SPSBIC 2017

4 - 5 May, Minna Nigeria

SCHOOL OF PHYSCIAL SCENCES
1ST BIENNIAL INTERNATIONAL CONFERENCE

PROCEEDINGS

Theme:
Science Technology and Innovation (STI):
The Vision for Poverty Reduction and Sustainable Development

FEDERAL UNIVERSITY OF TECHNOLOGY
MINNA, NIGER STATE, NIGERIA

PREFACE

This is the first international Conference organized by the school of Physical Sciences of the Federal University of Technology, Minna Nigeria the school is relatively new and consisting of the Departments of Physics, Chemistry, Mathematics, Statistics, Geology and Geography. It was exercised from the former school of Natural and Applied Sciences on the 6th of November 2014.

The school of Physical Sciences 1st Biennial International Conference is an interdisciplinary forum for the presentation of new ideas, recent developments and research findings in the field of Science and Technology. The Conference provides a platform to scholars, researchers in the academics and other establishments to meet, share and discuss how science and technology can help reduce poverty and bring about sustainable development. Submissions were received both nationally and internationally and severally reviewed by our international program committee. All contributions are neither published elsewhere nor submitted for publication as asserted by contributor.

We wish to express our gratitude to the school for challenging us to organize the first international conference. Special thanks to the Dean of the School Prof. A. S. Abubakar. Special thanks to all members of the organizing committee and sub-committee for their dedication, determination and sacrifice towards achieving a fruitful and successful conference.

The Local Organizing Committee Chairman
Kasim Uthman Isah (PhD).

Theme:

Science Technology and Innovation (STI): The Vision for Poverty Reduction and Sustainable Development

Sub-Themes

Scientific Research, Innovation and Entrepreneurship for Sustainable Development.

Scientific Research and Technological Development as tool for Poverty Reduction.

Scientific Research for Renewable Energy in Sustainable Energy Development.

Material Science, Nanoscience and Emerging Technologies in Sustainable Development.

Gender Issues in Quality Scientific Research Innovation and Sustainable Development.

CONTENT

INTERNATIONAL PLANNING COMMITTEE

Chemistry			
Prof. F. A. Adekola (PhD Analytical Chemistry) Department of Chemistry University of Ilorin, Nigeria Email: fadekola@hotmail.com	Prof. J. N. Egila (Analytical/Environmental Chemistry) Department of Chemistry University of Jos, Nigeria	Prof. Dagne Ermias (Natural Product Chemistry) African Laboratory of Natural Products, Department of Chemistry University (Art Kilo), Ethiopia Email: edagne@gmail.com	Dr. Hasmerya Maroof Computational Chemistry/Chemometrics, Department of Chemistry, University Teknologi Malaysia Email: hasmerya@kimia.fs.utm.my
Prof. Mohamed Noor Hasan Chemoinformatics/Chemometrics, Department of Chemistry, University Teknologi Malaysia Email: mnoor@utm.my, mnoor@yahoo.com	Dr. Nor Kartini Abu Bakar, Department of Chemistry, Faculty of Science, University of Malaya, Malaysia Email: kartini@um.edu.my	Dr. J. O. Jacob, Department of Chemistry, School of Physical Sciences, Federal University of Technology, Minna, Nigeria Email: john.jacob@futminna.edu.ng	Dr. Abdullahi Mann, Department of Chemistry, School of Physical Sciences, Federal University of Technology, Minna, Nigeria Email: abdumann@yahoo.com
Dr Hairul Anuar Tajuddin, Dept. of Chemistry, University of Malaya, Malaysia hairul@um.edu.my **hairultajuddin@gmail.com**			
Geography			
Prof. N.G. Nsofor Department of Geography Federal University of Technology Minna, Nigeria. Email: nsoforng50@yahoo.com	Prof. Haruna Kuje Ayuba Department of Geography Nasarawa State University, Keffi PMB 1022Keffi, Nigeria. Email: hkayuba@yahoo.com	Prof. S. M. Hassan Department of Geography and Environmental Management University of Abuja, Nigeria. Email; shuaibhassan123@gmail.com	Prof. A. I. Tanko Department of Geography Bayero University Kano, Nigeria Email; aitanko.geog@buk.edu.ng
Dr. Paul Tengbe Department of Geography Furra Bay College, University of Sierra Leone, Freetown Email; dr.paultengbe@yahoo.com	Prof. Alessandra Giannini International institute of Climate and Society (IRI) The Earth Institute University of Colorado, USA Email; Alesall@iri.columbia.edu		

Mathematics			
Dr. Farhad Ali Fluid Dynamics, Heat and Mass Transfer, Department of Mathematics. City University of Science and Information Technology, Pashewar, Pakistan Email: farhadali@cusit.edu.pk	Prof. Frank Sottile, Department of Mathematics, Texas A and M University, College Station, TX 77843, USA Email: sottile@math.tamu.edu	Prof. Oluwole D. Makinde, Applied Mathematics Department, University of the North, South Africa Email: dmakinde@yahoo.com makinded@sun.ac.za	Dr. Patrick Oseleka EZEPUE Director of Research Innovation and Creativity, Hallam University, SheffieldS1 1WB, UK Email: p.ezepue@shu.ac.uk
Dr. O. A. Ajala Department of pure and Applied Mathematics Ladoke Akintola University of Technology, Ogbomoso, Nigeria. E-mail**:** oaajala@lautech.edu.ng	Dr. A. J. Omowaye Department of Mathematics Federal University of Technology, Akure Nigeria E-mail: ajomowaye@futa.edu.ng omowaye_2004@yahoo.co.uk	Dr. Amos Popoola Department of Mathematics Osun State University, Osogbo, Nigeria E-mail: amos.popoola@uniosun.edu.ng	Prof. R. B. Adeniyi Numerical Analysis Department of Mathematics, University of Ilorin, Nigeria Email: raphade@unilorin.edu.ng
Materials Science/Nanoscience			
Professor Arunachala Kannan, Ira A. Fulton Schools of Engineering, The Polytechnic School PRLTA 335A, 7171 E Sonoran Arroyo Mall Arizona State University Mesa, AZ 85212; Email: amk@asu.edu	Dr. S. Ambali Department of Chemical Engineering, Federal University of Technology, Minna, Nigeria. Email: kasaka2003@futminna.edu.ng	Prof. A. S. Afolabi Department of Chemical and Metallurgical Engineering, Botswana University of Science and Tecgnology, Bostwana. Email: afolabi@biust.ac.bw	Dr, Nafarizal Bin Nayan, (nanoscience/nanotechnology and electronics) Email: nafa@uthm.edu.my Shamsuddin Research Centre, Office for Research, Innovation, Commercialization and Consultation, Universiti Tun Hussein Onn Malaysia
Prof. M. Aibinu, Department of Mechatronics, Federal University of Technology, Minna, Nigeria. Email: maibinu@gmail.com	Dr. Olayemi, Dept of Biology, F. U.T., Minna Email: isreal.olayemi@futminna.edu.ng	Dr. Mohammed Saidu Dept. Civil Engineering Department of Mechatronics, Federal University of Technology, Minna, Nigeria Email: mohammed_saidu@futminna.edu.ng	
Physics			
Prof. Fabian Ezema Department of Physics,	Dr. Mayeen Uddin Kahandaker, Department of Physics,	Prof. A. O. Musa, Department of Physics, Bayero University, Kano, Nigeria	Prof. K. J. Oyewumi, Department of Physics, University of Ilorin, Nigeria Email:

Federal University of Technology, Minna, Nigeria	University f Malaya, 50603, Kuala Lumpur, Email: mu_khandaker@um.edu.my	Email: aomusa2011@gmail.com	kjoyewumi@unilorin.edu.ng
Dr. Muhammad Arif in Agam Department of Physics, Universiti Tun Hussian Oon Malaysia Malaysia, Email: arif@uthm.edu.my	Dr. Oluwafemi Stephen Ojambati Department of Science and Technology, University of Twente, 7500 AE Enschede, The Netherlands Email: o.s.ojambati@utwente.ni	Dr. Zaidi Bin Embong, Department of Physics, Universiti Tun Hussian Oon Malaysia Malaysia Email: zembong@gmail.com	Dr. Umaru Ahmadu, Department of Physics, Federal University of Technology, Minna, Nigeria Email: u.ahmadu@yahoo.com
Prof. E. E Udensi, Department of Physics, Federal University of Technology, Minna, Nigeria Email: eeudensi@yahoo.com	Dr. Nasir Naeem Department of Physics, University of Abuja, Abuja, Nigeria. Email: nassnaeem@gmail.com	Prof. O. D Oyedum Department of Physics, Federal University of Technology, Minna, Nigeria Email: oyedidavid@futminna.edu.ng	Dr. Matthew T. Kolo Department of Physics, Federal University of Technology, Minna, Nigeria Email: mat_479@yahoo.com
Dr. Adetona Abbass Geophysics Department of Physics, Federal University of Technology, Minna, Nigeria Email: **tonabass@gmail.com**	Prof. SADIQ Umar, Nuclear Physics Department of Physics, Ahmadu Bello University, Zaria, Nigeria Email: sadiqumarx@yahoo.co.uk	Prof. V. Chukwuma, Atmospheric Physics Department of Physics, University of Ilorin, Nigeria Email: victorchukwuma@yahoo.com	Dr. Ibrahim Aku Department of Physics, Federal University of Technology, Minna, Nigeria ibrahimaku@futminna.edu.ng
Statistics			
Prof. Benjamin Agboola Oyejola Professor of Statistics (Biometry, Applied Statistics, Experimental Design and Econometrics) Department of Statistics University of Ilorin, Ilorin, Nigeria. **Email: boyejola@unilorin.edu.ng**	Prof. E.O. Asiribo Professor of Statistics (Biostatistics, Experimental Design and Time Series) Department of Statistics Federal University of Agriculture Abeokuta, Nigeria Email: asiribo@yahoo.com	Prof. Shehu Usman Gulumbe Professor of Statistics (Multivariate Statistics and Repeated Measures) Department of Mathematics Federal University Birin Kebbi Kebbi State, Nigeria. Email: shehu.gulumbe@fubk.edu.ng,	Dr. I. U. Shittu Associate Professor of Statistics (Time Series, Probability and Stochastic processes) Department of Statistics, Federal University of Technology, Minna, Nigeria. Email: shittu.olanrewaju@gmail.com, oi.shittu@ui.edu.ng

and boyejola2003@yahoo.com			
Dr. A. Isah Associate Professor of Statistics (Spatial Statistics, Probability theory, and Sample Survey) Department of Statistics, Federal University of Technology, Minna, Nigeria. Email: aish@futminna.edu.ng	Dr. Alexander Hapfelmeier *Ph.D.* Institut Fur Medizinsche Statistik UndEpidemiologe Technical University of Munich Klinikum rechts derIsar Ismaninger Str. 22. Email: alexander.hapfelmeier@tum.de.		
Geology			
Dr. U. S. Onoduku, Department of Geology, Federal University of Technology, Minna, Nigeria, **onoduku.usman@futminna.edu**	Prof. Wan Hasia Abdullahi, Department of Geology, University of Malaysia, Malaysia, wanhasia@um.edu.my	3. Dr. Idris-Nda Abdullahi, Department of Geology, Federal University of Technology, Minna, Nigeria, 08036273815, idrisnda@futminna.edu.ng	Prof. Okosun Edward Agboneni, Department of Geology, Federal University of Technology, Minna, Nigeria, eaokosun@yahoo.com
Dr. Waziri M. N., Department of Geology, Federal University of Technology, Minna, Nigeria **nuhuwaziri@futminna.edu.ng**	Dr. Che Vivian, Department of Geology, University of Buea, Cameroon, +237675030802, chevivian@gmail.com	Dr. Agyingi Christopher, PhD (Associate Professor of Sedimentology and Petroleum Geology) Department of Geology, University of Buea, Cameroon Tel: +237677875030 Email: agyingi@ubuea.cm and cm_agyingi@yahoo.co.uk	Cheo Emmanuel Suh, PhD (Professor of Economic Geology and Microtectonics) Department of Geology, University of Buea, Cameroon Tel: +237677292940 Email: chuhma@yahoo.com
Dr. Isah Goro Aliyu, Department of Geology, Federal University of Technology, Minna, Nigeria, isahgoro@futminna.edu.ng	Dr. Ako Thomas Agbor, Department of Geology, Federal University of Technology, Minna, Nigeria akoagbor@futminna.edu.ng		

LOCAL ORGANISING COMMITTEE

Dr. Kasim Uthman Isah (**Chairman)**

Dr. Abubakar Usman (**Secretary)**

Dr. Shehu Usman Onodoku

Dr. Mairo Muhammed

Dr. Umaru Mohammed

Mr. Elijah Yanda Shaba

TECHNICAL COMMITTEE

Dr. Adamu Alhaji Mohammed (**Chairman)**

Dr. T. A. Ako

Dr. T. O. Jimoh

Mr. Bello Adeshina

Mr. Salihu Saidu

Miss. Eichie Julia Ofure (**Secretary)**

LOGISTICS COMMITTEE

U. S. Onoduku (**Chairman)**
Dr. A. A. Rafiu
Dr. Samshideen Ajoye
Dr. J. O Jacob
Dr. (Mrs) S. H. Waziri
Dr. U. Mohammed
Mr. I. S. Onotu
Mr. S. E Abdulkabir (**Secretary)**

KEYNOTE SPEAKERS

Prof. Kenneth Ozoemena

Prof. Kenneth Ozoemena obtained his PhD degree in Chemistry in 2003 at Rhodes University, after which he completed postgraduate qualifications in Management Development (MDP), as well as in Higher Education (PGCHE) at the University of Pretoria. He is an Extraordinary Professor at the University of the Western Cape and was a Principal Researcher and Research Group Leader of the Electrochemical Energy Technologies at the CSIR Materials Science and Manufacturing Division. He recently joined School of Chemistry of the University of the Witwatersrand as Professor of Materials for Energy & Electrochemistry,

His research is highly interdisciplinary, spanning several areas of Materials Science and Electrochemistry. By February 2014, he had published 125 articles in leading scientific journals (such as *ChemComm*, *J Mater Chem*, *Energy Environ Sci*, *PCCP, ACS Appl Mater Interfaces, Langmuir, Electrochem Commun*, and *Electrochim Acta*) as well as six book chapters. He has been cited 2 674 times and holds an H-index of 30 and i10-index of 74. Ozoemena is listed amongst the world's top 1% of chemists by the Thomson Reuters' Web of Knowledge. He is a Fellow of the Royal Society of Chemistry (FRSC) (UK) and a Chartered Chemist (CChem) of the Royal Society of Chemistry (UK). He is a member of the editorial board of several scientific journals, (including *Electrochemistry Communications*), as well as Associate Editor of *Materials Focus*, and served as Guest Editor of *Electrochemical Acta* and *Journal of Porphyrins and Phthalocyanine*s.

Professor Cheo, Emmanuel Suh

Professor Cheo, Emmanuel Suh was born on the first of July, 1969 in Mankanikong in the North West Region of Cameroon. He attended Obafemi Awolowo University, Ile Ife, Nigeria from 1987 – 1990 were he obtained a Bachelor of Science (B.Sc) first class degree in Geology. He also obtained a Master of Science (M.Sc) degree from the same University in 1992. Prof. Cheo Emmanuel Suh obtained his PhD degree in Applied Geology in 1997 at Abubakar Tafawa University, Buachi, Nigeria in collaboration with Technical University of Berlin, Germany. He also had post-doctoral fellowships in the following institutions:

1. 2001 – Royal Society at the University of Bristol, UK
2. 2002 – Alexander Von Humboldt Foundation, Technical University of Clausthal, Germany
3. 2004 – Smithsonian Institution, Museum of National History, Mineral Science Department, Washington DC, USA.

He has consulted as an economic geologist for gold, iron ore and uranium deposits for Legend Mining, Australia, African Aura Resources, UK, Cameroon Mining Company and Cameroon Mining Action. He attended the Mining Indaba in Cape Town in February, 2012 where the Iron Resources in Cameroon and Central African sub-region were discussed. In August of the same year, he also participated in a training workshop on Sustainable Mining in Africa at Brisbane, Australia. He has won many grants, attended many conferences and published many articles in both local and international journals. He is a scientific member of so many geological associations.

COMPARATIVE ANALYSIS OF BASIC MODELS AND ARTIFICIAL NEURAL NETWORK BASED MODEL FOR PATH LOSS PREDICTION

Eichie, Julia Ofure[1*], Oyedum, Onyedi David[2], Ajewole, Moses Oludare[3] and Aibinu, Abiodun Musa[4]
[1,2]. Department of Physics, Federal University of Technology, Minna, Nigeria
[3]. Department of Physics, Federal University of Technology, Akure, Nigeria
[4]. Department of Mechatronics Engineering, Federal University of Technology, Minna, Nigeria
[1] juliaeichie@futminna.edu.ng,
[2] onyedidavid@futminna.edu.ng
[3] oludare.ajewole@futa.edu.ng
[4] abiodun.aibinu@futminna.edu.ng
* Corresponding author

Abstract

Propagation path loss models are useful for the prediction of received signal strength at a given distance from the transmitter, estimation of radio coverage areas of Base Transceiver Stations (BTS), frequency assignments, interference analysis, handover optimisation, and power level adjustment. Due to the differences in environmental structures, local terrain profiles and weather conditions, path loss prediction model for a given environment using any of the existing empirical models such as the Okumura-Hata's model has been shown to differ from the optimal model. In this paper, propagation parameters such as distance between transmitting and receiving antenna, transmitting power and terrain elevation, using sea level as reference point, were used as inputs to Artificial Neural Network (ANN) for the development of an ANN based path loss model. Data were acquired in a drive test through selected rural and suburban routes in Minna and environs. Multilayer perceptron (MLP) network parameters were varied during the performance evaluation process of developing the models. The weight and bias values and the architecture of the best performed MLP network were used in the development of the ANN based path loss model equations for rural and suburban routes. Amongst the considered basic empirical models, Hata model showed best performance on the rural routes with RMSE ranging from 5.05 to 9.30 dB but over predicted path loss on suburban routes with RMSE ranging from 19.50 to 82.14 dB. For the suburban routes, Egli model had the best performance with RMSE ranging from 3.81 to 8.18 dB. COST231 and Ericson models over predicted path loss for both rural and suburban routes. The developed ANN based path loss model performed better than the considered basic empirical path loss models with RMSE ranging from 3.96 to 7.07 on rural routes and 1.22 to 4.82 on suburban routes. Comparison of the ANN model-predicted path loss values with the basic empirical path loss models showed that the developed model has an acceptable accuracy.

Key words: Artificial Neural Network; path loss model: transmitting power

1.0 Introduction

Mobile telecommunications has rapidly become the most popular method of voice communication in Nigeria, since the inception of the Global System for Mobile Communication (GSM) in the country in August 2001 (NCC, 2015). The GSM service has spread from urban to suburban and rural areas of the country. However, like other wireless communication systems, GSM depends on the propagation of radio waves within the troposphere, the region of the atmosphere extending from the Earth's surface up to an altitude of about 16 km at the equator or 8 km at the poles (Reddy, 1987). Within the troposphere, the height of human-made structure and natural terrain elevation varies.

Based on human-made structures and natural terrain, land area can be classified into three major classes: urban, suburban and rural areas. These areas differ in type of buildings, density of buildings, presence of trees, foliage cover and other human-made structures. Rural areas are settlements outside towns and cities characterised by sparsely distributed buildings. These areas have less human-made structures and may have many trees and foliage cover. Suburban areas have more buildings and structures than rural areas, but less of trees and foliage cover. The heights of buildings in these areas are greater than that found in rural areas. Urban areas have dense human-made structures. Most of the buildings are tall and have reflecting walls. These areas have sparsely distributed trees and foliage cover when compared with rural and suburban areas.

The transmission path between a transmitter and a mobile receiver differs in the different areas (urban, suburban and rural areas) and varies from simple line-of-sight path to a path with obstructions such as hills, trees, buildings

and other human-made structures. The electric field strength of signals radiated from a transmitter is subject to propagation loss due to reflection, refraction, diffraction, absorption and scattering. Hills, buildings and other human-made obstacles often diffract, absorb or reflect radio waves. Weak received signal and path loss due to the reduction of power density of an electromagnetic wave, as it passes through multi-path propagation environment, is of great concern in mobile communication. Propagation path loss models are useful for prediction of received signal strength at a given distance from the transmitter, estimation of radio coverage areas of Base Transceiver Stations (BTS), frequency assignments, interference analysis, handover optimisation, and power level adjustment (Isabona *et al*., 2013).

Due to the differences in environmental structures, local terrain profiles and weather conditions, the signal strength and path loss prediction model for a given environment using any of the existing empirical models such as the Okumura-Hata's model has been shown to differ from the optimal model (Ekpenyong *et al*., 2010; Faruk *et al*., 2013; Nwalozie *et al*., 2014; Bakinde *et al*., 2012). Hence the need for a study that will investigates the effects of environmental conditions on mobile wireless signals with a view to determining the propagation characteristics required for the design of propagation path loss model that will aid optimal planning of mobile wireless communication networks in Minna and environs. Artificial Neural Network (ANN), one of the artificial intelligence techniques, has proven to be effective in the development of models for solving prediction problems.

ANN is flexible and has the capability to learn the underlying relationships between the inputs and outputs of a process, without needing the explicit knowledge of how these variables are related (Deligiorgi *et al*., 2013). It can therefore be useful in the development of path loss models.

The rest of this paper is organized as follows: Section 2 presents literature review while section 3 presents methodology for data acquisition and model development. Results and discussion is presented in section 4 while conclusion is in section 5.

2.0 Literature Review

This section has two sub-sections. Subsection 2.1, presents review of related research works from literature while Subsection 2.2 gives a brief overview of path loss model.

2.1 Related Research Works

Usman *et al.* (2015) investigated wireless mobile communication signal strength variation with weather and environmental factor in Bauchi. The research revealed variation of signal strength in different locations but similar values were obtained at different times in the same location. In the study of Sharma and Singh (2010), involving measurements on received power strength in urban, suburban and rural regions in Narnaul City, India, it was observed that path loss is less in the rural areas than in sub urban and urban areas.

Ayekomilogbon *et al.* (2013) study on signal degradation as a function of leaf density, revealed seasonal variability in the effect of tress on radio waves due to variation in the electrical constants (conductivity and permittivity) of the trees. Similarly, Nwawelu *et al.* (2012) revealed that trees and buildings have significant effect on the received power level of wireless mobile network.

Ogbulezie *et al.* (2013a) and Ogbulezie *et al.* (2013b) investigated the suitability of two basic propagation models for GSM 900 and 1800 MHz respectively for Port Harcourt and Enugu cities, and for Abuja, Kaduna and Kano cities in Nigeria. Measurements taken in cities were compared against predictions made by the Okumura Hata and COST-231 Hata models, and the classical models were observed to overestimate the path loss in all the cities. Similarly, Chebil *et al.* (2011) investigated path loss models for mobile communications in Malaysia. The results

revealed that SUI and COST-231 models over predicted the path loss while log-normal shadowing and lee models were in close agreement with the measured path loss.

Armoogum *et al.* (2010) carried out a comparative analysis of path loss for 3G networks for urban and rural regions of Mauritius Island, India. The research revealed that path loss is not constant at various locations for a constant distance around the respective Base Transceiver Station (BTS) due to the effect of terrain. Benmus *et al*. (2016) developed an empirical model, using ANN approach, for the prediction of propagation path loss at 900MHz, 1800 MHz and 2100 MHz in Tripoli, Libya. Results revealed that the ANN path loss model had acceptable agreement with the target path loss with MSE values ranging from 3.7 to 6.7.

2.2 Path Loss Model

Path loss is the reduction in power density of an electromagnetic wave as it propagates through a medium. Path loss for each measurement location is given by Seybold (2005) and Rappaport (2002) as:

$$PL_m(dB) = EIRP\ (dBm) - P_r(dBm) \quad (1)$$

where;

$EIRP_t$ = Effective Isotropic Radiated Power

P_r = received signal level

$$EIRP_t = P_{BTS} + G_{BTS} + G_{MS} - L_{FC} - L_{AB} + L_{CF} \quad (2)$$

The computation of path loss for all routes:

$$PL_m(dB) = P_{BTS} + G_{BTS} + G_{MS} - L_{FC} - L_{AB} + L_{CF} - P_r \quad (3)$$

where;

P_r = received signal level

P_{BTS} = transmitter power (dBm)

G_{BTS} = transmitting antenna gain (dBi)

G_{MS} = receiving antenna gain (dBi)

L_{AB} = antenna body loss (dB)

L_{FC} = feeder cable loss (dB)

L_{CF} = combiner and filter loss (dB)

A path loss model is a set of mathematical expressions and algorithms used for the characterisation of attenuation (reduction in power density) of an electromagnetic wave as a function of frequency, distance and other conditions in a given environment. The existing path loss models can be categorised into two, namely empirical models and theoretical models.

(a) Empirical Model: This model is based on observations and measurements. This model takes into account all environmental influences, but its accuracy depends on the similarities between the environment to be analysed and the environment used in the development of the model (Ajose and Imoize, 2013).

(b) Theoretical Model: This model deals with the fundamental principles of radio wave propagation. It utilises the governing laws of wave propagation to determine the received signal level at a particular location. They can be applied to different environments without altering the accuracy but they are usually very complex and lack computational efficiency (Benmus *et al*., 2016).

Since this research is based on observations and measurements, empirical models will be considered and some of the most frequently used basic empirical path loss model equations (Rappaport, 2002; Sharma and Singh, 2010; *Saunders* and Aragón-Zavala (2007; Ajose and Imoize, 2013; Chebil *et al*., 2011) are as follows:

(1) COST-231 Hata model

$$PL_{COST231} = 46.3 + 33.9log_{10}(f) - 13.82log_{10}(h_b) - a(h_m) + \{44.9 - 6.55log_{10}(h_b)\}log_{10}(d) + C_M \quad (4)$$

where $a(h_m) = (1.1log_{10}(f) - 0.7)h_m - (1.56log_{10}(f) - 0.8)$ and $C_M = 0$ dB

(2) Hata Model

$$PL(suburban)_{Hata} = 69.55 + 26.16log_{10}(f) - 13.82log_{10}(h_b) + \{44.9 - 6.55log_{10}(h_b)\}\, log_{10}(d) - 2[log_{10}(f/28)]^2 + 5.4 \quad (5)$$

$$PL(Rural)_{Hata} = 69.55 + 26.16log_{10}(f) - 13.82log_{10}(h_b) + \{44.9 - 6.55log_{10}(h_b)\}\, log_{10}(d) - 4.78(log_{10}(f)^2 + 18.33(log_{10}(f) + K \quad (6)$$

where k = 35.94

(3) Egli Model

$$PL_{Egli} = 20log_{10}f + 40\, log_{10}d - 20log_{10}h_b + 76.3 - 10log_{10}h_m \quad (7)$$

(4) Ericsson Model

$$PL_{Ericsom} \; a_0 + a_1log_{10}(d) + a_2log_{10}(h_b) + a_3log_{10}(h_b)log_{10}(d) - 3.2\big(log_{10}(11.75h_r)\big)^2 g(f) \quad (8)$$

where $g(f) = 44.49log_{10}(f) - 4.78\big(log_{10}(f)\big)^2$, a_0, a_1, a_2 *and* a_3 are constants given in Table 5 (Milanovic *et al*., 2010).

Table 5: Values of Constants in Ericsson Model

Environment	a_0	a_1	a_2	a_3
Suburban	43.20	68.93	12.0	0.1
Rural	45.95	100.6	12.0	0.1

3.0 Methodology

This section presents method of data acquisition and model development.

3.1 Data Acquisition

The measurement setup for data acquisition consists of a laptop equipped with Ericsson TEMS 9.1.4 drive test software, TEMS handsets and a Global Positioning System (GPS) receiver housed in a vehicle as shown in Figure 1.

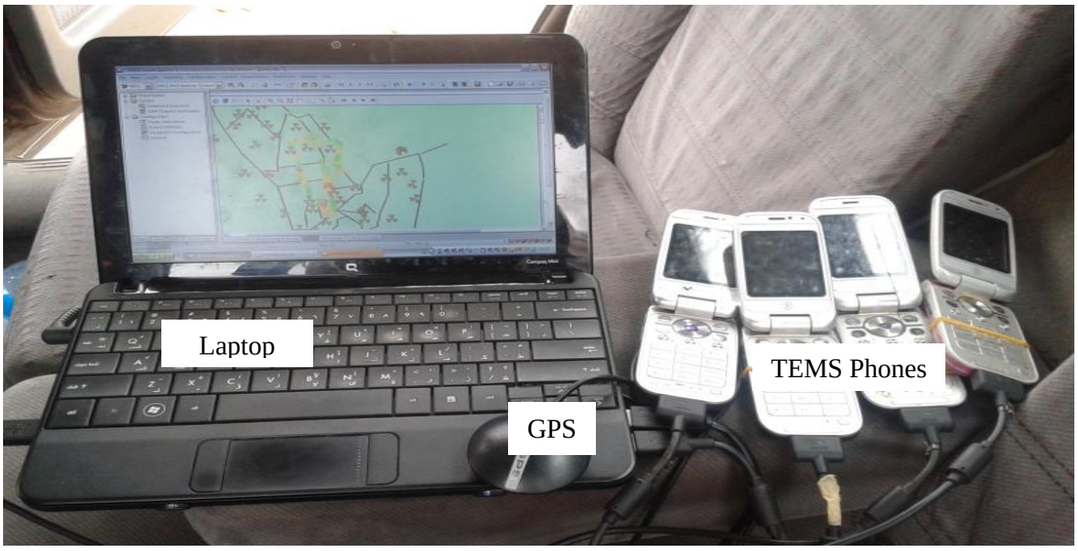

Figure 1: Drive Test Tools Housed in a Vehicle

Two TEMS mobile phones, one for each of the 2 selected wireless mobile communication networks (A and B) and a GPS, all connected to a laptop equipped with Ericsson TEMS 9.1.4 drive test software, and housed in a vehicle, were used for drive testing on some selected routes. The mobile phones were positioned at about 1 m distance from the earth surface. The RxLevels of the 2 Networks were measured in the drive test exercise in: the month of April (late dry season); the month of July (early wet season); and the month of October (late wet season) in Niger State. After each drive test exercise, the log files were replayed in TEMS investigation application software. In the replay process, the BTS serving each measurement points were displayed as shown in Figure 2.

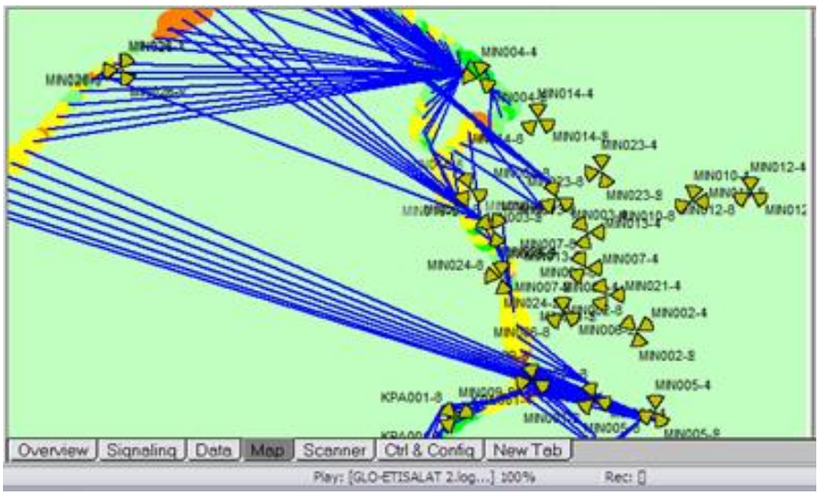

Figure 2: Screen Shot of Measurement Points and Serving BTS

Some BTS close to straight or nearly straight rural or suburban routes and serving measurement points without interference from neighbouring cells were selected and used as reference points for measurements. Figure 3 shows one of the selected BTS and the measurement points.

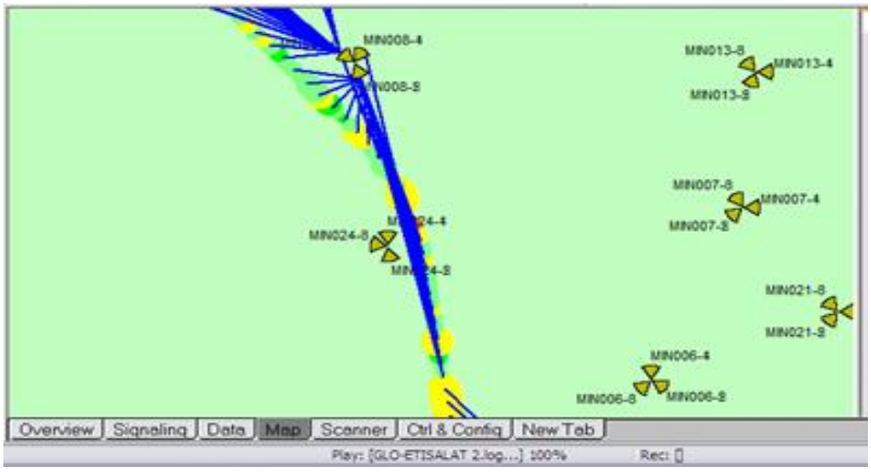

Figure 3: Screen Shot of a Selected BTS (MIN008) Serving Measurement Points

A total of 20 BTS were selected and used in this study. The geographical coordinates of the selected BTS were obtained and used to mark the BTSs locations on Google Earth application software as shown in Figure 4. The elevation above sea level of the marked locations (measurement points) corresponding to each BTS was determined. Each route had 2 reference BTS, 1 for each network. Based on population density, building density, building type and separation between buildings, measurement routes were classified as suburban and rural routes. The routes along which measurements were taken are:

- Rural Routes
  - Along Minna-Zungeru road, Beji
  - Along Minna-Bida road, Gidan Kwanu
- Suburban Routes
  - Along Minna-Bida road, Kpakungu
  - Along Western Bypass road, Dutsen Kura
  - Along Western Bypass road, Gbaiko
  - Along Bahagu Bypass road, Ugwandagi
  - Along Minna-Zungeru road, Tunga
  - Along Minna-Suleja road, Tunga
  - Along Kuta road, Maitumbi
  - Along Minna-Zungeru road, Tudun Fulani

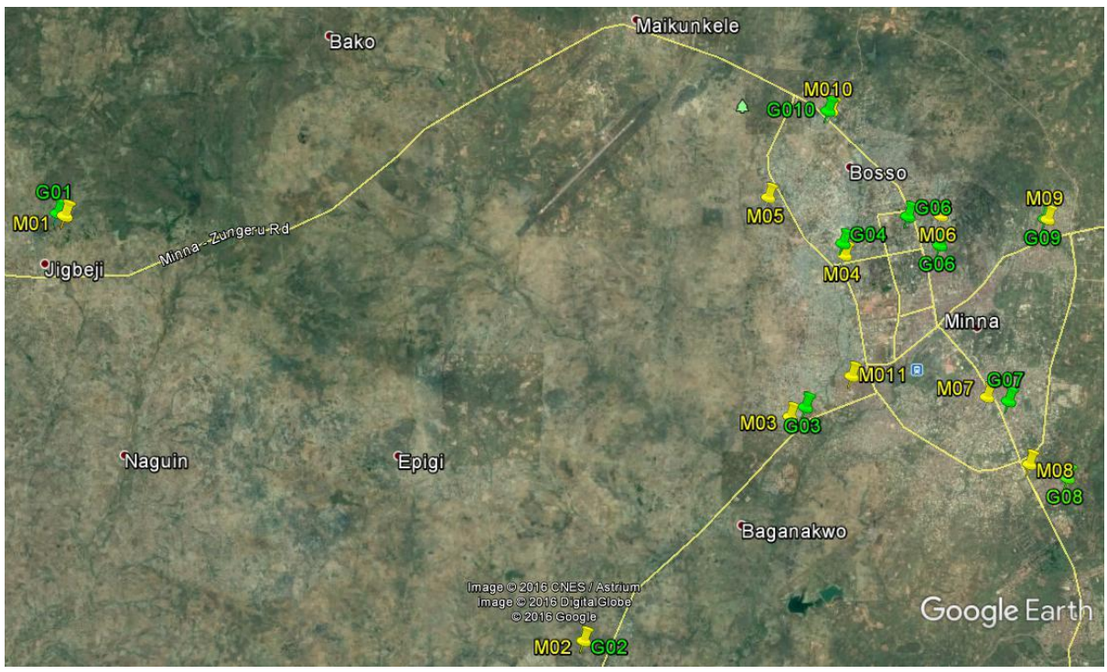

Figure 4: Reference BTS Points of Location (Google Earth, 2016)

Table 1 gives description of the measurement routes and Table 2 gives some details about the respective reference BTS.

Table 1 Description of Measurement Routes

Area	Route	Description
Rural	Beji (along Minna-Zungeru road)	Tarred road with scanty bungalow buildings and much vegetation/farm lands
	Gidan Kwanu (along Minna-Bida road)	Tarred road with scanty bungalow buildings and much vegetation/farm lands
Suburban	Kpakungu (along Minna-Bida road)	Tarred road with bungalow buildings and few vegetation

	Dutsen Kura (along Western Bypass road)	Tarred road with dense bungalow buildings and few vegetation
	Gbaiko (along Western Bypass road)	Tarred road with bungalow buildings and few vegetation on both sides of the road
	Ugwandagi (along Bahagu Bypass road)	Tarred road. Area is populated with bungalow buildings on one side of the road, and hills on the other side of road
	Tunga (along Minna-Zungeru road)	Tarred road and area is densely populated with bungalow buildings and few storey buildings
	Tunga (along Minna-Suleja road)	Tarred road and area is densely populated with bungalow buildings and few storey buildings
	Maitumbi (along Kuta road)	Tarred road and area is densely populated with bungalow buildings and few hills
	Tudun Fulani (along Minna-Zungeru road)	Tarred road with bungalow buildings and few vegetation

Table 2 Description of Reference BTS

Route	Reference BTS	Cell Name	Coordinates	Area	Transmitting Antenna Height (h_b)
1	M01	NI1554C	LatN0938.2166 LongE00620.1000	Beji	37
	G01	KON801	LatN0938.2961 LongE00619.9632	Beji	40
2	M02	NI0010E	LatN0932.1767 LongE00627.6300	Gidan Kwanu	37
	G02	FUM001	LatN0932.1744 LongE00627.6444	Gidan Kwanu	40
3	M03	NI4015E	LatN0935.3887 LongE00630.6457	Kpakungu	25
	G03	KPA001	LatN0935.5246 LongE00630.8694	Kpakungu	30
	M11	NI0064E	LatN0935.9698 LongE00631.5410	Kpakungu	25
4	M04	NI1585D	LatN0937.6958 LongE00631.4397	Dutsen Kura	30
	G04	MIN012	LatN0937.8692 LongE00631.4150	Dutsen Kura	33
5	M05	NI4030D	LatN0938.5267 LongE00630.3283	Gbaiko	30
6	M06	1424DB	LatN0938.2597 LongE00632.8373	Ugwandagi	25
	G06	MIN013	LatN0937.8402 LongE00632.8222	Ugwandagi	25
7	M07	NI4018E	LatN0935.6683 LongE00633.5083	Tunga	20
	G07	MIN005	LatN0935.6113 LongE00633.8217	Tunga	25
8	M08	NI0009E	LatN0934.7065 LongE00634.1400	Tunga	30
	G08	MIN015	LatN0934.5105 LongE00634.6790	Tunga	20
9	M09	NI0072E	LatN0938.2103 LongE00634.3901	Maitumbi	20
	G09	MIN010	LatN0938.2143 LongE00634.3576	Maitumbi	30
10	A10	1231DB	LatN0939.7681 LongE00631.2442	Tudun Fulani	35
	G10	MIN004	LatN0939.7637 LongE00631.1963	Tudun Fulani	35

The operating frequency, *f*, of each of the selected BTS was 1800 MHz and the receiving antenna height, h_m, on all routes was approximately 1 m. BTS transmitting power of 40 W was used during the drive test period. Using the TEMS drive test software, the RxLevel at distance intervals of 100 m from each BTS site, up till the cell coverage distance of the respective BTS, was determined for each of the 2 networks. Tables 3 and 4 shows sample of measurements on Beji route from Network A's BTS (M01) and Network B's BTS (G01).

Table 3 Sample of Measurements on Beji Route (Network A)

Distance (km)	Elevation Above Sea Level (m)	RxLevel (dBm)			
		April	July	October	Average
1.2	246	-79	-87	-81	-82
1.3	249	-80	-76	-76	-77
1.4	248	-84	-88	-93	-88
1.5	249	-67	-65	-83	-72
1.6	252	-68	-68	-81	-72
1.7	256	-65	-69	-93	-76
1.8	259	-74	-91	-94	-86
1.9	258	-80	-84	-97	-87
2.0	252	-86	-90	-102	-93
2.1	247	-86	-85	-104	-92
2.2	247	-90	-93	-91	-91
2.3	247	-93	-94	-107	-98
2.4	248	-98	-97	-107	-101
2.5	245	-99	-101	-99	-100
2.6	242	-99	-93	-98	-97
2.7	239	-95	-99	-95	-96
2.8	238	-90	-89	-88	-89
2.9	237	-94	-96	-100	-97
3.0	239	-98	-94	-88	-93
3.1	241	-95	-94	-94	-94
3.2	243	-92	-94	-89	-92
3.3	245	-88	-86	-89	-88
3.4	250	-90	-88	-89	-89
3.5	252	-86	-84	-81	-84
3.6	252	-90	-91	-87	-89
3.7	254	-92	-96	-89	-92
3.8	255	-90	-78	-88	-85
3.9	254	-88	-92	-92	-91

Table 4 Sample of Measurements on Beji Route (Network A)

Distance (km)	Elevation Above Sea Level (m)	RxLevel (dBm)			
		April	July	October	Average
1.4	250	-65	-71	-84	-73
1.5	250	-60	-63	-78	-67
1.6	251	-65	-65	-99	-76
1.7	250	-69	-68	-79	-72
1.8	253	-63	-65	-77	-68
1.9	259	-58	-57	-88	-68
2.0	263	-71	-79	-77	-76
2.1	260	-58	-60	-88	-69
2.2	254	-70	-77	-87	-78
2.3	248	-74	-80	-87	-80

2.4	249	-79	-78	-81	-79
2.5	248	-84	-79	-86	-83
2.6	247	-80	-83	-86	-83
2.7	244	-86	-85	-92	-88
2.8	242	-74	-78	-95	-82
2.9	242	-76	-78	-95	-83
3.0	241	-80	-78	-100	-86
3.1	240	-82	-78	-99	-86
3.2	240	-77	-72	-95	-81
3.3	241	-68	-69	-88	-75
3.4	243	-69	-73	-89	-77
3.5	245	-72	-66	-94	-77
3.6	247	-68	-73	-101	-81
3.7	249	-72	-75	-100	-82
3.8	252	-74	-73	-97	-81
3.9	255	-72	-70	-88	-77
4.0	255	-72	-76	-92	-80
4.1	254	-75	-78	-100	-84
4.2	252	-77	-78	-100	-85
4.3	248	-80	-84	-99	-88
4.4	247	-81	-79	-98	-86
4.5	246	-85	-87	-95	-89
4.6	250	-89	-88	-101	-93
4.7	253	-84	-80	-102	-89
4.8	254	-86	-89	-90	-88
4.9	256	-87	-90	-92	-90
5.0	258	-83	-83	-95	-87
5.1	259	-77	-81	-92	-83
5.2	260	-79	-82	-92	-84
5.3	262	-79	-78	-95	-84
5.4	263	-75	-76	-93	-81
5.5	265	-71	-74	-93	-79

3.2 Model Development

RxLevel variations in relation to elevation above sea level of measurement points were explored on all routes. The distance between each measurement point and their respective reference transmitting antenna, the height of the reference transmitting antenna and the elevation above sea level of measurement points were proposed as inputs in an MLP network used in the ANN design. The proposed MLP network consists of 3 nodes at the input layer, one hidden layer and 1 node at the output layer. The writing of the script files for the developed path loss models and the performance analysis to determine the weight and bias values, number of neurons and activation function type to be used in the optimal model equations was done using matlab.

A feedforward network topology and the default Matlab Neural Network Toolbox learning algorithm, Levenberg–Marquardt, were used. The number of neurons in the hidden layer was varied from 31 to 39 in incremental steps of 2. The most frequently used activation functions: logsig, purelin and tansig type of activation functions were used to create the 9 different pairs of activation functions used in the model development. Thus, each of the 5 different numbers of neurons was used with 9 different pairs of activation functions. Each run of the script file generates 45 networks. The script file was run 20 times and 20 runs generated 900 trained networks for performance evaluation. The flow diagram of the ANN script file is shown in Figure 5. A schematic of the proposed MLP network with variable neurons in the hidden layer is shown in Figure 6.

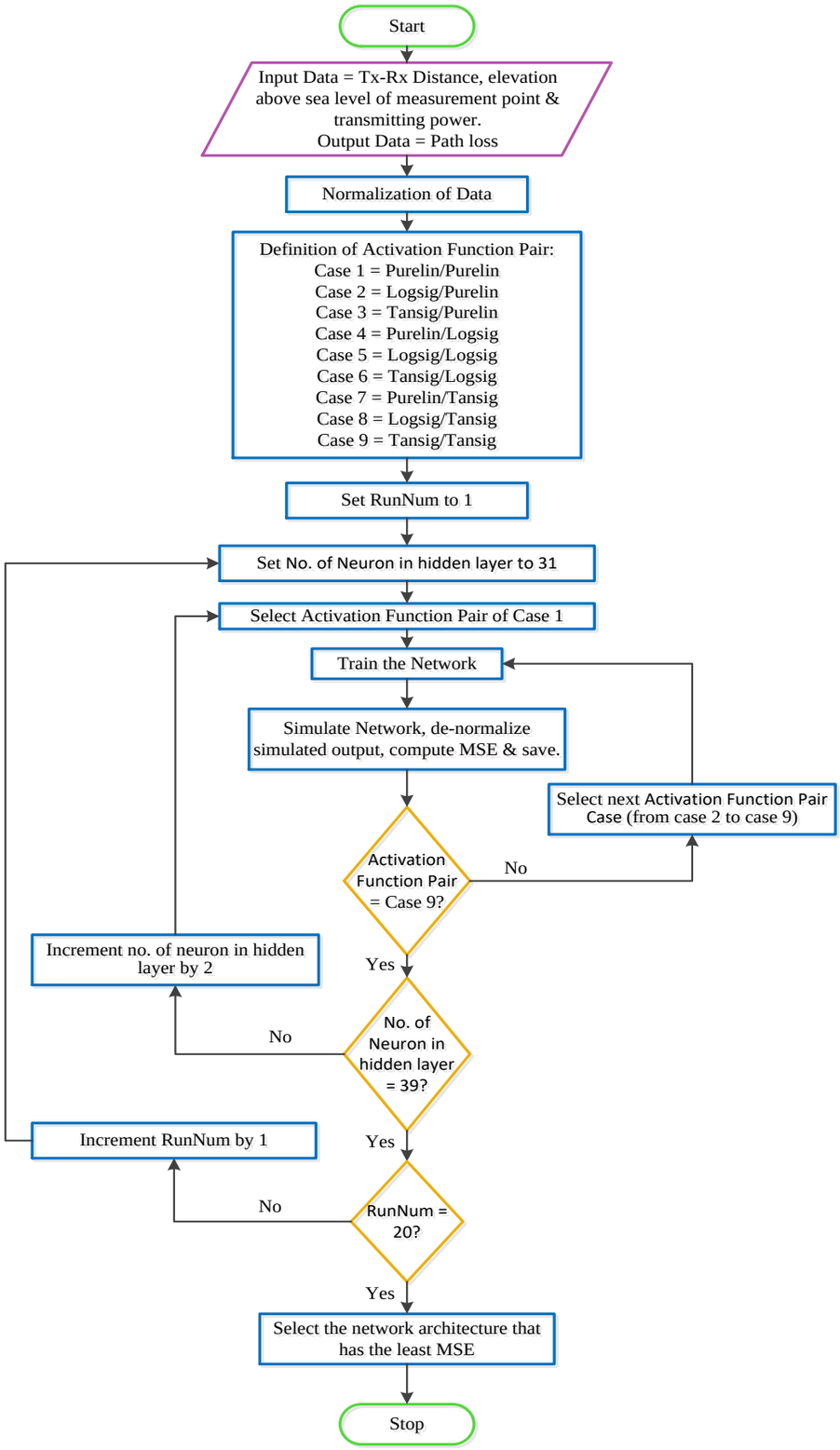

Figure 5: Flow Diagram of the ANN Script for Path loss Models

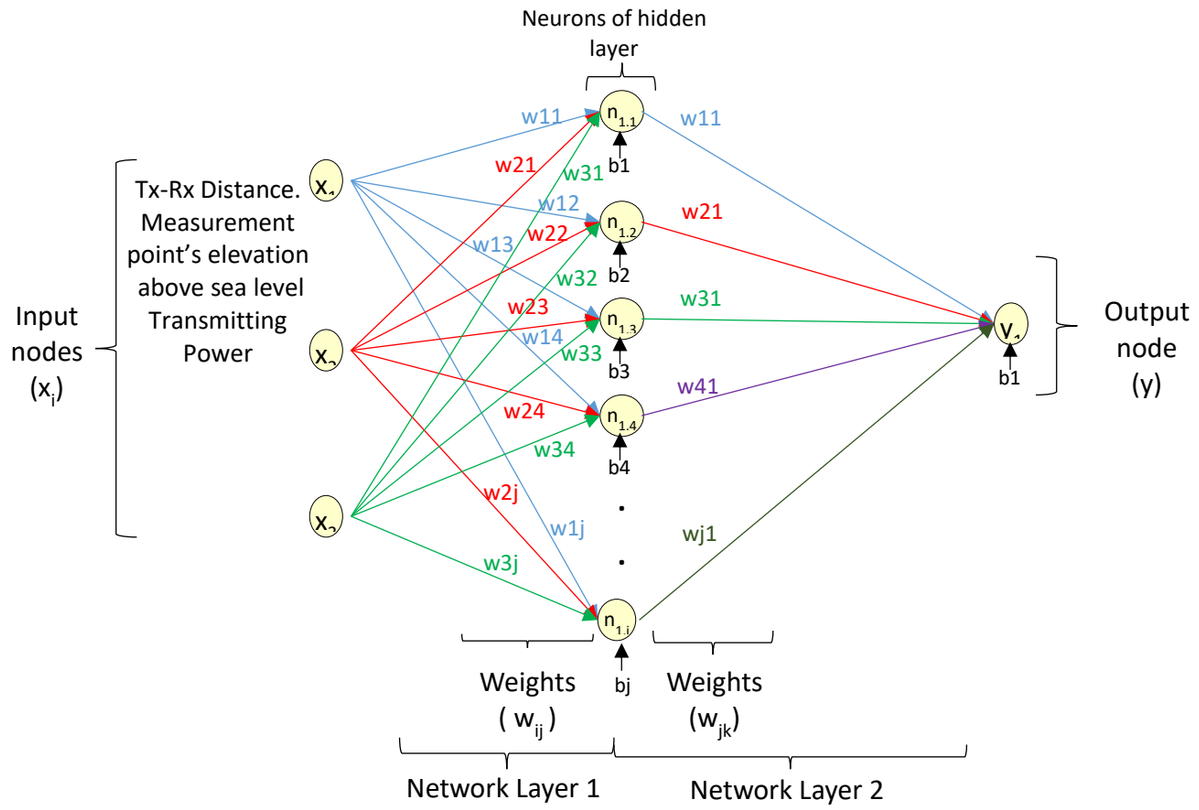

Figure 6: A 2 layered MLP Network for Path Loss Model

where x_i (where $1 \leq i \geq 3$) are the set of inputs; w_{ij} and w_{jk} are adjustable weight values: w_{ij} connects the i^{th} input to the j^{th} neuron in the hidden layer, w_{jk} connects the j^{th} output in the hidden layer to the k^{th} node in the output layer; y_k (where k = l) is the output. Each neuron and output node has associated adjustable bias values: b_j (where $j =$ number of neurons) is associated with the j^{th} neuron in network layer 1, b_k (where $k = 1$) is associated with the node in the network layer 2. Within each network layer are: the weights, w, the multiplication and summing operations, the bias, b, and the activation function, φ (Beale *et al*., 2011 and Aibinu *et al*, 2012). Mathematically, Figure 6 can be represented as Equation 9 (Eichie *et al*., 2016).

$$y = \varphi_2\left(\sum_{j=1}^{m} w_{jk}\varphi_1\left(\sum_{i=1}^{3} w_{ij}x_i + b_j\right) + b_k\right) \qquad (9)$$

where m is the total number of neurons in the hidden layer.

Two sets of input/output data were used separately with the ANN script file to develop 2 path loss model equations for rural route and suburban route. For the rural route path loss model, data from route 1 (76 samples) were used to train the network and for suburban route path loss model data from Network A on routes 3, 5, 7, 9 and 10, and data from Network B on routes 4, 6, 8 and 9 (total of 126 samples) were used while training the network. During the training process, the input and target output data were applied to the network and the network computed its output. The initial weight and bias values and their subsequent adjustments were done by the Matlab Neural Network Toolbox software. For each set of output in the output data, the error, e, (the difference between the target output, t, and the network's output, y,) was computed. Using Equation 10 MSE values were computed and used by the network performance function to optimize the network.

$$MSE = 1/N\left(\sum_{i=1}^{N}(t_i - y_i)^2\right) \qquad (10)$$

where N is the number of sets in the output data, t_i is the target output and y_i is the network's output. The weight and bias values were adjusted so as to minimize the MSE and thus increase the network performance. After the adjustments, the network underwent a retraining process, the MSE was recomputed and the weight and bias values

were readjusted. The retraining continued until the training data achieved the desired mapping that obtained minimum MSE value. The training and retraining processes were done for each of the 2 sets of input/output data.

4.0 Results and Discussion

In this section, performance evaluation results of the developed ANN based path loss model is discussed in subsection 1 while comparison of predicted path loss by ANN based path loss model and some basic empirical path loss models with measured path loss is discussed in subsection 2.

4.1 Evaluation of the Developed Path Loss Models

The network architecture of 9-39-4, with purelin/tansig pair of activation functions performed best with least MSE value of 24.10 for the rural routes. For the suburban route, network architecture of 1-37-3, with tansig/purelin pair of activation functions performed best with least MSE value of 8.36. Using the weight and bias values, and the architecture of the network with the best performance, the optimal model equations developed for path loss computation in rural and suburban route using transmitting antenna and receiving antenna distance, elevation above sea level of measurement points and transmitting power of reference BTS are:

Rural route:

$$y = \frac{2}{1+\exp\left(-2\left((\alpha x - 0.2152\ ) + 0.1205\right)\right)} - 1 \qquad (11)$$

where y = path loss, x is a (3x1) input vector of distance between transmitting and receiving antenna, elevation above sea level of measurement point and transmitting power of reference BTS. α is a (3x1) matrix shown in Equation 12.

$$\alpha = \lfloor 0.7068 \quad -0.5988 \quad -0.2808 \rfloor \qquad (12)$$

Suburban route:

$$y = \alpha\left(\frac{2}{1+\exp(-2(\beta x + \gamma))} - 1\right) + 1.1132 \qquad (13)$$

where y = path loss, x is a (3x1) input vector of distance between transmitting and receiving antenna, elevation above sea level of measurement point and transmitting power of reference BTS. The constants: α is a (1x37) matrix, β is a (37x3) matrix and γ is a (37x1) matrix shown in Appendix A.

Result obtained during the training process of the ANN based path loss model for the rural route is shown in Figure 7 while histogram of the margin of deviation between measured path loss and the predicted path loss is shown in Figure 8.

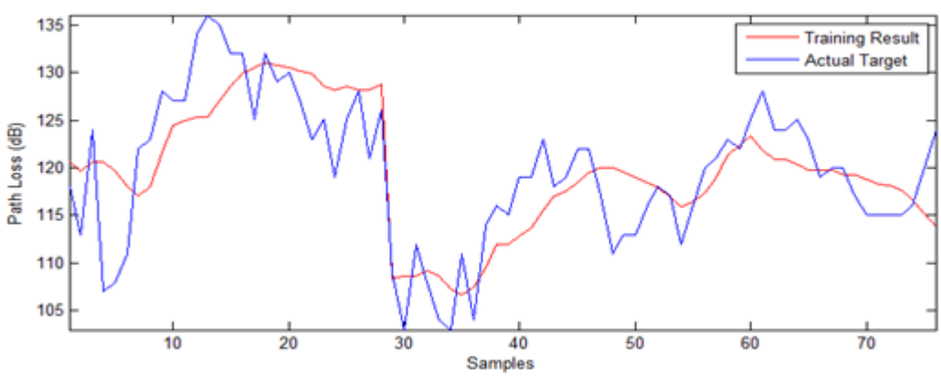

Figure 7: Comparison of Measured Path Loss and Model Predicted Path loss (Rural Route)

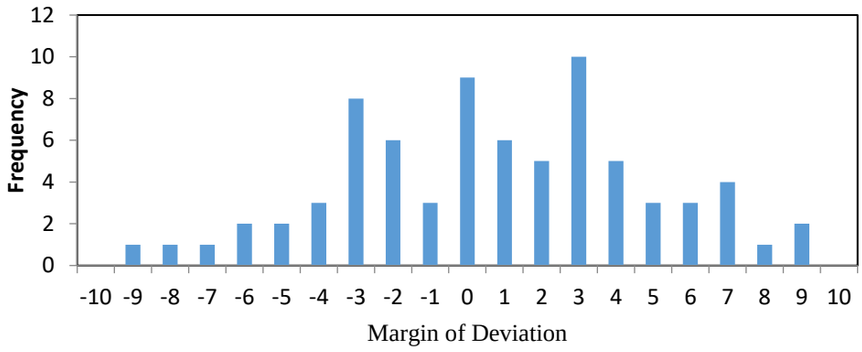

Figure 8: Histogram of Margin of Deviation for ANN Path Loss model (Rural).

From Figure 8, margin of deviation within the range of -6 to 6 is of high frequency and it is 86.67% of the total frequency distribution. Margin of deviation within the ranges of -7 to -10 and 7 to 10 is 13.33% of the total frequency distribution. The margin of deviation and the computed correlation coefficient value of 0.75 shows an acceptable accuracy. Figures 9 and 10 show the result of the training process of the ANN based path loss model for the suburban route, and histogram of the margin of deviation between measured and predicted path loss.

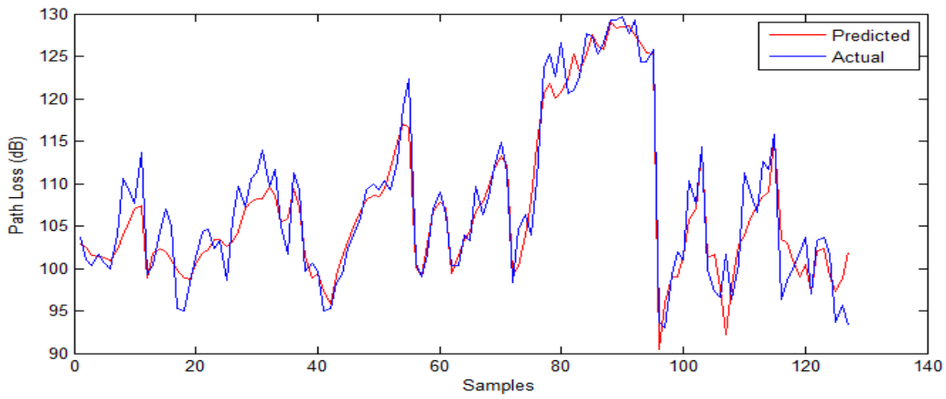

Figure 9: Comparison of Measured Path Loss and Model Predicted Path loss (Suburban Route)

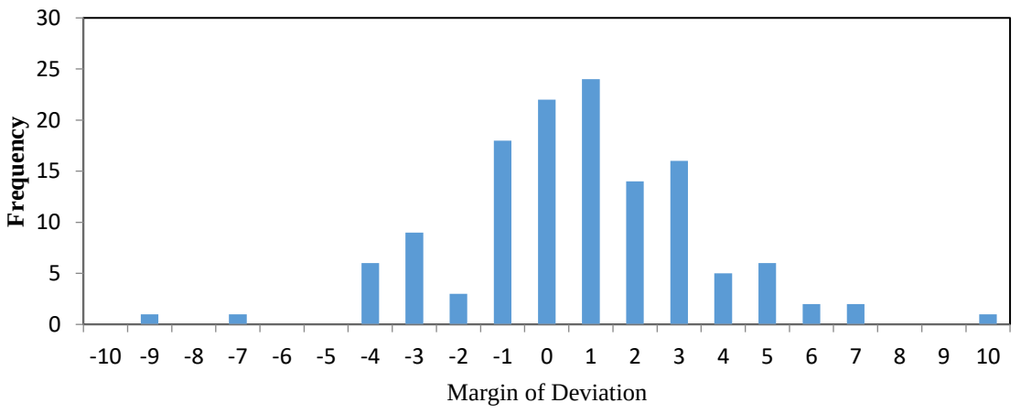

Figure 10: Histogram of Margin of Deviation for ANN Path Loss model (Suburban).

Figure 10 shows high frequency for deviation margin within the range of -6 to +6 and it is 96.15% of the total frequency distribution while 3.85% of the total frequency distribution had margin of deviation within the ranges of -7 to -10 and 7 to 10. The margin of deviation and the computed correlation coefficient value of 0.95 show an acceptable accuracy.

Result obtained from testing the ANN based path loss model for rural route on 70 samples of a rural route (Route 2) is shown in Figure 11 while result from the use of the ANN based path loss model for suburban route on 109 samples from suburban routes is shown in Figure 12.

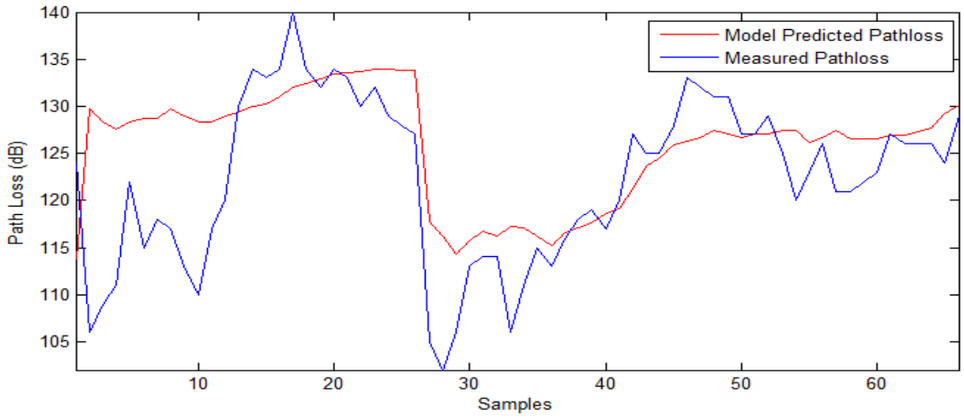

Figure 11: Testing of ANN Based Path Loss Model on 70 Samples (Rural Route)

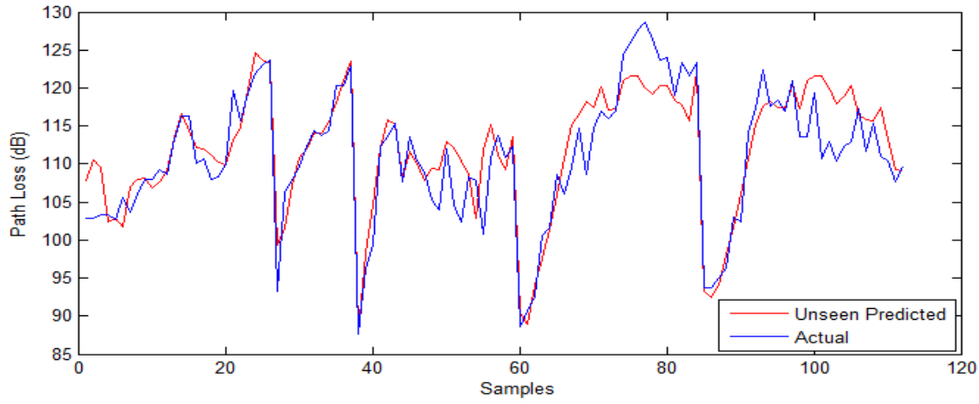

Figure 12 Testing of ANN Based Path Loss Model 109 Samples (Suburban Route)

Correlation coeficient values of 0.78 and 0.87 were computed for rural and suburban routes respectively. The effect of number of training data was observed in Figures 11 and 12. For the ANN based rural route path loss model, Network A, due to the short coverage distance of BTS M01, had 28 training samples (samples 1 to 28 of Figure 7) while Network B had 48 training samples (samples 29 to 76 of Figure 4.53). The results of testing the ANN based rural route path loss model on Route 2 shown in Figure 11 reveal that 32% of the 25 predicted values for Network A (samples 1 to 25 of Figure 12) had margin of deviation within the ranges of -7 to -10 and 7 to 10 while 68% had margin of deviation within the ranges of -6 to +6. The 48 training samples of Network B gave testing result (samples 26 to 70 of Figure 4.58) of 8.88% margin of deviation within the ranges of -7 to -10 and 7 to 10, and 91.11% margin of deviation within the ranges of -6 to +6.

The histogram of the margin of deviation between measured path loss and the ANN based model predicted path loss for rural and suburban routes are shown in Figures 13 and 14 respectively.

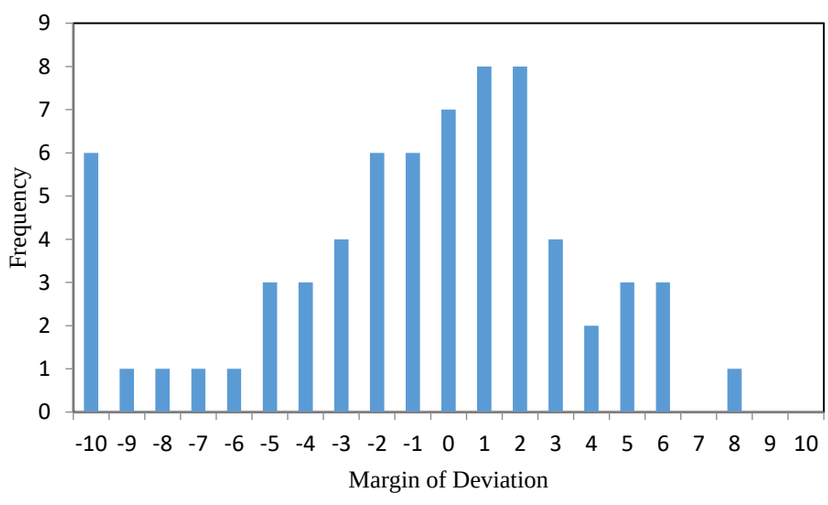

Figure 13. Histogram of Margin of Deviation for ANN Path Loss model (Rural)

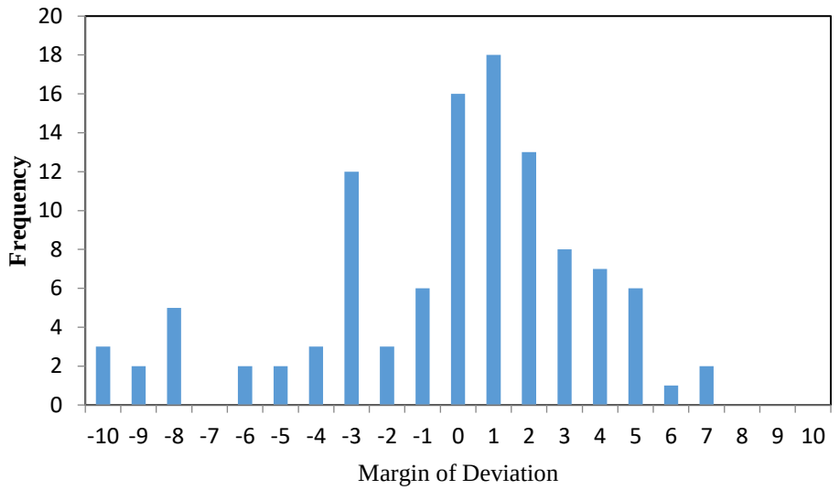

Figure 14. Histogram of Margin of Deviation for ANN Path Loss model (Suburban)

From Figure 13, margin of deviation within the range of -6 to 6 is of high frequency and it is 86.67% of the total frequency distribution. Margin of deviation within the ranges of -7 to -10 and 7 to 10 is 13.33% of the total frequency distribution. The margin of deviation and the computed correlation coefficient value of 0.75 show an acceptable accuracy. Figure 14 shows high frequency for margin of deviation within the range of -6 to 6 and it is 96.15% of the total frequency distribution while 3.85% of the total frequency distribution had margin of deviation within the ranges of -7 to -10 and 7 to 10. The margin of deviation and the computed correlation coefficient value of 0.95 show an acceptable accuracy.

4.2 Comparison of Model Predicted Path Loss with Measured Path Loss

The predicted path loss by some basic models and the proposed ANN model, were compared with the measured path loss for both the rural routes and the suburban routes. For the rural routes, as shown in Figures 15 and 16, Cost-231 model and Ericson model greatly over predict path loss on these routes. Hata and Egli models' predicted values are observed to be close to the measured path loss values, but the accuracy is low.

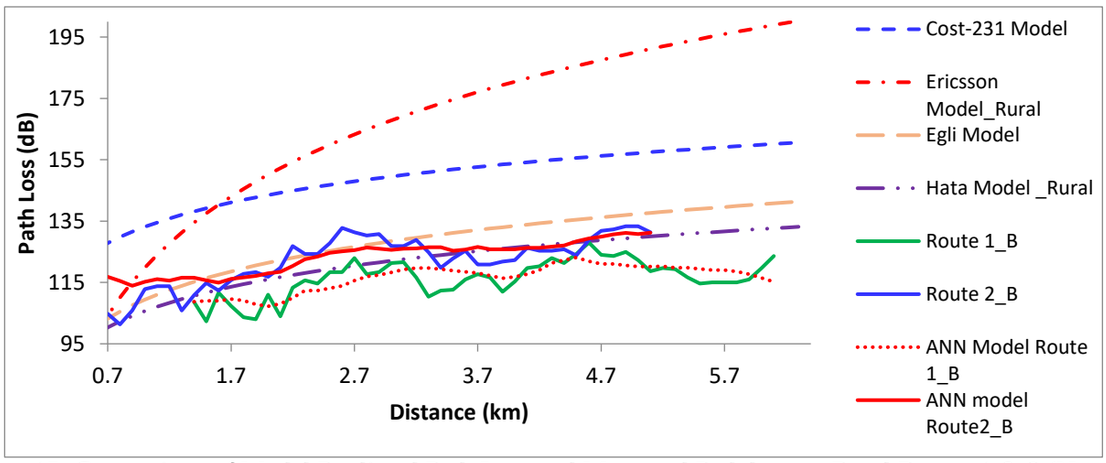

Figure 15: Comparison of Model Predicted Path Loss and Measured Path loss on Rural Routes 1 & 2 (Network B)

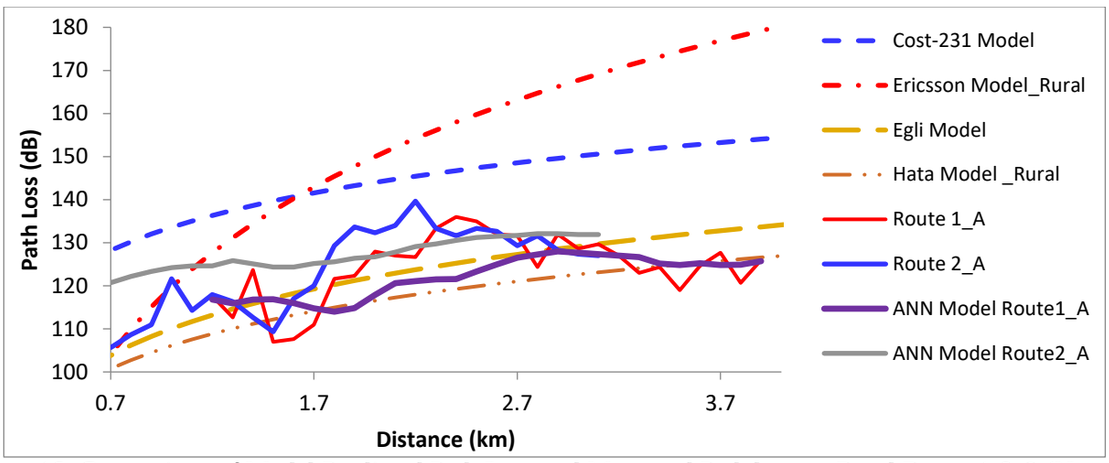

Figure 16: Comparison of Model Predicted Path Loss and Measured Path loss on Rural Routes1 & 2 (Network A)

For the suburban routes, as shown in Figures 17 to 19, Cost231 and Hata models greatly over predicted path loss values. Ericson model is also not in close agreement with the measured path loss values. Path loss predicted values by Egli model are observed to be in close agreement with measured path loss values in Figure 17 but the case was different in Figures 18 and 19.

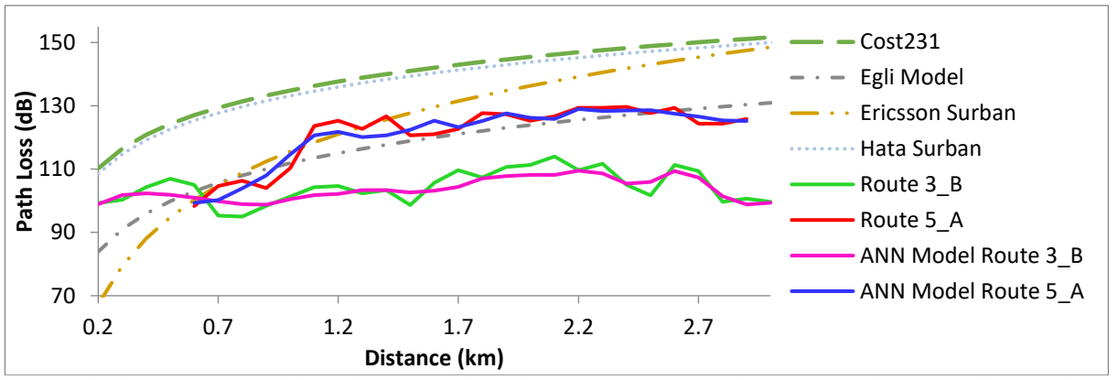

Figure 17: Comparison of Model Predicted Path Loss and Measured Path loss on Suburban Routes 3 & 5 (Networks A & B)

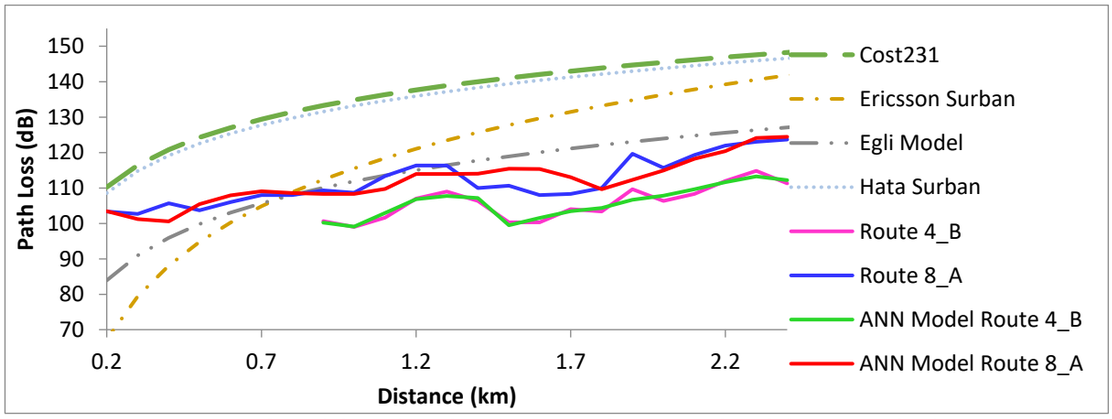

Figure 18: Comparison of Model Predicted Path Loss and Measured Path loss on Suburban Routes 4 & 8 (Networks A & B)

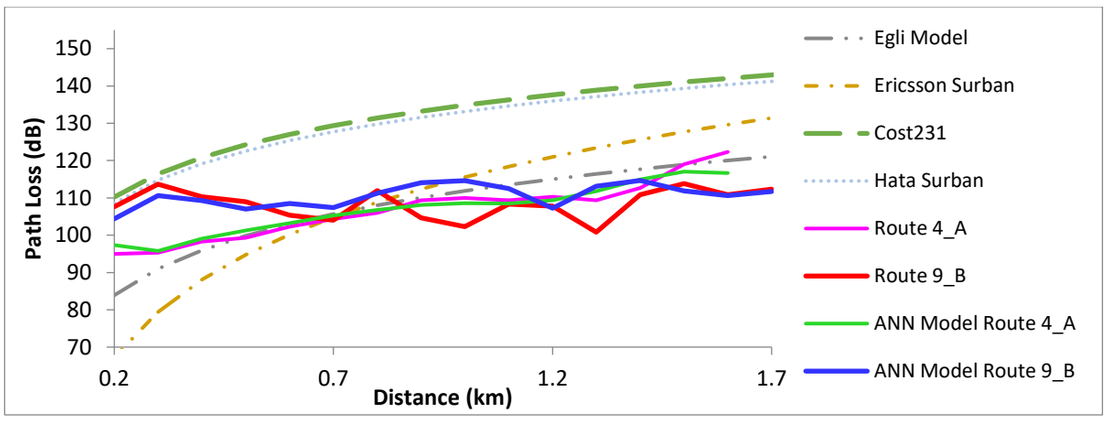

Figure 19: Comparison of Model Predicted Path Loss and Measured Path loss on Suburban Routes 4 & 9 (Networks A & B)

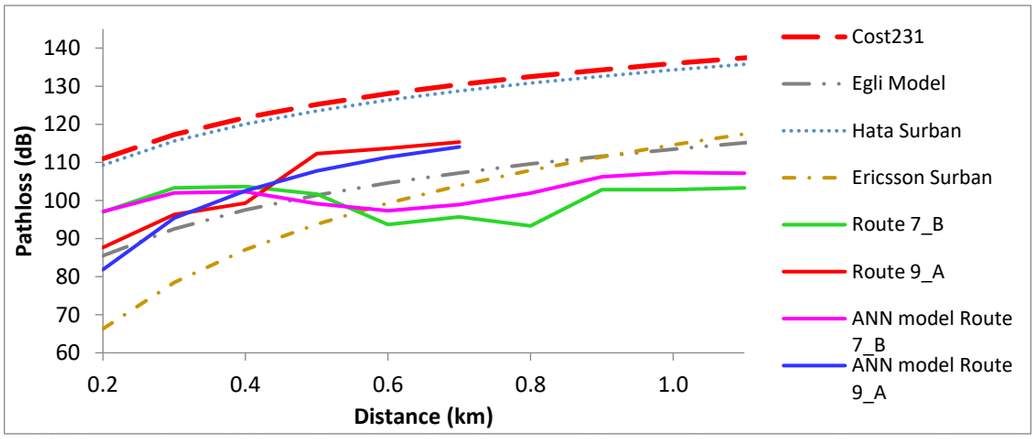

Figure 20: Comparison of Model Predicted Path Loss and Measured Path loss on Suburban Routes 7 & 9 (Networks A & B)

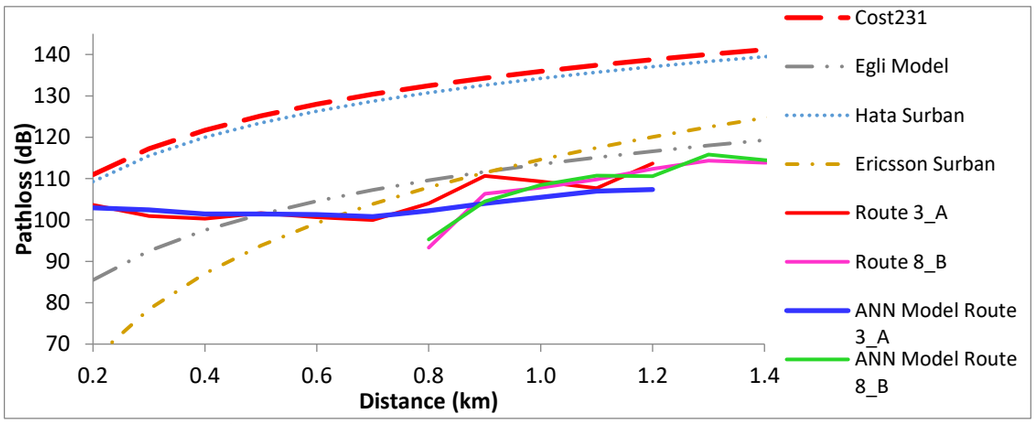

Figure 21: Comparison of Model Predicted Path Loss and Measured Path loss on Suburban Routes 3 & 8 (Networks A & B)

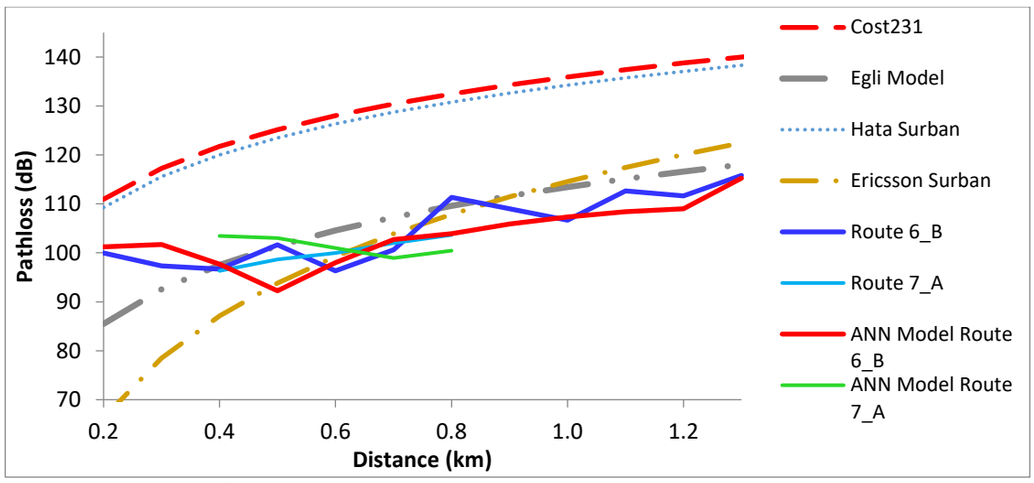

Figure 22: Comparison of Model Predicted Path Loss and Measured Path loss on Suburban Routes 6 & 7 (Networks A & B)

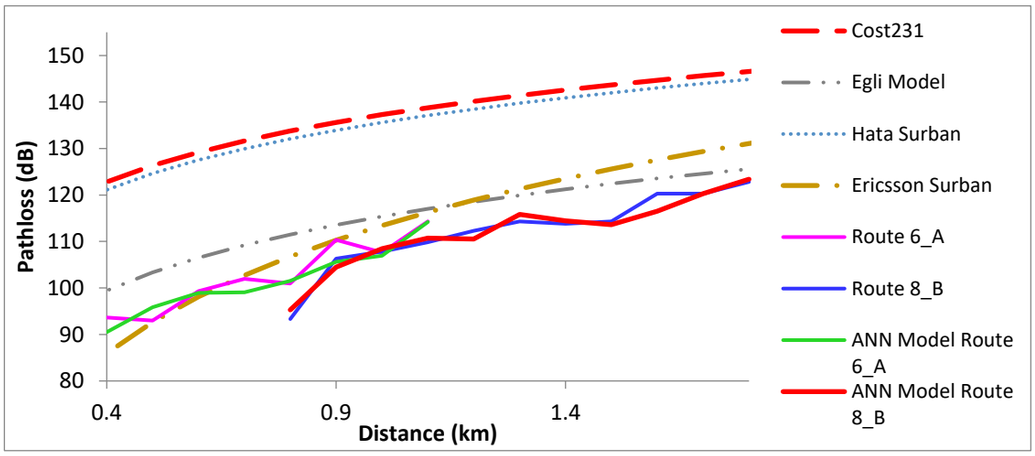

Figure 23: Comparison of Model Predicted Path Loss and Measured Path loss on Suburban Routes 6 & 8 (Networks A & B)

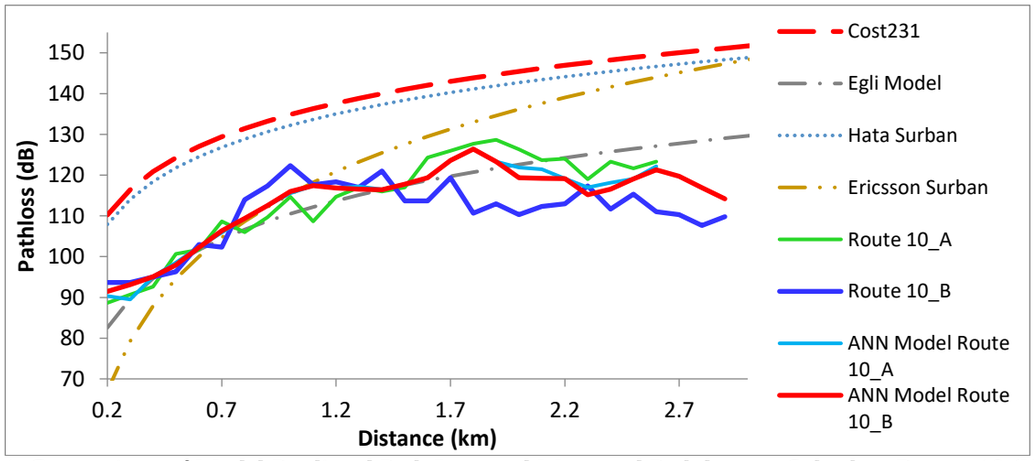

Figure 24: Comparison of Model Predicted Path Loss and Measured Path loss on Suburban Routes 10 (Networks A & B)

Figures 20 to 24 reveal that path loss prediction by basic path loss models such as Cost-231 model, Ericson model and Hata model are not in close agreement with measured path loss values. Egli model predicted in close agreement with the measured path loss but only on some routes. However, the ANN based path loss model predicted in close agreement to measured path loss.

To obtain a quantitative measure of the closeness of the predicted path loss to the measured path loss, Equation 14 (Ajose and Imoize, 2013) was used to compute Root Mean Square Error (RMSE) values as shown in Table 6.

$$RMSE = \sqrt{\frac{\sum_{i=1}^{N}(t_i - y_i)^2}{N}} \quad (14)$$

where N is the number of sets in the output data, t_i is the target output and y_i is the network's output.

Table 4.8: RMSE for Measurement Routes

Area	Route/ Network	Cost-231 Model	Hata Model	Egli Model	Ericsson Model	ANN Model
Rural	Route 1 A	23.51	8.3	6.97	36.32	6.53
	Route 1 B	35.63	9.3	15.58	59.66	3.96
	Route 2 A	22.98	8.33	6.06	32.99	7.07
	Route 2 B	25.48	5.05	6.13	42.44	4.63
Suburban	Route 3 A	24.49	22.87	7.33	14.57	3.13
	Route 3 B	36.06	34.44	16.67	27.7	2.89
	Route 4 A	24.29	22.62	4.31	11.24	3.62
	Route 4 B	35.48	33.81	13.57	24.32	1.22
	Route 5 A	21.14	19.5	4.82	11.02	2.64
	Route 6 A	28.18	26.5	5.6	4.39	2.49
	Route 6 B	24.94	23.3	6.04	12.52	4.17
	Route 7 A	23.25	21.64	7.77	18.17	4.25
	Route 7 B	29.05	27.45	10.64	16.18	3.93
	Route 8 A	25.09	23.47	7.73	16.73	3.21
	Route 8 B	26.2	24.57	8.18	16.4	4.82
	Route 9 A	26.45	24.9	11.47	18.84	3.48
	Route 9 B	83.36	82.14	69.44	77.57	2.47
	Route 10 A	22.27	20.61	3.81	13.98	2.89
	Route 10 B	26.21	24.59	8.37	19.71	6.16

Amongst the basic path loss models considered in this study, Hata model showed best performance on the rural routes with RMSE ranging from 5.05 to 9.30 dB as shown in Table 4.8. But Hata model over predicts path loss on suburban routes with RMSE ranging from 19.50 to 82.14 dB. For the suburban routes, Egli model had the best performance with RMSE ranging from 3.81 to 8.18 dB. COST231 and Ericson models over predicted path loss for both rural and suburban routes. The developed ANN based path loss model performed better than the considered basic path loss models with RMSE ranging from 3.96 to 7.07 on rural routes and 1.22 to 4.82 on suburban routes.

Conclusion

In this study using the distance between transmitting antenna and receiving antenna, elevation above sea level of measurement points and transmitting power of reference BTS as input to ANN, ANN based path loss models were developed for rural and suburban routes in Minna and environs. In the development of the models, network parameters such as number of neurons in the hidden layer and activation function were varied during the performance evaluation process. The use of Levenberg-Marquard algorithm, network architecture of 9-39-4, with purelin/tansig pair of activation functions performed best with least MSE value of 24.10 for the rural routes while network architecture of 1-37-3, with tansig/purelin pair of activation functions performed best with least MSE value of 8.36 for the suburban route.

The weight and bias values and the architecture of the MLP network were used in the development of the model equations. Comparisons of predicted path loss by some basic path loss models and the ANN based path loss model was done. Amongst the basic models, Hata model showed best performance on the rural routes with RMSE ranging from 5.05 to 9.30 dB but over predicted path loss on suburban routes with RMSE ranging from 19.50 to 82.14 dB. For the suburban routes, Egli model had the best performance with RMSE ranging from 3.81 to 8.18 dB. COST231 and Ericson models over predicted path loss for both rural and suburban routes. The developed ANN based path loss model performed better than the considered basic path loss models with RMSE ranging from 3.96 to 7.07 on rural routes and 1.22 to 4.82 on suburban routes

REFERENCES

Aibinu, A. M., Shafie, A. A., & Salami, M. J. (2012). Performance Analysis of ANN based YCbCr Skin Detection Algorithm. *Procedia Engineering*, 41, 1183–1189.

Ajose, S. O., & Imoize, A. I. (2013). Propagation measurements and modelling at 1800 MHz in Lagos Nigeria. *International Journal of Wireless and Mobile Computing*, 6(2), 154-173.

Armoogum, V., Munee, R., & Armoogum, S. (2010). Path Loss Analysis for 3G Mobile Networks for Urban and Rural Regions of Mauritius. Proceedings of the Sixth International Conference on Wireless and Mobile Communications (ICWMC), 164-169.

Ayekomilogbon, O., Famoriji, O., & Olasoji, O. (2013). UHF Band Radio Wave Propagation Mechanism in Forested Environments for Wireless Communication Systems. *Journal of Information Engineering and Applications*, 3(7), 11-16.

Bakinde, N. T., Faruk, N., Ayeni, A. A., Muhammad, M. Y., & Gumel, M. I. (2012). Comparison of Propagation Models for GSM 1800 and WCDMA Systems in Selected Urban Areas of Nigeria. *International Journal of Applied Information Systems (IJAIS)*, 2(7), 6-13.

Beale, M. H., Hagan, M. T., & Howard, B. O. (2011). Neural Network Toolbox™ 7. User Guide. R2011b.

Benmus, T. A., Abboud, R., & Shater, M. K. (2016). Neural Network Approach to Model the Propagation path Loss for Great Tripoli Area at 900, 1800 and 2100 MHz Bands. *Iinternational Journal of Sciences and Techniques of Automatic Control and Engineering*, 10(2), 2121-2126.

Chebil, J., Lwas, A. K., Islam, M. R., & Zyoud, A. (2011). Investigation of Path Loss Models for Mobile Communications in Malaysia. *Australian Journal of Basic and Applied Sciences*, 5(6), 365-371.

Deligiorgi, D., Philippopoulos, K., & Kouroupetroglou, G. (2013). Artificial Neural Network based Methodologies for the Spatial and Temporal Estimation of Air Temperature. *International Conference on Pattern Recognition Applications and Methods*, 669-578.

Dombayci, O. A., & Golcu, M. (2008). Daily Means Ambient Temperature Prediction using Artificial Neural Network method: A case study of Turkey. *Renewable Energy (Elsevier Journal)*, 34, 1158–1161.

Eichie, J. O., Oyedum, O. D., Ajewole, M. O. & Aibinu, A. M. (2016). Artificial Neural Network model for the determination of GSM Rxlevel from atmospheric parameters, *Engineering Science and Technology, an International Journal*, Retrieved from http://dx.doi.org/10.1016/j.jestch.2016.11.002.

Ekpenyong, M., Robinson, S., & Isabona, J. (2010). Macrocellular Propagation Prediction for Wireless Communications in Urban Environments. *JCS & T*, 10(3), 130-136.

Faruk, N., Adediran, Y. A., & Ayeni, A. A. (2013). On the Study of Empirical Pathloss Models. *Progress In Electromagnetics Research B*, 49, 155-176.

Isabona, J., Konyeha, C. C., Chinule, C. B., & Isaiah, G. P. (2013). Radio Field Strength Propagation Data and Path Loss Calculation Methods in UMTS Network. *Advances in Physics Theories and Applications*, 21, 54-68.

Milanovic, J., Rimac-Drlje, S., & Majerski, I. S. (2010). Radiowave propagation mechanisms and empirical models for fixed wireless access systems. *Technical Gazette*, 17(1), 43–52.

Nigerian Communications Commission (NCC) (2015). *Subscriber/Teledensity Data*. Retrieved July 2015 from http:// www.ncc.gov.ng.

Nwalozie, G. C., Ufoaroh, S. U., Ezeagwu, C. O., & Ejiofor, A. C. (2014). Pathloss Prediction for GSM Mobile Networks for Urban Region of Aba, South-East, Nigeria. *International Journal of Computer Science and Mobile Computing, 3*(2), 267-281.

Nwawelu, U. N., Nzeako, A. N., & Ahaneku, M. A. (2012). The Limitations of Campus Wireless Networks: A Case Study of University of Nigeria, Nsukka. *International Journal of Networks and Communications, 2*(5), 112-122.

Ogbulezie1, J. C., Onuu, M. U., Bassey, D. E., & Etienam-Umoh, S. (2013a). Site Specific Measurements and Propagation Models for GSM in Three Cities in Northern Nigeria. *American Journal of Scientific and Industrial Research, 4*(2), 238-245.

Ogbulezie1, J. C., Onuu, M. U., Ushie, J. O. and Usibe, B. E. (2013b). Propagation Models for GSM 900 and 1800 MHz for Port Harcourt and Enugu, Nigeria, *Network and Communication Technologies*, Vol. 2(2), 1-10.

Rappaport, T. S. (2002). *Wireless Communications: Principles and Practice* (2nd ed.). Upper Saddle River, New Jersey, USA: Prentice Hall.

Reddy, B. M. (1987). Physics of the Troposphere. In *Handbook on Radio Propagation for Tropical and Subtropical Countries, URSI Committee on Developing Countries, UNESCO subvention* (pp. 59-77). New Delhi: .

Saunders, S., & Aragón-Zavala, A. (2007). *Antennas and Propagation for Wireless Communication Systems* (2nd ed.). New York: John Wiley & Sons Inc.

Seybold, J. S. (2005). *Introduction to RF Propagation* (ed.). New York: John Wiley & Sons Inc.

Sharma, P. K., & Singh, R. K. (2010). Comparative Analysis of Propagation Path loss. *International Journal of Engineering Science and Technology, 2* (6), 2008-2013.

Usman, A. U., Okereke, O. U., & Omizegba, E. E. (2015). Instantaneous GSM Signal Strength Variation with weather and Environmental Factors. *American Journal of Engineering Research (AJSER), 4*(3), 104-115.

CHARACTERIZATION OF VIRGIN ASPHALTENES AND ITS SUBFRACTIONS USING UV-VISIBLE AND FTIR SPECTROSCOPY

[*1]Bisiriyu, M. T., [1]Idris, S., [2]Garba, H. A., [2]Yelwa, A. S., [2]Muhammad, A. B. and [2]Faruq, U. Z.

[1]Department of Chemistry, Federal University of Technology, Minna, Nigeria

Department of Pure and Applied Chemistry, Usmanu Danfodiyo University, Sokoto, Nigeria

[*]Corresponding Author's e-mail and Contact: m.bisiriyu@futminna.edu.ng

Abstract

Spectroscopic characterization of asphaltene is necessary in order to understand the changes it undergoes when heavy and extra-heavy oil types such as bitumen are subjected to catalytic aquathermolysis. The structural composition of asphaltene and its subfractions were investigated using UV/Visible and FTIR Spectroscopy. Raw bitumen sample was obtained from the bitumen deposit at Mile 2 in Odigbo, Ondo State, Nigeria. The sample was purified and the asphaltene fraction was precipitated with *n*-hexane, the precipitated asphaltene was fractionated into fractions A and B **based** on their difference in solubility and polarity with hexane/toluene mixture at a fixed ratio. The results showed that virgin asphaltene and **its** subfractions absorbed light of longer wavelength in the range (465 – 640 nm), indicating that they are made up of polynuclear aromatic compounds. The results also revealed the presence of alkyl side chains and major oxygenated groups in both virgin asphaltene and its subfractions (A and B). In general, asphaltene are complex molecular compound which consists of aromatic moieties with alkyl side chains, polar groups (esther, ether and carbonyl), acidic and basic groups (carboxylic and pyridine) which can interact at certain pH range by accepting or donating protons.

Keywords: Asphaltene, Bitumen, Subfractions A and B, UV/ Visible, FTIR,

1. Background

Asphaltenes are considered the most complex mixture of carbonaceous macromolecular compounds that have been found to pose many challenges which **include** obstruction of reservoirs, clogging of wells and pipeline as well fouling and stabilization of oil-water emulsions in the petroleum industry (Galoppini, 1994; Kokal and Sayegh, 1995; Khadim and Sarbar, 1999; Shedid and Zekri, 2006; Ma *et al*., 2008; Muhammad, 2015). Although, they are usually referred to as the heaviest fraction of petroleum but their solubility-based behaviour encompasses identical substances from coals and bitumen (Behar *et al*., 1984; William, 1985; Solli and Leplat, 1986) and base on composition the two are very identical (Badre *et al*., 2006; Muhammad, 2015). The composition of asphaltenes has remained a subject of interest and attention for many researchers (Bunger and Li, 1981; Peters, 1986; Sheu and Mullins, 1995; Sheu, 2002; Sabbah *et al*., 2011; Mullin *et al*., 2012; Muhammad and Abbott, 2013; Wu *et al*., 2013; Muhammad, 2015). **Generally,** asphaltenes macromolecules are considered to be composed of aliphatic side-chains joined to aromatic moieties through C-C, C-O and C-S linkages (Yen, 1974; Peng *et al*., 1997; Muhammad, 2015). The aromatic moieties are made up of large condensed pericyclic sheets of 4 and 20 rings (Groenzin and Mullins, 1999; Badre *et al*., 2006; Muhammad, 2015) whereas the alkyl moieties were found between C_3 to C_7 in size (Calemma *et al*., 1995; Muhammad, 2015), however, homologues occur between C_1 to C_{32} (del Rio *et al*., 1995; Peng *et al*., 1999; Muhammad and Abbott, 2013; Muhammad, 2015). More so, the aliphatic moieties are known to consist of both acyclic (n-alkyl and iso- alkyl) and cyclic (hopanoids, steroids etc.) alkyl groups (Mojelsky *et al*., 1992; Trifilieff *et al*., 1992; Peng *et al*., 1997; Strausz *et al*., 1999; Muhammad and Abbott, 2013; Muhammad, 2015). The aromatic moieties in a complex asphaltenes structure which are further interconnected to each other by aliphatic bridges (Polymeric structure) are still been study (Bunger and Li, 1981; Hammami *et al*., 1995; Speight, 2004; Badre *et al*., 2006; Strusz *et al*., 2008; Mullins, 2009; Muhammad, 2015). It has been reported that the molecular composition of aliphatic moieties and their stereochemistry are greatly affected by thermal stress (Muhammad and Abbott, 2013; Muhammad, 2015). But the aromatic moieties oxidation by ruthenium oxide makes it impossible to get clear image of the thermal evolution of the asphaltenes (Muhammad, 2015). In this paper, UV/Visible and FTIR Spectroscopy were employed to study virgin asphaltenes and its subfractions (A and B) to better understand the changes that might occur in asphaltenes structure and

composition when heavy and extra oils are subjected to catalytic aquathermolysis.

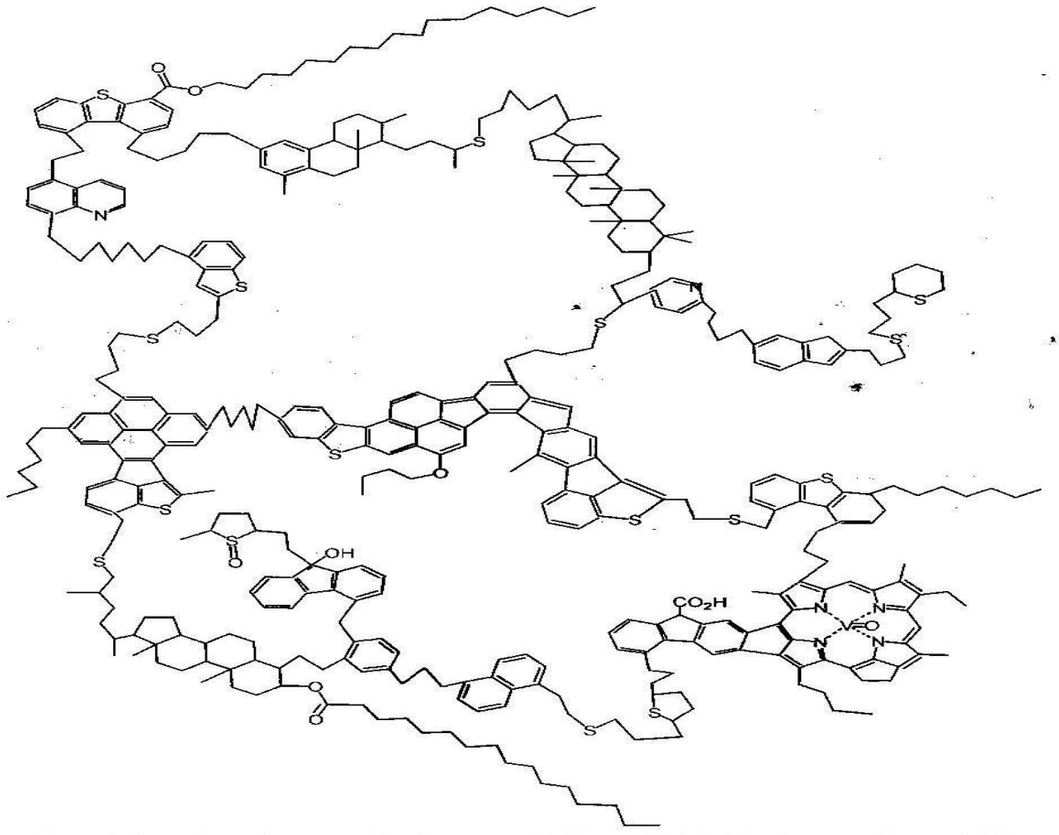

Figure 1: Hypothetical structure of asphaltene (Adapted from Anigbogu, 2011).

2. Material and Methods

2.1. *Sampling*

The bitumen sample was collected into a plastic container from the bitumen deposit at Mile 2 in Odigbo Local Government Area, Ondo State located in Nigerian bitumen belt of southwestern Nigeria. The belt lies on the onshore areas of eastern Dahomey (Benin) Basin, with Longitude 3º45'E and 5º45'E and Latitude 6º00'N and 7º00'N (Bakare *et al*., 2015).

2.2. *Purification of Raw Bitumen*

In other to remove particulate matter, bitumen (40 g) was dissolved with 200 cm^3 of DCM in a beaker using ultrasonicator (DR-LQ20) for 30 minutes. The solution obtained was filtered with a Whatman filter paper and the filtrate was left to dry completely (Muhammad, 2009).

2.3. *Precipitation of Asphaltenes*

Bitumen (1.00 g) was treated with *n*-hexane (40 cm^3) in a conical flask and was sonicated regularly. Firstly, the bitumen was dissolved with little amount of DCM before the asphaltenes **were** precipitated with *n*-hexane. The mixture was then stirred for 30 minutes and was allowed to equilibrate for 24 hours. The asphaltenes were recovered from the mixture by centrifuging at 3500 rpm for 10 minutes. The asphaltenes were then re-dissolved with DCM (1 cm^3) and re-precipitated with *n*-hexane (40 cm^3). The mixture was sonicated for 10 minutes and the asphaltene was then recovered by centrifugation. This procedure was repeated one more time and the asphaltene recovered was transferred into a pre-weighed beaker with little amount of DCM and left to dry (Muhammad, 2009).

2.2.4 *Fractionation and Characterization of Asphaltenes*

Fractionation of asphaltene was carried out by dissolving certain amount of asphaltene in toluene followed by the addition of *n*-hexane at a ratio of *n*-hexane:toluene (hextol) designed to precipitate only some asphaltenes (Barrera *et al*., 2013; Yamchi, 2014). Starting the fractionation, a clean beaker (100 cm^3) was weighed and exactly 3. 00 g of asphaltenes was measured into it. Toluene was then added to it and the mixture was left over night and later placed in an ultrasonic bath (DR-LQ20) for 5 minutes until the asphaltenes completely dissolved.

The corresponding volume of *n*-hexane according to the desired hextol ratio was added and the mixture was sonicated for another 45 minutes. After it was allowed to settle for 24 hours, the solution was centrifuged at 4000 rpm for 5 minutes to separate precipitated asphaltenes from the mixture. Supernatant was decanted and the solid

left was transferred with DCM into a clean beaker and this was named as fraction "A". The supernatant was then placed in a fumed cupboard to evaporate the hextol and the residue was named as fraction "B". The two subfractions were allowed to dry until there was no difference in mass (Yamchi, 2014).

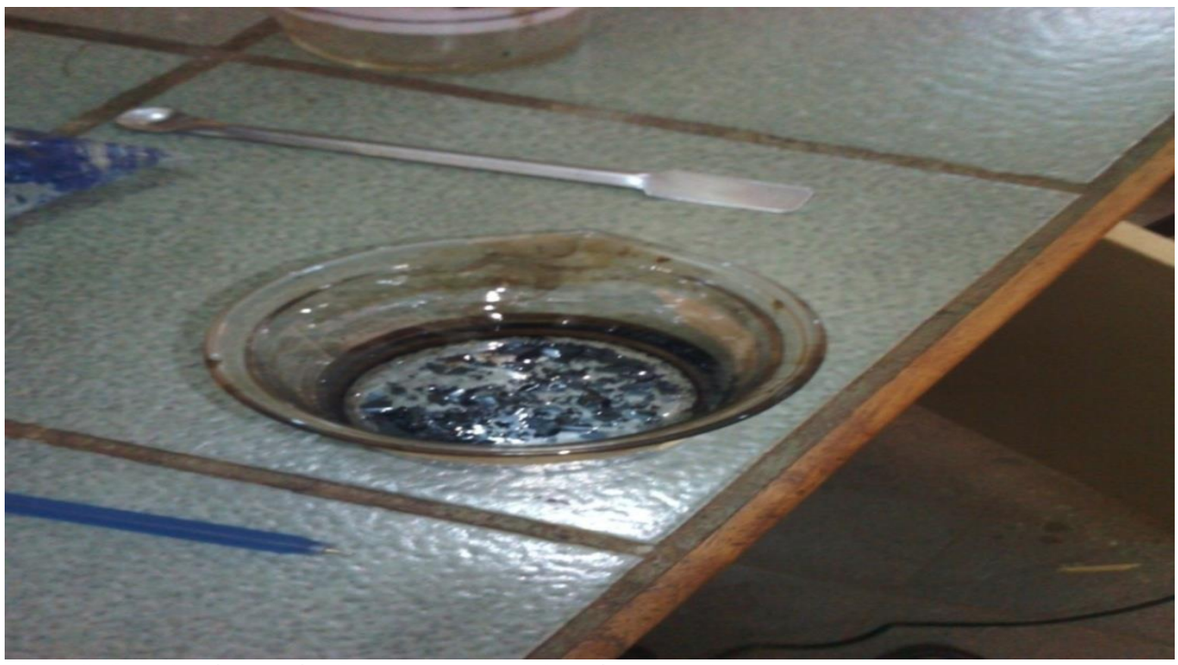

Figure 2: Showing flakes of *n*-C_6 asphaltenes obtained from the bitumen

(a) *UV/Visible Spectroscopic Measurements*

Asphaltenes (0.0001 g) was dissolved in dichloromethane (2.00 cm^3) to obtain asphaltenes solution and was transferred into a cuvet then it was placed in the sample compartment of the UV spectrophotometer. A UV/visible spectroscopic measurement of the solution was made between 400-800 nm on a spectrophotometer (UV-1800). The spectra information gave some insight into the polyaromatic structures in asphaltene and the extent of distribution of polyaromatic condensed ring system (Li *et al*., 2002). The same procedure was adopted for the characterization of its subfactions.

(b) *FTIR Analysis*

Asphaltene and its subfractions were analyzed on a Fourier transform infrared spectrometer (MB3000). The samples were measured using a transmission technique.

Small quantity of the sample dissolved in dichloromethane was carefully dropped into a firmly packed potassium bromide powder with a syringe. The mixture was ground into fine powder and a pellet was prepared. The infrared spectrum was scanned on the pellet 30 times using a detector at a resolution of 4 cm^{-1} in the range 4000 - 750 cm^{-1} (Li *et al*., 2002).

3. Results and Discussion

3.1 *Results of Characterization of Asphaltene and its Subfractions*

The results of the experiments conducted are hereby presented:

The UV/Visible spectra of asphaltene and its subfractions are presented in Figure 3(a – c) and were interpreted in Table 1.

Table 1: UV/Visible data of Asphaltene and its subfractions

Asphaltenes					
Virgin		Fraction A		Fraction B	
Absorbance	λ (nm)	Absorbance	λ (nm)	Absorbance	λ (nm)
3.70	510	3.50	570	3.20	465
3.20	515	2.00	575	3.00	470
2.00	520	1.40	600	2.90	475
1.40	530	0.80	640	2.30	480
1.20	535	----	-----	1.50	485

The spectra data of virgin asphaltene and its subfractions (Table 1) shows that they absorbed light in the visible region of the electromagnetic spectrum indicating that asphaltenes are highly unsaturated as shown in the hypothetical structure of asphaltene Figure 1.

The UV/Visible spectra of virgin asphaltene and its subfraction shows that they all contain polynuclear aromatic structures based on their absorbance at the following wavelengths: 465, 470, 475, 480, 510, 512, 520, 530, 570, 575, 600 and 640 nm, respectively.

The fact that asphaltenes are polycyclic aromatic compound, it's obvious that the wavelength of the individual aromatic constituents will vary considerably.

Their light absorption which occurred in the visible region of the spectrum (longer wavelength) suggests the presence of fused benzene rings or polynuclear aromatic system in asphaltene and its subfraction which are unsaturated and highly conjugated in nature. Their absorption is similar to those found in the literature. The range of absorption bands for both virgin asphaltenes and its subfraction are between 465 – 640 nm which correspond to the bands of highly conjugated polynuclear aromatics structures such as **benzenoid**. These are in accordance with asphaltenes and the UV/Visible absorption bands shows resemblance with those described elsewhere (Anigbogu, 2011; Concawe, 2012). The absorption bands which are in the range of 465 – 640 nm for both the virgin asphaltene and its subfractions are within the visible region which characterized the polynuclear aromatic compounds, indicating the presence of chromophore in the asphaltenes (Anigbogu, 2011). In the light of this, asphaltenes are coloured and the chromophore that maybe found in asphaltenes includes: conjugated double bonds involving aromatic hydrocarbon as indicated by the infrared spectra of the virgin asphaltene and fraction B. According to molecular orbital theory, the likely electronic transitions are: $\delta \rightarrow \delta^*$, $n \rightarrow \delta^*$, $\pi \rightarrow \pi^*$ and $n \rightarrow \pi^*$ where n = non-bonding orbital, δ = sigma orbital, π = pie orbital and those with asterisk are antibonding orbitals. The wavelengths of absorption range are in accordance with simple molecular orbital theory assumption. The assumption is that the difference in energy ΔE = HOMO - LUMO is small.

Therefore the longer the wavelength of absorption, the smaller the energy of irradiation. Hence, exposure of these compounds with small ΔE value and longer wavelength of absorption to high irradiation energy will denature them. Thus they could decompose under such condition (Anigbogu, 2011).

In Figure 4(a-c), the infrared spectra of virgin asphaltene and its subfractions are presented and were interpreted in Table 2 based on literature by Silversten and Webster (1998), Pavia *et al*. (2001) and were corroborated by Bakare *et al*. (2015).

Table 2: Assignment of Functional Groups to FTIR bands in Virgin Asphaltene and its Fractions

	Asphaltenes			
Wavenumber (cm^{-1})	Virgin	Fraction A	Fraction B	Interpretation
3450	+	+	+	O-H stretch (H- bonded)
2925	+	+	+	C-H stretch in alkyl (CH_2)
2850	+	+	+	C-H stretch in alkyl (CH)
1650	+	+	+	C=O (str.), in carboxylic acids
1500	+	-	+	C=C asymmetric str. in aromatics
1425	-	+	+	CH_2 (def.), in ketone
1350	-	+	-	C-N (str.), in aromatic amine
1275 - 1200	+	+	-	C-O (str.), in ester/ ether
1050	-	+	-	S=O (str.), in sulfoxides
750	+	+	-	C-H (def.), in ring with three adj. H-atoms

+ = present, - = absent, str. =stretch, def. = deformation, adj. = adjacent

The spectra of virgin asphaltene and its subfractions (Table 2) indicate strong and broad band absorption at 3450 cm^{-1} typical of O-H stretch (H-bonded). The two strong absorptions at 2925 cm^{-1} and 2850 cm^{-1} correspond to C-H stretch in (CH_2) and (CH) found in alkyl groups, respectively. The band at 1650 cm^{-1} may be attributed to C=O (stretch) in carboxylic acids, ketone and amide. A weak band at 1500 cm^{-1} which could be ascribed to C=C (stretch) in aromatic compounds was present in virgin asphaltene and fraction B but absent in fraction A while a band at 1425 cm^{-1} which is characteristics of CH_2 (def.) in ketone was absent in virgin asphaltenes but present in fraction A and B, respectively. Also, the spectra revealed a band at 1350 cm^{-1} which might be due to the availability of C-N (str.) in aromatic amine was absent in virgin asphaltene and fraction B but present in fraction A and the band observed in the range 1275 - 1200 cm^{-1} could be assigned to C-O (str.) in ester or ether was present in virgin asphaltene and fraction A but absent in fraction B. More so, a strong band at 1050 cm^{-1} which may be ascribed to S=O (str.) in sulfoxides or sulfonic acids was absent in virgin asphaltene and fraction B and present only in fraction A while an absorption band at 750 cm^{-1} is a characteristics of C-H (def.) in benzene ring with three adjacent hydrogen atoms was present in both virgin asphaltene and fraction A but absent in fraction B. The IR spectra bands (Table 2) are in conformity with observation of Muhammad (2015) and Bakare *et al*. (2015) in terms of functional groups. The spectra characteristics of virgin asphaltene showed the absence of some functionalities such as S=O and C-N which were present in one of its fractions described the heterogenousity of asphaltene. Although hydrocarbons are consistent with all the spectra, however, the presence of O-H and C=O groups in all the spectra confirmed that asphaltenes as a group are indeed polar because they aid asphaltene molecules in forming a mechanical barrier through hydrogen bonding around the water droplets and prevent coalescence (Li *et al*., 2002). These infrared results are in accordance with studies on Agbabu Natural Bitumen (Bakare *et al*., 2015).

4 Conclusions

The results showed that virgin asphaltene and it subfractions absorbed light of longer wavelength in the range (465 – 640 nm), indicating that they are made up of polynuclear aromatic compounds. The results also revealed the presence of alkyl side chains and major oxygenated groups in both virgin asphaltenes and its subfractions (A and B).

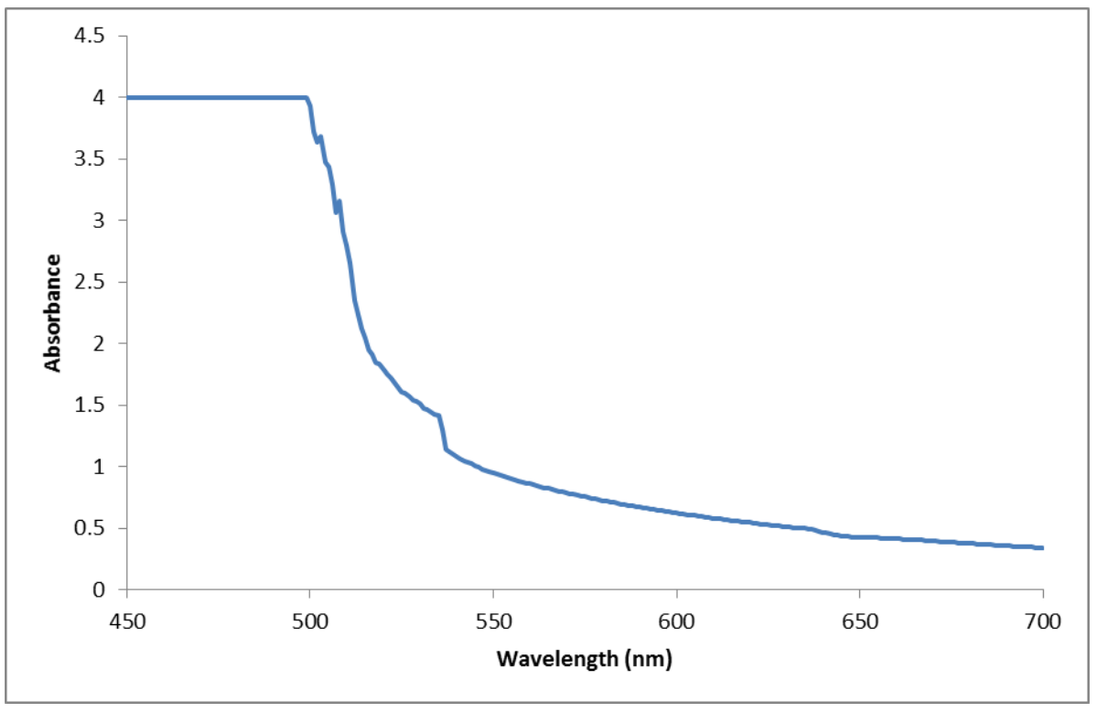

Figure 3a: UV- Visible spectra of virgin asphaltene

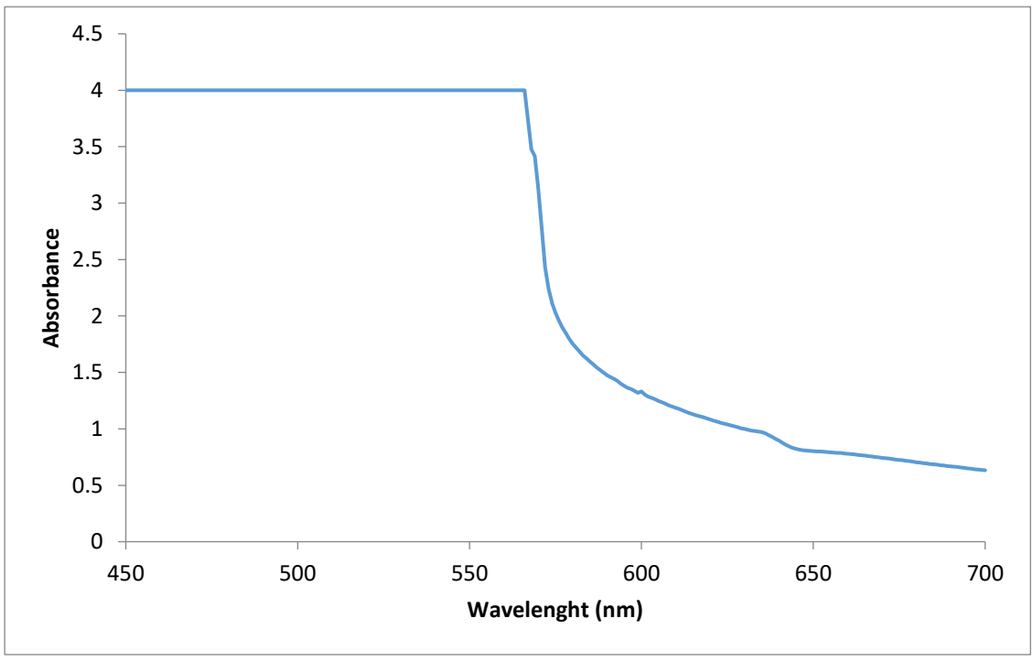

Figure 3b: UV-Visible spectra of asphaltene fraction A

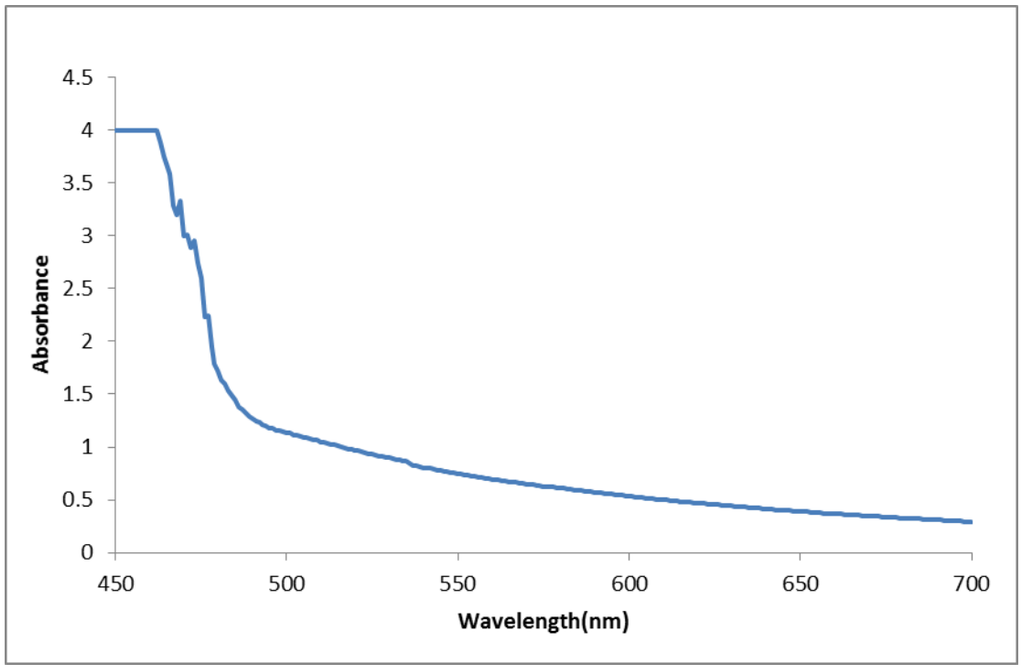

Figure 3c: UV-Visible spectra asphaltene fraction B

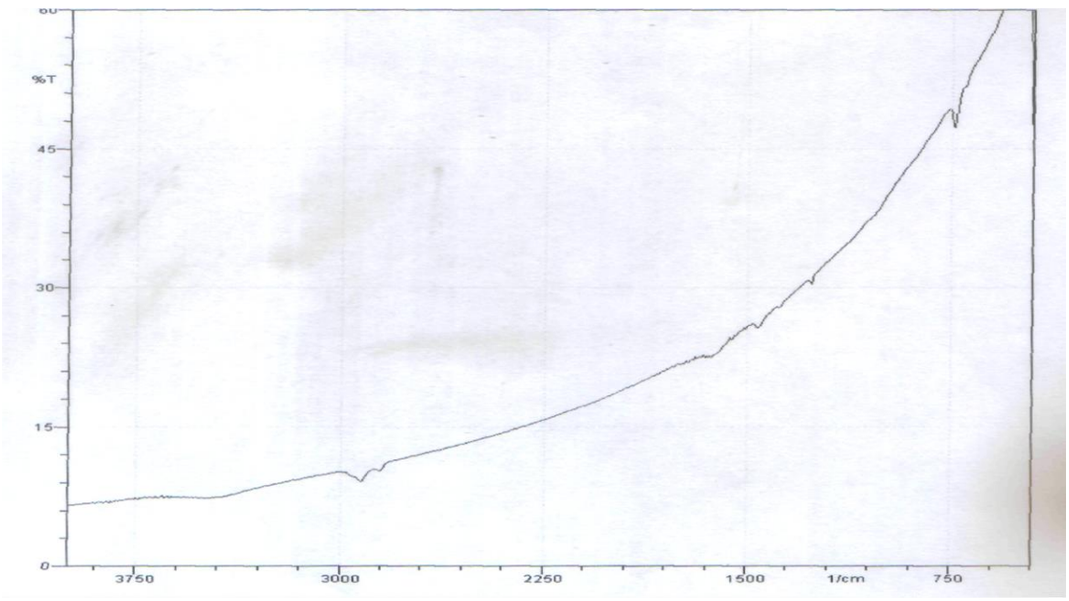

Figure 4a: FTIR spectra of virgin asphaltene

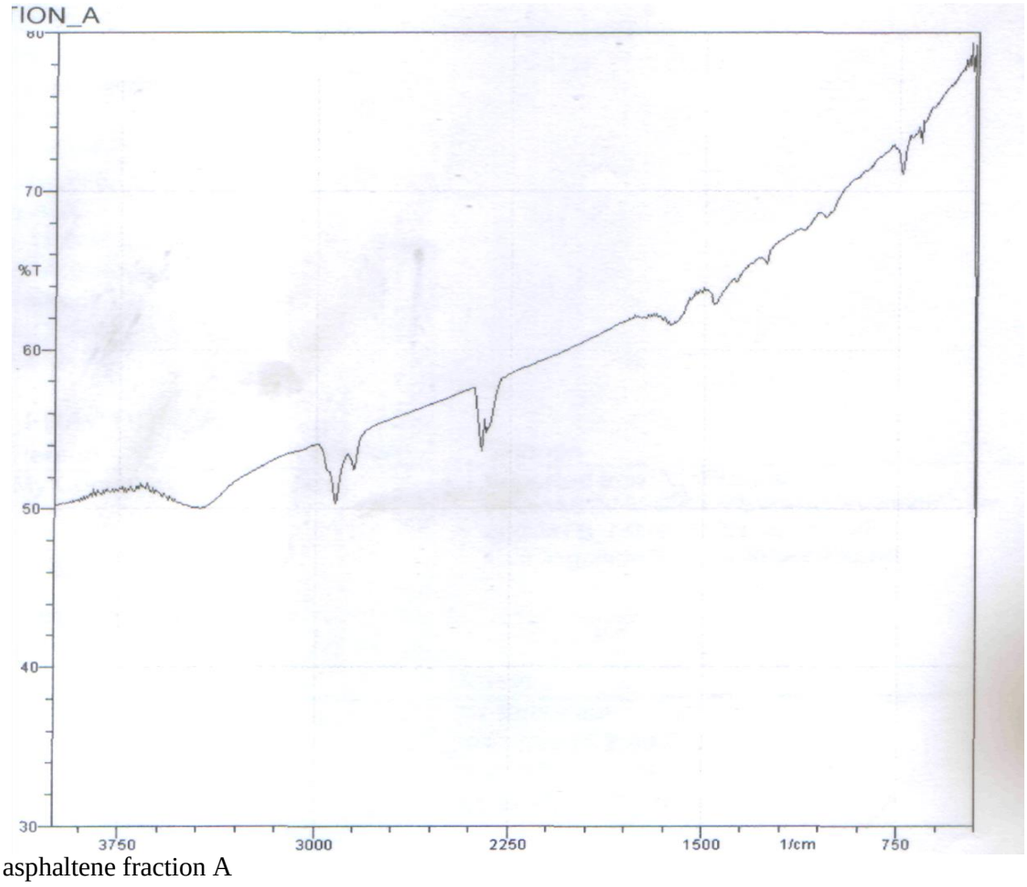

Figure 4b: FTIR spectra of asphaltene fraction A

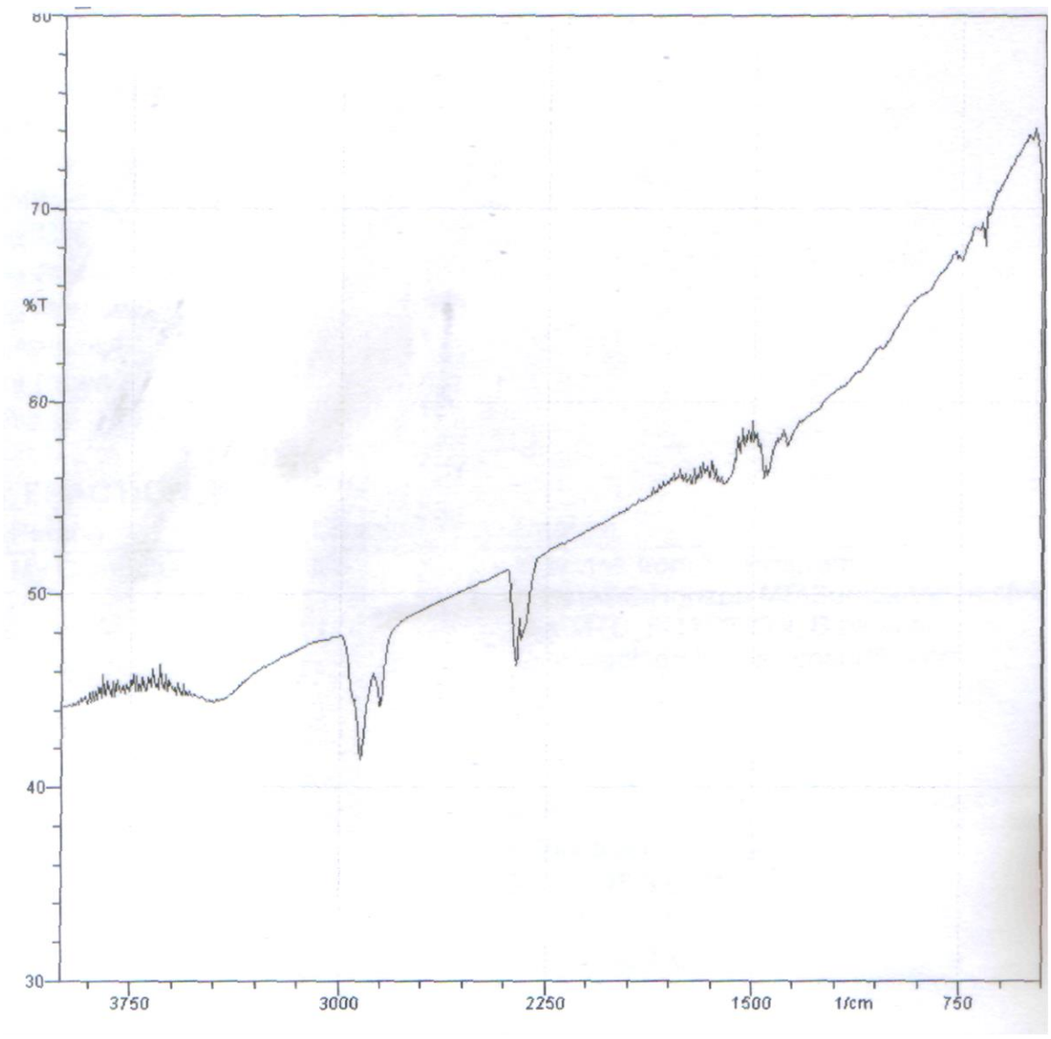

Figure 4c: FTIR spectra of asphaltene fraction B

Reference

Abdel-Raouf, M. E. (2012). Factors Affecting the Stability of Crude Oil Emulsions, Crude Oil Emulsions-Composition Stability and Characterization, Prof. Manar El-Sayed Abdul-Raouf (Ed.), ISBN: 978-953-51-0220-5, InTech, Available from: http://www.intechopen.com/books/crude-oil-emulsions-compositionstability-

Anigbogu, I. V. (2011). Precipitation of Asphaltenes, Quantification of Maltenes, UV and FTIR Spectroscopic Studies of C_7 and $C_5 + C_7$ Asphaltene from 350 ^oC Atmospheric Residuum Crudes. MSc. Dissertation, University of Nigeria, Nsukka. 130pp.

Badre, S., Goncalvesa, C. C., Norinagab, K. Gustavsona, G. and Mullins, O. C. (2006). Molecular Size and Weight of Asphaltene and Asphaltene Solubility Fractions from Coals, Crude Oils and Bitumen. *Fuel*, **85**, 1–11.

Bakare, H. O., Esan, A. O. and Olabemiwo, O. M. (2015). Characterization of Abgabu Natural Bitumen and Its Fractions Using Fourier Transform Infrared Spectrometry. *Chemistry and Materials Research*, [online], **7**, 1-11.

Barrera, D., Ortiz, D. and Yarranton, H. (2013). Molecular Weight and Density Distributions of Asphaltenes from Crude Oils. *Energy and Fuels*, **27**, 2474- 2487.

Behar, F., Pelet, R., Roucache, J. (1984). Geochemistry of Asphaltenes. *Organic Geochemistry*. **6**:587–595

Bunger, J. W. and Li, N. C. (eds) (1981). Chemistry of Asphaltenes, Advances in Chemistry Series 195, *American Chemical Society*, Washington D.C, p 260.

Calemma, V., Iwanski, P., Nali, M., Scotti, R. and Montanari, L. (1995). Structural Characterization of Asphaltenes of Different Origins. *Energy and Fuels*. **9**, 225–230.

Concawe's, PP/Analytical Information Task Force (2012). REACH- Analytical Characterization of Petroleum UVCM Substances. www.concawe.org. 118pp.

del Rio, J. C, Martin, F., Gonzalez-Vila, F. J. and Verdejo, T. (1995). Chemical Structural Investigation of Asphaltenes and Kerogens by Pyrolysis-Methylation. *Organic Geochemistry* **23,** (11–12), 1009–1022.

Galoppini, M. (1994). Asphaltene Deposition Monitoring and Removal Treatments: An Experience in Ultra Deep Wells. In: SPE Paper 27622, p 10.

Groenzin, H. and Mullins, O. C. (1999). Asphaltene Molecular Size and Structure. *Journal Physical Chemistry A.* **103**, (50), 11237–11245.

Hammami, A., Chang-Yen, D., Nighswander, J. A.and Stange, E. (1995). An Experimental Study of the Effect of Paraffinic Solvents on the Onset and Bulk Precipitation of Asphaltenes. *Fuel Science Technology International*. **13,** (9), 1167–1184.

Khadim, M., Sarbar, M. (1999). Role of Asphaltene and Resin in Oil field Emulsion. *Journal of Petroleun Science and Engineering*. **23**:213–221

Kokal, S. L. and Sayegh, S. G. (1995) . Asphaltenes: The Cholesterol of Petroleum. In: SPE Paper 29787, 169–181.

Li, M., Xu, M., Ma, Y., Wu, Z. and Christy, A. A. (2002). The Effect of Molecular Parameters on the Stability of Water-in-Crude Oil Emulsions Studied by IR and UV Spectroscopy: A Physicochemical and Engineering Aspect. *Colloids and Surfaces*, [online], **197**, 193-201.

Ma, A. Zhang, S. and Zhang, D. (2008). Ruthenium-Ion-Catalyzed Oxidation of Asphaltenes of Heavy Oils in Lunnan and Tahe Oilfields in Tarim Basin, NW China. *Organic Geochemistry* **39**(11):1502–1511.

Mojelsky, T. W., Ignasiak, T. M., Frakman, Z., McIntyre, D. D., Lown, E. M., Montgomery, D. S and Strausz, O. P. (1992). Structural Features of Alberta Oil Sand Bitumen and Heavy Oil Asphaltenes. *Energy and Fuels*. **6**, (1), 83–96

Muhammad, A. B. (2015) Thermal Evolution of Aliphatic and Aromatic Moieties of Asphaltenes from Coals of Different Rank: Possible Implication to the Molecular Architecture of Asphaltenes. *China Journal of Geochemistry.* doi:10.1007/s11631-015-0041-y. **34**, (3), 422–430.

Muhammad, A. B. (2009). The Molecular Composition and Geochemical Applications of Asphaltenes. PhD Thesis, Newcastle University, UK, 199pp.

Muhammad, A. B. and Abbott, G. D. (2013). The Thermal Evolution of Asphaltene-bound Biomarkers from Coals of different Rank: A Potential Information Resource During Coal Biodegradation. *International Journal of Coal Geology*. **107**:90–95.

Mullins, O. C. (2009). Rebuttal to Strausz et al. Regarding Time-Resolved Fluorescence Depolarization of Asphaltenes. *Energy and Fuels*, **23,** 2845–2854.

Mullins, O. C., Sabbah, H., Eyssautier, J., Pomerantz, A. E., Barre, L., Andrews, A. B., Ruiz-Morales, Y., Mostowfi, F., McFarlane, R., Goual, L., Lepkowicz, R., Cooper, T., Orbulescu, J, Leblanc, R. M., Edwards, J. and Zare, R. N. (2012). Advances in Asphaltene Science and the Yenmullins Model. *Energy Fuels*. **26**(7):3986–4003.

Pavia, D. L., Lampman, G. M. and Kris, G. S. (2001). Introduction to Spectroscopy: A Guide for Students of Organic Chemistry. USA: Thomson Learning, 680pp.

Peng, P., Fu, J., Sheng, G, Morales-Izquierdo , A., Lown, E. M. and Strausz, O. P. (1999). Ruthenium-Ions-Catalyzed Oxidation of an Immature Asphaltene: StructuralFeatures and Biomarker Distribution. *Energy and Fuels* **13,** (2), 266–277.

Peng, P., Morales-Izquierdo, A., Hogg, A. and Strausz O. P. (1997). Molecular Structure of Athabasca Asphaltene: Sulfide, Ether, and Ester Linkages. *Energy and Fuels* **11,** (6), 1171–1187.

Peters, K. E. (1986). Guidelines for Evaluating Petroleum Source Rock Using Programmed Pyrolysis. AAPG Bull **70**:318–329.

Sabbah, H., Morrow, A. L., Pomerantz, A. E. and Zare, R. N. (2011). Evidence for Island Structures as the Dominant Architecture of Asphaltenes. *Energy Fuels*, **25**(4):1597–1604.

Shedid, S. A., Zekri, A. Y. (2006). Formation Damage Caused by Simultaneous Sulfur and Asphaltene Deposition. In: SPE Paper 86553, 58–64.

Sheu, E. Y. (2002). Petroleum Asphaltene-Propertiesm, Characterization, and Issues. *Energy Fuels* 16(1):74–82.

Sheu, E. Y. and Mullins, O. C. (eds) (1995). Asphaltenes: Fundamentals and Applications. Plenum Press, New York, P245.

Silverstein, R. M. and Webster, F. X. (1998). Spectrometric Identification of Organic Compounds. New York: John Wiley and Sons, Inc., 495pp.

Solli, H. and Leplat, P. (1986). Pyrolysis-Gas Chromatography of Asphaltenes and Kerogens from Source Rocks and Coals–A Comparative Structural Study. *Organic Geochemistry* **10**(1–3):313–329.

Speight, J. G. (2004). Petroleum asphaltenes—Part 1: Asphaltenes, Resins and the Structure of Petroleum. *Oil Gas Science Technology*. **59,** (5), 467–477.

Strausz, O. P., Mojelsky, T. W., Lown, E. M., Kowalewski, I. and Behar, F. (1999). Structural Features of Boscan and Duri Asphaltenes. *Energy and Fuels*. **13**, (2), 228–247.

Strusz, O. P., Safarik, I., Lown, E. M. and Morales-Izquierdo, A. (2008). A Critique of Asphaltene Fluorescence Decay and Depolarization Based Claims about Molecular Weight and Molecular Architecture. *Energy and Fuels* **22** (2),1156–1166.

Trifilieff, S., Sieskind, O. and Albrecht, P. (1992). Biological Markers in Petroleum Asphaltenes: Possible Mode of Incorporation. In: Moldowan, J. M., Albrecht, P. and Philp, R. P. (eds). Biological Markersin Sediments and Petroleum. Prentice Hall, New Jersey, 350–369.

William, S. (1985). Coal Asphaltenes: A Review. *Fuel Process Technology* **10**(3):209–238.

Wu, Q., Pomerantz, A. E., Mullins, O. C. and Zare, R. N. (2013). Laser-Based Mass Spectrometric Determination of Aggregation Numbers for Petroleum- and Coal-Derived Asphaltenes. *Energy Fuels* **28**(1):475–482.

Yamchi, H. S. (2014). Effect of Refining on Asphaltene Property Distributions. M.Sc Thesis, University of Calgary, Alberta, 218pp.

Yen, T. (1974). Structure of Petroleum Asphaltenes and Its Significance. Energy Sources, Part A: Recovery, *Utilization and Environmental Effects*, **1**, 447 – 463.

STRUCTURAL AND MICROSTRUCTURAL STUDY OF GAMMA RAY-IRRADIATED CO-DOPED BARIUM TITANATE ($Ba_{0.88}Ca_{0.12}Ti_{0.975}Sn_{0.025}O_3$)

Umaru Ahmadu[1], Ahmad Abubakar Soje[2], Abdulwaliyu Bidemi Usman[1],
Auwal Muhammad Musa[3], Kasim Uthman Isah[1]
[1]Department of Physics, Federal University of Technology, P.M.B., 65, Minna, Nigeria
[2]College of Agriculture P.M.B.109, Mokwa, Niger State, Nigeria
[3]Centre for Energy Research and Training (CERT), Zaria, Nigeria

[1]u.ahmadu@yahoo.com
[2]ahmadsoje@gmail.com

Abstract
Barium calcium stannate titanate ($Ba_{0.88}Ca_{0.12}Ti_{0.975}Sn_{0.025}O_3$) ceramics, synthesized by solid state reaction method and sintered at 1100 °C/3 h, were exposed to gamma radiation dose of up to 1 kGy using a Cs-137 irradiation source at a dose rate of 100.46Gy/h. Structural analysis of the ceramics indicated a tetragonal perovskite crystalline structure for both pristine and irradiated ceramics with a minor secondary phase. However, slight changes of the lattice parameters and average crystallite size were observed for the irradiated samples. The lattice aspect ratio of the tetragonal phase (c/a) for the pristine ceramics was 1.0022 which decreased by 0.22% at maximum irradiation dose. Irradiation also causes some microstructural changes and slight decrease in grain size. Energy dispersive spectroscopic investigation of the $Ba_{0.88}Ca_{0.12}Ti_{0.975}Sn_{0.025}O_3$ showed small variation in its chemical composition as gamma radiation dose is increased.

Keywords: ceramics, gamma radiation, grain size, lattice parameters, surface morphology

1. Introduction
Barium titanate ($BaTiO_3$ or BT) has been used in capacitors, ultrasonic transducers, pyroelectric infrared sensors, and positive temperature coefficient (PTC) resistors (Fisher *et al.*, 2013; Sheela *et al*, 2010). BT is in ferroelectric perovskite (ABO_3) tetragonal phase from room temperature up to the Curie temperature (Tc,120 °C) (Fratini *et al.*, 2012) above which it transforms to paraelectric-cubic phase (Sheela *et al*, 2010). However, there are few drawbacks, such as low piezoelectric constants and structural phase transformations at low temperatures which limit the extensive application of the pure BT in piezoelectric devices (Aksel *et al*., 2010).

2. Literature Review
In recent years, there have been several attempts at improving its structural stability alongside other properties, such as ferroelectric and dielectric constants (Cai *et al*., 2011, Chen *et al*., 2012, Lijuan *et al*., 2013, Choudhury *et al*., 2008, Dash *et al*., 2014 Rao *et al*., 2013, Kim *et al*., 2009, Saikat *et al*., 2013, Kumar *et al*., 2009 and Dughaish *et al*., 2013).
Such attempts include the substitution of Ba^{2+} or Ti^{4+} by atoms of different sizes and oxidation states resulting in compounds of different physical and chemical properties, while still retaining the same structural phase (Chen *et al*., 2012, Lijuan *et al*., 2013, Choudhury *et al*., 2008, Dash *et al*., 2014, Rao *et al*., 2013, Kim *et al*., 2009, Saikat *et al*., 2013, Kumar *et al*., 2009, Dughaish *et al*., 2013, and Vitayakorn *et al*., 2016). The substitution on the A-site of BT (Ba^{2+}) by Ca^{2+} by up to 0.12mol prevents grain growth, improves electromechanical properties, structural stability (Choi *et al.*, 2010, Paunovic *et al*., 2004, and Matsuura *et al*., 2014) and decreases dielectric constant (Vitayakorn *et al*., 2016, Choi *et al*., 2010., and Paunovic *et al.*, 2004). On the other hand, substitution of the B-site (Ti^{4+}) by Sn^{4+} (0.025mol) increases permittivity and piezoelectric properties, but decreases the Tc (Nath and Medhi, 2012). Therefore, it is expected that simultaneous substitutions of Ba^{2+} by Ca^{2+} and Ti^{4+} by Sn^{4+} could lead to a piezoelectric ceramics having high permittivity, improved piezoelectric properties and structural stability.
Barium titanate-based materials have potential applications in nuclear radiation environments such as sensors in nuclear reactors, particle accelerators, detectors, space ship and satellites, among others (Medhi and Nath, 2013). The properties of such materials used in the fabrication of devices deployed in these environments should not be affected by nuclear radiation. Nuclear radiations, particularly gamma rays are of significant concern because they readily penetrate through protective shielding. The ionizing effect of gamma radiation may alter the structurally dependent properties of materials and hence their performance. The magnitude of such changes is largely dependent on radiation parameters such as linear energy transfer, dose and energy, nature of the material and its structural phase (Ogundare *et al*., 2016). However, the semiconducting and dielectric properties of BT ceramics have been found to depend on grain size and phase content (Hsiang *et al.*, 1996).
Recently, it was reported that structural properties of BT-based ceramics were altered on exposure to gamma radiation dose of up to 200Gy (Medhi and Nath, 2013, Nath and Medhi 2015) with subsequent decrease in grain size. Moreover, works on higher gamma ray exposure (dose) of BT-based ceramics is sparse in literature and extensive literature survey has revealed that so far, no work has been reported on gamma ray irradiated $Ba_{0.88}Ca_{0.12}Ti_{0.975}Sn_{0.025}O_3$ ceramics to the best of our knowledge. This work therefore aims to study the effect of gamma radiation on the microstructure of $Ba_{0.88}Ca_{0.12}Ti_{0.975}Sn_{0.025}O_3$ ceramics which might provide information on the stability of BT based devices for applications in space and radiation environments.

3. Methodology

$Ba_{0.88}Ca_{0.12}Ti_{0.975}Sn_{0.025}O_3$ (BCST) ceramics has been synthesized by solid state reaction method. Appropriate proportion of analytical grade $BaCO_3$ (≥99%, Kermel, China), TiO_2 and $CaCO_3$ (99.9%, Qualikems, India) and SnO_2 (99.99%, BDH, UK) were manually mixed thoroughly in an agate mortar and distilled water was added to the mixture to form a slurry in order to prevent selective sedimentation of the reagents. The slurry was dried in an oven at 150 °C for 1 hour and hand-ground using an agate mortar and pestle for about 4 hours to achieve homogeneity of the mixture. The homogenous mixture was placed in an alumina crucible and calcined at 1050 °C for 4 hours in a furnace to allow volatilization of bye-product, CO_2. The powder was further crushed for 1 hour and ground by adding 4wt% polyvinyl alcohol (PVA) as a binder before forming pellets. The pellets with diameter and thickness of 26mm and 1mm, respectively, were obtained at a pressure of 10 tons using a MiniPal4 Pw 4025/47B palletizing machine. The pellets were sintered at 1100 °C for 3 hours, and furnace-cooled for crystal phase formation. The sintered pellets were irradiated with gamma ray doses of 0.1, 0.3, 0.5, 0.7 and 1 kGy (the samples were labelled as BCST-0.1, BCST-0.3, BCST-0.5, BCST-0.7 and BCST- 1, respectively) using a Cesium-137 (Cs-137) irradiation source at a dose rate of 100.46Gy/h.

X-ray diffractometer (D8 Advance, Bruker AXS,40 kV,40mA) with monochromatic Cu-K_α (λ=1.54060Å) was used to characterize the structural phase composition of the pristine and irradiated ceramics. The instrument was operated in a step scan mode of size 0.034° and counts were accumulated for 88 s at each step for 2θ angles ranging from 20° to 90°. The ceramics were positioned on an aluminium stage with the aid of carbon adhesive tape and coated with AuPd (goldpalladium) using a sputter coater. Their surface morphology and elemental compositions were investigated using a high resolution scanning electron microscope (HRSEM, Zeiss) coupled with an EDS spectrometer. The HRSEM was operated at a voltage of 20 kV and images captured at 5 kV.

4. Results and Discussion

4.1. *Crystal Structure and Parameters*

Typical X-ray diffraction (XRD) patterns of the synthesized $Ba_{0.88}Ca_{0.12}Ti_{0.975}Sn_{0.025}O_3$ (BCST) ceramics at room temperature and irradiated with varying gamma ray doses are shown in Fig. 1. The prominent peaks in the XRD spectra correspond to the tetragonal phase of $BaTiO_3$ and matches well with JCPDS No. 00-005-0626 data. The XRD patterns are in agreement with reports of other groups who prepared BT-based ceramics using similar method (Rao *etal*., 2013 and Fasasi *etal*., 2006).

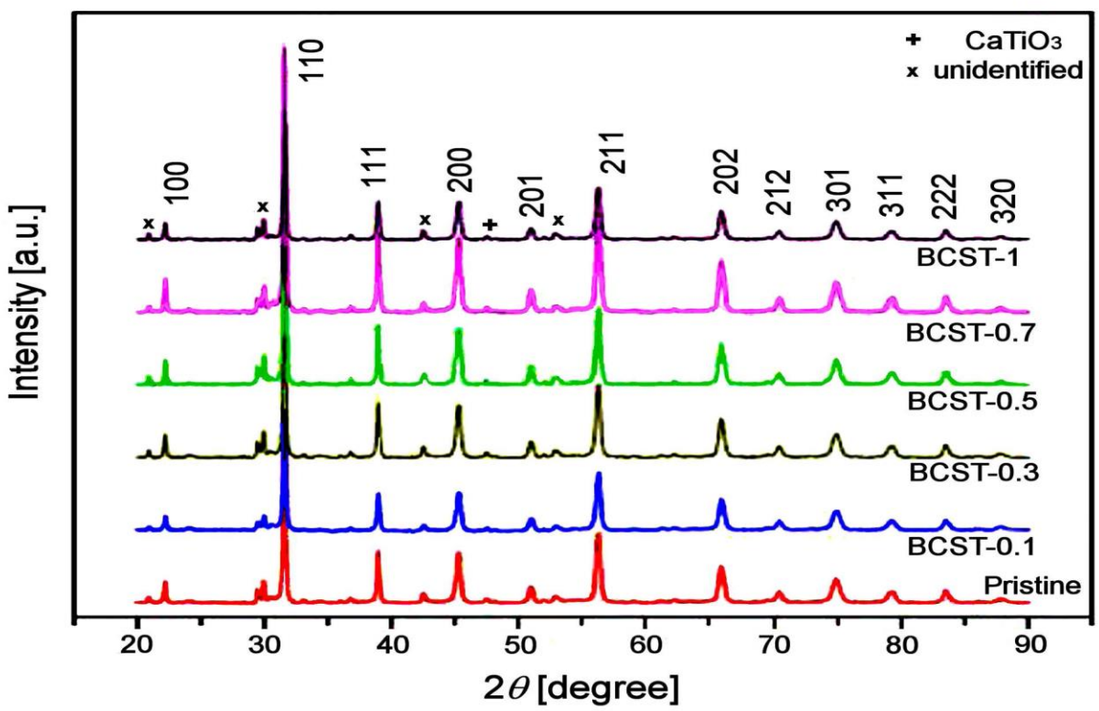

Figure 1. X-ray Diffraction Patterns of Pristine and Irradiated BCST Ceramic

Table 1. XRD Data (2θ Position (200), *d*-Spacing and FWHM) for the Peak 200 of Pristine and Irradiated BCST Ceramic

Sample	2θ	d-Spacing	FWHM
BCST	45.261	2.0019	0.410
BCST-A	45.285	1.9884	0.407

BCST-B	45.266	2.0017	0.418
BCST-C	45.278	2.0012	0.405
BCST-D	45.276	2.0013	0.397
BCST-E	45.270	2.0029	0.391

However, a minor peak around 47.5° 2θ can be observed and identified as orthorhombic $CaTiO_3$ phase (JCPDS file No. 00-022-0153). There were other diffraction peaks though with very low intensities whose match could not be found as indicated in the XRD spectra. The XRD pattern of the irradiated ceramics suggests a consistent phase and composition with the pristine sample. This corroborates the fact that gamma radiation does not change the perovskite structure of barium titanate based ceramics. Similar observations have been reported previously (Medhi and Nath, 2013, Nath and Medhi 2015).

Table 1 gives a quantitative analysis of the peak positions and parameters of the XRD patterns where the d values were obtained experimentally. It is observed that as the irradiation dose increases the structure sensitive XRD peak 200 slightly shifts towards higher 2θ angles. This can be discerned from the raw XRD data (not shown). Similar pattern has been observed when the A site of a typical ABO_3 structure is partially replaced by ions of smaller size (Chen *etal*., 2012, and Yun *etal*., 2007) and leads to distortion of the ABO_3 unit cell lattice (Chen *etal*., 2012) together with changes in the lattice parameters. Therefore, the slight shift of peaks to higher angles may be attributed to A-site defects due to the energetic gamma ray.

The average crystallite sizes (D) of the pristine and irradiated ceramics were calculated using the full width at half maximum (FWHM) of the most intense peak by the Scherrer formula (Dash *etal.*, 2014):

$$D = 0.9\lambda/\beta cos\theta \qquad (1)$$

where β is the FWHM of the diffraction peak in radians, θ the Bragg diffraction angle, λ the wavelength of the X-ray used and D the average crystallite size.

The calculated average crystallite size of the pristine ceramic is found to be approximately 38 nm. It can be seen from the plot of β and D versus irradiation dose (Fig. 2) that β values of the pristine increased while D values decreased on exposure to lower dose (up to 0.5 kGy). However, on further increasing the dose up to 1 kGy, β and D appear to be almost the same with the corresponding values for the pristine sample.

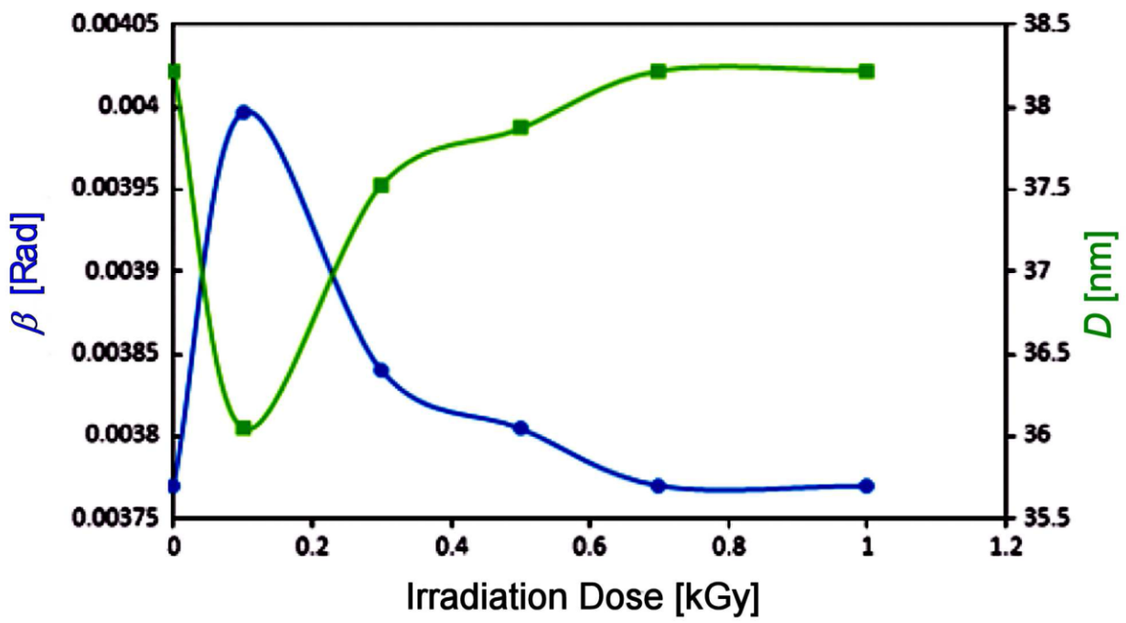

Figure 2. Variation of β and D against Irradiation Dose

Lattice parameters a and c of the pristine and irradiated ceramics were calculated from the XRD spectra using 100, 200 and 201 diffraction peaks. The calculated lattice aspect ratio of tetragonal phase (c/a = 1.0022) indicates a weak tetragonality of the pristine BCST ceramics in comparison with the referenced JCPDS data of BaTiO3 (c/a = 1.0110) prepared at higher temperature. Plot of lattice parameters (a and c) and c/a against irradiation dose is shown in Fig. 3. As can be seen, both a and c parameters are slightly changed, resulting in an increase of c/a ratio on exposure to lower irradiation dose (0.1 kGy). However, a value remained almost unchanged while the c values slightly decreased and consequently c/a ratio decreased with further increase in the irradiation dose. These results indicate a decrease in tetragonality of the perovskite structure of BCST ceramics upon gamma exposure. The variations in the lattice parameters can be understood in terms of the energy exchange between the gamma ray and

the lattice sites of some host atoms thereby leading to lattice distortion. This is consistent with the slight shift in peak positions to higher 2θ values. The increase in tetragonality is desirable in perovskite titanates because it increases polarizability and consequently leads to improved ferroelectric properties (Mady *etal*., 2011). However, the observed changes indicate on higher tendency towards phase transformation in the BCST ceramics on exposure to higher gamma irradiation dose (up to 1 kGy). Thus, it is expected that irradiation would ensue deterioration in ferroelectric properties of the BCST ceramics.

The unit cell volume is another structural parameter that can be used to indicate change in the structure of a crystal (Hsiang *etal*., 1996).The cell volume of the pristine ceramics was found to be 64.20Å^3. After gamma ray exposure, there were slight decreases of the cell volume. This is also consistent with the fact that energetic gamma rays possess the ability of ionizing the atoms of a material thereby resulting in electron-hole pairs. The observed decrease of the cell volume is corroborated by the slight shift of the XRD peak 200 toward higher angles with increasing gamma irradiation.

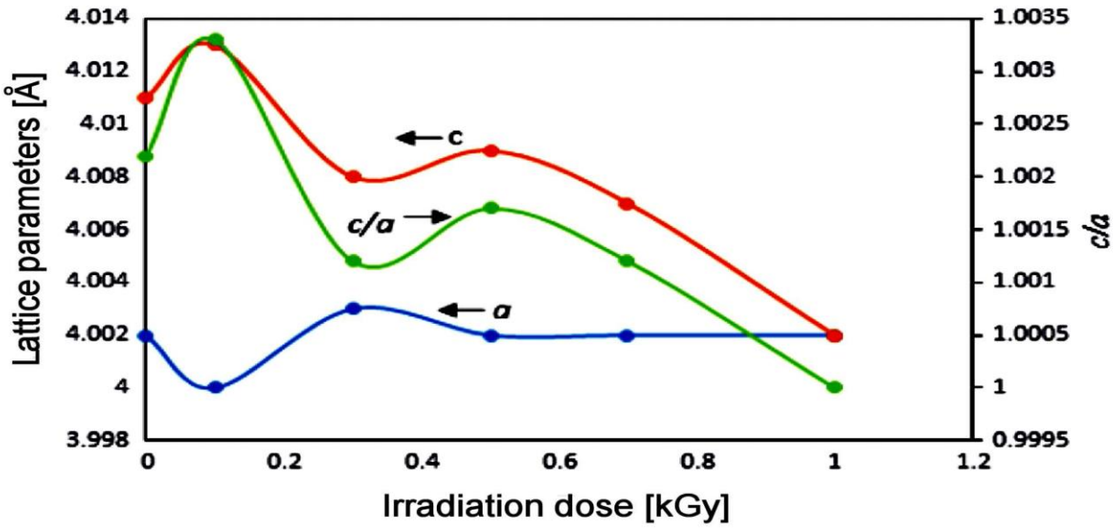

Figure 3. Variation of Lattice Parameters (a and c) and c/a Versus Irradiation Dose

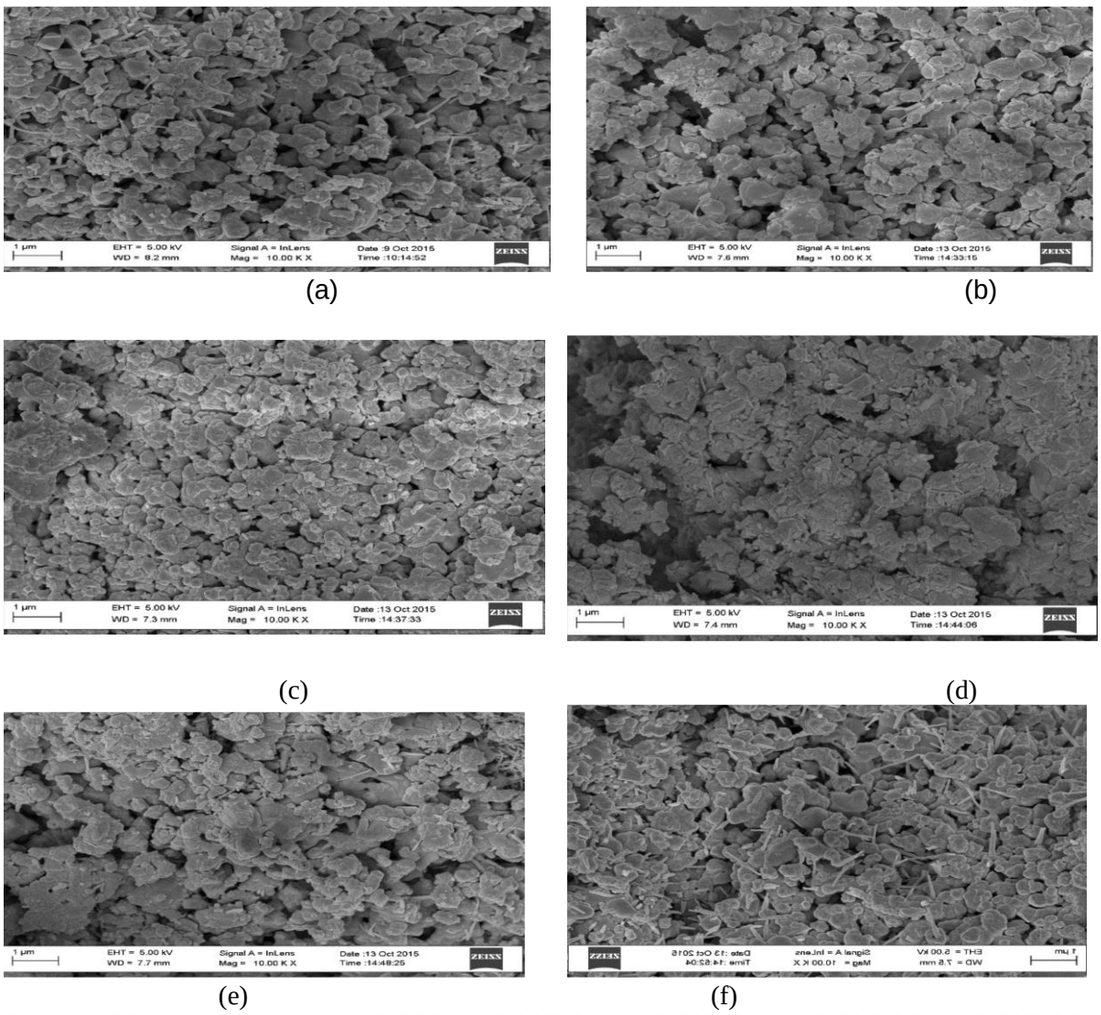

(a) (b)

(c) (d)

(e) (f)

Figure 4. SEM Micrograph of: (a) BCST, (b) BCST-0.1, (c) BCST-0.3, (d) BCST-0.5, (e) BCST-0.7 and (f) BCST-1

Figure 5. Variation of Average Grain Size with Irradiation Dose

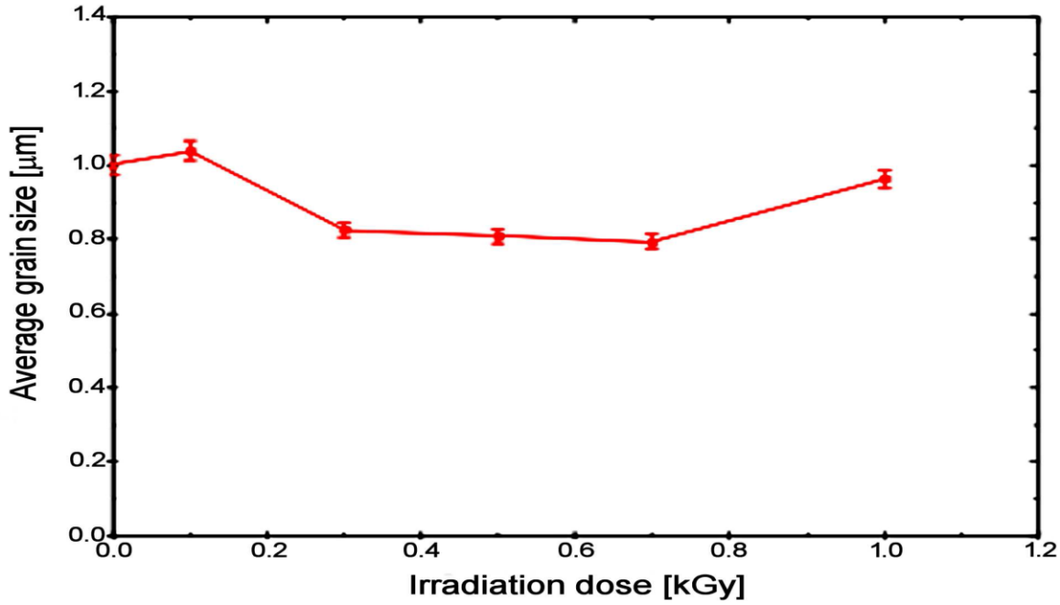

4.2.

Microstructural Analysis

Microstructural characterization of the pristine and irradiated BCST ceramics is depicted in Fig. 4. As can be seen from SEM micrograph of the pristine ceramics (Fig. 4a), there is non uniform distribution of grains. The pristine BCST ceramics contains two distinguishable microstructural features: i) a portion of agglomerates and some fairly fine grained microstructure and ii) a small portion of rod-like grains which could be attributed to rich Ca^{2+} regions necessitated by insufficient homogenization of the starting precursors (Paunovic *etal*., 2004). Further, the presence of some residual porosity is also evident. The average grain size as determined using ImageJ software is approximately 1.0 µm based on 100 grains. It is known that the initial powder preparation process and sintering temperature could result in inhomogeneous microstructure.

SEM micrographs reveal that gamma ray affects microstructure of the BCST ceramics, especially in the aspect of distribution of grain and average grain size (Fig.4). Thus, in the samples irradiated with lower gamma ray doses (0.1 to 0.7 kGy) rod-like grains are less visible and harder agglomeration of grains become more evident (Fig. 4). However, further increase in the irradiation dose (1 kGy) results in formation of BCST structure with higher portion of rod-like grains and fairly fined-grained microstructure (Fig. 4f). This result suggests that irradiation dose at this level affects the uniformity of the composition thereby leading to segregation in local part of the ceramic.

The determined average grain sizes of the irradiated samples are depicted in Fig. 5. As can be seen there is a small variation in the average grain. These variation in the average grain size could be due to fractured grains as a result of irradiation effect. The average grain size slightly increased after exposure to lower dose (0.1 kGy), but with further increase of irradiation dose thegrainsizedecreases.

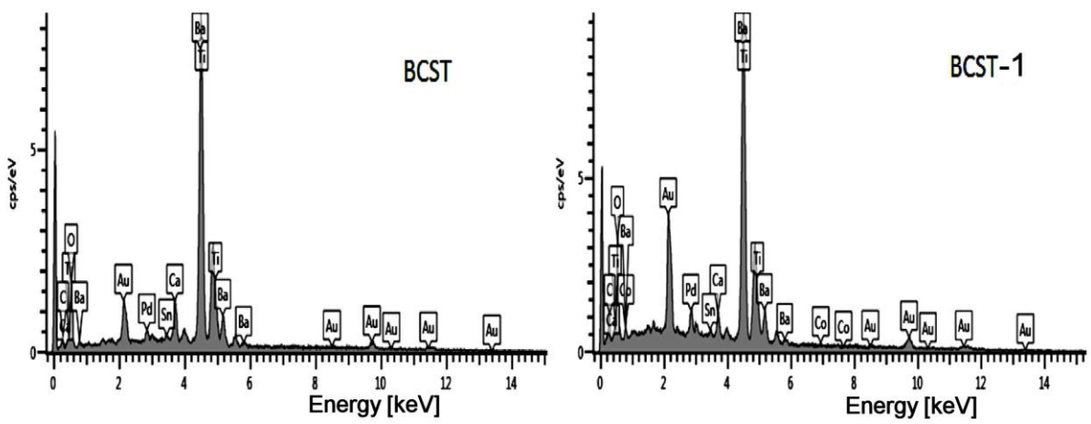

Figure 6. EDS Spectra of (a) Pristine BCST and (b) BCST-1 Ceramics

This result indicates that the average grain size of the BCST ceramics does not change considerably upon gamma ray exposure of up to 1 kGy and is contrary to some literature data (Medhi and Nath, 2013 and Nath and Medhi, 2014). However, grain size is closely connected with ferroelectric and piezoelectric properties of BT-based ceramics (Nath and Medhi, 2014). Ferroelectric and piezoelectric properties decrease when grain size decreases.

Thus, slight degradation of ferroelectric and piezoelectric properties is expected for the prepared BCST ceramic within the range of studied doses.

Table 2 Elemental Composition, Nominal Composition, Normalised EDS Derived Composition of Pristine and Irradiated BCST Ceramics

Samples	Ba	Ca	Sn	Ti	O	Total	Ba	Ca	Ti	Sn	O	Al	Co	Total
BCST	17.60	2.4	0.5	19.50	60	100.00	22.31	4.7	0.4	26.64	45.95	0.97	-	100
BCST-0.1	17.60	2.4	0.5	19.50	60	100.00	19.03	4.7	22.83	0.39	52.89	-	-	100
BCST-0.3	17.60	2.4	0.5	19.50	60	100.00	22.54	4.13	24.25	0.57	46.71	1.82	-	100
BCST-0.5	17.60	2.4	0.5	19.50	60	100.00	18.34	6.98	21.55	0.50	52.64	-	-	100
BCST-0.7	17.60	2.4	0.5	19.50	60	100.00	24.30	2.87	27.00	0.72	45..12	-	-	100
BCST- 1	17.60	2.4	0.5	19.50	60	100.00	19.3	2.19	22.29	0.51	55.52	0.18	0.24	100

4.3. *Chemical Composition*

Figure 6 depicts the EDS spectra showing the elemental composition of the pristine BCST ceramics. All of the peaks have been identified with the potential elements that match that peak. The spectra clearly indicate the presence of Ba, Ca, Ti, Sn, O, C, Au and Pd. The carbon (C) source could be traced to the carbon tape and AuPd (gold-paladium) is present in the compound in order to make it conducting.
Table 2 gives a quantitative comparison between the nominal and the normalized EDS derived composition of the pristine and irradiated BCST ceramics, where the major sources of error were removed and the remaining elements normalized to 100% to give a better relative representation of the remaining elements present in the material. However, trace amount of Al and Co were evident in the samples irradiated with 0.3 and 0.1 kGy, respectively. The presence of Al could be attributed to contamination during the processing of the material for SEM analysis and the presence of Co is not understood at present. The fluctuations in the normalized EDS derived composition in comparison with the nominal composition could be attributed to deficiency of oxygen during sintering in the ambient and difficulties in achieving macroscopic uniformity in solid state reaction method (Badapanda *et al*., 2010). A significant overlap for Ba and Ti is obvious in the spectra and makes it difficult to differentiate between them in the quantification results and this has been already reported (Korkmaz *et al*., 2012).

5. Conclusions

$Ba_{0.88}Ca_{0.12}Ti_{0.975}Sn_{0.025}O_3$ ceramics, prepared by solid state reaction and sintering at 1100 °C/3 h, were exposed to gamma radiation dose of up to 1 kGy. The pristine BCST ceramics has polycrystalline tetragonal structure with minor impurity $CaTiO_3$ phase. Gamma irradiation does not change the perovskite structure, but the structure sensitive 200 peak was found to shift to higher 2θ angles with increase in irradiation dose. It was also observed that the crystallite size decreases on exposure to irradiation dose up to 0.5 kGy and is almost the same with further increase of dose up to 1 kGy. XRD analysis indicates on decrease in the tetragonality of the perovskite BCST structure upon gamma irradiation, which is expected to lead to deterioration in the ferroelectric properties. The microstructure of the pristine BCST ceramics is characterized by agglomerates, rod-like grains and porosity with an average grain size of ~1.0 μm. In the samples irradiated with lower gamma dose (0.1 to 0.7 kGy) rod-like grains are less visible compared to those irradiated with higher dose (1 kGy).
It was observed that the average grain size of the BCST ceramics does not change appreciably upon gamma irradiation of up to 1 kGy. However, a slight degradation in ferroelectric and piezoelectric properties is expected.

References

Aksel, E and Jones, J. L. (2010), Advances in Lead-Free Piezoelectric Materials for Sensors and Actuators, *Journal of Sensors*, Vol. 10, 1935-1954.

Badapanda, T. (2010), Structural, Electrical and Optical Study of 'A' Site Deficient Heterovalent Ion Doped Barium Zirconium Titanate Perovskite. Doctoral Thesis *National Institute of Technology*, Rourkela-769008, Orissa India, 6-58.

Cai, W., Fu1, C. L., Gao, J. C., and Zhao, C. X. (2011), Dielectric Properties and Microstructure of Mg Doped Barium Titanate Ceramics, *Journal of Advances in Applied Ceramics*, Vol. 110 (3), 181 – 185.

Chen, Z. and Yuan-Fang, Q.U. (2012), Dielectric Properties and Phase Transitions of La2O3- and Sb2O3-Doped Barium Strontium Titanate Ceramics, *Transition of Nonferrous Meterial Society China,* Vol. 22, 2742–2748.

Choi, Y. K., Hoshina, .T., Takeda, H., and Tsurumi, T. (2010), Effects of Ca and Zr Additions and Stoichiometry on the Electrical Properties of Barium Titanate-Based Ceramics, *Journal of the Ceramic Society of Japan*, Vol. 118(10), 881-886.

Choudhury, S., Akter, S., Rahman, M.J., Bhuiyan, A.H. Rahman, S.N., Khatun, N., and Hossain, M.T. (2008), Structural, Dielectric and Electrical Properties of Zirconium Doped Barium Titanate Perovskite, *Journal of Bangladesh Academic of Sciences*, Vol. 32, 151–159.

Dash, S.K., Kant, S., Danlai, B., Swain, M.D., and Swain, B.B. (2014), Characterization and Dielectric Properties of Barium Zirconium Titanate Prepared by Solid State Reaction and High Energy Ball Milling Processes, *Indian Journal of Physics*, Vol. 88(2),129–135

Dughaish, Z. H. (2013), Dielectric Properties of $(BaTiO_3)_{(1-x)}$ $(SnO_2)_x$ Ceramics, *Journal of Natural Sciences and Mathematics Qassim University*, Vol. 6(2), 107-121.

Fasasi, A.Y., Balogun, F. A., Fasasi, M. K., Ogunyele, P. O., Mokobia, C.E., and Inyang, E.P. (2006), Thermoluminescence Properties of Barium Titanate Prepared by Solid-State Reaction, *Journal of Science Direct Sensors and Actuators* Vol. A 135, 598-604.

Fisher, J.G., Lee, D., Oh J., Kim, H., Nguyen D., Kim, J., Lee, S., and Lee, H. (2013), Low Temperature Sintering of Barium Calcium Zirconium Titanate Lead-Free Piezoelectric Ceramics, *Journal of Korean Ceramic Society*, Vol. 50(2), 157–162.

Frattini, A., Di Loreto, A., de Sanctis, O., and Benavidez, E. (2012), BCZT Ceramics Prepared from Activated Powders, *Procedia Material Sci*ence, Vol. 1, 359–365.

Hsiang, H.I., Yen, F.S., and Chang, Y.H. (1996), Effects of Doping with La and Mn on the Crystallite Growth and Phase Transition of BaTiO3 Powders, *Journal of Material Sciences*, Volume 31, 2417–2424.

Kim, Y. J., Hyun, J.W., Kim, H.S., Lee, J.H., Yun, M.Y., Noh, S.J., and Ahn, Y. H. (2009), Microstructural Cheracterization Dielectric Properties of Barium Titanate Solid Solutions with Donor Dopants, *Bull Korea Chemistry Soc*iety, Vol. 30(6), 1267-1273.

Korkmaz, E. and Kalaycioglu N.O. (2012), Synthesis and Luminescence Properties of $BaTiO_3$: RE (RE=Gd,$^{3+}$Dy,$^{3+}$Tb,$^{3+}$Lu,$^{3+}$) Phosphors. *Bull Material Sciences*, Vol. 35(6), 1011-1017.

Kumar, Y., Mohiddon, M. A., Srivastava, A., and Yadav, K. L. (2009), Effect of Doping on Structural and Dielectric Properties of $BaTiO_3$, *Indian Journal of Engineering and Materials Sciences*, Vol. 16, 390-394.

Lijuan, Z., Lihai, W., Jiandang, L., Bin, C., Minglei, Z., and Bangjiao., Y. (2013), Dielectric Properties and Structural Defects in $BaTi_{1-x}Sn_xO_3$ Ceramics, 16th International Conference on Positron Annihilation (ICPA-16), *Journal of Physics*, Conference Series 443,012014.

Mady, H.A. (2011), XRD and Electric Properties of Lead Barium Titanate Ferroelectric Ceramic, *Australian Journal of Basic Applied Sciences*, Vol. 5 (10), 1472–1477.

Matsuura, K., Hoshina, T., Takeda, H., Sakabe, Y., and Tsurumi, T. (2014), Effects of Ca Substitution on Room Temperature Resistivity of Donor-Doped Barium Titanate Based PTCR Ceramics, *Journal of the Ceramic Society of Japan*, Vol. 122(6), 402-405.

Medhi, N. and Nath, A. K. (2013), Gamma Ray Irradiation Effects on the Ferroelectric and Piezoelectric Properties of Barium Titanate Ceramics. *Journal Materials Engineering and Performance (EGJME)*, Vol. 22, 2716-2722.

[a]Nath, A. K. and Medhi, N. (2012), Density Variation and Piezoelectric Properties of $Ba(Ti_{1-x}Sn_x)O_3$ Ceramics Prepared from Nanocrystalline Powders, *Bull. Material Sciences*, Vol. 5(35), 847–852.

[b]Nath, A. K. and Medhi, N. (2015), Effect of Gamma ray Irradiation on the Piezoelectric and Ferroelectric Properties of Bismuth Doped Barium Titanate Ceramics, *Indian Journal of Physics*, Vol. 89(2), 131-136.

Ogundare, F.O. and Olarinoye, I.O. (2016), He^+ Induced Changes in the Surface Structure and Optical Properties of RF-Sputtered Amorphous Alumina Thin films, Journal of Non-Crystal Solids, Vol. 432, 292–299.

Paunovic, V., Zivkovic, L., Vracar, L., Mitic, V., and Milijkovic, M. (2004), Effects of Additive on Microstructure and Electrical Properties of $BaTiO_3$ Ceramics, *Serbian Journal of Electrical Engineering*, Vol. 3(1), 89-98.

Rao, M.V.S., Ramesh, V.K., Rames, M.N.V., and Rao, B.S. (2013), Effect of Copper Doping on Structural, Dielectric and DC Electrical Resistivity Properties of $BaTiO_3$, *Advance Material Physical Chemistry*, Vol. 3, 77–82.

Saikat, M. Mousumi B., Siddhartha M., Singh, P.K. (2013), Synthesis and Characterization of Cobalt Oxide Doped Barium Strontium Titanate, *Jounal of Austral Ceramics Society*, Vol. 49 (1), 79–83.

Sheela. D. and Jha. A. K. (2009), Structural, Dielectric and Ferroelectric Properties of Tungsten Substituted Barium Titanate Ceramics. Asian *Journal of Chemistry*, Vol. 21(10), 117-124.

Vitayakorn, N. (2006), Dielectric Properties of Bismuth Doped Barium Titanate (BaTiO3) Ceramics, Journal of Applied Sciences Resources, Vol. 2 (12), 1319–1322.

Yun, S., Wang X., Li,B., and Xu D. (2007), Dielectric Properties of Ca-Substituted Barium

Strontium Titanate Ferroelectric Ceramics, Journal of Solid State Community, Vol. 143, 461–465.

DESIGN OF STAND-ALONE SOLAR POWER SYSTEM FOR HOUSEHOLD ELECTRIFICATION IN MINNA, NIGER STATE, NIGERIA

Boluwaji M. Olomiyesan
Examination Development Department, National Examinations Council (NECO),
P.M.B. 159, Minna, Niger State, Nigeria.
E-mail: olomiyebolu@yahoo.com
Phone No: +234-806-625-8921

Abstract

The demand for electricity in Nigeria exceeds supply from the national grid. As a result of this many households, businesses and industries rely on generating plants for their power supply. However, there is abundance of sunshine all round the year that is capable of supplying the total energy need of the entire populace if properly tapped. This study focuses on how to harness the abundant solar resources around us for power generation through stand-alone PV system design. Stand-alone PV system for household electrification was designed for Minna using low power consuming appliances. PV Sizing worksheet was employed in the design of the system. The components and cost estimate of the designed systems for one bedroom and three bedrooms apartments were presented. The results show that the initial component cost for the two systems were ₦ 570,000 and ₦ 890,000 respectively.

Keywords: Solar, Sunshine hour, Load, Photovoltaic Sizing Worksheet, Minna

1.0 INTRODUCTION

Energy is one of the basic necessities of man. The socio-economic development of any country depends on the amount of energy consumed. Nigeria is endowed with huge resources of conventional energy resources such as: crude oil, tar sands, natural gas and coal, as well as reasonable amount of renewable energy resources (e.g. hydro, solar, wind and biomass). Currently, Nigeria is producing her electricity from hydro and gas (thermal) stations which are scattered across the country (Adaramola *et al*., 2011). The demand for electricity in the country exceeds supply from the national grid. Nigeria is expected to be generating 30,000 MW of electricity by the end of 2015 (Sambo, 2006). However, the current electricity production within the country is about 4000 MW due to fluctuations in the availability and maintenance of production sources. According to Nigerian energy policy report, it is estimated that the population connected to the grid system is short of power supply by over 60% of the time. Additionally, less than 40% of the population is connected to the grid. Thus, electricity generation is simply not enough to support the entire population (Kennedy *et al*., 2008).

As a result of the fluctuation and irregularity of electricity supply from the national grid many households, businesses and industries rely on generating plants for their power supply. This power source not only causes noise and environmental pollutions, but also contributes to global warming. In order to address this situation, there is an urgent need to explore the vast resources of solar energy around us as a source of clean and sustainable energy. Studies show that Nigeria receives an average solar radiation of about 25.2 $MJm^{-2}day^{-1}$ in the far north and about 12.6 $MJm^{-2}day^{-1}$ in the coastal latitudes (Ileoje, 1997), while the mean global radiation on a horizontal surface in Minna is found to be 20.45 $MJm^{-2}day^{-1}$ (Olomiyesan *et al*., 2014). This indicates that Niger State is one of the states with high insolation in Nigeria. There is abundance of sunshine all round the year, which is capable of supplying the total energy need of the entire populace if properly tapped. Despite this great potential, there is still shortage of electricity for household and industrial use in the state.

Electricity supply in Minna is characterized by load shedding and blackout almost on daily basis. This perennial power problem could be solved if the available solar energy resource in the state is properly harnessed for power generation through photovoltaic energy conversion. Proper design and installation of stand-alone PV systems can guarantee adequate power supply for households and small scale businesses in the state. However, outdoor characterisation of poly-crystalline module in Minna reveals that the design of photovoltaic systems for use in Minna and environs based on the rated performance of the PV module would be appropriate (Oyedum *et al*., 2014). This study focuses on how to harness the abundant solar resources around us for power generation through stand-alone PV system design.

2.0 SOLAR POWER GENERATION

Solar power is the conversion of sunlight into electricity, either directly using photovoltaic (PV) or indirectly using concentrated solar power (CSP). CSP systems use lenses or mirrors and tracking systems to focus a large area of sunlight into a beam. Solar PV technology offers an effective way of converting solar radiation from the sun directly to electricity using the photoelectric effect (Martin and Goswani, 2005).

Photovoltaic or solar cell represents the fundamental power conversion unit of a PV system. Solar cell is made of semiconducting materials that can convert incident radiation in the solar spectrum to electric currents. Solar cells can be classified as either crystalline (mono or poly-crystalline) or thin film (Amorphous Silicon, Copper Indium diselenide, Cadmium Telluride). Crystalline silicon based cells are more common and they have conversion efficiencies of between 15 – 20 percent. Solar cells produce direct current (d.c.) power, which fluctuates with the

intensity of the irradiating light. The cells are usually assembled into modules; the modules can then be connected in paralled-series configuration to form arrays. The number of modules connected together in an array depends on the amount of power output needed. PV technology is one of the fastest growing energy technologies in the world. Since 1993, the implementation of solar PV applications has increased every year. Solar PV application is growing rapidly, albeit from a small base, to a total global capacity of 227 GW at the end of 2015 (REN21, 2016).

2.1 PV System Components

In a PV power system, the solar module is the generator. The other components usually added to the system are called Balance of System (BOS). These include:

Charge controller – This monitors the battery's state-of-charge to ensure the battery is protected from deep discharge and overcharging.

Inverter – This is a device that changes the direct current (d.c.) power produced from the solar module or energy stored in the battery to alternating current (a.c.) power.

Battery – Stores the solar power generated by the modules and discharges the power as needed.

A PV system may not necessarily contain all the components mentioned above. It is designed based on the nature of the load to be powered by the system. Figure 1 shows typical components of a PV system.

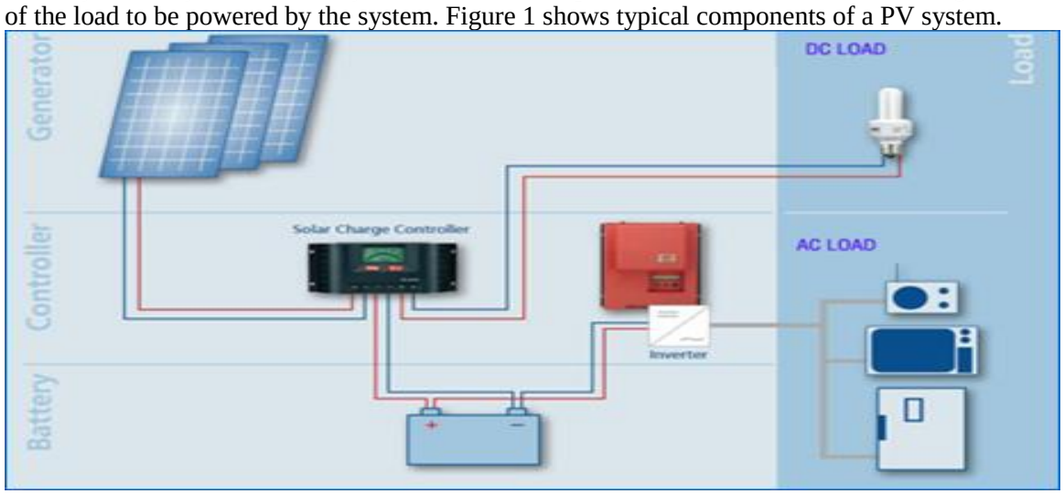

Figure 1: Components of a PV system.

3.0 METHODOLOGY

3.1 Design Considerations

PV systems design are location based, the global solar radiation at the site of interest as well as the energy consumption for the household must be considered for effective system design. In this study, stand-alone PV system sizing worksheet was used to determine the module and battery rating. The design was based on the month with the worst/lowest sunshine hours so that the system can meet the power requirement of the load all round the year. The systems were designed based on an estimate of the daily energy demands for two types of residential home (one-bedroom and three-bedroom flats) in Minna, using low-power consuming appliances. Inverter of 90% efficiency was considered and module selection was based on rated power, efficiency and price. Three days of rain or cloud covers was taking into consideration in the battery sizing. Lead-acid batteries were chosen due to their voltage requirement, cost limitation, ability to store electrical energy and ability to discharge by as much as 80% over thousands of charging and recharging cycles (Quanghuy, 2011).

3.2 Solar Radiation Data of the Site

The availability of solar radiation for solar power generation is dependent on the sunshine hours in any location. The sunshine hours data used in this work were obtained from the Nigeria Meteorological Agency (NIMET) at Minna Airport. The values of the monthly average of sunshine hours for Minna, for two years (2009 - 2010) is shown in Figure 2. This reveals the highest value of 9.7 hours per day in December and lowest value of 4.2 hours per day in July and August.

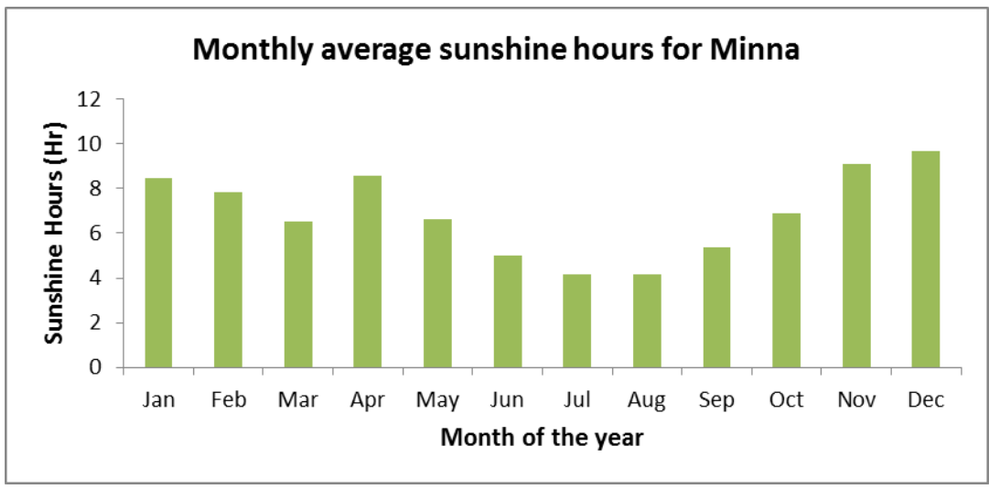

Figure 2: Monthly average sunshine hours for Minna

3.3 PV System Sizing Worksheet

For small systems, sizing worksheet is commonly used in calculating the amount of modules or batteries for particular load requirements. Tables 1 and 2 present the full sizing worksheets for stand-alone photovoltaic systems used for the one-bedroom and three-bedroom apartments respectively. The worksheet is separated into three sections.

The first section, labelled '**A**', represents the household loads. The numbers given under the "Adjusted Power" column take the inverter efficiency of 90% into consideration.

The second section, labelled '**B**', represents the battery sizing. The battery sizing takes into consideration three days of rain or cloud covers.

The third section, labelled '**C**' represents the PV array sizing. The array was designed for the month with the lowest sunshine hours.

Table 1: PV Sizing Worksheet for one-bedroom flat Household Electrification

Location: Minna, Nigeria **Latitude**: 9.37^0

A.	**Loads**				
A1	Inverter efficiency (decimal)				0.90
A2	Battery bus voltage				12 volts
A3	Inverter ac voltage				230 volts
	A4	A5	A6	A7	A8
Appliance	Rated Wattage	Adjustment Factor 1.0 for dc (A1) for ac	Adjusted Wattage (A4/A5)	Hours/day Used	Energy/day (A6×A7)
(5) 18 W bulbs	90	0.9	100	5	500
Television	85	0.9	94.4	3	283.2
(2) 80 W Fans	160	0.9	177.8	3	533.4
Laptops	65	0.9	72.2	2	144.4
Satellite Dish	30	0.9	33.3	3	99.9
DVD/VCD	12	0.9	13.3	2	26.6
(2) 4 W Phone Chargers	8	0.9	8.9	0.5	4.45
TOTAL	450		499.9		1592
A9	Total energy demand per day (Sum of A8)			1592 Watt-hours	
A10	Total amp-hour demand per day (A9/A2)			133 Amp-hours	
A11	Maximum ac power requirement (sum of A4)			450 Watts	
A12	Maximum dc power requirement (sum of A6)			499.9 Watts	

B.	Battery Sizing	
B1	Days o f storage desired/required	3 days
B2	Allowable depth-of discharge limit (decimal)	0.8
B3	Required battery capacity ((A10 × B1) / B2)	499 Amp-hours
B4	Amp-hour capacity of selected battery	200 Amp-hours
B5	Number of battery in parallel (B3 / B4)	3
B6	Number of battery in series (A2 / selected battery voltage)	1
B7	Total number of batteries (B5 × B6)	3
B8	Total battery amp-hour capacity (B5 × B4)	600 Amp-hours
B9	Total battery kilowatt-hour capacity (B8 × A2) / 1000)	7.2 kilowatt-hours
B10	Average daily depth of discharge (.75 × A10 / B8)	0.166

C.	PV Array Sizing	
	Design Tilt (Latitude + 15 degrees): 24.37	**Design Month**: July
C1	Total energy demand per day (A9)	1592 Watt-hour
C2	Battery round trip efficiency (0.70 – 0.85)	0.8
C3	Required array output per day (C1/C2)	1990 Watt-hours
C4	Selected PV module max power voltage at STC (× .85)	15.05 Volts
C5	Selected PV module guaranteed power output at STC	130 Watts
C6	Peek sun hours at design tilt for design month	4.2 hours
C7	Energy output per module (C5 × C6)	546 Watt-hours
C8	Module energy output at operating temperature. (DF × C7) DF = 0.80 for hot climates and critical applications. DF = 0.90 for moderate climates and non-critical applications.	491.4 Watt-hours
C9	Number of modules required to meet energy requirements (C3/C8)	4 modules
C10	Number of module required per string (A2/C4) rounded to next higher integer	1 modules
C11	Number of strings in parallel (C9/C10) rounded to next higher integer	4 strings
C12	Number of modules to be purchased (C10 × C11)	4 modules
C13	Nominal rated PV module output	130 Watts
C14	Nominal rated array output (C13 × C12)	520 Watts

Table 2: PV Sizing Worksheet for three-bedroom flat Household Electrification

A.	Loads	
A1	Inverter efficiency (decimal)	0.90
A2	Battery bus voltage	24 Volts
A3	Inverter ac voltage	230 Volts

	A4	A5	A6	A7	A8
Appliance	Rated Wattage	Adjustment Factor 1.0 for dc (A1) for ac	Adjusted Wattage (A4/A5)	Hours/day Used	Energy/day (A6×A7)
(8) 18 W bulbs	144	0.9	160	5	800
LCD TV	213	0.9	236.7	3	710.1
(4) 80 W Fans	320	0.9	356	3	1068
65 W Laptops	65	0.9	72.2	2	144.4
Satellite Dish	30	0.9	33.3	3	99.9
DVD/VCD	12	0.9	13.3	2	26.6

(3) 4 W Phone Chargers	12	0.9	13.3	0.5	6.7
TOTAL	796		884.8		2855.7

A9	Total energy demand per day (Sum of A8)	2855.7 Watt-hours
A10	Total amp-hour demand per day (A9/A2)	119 Amp-hours
A11	Maximum ac power requirement (sum of A4)	796 Watts
A12	Maximum dc power requirement (sum of A6)	884.8 Watts

B.	**Battery Sizing**	
B1	Days o f storage desired/required	3 days
B2	Allowable depth-of discharge limit (decimal)	0.8
B3	Required battery capacity ((A10 × B1) / B2)	446.3 Amp-hours
B4	Amp-hour capacity of selected battery	200 Amp-hours
B5	Number of battery in parallel (B3 / B4)	2
B6	Number of battery in series (A2 / selected battery voltage)	2
B7	Total number of batteries (B5 × B6)	4
B8	Total battery amp-hour capacity (B5 × B4)	400 Amp-hours
B9	Total battery kilowatt-hour capacity (B8 × A2) / 1000)	9.60 kilowatt-hours
B10	Average daily depth of discharge (.75 × A10 / B8)	0.223

C.	**PV Array Sizing**	
	Design Tilt (Latitude + 15 degrees): 24.37	**Design Month:** July
C1	Total energy demand per day (A9)	2855.7 Watt-hours
C2	Battery round trip efficiency (0.70 – 0.85)	0.8
C3	Required array output per day (C1/C2)	3569.6 Watt-hours
C4	Selected PV module max power voltage at STC (× .85)	25.33 Volts
C5	Selected PV module guaranteed power output at STC	300 Watts
C6	Peek sun hours at design tilt for design month	4.2 hours
C7	Energy output per module (C5 × C6)	1260 Watt-hours
C8	Module energy output at operating temperature. (DF × C7) DF = 0.80 for hot climates and critical applications. DF = 0.90 for moderate climates and non-critical applications.	1134 Watt-hours
C9	Number of modules required to meet energy requirements (C3/C8)	4 modules
C10	Number of module required per string (A2/C4) rounded to next higher integer	1 modules
C11	Number of strings in parallel (C9/C10) rounded to next higher integer	4 strings
C12	Number of modules to be purchased (C10 × C11)	4 modules
C13	Nominal rated PV module output	300 Watts
C14	Nominal rated array output (C13 × C12)	1200 Watts

The total energy demand per day for an average one-bedroom flat is 1.59 kWh, with as much as 450 W being drawn at once if all the appliances are in use, while the total energy demand per day for an average three-bedroom apartment is 2.86 kWh, with as much as 884.8 W being drawn at once if all the appliances are in use.

The inverter was selected based on the total power requirement of all the loads that can be run simultaneously, while the charge controller was chosen on the basis of its ability to handle the maximum current produce by the PV array.

From the design above, a one-bedroom flat apartment with a load estimate of 450 W will require a PV power system that comprises of: 520 W PV array, a charge controller (45 A), battery bank (600 Ah) and 1 kVA inverter, while a three-bedroom flat apartment with a load estimate of 884.8 W will require a PV power system comprising of: 1200 W PV array, a charge controller (45 A), battery bank (800 Ah) and 2 kVA inverter.

3.4 COST ANALYSIS THE PV SYSTEMS

The cost analysis for powering all the appliances in one-bedroom flat and three-bedroom flat using solar power based on the design above is presented in Tables 3 and 4 respectively. The components for each system were selected from the list of available models based on their capacity and price considerations. The estimate represents the components cost of the PV systems.

Table 3: Cost estimate of powering one-bedroom flat with solar modules

Component	Capacity	Quantity	Unit Price (₦)	Total Price (₦)
Solar Panel	130 W	4	40,000	160,000
Battery	200 Ah, 12 V	3	110,000	330,000
Inverter	1kVA	1	45,000	45,000
Charge Controller	45 A, 12-24 V	1	35,000	35,000
	Total Components Cost			570,000

Table 4: Cost estimate of powering three-bedroom flat with solar modules

Component	Capacity	Quantity	Unit Price (₦)	Total Price (₦)
Solar Panel	300 W	4	85,000	340,000
Battery	200 Ah, 12 V	4	110,000	440,000
Inverter	2.5 kVA	1	75,000	75,000
Charge Controller	45 A, 12-24 V	1	35,000	35,000
	Total Components Cost			890,000

The total cost of the PV system components for one-bedroom is ₦ 570,000, while total cost of the PV system components for the three-bedroom flat is ₦890,000.

.

4.0 CONCLUSION

Stand-alone power systems for powering the electrical loads of two types of home apartments (one-bedroom flat and three-bedroom flat) were designed and presented in this paper based on the total load demand of each apartment, using low power consuming appliances and PV Sizing worksheet.

The PV systems were designed for the month of July which has the least insolation so that the PV array would meet the energy need of the loads throughout the year. The design result shows that a one-bedroom flat apartment with electrical load of 450 W requires a PV power system of 520 W PV array, a 45A charge controller, 12 V battery bank (600 Ah) and an inverter (1 kVA) at an estimate cost of about ₦ 570,000. Also, a three-bedroom apartment with 884.8 W electrical load requires a PV system of 960 W PV array, a charge controller (45 A), 12 V battery bank (800 Ah) and inverter (2 kVA) at an estimate cost of about ₦ 890,000. These cost estimates represent the cost of components of the PV systems.

However, the initial cost of the system is very high compared to other competing choices such as using of generating set. This is the major constraint to the widespread application of solar power system. In other to minimize cost, PV power system can be initially designed for selected household appliances and not for the entire electrical load of the apartment, while other appliances can be later integrated into the design as cost implication improves.

5.0 RECOMMENDATIONS

The initial high cost of installing a PV power system is the main constraint to its widespread application for household electrification. In order to make PV applications attractive for household electrification, the following recommendations will be useful:

i. Government should establish PV Energy Company with the mandate to operate solar energy systems on a ‘fee for services’ basis at the home of interested client.

ii. Government, through the PV Energy Company or Financial Institutions, should make solar power system available at subsidised rate for civil servants to pay back from their salary for a period of 3-5 years.
iii. Since the major components of the PV system are imported, government should make the importation components of PV system tax free so as to encourage investors and reduce cost.
iv. Higher institutions of learning and research institutes should be encouraged to develop home-made solar modules that will be suitable for our environment through active research.
v. Awareness should be intensified about the benefits of renewable energy (especially solar energy) so as to arouse people's interest in this environmental friendly energy.

ACKNOWLEDGEMENT

The author is grateful to the management and staff of Nigerian Meteorological Agency, Minna, Niger state for making available the data of sunshine hours used in this work.

REFERENCES

Adaramola, M.S. & Oyewola, O.M. (2011). Wind Speed Distribution and Characteristics in Nigeria. *ARPN Journal of Engineering and Applied Sciences*, 6(2), 82-86.

CBN, (2014). Currency Exchange Rate. Retrieved on January 21, 2014 from http://www.cenbank.org/rates/ExchRateByCurrency.asp

Ileoje, O.C. (1997). Potentials for Renewable Energy Application in Nigeria. *Energy Commission of Nigeria*, 5-16.

Kennedy, J.D., Nick, H., Kyle, M., & Allison, R. (2008). The Energy Crisis of Nigeria; An Overview and Implications for the Future. *A Paper Presented at the University of Chicago*, 1-28.

Martin, C.L., & Goswami, D.Y. (2005). Concentrated Solar Power. Retrieved on April 12, 2012, from http://en.wikipedia.org/wiki/Concentrated_solar_power

Olomiyesan, B.M., Oyedum, O.D., Ugwuoke, P.E., Ezenwora, J.A. & Abdullahi, S.A. (2014). Estimation of Mean Monthly Global Solar Radiation For Minna Using Sunshine Hours. Journal of Sience, Tehnology, Mathematics and Eduation (JOSTMED), 10(3), 15-22.

Oyedum, O.D., Ugwuoke, P.E., Olomiyesan, B.M. & Ibrahim, A.G. (2014). Performance Evaluation of Polycrystalline Silicon Module under Outdoor Conditions in North Central, Nigeria. Nigeria Institute of Physics Journal,

Quanghuy L. (2011). *Off-grid Public Lighting System: Design and Characterization of an LED Luminaire* (Unpublished Master's Thesis). California Polytechnic State University, San Luis, Obispo.

Reincubate, (2012). Latest Major Exchange Rates. Retrieved on November 9, 2012, from www.xrates.net/?gclid=cp0q5p75x7mCFLtAodFy8ALQ

REN21, (2016). Renewables 2016: Global Status Report. Renewable Energy Network Policy for the 21st Century. Retrieved on February 2, 2017, from http://www.ren21.net/Portals/97/documents/GSR/GSR2016_Master18.pdf.

Sambo, A.S. (2006). Renewable energy electricity in Nigeria: *The way forward. Paper presented at the Renewable electricity policy conference, Abuja*, 11-12 December.

EVALUATION OF WIND ENERGY POTENTIAL FOR ELECTRIC POWER GENERATION IN GUSAU, NORTH WESTERN, NIGERIA

Oyedum, O.D.[1], Olomiyesan, B.M.[2] & Abolarin, M.S.[3]
[1]Department of Physics, Federal University of Technology,
P.M.B. 65, Minna, Niger State, Nigeria.
[2]Examination Development Department, National Examinations Council (NECO),
P.M.B. 159, Minna, Niger State, Nigeria.
[3]Mechanical Engineering Department, Federal University of Technology,
P.M.B. 65, Minna, Niger State, Nigeria.
E-mail: olomiyebolu@yahoo.com **Phone No:** +234-806-625-8921

Abstract

This study evaluates the wind energy potential in Gusau. The assessment involves statistical analysis of wind speed distribution in the study site using Weilbull distribution function and other relevant statistical equations. Twenty-two years wind speed data obtained from the Nigerian Meteorological Agency, Oshodi were used for the analysis. The result of the study shows that the monthly mean most probable and maximum energy carrying wind speeds in Gusau are respectively in the range $3.64 \leq v_{mp} \leq 8.50\ ms^{-1}$ *and* $4.30 \leq v_{max} \leq 10.79\ ms^{-1}$*.Also, the monthly mean wind power density in the study location ranged between 31.83 and 467.59* Wm^{-2}*, while the annual wind power density is 224.42* Wm^{-2}*. Thus, the wind energy resource in Gusau is not remarkable but it can be harnessed for small scale wind energy application with the use of appropriate wind turbines.*

.

Keyword: Wind, Energy, Power, Weibull, Gusau, Nigeria

1.0 Introduction

Wind energy is one of the fastest growing renewable energy options for electric power generation across the globe. The environmental benefit and advancement of its technology makes it highly competitive with conventional energy technology, thereby, wind energy is harnessed for grid and non-grid electricity generation (Dikko and Yahaya, 2012). The global cumulative installed capacity of wind power was estimated to be 369,553 MW in 2014 as against 7,600 MW in 1997 (GWEC, 2015). This attests to the growing interest in wind energy application around the world. In Africa, Morocco, Egypt, South Africa and Tunisia are the leading countries with installed capacity of 787 MW, 610 MW, 570 MW and 255 MW respectively, at the end of 2014 (GWEC, 2015).

Wind energy as source of power generation has not been given due attention in Nigeria. However, due to recent developments in wind energy mostly in developed countries (especially in Europe) with desire to reduce environmental impacts of the conventional energy resources, there is a general growing interest in the wind energy development in Nigeria (Adaramola and Oyewola, 2011). At present, there is no commercial wind power plants connected to the national grid in Nigeria. Also, there are only a few wind energy applications in Nigeria and many of such applications were installed in the early 1960s in some northern states for powering of water pumps.

Studies on wind speed data across Nigeria have been carried out by quite a number of researchers. Fagbenle *et al*. (1980) reported that the average wind speed across the country is $3ms^{-1}$ based on 9 years (1951-1960) wind data from twelve meteorological stations. Besides, they found that wind speed is generally higher in the northern part of the country than in the southern part. In another study, Ojosu and Salawu (1990) assessed the wind speed in the country using wind data for 24 years (1951-1975) from twenty-two meteorological stations. They reported that Sokoto has the highest wind speed of about 5.12 ms^{-1} in June and annual average of 3.92 ms^{-1}, while the middle and southern areas have wind speed of about 2 ms^{-1} or less. Further studies by Adekoya and Adewale (1992) and Fagbenle and Karayiannis (1994) are found to be consistent with the findings of Ojosu and Salawu (1990) and that of Fagbenle *et al*. (1980). In general, studies show that the northern part of Nigeria is endowed with great wind potential which could be exploited for power generation.

Researchers have attempted to assess the wind resource in the northern part of the country but not many detail studies have been done on the wind potential in Gusau. In 2006, Tijjani present the statistical analysis of wind power density based on the Weibull and Rayleigh models in selected locations in North-West Nigeria (Yelwa, Kaduna, Gusau, Sokoto and Kano) and found out that the average monthly wind power density of the region ranged between 1.87 Wm^{-2} and 108.8 Wm^{-2}. Fagbenle *et al*. (2011), assessed the wind energy potential of Potiskum and Maiduguri in North-Eastern Nigeria based on 2-parameter Weibull and other statistical analysis using 21 years (1987-2007) monthly mean wind data. They reported that monthly mean wind speed variation for Potiskum and Maiduguri ranged from 3.90 to 5.85 ms^{-1} and 4.35 to 6.33 ms^{-1} respectively, while the wind power density variation based on the Weibull analysis ranged from 102.54 to 300.15 Wm^{-2} for Potiskum and 114.77 to 360.04 Wm^{-2} for Maiduguri. They concluded that Maiduguri is a better site in terms of monthly and seasonal variation of mean wind speed, but both sites can be suitable for stand-alone and medium scale wind power generation. Ahmed *et al*. (2013) assessed the wind energy resource potential in Plateau, north central, Nigeria using Weibull distribution. Six years (2000-2006) monthly average wind speed data was used in the study and the highest wind speed for the location was found to be 15.4 ms^{-1} in January while the lowest wind speed was 8.7 ms^{-1} in August. The study also reveals that wind power density for the location varies between 368 and 1056 Wm^{-2}, hence Plateau is a good location for wind power generation.

The type of wind energy application suitable for a particular location depends on the wind energy potential of such location; hence assessment of wind energy resources is imperative. Therefore the focus of this study is to assess the wind energy potential in Gusau for electric power generation. Gusau is the capital city of Zamfara State and is located on latitude 12.10°N, longitude 6.15°E and at 450 m about the sea level.

2.0 Methodology

In this study, the Weibull two-parameter Probability Density Function (PDF) and its corresponding Cumulative Distribution Function (CDF) given by equations 1 and 2 were employed in analysing the wind distribution pattern. This statistical method was chosen because it has been found to be accurate and adequate in analysing and interpreting data of measured wind speed, and in predicting the characteristics of prevailing wind profile over a place (Fagbenle *et al*., 2011). The Weibull distribution function and its associated equations can be expressed as (Ahmed, 2011):

$$f_w(v) = \left(\frac{k}{c}\right)\left(\frac{v}{c}\right)^{k-1} exp\left[-\left(\frac{v}{c}\right)^{k}\right] \quad (1)$$

$$F_w(v) = 1 - exp\left[-\left(\frac{v}{c}\right)^{k}\right] \quad (2)$$

where:

$f_w(v)$ =Weibull Probability density function

$F_w(v)$ = cumulative probability function

v = wind speed (ms^{-1})

c = scale factor (ms^{-1})

k = shape factor (dimensionless)

The shape and scale factors are expressed in equations (3) and (4) as given by (Justus *et al*., 1978):

$$k = \left(\frac{\sigma}{v_m}\right)^{-1.086} \quad (3)$$

$$c = \frac{V_m}{\Gamma\left(1+\frac{1}{k}\right)} \quad (4)$$

$$\sigma = \left[\frac{1}{N-1}\sum_{i=1}^{N}(v_i - v_m)^2\right]^{1/2} \quad (5)$$

where:

σ = standard deviation

v_m = mean wind speed (ms^{-1})

v_i = observed wind speed (ms^{-1})

N = number of months in the period of time considered and

Γ(x) is the gamma function, which is defined as: $\Gamma(x) = \int_0^\infty t^{x-1}e^{-t}dt$

Most Probable Wind Speed (V_{mp}) and Maximum Energy Carrying Wind Speed (V_{Emax})

The most probable wind speed represents the modal wind speed for a given wind distribution, while the maximum energy carrying wind speed describes the wind speed carrying maximum energy which can be used to estimate the wind turbine design or rated wind speed (Akpinar and Akpinar, 2005). They can be expressed respectively as:

$$V_{mp} = c\left(\frac{k-1}{k}\right)^{\frac{1}{k}} \quad (6)$$

$$V_{Emax} = c\left(\frac{k+2}{k}\right)^{\frac{1}{k}} \quad (7)$$

Wind Power Density (WPD) and Wind Energy Density (WED)

Wind Power Density (WPD) is used to study the wind power available at a specific site. The estimation of the wind power density is an important factor when assessing the wind potential of a location as it indicates how much energy per unit of time and swept area of the blades is available at the selected area for conversion to electricity by a wind turbine (Fyrippis *et al*., 2010). The mean wind power density can be estimated directly from the wind speed or by using the Weibull two parameter method as expressed by (Kamau *et al*., 2010):

$$P(v) = \frac{1}{2}\rho v^3 \quad (8)$$

$$P(v) = \frac{1}{2}\rho c^3\,\Gamma\left(1+\frac{3}{k}\right) \quad (9)$$

where:

P(v) = Wind Power Density (Wm^{-2})

v = Wind speed

c = Weibull scale parameter

k = Weibull shape parameter.

ρ = Air density at the site, which can be expressed in the form:

$$\rho = \rho o - 1.194 \times 10^{-4} \times H_m \quad (10)$$

where ρo is the air density value at sea level usually taken as 1.225 kgm^{-3} and H_m is the site elevation in meters. The wind energy density (WED) is the product of the mean power density and the time (T) in hours. WED is usually expressed in $kWhm^{-2}$ and is given as:

$$WED = \frac{1}{2}\rho c^3\,\Gamma\left(1+\frac{3}{k}\right)T \quad (11)$$

Classification of Wind Power Using WPD

A classification zone for wind with respect to its WPD in Wm^{-2} has been developed by the Battelle-Pacific Northwest Laboratory (PNL) as part of the US Department of Energy (DOE's) Federal Wind Energy Program.

This classification is divided the wind power to seven different classes ranging from the lowest (Class 1) to the highest (Class 7) (Ordóñez *et al*., 2013). The PNL wind power classification is shown in Table 1.

Table 1: PNL Wind Power Classification

Wind Power Class	WPD at 10 m (Wm^{-2})	Wind Applications
1	0-99	Not Suitable
2	100-149	Poor
3	150-199	Marginal
4	200-249	Good
5	250-299	Very Good
6	300-399	Excellent
7	400-1000	Excellent

(Source: Saeidi *et al*., 2011)

3.0 Result and Discussion

3.1 Variation of wind speed

The monthly mean wind speed data used in this study were measured at anemometer height of 10 m and is presented in Figure 1. The data covered a period of 22 years between 1984 and 2005.

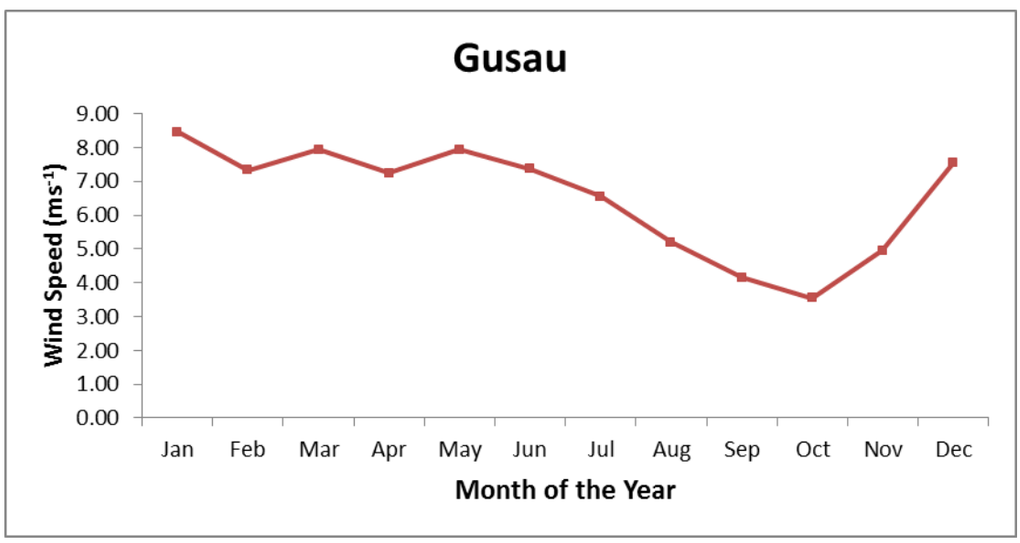

Figure 1: Monthly Average Wind Speeds for Gusau

Figure 1 shows that the highest and lowest monthly mean wind speed values for the period of the study are between 8.46 ms^{-1} in January and 3.54 ms^{-1} in October. The annual mean wind speed recorded for the period of the study is 6.52 ms^{-1}. This value is in agreement with previous study by Fagbenle and Karayiannis (1994), but is higher than the values reported by Fagbenle *et al*. (1980) and Chineke (2009). The wind speed is observed to be lower in the rainy season months (August – November) than the dry season months.

3.2 Wind Speed Frequency Distribution

The plot of the probability density function (PDF) illustrates the fraction of time for which a given wind speed possibly prevails at a location. The peak of the PDF curve indicates the most frequent velocity, whereas the plot of the cumulative distribution function is used for estimating the time for which wind speed is within a certain speed interval. The monthly probability density and cumulative distribution derived from the time series data for the whole years for Gusau is shown in Figures 2 and 3 respectively. The PDF and CDF plots show that all the curves of the monthly wind profiles follow the same distribution pattern. The variation in shapes of PDF and

CDF plots were the results of the varying values of the Weibull parameters c and k. The shape parameter, k, indicates how peak the wind distribution is, while the scale parameter, c, determines the spread of the distribution.

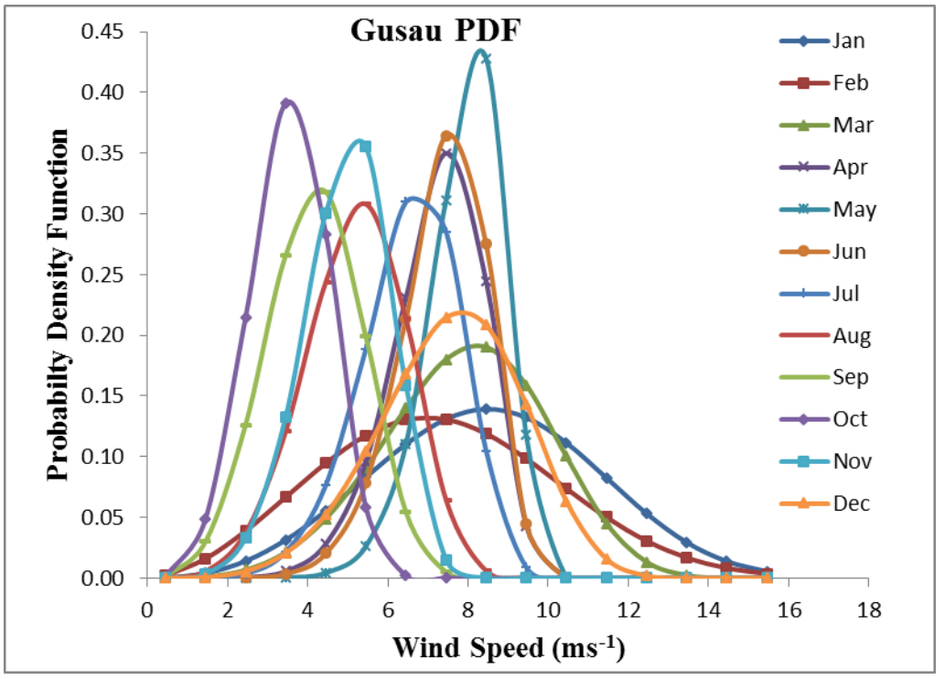

Figure 2: Monthly Probability Density Function (PDF) for Gusau

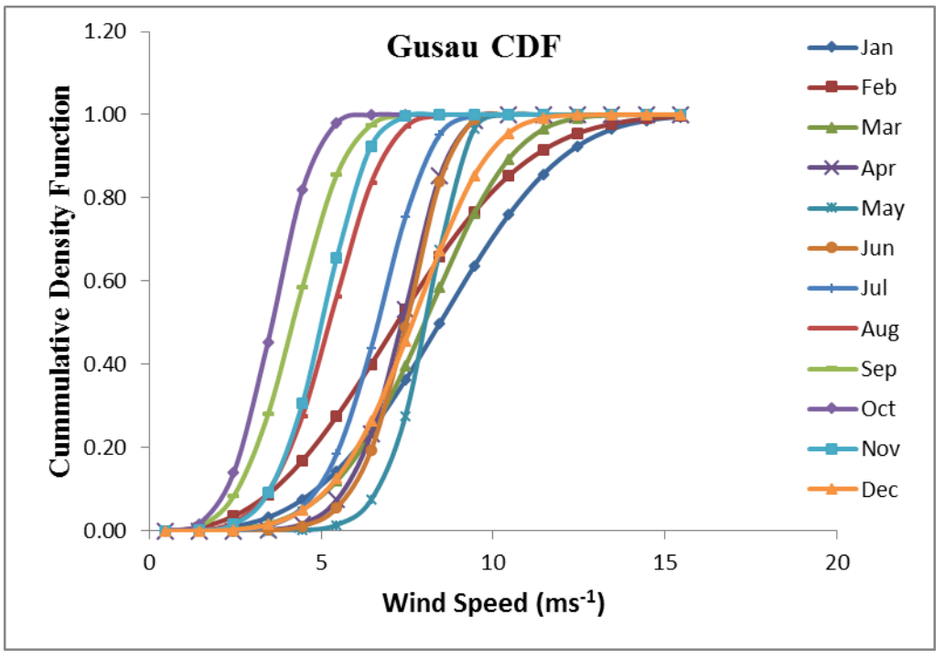

Figure 3: Monthly Cumulative Distribution Function (CDF) for Gusau

The plot of the monthly PDF shown in Figure 2 demonstrates that the wind profiles for all the months follow the same distribution pattern. The figure further reveal that the peak of the density function frequencies (i.e. most frequent wind speeds) skewed towards the higher values of mean wind speed. It can further be noted that the PDF plot show a good data spread in a number of months of the year with December, January, February and March having the widest spread of wind speed.

Also, the CDF plot in Figure 3 show that at Gusau, 40% of the data are in the wind speed range of 3.2 – 7.9 ms^{-1} and below, while 80% of the data are within wind speed interval of 4.2 – 11.0 ms^{-1} and below.

The annual probability and cumulative density functions obtained using the Weibull distribution function for Gusau is shown in Figures 4a and 4b.

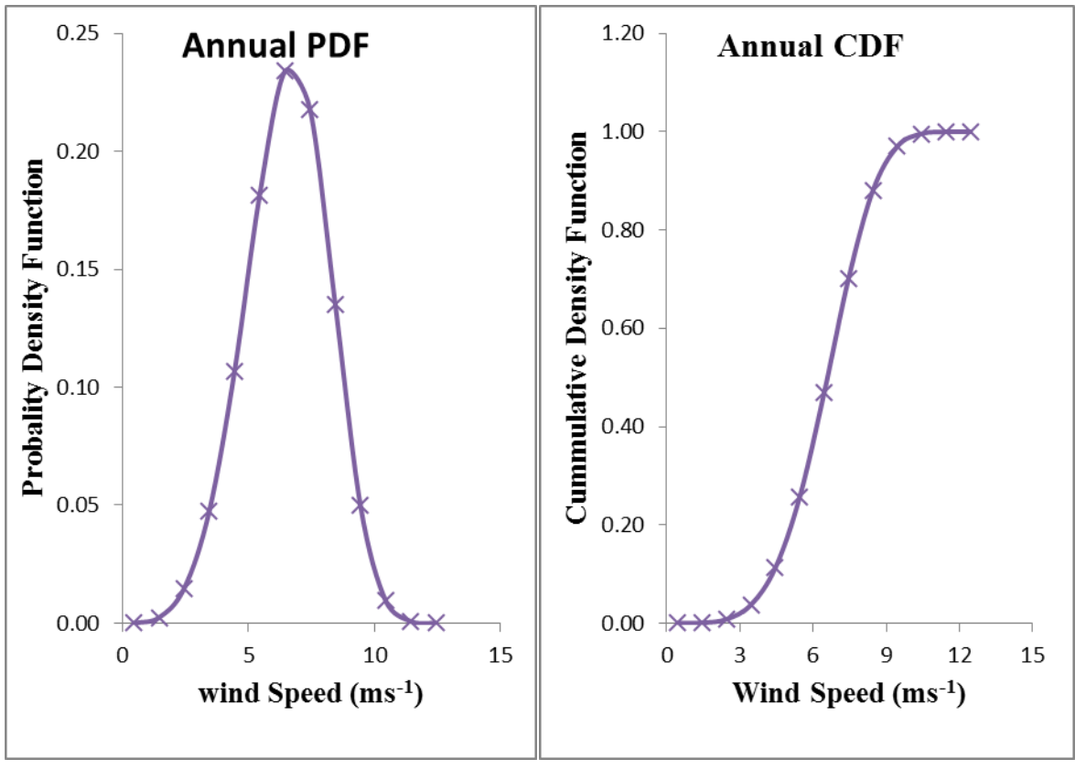

Figure 4: Annual Wind Distribution for Gusau (a) PDF and (b) CDF

From Figure 4(a), it can be noted that the most frequent wind speed expected from January to December in Gusau is about 6.80 ms^{-1}.

The cut-in wind speed which contributes to the generation of electricity from wind in most new wind turbine designs is about 3.0 ms^{-1} and above (Nze-Esiaga and Okogbue, 2014). However, if wind turbines with cut-in wind speed of 4 ms^{-1} and 6 ms^{-1} are selected for use in the sites, it can be observed from the CDF curves in Figure 4(b) that, the percentage of the annual wind energy above the 4.0 and 6.0 ms^{-1} cut-in wind speed which can contribute to the generation of electricity are respectively 93% and 64% for Gusua. This implies that if a wind turbine with a design cut-in wind speed of 4.0 ms^{-1} is installed for electricity generation in this site, the turbine will work for about 95% of the time.

3.3 Wind Speed Characteristics and Wind Power Density

The most probable wind speed (V_{mp}) and the maximum energy carrying wind speed (V_{Emax}) for the studied locations were calculated using equations 6 and 7 respectively. The monthly and annual values of the wind speed characteristics, Weibull parameters (c and k), wind power density (WPD) and wind energy density (WED) of the study site at a height of 10 m AGL is presented in Tables 2.

Table 2: Wind Speed Characteristics and Other Parameters at 10 m in Gusau

Period	Vm (ms^{-1})	Vmp (ms^{-1})	Vmax (ms^{-1})	k	c (ms^{-1})	WPD (Wm^{-2})	WED ($kWhm^{-2}d^{-1}$)
Jan	8.46	8.50	10.79	3.40	9.42	467.59	11.222
Feb	7.33	6.98	10.06	2.74	8.24	341.79	8.203
Mar	7.93	8.21	9.47	4.41	8.70	349.11	8.379
Apr	7.25	7.58	7.99	7.34	7.73	240.04	5.761

May	7.94	8.26	8.51	9.91	8.35	305.77	7.339
Jun	7.37	7.70	8.06	7.91	7.83	249.85	5.996
Jul	6.55	6.85	7.38	6.17	7.05	181.77	4.362
Aug	5.19	5.39	6.13	4.64	5.68	96.37	2.313
Sep	4.16	4.26	5.12	3.88	4.60	52.62	1.263
Oct	3.54	3.64	4.30	4.08	3.90	31.83	0.764
Nov	4.96	5.18	5.72	5.28	5.39	81.43	1.954
Dec	7.56	7.86	8.87	4.82	8.25	294.83	7.076
Average	6.52	6.70	7.70	5.38	7.09	224.42	5.386

NOTE: WPD is the Weilbull Wind Power Density while, WED is the Wind Energy Density.

From Table 2 it is observed that the monthly Weibull shape parameter, k, for Gusau is in the range of 2.74 – 9.91. Also, the monthly Weibull scale parameter, c, is in the range of 3.90 – 9.42 ms^{-1}, thus corresponding to monthly mean wind speeds in the range of 3.54 – 8.46 ms^{-1}. Furthermore, Table 2 reveals that the monthly values of v_{mp} and v_{max} for Gusau are respectively in the range $3.64 \leq v_{mp} \leq 8.50$ ms^{-1} and $4.30 \leq v_{max} \leq 10.79$ ms^{-1}. The monthly Weibull WPD is in the range of 31.83 – 467.59 Wm^{-2}, which falls into the Wind Classes between 1 and 7 of the PNL wind classification. The annual average WED was estimated to be 5.386 $kWhm^{-2}day^{-1}$, while the annual WPD is 224.42 Wm^{-2}. According to PNL classification, Gusau falls into class 3, this indicates that Gusau will only be suitable for small-scale electricity generation by using special wind turbines which have low cut-in speeds, water pumping and other low-energy capacity applications that require intermittent power supply.

4.0 Conclusion

Wind speed distribution and wind power density in Gusau was assessed using Weibull two-parameter and other statistical equations. This analysis reveals that the highest (8.46 ms^{-1}) and lowest (3.54 ms^{-1}) monthly mean wind speed values in Gusau were respectively recorded in January and October, while the annual mean wind speed is estimated to be 5.31 ms^{-1}. Similarly, the annual values of the most probable wind speed and the maximum energy-carrying wind speed in the study site are respectively 6.70 and 7.70 ms^{-1}. The value of the WPD varies from 31.83 Wm^{-2} to 467.59 Wm^{-2}. The annual WPD and WED in Gusau are respectively 224.42 Wm^{-2} and 5.386 $kWhm^{-2}day^{-1}$. The value of the WPD obtained indicates that Gusau to wind power class 3. This in-turn indicates that the location is not suitable for large scale wind application but the wind resources in the location sufficient for small scale wind applications and other low-energy capacity applications that require intermittent power supply.

ACKNOWLEDGEMENT: The authors gratefully acknowledge the assistance of the Nigerian Meteorological Agency (NIMET) for providing the wind speed data used in this research.

Reference

Adaramola, M. S., & Oyewola, O. M. (2011). Wind Speed Distribution and Characteristics in Nigeria. *ARPN Journal of Engineering and Applied Sciences*, 6(2), 82-86.

Adekoya L. O., & Adewale A. A. (1992). Wind Energy Potential of Nigeria. *Renewable Energy*, 2, 35-39.

Ahmed, A., El-Suleiman, A., & Nasir, A. (2013). An Assessment of Wind Energy Resource in North Central Nigeria, Plateau. *Science Journal of Energy Engineering*, 1(3), 13-17. doi: 10.11648/j.sjee.20130103.11

Ahmed, S. A. (2011). Investigation of Wind Characteristics and Wind Energy Potential at Ras Ghareb Egypt. *Renewable and Sustainable Energy Reviews*, 15, 2750- 2755.

Akpinar, E. K., & Akpinar, S. (2005). An Assessment on Seasonal Analysis of Wind Energy Characteristics and Wind Turbine Characteristics. Energy Conversion and Management, 46, 1848–1867.

Chineke, C. T. (2009). Boosting Electricity Supply in Nigeria: Wind Energy to the Rescue? *The Pacific Journal of Science and Technology*, 10(2), 553-560.

Dikko, I., & Yahaya, D. B. (2012). Evaluation of Wind Power Density in Gombe, Yola and Maiduguri, North Eastern Nigeria. *Journal of Research in Peace, Gender and Development*, 2(5), 115-122.

Fagbenle R. L., & Karayiannis T. G. (1994). On the Wind Energy Resource of Nigeria. *International Journal of Energy Research*, 18, 493-508.

Fagbenle R. L., Fasade A. O., Amuludun A. K., & Lala P. O. (1980). Wind Power Potentials of Nigeria. 12th Biennial conference of the West African Science Association, University of Ife, Nigeria.

Fagbenle, R. O., Katende, J., Ajayi, O. O., & Okeniyi, J. O. (2011). Assessment of Wind Energy Potential of Two Sites in North-East, Nigeria. *Renewable Energy*, 36, 1277-1283.

Fyrippis, I., Axaopoulos, P. J., & Panayiotou, G. (2010). Wind Energy Potential Assessment in Naxos Island, Greece. *Applied Energy*, 87, 577-586.

GWEC (2015). Global Wind Energy Council, Global wind 2014 Report, Pp 1.

Nze-Esiaga, N., & Okogbue, E. C. (2014). Assessment of Wind Energy Potential as a Power Generation Source in Five Locations of South Western Nigeria. *Journal of Power and Energy Engineering*, 2, 1-13. doi.org/10.4236/jpee.2014.25001

Ojosu, J. O., & Salawu, R. I. (1990). A Survey of Wind Energy Potential in Nigeria. *Solar and Wind Technology*, 7, 155-167.

Ordóñez, G., Osma, G., Vergara, P., & Rey, J. (2013). Wind and Solar Energy Potential Assessment for Development of Renewables Energies Applications in Bucaramanga, Colombia. *The International Congress of Mechanical Engineering and Agricultural Sciences*, 59, 1-6. doi:10.1088/1757-899X/59/1/012004

Tijjani, A. A. (2006). Statistical Analysis of Wind Power Density Based on the Weibull and Rayleigh Models in North Western Nigeria. *African Engineering Seminar*, Bayero University, Kano.

INTEGRATED GEOLOGY, MINERALOGY AND GEOCHEMISTRY INVESTIGATIONS OF THE MINNA-TEGINA-MAKERA ROAD NORTH WESTERN NIGERIA: IMPLICATION ON FAILED PORTION

***Alabi A. A., Unuevho C., Jimoh M. O., Akande W. G., Ejepu S. J., Asema A. I.**
Department of Geology Federal University of Technology
*Corresponding author: alabiadekola@futminn.edu.ng

ABTRACT

Minna - Tegina - Makera federal road links the north to the southwest and serve as major route for transportation of goods and services. The road has been repaired severally, but continues to fail at particular portion a short time after repair. This study therefore integrated geology, mineralogy and geochemistry to investigate the cause of the failure. The area is underlain by basement and sedimentary rocks of varying texture, mineralogy and geochemistry. The stable portion is underlain by granite-gneiss, granites, amphibolites schist quartz schist and sandstone while the failed road sections are underlain by mica schist, phyllite and coarse grain granite It is evidently clear from this finding that low grade metasedimentary rocks constitute the foundation of the failed section, the presence of clayey and sandy (weathered product) and interaction with climate have contributed to road failure witnessed on the study road section.

INTRODUCTION

Roads in Nigeria are constructed on monotonous basement and sedimentary terrains with failed portions been attributed to inadequate engineering study and poor construction materials. Shear strength, compaction and compressibility studies have shown that basement and sedimentary rocks could respond considerably to stress and environmental influence as a result of their variation in mineralogical and chemical composition. The understanding of the lithology of the underlying parent rocks and soils used in the construction of road play important role in the stability and performance of any road. However, bad portion of roads are as a result of incompetent base materials and basement rocks or poor construction. This is responsible for fatal road carnage, wearing down of vehicles and waste of valuable time during transportation of goods and services.

Adewoye *et al*., (2012) attributed the failure of Oyo – Ogbomoso federal road to environmental factors, while Osinowo (2011) identified anomalous low resistivity zone and delineated major and minor linear fractures that aid in the interaction of water with basement rocks and greatly reduced the base-rock and subsoil shear strengths resulting into incessant road carnage. Akintorinwa *et al.* (2011) studied the cause of road failure along Ilesa – Akura highway using remotely sensed and geotechnical data and concluded that linear (geological) features are zone of weakness that enhance the accumulation of water leading to failure of some segments in the study road. Integration of geological, mineralogical and geochemical investigation of the underlying parent rocks to compliment geotechnical study in foundation engineering problems cannot be overemphasized. This study therefore integrated geology, mineralogy and geochemistry to investigate the cause of failure of Minna - Tegina - Makera federal high way north western Nigeria.

LOCATION AND GEOLOGY OF THE STUDY AREA

The Minna - Tegina - Makera federal road is located within Latitudes 9˚ 10'N - 10˚ 05'N and 4˚ 50'E - 6˚ 10'E, and is approximately 155 kilometers long trending in southeast – northwest and northwest-southwest directions (Figure 1) and underlain by Precambrian Basement Complex of northwestern Nigeria and Cretaceous sedimentary

rocks of the Bida basin. The basement rocks occur in the southern and northern part of the study area and falls within the Ushama and Birnin Gwari formations while the sedimentary rock is to the northeast and falls within the Bida sandstone formation. The Birnin Gwari formation is composed of metamorphosed clastic sedimentary rocks, mainly phyllites and mica schist with which metagreywackes, pebbly occur as fragments. The phyllites are finely laminated which is defined by alternation of quartz-rich and sericite/chlorite-rich layers that vary in width from 0.5 millimeters to 5 millimeters, while the Ushama formation is consist of mica schist, quartz schist, and quartzite with some amphibolites layers composed of quartz, muscovite, biotite and plagioclase (Ajibade, *et al* 2008). Alabi (2016) identified the presence thin beds of kaolinitic clay overlain by lateritic soil and sandstone/ferruginous sandstone within the Bida sandstone formation, and suggest basement provenance of the kaolinitic clay.

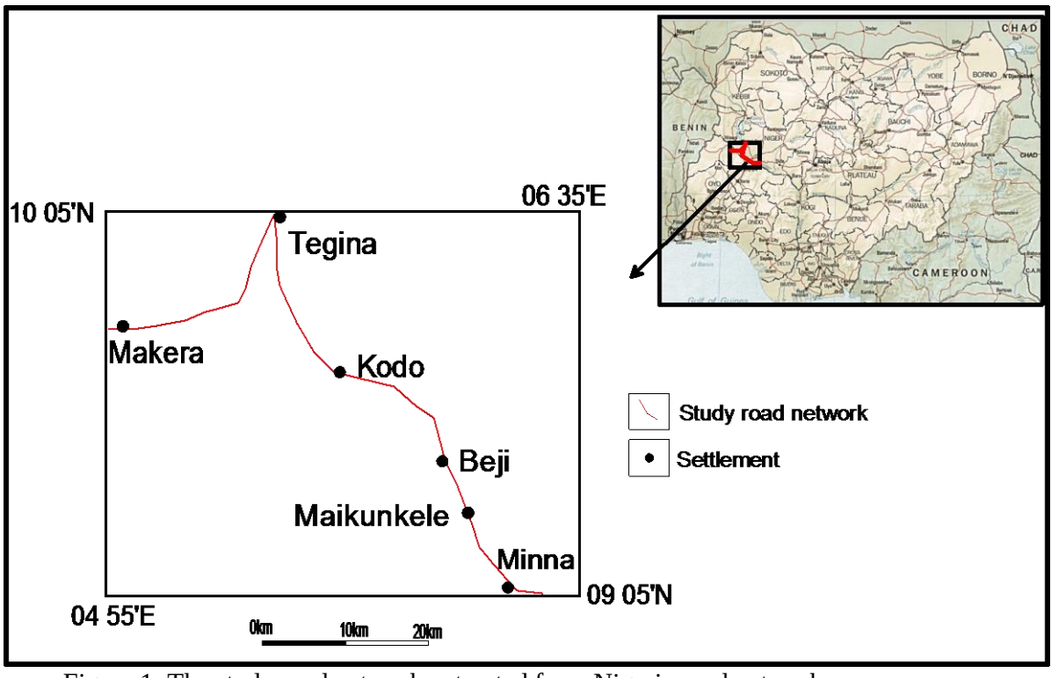

Figure 1: The study road network extracted from Nigeria road network

Research Methodology

Geological mapping was carried in the study area with more emphasis on outcrops along the study road network. All the rock types encountered were studied in hand specimen for their mineralogy composition, texture, structure, color and their relationship with each other. Rock samples were obtained at different locations (stable and failed road sections) using geological hammer and their coordinate recorded. Ten representative basement rock and two representative sedimentary rock samples from the study area were taken to the laboratory at the Department of Geology, Federal University of Technology Minna and prepared for whole-rock chemical analyses and rock mineral analysis. The samples were broken into smaller pieces using geologic hammer, crushed using jaw crusher and pulverizedusing using FRITSCH Pulverisette. Pulverized rock samples of 7. 5grams that pass through 20 mesh for mineralogical and geochemical analysis, using X-ray Diffraction (XRD) and Inductively Coupled Plasma mass spectrometry (ICP-MS) methods at Activation Laboratory Ontario, Canada.

Results and Discussion

Geology and Mineralogy

The rock types along the study road network includes; granite-gneiss, medium grain biotite and muscovite granite, phorphyritic granite, mica schist, amphibolites schist quartz schist phyllite and sandstone as revealed through geological mapping (Figure 2).

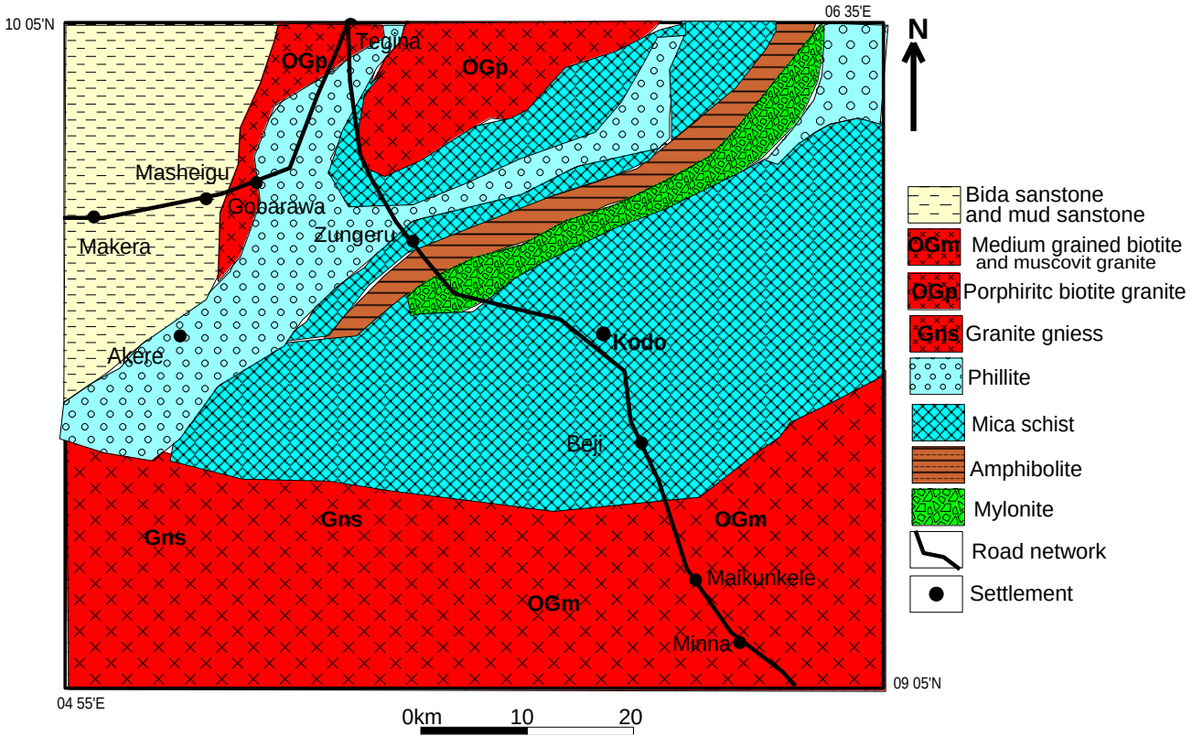

Figure 2: Geological map of the study area showing the studied road network

The rock that underlain the stable road sections are made up of granite-gneiss, granites, amphibolites schist and quartz schist and sandstone while the failed road sections are underlain by mica schist, phyllite and coarse grained granite (Fig. 4). Structurally, most of the granites are open jointed (Figure 3) and in some areas dissected by quartzo-feldspartic veins. The granitic rock underlies about 45% of the study area while phyllite, schist and smphibolite schist are about 45% and sandstone 5%. Schist is strongly foliated ranging from muscovite schist to biotite schist, trending in NE - SW and occurred mostly in the northern section of the study road network. In hand specimen the schist varies from leucocratic to melanocratic, the leucocratic show effects of chemical weathering (Figure 5). Amphibolite schist occurred in Zungeru inter-layered with quartz schist and mylonite, this rock is restricted to Zungeru area and a times seen intruding the schist (Figure 6). Phyllite are also common in the northeast and northwest sections of the study area and are closely associated with schist, characterized by a silky sheen on the cleavage surface and show evidence of intensive weathering at the surface where they outcrop. Field evidence along the study road network show that the failed road section is underlies by mica schist, porphyritic granite and phyllite. The fairly stable section is underlain by granite while the stable section is underlain by medium graine granite/granite-gneiss, amphibolite schist and sandstone.

Mineralogy

X-ray diffraction patterns of the basement rocks samples indicate predominance presence of quartz, biotite, muscovite, feldspar, and actinolite (Plate 9a – i) while quartz, kaolinite, muscovite and anatase for sandstone/mudstone (Plate 9j). Percentage mineralogical composition of granitnitic rocks from XRD result shows average composition of 33.5% quartz, 28.3% feldspar and 21.06% actinolite, muscovite schist show average composition of 31.9% quartz, 30.3% feldspar and 22.4% muscovite while muscovite schist show 33.1% quartz, 47.1% feldspar and 19.2% muscovite. Amphibolite schist shows 31.9% quartz, 27.1% feldspar and 21.06% actinolite. Phyllite shows average mineralogy composition of 44% quartz, 57% feldspar and 21% muscovite. Sandstone/mudstone shows average composition of 75% quartz, 22.1% Kaolinite, 2.2% muscovite and anatase 2.5%.

Figure 3: Jointed granite in Maikunkele area

Figure 4: Coarse grain granite in Gobarawa area

Figure 5: Weathered Leucocratic schist

Figure 6: intruded amphibolites

Percentage mineralogical composition of the rocks that underlain the failed section revealed high proportion of feldspar minerals (microcline, orthoclase and albite) ranging between 30.3% and 57%, and quartz ranges between 32.1% and 34.9% (Table 1). The high feldspar content of these rocks coupled with the interaction of water will facilitate the chemical weathering of these rocks that may eventually yield clay minerals.

Table 1: Percentage Mineralogical Composition of Basment Complex and sedimentary rock Samples

Location	1	2	3	4	5	6	7	8	9	10	11	12	Total
Granite (Maikunkele)	33	15	n.d	n.d	12.8	n.d	n.d	23.5	n.d	15.5	n.d	n.d	99.8
Muscovite schist (Beji)	33.4	n.d	19.2	23.9	n.d	n.d	n.d	23.4	n.d	n.d	n.d	n.d	99.9
Muscovte schist (Kodo)	32.1	n.d	18.8	28.5	n.d	n.d	n.d	20.6	n.d	n.d	n.d	n.d	100

Muscovite schist (Tegina 1)	33.6	n.d	26.1	n.d	n.d	n.d	n.d	40.3	n.d	n.d	n.d	n.d	100
Muscovite schist (Gobrwa2)	38.1	n.d	32.2	n.d	n.d	n.d	n.d	29.5	n.d	n.d	n.d	n.d	99.8
Ampbibolite (Zungeru 2)	17.5	13	n.d	n.d	34.4	n.d	n.d	34.9	n.d	n.d	n.d	n.d	99.8
Phyllite (Zungeru 1)	34.9	21.0	n.d	n.d	nd	23.6	n.d	20.4	n.d	n.d	n.d	n.d	99.9
Granite (Gobarawa)	32.5	n.d	n.d	n.d	20.6	n.d	n.d	27.9	18.8	n.d	n.d	n.d	99.8
Granite gniess (Tegina 2)	48.2	20.8	n.d	n.d	nd	n.d	n.d	20.9	n.d	n.d	n.d	n.d	99.9
Gniess mylonite (Zungeru3)	38.3	n.d n.d	n.d 2.1	n.d n.d	27.8	n.d n.d	7.8	25.9	n.d n.d	n.d n.d	n.d 21.2	n.d 2.5	99.8 99.6
Sandstone (Masheigu)	73.4	n.d	2.2	n.d	n.d n.d	n.d	n.d n.d	n.d n.d	n.d	n.d	20.1		99.6
Sandstone (Makera)	74.8						n.d						

1= Quartz 2= Biotite 3=Muscovite 4= Microcline 5= Actinolite 6= Othorclase 7= Chalcopyrite 8=Albite 9=Cordierite 10=Iron magnesium aluminium silicate hydroxide n.d=not detected 11= Kaolinite 12=Anatase

Geochemistry

The results of the geochemical analysis (expressed in weight percentage) of the rocks from the study road network is presented in Table 2, which aided in the calculation and binary plots of the provenance and weathering intensity. The chemical composition of the rock samples are direct reflection of the percentage composition of the rocks in the study area. Granite, Gneiss mylonite and granite gneiss are characterized by SiO_2 in the range of 62.93% and 71.78%, the schist and phyllite in the range of 58.66% and 43.94%, while amphibolite schist is 49.12%. The relative enrichment of Al_2O_3 (17.08 – 17.20%), Na_2O and K_2O in mica schist is an indication of it felsic character, feldspar and mica enrichment. The Fe_2O_3 and MgO enrichment in amphibolite schist and gneiss mylonite reflects mafic character of these rocks. The sandstone is enriched in SiO_2 of 74.1% average composition, 20.1% kaolinite, 2.2% muscovite and 2.5% anatase.

Table 2: Major oxides in wt% of Basement rocks

Oxides	Mk	Bj	Kod	Zn1	Zn 2	Zn 3	Teg 1	Teg 2	Mak 1	Gob 1
SiO_2	68.77	57.68	58.66	43.94	49.12	61.93	51.01	69.94	71.78	62.93
Al_2O_3	14.59	17.08	17.19	17.20	15.20	13.09	13.45	14.60	15.26	17.09
Fe_2O_3	4.71	7.70	7.81	11.63	14.63	3.52	3.43	3.51	0.82	5.15
CaO	1.99	0.24	0.24	0.68	10.18	3.03	9.75	1.58	1.27	0.03
MgO	2.17	3.15	3.15	8.90	10.90	10.51	5.09	0.94	0.13	1.51
Na_2O	3.66	0.19	0.19	3.17	3.34	3.34	2.39	3.52	3.94	2.84
K_2O	2.53	4.76	4.76	6.41	3.16	2.14	6.44	4.76	5.43	2.14
MnO	0.06	1.38	0.38	0.22	0.13	0.41	0.06	0.06	0.02	0.10
TiO_2	0.51	1.85	1.55	1.71	1.18	0.68	1.58	0.49	0.07	1.98
P_2O_5	0.14	0.04	0.04	0.04	0.14	0.12	0.03	0.14	0.02	0.05
Cr_2O_3	0.065	0.036	0.036	0.133	0.003	0.064	0.052	0.052	0.068	0.064
LOI	0.66	5.99	5.99	6.09	6.09	1.38	6.44	0.48	0.50	6.38
TOTAL	99.86	100	99.99	100.1	99.27	100.2	100	100	103	99.81

Mk = Medium grained granite around Maikunkele area Teg 2 = Granite gneiss from Tegina area

Zn1 = Phyllite around Zungeru area Gob1 =Muscovite schist around Makera area

Kod = Muscovite schist around Kodo area Teg 1 = Mica schist around Zungeru area

Bj = Muscovite schist around Beji area Zun 3= Gneiss mylonite around Zungeru area

Zn 2 = Muscovite schist around Kodan area

Mak = Sandstone around Makera area

Geochemical binary plot of Na_2O/Al_2O_3 versus K_2O/Al_2O_3 show that the mica schist, phyllite and amphibolite schist are of sedimentary provenance while granite and granite gneiss are of igneous provenance (Figure 7).

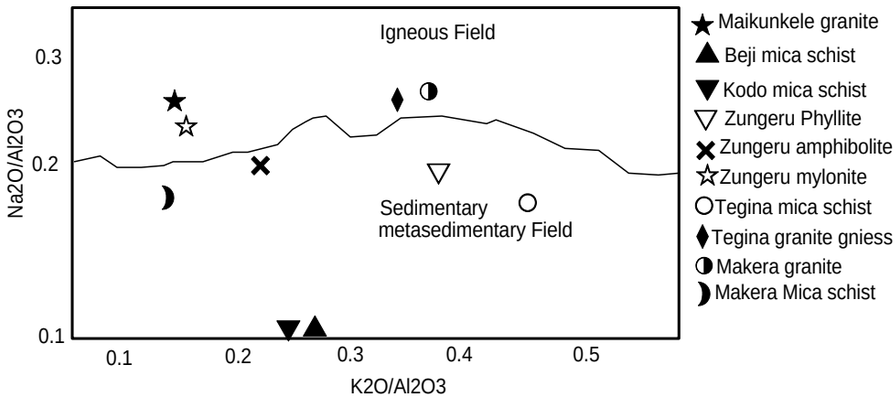

Figure 7: Na_2O versus K_2O plot for study area rocks (after Garrels and Mackenzie, 1971)

Weathering intensity of igneous and metamorphic rocks in humid climatic region can be determine using Ruxto Ratio (SiO_2/ Al_2O_3) proposed by Ruxton (1968). He proposed Ruxton Ratio value of <3.8 for intensively weathered rocks, 4 – 4.5 moderately weathered rocks and >4.5 least weathered rocks. The Ruxton Ratio values of between 2.6 – 3.7 revealed the mica schist of Tegina, Makera, Kodo, Beji, Zungeru phyllite and Zungeru amphibolite schist to have been intensively weathered and constituted the underlying basement rocks of the failed sections of the study road networks while values of between 4.7 – 4.8 revealed the granite/granite gneiss of Maikunkele, Tegina, and Zungeru mylonte to be of least weathered intensity constituted the underlying basement rocks of the stable section of the study road networks (Figure 8). Combined field evidence, provenance study and weathering intensity result shows that the meta-sedimentary rocks are of low grade metamorphism and have been intensively weathered while the meta-igneous rocks are more stable and resistant to chemical weathering. Weathering processes penetrate down discontinuities (planes of weakness), such as faults and joints, in the metasedimentary rock mass and then attack the faces, corners and edges of the joints in rock, which produces flakes of clay and sand. As the weight of cars and trucks pass over the weak spot (clay and sand) along the study road, pieces of the weathered material is weaken and cause the material to be displaced or broken down due to vehicle over weight, creating potholes. Interaction of weathered materials (clay and sand) with water and frequent movement of cars and trucks causes the enlargement of potholes that resulted in total failure of the road section.

The stable section of the study road that falls within the Bida Formation of Bida basin is composed of sandstone and lateritic soil, that are formed by in-situ leaching of sediments and precipitate quartz grain as sandstone while the leaching of soluble ions leaves the more insoluble ions, predominantly Kaolinite, iron and aluminium that precipitate of iron aluminium hydroxide as laterite.

Sandstone is more resistant to water influence and chemical weathering compared to rocks composed of silicates. Some clays generally influence swelling of weathered geological materials, the presence of thin layer of kaolinite a non swelling clay minerals in the sedimentary section of the study road does not have any swelling impact on the road. Also, diagenesis processes (compaction and cementation) influenced harding of the sandstone and thus make the road on the sedimentary section stable.

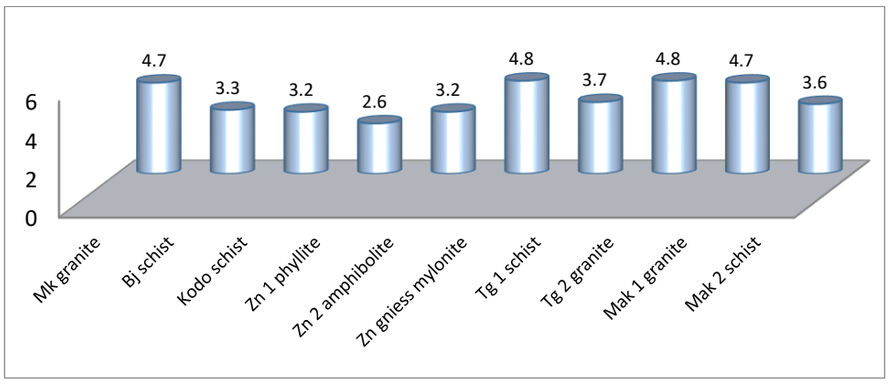

Figure 8: Weathering Intensity for study area (after Ruxton, 1968)

Conclusion

In this study, combined mineralogy and geochemical evaluations of the monotonous basement rocks and sandstone has been used to investigate the cause of road network failure along Minna – Tegina - Makera road, northwestern Nigeria. Results from this study identified the meta-sedimentary rocks which are of low grade metamorphism, enriched in feldspar minerals to underlie the failed sections of the study road network and meta-igneous rocks underlying the stable sections. The enrichment of feldspar combined with foliation, joints in the rocks and humid climatic condition promote the weathering of the meta-sedimentary rocks that lead to intensive weathering of these rocks and cause the failure of sections of the study road network and road carnage of various degree. Effort to maintain the study road section by government agency have not yield any result because the maintenance carried out was approached wrongly. It is evidently clear from this finding that low grade metasedimentary rocks constitute the foundation of the failed section, the presence of clayey and sandy (weathered product) and interaction with climate have contributed to road failure witnessed on the study road section.

In the light of this study, the failed portions of the study road need serious engineering attention. Excavation to fresh basement is required and filling with competent rocks to serve as basement and prevent persistent failure of this road.

(a) (b)

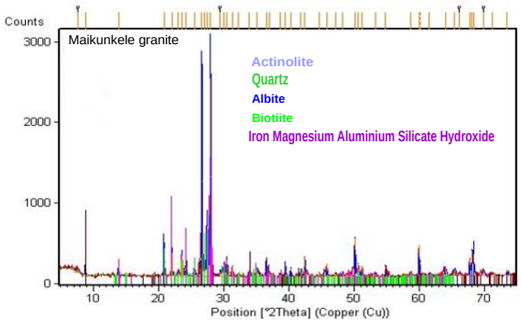
Counts
Maikunkele granite
Actinolite
Quartz
Albite
Biotiite
Iron Magnesium Aluminium Silicate Hydroxide
3000
2000
1000
0
10
20
30
40
50
60
70
Position [°2Theta] (Copper (Cu))

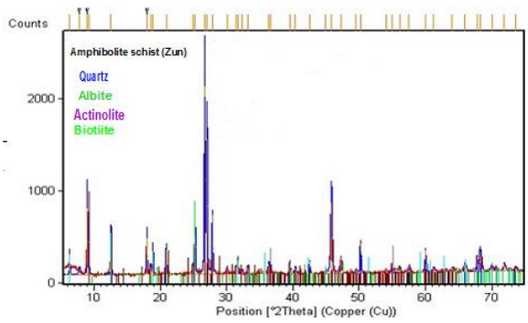
Counts
Amphibolite schist (Zun)
Quartz
Albite
Actinolite
Biotiite
2000
1000
0
10
20
30
40
50
60
70
Position [°2Theta] (Copper (Cu))

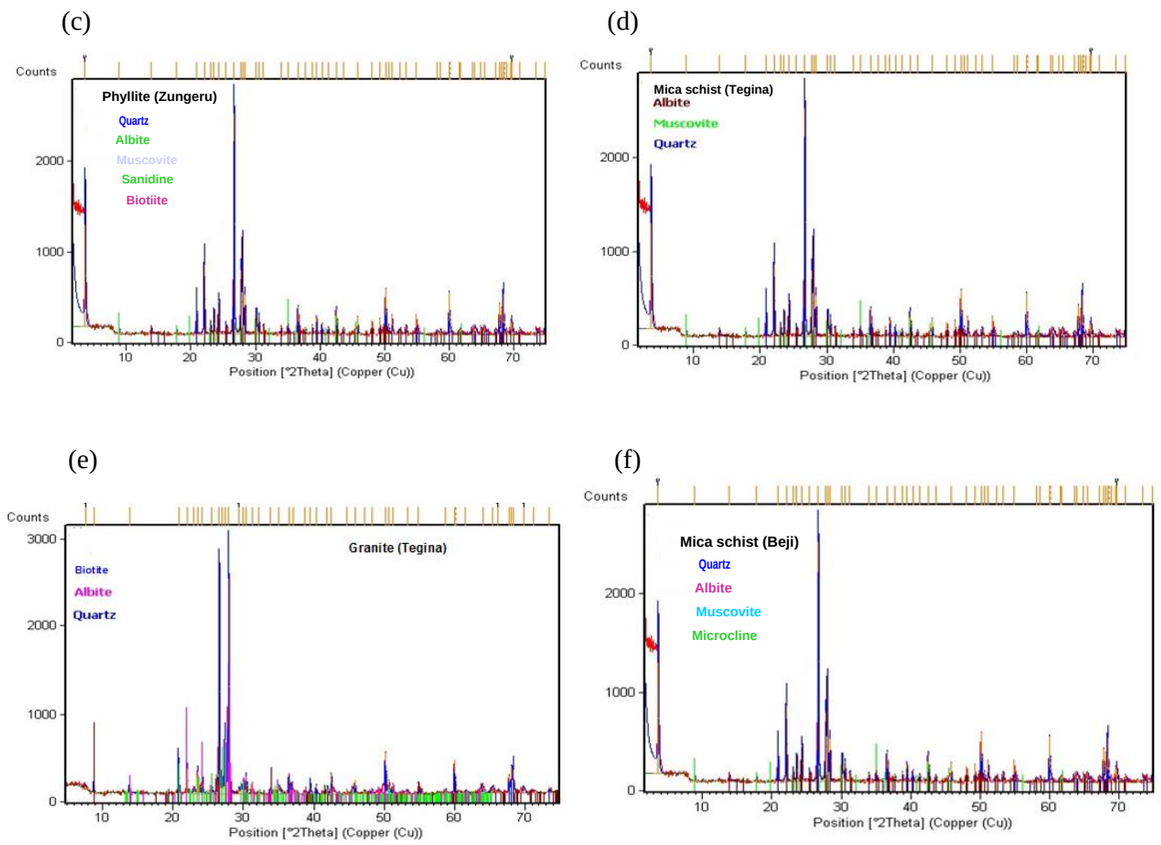

Figure 9: XRD Refractograms of rocks from the study area

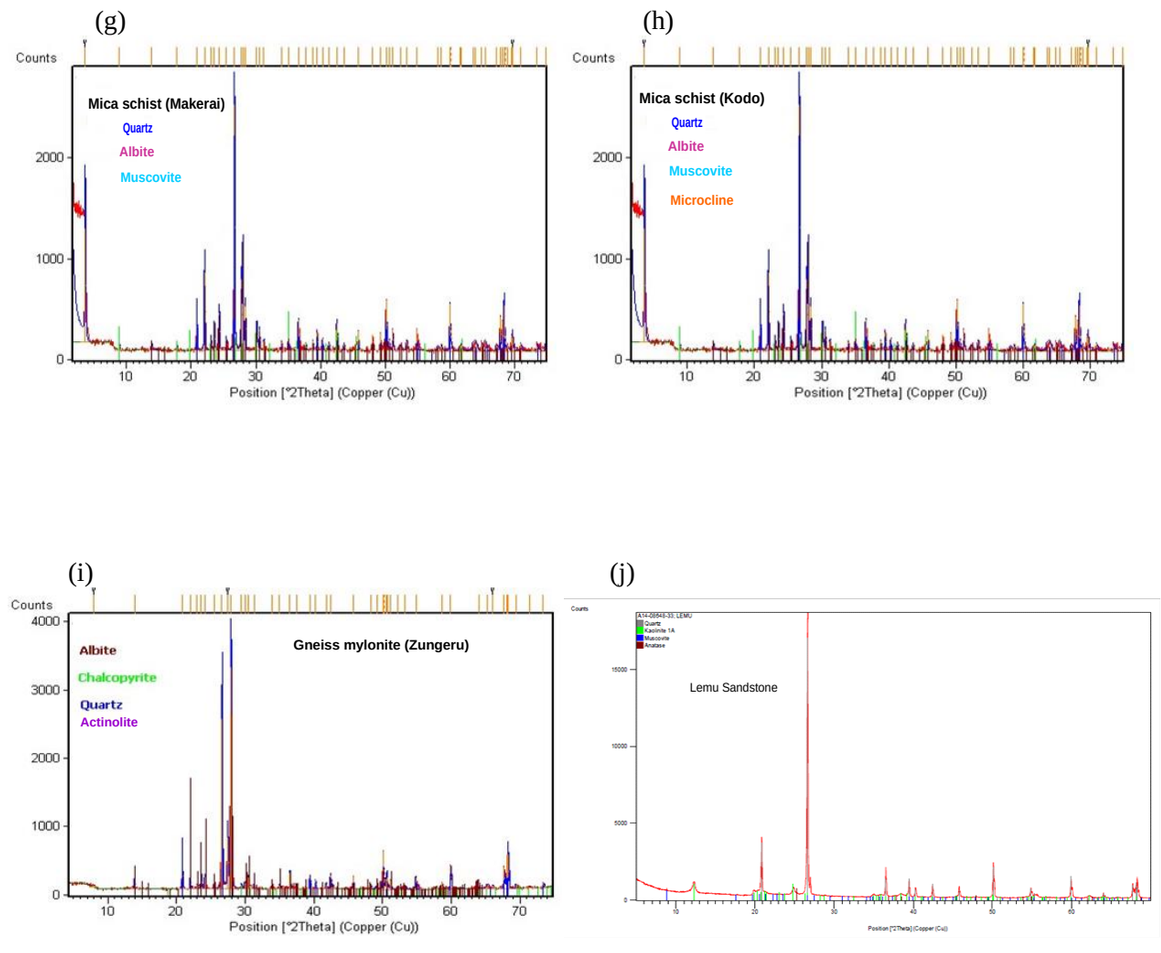

Figure 9: XRD Refractograms of rocks from the study area

Plate 10: Failed road sections along Minna – Tegina and Tegina - Makera federal road

REFERENCES

Adewoye, A. O., Adegbola, A. A., Bolaji, A. A. and Opebiyi, D. F. (2012). Engineering Properties of Foundational Materials of Oyo Ogbomoso Road, in Southwestern Nigeria: *Science Focus* 9: 42-47.

Ajibade, A.C., Anyanwu, N.C.P., Okoro, A.U., and Nwajide, C.S. (2008). The geology of Minna area. *Nigeria Geological Survey Agency Bulletin* No. 43.

Alabi, A. A (2016). Geology, Mineralogy, Geochemical Charaterization And Provenance Study Of Clay Occurrences In Central Bida/Niger Basin, Central Nigeria (Unpublishe Ph.D Thesis), Ahmadu Bello Universitt Zaria, Nigeria.

Akintorinwa, O. J., Ojo J. S. and Olorunfemi M. O. (2011) Appraisal of the causes of Pavement Failure Along The Ilesa - Akure Highway, Southwestern Nigeria Using Remotely Sensed and Geotechnical Data. *Ife Journal of Science* vol. 13, No.1. 185 – 197.

Garrels, R.M. and Mackenzie, F.T., (1971). *Evolution of metasedimentary rocks New York*: Norton and Company, page 394.

Osinowo O. O., Akanji A. O. and Akinmosin A. (2011). Integrated geophysical and geotechnical investigation of the failed portion of a road in basement complex Terrain, Southwest Nigeria, RMZ –*Materials and Geoenvironment*, 58(2): 143–162.

Ruxton, B.P. (1968). Measurment of the Degree of Chemical Weathering of rocks. *Journal of Geology 76*, page 518-527.

PALM BUNCH MANAGEMENT AND DISPOSAL AS SOLID WASTE AND THE STABILIZATION OF OLOKORO LATERITIC SOIL FOR ROAD CONSTRUCTION PURPOSES IN ABIA STATE, NIGERIA

Onyelowe, K. C.

Department of Civil Engineering, Michael Okpara University of Agriculture, Umudike, P. M. B. 7267, Umuahia 440109, Abia State, Nigeria. Email: konyelowe@mouau.edu.ng, konyelowe@gmail.com, konyelowe@yahoo.com.

Abstract

Palm bunch management and disposal as solid waste have been studied for the amount discharged from selected palm oil mills in Abia State. The process of personal interviews was conducted and responses evaluated and tabulated. A correlation was drawn between the responses and previous research work on the use of palm bunch ash as admixture in the stabilization of soil for road construction works in Abia State. Palm bunch as solid waste has proven to be a good material in both ash and nanosized ash additive to soil in improving its strength properties which satisfied the standards for the materials' use in pavement construction and rehabilitation. The results have encouraged the Ministries of Environment and Works to collaborate in this task to convert solid waste to usable materials in Geoengineering and "Geowaste" Engineering.

Keywords: Palm Bunch; Management; Disposal; Solid Waste; Stabilization; Lateritic Soil; Road Construction.

1. Introduction

Palm bunch is a product of palm oil production and processing from agro industries and local farmers whose concentration is the processing and production of palm oil. The task of palm bunch management and disposal has been a huge one except for its use as biofuel; a process that has helped in reducing the quantity of bunch indiscriminately disposed on the streets every day (Isaac and Eunice 2014). With the introduction of Geowaste Engineering, the disposal and management of palm bunch as a solid waste has gained interests. "Geowaste" Engineering is the area of Geoenvironmental Engineering where solid waste materials are used to improve the mechanical and Geotechnical properties of lateritic soil used in pavement constructions. Nigeria as a developing country whose hope of breaking loose from the shackles of underdevelopment, has been faced with solid waste disposal and management problem (Burmamu et al. 2014; Ochuko 2014). This is primarily because we lack the technologies and expertise to recycle and reuse these waste materials. Over the years, researches have shown that palm bunch could be used in the stabilization of lateritic soil, which is used in different Geotechnical engineering works. While we are faced with the hazards of dumping a palm bunch on our environment, we are equally faced with a dilapidated and failed environment with respect to facilities and structures that could be saved with these same waste materials. In 2015, a research was carried out to evaluate the effect of palm bunch ash on the Geotechnical properties of lateritic soil used for construction purposes and results showed significant improvements on the mechanical and Geotechnical properties of soil when mixed with varying proportions of palm bunch ash (Onyelowe and Ubachukwu 2015). In 2016, an extended research work was also conducted on the effect of nanosized palm bunch ash on the Geotechnical properties of lateritic soil used for the same purpose. The results also showed great improvements in the soil properties which satisfied engineering standards for use as admixture in the stabilization of the soil for Geotechnical engineering works (Onyelowe et al., in review). Consequently, the aim of this research work is to evaluate the need for efficient disposal and management of palm bunch and its use in the soil improvement for road pavement construction and rehabilitation and other Geo-engineering works in Abia State.

2. Methodology

Abia State is located on latitude 5.4309° N and longitude 7.5247° E covering an area of 6, 320km^2 with an average rainfall of 2050mm. Abia State has a variety of land forms, despite the fact that it is dominated by flat and low-lying land, generally less than 120m above sea-level. The low-lying plain is the inland extension of the coastal plain from the Bight of Benin. The central part of the state is characterized by undulating land with many hills. The highland areas are part of the Enugu - Nsukka - Okigwe cuesta. This area has an average height of between 120m and 180m above sea-level. From Okigwe (Imo State), this escarpment extends in a west-east direction and, on getting to Afikpo (Ebonyi State), veers southeastwards to Arochukwu where it terminates. Palm tree farming and palm oil processing and production are the major activities of the people living within the studied area. As a result, palm oil milling factories and farms are predominantly located in every village within the state of Abia. The waste products of these factories are palm bunch, palm kernel, palm leaves, etc., which are disposed

indiscriminately along pathways, roads and even on farmlands making its use a difficult task. The present research has sampled through questionnaires the average yield of few selected palm oil mills in Abia State and come up with the results of their responses which will help the state ministry of environment to establish modalities on how to manage these solid waste materials in collaboration with the state ministry of works. The selected palm oil mills are located in Ndiolumbe, Omoba, Nbawsi, Ohafia, Arochukwu, Obohia and Ndoki all in Abia State. The management of these palm oil mills were interviewed on the quantity of palm bunch they produce daily and their disposal procedures. At the end of the exercise, results were collected and tabulated.

3. Results and Discussions

From the seven selected Palm Oil Mills in Abia State, a total of 1113tonnes of palm bunch is discharged and disposed daily as shown in Tables 1 and 2.

Table 1: Daily Discharge of Palm Bunch from Palm Oil Mills in Abia State

Palm Oil Mill	Ndiolumbe	Omoba	Nbawsi	Ohafia	Arochukwu	Obohia	Ndoki
Palm Bunch Discharge Quantity (Tonnes/day)	342	192	157	118	87	120	97

1 Tonne = 1000kg

Table 2: Daily Disposal of Palm Bunch from Palm Oil Mills in Abia State

Discharge Point	Biofuel	Farmland	Road Sides	Drains	Dilapidated Road Points	Organic Fertilizer	Solid waste Bins	Uncertain
Tonnes/day	520	21	146	136	201	23	53	19

1 Tonne = 1000kg

It can be observed that the palm oil mills in the southern part of Abia and close to the rural and suburb communities produce the highest amount of palm bunch. The daily discharge of palm bunch from the selected oil mills in Abia State is a clear indication of the amount of solid waste disposed indiscriminately that should be put into engineering use to save our environment. Among the hazards of indiscriminate disposing this solid waste are; (i) blocking rural and urban roads where these wastes are dumped, (ii) blocking drain facilities, thereby making them non-functional, (iii) puncturing of vehicle tyres and also making the roads untidy to be used, iv) rendering farmlands useless to intended use, and (v) occupying the waste bins unnecessarily. It can also be observed that the highest quantity is used as a biofuel in homes and the same oil processing factories to boil the palm fruits during processing. This is because all the oil mills don't have access to industrial boilers used to boil palm fruits during processing. The above mentioned hazards could be mitigated if the ministries of Environment and Works had come together to collaborate on the management and discharge of solid waste in Abia state under a procedure I would call "waste to safety" of our decaying environment. There is plenty to be achieved with this procedure; (i) save our farmlands, roadways, drains, waste bins and more by ridding the environment of this solid waste and pushing them into the stabilization of soil for Geotechnical engineering purposes. The subgrade soils of our flexible pavements fail in different parts of the state when we can actually improve the strength characteristics of the lateritic soil used as subgrade soils by using palm bunch ash as admixture to the stabilized soil and ordinary Portland cement as the binder. Previous research has shown that the addition of 15% of Palm Bunch Ash by weight of the stabilized sample is suitable to improve the strength properties of the stabilized soil and the addition of 12% of Nanosized Palm Bunch Ash is also suitable for the same purpose. It follows that if the entire palm bunch generated in this state from palm oil processing, the environment will be free of this solid waste and at the same time get better in terms of pavement facilities' strength improvement.

4. Conclusion

From the foregoing, we can deduce that the management and disposal of palm bunch and reusable solid waste generated in Abia State is a combined activity of the Ministries of Environment and Works in that both government agencies have a need for this solid waste to make our environment better in both lines.

Acknowledgement

The data collected was made possible by the operators of the selected Palm Oil Mills in Abia State.

References

Isaac OA and Eunice OA. 2014. “Environmental Risk-Factors of Indiscriminate Refuse Disposal in Ekiti State, Nigeria”, IOSR Journal of Research & Method in Education (IOSR-JRME), Volume 4, Issue 5 Ver. II, PP 54-59.

Burmamu BR, Law PL, Aliyu HH and Ibrahim Y. 2014. “Environmental Impacts and Management Strategies of Solid Waste Disposal in Jimeta-Yola, Nigeria”, International Journal of Environmental Engineering Science and Technology Research Vol. 2, No. 3, PP: 1 – 8.

Ochuko MO. 2014. “Solid Waste Management in Obantoko Area of Abeokuta, Nigeria”, Journal of Emerging Trends in Engineering and Applied Sciences (JETEAS) 5 (2): 111-115.

Onyelowe KC and Ubachukwu OA. 2015. “Stabilization of Olokoro-Umuahia Lateritic Soil with Palm Bunch Ash as Admixture”, Umudike Journal of Technology, Vol.2, No. 2: 67-77.

GEOTECHNICAL INVESTIGATION OF THE SUBSURFACE FORMATIONS USING ELECTRICAL RESISTIVITY METHOD IN NORTHERN PART OF PAIKO TOWN, NIGER STATE, NIGERIA

[1]Alhassan D.U, [2]Obiora D. N, and [2]Okeke F. N

[1]Department of Physics, Federal University of Technology, Minna

[2]Department of Physics and Astronomy, University of Nigeria, Nsukka

Correspondence author – a.usman@futminna.edu.ng

Abstract

Vertical electrical sounding (VES) was carried out in the study area, using Abem Terrameter model SAS 4000. The study was carried out with a view to determine the subsurface layer parameters (resistivity, depth, thickness and lithologies) which were employed in delineating the sites for building construction. Six transverses with ten VES stations along each traverse, having separation of 50 m apart were investigated. It has a maximum current electrode separation (AB/2) of 100 m. Three to four distinct geoelectric layers were observed namely; Top layer which consist of gravel, sand, laterite and alluvial, weathered/fractured layer consist of clay and laterite, and fresh basement layer that consist of granite, gneiss and igneous rock. The observed frequencies in curve types include 21.6% of H, 0.6% of HA, 2.4% of K, 0.6% of A, 3.6% of KH, 6% of QA and 1.2% of HK. Sixteen VES stations were delineated for building construction, having depths to fresh basement varying between 2.18 m and 3.93 m with fresh basement resistivity ranged between 1038 Ωm and 194453 Ωm

Key words: Building construction, vertical electrical sounding, resistivity, depth, geoelectric layer, bedrock, Abem Terrameter

Introduction

The study area is located in the north central part of Nigeria. The population of Paiko is increasing rapidly as a result of people migrating from rural areas to urban towns to earn a living. As such, there is need for more estate development to accommodate the growing population of the area. However, presently in Nigeria there are several cases of building collapse and cracking of walls as a result of poor foundation and lack of site investigation (Alhassan *et al*., 2015). There is need to search for the areas where the consolidated basement is shallow and can provide strong base for building construction. Therefore, the aim of this work is to employ geophysical method to determine sites where the fresh basement is intruded close to the surface that can support foundations to buildings. Among several geophysical methods employed in determining depth to bedrock (electrical resistivity, gravity, seismic, magnetic, remote sensing, and electromagnetic), the electrical resistivity method is the most effective (Kearey *et al*., 2002; Alhassan *et al*., 2017). It is an effective and a reliable tool in slicing the earth into geoelectric layers. It has the advantage of non-destructive effect on the environment, cost effective, rapid and quick survey time and less ambiguity in interpretations of results when compared to other geophysical survey methods (Todd, 1980). The vertical electrical sounding (VES) technique provides information on the vertical variations in the resistivity of the ground with depth (Ariyo, 2005; Alhassan *et al*., 2015; Obiora *et al*., 2016). It is used to solve a wide variety of problems, such as; determination of depth, thickness and boundary of aquifer (Asfahani, 2006; Bello and Makinde, 2007).

GEOLOGY OF THE STUDY AREA

The study area is located within the north central Nigerian basement complex. It has an elevation of 304 m above sea level with population of about 736,133 people as at 2006 census. It is bounded by latitudes 9° 25′N and 9° 27′N and longitudes 6 ° 37′E and 6 ° 39′E. Generally, the area mapped forms part of the Minna- granitic formation that consists of Metasediment `and metavolcanics. The Metasediment include quartzites, gneisses and the metavolcanics are mainly granites. Among the main rock groups are granites which occur at the central and northern parts of the area, while on the south and east, cobbles of quartzite are found especially along the channels and valley. However, the other bodies like pegmatites and quartz veins also occur within the major rock types (Figure 1). The rocks are mainly biotite –granites with medium to coarse grained, light colored rocks with some variation in biotite content. The mineral constituents are leucocratic to mesocratic. However, the biotite minerals are thread like and are arranged rough parallel streak, although some are disoriented in the groundmass. The feldspar minerals occur as fine to medium grained, though grains are cloudy as a result of alteration mostly along the twin planes, while the quartz minerals are constituents of the granitic rocks which show strong fracturing in the granitic rocks of the area (Ajibade, 1980).

The area is therefore, underlain by four lithological formations as it is evident from the rocks in the area. The rock types in this region include granites, gneisses quartzite as well as laterites while most of the granites are older granites and this distinguishes them from the younger granites found in Jos area. From field observation, granitic rocks are the most abundant and they are widely distributed in the study area, as well characterized by hills with relative low lands and slightly drained by streams of intermittent and ephemeral types and also some tributaries. The area mapped is underlain by coarse to medium grained granite. These rocks are well exposed at the southern and eastern parts of the area. In hand specimen they have a coarse texture. The outcrops are all light in colour and the major minerals contained are quartz, feldspar and biotite as revealed under the thin section studies by the use of a petrological microscope.

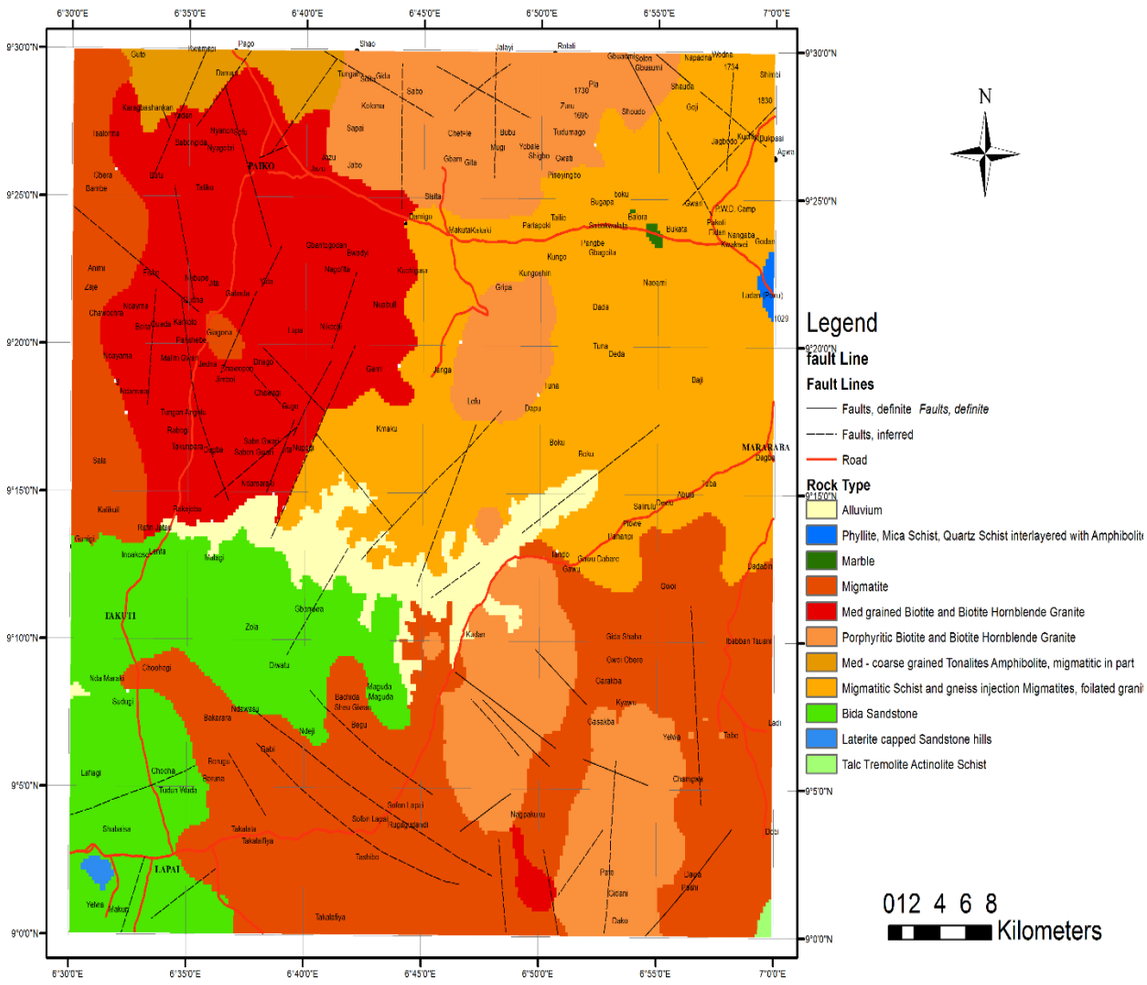

Figure 1: Geological Map of Paiko area (Modified after NGSA 2010).

METHODOLOGY

This research has utilized the electrical resistivity method in delineating the shallow consolidated basement of the study area. Sixty vertical electrical soundings were carried out using SAS 4000 model Terrameter and its accessories. The conventional Schlumberger array pattern with half electrode spacing (AB/2) varying from 1 m to a maximum of 100 m was adopted. The apparent resistivity was computed using equation 1

$$\rho_a = KR \qquad (1)$$

Where ρ_a is an apparent resistivity and the earth resistance (R) is given as

$$R = \frac{\Delta V}{I} \qquad (2)$$

The geometric factor, K, is expressed as

$$K = \pi\left(\frac{\left(\frac{AB}{2}\right)^2 - \left(\frac{MN}{2}\right)^2}{MN}\right) \qquad (3)$$

The apparent resistivity values obtained from equation (1) were plotted against the half current electrode separation spacing using IPI2WIN software. From these plots, vertical electrical sounding curves were obtained (Figure 2) and qualitative deductions such as resistivity of the layers, the depth of each layer, the thickness of each layer, number of layers, curve types and geologic cross section of the area were made.

RESULTS AND DISCUSSION

The summary of the interpreted electrical resistivity survey is presented in Tables 1, 2, 3 and 4. Table 1 consists of VES stations $G_1$to I_{10} while table 2 comprised of VES stations J_1 to L_{10}. The tables 3 and 4 show the depth to consolidated basement. From the plot of apparent resistivity versus half current electrode spacing, geoelectric sections were produced (figure 2), where resistivity of the layers, the depth of each layer, the thickness of each layer, and number of layers, were obtained.

The geologic cross section (Figure 3a-f) reveals that the area is characterized by 3 to 4 geologic subsurface layers. Six profiles with sixty VES stations were covered and their subsurface geologic cross sections were presented in figure 3. The geologic cross section shows the layers in vertical sequence with colorations differentiate one layer from another layer (figure 3a-f). From the figure, 3- layer type occurring more and are characterized by H curve type. Some are characterized by A and K curve types. The 3- layer geologic sections are generally made up of topsoil, weathered/fractured layer and fresh basement rock from top to the bottom with variable depths, thicknesses and resistivities. The 4- layer geoelectric sections are characterized by HA, KH and HK curve types. The observed frequencies in curve types include 21.6 % of H, 3.0 % of HK, 4.2 % of HA, 3.6 % of A, 2.4 % of K, and 1.2 % of KH

The 4- layer geoelectric section is made up of topsoil, weathered layer, fractured layer and fresh basement rock. Generally, the topsoil of the area is made up of loose sand, gravels, sandy clay, laterite and clay. In a basement complex terrain, areas with fresh basement layer depth less or equal to 4 m are favorable and good for building construction (Alhassan *et al*., 2015).

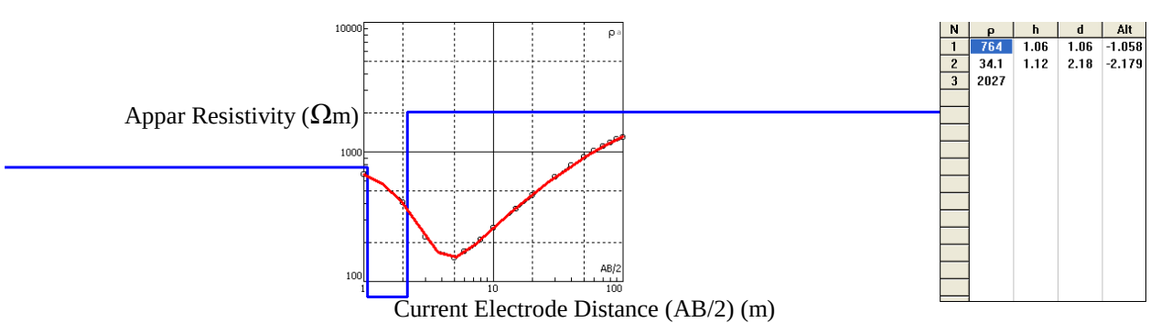

Figure 2a: VES Curve I_7

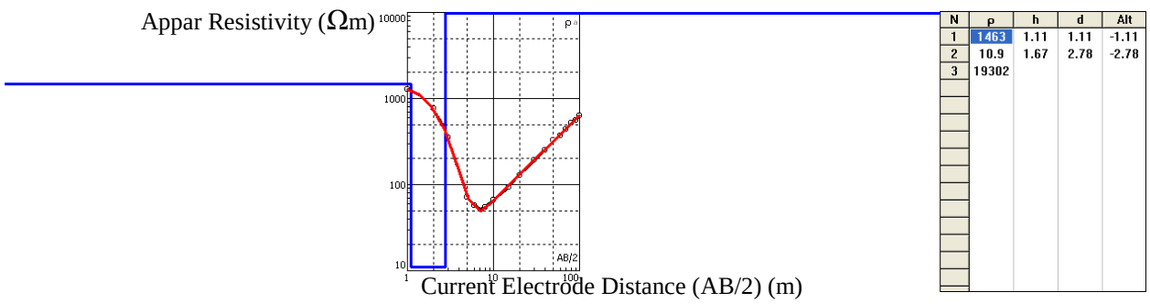

Figure 2b: VES Curve I_{10}

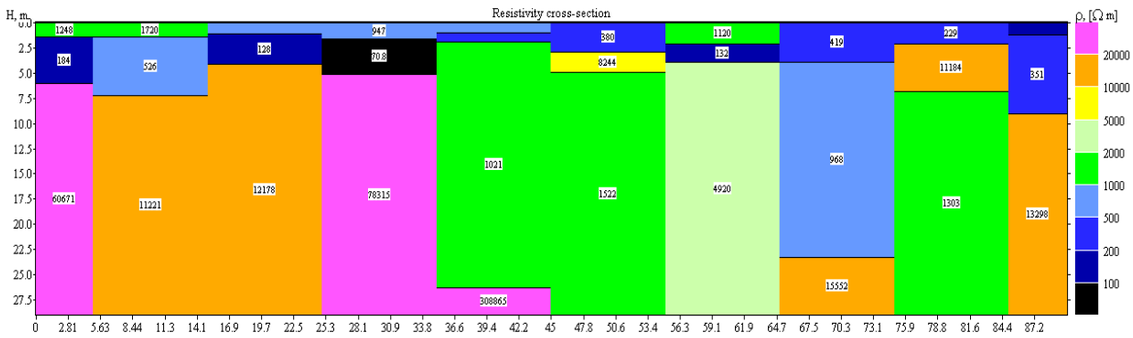

Figure 3a: Geologic Cross-Section of Profile G

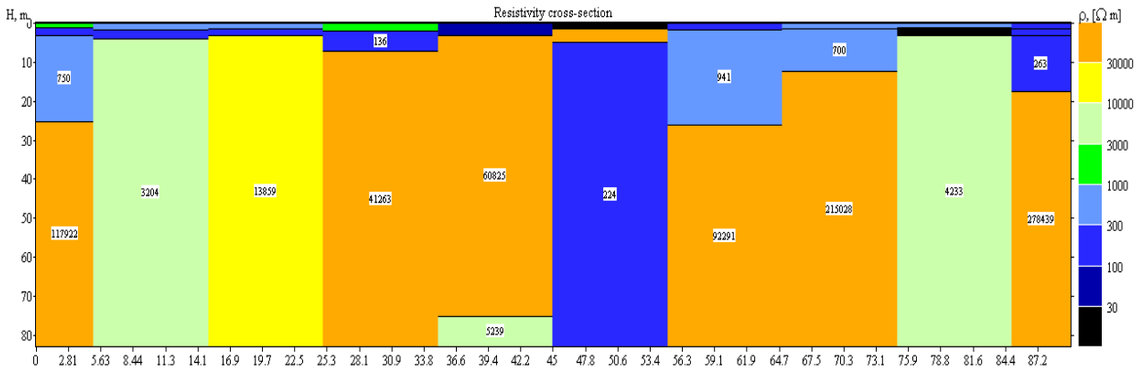

Figure 3b: Geologic Cross-Section of Profile H

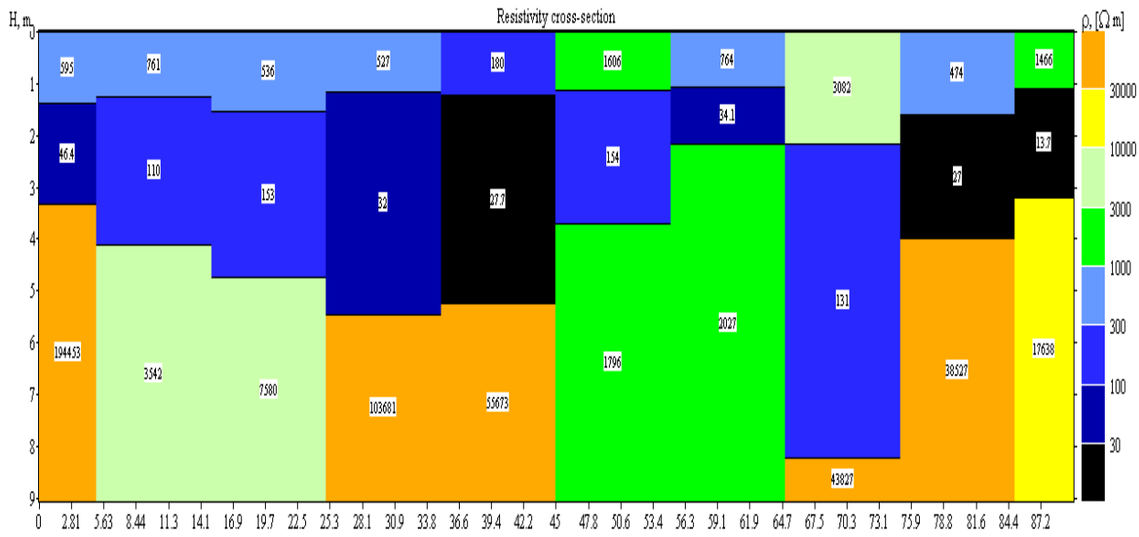

Figure 3c: Geologic Cross-Section of Profile I

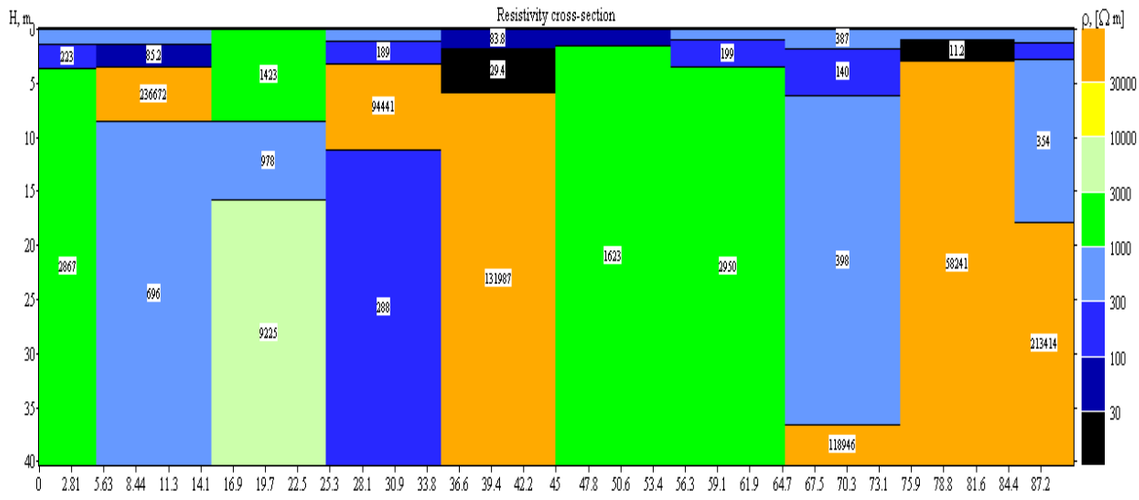

Figure 3d: Geologic Cross-Section of Profile J

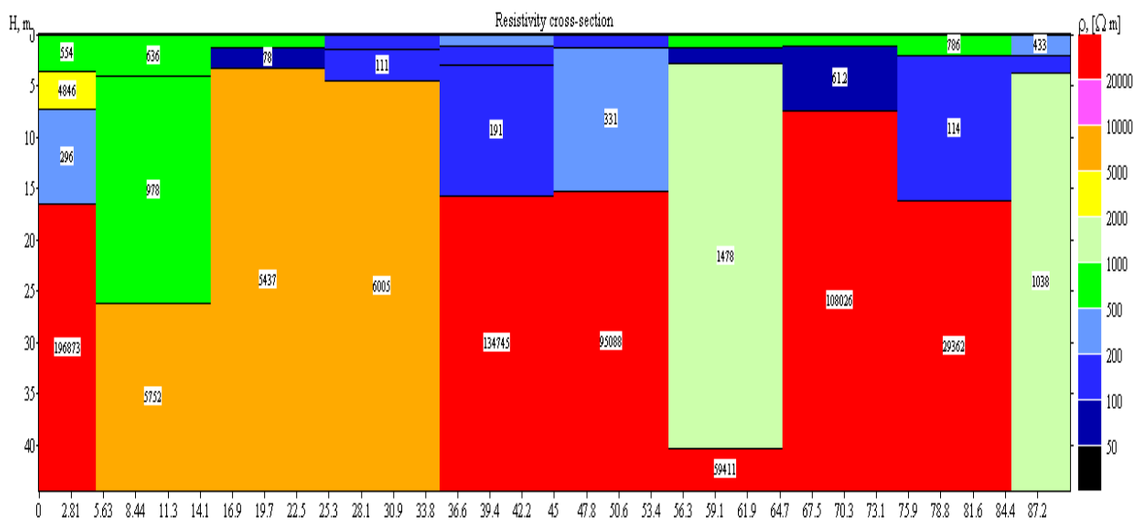

Figure 3e: Geologic Cross-Section of Profile K

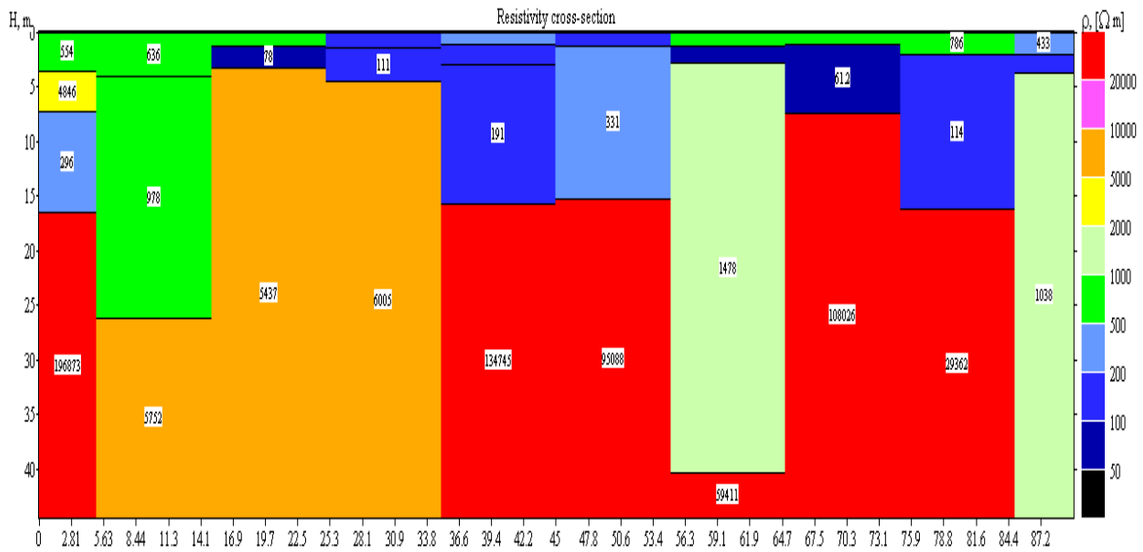

Figure 3f: Geologic Cross-Section of Profile L

In investigating the continuous variation of resistivity with depth, iso-resistivity maps using Golden software (Surfer 11.0) version were obtained for the layers (Figure 4). It shows the color range corresponding to resistivity range of the earth materials. The iso-resistivity map of the first layer reveal that blue represent gravels, sky blue represent sand, green correspond to laterite and yellow represent alluvial deposits (Figure 4a).

The iso-resistivity map of the second layer shows that blue color corresponds to clay and sky blue represent laterite (Figure 4b). Third layer iso-resistivity maps reveal that blue represent granite, sky blue represent gneiss, green correspond to igneous rock, and yellow represent gabbro rock (Figure 4c).

The depth to consolidated basement map shows the depth distribution within the area (figure 5). From the map, the area with blue coloration corresponds to the shallow depth to fresh basement with high resistivity values and therefore be the suitable areas delineated for building construction.

Table 1: Layers resistivity, depth, thickness and curve types

VES station	No of Layer	Layer resistivity (Ωm)				Layer depth (m)				Layer Thickness (m)				Curve type
		ρ_1	ρ_2	ρ_3	ρ_4	d_1	d_2	d_3	d_4	h_1	h_2	h_3	h_4	
G_1	3	1248	184	60671		1.40	6.00	∞		1.40	4.60	∞		H
G_2	3	1720	526	11221		1.38	7.27	∞		1.38	5.89	∞		H
G_3	3	667	126	12178		1.14	4.07	∞		1.15	2.92	∞		H
G_4	3	947	70.80	78315		1.63	5.11	∞		1.63	3.47	∞		H
G_5	4	820	247	1021	308865	1.04	1.88	26.30	∞	1.04	0.85	24.40	∞	HA
G_6	3	380	8244	1522		2.87	4.91	∞		2.07	2.04	∞		K
G_7	3	1120	132	4920		2.07	3.93	∞		2.07	1.06	∞		H
G_8	3	419	968	15552		3.91	23.30	∞		3.91	19.40	∞		A
G_9	3	229	11184	1303		2.11	6.87	∞		2.11	4.75	∞		K
G_{10}	3	117	351	13298		1.18	9.07	∞		1.19	7.88	∞		A
H_1	4	1490	152	750	117922	1.18	3.21	25.40	∞	1.18	2.03	22.10	∞	HA
H_2	3	415	124	3204		1.69	3.93	∞		1.69	2.24	∞		H
H_3	3	308	130	13859		1.42	3.28	∞		1.42	1.86	∞		H

H_4	3	1114	136	41263		1.93	7.16	∞		1.93	5.23	∞		H
H_5	3	39.90	60825	5239		3.07	75.10	∞		3.07	72.00	∞		K
H_6	3	1070	80368	224		1.38	4.81	∞		1.38	3.43	∞		K
H_7	3	243	941	92291		1.85	26.10	∞		1.05	24.30	∞		A
H_8	3	457	700	215028		1.45	12.40	∞		1.45	10.90	∞		A
H_9	3	550	28	4233		1.12	3.30	∞		1.12	2.17	∞		H
H_{10}	4	191	106	263	278439	1.43	3.03	17.60	∞	1.43	1.60	14.60	∞	HA
I_1	3	595	46.40	194453		1.37	3.34	∞		1.37	1.96	∞		H
I_2	3	761	110	3542		1.25	4.10	∞		1.25	2.86	∞		H
I_3	3	536	153	7580		1.52	4.75	∞		1.52	3.23	∞		H
I_4	3	527	32	103681		1.16	5.47	∞		1.16	4.31	∞		H
I_5	3	180	27.70	55673		1.22	5.23	∞		1.22	4.02	∞		H
I_6	3	1606	154	1796		1.12	3.72	∞		1.12	2.60	∞		H
I_7	3	764	34.10	2027		1.06	2.18	∞		1.06	1.12	∞		H
I_8	3	3082	131	43827		2.15	8.22	∞		2.15	6.06	∞		H
I_9	3	474	27	38527		1.61	3.97	∞		1.61	2.36	∞		H
I_{10}	3	1463	10.90	19302		1.11	2.78	∞		1.11	1.67	∞		H

VES-vertical electrical sounding; ρ-layer resistivity; d- layer depth; h – layer thickness; m-metre

Table 2: Layers resistivity, depth, thickness and curve types

VES station	No of Layer	Layer resistivity (Ωm)				Layer depth (m)				Layer Thickness (m)				Curve type
		ρ_1	ρ_2	ρ_3	ρ_4	d_1	d_2	d_3	d_4	h_1	h_2	h_3	h_4	
J_1	3	841	223	2867		1.36	3.61	∞		1.36	2.25	∞		H
J_2	4	439	85.20	236672	696	1.35	3.53	8.57	∞	1.35	2.18	5.04	∞	HK
J_3	3	1423	978	9225		8.53	15.70	∞		8.53	7.20	∞		H
J_4	4	985	189	94441	288	1.05	3.27	11.20	∞	1.05	2.22	7.93	∞	HK
J_5	3	83.80	29.40	131987		1.86	5.86	∞		1.86	3.99	∞		H
J_6	2	62.20	1623			1.56	∞			1.56	∞			A
J_7	3	982	199	2950		0.95	3.54	∞		0.95	2.59	∞		H
J_8	4	387	140	398	118946	1.86	6.09	36.60	∞	1.86	4.22	30.50	∞	HA
J_9	3	620	11.20	58241		1.00	3.00	∞		1.00	2.00	∞		H
J_{10}	4	571	124	354	213414	1.30	2.73	17.80	∞	1.30	1.43	15.10	∞	HA
K_1	4	554	4846	296	196873	3.57	7.19	16.40	∞	3.57	3.61	9.22	∞	KH
K_2	3	636	978	5752		4.06	26.20	∞		4.06	22.10	∞		A
K_3	3	517	78	5437		1.17	3.22	∞		1.17	2.05	∞		H
K_4	3	178	111	6005		1.42	4.47	∞		1.42	3.05	∞		H
K_5	4	469	117	191	134745	1.07	3.00	15.70	∞	1.07	1.93	12.70	∞	HA
K_6	3	198	331	95088		1.30	15.20	∞		1.30	13.90	∞		A
K_7	4	776	61.30	1478	59411	1.21	2.76	40.30	∞	1.21	1.54	37.50	∞	HA
K_8	3	712	61.20	108026		1.06	7.45	∞		1.06	6.39	∞		H
K_9	3	786	114	29362		2.02	16.10	∞		2.02	14.10	∞		H

K_{10}	3	433	113	1038		2.02	3.62	∞		2.02	1.60	∞		H
L_1	4	300	196	27962	79.90	2.69	7.93	15.30	∞	2.69	5.23	7.41	∞	HK
L_2	4	620	154	38600	130	1.18	3.24	8.02	∞	1.18	2.06	4.78	∞	HK
L_3	4	625	132	113317	303	1.28	3.03	6.78	∞	1.28	1.75	3.75	∞	HK
L_4	3	1052	232	172184		1.24	12.70	∞		1.24	11.40	∞		H
L_5	3	656	289	4230		1.49	13.60	∞		1.49	12.10	∞		H
L_6	3	85	15.20	78682		1.13	5.26	∞		1.13	4.13	∞		H
L_7	3	584	156	2853		1.18	3.73	∞		1.18	2.55	∞		H
L_8	3	1003	59.80	31877		2.54	7.28	∞		2.54	4.75	∞		H
L_9	3	546	43.20	107599		1.42	7.54	∞		1.42	6.12	∞		H
L_{10}	3	420	170	110943		2.31	14.40	∞		2.31	12.10	∞		H

VES-vertical electrical sounding; ρ-layer resistivity; d- layer depth; h – layer thickness; m-metre

Table 3: Depths to Fresh Basement of the Area

VES STATION	Latitude (degrees)	Longitude (degrees)	Elevation (m)	Depth to Basement (m)
G_1	09.46521	006.63871	320	6.00
G_2	09.46500	006.63832	312	7.27
G_3	09.46463	006.63797	307	4.07
G_4	09.46435	006.63756	311	5.11
G_5	09.46410	006.63720	310	26.30
G_6	09.46379	006.63683	313	4.91
G_7	09.46360	006.63642	307	3.93
G_8	09.46330	006.63602	306	23.30
G_9	09.46294	006.63575	308	6.87
G_{10}	09.46264	006.63533	312	9.07
H_1	09.46567	006.63856	313	25.40
H_2	09.46538	006.63799	305	3.93
H_3	09.46502	006.63739	299	3.28
H_4	09.46469	006.63698	304	7.16

H_5	09.46443	006.63658	307	75.10
H_6	09.46413	006.63629	307	4.81
H_7	09.46382	006.63595	310	26.10
H_8	09.46353	006.63560	305	12.40
H_9	09.46279	006.63505	303	3.30
H_{10}	09.46278	006.63501	305	17.60
I_1	09.46609	006.63838	309	3.34
I_2	09.46596	006.63795	313	4.10
I_3	09.46572	006.63758	310	4.75
I_4	09.46551	006.63718	305	5.47
I_5	09.46535	006.63672	305	5.23
I_6	09.46510	006.63634	306	3.72
I_7	09.46483	006.63597	306	2.18
I_8	09.46458	006.63562	305	8.22
I_9	09.46424	006.63528	308	3.97
I_{10}	09.46383	006.63491	296	2.78

Table 4: Depths to Fresh Basement of the Area

VES STATION	Latitude (degrees)	Longitude (degrees)	Elevation (m)	Depth to Basement (m)
J_1	09.46655	006.63817	312	3.61
J_2	09.4663	006.63778	311	8.57
J_3	09.46610	006.63736	310	15.70
J_4	09.46587	006.63693	303	11.20
J_5	09.46569	006.63650	291	5.86
J_6	09.46538	006.63613	301	3.00
J_7	09.46520	006.63573	305	3.54
J_8	09.46494	006.63538	304	36.60
J_9	09.46465	006.63501	303	3.00
J_{10}	09.46429	006.63460	303	17.80
K_1	09.46704	006.63790	316	16.40
K_2	09.46672	006.63721	311	26.20
K_3	09.46640	006.63688	301	3.22
K_4	09.46617	006.63649	302	4.47
K_5	09.46588	006.63613	300	15.70
K_6	09.46560	006.63574	301	15.20
K_7	09.46533	006.63533	302	40.30
K_8	09.46504	006.63494	303	7.45
K_9	09.46473	006.63451	298	16.10
K_{10}	09.46443	006.63412	305	3.62

L_1	09.46746	006.63768	314	15.30
L_2	09.46734	006.63724	310	8.02
L_3	09.46703	006.63681	314	6.78
L_4	09.46677	006.63638	312	12.70
L_5	09.46650	006.63600	313	13.60
L_6	09.46621	006.63557	306	5.26
L_7	09.46585	006.63514	299	3.73
L_8	09.46552	006.63486	296	7.28
L_9	09.46529	006.63436	304	7.54
L_{10}	09.46497	006.63390	314	14.40

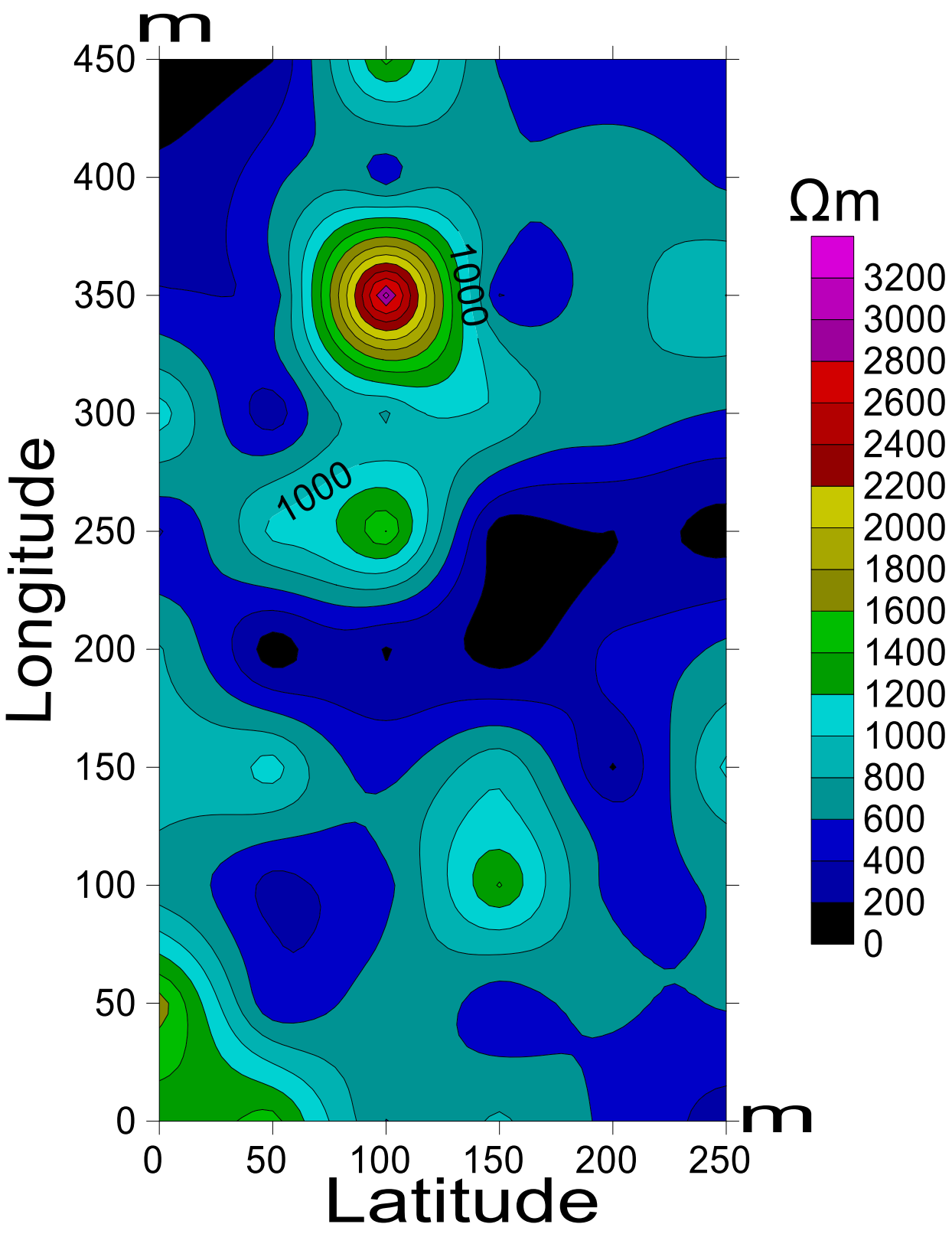

Figure 4a: Iso resistivity Map of the First Layer

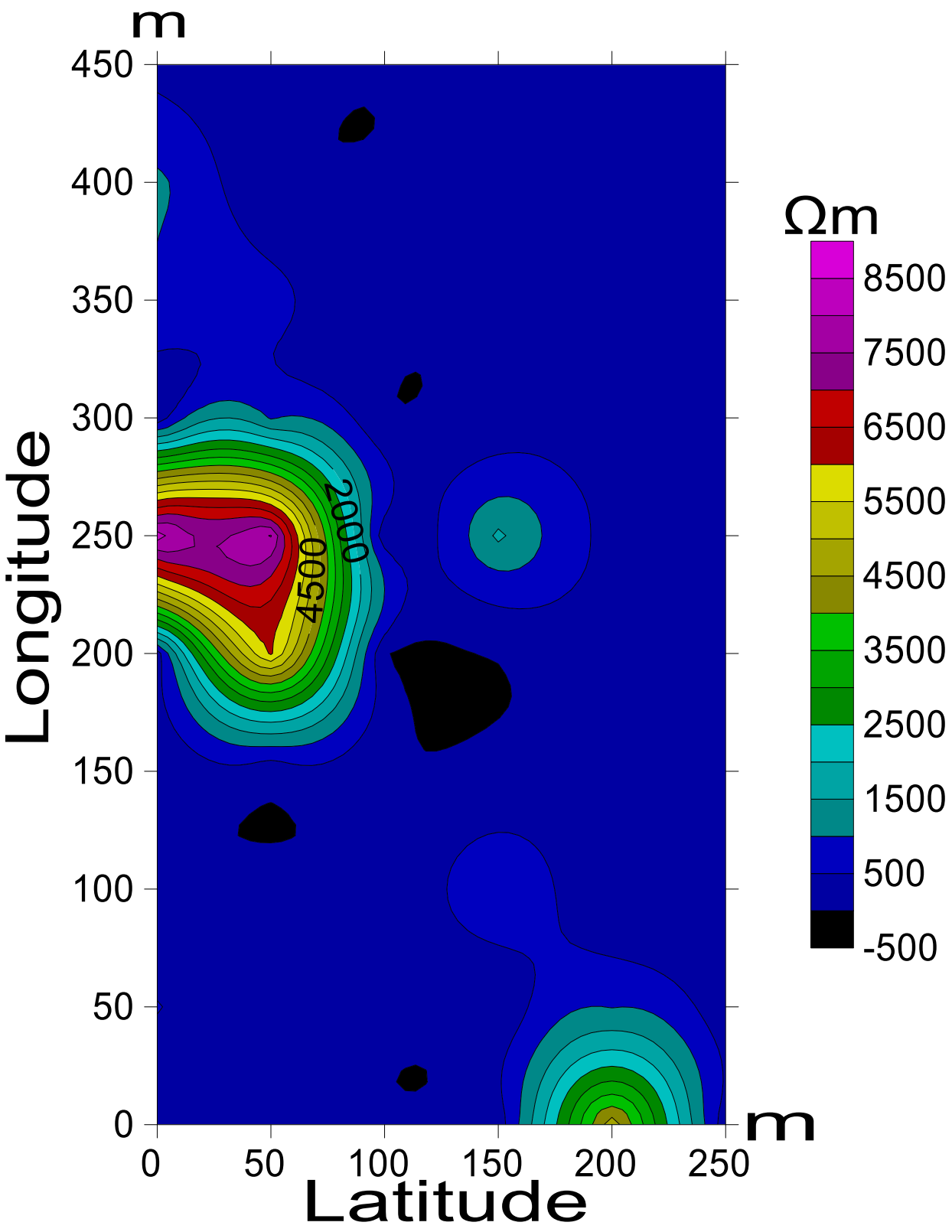

Figure 4b: Iso resistivity Map of the Second Layer

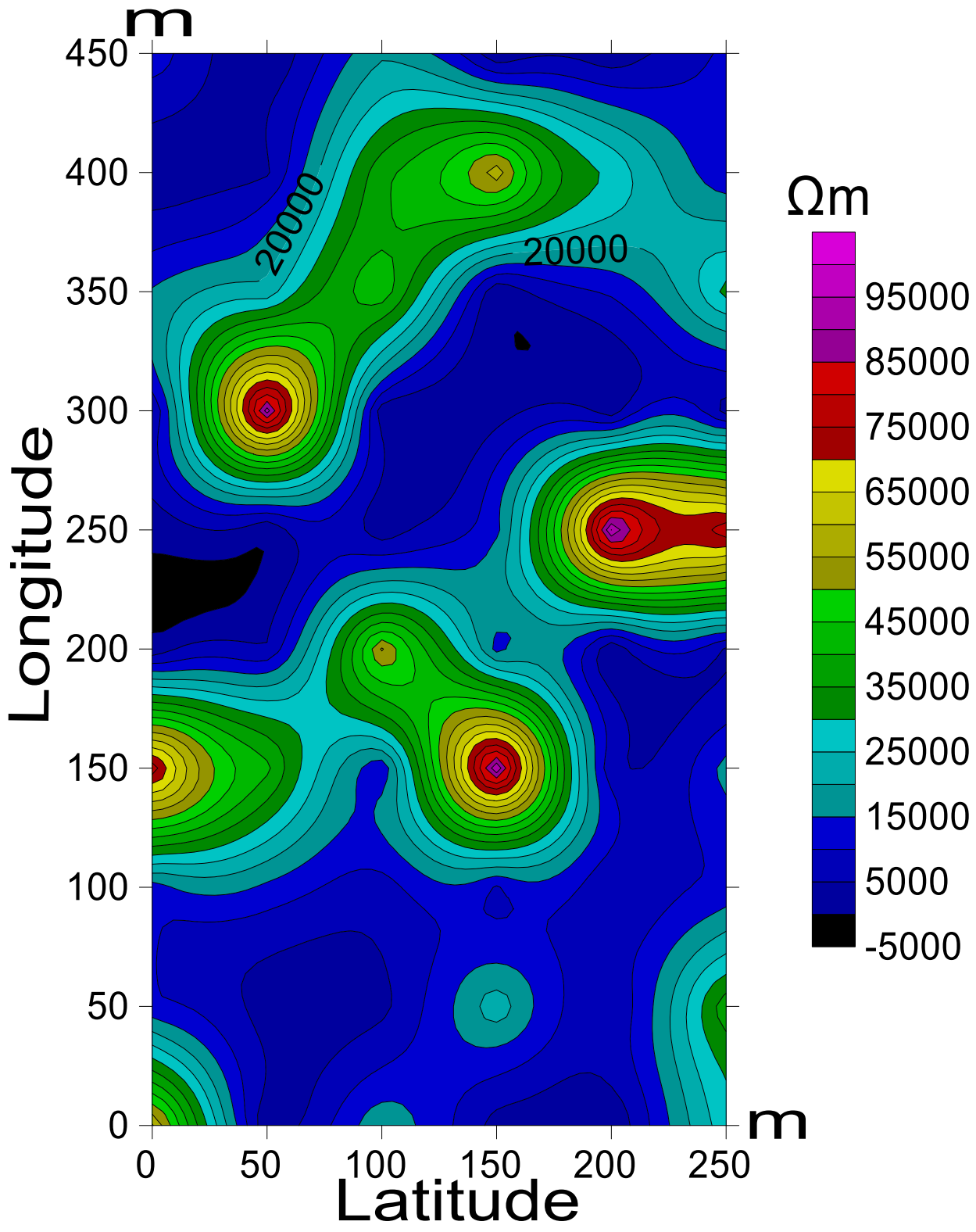
m
450
400
350
300
250
200
150
100
50
0
Longitude
20000
20000
Ωm
95000
85000
75000
65000
55000
45000
35000
25000
15000
5000
-5000
m
0
50
100
150
200
250
Latitude

Figure 4c: Iso resistivity Map of the Third Layer

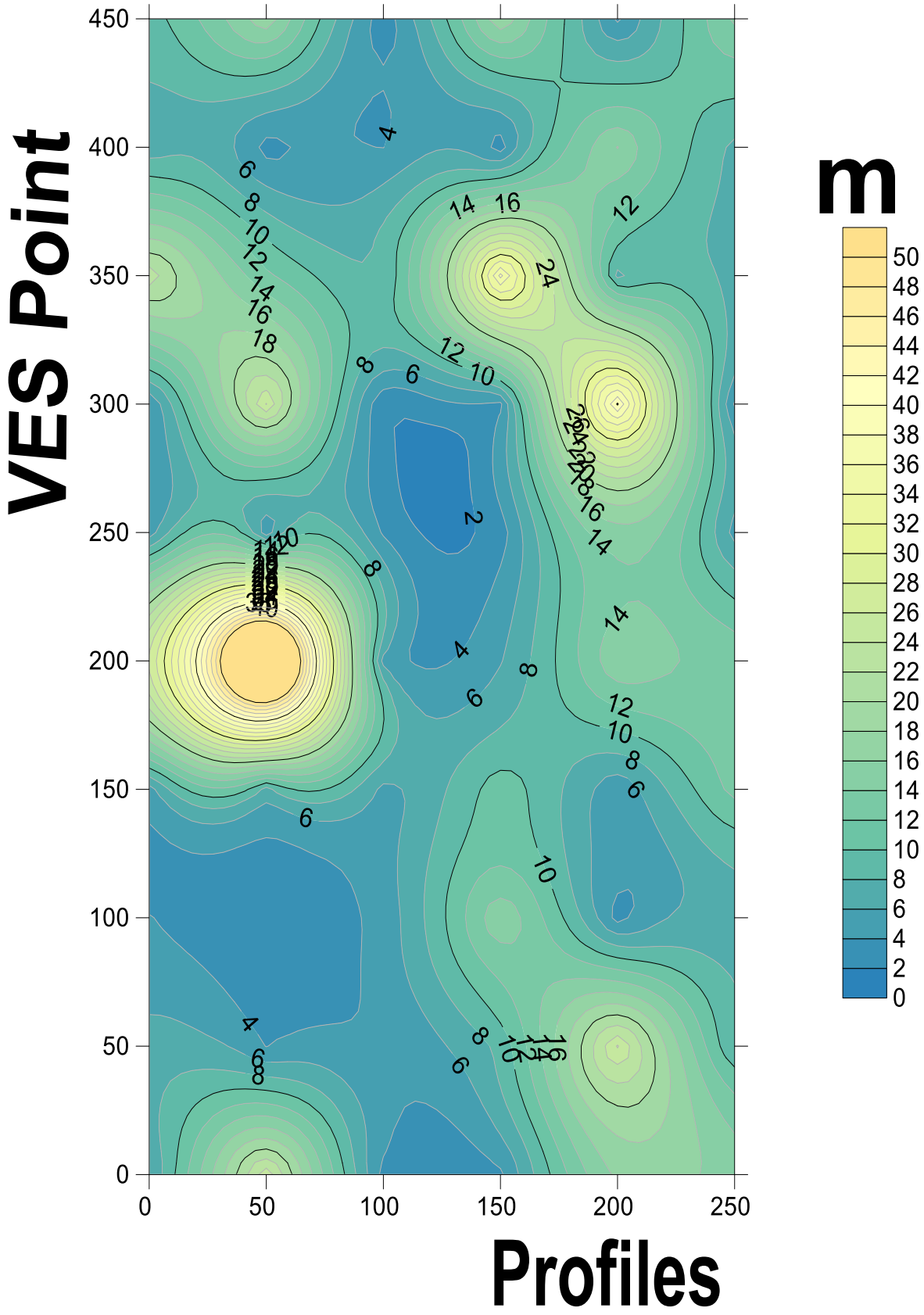
VES Point
Profiles
m
450
400
350
300
250
200
150
100
50
0
0
50
100
150
200
250
50
48
46
44
42
40
38
36
34
32
30
28
26
24
22
20
18
16
14
12
10
8
6
4
2
0

Figure 4d: Depths to Fresh Basement Contour Map

Table 5: Areas Delineated for Building Construction

VES STATION	Latitude (degrees)	Longitude (degrees)	Elevation (m)	Depth to Basement (m)
G_7	09.46360	006.63642	307	3.93
H_2	09.46538	006.63799	305	3.93
H_3	09.46502	006.63739	299	3.28
H_9	09.46279	006.63505	303	3.30
I_1	09.46609	006.63838	309	3.34
I_6	09.46510	006.63634	306	3.72
I_7	09.46483	006.63597	306	2.18
I_9	09.46424	006.63528	308	3.97
I_{10}	09.46383	006.63491	296	2.78
J_1	09.46655	006.63817	312	3.61
J_6	09.46538	006.63613	301	3.00
J_7	09.46520	006.63573	305	3.54
J_9	09.46465	006.63501	303	3.00
K_3	09.46640	006.63688	301	3.22
K_{10}	09.46443	006.63412	305	3.62
L_7	09.46585	006.63514	299	3.73

Sixteen VES stations were delineated for building construction having depths to fresh basement varying between 2.18 m and 3.93 m and resistivity values ranged between 1038 Ωm and 194453 Ωm, where consolidated basement is shallow as indicated in table 5.

Conclusion

The use of various electrical resistivity parameters (resistivity of the layer, depth of the layer, thickness of the layer) were employed to determine the suitable site for building construction. Three to four distinct geoelectric layers were observed namely; Top layer, weathered layer, fractured layer, and fresh basement layer. The observed frequencies in curve types include 21.6% of H, 4.2% of HA, 2.4% of K, 3.6% of A, 1.2% of KH, and 3% of HK. Sixteen VES stations were delineated for building construction, having depths to fresh basement varying between 2.18 m and 3.97 m and fresh basement resistivities ranged from 1038 Ωm to 194453 Ωm. Government and estate developers in the area are encouraged to make use of the results of this study for building construction site selection to reduce the problem of building collapse and cracking of walls. More research work in this area would contribute to solving the problem of collapse of building completely.

References

Ajibade, A.C., (1980). The Geology of the Country around Zungeru, Northwestern state of Nigeria. M.Sc. thesis, University of Ibadan, Ibadan, Nigeria

Alhassan, D.U, Obiora, A.N, Okeke F.N (2015). The assessment of aquifer potentials and aquifer vulnerability of southern Paiko, north central Nigeria, using geoelectric method. *Global Journal of Pure and Applied Sciences*. Vol. 21, pp 51- 70

Alhassan, D.U, Mamodu, A, Jimoh, M. O and Mohammed, A (2015). Geotechnical Investigation of the Earth Subsurface Formation for its Suitability for High-Rise Buildings in Southern Part of Paiko, Niger State, North Central Nigeria. *Journal of Science, Technology and Mathematics Education (JOSTMED)*, Vol.11, No. 3, pp10-22

Alhassan, D.U., Obiora, D.N. and Okeke, F.N. (2017). Geoelectrical investigation of groundwater potentials of northern Paiko, Niger State, north central Nigeria. Journal of Earth Science, vol. 28, no. 1, pp. 103-112

Ariyo, S. O., (2005). Geoelectrical Characterization of Aquifers and Geochemical study of Groundwater in the Basement Complex/Sedimentary Transition Zone around Isharsa, Southwest Nigeria. M.Sc. thesis, University of Ibadan, Ibadan, Nigeria

Asfahani, J., (2006): Geoelectrical investigation for characterizing the hydrogeological conditions in semi-arid region in Khanasser valley, Syria. *J. Arid Environ.* 68: 31 – 52

Bello, A. A., Makinde, V., (2007): Delineation of the aquifer in the Sout-Western part of the Nupe Basin, Kwara State, Nigeria. *J. Am. Sci.*, 3: 36 – 44

Dangana, L.M., (2007): Geoelectric survey for subsurface water in Paiko town, Niger State, Nigeria. Ph.D thesis, University of Abuja, Nigeria

Obiora, D. N., Alhassan U.D, Johnson C. I, and Okeke F.N (2016): Geoelectric Evaluation of Aquifer Potential and Vulnerability of Northern Paiko, Niger State, Nigeria. *Water Environment Research*, Vol.88, No 7, pp 644 – 651

Niger state water and sanitation Board (2001).

Todd, K.D., (1980): Groundwater Hydrology, 2nd edition. John Wiley and Sons, New York.

A 4- STAGE RUNGE-KUTTA TYPE METHOD FOR SOLUTION OF STIFF ORDINARY DIFFERENTIAL EQUATIONS

Muhammad R[1*]. Y. A Yahaya[2] A.S Abdulkareem[3].

[3]Department of Chemical Engineering, Federal University of Technology, Minna.

[1&2]Department of Mathematics/Statistics , Federal University of Technology, Minna.

[3]kasaka2003@futminna.edu.ng

[2]yusuphyahaya@futminna.edu.ng

[1]r.muhd@futminna.edu.ng

[*]Corresponding author

Abstract

In this paper, a 2 step implicit block hybrid linear multistep method was reformulated into a 4-stage block hybrid Runge-Kutta Type Method via the butcher analysis. The method can be use to solve first order stiff ordinary differential equation. A numerical example solved with the proposed method showed a better result in comparison with an existing method.

Keywords:hybrid,implicit, runge-kutta type

1. Introduction

Ordinary Differential Equations (ODEs) arise frequently in the study of physical problems. Unfortunately many of these equations cannot be solved exactly. This is why solving these equations numerically is important. Traditionally, mathematicians have used one of two classes of methods for solving numerically ordinary differential equations. These are one step methods and Linear Multistep Methods (LMMs) (Rattenbury, 2005).

Runge-Kutta methods are very popular because of their simple coefficients, efficiency and numerical stability (Agam, 2013). The methods are fairly simple to program, easy to implement and their truncation error can be controlled in a more straight forward manner than multistep methods (Kendall,1989). The application of Runge-Kutta methods have provided many satisfactory solutions to many problems that have been regarded as insolvable. The popularity and growth of these methods, coupled with the amount of research effort being undertaken, are further evidence that the applications are still the leading source of inspiration for mathematical creativity (Adegboye, 2013). With the advancement in computer technology, numerical methods are now an increasingly attractive and efficient way to obtain approximate or nearly accurate solutions to differential equations which have hitherto proved difficult or even impossible to solve analytically.

2. Literature Review

Yahaya and Adegboye (2011**)** reformulated the block hybrid Quade's method into Runge-Kutta type method of order 6. The method was extended to the case in which the approximate to a second order

(special or general) as well as first order initial value problem can be calculated. The method was A-stable, possessed the Runge-Kutta stability property, however it was limited to the step number $k = 4$. Chollom *et al.* (2012) constructed a class of A-stable Block Adams Bashforth Explicit Method (BABE) including their hybrid forms. The method tested on non-linear initial value problem performed well and compete favourably with the block hybrid Adams Moulton of higher order, but the step number was restricted to 2. Yahaya and Ajibade (2012**)** reformulated the two step hybrid linear multistep method into a 3-Stage Runge-Kutta Type method through the idea of general linear method. The method was used to solve only first order initial value problem.

Sofoluwe *et al.* (2012) derived some Backward Differentiation Formulae (BDF) capable of generating solution to stiff initial value problem using lagrangian interpolation technique. The BDF derived were implemented on some standard initial value problem. The region of absolute stability was constructed and the nature so obtained established some facts about the choice of BDF for numerical treatment of stiff problems. The non-stiff problems were not considered. Okunuga *et al.* (2012) presented a direct integration of second order ordinary differential equation using only Explicit Runge-Kutta Nystrom (RKN) method with higher derivative. They derived and tested various numerical schemes on standard problems. Due to the limitations of Explicit Runge-Kutta (ERK) in handling stiff problems, the extension to higher order Explicit Runge-Kutta Nystrom (RKN) was considered and results obtained showed an improvement over conventional Explicit Runge-Kutta schemes. The Implicit Runge-Kutta scheme was however not considered.

3. Methodology

Butcher defined an S-stage Runge-Kutta methods for the first order differential equation in the form

$$y_{n+1} = y_n + h\sum_{i,j=1}^{s} a_{ij}k_i \qquad (1)$$

where for $i = 1,2 \ldots \ldots s$

$$k_i = f(x_i + \alpha_j h, y_n + h\sum_{i,j=1}^{s} a_{ij}k_j) \qquad (2)$$

The real parameters α_j, k_i, a_{ij} define the method. The method in Butcher array form can be written as

α	β
	b^T

Where $a_{ij} = \beta$

Consider the approximate solution to (3.1) in the form of power series given as

$$y(x) = \sum_{j=0}^{t+m-1} \alpha_j x^j = y_{n+j} \qquad (3)$$

$$\alpha \in R, j = 0(1)t + m - 1, y \in C^m(a,b) \subset P(x) \qquad (4)$$

$$y'(x) = \sum_{j=1}^{t+m-1} j\alpha_j x^{j-1} = f(x,y) \qquad (5)$$

Where α_j's are the parameters to be determined, t and m are the points of interpolation and collocation respectively

For $K = 2$, we choose $t = 3$ and $m = 1$ at (3). Also interpolate (3) at $x = x_{n+i}, i = 0, \frac{1}{2}, 1$ and collocate (4) at $x = x_{n+i}, i = 2$ to have the following system of linear equations of the form

$$y(x) = \sum_{j=0}^{t+m-1} \alpha_j x^j = y_{n+i} \qquad i = 0, \frac{1}{2}, 1 \tag{6}$$

$$y'(x) = \sum_{j=0}^{t+m-1} j\alpha_j x^{j-1} = f_{n+i} \qquad i = 2 \tag{7}$$

The general form of the method upon addition of one off grid point is expressed as;

$$\bar{y}(x) = \alpha_1(x) y_n + \alpha_2(x) y_{n+1} + \alpha_3 y_{n+\frac{1}{2}} + h\beta_0(x) f_{n+2} \tag{8}$$

The matrix D of dimension $(t + m) * (t + m)$ of the proposed method is expressed as:

$$D = \begin{bmatrix} 1 & x_n & x_n^2 & x_n^3 \\ 1 & x_n + h & (x_n + h)^2 & (x_n + h)^3 \\ 1 & x_n + \frac{1}{2}h & \left(x_n + \frac{1}{2}h\right)^2 & \left(x_n + \frac{1}{2}h\right)^3 \\ 0 & 1 & 2x_n + 4h & 3(x_n + 2h)^2 \end{bmatrix}$$

We invert the matrix D, to obtain columns which form the matrix C i:e $C = D^{-1}$. The elements of C are used to generate the continous coefficients of the method equations:

$$\left.\begin{aligned} \alpha_1(x) &= C_{11} + C_{21}x + C_{31}x^2 + C_{41}x^3 \\ \alpha_2(x) &= C_{12} + C_{22}x + C_{32}x^2 + C_{42}x^3 \\ \alpha_3(x) &= C_{13} + C_{23}x + C_{33}x^2 + C_{43}x^3 \\ \beta_0(x) &= C_{14} + C_{24}x + C_{34}x^2 + C_{44}x^3 \end{aligned}\right\} \tag{9}$$

The values of the continuous coefficients (9) are substituted into (8) to give the continuous form of the two step block hybrid BDF with one off step interpolation point.

$$\left.\begin{aligned} y(x) = &\left[1-\frac{44}{13h}(x-x_n)+\frac{41}{13h^2}(x-x_n)^2-\frac{10}{13h^3}(x-x_n)^3\right]y_n + \\ &\left[-\frac{20}{13h}(x-x_n)+\frac{47}{13h^2}(x-x_n)^2-\frac{14}{13h^3}(x-x_n)^3\right]y_{n+1} + \\ &\left[\frac{64}{13h}(x-x_n)-\frac{88}{13h^2}(x-x_n)^2+\frac{10}{13h^3}(x-x_n)^3\right]y_{n+\frac{1}{2}} + \\ &\left[\frac{1}{13h}(x-x_n)-\frac{3}{13h}(x-x_n)^2+\frac{2}{13h^2}(x-x_n)^3\right]f_{n+2} \end{aligned}\right\} \quad (10)$$

Evaluating (10) at point $x = x_{n+2}$ and its derivative at $x = x_{n+1/2}, x = x_{n+1}$ yields the following three discrete hybrid schemes which are used as block integrator;

$$\left.\begin{aligned} \tfrac{-36}{13}y_{n+1} + y_{n+2} + \tfrac{32}{13}y_{n+\frac{1}{2}} &= \tfrac{9}{13}y_n + \tfrac{6}{13}hf_{n+2} \\ \tfrac{33}{12}y_{n+1} + y_{n+\frac{1}{2}} &= \tfrac{21}{12}y_n + \tfrac{26}{12}hf_{n+\frac{1}{2}} + \tfrac{1}{12}hf_{n+2} \\ y_{n+1} - \tfrac{40}{32}y_{n+\frac{1}{2}} &= -\tfrac{8}{32}y_n + \tfrac{13}{32}hf_{n+1} - \tfrac{1}{32}hf_{n+2} \end{aligned}\right\} \quad (11)$$

The equation (11) is of order $[3,3,3]^T$ with error constant $\left[-\frac{3}{52}, \frac{17}{832}, -\frac{19}{624}\right]^T$ respectively.

Equation (11) is transformed as

$$\left.\begin{aligned} y_{n+\frac{1}{2}} &= y_n + \tfrac{h}{72}(0f_n + 64f_{n+\frac{1}{2}} - 33f_{n+1} + 5f_{n+2}) \\ y_{n+1} &= y_n + \tfrac{h}{72}\left(0f_n + 80f_{n+\frac{1}{2}} - 12f_{n+1} + 4f_{n+2}\right) \\ y_{n+2} &= y_n + \tfrac{h}{9}\left(0f_n + 8f_{n+\frac{1}{2}} + 6f_{n+1} + 4f_{n+2}\right) \end{aligned}\right\} \quad (12)$$

Reformulating the block hybrid method with the coefficient as characterized by the Butcher array form as

α	β
	b^T

Where $a_{ij} = \beta$ Gives Table 3.1

Table 3.1: The Butcher Table for method (12)

0	0	0	0	0
$\frac{1}{2}$	0	$\frac{8}{9}$	$\frac{-11}{24}$	$\frac{5}{72}$
2	0	$\frac{8}{9}$	$\frac{2}{3}$	$\frac{4}{9}$
1	0	$\frac{10}{9}$	$\frac{-1}{6}$	$\frac{1}{18}$
	0	$\frac{10}{9}$	$\frac{-1}{6}$	$\frac{1}{18}$

NOTE:

The Butcher table is being rearranged with the off grid points appearing first, followed by the $c_{i's}$ in descending order. This is done in other to satisfy the consistency condition.

Using equation (1), we obtained an implicit 4-stage block Runge-Kutta Type method of uniform order 3.

$$\left.\begin{aligned} y_{n+\frac{1}{2}} &= y_n + h(0k_1 + \tfrac{8}{9}k_2 - \tfrac{11}{24}k_3 + \tfrac{5}{72}k_4) \\ y_{n+2} &= y_n + h\left(0k_1 + \tfrac{8}{9}k_2 + \tfrac{2}{3}k_3 + \tfrac{4}{9}k_4\right) \\ y_{n+1} &= y_n + h\left(0k_1 + \tfrac{10}{9}k_2 - \tfrac{1}{6}k_3 + \tfrac{1}{18}k_4\right) \end{aligned}\right\} \quad (13)$$

Where

$$\left.\begin{aligned} k_1 &= f(x_n, y_n) \\ k_2 &= f(x_n + \tfrac{1}{2}h, y_n + h\{\tfrac{8}{9}k_2 - \tfrac{11}{24}k_3 + \tfrac{5}{72}k_4\}) \\ k_3 &= f(x_n + h, y_n + h\{\tfrac{10}{9}k_2 - \tfrac{1}{6}k_3 + \tfrac{1}{8}k_4\}) \\ k_4 &= f(x_n + 2h, y_n + h\{\tfrac{8}{9}k_2 + \tfrac{2}{3}k_3 + \tfrac{4}{9}k_4\}) \end{aligned}\right\} \quad (14)$$

4. Results and Discussion

The newly derived block integrators were used to solve this problem within the interval $0 \leq x \leq 0.1$. Okunuga *et al.* (2013) solved this stiff problem by adopting a new 3-point block method of order five. Consider the highly stiff Ordinary Differential Equation (ODE)

$y' = -10(y-1)^2,\ y(0) = 2\,,\ \ h = 0.01$

Exact Solution: $y(x) = 1 + \frac{1}{1+10x}$

Applying the proposed Runge-kutta Type Method (RKTM) to this problem yields the following results in Table 4.1

.

Table 4.1: Absolute Error and Comparison of Result with Okunuga *et al.* (2013) for Problem 1 Using method (13)

t	Exact Solution	Computed Solution	Error RKTM	Error Okunuga [2013]
0.01	1.909090909	1.909125964	3.51E-05	1.07E-04
0.02	1.833333333	1.833397888	6.46E-05	2.38E-04

0.03	1.769230769	1.769301368	7.06E-05	4.51E-04
0.04	1.714285714	1.714362172	7.65E-05	6.20E-04
0.05	1.666666667	1.666741036	7.44E-05	8.84E-04
0.06	1.625000000	1.625073119	7.31E-05	1.03E-03
0.07	1.588235294	1.588304277	6.90E-05	1.27E-03
0.08	1.555555556	1.555621291	6.57E-05	1.53E-03
0.09	1.526315789	1.526377230	6.14E-05	1.75E-03
0.1	1.500000000	1.500057888	5.79E-05	1.81E-03

Results of the proposed method of order 3 with fewer function evaluations displayed in the table able showed a better than accuracy than results obtained by okunuga *et al.(*2013) of order five .Also there is an increase in accuracy as the computed solution moves closer to the exact solution.

5. Conclusion

This research work shows the link between a k-step linear multistep methods and Runge-Kutta methods which leads to a more accurate Block implicit Runge-Kutta Type Method (RKTM) for solving first order stiff

ordinary differential equation (ODE).The method can also be extended to second and higher order as derivation is done only once.

References

Adegboye, Z.A (2013), Construction and implementation of some reformulated block implicit linear multistep method into Runge-Kutta type method for initial value problems of general second and third order ordinary differential equations. Unpublished doctoral dissertation, Nigerian Defence Academy, Kaduna .

Agam, A.S (2012), A sixth order multiply implicit Runge-Kutta method for the solution of first and second order ordinary differential equations. Unpublished doctoral dissertation, Nigerian Defence Academy, Kaduna .

Butcher, J.C (2008), *Numerical methods for ordinary differential equations.* John Wiley & Sons. C ,463.

Chollom J.P.,Olatun-bosun I.O, & Omagu S. (2012). A class of A-stable block explicit methods for the solutions of ordinary differential equations. *Research Journal of Mathematics and Statistics,* Vol. *4(2),*52-56.

Kendall, E. A (1989). *An introduction to numerical analysis*, (2nd ed), John Wiley & Sons.367.

Okunuga, S.A, Sofulowe, A.B, Ehigie, J.O, & Akanbi, M.A. (2012). Fifth order 2-stage explicit runge kutta nystrom (erkn) method for the direct integration of second order ode. *Scientific Research and Essays*, Vol. *7(2),* 134-144.

Rattenbury, N. (2005). *Almost runge kutta methods for stiff and non-stiff problems*. Unpublished doctoral dissertation, University of Auckland.

Sofulowe, A.B., Okunuga, S.A, & Ehigie, J.O (2012). Treatment of stiff initial value problem using block backward differentiation formulae. *Journal of Nigerian Association of Mathematical Physics,* Vol. *20,* 75-82.

Yahaya, Y.A. & Adegboye, Z.A. (2011). Reformulation of quade's type four-step block hybrid multstep method into Runge-Kutta method for solution of first and second order ordinary differential equations. *Abacus,* Vol. *38(2)*, 114-124.

Yahaya, Y.A. & Ajibade, M.T. (2012). A reformulation of a two-step hybrid linear multistep method (lmm) into a 3-stage runge-kutta type (rkt) method for solution of ordinary differential equation. *Book of Readings of the 4th Annual National Conference of the School of Science and Science Education, Federal University of Technology Minna, Nigeria,*Vol. *2(4), 193-198.*

THE MENACE OF THE GEO-ENVIRONMENTAL HAZARD CAUSED BY GULLY EROSION IN ABIA STATE, NIGERIA

Onyelowe KC* and Michael M

Department of Civil Engineering, Michael Okpara University of Agriculture, Umudike, P. M. B. 7267, Umuahia 440109, Abia State, Nigeria. Email: konyelowe@mouau.edu.ng, konyelowe@gmail.com, konyelowe@yahoo.com.

*Corresponding Author

Abstract

The menace of Gully Erosion in Abia State has been studied and evaluated and the results of the reconnaissance and observation survey showed that most of the communities in the state are faced with this problem. The present research has proposed methods on how to mitigate this Geo-Environmental problem which included the use of slope drainage, turfing, shotcreting, retaining walls, sheet pile walls, change of slope geometry, reinforced soil wall, crib wall, gabion wall, contiguous bored pile wall, Geotextiles and soil nailing. The state Ministries of Environment and Works should consult experts in the field of Geotechnical Engineering towards putting to an end the menace of gully erosion in Abia State.

Keywords: Menace; Geo-Environmental; Hazard; Gully Erosion; Abia State.

1. Introduction

Gully Erosion has been a source of worry in almost all the 17 local governments and most communities in Abia State. This has led to Geo-Environmental decay and loss of major roads in the state. Many communities have been cut off from the major urban dwellings where they carry their farm produce for sale. Unfortunately, the government has not taken any step towards the evaluation of the extent of decay caused by gully sites to proffer solutions to end this menace. Gullies start unnoticed most times, but end up washing farmlands, pavements, and other Geotechnical facilities on its route, thereby leaving the environment in a state of decay. When this happens, the socioeconomic life of the affected localities is thrown into disarray. This is because when farmlands are washed away, farmers whose source of livelihood rests on the farm produce are left with the pain of the loss of their crops, road users are left to suffer the decay on the pavement facilities or in most cases they are cut off completely from the rest of the other suburbs and urban settlements. Observation and reconnaissance survey of the major gully sites has shown that Umuada-Umuetegha Nvosi road, Umuetegha-Umungbogho road, Umuhu-Umuehim road, etc in Isiala Ngwa South LGA, Bende-Ohafia road, Ebem-Okuno road, Bende-Igbere road, etc., in Bende and Ohafia Local Government Area, Umuakwu-Amachi Nsulu road in Isiala Ngwa North Area, Amuzukwu, Olokoro etc., roads in Umuahia South LGA, Umuda Isingwu and Okpara Square gully sites in Umuahia North LGA, Uturu gully site in Isikwuato LGA, Oboro gully sites in Ikwuano LGA, etc., have been destroyed or completely cut off from neighboring communities or cities by gully erosion. Geotechnical and Geo-Environmental engineering offer procedures towards solving gully erosion problems ranging from slope stabilization, landscaping, channels and drains, etc. The main aim of this work was to study the erosion sites and suggest possible Geotechnical engineering solutions to end this scourge.

2. Methodology

Reconnaissance and observation survey was the method adopted to evaluate the extent of decay caused by gully erosion in the state of Abia. Data collected by oral questionnaire from the people actually affected in these localities were studied and analyzed. Abia State is located on latitude 5.4309° N and longitude 7.5247° E covering an area of 6, 320km^2 with an average rainfall of 2050mm between its northern and southern ends. Abia State has a variety of land forms, despite the fact that it is dominated by flat and low-lying land, generally less than 120m above sea-level. The low-lying plain is the inland extension of the coastal plain from the Bight of Benin. The central part of the state is characterized by undulating land with many hills. The highland areas are part of the Enugu - Nsukka - Okigwe cuesta. This area has an average height of between 120m and 180m above sea-level. From Okigwe (Imo State), this escarpment extends in a west-east direction and, on getting to Afikpo (Ebonyi State), veers southeastwards to Arochukwu where it terminates. During the survey, the following causes of gullies were identified; (i) lack of drain facilities, (ii) badly constructed road pavements, (iii) negligence to rainfall and runoff volume during the design stage of drains, (iv) dumping of solid waste on drain channels and (v) wrongly located building structures as a result of wrong planning.

3. Results and Discussions

For the purpose of handling, the identified causes of gully erosion in Abia State were labelled GE-Cause A: lack of drain facilities, GE-Cause B: badly constructed road pavements, GE-Cause C: negligence to rainfall and runoff volume during the design stage of drains, GE-Cause D: dumping of solid waste on drain channels and GE-Cause E: wrongly located building structures as a result of wrong planning, (where GE is Gully Erosion) and the responses from the affected local governments in Abia state were evaluated in percentage. The evaluated responses from the eight local government areas of Abia State badly affected by gully erosion are tabulated and plotted in Figures 1, 2, 3, 4, 5, 6, 7, and 8. The figures show the responses based on the degree of effect on the people and their socioeconomic lives.

3.1 Erosion Menace Responses at Bende Local Government Area

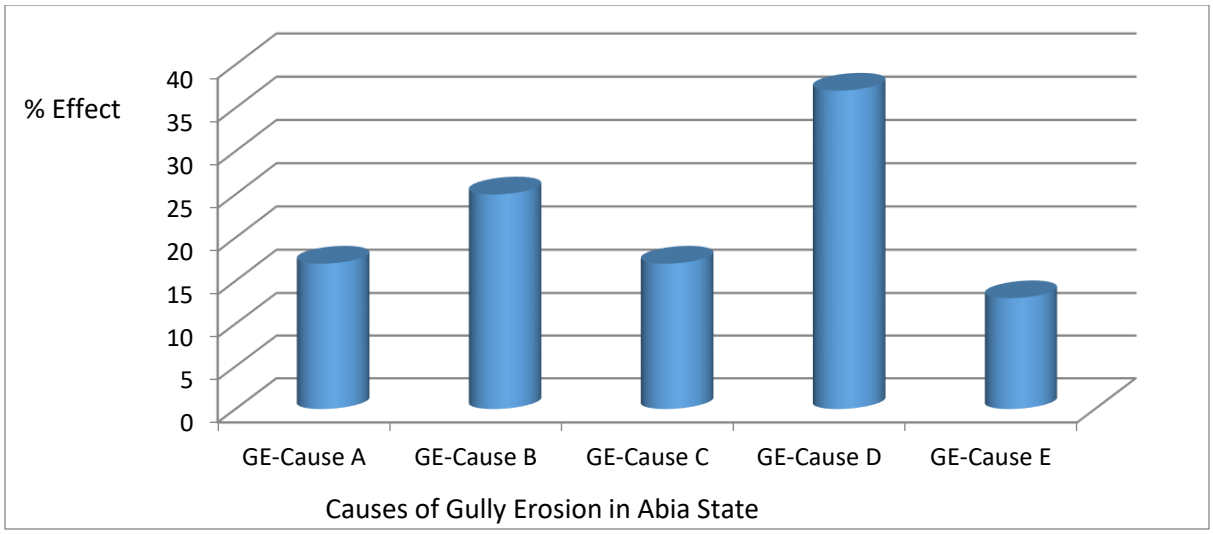

Figure 1: Percentage effect of the causes of Gully Erosion in Bende LGA

3.2 Erosion Menace Responses at Ikwuano Local Government Area

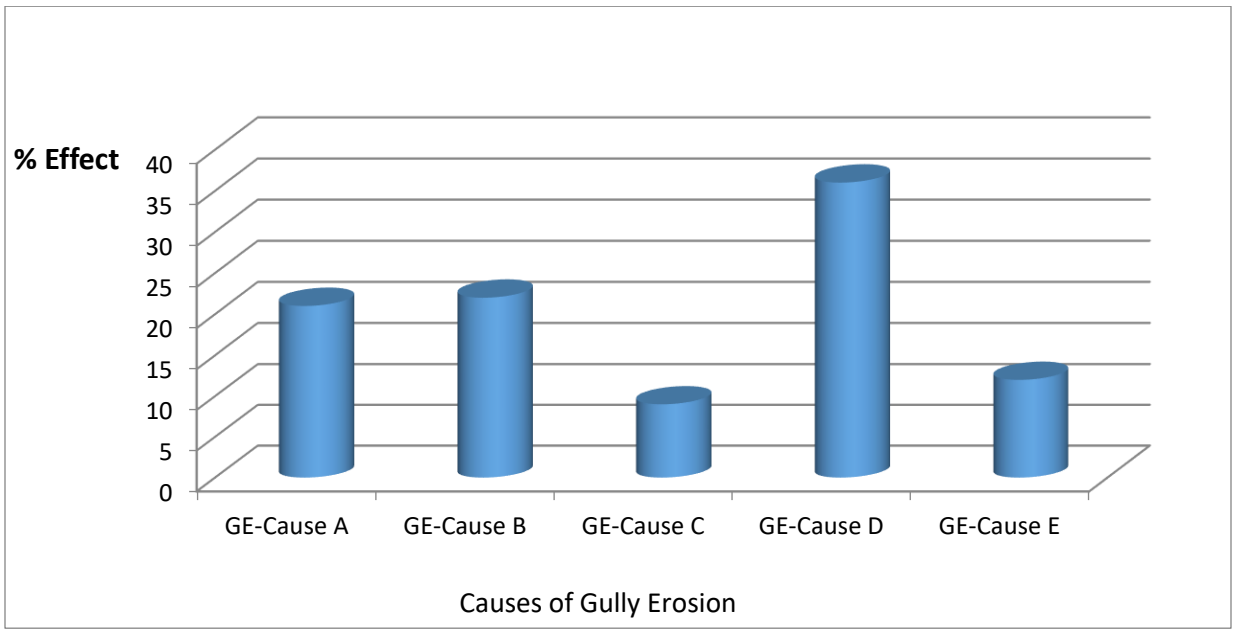

Figure 2: Percentage effect of the causes of Gully Erosion in Ikwuano LGA

3.3 Erosion Menace Responses at Isiala Ngwa North Local Government Area

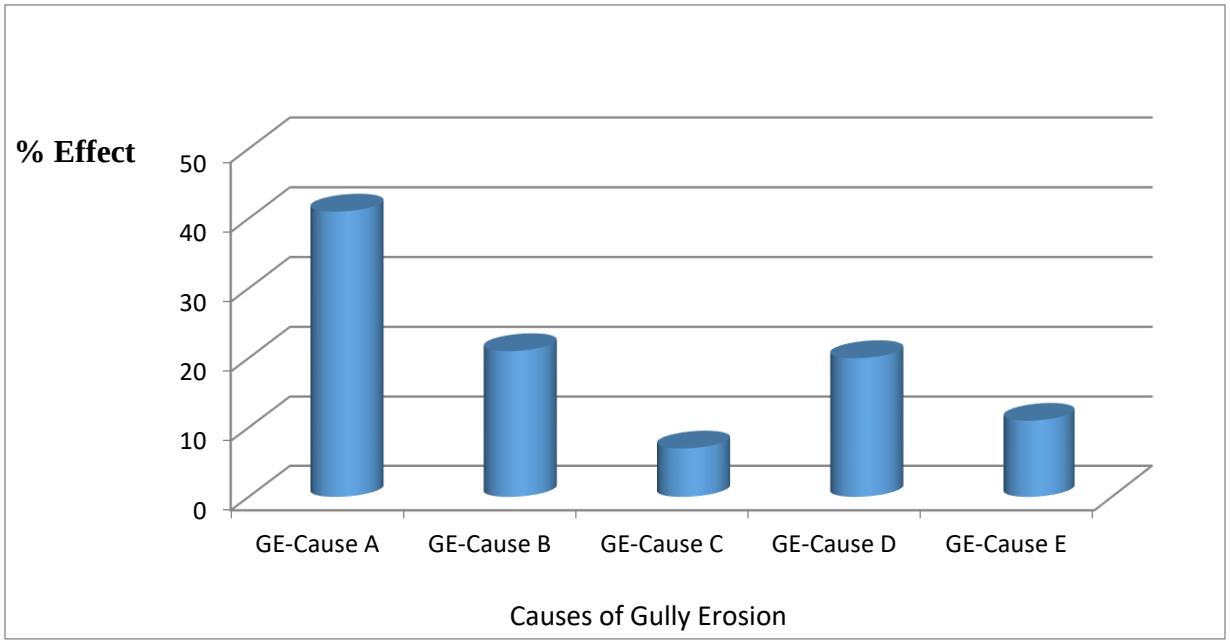

Figure 3: Percentage effect of the causes of Gully Erosion in Isiala Ngwa North LGA

3.4 Erosion Menace Responses at Isiala Ngwa South Local Government Area

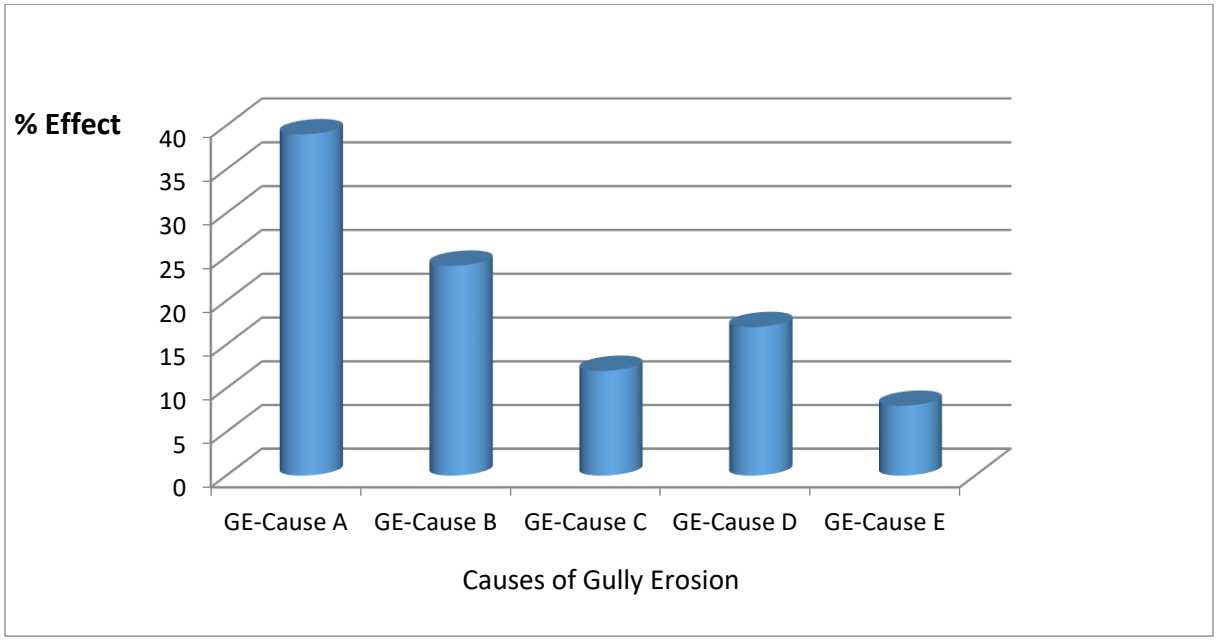

Figure 4: Percentage effect of the causes of Gully Erosion in Isiala Ngwa South LGA

3.5 Erosion Menace Responses at Isikwuato Local Government Area

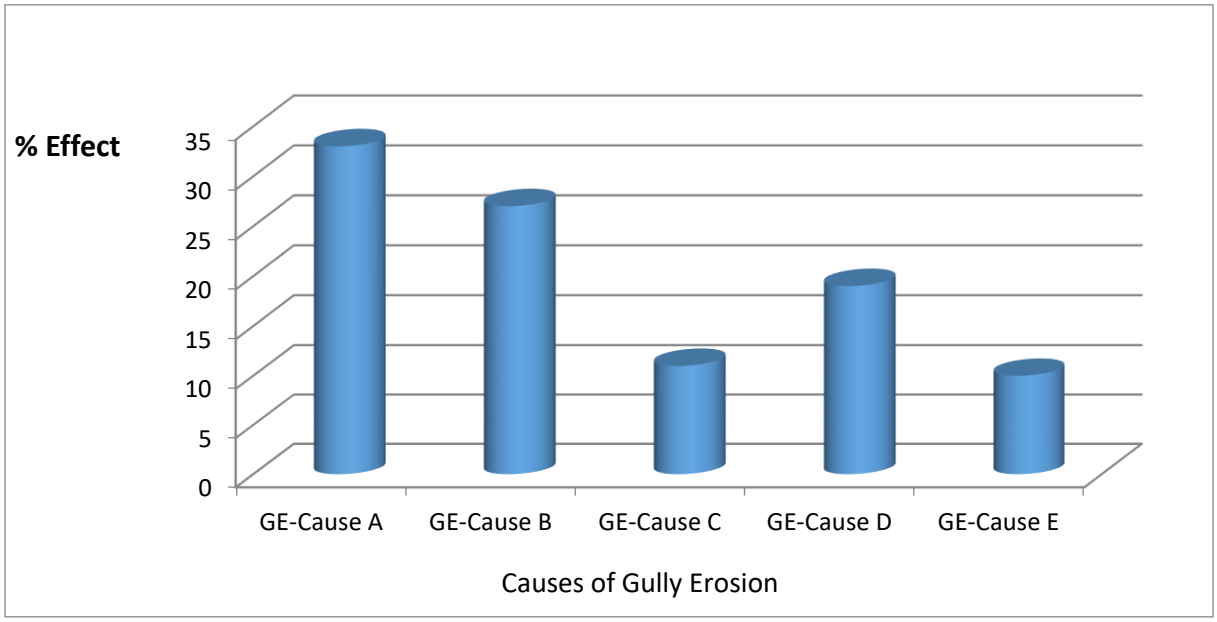

Figure 5: Percentage effect of the causes of Gully Erosion in Isikwuato LGA

3.6 Erosion Menace Responses at Ohafia Local Government Area

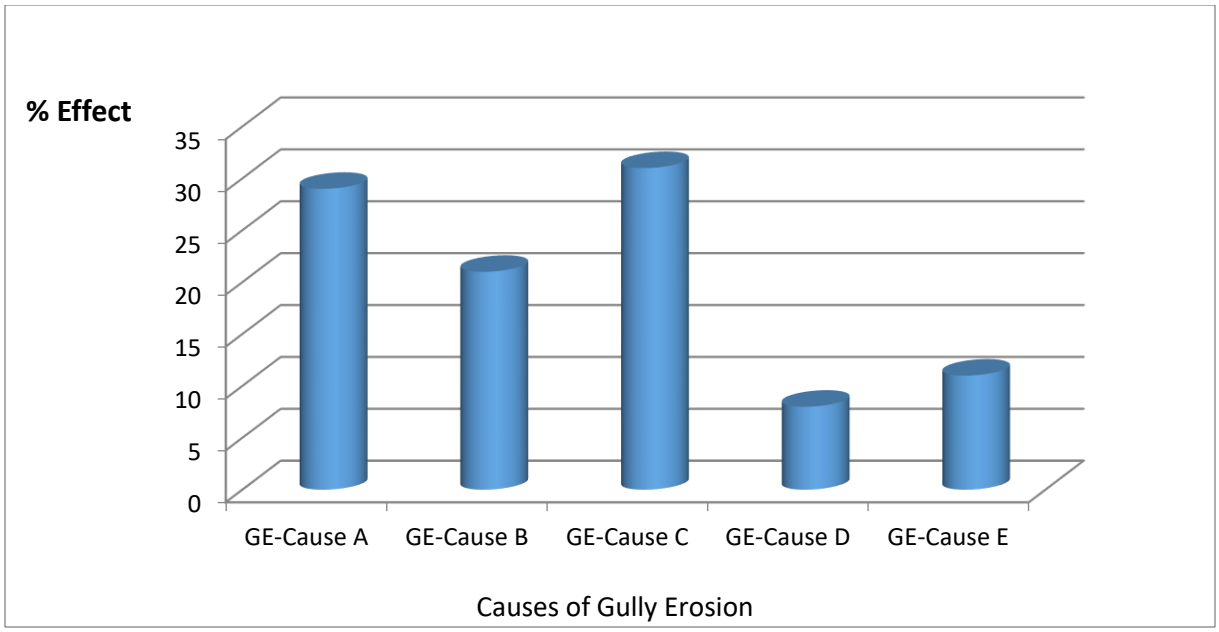

Figure 6: Percentage effect of the causes of Gully Erosion in Ohafia LGA

3.7 Erosion Menace Responses at Umuahia North Local Government Area

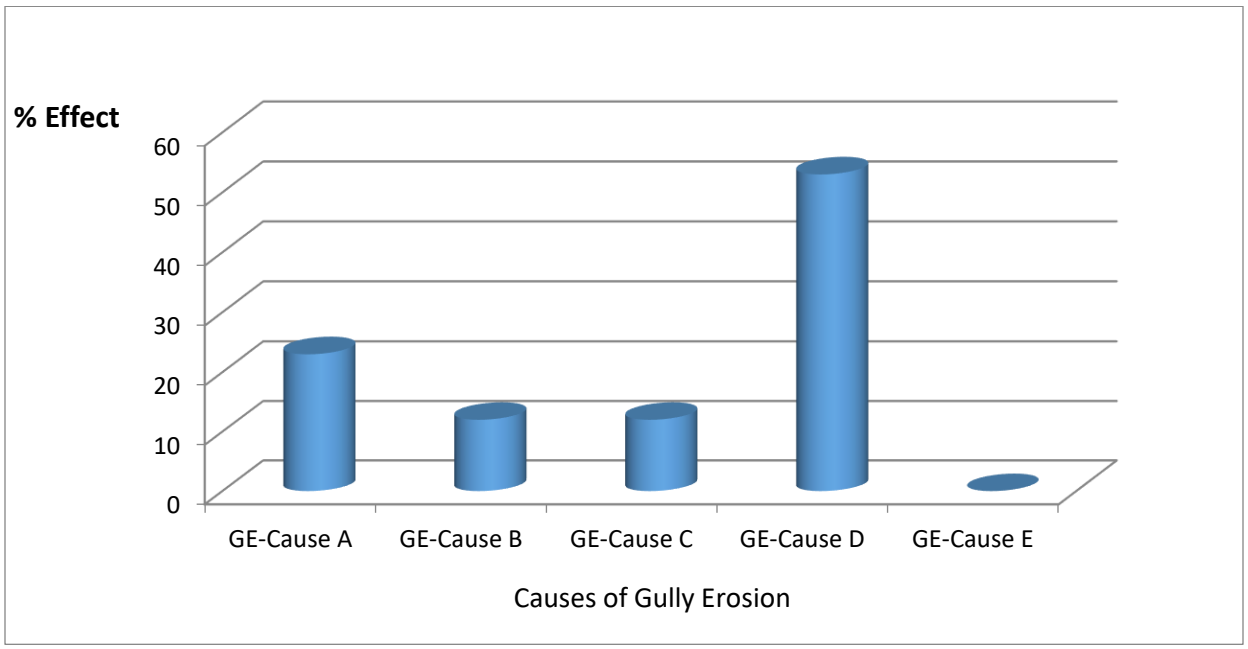

Figure 7: Percentage effect of the causes of Gully Erosion in Umuahia North LGA

3.8 Erosion Menace Responses at Umuahia South Local Government Area

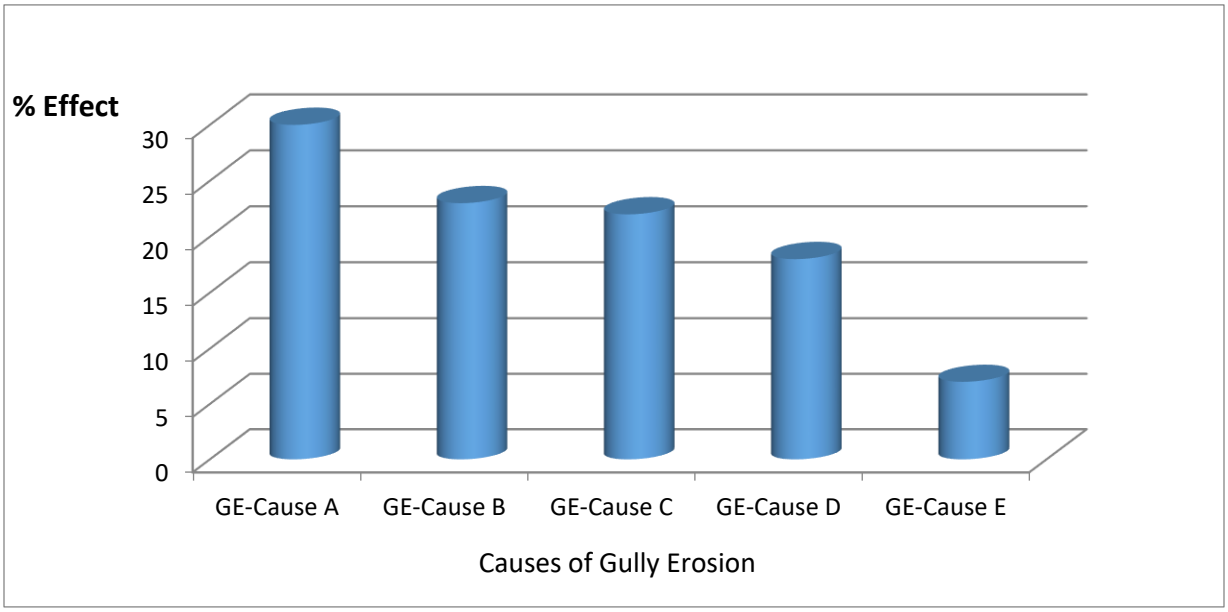

Figure 8: Percentage effect of the causes of Gully Erosion in Umuahia South LGA

4. Conclusion

From the foregoing, it will be concluded that the responses from the people of the areas based on the effect of the causes of Gully Erosion on their collective existence vary from location to location. This is as a result of the main activities going on these areas. The areas within the rural dwellings are more affected by lack of drainage facilities; GE-Cause A and badly constructed road pavements; GE-Cause B while those located in the urban centers are affected by GE-Causes C, D and E. It is the duty of this research finding to suggest a more Geotechnical engineering approach to solving many of these Geo-Environmental decay facing the Abia State and its communities. Researchers have shown that when the soil being washed away is stabilized to improve its mechanical properties, the ease with which erosion affects the top soil will be reduced. Moreover, adopting landscaping procedures with concrete or stabilizing the slopes on pavement will go a long way in mitigating the environmental problems facing Abia State. Moreover, slope drainage, turfing, shotcreting, retaining walls, sheet pile walls, change of slope geometry, reinforced soil wall, crib wall, gabion wall, contiguous bored pile wall, Geotextiles and soil nailing are the Geotechnical engineering procedures to be used to ensure that erosion menace is checked.

Acknowledgement

The data used in this research presentation were gotten from the people of the various affected local governments in Abia State through their cooperation.

References

Abdulfatai, I.A, Okunlola, I. A, Akande, W. G, Momoh, L.O, and Ibrahim, K. O, (2014), "Review of Gully Erosion in Nigeria: Causes, Impacts and Possible Solutions", Journal of Geosciences and Geomatics, Vol. 2, No. 3, 125-129. DOI: 10.12691/jgg-2-3-8.

Hamed, N., Khairul, A., Kassim, Amin G., Ramli N., Sayyed Y. Z. F., (2012), Investigation of Slope Failures in Soil Mechanics, Electronic Journal of Geotechnical Engineering, Vol. 17, Bundle R, Pp. 2703-2720.

Imasuen, O.I, Omali A.O and Ibrahim, I, (2011), "Assessment of environmental impacts and remedies for gully erosion in Ankpa Metropolis and environs, Kogi State, Nigeria", Advances in Applied Science Research, 2011, 2 (5):372-384

Nemes, I and Constantinescu L, (2011), The Gully Erosion Effect on the Environment, Proceedings of the International Conference on Information and Communication Technologies for Sustainable Agri-production and Environment (HAICTA 2011), Skiathos, 8-11 September, 2011. Pp. 621-629.

Nwilo, P. C., Olayinka, D. N., Uwadiegwu, I., and Adzandeh, A.E., (2011), "An Assessment and Mapping of Gully Erosion Hazards in Abia State: A GIS Approach", Journal of Sustainable Development, Vol. 4, No.5. doi:10.5539/jsd.v4n5p196.

FIFTH-ORDER FIVE-STAGE EXPLICIT ALMOST RUNGE-KUTTA METHODS

[1]Abdulrahman Ndanusa[*] [2]Zainab Ishaq Abdulazeez

[1,2]Department of Mathematics, Federal University of Technology, Minna, Nigeria

[1]as.ndanusa@futminna.edu.ng

[2]zaqinternational@yahoo.com

[*]Corresponding author

Abstract

Two new Almost Runge-Kutta methods of orders five with five stages are introduced through a judicious and careful choice of free parameters to the general form of deriving order five methods. Appropriate convergence analysis established that the methods are consistent and stable, hence their convergence. The proposed methods, christened ARK5a and ARK5b, were implemented using sample initial value problems and the results compared with those of some existing ARK methods of the same order. Experimental results revealed that the methods are more efficient and effective than the existing methods by producing lesser errors and lesser computational rigour.

Keywords: stability, convergence, almost runge-kutta, order conditions

1. Introduction

The class of numerical methods known as the General Linear Methods came into being as a result of the work of Butcher (1996), in an effort to formulate a general class of methods that incorporate the multivalue attributes of linear multistep methods into the multistage attributes of Runge-Kutta methods (Rattenbury, 2005). Almost Runge-Kutta (ARK) methods, introduced by Butcher (1996), are a special class of General Linear Methods whose properties have close affinity to those of explicit Runge-Kutta methods. ARK methods are able to attain the multivalue character of Linear Multistep Methods by allowing more than one value to be passed from step to step, even as the multistage nature of Runge-Kutta methods is retained. They share a lot of features with single step schemes and possess stability features of Runge-Kutta schemes.

Since the introduction of this class of methods, many researchers have contributed in no small measure towards improvement of the method for greater effectiveness and efficiency. In this direction, (Rattenbury, 2005) derived some Almost Runge-Kutta methods. This research which focused mainly on explicit schemes concentrated more on a unique fourth order numerical scheme for numerical integration of non-stiff differential equations, which when put into effect in the right way, operates like a fifth order scheme. She further derived low order diagonally implicit schemes for solving stiff differential equations. In Abraham (2010) some new ARK methods for the solution of non-stiff differential equations were derived; a comparison of relative performance of the methods with Runge-

Kutta methods established that the ARK methods compete favourably with traditional Runge-Kutta methods. Alimi (2014) found out that the investigated effectiveness of Richardson Extrapolation Technique in estimating the error associated with Almost Runge-Kutta schemes. The outcome of the investigation indicates that Richardson extrapolation technique is not effective in achieving error estimates associated with Almost Runge-Kutta schemes. He also generated a numerical solver for carrying out experimentin numerical analysis. Furthermore, Ndanusa and Audu (2016)a derived two explicit ARK methods, a three stage third order method, and a four-stage third-order method for the numerical integration of initial value problems. In Ndanusa and Audu (2016)b, two ARK methods of orders four and five (ARK5) were constructed. Numerical examples justified the introduction of these methods in that they methods performed better than some existing ARK methods of equal standing.

2. Materials and Methods

Following Butcher (2008), the general fifth-order five-stage ARK method takes form

$$\left[\begin{array}{c|c} A & U \\ \hline B & V \end{array}\right] = \left[\begin{array}{ccccc|c|cc} 0 & 0 & 0 & 0 & 0 & 1 & c_1 & \frac{1}{2}c_1^2 \\ a_{21} & 0 & 0 & 0 & 0 & 1 & c_2 - a_{21} & \frac{1}{2}c_2^2 - a_{21}c_1 \\ a_{31} & a_{32} & 0 & 0 & 0 & 1 & c_3 - a_{31} - a_{32} & \frac{1}{2}c_3^2 - a_{31}c_1 - a_{32}c_2 \\ a_{41} & a_{42} & a_{43} & 0 & 0 & 1 & c_4 - a_{41} - a_{42} - a_{43} & \frac{1}{2}c_4^2 - a_{41}c_1 - a_{42}c_2 - a_{43}c_3 \\ b_1 & b_2 & b_3 & b_4 & 0 & 1 & b_0 & 0 \\ \hline b_1 & b_2 & b_3 & b_4 & 0 & 1 & b_0 & 0 \\ 0 & 0 & 0 & 0 & 1 & 0 & 0 & 0 \\ \beta_1 & \beta_2 & \beta_3 & \beta_4 & \beta_5 & 0 & \beta_0 & 0 \end{array}\right] \quad (1)$$

where $c_5 = 1$; the Order conditions are:

$$\left.\begin{array}{c} b^T c = \frac{1}{2}, b^T c^2 = \frac{1}{3}, b^T c^3 = \frac{1}{4}, b^T c^4 = \frac{1}{5} \\ b_0 + b^T e = 1, b^T A = b^T (1 - C), \\ b^T (1 - c) Ac = \frac{1}{24}, b^T (1 - c) Ac^2 = \frac{1}{60}, \\ c_1 = -2 \frac{exp_5(-\beta_5)}{\beta_5 exp_4(-\beta_5)}, \beta^T e + \beta_0 = 0, \\ \beta^T (I + \beta_5 A) = \beta_5 e_5^T \\ \left(1 + \frac{1}{2}\beta_5 c_1\right) b^T A^3 c = \frac{1}{120} \end{array}\right\} \quad (2)$$

From the order conditions (2) we obtain

$$c_1 = \frac{-2\left(1 - \beta_5 + \frac{1}{2}\beta_5^2 - \frac{1}{6}\beta_5^3 + \frac{1}{24}\beta_5^4 + \frac{1}{120}\beta_5^5\right)}{\beta_5\left(1 - \beta_5 + \frac{1}{2}\beta_5^2 - \frac{1}{6}\beta_5^3 + \frac{1}{24}\beta_5^4\right)} \quad (3)$$

$$a_{32} = \frac{2 - 5c_1}{120 b_3 (c_2^2 - c_1 c_2 - c_2^2 c_3 + c_1 c_2 c_3)} \quad (4)$$

$$a_{31} = \frac{\frac{1}{24} - b_2 a_{21} c_1 (1 - c_2) - b_3 a_{32} c_2 (1 - c_3)}{b_3 c_1 (1 - c_3)} \quad (5)$$

$$a_{21} = \frac{2c_2(c_2 - c_1)}{c_1(2 - 5c_1)(2 + c_1\beta_5)} \quad (6)$$

$$a_{41} = \frac{b_1 - b_1 c_1 - b_2 a_{32} - b_3 a_{31}}{b_4} \quad (7)$$

$$a_{42} = \frac{b_1 - b_2 c_2 - b_3 a_{32}}{b_4} \quad (8)$$

$$a_{43} = \frac{b_3 - b_3 c_3}{b_3} \quad (9)$$

$$\left.\begin{array}{c} b_1 c_1 + b_2 c_2 + b_3 c_3 + b_4 c_4 = \frac{1}{2} \\ b_1 c_1 + b_2 c_2 + b_3 c_3 + b_4 c_4 = \frac{1}{2} \\ b_1 c_1^3 + b_2 c_2^3 + b_3 c_3^3 + b_4 c_4^3 = \frac{1}{4} \\ b_1 c_1^4 + b_2 c_2^4 + b_3 c_3^4 + b_4 c_4^4 = \frac{1}{5} \\ b_0 + b_1 + b_2 + b_3 + b_4 = 1 \end{array}\right\} \quad (10)$$

Solving system (10) results in

$$b_1 = \frac{5c_2 + 5c_3 - 10c_2c_3 - 3}{60\,(c_1 - 1)c_1(c_1 - c_2)(c_1 - c_3)} \tag{11}$$

$$b_2 = \frac{10\,c_1c_3 - 5c_1 - 5c_3 + 3}{60c_2(c_1 - c_2)(c_2 - 1)(c_2 - c_3)} \tag{12}$$

$$b_3 = -\frac{1}{60}\left[\frac{10\,c_1c_2 - 5c_1 - 5c_2 + 3}{c_3(c_3 - 1)(c_2 - c_3)(c_1 - c_3)}\right] \tag{13}$$

$$b_4 = \frac{30c_1c_2c_3 - 20c_1c_2 - 20c_1c_3 - 20c_2c_3 + 15c_1 + 15c_2 + 15c_3 - c_2}{60(c_3 - 1)(c_2 - 1)(c_1 - 1)} \tag{14}$$

$$b_0 = \frac{30c_1c_2c_3 - 10c_1c_2 - 10c_1c_3 - 10c_2c_3 + 5c_1 + 5c_2 + 5c_3 - 3}{60\,c_1c_2c_3} \tag{15}$$

And from $\beta^T(I + \beta_5 A) = \beta_5 e_5^T$ of (2) results

$$\beta_1 + a_{21}a_{32}a_{43}b_4\beta_5^5 - a_{21}a_{32}b_3\beta_5^4 - a_{21}a_{42}b_4\beta_5^4 + a_{21}b_2\beta_5^4 - a_{31}a_{43}b_4\beta_5^4 + a_{31}b_3\beta_5^3 + a_{41}b_4\beta_5^3$$

$$-b_1\beta_5^2, \beta_2 - a_{32}a_{43}b_4\beta_5^4 + a_{42}b_4\beta_5^3 + a_{32}b_3\beta_5^3 - b_2\beta_5^2, \beta_3 + a_{43}b_4\beta_5^3 - b_3\beta_5^2, \beta_4 - b_4\beta_5^2, \beta_5$$

$$= 0,0,0,0,\beta_5 \tag{16}$$

Thus,

$$\beta_1 = a_{21}a_{32}a_{43}b_4\beta_5^5 - a_{21}a_{32}b_3\beta_5^4 - a_{21}a_{42}b_4\beta_5^4 + a_{21}b_2\beta_5^4 - a_{31}a_{43}b_4\beta_5^4 + a_{31}b_3\beta_5^3$$

$$+a_{41}b_4\beta_5^3 - b_1\beta_5^2 \tag{17}$$

$$\beta_2 = -a_{32}a_{43}b_4\beta_5^4 + a_{42}b_4\beta_5^3 + a_{32}b_3\beta_5^3 - b_2\beta_5^2 \tag{18}$$

$$\beta_3 = a_{43}b_4\beta_5^3 - b_3\beta_5^2 \tag{19}$$

$$\beta_4 = -b_4\beta_5^2 \tag{20}$$

$$\beta_5 = \beta_5 \tag{21}$$

$$\beta_0 = -\beta_1 - \beta_2 - \beta_3 - \beta_4 - \beta_5 \tag{22}$$

And the following fifth-order five-stage ARK schemes, christened ARK5a and ARK5b are obtained

ARK5a with $c^T = \left[\frac{53}{150}, \frac{1}{2}, , \frac{3}{4}, 1, 1\right]$

$$\left[\begin{array}{c|c} A & U \\ \hline B & V \end{array}\right] = \left[\begin{array}{ccccc|c|cc} 0 & 0 & 0 & 0 & 0 & 1 & \frac{53}{150} & \frac{2809}{45000} \\ \frac{12375}{23744} & 0 & 0 & 0 & 0 & 1 & -\frac{503}{23744} & -\frac{53}{896} \\ \frac{95625}{74624} & \frac{833}{3520} & 0 & 0 & 0 & 1 & -\frac{26053}{33920} & -\frac{371}{1280} \\ -\frac{982125}{1466828} & -\frac{1455}{407} & \frac{7760}{4403} & 0 & 0 & 1 & \frac{191193}{54908} & \frac{2491}{2072} \\ \frac{4218750}{6729569} & -\frac{8}{33} & \frac{160}{357} & \frac{37}{582} & 0 & 1 & \frac{11}{106} & 0 \\ \hline \frac{4218750}{6729569} & -\frac{8}{33} & \frac{160}{357} & \frac{37}{582} & 0 & 1 & \frac{11}{106} & 0 \\ 0 & 0 & 0 & 0 & 1 & 0 & 0 & 0 \\ \frac{48750}{5141} & -\frac{32}{3} & 0 & -\frac{296}{291} & 4 & 0 & -\frac{286}{159} & 0 \end{array}\right] \tag{23}$$

ARK5b with $c^T = \left[\frac{53}{150}, \frac{1}{3}, \frac{2}{3}, 1, 1\right]$

$$\left[\begin{array}{c|c} A & U \\ \hline B & V \end{array}\right] = \left[\begin{array}{ccccc|c|cc} 0 & 0 & 0 & 0 & 0 & 1 & \frac{53}{150} & \frac{2809}{45000} \\ -\frac{1125}{23744} & 0 & 0 & 0 & 0 & 1 & \frac{27119}{71232} & \frac{583}{8064} \\ \frac{6480125}{2386272} & -\frac{329}{201} & 0 & 0 & 0 & 1 & -\frac{983389}{2386272} & -\frac{51781}{270144} \\ -\frac{7763140375}{257788608} & \frac{6499}{231} & \frac{6499}{3619} & 0 & 0 & 1 & \frac{2165363}{1828288} & \frac{116971}{206976} \\ -\frac{625000}{241627} & \frac{23}{8} & \frac{201}{376} & \frac{77}{376} & 0 & 1 & \frac{33}{424} & 0 \\ \hline -\frac{625000}{241627} & \frac{23}{8} & \frac{201}{376} & \frac{77}{376} & 0 & 1 & \frac{33}{424} & 0 \\ 0 & 0 & 0 & 0 & 1 & 0 & 0 & 0 \\ -\frac{110286250}{724881} & \frac{454}{3} & \frac{134}{47} & -\frac{154}{97} & 4 & 0 & -\frac{236}{53} & 0 \end{array}\right] \tag{24}$$

3. Convergence Analysis

For the scheme ARK5a, its V matrix is

$$V = \begin{bmatrix} 1 & \frac{11}{106} & 0 \\ 0 & 0 & 0 \\ 0 & -\frac{286}{159} & 0 \end{bmatrix} \tag{25}$$

From the characteristic polynomial of V

$$\rho(\lambda) = \det(\lambda \mathrm{I}_3 - V) \tag{26}$$

$$\begin{vmatrix} \lambda - 1 & -\frac{11}{106} & 0 \\ 0 & \lambda & 0 \\ 0 & \frac{286}{159} & \lambda \end{vmatrix} = \lambda^3 - \lambda^2 \tag{27}$$

Following Cayley-Hamilton theorem,

$$\rho(V) = V^3 - V^2 = 0 \tag{28}$$

$$\begin{bmatrix} 1 & \frac{11}{106} & 0 \\ 0 & 0 & 0 \\ 0 & 0 & 0 \end{bmatrix} - \begin{bmatrix} 1 & \frac{11}{106} & 0 \\ 0 & 0 & 0 \\ 0 & 0 & 0 \end{bmatrix} = \begin{bmatrix} 0 & 0 & 0 \\ 0 & 0 & 0 \\ 0 & 0 & 0 \end{bmatrix} \tag{29}$$

It implies

$$V^3 = V^2 \tag{30}$$

Similarly, $V^4 - V^2 = 0 \ \ => V^4 = V^2, \cdots,$ and $V^n = V^2$ for every n greater than 2, meaning V^n is bounded which shows that the method is stable. Also, the method is consistent since it is of order $p = 5 > 1$. Therefore ARK5a method is convergent.

And for ARK5b, the matrix is given as:

$$V = \begin{bmatrix} 1 & \frac{33}{424} & 0 \\ 0 & 0 & 0 \\ 0 & -\frac{236}{53} & 0 \end{bmatrix} \tag{31}$$

whose characteristic polynomial is

$$\rho(\lambda) = \lambda^3 - \lambda^2 \tag{32}$$

with the eigenvalues calculated to be $\lambda = 1, 0, 0$, and it satisfies the Cayley-Hamilton theorem thus

$$\rho(V) = V^3 - V^2 = 0 \tag{33}$$

$$\begin{bmatrix} 1 & \frac{33}{424} & 0 \\ 0 & 0 & 0 \\ 0 & 0 & 0 \end{bmatrix} - \begin{bmatrix} 1 & \frac{33}{424} & 0 \\ 0 & 0 & 0 \\ 0 & 0 & 0 \end{bmatrix} = \begin{bmatrix} 0 & 0 & 0 \\ 0 & 0 & 0 \\ 0 & 0 & 0 \end{bmatrix} \tag{34}$$

Consequently,

$$V^4 - V^2 = 0 \quad => V^4 = V^2 \ \cdots \ V^n = V^2 \tag{35}$$

for every n greater than 2, meaning V^n is bounded; thus the method is stable. The method is also consistent since it it of order $p = 5 > 1$. Therefore the scheme ARK5b is convergent.

4. Numerical Experiments

The proposed schemes ARK5a AND ARK5b are applied to problems 1 and 2 and the results compared with those of Ndanusa and Audu (2016)b in order to ascertain their efficacy. It is instructive to note that the fifth order method of Ndanusa and Audu (2016)b (nicknamed [NA]) is more accurate than the methods of Abraham (2010) and Alimi (2014). The results are presented in Tables 1 and 2.

Problem 1**:**

$$\left.\begin{array}{c} y' = x + y, \quad y(0) = 1 \\ h = 0.1, \quad x \in [0,1] \\ y(x) = 2e^x - x - 1 \end{array}\right\} \tag{36}$$

Problem 2**:**

$$\left.\begin{array}{c} y' = x + 2y, \quad y(0) = 1 \\ h = 0.1\,, \quad x \in [0,1] \\ y(x) = -\frac{1}{2}x - \frac{1}{4} + \frac{5}{4}e^{2x} \end{array}\right\} \tag{37}$$

Table 1: Results Of Problem 1

x	y_{exact}	$y_{([NA])}$	$Error_{([NA])}$	$y_{([ARK5a])}$	$Error_{([ARK5a])}$	$y_{([ARK5b])}$	$Error_{([ARK5b])}$
0.0	1.000000000	1.000000000	0.000000000	1.000000000	0.000000000	1.000000000	0.000000000

0.1	1.110341836	1.110341835	0.000000001	1.110341836	0. 000000000	1.1103418356	0. 000000000
0.2	1.242805516	1.242805512	0.000000004	1.242805513	0.000000003	1. 242805513	0.000000003
0.3	1.399717615	1.399717607	0.000000008	1.399717608	0.000000007	1. 399717609	0.000000006
0.4	1.583649395	1.583649382	0.000000012	1.583649385	0.000000010	1. 583649384	0.000000011
0.5	1.797442541	1.797442523	0.000000018	1.797442526	0.000000015	1. 797442526	0.000000016
0.6	2.044237601	2.044237576	0.000000025	2.044237580	0.000000021	2. 044237579	0.000000022
0.7	2.327505415	2.327505382	0.000000033	2.377505387	0.000000028	2. 377505386	0.000000029
0.8	2.651081857	2.651081815	0.000000042	2.651081820	0.000000037	2. 651081819	0.000000038
0.9	3.019206222	3.019206169	0.000000052	3.019206175	0.000000047	3. 019206174	0.000000048
1.0	3.436563657	3.436563592	0.000000065	3.436563598	0.000000059	3. 436563597	0.000000060

Table 2: Results Of Problem 2

x	y_{exact}	$y_{([NA])}$	$Error_{([NA])}$	$y_{([ARK5a])}$	$Error_{([ARK5a])}$	$y_{([ARK5b])}$	$Error_{([ARK5b])}$
0.0	1.000000000	1.000000000	0.000000000	1.000000000	0.000000000	1.000000000	0.000000000
0.1	1.226753448	1.226753383	0.000000065	1.226753402	0.000000046	1.226753401	0.000000047
0.2	1.514780872	1.514780653	0.000000219	1.514780677	0.000000195	1.514780676	0.000000196
0.3	1.877648500	1.877648062	0.000000438	1.877648091	0.000000409	1.877648090	0.000000410
0.4	2.331926160	2.331925417	0.000000743	2.331925452	0.000001120	2.331925451	0.000001121
0.5	2.897852285	2.897851123	0.000001162	2.897851165	0.000001681	2.897851164	0.000001682
0.6	3.600146154	3.600144423	0.000001731	3.600144473	0.000002433	3.600144472	0.000002434
0.7	4.468999959	4.468997466	0.000002493	4.468997526	0.000003434	4.468997525	0.000003435
0.8	5.541290530	5.541287022	0.000003508	5.541287096	0.000004762	5.541287095	0.000004763
0.9	6.862059330	6.862054478	0.000004852	6.862054568	0.000004762	6.862054567	0.000004763
1.0	8.486320124	8.486313504	0.000006620	8.486313614	0.000006510	8.486313613	0.000006511

5. Discussion of Results

Tables 1 and 2 depict the results of applying the proposed methods ARK5a and ARK5b to the test Problems 1 and 2. From the tables, x stands for the integration points at which the solutions are sought, y_{exact} is the exact solutions at the various integration points, $y_{([7])}$ is the approximate solutions for the method of Ndanusa and Audu (2016)b, $y_{([ARK5a])}$ is the approximate solution of ARK5a, $y_{([ARK5b])}$ is the approximate solution of ARK5b, while $Error_{([7])}$, $Error_{([ARK5a])}$ and $Error_{([ARK5b])}$ are the errors

produced by the methods of Ndanusa and Audu (2016)b, ARK5a and ARK5b respectively. In summary, it is evident that the proposed methods ARK5a and ARK5b exhibit lesser errors than the method of Ndanusa and Audu (2016)b, and by extension the methods of Abraham (2010) and Alimi (2014).

6. Conclusion

This research has succeeded in producing two new explicit Almost Runge-Kutta methods each of order 5. The methods are proven to be convergent by subjecting them to standard convergence criteria. Numerical examples further established that the methods are not only effective but also compare favourably with other known methods in existence.

References

Abraham, O. (2010). *Development of some new classes of explicit Almost Runge-Kutta methods for non-stiff differential equations*, unpublished Ph.D thesis, Federal University of Technology, Minna, Nigeria.

Alimi, O. K. (2014). *On the performance of Richardson extrapolation technique in estimating local truncation errors for explicit Almost Runge-Kutta methods*, unpublished, Master's thesis, Federal University of Technology Minna, Nigeria.

Butcher, J. C. (1996). General linear methods, *Computer Mathematics Application*, Vol. 31, 105-112.

Butcher, J. C. (1997). An introduction to Almost Runge-Kutta methods, *Applied Numerical Mathematics*, Vol. 24, 331-342.

Butcher, J. C. (2008). *Numerical methods for ordinary differential equations,* 2nd ed., Great Britain: John Wiley & Sons, Ltd.

Ndanusa, A. and Audu, K. J. (2016)a. Design and analysis of some third order explicit Almost Runge - Kutta methods, *Applied Mathematics,* Vol. 7, 13 – 21.

Ndanusa, A. and Audu, K. J. (2016)b. On fourth and fifth order explicit Almost Runge – Kutta methods, *International Journal of Scientific and Innovative Mathematical Research,* Vol. 4(1), 88 – 96.

Rattenbury, N. (2005). *Almost Runge-Kutta methods for stiff and non-stiff problems*, unpublished Ph.D thesis, University of Auckland, New Zealand.

FOURTH ORDER TRIGONOMETRICALLY-FITTED IMPROVED RUNGE-KUTTA METHOD

Abdulrahman Ndanusa[1*] Aliyu Umar Mustapha[2]

[1, 2]Department of Mathematics, Federal University of Technology, Minna, Nigeria

[1]as.ndanusa@futminna.edu.ng

[2]aliyuumar423@gmail.com

[*]Corresponding author

Abstract

A trigonometrically - fitted fourth order Improved Runge – Kutta (IRK) method whose coefficients depend on the frequency and step – size is constructed. The method is applied to solve sample initial value problems (IVPs) with oscillatory solutions. Numerical results obtained are compared with those of the non - fitted IRK method of the same order. The comparison shows that the trigonometrically fitted method is much more effective and efficient than the non – fitted method, with similar cost.

Keywords: improved Runge–kutta method, initial value problem, oscillatory solution, trigonometrically – fitted, Taylor series

1. Introduction

A great many numerical methods for approximating the solution of initial value problems (IVP) of order ordinary differential equations have been in use. Runge – Kutta (RK) method is just one class of such methods while the Improved Runge - Kutta (IRK) method arises from the classical RK method. Most efforts to increase the order of RK methods have been accomplished by increasing the number of Taylors series terms used and thus the number of function evaluations required (Gear 1971; Butcher 1987). Many authors have attempted to increase the efficiency of RK methods by trying to lower the number of function evaluations required (Rabiei *et al*., 2013). The IRK methods are a special class of two-step methods, that is, the approximate solution y_{n+1} is calculated using the value of y_n and y_{n-1}. The method introduces the new terms of k_{-i}, which are calculated using $k_i (i \geq 2)$, from the previous step. The schemes usually have lower number of function evaluations than the Runge-Kutta methods. The general $s - stage$ IRK method has the form

$$y_{n+1} = y_n + h\left(b_1 k_1 - b_{-1} k_{-1} + \sum_{i=2}^{s} b_i (k_i - k_{-i})\right) \qquad (1)$$

for $1 \leq n \leq N - 1$, where

$$\left.\begin{aligned} k_1 = f(x_n, y_n), \qquad k_{-1} = f(x_{n-1}, y_{n-1}) \\ k_i = f\left(x_n + c_i h, y_n + h\sum_{j=1}^{i-1} a_{i,j} k_j\right), \qquad 2 \leq i \leq s \\ k_{-i} = f\left(x_{n-1} + c_i h, y_{n-1} + h\sum_{j=1}^{i-1} a_{i,j} k_{-j}\right), \qquad 2 \leq i \leq s \end{aligned}\right\} \tag{2}$$

for $c_2 \ldots c_s \epsilon [0,1]$ and f depends on both x and y while k_i and k_{-i} depend on the values of k_j and k_{-j} for $j = 1, \ldots\ldots, i-1$. Here s is the number of function evaluations performed at each step and increases with the order of local accuracy of the IRK method. The IRK method is not self- starting therefore a one-step method must provide the approximate solution of y_1 at the first step. The one-step method must be of appropriate order to ensure that the difference $\left(y_1 - y(x_1)\right)$ is order of p or higher (Rabiei and Ismail, 2012).

Trigonometrically – fitted methods are especially developed to improve the accuracy of numerical solutions of initial value problems. In particular, when the solution exhibits periodic or oscillatory behaviour, trigonometrically fitted methods are much more efficient than non-fitted methods, with the same cost. These methods are generally obtained to exactly solve IVPs whose solutions are linear combinations of the functions $\{1, x, x^2, \ldots, \cos(\omega x), \sin(\omega x)\}$. The procedure has been applied to linear multistep methods, Runge_Kutta-type methods, and hybrid methods (Ramos and Vigo-Aguiar, 2010). The pioneering work in the development of trigonometrically – fitted methods is attributed to Gautschi (1961); ever since, authors who have made their contributions in this direction include, Franco (2004), Wang (2006), Fang and Wu (2008), to mention but just a few. This present research is an attempt to design a trigonometrically – fitted IRK method of order four, thereby improving its efficiency and effectiveness.

2. Materials and Methods

An alternative form of the general IRK method (1) and (2) is

$$\begin{aligned} y_{n+1} = y_n + hb_1 f(x_n, y_n) - hb_{-1} f(x_{n-1}, y_{n-1}) \\ + h\sum_{i=2}^{s} b_i \left(f(x_n + c_i h, Y_i) - f(x_{n-1} + c_i h, Y_{-i})\right) \end{aligned} \tag{3}$$

where,

$$Y_i = y_n + h\sum_{j=1}^{i-1} a_{i,j} f(x_n + c_j h, Y_j) \tag{4}$$

$$Y_{-i} = y_{n-1} + h\sum_{j=1}^{i-1} a_{i,j} f\left(x_{n-1} + c_j h, Y_{-j}\right) \tag{5}$$

where y_{n+1} and y_n are approximations to $y(x_{n+1})$ and $y(x_n)$ respectively.

If a function $y(x)$ is integrated exactly by TFIRK method for all problems whose solution is $y(x)$ then,

$$y_n = y(x_n) = e^{i\omega x_n} \tag{6}$$

$$y_{n-1} = y(x_{n-1}) = y(x_n - h) = e^{i\omega(x_n - h)} \tag{7}$$

Thus

$$y_n^{'} = i\omega e^{i\omega x_n} = f\left(x_n, y_n\right) \tag{8}$$

$$y_{n-1}^{'} = i\omega e^{i\omega(x_n - h)} = f\left(x_{n-1}, y_{n-1}\right) \tag{9}$$

$$Y_i = e^{i\omega(x_n + c_i h)} \tag{10}$$

$$Y_{-i} = e^{i\omega(x_{n-1} + c_i h)} \tag{11}$$

Consequently, we obtain the recursive relations

$$cos(c_i z) = 1 - z\sum_{j=1}^{i-1} a_{ij} \sin\left(c_j z\right), \qquad i = 2,3,\ldots,s \tag{12}$$

$$sin(c_i z) = z\sum_{j=1}^{i-1} a_{ij}\, cos\left(c_j z\right), i = 2,3,\ldots,s \tag{13}$$

$$cos(z) = 1 - zb_{-1}\, sin(z) - z\sum_{i=2}^{s} b_i\, sin(c_i z) + z\sum_{i=2}^{s} b_i\, sin\left(z(c_i - 1)\right) \tag{14}$$

$$sin(z) = zb_1 - zb_{-1}\, cos(z) + z\sum_{i=2}^{s} b_i\, cos(c_i z) - z\sum_{i=2}^{s} b_i\, cos\left(z(c_i - 1)\right) \tag{15}$$

The relations (12), (13), (14) and (15) are the relations of order conditions of the trigonometrically-fitted method. They replace the equations of order conditions of two-step Improved Runge-Kutta (IRK) method, which can be solved to give the coefficients of a particular method based on existing coefficients.

For the proposed fourth order three stage trigonometrically – fitted IRK (TFIRK43) method ($s = 3, p = 4$), the order conditions up to order four for classical IRK methods, according to Rabiei *et al*. (2013), is

$$\left.\begin{aligned}
&\text{First order:} && b_1 - b_{-1} = 1 \\
&\text{Sercond order:} && b_{-1} + \sum_{i=2}^{s} b_i = \frac{1}{2} \\
&\text{Third order 3} && : \sum_{i=2}^{s} b_i\, c_i = \frac{5}{12} \\
& && \sum_{i=2}^{s} b_i\, c_i^2 = \frac{1}{3} \\
&\text{Fourth order 4:} && \sum_{i=2,j=1}^{s} b_i\, a_{ij} c_j = \frac{1}{6} \\
& && \sum_{i=1}^{s} b_i\, c_i^3 = \frac{31}{120}
\end{aligned}\right\} \qquad (16)$$

And the classical fourth order three stage IRK method (IRK43) has the butcher tableau as

Table 1 Butcher Tableau for IRK43

0			
$\frac{31}{60}$	$\frac{31}{60}$		
$\frac{62}{85}$	$\frac{7502}{24565}$	$\frac{10416}{24565}$	
$\frac{157}{23064}$	$\frac{23221}{23064}$	$-\frac{1800}{6727}$	$\frac{122825}{161448}$

Substituting $s = 3, c_1 = 0$ in the recursive relations (12) and (13)

when $i = 2$

$$\cos(c_2 z) - 1 = 0 \qquad (17)$$

$$\sin(c_2 z) - z a_{2,1} = 0 \tag{18}$$

when $i = 3$

$$cos(c_3 z) - 1 + z a_{3,2}\, sin(c_2 z) = 0 \tag{19}$$

$$sin(c_3 z) - z\left[a_{3,1} + a_{3,2}\, cos(c_2 z)\right] = 0 \tag{20}$$

Substituting $s = 3, c_1 = 0$ into (14) and (15)

$$cos(z) - 1 + z b_{-1}\, sin(z) + z[b_2\, sin(c_2 z) + b_3\, sin(c_3 z)] - z\left[b_2\, sin\big((c_2 - 1)z\big) + b_3\, sin\big((c_3 - 1)z\big)\right] = 0 \tag{21}$$

$$sin(z) - z b_1 + z b_{-1}\, cos(z) - z[b_2\, cos(c_2 z) + b_3\, cos\, c_3 z] + z\left[b_2\, cos\big((c_2 - 1)z\big) + b_3\, cos\big((c_3 - 1)z\big)\right] = 0 \tag{22}$$

Equations $(19) - (22)$ are now the equations of order conditions for the fourth order three stage trigonometrically-fitted IRK method which replaces the order conditions of the original method.

Equations (21) and (22), together with two additional equations from the order conditions (16), that is,

$$b_1 - b_{-1} = 1 \tag{23}$$

$$b_{-1} + b_2 + b_3 = \frac{1}{2} \tag{24}$$

are combined to constitute a system a four equations in six unknowns $(b_{-1}, b_1, b_2, b_3, c_2 \text{and} c_3)$. The resulting system is solved in terms of two free parameters $(c_2 = \frac{31}{60}, c_3 = \frac{62}{85})$ whose values are obtained from Table 1. Using Maple software, the following values are obtained for the unknowns.

$$\left.\begin{aligned} b_{-1} &= -\frac{1}{2}\frac{M_1}{M_2} \\ b_1 &= \frac{1}{2}\frac{\mathrm{M}_3}{\mathrm{M}_4} \\ b_2 &= -\frac{1}{2}\frac{\mathrm{M}_5}{\mathrm{M}_6} \\ b_3 &= \frac{1}{2}\frac{M_7}{M_8} \end{aligned}\right\} \tag{25}$$

where,

$$M_1 = -\frac{1}{2}\left[-2z\, sin\left(\frac{31}{60}z\right) - 2z\, sin\left(\frac{29}{60}z\right) - 2cos\left(\frac{31}{60}z\right) + 2cos\left(\frac{62}{85}z\right) + 2cos\left(\frac{29}{60}z\right)\right.$$

$$-2cos\left(\frac{23}{85}z\right) + 2cos\left(\frac{31}{60}z\right)\cos(z) - 2cos\left(\frac{29}{60}z\right)cos(z) + 2sin(z)sin\left(\frac{31}{60}z\right)$$

$$\left.+2sin(z)sin\left(\frac{29}{60}z\right) - zcos\left(\frac{29}{60}z\right)sin\left(\frac{62}{85}z\right) - zcos\left(\frac{29}{60}z\right)sin\left(\frac{23}{85}z\right) - 2sin\left(\frac{62}{85}z\right)\sin(z)\right.$$

$$+2sin\left(\frac{62}{85}z\right) - 2sin\left(\frac{23}{85}z\right)sin(z) + 2zsin\left(\frac{23}{85}z\right) - 2cos(z)cos\left(\frac{62}{85}z\right)\sin(z)$$

$$+2cos(z)cos\left(\frac{23}{85}z\right) + zcos\left(\frac{23}{85}z\right)sin\left(\frac{29}{60}z\right) + zcos\left(\frac{23}{85}z\right)sin\left(\frac{31}{60}z\right)$$

$$-zcos\left(\frac{62}{85}z\right)sin\left(\frac{29}{60}z\right) - zcos\left(\frac{62}{85}z\right)sin\left(\frac{31}{60}z\right) + zcos\left(\frac{31}{60}z\right)sin\left(\frac{62}{85}z\right)$$

$$+zcos\left(\frac{31}{60}z\right)sin\left(\frac{23}{85}z\right)] \quad (26)$$

$$M_2 = z[\cos(z)\,sin\left(\frac{31}{60}z\right) + cos(z)sin\left(\frac{29}{60}z\right) - sin\left(\frac{31}{60}z\right) - cos\left(\frac{62}{85}z\right)\sin(z)$$

$$+cos\left(\frac{62}{85}z\right)sin\left(\frac{31}{60}z\right) + cos\left(\frac{62}{85}z\right)sin\left(\frac{29}{60}z\right) + cos\left(\frac{23}{85}z\right)sin(z)$$

$$-cos\left(\frac{23}{85}z\right)sin\left(\frac{31}{60}z\right) - cos\left(\frac{23}{85}z\right)sin\left(\frac{29}{60}z\right) - cos(z)sin\left(\frac{62}{85}z\right) - cos(z)sin\left(\frac{23}{85}z\right)$$

$$+sin\left(\frac{62}{85}z\right) + sin\left(\frac{23}{85}z\right) + cos\left(\frac{31}{60}z\right)sin(z) - cos\left(\frac{31}{60}z\right)sin\left(\frac{31}{60}z\right)$$

$$-cos\left(\frac{31}{60}z\right)sin\left(\frac{23}{85}z\right) - cos\left(\frac{29}{60}z\right)sin(z) + cos\left(\frac{29}{60}z\right) + cos\left(\frac{29}{60}z\right)sin\left(\frac{62}{85}z\right)$$

$$+cos\left(\frac{29}{60}z\right)sin\left(\frac{23}{85}z\right)] \quad (27)$$

$$M_3 = \frac{1}{2}[2\,sin\left(\frac{23}{85}z\right) + 2\,sin\left(\frac{62}{85}z\right)sin(z) + 2cos(z)cos\left(\frac{62}{85}z\right) - 2cos(z)cos\left(\frac{23}{85}z\right)$$

$$+2cos\left(\frac{31}{60}z\right) - 2cos\left(\frac{62}{85}z\right) - 2cos\left(\frac{29}{60}z\right) + 2cos\left(\frac{23}{85}z\right) + 2cos\left(\frac{31}{60}z\right)\sin(z)$$

$$-2cos\left(\frac{31}{60}z\right)cos(z) + 2cos\left(\frac{29}{60}z\right)cos(z) - 2sin(z)sin\left(\frac{31}{60}z\right) - 2sin(z)sin\left(\frac{29}{60}z\right)$$

$$+2zcos(z)sin\left(\frac{31}{60}z\right) + 2zcos(z)sin\left(\frac{29}{60}z\right) - cos\left(\frac{29}{60}z\right)zsin(z)$$

$$+3zcos\left(\frac{29}{60}z\right)sin\left(\frac{62}{85}z\right) + 3zcos\left(\frac{29}{60}z\right)sin\left(\frac{23}{85}z\right) - 3zcos\left(\frac{23}{85}z\right)sin\left(\frac{29}{60}z\right)$$

$$-3zcos\left(\frac{23}{85}z\right)sin\left(\frac{31}{60}z\right) + 3zcos\left(\frac{62}{85}z\right)sin\left(\frac{29}{60}z\right) + 3zcos\left(\frac{62}{85}z\right)sin\left(\frac{31}{60}z\right)$$

$$-3zcos\left(\frac{31}{60}z\right)sin\left(\frac{62}{85}z\right) - 3zcos\left(\frac{31}{60}z\right)sin\left(\frac{23}{85}z\right) - 2zsin(z)cos\left(\frac{62}{85}z\right)]$$

$$-2zsin(z)cos\left(\frac{23}{85}z\right)-2sin\left(\frac{62}{85}z\right)zcos(z)sin\left(\frac{23}{85}z\right)-2sin\left(\frac{23}{85}z\right)zcos(z)] \quad (28)$$

$$M_4 = z[\cos(z)\,sin\left(\frac{31}{60}z\right)+cos(z)sin\left(\frac{29}{60}z\right)-sin\left(\frac{31}{60}z\right)-sin\left(\frac{29}{60}z\right)$$

$$-cos\left(\frac{62}{85}z\right)sin(z)+cos\left(\frac{62}{85}z\right)sin\left(\frac{31}{60}z\right)+cos\left(\frac{62}{85}z\right)sin\left(\frac{29}{60}z\right)+\cos\left(\frac{23}{85}z\right)sin(z)$$

$$-cos\left(\frac{23}{85}z\right)sin\left(\frac{31}{60}z\right)-cos\left(\frac{23}{85}z\right)sin\left(\frac{29}{60}z\right)-cos(z)sin\left(\frac{62}{85}z\right)-cos(z)sin\left(\frac{23}{85}z\right)$$

$$+sin\left(\frac{62}{85}z\right)sin\left(\frac{23}{85}z\right)+cos\left(\frac{31}{60}z\right)sin(z)-cos\left(\frac{31}{60}z\right)sin\left(\frac{62}{85}z\right)$$

$$-cos\left(\frac{31}{60}z\right)sin\left(\frac{23}{85}z\right)-cos\left(\frac{29}{60}z\right)sin(z)+cos\left(\frac{29}{60}z\right)sin\left(\frac{62}{85}z\right)$$

$$+cos\left(\frac{29}{60}z\right)sin\left(\frac{23}{85}z\right)] \quad (29)$$

$$M_5 = [-2sin(z^2)-4\,cos(z)+2zsin(z)+2sin\left(\frac{23}{85}z\right)sin(z)+zsin(z)cos\left(\frac{62}{85}z\right)$$

$$-zsin(z)cos\left(\frac{23}{85}z\right)+2sin\left(\frac{62}{85}z\right)sin(z)+2-4cos\lfloor z\rfloor-2cos\left(\frac{62}{85}z\right)+2cos\left(\frac{23}{85}z\right)$$

$$+2cos(z^2)+sin\left(\frac{62}{85}z\right)cos(z)+sin\left(\frac{23}{85}z\right)zcos(z)-3zsin\left(\frac{62}{85}z\right)-3zsin\left(\frac{23}{85}z\right)$$

$$+2cos(z)cos\left(\frac{62}{85}z\right)-2cos(z)cos\left(\frac{23}{85}z\right) \quad (30)$$

$$M_6 = [z[\cos(z)\,sin\left(\frac{31}{60}z\right)+cos(z)sin\left(\frac{29}{60}z\right)-sin\left(\frac{31}{60}z\right)-sin\left(\frac{26}{60}z\right)$$

$$-cos\left(\frac{62}{85}z\right)sin\left(\frac{31}{60}z\right)+cos\left(\frac{62}{85}z\right)sin\left(\frac{31}{60}z\right)+cos\left(\frac{62}{85}z\right)sin\left(\frac{29}{60}z\right)$$

$$+cos\left(\frac{23}{85}z\right)sin(z)-cos\left(\frac{23}{85}z\right)sin\left(\frac{31}{60}z\right)-cos\left(\frac{23}{85}z\right)sin\left(\frac{29}{60}z\right)$$

$$-cos(z)sin\left(\frac{62}{85}z\right)-cos(z)sin\left(\frac{23}{85}z\right)+sin\left(\frac{62}{85}z\right)+sin\left(\frac{23}{85}z\right)]+cos\left(\frac{31}{60}z\right)sin(z)$$

$$-cos\left(\frac{31}{60}z\right)sin\left(\frac{62}{85}z\right)-cos\left(\frac{31}{60}z\right)sin\left(\frac{23}{85}z\right)-cos\left(\frac{29}{60}z\right)sin(z)+cos\left(\frac{29}{60}z\right)sin\left(\frac{62}{85}z\right)$$

$$+cos\left(\frac{29}{60}z\right)sin\left(\frac{23}{85}z\right)]] \quad (31)$$

$$M_7 = [2cos(z^2) - 4\,cos(z) + 2zsin(z) + 2 + cos\left(\frac{31}{60}z\right)zsin(z)$$

$$+2cos\left(\frac{31}{60}z\right)cos(z) - 2cos\left(\frac{31}{60}z\right) - cos\left(\frac{29}{60}z\right)zsin(z) - 2cos\left(\frac{29}{60}z\right)cos(z)$$

$$+2cos\left(\frac{29}{60}z\right) - 2sin(z^2) + 2\sin(z)\,sin\left(\frac{31}{60}z\right) + 2sin(z)sin\left(\frac{29}{60}z\right)$$

$$+cos(z)sin\left(\frac{31}{60}z\right) + zcos(z)cos\left(\frac{29}{60}z\right) - 3zsin\left(\frac{31}{60}z\right) - 3zsin\left(\frac{29}{60}z\right) \quad (32)$$

$$M_8 = [z[\cos(z)\,sin\left(\frac{31}{60}z\right) + cos(z)sin\left(\frac{29}{60}z\right) - sin\left(\frac{31}{60}z\right) - sin\left(\frac{26}{60}z\right)$$

$$-cos\left(\frac{62}{85}z\right)sin(z) + cos\left(\frac{62}{85}z\right)sin\left(\frac{31}{60}z\right) + cos\left(\frac{62}{85}z\right)sin\left(\frac{29}{60}z\right)$$

$$+cos\left(\frac{23}{85}z\right)sin(z) - cos\left(\frac{23}{85}z\right)sin\left(\frac{32}{60}z\right) - cos\left(\frac{23}{85}z\right)sin\left(\frac{23}{85}z\right)$$

$$+sin\left(\frac{62}{85}z\right) + sin\left(\frac{23}{85}z\right) + cos\left(\frac{31}{60}z\right)sin(z) - cos\left(\frac{31}{60}z\right)sin\left(\frac{62}{85}z\right)$$

$$-cos\left(\frac{31}{60}z\right)sin\left(\frac{23}{85}z\right) - cos\left(\frac{29}{60}z\right)sin(z) + cos\left(\frac{29}{60}z\right)sin\left(\frac{62}{85}z\right)$$

$$+cos\left(\frac{29}{60}z\right)sin\left(\frac{23}{85}z\right)] \quad (33)$$

The Taylor series expansions of the coefficients $b_{-1}, b_1, b_2, \text{and} b_3$ in (25) are obtained as

$$\left.\begin{aligned} b_{-1} &= \frac{157}{23064} - \frac{455}{553536}z^2 + o(z^4) \\ b_1 &= \frac{23221}{23064} - \frac{445}{553536}z^2 + o(z^4) \\ b_2 &= -\frac{1800}{6727} + \frac{65}{23064}z^2 + o(z^4) \\ b_3 &= \frac{122825}{161448} - \frac{1105}{553536}z^2 + o(z^4) \end{aligned}\right\} \quad (34)$$

From (34), it is evident that the classical IRK43 method, shown in Table 1, is recovered as z approaches zero. And in order to re-establish the order of the method as four, the Taylor expansions of the order conditions from the order conditions (16) is obtained after substituting the coefficients (34).

$$\left.\begin{aligned}
&\text{First order}: && b_1 - b_{-1} = 1 + o(z^4)\\
&\text{Second order}: && b_{-1} + \sum_{i=2}^{s} b_i = \frac{1}{2} + o(z^4)\\
&\text{Third order}: && \sum_{i=2}^{s} b_i\, c_i = \frac{5}{12} + o(z^4)\\
& && \sum_{i=2}^{s} b_i\, c_i^2 = \frac{1}{3} - \frac{91}{293760} z^2 + o(z^4)\\
&\text{Fourth order}: && \sum_{i=2,j=1}^{s} b_i a_{ij}\, c_j = \frac{1}{6} - \frac{91}{208080} z^2 + o(z^4)
\end{aligned}\right\} \qquad (35)$$

From (35) it observed that as z approaches zero the order conditions (16) of the IRK methodsare recovered up to order four, implying that the coefficients of the TFIRK43 method satisfies the IRK order four conditions.

3. Numerical Examples

In the following numerical examples, the approximate solutions are sought on the partition$[x_0,\ x_N]$, and the errors are calculated at the endpoints as $|y_n - y(x_n)|$, where y_n and $y(x_n)$ are the approximate and exact solutions at the point x_n respectively. The sample problems are solved with the aid of Maple software and the results presented in Table 2 - 5

Example 1

$y'(x) = x\cos(x) + \sin(x), \quad y(0) = 0, \quad$ Exact solution: $y(x) = x\sin(x), \qquad \omega = 1$

Example 2

$y'(x) = -\pi\sin(\pi x), \qquad y(0) = 0;$ Exact solution: $y(x) = \cos(\pi x)\,, \qquad \omega = \pi$

Table 2: Results of Example 1 on [0, 1], $h = 0.05$, $\omega = 1$

x	Exact	TFIRK43	Error	IRK43	Error
0.05	0.0024989585	4.9958341150E-03	2.4968756150E-03	4.9958341150E-03	2.4968756150E-03
0.10	0.0099833417	9.9833416599E-03	4.8246343683E-12	9.9833416502E-03	1.4478106272E-11
0.15	0.0224157199	2.2415719861E-02	9.6220972565E-12	2.2415719842E-02	2.8867686620E-11

0.20	0.0397338662	3.9733866145E-02	1.4380397506E-11	3.9733866116E-02	4.3120760966E-11
0.25	0.0618509898	6.1850989795E-02	1.9087641844E-11	6.1850989756E-02	5.7189775782E-11
0.30	0.0886560620	8.8656061975E-02	2.3732064611E-11	8.8656061927E-02	7.1027752760E-11
0.35	0.1200142326	1.2001423258E-01	2.8302057169E-11	1.2001423252E-01	8.4588435762E-11
0.40	0.1557673369	1.5576733689E-01	3.2786196916E-11	1.5576733683E-01	9.7826435600E-11
0.45	0.1957344904	1.9557344903E-01	3.7173275840E-11	1.9573449024E-01	1.1069737222E-11
0.50	0.2397127693	2.3971276926E-01	4.1452328526E-11	2.3971276918E-01	1.2315801384E-11
0.55	0.2874779759	2.8747797587E-01	4.5612659572E-11	2.8747797577E-01	1.3516641267E-11
0.60	0.3387854840	3.3887854840E-01	4.9643870317E-11	3.3878548389E-01	1.4668203676E-10
0.65	0.3933711637	3.9337116367E-01	5.3535884834E-11	3.9337116357E-01	1.5766589752E-10
0.70	0.4509523811	4.5095238101E-01	5.7278975112E-11	4.5095238090E-01	1.6808067100E-10
0.75	0.5112290700	5.1122906996E-01	6.0863785376E-11	5.1122906984E-01	1.7789082521E-10
0.80	0.5738848727	5.7388487266E-01	6.4281355468E011	5.7388487253E-01	1.8706271336E-10
0.85	0.6385883444	6.3858834430E-01	6.7523143240E-11	6.3858834417E-01	1.9556470038E-10
0.90	0.7049942187	7.0449942186E-01	7.0581045914E-11	7.0499421846E-01	2.0336725388E-10
0.95	0.7727447295	7.7274472948E-01	7.3447420323E-11	7.7274472934E-01	2.1044304064E-10
1.00	0.8414709848	8.4147098473E-01	7.6115102026E-11	8.4147098459E-01	2.1676701450E-10

Table 3: Results of Example 2 on [0, 1], $h = 0.05$, $\omega = \pi$

x	Exact	TFIRK43	Error	IRK43	Error
0.05	0.9876883400	-0.0245726683	1.0122610080+000	-0.0245726683	1.0122610080+000
0.10	0.9510565163	0.9510565163	4.5570800000E-25	0.9510565186	2.2762336676E-09

0.15	0.8910065242	0.8910065242	1.1772170000E-24	0.8910065286	4.4488188493E-09
0.20	0.8090169944	0.8090169944	2.1467630000E-24	0.8090170008	6.4642592875E-09
0.25	0.7071067812	0.7071067812	3.3404710000E-24	0.7071067895	8.2729281496E-09
0.30	0.5877852523	0.5877852523	4.7289480000E-24	0.5877852600	9.8302900058E-09
0.35	0.4539904997	0.4539904997	6.2780070000E-24	0.4539905108	1.1097997439E-08
0.40	0.3090169944	0.3090169944	7.9494970000E-24	0.3090170064	1.2044835283E-08
0.45	0.1564344650	0.1564344650	9.7022770000E-24	0.1564344777	1.2647489251E-08
0.50	0.0000000000	0.0000000000	1.1493168000E-23	1.2891119999	1.2891119999E-08
0.55	-0.1564344650	-0.1564344650	1.3278081000E-23	-0.1564344523	1.2769728531E-08
0.60	-0.3090169944	-0.3090169944	1.5013077000E-23	-0.3090169821	1.2286303908E-08
0.65	-0.4539904997	-0.4539904997	1.6655413000E-23	-0.4539904883	1.1452749648E-08
0.70	-0.5877852523	-0.5877852523	1.8164670000E-23	-0.5877852420	1.0289590624E-08
0.75	-0.7071067812	-0.7071067812	1.9503666000E-23	-0.7071067724	8.8254676701E-09
0.80	-0.8090169944	-0.8090169944	1.0639442000E-23	-0.8090169873	7.0964323538E-09
0.85	-0.8910065242	-0.8910065242	2.1544032000E-23	-0.8910065190	5.1450592626E-09
0.90	-0.9510565163	-0.9510565163	2.2195157000E-23	-0.9510565133	3.0193976782E-09
0.95	-0.9876883406	-0.9876883406	2.2576787000E-23	-0.9876883398	7.7178844349E-10
1.00	-1.0000000000	-0.9999999999	2.2679523000E-23	-1.0000000015	1.5424248428E-09

Table 4: Maximum errors for Example 1 on [0, 100], $\omega = 1$

h	TFIRK43	IRK43	NFEs
$\frac{1}{20}$	1.0291918182E-10	4.7352725236E-09	6000
$\frac{1}{40}$	3.1201619496E-12	1.4777985444E-10	12000
$\frac{1}{80}$	9.6134575308E-14	4.6151065805E-12	24000
$\frac{1}{160}$	1.2950265575E-14	1.4417554518E-13	48000
$\frac{1}{320}$	3.7783169258E-12	4.5047630316E-15	96000
$\frac{1}{640}$	5.1468240093E-11	1.4076266174E-16	192000

Table 5: Maximum errors for Example 2 on [0, 100], $\omega = \pi$

h	TFIRK43	IRK43	NFEs
$\frac{1}{20}$	1.6696492000E-23	1.6757378568E-08	6000
$\frac{1}{40}$	1.0045783210E-21	4.9322096769E-10	12000
$\frac{1}{80}$	2.0575750783E-20	1.4938496673E-11	24000
$\frac{1}{160}$	8.3151927728E-19	4.5942435517E-13	48000
$\frac{1}{320}$	2.0753909807E-17	1.4241446777E-14	96000
$\frac{1}{640}$	4.8402497964E-15	4.4324050858E-16	192000

4. Discussion of Results

Table 2 displays the results of comparison of performance between TFIRK43 and IRK43 when applied to solve Example 1 on the interval $[0, 1]$. It is observed that TFIRK43 performs better than the classical IRK43 by exhibiting lesser errors. Similarly, Table 3 shows the results of comparing the performance of TFIRK43 and IRK43 applied to the solution of the problem of Example 2. There is an observable display of better accuracy by TFIRK43, considering its minimal display of errors relative to the errors of IRK43. Table 4 gives the results of the maximum errors obtained on the interval $[0, 100]$ by TFIRK43 and IRK43 applied to Problem 1. There is a general observation of better performance by TFIRK even though this reduces as the step size tends towards zero. And, in Table 5, similar observation to the results of Table 4 is noted.

5. Conclusion

We have derived a fourth order three stage trigonometrically – fitted Improved Runge – Kutta method. The methods were applied to solve highly oscillatory initial value problems of first order ordinary differential equations. The results established that the trigonometrically – fitted method is more accurate than the non – fitted method. Also, the TFIRK43 requires only three function evaluations at each integration step and in general requires $\left(3 \cdot \left(\frac{T}{h}\right)\right)$ NFEs on the entire interval of integration.

References

Butcher, J. C. (1987). *The numerical analysis of ordinary differential equations*: *Runge - Kutta and general linear methods.* Chichester: Wiley.

Fang, Y. and Wu, X. (2008). A trigonometrically fitted explicit Numerov-type method for second-order initial value problems with oscillating solutions, *Applied Numerical Mathematics*, Vol. 585, 341-351.

Franco, J. M. (2004). Runge_Kutta methods adapted to the numerical integration of oscillatory Problems, *Applied Numerical Mathematics,* Vol. 50, 427 - 443.

Gautschi, W. (1961). Numerical integration of ordinary differential equations based on trigonometric polynomials, *Numerische Mathematik,* Vol. 3, 381 - 397.

Gear, C. W. (1971). *Numerical initial value problems in ordinary differential equations*. Englewood Cliffs, New Jersy: Prentice-Hall.

Rabiei, F. and Ismail, F. (2012). Fifth-order Improved Runge-Kutta method with reduced number of function evaluations, *Australian Journal of Basic and Applied Sciences,* Vol. 6 (3), 97-105.

Rabiei, F., Ismail, F. and Suleiman, M. (2013). Improved Runge-Kutta methods for solving ordinary differential equations, *Sains Malaysiana*, Vol. 42(11), 1679 - 1687.

Ramos, H. and Vigo-Aguiar, J. (2010). On the frequency choice in trigonometrically fitted methods. *Applied Mathematics Letters*, Vol. 23, 1378 – 1381.

Wang, Z. (2006). Trigonometrically-fitted method for a periodic initial value problem with two Frequencies. *Comput. Phys. Comm*., Vol. 175, 241 - 249.

ASSESSMENT OF IMPACT OF ACTIVITIES OF LOCAL ROAD MAINTENANCE ON THE MINNA-KATAEREGI HIGHWAY, NORTH CENTRAL NIGERIA

[1]WAZIRI, S. H*., [1]GORO, A. I. and [2]WAZIRI, J. A

[1] Federal University of Technology, Minna, Nigeria [2] Covenant University, Otta, Nigeria

* Corresponding author

Salwaz1969@gmail.com 07035983684

Abstract

It is important to ensure that water is prevented from getting in contact with the subgrade in order to maintain its stability and a stable road pavement. The activities of the local road maintenance as well as the groundwater fluctuation along Minna-Kataeregi road were investigated. This was in order to ascertain the impact of the local road maintenance on the performance of this road. The result shows that there is considerable seasonal moisture change along the studied road. The activities of the Local road maintenance expose the subgrade to water as well as raising the water table. This resulted in instability of the subgrade that has translated to poor performance of the road instead of improving the road.

Keywords: Groundwater, Minna, Performance, Local Road Maintenance,

1. Introduction

A road is a path established over land for the passage of people, vehicles and animals. Roads provide dependable pathways for moving people and goods from one place to another. They differ in quality from dirt roads to concrete paved multi lane highways. There are many types of roads ranging from multi-lane freeways and expressways to two way country roads. They can be classified into three major categories: highways, urban or city streets and rural roads. The road considered in this study may be categorized as a highway.

Road is usually built up in several layers as shown in Figure 1 below. To be able to support heavy vehicular movement at high speeds, each layer has a specific function and helps the one above it in supporting the weight and pressure of moving traffic. The number of layers in a road depends on the inferred use of the road, but generally roads are made up of three layers consisting of the sub-grade, base and sub-base below the wearing surface. The sub-grade refers to the soil immediately beneath the sub-base followed by the base and sub-base which is below the wearing surface.

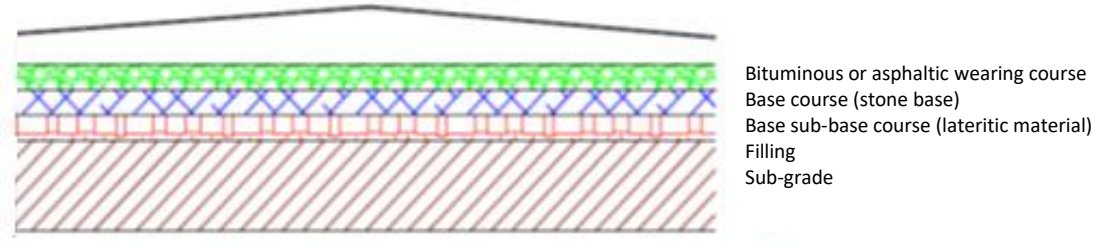

Figure 1. Typical Layers Of A Road Pavement

The road pavement is the hard crust placed on the soil formation after the completion of the earthworks. Its main functions are to provide a smooth riding surface, to distribute the traffic loads over the soil

formation sufficiently to prevent the soil from being overstretched and to protect the soil formation from the adverse effect of weather.

The characteristics of the pavement are therefore dependent on the nature of the traffic and on the property of the soil on which the pavement is constructed. The soil foundation which receives the traffic loads directly from the pavement is referred to as the subgrade as earlier mentioned. The base may be surfaced with either a concrete (rigid) or bituminous (flexible) surfacing.

A successful subgrade should be able to resist the effects of both traffic and weather. A reduction in the supporting power of the subgrade as a result of either of these causes is sometimes referred to as regression.

In this paper, the impact of activities of local road maintenance along the Minna-Kataeregi Road, Central Nigeria is analyzed. The study area is located along the Minna-Kataeregi Road. It lies along longitude (06°31'32.4"E) to (06°22'53.8"E) and latitude ($09^0$35′44.4″ N) to (09^0 05' 38.3"N).

This road has continued to experience failure after construction and frequent maintenance almost on a yearly basis by the locally untrained road maintenance. Thus, this research was carried out to determine the possible impact of this unprofessional road maintenance on the performance of the road.

2. Literature Review

According to the (U.S. Army Corps of Engineers, 1984), the soil in the subgrade exists above the water table and beneath a sealed surface; this does not stop the ingress of water. As a consequence, partially saturated or saturated conditions can exist in the soil. Also, road pavements are constructed at a level where the subgrade is affected by wetting and drying, which may lead to swelling and shrinkage, respectively, if the subgrade consists of expansive clay. Such volume changes are non-uniform, and the associated movements may damage the pavement.

Workers like (Gidigasu, 1972), (Gidigasu, 1978), (Ajayi, 1982), (Ayangade, 1992), (Adeyemi, 1992), (Okagbue and Ifedigbo, 1995), (Adeyemi and Oyeyemi, 1998), (Jegede and Oguniyi, 2004) have attributed the causes of road instability to factors ranging from minerallogic, geotechnical and soil conditions. (Gidigasu, 1972) attributed the majority of road pavement failures in the tropics to mineralogical and geotechnical factors. (Ajayi, 1982) noted that the road failure he studied occurred where the pavement was founded on saprolite rather than the strong lateritic horizons. (Adeyemi, 1992) noted that the degree of stability of the road he studied increased with the amount of kaolinite present in the subgrade soil and with increase in the California Bearing Ratio (CBR) and unconfined compressive strength (UCS) of the sub-grade soils. (Ayangade, 1992) observed that there was a positive correlation between the strength characteristics of the foundation soils and the stability of the pavement along the Oshogbo – Gbongan road, south western Nigeria. (Jegede and Oguniyi, 2004) attributed the incidence of highway pavement failures for Nigerian highways to improperly compacted edges of the pavements to non- provision of drainage facility along the roads, and low California Bearing values among others.

The rock types mapped include fine to medium grained biotite granite, granite gneiss, schist and sandstone. The granite was affected by the Pan African Orogeny with late tectonic emplacement of granites and granodiorites. The end of the orogeny was marked by faulting and fracturing (Abaa 1983, Gandu *et al*.,1986, and Waziri, 2015). The granites are thus fractured, jointed and deeply weathered in some places.

The area has an average annual rainfall of about 1,000 mm. Rainy season usually starts during the month of April, and reaches the peak by August/September and ends in October. Low average temperature of 24ºC is recorded between the months of July and September while high temperature is usually recorded during the months of February to April, at an average of 35^0C. The harmattan wind is experienced between December and January.

3. Methodology

Groundwater fluctuation that may affect moisture content of subgrade was monitored. Static water levels were measured from hand-dug wells located very close to or along the road (Figure 2) during the peak of the dry (April) and rainy (September) seasons. A water level meter was used in taking the measurements while a GPS was used in taking the ground elevation as well as the co-ordinates of the wells. The total depths of the wells were also measured. The following parameters were determined;

i. Total depth of well D (m)

ii. Dry season static water level A (m)

iii. Wet season static water level B (m)

iv. Level of fluctuation of ground water C (m) = A-B

v. Percentage of variation E (%) = B/A X 100

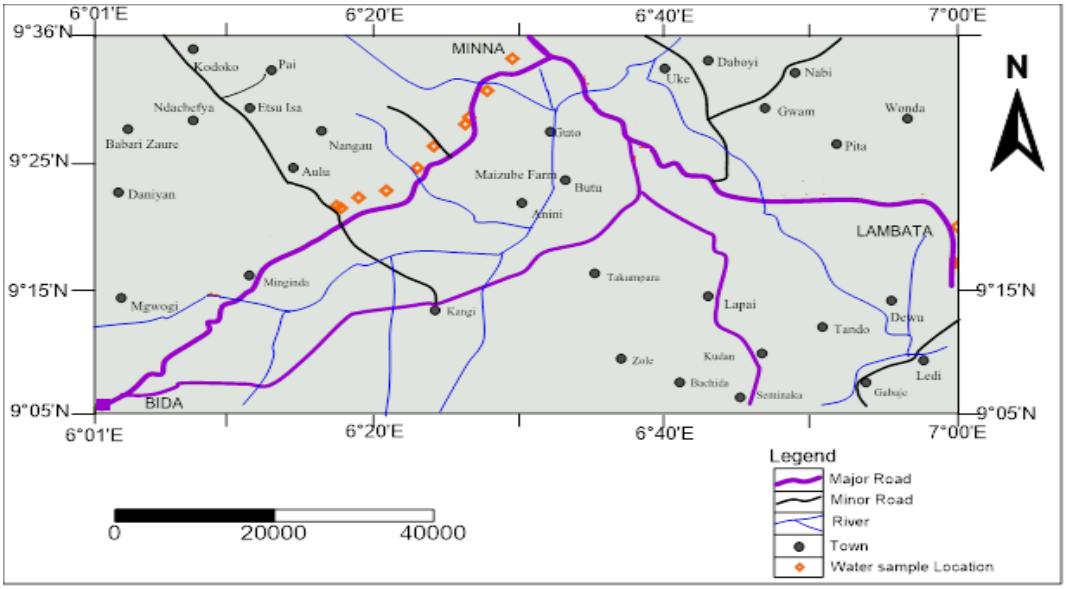

Figure 2. Map Showing The Location Of Water Inventory Along Minna-Kataeregi Road, North Central Nigeria.

4. Results and Discussion

The result of the groundwater inventory is shown in table 1. The result shows that the groundwater fluctuation is high with very low water table especially during the rainy season.

It was observed that pits that range from few centimeters to five meters were dug either on the failed shoulders of the road pavement or very close to the shoulders (Figure 3). Geologic/soil materials recovered from these pits were used in filling the pot-holes (failed portions on the road pavement). Rain

water is normally collected in the dug holes during the rainy season. A closer observation further reveals that some of the dug geologic materials are part of the subgrade especially where the pits are as deep as five meters (Figure 3).

Studies by (Waziri *et al.*, 2012) and (Waziri, 2015) showed that the portion of the road pavement under study is underlain by granites, gneisses and ampobilite schist. The minerals that make up the rocks include nacaphite, vallerite, ferriwinchite, birnessite, caicium titanium oxide, hornblende, albite, quartz, actinolite, plagioclase (Labrodorite), and silicate minerals (Waziri, 2015).

These rocks have undergone fracturing and weathering resulting in formation of clayey secondary minerals. Thus the subgrade materials along this road consist of clayey materials that can swell and shrink when exposed to wet and dry conditions. Groundwater inventory from hand-dug wells located close to the studied road show a high percentage of variation which suggests that the groundwater table variation along the road is high.

The activities of the untrained local road maintenance along this road expose the subgrade to water. Water in pavement subgrade has long been recognized as a primary cause of premature pavement distress, deterioration and failure. When present in subgrade or base course for any length of time, water has been shown to weaken both concrete and asphalt pavements. In addition to its purely physical properties, the water in soil is of interest to engineer due to its action as a solvent. The chemical action of water during leaching further breakdown the subgrade and bring the soluble salts in to solution.

The dissolution of these salts gives rise to positively charged ions such as calcium, magnesium and sodium which can be adsorbed unto the surfaces of the soil particles. These exchangeable bases and the type of exchangeable bases in the soil can affect its physical properties to a considerable extend. The soluble salts can affect the soil and engineering properties by attacking concrete and other materials containing cement and corroding metals such as iron pipes. Montmorillinitic clay and illites are among the secondary minerals identified from the weathered products of the rocks underlying this road (Waziri *et al*, 2012).

Table 1: Groundwater fluctuation along Minna-Kataeregi Road, North Central Nigeria

Location	Well Depth (m)	SWL * Dry Season A (m)	SWL * Wet Season B (m)	Variation (A-B)	% of Variation	Rock Type	Lat. (N)	Long. (E)	Elev. Amsl(m)
Kataeregi	10.1	9.3	8.0	1.3	116.3	Granite gneiss	9^0 21' 45.1"	6^0 17' 44.0	155
SabonYeregi	8.5	8.2	6.8	1.4	103.7	Migmatite	9^0 22'36.5"	6^0 18'56.5"	136
Gadda	4.0	3.8	2.8	1.0	135.7	Schist	9^0 23'11.4"	6^0 20'50.1"	131
Sabon Dagga	7.9	6.7	6.0	0.7	111.7	Granite	9^0 25'02.2"	6^0 22'57.3"	180

Bisisi	9.8	9	7.6	1.4	118.4	Granite	9^0 26'48.7"	6^0 24'04.3"	189
Garatu	9.6	9.4	2.1	7.3	447.6	Granite	9^0 28'36.6"	6^0 26'12.4"	219
Pompom	7.0	5.5	2.7	2.2	203.7	Granite	9^0 31'19.7"	6^0 27'41.6"	239
GidanMangoro	9.5	8.9	8.0	0.9	111.3	Granite	$9^0$33'56.9"	6^0 29'24.3"	237
Garatu	5.4	4.9	0.2	4.7	110	Granite	9^0 29'09.9"	6^0 26'28.8"	224

*SWL – Static Water Level

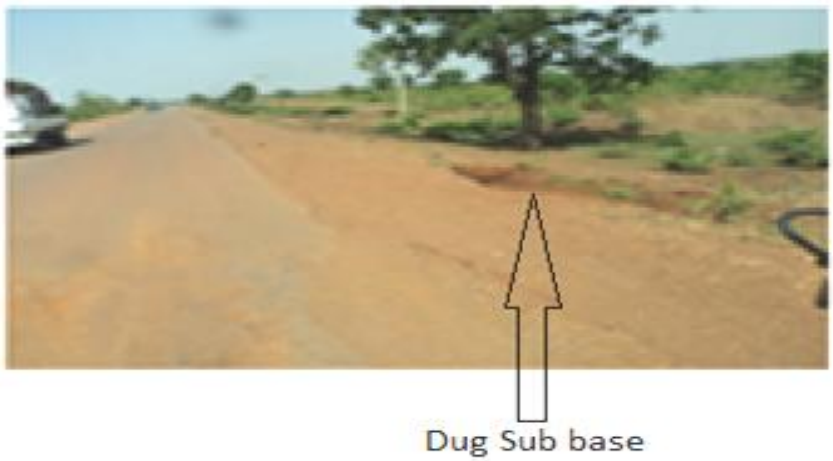

Figure 3. Water Collected In A Hole Dug In The Subgrade By Local Road Maintenance Along Minna-Kataeregi Road North Central Nigeria.

Works by Beaver and Winterkorn (1942) has shown that these clay minerals are flat, elongated or lamellar and have a large surface area per unit weight than would be the case if they were more spherical in shape. The plate –like shape is a major factor causing the plasticity exhibited by clay particles when in contact with water.

The activities of the untrained local road maintenance have led to further degrading the road pavement. This is because they expose the subgrade to water which results in weakening the subgrade since nearly all soils decrease in strength with increasing moisture content and this effect is marked in clayey soils. This has caused severe longitudinal cracks in pavement roads. The subgrade need to be adequately

protected from moisture. The water collected in the holes dug by the local road maintenance could infiltrate into the subgrade leading to a rise in the water table thereby increasing the moisture content of the subgrade material. The subgrade is close to the surface and can be affected by the seasonal weather changes that lead to fluctuations in the moisture content of the subgrade. This is mostly pronounced in the verges of the road.

The effect of these changes in moisture content in the verges is often found to extend for some distance under the edges of the road into the subgrade (Research Laboratory, 1974). According to (Transport and Road Research Laboratory, 1974), when the subgrade is composed of heavy clay, these seasonal fluctuations in moisture content are accompanied by corresponding changes in the volume of the soil. In such cases, the edges of the roads have been found to be subject to a seasonal rise and fall, with respect to the center of the road, of as much as 2 inches. During droughts, these movements are greater and may result in the serious cracking of bituminous surfaces as observed in the studied road.

5. Conclusion

This study reveals that the activities of local road maintenance along the Minna – Kataeregi highway in Niger State, Nigeria has led to poorer performance of the road instead of improving the performance of the road. This is due to introduction of water to the subgrade layer of the road through digging of pits near the road to collect geologic/soil material used in filling the potholes. Water in the subgrade layer weakens the road and leads to failure manifested by the presence of more potholes. This study therefore suggests that their activities be discouraged.

References

Abaa, S.I. (1983), The structure and petrography of alkaline rocks of the Mada Younger Granite Complex, Nigeria. Journal African Earth Sciences Vol. 3, 107-113

Adeyemi, G.O. (1992), Highway geotechnical properties in the Ajeb0-Ishara geological transition zone of Southwestern Nigeria. Unpublished doctoral thesis, OAU, Ile Ife, Nigeria

Adeyemi, G.O. and Oyeyemi, F. (2000), Geotechnical basis for failure of sections of the Lagos – Ibadan expressway, south western Nigeria. Bulletin of Engineering Geology and the Environment 55, 39 – 45

Ajayi, I.A. (1982), Proposal for engineering of laterised residual soils in the Ajebo – Ishara geological transition zone of Southwestern Nigeria

Ajayi, I.A. (1987), Geology in a tropical environment. *Global journal of Geological Sciences* Vol.3 No 2, 99-108

Ayangade (1992), Some geotechnical properties of two highway subgrade along Gbongan-Oshogbo road, South western Nigeria

Baver, L.D., and Winterkorn, H.F. (1935), Sorption of liquids by soil colloids. II. Surface behavior in the hydration of clays. Soil Sci., 1935, 40, 403-19

Gandu, A.H., Ojo S.B. and Jakaiye, D.E (1986), A gravity study of The Precambrian rocks in the Malumfashi area of Kaduna state, Nigeria. Tectonophyics 126, 181-194

Gidugasu, M.D. (1972), Mode of formation and geotechnical characteristics of laterite materials of Ghana in relation to soil forming factors. Eng.Geol., 6, 79-150

Okagbue C.O. and Ifedigbo O .T. (1995), Engineering properties and slope stability of road cuttings along the Enugu – Onitsha express road southeastern Nigeria. *Bull. of the International Association of Engineering geology. Paris – no 52,85 – 93*

Transport and Road Research Laboratory (1974), Transport and Road Research Laboratory, Harmondsworth, Middlesex

U.S. Army Corps of Engineers (1984), Engineering and Designs, Department of the Army Corps of Engineers, U.S. Army Corps of Engineers, Washington D.C.

Waziri S.H., Okunlola I.A., S. Abafiran, T. Ako. and A. Nduka (2012), The mineralogical, geotechnical and industrial uses of clay derived from granitic rock: case study of Gidanmangoro and Gidan-kwano area, part of Minna sheet 184 SW. Book of abstracts Natonal Association of Hydrogeologists National conference Benin 2012.p. 20

Waziri, S. H. (2015), Impact of geology on the stability of Lambata-Minna and Minna-Bida roads, Central Nigeria. Unpl.Ph.D thesis, University of Nigeria, Nsukka.

PALYNOFACIES ANALYSIS OF IDA 4 WELL, NIGER DELTA, NIGERIA

Jacinta Chukwuma-Orji[1*] Edward Okosun[1] Emmanuel Udensi[2] Peter Olasehinde[1] Usman Onuduku[1] Yahaya Alkali[1]

[1]Department of Geology, Federal University of Technology, Minna, Niger State, Nigeria.

[2]Department of Physics, Federal University of Technology, Minna, Niger State, Nigeria.

[1]jacinta@futminna.edu.ng

[1]eaokosun@futminna.edu.ng

[2]udensi.emmanuel@futminna.edu.ng

[1]onoduku.usman@futminna.edu.ng

[1]yalkali@futminna.edu.ng

* Corresponding author

Abstract

Palynofacies analyses of the strata penetrated by Ida-4 wells were carried out with the aim of studying the stratigraphic sequence penetrated by the well in order to establish palynostratigraphic zones, relative age and the paleoenvironment of deposition. Fifty ditch cutting samples within the interval of 2179 – 3523 m were analyzed. The acid methods of sample preparation for palynofacies analyses were followed. The result of the analyses yielded low to abundant occurrences of pollen and spores with abundance of small, medium and large sizes of palynomacerals 1 and 2, few occurrences of palynomacerals 3 and 4. The lithology consists of alternation of shale and sandstone units with few intercalations of argillaceous sandstone units, indicating that the studied interval belongs to the Agbada Formation. The studied intervals were dated middle Miocene to late Miocene based on the recovered age diagnostic marker species such as *Zonocostatites ramonae, Multiareolites formosus, Verrutricolporites rotundiporus, Crassoretitriletes vanraadshoveni* and *Racemonocolpites hians.* Two interval range palynostratigraphic zones: *Multiareolites formosus – Zonocostatites ramonae, Verrutricolporites rotundiporus - Crassoretitriletes vanraadshoveni* and a taxon range zone: *Ainipollinite verus* zone were proposed. Paleoenvironmental interpretation was based on the palynofacies association and the lithology which revealed that the stratigraphic interval studied was deposited in the Coastal-deltaic (marginal marine) environments.

Keywords: Ida 4, paleoenvironment, palynofacies

1. Introduction

Palynofacies could be described as the entire acid resistant organic matter (palynological matter) constituents of sedimentary deposit. The term was first introduced by Combaz (1964) to describe the total microscopic image of the organic components in sedimentary rock samples. Subsequent authors have assigned different names to the organic components such as organic matter (Gehmann, 1962; Lorente, 1990; Batten and Stead, 2005), palynodebris (Boulter & Riddick 1986; Van der Zwan, 1990; Boulter, 1994) and kerogen or palynomacerals (Tyson, 1995; Araujo *et al*., 1998; Whitaker, 1985; Oyede, 1992; Thomas *et al.*, 2015). Palynofacies was defined by Tyson (1995) as a body of sediment containing a distinctive assemblage of palynological organic matter thought to reflect a specific set of environmental conditions or to be associated with a characteristic range of hydrocarbon-generating potential. Batten and Stead (2005) defined palynofacies (palynological facies) generally to mean organic matter that is recovered from a rock or unconsolidated sediment by the standard palynological processing technique of digesting a sample in HCl and /or HF. Every sedimentary deposits containing organic matter have an associated palynofacies, which could be miospores (small spores and pollen grains), prasinophyte algal bodies, dinoflagellate cysts,

acritarch, foraminfera linings, structured fragments such as cuticles and wood tissues (phytoclasts or fragments of plants) and unstructured materials having an amorphous appearance. These organic matters are common, occurring in abundance in both continental and marine deposits. They are equally resistant to acid, high temperature and pressure, microbial decay and solutioning in water. Palynofacies analysis has several stratigraphic applications such as in chronostratigraphy, biostratigraphy and sequence stratigraphy. Its stratigrapic application is very useful on a local scale for fine correlation of reservoir units within oil-fields and to some extent on scale especially in areas or within successions which more conventional boistratigraphic markers are scarce or lacking (Batten and Stead, 2005). Palynofacies analysis is useful in the interpretation of the processes controlling deposition. It also provides basis for reconstruction of paleogeography, paleoecology, paleoenvironment and paleoclimate. Therefore this work is aimed at carrying out the palynofacies analyses of the ditch cuttings retrieved from Ida-4 well in order to establish the palynostratigraphic zonation, biochronology and paleoenvironment of deposition of the strata penetrated by the well. The studied well (IDA-4 well) is located in Ida field in the Niger delta. The coordinates that describe the locations of Ida-4 on the base map of Ida field is 69550 m North and 481875 m East (figure 1).

2. Literature Review

Niger delta lies between latitudes 4º and 6º N and longitudes 3º and 9º E in the Southern part of Nigeria (figure 2). Short and Stauble (1967) recognized three formations in the subsurface of the Niger delta. In ascending order, these formations are; the Akata, Agbada and Benin formations. The Akata Formation generally consists of open marine and prodelta dark grey shale with lenses of siltstone and sandstone. The Agbada Formation consists of cyclic coarsening-upward regressive sequences. The coarsening upward sequences are composed of shales, siltstones, and sandstones which include delta front and lower delta plain deposits (Weber, 1971). The Benin Formation comprises a succession of massive poorly indurated sandstones, thin shales, coals, and gravels of continental to upper delta plain origin. The three formations were deposited in continental, transitional and marine environments (Ola and Adewale, 2014). Doust and Omatsola, (1990) recognized depositional belts in the Niger Delta, These are: the Northern Delta, Greater Ughelli, Central Swamp, Coastal Swamp, and Offshore depobelts (figure 2).

They are distinguished by their age and most importantly their location. The most comprehensive contribution to the knowledge on the palynology of the Niger Delta was made by Germeraad *et al.* (1968). Their study was based on the palynomorph assemblages of the Tertiary sediments of three tropical areas: parts of South America, Asia and Africa (Nigeria). They established nine pantropical zones using quantitative base and top occurrence (numeric method) of diagnostic species such as *Echitricolporite spinosus, Crassoretitriletes vanradshoveni, Magnastrites howardi, Verrucatosporites usmensis, Monoporites annulatus* and *Proxapertites operculatus*. Evamy *et al*. (1978) established twenty nine informal palynological zones of the Niger delta using alphanumeric coding method which seems to form the background information for in-house zonal scheme of Shell Petroleum Development Company. Oboh *et al*. (1992) carried out palynological interpretation of the palaeoenvironments of Miocene strata of the well Igbomotoru-1, Niger delta. They used the lithology and the abundance or scarce occurrence of *Zonocostites ramonae* in the samples to interpret the environment of deposition to be largely transitional with marine influence.

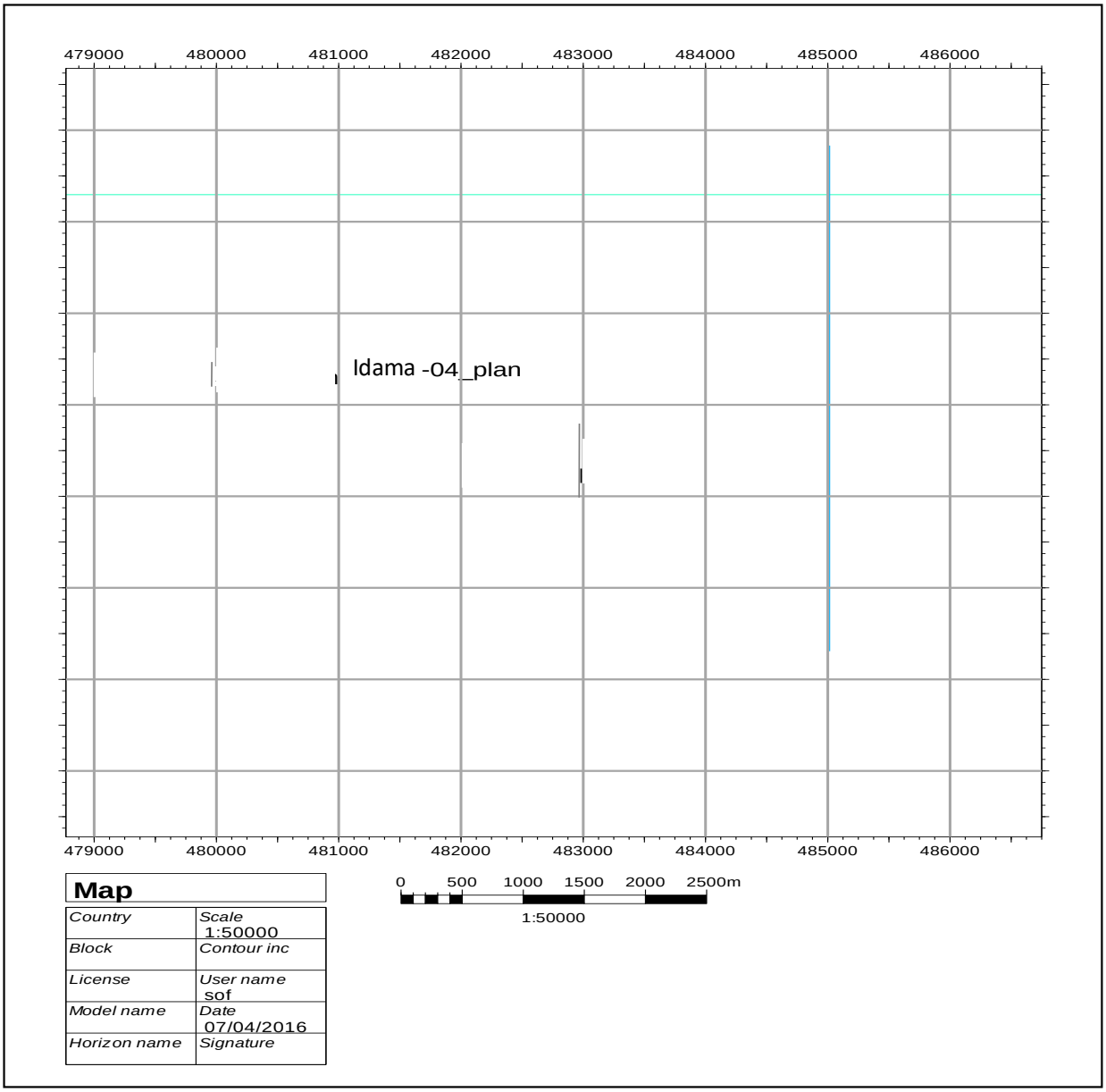

Figure 1: Base map of the study area and the locations of Ida-4 well in the Niger Delta.

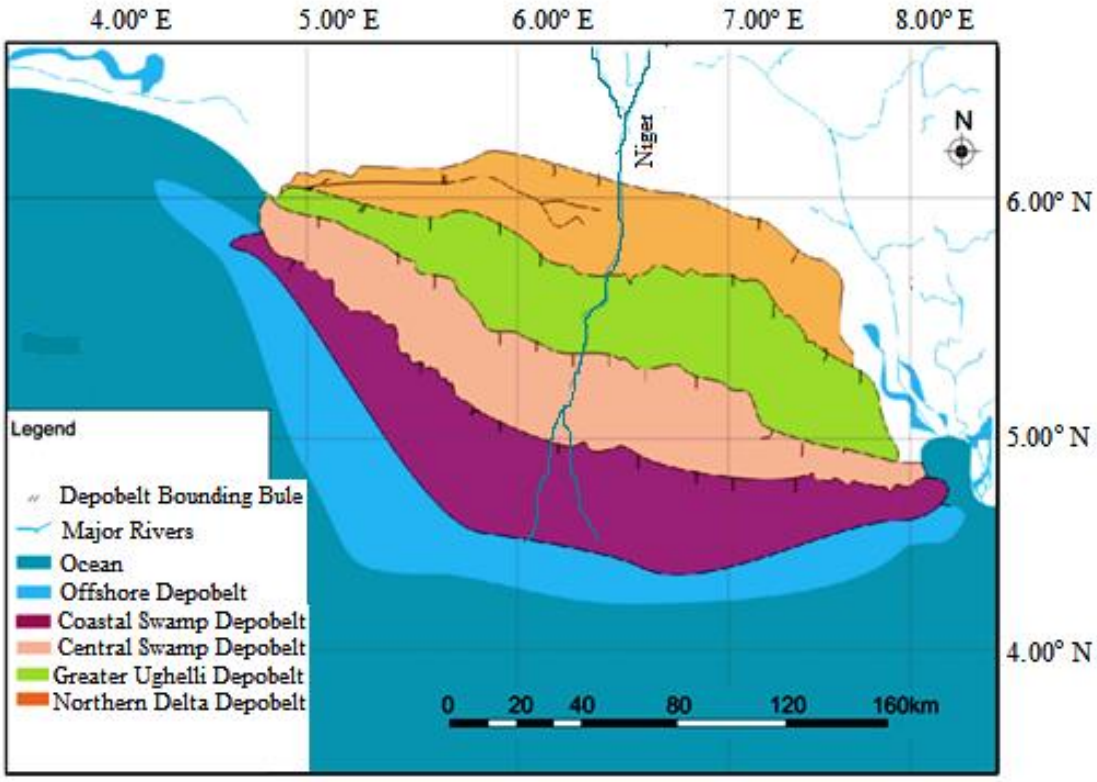

Figure 2: Depobelt map of the Niger Delta (modified after Okosun and Chukwuma-Orji, 2016)

3. Methodology

The materials used for this study include ditch cutting samples and wireline logs of Ida-4 well and they were provided by Chevron Nigeria Plc. All the laboratory facilities required were made available by Crystal Age Limited, Lagos where the laboratory analyses were carried out.

3.1 Lithologic description

Lithologic description of the stratigraphic intervals studied was done by physical observation and feeling of the samples between fingers. Fissile or platy samples indicate shale while samples with fine to coarse grained sizes indicate sandstone units. The description was enhanced by the Gamma-ray log since high and low values of Gamma log signify shale and sandstone lithologies, respectively (Adegoke, 2002; Olayiwola and Bamford 2016).

3.2 Samples preparation for organic matter recovery

The standard acid method of sample preparation for organic matter recovery was followed. Fifty ditch cutting samples from Ida-4 well within the interval of 2152 – 3523 m were analyzed. Fifteen grammas of each sample were treated with 10% HCl under a fume cupboard for the complete removal of carbonates that may be present in the samples. This was followed by complete neutralization with distilled water before the next procedure. Then 40% HF was added to the sample which was placed on a shaker for 24 hours to speed up the reaction rate and to ensure a complete dissolution of the silicates that may be present in the samples and for the particles to settle down. Thereafter, the HF was carefully decanted, then followed by complete neutralisation with distilled water in order to remove fluoro-silicate compounds usually formed from the reaction with HF. Sieving and separation were performed using Brason Sonifier 250 to filter away the remaining inorganic matter (silicates, clay, and mud) and heavy minerals to recover organic matters. Brason Sonifier is an electric device used with the aid of 5 micron sieve and it operates in a sonic vibration

to filter out inorganic matter and heavy minerals. The sieved residue was given controlled oxidation using concentrated nitric acid (HNO_3). The level of oxidation required by each sample was closely monitored under a palynological microscope.

For palynomacerals recovery, the same procedure for sample preparation for palynomorphs recovery was followed, except that the oxidation process with HNO_3 was omitted in order not to bleach the palyno debris. The recovered organic matters were uniformly spotted on arranged cover slips of 22/32 mm and were then allowed to dry for mounting. The mounting medium used for permanent mounting of cover slip onto glass slide was Loctite (Impruv) and was dried with natural sunlight for 5 minutes. The slides were then stained with safranin-O in order to enhance the study of dinoflagellete cysts.

Both palynology and palynomaceral slides were examined under the Olympus Binocular light transmitted microscope. The palynomaceral slides were subjected to quantitative analysis of different types of palynomacerals (type 1, 2, 3, and 4) as well as structureless organic matter (SOM). Identification of palynomorph and palynomacerals were done through the use of palynological albums and the published works of previous researchers (Germeeraad *et al*., 1968; Ajaegwu *et al*., 2012; Bankole, 2010; Durugbo and Aroyewun, 2012; Ige, 2009; Ige *et al*., 2011; Ola and Adewale, 2014; Oyede, 1992 and Thomas *et al*., 2015).

4. Results and Discussion

4.1 Lithology

The lithology of the studied interval consists of alternating shale/mudstone and sandstone unites with few intercalations of argillaceous sandstone (sandy shale and siltstone) units (figure 3). This suggests that the studied interval belongs to Agbada Formation. The shale/mudstones are mostly grey to brownish grey in colour, moderately hard to hard, platy to flaggy in appearance. The sandstones are predominantly milky white to smoky, coarse to fine grained, angular to subangular to rounded, and poorly to well sorted in texture.

4.2 Palynology

The results of palynological analysis are presented in palynomorph and palynomacerals distribution charts of Ida 4 well (figure 3). The chart presents the different palynomorph taxa and types of palynomacerals encountered at the different studied depth intervals. Palynological analysis of the slides of Ida 4 well yielded significant number of pollen and spores with low to moderate diversity. Pollen and spores were dominant. Photomicrographs of some of the recovered forms are illustrated in plate 1.

The spores recorded include the species of *Laevigatosporites* sp, *Verrucatosprites* sp, *Aletisporites* sp, *Cyperaceaepollis* sp, *Lycopodium* sp, *Selaginella myosorus, Pteris* sp, *Stereiosporites, Crassoretitriletes vanraadshoveni, Acostichum aureum* and *Magnastriatites howardi.*

The pollen species recovered are: *Zonocostites ramonae, Monoporites annulatus, Racemonocolpites hians, Retistephanocolpites gracilis, Praedapollis flexibilis, Striatricolpites catatumbus, Retibrevitricolporites protudens, Pachydermites diederixi, Psilatricoloporites crasssus, Retitricolporites irregularis, Fenestrites spinosus, Peregrinipollis nigericus, Gemamonocolpites* sp, *Multiareolites formosus, Verrutricolporites rotundiporus, Nummulipollis neogericus, Canthium* sp, *Coryius* sp, *Psilatricolporites* sp, *Elaeis guineensis, Alnipollinites verus, Podocarpidites* sp and *Retitricolporites* sp.

The algal cysts present are *Botryococcus brannii and* no dinoflagellate cyst was recovered.

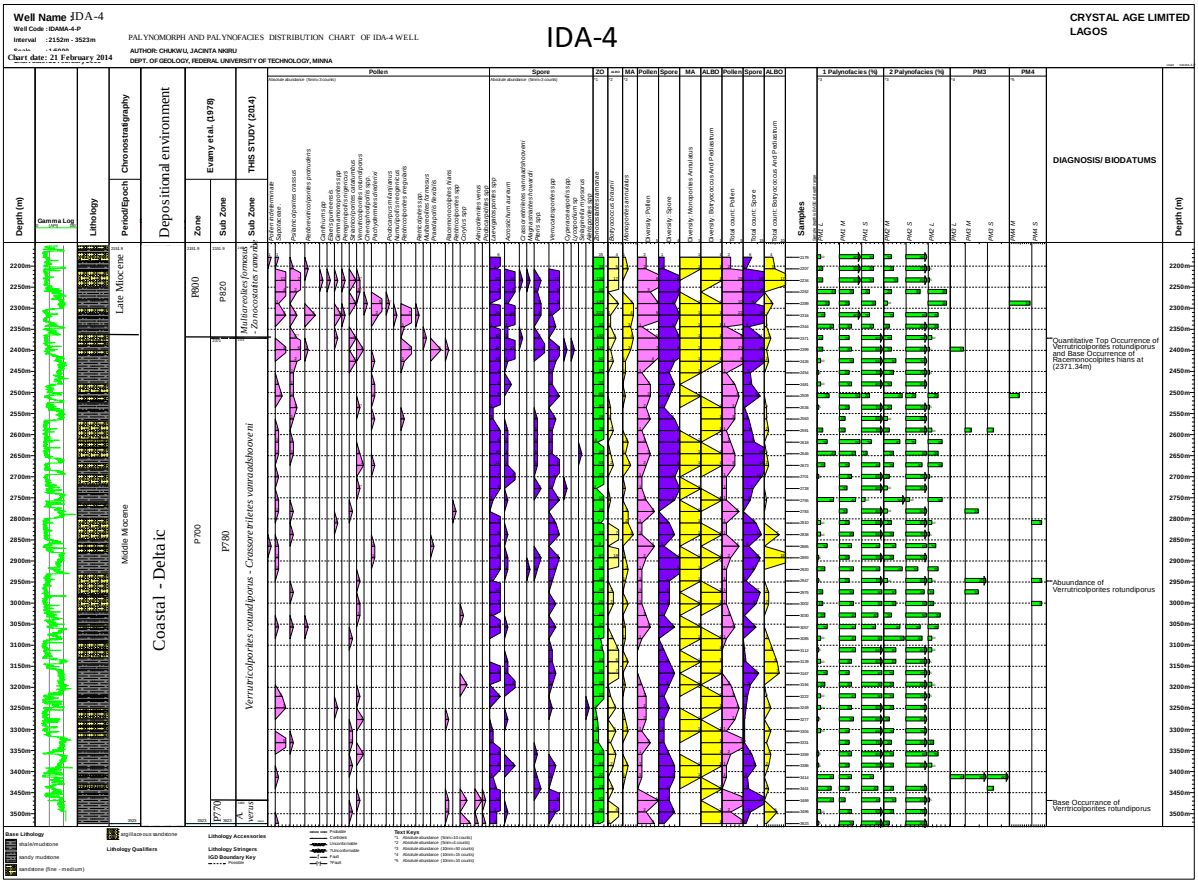

Figure 3: Palynomorph and palynofacies distribution chart of Idama-4 well

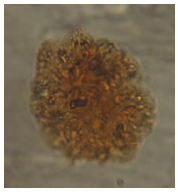

Botryococcus braunii

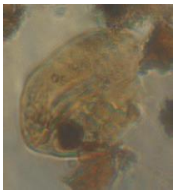

Gemmamonoporites sp

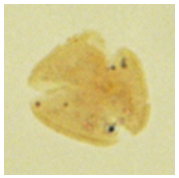

Retitricolporites sp

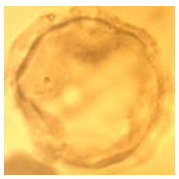

Monoporites annlatus

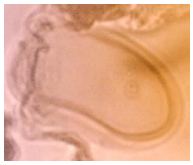

Cyperaceaepollis sp

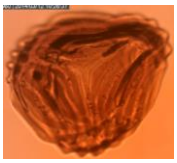

Magnasriatites howardii

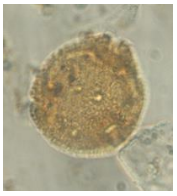

Retibrevitricolporites protrudens

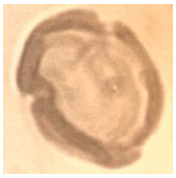

Zonocostites ramonae

Acrostichum aureum

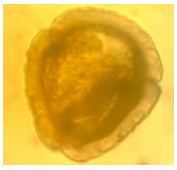

Psilatricolporites crassus

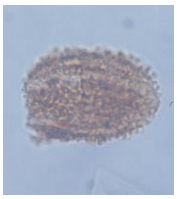

Racemonocolpites hians

Mutiareolites formosus

Laevigatosporites sp

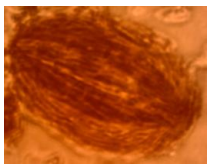

Striaticolpites catatumbus

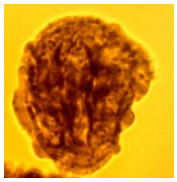

Peregrinipollis nigericus

Numulipollis neogenicus

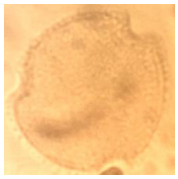

Canthium spp

Crassoretitriletes vanraadshooveni

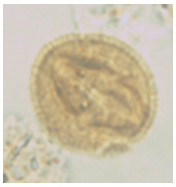

Verrutricolporites rotundiporus

Plate 1: Palynomorphs recovered from the studied wells (x400)

4.3 Palynomacerals

The palynomacerals analysis yielded abundant records of palynomercerals 1 and 2, few occurrences of palynomacerals 3 and 4 and no record of (SOM) structureless organic matter (plate 2, figure 3).

4.3.1 Palynomaceral 1 (PM1)

In this study, the observed palynomaceral 1 appeared orange-brown to dark-brown in colour, opaque, irregular in shape, structureless and varies in preservation (plate 2). Oyede (1992) described Palynomaceral 1 as particulate organic matter (Alginite) that is orange-brown to dark-brown in colour, dense in appearance, irregular in shape, structureless and varies in preservation. It is heterogeneous and of higher plant in origin and some are products of exudation processes such as the gelification of plant debris in the sediments. Palynomaceral 1 includes small, medium and large sizes of flora debris, humic gel-like substances and resinous cortex irregularly shaped materials (Oyede, 1992 and Thomas *et al.*, 2015).

4.3.2 Palynomaceral 2 (PM 2)

The PM 2 observed in this study is irregular in shape, brown-orange in colour, and platy in structure (plate 2). According to Oyede, 1992, palynomaceral 2 (Exinites) is usually brown–orange colour, structured but irregular in shape. It encompasses platy like structured plant materials (leaves, stems or small rootlet

debris), algae debris and a few amounts of humic gels and resinous substances. It is more buoyant than palynomaceral 1 because of its thinner lath-shaped character.

4.3.3 Palynomaceral 3 (PM 3)

The PM 3 observed in this study, generally is translucent and contained stomata, pale to brown in colour and is irregular in shape (plate 2). Oyede, 1992 stated that PM 3 (Vitrinite) is pale, relatively thin and irregularly shaped and occasionally contains stomata. Also, it includes structured plant material, mainly of cuticular origin and degraded aqueous plant material. It is more buoyant than palynomaceral 2 (Thomas *et al.*, 2015).

4.3.4 Palynomaceral 4 (PM 4)

The observed PM 4 in this study varies from black to dark brown in colour, with blade or needle like shapes (plate 2). Oyede (1992) described PM 4 (Inertnite) as being black to charcoal black in colour. Also, it is equidimensional, blade or needle shaped material. It is uniformly opaque and structureless, but may occasionally show cellular structure. The components of this palynomaceral are of different origins and they include compressed humic gels, charcoal and geothermally fusinized material. Blade-shaped palynomaceral 4 is extremely buoyant and resistant to degradation. Thus, they are often transported over long distances (Oyede, 1992 and Thomas *et al.*, 2015). Concentration of PM-4 characterizes high energy environment.

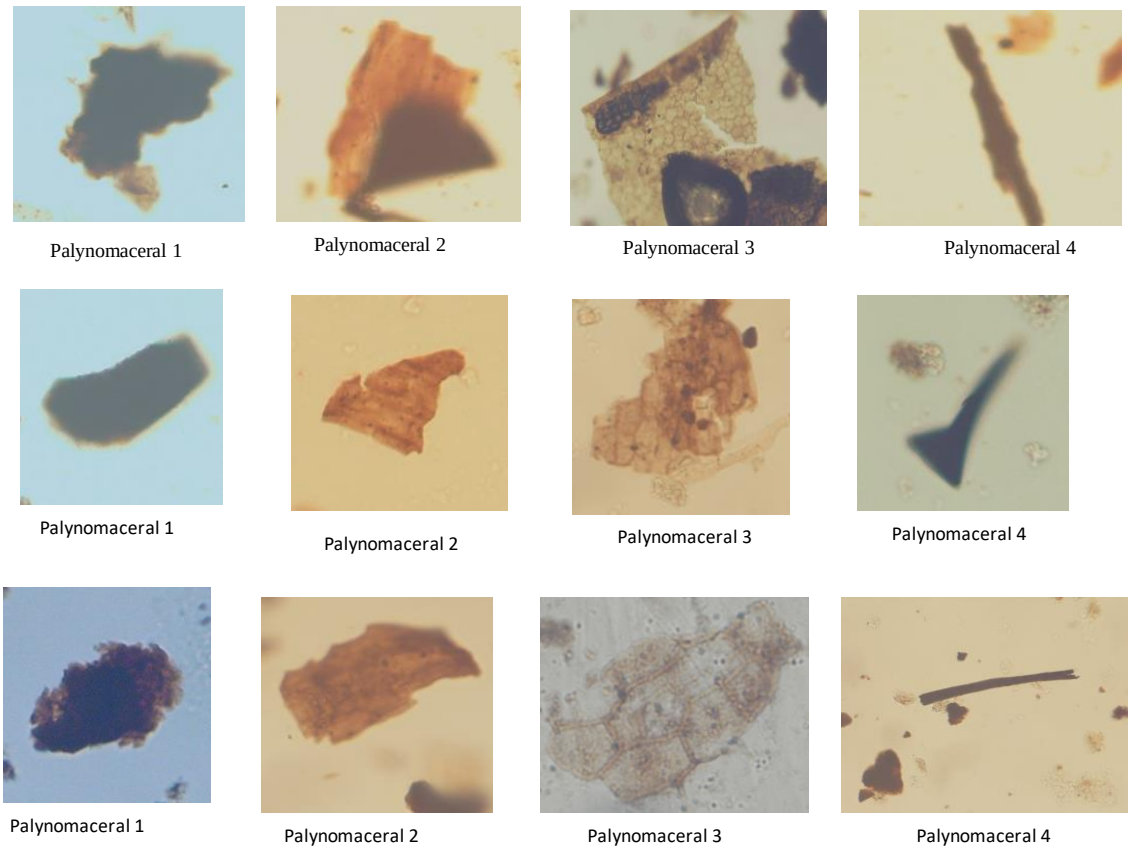

Plate 2: Types of palynomacerals recovered (x400).

4.4 Palynostratigraphic zonations and biochronology

The palynostratigraphic zones proposed in this study were based on the international stratigraphic guide - an abridged version of Murphy and Salvador (1999). The works of Germeraad *et al.*, (1968); Evamy *et al.*,

(1978); Ige, (2009); Oboh *et al*. (1992), Bankole, (2010); Aturamu & Ojo, (2015) and Olayiwola, & Bamford, (2016) were consulted. Age diagnostic marker species were used to determine the age of the studied intervals in the well. Three biozones were proposed in the studied wells: *Multiareolites formosus – Zonocostatites ramonae, Verrutricolporites rotundiporus - Crassoretitriletes vanraadshoveni* and *Ainipollinite verus* zones.

i. Multiareolites formosus – Zonocostatites ramonae Zone (Interval zone)

Stratigraphic interval: 2179 – 2371 m

Definition: The top of the zone is defined by the first downhole occurrence (FDO) of *Zonocostatites ramonae* at 2179 m while the base is marked by the last downhole occurrence (LDO) of *Multiareolites formosus* and *Crassoretitriletes vanraadshoveni* at 2371 m.

Characteristics: The assemblages of palynomorphs taxa that characterize this zone include *Zonocostatites ramonae, Crassoretitriletes vanraadshoveni*, *Nummulipollis neogericus, Multiareolites formosus* and *Retibrevitricolporites protrudens.* Other taxa occurring within the zone are sapotacea, *Psilatricoloporites crasssus, Peregrinipollis nigericus, Laevigatosporites* sp, *Verrucatosprites* sp, *Aletisporites* sp, *Pteris* sp, *Acostichum aureum* and *Magnastriatites howardi*.

Age: The zone is dated late Miocene because of the presence of *Crassoretitriletes vanraadshoveni, Multiareolites formosus* and *Peregrinipollis nigericus.*

Remark: The zone is equivalent to P800 zone and P820 subzone of Evamy *et al*, (1978). The zone is marked by very rich recovery of *Zonocostatites ramonae, Monoporites annulatus, Botryococcus braunii* and *Laevigatosporites* sp. There is single occurrence of *Podocarpus milanjianus* within the zone. The base occurrence of this species marks late Miocene – early Pliocene boundary (Morley, 1997). Its occurrence within the zone could have resulted from caving in and mixing of rock cuttings during drilling. Also occurring within the zone is pollen indeterminate which could probably be reworked specimens because it is not well preserved. The single occurrence of *Proxapertites cursus* an Early Eocene to Early Miocene species at 2371 m could have resulted from reworking of older sediments into younger sediments.

ii. Verrutricolporites rotundiporus - Crassoretitriletes vanraadshoveni Zone (Interval zone)

Stratigraphic interval: 2371 - 3469 m

Definition: The top of the zone is defined by the last downhole occurrence (LDO) of *Crassoretitriletes vanraadshoveni*, *Multiareolites formosus* and base regular occurrence of *Gemamonocolpites* sp at 2371 m while the base is marked by the last downhole occurrence of *Verrutricolporites rotundiporus* at 3469 m.

Characteristics: The zone is characterized by the presence and lowermost documented occurrence of *Racemonocolpites hians, Retibrevitricolporites protudens, Pachydermites diederixi, Psilatricoloporites crasssus, Gemamonocolpites* sp, *Multiareolites formosus, Verrutricolporites rotundiporus* and sapotaceae within the zone. The occurrence of *Zonocostites ramonae* and *Monoporites annulatus* are rich within this zone.

Age: The zone is dated middle Miocene because taxa such as *Verrutricolporites rotundiporus, Retibrevitricolporites protudens,* and *Racemonocolpites hians* are diagnostic of middle Miocene.

Remark: The is equivalent to P700 zone and P780 subzone of Evamy *et al*, (1978)

iii. Ainipollinite verus Zone (Taxon-range zone)

Stratigraphic interval: 3469 - 3523 m

Definition: The top and base of the zone is defined by the first and last downhole occurrence of *Ainipollinite verus* at the depth of 3469 and 3523 m respectively. The first and last downhole occurrence of *Podocarpidites* sp also marks the top and base of the zone.

Characteristics: The zone is characterized by the lowermost documented occurrence of *Striatricolporites catatumbus, Laevigatosporites* sp, sapotaceae, *Zonocostates ramonae, Acrostichum aureum, Monoporites annulatus* and *Racemonocolpites hians*. *Retibrevitricolporites protrudens*- a species with an age range of Oligocene to Pliocene has its LOD within the zone.

Age: The zone is dated middle Miocene. The stratigraphic position of the zone and the presence of the above mentioned taxa that defined and characterized the zone aided its age assignment.
Remark: The zone is equivalent to P700 zone and P770 subzone of Evamy *et al*, (1978).

4.5 Correlation of the established palynostratigraphic zones with the Niger delta Cenozoic chart
The established zones of this study and the P zones equivalent of Evamy *et al*., (1978) are correlated with the Niger delta Cenozoic chart (figure 4). The correlation reveals that the studied well is located in the coastal swamp depobelt. It also confirms the assigned age of the studied interval to be middle to late Miocene.

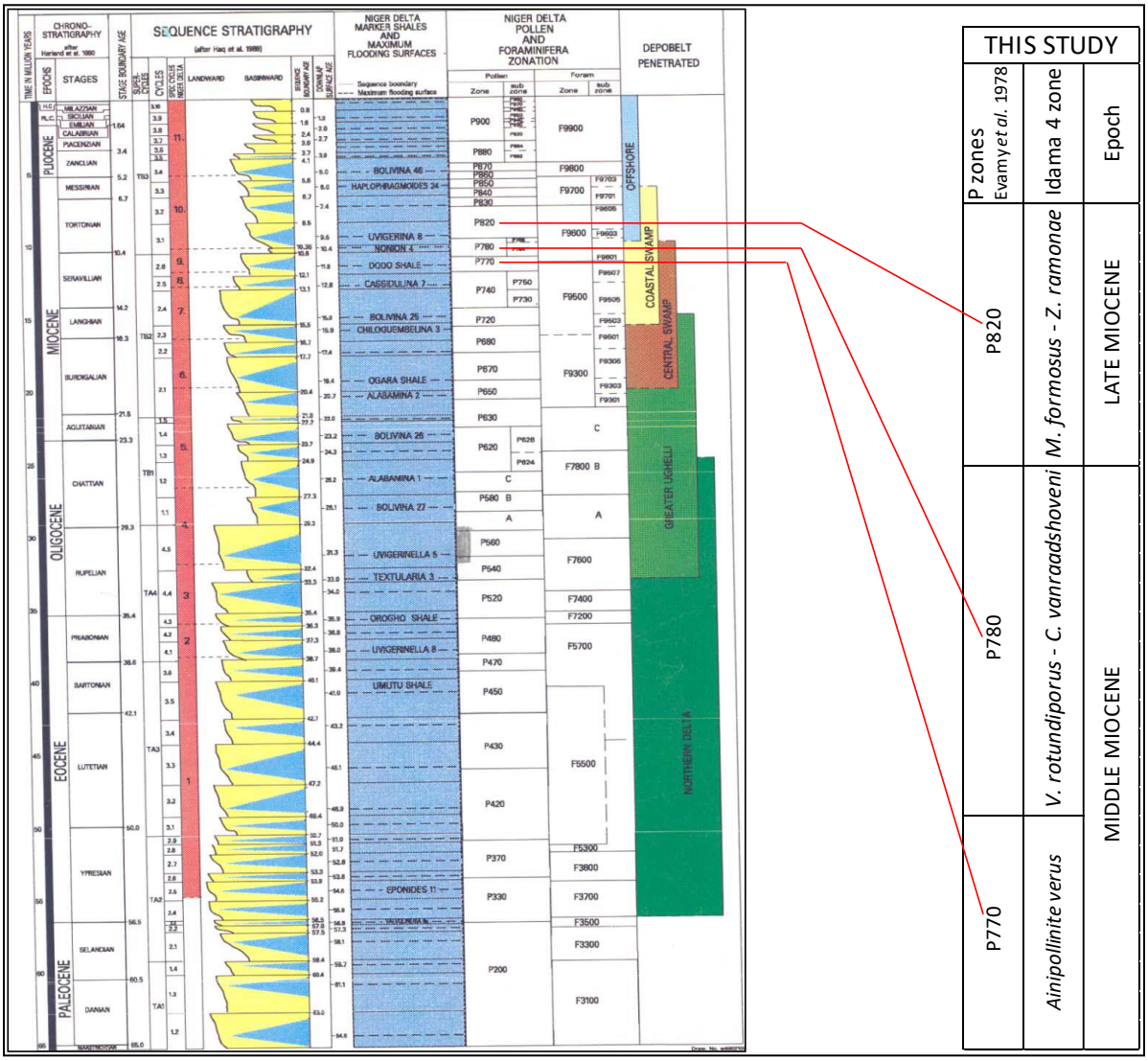

Figure 4: palynostratigraphic zones correlation with the Niger delta Cenozoic chart

4.6 Paleoenvironment of deposition
This involves the periodic changes in the depositional environment over geologic time. Evaluation of paleoenvironment of deposition is essential because different depositional environment give rise to reservoirs with different qualities and characteristics such as porosity, permeability, heterogeneity and

architecture. Inference of the paleodepositional environments of the studied wells was made based on the following criteria:

i. The nature of organic matter (palynomercerals) recovered in the studied interval. The terrestrial/coastal and marine depositional environments have been distinguished to have distinctive and characteristic palynofacies (Oyede, 1992 and Thomas *et al*., 2015). The terrestrial/coastal environments are characterized by poorly sorted palynomacerals 1 and 2, absence of dinocysts and common to abundant occurrence of fungal spores while marine environment is characterized by a good sorting of organic matter predominantly small to medium, common to abundant palynomacerals 1 and 2, some needle-shaped to lath-shaped palynomaceral 4 and presence of dinocysts and or foraminifera linings (Oyede, 1992).

ii. Association of environmentally restricted diagnostic species such as *Zonocostites ramonae, Monoporites annulatus, Pachydermites diederixi, Psilatricoloporites crasssus, Laevigatosporites* sp and *Botryococcus braunii.*

Based on the above mentioned criteria, lower delta plain to delta front and prodelta (subaerial delta to subaqueous delta plains) environment within coastal – deltaic environment of deposition have been inferred for the sediments encountered in the analyzed intervals of Idama 4 well (table 1 and figure 5).

The intervals; 2179 – 2800 m, in Idama 4 well was delineated to have been deposited in the lower delta plain environment. The lower delta plain is equivalent to fore shore and fluvio-marine environment (figure 5). The reasons for this deduction are:

i. The intervals are characterized by high representation of mangrove, freshwater swamp and rainforest swamp taxa, freshwater algae, savana and montane taxa such as *Zonocostites ramonae, Monoporites annulatus, Striatricolpites catatumbus, Retibrevitricolporites protudens, Pachydermites diederixi, Psilatricoloporites crasssus, Verrutricolporites rotundiporus, Botryococcus braunii, Acrostichum aureum, Pachydermites diederixi* and *Laevigatosporites sp.*

ii. The abundant records of palynomacerals 1 and 2 indicate coastal deltaic environment of deposition with influx of fresh water from the moderate quantities of *Botryococcus braunii*, and *Laevigatosporites* sp recorded within the interval in Idama 4 well.

iii. Aggradational, progradational and retrogradational log motifs characterize the sands (intercalated by shales) in the interval suggest their deposition as channel / bar complexes in a delta plain – delta front setting. Lithologically, the sands are milky white, very fine to medium – grained, occasionally coarse to very coarse –grained/ granule -sized, poorly to well sorted and sub-angular to sub-rounded. The shales are reddish brown to grey, silty, platy and moderately soft to moderately hard. These criteria indicate deposition in lower deltaic plain environments.

Table 4.1: Environment of Deposition in Idama 4

Idama 4 well intervals (m)	Inferred Depositional environment
2179 – 2800	Subaerial delta (lower delta plain/fore shore)
2800 – 2885	Subaqueous delta (delta front/lower shore face) plain
2885 – 3523	Subaqueous delta (delta front to prodelta) plain

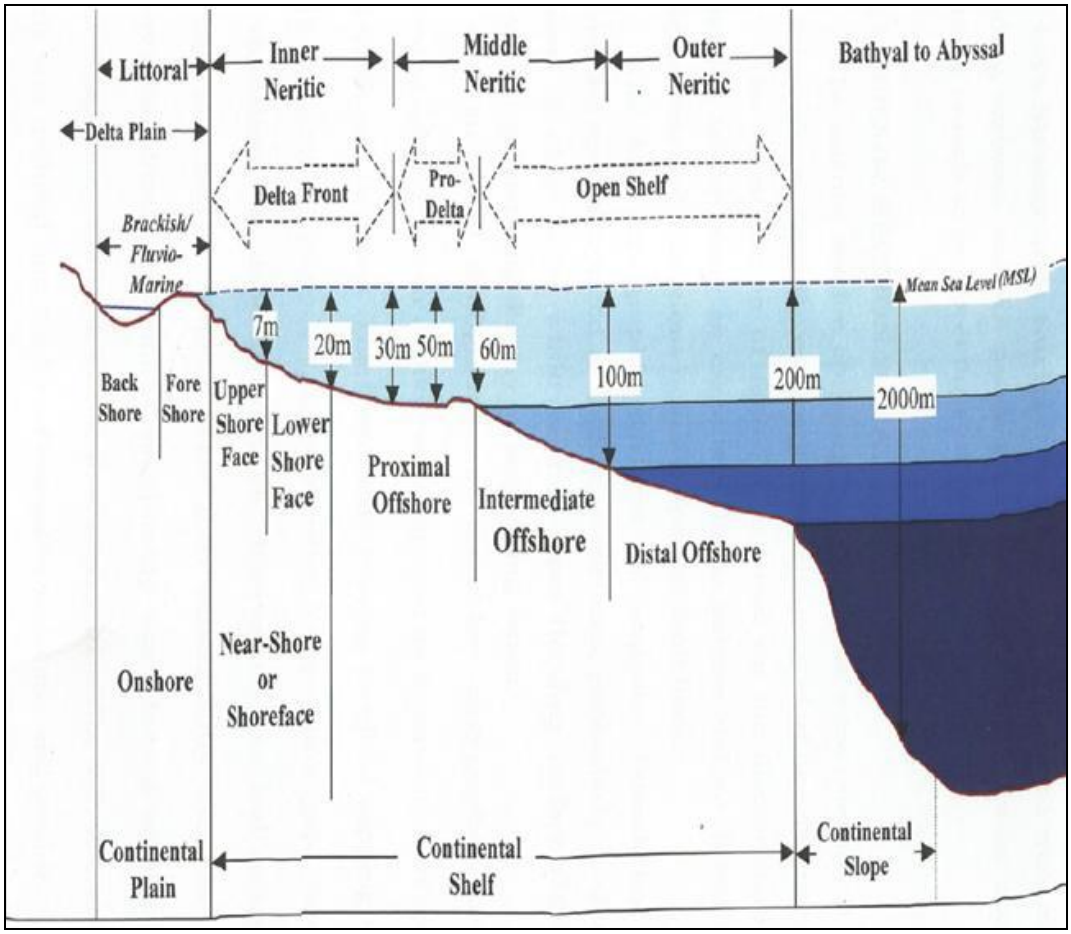

Figure 5: Depositional environments and bathymetric ranges used in paleoenviromental interpretation (Ijomah *et al*., 2016)

Similarly, the interval: 2800 – 2885 m well was delineated to have been deposited in delta front (inner neritic) environment of deposition. The criteria for this deduction are:

i. The intervals are characterized by increased representation of montane taxa such as *Monoporite annulatus*, reduced occurrences of mangrove, freshwater swamp and rainforest swamp taxa compared to the above intervals.
ii. The palynomacerals 1 and 2 that occur are more of large and medium sizes than the small size.
iii. The sands and shale intercalations in this interval are characterized by blocky / aggradational log motifs (slightly serrate cylinder on funnel – shaped log character); suggesting their deposition as channels / channel fills in a delta front setting.

The lowermost segment: 2885 – 3523 m of Idama 4 well is also inferred to have been deposited in delta front to prodelta environment of deposition. The reasons for this inference are:

i. The intervals are characterized by moderate representation of mangrove, freshwater swamp and rainforest swamp taxa *Zonocostites ramonae, Monoporites annulatus, Striatricolpites catatumbus, Retibrevitricolporites protudens, Pachydermites diederixi, Psilatricoloporites crasssus, Verrutricolporites rotundiporus, Botryococcus braunii, Acrostichum aureum, Laevigatosporites sp* and *Pachydermites diederixi*, rare to non representation of savanna and montane taxa suggesting subaqueous delta environment.
ii. They are characterized by moderate to good sorting of palynomacerals 1 and 2, predominantly common to abundant small to medium sizes.

iii. The lithology is mostly shaly intercalated with sandstone units. The sand units exhibited multiserrate funnel, cylinder/ subtle bell-shaped GR log profiles interpreted as subaqeous mouth bars and distributary channel deposits indicates prograding shoreline.

5. Conclusion

Palynofacies were carried out on the strata penetrated by Idama 4 well using the ditch cuttings and gamma ray log provided by Chevron Nigeria Limited. Fifty ditch cutting samples within the interval of 2152 – 3523 m, in Idama 4 well were analyzed. The analysis yielded low to abundant recovery of pollen and spores, small to large sizes of palynomacerals 1 and 2, few occurrences of palynomacerals 3 and 4. The lithology showed alternation of shale and sandstone units with few intercalations of argillaceous units, indicating Agbada Formation. The alternation of shale and sandstone units forms good targets in petroleum exploration because they act as seal and reservoir rock units. The studied intervals were dated middle Miocene to late Miocene based on the recovered age diagnostic marker species such as *Multiareolites formosus, Verrutricolporites rotundiporus, Crassoretitriletes vanraadshoveni* and *Racemonocolpites hians.* Three palynostratigraphic zones were established in the three wells using the international stratigraphic guide for establishment of biozones. *Multiareolites formosus – Zonocostatites ramonae*, *Verrutricolporites rotundiporus - Crassoretitriletes vanraadshoveni* and *Ainipollinite verus* zones were established. The three zones proposed are equivalent to P770, P780 and P820 of Evamy *et al*., (1978). These were correlated to the Niger delta Chronostratigraphic chart. The correlation shows that the age of the studied interval of the well is middle to late Miocene and falls in the coastal swamp depobelt of the Niger delta. The proposed palynostratigraphic zones of this study could contribute to the harmonization of Niger delta floral biozonation scheme. Coastal-deltaic (lower delta plain to prodelta) environments of deposition have been inferred for the studied interval based on the lithology and the palynofacies association.

References

Adegoke, O.S. (2002) High resolution biostratigraphy, sequence stratigraphy and 3-D modeling. Indispensable tools for E & P activities in the New Millenium, *Nigerian Association of Petroleum Exploration*, Vol.16, 46-65.

Ajaegwu, N. E., Odoh, B. I., Akpunonu, E. O., Obiadi, I. I. and Anakwuba, E.K. (2012). Late Miocene to Early Pliocene Palynostratigraphy and Palaeoenvironments of ANE-1 Well, Eastern Niger Delta, *Nigeria Journal of Mining and Geology*, Vol. 48, 31–43.

Araujo, C. V., Condé, V. C., Botelho-Neto, J., Pedrão, E., and Conceição, J. C. J. (1998). Palynofacies in a sequence stratigraphy context, an example of an upper Aptian section from Almada Basin, Brazil. *The American Association of Petroleum Geologists, International Conference and Exhibition, abstracts*, Vol. 82, 1886-1887.

Aturamu, A. O. and Ojo, A. O. (2015). Integrated biostratigraphic analysis of the Agbada Formation (Nep-1 Well) offshore, Eastern Niger-Delta Basin, Nigeria, *Australian Journal of Biology and Environment Research*, Vol. 2, 1 - 14.

Bankole, S. I. (2010). Palynology and stratigraphy of three deep wells in the Neogene Agbada Formation, Niger Delta, Nigeria. Implications for petroleum exploration and paleoecology, PhD thesis, der Technischen Universität Berlin, 1-190

Batten, D. J. and Stead, D. T. (2005). Palynofacies analysis and its stratigraphic application. In: E. A. M. Koutsoukos (Ed.), *Applied stratigraphy*, Netherland, Springer, 203-226.

Boulter, M. C. (1994). An approach to a standard terminology for palynodebris. In: A. Traverse (Ed.), *Sedimentation of organic particles* Cambridge University Press, 199-216.

Boulter, M. C. and Riddick, A. (1986). Classification and analysis of palynodebris from the Palaeocene sediments of the Forties Field. *Sedimentology*, Vol. 33, 871-886.

Combaz, A. (1964). Les palynofacies. *Revue de Micropaléontologie*, Vol. **7**, 205-218.

Doust, H. and Omatsola, E. (1990). Niger Delta divergent/passive margin basins, *American Association of Petroleum Geologists Memoir*, Vol. 48, 201-238.

Durugbo, E. U. and Aroyewun, R. F. (2012). Palynology and Paleoenvironments of the Upper Araromi Formation, Dahomey Basin, Nigeria. *Asian Journal of Earth Sciences*, Vol. 5, 50-62.

Evamy, B. D., Haremboure, J., Karmerling, P., Knaap, W. A., Molloy, F. A. and Rowlands, P. H. (1978). Hydrocarbon habitat of the Tertiary Niger Delta. *American Association of Petroleum Geologists Bulletin*, Vol. 62, 1-39.

Gehmann Jr., H. M., (1962). Organic matter in limestones. *Geochimica et Cosmochimica Acta*, Vol. 26**,** 885-897.

Germeraad J. J., Hopping, G. A. and Muller, J. (1968). Palynology of Tertiary sediments from tropical areas. *Review of Paleobotany and Palynology*, Vol. 6, 189-348.

Ige, O. E. (2009). A Late Tertiary Pollen record from Niger Delta, Nigeria, *International Journal of Botany,* Vol. 5, 203-215.

Ige, O. E., Datta, K., Sahai, K. and Rawat, K. K. (2011). Palynological Studies of Sediments from North Chioma-3 Well, Niger Delta and its Palaeoenvironmental Interpretations. *American Journal of Applied Sciences*, Vol. 8, 1249-1257.

Ijomah, A. K., Amajor, L. C. and Ugwueze, C. (2016). Sequence Stratigraphy and Hydrocarbon Analysis of Coastal Swamp Depobelt, Niger Delta, Nigeria. *Journal of Scientific and Engineering Research,* Vol. 3, 285 – 294.

Lorente, M. A. (1990). Textural characteristics of organic matter in several subenvironments of Orinoco Upper delta. *Geologie en Mijnbouw*, Vol. 69, 263-278.

Morley, R. J. (1997). Offshore Niger Delta palynological zonation, prepared for the Niger Delta Stratigraphic Commission, *Palynova*, Vol. 1, 1 – 6.

Murphy, M. A. and Salvador, A. (eds.) (1999) International Stratigraphic Guide - An abridged version, International Subcommission on Stratigraphic Classification of IUGS, International Commission on Stratigraphy, *Special Episodes*, Vol. 22, pp. 255 – 272.

Oboh, F. E., Salami M. B. and Chapman, J. L. (1992). Palynological interpretation of the palaeoenvironments of Miocene strata of the well Igbomotoru-1, Niger delta. *Journal of Micropalaeontology,* Vol. 11, 1-6.

Ola, P. S., and Adewale, B. K. (2014) Palynostratigraphy and Paleoclimate of the sequences penetrated by Meren 31 side tract-2 well, offshore Niger delta. International Journal of Geosciences, Vol. 5, 1206 – 1218.

Olayiwola, M. A. and Bamford, M. K. (2016). Petroleum of the Deep: Palynological proxies for palaeoenvironment of deep offshore upper Miocene-Pliocene sediments from Niger Delta, Nigeria *Palaeontologia Africana*, Vol. 50, 31–47.

Oyede, A. C. (1992). Palynofacies in deltaic stratigraphy. *Nigerian Association of Petroleum Explorationist Bulletin.* Vol. 7, 10 – 16.

Short, K. C. and Stauble, A. J. (1967). Outline of the geology of Niger Delta, *American Association of Petroleum Geologists Bulletin*, Vol. 51, 761 - 779.

Thomas, M. L., Pocknall, D. T., Warney, S., Bentley, S. J. Sr., Droxler, A. W. and Nittrouer, C. A. (2015). Assessing palaeobathymetry and sedimentation rates using palynomarceral analysis: a study of modern sediments from the Gulf of Papua, offshore Papua New Guinea. *Palynology*, Vol. 0, 1 – 24.

Tyson, R. V. (1995). *Sedimentary Organic Matter: organic facies and palynofacies* London: Chapman & Hall, 600 - 615.

Van der Zwan, C. J. (1990). Palynostratigraphy and palynofacies reconstruction of the upper Jurassic to lowermost Cretaceous of the Draugen Field, offshore mid Norway. *Review of Palaeobotany and Palynology*, Vol. 62, 157-186.

Weber, K. J. (1971). Sedimentological aspects of oil fields in the Niger Delta, *Geologie en Mijnbouw*, Vol.50, 559 – 576.

Whitaker, M. F. (1985). Palynofacies analysis as applied to basin evaluation in the northern North Sea. *Shell Exploration Bulletin*, 217

INFLUENCE OF GEOLOGY AND HYDROGEOLOGICAL CONDITIONS ON THE PERFORMANCE OF A ROAD PAVEMENT BETWEEN SHANGO AND CHANCHAGA ALONG MINNA –LAMBATA ROAD, CENTRAL NIGERIA

[1]Waziri S.H[*].,[2]Okogbue C.O, [3]Okonlola, I.A. and [1]ABDULLAHI, I.N.
[1]Department of Geology, Federal University of Technology, P.M.B 65, Minna, Niger state
[2]Department of Geology, University of Nigeria, Nsukka
[3]Department of Chemistry and Geology, Al-Hakimah University Ilorin, Nigeria
* Corresponding author
salwaz1969@gmail.com **+2347035983684**

Abstract

The dual carriageway along Shango – Chanchaga, in Minna, Central Nigeria, has continued to experience failure at a particular section, opposite the Public Works (PW) LTD yard, Tungan-Goro). This section of the road, which, unlike others, does not response to frequent and routine maintenance, is underlain by schist that is deeply weathered. Evidence shows that the failure experienced by the road is attributed to the geological/hydrogeological conditions underlying the road. This is because the frequently failed portion of this road is constructed on a fractured and deeply weathered schist as a subgrade material with low bearing capacity. The segment of this road is at a depression associated with concentration of groundwater discharge. Storage in the groundwater has increased as a result of blockage in most of the seepages culminating in fast disintegration of the base course materials. The schist under this portion of the highway is weathered to the depth of more than 10 meters into clay minerals with resistivity values as low as 21 Ohm. The clay minerals absorb water and swell in the wet season and compact at the dry season. The percentage of groundwater variation ranges between 154% - 2400% indicating medium to very high percentage of variation of groundwater fluctuation. These clay minerals absorb water and swell at the raining season and dries in the dry period. The road needs to be properly designed and provided with good drainage that will reduce the ingress of water.

Keywords:hydrogeologic conditions, instability, weathering, sub-base material

1. Introduction

The Nigerian government spends billions of Naira on road construction and maintenance and yet most of these roads are not found in stable and good conditions most of the time. In Nigerian highway construction, a lot of importance is attached to testing of the aggregates that are necessary for a sound and durable pavement and in very few cases, the geologic materials that provides support for the highway.

When considering a suitable route for the highway, the geological setting and the groundwater condition of the area are some of the important factors to be considered. Studies have shown (Weinert, 1960; Farquhar,

1980; Okabue and Uma, 1988) that geological and hydrogeological conditions underlying a highway route are important factors in the effective performance of the road. Analysis of the impact of geology on the effectiveness of a portion of a highway in Minna is been made in this paper. A particular point opposite the Public Works Nig. Ldt yard (Tungan-Goro-Chanchaga) experiences frequent failures as seen in figure 1.

Figure1 A failed portion of the studied road

The topography of the Minna and environs is largely affected by the geology that comprises of schist, amphibolites, gneisses and granites which constitute part of the Basement Complex rocks of Nigeria. The granitic hills are massive undulating terrains that range from 380m-850m high above mean sea level. The study area is within the middle belt of Nigeria and record a mean rainfall of about 1,000mm annually. Rainfall begins in April, August/ September records the maximum rainfall and stops in October. The months of August and September records low temperatures of about 24^{o}C. High temperature is usually recorded during the months of February to March, at an average of 35^{0}C. The harmattan wind is experienced during December and January.

2. Literature Review

Research has shown that the stability of roads in tropical area is controlled by the geologic/ hydrogeologic, soil, climatic and drainage conditions among other factors (Clare and Beaven, 1962; Tanner, 1963; Gidigasu, 1974, 1983; *Okogbue C.O., 1988;*Okagbue and Uma, 1988). Deterioration of the materials that make up the base and sub-base and improper drainage that result to water having access to the pavement structure are among the causes attributed to road failure (Gidigasu, 1983). Base and sub-base materials disintegrate faster when water comes in to contact with it and areas that are not properly drained do not meet proper specifications on allowable plasticity and content of fines. Road failure could also result when inferior base and sub-base materials are used. Road failure also result when specifications for the pavement thickness is not followed. (Gidigasu, 1983) observed that breakdown of the road pavement increases when

water percolate during the rainy period and reduce the strength of the highway material and when moisture suction occur from when the shoulder material loses moisture during the dry season.

Geology and hydrogeological conditions are considered critical when other factors are met in road construction. (Clare and Beaven, 1962; Okogbue and Uma, 1988) have observed that the patterns of road effectiveness in West Africa are controlled by geology, topography, soil and drainage conditions. (Russan and Croney, 1961; Gidigasu, 1983; Okogbue and Uma 1988), have noted that depth to water table tends to be the most prevalent of the climatic, physiography and drainage factors that control road effectiveness.

3. Methodology

Road grade elevations: A geographical Positioning System (GPS) was used in taking the road grade elevations.

Well water level fluctuation: Static water levels were measured from four hand-dug wells located very close to the road during the peak of the dry (April) and rainy (September) seasons. A water meter was used in taking the measurements while a GPS was used in taking the ground elevation as well as the co-ordinates of the wells. The total depths of the wells were also measured.

Geophysical survey: Vertical electrical sounding (VES) also referred to as electrical resistivity sounding was employed during this study. Current was sent into the subsurface by means of two current electrodes (C_1 and C_2) and a second pair of electrode (P_1 and P_2) measured the drop in potential. The electrode spacing interval was constantly changed while maintaining a fixed location from the center of the electrode spread.

laboratory tests: Atterberg Limits tests were conducted on five samples collected from five trial pits along the portion of the studied road. The liquid limit (LL) and plastic limit (PL) were each determined with about 300 grams of soil samples passing 0.425mm sieve in accordance with BS 1377 (1990). The difference between LL and PL gave the plasticity index (PI). The cone penetration method as described by (Brain, 1983) was used. A graph of cone penetration versus moisture content was plotted both on a linear scale and a straight line graph obtained. The LL was taken as the moisture content at which the standard cone penetrated 20mm into the soil paste.

4. Results and Discussion

The geology of Minna area reveals that the schist has been intruded in places by the older granite (figure 2). The emplacement of the older granite has led to intense jointing and fracturing of the schist. The schist is fine grained, foliated and dips at about 28^0W. Most of the drainages cut the narrow valley and water moves from the hills to the valley during raining season. The schist is mostly exposed along these river channels (River Chancgaga). Drainage pattern is the trellis while the major river found along the road is the Chanchaga River which is a tributary of the Kaduna River.

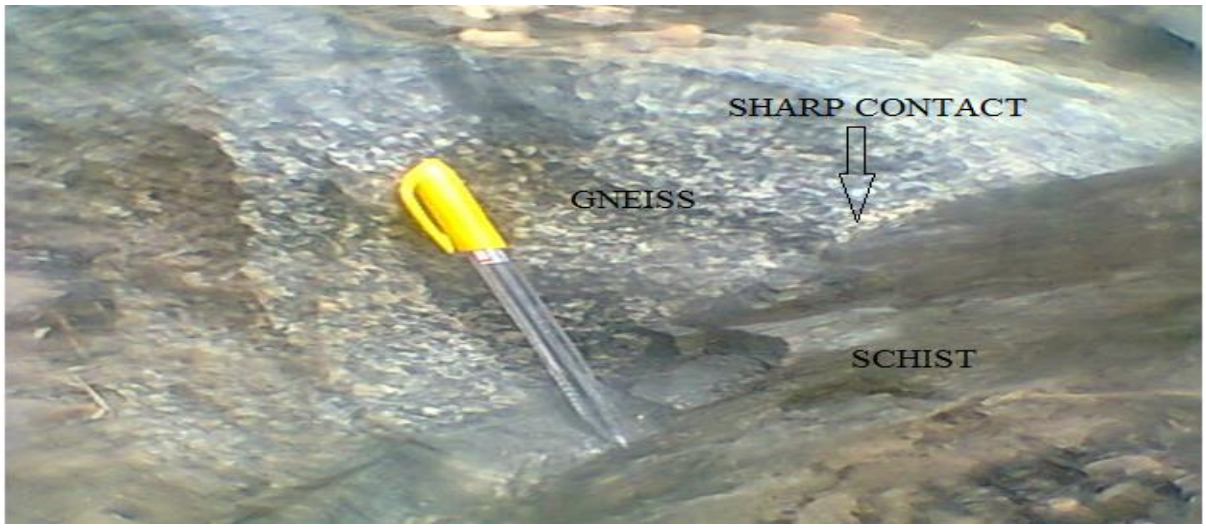

Figure 2: Schist intruded by granite gneiss in Minna area

The VES result is shown in figure 3, the groundwater fluctuation on table 1 while the Atterbege limits are presented on table 2.

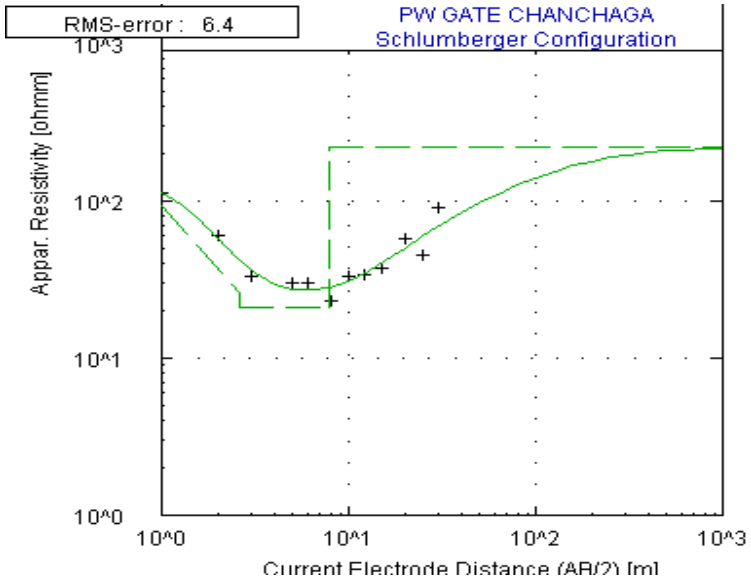

No	Res	Thick	Depth
1	146.6	0.7	0.7
2	26.0	1.9	2.6
3	21.2	5.2	7.8
4	219.2	-.-	-.-

Figure3: Subsurface geology of the problem area

Table 1: Groundwater fluctuation along Shango-Chanchaga Road

Location	Well depth (m)	SWL Dry Season A (m)	SWL Wet Season B (m)	Variation (A – B)	% of Variation	Rock Type	Lat.(N)	Long.(E)	Elev. amsl (m)
CHANCHAGA1	2.1m	1.5m	0.5m	0.4m	300	Schist	9^0 32' 15.6"	6^0 34' 46.3"	230
CHANCHAGA 11	5.4m	4.5m	1.5m	3m	346	Schist	9^0 32' 33.5"	6^0 34' 53.5"	202
CHANCHAGA111	5.5m	5.1m	1.7 m	3.4m	300	Schist	9^0 47'.2"	6^0 39.7"	241
SHANGO	8.2	5.0m	1.9	3.1m	263	Schist	9^0 34' 25.9"	6^0 34' 18.4"	256

Table 2 Classification of the soils based on Atterberge Limits along Shango-Chanchaga Road

ATTERBEG LIMITS				*Plasticity adjective*
LL %	PL	PI	*USSC classification*	
33	4.0	29	CL	High
41	3.0	38	CH	High
39	3.5	35.5	CH	High
48	4	44	CH	Very high
38.5	15.4	23.1	CL	High

The geology as revealed affects the nature and ground in the area. The Basement complex rocks at their time of formation were none porous and highly impermeable. The rocks however, have been affected by tectonic activities that lead to the faulting and fracturing of the rocks (Gandu*et al*., 1986; Olayinka, 1992; Obaje, 2009) resulting in secondary porosity. The fractures provided access to rain water into the schist that has \resulted in weathering of the schist thereby making the overburden thick. The resistivity values recorded from this segment of the road is low (between 21and 26 Ohm) and the depth of weathering beyond ten meters (figure 3). The presence of water has further enhanced chemical weathering of the primary minerals to secondary minerals that are mostly clayey. The clayey weathered products of the schist absorb rain water but do not allow downward movement of the water, the clay being an aquiclude. This results in the rise of the water table to less than 1m thereby making the sub-base and subgrade materials permanently wet during the wet season. The percentage variation of groundwater fluctuation is between 263 and 340 as shown in table 1.

This is high and indicates that the under lying geologic materials are impermeable.

The Shango-Chanchaga Road was constructed using granite (which was sourced for locally) as base course. This possibly shows that the type of material used for the construction of the highway may not be mainly responsible for the failure. Swelling soils are a major constituent of the subgrade soils of the area as shown in (table 2). This type of soil is associated with natural low bearing capacity. The cause of the failure could be attributed to the groundwater condition that is being controlled by the geology of the problem area. Close observations of figures 1 and 2 show that the problem area is underlain by schist at a low elevation. It has already been shown that this schist was highly affected by fracturing and jointing that accompanied the intrusion of the older granites in the Minna area. Its intense fracturing and jointing have allowed the percolation of rain water and has considerably weakened the schist and led to its unsuitability as an underlying material. The performance of the subgrade of the failed portion of the highway is thought to have been influenced by the resulting lowered bearing capacity of the weathered schist. The studied rocks are composed of calcium-rich feldspars and dark minerals that are easily susceptible to high weathering (i.e., unstable).

Most of these rock components have weathered in to highly impermeable amorphous hydrous oxides and mostly clay-sized plastic soils. Some of the minerals identified in the metamorphic rocks in the study area include hornblende, biotite, chlorite and sericite. Because the mafic minerals (most weatherable) are concentrated in the schist, they have become more susceptible to weathering. This property has proved troublesome in engineering according to (Rahn, 1996).

The weathered rocks could have formed clay minerals mostly kaolonite and montmorillonite. According to (Okeke, 2008; Attewell and Farmer 1976), the active clay mineral that is responsible for the swelling in expansive soil is montmorillonite. The presence of secondary minerals (halloysite, illite and montmorillonite) is very

important from the engineering point of view (Gidigasu, 1974; Townsend *et al*., 1969). The granular structure (that makes the soils suitable for engineering purposes) in the study soils appears to have been lost upon working the soils resulting in an increase in the clay-size content and plasticity. This has resulted in the soils having lower strengths, high pore pressure, high swelling potentials and other undesirable properties.

5. Conclusion

The hydrogeologic conditions together with the poor drainage that have resulted to the lowered strength of the subgrade could be responsible for the failed pavement. The significance of understanding the geology/hydrogeology in selection, design, construction and wellbeing of highways therefore, should not be under estimated.

The incessant failures of the portion of the road opposite the PW gate along Shango –Chanchaga dual carriageway Minna is linked to the geology/hydrogeology of the area. This portion of the road is built on weak sub-grade (jointed, fractured and weathered schist) that has lost its ability to carry load. The road is at a low elevated area with an accumulation of groundwater seeping out. Majority of the seepages have become obstructed leading to rise in water table under the highway due to increased groundwater storage. This results in the base course being prone to fast disintegration. The schist has weathered to plastic clayey materials that absorb water, swells and expands in the wet period and contracts during the dry period. This has led to longtime wetting of the base and sub-base materials during the wet season. The provision of adequate sub-base drainage facilities will help minimize in the subgrade

REFERENCES

Atterwel, P.B. and Farmer, I.W. 1976. Principles of Engineering Geology, Chapman & Hall

Brain, V. 1983. Laboratory works in soil mechanics. Granada publishing limited.

British Standards (BS) 1377, 1990.Methods of testing soils for civil engineering purposes. British Standards Institution, London.

Clare,K.E. and P.J. Beaven, 1962.Oils and other road making materials in Nigeria. Brit. Road Res. Lab. Tech. Paper, No. 57.

Farquhar, O.C. 1980. Geologic processes affecting the stability of rock slopes along Massachusetts highways.*Eng. Geol.* 16, 135-145.

Gandu, A.H., S.B. Ojo and D.E Jakaiye, 1986. A gravity study of The Precambrian rocks in the Malumfashi area of Kaduna state, Nigeria. Tectonophyics 126:181-194.

Gidigasu, M.D. 1983.Development of acceptance specifications for Tropical Gravel paving materials.*Eng. Geol.* 19, 213-240.

GIDIGASU, M.D. 1974.The degree of weathering in the identification of laterite materials for engineering purposes.Eng. Geol 8. P. 213 – 266.

Obaje, N.G. 2009. Geology and Mineral Resources of Nigeria, Lecture notes in Earth Sciences 120, Do1 10.1007/978-3-540-92685-91, C_ Springer-Verlag Berlin Heidelberg 2009

Okeke, O. C. 2008. Distribution, characteristerization and improvement of expansive soils in parts of southeasthern Nigeria for engineering construction. Unpublished ph.D thesis, department of Geology, University of Nigeria, Nsukka, Nigeria.

Okogbue C.O. 1988. The impact of geology on the performance of a bituminous surfaced pavement – a case study from South eastern Nigeria. Journal of African Earth Sciences 1988.

Okogbue, C.O. and K.O Uma. 1988: The impact of geology on the performance of a bituminous surfaced pavement – a case study from southern Nigeria. Journal of African Earth Sci., Vol.7.No.1.pp.257-264.

Olayinka AI. 1992. Geophysical siting of boreholes in crystalline basement areas of Africa. J Afr

Rahn P.H. (1996): Engineering Geology: An Environmental Approach Earth Sci 14:197–207

Russan, K. and J.D. Croney, 1961.Effect of climatic factors on subgrade conditions.*Geotech.London* **11** (1), 22.28.

Townsend, F.C., Manke, G.P. and Parcher, J.V. (1969): Effects of remolding on the properties of laterite soils. Highway Res. Rec., 284pp 76-84

Tanner, J.S.1963. A review of the methods of pavement design used in overseas territories and the performance of roads constructed by the various design method.*Proc.Reg. Conf. Africa soilMech. Found. Eng.*, 3rd, Salibury, vol.1,pp. 93-100.

Weinert, H.H. 1960. Engineering petrology for roads in South Africa.*Eng. Geol. Handbook* (edited by Woods, K.B.), pp.25.1-25, 52., McGraw-Hill, New York.

ANALYSIS OF STRUCTURE, MICROSTRUCTURE AND CHEMICAL COMPOSITION OF SOLID SOLUTION OF CO-DOPED BARIUM CALCIUM STANNATE TITANATE ($BA_{1-X}CA_XTI_{0.975}SN_{0.025}O_3$) ($0 \leq X \geq 0.12$)

U. Ahmadu, M.I. Abdullahi, Abdulwaliyu B. Usman, Uno, E. Uno. and Moses Agida

Department of Physics, Federal University of Technology, P.M.B., 65, Minna, Nigeria

Corresponding author: u.ahmadu@yahoo.com

Abstract

$Ba_{1-x}Ca_x(Ti_{0.975}Sn_{0.025})O_3$ ($0.00 \leq x \leq 0.12$) ceramics have been synthesized by solid state reaction method. Structural analyses have been carried out to determine the effect of Ca^{2+} substitution on the structural parameters of the ceramic. The average crystallite size decreased from 36.39 nm to 35.39 nm for highly doped Ca^{2+}. Highest increase in c/a ratio was observed at x = 0.06. Microstructural evaluation of the material revealed decrease in grain size from 1 μm to 0.45 μm upon incorporation of Ca^{2+}. Energy Dispersive Spectroscopy (EDS) investigation showed variation in chemical composition but no structural transformation was observed.

Keywords: ceramic; X-ray diffraction; crystallinity; microstructure; grain size.

1. Introduction

Lead based perovskite ceramics have shown high dielectric and piezoelectric properties which are widely used in piezoelectric devices (Mahajan et al, 2011). Unfortunately, the lead content in such ceramics is a very toxic substance that can pollute environment, cause damage to brain and nervous system (Shi *et al*, 2013), hence from environmental point of view and human health protection, there is need to replace these materials with lead-free composition. Over the years, there have been growing researches in developing lead-free piezoelectric materials which may replace their lead-based counterparts. Perovskite Barium Titanate ($BaTiO_3$ or BT) has been recognized as a promising candidate due to its potential application in multilayer ceramic capacitors, piezoelectric transducers, sensors, Fe-RAM (Medhi and Nath, 2013), among others. BT is a typical ferroelectric which exhibits a perovskite (ABO_3) structure. However, some of its drawbacks have limited its extensive application in its pure form due to conflict between significant hysteresis in the strain and electric field dependence of the material which has led to difficulties in controlling the piezoelectric ceramic (Medhi and Nath, 2013), alongside its low piezoelectric constant (Aksel and Jones, 2010). Thermal instability of its structural phase and other dependent properties is also of major concern. BT exhibits a relatively low transition temperature (T_c =120 ℃) and thus suffers structural phase transformation (ferroelectric-tetragonal to paraelectric-cubic phase) at low temperatures (Frattini *et al*, 2012; Aksel and Jones, 2010). Several attempts at improving its structural stability and other dependent properties such as ferroelectric and dielectric properties have been made (Dash *et al*, 2014; Kumar *et al*, 2009 and Woodecka-Duš *et al*, 2007). These include the substitution of Ba^{2+} or Ti^{4+} by atoms of different sizes and oxidation states resulting in compounds of different physical and chemical properties, while still retaining the same structural phase (Dash *et al*, 2014; Cai *et al*, 2011 and Kumar *et al*, 2009). It has been reported that partial substitution of Ba^{2+} by Ca^{2+} prevents grain growth, improves electromechanical properties and structural stability (Matsura *et al*, 2014;Choi *et al*, 2010 and Paunovic *et al*, 2004). However, it was observed that the substitution decreased the dielectric constant (Choi et al, 2010; Yun *et al*, 2007). But the substitution of Ti^{4+} by 0.025 mol of Sn^{4+} leads to increased permittivity, enhanced piezoelectric properties and decreased T_c [(Nath and Medhi, 2012). As such, it is expected that simultaneous substitutions of Ba^{2+} by Ca^{2+} and Ti^{4+} by Sn^{4+} (0.025 mol) may offer the possibility of developing a lead free piezoelectric ceramic. However, secondary phases which affect the crystal structure and other dependent properties of BT upon substitution of inappropriate Ca^{2+} concentration have been reported (Choi *et al*, 2010). Therefore, the appropriate concentration of Ca^{2+} that may improve the structural phase of the ceramic is worth

investigating. To the best of our knowledge, structural and microstructural properties of BT partially substituted by Ca^{2+} and Sn^{4+} (0.025 mol) have not been investigated apart from our earlier work (Ahmadu *et al*, 2016).
In the present work, the effect of Ca^{2+} substitution (on the Ba^{2+} site of $BaTiO_3$) on the structural and microstructural properties of $Ba_{1-x}Ca_x(Ti_{0.975}Sn_{0.025})O_3$ ceramics (where, $0.00 \leq x \leq 0.12$) has been investigated and the evolution of these properties with doping have been reported.

2. Experimental Procedures

$Ba_{1-x}Ca_x(Ti_{0.975}Sn_{0.025})O_3$ (BCST) ceramics where $0.00 \leq x \leq 0.12$ were synthesized by solid state reaction method. Analytical grade $BaCO_3$ ($\geq 99\%$, Kermel, China.), TiO_2 and $CaCO_3$ (99.9 %, Qualikems, India) and SnO_2 (99.99 %, BDH, U.K) were used as starting precursors. Stoichiometric amounts of these materials for the required specimens were weighed and dry- mixed thoroughly followed by wet mixing with distilled water as the medium. The amount of distilled water used was just enough to form slurry to prevent selective sedimentation of the reagents. The slurry was dried in an oven at 150 ℃ for 1 hour. The dried mixture was hand- ground thoroughly for homogeneity using agate mortar and pestle for 4 hours. The homogenous mixture was placed in an alumina crucible and calcined at 1050 °C for 4 hours in a furnace to allow volatilization of bye-product, CO_2. The obtained mixed powder was further ground for 1 hour and granulated by adding 4 wt% polyvinyl alcohol (PVA) as binder to reduce brittleness and to have better compactness and then pressed into 26 mm diameter and 1 mm thickness pellets at a pressure of 10 tons. Finally, the prepared pellets were sintered at 1100 ℃ for 3 hours, and furnace-cooled to obtain a crystal phase formation.
X-ray Diffractometer (D8 Advance, BRUKER AXS, 40 kV, 40 mA) with monochromatic Cu-K_α radiation (λ = 1.54060 Å) at iThemba LABs, South Africa, was used to characterize the structural phase composition of the synthesized ceramics over a 2θ range from 20° to 90° with scan step and acquisition time of 0.034° and 88 seconds, respectively. The morphology and the elemental composition of the ceramics were analyzed using High Resolution Scanning Electron Microscope (HRSEM, Zeiss) coupled with EDS spectrometer, working at a voltage of 20 kV at the Electron Microscopy Unit, Department of Physics at the University of the Western Cape (UWC), Cape Town, South Africa. Images were captured at 5 kV. Prior to the analysis, the samples were placed on a carbon adhesive tape and backed on an aluminium stage. As the samples are non-conducting, a thin layer of AuPd was coated using a sputter coater and then vacuumed in the HRSEM. For measurement of the grain sizes, Imagej software was used.

3. Results and Discussion

3.1 Crystal Structure Analysis

X-ray Diffraction (XRD) patterns of the synthesized $Ba_{1-x}Ca_x(Ti_{0.975}Sn_{0.025})O_3$ ceramics, with x = 0.00, 0.06 and 0.12 mol is depicted in Fig. 1.The XRD patterns confirm that the ceramics are polycrystalline with single phase perovskite structure which compares well with JCPDS no: 00-005-0626 reference data of tetragonal $BaTiO_3$. The XRD patterns are also in agreement with the reports of other workers who prepared BT-based ceramics using similar method (Kim *et al*, 2009;Fasasi *et al*, 2006).

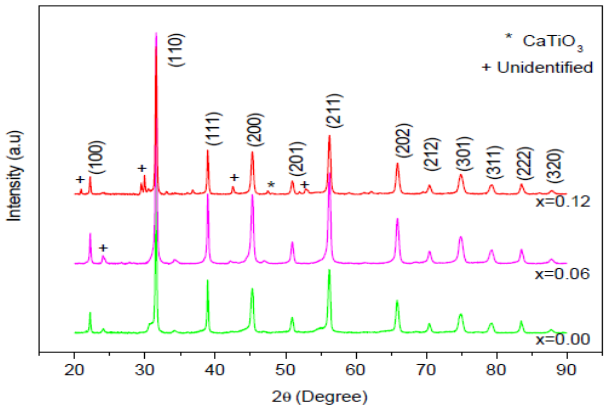

Figure 1. X-Ray Diffraction Pattern of $Ba_{1-x}Ca_x(Ti_{0.975}Sn_{0.025})O_3$ ($0.00 \leq x \leq 0.12$)

However, a minor peak around 47.5° 2θ scan was observed at x = 0.12 which has been identified as orthorhombic $CaTiO_3$ phase (JCPDS file no: 00-022-0153) and attributed to the solubility limit of Ca^{2+} in BCST. This suggests that Ca^{2+} is soluble in BCST up to 0.06 mol. There were other diffraction peaks though with very low intensities whose match could not be found as indicated in the XRD spectra. Further, it was observed that the structure sensitive peak (200) slightly shift towards higher 2θ angles from 45.246 to 45.261° with increasing Ca^{2+} concentration. This suggests distortion of the ABO_3 unit cell lattice (Chen and Yuan-fang, 2012) which could lead to changes in the lattice parameters and is consistent with fact that the radius of Ca^{2+} ions (0.99 Å) is smaller than that of Ba^{2+} ions (1.34 Å) (Yun *et al*, 2007).
Average crystallite size (s) were calculated by eqn. (1) (Dash *et al*, 2014) using the full width at half maximum (FWHM) of the most intense peak.

$$D = \frac{0.9\lambda}{\beta \cos\theta} \qquad (1)$$

where β is the FWHM of the diffraction peak expressed in radians, θ is the Bragg diffraction angle of the XRD peak, λ is the wavelength of the X-ray used which is 1.54060 Å and D is the crystallite size in nanometers.

The calculated average crystallite size is presented in table 1 where it can be seen that the crystallite size decreased because FWHMs increased with increase in doping concentration. This is due to the fact that smaller Ca^{2+} ions replace larger Ba^{2+} ions and their reactivity with the host compound decreased giving rise to decreased crystallinity.

Table 1: Ca^{2+} Concentration (x), Peak Position (2θ) and FWHM (β) at (110) and Average Crystallite size (D)

x	2θ (Degree)	$\beta \times 10^{-3}$ (Radians)	D (nm)
0.00	31.57	3.61	36.93
0.06	31.59	3.94	33.82
0.12	31.58	3.77	35.39

Lattice parameters *a* and *c* of the ceramics were calculated from the XRD spectra using the (100), (200) and (201) diffraction peaks and compared with the JCPDS no: 00-005-0626 data of $BaTiO_3$ (table 2).

Table 2: Determined Lattice Constants a and c, c/a and Cell Volume of $Ba_{1-x}Ca_x(Ti_{0.975}Sn_{0.025})O_3$ Ceramics

X	a (Å)	c (Å)	c/a (Å)	Cell Volume ($Å^3$)
Referenced BT	3.994	4.038	1.0110	64.410
0.00	4.0048	4.0092	1.0011	64.30
0.06	4.0030	4.0149	1.0030	64.30
0.12	4.0020	4.0110	1.0022	64.20

It can be seen that x = 0.00 is weakly tetragonal in comparison with the JCPDS data of $BaTiO_3$ prepared at higher temperature. But on substitution of Ca^{2+} for Ba^{2+}, the lattice parameters *a* decreased while *c* increased and consequently *c/a* ratio (tetragonality) increased. However, x = 0.06 is seen to have the highest value, which could be attributed to the solubility limit of Ca^{2+}. It has been suggested that the increase of the space available to the Ca^{2+} at the Ba^{2+} site induced ferroelectricity in dielectrics (Choi *et al*, 2010). It is hypothesized this could be the reason for the increase in tetragonality observed on substitution of Ba^{2+} by Ca^{2+}. Also presented in table 2 is the cell volume where it is seen to slightly decrease as the concentration of Ca^{2+} increased. This has been corroborated by shifting of (200) peaks to higher angles with increasing Ca^{2+} concentration. Moreover, increase in *c/a* is a desirable characteristic of perovskite titanates because higher *c/a* normally increases the polarizability and improves the ferroelectric properties (Mady, 2011). Thus the observed increase in tetragonality of $Ba_{1-x}Ca_x(Ti_{0.975}Sn_{0.025})O_3$ ($0.00 \leq x \leq 0.12$) may lead to improved ferroelectric properties. Thus it was found that the most appropriate structural properties of $Ba_{1-x}Ca_x(Ti_{0.975}Sn_{0.025})O_3$ ceramics can be obtained with x = 0.06.

3.2 Microstructural Analysis

Fig. 2 depicts HRSEM micrographs of $Ba_{1-x}Ca_x(Ti_{0.975}Sn_{0.025})O_3$ ($0.00 \leq x \leq 0.12$). From Fig. 2(a), it can be seen that the particles agglomerate alongside fairly homogeneous and porous microstructure.

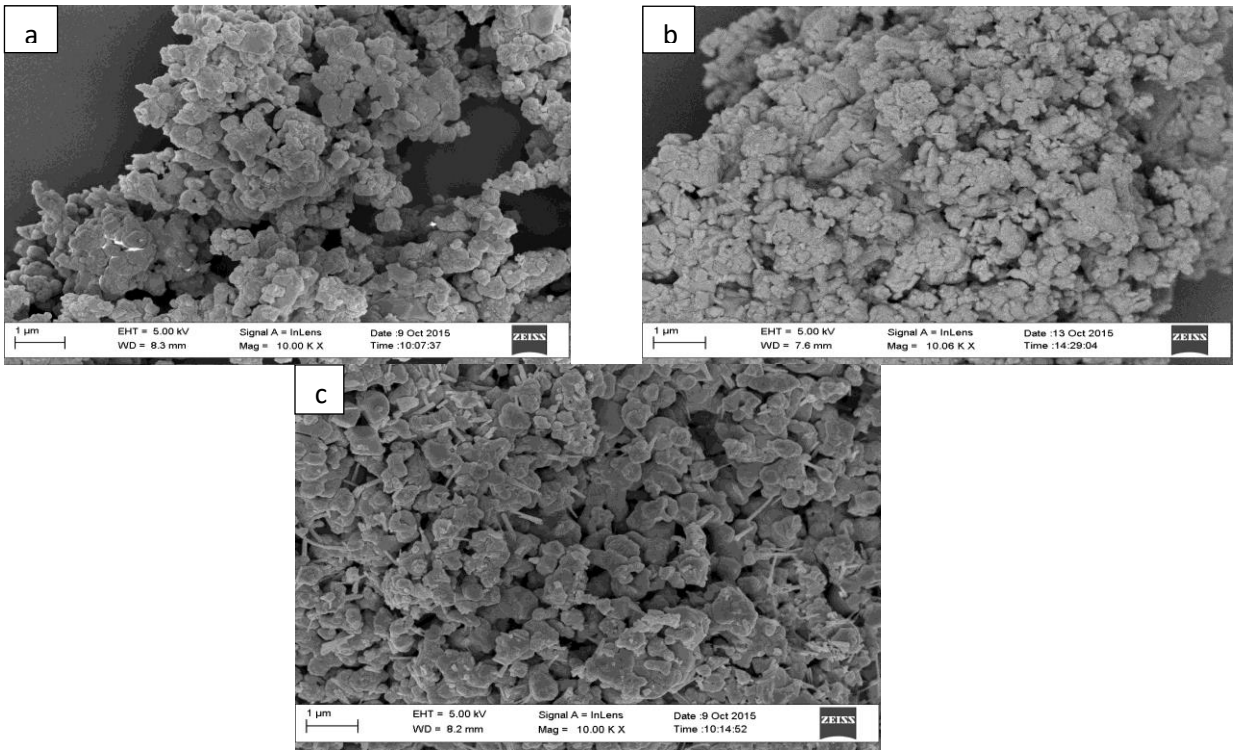

Figure2. HRSEM Micrographs of (a) x = 0.00 (b) x = 0.06 (c) x = 0.12

The average grain size of the ceramics is about 1 µm which is smaller than those observed in traditional BT ceramics sintered at higher temperature (1450 ℃) (Nath and Medhi, 2014). The small value of grain size may be due to insufficient sintering temperature. On addition of Ca^{2+} (x = 0.06), harder agglomeration of grains is observed and the average grain size decreased to about 0.45 µm and this eventually gives rise to poor microstructure (Figure 2b). As Ca^{2+} concentration increased (x = 0.12), two regions are distinguishable in their grain size and phase compositions. The first shows a fairly fine-grained microstructure with average grain size of 0.7 µm , while the other has rod-like grains (Figure 2c). Some residual porosity is evident. The distinct feature of this sample is the presence of non-homogeneous microstructure throughout the sample. The observed rod-like grains are due to non-uniform distribution of starting powders (Paunovic *et al.*, 2004). It is generally known that the initial powder preparation process and possibly insufficient mixing of starting powders or insufficient sintering temperature could result in poor and non-homogeneous microstructure. The decrease in average grain size of the ceramic upon substitution of Ca^{2+} for Ba^{2+} indicates that Ca^{2+} inhibits grain growth (Choi *et al.*, 2010). Moreover, ferroelectric properties of BT-based ceramics have been strongly linked to grain size (Nath and Medhi, 2014) where it is found to decrease when grain size decreases. Decrease in dielectric constant may also be expected because the grain boundary is non-ferroelectric and the dielectric constant of grain boundary is much less than that of grain (Cai *et al.*, 2011). The smaller the grain size is, the more the grain boundary is, and therefore the lower the dielectric constant is.

3.3 Chemical Composition

Fig. 3 is the EDS spectrum showing the elemental composition of $Ba_{1-x}Ca_x(Ti_{0.975}Sn_{0.025})O_3$ ceramics. All the peaks have been identified with the potential elements that match that peak. The spectra clearly reveal the presence of Ba,

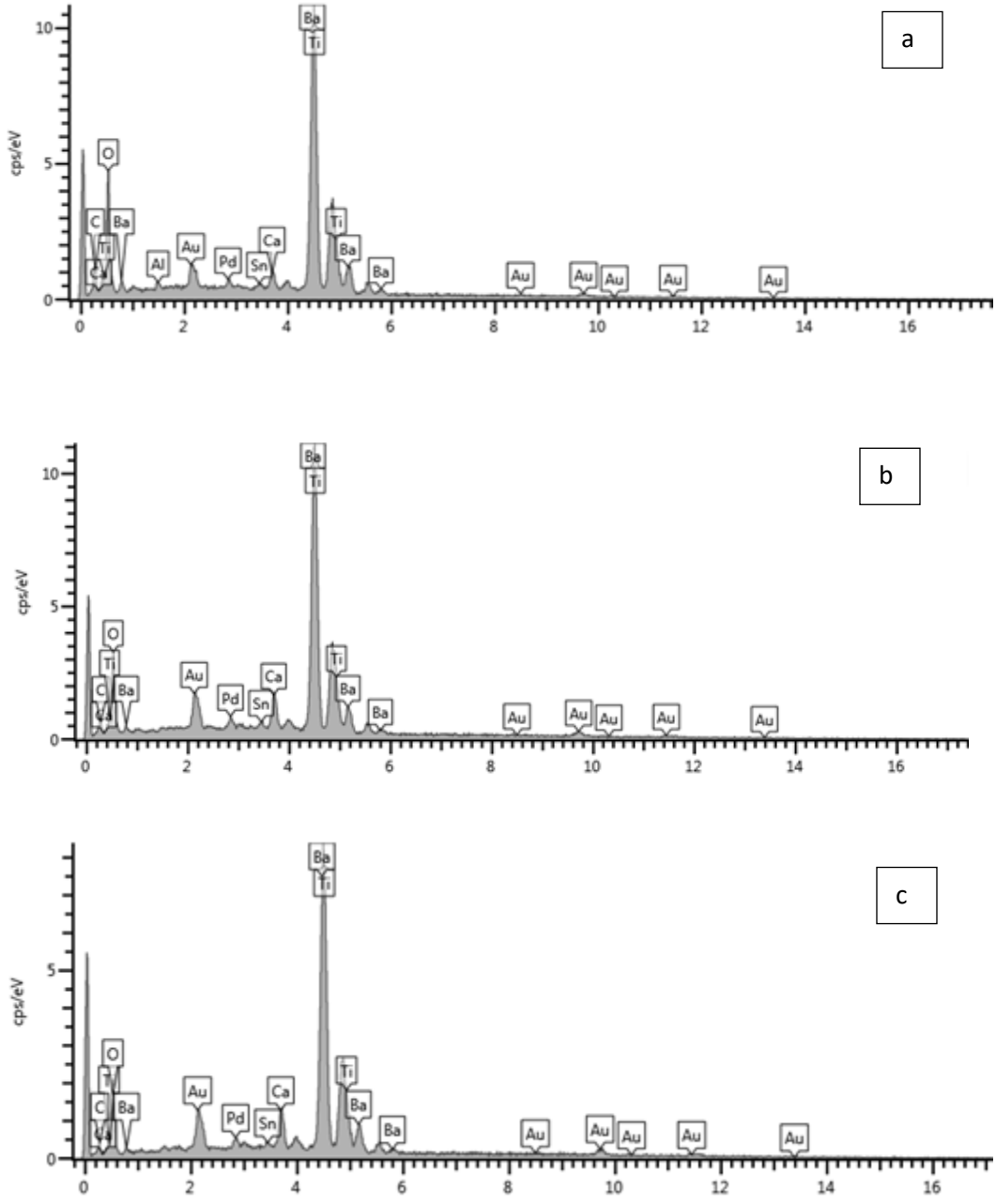

Fig. 3: EDS spectrum of (a) x = 0.00 (b) x = 0.06 (c) x =0.12

The C (carbon) source could have come from the carbon tape. AuPd (Gold-Paladium) is present in the compound in order to make it conducting and the Al may be attributed to contamination during the preparation of samples for SEM analysis. Table 3 gives a quantitative comparison of the nominal composition and the normalized EDS derived composition where the major sources of error have been removed and the remaining elements normalized to 100% to give a representation of the elements present in the compound. The variations in the normalized EDS

derived composition in comparison with the nominal composition could be assigned to deficiency of oxygen during sintering in the ambient (Bapanda, 2010). The overlap of Ba and Ti is clear in the spectra and makes it difficult to distinguish between them in the quantification results. This observation has been reported by other workers (Kim *et al*, 2009;Fasasi *et al*, 2006). However, further investigations are required to elucidate the higher values of the normalized EDS derived results.

Table 3.Nominal and Normalized EDS-derived Elemental Composition

	Nominal Composition (atomic %)						Normalized EDS Derived Composition (atomic %)					
Sample (x)	Ba	Ca	Sn	Ti	O	Total	Ba	Ca	Sn	Ti	O	Total
0.00	20.00	-	0.50	19.50	60.00	100	18.41	-	0.33	19.11	62.15	100
0.06	18.80	1.20	0.50	19.50	60.00	100	19.59	3.59	0.63	22.97	52.69	100
0.12	17.60	2.4	0.50	19.50	60.00	100	22.31	4.7	0.4	26.64	45.95	100

4. Conclusion

Polycrystalline $Ba_{1-x}Ca_x(Ti_{0.975}Sn_{0.025})O_3$ ($0.00 \leq x \leq 0.12$) ceramics were prepared by solid state reaction method. The results indicate that the FWHM increased, crystallite size and grain size decreased as the concentration of Ca^{2+} increased, all of which lead to reduced crystallinity. Variations are observed in the lattice parameters which cause lattice distortion and consequently lead to increase in *c/a* ratio alongside slight contraction of unit cell volume. The changes in the structural and microstructural properties observed on substitution of Ca^{2+} for Ba^{2+} in BCST ceramic could lead to changes in the dielectric and other properties.

References

Ahmadu Umaru, Ahmad Abubakar Soje, Abdulwaliyu Bidemi, Muhammad Auwal Musa, Isah Kasim Uthman. (2016).Structural and Microstructural Study of Gamma Ray-Irradiated Co-doped Barium Titanate ($Ba_{0.98}Ca_{0.12}Ti_{0.975}Sn_{0.025}O_3$).*Processing and Application of Ceramics*,10 (2):79-85.

Aksel, E. and Jones, J.L. (2010) Advances in Lead-Free Piezoelectric Materials for Sensors and Actuators. *Sensors*, **10**, 1935-1954.

Badapanda, T. (2010). Structural, Electrical and Optical Study of 'A' Site Deficient Heterovalent Ion Doped Barium Zirconium Titanate Perovskite. *Department of physics, National Institute of Technology*.Rourkela-769008.Orissa India, 6-58.

Cai, W., Fu, C.L., Gao, J.C. and Zhao, C.X. (2011) Dielectric Properties and Microstructure of Mg doped barium titanate ceramics. *Adances in Applied Ceramics*, **110**, 3, 181-185.

Chen, Z. and Yuan-fang, Q.U. (2012) Dielectric Properties and Phase Transitions of La_2O_3- and Sb_2O_3-Doped Barium Strontium Titanate Ceramics. *Transactions of Nonferrous Metals Society of China*, **22**, 2742−2748.-I

Choi, Y.k., Hoshina, T., Takeda, H. and Tsurumi, T. (2010) Effects of Ca and Zr Additions and Stoichiometry on the Electrical Properties of Barium Titanate-Based Ceramics. *Journal of the Ceramic Society of Japan*, **118**, 10, 881-886.

Dash, S.K., Kant, S., Danlai, B., Swain, M.D. and Swain, B.B. (2014) Characterization and Dielectric Properties of Barium Zirconium Titanate Prepared by Solid State Reaction and High Energy ball milling processes. *Indian Journal of Physics*, **88**, 2, 129-135.

Fasasi, A.Y., Balogun, F.A., Fasasi, M.K., Ogunyele, P.O., Mokobia, C.E. and Inyang, E.P. (2006) Thermoluminescence Properties of Barium Titanate Prepared by Solid-State Reaction, *Sensors and Actuators A*, **135**, , 598-604.

Frattini, A., Di Loreto, A., de Sanctis, O. and Benavidez, E. (2012) BCZT Ceramics Prepared from Activated Powders. *Procedia Material Science*, **1**, 359-365.
HSIANG, FU-SU YEN, YEN-HWEI

Kim, Y.J., Hyun, J.W., Kim, H.S., Lee, J.H., Yun, M.Y., Noh, S.J. and Ahn, Y.H. (2009) Microstructural Characterization and Dielectric Properties of Barium Titanate Solid Solutions with Donor Dopants. *Bulletin of the Korean Chemical Society*, **30**, 6, 1267-1273.

Kumar, Y., Mohiddon, A. Md., Srivastava, A. and Yadav, K.L. (2009) Effect of Ni Doping on Structural and Dielectric Properties of $BaTiO_3$. *Indian Journal of Engineering & Material Sciences*, **16**, 390-394.

Mady, H. A. (2011) XRD and Electric properties of lead barium Titanate Ferroelectric Ceramic. *Australian Journal of Basic and Applied Sciences*, **5,** 10, 1472-1477.

Mahajan, S., Thakur, O.P., Prakash, C. and Sreenivas, K. (2011) Effect of Zr on Dielectric, Ferroelectric and impedance properties of BaTiO3 ceramic. *Bulletin of Materials Science*, **34**, 7, 1483–1489.

Matsuura, K., Hoshina, T., Takeda, H., Sakabe, Y. and Tsurumi, T. (2014) Effects of Ca Substitution on Room Temperature Resistivity of Donor-Doped Barium Titanate Based PTCR Ceramics. *Journal of the Ceramic Society of Japan*, **122**, 6, 402-405.

Medhi, N. and Nath, A.K. (2013) Gamma ray Irradiation Effects on Ferroelectric and Piezoelectric Properties of Barium Titanate Ceramics. *Journal of Material Engineering and Performance*, **22**, 2716-2722.

Nath A.K. and Medhi, A. (2014) Effect of Gamma Ray Irradiation on the Piezoelectric and Ferroelectric Properties of Bismuth Doped Barium Titanate Ceramics. *Indian Journal of Physics,* Doi:10.1007/s12648-014-0531-5.

Nath, A.K. and Medhi, N. (2012) Density Variation and Piezoelectric Properties of $Ba(Ti_{1-x}Sn_x)O_3$ Ceramics Prepared from Nanocrystalline Powders. *Bulletin of Materials Science,* **35**, 5, 847–852.

Paunovic, V., Zivkocic, Z., Vracar, L., Mitic, V. and Miljkovic, M. (2004) The effect of additive on Microstructural and Electrical Properties of $BaTiO_3$. *Serbian Journal of Electrical Engineering,* **1**, 3, 89-98.

Shi, M., Zhong, J., Zuo, R., Xu, Y., Wang, L., Su, H. and Gu, C. (2013) Effect of Annealing Processes on the Structural and Electrical Properties of the Lead-Free Thin Films of $(Ba_{0.9}Ca_{0.1})(Ti_{0.9}Zr_{0.1})O_3$. *Journal of Alloys and Compounds*, **562**, 116–122.

Wodecka-Duś, B., Lisińska-Czekaj, A., Orkisz, T., Adamczyk, M., Osińska, K., Kozielski, L. and Czekaj, D. (2007) The Sol-gel Synthesis of Barium Strontium Titanate. *Materials Science-Poland,* **25**, 3, 719-799.

Yun, S., Wang, X., Li, B. and Xu, D. (2007) Dielectric Properties of Ca-Substituted Barium strontium Titanate Ferroelectric Ceramics. *Solid State Communications,* **143**, 461–465.

STRUCTURAL AND UV-VIS SPECTROSCOPY STUDIES OF GAMMA IRRADIATED STARCH FROM *DIOSCOREA ROTUNDATA*

Ahmadu Umaru[1], Muhammad Habeebah Ndakpayi[1], Kasim Uthman Isah[1], Auwal Muhammad Musa[2], Moses Agida[1]

[1]Department of Physics, Federal University of Technology, Minna, Nigeria

[2]Centre for Energy Research and Training (CERT), Ahmadu Bello University, Zaria, Nigeria.

Corresponding author: u.ahmadu@yahoo.com

Abstract

White yams (Dioscorea rotundata) Kwasi species was irradiated with gamma rays at different doses of 0.05 kGy, 0.1 kGy, 0.2 kGy 0.6 kGy and 1.0 kGy from Cesium-137 gamma source and were assigned codes KA, KB, KC, KD, KE and KF respectively. The native and irradiated sample were investigated and characterised by X-ray diffraction, SEM and UV-Vis spectroscopy. XRD peaks of highest intensity are at 17.14, 17.12, 17.12, 17.12, 17.13 and 17.13 ° 2θ with % crystallinities of 50.26, 50.40, 50.62, 50.15, 50.85 for 0.05 to 1.0 kGy respectively and 50.48 % for native. Their microstructure has average grain sizes of 22.80, 12.38, 40.31, 165.07, 22.90 and 112.84 µm respectively. The grains are ellipsoidal, ovoid and oval-shaped and are of crystal type B for both native and irradiated samples. The crystallize sizes are 1.68, 1.71, 1.71, 1.73, 1.72 and 1.71 nm for native, 0.05 to 1.0 kGy respectively. UV-Vis spectroscopy studies show maximum absorbance of 1.373 at 290 nm wavelength in the UV region which was obtained for the 0.2 kGy dose. The TGA plot shows that *kwasi* starch sample decomposes from 699 ºC with water content loss of ~10 % at ~ 122ºC. DTA shows it glass transition temperature ~90ºC and melting at 391ºC. It is concluded that *kwasi* starch structure was not altered by gamma irradiation and may be suitable for many industrial applications in both food and non-food industries provided the dose needed would not exceed 1 kGy of irradiation.

Keywords: gamma-irradiation, Starch, SEM, TGA, UV-Vis, XRD

1. Introduction

Starch is widely available as naturally occurring carbohydrates reserve in plant tubers and seed endosperm where it is found as granules each typically containing amylopectin molecules accompanied by amylose molecules. World production of starch reached 27.5 million tons (Bujang, 2010). There has been growing interest in its use for various applications such as in the food industry, paper, textile, pharmaceutical and medical among others (Neelam *et al.,* 2012). It is used in the polymer industry because of its environmental friendliness (Ummi-Shafiqah *et al.,* 2012) as it is a natural polymer. This is due to the many advantages such as being safe, renewable and biodegradable among others. The physical properties of its native form need to be studied and correlated for the proper exploitation of their functional properties.

2. Literature Review

Due to several disadvantages of native starch such as been structurally too weak, low shear stress resistance, thermal decomposition, relatively inert and have limitations to high viscosity, low solubility in cold water and paste instability; granules hydrate easily, swell rapidly (Singh *et al.*, 2010; Ibrahim and Achudan, 2011; Neelam *et al.*, 2012). The need for the modifications of its properties becomes necessary. Chemical, enzymatic and genetic modifications have been used (Desai and Park, 2006; Singh *et al.*, 2010; Neelam *et al.*, 2012; Lamanna *et al.*, 2013) among others. However, these methods are often expensive, complex, time consuming, not safe and often associated with environmental concerns. The physical methods such as gamma irradiation has been found to be cost effective, environmentally friendly, requires simple sample preparations and is fast. Different starch sources have shown different thresholds for their structure to be modified by irradiation (Desai and Park, 2006; Singh *et al.*, 2010; Lamanna *et al.*, 2013; Bettaïeb *et al.*, 2014), and the onset of damage due to irradiation amongst others. It is only by subjecting samples to different doses that the effects can be known and therefore good to start with small doses. The structural properties of starch are fundamental to their functional properties. In this work, the effect of different gamma irradiation doses (0.0, 0.05, 0.1, 0.2, 0.6 and 1.0 kGy) on the structural, morphological and UV-Vis spectrum of *kwasi* starch, locally grown in Nigeria, have been evaluated in order to assess the suitability of some parameters for relevant applications, in particular, in the food, polymer electrolytes and radiation environments.

3. Methodology

3.1 Sample Preparation

Tubers of *dioscorea rotundata* (Kwasi) were purchased fresh at Tatiko village Minna, Nigeria, in December, 2014 and were taken to laboratory for extraction. Each tuber of yam was washed and weighed before peeling with top loading balance. The peeled tuber, was cut into pieces and blended with 1000 ml of distil water for purity of starch using electrically powered blender. The blended tuber was sieved through an 80-mesh sieve with 5 litres of distil water, the sieve was allowed to settle for 10 mins and decanted. Decantation was repeated 3 times to obtain pure starch sediment. The starch collected was spread on a clean plastic tray and allowed to dry at room temperature

for 24 hours. The dried starch was weighed and the percentage starch content was determined using the equation below:

$$Percentage\ starch = \frac{weight\ of\ the\ dry\ starch}{weight\ of\ the\ peeled\ yam} \times 100\ \% \qquad (1)$$

The dried lumps of the starch were further ground into powder form using ceramic mortar and pestle, sieved with 80-mesh sieve. Fine samples were put in universal sample bottle.

3.2 Thermogravimetric Analysis

Thermogravimetric Analysis measurement was carried out using a thermogravimetric analyzer (TGA 4000 PerkinElmer UK). 38.16 mg of the native starch sample was weighed directly into an aluminum pan. The pan was heated from 30 ºC to 700 ºC at a heating rate of 10 ºC/min under N_2 gas flow at 20 ml/min. The weight loss and weight derivatives were determined from the TGA curves by means of the universal analysis 2000 software.

3.3 Gamma-Irradiation Process

The samples were irradiated with gamma rays at different doses of 0.05 kGy, 0.1 kGy, 0.2 kGy 0.6 kGy and 1.0 kGy from Cesium-137 gamma source having activity of 1850 MBq and a dose rate of 100.9918 Sv/hr. In this study the activity of the source was converted to dose rate using Radpro calculator software.

3.4 X-ray Diffraction

X-ray diffractograms of starch powders were recorded using D8 Advance X-ray diffractometer (BRUKER AXS Germany). Cu-K$\propto_1$ radiation, with wavelength of 1.5406 Å, was used in the experiment and the radiation was generated at a voltage of 40 kV and current 40 mA. The sample was placed in the XRD sample holder and then scanned between (2θ) 10 to 79 º with scan step size of 0.034 º and scan step time of 176 s with a continuous scan type at a measurement temperature of 25ºC. The procedure was the same for both the native and irradiated starch samples.

3.5 Scanning electron microscope

Scanning Electron Microscope was used to study the surface morphology using Phenom Pro X at an accelerator potential of 15 kV. 1 g each of native and the irradiated samples were stuck separately on a specimen holder using

a silver plate and then coated with palladium in a vacuum evaporator to reduce the deposited charge on the sample surface.

3.6 UV-Vis spectroscopy

An ultraviolet-visible radiation study was carried out in the wavelength range of 200-600 nm for both native and each of the irradiated starch samples. 0.05 g of each sample was dissolved in 30 ml distilled water. The absorbance of the starch samples were measured by means of a UV-Vis spectrophotometer (Jenway 6405).

4. Results and Discussion

4.1 TGA/DTA Thermal Stability

The TGA (green)/DTA (brown) curve of native starch is shown in Fig. 1. The curve shows mass loss in two steps. The first mass loss observed is at temperature range 30-122 ^{o}C with ~10 % mass loss .There is an endothermic peak at 90^{o}C, attributed to glass transition observed in the DTA curve. This range is in accordance with literature (Costa *et al.*, 2011; Ayala *et al.*, 2011) for cassava starch. The initial weight loss is attributed to the loss of water .The endothermic peak at temperature 391^{o}C is the melting point. The temperature range is similar to that reported by other workers (Mano *et al.*, 2003; Lamanna *et al.*, 2013; Hebeish *et al.*, 2013). The TGA plot shows that *kwasi* starch is stable at ~ 699 ^{o}C after all volatiles have been removed.

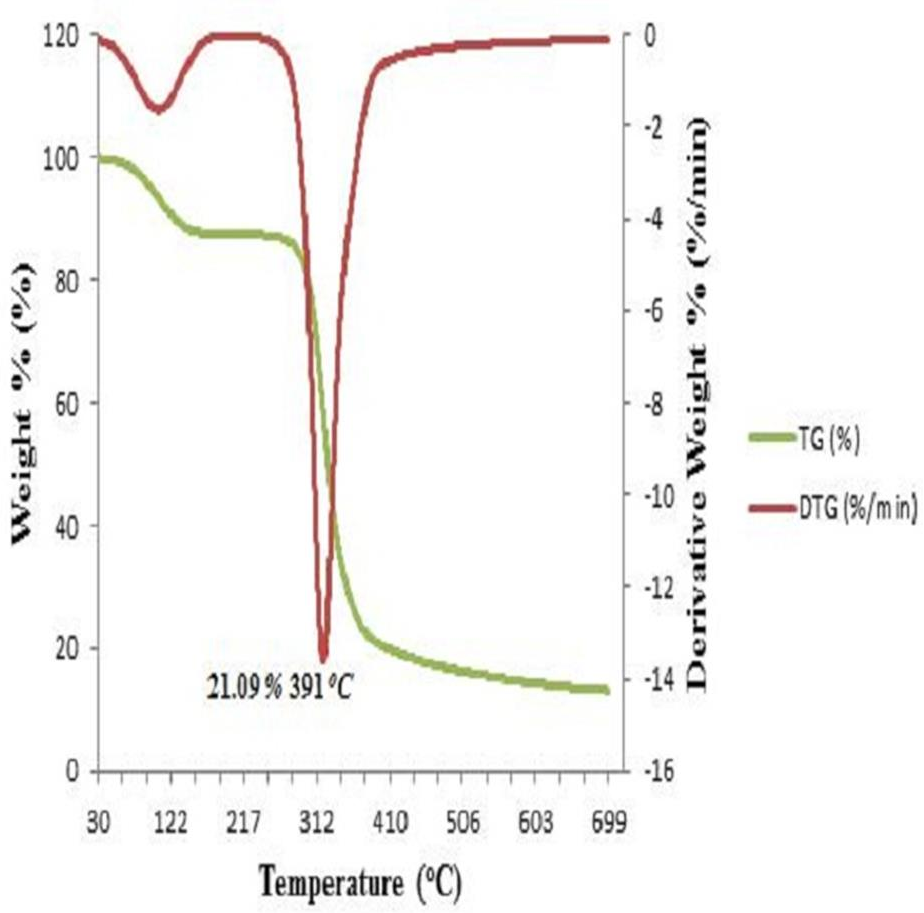

Figure 1. TGA/DTA Plots for Native Starch

4.2 XRD Structural Investigation

The crystalline and amorphous natures of the samples at different doses were obtained by X-ray diffraction. Fig. 2 shows the XRD pattern of both native and irradiated *kwasi* starch samples used. The X-ray diffraction patterns clearly indicate that the samples are semi-crystalline in nature. Similarity of their X-ray diffraction patterns indicate that the organization of crystalline structure of starch was not affected by gamma irradiation. There was no peak at higher than 50°, which is considered an area for amorphous structure. It seemed that gamma irradiation of *kwasi* starch did not provide any molecular movement of starch, so there may not be any interactions between starch molecules, leading to no change in crystallinity.

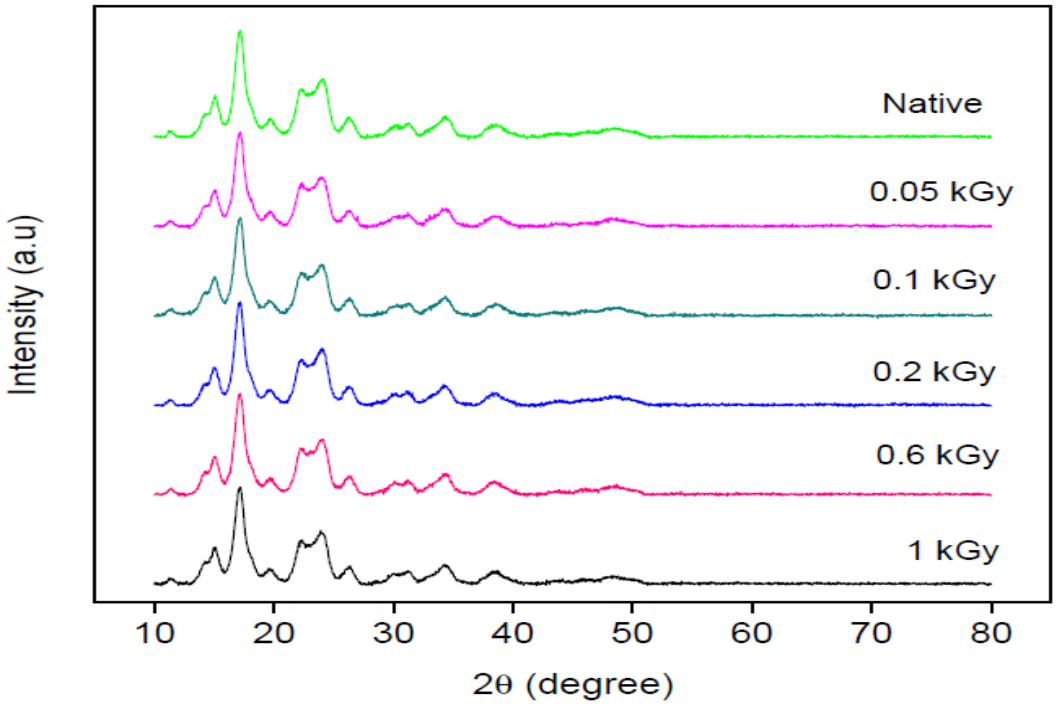

Figure 2. X-Ray Diffraction Pattern of *Kwasi* (*Dioscorea Rotundata*) Starch Samples at Diffraction Angular Range of $10 \leq 2\theta \leq 79°$ Showing Native and all Gamma Irradiated Starch at Different Doses.

It can be observed from XRD patterns that the peaks for all samples were observed at diffraction angle (2θ) of 17.14, 17.12, 17.12, 17.12, 17.13 and17.13 ° for native, 0.05, 0.1, 0.2, 0.6 and 1.0 kGys, respectively. The values are similar to those reported by (Ahmadu *et al.*, 2015) for *Dioscorea rotundata* starch. Strongest diffraction peak at 17° 2θ confirmed that *Kwasi* starch has a typical B-type diffraction pattern. The diffraction pattern may depend on starch origin as well as environmental growth conditions (Marimuthu *et al.*, 2013). This pattern is the same with that reported by (Brunnschweiler *et al.*, 2005).

The Crystallite sizes (D) were calculated using Debye-Scherrer equation

$$D = \frac{K\lambda}{B COS\theta}, (nanometers) \qquad (2)$$

where k =1, B, **λ** and θ are the full width at half maxima (FWHM), wavelength and Bragg peak respectively (Hebeish *et al.*, 2013; Sownthari and Suthanthiraraj, 2013). The result indicates that all samples have approximately similar crystallite sizes because there were no structural modification at all doses of irradiation.

The percent crystallinity was determined using equation

$$X_c\ (\%)\ = \frac{A_c}{A_c + A_a} \times 100\ \% \qquad (3)$$

A_c is the area under the peaks representing the total crystalline region and A_a the area under the peaks representing the total amorphous region. This formula has been reported variously (Rani *et al.*, 2013; Abd El-Kader and Ragab, 2013; Abdul Rahman *et al.*, 2014). Table 2 list the values of % crystallinity for each sample. The % crystalinity was found to decrease from 50.26 % for native to 50.15 % at 0.2 kGy, but it increases in other doses as the dose increases. However, all the values are similar to those reported in literatures by (Lamanna *et al.*, 2013) for Cassava and waxy maize starch. There was no trend in the results obtained but values are so close to suggest that irradiation had little effect on the starch.

Table 1 Summary of Peak (2θ) Positions, Crystallinity, Crystallite Size, FWHM and Crystal Type of *Kwasi* Starch.

Samples (kGy)	d (Å)	2θ (°)	Crystallinity (%)	Crystallite size (nm)	FWHM	Crystal type
Native	5.17007	17.14	50.26	1.68	0.928	B
0.05	5.1753	17.12	50.40	1.71	0.911	B
0.1	5.17387	17.12	50.62	1.71	0.908	B
0.2	5.17387	17.12	50.15	1.73	0.900	B
0.6	5.17127	17.13	50.85	1.72	0.905	B
1.0	5.17007	17.127	50.45	1.71	0.910	B

4.3 Microstructure

The native and gamma irradiated (0.05-1.0 kGy) starch samples were examined using SEM scanned at x1000 magnification, Fig. 3. It was observed that native starch granules and all gamma-irradiated starch samples showed ellipsoidal, ovoid and oval-shaped granules with a smooth surface. The shapes observed are typical shapes of *dioscorea* starch as has been reported (Riley *et al.*, 2006; Odeku, 2012; Singh *et al.*, 2010) for potato starch since they are root and tuber crops. The granule structure was not changed even after the treatment with 1 kGy of gamma

irradiation. The result is in agreement with previous findings of (Bettaïeb *et al.*, 2014) who reported the absence of evident physical damage on corn starch. Therefore, gamma radiation damage to *kwasi* starch seems to be only at the microstructural level. The observation is the same as reported by (Desai and Park, 2006; Lee *et al.*, 2013). However, scratches were observed on the granules surface of few other irradiated starch samples. The presence of scratches on the surface of starch was due to the highly energetic and penetrating radiations and also the source. There was also an observed clustering of starch granules on irradiated samples at 0.1 kGy and 0.2 kGy. This is attributed to the free radicals produced by gamma irradiation on starch molecules (Lee *et al.*, 2006; Kumar *et al.*, 2013; Polesi *et al.*, 2015).

The average grain size (µm) of *kwasi* starch was measured at x1000 magnification using image J software. The values obtained are 22.80, 12.38, 40.31, 165.07, 22.90 and 112.84 μm for native, 0.05, 0.1, 0.2, 0.6, and 1.0 kGy respectively.

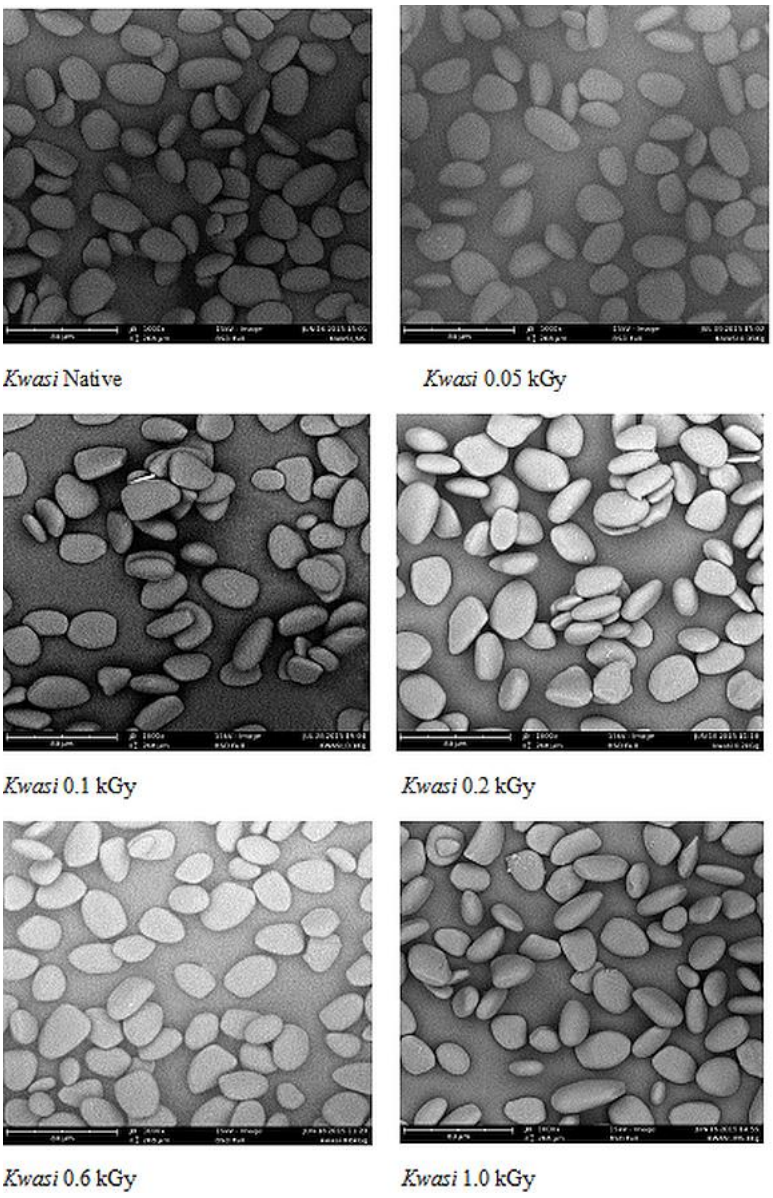

Figure 3. Sem Images of *Kwasi* Starch at x1000 Magnification for both Native and Gamma Irradiated Samples.

The comparison of the pattern of UV-Vis spectra of *kwasi* starch from irradiated and un-irradiated (recorded in the range 200-600 nm) samples, it was possible to verify that the absorbance of *kwasi* starch are affected at different doses of gamma irradiation. The result is similar to that reported by Desai and Park (2006). It was observed that the highest absorbance peak of *kwasi* starch was at 0.2 kGy with a value of 1.373 at 290 nm wavelength (Fig.4).

These results confirm that ionizing radiation altered the absorbance of *kwasi* starch with respect to dose. All the doses absorbed are in the ultra-violet region (190-400 nm) and so there was no indication of any light being absorbed making Kwasi starch colourless.

Due to the lack of relevant literature about *dioscorea rotundata* starch, very little information was found on UV-Vis study of gamma-irradiated starch. However, in a similar study, Bajer and Kaczmarek (2010) reported an increase in absorbance of starch due to the increase of UV-irradiation of starch from 0-13 hours. Abdel-Razik *et al.* (2015) and Sownthari and Suthanthiraraj (2013) also reported increase in chemical modified corn and potato starches, respectively. Gunasekaran and Devi (2007) reported a variation in the absorbance of chemically modified corn and wheat starches.

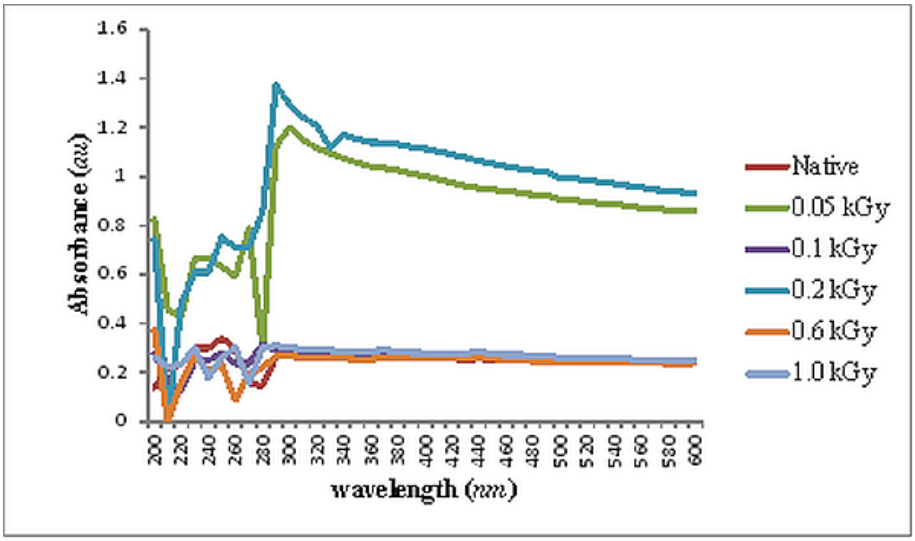

Figure 4. UV-Vis Spectral of Irradiated and Non-Irradiated *Kwasi* Starch Samples at Different Doses.

Table 2 Highest Absorbance for Native and Each of the Irradiated Starch Sample at Different Doses.

Sample (*kGy*)	Absorbance (*au*)	Wavelength (*nm*)
Native	0.339	250
0.05	1.202	300
0.1	0.317	280
0.2	1.373	290
0.6	0.374	200
1.0	0.310	290

5. Conclusions

The XRD characterisation shows that *Kwasi* starch is semi-crystalline in nature. There was no trend in the values recoded for percent crystallinity and crystallite sizes of both the irradiated and un-irradiated starch samples, these values were approximately similar. It also shows the maximum decrease in percentage crystallinity, the maximum crystal size, the slight decrease in intensity and the full width at half maxima at 0.2 kGy.

An Oval shape of starch granules was observed by SEM, and a strong intensity at (2θ) of 17 ^{o} indicated that it is B-type X-ray pattern characteristic of tubers. The DTA plot indicates phase transformations took place at temperatures of ~ 88 and 319 ^{o}C. However, TGA plot shows that *kwasi* starch is stable at 699 ^{o}C with weight loss of ~14.19 %.

These results are an indication that *kwasi* starch structure is stable to gamma irradiation of up to a maximum dose of 1 kGy and has high crystalllinity compared to other starches, particularly within the *dioscorea* family. These properties therefore make it promising for application in polymer electrolytes, for food preservation. It would also be environmentally friendly when used in radiation environment not exceeding 1 kGy.

References

Abd El-Kader, M. F. H. and Ragab, H. S. (2013). Dc Conductivity and Dielectric Properties of Maize Starch/Methylcellulose Blend Films. *Ionics*, Vol. 19, 361–369.

Abdel-Razik, E. A., Badawy, D. S. and El Nahas, E. A. (2015). Graft Copolymerization of Acrylamide onto Corn Starch using Mohr's Salt/Hydrogen Peroxide Redox System in Aqueous Media Under Visible Light. *International Journal of Modern Organic Chemistry*, Vol. 4(1), 1-17.

Abdul Rahman, M. H., Khandaker, M. U., Khan, Z. R., Kufian, M. Z., Noor, I. S. M., and Arof, (2014). A. Effect of Gamma Irradiation on Poly (Vinyledene Difluoride) Lithium Bis (Oxalato) Borate Electrolyte. *Royal Society of Chemistry: Chemistry Physics*, Vol. 16, 11527-11537.

Ahmadu, U., Agbomeji, O., Mohammed, Y. and Odeku, O. (2015) Physical and Crystallographic Parameters of Starch from *Dioscorea Rotundata*. Submitted.

Ayala, G., Agudelo, A. and Vargas, R. (2011). Effect of Glycerol on the Electrical Properties and Phase Behavior of Cassava Starch Biopolmers. *Network of Scientific Journal*, Vol. 171, 138-147.

Bajer, D. and Kaczmarek, H. (2010). Study of the Influence of uv radiation on Biodegradable Blends Based on Chitosan and Starch. *Progress on Chemistry and Application of Chitin and its Derivatives*, Vol. 15, 17-24.

Bettaïeb, N. B., Jerbi, M. T. and Ghorbel, D. (2014), Gamma Radiation Influences Pasting, Thermal and Structural Properties of Corn Starch. *Radiation Physics and Chemistry*, Vol. 103, 1-8.

Brunnschweiler, J., Luethi, D., Handschin, S., Fara, Z., Escher, F. and Conde-Petit, B. (2005). Isolation, Physicochemical Characterization and Application of Yam (*Dioscorea Spp*.). Starches as Thickening and Gelling Agent. *Starch/Stärke57*, 107-117.

Bujang, K.B. (2010). Production and Processing of Sago: A Food and Fuel Alternative *International Seminar on Sago and Spices for Food Security*. Ambon. Rep. Indonesia.1-6. Retrieved from www.researchgate.net.

Costa, F. J. O. G., Almeida, R. R., Lacerda, L. G., Carvalho-Filho, M. A. S., Bonnach, G. and Schnitzler, E. (2011), Thermo Analytical Study of Native Cassava Starch and Treated with Hydrogen Peroxide. *Alim Nutrition*, Vol. 22 (1), 7-15.

Desai, K. G. and Park, H. J. (2006), Study of Gamma-Irradiation Effects on Chitosan Microparticles, *Drug Delivery*, Vol. 39, 13–50.

Gunasekaran, S. and Devi, M. K. (2007). UV-Vis Spectroscopic Investigation on Hydrolysis of Starch and Starch-Drug Interaction. *Asian Journal of Chemistry*, Vol. 19 (5), 3363-3374.

Hebeish, A., El-Rafie, M. H., El-Sheikh, M. A. and El-Naggar, M. E. (2013).Nanostructural Features of Silver Nanoparticles Powder Synthesized through Concurrent Formation of the Nanosized Particles of Both Starch and Silver. Journal of Nanotechnology, 1-10.

Ibrahim, N. H. and Achudan, S. N. (2011). Physical Properties and Stability of Emulsions as Affected by Native and Modified Yam Starches. *International Scholarly and Scientific Research and Innovation* Vol. 5, 394-398.

Kumar, P., Ganure, A. L., Subudhi, B. B., and Shukla, S. (2013). Synthesis and Characterization of ph Sensitive Ampiphillic new Copolymer of Methyl Methacrylate Grafted on Modified Starch: Influences of Reaction Variables on Grafting Parameters. *International Journal of Pharmacy and Pharmaceutical Sciences*, Vol. 6, (1), 868-880.

Lamanna, M., Morales, N. J., Garcia, N. L., and Goyanes, S. (2013). Development and Characterization of Starch Nanoparticles by Gamma Irradiation: Potential Application as Starch Matrix Filler, *Carbohydrate Polymers*, Vol. 97, 90-97.

Lee, J.-S., Ee, M.-L., Chung, K.-H. and Othman, Z. (2013) Formation of Resistant Corn Starches Induced by Gamma-Irradiation. *Carbohydrate Polymers*, Vol. 97, 614-617.

Lee, Y.-J., Kim, S. Y., Lim, S.-T., Han, S.-M., Kim, H.-M., Kang, I.-J. (2006). Physicochemical Properties of Gamma-Irradiated Corn Starch. *Journal of Food Science and Nutrition*, Vol. 11,146-154.

Mano, J. F., Koniarova, D. and Reis, R. L. (2003). Thermal Properties of Thermoplastic Starch/Synthetic Polymer Blends with Potential Biomedical Applicability. *Journal of Materials Science: Materials in Medicine*, Vol. 14, 127-135.

Marimuthu, M., Sundaram, U. and Gurumoorthi, P. (2013). X-ray Diffraction and Starch Analysis of Nano Sized Seed Powder of Velvet Bean (*Mucuna Pruriens*). *Indo American Journal of Pharmaceutical Research*, Vol. 3(6), 4319-4329.

Neelam, K., Vijay, S., and Lalit, S. (2012), Various Techniques for the Modification of Starch and the Applications of its *Derivatives. International Research Journal of Pharmacy*, vol. 3(5), 25-31.

Odeku, O. A. (2012) Potentials of Tropical Starches as Pharmaceutical Excipients. *Starch/Stärke* 00, 1–18.

Polesi, L. F., Sarmento, S. B. S., Moraes, J., Franco, C. M. L. and Canniatti-Brazaca, S. G. (2015). Physicochemical and Structural Characteristics of Rice Starch Modified by Irradiation. *Food Chemistry*, 191, 59-66.

Rani, N. S., Sannappa, J., Demappa, T. and Mahadevaiah, (2013). Gamma Radiation Induced Conductivity Control and Characterisation of Structural and Thermal Properties of Hydroxyl Propyl Methyl Cellulose (HPMC) Polymer Complexed with Sodium Iodide (Nal). *Advances in Applied Science Research*, Vol. 4 (3), 195-219.

Riley, C. K., Wheatley, A. O. and Asemota, H. N. (2006). Isolation and Characterization of Starches from Eight *Dioscorea Alata* Cultivars Grown in Jamaica. *African Journal of Biotechnology*, Vol. 5(17), 1528-1536.

Singh, S., Singh, N., Ezekiel R. and Kaur, A. (2010), Effects of Gamma-Irradiation on the Morphological, Structural, Thermal and Rheological Properties of Potato Starches, *Carbohydrate Polymers*, xxx, xxx xxx.

Sownthari, K. and Suthanthiraraj, S. A. (2013). Synthesis and Characterization of an Electrolyte System Based on Biodegradable Polymer. *Express Polymer Letters*, Vol. 7(6), 495-504.

Ummi-Shafiqa, M. S, Fazilah, A., Karim, A. A., Kaur, B. and Yusup, Y. (2012). The Effects of UV Treatment on the Properties of Sago and Mung Bean Films. *International Food Research Journal* Vol. 19(1), 265-270.

BEHAVIOURAL ANALYSIS OF DAILY RAINFALL PATTERN IN KATSINA

E.V. Tikyaa, A. N. Baba-Kutigi and E. Joseph

Department of Physics, Federal University Dutsin-ma, Katsina State, Nigeria

Corresponding Author: etikyaa@fudutsinma.edu.ng, +2347032096960.

ABSTRACT

Rainfall is the most important meteorological parameter as far as agriculture is concerned. This is because about 70% of living things is composed of water and so without water living things cannot thrive. In northern Nigeria today, the treat of desertification is looming large, hence the need for a thorough analysis of our hydrological resources. This paper seeks to undertake a behavioral analysis of the rainfall pattern in Katsina State, Nigeria. The analysis involves a complete statistical, trend and nonlinear analysis of the daily rainfall time series from 1990 to 2015 in a view to characterizing the data and describing its dynamics so that adequate recommendations can be made for its modelling. The outcome of this analysis indicates that the rainfall in Katsina exhibits an increasing trend over the past 26 years with a high variance and low dimensional chaotic attractor ($\nu = 0.96$). A minimum of 11 and maximum of 27 independent variables are required to model the daily rainfall in Katsina. The largest Lyapunov exponent for the rainfall time series in Katsina was also computed and found to be 0.002799/day while the Kolmogorov-Sinai (K-S) entropy was found to be 0.003633/day. The positive value of the Lyapunov exponent and finite value of the K-S entropy indicates a strong signature of chaos in the daily rainfall in Katsina over the last 26 years. This also indicates that the daily rainfall in Katsina is predictable for the next 190 to 357 days. It is recommended that adequate measures such as afforestation programmes be taken more seriously to curb the menace of global warming and climate change which is responsible for the increased fluctuations in rainfall pattern in Katsina State making it more difficult for farmers to plan and optimize their agricultural yield.

Keywords: Trend analysis, chaos, phase space reconstruction, phase portrait, correlation dimension, Lyapunov exponent, Kolmogorov-Sinai entropy.

1. INTRODUCTION

Nowadays meteorological and hydrological studies, lays huge emphasis on the modelling of time series so as to ease the designing, planning and forecasting of these natural resources. Time series represents a dynamic measure of a physical process over a given period of time and may be discrete or continuous (Fathima and Jothiprakash, 2014). The discovery of Chaos by Edward Lorenz in 1961 (Lorenz, 1963), has brought about a great revolution on the mode of understanding and expressing most of these phenomena in nature. Chaos theory, the basis and foundation of nonlinear dynamics, is a tool that can be used for characterizing and modelling complex phenomena in nature such as rainfall data which has a higher variation coefficient (Rasoul *et al.*, 2014). Weather is a continuous, data-intensive, multidimensional, dynamic and chaotic process and these properties make weather prediction a big challenge as the chaotic nature of the atmosphere implies the need for massive computational power required to solve the equations that describe the atmospheric conditions (Lai *et al.*, 2004). Climate indeed varies nonlinearly too, but this has not prevented scientists from making good predictions using advance regression techniques. Science and technology has been applied to predict the state of the atmosphere in future time for a given location and this is very important as it affects life on earth. Today, computational weather forecasts are made by collecting quantitative data about the current state of the atmosphere and using scientific understanding of atmospheric processes to numerically project how the atmosphere will evolve, but due to an incomplete understanding of the chaotic atmospheric processes, forecasts become less accurate as the range of forecast increases (Sharma and Manoria, 2007).
In this paper is aimed at undertaking a detailed behavioral analysis of the rainfall in Katsina over the last twenty-six years so as to unveil its dynamics thereby characterizing the data for modelling and forecasting to boost the planning of agricultural activities in the nearest future.

2. METHODOLOGY

The behavioral analysis of daily rainfall in Katsina state will be undertaken in this research by applying the following techniques:

i. Statistical analysis of the data,
ii. Trend analysis, and
iii. Nonlinear analysis.

Statistical Analysis

Statistical analysis involves the computation of the arithmetic mean, variance, standard deviation, coefficient of variation, signal-to-noise ratio, range, kurtosis and skewness. MATLAB statistics toolbox (R2014a) is used to achieve this.

Trend Analysis

In order to check the overall effect of greenhouse effect and global warming on the rainfall pattern in Katsina, trend analysis was carried out using the following statistical tools:

i. the correlation coefficient of the rainfall data with time was computed to determine the strength of the linear relationship the daily rainfall data with time,
ii. the monotonic increasing or decreasing trend was tested using the non-parametric Mann-Kendall test, and
iii. the slope of a linear trend is estimated with the nonparametric Sen's slope estimator.

i. Correlation Coefficient

The Pearson product moment correlation coefficient R, measures the strength and the pattern of a linear relationship between two variables. It is mathematical given by (MathBits, 2015):

$$R = \frac{n\sum xy - (\sum x)(\sum y)}{\sqrt{n(\sum x^2) - (\sum x)^2}\sqrt{n(\sum y^2) - (\sum y)^2}} \quad (1)$$

R value ranges from –1 to +1, with +1 or –1 indicating a perfect correlation and a correlation coefficient close to or equal to zero indicating no relationship between the variables. A correlation greater than 0.8 is generally described as strong, whereas a correlation less than 0.5 is generally described as weak. While a positive correlation coefficient indicates an increasing trend, a negative correlation coefficient indicates a decreasing trend.

ii. Mann-Kendall Analysis

The nonparametric Mann-Kendall test is usually used to detect trends that are monotonic but not necessarily linear. The Mann-Kendall test statistic S is computed using the formula (McBean and Motiee, 2008):

$$S = \sum_{k=1}^{n-1} \sum_{j=k+1}^{n} sign(x_j - x_k), \quad (2)$$

Where x_j and x_k are the daily rainfall values and time in days j and k, with $j > k$, respectively.
The sign ( ) function is defined as (Christoph, and Frei, 2015):

$$sign(x_j - x_k) = \begin{cases} 1 & if\ x_j - x_k > 0 \\ 0 & if\ x_j - x_k = 0 \\ -1 & if\ x_j - x_k < 0 \end{cases} \quad (3)$$

A very high positive value of S (>120) is an indicator of an increasing trend, while a very low negative value indicates a decreasing trend (Olofintoye, and Sule, 2010). The Man-Kendall parameter S and its variance $VAR(S)$ are used to compute the test statistic Z as follows (McBean and Motiee, 2008):

$$Z = \begin{cases} \frac{S-1}{\sqrt{VAR(S)}} & if\ S > 0 \\ 0 & if\ S = 0 \\ \frac{S+1}{\sqrt{VAR(S)}} & if\ S < 0 \end{cases} \quad (4)$$

The Z statistic follows a normal distribution trend, is tested at 95% (α=0.05) level of significance ($Z_{\frac{\alpha}{2}} = 1.96$) and its value describes the trend as (Khambhammettu, 2005):

a) decreasing if Z is negative and the absolute value is greater than the level of significance,
b) increasing if Z is positive and greater than the level of significance, and
c) no trend if the absolute value of Z is less than the level of significance.

iii. Sen's Slope Estimator

The Sen's test estimates the true slope of an existing trend (i.e. change per day). The Sen's method is used in cases where the trend can expressed as linear:

$$y(t) = Qt + B \quad (5)$$

Where Q is the slope, B is a constant and t is time.

$$Sen's\ estimator,\ Q = \underbrace{median}_{j>k} \left(\frac{x_j - x_k}{j-k}\right) \quad (6)$$

For n values x_j in the time series there will be as many as $N = \frac{n(n-1)}{2}$ slope estimates Q_i of which the median value gives the Sen's estimator, Q. In order to get an estimate of the intercept B in equation (5), the n values of differences $x_i - Qt_i$ are calculated and the median of these values gives an estimate of B (Salmi *et al.*, 2002).

Nonlinear analysis

The tools of nonlinear analysis used to characterize the daily rainfall data in this paper include: time series plot, phase portrait and Poincaré map, correlation dimension, Lyapunov exponents and Kolmogorov-Sinai entropy.

i. Time Series Plot

Time series plot involves plotting the daily, monthly and yearly rainfall data and observing the trend. If they exhibit irregular, aperiodic or unpredictable behavior, then it could be described as random or chaotic. On the other hand if they exhibit a regular repeating pattern, then the system exhibits either a periodic and quasi periodic behavior (Echi *et al.*, 2015).

ii. Phase Portrait

A phase portrait is a two-dimensional visualization of the phase-space. It displays the attractor and unveils its dynamics. Chaotic systems exhibit distinct shapes, periodic systems exhibit limit cycle (closed curves) while quasi periodic systems exhibit torus shape (Ozer and Akin, 2005).

iii. Poincaré maps

The Poincaré map is that it represents a slice through the attractor of the dynamical system and it is a stroboscopic view of the phase portrait of the dynamical system; hence it can also be referred to as a stroboscopic map (Velickov, 2006). Poincaré maps of periodic systems shows a single point, quasi-periodic systems shows a closed curve while chaotic systems show distinct points (Ozer and Akin, 2005).

iv. Correlation Dimension

The correlation dimension actually measures the number of "degrees of freedom" excited by the system. The Grassberger-Procaccia algorithm is used to compute the correlation dimension in this work using the correlation integral. For any set of M points in an *m*-dimensional phase space, the correlation integral or correlation sum (spatial correlation of points) *C*(r) is computed by the equation (Grassberger and Procaccia, 1983):

$$C_m(r) = \lim_{N\to\infty} \frac{2}{N(N-1)} \sum_{i=1}^{M} \sum_{j=i+1}^{M} H\left(r - \left\|\overrightarrow{x_i} - \overrightarrow{x_j}\right\|\right) \quad (7)$$

H(*x*) is the Heaviside function and ||... || is the Euclidean norm, while r is the scaling parameter. The correlation integral measures the fraction of the total number of pairs of phase points that are within a distance r from each other. For chaotic time series, the correlation integral power law for small values of r takes the form:

$$C(r) \sim r^{\nu} \quad (8)$$

Thus, the correlation dimension ν is given by:

$$\nu = \lim_{r\to 0} \lim_{M\to\infty} \frac{\log C(r)}{\log r} \quad (9)$$

Hence, a log-log graph of the correlation integral versus the scaling parameter, r will yield an estimate of the correlation dimension *ν,* which is computed from the slope of a least-square fit of a straight line over a large length scale of r. Chaotic systems exhibit low dimensionality i.e. ν <20 and its correlation exponent curve for a range of values of embedding dimension (say m = 1 to 30) usually saturates at values beyond its actual embedding dimension. The saturation value of the correlation exponent plot gives the correlation dimension and the value of the embedding dimension at which the saturation of the correlation exponent curve occurs generally provides an upper bound on the number of variables sufficient to model the dynamics (Echi *et al.*, 2015).

v. Lyapunov Exponents

Lyapunov exponents (λ) are the average rates of exponential divergence or convergence of nearby orbits in phase space and is a fundamental property that characterizes the rate of separation of infinitesimally close trajectories (Takens, 1980). It is mathematical given by:

$$\lambda_1(i) = \frac{1}{i.\Delta t} \cdot \frac{1}{M-i} \cdot \sum_{j=1}^{M-i} \ln \frac{d_j(i)}{d_j(0)} \quad (10)$$

Δt is the sampling period of the time series, M is the number of reconstructed phase points and $d_j(i)$ is the distance between the jth pair of nearest neighbors after i discrete-time steps, i.e., $i.\Delta t$ seconds. The nearest neighbor, X_j, is found by searching for the point that has the least distance to the particular reference point, X_j. This is expressed as:

$$d_j(0) = \min_{X_{\hat{j}}} \left\| X_j - X_{\hat{j}} \right\| \quad (11)$$

$d_j(0)$ is the initial distance from the jth point to its nearest neighbor $\hat{j}$. A positive Lyapunov exponent indicates chaotic behavior, a negative value indicates periodic behavior while a zero Lyapunov exponent indicates quasi-periodicity (transition to chaos). The method used in computing the largest Lyapunov exponent was developed by Rosenstein *et al* (1992). The Lyapunov (e-folding) time or predictability T (upper bound) is the time within which it is possible to predict the system forward and can be computed in terms of the largest Lyapunov exponent λ using the expression (Stehlik, 2006):

$$T_{max} = \frac{\Delta t}{\lambda} \quad (12)$$

vi. Kolmogorov-Sinai entropy

Eckmann and Ruelle (1985) defined Kolmogorov-Sinai entropy as the mean rate of information gain or loss in a dynamical system. The predictability of time series can also be indicated by metric entropy which is a measure of the rate of loss of predictability. Metric entropy measures how far the future can be predicted with given initial information (Hakki, 2006):

The value of the K-S entropy could be used to describe the type of system; e.g. in random systems the K-S entropy is equal to infinity, it is finite for chaotic systems and is zero for a quasi-periodic and periodic systems (Kolmogorov, 1961).

In this work, an upper bound of the K-S entropy is computed using Pesin's theorem (Pesin, 1977). This states that the metric entropy is equal to the sum of positive Lyapunov exponents due to the fact that the system invariants are absolutely continuous in all expanding dimensions. The Lyapunov exponent spectrum was determined from a range of values of embedding dimension (i.e. 1 to m) and the K-S entropy can be estimated using Pesin's identity, which seems to hold for typical attractors. This relation can be written mathematically as (Rosenstein *et al.*, 1992):

$$K = \sum_{i,\lambda_i>0} \lambda_i \quad (13)$$

The K-S entropy can also give a lower bound for the predictability of the system viz (Zeng et al., 1993):

$$T_{min} = \frac{\ln 2}{K} \quad (14)$$

vii. Phase Space Reconstitution

In order to effectively carry out nonlinear analysis, phase space reconstruction has to be done so as to draw out a multi-dimensional description of system in an embedded space called state space. The method of delays was thus employed to achieve this [Takens (1980) and Packard *et al.* (1980)]. For a generalized time series $\{x_1, x_2, \ldots, x_N\}$, the attractor can be reconstructed in a m-dimensional phase space of delay coordinates in form of the vectors:

$$X_n = [x_n, x_{n+\tau}, x_{n+2\tau}, \ldots, x_{n+(m-1)\tau}] \quad (14)$$

τ is the time lag, and m is the embedding dimension. The time lag τ is evaluated in this work using the method of autocorrelation function criterion put forward by Ramsey and Yuan (1989), who showed that if a plot of the autocorrelation function against a range of values of the time lag τ is made, τ is chosen to be the time of the first zero in the autocorrelation function (ACF) of the data series. The minimum embedding dimension, m was computed using the method of "False Nearest Neighbors (FNN)" which was developed by Kennel *et al.* (1992). By plotting the percentage of FNN against increasing embedding dimension values, a monotonic decreasing curve is observed and the minimum embedding dimension can be evaluated from the point where the percentage of FNN drops to almost zero or a minimum value.

3. STUDY AREA AND DATA SOURCE

Katsina state, also known as the home of hospitality, is located in the North-Western region of Nigeria. The state is located within the coordinates $12°15'N$, $7°30'E/12°25'N$, $7°50'$E and was created on 23rd September, 1987. It covers a total land area of 24,192km^2 with a population density of 160/km^2 and its landscape is largely dominated by the Sahel savannah vegetation. Katsina state experiences two dominant seasons: the rainy and dry season, with the Hausa-Fulani who are predominantly farmers being the largest ethnic group in the state (Wikipedia.org/Katsina_state, 2017). The data used in this research was obtained from the Nigerian

Meteorological Agency (NIMET) Abuja. It comprises of secondary data made up of daily average rainfall (mm) recorded in Katsina from 1st January, 1990 to 31st December 2015, a period of twenty-six years.

4. RESULTS AND DISCUSSION

The statistics of daily rainfall (mm) is displayed in Tables 1:

Table 1: Statistics of daily rainfall in Katsina

Statistic	Value
No. of data	9490
No. of zeros	8241 (86.8%)
Mean (mm)	1.5943
Standard Deviation (mm)	6.5249
Variance (mm)	42.5743
Coefficient of Variation	4.0926
Signal-to-noise ratio	0.2443
Maximum value (mm)	156.0
Minimum value (mm)	0.00
Kurtosis	78.2994
Skewness	6.8979

Figures 1(a), (b) and (c) shows time series plots of daily, monthly and yearly rainfall in Katsina.

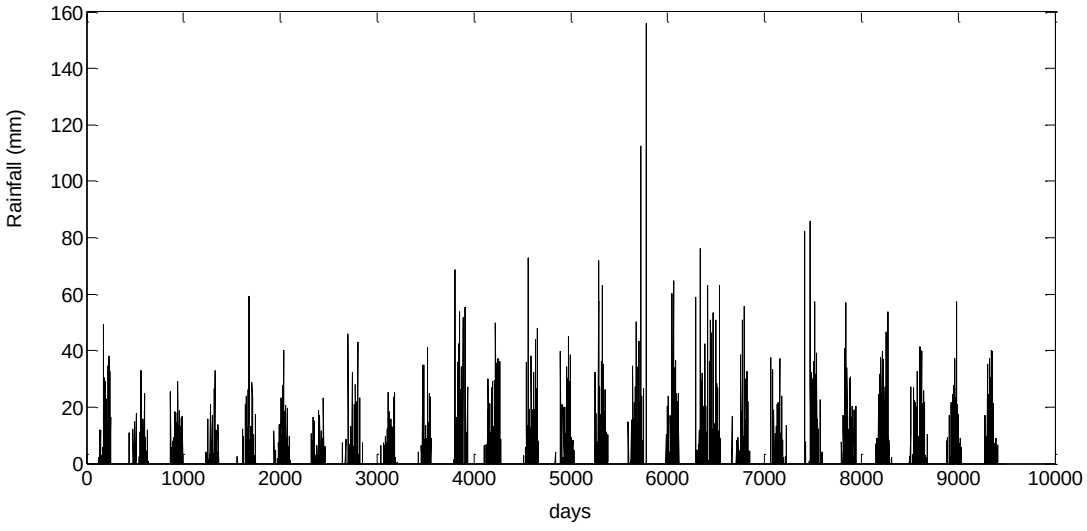

(a)

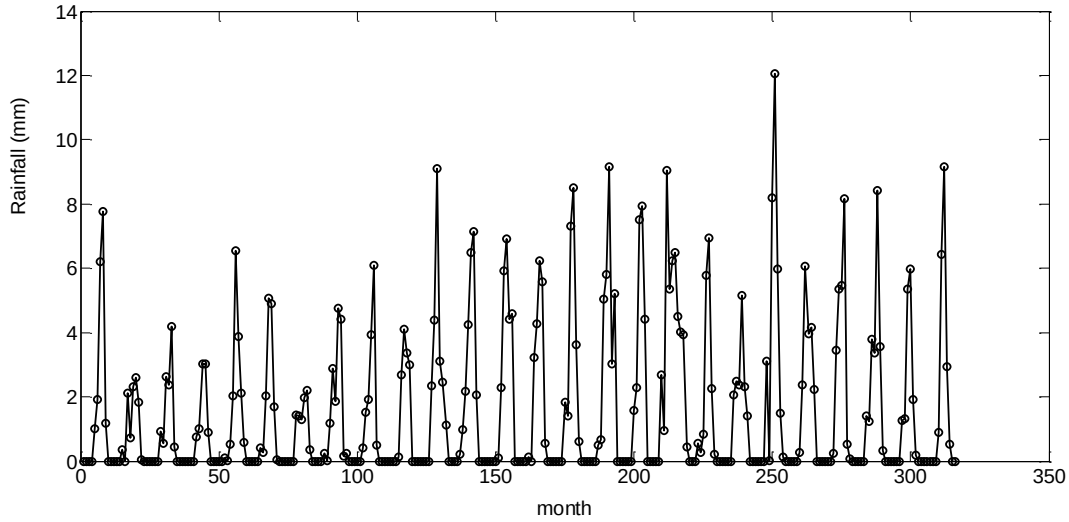

(b)

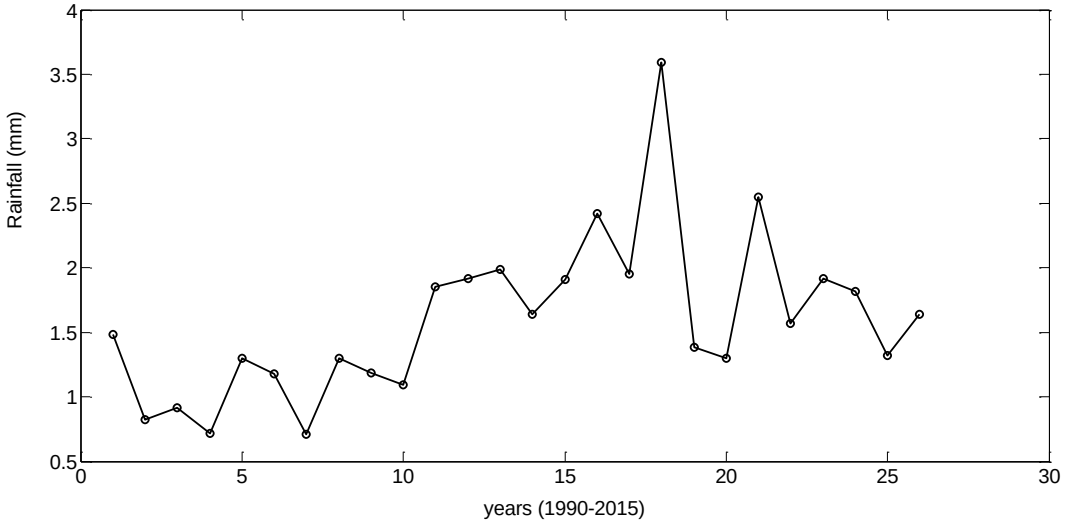

(c)

Figure 1: Time series for (a) daily, (b) monthly, (c) Yearly rainfall in Katsina from 1990-2015.

The summary of the trend analysis of the converted annual rainfall data using the Mann-Kendall trend test, Sen's slope estimator and Pearson's correlation coefficient are displayed in Table 2 and figure 2.

Table 2: Summary of the Mann-Kendall analysis for monthly and yearly rainfall in Katsina

Variable	Annual Rainfall (mm)
Pearson's correlation coefficient (*R*)	0.5029

Kendall tau	0.3846
Mann-Kendell coefficient S	125
Z statistic	2.7332
Hypothesis test (h=1: significant, h=0: not significant)	h=1
Trend description (from R and Z values)	Increasing trend
Trend Significance	Significant

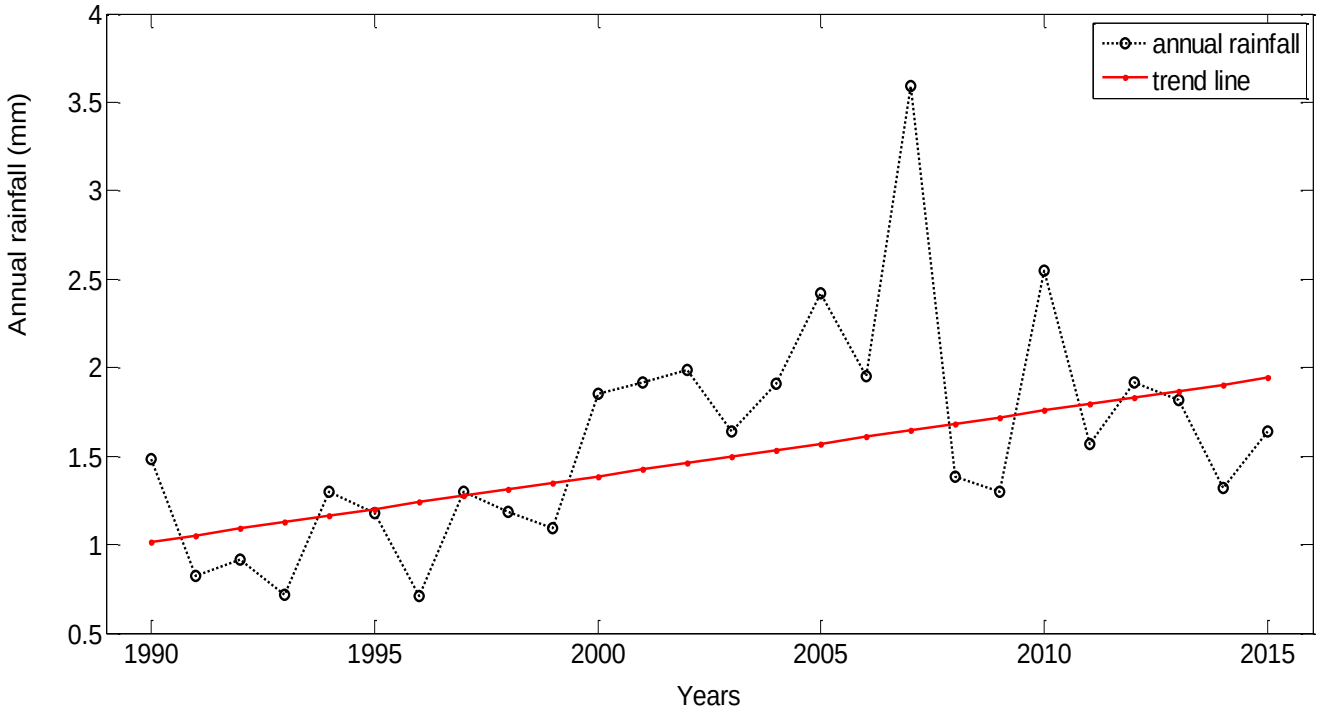

Figure 2: Rainfall trend for Katsina using Sen's slope model, $y = 0.037t - 72.64$ (increasing trend)

The trend analysis results in Table 2 (Mann-Kendall test) and figure 2 (Sen's slope estimator) indicates that the trends of the annual rainfall in Katsina is significant as the Z-statistic computed (2.73) is greater than the z-value at the level of significance (1.96). This implies an increasing trend in the mean annual rainfall in Katsina state. Hence there could be an increased risk of occurrences of flooding and surface run-off/erosion in the nearest future.

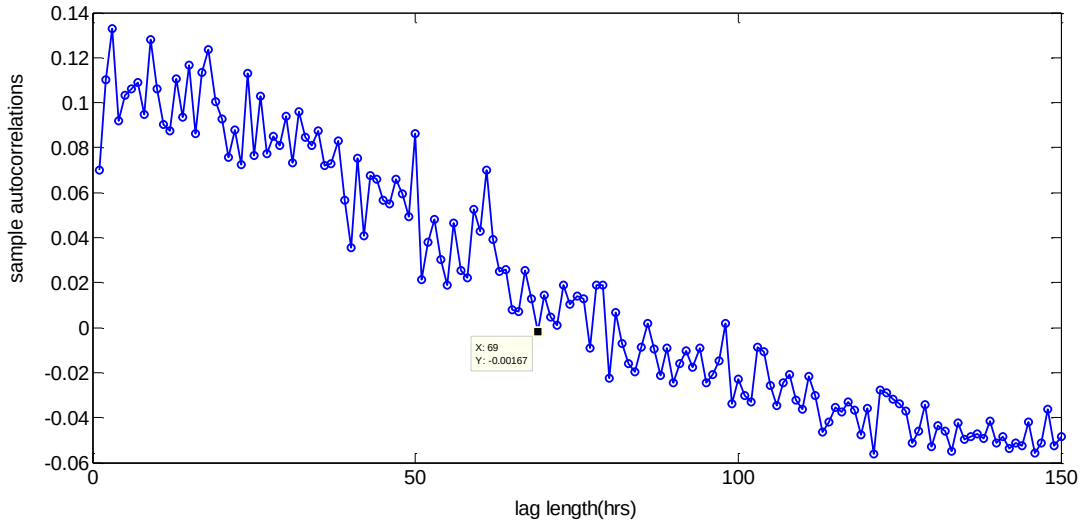

Figure 3: shows the estimation of time lag using the method of autocorrelation function criterion (ACF). A delay time of 69 days was calculated for the rainfall dataset.

Figure 4 illustrates the determination of the optimum embedding dimension using the method of false nearest neighbors (FNN). The rainfall data for Katsina was found to have an embedding dimension of eleven (m=11).

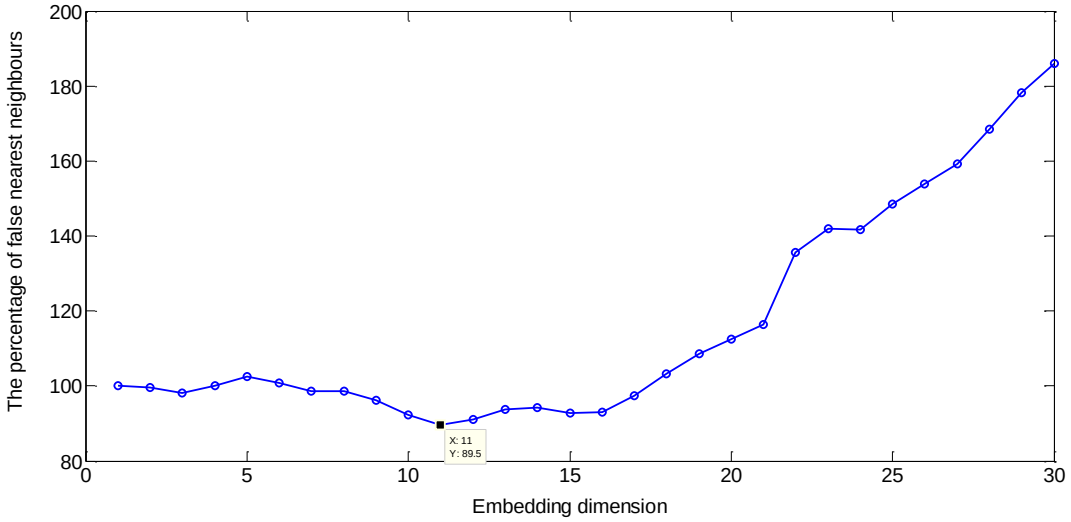

Figure 4: Percentage of FNN for Rainfall in Katsina (m=11)

Figure 5 (a) and (b) show the phase portrait and Poincaré map for rainfall constructed using the time lag and embedding dimensions calculated. The phase portrait exhibits a sponge-like geometry of distinct shapes while the Poincaré map shows scattered distinct points indicating the presence of random and chaotic dynamics in the rainfall time series. These plotted phase points are concentrated at the origin due to the numerous zeros (86.8%) in the rainfall dataset.

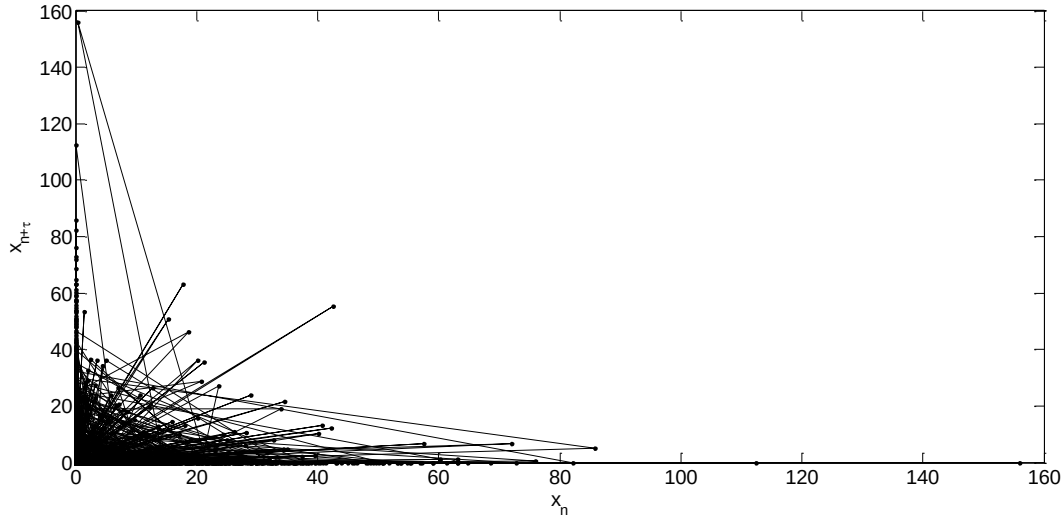

(a)

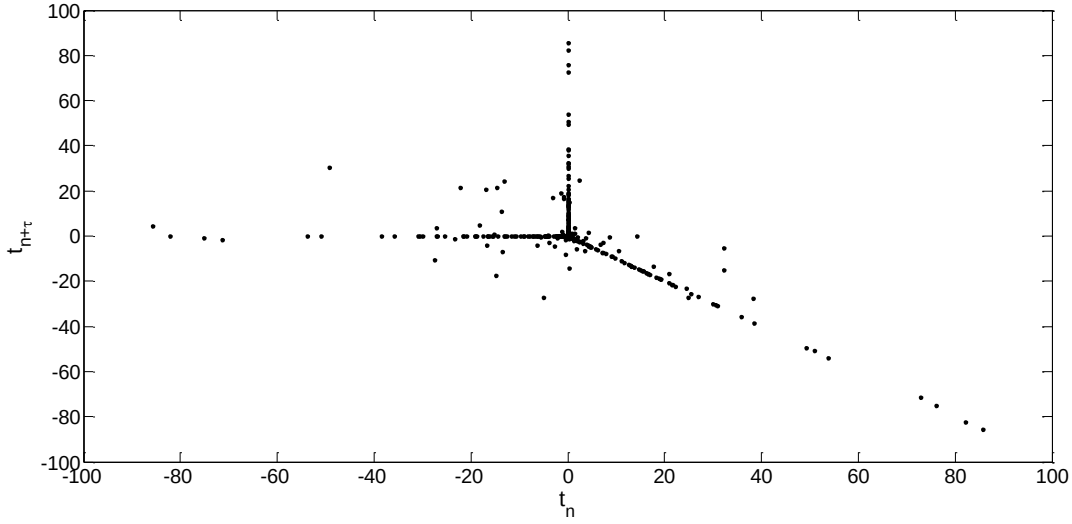

(b)

Figure 5: (a) Phase portrait, (b) Poincaré map of rainfall in Katsina

The correlation dimension was then calculated for the rainfall datasets using the time lag τ =2 and for increasing embedding dimensions, *m*, from 1 to 30.

Figure 5(a) is a plot showing the relationship between the correlation function *C(r)* and the radius *r* (i.e. $\log C(r)$ versus $\log r$) for increasing embedding dimension *m* while figure 6(b) shows the relationship between the correlation exponents and the embedding dimension values *m*. The correlation dimension ($\nu \approx 0.96$) is the saturation value of this plot.

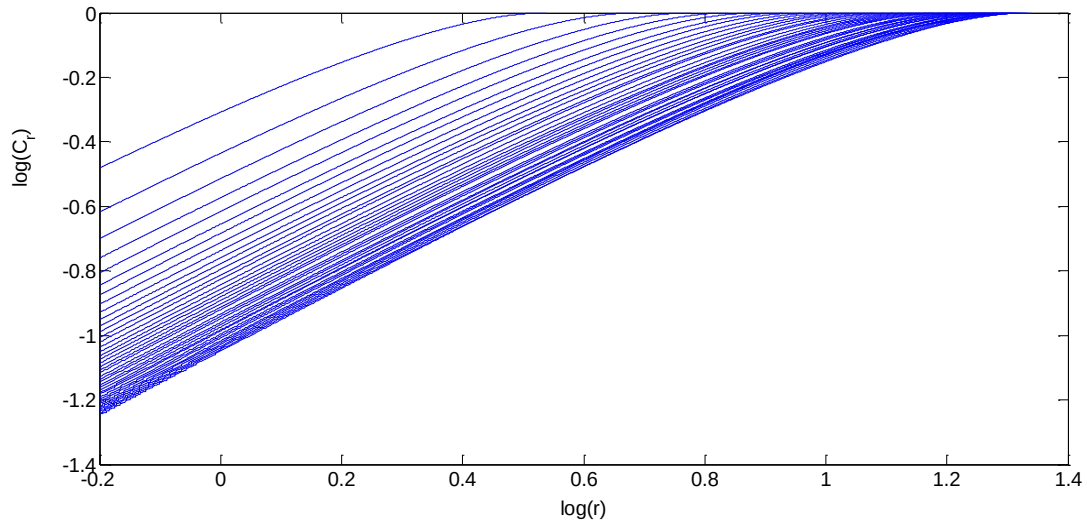

(a)

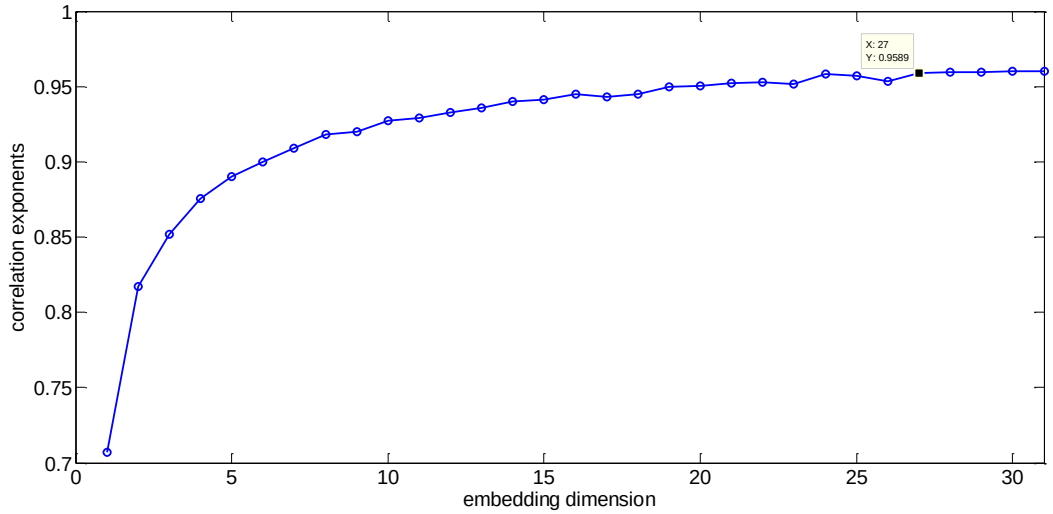

(b)

Figure 6: (a) Relationship between the correlation integral *C(r)* and the scaling radius *r*, (b) Relation between correlation exponent and embedding dimension *m* for Rainfall in Katsina (υ =0.9589 at m = 27).

The figures above, confirms the presence of low dimensional behavior in the rainfall time series as the value of the correlation exponents increase with the embedding dimension up to certain value and then begins to saturate. The saturation of the correlation exponent is an indication of the existence of chaotic dynamics. The correlation dimension computed is 0.96 for rainfall. This low value (ν<20) of correlation dimension suggest that there are some fractal characteristics in the rainfall time series. Similarly from the correlation exponent curves in figure 6(b), we can infer that the daily rainfall in Katsina requires about 11 to 27 independent variables to model its dynamics.

The results of the Lyapunov exponent, Kolmogorov-Sinai entropy and predictability computation for rainfall in Katsina using Rosenstein's algorithm are presented in the next section (figure 7).

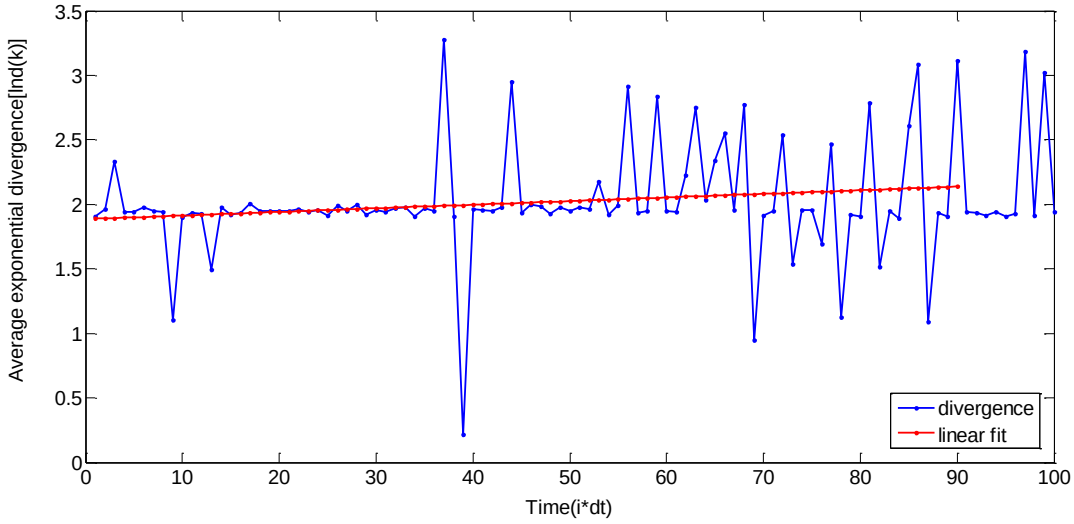

Figure 7: The Lyapunov spectrum for the estimation of the largest Lyapunov exponent for rainfall in Katsina state (λ = 0.00)

Table 3: the Lyapunov exponent values from m=1 to 11

Embedding dimension (m)	Lyapunov exponent (λ)
1	-0.000276756518481
2	-0.001538824833904
3	0.002798582842560
4	0.000583022388456
5	0.000177616855977
6	-0.000095179646034
7	0.000073595529012
8	-0.000044529646047
9	-0.000615826399598
10	-0.000628499196789
11	-0.000685778959816

Largest Lyapunov exponent, λ = 0.002799/day

Kolmogorov-Sinai entropy, K = 0.003633/day

Predictability, T_{max} = 357.32 days

T_{min} = 190.80 days

The largest Lyapunov exponent for the rainfall time series in Katsina was computed and found to be 0.002799/day while the K-S entropy was found to be 0.003633/day. The positive value of the Lyapunov exponent and finite value of the K-S entropy indicate a strong signature of chaos in the daily rainfall in Katsina over the last 26 years. This also indicates that the daily rainfall in Katsina is predictable for the next 190 to 357 days.

5. CONCLUSION

In this paper, a behavioral analysis of rainfall pattern in Katsina from the year 1990-2015 was carried out. The outcome of this analysis indicates that the rainfall in Katsina exhibits an increasing trend with high variance and low dimensional chaotic behavior. A minimum (maximum) of 11(27) independent variables is required to model the daily rainfall in Katsina while the rainfall is predictable in the next 190-357 days. It is recommended

that adequate measures such as accelerated afforestation programmes be launched to curb the effect of global warming and climate change which is responsible for increased fluctuations and chaos in weather making it more difficult for farmers to plan and optimize their agricultural activities.

6. ACKNOWLEDGEMENT

The authors wish to acknowledge the authorities of the Federal University Dutsin-ma, Katsina State, Nigeria for supporting them technically and financially during the period of this research.

REFERENCES

Christoph, A. and Frei. S. (2015) Analysis of Climate and Weather Data: Trend Analysis. http://www.iac.ethz.ch/edu/courses/master/electives/acwd/trend.pdf. Accessed on 10/10/2015.

Echi, M.I., Tikyaa, E.V. and Isikwue, B.C. (2015). Dynamics of Rainfall and Temperature in Makurdi, *International Journal of Science and Research*, 4(7), 493-499.

Ekmann, J. and Ruelle, D. (1985). Ergodic theory of chaos and strange attractors. *Review of Modern Physics*, 57, 617-656.

Fathima, T. and Jothiprakash, V. (2014). Behavioural Analysis of a Time Series-A Chaotic Approach, *Sâadhanâ,* 39(3), 659-676.

Grassberger, P. and Procaccia, I. (1983). Characterisation of Strange Attractors, *Physics Review letters*, 50, 346-349.

Hakki, E. (2006). On the Predictability of Time Series by Metric Entropy. M.Sc. Thesis, Graduate School of Engineering and Sciences, Izmir Institute of Technology, 211pp.

http://en.wikipedia.org/wiki/katsina_state.[Accessed: February 18, 2017].

Kennel, M., Brown, R. and Abarbanel, H. (1992). Determining embedding dimension for phase-space reconstruction using a geometrical construction, *Physical Review A*, 45(6), 3403-3411.

Khambhammettu, P. (2005). Mann-Kendall Analysis, Annual Groundwater Monitoring. *Report of HydroGeologic Inc.*, Fort Ord, California.

Kolmogorov, A.N. (1961). Local structure of turbulence in an incompressible liquid for very large Reynolds numbers. In Friedlander, S. K. and Topper, L. (eds). Turbulence: Classic papers statistical theory. New York, Interscience, p. 36.

Lai, L. (2004). Intelligent weather forecast. Third international conference on machine learning and cybernetics, Shanghai.

Lorenz, E. (1963). Deterministic non-periodic flow, *Journal of the Atmospheric Sciences*, 20(2), 41.

MathBits.com (2015). Statistics 2-Correlation Coefficient and Coefficient of Determination. http:// mathbits.com/MathBits/TISection/Statistics2/Correlation.html

McBean, E and Motiee, H. (2008). Assessment of Impact of Climate Change on Water Resources: A Long Term Analysis of the Great Lakes of North America, *Hydrology and Earth System Sciences*, 12**,** 239–255.

Olofintoye, O and Sule, B.F. (2010) Impact of Global Warming on the Rainfall and Temperature in the Niger Delta of Nigeria. *USEP: Journal of Research Information in Civil Engineering*, **7(**2), 33-48.

Ozer, B. and Akin, E. (2005) Tools for Detecting Chaos, *Sau Fen Bilimleri EnstitusuDergisi*, 9(1), 60-66.

Packard, N., Crutchfield, J., Farmer, J. and Shaw, R. (1980). Geometry from a Time Series, Physics *Review Letters*, 45, 712.

Pesin, Y. B. (1977). Characteristic Lyapunov exponents and smooth Ergodic theory. *Russian Mathematical Surveys*, 32, *55.*

Ramsey, J.B. and Yuan, B. J. (1989). Bias and error bars in dimension calculations and their evaluation in some simple models. *Physics Letters A*, 134, 397-398.

Rasoul, J., Mohammad, G. and Abolfaz, S. (2014). Dynamics of Rainfall in Ramsar, *Journal of Applied Science and Agriculture*, 9(4), 1371-1378.

Rosenstein, M., Collins, J. and De Luca, C. (1992). A practical method for calculating largest Lyapunov exponents from small data sets, *Physica D*, 65, 117-134.

Salmi T., Määttä A., Anttila P., Ruoho-Airola T., and Amnell T. (2002). Detecting Trends of Annual Values of Atmospheric Pollutants by the Mann-Kendall Test and Sen's Slope Estimates –The Excel Template

Application Makesens. *Finnish Meteorological Institute Publications on Air Quality*, No.31, Helsinki, Finland.
Sharma, A. and Manoria, M. (2007). A Weather Forecasting System using concept of Soft Computing: a new approach. *AIP conference proceedings India*, 923, 275.
Stehlík, J. (2006). Searching for Chaos in Rainfall and Temperature Records – a Nonlinear Analysis of Time Series from an Experimental Basin, *Na Sabatce*, 17(143), 4.
Takens, F. (1980). Detecting Strange Attractors in Turbulence, *Lecture Notes in Mathematics*, 898, 366.
Velickov, S. (2006). Nonlinear Dynamics and Chaos with Applications to Hydrodynamics and Hydrological Modeling. London, Taylor and Francis Group plc, pp. 76-79.
Zeng, X. (1993) Chaos Theory and its Application in the Atmosphere, *Atmospheric Science*, 504, 5-44.

DETERMINATION OF HEAVY METALS IN SELECTED VEGETABLES, ALONG LANDZUN RIVER OF BIDA, NIGER STATE, NIGERIA

Ajai, A. I[1]*., [1]Hassan, I. B[1] and Inobeme, A[2].
1. Department of Chemistry, Federal University of Technology, Minna
2. Department of Chemistry, Edo University Iyamho, Edo State

Ajai.ike@futminna.edu.ng; talk2alexajai@gmail.com
abelmichael4@gmail.com
* Corresponding Author

Abstract

The concentrations of heavy metals in selected vegetables along Landzun River of Bida, Niger State were determined in order to establish the levels of their contamination. The Vegetables samples (African Spinach, Jute mallow and Pumpkin) were collected from Bangaie-Bantuwa and Nasarafu-Edogifu along Landzun River (from upper, middle and down streams) and were analyzed for Cd, Cr, Mn, Ni and Pb using Atomic Absorption Spectrophotometer (AAS). The highest concentration of Cd (0.493±0.6mg/kg) was found in Pumpkin. This was higher than the permissible limit of 0.2mg/kg. Pumpkin leaves also recorded the highest concentration of Ni (1.33±0.03mg/kg), while Spinach had the highest concentration of Pb. With the exception of Cr and Pb, the contents of Mn, Cd and Ni were high in most of the samples analyzed when compared to the WHO/FAO standard hence may posed health challenge to the consumer. The concentrations of the metals were generally in the order Mn>Pb>Ni>Cd>Cr.

Key Words: Concentrations Vegetables, Heavy metal, Contamination, Spectrophotometer

1. Introduction

Vegetables are essential part of human's diets (Mercola, 2014). In addition to their possible source of important nutrients, they constitute important functional food components by contributing protein, vitamins, iron and calcium to human diet (Shobhana *et al.,* 2016). Sewage effluents apart from being a source of nutrient for plants also result to increase in the concentration of heavy metals in soil and passage of these metals along the food chain (Tasrina *et al.,* 2015). Plants and vegetables generally take in trace elements from contaminated soils and waste water used for irrigating as well as from deposits on different parts of the plants exposed to air from polluted environment (Hajeb, *et al.,* 2014). The leafy vegetables grown in heavy metals contaminated soils accumulate higher amounts of metals than those grown in uncontaminated soils because they absorb these metals through their root from the contaminated soil (Pathak, *et al.,* 2013). The uptake and accumulation of mineral nutrients by plants may usually follow two main paths i.e., through the roots and folia surface (Lugwisha and Othman, 2016). Uptake of trace metals from the soil is affected by several factors which include soil pH, plant growth stages, types of species, fertilizers and soil (Opajobe, *et al*., 2011).

Heavy metal refers to any metallic element that has comparatively high density and is toxic even at low concentration. It is a general collective term, which applies to the group of metals and metalloids with atomic density greater than 5g/cm^3 (Abimbola *et al.,* 2015). Heavy metals include Cadmium (Cd), Zinc (Zn), Mercury (Hg), Arsenic (As), Silver (Ag), Lead (Pb) Chromium (Cr), Copper (Cu), Iron (Fe) and Platinum group elements (Zhang, *et al.,* 2012). Heavy metals are not easily biodegradable and consequently can be accumulated in human vital organs and tissues resulting to various degrees of illness based on the level of exposures (Salawu *et al.,* 2015). Several heavy metals have been reported in edible plants consumed in different parts of the world. Among the heavy metals cadmium, mercury, arsenic and lead pose more challenges to human health on exposure (Echem, 2014).

The high consumption of vegetables from Landzun River bank of Bida area and their vast application in industries has prompted the need for the constant monitoring of the heavy metals present in them to ensure

they are not beyond permissible limit for consumption. Although studies have been conducted to assess the safety level of vegetables in different places around irrigation source, there is dearth of information from the River bank of Bida. Since some of these metals even at low concentrations can cause serious toxic effects in organisms, it is paramount to continually determine their levels in vegetables that are intended for human consumption from the view of public health. Thus, the aim of this study is to assess the level of heavy metal in selected Vegetable Plants along Bangaie-Bantuwa and Edogifu-Nasasrafu river Landzum of Bida local government, Niger State.

2. Materials and Methods

2.1 Study Area

River Landzun is located in Bida. Bida is the second largest city in Niger State, it is located Southwest of Minna, the Capital of the State. Niger State is located between latitudes 8Â°20'N and 11Â°30'N and longitude 3Â°30'E and 7Â°20'E. The state is bordered to the North by Zamfara State, to the Northwest by Kebbi State, to the South by Kogi State, to Southwest by Kwara State; while Kaduna State and the Federal Capital Territory border the state to the Northeast and Southeast, respectively (Ogbebor *et al.*, 2015).

2.2 Sample Collection and Preparation

Three different species of vegetable were used for this study. The specie includes Africa Spinach (*Amaranthus hybridus*), Jute mallow (*Corchurus olitorious*) and Pumpkin (T*elfara occidentalis*). The African Spinach and Jute mallow were collected from Bangai – Bantuwa (B-B) while Pumpkin (T*elfara occidentalis*) was collected from Edogifu−Nasarafu (E-N) Landzun river banks areas of Bida from upper (B-B_1 or E-N_1), middle (B-B_2 or E-N_2) and down (B-B_3 or E-N_3) streams. The samples were collected in June, 2015 and labeled in a polythene bags. The vegetables were washed with distilled water to remove any possible foliar contaminants, such as pesticides, fertilizers, dust and mud. The freshly collected samples were dried at room temperature. Each sample was separated into leaves and stems and the leaves were then grinded into finely particles using wooden mortar and pestle and sieved for wet digestion.

2.3 Method of Digestion and Analysis of Metals

2.0 g of the sieved impoverished samples was weighed into 50cm^3 beakers. 12cm^3 of HNO_3 and $HClO_4$ (3:1) were then added. The digestion was performed at a temperature of about 120^{0}C for two and half hours. After cooling, the digested solution was filtered and made up to mark with distilled water. The metals concentrations were determined using Atomic absorption spectrophotometer (AA240FS model). Each of the samples from different spot was analyzed in triplicates to obtain a representative result and the data reported in mg/kg.

2.4 Quality Control

All chemicals and reagents used in the experiments were of analytical grade and purchased from Merck (Darmstadt, Germany). All glassware used for digestion and preservation of the digested samples were washed with a solution of 10% of nitric acid followed by washing with double deionized water.

2.5 Data Analysis

The results obtained were subjected to statistical analysis by Analysis of variance (ANOVA) using SPSS 16 software. Mean values were analyzed by the Duncan's test.

3. Results and Discussion

Table1: Heavy Metal Concentrations in Jute Mallow (mg/kg)

Metals	B-B_1	B-B_2	B-B_3	Maximum limit FAO/WHO (2012)

Cd	0.153±0.006[a]	0.183±0.042[a]	0.117±0.081[a]	0.2
Cr	0.183±0.190[a]	ND	ND	2.3
Mn	4.500±1.817[b]	5.160±2.917[c]	3.55±0.385[a]	-
Ni	0.723±0.150[b]	0.577±0.117[a]	0.920±0.098[c]	0.2
Pb	3.713±0.227[a]	3.437±0.515[a]	3.020±0.599[a]	5.0

Results are expressed as mean ± standard deviation. Values with the same superscript on the same row do not differ significantly at $P<0.05$.

Key: B-B_1: Bangaie-bantuwa (upper area); B-B_2; Bangaie-bantuwa (middle area) and Bangaie-bantuwa (down areas); ND- Not Detected

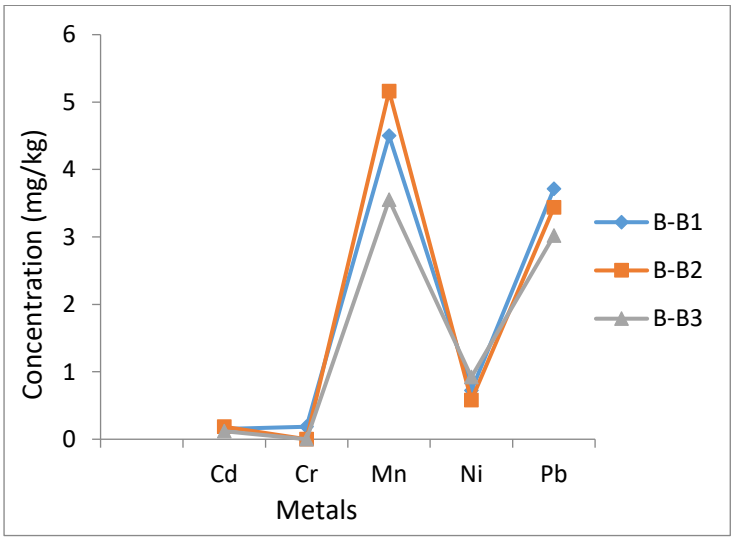

Fig. 1: Heavy Metal Concentrations in Jute Mallow (mg/kg)

Table 1 and figure 1 show the mean concentrations of heavy metals in Jute Mallows. The concentration of Cadmium ranged from 0.117±0.08 to 0.153±0.006mg/kg. Values for Cadmium obtained for Jute were not significantly different among the different areas at $p<0.05$. The upper stream has the least cadmium content. The range of values obtained for Cd is lower when compared to permissible limit of 0.2mg/kg documented in FAO/WHO, 2012. The content of Cd obtained is within the range of 0-2.4 mg/kg reported by Mutune *et al*., 2013 in a similar study. Cr was only found in the Upper stream were its concentration was 0.183±0.19mg/kg and lower than the allowed limit of 2.30mg/kg. It is also less than 1.50mg/kg reported by Abimbola *et al*., 2015. The concentration of Mn among the different areas differed significantly. The lowest concentration of Mn was 3.55mg/kg while highest was 5.160mg/kg; these were obtained at Downstream and Middle stream respectively. Nickel differed significantly among the different areas. The range of Nickel

content was from 0.577±0.12 to 0.920±0.10mg/kg. The concentration of Nickel is higher than the recommended standard of 0.2mg/kg recorded by FAO/WHO 2012. The highest and lowest concentrations of Pb in Jute Mallow were 3.713±0.227 and 3.020±0.599 mg/kg respectively. This is lower than the permissible level of 5.0 mg/kg. From table 1, it is clear that only chromium contamination in the Jute Mallow is observed as the concentration of the other metals are below their permissible limit of contamination. The high values of some of these metals is closely associated to the water absorb by the vegetables which might also show a high content of these metals. High concentration of Chromium in diet has deleterious effect to humans; it attacks DNA, proteins, and membrane lipids, thereby disrupting cellular integrity and functions (Naz, *et al*., 2015).

Table 2: Heavy Metal Concentrations in Spinach (mg/kg)

Metals	**B-B_1**	**B-B_2**	**B-B_3**	**Maximum limit FAO/WHO(2012)**
Cd	0.133±0.0153^{a}	0.197±0.021^{b}	0.177±0.252^{b}	0.2
Cr	ND	0.687±0.597^{ab}	1.243±0.616^{b}	2.3
Mn	8.523±1.392^{b}	3.160±0.496^{a}	3.343±0.461^{a}	-
Ni	0.810±0.210^{a}	0.753±0.106^{a}	0.773±0.138^{a}	0.2
Pb	3.960±0.269^{a}	3.613±0.370^{a}	3.600±0.118^{a}	5.0

Results are expressed as mean ± standard deviation. Values with the same superscript on the same row do not differ significantly at P<0.05.

Key: B-B_{1-3} -Bangaie-bantuwa (upper, middle and down streams) and ND: Not Detected

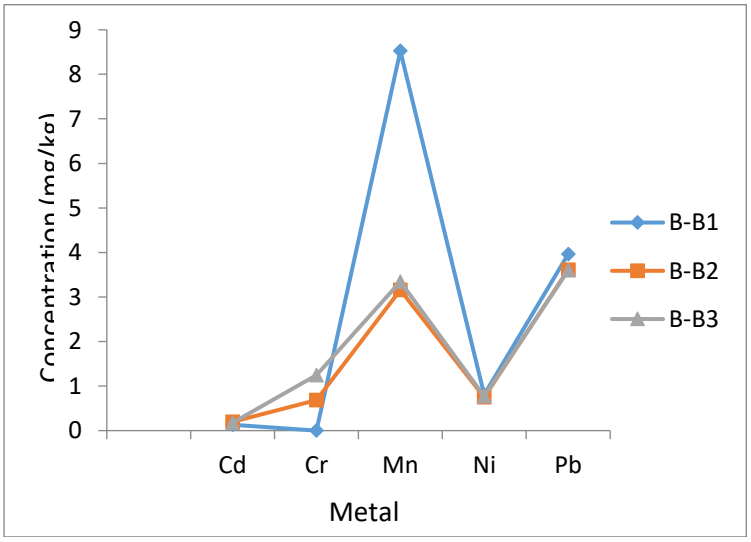

Fig. 2: Heavy Metal Concentrations in mg/kg of Spinach

From table 2 and fig. 2, the concentration of Cd in all the areas was lower than the permissible limit of 0.2mg/kg. The highest concentration of Cd was 0.197mg/kg which was at the middle stream. The value obtained for Cd in this study is higher than 0.03 µg/g obtained by Lugwisha and Othman, 2016 in a similar study on cabbage**.** Cr was not detected at the upstream. The highest value recorded for Cr in Spinach was 1.24mg/kg. The value obtained in this study is comparable to 0-1.2 mg/kg documented by Mutune *et al*., 2015 in his study on heavy metals in vegetables. There was a significant difference in the concentration of Mn in Spinach between the Upper and the other two areas. The highest concentration of Mn was 8.523±1.392 mg/kg while the lowest in Spinach was 3.160±0.496mg/kg. The concentration of Mn in the Spinach at upper stream was significantly higher than all others. The consumption of these vegetables may cause poisoning of the central nervous system and manganic pneumonia. The contents of Ni obtained in this study were generally lower than the permissible limit of 0.2mg/kg documented by WHO/FAO (2012). Pb contents in the Spinach were not significantly different at P<0.05. The values obtained were all below the tolerable limit.

Table 3: Heavy Metal Concentrations in mg/kg of Pumpkin

Metals	**E-N_1**	**E-N_2**	**E-N_3**	**Maximum limit WHO/FAO(2012)**
Cd	0.073±0.006^{a}	0.087±0.015^{a}	0.493±0.611^{b}	0.2
Cr	ND	ND	0.0015±0.023^{a}	2.3
Mn	15.230±1.796^{a}	32.333±1.974^{c}	17.660±2.266^{ab}	-
Ni	0.920±0.050^{a}	1.133±0.038^{b}	0.990±0.087^{a}	0.2
Pb	2.960±0.171^{a}	2.830±0.154^{a}	3.303±0.072^{b}	5.0

Results are expressed as mean ± standard deviation. Values with the same superscript on the same row do not differ significantly at P<0.05.

Key: E-N_{1-3}Edogifu-Nasarafu areas (upper, middle and down)

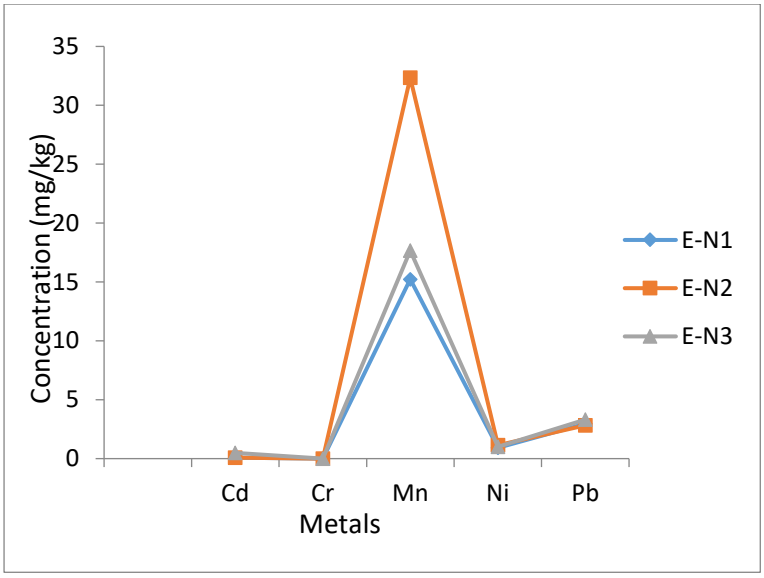

Fig. 3: Heavy Metal Concentrations in mg/kg of Pumpkin

The concentrations of trace metals in Pumpkin are shown in table 3. The highest concentration of Cd (0.493±0.611mg/kg) was at down area. The concentration at this area is significantly higher than others at $p<0.05$. The concentration of Cd obtained in this study is less than 0.1mg/kg reported by Tasrina *et al.*, 2015 in a similar study and 0.76± 0.2 reported by Lami, *et al.*, 2015. It is however above the permissible limit of 0.2mg/kg recorded in WHO standard above. Cr in pumkin was also detected at the samples from the Down area were the value recorded was 0.0015±0.02mg/kg. The result obtained for Cr is lower than the range of 8.5-21.0 reported by Akpan *et al*, 2015 in their study on Pumpkin leaves. The highest and lowest concentrations of Mn in the Pumpkin were 32.333±1.97 and 15.230±1.79mg/kg respectively. This is comparable to the findings of Akpan *et al.*, 2015. The values for Mn among the three areas were significantly different. Ni contents in the pumpkin were relatively higher when compared to the allowed limit of 0.2mg/kg. The highest concentration of Ni was 0.990±0.087 mg/kg, which is almost five times the permissible limit based on WHO/FAO, 2012. A number a researcher also reported also reported that consumption of heavy metals contaminated vegetables can pose serious health (Heidarieh, *et al*., 2013). The high levels of these metals in the water might be attributed to, apart from the natural sources, the indiscriminate discharge of wastes from nearby mechanic workshops, which could be from motor battery of Ni–Cd base, car paints, car panel beating wastes and solder for soldering car components as well as run-off from roadside car-wash sites. The highest concentration of Pb recorded in Pumpkin was 3.303±0.072 mg/kg. The concentration of Pb from this study is higher when compared to 0.119 mg/kg to 1.596 mg/kg reported by Tasrina *et al.*, 2015. It is also higher when compared to 0.005mg/kg in pumpkin reported by Otitoju *et al*, 2012. As well as 0.613 ± 0.0009mg/kg reported by Salawu *et al*., 2015. The order of trace metal content in the Pumpkin (Mn>Pb>Ni>Cd>Cr) is similar to the findings by Lami *et al.*, 2013 in a similar study.

4. Conclusion

The findings from this study show different levels of heavy metals concentrations in vegetables studied. With the exception of Cr and Pb whose concentrations in some of the samples being below their approved standard limit, the concentration of the other metals determined were higher than the WHO/FAO (2012) recommended

limit in vegetables, which implies that they could pose health threat to man. Generally, the increasing trend for the levels of heavy metals analyzed in the samples from this study are the order of Mn>Pb>Ni>Cd>Cr. However, the findings suggest that further work should be conducted on metals uptake by other species of vegetables and to continually monitor the concentrations of these metals in vegetables from water ways so as to ensure that they are within the permissible limit for human consumption.

References

Abimbola, W., Akindele, A., Agbolade, O. and Sam-Wobo S. (2015). Analysis of Heavy Metals in Vegetables Sold in Ijebu-Igbo, Ijebu North Local Government, Ogun State, Nigeria. *International Journal of Scientific and Engineering Research,* Vol. 6(11), 130-139

Akpan, I., William, E., and Inyang, E. (2015). Determination of Heavy Metal Contents in Fluted Pumpkin Leaves (*Telfairia Occidentalis*). Along Roadsides in Calabar, Nigeria. *European Scientific Journal*, Vol. 11(33), 1857 – 7881.

Echem, O. G (2014). Determination of the levels of Heavy Metal (Cu, Fe, Ni, Pb and Cd) Up take of Pumpkin (*Telfairia occidentalis*) Leaves Cultivated on Contaminated Soil. *Journal of Applied Science Environ. Management*, Vol. 18 (1), 71-77.

Hajeb, P., Sloth, J. J., Shakibazadeh, S., Mahyudin, N. A. and Afsah-Hejri, L. (2014). Toxic Elements in Food: Occurrence, Binding and Reduction Approaches. *Comprehensive Reviews in Food Science and Food Safety*, Vol. 13, 457-472.

Heidarieh, M., Maragheh, M. G., Shamami, M. A., Behgar, M. and Ziaei, F. (2013). Evaluation of Heavy Metal Concentration in Shrimp (*Penaeus semisulcatus*) and Crab (*Portunus pelagicus*) with INAA Method. Springer Plus, Vol. 2, 72.

Lami A., Nnamonu, O. A., Ogidi I. and Eneji, S. (2015). Analysis of Heavy Metals Content of Fluted Pumpkin (*Telfairia occidentalis*) leaves Cultivated on the North Bank of River Benue, Nigeria. *Food Science and Quality Management,* Vol. 39, 1-9.

Lugwisha E. H. and Othman C. O. (2016). Heavy Metal Levels in Soil, Tomatoes and Selected Vegetables from Morogoro Region, Tanzania, I*nternational Journal of Environmental Monitoring and Analysis,* Vol. 4(3), 82-88.

Mercola, J. (2014). Surprising Health Benefits of Vegetables. Available at: www.mercola.com. Accessed 23/01/2017.

Mutune, A. N., Makobe, M. A. and Abukutsa-Onyango, M. (2014). Heavy Metal Content of Selected African Leafy Vegetables Planted in Urban and Peri-Urban Nairobi, Kenya. *African Journal of Environmental Science and Technology,* Vol. 8(1), 66-74.

Naz, A., Khan, S., Muhammad, S., Khalid S., Alam, S., Siddique, S., Ahmed, T. and Scholz M. (2015). Toxicity and Bioaccumulation of Heavy Metals in Spinach (*Spinacia oleracea*) Grown in a Controlled Environment. *International Journal of Environmental Research and Public Health*, Vol. 12(7): 7400

Ogbebor, O. G., Obisesan, B., Madukwe, I. U. and Clement C. A. (2015). Prevalence of Undiagnosed HIV Infection among Dental Patients in a Nigerian Secondary Healthcare Facility. *Journal of International Society of Preventive and Community Dentistry*, Vol. 5(3), 2-3.

Opajobe, A. O, Esume, C. O, Osasuyi, A., Okehie, C. C. (2011). Determination of the Lead Content of Pumpkin Leaf (*Telfairia occidentalis*) in Selected Towns of Delta State Covering the three (3) Senatorial Districts of the State. *Curriculum and World Environment*, Vol. 6(1), 39-44.

Otitoju, O., Akpanabiatu, M. I., Otitoju, G. T. O., Ndem, J. I., Uwah, A. F., Akpanyung, E. O. and Ekanem J. T. (2012). Heavy Metal Contamination of Green Leafy Vegetable Gardens in Itam Road Construction Site in Uyo, Nigeria. *Research Journal of Environmental and Earth Sciences* Vol. 4(4), 371-375.

Pathak, C., Chopra, A. K. and Srivastava, S. (2013). Accumulation of Heavy Metals in *Spinacia oleracea* Irrigated with Paper Mill Effluent and Sewage. *Environment Monitoring and Assessment*, Vol. 185, 7343-7352.

Salawu, K., Barau, M. M., Mohammed, D., Mikailu, D. A., Abdullahi, B. H. and Uroko, R. I. (2015). Determination of some selected heavy metals in spinach and irrigated water from Samaru Area within Gusau Metropolis in Zamfara State. *Nigeria, Academic Journals*, Vol. 7(8), 76-80.

Shobhana R., Bharat L., Nohar S. D., Khageshwar S. P., Borislav B, and Laurent M. (2016). Heavy Metal Contamination of Vegetables. *Journal of Environmental Protection*, Vol. 7, 996-1004.

Tasrina, R. C, Rowshon, A., Mustafizur, A. M. R, Rafiqul, I. and Ali, M. P. (2015). Heavy Metals Contamination in Vegetables and its Growing Soil. *Journal of Environmental Analytical Chemistry* Vol. 2 (3), 2380-2391.

ANALYSIS OF EFFECTS OF UNDESIRED COURSE OF STUDY ON STUDENTS' ACADEMIC ACHIEVEMENT IN NIGERIA, USING BINARY LOGISTIC REGRESSION APPROACH

O. M. Adetutu*, O. M. Otu, A. O. Bello, I. S. Onotu and U. Abdullahi
Department of Statistics, Federal University of Technology, Minna, Niger State, Nigeria

*ola.adetutu@futminna.edu.ng
mjamiu4u@yahoo.com
oyedele.bello@futminna.edu.ng
idris.onotu@futminna.edu.ng
u.abdullahi@futminna.edu.ng

Abstract

The obvious important of knowledge creation to development has long place University at the Centre of the effort of Governments to increase the rate at which their economies grow.
Education been the best legacy any nation can give her citizens especially the youth, the development of any nation depend largely on the quality of education of such nation. Therefore, Students' academic achievement plays a significant role in producing the pre-eminent quality graduates who will become great leader and manpower of the country and hence responsible for the country's economic and social development.
This research work was conducted to examine the effects of undesired course of study on students' academic performance in tertiary institution in Nigeria. The main method of data collection was through questionnaire which was administered to 400 students in Federal University of Technology, Minna Nigeria. The specific objectives of the study were to determine the effects of undesired course of study on students' academic performance, and to examine if factors such as gender, age, satisfaction with the course of study affect students' academic performance. The student cumulative grade point average (CGPA) was used as a measure of academic performance. The data were analyzed quantitatively using binary logistic regression approach and the results revealed that factors such as satisfaction with course of study and undesired course of study affected students academic performance. However factors like age and gender difference did not significantly affect students' academic performance.

Keywords: academic, performance, undesired, questionnaire, *binary logistic regression, cumulative grade point average (CGPA)*

1. Introduction

All centres of learning such as schools, colleges and universities are worthless without students; this is because students are the most indispensable asset of any institution. The social and economic growth of any nation is directly allied with students' academic performance, because education is a strategic factor for achieving a long-term economic development.
The Nigerian educational system has extremely improved in the last-decades. However, this progress keeps Nigeria at other country's tail end due to its high rates of students' failure and drop out.
According to Ali and et.al (2009) students' academic achievement plays a significant role in producing the pre-eminent quality graduates who will become great leader and manpower of the country and hence responsible for the country's economic and social development: Ali and et.al (2009).
According to Cambridge University Reporter (2013) success has a great influence on a student's self-confidence, enthusiasm, and perseverance in higher education. High rate of academic failure may have results due to lack of satisfaction with the course of study, levels of attrition, and increased cost of education. And this might reduce admission opportunities for students seeking higher degrees or further study.
Academic achievement of students has being an interested topic for educators and researchers. They have been fascinated in identifying and understanding the factors that contribute to students' academic excellence as well as that of its failure. Student academic performance measurement has considerably received attention in previous studies. Various researchers have researched on issues including gender and age difference, lecturers'

or teachers' level of education and their teaching styles, class environment, social economic factors, and educational back-ground of the parents etc. and their discoveries from this studies varies from region to region and their results differs in cities and rural areas.
However, students enrolled in various tertiary institutions in Nigeria may have come from different educational backgrounds, but still, they are provided with the same educational services and equipment in their respective institutions; and some of them still perform significantly better than others academically. Could this be as a result of given such students their desired course of study?
This research is to ascertain the effect or non-effect of undesired course of study on students' academic performance and make recommendations to the policy maker on ways of addressing them so that educational performance of students can be enhanced. Student academic performance was measured through their cumulative grade point average (CGPA) and students CGPA being an important contributing factor in the future of any student's career. We decided to conduct this research to investigate the hidden relation between undesired course of study and students' performance using Federal University of Technology, Minna (FUTMINNA) as case study. Making assumption that, students who are given a desired course of study will achieve a CGPA of 3.00 and above, and have a higher level of concentration.

This research work aim to contribute to the prevalent knowledge by statistically documenting the effect of undesired course of study on students' academic success or failure in tertiary institution in Nigeria, using FUT Minna as a case studied.

Null Hypothesis (Ho)
There is no significant relationship between the explanatory variables (undesired course, level of satisfaction, age and gender differences) and the dependent variable (academic performance).

Alternative Hypothesis (Ha)
There is a significant relationship between the explanatory variables (undesired course, level of satisfaction, age and gender differences) and the dependent variable (academic performance).

Decision rule:
The null hypothesis will be rejected if the sig-value is less than Alpha (α) at 5% level of significance.

2. Literature Review
Educational achievements of youths require urgent attentions to achieve their goals. Various researches have been made to determine factors that contribute to the educational success of students. Customarily, in any research a researcher always takes the advantages of the information and knowledge that had been accumulated in the past as a result of constant investigation endeavour by mankind.
Previous researches studies have identified several factors that affect students' academic performance in various educational centres. Some of these factors include gender, class attendance, class size, age, entry qualifications, learning style or preferences, family educational background and income etc.
Researchers such as Borde (1998), Hedges and Newell (1999) and Woofield and et al (2006); considered the rate of gender to academic performance. Borde (1998) in his own work stated that gender play a significant role in students' performance. However, he noted that gender difference of student varies from one setting to another. There are setting where female student outer-performed their male counter-part and some other setting where the male performed better than the female. This suggests the need for every research considering gender be performed uniquely to the desired settings. Hedges and Navel (1999) further unveiled the settings where male is expected to perform better than female and vis-visa. Hedge and Navel (1999) concluded that male performed better than female in science subjects and while female performed better in reading and writing just as Aggrawal (1993) has discovered years earlier.

Several studies have shown that academic achievement differs across nationality. Yousef (2011) makes an investigation on academic performance of foreign students. The result of this study revealed that foreign students performed better than local students in business studies.
Gareth and et al (2013) statistically predicted the causes of poor academic performance of school students in a research he conducted on a sample of 200 high school students' of Zimbabwe. Data were gathered through interview he carries out with students. The outcomes of the study revealed that there is dissimilarity in

academic achievement of female and male students with male students performing better while educational background of parents had a significant effect on academic achievement of students.
Bahago (2011) conducted a research on the influence of educational motivation and demographic characteristics on academic performance of nomadic Fulani girls in Adamawa state, Nigeria. The data for the research was collected from a sample of 300 girls randomly selected from polytechnics by administering active-motivation rating scale and nomadic girls' achievement test. The outcome of the research showed that educational levels of parents significantly influence students' academic performance.

3. Methodology

This section described precisely the methodology that was used to reveal some statistical evidence about the effects of undesired course of study on students' academic performance.

3.1 Data Collection

The data for this research work was collected randomly using questionnaire from students of Federal University of Technology Minna, Nigeria. Total samples of 400 questionnaires were distributed and 347 were analysed due to some non-respondents.
In the questionnaire, Students were asked to indicate their gender, level, Cumulative Grade Point Average (CGPA). They were asked to specify whether they are given their desired course of interest at the time of admission and there level of satisfaction base on the given course of study. Additionally, they were asked to indicate there level, school (faculty), and department.
The data obtained from respondents were analysed using binary logistic regression analysis. Students' academic performance was measured using their Cumulative Grade Point Average (CGPA) and were identified as the dependent variable and were categorised in to dichotomous values (0, 1). CGPA of 3.00 and above was represented as 1, while CGPA of 2.99 and below was represented as 0. Other variables (undesired course, age, sex, and level of satisfaction) were used as the explanatory variable to predict the performance of students. All the data collected from this survey was processed using SPSS software (Statistical Package for the Social Sciences).
After the completion of each questionnaire by the respondents, we (researcher) reviewed them so as to ensure that there are no missing items. The resulting data was entered into a database for processing using SPSS. Descriptive statistics were used to make a description of the responded population.

3.2 Method of Statistical Analysis

The method of analysis used in this research work is binary logistic regression analysis. Binary logistic regression is more appropriate since the dependent variables are either categorical or continuous variables. Logistic regression analysis is a statistical analysis that determines the influence of various factors on a dichotomous outcome by calculating the changes in the log odds of the dependent as opposed to the variable itself. In logistic regression, log odds ratio provides a basic description of the probabilistic relationship of the variables and the outcome in comparison to a linear regression by which more information about the linear relationship can be drawn.
Logistic regression is a special case of the generalized linear model and is comparable in certain respect to linear regression. However, the assumption of logistic regression model is quite different from ordinary linear regression model in that the logistic regression takes on a linear relationship between the logit of the outcome variables and the predictor variables. However, it does not assume a linear relationship between the actual outcome and the predictor variable. Secondly, the sample is 'large'-reliability of estimate declines when there are only a few cases, noting that the predictor variables are not linear functions of each other and the usual normal distribution is not necessary or assumed for the outcome variable. Lastly, each and every levels of the independent variable are not necessarily homoscedasticity, as the explanatory variables need not to be interval level.

3.3 The Logistic Regression Model

The aim of a logistic regression is to find the most suitable fitting model to describe the relationship between the dichotomous characteristics of interest (dependent variable or outcome variable) and a set of independent (predictor or explanatory) variables.

Suppose a binary variable y follows a Bernoulli distribution, that is, y takes either the value 1 or the value 0 with probabilities π(x) or $1 - \pi(x)$ respectively, where $x = (x_0, x_1, \dots x_p) \in R$ is a vector of p explanatory variables. This means, π(x) represents the conditional probability $p(y/x)$ of $y = 1$ given x. Based on the binary outcome variable, we use the logistic distribution and specific form of logistic regression model with unknown parameters $\beta_0, \beta_1, \dots \beta_p$ is given as,

$$\pi(x) = \frac{\exp(\beta_0 + \beta_{1x_1,\dots+}\beta_{px_p})}{1+\exp(\beta_0 + \beta_{1x_1,\dots+}\beta_{px_p})} \qquad equation\ (1)$$

At times, it is convenient to change the notation slightly writing $x_0 = 1$, thus the above model becomes, $\exp(x^{T\beta})$

$$\pi(x) = \frac{e^{x^{T\beta}}}{1+e^{x^{T\beta}}} \qquad equation\ (2)$$

Where $(x_0, x_1, \dots x_p)^T$ and $\beta = (\beta_0, \beta_1, \dots \beta_p)^T$

A transformation of $\pi(x)$ is called the logit transformation and is given by

$$Logit\ \pi(x) = ln\frac{\pi(x)}{1-\pi(x)} \qquad equation\ (3)$$

Under the above transformation, we can write the regression model as,

$$Logit\ \pi(x) = x^{T\beta} \qquad equation\ (4)$$

This implies that $Logit\ p = b_0 + b_{1x_1}, \dots + b_{kx_k}$ $\qquad equation\ (5)$

Where p, is the probability of presence of the characteristic of interest and the logit transformation is defined as the logged odds.

$$Odds = \frac{p}{1-p} = \frac{\text{probability of presence of characteristic}}{\text{probability of absence of characteristic}}$$

And $Logit\ (p) = \ln(\frac{p}{1-p})$ $\qquad equation\ (6)$

3.4 Wald Test

Wald test is a statistic that examines the contributions of each of the predictors in a given model. The Wald statistic is comparable to the T-test in linear regression, which assesses the significance of the coefficients. Wald test is defined as the ratio of the square of the regression coefficient to the square of the standard error of the coefficient and it is asymptotically distributed as a chi-square distribution. It tests the following hypotheses:

H_0: The regression coefficients are zero

H_1: The regression coefficients are not zero

The Wald statistic is given as; $W = \frac{\beta}{SE(\beta)}$

3.5 Odds and Odds Ratio

The odds ratio is a measure of relationship which expresses the association between an exposure and outcome from a comparatives study. In other words, the odds ratio is one of a range of statistics used to assess the risk of a particular outcome, if a certain factor (or exposure) is present. It is a relative measure of risk, telling us how much likely it is that someone who is exposed to the factor under study will develop the outcome as compared to someone who is not exposed. While, the term "Odds" are method of presenting chances. That is, the odds of an event happening is the probability that the event will happen divided by the probability that the event will not happen.

Odds ratio is used because it does adequately provide an estimate (with confidence interval) for the relationship between the two dichotomous variables also enable us to thoroughly determine the influences of other variables on the relation, using logistic regression and their interpretation is special and convenient. Therefore, it is essential to introduce the term odds and odds ratio to discourse binary data and to interpret the logistic regression coefficients. For a probability π of success, the odds are defined to be;

$$\text{Odds} = \frac{\pi}{1-\pi}$$

The odds are nonnegative and odds > 1.0 when a success is more likely than a failure.

In a 2×2 table, the probability of success is π_1 in row 1 and π_2 in row 2. Within row 1, the odds of success and defined to be,

$$Odds_1 = \frac{\pi_1}{1-\pi_1}$$

And within row 2, the odds of success are defined to be,

$$Odds_2 = \frac{\pi_2}{1-\pi_2}$$

The ratio of the odds from the two rows is called the odds ratio, which is given by, $Odds\ Ratio = = \frac{\frac{\pi_1}{1-\pi_1}}{\frac{\pi_2}{1-\pi_2}}$

4. Results and Discussion

Table 4.1: Case processing summary table

Case Processing Summary

Unweighted Cases[a]		**N**	**Percent**
Selected Cases	Included in Analysis	290	83.6
	Missing Cases	57	16.4
	Total	347	100.0
Unselected Cases		0	.0
Total		347	100.0

a. If weight is in effect, see classification table for the total number of cases.

Table 4.1 provides us with the summary of the analysis. Thus there are 347 (100%) total cases for the analysis for which 290 (83.6%) cases are included in the analysis. However, 57 (16.4%) of the cases were missing which result due to the fact that some of the students were not having cumulative grade point average (CGPA)

Table 4.2: Variables in the Equation

Variables in the Equation

		B	**S.E.**	**Wald**	**Df**	**Sig.**	**Exp(B)**
Step 1[a]	SATISFACTION			39.321	4	.000	
	SATISFACTION(1)	-.156	.497	.099	1	.753	.855
	SATISFACTION(2)	-1.298	.473	7.532	1	.006	.273
	SATISFACTION(3)	-3.249	.652	24.831	1	.000	.039
	SATISFACTION(4)	-1.645	1.014	2.629	1	.105	.193
	GUC(1)	-.578	.287	4.058	1	.044	.561
	SEX(1)	.533	.287	3.448	1	.063	1.704
	AGE	-.030	.053	.321	1	.571	.970
	Constant	2.079	1.296	2.574	1	.109	7.996

a. Variable(s) entered on step 1: SATISFACTION, GUC, SEX, AGE.

Table 4.2 provides detail information about the contributions and significance of each of the explanatory variables. It shows the logistic coefficient (B), Wald test and odds ratio for each predictor variable. The logistic coefficient is the expected amount of change in the logit for each one unit change in the predictor variable. The logit is what is being predicted, it is the odds of membership in the category of the outcome variable with the numerically higher value (here 1 rather than 0) the closer a logistic coefficient is to zero, the less influence

it has in the predicting the logit. The variables that contribute significantly to the predictive ability of the model are GUC and SATISFACTION. The following are the interpretation of the respective predictor variables.

4.1 Satisfaction

Satisfaction is a significant predictor of academic performance with sig (p-value) equal 0.000, which is less than 0.05, looking at individual's contributions of the dummy variable. For the first dummy variable SATISFACTION(1) which stand for satisfaction and the negative sign in its coefficient means that, the odds of achieving a CGPA of 3.00 or above is lower for students that are satisfied with the course of study compare to those that are highly satisfied. This implies that, the probability of achieving a CGPA of 3.00 or above for students that are satisfied with the course of study is lower compare to students that are highly satisfied with the course of study.

The odds ratio for SATISFACTION (1) is 0.855 and this implies that, students that are satisfied with the course of study are 0.855 times less likely to achieve a CGPA of 3.00 or above than those that are highly satisfied with the course of study holding other independent variables fixed. In percentage, the odds of achieving a CGPA of 3.00 or above is 14.5% = {(0.855-1)*100%} lower for students that are satisfied with the course of study compare to those that are highly satisfied with the course of study.

For the second dummy variable SATISFACTION(2) which stand for moderately satisfied and the negative sign in its coefficient mean that the odds of achieving a CGPA of 3.00 or above is going to be lower for students that are moderately satisfied with the course of study compare to those that are highly satisfied with the course of study. This implies that the probability of students to achieve a CGPA of 3.00 or above given that they are moderately satisfied with the course of study is lower compare to those that are highly satisfied.

The odds ratio is 0.273 and this shows that, students that are moderately satisfied with the course of study are 0.273 times less likely to achieve a CGPA of 3.00 or above than those that are highly satisfied with the course of study holding other independent variables fixed. In percentage, the odds of achieving a CGPA of 3.00 or above is 72.7% = {(0.273-1)*100%} lower for students that are moderately satisfied with the course of study than those that are highly satisfied holding other independent variable fixed.

For the third dummy variable SATISFACTION(3) which stand for dissatisfied and the negative sign in its coefficient indicate that the odds of achieving a CGPA of 3.00 or above is going to be lower for students that are dissatisfied with the course of study compare to those that are highly satisfied. This implies that the probability of students to achieve a CGPA of 3.00 or above given that they are dissatisfied with the course of study is lower compare to those that are highly satisfied.

The odds ratio for SATISFACTION (3) is 0.039 and this means that the odds of achieving a CGPA of 3.00 or above for students that are dissatisfied with the course of study is 0.039 times lower than the odds of students that are highly satisfied with the course of study holding other independent variable fixed. In percentage, the odds of achieving a CGPA of 3.00 or above is 96.1% = {(0.039-1)*100%} lower for students that are dissatisfied with the course of study than those that are highly satisfied, holding other independent variables fixed.

For the fourth dummy variable SATISFACTION(4) which stand for highly dissatisfied, the negative sign in its coefficient those that the odds of achieving a CGPA of 3.00 or above is going to be lower for students that are highly dissatisfied with the course of study compare to those that are highly satisfied. This implies that the probability of students to achieve a CGPA of 3.00 or above given that they are highly dissatisfied with the course of study is lower compare to those that are highly satisfied with the course of study. The odds ratio for SATISFACTION (4) is 0.193 and this implies that, students that are highly dissatisfied with the course of study are 0.193 times less likely to achieve a CGPA of 3.00 or above than those that are highly satisfied, holding other independent variables fixed. In percentage, the odds of achieving a CGPA of 3.00 or above is 77.6% = {(0.193-1)*100%} lower for students that are highly dissatisfied with the course of study than those that are highly satisfied with the course of study holding other independent variables fixed.

4.2 Given Undesired Course of Study GUC

Since the sig (p-value) is 0.044, which is less than 0.05, therefore this predictor variable (GUC) is statistically significant and the negative sign in its coefficient means that, the odds of achieving a CGPA of 3.00 or above is going to be lower for students that are given an undesired course of study (GUC) than those that are not.

This implies that the probability of students to achieve a CGPA of 3.00 or above given that they are given an undesired course of study is lower compare to those that are given a desired course of study.
The odds ratio for GUC is 0.561 and this implies that, when holding all other variables constant, students that are given an undesired course of study are 0.561 times less likely to achieve a CGPA of 3.00 or above than those that are given a desired course of study. In percentage, the odds of achieving a CGPA of 3.00 or above is 43.9% = {(0.561-1)*100%} lower for students that are given an undesired course of than those that are given a desired course of study holding other independent variables fixed.

4.3 Sex

Since the sig (p-value) is 0.063 which is greater than 0.05, therefore this predictor variable (SEX) is not statistically significant. The positive sign in its coefficient implies that the odds of achieving a CGPA of 3.00 or above are higher for male students than female students. In other word, the probability achieving a CGPA of 3.00 or above for male students is higher compare to female students. The odds ratio for SEX is 1.704 and this implies male students are1.704 times more likely to achieve a CGPA of 3.00 or above than female students. In percentage, the odds of achieving a CGPA of 3.00 or above is 70.4% = {(1.704-1)*100%} higher for male students than female students holding other independent variables fixed.

4.4 Age

Since the sig (p-value) is 0.571, which is greater than 0.05, thus it is not statistically significant. The negative coefficient means those students that are of young age are more likely to achieve a CGPA of 3.00 or above compare to those that are of old age. The odds ratio for AGE is .970 and this implies when holding all other variables constant, students of young age are 0.970 times more likely to achieve a CGPA of 3.00 or above than those of old age.
In percentage, the odds of achieving a CGPA of 3.00 or above is 3.0% = {(0.970-1)*100%} higher for younger age students than those that are of old age, holding other independent variable fixed.

4.5 Discussions

The outcome of this research work revealed that given students a desired course of his interest improved its cumulative grade point average (CGPA) significantly; also students that were given an undesired course to study find it difficult to achieve a cumulative grade point average (CGPA) of 3.00 or above. We also observed that students that were highly satisfied with their course of study are more likely to achieve a CGPA of 3.00 or above, where those that highly dissatisfied are more likely to achieve a cumulative grade point (CGPA) of 2.99 or below.
We also have discovered from our findings that students that are of young age have a high probability of achieving a CGPA of 3.00 or above in comparison to students that of old age. However, research statistically revealed that both age, sex are not a good predictor of students' academic performance base on this research work. These results also revealed that students of young age are more likely to achieve a better academic performance than their old students' counterpart.

5.0 Conclusion

It appeared that many students tend to be struggling to maintain a CGPA of 3.00. Consequently, there must be copious debatable factors that can possibly contribute to the deterioration of student's academic performance and one major responsible factor could be undesired course of study.
The factors investigated in this research work were not exhaustive; there are numerous additional factors that affect academic achievement of students. However, it can be concluded from this study that given students undesired course of study significantly affect his/her academic achievement. And also, it is of prominence to conclude that lack of satisfaction on the course of study greatly affected the performance of student.

5.1 Recommendations

The following are the recommendations I think may be of useful solution to the identified factors and other factor as they affect students' academic achievement in Nigeria.

The Nigerian university commission (NUC), tertiary institutions, and other Centre of learning in Nigeria, if not stop should reduce the rate at which students are been given an undesired course to study so that student academic performance can be improve and the economy of the country.
Parents should exempt from deviating their children from their desires course for their own interest. And various center of learning should ensure that necessary orientation is given to student after admission.
Tertiary institution should provide those students who are achieving at lower levels with educational support and educational resources in order to bridge the achievement gap.
More research is suggested to explore other variables that influence students' academic achievement.

References

Aggarwal, V.R. (1993) A Study of Reading Ability in Relation to Certain Cognitive and Non-cognitive Factors.Asian Journal of Psychological Education11, 3, 41

Ali, Norhidayah, Jusoff, Kamaruzaman, Ali, Syukriah, Mokhtar, Najah and Salamt, Azni Syafena Andin.(2009). 'The Factors Influencing Students' Performance at Universiti Teknologi MARA Kedah, Malaysia'. Canadian Research and Development Center of Sciences and Cultures: Vol.3 No.4.

Ali, S., Haider,Z., Munir, F., Khan, H., and Ahmed, A. (2013). Factors Contributing to the Students' Academic Performance: A Case Study of Islamia University Sub-Campus. American Journal of Educational Research, 1, 283-289.

Bahago,Beatrice Ahmadu (2011) Intelligence of Achievement Motivation and Demographic Characteristic on Academic Performance of Nomadic Fulani Girls in Adamawa State. Submitted to the School of Postgraduate Studies, University of Jos. Retrieved from Internet on July 20, 2011.

Borde, S. F. (1998). Predictors of student academic performance in the introductory marketing course. Journal of Education for Business, 73, 302-307.

Cambridge university reporter (2013). Indicators of academic performance available: http://www.admin.cam.ac.uk/reporter/2002-03/weekly/5915/[accessd Feb. 12, 2014]

Gareth James; Daniela Witten; Trevor Hastie; Robert Tibshirani (2013). An Introduction to Statistical Learning

Hedges, L., Newell, A. (1999). Changes in the Black-White gap in achievement scores. Sociology of Education, 72(2), 111-135.

Woodfield, R., Earl-Novell, S. (2006). An assessment of the extent to which subject variation in relation to the award of first class degree between the arts and sciences can explain the 'gender gap'. British Journal of Sociology of Education, 27(3), 355-372.

Yousef, D. A. (2011). Academic Performance of Business Students in Quantitative Courses: A Study in the Faculty of Business and Economics at the UAE University. Decision Sciences Journal of Innovative Education, 9, 255-267.

SENSITIVITY ANALYSIS FOR THE MATHEMATICAL MODELING OF MEASLES DISEASE INCORPORATING TEMPORARY PASSIVE IMMUNITY

Samuel Abu Somma[1*] and Ninuola Ifeoluwa Akinwande[2]

[1,2]Department of Mathematics, Federal University of Technology, Minna, Nigeria.

[1*]Sam.abu@futminna.edu.ng

[2]aninuola@gmail.com

Abstract

Measles is an airborne disease which spreads easily through the coughs and sneezes of those infected. Measles antibodies are transferred from mothers who have been vaccinated against measles or have been previously infected with measles to their newborn children. These antibodies are transferred in low amounts and usually last six months or less. In this paper a mathematical model of measles disease was formulated incorporating temporary passive immunity. There exist two equilibria in the model; Disease Free Equilibrium (DFE) and Endemic Equilibrium (EE). The Disease Free Equilibrium (DFE) state was analyzed for local and global stability. The Basic Reproduction Number R_0 was computed and used to carried out the sensitivity analysis with some parameters of the mode. The analysis shows that as contact rate α increases the R_0 increases and as the vaccination rate v increases the R_0 decreases. Sensitive parameters with the R_0 were presented graphically. The disease will die out of the population if the attention is given to high level immunization.

Keywords: Basic Reproduction Number; equilibrium state; sensitivity; stability.

1. Introduction

Measles is an airborne disease which spreads easily through the coughs and sneezes of those infected. It may also be spread through contact with saliva or nasal secretions. Nine out of ten people who are not immune and share living space with an infected person will likely catch it. People are infectious to others from four days before to four days after the start of the rash. People usually do not get the disease more than once in a life time; indicating that once recovered from the disease, the person become permanently immune (Atkinson, 2011).

According to WHO, measles is one of the leading causes of death among young children even though a safe and cost-effective vaccine is available. In 2015, there were 134 200 measles deaths globally – about 367 deaths every day or 15 deaths every hour. Measles vaccination resulted in a 79% drop in measles deaths between 2000 and 2015 worldwide. In 2015, about 85% of the world's children receive 'xone dose of measles vaccine by their first birthday through routine health services – up from 73% in 2000. During 2000-2015, measles vaccination prevented an estimated 20.3 million deaths making measles vaccine one of the best buys in public health.

According to, Leuridan *et al*. (2012), *i*n developed countries, children are immunized against measles at 12 months, generally as part of a three-part measles, mumps, and rubella (MMR) vaccine. The vaccination is generally not given before this age because such infants respond inadequately to the vaccine due to an

immature immune system. Measles antibodies are transferred from mothers who have been vaccinated against measles or have been previously infected with measles to their newborn children. However, such antibodies are transferred in low amounts and usually last six months or less. Infants under one year of age whose maternal anti-measles antibodies have disappeared become susceptible to infection with the measles virus. A second dose of the vaccine is usually given to children between the ages of four and five, to increase rates of immunity.

Sensitivity analysis tells us how important each parameter is to disease transmission. Such information is crucial not only for experimental design, but also to data assimilation and reduction of complex nonlinear models, (Powell *et al.,* 2005). Sensitivity analysis is commonly used to determine the robustness of model predictions to parameter values, since there are usually errors in data collection and presumed parameter values. It is used to discover parameters that have a high impact on R_0 and should be targeted for intervention strategies.

In this paper, we formulated a mathematical model of disease incorporating temporary passive immunity. The existence of equilibrium point was verified and the local and global stability of Disease Free Equilibrium (DFE) were analyzed using basic reproduction number. We also carried out the sensitivity analysis of the basic reproduction number with some parameters of the model.

2. Literature Review

Abubakar *et al,* (2012), formulated a mathematical model for measles disease dynamics. They divided the total population into three compartments of: Susceptible S(t), Infected I(t) and Recovered R(t). In their model they did not consider vaccination rate, they did not compute basic reproduction number.

Somma *et al.,* (2015), modified the Maternally-Derived-Immunity Susceptible Infectious Recovered (MSIR) Model by adding the vaccination rate and death rate due to the disease to the existing MSIR model. They determined the basic reproduction number using next generation Matrix and Jacobian matrix methods. In their model they did not considered the immunity rate.

Okyere-Siabouh and Adetunde (2013), they formulated a mathematical model of Measles with respect to Cape-Coast Metropolis. They consider Susceptible-Exposed-Infected-Recovered (SEIR) epidemiological model. Their model assumes that individuals are equally likely to be infected by the infectious individuals in a case of an outbreak, except those who are immune.

Fred *et al.* (2014), used a population with variable size to provide a framework. Their model relied on a compartmental model expressed by a set of ordinary differential equations (O.D.E) and partial differential equations (P.D.E) based on the dynamics of measles infections. The mathematical model equations, the mathematical analysis and the numerical simulations that followed served to reveal quantitatively as well as qualitatively the consequences of the mathematical modeling on measles vaccination. They performed the numerical and qualitative analyses of the model at different state variables.

Derdei *et al.,* (2014), formulated a MSIR model, they did not incorporate vaccination rate into their model. They did not analyze the stability of the model.

Yano *et al.* (2016), investigate the transmission dynamics of a Childhood disease outbreak in a community with direct inflow of susceptible and vaccinated new-born. In their model they did not considered the maternally-derive- immunity and immunity rate.

3. Methodology

3.1 Model Formulation

The total population $N(t)$ is divided into four compartment based on the epidemiological status of individuals: Maternally-Derive-Immunity $M(t)$, Susceptible $S(t)$, Infected $I(t)$ and Recovered/Immuned $R(t)$, $t = \text{time}$. In this model it is assume that the new babies are born into M class and S at constant rate Λ. The proportion of the new born with immunity is θ while the proportion of the new born without immunity is $(1-\theta)$. The new babies loss their immunity after some time at a rate ω and move to susceptible class. The susceptible individuals become infected with measles at a contact rate α. The susceptible class is vaccinated at a rate v and thereby move to recovered/immuned class. The treated infected individuals recover at a rate γ and move to recovered/immuned class. The death rate due to disease δ while the natural death rate of the entire population is μ. The schematic diagram and model equations for the measles transmission as discuss in this paper is presented below:

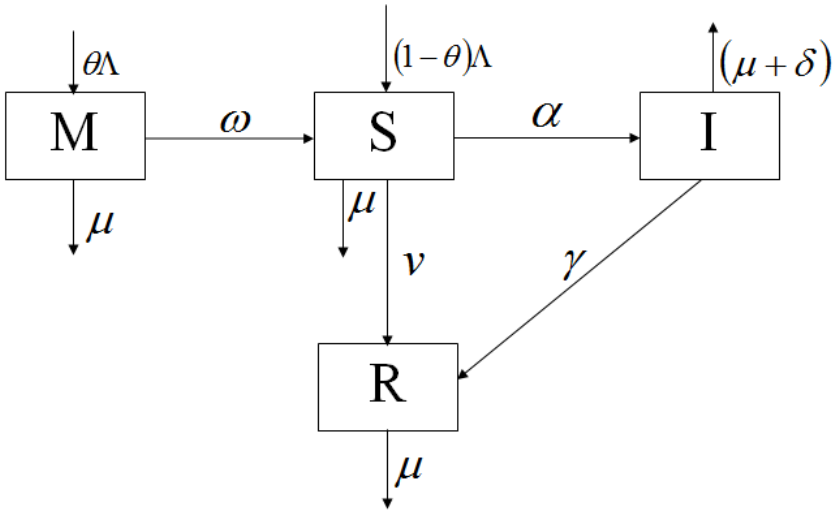

Figure 3.1: Schematic Diagram of the Model

$$\frac{dM}{dt} = \theta\Lambda - (\omega + \mu)M \tag{3.1}$$

$$\frac{dS}{dt} = (1-\theta)\Lambda - \frac{\alpha SI}{N} + \omega M - (v + \mu)S \tag{3.2}$$

$$\frac{dI}{dt} = \frac{\alpha SI}{N} - (\mu + \delta + \gamma)I \tag{3.3}$$

$$\frac{dR}{dt} = \gamma I + vS - \mu R \tag{3.4}$$

Where

$$N = M + S + I + R \tag{3.5}$$

Table 3.1: Variables and Parameters of the Model

Variables/Parameter	Description
N	Total Population
M	Maternally-Derived –Immunity
S	Susceptible
I	Infected
R	Recovered/Immune
Λ	Recruitment rate
θ	Immunity Rate
α	Contact Rate
δ	Death Rate due to Disease
γ	Recovery Rate
μ	Natural Death Rate
v	Vaccination Rate
ω	Loss of Immunity Rate

3.2 *Existence of Equilibrium Points of the Model*

At equilibrium point

$$\frac{dM}{dt} = \frac{dS}{dt} = \frac{dI}{dt} = \frac{dR}{dt} = 0 \tag{3.6}$$

Let

$$\left(M,\ S,\ I,\ R\right) = \left(M^*,\ S^*,\ I^*,\ R^*\right) \tag{3.7}$$

be arbitrarily equilibrium point

$$\theta\Lambda - A_1 M^* = 0 \tag{3.8}$$

$$\left(1-\theta\right)\Lambda - \frac{\alpha S^* I^*}{N^*} + \omega M^* - A_2 S^* = 0 \tag{3.9}$$

$$\frac{\alpha S^* I^*}{N^*} - A_3 I^* = 0 \tag{3.10}$$

$$\gamma I^* + vS^* - \mu R^* = 0 \tag{3.11}$$

Where

$$A_1 = \left(\omega + \mu\right),\ A_2 = \left(v + \mu\right) \text{ and } A_3 = \left(\mu + \delta + \gamma\right) \tag{3.12}$$

From (3.10) we have

$$\left(\frac{\alpha S^*}{N^*} - A_3\right) I^* = 0 \tag{3.13}$$

$$I^* = 0 \tag{3.14}$$

Or

$$\left(\frac{\alpha S^*}{N^*} - A_3\right) = 0 \tag{3.15}$$

Equations (3.14) and (3.15) shows the existence of two equilibria; Disease Free Equilibrium (DEF) and Endemic Equilibrium (EE) respectively.

3.3 Disease Free Equilibrium (DEF) Point

The Disease Free Equilibrium (DEF) is the absence of the disease in a population and equation (3.14) show the implies the disease.

Let

$$\left(M,\ S,\ I,\ R\right)=\left(M^{0},\ S^{0},\ I^{0},\ R^{0}\right)=E^{0} \tag{3.16}$$

Disease Free Equilibrium (DEF) point.

Substituting (3.14) into equations (3.9) and (3.11) gives

$$M^{0}=\frac{\theta\Lambda}{A_1} \tag{3.17}$$

$$S^{0}=\frac{A_1(1-\theta)\Lambda+\omega\theta\Lambda}{A_1A_2} \tag{3.18}$$

$$R^{0}=\frac{v\left[A_1(1-\theta)\Lambda+\omega\theta\Lambda\right]}{\mu A_1A_2} \tag{3.19}$$

The Disease Free Equilibrium (DFE) point is given as

$$\left(M^{0},\ S^{0},\ I^{0},\ R^{0}\right)=\left(\frac{\theta\Lambda}{A_1},\ \frac{A_1(1-\theta)\Lambda+\omega\theta\Lambda}{A_1A_2},\ 0,\ \frac{v\left[A_1(1-\theta)\Lambda+\omega\theta\Lambda\right]}{\mu A_1A_2}\right) \tag{3.20}$$

3.4 Basic Reproduction Number R_0

Basic reproduction number R_0, is average number of secondary cases produced by a single infection in a completely susceptible population.

Applying next generation matrix operator to compute the Basic Reproduction Number of the model as used by Diekmann, *et al.*, (1990), and improved by (Driessche, *et al.*, 2002).

$$FV^{-1}=\left[\frac{\partial F_i\left(E^{0}\right)}{\partial x_i}\right]\left[\frac{\partial V_i\left(E^{0}\right)}{\partial x_i}\right]^{-1} \tag{3.21}$$

Where

F_i are the new infections, while the V_i are transfers of infections from one compartment to another. E^{0} is the disease-free equilibrium point. The basic reproduction number, R_0 is the largest eigenvalue or spectral radius of FV^{-1}.

$$F = \frac{\alpha S^0}{N^0} \tag{3.21}$$

$$V = A_3 \tag{3.22}$$

$$V^{-1} = \frac{1}{A_3} \tag{3.23}$$

$$FV^{-1} = \frac{\alpha S^0}{A_3 N^0} \tag{3.34}$$

At DFE

$$FV^{-1} = \frac{\alpha\mu\left[A_1(1-\theta)+\omega\theta\right]}{A_1A_2A_3} \tag{3.25}$$

$$R_0 = \frac{\alpha\mu\left[A_1(1-\theta)+\omega\theta\right]}{A_1A_2A_3} \tag{3.26}$$

3.5 Local Stability of Disease Free Equilibrium (DFE) E^0

Theorem 3.1: The Disease Free Equilibrium of the model system (3.1)-(3.4) is locally asymptotically stable if $R_0 < 1$.

Proof

In order to prove the theorem above, we are going to use the Jacobian Matrix stability techniques. The all eigenvalues of the matrix are expected to be less than zero (i.e. $\lambda_i < 0$).

$$J\left(E^0\right) = \begin{bmatrix} -A_1 & 0 & 0 & 0 \\ \omega & -A_2 & -\dfrac{\alpha\mu\left[A_1(1-\theta)+\omega\theta\right]}{A_1A_2} & 0 \\ 0 & 0 & \dfrac{\alpha\mu\left[A_1(1-\theta)+\omega\theta\right]-A_1A_2A_3}{A_1A_2} & 0 \\ 0 & \nu & \gamma & -\mu \end{bmatrix} \tag{3.27}$$

$$\left|J\left(E^0\right)-\lambda I\right| = 0 \tag{3.28}$$

$$\begin{vmatrix} -A_1-\lambda & 0 & 0 & 0 \\ \omega & -A_2-\lambda & -\dfrac{\alpha\mu\left[A_1(1-\theta)+\omega\theta\right]}{A_1A_2} & 0 \\ 0 & 0 & \dfrac{\alpha\mu\left[A_1(1-\theta)+\omega\theta\right]-A_1A_2A_3}{A_1A_2}-\lambda & 0 \\ 0 & \nu & \gamma & -\mu-\lambda \end{vmatrix} = 0 \qquad (3.29)$$

The characteristic equation of (3.29) is given as

$$(-A_1-\lambda)(-A_2-\lambda)\left[\left[\alpha\mu\left[A_1(1-\theta)+\omega\theta\right]-A_1A_2A_3\right]-\lambda\right](-\mu-\lambda)=0 \qquad (3.30)$$

$$\lambda_1=-A_1,\ \lambda_2=-A_2,\ \lambda_3=-\mu \qquad (3.31)$$

It is observed that, $\lambda_1,\ \lambda_2,\ \lambda_3<0$

But, $\lambda_4<0$ if

$$\alpha\mu\left[A_1(1-\theta)+\omega\theta\right]-A_1A_2A_3<0 \qquad (3.32)$$

$$\frac{\alpha\mu\left[A_1(1-\theta)+\omega\theta\right]}{A_1A_2A_3}<1 \qquad (3.33)$$

The Left Hand Side (LHS) of equation (3.33) is equivalent to the Right Hand Side of (3.26), therefore,

$$R_0<1 \qquad (3.34)$$

Equation (3.34) proved the theorem 3.1. Equation (3.34), implies that, the disease will not persist in the population.

3.7 Global Stability of Disease Free Equilibrium (DFE), E^0

Theorem 3.2: The DFE, E_0 of the model system is globally asymptotically stable if $R_0 \leq 1$.

Proof
To establish the global stability of the disease-free equilibrium, we construct the following Lyapunov function:

$$V(M, S, I, R) = A_3 I \tag{3.35}$$

Differentiating (3.35) with respect to t gives

$$\frac{dV}{dt} = A_3 \frac{dI}{dt} \tag{3.36}$$

$$\frac{dV}{dt} = A_3\left(\frac{\alpha S}{N} - A_3\right)I \tag{3.37}$$

Since $S \leq S^0$ and $N \leq N^0$

$$\frac{dV}{dt} \leq A_3\left(\frac{\alpha S^0}{N^0} - A_3\right)I \tag{3.38}$$

$$\frac{dV}{dt} \leq A_3\left[\frac{\alpha\mu\left[A_1(1-\theta)+\omega\theta\right]}{A_1 A_2} - A_3\right]I \tag{3.39}$$

$$\frac{dV}{dt} \le A_3{}^2 (R_0 - 1) I \tag{3.40}$$

When $R_0 < 1$, the derivative $\frac{dV}{dt} < 0$ and $R_0 = 1$, the derivative $\frac{dV}{dt} = 0$ Consequently, the largest compact invariant set in $\left\{ (M, S, I, R) \in \Omega, \frac{dV}{dt} = 0 \right\}$, when $R_0 \le 1$, is the singelton E^0. Hence, LaSalle's invariance principle, LaSalle (1976) implies that E^0 is globally asymptotically stable in Ω. This completes the proof.

3.8 Endemic Equilibrium (EE) Point

The Endemic Equilibrium (EE) is the persistence of the disease in a population and equation.

Let

$$(M, S, I, R) = (M^{**}, S^{**}, I^{**}, R^{**}) = E^1 \tag{3.41}$$

$$\left.\begin{aligned} &\theta\Lambda - A_1 M^{**} = 0 \\ &(1-\theta)\Lambda - \frac{\alpha S^{**} I^{**}}{N^{**}} + \omega M^{**} - A_2 S^{**} = 0 \\ &\frac{\alpha S^{**} I^{**}}{N^{**}} - A_3 I^{**} = 0 \\ &\gamma I^{**} + \nu S^{**} - \mu R^{**} = 0 \end{aligned}\right\} \tag{3.42}$$

$$\left.\begin{aligned} &\theta\Lambda - A_1 M^{**} = 0 \\ &(1-\theta)\Lambda - \lambda^{**} S^{**} + \omega M^{**} - A_2 S^{**} = 0 \\ &\lambda^{**} S^{**} - A_3 I^{**} = 0 \\ &\gamma I^{**} + \nu S^{**} - \mu R^{**} = 0 \end{aligned}\right\} \tag{3.43}$$

Where,

$$\lambda^{**} = \frac{\alpha I^{**}}{N^{**}} \tag{3.44}$$

Is the force of infection

From (3.43)

$$\left.\begin{aligned} M^{**} &= \frac{\theta\Lambda}{A_1} \\ S^{**} &= \frac{A_1\Lambda(1-\theta)+\theta\omega\Lambda}{A_1\left(\lambda^{**}+A_2\right)} \\ I^{**} &= \frac{\lambda^{**}\left[A_1\Lambda(1-\theta)+\theta\omega\Lambda\right]}{A_1A_3\left(\lambda^{**}+A_2\right)} \\ R^{**} &= \frac{vA_3\left[A_1\Lambda(1-\theta)+\theta\omega\Lambda\right]+\gamma\left[A_1\Lambda(1-\theta)+\theta\omega\Lambda\right]\lambda^{**}}{A_1A_3\mu\left(\lambda^{**}+A_2\right)} \end{aligned}\right\} \tag{3.45}$$

$$N^{**} = M^{**} + S^{**} + I^{**} + R^{**} \tag{3.46}$$

$$N^{**} = \frac{A_3\theta\Lambda\mu\left(\lambda^{**}+A_2\right)+\left[A_1\Lambda(1-\theta)+\theta\omega\Lambda\right]\left[(\mu+\gamma)\lambda^{**}+A_2A_3\right]}{A_1A_3\mu\left(\lambda^{**}+A_2\right)} \tag{3.47}$$

Substituting I^{**} and N^{**} into (3.44) gives

$$\begin{aligned}\left[A_3\theta\Lambda\mu+(\mu+\gamma)\left[A_1\Lambda(1-\theta)+\theta\omega\Lambda\right]\right]\lambda^{**} + A_2A_3\theta\Lambda\mu + A_2A_3\left[A_1\Lambda(1-\theta)+\theta\omega\Lambda\right] \\ -\alpha\mu\left[A_1\Lambda(1-\theta)+\theta\omega\Lambda\right]=0\end{aligned} \tag{3.48}$$

$$B_1\lambda^{**} + B_2 = 0 \tag{3.49}$$

Where,

$$\left.\begin{aligned} B_1 &= A_3\theta\Lambda\mu+(\mu+\gamma)\left[A_1\Lambda(1-\theta)+\theta\omega\Lambda\right] \\ B_2 &= A_2A_3\left[\theta\Lambda\mu+\left[A_1\Lambda(1-\theta)+\theta\omega\Lambda\right]\right]-\alpha\mu\left[A_1\Lambda(1-\theta)+\theta\omega\Lambda\right] \end{aligned}\right\} \tag{3.50}$$

$$B_2 = A_1A_2A_3\Lambda(1-R_0) \tag{3.51}$$

Therefore, equation (3.49) becomes

$$B_1\lambda^{**} + A_1A_2A_3\Lambda(1-R_0) = 0 \tag{3.52}$$

3.9 Bifurcation Analysis

We illustrate the phenomenon of Bifurcation by considering the equation (3.52) resulting from the endemic equilibrium. The estimated parameter values in table 4.1 are used to plot the diagram.

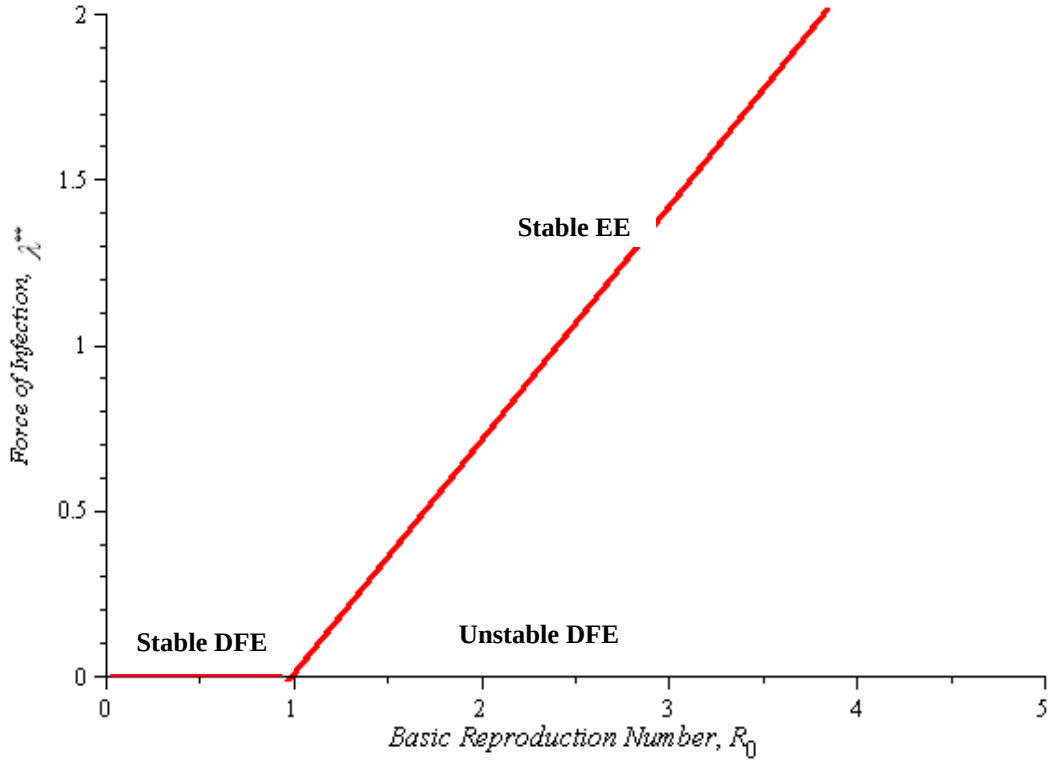

Figure 3.2: Forward Bifurcation Diagram for the Model

In figure 3.2 above, the two equilibrium points exchange stabilities depending on the value of R_0. A transcritical/forward bifurcation in the equilibrium points occur at $R_0 = 1$. If, $R_0 < 1$ the disease free equilibrium (DFE) is stable. But if $R_0 > 1$, the endemic equilibrium exists and it is stable while the disease free equilibrium is a saddle point. Thus there is a forward bifurcation because in the neighbourhood of the bifurcation point, the force of infection, λ^{**} is an increasing function of R_0.

4 Results and Discussion

4.1 Sensitivity Analysis of the Basic Reproduction Number, R_0 with Some Parameter of the Model

Sensitivity indices allow us to measure the relative change in a variable when a parameter changes. The normalized forward sensitivity index of a variable with respect to a parameter is the ratio of the relative change in the variable to the relative change in the parameter. When the variable is a differentiable function of the parameter, the sensitivity index may be alternatively defined using partial derivatives.

In determining how best to reduce human mortality and morbidity due to measles, the sensitivity indices of the basic reproduction number to the parameters of the model was calculated following similar approaches as in Arriola and Hyman (2005), Chitnis *et al.* (2008), Mikuchi *et al.* (2012) and Abdulrahman *et al.* (2013). The normalized forward sensitivity indices with respect to a parameter value, P is defined as

$$S_P^{R_0} = \frac{\partial R_0}{\partial P} \times \frac{P}{R_0} \tag{4.1}$$

Where,

$$P = \{\alpha,\ \gamma,\ \nu,\ \theta\} \tag{4.2}$$

The sensitivity indices of the parameters of the basic reproduction number R_0 were calculated using Maple 13 software. See appendix B, for the estimation of variables and parameter values used in sensitivity analysis as shown on Table 4.1 below.

Table 4.1: Values for Parameters used for Sensitivity Analysis

Variables	Values per year	Source
$M(0)$	82,010,000	B9
$S(0)$	7,099,464,364	B10
$I(0)$	254,918	B3
$R(0)$	118,270,718	B4
N	7,300,000,000	B1
Λ	139,000,000	B2
α	0.9	B12
δ	0.53	B6
γ	0.47	B5
μ	0.008	B7
ω	0.39	B11
ν	0.85	B8
θ	0.61	B13

Table 4.2: Sensitivity Indices of R_0 to Parameters of the model, evaluated at the parameter values given in Table 4.1

Parameter	Low transmission	High transmission
	Sensitivity Index	Sensitivity Index
α	1.000000000	1.00000000
γ	-0.466269843	-0.3172588832
v	-0.9906759907	-0.9878419453
θ	-0.01241351242	-0.006270226538

Table 4.2 shows that all the parameters have either positive or negative effects on the basic reproduction number, R_0. The positive parameters will increase the basic reproduction number while the negative parameters will decrease the basic reproduction number. The contact rate, α has the highest sensitivity index follow by vaccination rate, v and recovery rate, γ and immunity rate θ has the lowest sensitivity analysis.

4.2 Graphical Representation of Basic Reproduction Number with Sensitive Parameter

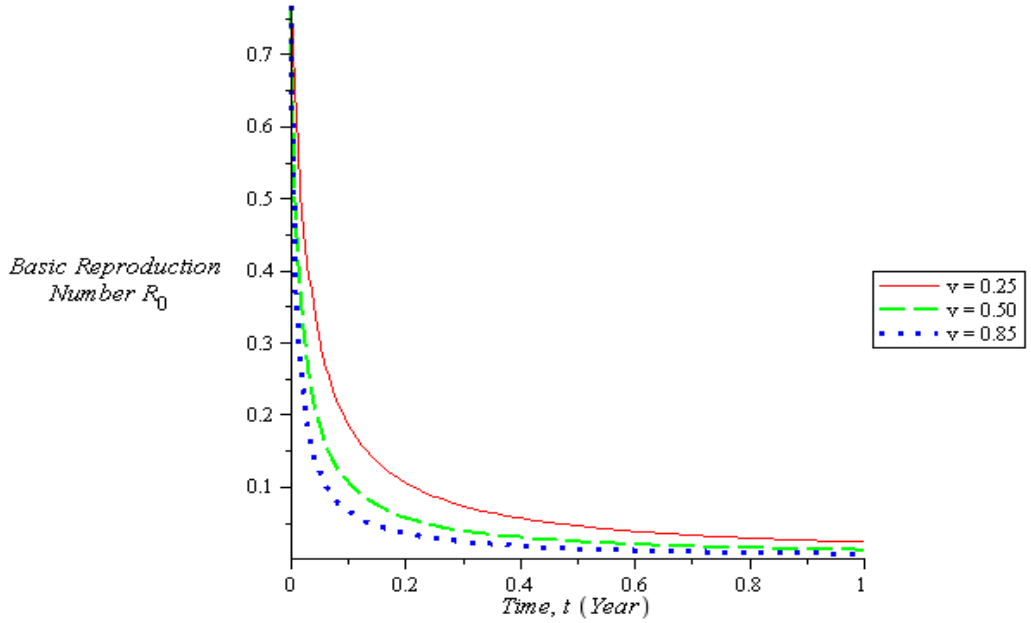

Figure 4.1: The Graph of Basic Reproduction Number against different values of Vaccination Rate

Figure 4.1 shows that as vaccination rate increases with time the Basic reproduction number decreases. It is observe that, with increase in vaccination rate, the basic reproduction number decrease to almost zero.

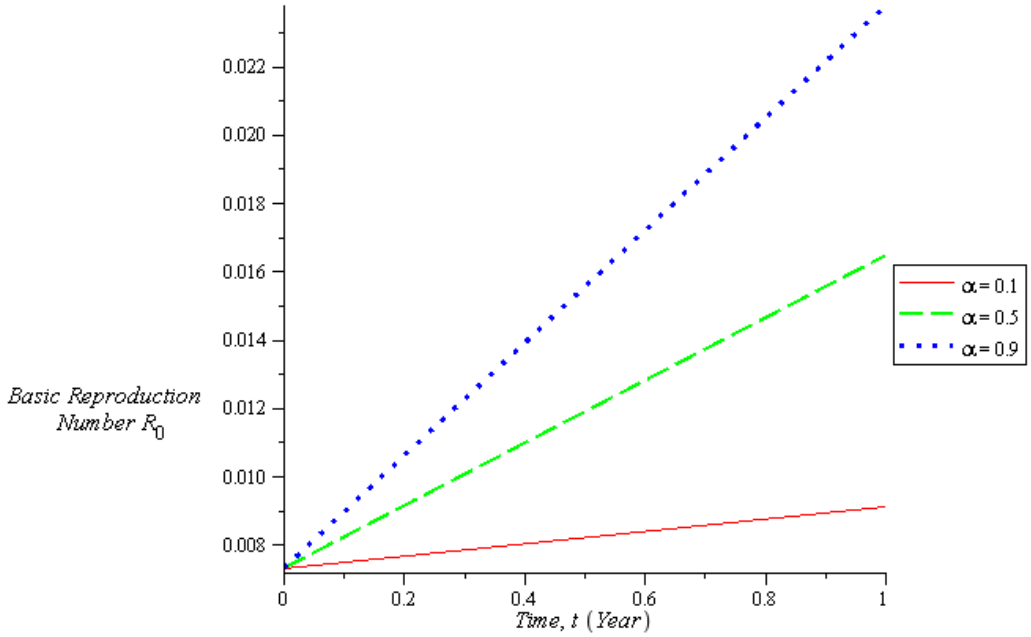

Figure 4.2: The Graph of Basic Reproduction Number against different values of Contact Rate

Figure 4.2 shows that as contact rate increases with time the Basic reproduction number increases. It also show that low contact rate gives low basic reproduction number. The children infected with measles should be separated from those that are not infected.

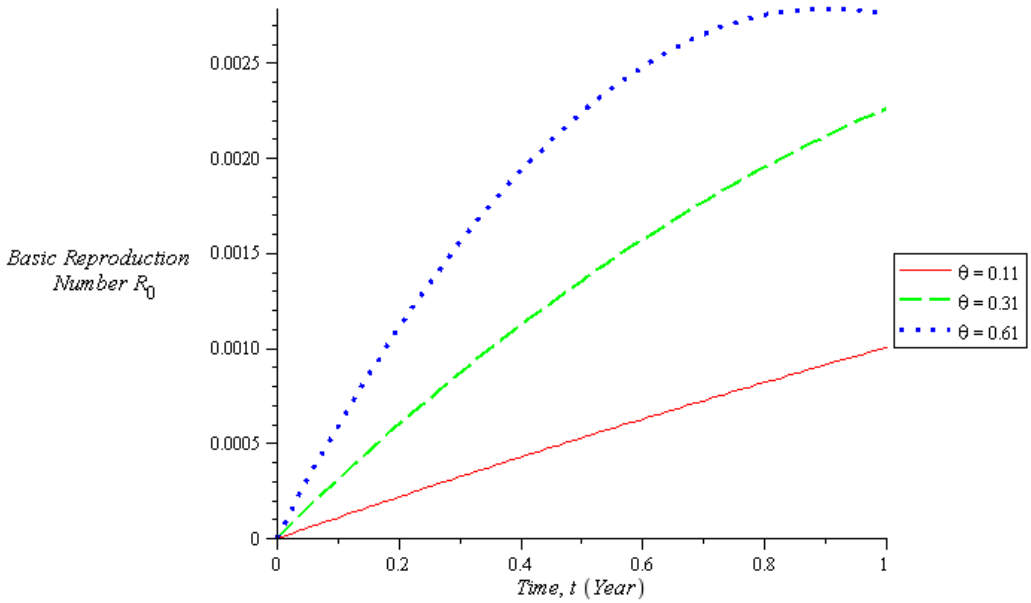

Figure 4.3: The Graph of Basic Reproduction Number against different values of Immunity Rate
Figure 4.3 shows that as immunity rate increases with time the Basic reproduction number decreases. The immunity depends on vaccination and treatment.

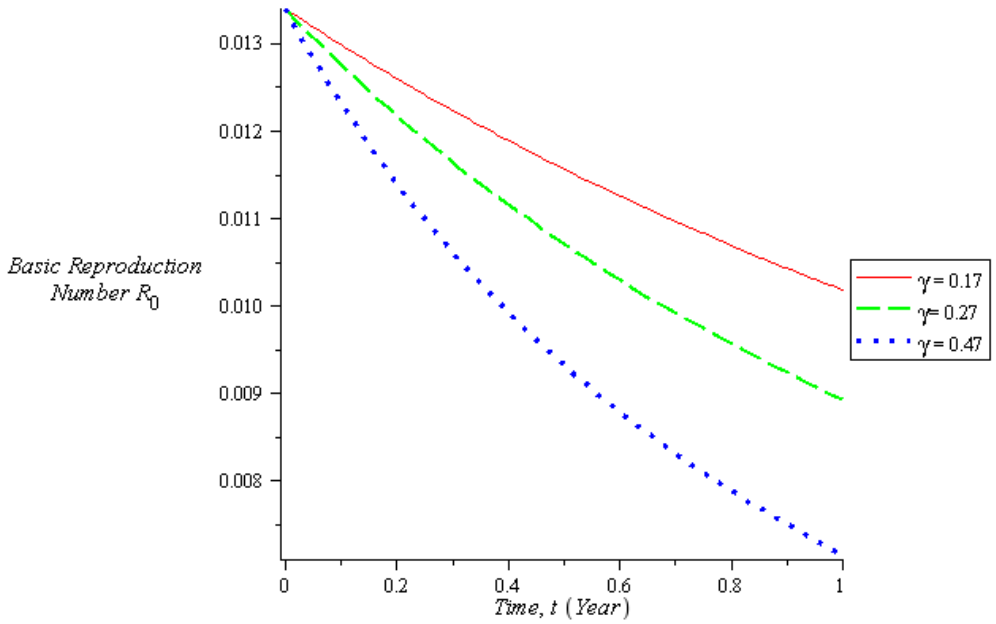

Figure 4.4: The Graph of Basic Reproduction Number against different values of Recovery Rate

Figure 4.4 shows that as recovery rate increases with time the basic reproduction number decreases. It is observe that, with increase in recovery rate, the basic reproduction number decrease to almost zero.

5 Conclusion

The model equations are formulated using first order ordinary differential equation. The existence of Disease Free Equilibrium (DFE) and Endemic Equilibrium (EE) was proved. The Disease Free Equilibrium (DFE) is locally asymptotically stable if $R_0 < 1$ and globally asymptotically stable if $R_0 \leq 1$. The bifurcation analysis reveal that the model exhibit forward bifurcation if $R_0 = 1$.

Four parameters of the model were used to carried out the sensitivity analysis with the basic reproduction number R_0. The contact rate α , is the most sensitive parameter that will increase the basic reproduction number R_0 while the vaccination rate v is the most sensitive parameter that will decrease the basic reproduction number R_0. Other parameter that were used in sensitivity analysis are immunity rate θ and recovery rate γ .

The graphical representation of the basic reproduction number R_0 with these sensitive parameters give the better understanding on how the parameters affect the basic reproduction number R_0 negatively or positively. Measles will die out of the population if attention is given to high level immunization of children. The rural dweller should be sensitizing on the risk of contracting the disease. The susceptible individuals should not share the same living space with the infected individuals

Reference

Abubakar, S., Akinwande, N. I. &Abdulrahman, S. (2012), A Mathematical Model of Measles Disease Dynamics. *Journal of Science, Technology, Mathematics and Education (JOSTMED)* 8(3), 144-152**.**

Abdulrahman, S., Akinwande, N. I., Awojoyogbe, O. B. & Abubakar, U.Y. (2013). Sensitivity analysis of the parameters of a mathematical model of Hepatitis B virus transmission. *Universal Journal of Applied Mathematics*, 1(4), 230-240.

Atkinson, William (2011). *Epidemiology and Prevention of Vaccine-Preventable Diseases* (12 ed.). *Public Health Foundation. pp. 301–323. ISBN 9780983263135. Retrieved 5 February 2015.*

Arriola, L. and Hyman, J. (2005).'Forward and adjoint sensitivity analysis with applications in dynamical systems' Lecture Notes in Linear Algebra and Optimization.

Chitnis, N., Hyman, J. M. & Cushing, J. M. (2008).Determining Important Parameters in the Spread of Malaria through the Sensitivity Analysis of a Mathematical Model, *Bulletin of Mathematical Biology*, DOI 10.1007/s11538-008-9299-0.

Diekmann, O, Heesterbeek, J. A. P. & Metz, J. A. J. (1990)."On the Definition and the Computation of the Basic Reproduction Ratio R_0 in Models for Infectious Diseases in Heterogeneous Populations".*Journal of Mathematical Biology*, 28 (4): 365–382.

Derdei B., Abderrahman I., and Gauthier S. (2014), Global Analysis of Multi-strains SIS, SIR and MSIR Epidemic Models. *Journal of Applied Mathematics and Computing, Springer*, 44 (1-2), pp.273-292.

Driessche V., P. & Watmough, J. (2002). "Reproduction Numbers and Sub-threshold Endemic Equilibria for Compartmental Models of Disease Transmission".*Mathematical Biosciences*180 (1–2): 29–48.

Fred M. O., Sigey J. K., Okello J. A., Okwoyo J. M. & Kang'ethe G. J. (2014), Mathematical Modeling on the Control of Measles by Vaccination : Case Study of KISII County, Kenya, *The SIJ Transactions on Computer Science Engineering & its Applications (CSEA)*, Vol. 2 (3), 61-69.

LaSalle J. P.(1976), *The Stability of Dynamical Systems*, Regional Conference Series in Applied Mathematics, SIAM, Philadelphia, Pa, USA.

Leuridan E, Sabbe M, Van Damme P (September 2012). *"Measles outbreak in Europe: susceptibility of infants too young to be immunized". Vaccine* ***30*** *(41): 5905–13. doi:10.1016/j*

Mikuchi, M.A. (2012). Sensitivity Analysis of the Basic Reproduction Number and other Quantities for Infectious Disease Models. An M.Sc. thesis, Colorado State University Fort Collins, Colorado, Spring.

Okyere-Siabouh S. and Adetunde I. A. (2013), Mathematical Model for the Study of Measles in Cape Coast Metropolis, *International Journal of Modern Biology and Medicine*, Vol. 4(2), 110-133.

Powell D. R., Fair J., LeClaire R. J., Moore L. M., and Thompson D.(2005), Sensitivity Analysis of an Infectious Disease Model. *International System Dynamics Conference, Boston*, MA,

.

Somma, S. A., Akinwande, N. I., Gana, P., Abdulrahaman, S. & Ashezua, T. T., (2015), Modified Maternally-Derived-Immunity Susceptible Infectious Recovered (MSIR) Model of Infectious Disease: Existence of Equilibrium and Basic Reproduction Number., *Nigerian Journal of Technological Research* (NJTR). 10(1):40-43.

Yano T. K., Makinde O. D. and Malonza D. (2016). Modelling childhood disease outbreak in a community with inflow of susceptible and vaccinated new-born. *Global Journal of Pure and Applied Mathematics,* 12(5), 3895-3916.

Appendices

Appendix A: Reported Measles Cases by WHO Region 2015 and 2016, as of November 2016

Table A1: Reported Measles Cases by WHO Region 2015, as of November 2016

WHO Region	Member States Reported (Expected)	Total Suspected	Total Measles	Clinical Confirmed	Epidemiological Link	Laboratory Confirmed	Data Received
Africa	41(47)	86984	55263	21111	26163	7989	Nov-16
America	34(35)	18670	210	0	0	210	Nov-16
Eastern Mediterranean	21(21)	34654	14053	639	4559	8855	Nov-16
Europe	50(53)	28025	26776	19835	1014	5926	Nov-16
South-East Asia	11(11)	114726	90860	64484	22353	4023	Nov-16
Western Pacific	27(27)	143289	67756	22337	611	44808	Nov-16
Total	**184(194)**	**426348**	**254918**	**128406**	**54700**	**71811**	

Source: WHO (2016)

Table A2: Reported Measles Cases by WHO Region 2016, as of November 2016

WHO Region	Member States Reported (Expected)	Total Suspected	Total Measles	Clinical Confirmed	Epidemiological Link	Laboratory Confirmed	Data Received
Africa	42(47)	46474	28126	12459	11085	4582	Nov-16
America	34(35)	9564	65	0	0	65	Nov-16
Eastern Mediterranean	20(21)	19763	4518	153	947	3418	Nov-16
Europe	50(53)	3849	2537	241	385	1910	Nov-16
South-East Asia	11(11)	86302	63169	51015	11004	1150	Nov-16
Western Pacific	27(27)	100517	55620	27594	638	27388	Nov-16
Total	**184(194)**	**266469**	**154035**	**91462**	**24059**	**38513**	

Source: WHO (2016)

Appendix B: Estimation of Variables and Parameter Values

It is difficult to get a reliable data, we estimated the parameter values based on the available data from the World Health Organization (WHO), Population Reference Bureau and reliable related literature. The estimates are clearly explained in the following sub-sections.

B1: The Total Population, N

According to Population Reference Bureau, the world total population at 2015, is 7.3 billion.

$$N = 7{,}300{,}000{,}000$$

B2: Recruitment Number, Λ

According to Population Reference Bureau the birth rate per year is $\frac{19}{1{,}000}$

The number of new birth in 2015 is 139, 000, 000.

Therefore,

$$\Lambda = 139{,}000{,}000$$

B3: Number of Infected, I

The WHO estimate that, there are 254, 918 cases of measles worldwide each year, resulting in 134,200 deaths. (See Table A1)

$$I = 254,\ 918$$

B4: Number of Recovered/Immune, R

Recovered/Immune Human population, R = recovered + immune

From B3 the number of cases is 254, 918 and number of death is 134,200.

Recovered= 254, 918 -134,200 = 120,718 the number of surviving infants in 2015 is 139,000,000

and the percentage of vaccinated is 85%. Therefore,

Vaccinated = 85% of 139,000,000 =118,150,000.

Hence,

Recovered/Immune Human population, $R = 120{,}718 + 118{,}150{,}000$

$R = 118{,}270{,}718$

B5: Recovery Rate, γ

From B3 and B4

$$\gamma = \frac{\text{Recovered}}{\text{Number of cases}}$$

$$\gamma = \frac{120{,}718}{254{,}918} = 0.47$$

B6: Disease Induce death rate, δ

From B3 the number of cases of measles is 254,918 and the number of death from measles is 134,200

$$\delta = \frac{\text{Number of Death from measles}}{\text{Number of cases}}$$

$$\delta = \frac{134{,}200}{254{,}918} = 0.53$$

B7: Natural Death Rate, μ

According to WHO, the death rate is 8 deaths per 1,000. Therefore,

$$\mu = \frac{8}{1000} = 0.008$$

B8: Vaccination rate, v

According to, WHO in 2015, about 85% of the world's children received one dose of measles vaccine. Therefore,

$$v = 0.85$$

B9: Maternally-Derived-Immunity, M

According to Millennium Development Goal (MDG4), every year nearly 41% of all under-five child deaths are among newborn infants, babies in their first 28 days of life or the neonatal

period.

$$M = 59\% \text{ of } 139{,}000{,}000$$

$$M = 82{,}010{,}000$$

B10: Number of Susceptible, S

Recall $N = M + S + I + R$ therefore,

$$S = N - (M + I + R)$$

$$S = 7{,}300{,}000{,}000 - (82{,}010{,}000 + 254{,}918 + 118{,}270{,}718)$$

$$S = 7{,}300{,}000{,}000 - 200{,}535{,}636$$

$$S = 7{,}099{,}464{,}364$$

B11: Loss of immunity, ω

According to WHO Immunization coverage fact sheet, national immunization schedule reported that, only 61% of children received 2 doses of measles. Therefore,

$$\omega = 39\% = 0.39$$

B12: Contact Rate, α

According to, Atkinson, (2011), nine out of ten people who are not immune and share living space with an infected person will catch it. Therefore

$$\alpha = \frac{9}{10} = 0.9$$

B13: Immunity Rate, θ

WHO doctors recommend that two doses of the vaccine be given at six and nine months of age to ensure immunity and prevent outbreaks, as about 15% of vaccinated children fail to develop immunity from the first dose. According to WHO Immunization coverage fact sheet, national immunization schedule reported that, only 61% of children received 2 doses of measles. Therefore, the Immunity Rate, θ is assumed to be

$$\theta = 0.61$$

TOPOLOGIES FOR PERMANENT MAGNET FLUX SWITCHING MOTORI OUT-RUNNER SEGMENTED ROTOR

Enwelum Mbadiwe I[1] Ibrahim Kasim Mohammed [2]

[1]Department of Electrical/Electronic Engineering, [2]Department of Physical Sciences, Niger State Polytechnic, Zungeru, Nigeria

[1]mb.fkee.uthm@gmail.com

[2]kasimzabbo1976@gmail.com

Abstract

This paper presents topologies for three phase permanent magnet flux switching motor (PMFSM) in out-runner segmented rotor employing radial magnetic direction. PMFSM is the electric machine in which all the active components are located on the stator leaving its rotor completely robust for high speed application. The basic operating principle of this category of motor using segmented rotor is based on an unconventional configuration to modulate the polarity of the flux linkages in the stationary stator with clear benefits. 2D Finite Element Analysis (FEA) is carried using JMAG Software version 14 released by the Japanese Research Institute to examine the performances of the topologies in terms of magnetic flux linkages, cogging torque, induced back-emf and average torque respectively. Results show that 24slot-14poles has the highest average torque suitable for high speed application.

Keywords: flux switching motor, loss-free excitation, out-runner, permanent magnet, radial magnetic direction segmented rotor, topology

1. Introduction

Recently, segmented rotor was used in flux switching machine (FSM) in which all active parts are located on the stator leaving the rotor completely robust to contain high speed and the performance in terms of torque is greatly improved (Mecrow *et al*., 2006). It is very obvious that this configuration of using segmented rotor and deployment of permanent magnet (PM) and armature windings on the stator provides gains for operating with bipolar flux in the magnetic circuit (Zulu and Mecrow, 2012; Raminosoa *et al*., 2011). The segmented rotor is used to create bipolar flux linkages in the armature windings with also bipolar flux in the armature tooth for a single cycle of operation. An investigation into the design of PMFS motor in out runner structure employing segmented rotor is described in this paper. This is necessitated with the reference for the application and specification associated with far distance travel. The design is concerned with securing very high torque without compromising other constraints needed for long distance travel such as weight of motor. In general, flux switching motor is developed by combing two conventional motors namely, induction motor (IM) and switched reluctance motor (SRM) respectively (Thomas *et al*., 2010; Zhu *et al*., 2008). For the rotor rotation to go through poles of each of the motors under investigation, their flux linkages in the armature undergo the period of revolution of each motor's number of poles (Ahmad *et al*., 2012).

Generally, rotor speed of FSM is as expressed in Eq. (1). Also, electrical frequency is stated in Eq. (2).

$$N_s = \frac{60f}{p} \qquad (1)$$

Where, N_s rotor speed, f is frequency, p number of poles.

$$f_e = N_r \times f_m \quad (2)$$

Where, f_e is electrical frequency, N_r is number of rotor and f_m is mechanical frequency.

Permanent magnet FS motors have attracted researchers' interest due its beneficial attributes of end short coils, short flux path and high torque density. Regrettably, almost PMFSMs in published literatures have been in conventional toothed rotor without any attention considering segmented rotor which provides high torque for high speed purposes (Fei *et al*., 2009; Galea *et al*., 2012). First of all, I will describe the operating principle of this motor employing out-runner segmented rotor and PM source of flux excitation and introduce the various design topologies. The performance results of each motor is examined which include magnetic flux linkages, cogging flux, induced back-emf and average torque.

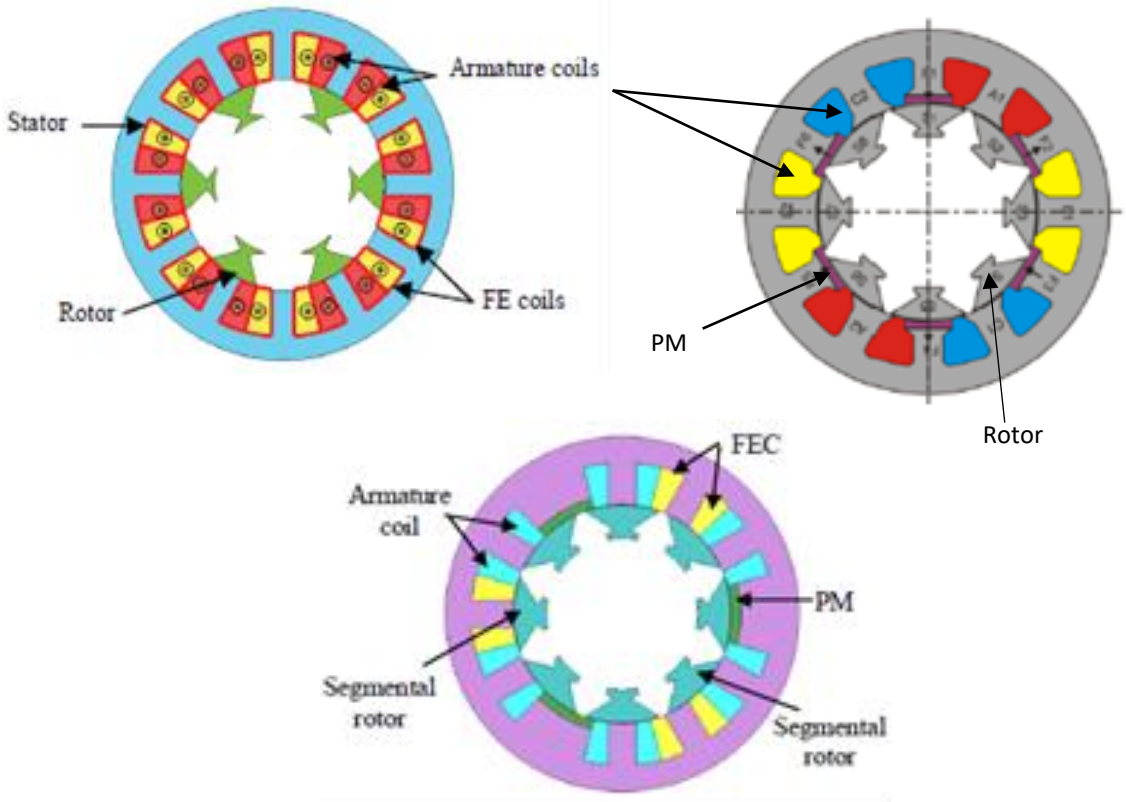

2. Topologies for Three Phase Motors

Flux switching motor (FSM) is categorized into three kinds namely, permanent magnet FSM, Field excitation FSM and Hybrid Excitation FSM respectively. These three kinds are due to different means of flux excitation. Examples of FSMs are illustrated in Fig. 1. In PMFSM, PM is the source of field excitation, FEFSM utilizes field coil while HEFSM employs both PM and FE as main and secondary sources of excitation. For three phase motor design, it often appears that six number is the minimum of teeth necessary for AC working but this is not true as three of the six teeth are deployed as armature and the remaining six will be insufficient to form alternate pairs. Under this constraint, the minimum number of teeth for three phase configuration is 12 or 24 in this multiple as the case might be (Zulu *et al*., 2010). This design considers a 24 tooth stator to allow four sets of three- phase series windings using the convention in Eq.3 (Fei *et al*., 2011).

$$N_r = N_s\left(2 \pm \frac{k}{2p}\right) \quad (3)$$

Where, Nr is the number of rotor poles, Ns number of stator poles, k is a positive integer 1,2,3, etc. and p is phase.

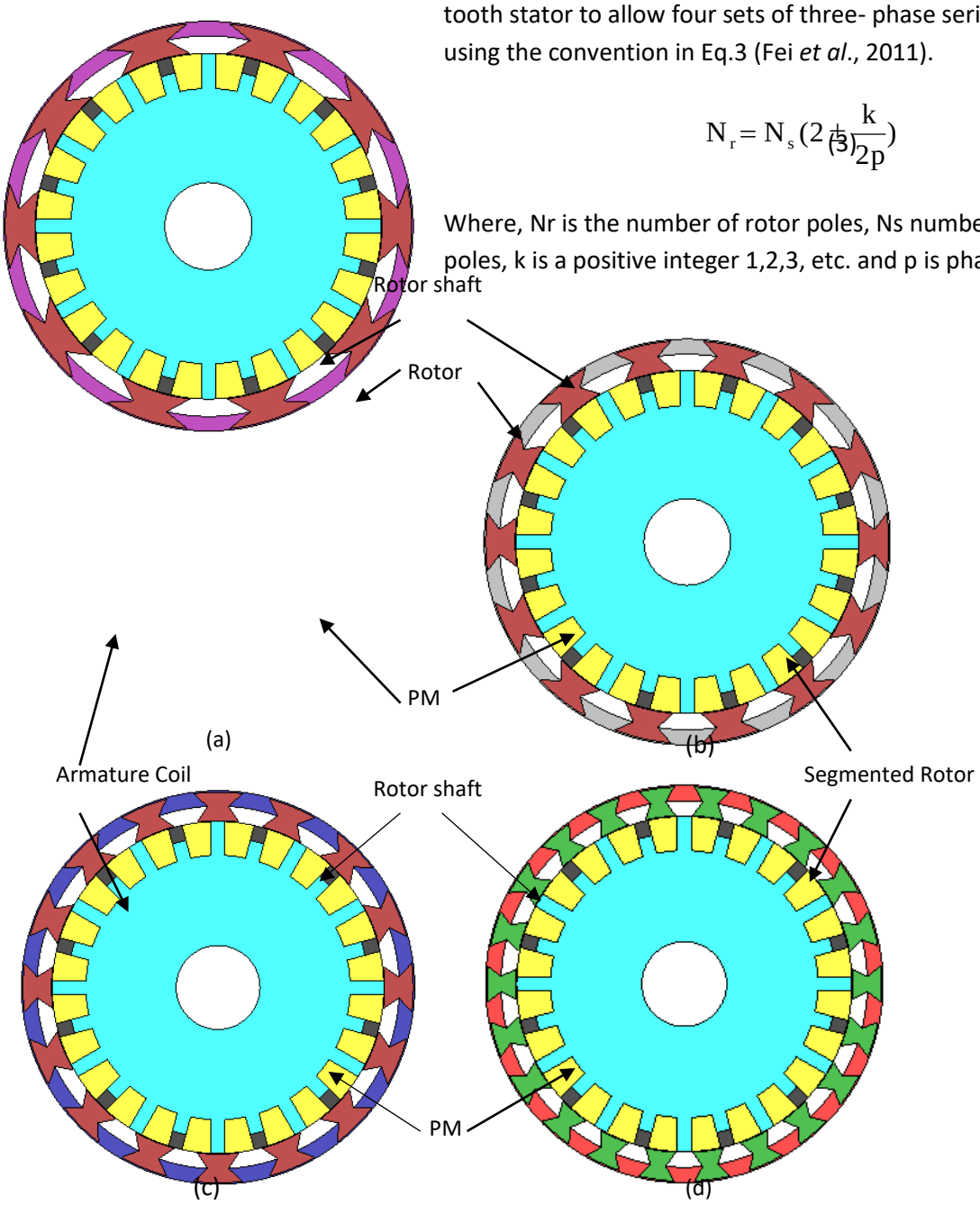

Fig. 2. Cross sections of PMFSMs in out-runner segmented
(a) 24Slot-10Pole (b) 24Slot-14Pole (c) 24Slot-16Pole (d) 24Slot-22Pole

3. Operating Principle of Out-Runner PMFSM Segmented Outer Rotor

Shown in Fig.2 are the cross sections of the four motors of different rotor configurations under investigation. For the operating principle, the rectilinear cell arrangement is presented in Fig. 3. The flux switching mechanism is explained using PM1 and armature coil. At the initial condition when stator tooth is in alignment with rotor S1, there is flux flow from PM1 into S1 in upward direction linking with S1 and back to the stator back iron as shown in Fig. 3 (a). However, in the second alignment, when segment rotor S1 begins to rotate in counter-clockwise direction, flux begins to flow from PM1 through S1 into the stator pole. Therefore, as S1 continues to rotate and at the third quadrant, there is switch of flux at S1 from PM1 to the downward direction as shown in Fig. 3 (b). The design requirements, specifications and restrictions of the proposed motor are provided in Table 1.

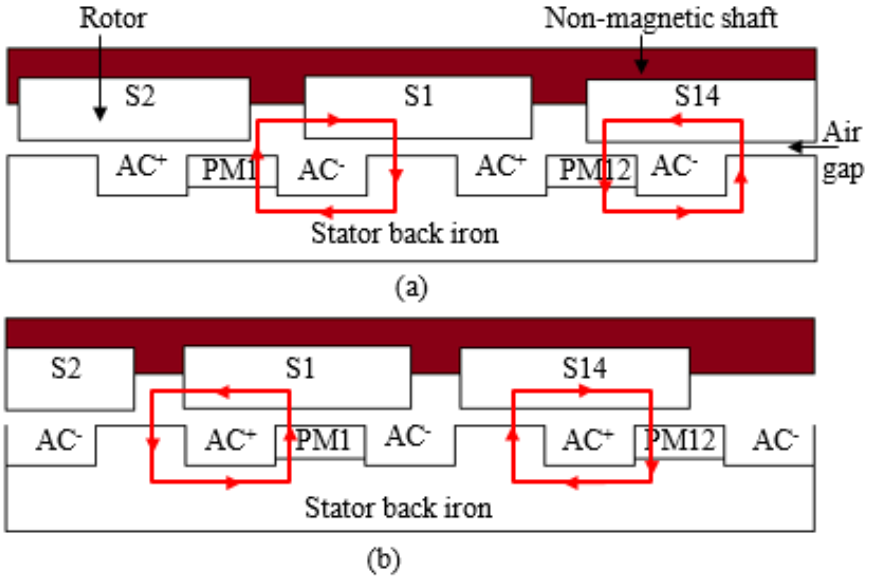

Fig. 3. Operating principle of out-runner PMFSM

(a) First alignment (b) Second alignment

Table1: Motor Specifications

Descriptions	Out-runner segmented rotor PMFSM
No. of Phases	3
No. of Rotor Pole	10, 14, 16, 22
No. of Stator Pole	24
Diameter of Motor	11inches/279.4mm
PM mass (kg)	1
Stack-length (mm)	100
Stator shaft (mm)	30
DC- voltage inverter (V)	415
Inverter current (A_{rms})	360
No. of Conductors	18
Armature Slot Area (mm^2)	432

4. Design Methodology

To know and select the excellent motor in terms of high torque and torque density, five different motors are designed and investigated. In designing each motor which is carried out using JMAG Geometry editor environment and later uploaded into Designer for simulation and analysis. The motor parts which include rotor, stator armature coil and PM are designed in the Geometry editor while setting in the materials, conditions circuit mesh setting are developed in the Designer.

The material used for the rotor and stator is electrical steel 35H210 while the PM is Neomax-35AH. Design flow chart is illustrated in Fig. The four motors under investigation are 24slot-10poles, 24 slots-14 poles, 24 slots-16poles and 24 slots-22poles on the part of 24 number stator pole teeth only Furthermore, the design of rotor employed the relationship between rotor segment angle and rotor tooth width and is similar to segment of a circle to length of arc given in Eq. 4

$$\theta = \frac{180 \times \text{rotor tooth width}}{\pi \times \text{outer rotor inner} - \text{radius}} \quad (4)$$

Where θ is the spanned angle of the rotor segment.

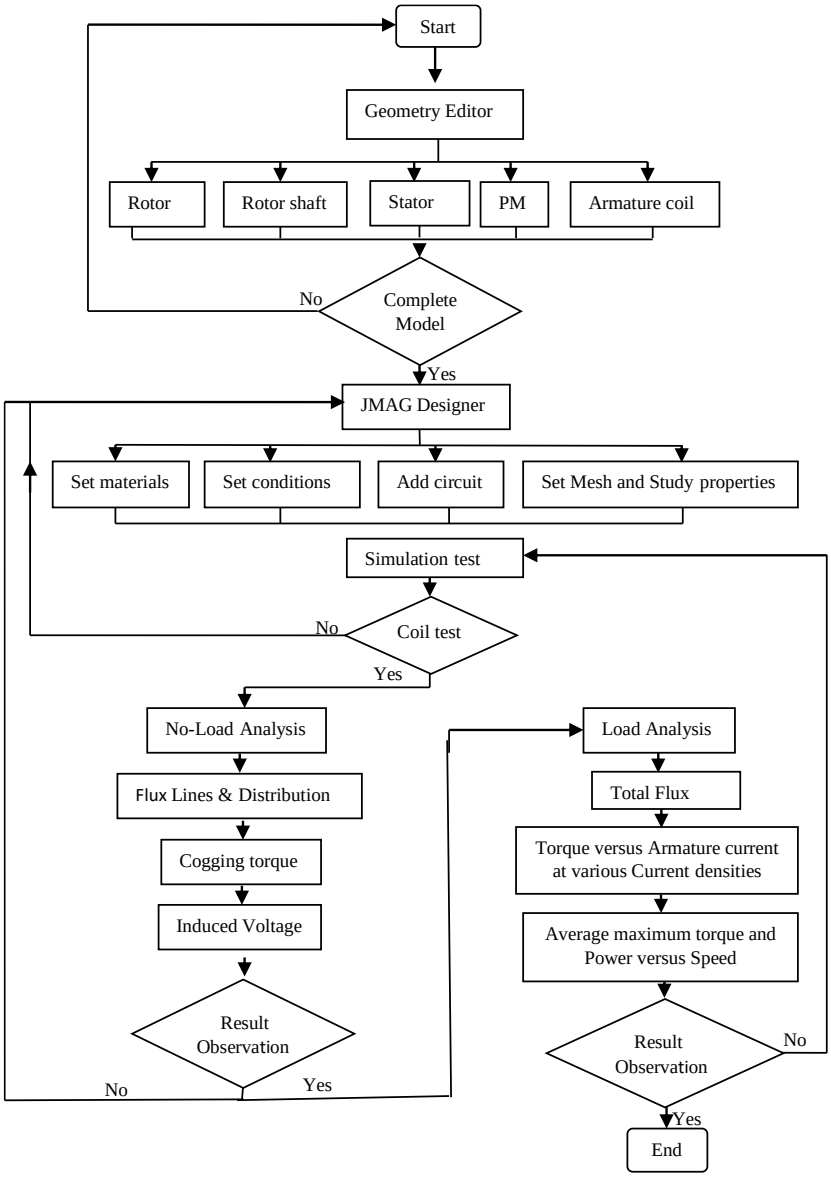

Fig.4. Work flow chart of motor design in Geometry Editor and JMAG- Designer

5. Performance Analysis

5.1. No load condition: Magnetic flux linkage

Flux and flux linkage present the initial performance of motor whether it would lead to low torque or high torque. It is not all the time that high profile flux amplitude leads to high torque under load condition In Fig. 5, the magnetic flux amplitude of the five motors under investigation are presented. Smooth sinusoidal waveform provides the benefit of being a suitable motor. It is seen that the amplitude of U-phase flux profile of the five motors, 24slots-10poles gauged the highest followed by 24slots-14poles. Furthermore, 24slots-16poles did not sinusoidal waveform, 24slots-22poles achieves low sinusoidal waveform.

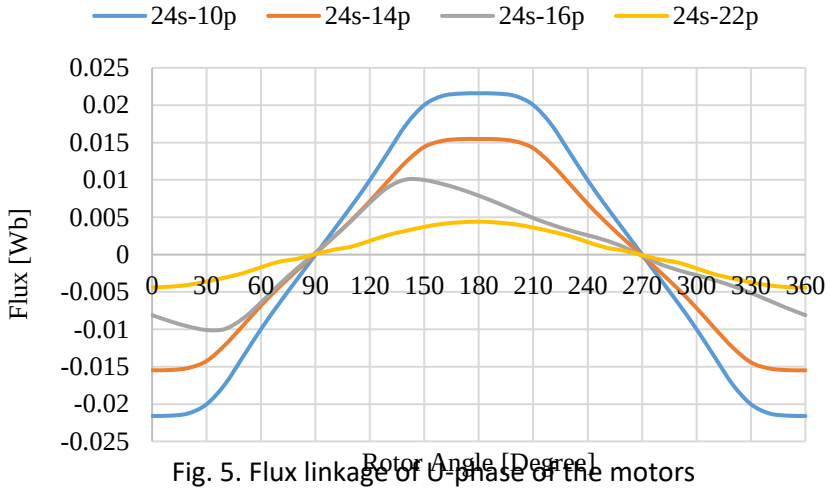

Fig. 5. Flux linkage of U-phase of the motors

5.2. Cogging torque

The plot of cogging torques of the motors, all operating at 1900rpm are shown in Fig. 6. A cursory look at them, 24s-16p has three electric cycles securing the highest cogging torque of 75Nm peak to peak, and high cogging torque is not suitable for motor operation as it causes vibration as a result. Furthermore, the configurations of 24s-10p, 24s-14p and 24s-22p respectively have low cogging torques but 24s-14p has the favorable waveform. Therefore, further design improvement will reduce the cogging torque to the lowest minimum some effective and efficient performance of the proposed motor (Zang *et al*., 2014; Omar *et al*., 2013).

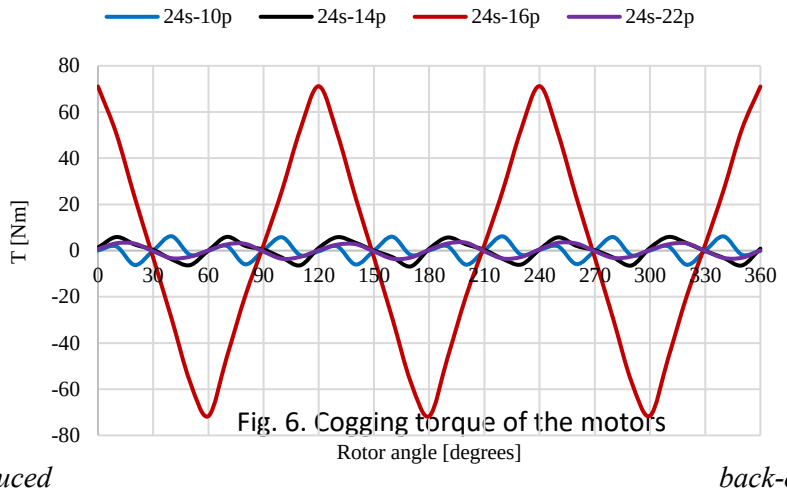

Fig. 6. Cogging torque of the motors

5.3. Induced back-emf

At no-load condition such that at current Ja 0 A/mm^2 the back-emf of the motors induced from the performance of PM and armature coil at the speed of 1900rpm is illustrated in Fig. 7. The purpose is to verify if the designed motor is working in a safe region. A cursory look at each of the motor, it is observed that 12slots-10poles delivered the highest amplitude of induced voltage. Adversely, the sinusoidal waveform is characterized with harmonics. This is followed by 12slots-14poles which has also sinusoidal waveform. Motor 12slots 7pole and 24slots-22poles have gross ripples while 24slots-16poles did not secure sinusoidal waveform. Therefore 24slots-10 and 14poles respectively have displayed favourable sinusoidal waveform and this gives them advantage to perform better after further refinement to provide protection in case of uncertain system fault (Wang *et al.*, 2008).

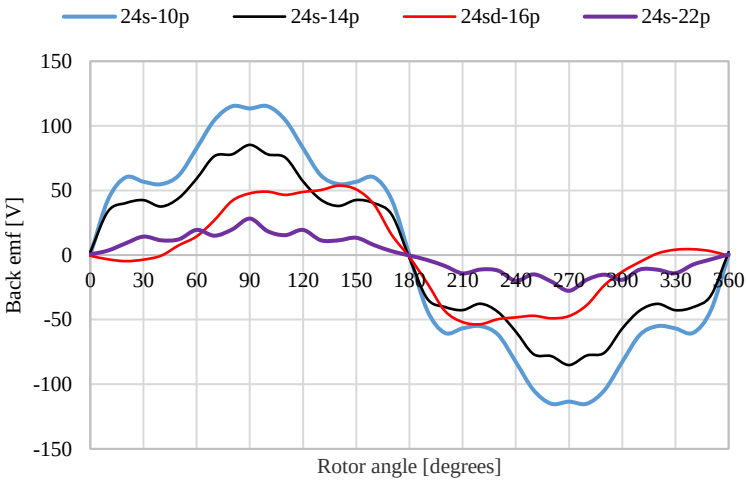

Fig. 7. Induced back-emf at 1900rpm

6. Torque versus speed characteristics

6.1 Load Condition

Plot of torque versus speed of the motors under investigation are shown in Fig. 8. Each motor's performance is presented and could be seen at the y- axis. 12slots-7poles achieves the lowest torque while 24slots-14 pole secures the highest torque of 208Nm. 24slots-10poles secures 184Nm and 24slots-16poles yields 175Nm while 24slots-22poles gets 66Nm respectively. Again, achieving the highest torque, 24slots-14poles has secured the

rotor number necessary for high torque that provides the acceleration for long distance travel. Equation 5 defines the convention theory used for torque production in electric motors: (Zhu *et al*., 2008)

$$T = P_n * (\phi_m) i_q \qquad (5)$$

Where P_n is the number of pole pairs, ϕ_m is the PM flux linkage while i_q is the quadrature axis current.

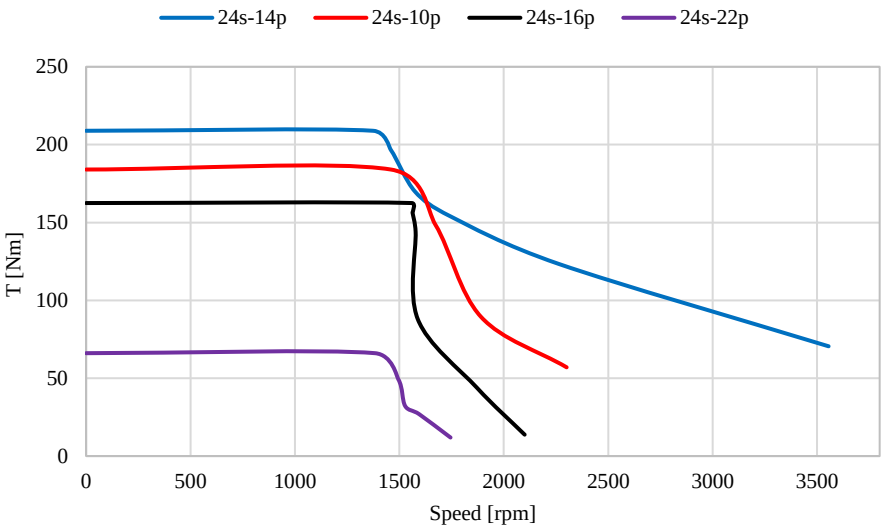

Fig. 8. Torque versus speed

7. Conclusion

This paper has presented four topologies of three phase out-runner segmented rotor permanent magnet flux switching motor having different rotor number from which the best will be selected for further improvement and analysis . The span angle of each pole segment is in accordance with the relationship between arc of length and segment of circle. Out of these motors designed, two motors only achieved favourable high magnetic flux amplitude, low cogging torque, induced back-emf necessary for high torque production. However, at load condition, 24slots-14poles secured the highest average torque of 208Nm. Therefore, with this excellent performance, the motor is selected for further improvement and optimization to improve its torque and general performance. And this will be reported soon.

References

Mecrow, B.C. , Bedford, T. J., Bennet, J.W., and Celik, T. (2006). The use of segmental rotors for 2-phase flux switching motors, *Proc. 17 International Conf. on Electrical Machines, ICEM'* paper 608.

Zulu, A. & Mecrow, B. C. (2012) Permanent magnet flux switching synchronous motor employing a segmental rotor, *IEEE Transactions on Industry Appl*. vol., 48.

Raminosoa, T., Gerada, C. & Galea, M. (2011). Design considerations for a fault tolerant flux switching permanent magnet machine, *IEEE Trans. Ind. Electrons*., vol.58, no. 7, pp. 2818-2825.

Thomas, A.S., Zhu, Z. Q., Zhang, A.S., & Jewell, G. W. (2010). Comparison of flux switching an dsurface mounted permanent magnet generators for aerospace applications, *Proc, IET PEMD,* pp. 1-5.

Zhu, Z.Q. (2011). Switched flux permanent magnet- machines innovation continues, *Proc. International Conf. on Elect. Mach. Systems,* pp. 1-10.

Zhu Z., Chen, Q, J., Pang, Y., Howe, D., Iwasaki, S. & Deodhar, R. (2008). Analysis of a novel multitooth flux switching PM brushless AC machine for high torque direct drive application, *IEEE Trans. Magnetics,* vol. 44, no. 11, pp.4313-4316.

Ahmad, M. Z., Sulaiman, E., Haron, Z. A. & Kosaka, T. (2012). Preliminary studies on a new ourt – rotor permanent magnet flux switching machine with hybrid excitation flux for direct drive EV application, *Proc. IEEE Int Conf., Power and Energy,* pp. 928-933

Fei, W., Luk, P. C. K., Shen J. X., Wang Y. & Jin, M. (2009). A novel outer –rotor permanent magnet flux switching machine for urban electric vehicle applications, *Pro. 3rd Inter. Conf., Power Elect. Systems Applications,* pp. 1-6.

Sulaiman, E., Kosaka, T., Matsui, N. & Ahmad, M.Z. (2012). Design studies on high torque and high power density hybrid excitation flux switching synchronous motor for HEV applications, *Proc. IEEE Int. Power Engineering and Optimisation Conference,* pp. 333-338.

Wroble, R. & Mellor, P. H. (2008). Design considerations of direct drive brushless machine with concentrated windings, *IEEE Trans. Energy Convers.*, vol. 23, no. 1, pp. 1-8.

Mecrow, B.C., El-Kharashi, E. A., Finch, J. W. & Jack, A.G. (2003). Segmental rotor switched reluctance motor with single tooth windings, *Electric Power Application*, *IEEE Proceedings*, vol. 15, pp. 591-599.

Galea, M., Gerada, C. & Hamiti, T. (2012). Design considerations for an outer rotor Field wound, flux switching machine," *XXth inter. Conf. on Electrical. Machines*, *(ICEM)*.

Zulu, A., Mecrow, B. C. & Armstrong, M. (2010). Topologies for wound field three phase segmented rotor flux switching machines, *Power Electronics, Machines and Drives (PEMD) 5th Inter., Conf.* pp. 1-6.

Fei, W., Chi-Kwong, P. & Shen, J. (2011). Design and analysis of a new outer rotor permanent magnet flux switching machine for electric vehicle propulsion, *The International Journal for computation and Mathematics in Electrical and Electronic Engineering (COMPEL),* vol. 30, Issue 1, pp. 48-61

Sulaiman, E., Khan, F. & Ahmad, M. Z. (2013). Investigation of field excitation switched flux motor with segmental rotor, *IEEE Conference on Clean Energy and Technology (CEAT),*pp. 317- 322.

Wang, C. F., Shen, J. X., Wang, L. L. & Wang, K. (2008). A novel permanent magnet flux switching linear motor, *Proc. 4th IET Conf..Power Electron, Machines and Drives,* pp. 116-119.

Zang, H., Hee Le, D., Woo-Lee, C. & Woo Ahn, J. (2014). Design and analysis of a segmental rotor type12/8 switched reluctance motor, *Journal of Power Electronics,* vol. 14 no. 5, pp. 866-873.

Omar, M. F., Sulaiman, E. & Soomro, H. A. (2013). A new topology of single phase field excitation flux switching machine for high density air-condition with segmental rotor, *ARPN Journal of Engineering and Applied Sciences*.

NEUTRON AND PHOTON SHIELDING PARAMETERS OF SOME HYDRIDES AND BOROHYDRIDES

[a]*Olarinoye, I.O., [b]Suraju, K.O.

[a]*Department of Physics, Federal University of Technology, Minna. Nigeria.

[b]Department of Physics/Geology/Geophysics, Federal University, Ndufu Alike Ikwo, Ebonyin State.

leke.olarinoye@futminna.edu.ng; lekeola2005@yahoo.com

Abstract

The mass attenuation coefficients and effective atomic numbers of three hydrides (MgH_2, TiH_2, and VH_2), seven borohydrides ($NaBH_4$, $Mg(BH_4)_2$, $Al(BH_4)_3$, KBH_4, $Ca(BH_4)_2$, $Mn(BH_4)_2$, and $RbBH_4$) and water were calculated and compared for photon energies in the range 0.015-15 MeV. The fast neutron removal cross-section of the 11 substances were also estimated. The mass attenuation coefficients and effective atomic numbers of the materials were observed to vary with photon energy and chemical composition. The effective atomic number and photon shielding capacity was found to be highest for $RbBH_4$ and least for water throughout the photon energy spectrum. The total fast neutron removal cross section for MgH_2, TiH_2, VH_2, $NaBH_4$, $Mg(BH_4)_2$, $Al(BH_4)_3$, KBH_4, $Ca(BH_4)_2$, $Mn(BH_4)_2$, $RbBH_4$ and water were 0.111, 0.1652, 0.1998, 0.109, 0.1322, 0.0725, 0.0867, 0.0781, 0.0737, 0.0847 and 0.1029, respectively. Neutron shielding capacity of the materials depended on their hydrogen partial fraction. The hydrides are better neutron shields compared to the borohydrides and water.

Keywords: Photons; Neutrons, Interaction cross-section; Hydrides; Borohydrides

1. Introduction

Over the years, research in nuclear science and technology has been very active. This is due to the wide applications of nuclear energy in diverse fields such as agriculture, medicine, industries and for research. Nuclear radiations are often released in many nuclear processes involved in these applications. Although, nuclear energy presents immense benefits for mankind, however, uncontrolled exposure of man and the biota to components of nuclear radiation has dangerous health and environmental implications. The continuous and effective use of nuclear energy and technology consequently depends to a large extent on the ability to confine the radiations in such a way that it does not cause harm to man and his environment.

One of the methods of radiation protection is through the use of radiation shield. Radiation shielding involves confining the nuclear radiation to a volume of space. Shielding requires no administrative control unlike other forms of radiation protection. An ideal shield would not only attenuate considerably the primary radiation, but should also not be a source of secondary radiation. The effectiveness of any shield depends on its chemical composition and radiation parameters such as type (particulate or electromagnetic) and energy. In a nuclear reactor facility, neutrons and photons (gamma rays are of major concern to nuclear engineers when designing structures for the purpose of radiation shielding. This is due to their massless (photons only) and uncharged nature which enables them to penetrate deeper into any given medium. Materials for gamma rays attenuation are required to be of high density, on the other hand, fast neutron shields require low density hydrogenous materials as moderators and materials rich in elements (B, Eu, Pu, Cd) that have high neutron absorption cross-section for the absorption of the moderated neutrons. However, low density materials emit gamma rays whose energy is in the range 0.10- 10 MeV [1] when used for neutron shielding. Obviously, a combination of low density hydrogen rich materials and high atomic number materials are required for the construction of an

effective absorber for neutrons [2-4]. This would not only provide adequate absorption for neutrons as well as for the secondary radiation (captured gamma rays).

Traditionally, radiation shield materials include lead, water, depleted uranium, polythene, light and heavy concretes [5-10]. Nevertheless, some of these materials have major drawbacks- the toxicity of lead has limited its use; depleted uranium is relatively less abundant, and also has radiation issues; concrete has durability and space issues as a result of its bulkiness [11, 12]. In addition to these, concrete loose its water and hence its hydrogen content as temperature increases [12]. Water on the other hand, is a liquid and thus require a container. These and many more problems have made research into alternative shielding materials very active and necessary.

Hydrides and borohydrides have been considered as good hydrogen storage materials due to their high hydrogen densities. Consequently, they have attracted much research interest especially in the area of energy storage [13-15]. Their high hydrogen content has also made them potentially effective moderators and absorbers of fast neutrons but they may not be effective in shielding the secondary photons that accompanies such interactions due to their low atomic masses. This report thus aims at evaluating the shielding effectiveness of three heavy hydrides (VH_2, MgH_2 and TiH_2), seven borohydride ($NaBH_4$, $Mg(BH_4)_2$, $Al(BH_4)_3$, KBH_4, $Ca(BH_4)_2$, $Mn(BH_4)_2$, and $Rb(BH_4)_2$) materials and water with respect to gamma rays and fast neutrons. The relationship between their shielding capacity and hydrogen content is explained. Shielding parameters such as; fast neutron removal cross section, mass attenuation coefficient, effective atomic numbers of the 11 hydrogen rich materials were also estimated and compared.

2. Theory and Calculations

2.1. Fast neutron removal cross section: The macroscopic effective removal cross section is a parameter that can be used to characterise neutron penetration in a material. It represents the probability that a fast neutron is removed from incident neutron beam [16, 17]. For fast neutron energy in the range 2-12 MeV, the effective removal cross section is a constant [18]. A lot of formulae has been suggested for the evaluation of the macroscopic effective removal cross-section (Σ_R) of fast neutrons (19, 18-22). These expressions have also been used for the evaluation of Σ_R for many elements [18-20]. For homogenous materials, Σ_R can be evaluated using the mixture rule [16]:

$$\Sigma_R = \sum_i w_i \left(\Sigma_R/\rho\right)_i \quad (1)$$

Where, w_i and Σ_R/ρ represent the partial density and mass removal cross section of the i^{th} element in the compound respectively.

2.2. Mass Attenuation Coefficients

The mass attenuation coefficient (μ_m) of a medium is a quantity that characterises its interaction with photons. According to the Beer- Lambert's law the transmission photon flux (I) through a medium of thickness t, when photon flux (I_o) is incident on it is predicted by the equation:

$$I = I_o e^{-\mu_m t} \quad (2)$$

The mass attenuation coefficient depends on atomic number of the medium and the photon energy. For composite material (chemical compound or homogeneous mixture), μ_m is expressed as:

$$\mu_m = \sum_i w_i (\mu_m)_i \quad (3)$$

Where w_i and $(\mu_m)_i$ are the weight fraction and mass attenuation coefficient of the *i*th elemental constituents in the compound. The μ_m of any medium at a specified energy also depends majorly on the photoelectric, Compton scattering and the pair production interaction coefficients [23]. The dominance of any of these three interaction modes dictates the magnitude of μ_m. Generally, μ_m measures the degree to which a material can attenuate photons.

2.3. Effective atomic number (Z_{eff})

The interaction cross section of photon with any medium is a function of its chemical constituents. For pure elements, their chemical characteristics may be described by their atomic number. However, for a composite material (mixture or compound), the effective atomic number (Z_{eff}) is used to define their response to electromagnetic radiation. The Z_{eff} is a parameter that conveniently represents the interaction of a medium with photons for the purpose of radiation absorbed dose measurement, shielding construction and identification of tissue equivalent material. Unlike the atomic number of pure elements, Z_{eff} is not a constant but rather depends on photon energy.

3. Methodology

Three hydrides (VH_2, TiH_2, and MgH_2), 7 borohydride ($NaBH_4$, $Mg(BH_4)_2$, $Al(BH_4)_3$, KBH_4, $Ca(BH_4)_2$, $Mn(BH_4)_2$, and $Rb(BH_4)_2$) and water were analysed for their neutron and photon shielding capacity. The chemical formulae, physical density and hydrogen density in these materials were obtained from literature [13, 18, 24] and presented in Table 1.

3.1 **neutron removal cross section:** The macroscopic effective removal cross section (Σ_R) for the hydrides and borohydrides were evaluated through the use of a computer program- WinNC-toolkit [22]. The program was designed for theoretical determination of attenuation coefficients of fast neutrons in composite materials. The results from the toolkit has been verified to agree with good accuracy to experimental data [22].

3.2 **Mass attenuation coefficient:** The mass attenuation coefficients of the materials were estimated theoretically via the use of the WinXCom computer code [25] for photon energies from 0.01-15 MeV. This code is the window version of an earlier program (Xcom) developed by Berger and Hubbel [26]. The program can be used to calculate photon interaction cross section for element, compound and mixture in the energy spectrum of 1 keV-1 GeV.

3.3. **Estimation of the Effective atomic number (Z_{eff}):** the values of $(\mu_m)_i$ for each compound obtained from WinXCom was used to calculate the total molecular cross section according to the equation:

$$\sigma = \mu_m \frac{M}{N_A} \tag{4}$$

.Where, M and N_A is the molecular weight of each compound and the Avogadro's number respectively. The total atomic cross section (σ_t) was then calculated using the equation:

$$\sigma_t = \sigma / \sum_i n_i \tag{5}$$

Here, n_i is the number of formula unit of the i^{th} element. The effective atomic number of the water, halides and boro-hydrides was then calculated using the equation [27]:

$$Z_{eff} = {}^{\sigma_t}/_{\sigma_e} \tag{6}$$

Where, σ_e is the total electronic cross section of the material and it is given as [23]:

$$\sigma_e = \frac{1}{N_A}\sum_i \frac{(fA)_i}{Z_i}\mu_i \quad (7)$$

The weight proportion of the i^{th} element with atomic mass number in a compound is represented by f and A respectively in equation x.

4. Results and Discussions

The fast neutron removal cross-section for the hydrides is presented in Figure 1. The cross section was 0.111, 0.1652 and 0.1998 for MgH_2, TiH_2 and VH_2 respectively. The increase in neutron removal ability was consistent with their hydrogen (content neutron removal cross section) partial density as depicted in the same figure (Figure 1). This is due to the fact that hydrogen has higher neutron cross section compare to any of Mg, Ti or V. Consequently higher hydrogen partial density implies higher affinity for neutron removal. The removal cross section for the considered borohydrides, partial removal cross section of hydrogen and boron in the compounds are shown in Figure 2. The removal cross section was higher for borohydride with higher combination of boron and hydrogen removal cross sections irrespective of the physical densities and atomic molar masses of the borohydrides. The total fast neutron removal cross section for $NaBH_4$, $Mg(BH_4)_2$, $Al(BH_4)_3$, KBH_4, $Ca(BH_4)_2$, $Mn(BH_4)_2$, and $RbBH_4$ are: 0.109, 0.1322, 0.0725, 0.0867, 0.0781, 0.0737, and 0.0847 respectively, while that of water was found to be 0.1029. From the results, MgH_2, VH_2, $NaBH_4$, and $Mg(BH_4)_2$ are better fast neutron moderators than water and thus could be used for the construction of neutron shield in a nuclear facility. The partial neutron removal cross section for hydrogen which is directly linked with the hydrogen partial density is a vital factor for the relative shielding efficacy of neutron of all the considered materials.

The mass attenuation coefficients **(μ_m)** for the eleven substances in the low energy (0.015-0.1 MeV) and high energy (0.2-15 MeV) ranges are presented in Figures 3a and 3b respectively. The changes in the mass attenuation coefficients of the hydrides, borohydrides and water behave similarly within the presented photon energy spectrum. The $\mu_m$were higher at lower energy region and vice versa for all the materials. Between 0.015 and 0.04 MeV, mass attenuation was highest. Beyond this energy, the μ_m decreased rapidly with energy up to 0.1 MeV. From 0.1 MeV to 4 MeV the mass attenuation coefficients remain relatively stable for all considered substances after which a rise in value begins (Figure 3b). This trend is consistent with theoretical argument which predicted high attenuation coefficients for low energy photons in any material due to the removal of low energy photon from photon beam after interaction with any medium [23]. This removal can be attributed to two main reasons; firstly, low energy photons have high interaction coefficient thus possess more tendency to loss a good part of their energy during collision with the atoms of the interacting medium. This leads to further loss of photon energy and ultimately their absorption. Secondly, photoelectric effect and Compton scattering are two major interaction modes that takes place within the region below 2 MeV. These two modes of interaction depletes the population of photons in a beam incident on a material medium. While the photoelectric effect removes completely photons from a beam, incoherent scattering reduce considerably the energy of the interacting photons. These two events account for the loss of photons at the lower end of the spectrum and thus accounts for the relative high attenuation coefficient for a material when compared to the high energy region. At the higher energy region, the photons are very energetic and penetrate deeper into the material without interacting. This explains why the attenuation is low at low energy. although pair production takes place at energies greater than 1.02 MeV, and also annihilate photons, this is not enough to cause a rapid increase in the attenuation but rather gradual as shown in the figure beyond 4 MeV. Comparatively, from the figures, and Table 1, it appears that the physical density of the substances play no major role in their photon shielding efficacies as may be expected. This is probably due to the fact that the use of physical density for selecting photon shielding materials is only applicable to mixtures of similarly compound such as concretes

with different mixture composition. For pure compounds, the chemical constituents and their concentrations play a more vital role. In the low energy region, the mass attenuation coefficients for the substances in the following order: $RbBH_4$ > VH_2 > TiH_2 > $Mn(BH_4)_2$ > KBH_4 > $Ca(BH_4)_2$ MgH_2 > $NaBH_4$ > $Al(BH_4)_3$ >H_2O> $Mg(BH_4)_2$. However, in the high energy region, there seems to be no noticeable difference between the mass attenuation coefficients of all the substances considered.

The effective atomic numbers and their variations with photon energy within the range 0.015-15 MeV is shown in Figure 4. Obviously, the changes in Z_{eff} with respect to photon energy is almost similar for all the eleven substances considered. From the figure, the Z_{eff} decreased steadily from their maximum value in the low energy region (0.015-0.1 MeV) of the spectrum. Thereafter, the values become relatively stable before increasing slightly towards the end of the energy spectrum. The peak value of Z_{eff} for all the materials was obtained at 15 KeV while the minimum values were observed at different energies for different material between photon energy range of 0.5 MeV and 1 MeV. The observed changes in Z_{eff} with energy of photons can be attributed to photon interaction modes with each substances. Within the energy region of interest in this study, the photoelectric effect, Compton (incoherent) scattering and pair production are the three dominant interaction modes for photons. In the low energy region (0.015-0.04 MeV), photoelectric effect dominates, while Compton scattering and pair production dominated at intermediate (0.05-1 MeV) and high energy (above 1.5 MeV) regions respectively. The photoelectric effect (τ), Compton scattering (σ) and pair production (κ) interaction coefficients depends on energy and atomic number according to the following equations [27]:

$$\tau = a\frac{Z^5}{E^3} \quad (8)$$

$$\sigma = b\frac{Z}{E} \quad (9)$$

$$\kappa = cZ^2(E - 1.02) \quad (10)$$

Where *a, b, c* are constants. Consequently, the effective atomic numbers of the substances are higher in the lower energy region where photoelectric effect is dominant and least in the region of Compton scattering as predicted by the equation 1-3. The final rise in the Zeff at the later energy region is predicted nby equation 2 due to the predominance of pair production.

From the results, for each of the eleven materials, the upper and the lower limits of the Zeff depend on the atomic composition of the compounds. The upper and lower limits did not exceed the atomic number of the heaviest and lightest atoms respectively in the composite material. This explains why compound with high atomic number atoms have higher effective atomic number at all energies and vice versa. $RbBH_4$ had the highest Zeff throughout the considered energy spectrum while water and Al(BH4)3 had the least in the low energy region and high energy region respectively. The Zeff of the materials varied from 4.66; 8.01; 8.34; 3.33; 2.73; 2.50; 18.26; 3.46; 3.92; 7.76; and 3.33 to 11.38; 21.80; 22.82; 9.28; 9.37; 9.76; 4.67; 18.70; 24.07; 35.14 and 6.74 respectively for: MgH_2; TiH_2; VH_2; $NaBH_4$; $Mg(BH_4)_2$; $Al(BH_4)_3$; KBH_4; $Ca(BH_4)_2$; $Mn(BH_4)_2$; $RbBH_4$;and water.

Table 1. Mass number, physical density and hydrogen density of the hydride, borohydride and water.

Material	Mass Number	Density (gcm^{-3})	Hydrogen Density ($10^{22}\ cm^{-3}$)
MgH_2	26.32	1.45	6.6
TiH_2	49.88	3.77	9.1
VH_2	52.96	4.62	10.5
$NaBH_4$	37.83	1.08	6.9
$Mg(BH_4)_2$	53.99	1.48	13.2
$Al(BH_4)_3$	71.51	0.79	8
KBH_4	53.94	1.17	5.3
$Ca(BH_4)_2$	69.76	1.07	7.5
$Mn(BH_4)_2$	84.62	1.24	7.1
$RbBH_4$	100.31	1.92	4.6
Water	18.02	1	6.7

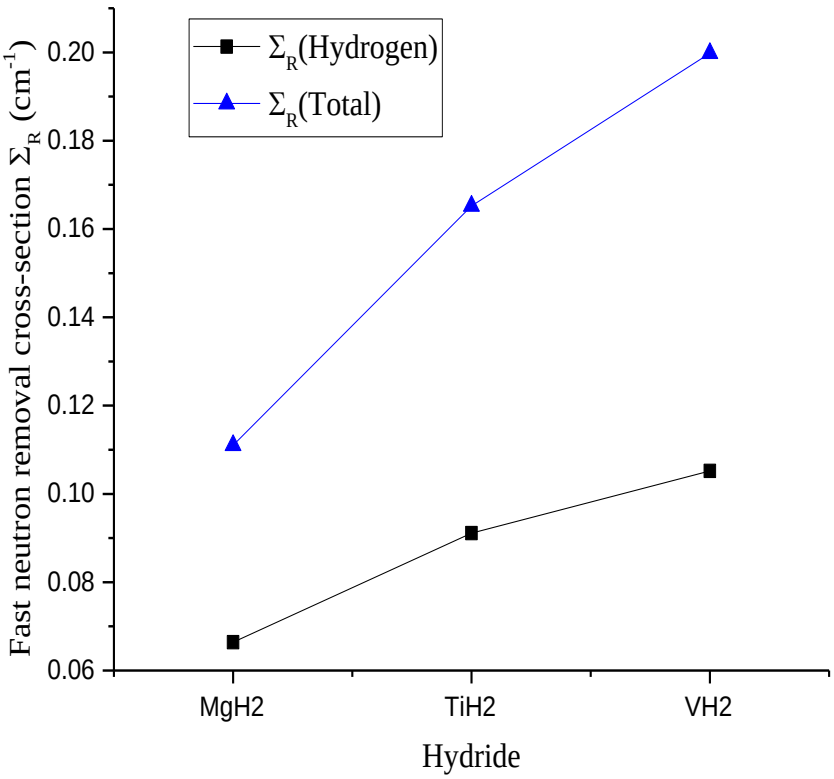

Figure 1. Fast neutron removal cross-section for the hydrides and hydrogen content

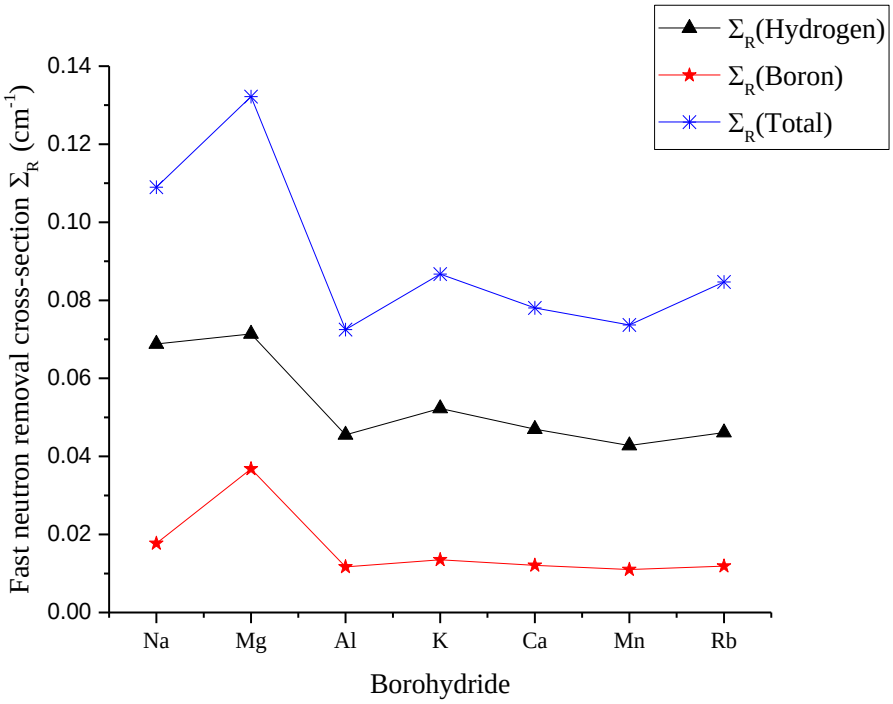

Figure 2. Fast neutron removal cross section for the borohydrides and boron and hydrogen content.

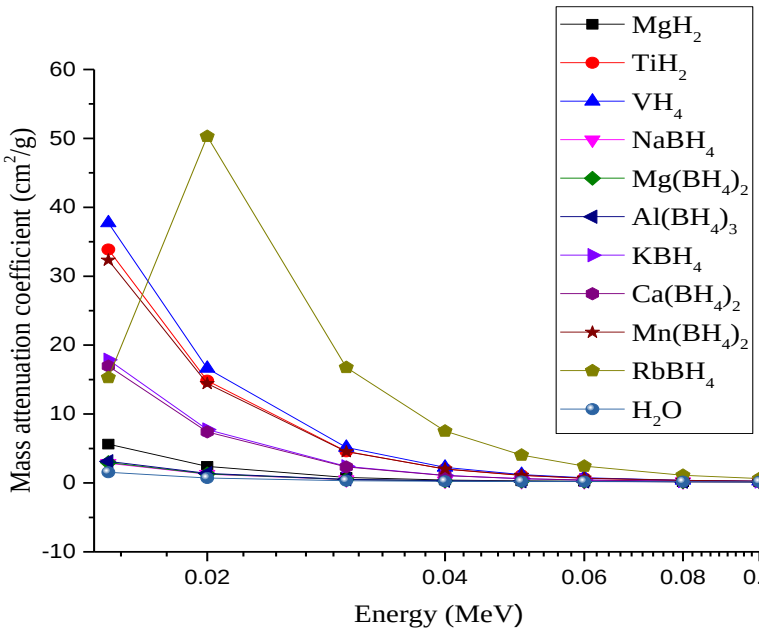

Figure 3a. Mass attenuation Coefficieents of the substances in the low energy region.

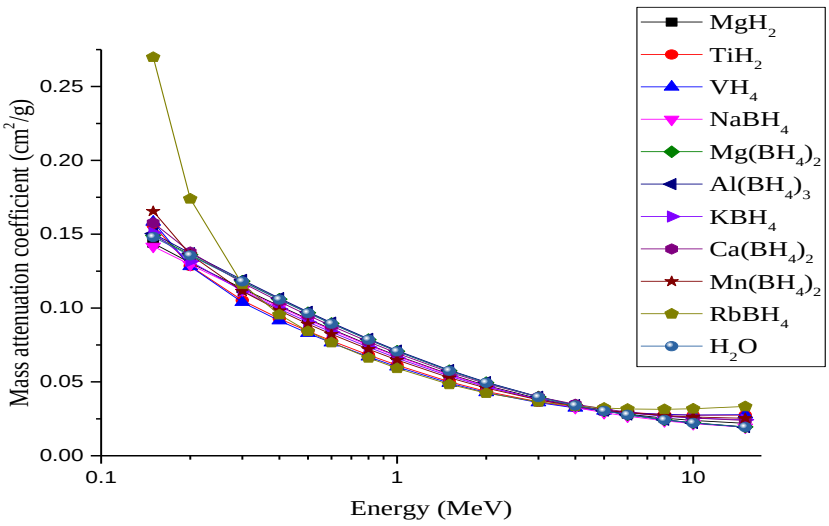

Figure 3b. Mass attenuation coefficients of the substances in the high energy region.

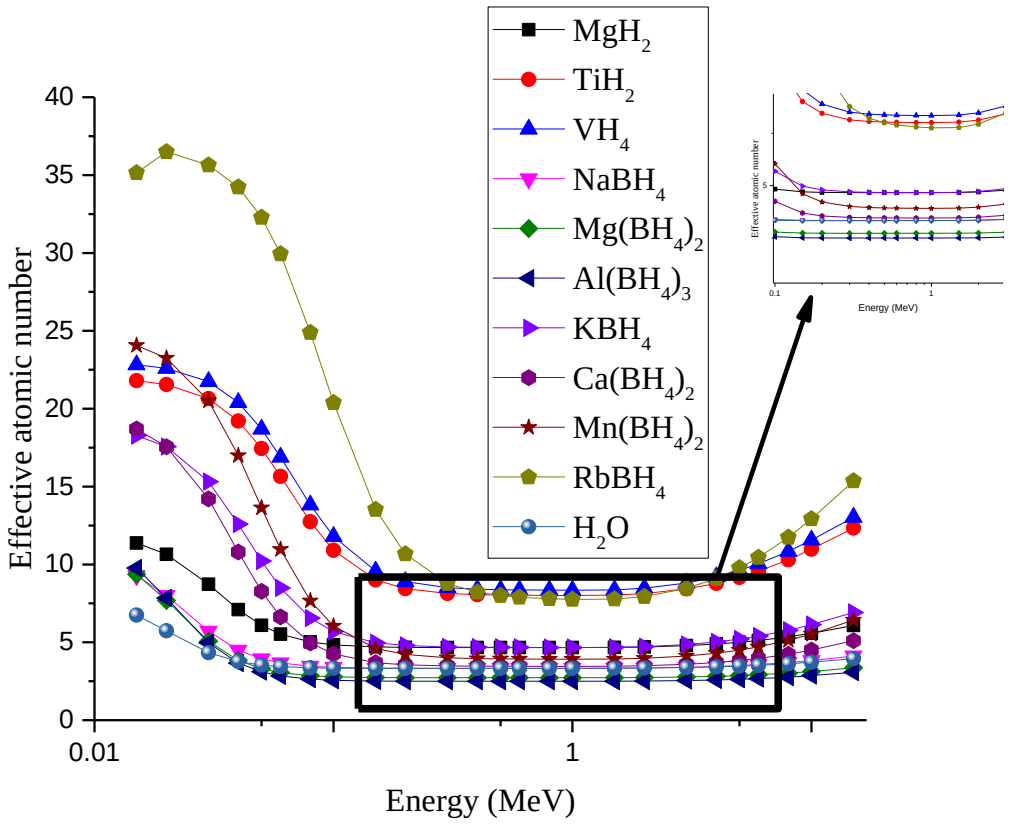

Figure 4. Effective atomic number of the substances.

5. Conclusion

The neutron and photon shielding capacities of three hydrides (MgH_2, TiH_2, and VH_2), seven borohydrides ($NaBH_4$, $Mg(BH_4)_2$, $Al(BH_4)_3$, KBH_4, $Ca(BH_4)_2$, $Mn(BH_4)_2$, and $RbBH_4$) and water were calculated and

compared. For the purpose of fast neutron moderation or shielding, the partial hydrogen density and neutron removal cross section plays a vital role irrespective of physical densities of the materials. The calculated mass attenuation coefficients of the materials vary with photon energies in similar version but differ in magnitude from one material to the other. The mass attenuation coefficient was higher for compound containing denser atoms and smaller for compound with less heavy atoms. From the results, $RbBH_4$ showed better photon shielding capacity compared to other compounds while water was the least effective for photon shielding. The effective atomic number varied with photon energy as predicted by the partial photon interaction modes (photoelectric effect, Compton scattering and pair production) dominant at a particular energy. Although the effective atomic number is an approximation and similar in function to the atomic number of elements for the purpose of radiation control and measurements, the observed variation with photon energy thus suggest that a single digit cannot be used to represent it for compounds and mixtures. Rather, the value to be used for this purpose will depend greatly on the spectrum of photon energy of interest.

Generally, the requirement for good neutron shield are not the same for photon shield, consequently, the same material cannot be used for the same function with equal efficiencies. From the results of this research, $RbBH_4$ shield photons better while VH_2 presents a better neutron shield out of all the materials considered. However in a mixed radiation environment comprising fast neutron and photons, a combination of shielding materials to serve for both photons and neutrons are recommended. A combination of VH_2 and $RbBH_4$ or a material containing both compounds could be a perfect shield for radiation protection of man and the biota against the harmful effects of the radiations.

References

[1]. V.P. Singh, M.E. Medhat, N.M. Badiger, Nuclear Engineering Design, 270 (2014) 90-100.

[2]. S.W. Gary, Fundamental of Radiation Material Science, Springer-Verlag, Berlin, 2007.

[3]. T. Hayashi, K. Tobita, Y. Nakamori, S. Oriomo, Journal of Nuclear Materials 386-388 (2009) 119-121.

[4]. T. Hayashi, K. Tobita, S. Nishino, et al., Fus. Eng. Des. 81 (2006) 1285.

[5]. A.S. Makarious, et al., Ann. Nucl Eng. 23 (1996) 3, 195-206.

[6]. S. M. J. Mortazavi, Radiat. Prot. Dosimetry, 142 (2010), 2-4, 120-124.

[7]. I.I. Bashter, Ann. Nucl. Energy, 24 (1997), 17, 1389-1401.

[8]. Oyeleke O.I. (2009). *Journal of science, education and technology, 2(1). 197-202.*

[9]. M.R. Shavers, N. Zapp, R.E. Barber, J.W. Wilson, G. Qualls, L. Toupes, S. Ramsey, V. Vinci, G. Smith, F.A. Cucinnotta. Adv. Space Res. (2004) 1333-1337.

[10]. J. Miller, C. Zethlm, F.A. Cicinotta, L. Heilbronn, D. Stephens, J.W. Wilson. Radiat. Res. 159 (2003) 381-390.

[11]. Elbio Calzada et al., Nucl. Instruments and Methods in Physics Research, A 651 (2011), 77-80.

[12]. A. Akkurt et al., Radiat. Meas. 45 (2010) 827-830.

[13]. S. Oriomo, Y. Nakamori, J. Eliseo, A. Zuttel, C.M. Jensen.Chem. Rev. 107 (2007) 4111-4132.

[14]. Y. Nakamori, K. Miwa, A. Ninomya, H. W. Li, N. Ohba, S. Towata, Z. Zuttel, S. Orimo, Phys. Rev. B. 74 (2006) 045126 (1).

[15]. S. Oriomo, Y. Nakamori, A. Zuttel, Mater. Sci. Eng. B 108 (2004) 51.

[16]. E.P. Blizard, L.S. Abbott, Reactor Handbook, Vol. III, part B, Shielding Wiley, New York, 1962.

[17]. J.J. Duderstadt, L.J. Hamilton, Nuclear Reactor Analysis (Wiley, New York) 1976.

[18]. M. F. Kaplan, concrete Radiation Shielding, Wiley, New York, 1982.

[19]. V.P. Singh, N. M. Badiger, J. Fusion Energ. 2014 DOI10.1007/S10894-014-9679.4

[20]. A.E. Profio, Radiation Shielding and Dosimetry, Wiley, New York, 1979.

[21]. A.B. Chitton, J.K. Shultis, R.E. Faw, Principles of Radiation Shielding, Prentice-Hall, Eaglewood Cliffs, N.J. 1984.

[22]. K.S. Mann., Toolkit for fast neutron removal cross-section, 3rd international Conference Advancements in Engineering and Technology, Bhai Gurdas Institute of Engineering and Technology, Sangrur (Puanjab), India.

[23]. Olarinoye, I.O. Res. J. Chem Sci. 1(2) (2011) 64-69.

[24]. K. Tobita, S. Konishi, S. Nishio, K. Kosako, T. Tabaro, Letters 10, (2001) 1035-1039.

[25]. L. Gerward, N. Guibert, K.B. Jensen, H. Levring. 2004. WinXCom: a program for calculating X-ray attenuation Coefficients. Radiat. Phys. Chem. 71, 653-654.

[26]. M.J. Berger, J.H. Hubbel, 1987 NBSIR 87-3597, XCOM: photon cross section on personal computer. National institute of standards. Gaithersberg, M.D. 20899, U.S.A.

[27]. E.M. James (2006)Physics for radiation protection: a handbook. Wiley-VCH, Verlag GmbH and Co. Weinheim, 822.

A UNIFORM ORDER CONTINUOUS HYBRID INTEGRATION FOR SOLVING THIRD ORDER ORDINARY DIFFRENTIAL EQUATIONS

Umaru Mohammad[*1] Aliyu Ishaku Ma'ali[2] and Raphael Babatunde Adeniyi [3]

[1*]Department of Mathematics, Federal University of Technology, Minna, Niger State, Nigeria.

[2]Department of Mathematics/ Computer Science, Ibrahim Badamasi University Lapai, Nigeria

[3] Mathematics Department, University of ILorin, ILorin, Nigeria.

[1]umaru.mohd@futminna.edu.ng

[2]aai_maali@yahoo.com

[3]raphade@unilorin.edu.ng

Abstract

A three -step Continuous Block Hybrid Method (CBHM) with two non-step points of order (6,6,6,6,6) is proposed for direct solution of the special and general third order initial value problems (IVPs). The main method and additional methods are obtained from the same continuous schemes derived via interpolation and collocation procedures. The stability properties of the methods are discussed and the stability region shown. The methods are applied in block form as simultaneous numerical integrators over non-overlaping interval. The efficiency of the proposed method was tested and was found to compete favorable with the existing methods.

Keywords: Collocation, Interpolation, Power series approximant, Grid points, Off-grid points and Block methods

1. Introduction

This paper considers the solution of special and general third order initial value problem of the form:

$$y''' = f(x, y),\ y(a) = y_0\ ,\ y'(a) = \eta_0\ ,\ y''(a) = \eta_1 \tag{1}$$

$$y''' = f(x, y, y', y''),\ y(a) = y_0\ ,\ y'(a) = \eta_0\ ,\ y''(a) = \eta_1 \tag{2}$$

However, only a limited number of numerical methods are available for solving (1) and (2) directly without reducing to a first order system of initial value problems. Some authors have proposed solution to higher order initial value problems of ordinary differential equations using different approaches (Awoyemi (1991),Awoyemi (2000),Kayode (2005) and Adekunle et al. (2013)). These methods mentioned which were implemented in Predictor-Corrector mode, like linear multistep methods and other standard method are usually applied to initial value problem as a single formula but the setbacks of this method are: (1) They are not self-starting (2) they advance the numerical integration of ordinary differential equation in one step at a time which lead to overlapping of piecewise polynomial solution mode. See (Mohammed and Adeniyi (2014) and Mohammed and Adeniyi (2015)) for details. The advantages of continuous method are widely reported by Awoyemi (2003).

In order to correct the setback of the method of Predictor-Corrector method, Fatunla(1991), Olabode (2009), Olabode and Yusuph (2009) and Yahaya and Mohammed (2010) proposed block methods for the solution of higher order differential equations with limitation to special type of tODEs

In view of the above mention, we extended the work of Olabode and Yusuph (2009) into a modified linear multi-step method by considering one-three off step point at collocation to handle both special and general third ordinary differential equations. The three step block hybrid method proposed is zero stable, consistent and more accurate than the existing one. Experimental results confirm the superiority of the new schemes over the existing method.

2. Derivation of the method

In this section the objective is to derive Hybrid Linear Multi-step Method (HLMM) of the form

$$\sum_{j=0}^{r-1}\alpha_j y_{n+j} = h^3\sum_{j=0}^{s-1}\beta_j f_{n+j} + h^3\beta_\mu f_{n+\mu} + h^3\beta_v f_{n+v} \qquad (2)$$

Where α_j , β_j and β_v are unknown constants and v_j is not an integer. We note that α_k =1, $\beta_j \neq 0$, α_0 and β_0 do not both vanish. In order to obtain (2), we proceed by seeking to approximate the exact solution Y(x) of the form

$$Y(x) = \sum_{j=0}^{r+s-1} a_j x^j , \qquad (3)$$

Where $x \in [a,b], a_j$ are unknown coefficients to be determined and $1 \le r < k$, $S > 0$ are the number of interpolation and collocation points respectively. We construct the continuous approximation by imposing the following conditions.

$$Y(x_{n+j}) = y_{n+j} , \quad j = 0,1.2,....., r-1 \qquad (4)$$

$$Y'''(x_{n+j}) = f_{n+j} \qquad (5)$$

Equation (4) and (5) lead to a system of (r+s) equations which is solved by Cramer's rule to obtain a_j . The continuous approximation is constructed by substituting the values of a_j into equation (3). After simplification, the continuous method is expressed as

$$Y(x) = \sum_{j=0}^{r-1}\alpha_j(x) y_{n+j} + h^3\sum_{j=0}^{s-1}\beta_j(x) f_{n+j} + h^3\beta_\mu(x) f_{n+\mu} + h^3\beta_v(x) f_{n+v} \qquad (6)$$

where $\alpha_j(x), \beta_j(x), \beta_\mu(x)$ and $\beta_v(x)$ are continuous coefficients. We note that since

equation (1) involves first and second derivatives, the first and second derivative formula

$$Y'(x)=\frac{1}{h}\left(\sum_{j=0}^{r-1}\alpha'_j(x)y_{n+j}+h^3\sum_{j=0}^{s-1}\beta'_j(x)f_{n+j}+h^3\beta'_\mu(x)f_{n+\mu}+h^3\beta'_v(x)f_{n+v}\right)$$
$$Y''(x)=\frac{1}{h^2}\left(\sum_{j=0}^{r-1}\alpha''_j(x)y_{n+j}+h^3\sum_{j=0}^{s-1}\beta''_j(x)f_{n+j}+h^3\beta'_\mu(x)f_{n+\mu}+h^3\beta''_v(x)f_{n+v}\right) \quad (7)$$

Equation (7) is easily obtained from (6) and is used to provide the first and second derivatives for the methods by imposing the condition

$$Y'(x)=\delta(x),\ Y''(x)=\gamma(x) \quad (8)$$
$$Y'(a)=\delta_0,\ Y''(a)=\gamma_0 \quad (9)$$

3. Three Step Block Hybrid Method with two off Step Collocation Point

To derive this methods, we use Eq.(6) to obtained a continuous 3-step HLM method with the following specification : r=3,s=6,k=3, $v=\frac{8}{3},\mu=\frac{5}{2},\gamma_i(x)=x^i,i=0,1,...,8$.

We also express $\alpha_j(x),\beta_j(x)$ and $\beta_v(x)$ as a functions of t, where $t=\frac{x-x_n}{h}$ to obtain the continuous form as follows:

$$\alpha_0=\left(1-\frac{3}{2}t+\frac{1}{2}t^2\right),\ \alpha_1=\left(2t-t^2\right),\ \alpha_2=\left(-\frac{1}{2}t+\frac{1}{2}t^2\right)$$

$$\beta_0(x)=\frac{1}{201600}\left(10078t-28615t^2+33600t^3-21910t^4+8638t^5-2044t^6+268t^7-15t^8\right)$$

$$\beta_1(x)=\frac{1}{25200}\left(10016t-14400t^2+8400t^4-5404t^5+1617t^6-244t^7+15t^8\right)$$

$$\beta_2(x)=\frac{1}{3360}\left(-2082t+3809t^2-4200t^4+3542t^5-1274t^6+220t^7-15t^8\right)$$

$$\beta_{\frac{5}{2}}(x)=\frac{1}{1575}\left(3244t-5910t^2+6720t^4-5936t^5+2268t^6-416t^7+30t^8\right)$$

$$\beta_{\frac{8}{3}}(x)=\frac{1}{22400}\left(-40662t+74115t^2-85050t^4+75978t^5-29484t^6+5508t^7-40t^8\right)$$

$$\beta_3(x)=\frac{1}{5040}\left(1316t-2402t^2+2800t^4-2548t^5+1015t^6-196t^7+15t^8\right) \quad (10)$$

The MFDMs are obtained by evaluating (10) at $x = \left\{ x_{n+3}, x_{n+\frac{8}{3}}, x_{n+\frac{5}{2}} \right\}$ to obtain the following

$$y_{n+3} = y_n - 3y_{n+1} + 3y_{n+2} + \frac{h^3}{1200}\left[11f_n + 536f_{n+1} + 900f_{n+2} - 896f_{n+\frac{5}{2}} + 729f_{n+\frac{8}{3}} - 80f_{n+3}\right] \quad (11)$$

$$y_{n+\frac{8}{3}} = \frac{5}{9}y_n - \frac{16}{9}y_{n+1} + \frac{20}{9}y_{n+2} + \frac{h^3}{52488}\left[271f_n + 12928f_{n+1} + 19716f_{n+2} - 21760f_{n+\frac{5}{2}} + 16605f_{n+\frac{8}{3}} - 1840f_{n+3}\right] \quad (12)$$

$$y_{n+\frac{5}{2}} = \frac{3}{8}y_n - \frac{5}{4}y_{n+1} + \frac{15}{8}y_{n+2} + \frac{h^3}{491520}\left[1729f_n + 81304f_{n+1} + 115740f_{n+2} - 135424f_{n+\frac{5}{2}} + 101331f_{n+\frac{8}{3}} - 11080f_{n+3}\right] \quad (13)$$

In particular, to start the initial value problem for n = 0, we obtain the following equations from (9):

$$h\delta_0 = -\frac{3}{2}y_0 + 2y_1 - \frac{1}{2}y_2 + h^3\left[\frac{5039}{100800}f_0 + \frac{626}{1575}f_1 - \frac{347}{560}f_2 + \frac{3244}{1575}f_{\frac{5}{2}} - \frac{20331}{11200}f_{\frac{8}{3}} + \frac{47}{180}f_3\right] \quad (14)$$

$$h^2\gamma_0 = y_0 - 2y_1 + y_2 + h^3\left[-\frac{5723}{20160}f_0 - \frac{8}{7}f_1 + \frac{3809}{1680}f_2 - \frac{788}{105}f_{\frac{5}{2}} + \frac{14823}{2240}f_{\frac{8}{3}} - \frac{1201}{1260}f_3\right] \quad (15)$$

The derivatives are derived by

$\delta(x_{n+\tau}) = \delta_{n+\tau}$ *and* $\gamma(x_{n+\tau}) = \gamma_{n+\tau}$, $\tau = 1,2,\frac{5}{2},\frac{8}{3}$ *and* 3 as follows:

$$h\delta_{n+1} = -\frac{1}{2}y_n + \frac{1}{2}y_{n+2} - \frac{h^3}{20160}\left[131f_n + 3272f_{n+1} - 1332f_{n+2} + 5632f_{n+\frac{5}{2}} - 5103f_{n+\frac{8}{3}} + 760f_{n+3}\right]$$

$$h\delta_{n+2} = \frac{1}{2}y_n - 2y_{n+1} + \frac{3}{2}y_{n+2} + \frac{h^3}{100800}\left[49f_n + 21632f_{n+1} + 21130f_{n+2} - 27392f_{n+\frac{5}{2}} + 19683f_{n+\frac{8}{3}} - 200f_{n+3}\right]$$

$$h\delta_{n+\frac{5}{2}} = y_n - 3y_{n+1} + 2y_{n+2} + \frac{h^3}{806400}\left[7387f_n + 360262f_{n+1} + 602370f_{n+2} - 628672f_{n+\frac{5}{2}} + 486243f_{n+\frac{8}{3}} - 54790f_{n+3}\right]$$

$$h\delta_{n+\frac{8}{3}} = \frac{7}{6}y_n - \frac{10}{3}y_{n+1} + \frac{13}{6}y_{n+2} + h^3\left[\frac{31111}{2939328}f_n + \frac{120314}{229635}f_{n+1} + \frac{1144879}{1224720}f_{n+2} - \frac{29084}{32805}f_{n+\frac{5}{2}} + \frac{43651}{60480}f_{n+\frac{8}{3}} - \frac{15115}{183708}f_{n+3}\right]$$

$$h\delta_{n+3} = \frac{3}{2}y_n - 4y_{n+1} + \frac{5}{2}y_{n+2} + \frac{h^3}{20160}\left[271f_n + 13672f_{n+1} + 26460f_{n+2} - 22528f_{n+\frac{5}{2}} + 21141f_{n+\frac{8}{3}} - 2056f_{n+3}\right]$$

$$h^2\gamma_{n+1} = y_n - 2y_{n+1} + y_{n+2} + \frac{h^3}{100800}\left[1653f_n + 12088f_{n+1} - 52860f_{n+2} + 150272f_{n+\frac{5}{2}} - 129033f_{n+\frac{8}{3}} + 17880f_{n+3}\right]$$

$$h^2\gamma_{n+2} = y_n - 2y_{n+1} + y_{n+2} + \frac{h^3}{100800}\left[841f_n + 46976f_{n+1} + 94140f_{n+2} - 125696f_{n+\frac{5}{2}} + 95499f_{n+\frac{8}{3}} - 10960f_{n+3}\right]$$

$$h^2\gamma_{n+\frac{5}{2}} = y_n - 2y_{n+1} + y_{n+2} + \frac{h^3}{322560}\left[2757f_n + 149360f_{n+1} + 363828f_{n+2} - 225536f_{n+\frac{5}{2}} + 220887f_{n+\frac{8}{3}} - 27456f_{n+3}\right]$$

$$h^2\gamma_{n+\frac{8}{3}} = y_n - 2y_{n+1} + y_{n+2} + h^3\left[\frac{209179}{24494400}f_n + \frac{177256}{382725}f_{n+1} + \frac{459667}{408240}f_{n+2} - \frac{234436}{382725}f_{n+\frac{5}{2}} + \frac{77467}{100800}f_{n+\frac{8}{3}} - \frac{26627}{306108}f_{n+3}\right]$$

$$h^2\gamma_{n+3} = y_n - 2y_{n+1} + y_{n+2} + \frac{h^3}{100800}\left[869f_n + 46584f_{n+1} + 115140f_{n+2} - 79104f_{n+\frac{5}{2}} + 115911f_{n+\frac{8}{3}} + 2200f_{n+3}\right]$$

This proposed method is consistent since its order is 6, its also zero-stable; above all, it has moderate interval of absolute stability as can be seen in figure 1. The proposed three step method (11)-(15) have order 6 and error constants given by the vector $C_9 = \left(\frac{1}{201600}, -\frac{5167}{1785641760}, -\frac{571}{123863-40}, \frac{1141}{12}, \frac{283}{4}\right)^T$

4. Convergence

The convergence of the proposed block hybrid methods is determined using the approach of Fatunla (1991) for hybrid linear multistep method, where the block hybrid method are represented in a single block, r point multistep method of the form

$$A^{(0)}Y_m = \sum_{i=1}^{k} A^i Y_{m-i} + h \sum_{i=0}^{k} B^{(i)}F_{m-i}, \qquad (16)$$

Where *h* is a fixed mesh size within a block, A^i,B^i, i=O(1)k are r by r matrix coefficients and

A^0 is r by r identity matrix.

Y_m, Y_{m-1} , F_m and F_{m-1} are vectors of numerical estimates

Definition 1. The block method is zero stable provided the root $R_{i,j} = 1(1)k$ of the first characteristic polynomial $p(R)$ specified as

$$\rho(R) = \det\left|\sum_{i=0}^{k} A^{(i)} R^{k-i}\right| = 0 \qquad (17)$$

Satisfies $|R_j| \leq 1$ and for those roots with $|R_j| \leq 1$, the multiplicity must not exceed 2.

We can put the five integrator represented by equations (11) - (15) into the matrix-equation form and for easy analysis the result was normalized to obtain;

$$\begin{pmatrix} 1 & 0 & 0 & 0 & 0 \\ 0 & 1 & 0 & 0 & 0 \\ 0 & 0 & 1 & 0 & 0 \\ 1 & 0 & 0 & 1 & 0 \\ 0 & 0 & 0 & 0 & 1 \end{pmatrix} \begin{pmatrix} f_{n+1} \\ f_{n+2} \\ f_{n+\frac{5}{2}} \\ f_{n+\frac{8}{3}} \\ f_{n+3} \end{pmatrix} = \begin{pmatrix} 0 & 0 & 0 & 0 & 1 \\ 0 & 0 & 0 & 0 & 1 \\ 0 & 0 & 0 & 0 & 1 \\ 0 & 0 & 0 & 0 & 1 \\ 0 & 0 & 0 & 0 & 1 \end{pmatrix} \begin{pmatrix} y_{n-4} \\ y_{n-3} \\ y_{n-2} \\ y_{n-1} \\ y_n \end{pmatrix}$$

$$+h^3 \begin{pmatrix} \frac{274}{1575} & -\frac{1727}{3360} & -\frac{2666}{1575} & -\frac{4779}{3200} & \frac{181}{840} \\ \frac{2348}{1575} & -\frac{346}{105} & \frac{17152}{1575} & -\frac{6723}{700} & \frac{436}{315} \\ \frac{101125}{36864} & -\frac{911875}{172032} & \frac{145375}{8064} & -\frac{3655125}{229376} & \frac{198125}{86016} \\ \frac{3731456}{1148175} & -\frac{461824}{76545} & \frac{3407872}{164025} & -\frac{260416}{14175} & \frac{610304}{229635} \\ \frac{1539}{350} & -\frac{243}{32} & \frac{4698}{175} & -\frac{531441}{22400} & \frac{963}{280} \end{pmatrix} \begin{pmatrix} f_{n+1} \\ f_{n+2} \\ f_{n+\frac{5}{2}} \\ f_{n+\frac{8}{3}} \\ f_{n+3} \end{pmatrix} + h \begin{pmatrix} 0 & 0 & 0 & 0 & \frac{6179}{67200} \\ 0 & 0 & 0 & 0 & \frac{421}{900} \\ 0 & 0 & 0 & 0 & \frac{175625}{229376} \\ 0 & 0 & 0 & 0 & \frac{1011776}{1148175} \\ 0 & 0 & 0 & 0 & \frac{25461}{22400} \end{pmatrix} \begin{pmatrix} f_{n-4} \\ f_{n-3} \\ f_{n-2} \\ f_{n-1} \\ f_n \end{pmatrix}$$

(18)

The first characteristic polynomial of the block hybrid method (18) is given by

$$\rho(R) = \det\left(RA^0 - A^1\right)$$

Substituting the value of A^0 and A^1 into the function above gives

$$\rho(R) = \det\left[R\begin{pmatrix} 1 & 0 & 0 & 0 & 0 \\ 0 & 1 & 0 & 0 & 0 \\ 0 & 0 & 1 & 0 & 0 \\ 0 & 0 & 0 & 1 & 0 \\ 0 & 0 & 0 & 0 & 1 \end{pmatrix} - \begin{pmatrix} 0 & 0 & 0 & 0 & 1 \\ 0 & 0 & 0 & 0 & 1 \\ 0 & 0 & 0 & 0 & 1 \\ 0 & 0 & 0 & 0 & 1 \\ 0 & 0 & 0 & 0 & 1 \end{pmatrix} \right]$$

$$= \det\begin{pmatrix} R & 0 & 0 & 0 & -1 \\ 0 & R & 0 & 0 & -1 \\ 0 & 0 & R & 0 & -1 \\ 0 & 0 & 0 & R & -1 \\ 0 & 0 & 0 & 0 & R-1 \end{pmatrix}$$

$$= \left[R^4(R-1)\right] \qquad (19)$$

Therefore, R=0, R=1. The block method is zero stable and consistent since the order of the method p=6>1, and by Henrici (1962), the block method is convergent.

5. Region of Absolute Stability

The absolute stability region of the newly constructed hybrid linear multi-step methods (11)-(15) is plotted using Chollom (2004) by reformulating the methods as general linear methods and is shown in Figure 1 below.

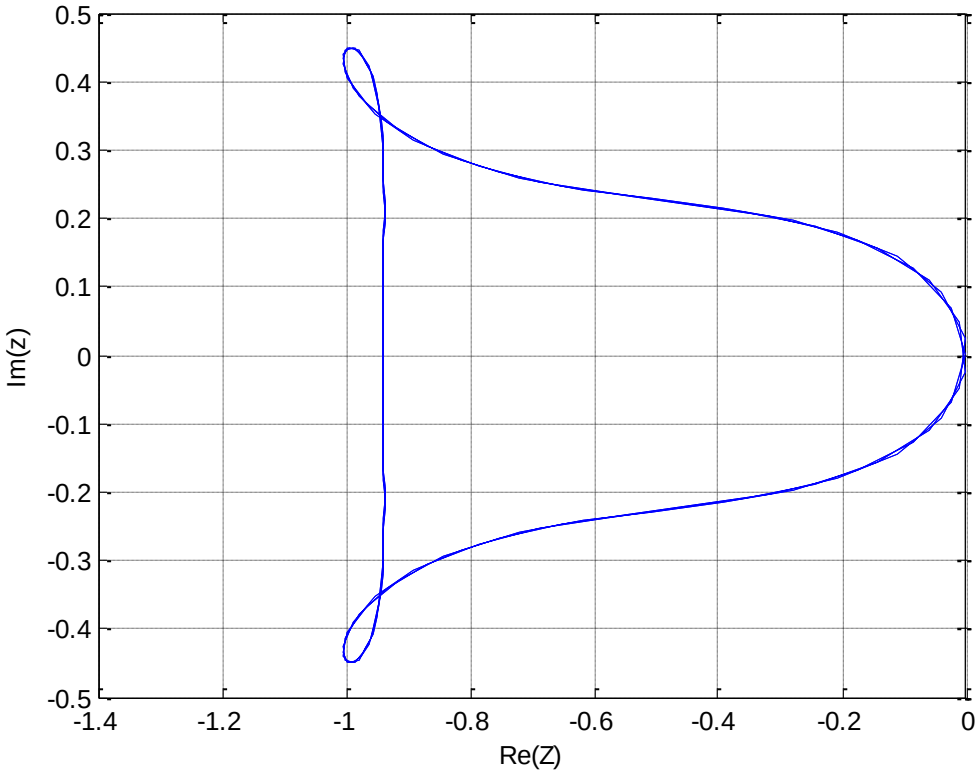

Fig. 1: Region of Absolute Stability Region of Hybrid Linear Multi-Step Method (HLMM)

6. Numerical Examples

We report here seven numerical examples taken from literature for the bases of comparison (see Tables 1-7).

Problem 1

$$y''' + e^{-y} - 3e^{-2y} + 2e^{-3y}$$

$$y(0) = \ln 2, \quad y'(0) = \tfrac{1}{2}, \quad y''(0) = \frac{1}{4}$$

Exact Solution is $y(x) = \ln\left(e^{x} + 1\right)$

Table 1: Showing Exact solutions and the computed results from the proposed methods for Problem 1

X	Exact Solution	Numerical Solution	Error	Error in R-K Method
0.1	0.7443966600	0.7443966601	1E-10	5.755E-09
0.2	0.7981388693	0.7981388694	1E-10	1.150E-07
0.3	0.8543552446	0.8543552445	1E-10	1.205E-07
0.4	0.9130152525	0.9130152524	1E-10	4.059E-08
0.5	0.9740769843	0.9740769842	1E-10	1.127E-07
0.6	1.037487950	1.037487951	1E-09	1.092E-07
0.7	1.103186049	1.103186049	0	7.339E-08
0.8	1.171100666	1.171100666	0	1.230E-07
0.9	1.241153875	1.241153875	0	9.167E-08
1.0	1.313261687	1.313261687	0	1.149E-07

Problem 2 $y''' = 3\sin x$ (Olabode and Yusuph (2009))

$y(0) = 1, \quad y'(0) = 0, \quad y''(0) = -2, h = 0.1$

Exact Solution is $y(x) = 3\cos x + \frac{x^2}{2} - 2$

Table 2: Showing Exact solutions and the computed results from the proposed methods for Problem 2

X	Exact Solution	Numerical Solution	Error	Olabode and Yusuph (2009)
0.1	0.990012496	0.990012496	0	1.65922E-10
0.2	0.960199733	0.9601997335	5E-10	4.76275E-10
0.3	0.911009467	0.9110094673	3E-10	6.23182E-10
0.4	0.843182982	0.8431829819	1E-10	2.91345E-10
0.5	0.757747686	0.7577476855	5E-10	8.71118E-10
0.6	0.656006845	0.6560068445	5E-10	3.92904E-09
0.7	0.539526562	0.5395265615	5E-10	9.55347E-09
0.8	0.410120128	0.4101201276	4E-10	1.80415E-08
0.9	0.269829905	0.2698299042	8E-10	3.03120E-08
1.0	0.120906918	**0.1209069177**	3E-10	4.73044E-08

Problem 3 (Awoyemi et al (2014))

$$y''' + 4y' = x$$

$$y(0) = 0, \quad y'(0) = 0, \quad y''(0) = 1, h = 0.1$$

Exact Solution is $y(x) = -\frac{3}{16}\cos 2x + \frac{5}{16}$

Table 3: Showing Exact solutions and the computed results from the proposed methods for Problem 3

X	Exact Solution	Numerical Solution	Error	Error in Awoyemi et al (2014)
0.1	0.004987516700	0.004987516680	2E-11	1.1899E-11
0.2	0.01980106360	0.01980106378	1.8E-10	3.0422E-09
0.3	0.04399957220	0.04399957259	3.9E-10	7.7796E-08
0.4	0.07686749200	0.07686749244	4.4E-10	1.5559E-07
0.5	0.1174433176	0.1174433185	9E-10	3.0541E-07
0.6	0.1645579210	0.1645579226	1.6E-09	4.6102E-07
0.7	0.2168811607	0.2168811622	1.5E-09	3.138E-07
0.8	0.2729749104	0.2729749122	1.8E-09	7.0374E-07
0.9	0.3313503928	0.3313503951	2.3E-09	1.0177E-06
1.0	0.3905275319	0.3905275341	2.2E-09	1.6528E-06

Problem 4 (Sagir (2014))

$$y''' + 5y'' + 7y' + 3y = 0$$

$$y(0) = 1, \quad y'(0) = 0, \quad y''(0) = -1, h = 0.1$$

Exact Solution is $y(x) = e^{-x} + xe^{-x}$

Table 4: Showing Exact solutions and the computed results from the proposed methods for Problem 4

X	Exact Solution	Numerical Solution	Error	Error in Sagir (2014)
0.1	0.9953211598	0.9953211602	4E-10	6.4300E-08
0.2	0.9824769037	0.9824769045	8E-10	2.7200E-08
0.3	0.9630636869	0.9630636870	1E-10	3.0500E-08
0.4	0.9384480644	0.9384480648	4E-10	8.9800E-08
0.5	0.9097959895	0.9097959906	1.1E-09	4.4260E-07
0.6	0.8780986178	0.8780986179	1E-10	7.7260E-07
0.7	0.8441950165	0.8441950160	5E-10	1.9523E-06
0.8	0.8087921354	0.8087921343	1.1E-09	1.0274E-06
0.9	0.7724823534	0.7724823510	2.4E-09	1.3509E-06
1.0	0.7357588824	0. 7357588850	2.6E-09	1.3470E-05

Problem 5 Consider the linear singular IVP

$$y''' + \frac{\cos x}{\sin x} y'' = \sin x \cos x$$

$$y(0) = 1, \quad y'(0) = -2, \quad y''(0) = 0, h = 0.1$$

Exact Solution is $y(x) = 1 - 2x + \frac{x^2}{12} - \frac{\sin^2 x}{12}$

Table 5: Showing Exact solutions and the computed results from the proposed methods for Problem 5

X	Exact Solution	Numerical Solution	Error
0.1	0.8000027740	0.8000027741	1E-10
0.2	0.6000442080	0.6000442081	1E-10
0.3	0.4002223173	0.4002223172	1E-10
0.4	0.2006961129	0.2006961128	1E-10
0.5	0.00167926274	0.001679262669	7.1E-11
0.6	-0.1965684269	-0.1965684270	1E-10
0.7	-0.3937513691	-0.3937513692	1E-10
0.8	-0.5895499801		3E-10

		-0.5895499804	
0.9	-0.7836334206	-0.7836334211	5E-10
1.0	-0.9756727849	-0.9756727850	1E-10

Problem 6 Non-linear Blasius equations

$$2y''' + yy'' = 0$$

$$y(0) = 0, \quad y'(0) = 0, \quad y''(0) = 1, h = 0.1$$

The exact solution does not exist.

We compare our method with fourth order Runge-Kutta Method which shows an agreement with each other.

Table 6:Numerical methods for problem 6

x	Numerical Solution	R-K METHOD
0.1	0.0049999583	0.0049999552
0.2	0.0199986668	0.0199986591
0.3	0.0449898795	0.0449898741
0.4	0.0799573780	0.0799573773
0.4	0.1248700575	0.1248700476
0.6	0.1796771413	0.1796771264
0.7	0.2443036171	0.2443036129
0.8	0.3186460094	0.3186459795
0.9	0.4025686206	0.4025686062
1.0	0.4959003415	0.4959003376

Problem 7

Consider linear system

$$y''' = \frac{1}{68}(817y + 1393z + 448w)$$

$$z''' = -\frac{1}{68}(1141y + 2837z + 896w)$$

$$w''' = \frac{1}{68}(3059y + 4319z + 1592w)$$

With initial conditions

$$\begin{cases} y(0) = -2,\ z(0) = -2, w(0) = -12 \\ y'(0) = -12,\ z'(0) = 28, w'(0) = -33 \\ y''(0) = 20,\ z''(0) = -52,\ w''(0) = 5 \end{cases}$$

The analytical solution of the problem is given by

$$\begin{cases} y = e^{x} - 2e^{2x} + 3e^{-3x} \\ z = 3e^{x} + 2e^{2x} - 7e^{-3x} \\ w = -11e^{x} - 5e^{2x} + 4e^{-3x} \end{cases}$$

Table 13: Example 7 for k=3 with Two off-grid point at Collocation

X	Exact Solution			Numerical Solution			Error		
	y(x)	Z(x)	W(x)	Y(x)	Z(x)	W(x)	Y(x)	Z(x)	W(x)
0.1	0.884820064	0.572590725	-15.30062101	0.8848200328	0.5725907975	-15.30062105	3.12E-08	7.25E-08	4E-08
0.2	-0.115811730	2.806176217	-18.69930729	-0.115811924	2.806176663	18.69930753	1.93E-07	4.46E-07	2.4E-07
0.3	-1.074669813	4.847826406	-22.33276225	-1.074670301	4.847827514	-22.33276288	4.88E-07	1.11E-06	6.3E-07
0.4	-2.055674522	6.818196467	-26.33299947	-2.055675432	6.818198548	26.33300066	9.09E-07	2.08E-06	1.19E-06
0.5	-3.118451905	8.820816349	-30.83482248	-3.118453394	8.820819761	-30.83482447	1.48E-06	3.41E-06	1.99E-06
0.6	-4.322218381	10.94949803	-35.98269587	-4.322220576	10.94950306	-35.98269878	2.19E-06	5.03E-06	2.91E-06
0.7	-5.729277942	13.29446306	-41.93745391	-5.729280922	13.29446992	-41.93745794	2.98E-06	6.86E-06	4.03E-06
0.8	-7.408370060	15.94766196	-48.88324052	-7.408373873	15.94767075	-48.88324578	3.81E-06	8.79E-06	5.26E-06

0.9	-9.438075281	19.00766567	-57.03504949	-9.438079890	19.00767630	-57.03505590	4.61E-06	1.06E-05	6.41E-06
1.0	-11.91046916	22.58444820	-66.64723234	-11.9104655489	22.58446732	-66.647239321	3.61E-06	1.91E-05	6.98E-06

5. Conclusion

We have derived a three-step continuous Hybrid Linear Multi-step Method (HLMM) from which Multiple Finite Difference Methods (MFDMs) are obtained and applied to solve third order ordinary differential equations (ODE) without first adapting the ODE to an equivalent first order system. The MFDMs are applied as simultaneous numerical integrators over sub-intervals which do not overlap and hence they are more accurate than Single Finite Difference Methods (SFDMs) which are generally applied as single formulas over overlapping intervals. We have shown that the methods are convergent and have large intervals of absolute stability, which make them suitable candidates for computing solutions on wider intervals. In addition to providing additional methods and derivatives, the continuous HLMM can be used to obtain global error estimates. Our future research will be focused on adapting the MFDMs to solve third order partial differential equations.

References

Adekule, M. R., Egwurube, M. O. and Adesanya, A. O. and Udo, M. O. (2014). Five steps block predictor-block corrector method for the solution of ODEs, Applied mathematics, Vol. 5, 1252-1266.}

Awoyemi, D.O (1991). A class of continuous linear multi step method for general second order initial value problems in ordinary differential equation. International Journal of Computer Mathematics, 72, pp. 29 - 37.

Awoyemi, D.O (2003). A P-stable linear multistep method for solving third order ordinary mdifferential equation. International Journal of Computer Mathematics, 80(8), 85-991.

Awoyemi, D.O. (2000). A new six order algorithm for the general second order ordinary differential equation. International Journal of Computer Mathematics, 77, pp. 177- 124}

Awoyemi,D.O,Kayode,S.J and Adoghe, L.O (2014). A four ?point fully implicit method for numerical integration of third-order ordinary differential equations, Int. J. Physical Sciences, 9(1) , 7-12.

Fatunla, S.O (1991). Block method for second order initial value problem (IVP), \textit{International Journal of Computer Mathematics, 41, 55-63.}

Chollom J.P (2004): A Study of Block Hybrid Adam`s Methods With Link to Two Step Runge- Kutta Methods for First Order Ordinary Differential Equations Ph.D Dissertation (unpublished) University of jos, Nigeria.

Henrici,P (1962). Discrete Variable Methods for ODE`s, New York USA, John Wiley and Sons.

Kayode, S, J., Awoyemi, D. O (2005). A 5 steps maximal order method for direct solution of second order ordinary differential equation, Journal of the Nigerian Mathematical Physics, 9, 2005, 279-284.

Lambert, J. D, Computational method in ordinary differential equation, John Wiley and Sons, London, U. K, 1973.}

Mohammed, U. and Adeniyi, R.B (2014). A Three Step Implicit Hybrid Linear Multistep Method for the Solution of Third Order Ordinary Differential Equations. Gen. Math. Notes (GMN), Vol. 25, No. 1, November 2014, pp. xx-xx.

Mohammed, U. and Adeniyi,R.B (2015). A Class of Implicit Six Step Hybrid Backward Differentiation Formulas for the Solution of Second Order Differential Equations. British Journal of Mathematics/Computer Science (BJMC), Vol. 6,NO 1, pp. 41-52.

Olabode, B.T (2009).An accurate scheme by block method for the third order ordinary differential equation. Pacific journal of science and technology 10(1).

Olabode, B.T, Yusuf, Y (2009). A new block method for special third order ordinary differential equation. Journal of Mathematics and Statistics, 5(3), 2009,167-170.

Sagir, A.M (20014) On the approximate solution of continuous coefficients for solving third order ordinary differential equations, *International Journal of Mathematical, Computational Science and Engineering*, 8(3) (2014), 39-43.

Taiwo O. A. and Falade, K. J. (2015). Numerical solution of third order non-homogeneous singular initial value problem by exponentially fitted collocation approximation method. International Mathematics Conference, University of Ibadan (27-30, January 2015).

Yahaya,Y.A and Mohammed,U (2010). A 5-step Block Method for Special Second Order Ordinary Differential Equations. Journal of Nigerian Mathematical Society (JNMS). vol.29, pp113-126.

MHD MIXED CONVECTION FLOW IN MELTING FROM A HEATED VERTICAL PLATE EMBEDDED IN POROUS MEDIUM

Aliyu Ishaku Ma'ali[1] Umaru Mohammed[2]*, Abdulkadir Abubakar[1] and Abdullahi Idris Enagi[2]

[1]Department of Mathematics/ Computer Science Ibrahim Badamasi Babangida,

university Lapai, Nigeria

[2]Department of Mathematics, Federal university of Technology, Minna, Nigeria

1aai_maali@yahoo.com

2umaru.mohd@futminna.edu.ng

[1]aabubakar01@yahoo.com

[2]enagi.idris@futminna.edu.ng

* Corresponding author

Abstract

The MHD mixed convection flow in melting from a heated vertical plate embedded in porous medium is investigated. The similarity equations are derived and solved numerically using Nachtsheim–Swigert shooting iteration technique along with the sixth order Runge–Kutta integration scheme. Comparisons with previously published work are performed, and the results are found to be in excellent agreement. Results for the non-dimensional velocity and temperature are displayed graphically. During the investigation, it was found that the melting phenomenon decreases the local Nusselt number at the solid-liquid interface.

Keywords: Liquid phase,mixed convection, Magnetic effect, Buoyancy forces

Nomenclature

B_0 Magnetic flux density [T]

C_ρ Liquid specific heat capacity [J/kg K]

C_s Solid specific heat capacity [J/kg K]

Da Darcy number, $\frac{K}{x^2}$

Λ Inertia parameter $\mathrm{Re}\, F\sqrt{Da}$

f Dimensionless stream function

G_r Grashof number ν^2

h Heat transfer coefficient [W/m^2 K]

Ha Hartman number, $\sqrt{\ } \rho\nu$

Ec Eckert Number $C_p(T_\infty - T_m)$

K Permeability of porous media [m^2]

[2] (Corresponding author) Permanent Address: Department of mathematics/statistics, federal university of technology, minna, Nigeria,
E-mail: 2umaru.mohd@futminna.edu.ng

κ Thermal conductivity [W/m K]

L Plate length [m]

M Melting parameter, $1 + C_s(T_m - T_s)$

Nu Nusselt number k

q_w Heat flux [W/m^2]

Re Reynolds number ν

T Temperature [K]

T_m Melting Temperature [K]

T_s Solid temperature [K]

T_∞ Liquid temperature [K]

u_∞ External flow velocity [m/s]

U, V Velocity in x and y direction [m/s]

x, y Coordinate axes along and perpendicular to plate [m]

Greeks

α Thermal diffusivity [m^2/s]

β Coefficient of kinematic viscosity [m^2/s]

η Dimensionless similarity variable

ρ Liquid density [kg/m^3]

ν Kinematic viscosity [m^2/s]

σ Electrical conductivity of fluid [mho m^{-1}]

θ Dimensionless Temperature, $\frac{T - T_m}{T_\infty - T_m}$

ψ Dimensionless stream function [m^2/s]

λ constant defined in equation (4)

1. Introduction

The Problem of MHD laminar flow through a porous medium has become very important in recent years because of its possible applications in many branches of Science and Technology, particularly in the field of Agricultural Engineering to study the underground water resources, seepage of water in river beds; in Chemical Engineering for filtration and purification process; in Petroleum Technology to study the movement of natural gas, oil and water through the oil reservoirs. There has been a renewed interest in MHD flow and heat transfer in porous and clear domains due to the important effect of magnetic field on the boundary layer flow control and on the performance of many systems using electrically conducting fluid such as MHD power generators, the cooling of nuclear reactors, plasma studies, purification of molten metal's from non-metallic inclusion, geothermal energy extractions etc. Many problems of MHD Darcian and non- Darcian flow of Newtonian fluid in porous media have been analyzed and reported in the literature. Chamkha (1997) analyzed the hydromagnetic natural convection flow from an isothermal inclined surface adjacent to thermally stratified porous medium. Bian *et al.* (1996) have studied the natural convection in an inclined porous medium with the effect of electromagnetic field. Aldoss *et* al. (1995) has considered the magneto hydrodynamic mixed convection flow from a vertical plate embedded in a porous medium. Tashtoush (2005) analyzed the effects of magnetic and buoyancy on melting from a vertical plate embedded in saturated porous media. The unsteady MHD combined convection over a moving vertical

sheet in a fluid saturated porous medium with uniform surface heat flux was studied by El-Kabeira *et al.* (2007). Afify (2007) analyzed the effects of variable viscosity on non-Darcy MHD free convection along a non-isothermal vertical surface in a thermally stratified porous medium.

Effect of melting and thermo diffusion on natural convection heat and mass transfer of a non-Newtonian fluid in a saturated non-Darcy porous medium was studied by Kairi and Murthy (2009). It is noted that the velocity, temperature and concentration profiles as well as the heat and mass transfer coefficients are significantly affected by the melting phenomena and thermal-diffusion in the medium. If the temperature of the surrounding fluid is rather high, radiation effects play an important role and this situation does exist in space technology. In such cases, one has to take into account the effect of thermal radiation and mass diffusion. Bakier *et al.* (2009) studied Group method analysis of melting effect on MHD mixed convection flow from a radiative vertical plate embedded in saturated porous medium for Newtonian fluids. He developed linear transformation group approach to simulate problem of hydro magnetic heat transfer by mixed convection along vertical plate in a liquid saturated porous medium in the presence of melting and thermal radiation effects for opposing external flow. He studied the effects of the pertinent parameters on the rate of the heat transfer in terms of the local Nusselt number at the solid-liquid interface. More recently melting and radiation effects on mixed convection from a vertical surface embedded in a non-Newtonian fluid saturated non-Darcy porous medium for aiding and opposing external flows is analyzed by Chamkha *et al*. (2010). They obtained representative flow and heat transfer results for various combinations of physical parameters.

Of interest, among the reviewed articles in this work is Tashtoush (2005), in which the combined effect of magnetic and buoyancy influences is considered on melting with constant temperature from a vertical plate. However, several fluids of interest exist with variable temperature for which results in (2005) are not applicable. The present article therefore is aimed at addressing the limitation and extends its results to fluids with variable properties in presence of viscous dissipation.

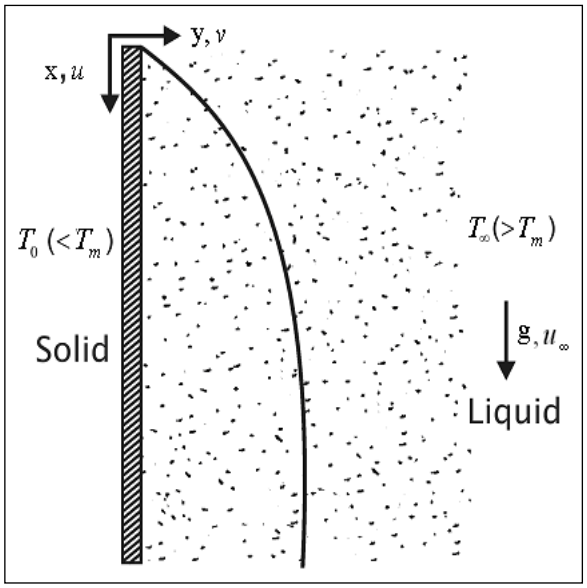

2. Mathematical Formulation

Let us consider the problem of magnetohydrodynamic combined heat convective steady incompressible laminar boundary layer flow of a gray optically thick electrically conducting viscous Newtonian fluid in a porous medium adjacent to vertical flat plate with opposing external flow U_∞ in the presence of a transverse magnetic field. It is assumed that this plate constitutes the interface between and solid phases during melting inside the porous matrix as shown in Fig. 1. The uniform transverse magnetic field to the plate surface is applied. The temperature of the plate, T_m is the melting temperature of the material occupying the porous matrix. The liquid phase temperature is T_∞. The temperature of the solid far from the interface is T_0. The governing equations for the problem can be written as Bakier (1997) and Tashtoush (2005)

$$\frac{\partial u}{\partial x}+\frac{\partial v}{\partial y}=0 \qquad \textbf{(1)}$$

$$\left(1+\frac{\sigma B_0^2}{\rho \nu}+\frac{2F\sqrt{K}}{\upsilon}u\right)\frac{\partial u}{\partial y}=\frac{-Kg\beta}{\nu}\frac{\partial T}{\partial y} \qquad \textbf{(2)}$$

$$u\frac{\partial T}{\partial x}+v\frac{\partial T}{\partial y}=\alpha\frac{\partial^2 T}{\partial y^2}+\mu\left(\frac{\partial u}{\partial y}\right)^2+\sigma B_0^2 u^2 \qquad \textbf{(3)}$$

The boundary conditions for the present problem are as follows:

$$y=0,\quad T=T_m(=T_\infty+Ax^\lambda),\ k\frac{\partial T}{\partial y}=\rho\left[1+C_s\left(T_m-T_s\right)\right]\nu(x,0) \tag{4}$$

$$y\to\infty,\ T\to T_\infty,\ u\to U_\infty \tag{5}$$

Where u and v are Darcy's velocity in the x and y directions, also K,α,ρ,σ,ν, β, g and T are the inertia coefficient, the permeability, liquid thermal diffusivity , liquid density, electric conductivity, kinematic viscosity, thermal expansion coefficient, acceleration due to gravity and temperature respectively. The first boundary conditions on the melting surface simply stated that the temperature of the interface equals the melting temperature of the material saturating the porousmatrix. The second condition at y = 0 is a direct result of a heat balance. It states that the heat conducted to the melting surfaceis equal to the heat of melting plus the sensible heat required to raise the temperature of the solid T_0 to is melting temperature T_m, (Baker (997), Epstein and Cho (1976)]).

To seek similarity solution to equation (2) and (3) with boundary condition (4) and (5), we introduce the following dimensionless variables

$$\eta=\sqrt{\frac{u_\infty}{\alpha}}\ y\ x^{\frac{\lambda-1}{2}}\quad \psi=\sqrt{\alpha u_\infty}\,x^{\frac{\lambda+1}{2}}\,f(\eta),\quad \theta(\eta)=\frac{T-T_m}{T_\infty-T_m} \tag{6}$$

Substituting equation (6) into equation (2) and (3), we obtain the following transformed governing equations:

$$\left(1+Ha^2+2\Lambda f'\right)f''+\frac{Gr}{\mathrm{Re}}\theta'=0 \tag{7}$$

$$\theta''+\frac{1}{2}(1+\lambda)f\theta'-\lambda f'\theta+Ec\left(f''\right)^2+\frac{Ha^2Ec}{Da}f'^2=0 \tag{8}$$

The boundary conditions are

$$\eta=0,\theta=0,\ f(0)+2M\theta'(0)=0 \tag{9}$$

$$\eta\to\infty,\theta=1,\ f'=1 \tag{10}$$

Where $M=\dfrac{C_p\left(T_\infty-T_m\right)}{1+C_s\left(T_m-T_s\right)}$ is the melting parameter, $\mathrm{Re}=\dfrac{U_\infty x}{\nu}$ is the Reynolds number,

$\Lambda=\mathrm{Re}\,F\sqrt{Da}$ is the inertia parameter, $Gr=\dfrac{Kg\beta_T\left(T_\infty-T_m\right)x}{\nu^2}$ is the Grashof number,

$Ec = \frac{u_0^2}{C_p(T_\infty - T_m)}$ is the Eckert number, $Da = \frac{K}{x^2}$ is the Darcy number and $Ha = \sqrt{\frac{\sigma B_0^2}{\rho \nu}}$ is the Hartman number.

The ratio $\frac{Gr}{\mathrm{Re}}$ in equation (7) is a measure of the relative importance of free and force convection and is the controlling parameter for the present problem.

The heat transfer rate along the surface of the plate q_w can be computed from the Fourier heat conduction law.

$$q_w = -k \left.\frac{\partial T}{\partial y}\right|_{y=0} \tag{11}$$

The heat transfer results can be represented by the local Nusselt number Nu, which is defined as

$$Nu = \frac{hx}{k} = \frac{q_w x}{k(T_m - T_\infty)} \tag{12}$$

Where h denotes the local heat transfer coefficient and k represent the liquid phase thermal conductivity. Substituting equation (6) and (11) into equation (12) we obtain

$$\frac{Nu}{Ra^{\frac{1}{2}}} = \theta'(0). \tag{13}$$

3. Numerical Methods

The dimensionless equations (7)-(8) together with the boundary condition (9)-(10) are solved numerically by means of sixth order Runge-kutta methods coupled with shooting technique. The solution thus obtained is matched with the given values of $f'(\infty)\ and\ \theta(0)$. In addition, the boundary condition $\eta \to \infty$ is approximated by $\eta_{\max} = 4$ which is found sufficiently large for the velocity and temperature to approach the relevant free stream properties.

Table I. : Values of $\theta'(0)$ and $f(0)$ for different values of buoyancy parameter and melting parameters, $Ha = 0, \lambda = 0, \Lambda = 0$

		Tashtoush (2005)		Present work	
M	Gr/Re	$\theta'(0)$	$f(0)$	$\theta'(0)$	$f(0)$
0.4	0.0	0.4571	-0.3657	0.4570	-0.3656
	1.4	0.6278	-0.5023	0.6278	-0.5022
	20	1.6866	-1.3493	1.6866	-1.3493
2.0	0.0	0.2743	-1.097	0.2743	-1.097
	1.4	0.3807	-1.5231	0.3808	-1.5232
	3.0	0.4747	-1.8988	0.4747	-1.8988
	8.0	0.6902	-2.7607	0.6902	-2.7607
	10.0	0.7587	-3.0290	0.7593	-3.0375
	20.0	1.0382	-4.1529	1.0382	-4.1529

4. Result and discussion

In order to test the accuracy of our results, we have compared our result with those of Tashtoush (2005) without the constant λ. The comparison is found to be in excellent agreement, as presented in table1. Numerical results are presented graphically for the mixed convection (Gr/Re) ranging from 0.0 to 30.0, melting parameter ranging from 0.0 to 10, magnetic field ranging from 0.0 to 0.4, constant λ ranging from 0.0 to 0.4 and Eckert number ranging from 0.0 to 2.0. Figures 2 and 3 depict the effect of mixed convection parameter (Gr/Re) in velocity and temperature distribution for λ=1/5 respectively. It should be mentioned that increases in the values of Gr/Re have a tendency to increase the buoyancy effect due to temperature differences and this leads to increase in slip velocity on the plate in Fig. 2. However, the thermal boundary layer thickness decreases with increase in Gr/Re and it results to increase in the fluid temperature as shown in Figure 3.

Figures 4 and 5 depict the influence of melting parameter (M) on velocity and Temperature profiles respectively. It is obvious that increasing the melting parameter causes higher acceleration to the fluid flow which in turn, increases its motion and causes decrease in temperature. This is established by respective increases in the boundary layer thickness of velocity and temperature..

The effect of flow inertia (Λ) on the velocity profiles is shown in figure 6. It can be seen that as Λ increases the velocity of the slip on the plate decreases, this decrease in slip velocity is observed to cause an increase in the thermal boundary layer thickness which consequently lead to a decrease in the temperature as shown in figure 7.

Figures 8, 9 depict the effect of magnetic parameter (Ha) on the velocity and temperature distribution, respectively. It can be seen that application of magnetic field normal to the flow of an electrically conducting fluid gives rise to a resistive force that acts in the direction opposite to that of flow. Thus, thermal boundary

layer thickness is significantly increased. These behaviors are depicted in the respective decrease in velocity as well as an increase in the temperature as the magnetic parameter Ha is increased.

Fig 10, 11 depict the influence of increasing the constant parameter (λ) on the behavior of the velocity and temperature profile, respectively. It can be seen that increasing the value of constant λ increases the temperature of the plate and has a tendency to accelerate the flow. This in turn increases the velocity and decreases the temperature profile. Moreover, as λ increases, hydrodynamic and thermal boundary layers increase.

Figures 12, 13 show the effect of Eckert number (*Ec)* on velocity and temperature profiles in the mixed convection flow. It is seen from the figures that the velocity curve decreases with the increase of Eckert number. However, with the increase of Eckert number, there is significant increase in heat generation due to fluid motion and this translates to temperature increase as shown in figure 13.

FIGURES

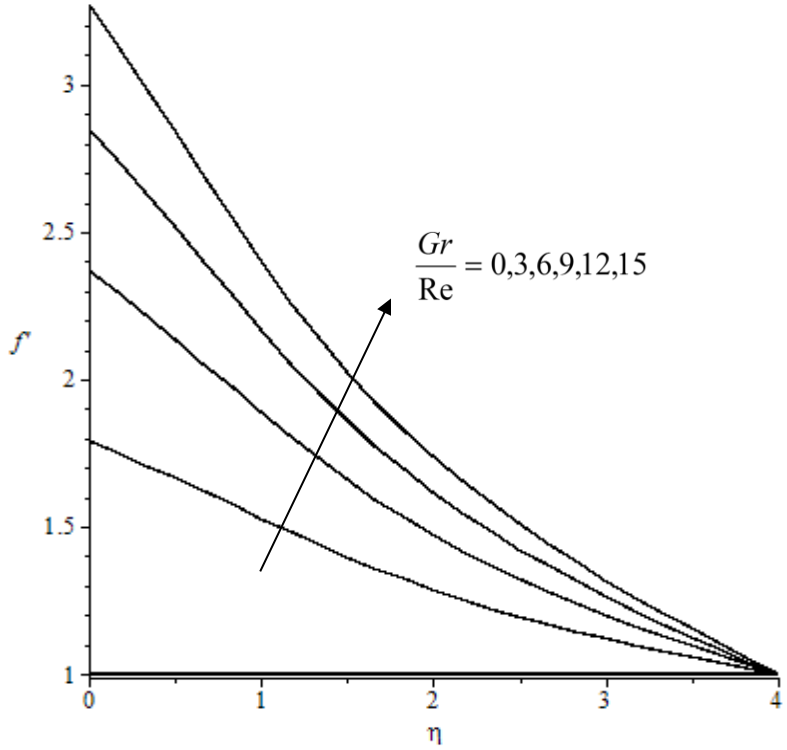

Fig. 2. Velocity profile for different values of Gr/Re, λ=0.3,M=1.0,$\Lambda = 1.0$,Ec=0.1, Ha=0.1 and Da=0.1

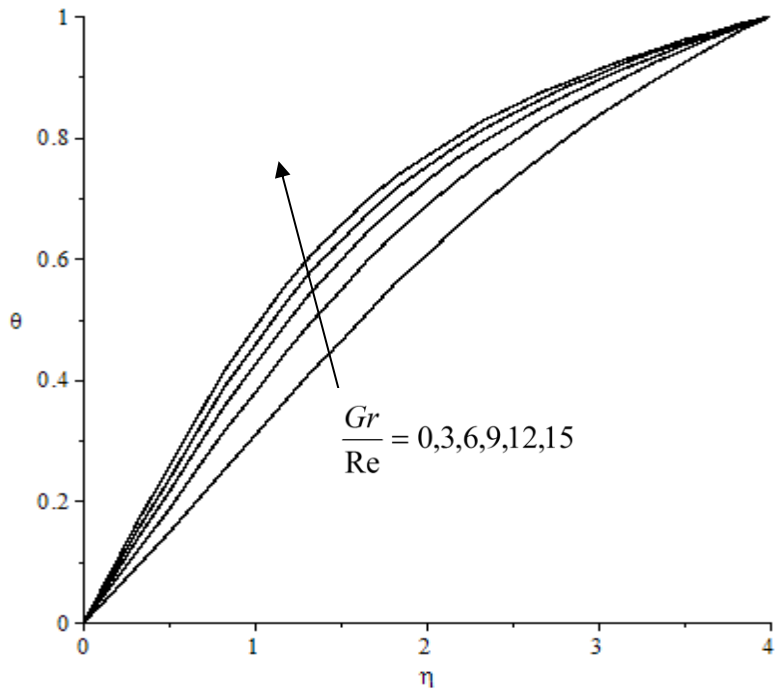

Fig. 3. Temperature profile for different values of Gr/Re, λ=0.3,M=1.0, $\Lambda = 1.0$,Ec=0.1, Ha=0.1 and Da=0.1

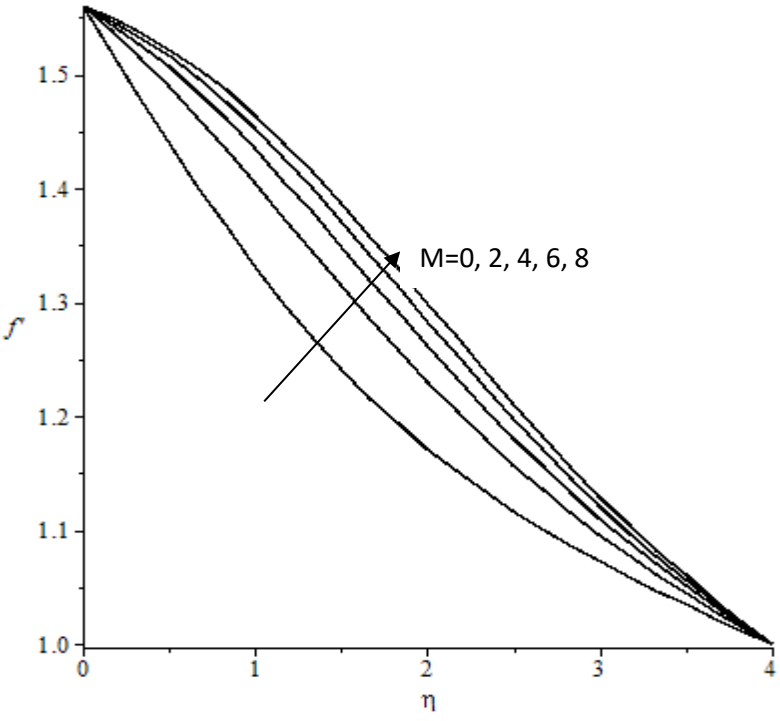

Fig. 4. Velocity profile for different values of M,Gr/Re=2.0, λ=0.3, $\Lambda = 1.0$,Ec=0.1, Ha=0.1 and Da=0.1

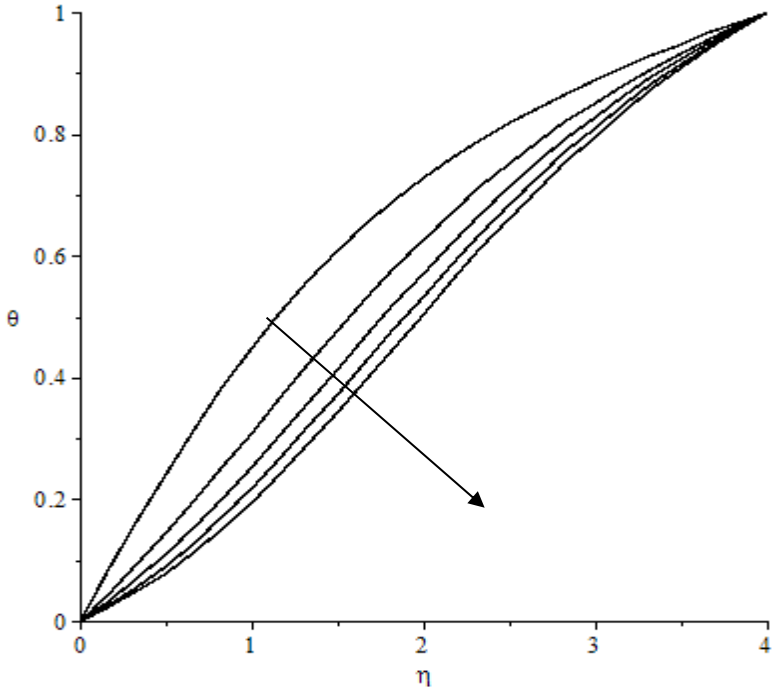

Fig. 5. Temperature profile for different values of M,Gr/Re=2.0, λ=0.3,$\Lambda = 1.0$,Ec=0.1, Ha=0.1 and Da=0.1

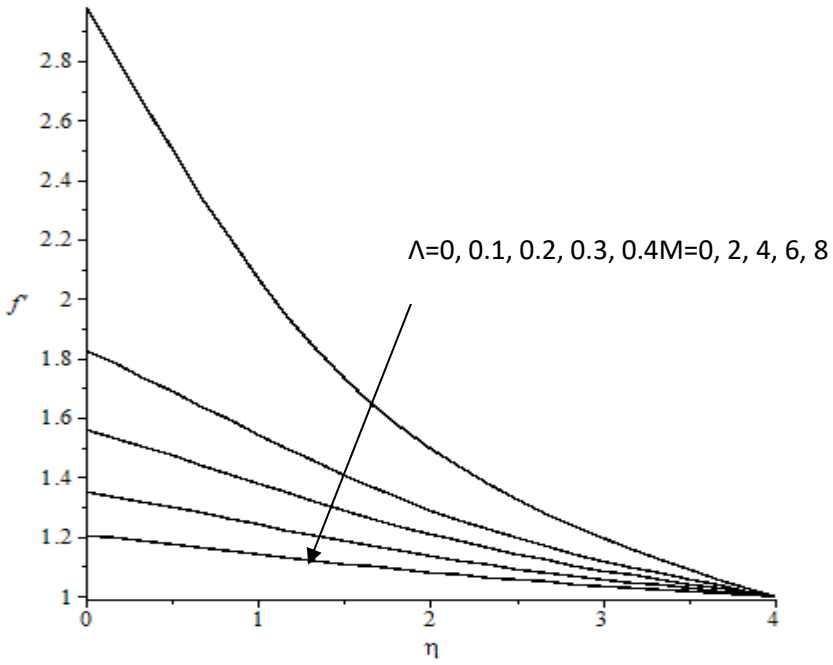

Fig. 6. Velocity profile for different values of Λ M=0.5,Gr/Re=3.0, λ=0.2,Ec=0.1, Ha=0.5 and Da=0.1

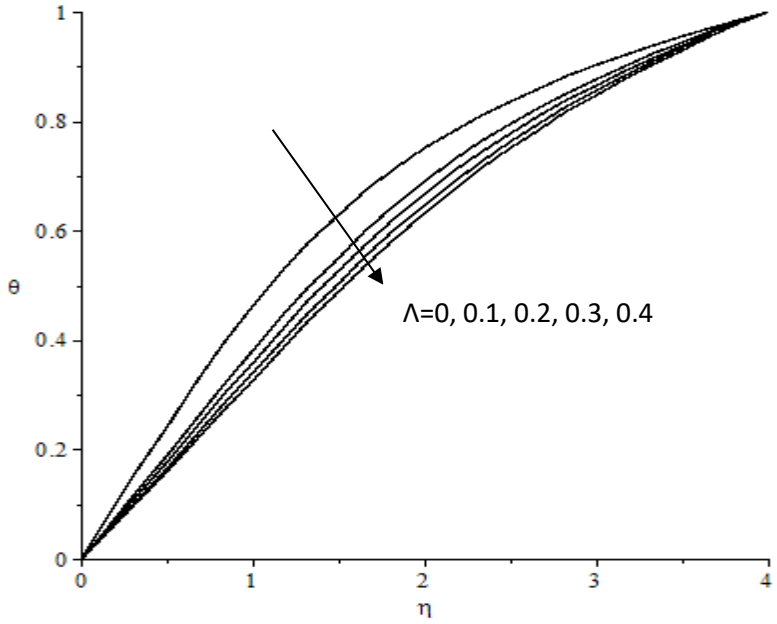

Fig. 7. Temperature profile for different values of Λ M=1.0,Gr/Re=2.0, λ=0.3,Ec=0.1, Ha=0.1 and Da=0.1

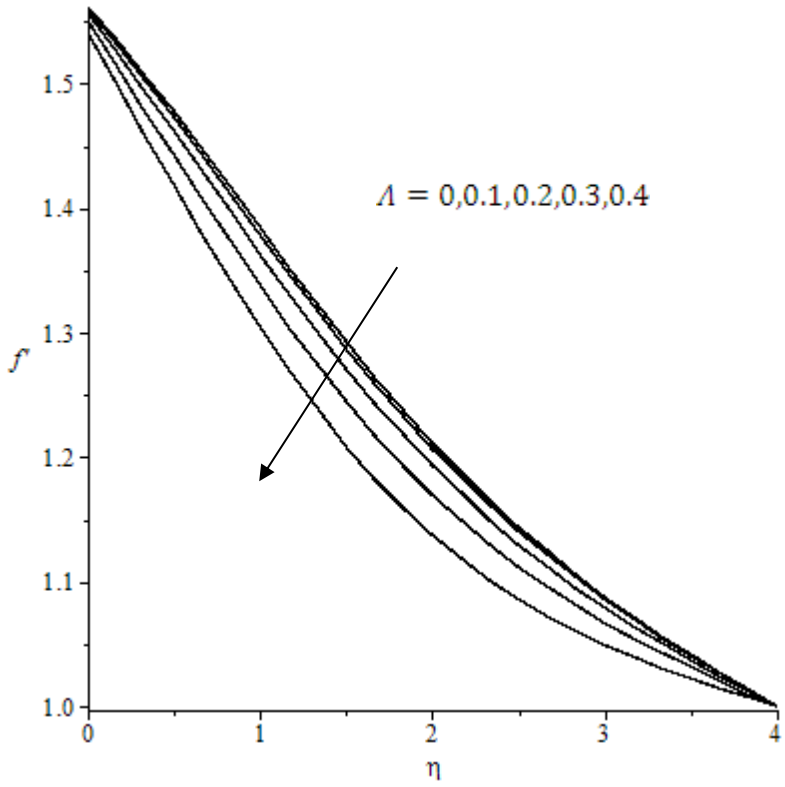

Fig. 8. Velocity profile for different values of Ha, M=1.0, Gr/Re=2.0, λ=0.3,$\Lambda = 1.0$, Ec=0.1, Ha=0.1 and Da=0.1

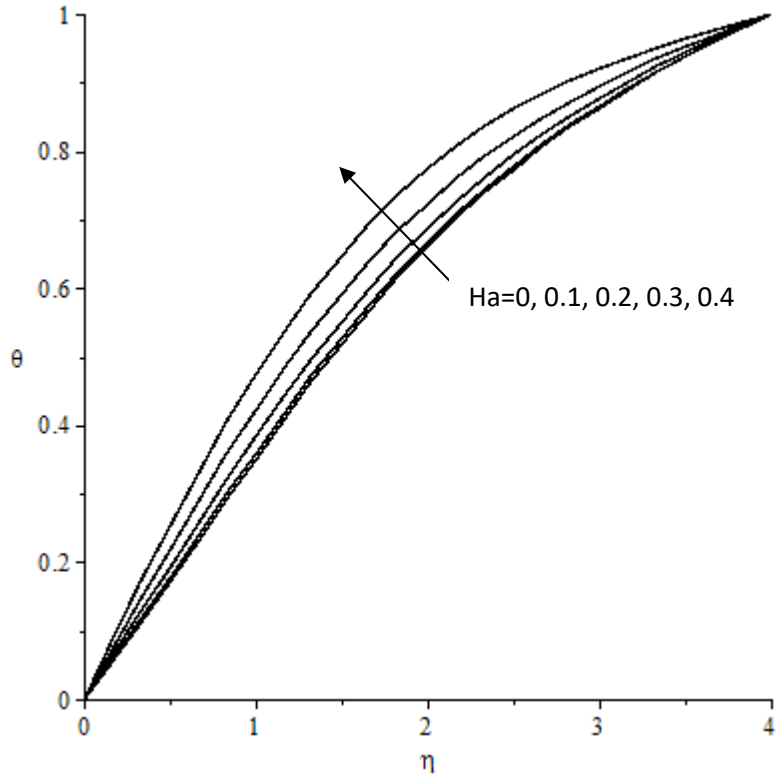

Fig.9. Temperature profile for different values of Ha, M=1.0,Gr/Re=2.0, λ=0.3, $\Lambda = 1.0$, Ec=0.1, Ha=0.1 and Da=0.1

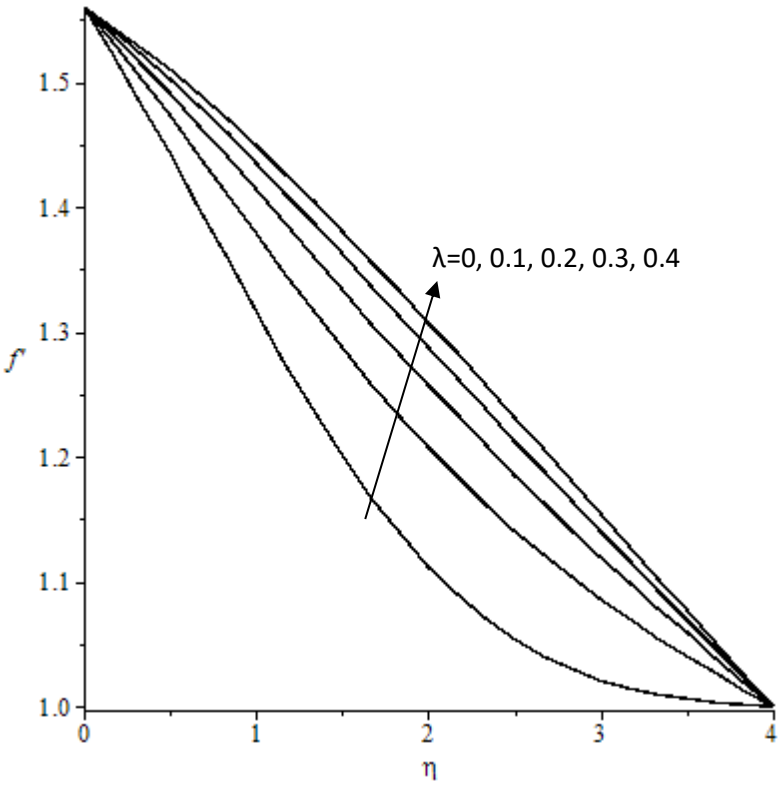

Fig. 10. Velocity profile for different values of λ , M=1.0,Gr/Re=2.0, $\Lambda = 1.0$,Ec=0.1, Ha=0.1 and Da=0.1

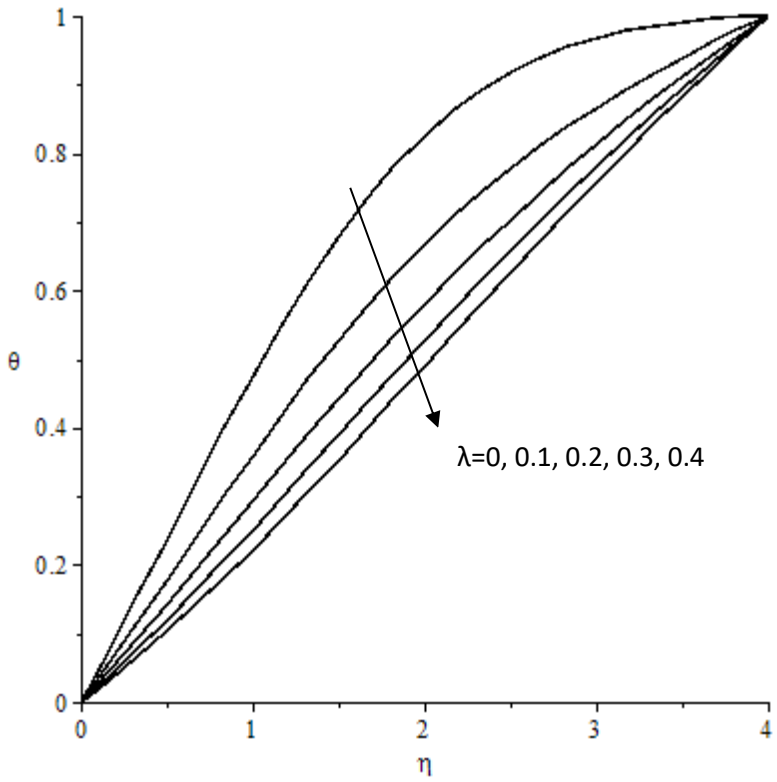

Fig. 11. Temperature profile for different values of λ=0.3 , M=1.0, Gr/Re=2.0, $\Lambda = 1.0$,Ec=0.1, Ha=0.1 and Da=0.1

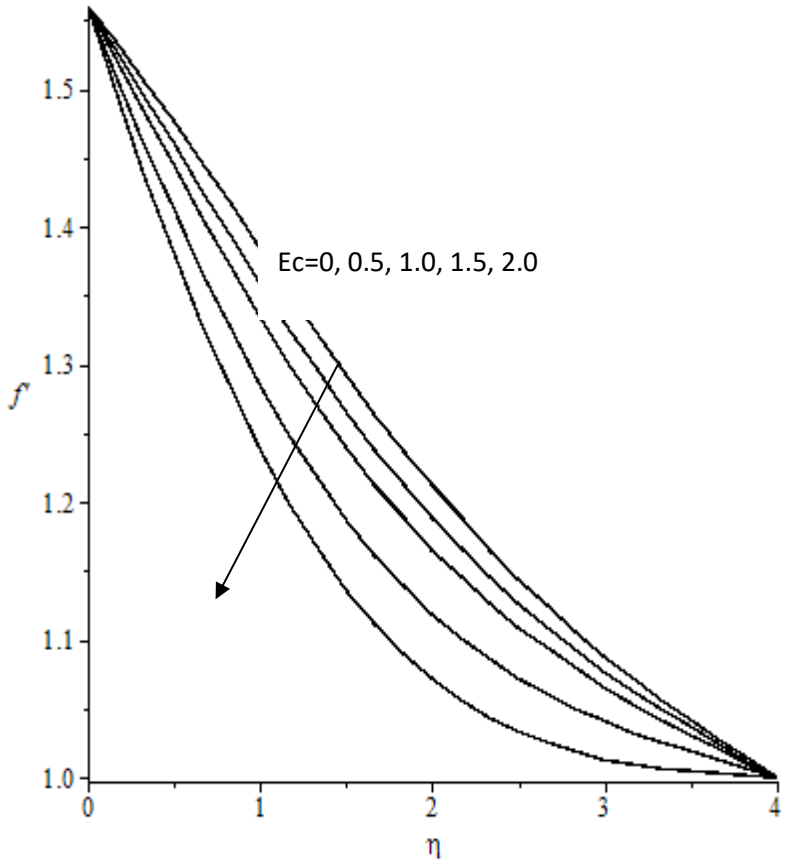

Fig. 12. Velocity profile for different values of Ec,λ =0.3, M=1.0,Gr/Re=2.0, $\Lambda = 1.0$, Ha=0.1 and Da=0.1

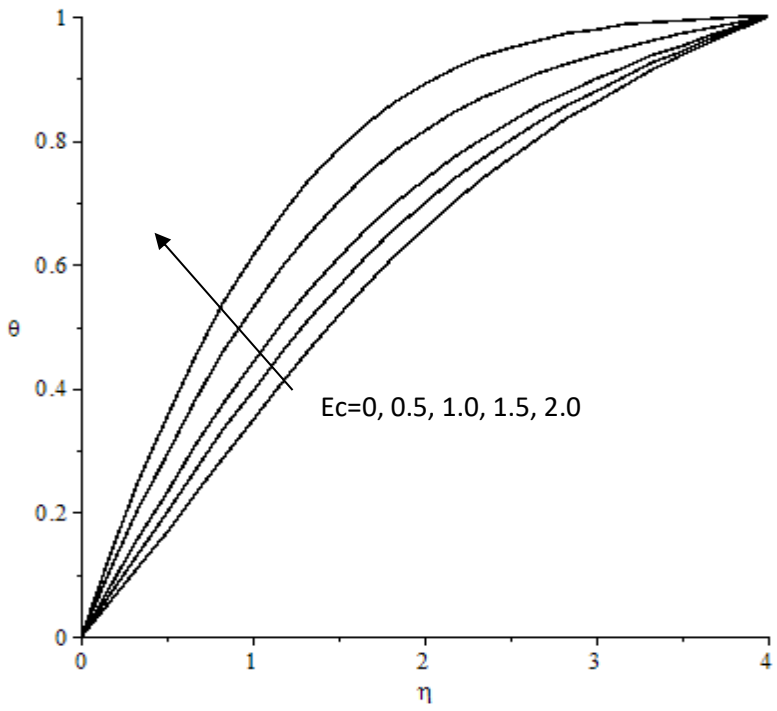

Fig. 13. Temperature profile for different values of Ec,λ =0.3, M=1.0,Gr/Re=2.0, $\Lambda = 1.0$, Ha=0.1 and Da=0.1

5. Conclusion

In this study The MHD mixed convection flow in melting from a heated vertical plate having variable temperature embedded in porous medium is analyzed. The heat transfer coefficients are obtained for various values of flow influencing parameters. It is noted that the velocity and temperature profiles as well as the heat transfer coefficients are significantly affected by the melting in the medium. The major conclusion is that the heat transfer coefficients are reduced with increasing melting parameter and grows with increasing Gr/Re. The results obtained in the present work have been validated by works in existing literature and an excellent agreement is found.

REFERENCES

Afify, A. A., (2007) Effects of variable viscosity on non-Darcy MHD free convection along a non-isothermal vertical surface in a thermally stratified porous medium. Applied Mathematical Modeling 31,1621-1634.

Aldoss, T. K., Al-Nimr, M.A., Jarrah, M.A., Al-Shaer, B.J.,(1995) Magneto hydrodynamic mixed convection from a vertical plate embedded in a porous medium. Numer Heat Transfer 28, 635-645.

Bakier, A.Y., (1997) Aiding and opposing mixed convection flow in melting from a vertical flat plate embedded in a porous medium. Transport in Porous Media 29, 127–139.

Bakier, A.Y., Rashad, A.M., Monsour, M.A., (2009) Group method analysis of melting effect on MHD mixed convection flow from a radiate vertical plate embedded in a saturated porous media. Commun. Nonlinear Sci. Numer. Simulat 14, 2160-2170

Bian, W., Vasseur, P., Bilgen, E., Meng, F., Effect of electromagnetic field on natural convection in an inclined porous medium. Int J Heat Fluid Flow 17, 36-44.

Chamkha, A.J., Ahmed, S.E., Aloraier, A.S., (2010)Melting and radiation effects on mixed convection from a vertical surface embedded in a non-Newtonian fluid saturated non-Darcy porous medium for aiding and opposing eternal flows. International Journal of the Physical Sciences 25 (7), 1212- 1224.

Chamkha, A.J.,(1997) Hydromagnetic natural convection from an isothermal inclined surface adjacent to thermally stratified porous medium. Int J Eng Sci 35, 975-986.

EL-Kabeira, S.M.M., Rashada, M.A., Gorla, R.S.R.,(2007) Unsteady MHD combined convection over a moving vertical sheet in a fluid saturated porous medium with uniform surface heat flux. Mathematical and Computer Modelling 46 ,384-397.

Epstein, M., Cho, D.H.,(1976) Laminar film condensation on a vertical melting surface. ASMEJ. Heat Transfer 98,108-113.

Kairi, R.R., Murthy, P.V.S.N., (2009) Murthy, Effect of melting and thermo-diffusion on natural convection heat mass transfer in a non-Newtonian fluid saturated non-Darcy porous medium. The open transport phenomena journal. 1, 7-14

Tashtoush, B., (2005) Magnetic and buoyancy effects on melting from a vertical plate embedded in saturated porous media. Energy Conversion and Management 46, 2566–2577.

INFLUENCE OF ZERO-ORDER SOURCE AND DECAY COEFFICIENTS ON THE CONCENTRATION OF CONTAMINANTS IN TWO-DIMENSIONAL CONTAMINANT FLOW

[*1]Jimoh, O. R., [2]Aiyesimi, Y. M., [3]Jiya, M. and [4]Bolarin, G. A.

[1,2,3,4]Department of Mathematics, Federal University of Technology, Minna, Nigeria.

[4]g.bolarin@futminna.edu.ng

[3]jiyason2010@gmail.com

[2]yomiaiyesimi2007@yahoo.co.uk

[*1]razaq.jimoh@futminna.edu.ng

*Corresponding author

Abstract

In this article, an eigenfunctions expansion method is used in studying the behavior of two-dimensional contaminant flow problem with non-zero initial concentration. The mathematical model describing the contaminant flow is described by advection, dispersion, adsorption, first order decay and zero-order source. It is assumed that the adsorption term is modeled by Freudlich isotherm. Before the application of the eigenfunctions method, the parameter expanding method is applied on the model and the boundary conditions are transformed to the homogeneous type. Thereafter, the approximate solution of the resulting initial value problem was obtained successively. The results obtained are expressed graphically to show the effect of change in the zero-order source and decay coefficients on the concentration of the contaminants. From the analysis of the results, it was discovered that the contaminant concentration decreases with increase in the distance from the origin as the zero-order source and decay coefficient increases.

Keywords: Advection, adsorption, contaminant, dispersion, eigenfunctions.

1. Introduction

The problem of contaminant transport in soil, groundwater and surface water has been a research of great concern in hydro-geology for many years. This is largely due to immense contamination of groundwater and surface water by industrial and human activities such as agricultural chemicals, accidental spills, landfills and buried hazardous materials. Though, agricultural chemicals could generally be useful in the surface of the soil, their penetration into the saturated and unsaturated zone of groundwater could contaminate groundwater.

Groundwater in its natural state is generally of excellent quality because the physical structure and mineral constituents of rock have facility for purifying water. Before the coming of industries and factories, the major threats to groundwater are viruses and bacteria. The presence of these microbiological contaminants like bacteria, viruses and parasites in groundwater may pose some threat to our community health.

The transport equation which models the movement of contaminants through groundwater and surface water environments was reported by (Bear, 1997). They are often advection-dominated and require a lot of care when solved numerically. In order to predict the contaminant migration in the geological formation more accurately, a tasking job emerges for scientists. The involves defining the flow lines of groundwater of the

aquifers, the travel time of water along the flow lines and to predict the chemical reaction and zero order source coefficient which alter the concentration during transport.

2. **Literature Review**

Most researchers are of the view that the flow in the solute transport or contaminant flow model is predominantly horizontal as found in (Bear, 1997). Further research by (Brainard and Gelhar, 1991) discovered that appreciable vertical flow components do occur in the domain of vertically penetrating wells and streams.

In an effort to provide solutions to the contaminant flow problems, a lot of successes were achieved by some researchers but mostly on one-dimensional cases with various initial and boundary conditions. (Okedayo and Aiyesimi, 2005) came out with the influence of retardation factor on the nonlinear contaminant flow problem. (Okedayo *et al*. 2011) studied on the 1-Dimensional nonlinear contaminant transport equation with an initial and instantaneous point source. Their investigation revealed that the contaminant concentration decreases with increase in the distance from the origin. On the dispersion of solute, (Ramakanta and Mehta, 2010) explored the effect of longitudinal dispersion of miscible fluid flow through porous media.

The analytical solution to temporally dependent dispersion through semi-infinite homogeneous porous media by Laplace transform technique (LTT) was provided by (Yadav *et al.* 2011). On the effect of reactive and non-reactive contaminant on the flow, (Aiyesimi and Jimoh, 2012,2013) embarked on computational analysis of 1-dimensional non-linear contaminant flow problem with an initial continuous point source using homotopy perturbation method. They discovered that the concentration decreases with increase in time and distance from the origin for the non-reactive case.

In order to understand the movement of contaminants in a flow, several models were formulated. i.e., Bear (1972), Cherry *et al.* (1979), Yadav *et al.* (2011), Yadav and Jaiswal (2011), etc. In their formulations, assumptions were made. Bear (1972) assumed that flow takes place only in the horizontal direction. Yadav et al. (2011), Chen *et al.* (2006), Singh *et al*. (2014) and Yadav and Jaiswal (2011) believed that both advection and dispersion happen in the horizontal and vertical direction but did not anticipate that there could be any reaction between the contaminants in the flow.

In this paper, the two-dimensional contaminant flow problem incorporating flow in both horizontal and vertical direction in addition to first-order decay and zero order sources is studied using the combination of parameter expanding method (PEM) and eigenfunctions method.

3. **Methodology**

3.1 Formulation of the Model

We consider an incompressible fluid flow through a semi-infinite homogeneous porous media with non-zero initial concentration in the transport domain. We assume that the flow is two-dimensional and in the direction of *x* and *y*-axis. The source concentration is assumed at the origin (i.e. at $x = 0$ and $y = 0$). The contaminant concentration is a function of space and time.

Following (Bear, 1997), (Yadav, *et al.* 2011), (Freezer and Cherry, 1979), Batu (2006), Ujile (2013), Singh (2013) and Singh *et al*. (2015), the two dimensional partial differential equation describing hydrodynamic dispersion in adsorbing, homogeneous and isotropic porous medium can be written as

$$\frac{\partial C}{\partial t}+\frac{\partial S}{\partial t}=D_{xx}\frac{\partial^2 C}{\partial x^2}+D_{yy}\frac{\partial^2 C}{\partial y^2}-u(t)\frac{\partial C}{\partial x}-v(t)\frac{\partial C}{\partial y}-\gamma(t)C+\mu(t) \quad (1)$$ Where,

$$\left.\begin{aligned} D_{xx}&=\frac{\alpha_L u^2}{\sqrt{u^2+v^2}}+\frac{\alpha_T v^2}{\sqrt{u^2+v^2}}\\ D_{yy}&=\frac{\alpha_L v^2}{\sqrt{u^2+v^2}}+\frac{\alpha_T u^2}{\sqrt{u^2+v^2}}\end{aligned}\right\} \quad (2)$$

as used in Batu (2006). This is an extension of the advection-diffusion equations. The concentration of adsorbed contaminant in the medium is directly proportional to that of the dissolved contaminant iin the flow (Schiedegger, 1961). i.e., $S=K_d C$ where C is the concentration of the dissolved contaminant and S is the concentration of the adsorbed contaminant.

$$\frac{\partial S}{\partial t}=K_d\frac{\partial C}{\partial t} \quad (3)$$

Hence, equation (3.3) yields

$$R\frac{\partial C}{\partial t}=D_{xx}\frac{\partial^2 C}{\partial x^2}+D_{yy}\frac{\partial^2 C}{\partial y^2}-u(t)\frac{\partial C}{\partial x}-v(t)\frac{\partial C}{\partial y}-\gamma(t)C+\mu(t) \quad (4)$$

where,

$R=1+K_d$, is the retardation coefficient, accounting for equilibrium linear sorption process

K_d is the distribution coefficient which is defined as the ratio of the adsorbed contaminant to the dissolved contaminants

D_{xx} is the longitudinal dispersivity

D_{yy} is the transverse dispersivity

t is the time

x is the distance measured from the origin in the longitudinal direction

y is the distance measured from the origin in the transverse direction

$\gamma(t)$ is a first order decay term

$\mu(t)$ is the zero order source term.

As initial and boundary conditions, we choose

$$\left.\begin{aligned} C(x,y,t) &= c_i; x \geq 0, y \geq 0, t = 0 \\ C(x,y,t) &= C_0(1+\exp(-qt)); x = 0, y = 0, t > 0 \\ C(x,y,t) &= c_p; x \to l, y \to l, t \geq 0 \end{aligned}\right\} \quad (5)$$

where C_0 is the solute concentration and q is the parameter like flow resistance coefficient.

We let

$$\left.\begin{aligned} v(t) &= v_0 f(t) \\ u(t) &= u_0 f(t) \\ D_{xx} &= D_{x0} f(t) \\ D_{yy} &= D_{y0} f(t) \\ \gamma(t) &= \gamma_0 f(t) \\ \mu(t) &= \mu_0 f(t) \end{aligned}\right\} \quad (6)$$

where $f(t)$ is arbitrary function of time. By substituting equation (6) into (4), we obtain

$$\frac{R}{f(t)}\frac{\partial C}{\partial t} = D_{x0}\frac{\partial^2 C}{\partial x^2} + D_{y0}\frac{\partial^2 C}{\partial y^2} - u_0\frac{\partial C}{\partial x} - v_0\frac{\partial C}{\partial y} - \gamma_0 C + \mu_0 \quad (7)$$

where

$$D_{x0} f(t) = \frac{\alpha_L {u_0}^2 + \alpha_T {v_0}^2}{\sqrt{{u_0}^2 + {v_0}^2}} \quad (8)$$

$$D_{y0} f(t) = \frac{\alpha_L {v_0}^2 + \alpha_T {u_0}^2}{\sqrt{{u_0}^2 + {v_0}^2}} \quad (9)$$

as cited in Batu (2006) and $f(t)$ is the arbitrary function of time.

D_{x0} is the initial dispersion coefficient in x direction

D_{y0} is the initial dispersion in the y direction

u_0 is the initial velocity component in the x-direction

v_0 is the initial velocity component in the y-direction

γ_0 is the initial first order decay term

μ_0 is the initial zero-order source term.

A new time variable is introduced as in Crank (1975) and Olayiwola *et al*. (2013)

$$\tau = \frac{1}{R}\int_0^t f(t)dt \tag{10}$$

and

$$f(t) = \mathrm{Re}^{-qt} \tag{11}$$

such that from equation (10),

$$\frac{d\tau}{dt} = \frac{f(t)}{R} \text{ and } \frac{dt}{d\tau} = \frac{R}{f(t)} \tag{12}$$

By substituting equations (10), (11) and (12) in equations (5) and (7), we obtain

$$\left.\begin{aligned} &\frac{\partial C}{\partial \tau} = D_{x0}\frac{\partial^2 C}{\partial x^2} + D_{y0}\frac{\partial^2 C}{\partial y^2} - u_0\frac{\partial C}{\partial x} - v_0\frac{\partial C}{\partial y} - \gamma_0 C + \mu_0 \\ &C(x,y,\tau) = c_i; x \geq 0, y \geq 0, \tau = 0 \\ &C(x,y,\tau) = C_0(2 - q\tau); x = 0, y = 0, \tau < 0 \\ &C(x,y,\tau) = c_p; x \to l, y \to l, \tau \geq 0 \end{aligned}\right\} \tag{13}$$

3.2 Solutions of the Model

We introduce a new space variable as found in Yadav *et al.* (2011), Mahato *et al*. (2015) and Yadav *and* Jaiswal (2011) as follows:

$$\eta = x + y\sqrt{\frac{D_{y0}}{D_{x0}}} \tag{14}$$

into equation (13) and obtain

$$\frac{\partial C}{\partial \tau} = D\frac{\partial^2 C}{\partial \eta^2} - U\frac{\partial C}{\partial \eta} - \gamma_0 C + \mu_0 \tag{15}$$

with the corresponding initial and boundary conditions

$$\left.\begin{aligned} &C(\eta,\tau) = c_i; \eta \geq 0, \tau = 0 \\ &C(\eta,\tau) = C_0(2 - q\tau); \eta = 0, \tau > 0 \\ &C(\eta,\tau) = c_p; \eta \to l, \tau \geq 0 \end{aligned}\right\} \tag{16}$$

where,

$$D = D_{x0}\left(1 + \left(\frac{D_{y0}}{D_{x0}}\right)^2\right) \tag{17}$$

$$U = \left(u_0 + v_0 \sqrt{\frac{D_{y0}}{D_{x0}}} \right) \tag{18}$$

3.3 Non-Dimensionalization

The following dimensionless variables are used to non-dimensionalize the equation (15)

$$\left.\begin{aligned} \tau &= \frac{L}{U}\tau' \\ \eta &= \eta' L \\ C &= C_0 C' \\ \partial\tau &= \frac{L}{U}\partial\tau' \\ \partial\eta &= L\eta' \end{aligned}\right\} \tag{16}$$

and we obtain

$$\Rightarrow \frac{\partial C}{\partial \tau} = D_1 \frac{\partial^2 C}{\partial \eta^2} - \frac{\partial C}{\partial \eta} - \gamma_0 C + \mu_0 \tag{17}$$

where ,

$$D_1 = \frac{D}{LU} \tag{18}$$

The non-dimensionalized equation together with the initial and boundary conditions is

$$\left.\begin{aligned} &\frac{\partial C}{\partial \tau} = D_1 \frac{\partial^2 C}{\partial \eta^2} - \frac{\partial C}{\partial \eta} - \gamma_0 C + \mu_0 \\ &C(\eta,0) = \frac{c_i}{c_0} \\ &C(0,\tau) = 2 - q\tau,\ \tau \geq 0 \\ &C(1,\tau) = \frac{c_p}{c_0},\ \tau \geq 0 \end{aligned}\right\} \tag{19}$$

3.4 Parameters Expanding Method (PEM)

The above initial boundary value problem is solved for when the initial spatial concentration c_i is non-zero. By using parameter expanding method and let $1 = a\gamma_0$ in the advection term of equation (19) and

$$C(\eta,\tau) = C_0(\eta,\tau) + \gamma_0 C_1(\eta,\tau) \tag{20}$$

as used by Olayiwola *et al*. (2013), He (2006) and Sweilam and Khader (2010),

Equation (19) becomes

$$\begin{aligned}&\frac{\partial}{\partial\tau}(C_0(\eta,\tau)+\gamma_0C_1(\eta,\tau)+\gamma_0{}^2C_2(\eta,\tau)+...)\\&=D_1\frac{\partial^2}{\partial\eta^2}(C_0(\eta,\tau)+\gamma_0C_1(\eta,\tau)+\gamma_0{}^2C_2(\eta,\tau)+...)\\&-a\gamma_0\frac{\partial}{\partial\eta}(C_0(\eta,\tau)+\gamma_0C_1(\eta,\tau)+\gamma_0{}^2C_2(\eta,\tau)+...)\\&-\gamma_0(C_0(\eta,\tau)+\gamma_0C_1(\eta,\tau)+\gamma_0{}^2C_2(\eta,\tau)+...)+\mu_0\end{aligned}\tag{21}$$

Equating corresponding coefficients on both sides of equation (21), we obtain the following initial boundary problems:

$$\left.\begin{aligned}&\frac{\partial C_0}{\partial\tau}=D_1\frac{\partial^2C_0}{\partial\eta^2}+\mu_0\\&C_0(\eta,0)=\frac{c_i}{c_0}\\&C_0(0,\tau)=2-q\tau\\&C_0(1,\tau)=\frac{c_p}{c_0}\end{aligned}\right\}\tag{22}$$

$$\left.\begin{aligned}&\frac{\partial C_1(\eta,\tau)}{\partial\tau}=D_1\frac{\partial^2C_1}{\partial\eta^2}-a\frac{\partial C_0}{\partial\eta}-C_0\\&C_0(\eta,0)=0\\&C_0(0,\tau)=0\\&C_0(1,\tau)=0\end{aligned}\right\}\tag{23}$$

We transform equations (22) and (23) to homogeneous boundary conditions problem as follows:

From (22), let

$$w_0(\tau)=\alpha(\tau)+\frac{\eta}{l}(\beta(\tau)-\alpha(\tau)),\quad l=1\tag{24}$$

where $\alpha(\tau)=2-q\tau$ and $\beta(\tau)=\frac{c_p}{c_0}$,

$$C_0(\eta,\tau)=v_0(\eta,\tau)+w_0(\tau)\tag{25}$$

i.e.,

$$C_0(\eta,\tau)=v_0(\eta,\tau)+(2-q\tau)+\eta\left(\frac{c_p}{c_0}-(2-q\tau)\right)\tag{26}$$

We transform equation (23) and (23) using equation (26) and obtained the following equations

$$\left.\begin{aligned} &\frac{\partial v_0}{\partial \tau} = D_1 \frac{\partial^2 v_0}{\partial \eta^2} + \mu_0 - (\eta - 1)q \\ &v_0(0,\tau) = 0 \\ &v_0(1,\tau) = 0 \\ &v_0(\eta,0) = \frac{c_i}{c_0} - 2(\eta - 1) - \eta \frac{c_p}{c_0} \end{aligned}\right\} \tag{27}$$

$$\left.\begin{aligned} &\frac{\partial v_1(\eta,\tau)}{\partial \tau} = D_1 \frac{\partial^2 v_1}{\partial \eta^2} - a \frac{\partial v_0}{\partial \eta} - v_0 \\ &v_0(\eta,0) = 0 \\ &v_0(0,\tau) = 0 \\ &v_0(1,\tau) = 0 \end{aligned}\right\} \tag{28}$$

The initial boundary value problem (27) is solved by eigenfunctions expansion technique

From (27), we have

$$F(\eta,\tau) = \mu_0 - (\eta - 1)q \tag{29}$$

$$F(\eta) = \frac{c_i}{c_0} + 2(\eta - 1) - \eta \frac{c_p}{c_0} \tag{30}$$

In Fourier series expansion,

$$b_n = 2\int_0^1 F(\eta)\sin(n\pi)\eta d\eta \tag{31}$$

$$b_n = 2\int_0^1 \left(\frac{c_i}{c_0} + 2(\eta - 1) - \eta \frac{c_p}{c_0}\right)\sin(n\pi)\eta d\eta \tag{32}$$

$$b_n = -\frac{2c_i}{n\pi c_0}(\cos(n\pi) - 1) - \frac{4}{n\pi} + \frac{2c_p}{n\pi c_0}\cos n\pi \tag{33}$$

$$F_n(\tau) = 2\int_0^1 (\mu - (\eta - 1)q)\sin(n\pi\eta d\eta) \tag{34}$$

$$F_n(\tau) = -\frac{2\mu_0}{n\pi}(\cos(n\pi) - 1) + \frac{2q}{n\pi} \tag{35}$$

$$C_n(\tau) = \int_0^\tau e^{\left(\alpha - k(n\pi)^2(\tau - t)\right)} F_n(t)dt + b_n e^{\left(\alpha - k(n\pi)^2 \tau\right)} \tag{36}$$

Therefore,

$$C_n(\tau)=\frac{2}{D_1(n\pi)^3}\left(q-\mu_0\left(\cos(n\pi)-1\right)\right)\left(1-e^{\left(-D_1(n\pi)^2\tau\right)}\right)+\begin{pmatrix}-\dfrac{2c_i}{n\pi c_0}\left(\cos(n\pi)-1\right)\\-\dfrac{4}{n\pi}+\dfrac{2c_p}{n\pi c_0}\cos n\pi\end{pmatrix}e^{\left(-D_1(n\pi)^2\tau\right)} \quad (37)$$

$$C_0(\eta,\tau)=v_0(\eta,\tau)+w_0(\tau) \quad (38)$$

i.e.,

$$C_0(\eta,\tau)=w_0(\tau)+\sum_{n=1}^{\infty}C_n(\tau)\sin(n\pi\eta) \quad (39)$$

$$\begin{aligned}C_0(\eta,\tau)&=(2-q\tau)(1-\eta)+\eta c_p\\&+\sum_{n=1}^{\infty}\begin{pmatrix}\dfrac{2}{D_1(n\pi)^3}\left(q-\mu_0\left(\cos(n\pi)-1\right)\right)\left(1-e^{\left(-D_1(n\pi)^2\tau\right)}\right)\\+\begin{pmatrix}-\dfrac{2c_i}{n\pi c_0}\left(\cos(n\pi)-1\right)-\dfrac{4}{n\pi}\\+\dfrac{2c_p}{n\pi c_0}\cos n\pi\end{pmatrix}e^{\left(-D_1(n\pi)^2\tau\right)}\end{pmatrix}\sin(n\pi\eta)\end{aligned} \quad (40)$$

Similarly, the solution of equation (27) is substituted in equation (28) and solved using the eigenfunctions method and obtained the following results.

$$\begin{aligned}C_1(\eta,\tau)=-\sum_{n=1}^{\infty}&\left(\sum_{n=1}^{\infty}\frac{2}{D_1(n\pi)^3}\left(q-\mu_0\left(\cos(n\pi)-1\right)\right)\begin{pmatrix}\dfrac{1}{D_1(n\pi)^2}-\tau e^{\left(-D_1(n\pi)^2\tau\right)}\\-\dfrac{e^{\left(-D_1(n\pi)^2\tau\right)}}{D_1(n\pi)^2}\end{pmatrix}\right)\sin(n\pi\eta)\\&-\sum_{n=1}^{\infty}\left(\sum_{n=1}^{\infty}\begin{pmatrix}-\dfrac{2c_i}{n\pi c_0}\left(\cos(n\pi)-1\right)-\dfrac{4}{n\pi}\\+\dfrac{2c_p}{n\pi c_0}\cos n\pi\end{pmatrix}e^{\left(-D_1(n\pi)^2\tau\right)}\tau\right)\sin(n\pi\eta)\end{aligned} \quad (41)$$

The solution of the contaminant flow problem (13) when $c_i \neq 0$ is therefore

$$C(\eta,\tau)=C_0(\eta,\tau)+\gamma_0 C_1(\eta,\tau) \quad (42)$$

Where $C_0(\eta,\tau)$ and $C_1(\eta,\tau)$ are as given in (40) and (41).

4. **Results and Discussion**

The analytical solution obtained in equation (42) is used to study the behavior of the contaminant concentration in the flow for values of $C_i = 2,\ C_0 = 1,\ q = 3,\ \gamma = 0.1,\ \mu = 0.3,\ D_{x0} = 1,\ u_0 = 0.1,\ v_0 = 0.1$ with D_{y0} varying as 1.5, 1.6, 1.7 and the graph presented in figure 1. Similarly, with μ_0 varying as 0.3, 0.6, 0.9, we obtained the graphs in figure 2 and 3. Figure 4 is obtained by varying the first order decay coefficient γ as 0.1, 0.5 and 0.9.

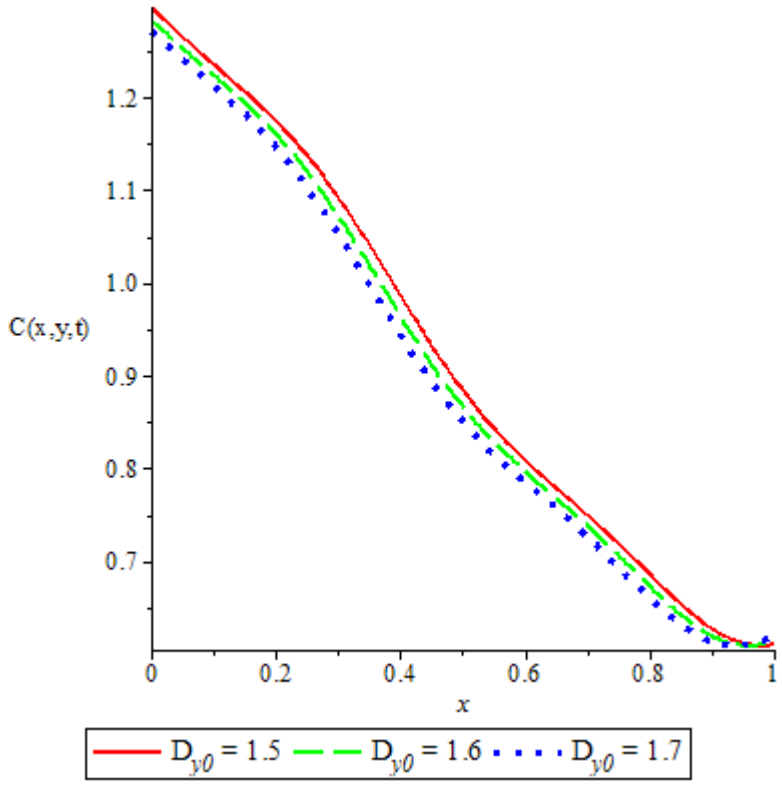

Figure 1: Contaminant Concentration profile for $D_{y0} = 1.5, D_{y0} = 1.6,\ D_{y0} = 1.7$ when $c_0 = 1, c_p = 1,$ $q = 3,\ \gamma_0 = 0.1,\ \mu_0 = 0.3,\ D_{x0} = 1,\ u_0 = 0.1, v_0 = 0.1$ with y and t fixed as 0.5.

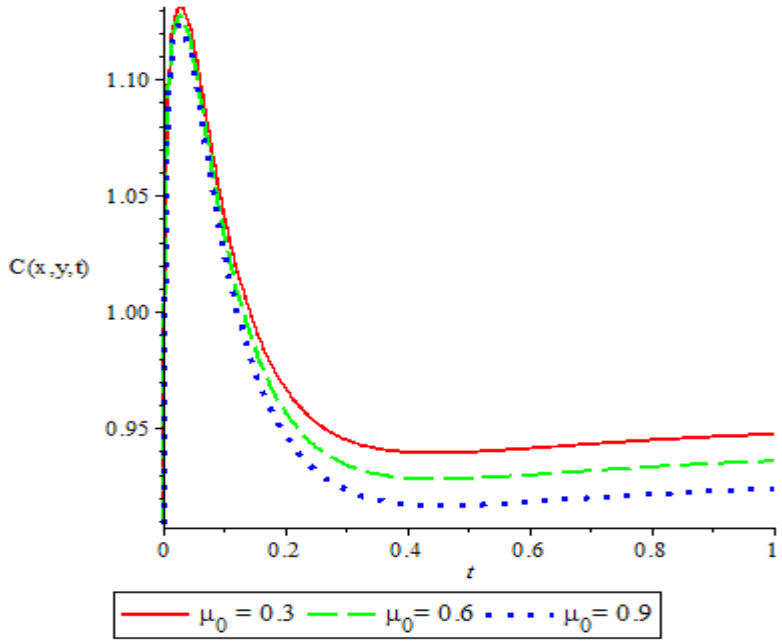

Figure 2: Contaminant Concentration profile for $\mu_0 = 0.3, \mu_0 = 0.6,\ \mu_0 = 0.9$ when $c_0 = 1, c_p = 1,$ $q = 3,\ \gamma_0 = 0.1,\ D_{x0} = 1,\ D_{y0} = 1.5,\ u_0 = 0.1, v_0 = 0.1$ with y and x fixed as 0.5.

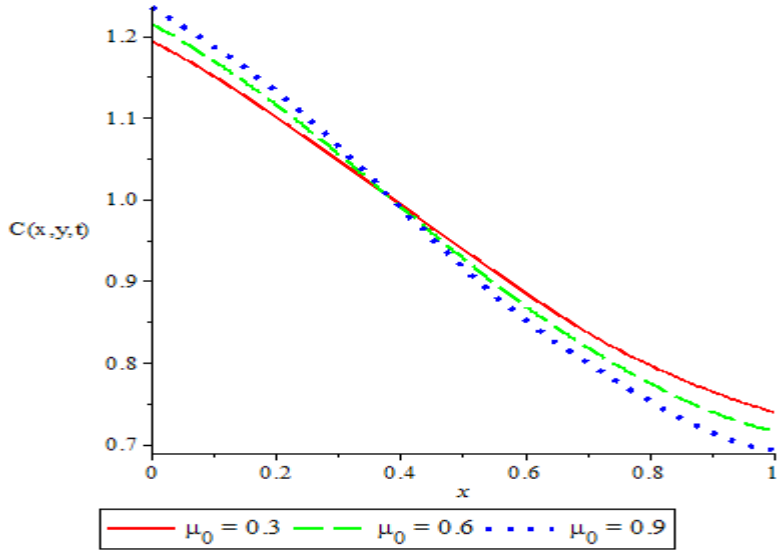

Figure 3: Contaminant Concentration profile for $\mu_0 = 0.3, \mu_0 = 0.6,\ \mu_0 = 0.9$ when $c_0 = 1, c_p = 1,$ $q = 3,\ \gamma_0 = 0.1,\ D_{xo} = 1,\ D_{y0} = 1.5,\ u_0 = 0.1, v_0 = 0.1$ with y and t fixed as 0.5.

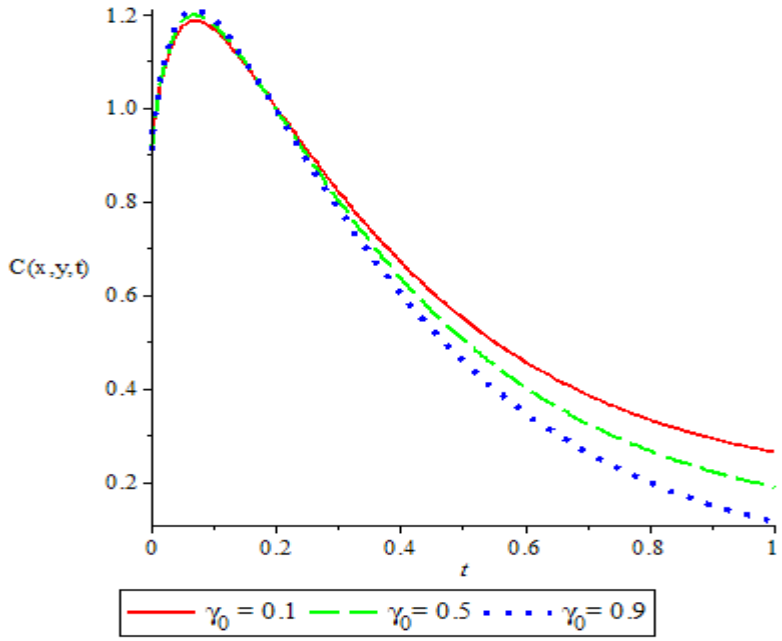

Figure 4: Contaminant Concentration profile for $\gamma_0 = 0.1, \gamma_0 = 0.5$, $\gamma_0 = 0.9$ when $c_0 = 1$, $\mu_0 = 0.3$, $c_p = 1$, $q = 3$, $D_{xo} = 1$, $D_{y0} = 1.5$, $u_0 = 0.1, v_0 = 0.1$ with y and x fixed as 0.5.

Figure 1 shows the contaminant concentration profile with distance x for varying vertical dispersion coefficient. The graph shows that the contaminant concentration decreases as the vertical dispersion coefficient increases. Figure 2 is the contaminant concentration profile with time for varying zero-order source coefficient. It shows that as the zero-order source coefficient increases, the contaminant concentration decreases with time. Figure 3, which is the graph of contaminant concentration against distance x shows that the contaminant concentration decreases with increase in distance as the zero-order source coefficient increases. Similarly, figure 4 also reveal that as the contaminant concentration decreases with time as the decay coefficient increases.

5. **Conclusion**

A two-dimensional contaminant flow model with non-zero initial concentration is solved to predict the effect of change in the zero-order source and decay coefficients on the contaminant concentration along transient groundwater in a finite homogeneous medium by eigenfunctions expansion method. The zero-order source and decay coefficient are varied to study the contaminant behavior along the flow. Our findings reveal that the contaminant concentration decreases along the spatial direction as the zero-order source and decay coefficient increases. This model, if properly implemented could help the geologist in locating the point at which the contaminant concentration is approximately zero.

References

Aiyesimi, Y. M. and Jimoh, O. R. (2012). Computational Analysis of 1-D non-linear reactive contaminant flow problem with an initial continuous point source. *Journal of Nigerian Association of Mathematical Physics*, 22, 543-543.

Aiyesimi, Y. M. and Jimoh, O. R. (2013). Analytical solution of non-linear contaminant flow problems with initial continuous point source by homotopy perturbation method. *Nigerian Journal of Technological Research*, 8(1), 43-46.

Batu, V. (2006). *Applied Flow and Solute Transport Modeling in Aquifers: Fundamental Principles and Analytical and Numerical Methods*. USA: CRC Press, Taylor and Francis.

Bear, J. (1972). *Dynamics of Fluid in Porous Media*. New York: Elsevier publishing company.

Bear, J. (1997). *Hydraulics of Groundwater.* New York: McGraw-Hill.

Brainard, E. C. & Gelhar, L. W. (1991). Influence of vertical flow on groundwater transport. *Groundwater*, 2915, 693-701.

Chen, Z., Huan., G and Ma, Y. (2006). Computational methods for multiphase flows in porous media. *Society for Industrial and Applied Mathematics*, 1, 9-49.

Crank, J. (1975). *The Mathematics of Diffusion.* United Kingdom, Oxford University Press.

Freezer, R. A. & Cherry, J.A. (1979). *Groundwater*. Englewood Cliffs, New Jersey: Prentice Hall, Incorporation.

He, J. H. (2006). Some assymptotic methods for strongly nonlinear equations. *International Journal of Modern Physics,* 20(10), 1141-1199.

Mahato, N. K., Begam, S., Das, Pintu & Singh, M. K. (2015). Two-dimensional solute dispersion along the unsteady groundwater flow in aquifer. *Journal of Groundwater research*, 3(4), 44-67.

Okedayo, T. G. & Aiyesimi, Y. M. (2005). Influence of retardation factor on the non-linear contaminant flow. *The Journal of Education*, 4,27-32.

Okedayo, T. G., Owoloko, E. A. & Osafile, O.E. (2011). A regular perturbation analysis of the non-linear contaminant transport equation with initial and instantaneous point source. *Australia Journal of Basic and Applied Sciences*, 5(8),1273-1277.

Olayiwola, R. O., Jimoh, O. R., Yusuf, A. & Abubakar, S. (2013). A mathematical Study of contaminant transport with first order decay and time-dependent source concentration in an aquifer. *Universal Journal of Mathematics,* 1(2), 112-119.

Ramakanta, M. & Mehta, M. N. (2010). Effect of longitudinal dispersion of miscible fluid flow through porous media. *Advanced Theoretical and Applied Mechanics*, 3(5), 211-220.

Schiedegger, A. F. (1961). General theory of dispersion in porous media. *Journal of general theory of Research*. 66:1-10.

Singh, M. K. (2013). Two-dimensional solute transport in finite homogeneous porous formations. *International Journal of Geology, Earth and Environmental Sciences,* 3(2), 35-48.

Singh, M. K., Ahamed , S. & Singh , V. P. (2014). One-dimensional uniform and time varying solute dispersion along transient groundwater flow in a semi-infinite aquifer. *Acta Geophysica*, 6(4), 872-892.

Singh, M. K., Mahato, N. K. & Kumar, N. (2015). Pollutant's horizontal dispersion along and against sinusoidally varying velocity from a pulse type source. *Acta Geophysica*, 63(1), 214-261.

Sweilam, N. A. & Khader, M. M. (2010). A note on parameter expansion method of coupled Van der pol-Duffing oscillations. *Applications and Applied Mathematics* (*An International Journal*), 1, 94-100.

Ujile, A. A. (2013). Evaluating mass transfer process for groundwater contaminants flow models in Yenegoa, Nigeria. *International Journal of Engineering and Technology*, 3, 824-833.

Yadav, R. R. & Jaiswal, D. K. (2011). Two-dimensional analytical solutions for point source contaminants transport in semi-infinite homogeneous porous medium. *Journal of Engineering Science and Technology*, 6(4), 459-468.

Yadav, R. R., Jaiswal, D. K., Yadav, H. K. & Gulrana (2011). Temporary dependent dispersion through semi-infinite homogeneous porous media: an analytical solution. *International Journal of Research and Reviews in Applied Sciences*, 6(2), 158-164.

VHF RADIOWAVE PROPAGATION MEASUREMENTS IN MINNA, NORTH CENTRAL NIGERIA

K. C. Igwe[1*], O. D. Oyedum[1], M.O. Ajewole[2] and A. A. Aibinu[3]

[1]Department of Physics, Federal University of Technology, Minna, Niger State

[2]Department of Physics, Federal University of Technology, Akure, Ondo State

[3]Department of Mechatronics Engineering, Federal University of Technology, Minna, Niger State

[1*]Corresponding author: k.igwe@futminna.edu.ng

Abstract

In designing an efficient radio communication system, the engineer is faced with the task of being able to predict the behaviour of the radio signal from the transmitter to the receiver and in doing this, preliminary calculations including the expected signal strength at the receiver has to be made. Signal strength measurement was made from a broadcasting station transmitting at a frequency of 92.3 MHz along a 14.85 Km path. The results obtained show that received signal strength (RSS) values were higher during the wet season as compared to lower values recorded during the dry season for the link. Also, the RSS was higher during the morning and evening/night hours while lower values were recorded during the afternoon time. Signal attenuation caused by atmospheric and environmental losses was calculated and for the dry season, average clear-air attenuation fluctuated between -2 dB to 2.3 dB while wet season values fluctuated between 0 dB and -2.9 dB. Also, the RSS was modeled using ITU-R P.526-12 to predict path losses due to diffraction over the earth's curvature and result obtained reveal that this model underestimated the RSS for the radio link while 206 (12.46%) enhanced field strength was recorded out of the measured 1,639 data.

Key words: Signal strength, Attenuation, Diffraction

1. Introduction

Radio waves form part of the electromagnetic spectrum that extends from the very low frequencies (3-30 kHz) to the extremely high frequencies (30-300 GHz). In the middle of these two extreme frequencies are bands of frequencies that are found in every day uses. These are audio frequencies used in systems for the reproduction of audible sounds, radio frequencies, infrared light, ultraviolet light and x-rays (Barringer and Springer, 1999). The influence of the propagating medium on electromagnetic waves determines the success of any communication.

The daily changes of water vapour in the troposphere and the ionization by the sun in the ionosphere affect radio propagation. Practical applications from the understanding of the effects of these varying conditions on radio propagation abound, from choosing frequencies for international shortwave broadcasters, designing efficient mobile telephone systems, radio navigation to radar systems operation. Radio propagation is also affected by a number of other factors determined by its path from one point to the other (Hall and Barclay, 1991). The path can be a direct line-of-sight path or over-the-horizon path aided by refraction in the atmosphere. For most communication links, the presence of the earth, the atmosphere, the ionosphere, atmospheric hydrometeors such as raindrops, snow and hail modifies the signal propagation. The natural environment has an influence on the propagation of radio waves and this influence is highly dependent on the frequency used, the directivity of the antennas involved and the proximity of the antennas to the ground. The physical nature of the intervening path may also have a significant effect on the propagation of radio waves since propagation over land is different from propagation over water, which is also different from propagation over heavy vegetation or over urbanised areas where tall buildings produce different scattering and diffraction effects (Collin, 1985). Since radio waves are a form of electromagnetic radiation, like light waves, when they travel, they interact with objects and the media in which they travel. As a result, they are affected by the phenomena of reflection, refraction, diffraction, absorption, polarisation and scattering (Paris and Hurd, 1969).

In order to achieve a reliable and efficient communication between a transmitter and a receiver, knowledge of the spatial and temporal variability of field strength is required. Where the user expects a very high quality signal, especially in broadcast applications, this assumes greater significance. Also the performance of any communication circuit depends on the models employed to calculate the coverage area and interference problems (Prasad *et al.*, 2006). At VHF and higher frequencies for which the effects of the ionosphere are generally considered negligible, the troposphere greatly influences the received signal, especially at a distant terminal. This is in addition to any influence caused by the electrical properties of the terrain over which the wave is propagated. Also, propagation conditions often changes greatly from month to month and the monthly variability can vary significantly from year to year. These statistics of signal variability is needed for spectrum planning and for predicting the performance of radio systems (Aboaba and Jegede, 2001; Middleton, 2003).

2. Relevant theory

The power flux per unit area P_a (W/m^2) at a distance r (m) from a loss free isotropic antenna radiating a power P_T (W) is given by (Freeman, 1997):

$$P_a = {}^{P_T}/_{4\pi r^2} \quad (1)$$

where $4\pi r^2$ is the surface area of a sphere at a distance d (m) from the source.

The power at the receiver is given by:

$$P_R = P_T \left(\frac{\lambda}{4\pi r^2}\right)^2 \quad (2)$$

The free space loss, L_{FSL} between transmitter and receiver antennas is defined by:

$$L_{FSL}(dB) = 10Log(\frac{P_T}{P_R}) \quad (3)$$

Combining equations (2) and (3), the free space loss is given as:

$$L_{FSL}(dB) = 20Log(\frac{4\pi r}{\lambda}) \quad (4)$$

Equation (4) is restated more conveniently as

$$L_{FSL}(dB) = 32.45 + 20Log(r_{km}) + 20Log(F_{MHz}) \quad (5)$$

Or as (ITU-R, 2009):

$$L_{FSL}(dB) = 139.3 - E + 20Log(F_{MHz}) \quad (6)$$

And the free space field strength for 1 kW e.r.p. , E_{FS} is given by:

$$E_{FS}(dB\mu V/m) = 106.9 - 20Log(r_{km}) \quad (7)$$

For a non free-space environment, the field strength can be related to the basic free space loss by (Barringer and Springer, 1999):

$$L_{FSL}(dB) = 137 + 20Log(F_{MHz}) + P_T + G_T - E(dB\mu V/m) \quad (8)$$

Also, field strength can be expressed as a function of received voltage, receiving antenna gain and frequency when applied to an antenna whose impedance is 50 ohms. This is given as:

$$E(dB\mu V/m) = E(dB\mu V) - G_r(dBi) + 20Log(F_{MHz}) - 29.8 \quad (9)$$

For received voltage calculation, this equation becomes:

$$E(dB\mu V) = E(dB\mu V/m) + G_r(dBi) - 20Log(F_{MHz}) + 29.8 \quad (10)$$

where G_r is the isotropic gain of the receiving antenna

The diffraction path loss is taken as the sum of the free space loss that exists in the absence of obstacles and the diffraction loss introduced by the obstacles (Roda, 1988). The diffraction field strength, E, relative to the free-space field strength, E_0, is given by (ITU-R, 2012):

$$20\ log\frac{E}{E_0} = F(X) + G(Y_1) + G(Y_2)\ dB \quad (11)$$

where X is the normalised length of the path between the antennas at normalised heights Y_1 and Y_2.

$$X = 2.188\beta f^{1/3} a_e^{-2/3} d \quad (12a)$$

$$Y = 9.575\ X\ 10^{-3} \beta f^{2/3} a_e^{-1/3} h \quad (12b)$$

where: d = path length (km)

a_e = equivalent Earth's radius (km)

h = antenna height (m)

f = frequency (MHz)

β is a parameter allowing for the type of ground and for polarisation. It is related to K, the surface admittance by the following semi-empirical formula:

$$\beta = \frac{1+1.6\ K^2+ 0.67\ K^4}{1+4.5\ K^2+ 1.53\ K^4} \quad (13)$$

The distance term is given by:

$$F(X) = 11 + 10\ log(X) - 17.6\ X \quad \text{for X} \geq 1.6 \quad (14a)$$

$$F(X) = -20\ log(X) - 5.6488X^{1.425} \text{ for X} < 1.6 \quad (14b)$$

The height gain term G(Y) is given by the following formula:

$$G(Y) \equiv 17.6\ (B - 1.1)^{1/2} - 5log(B - 1.1) - 8 \text{ for B} > 2 \quad (15a)$$

$$G(Y) \equiv 20log(B + 0.1B^3) - 5log\ (B - 1.1) \quad \text{for B} \leq 2 \quad (15b)$$

where: $B = \beta Y$ (15c)

3. Methodology

Experimental Setup: The transmitter, a broadcast station is the Federal University of Technology, Minna FM station broadcasting at 92.3 MHz. It is located at the main campus of the University, Gidan Kwano, Minna. It is 14.85 Km from the receiver, which is located at the mini campus, Bosso, Minna. The climatic condition in Minna is a tropical one with two main seasons, the dry or harmattan season which occurs from November to March and the wet or rainy season which commences from April and ends in October every year. The measurement was done from January to March and from May to July, that is, three months of dry season and three months of wet season.

The instrument used for the signal strength measurement is the Geberit Digital Signal Level Meter, GE-5499 covering the signal range of 30-120 dBμV (Figure 1). Figure 2 shows the map of the transmitting and receiving stations while table 1 gives details of the parameters of the experiment.

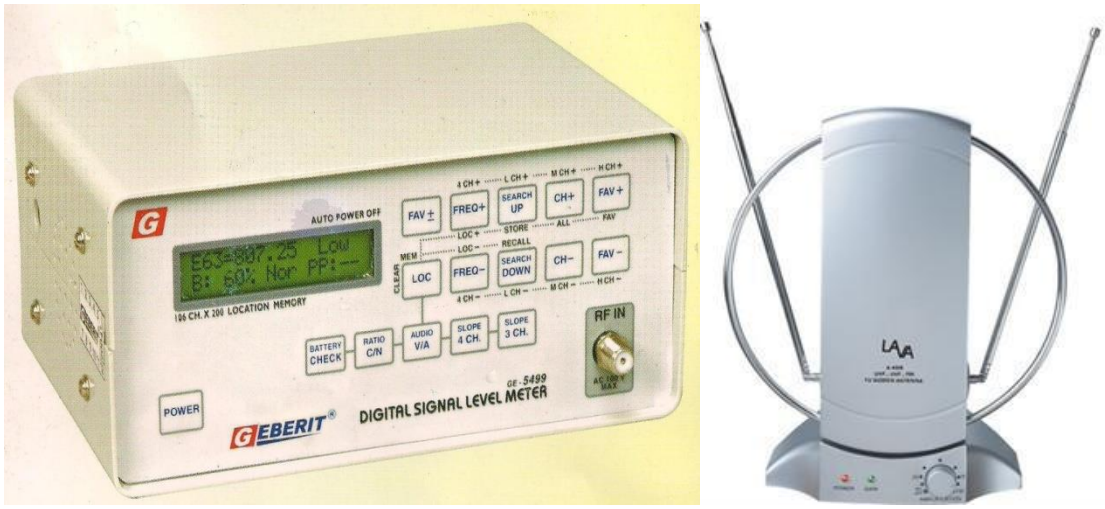

Figure 1: Geberit field strength meter and antenna

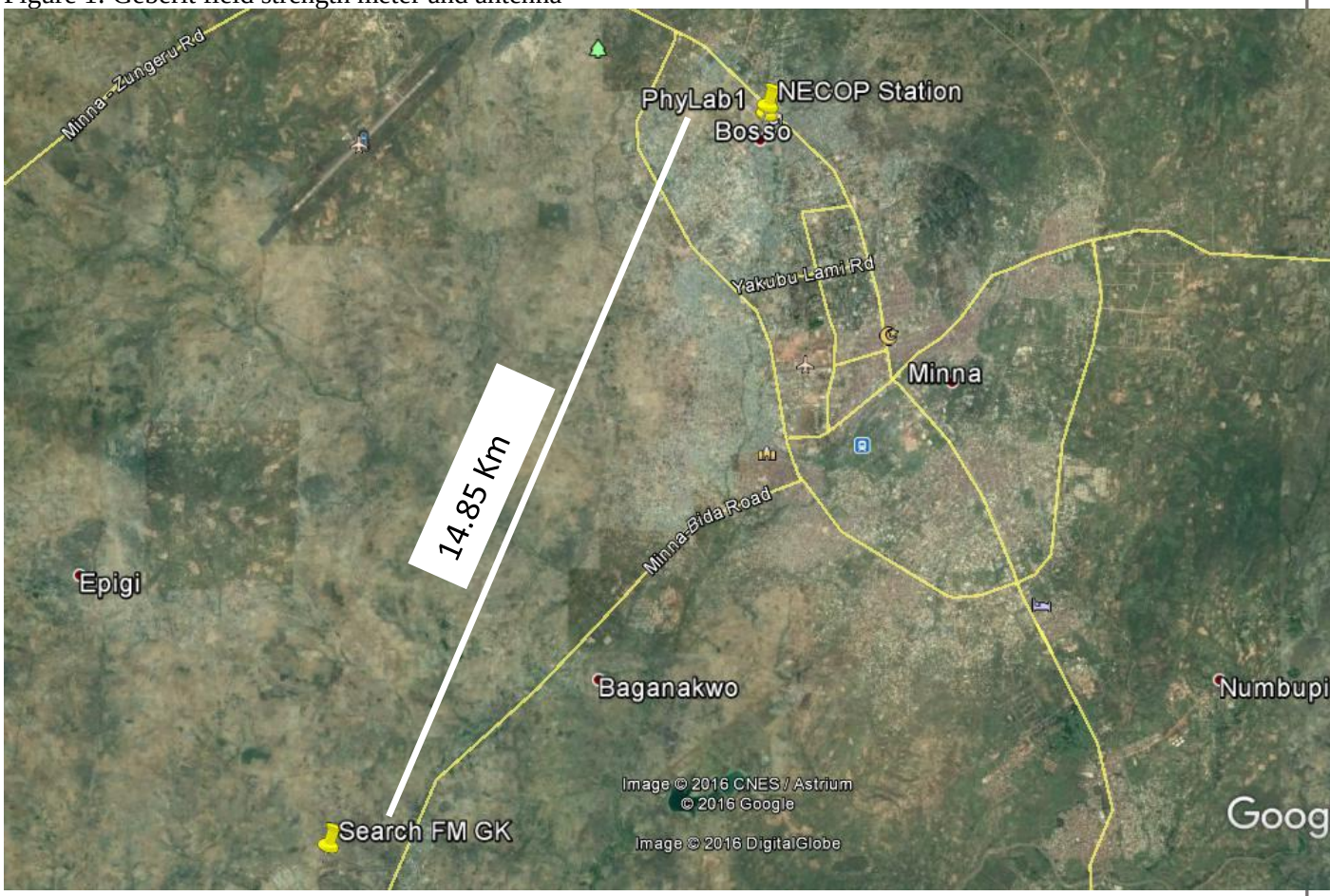

Figure 2: The transmitting station (Search FM) and the measurement site (Physics Lab 1)

Table 1: Measurement parameters

Frequency (MHz)	92.3
Tx height (m)	180
Rx height (m)	3.2
Path distance (km)	14.85

Tx Power (kW)	0.3

4. Results and Discussion

4.1 Seasonal Variation of Signal Strength

Although measurements were made for six months, only few months are shown here because of space constraints. Figures 4.1a-b show the mean monthly variation of Signal Strength for the VHF link for a typical dry season month and a typical wet season month. Using the month of March for a typical dry month, mean signal strength measured for the link varied from 72 dBµV to 93 dBµV.
Measurement made for the wet season months reveal that higher signal strength values were recorded for the link. For the month of July, a typical wet month, mean signal strength measured for the link ranged between 88 dBµV and 106 dBµV.

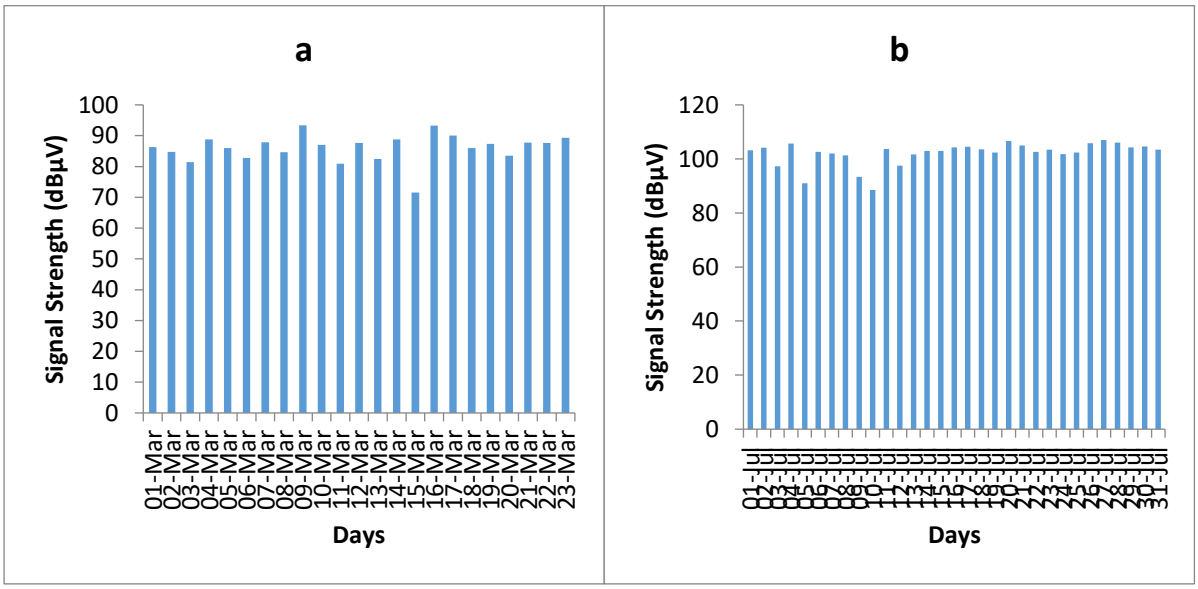

Figure 4.1a&b: Mean daily VHF Signal Strength Variation for a typical dry month (March) and a typical wet month (July)

4.2 Mean Diurnal variation of Signal Strength

Figures 4.2a-b show the mean values of diurnal variation of the received signal strength during broadcast hours. The measurement was taken from 9 am to 10 pm when the radio station ends broadcast daily. From the results, it is observed that hourly signal strength shows a noticeable diurnal trend. The received signal strength (RSS) was generally higher during the morning and evening/night hours while lower values were recorded during the afternoon time. Using the month of February as an example, a peak value of RSS of 77 dBµV was recorded around 9.00 am local time but thereafter the RSS decreases towards afternoon until a minimum value of 67 dBµV was reached by 2.00 pm. The RSS value then began an upward rise with a value of 71 dBµV from 3.00 pm until another peak value of 75 dBµV was reached by 5.00 pm. There was a slight decrease in RSS to 71 dBµV at 6 pm before another rise from 72 dBµV at 7.00 pm to a peak value of 75 dBµV by 8.00 pm which was maintained during the night. This trend of morning/night peak and midday minimum was observed in the other months.

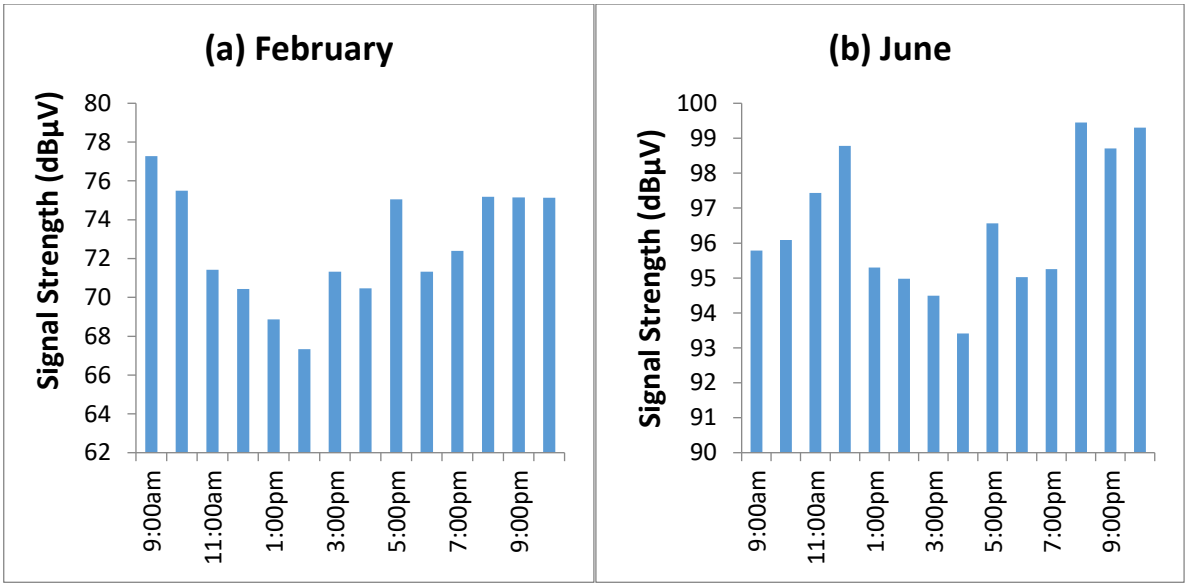

Figure 4.2a&b: Mean Diurnal Variation of Signal Strength for a typical dry month (February) and a typical wet month (June)

4.3 Cumulative Frequency Distribution of Signal Strength

The cumulative frequency distribution of the received signal strength (RSS) for the link for the entire database is presented in Figure 4.3. This curve show the fraction of the total time for which the received signal exceeded a specified power. For this link, 1,639 RSS value was recorded in the entire database. Of these values, the highest number of samples in the entire data base is 105 dBµV which occurred 313 times, corresponding to 48.38% of time of measurement while the field strength value with the lowest number of samples in the entire data base is 55 dBµV and 115 dBµV, both occurring twice during measurement and this represented 0.12% of time. Also, figure 4.3 reveals that the RSS exceed 35 dBµV in 95.5% of the measurement time.

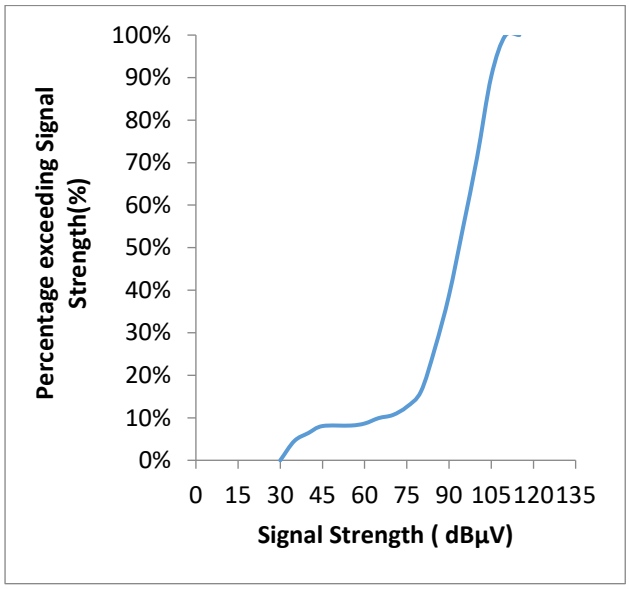

Figure 4.3: Cumulative Frequency Distribution for Search FM Minna

4.4 Attenuation of received signals

During transmission, there is a certain power expected at the receiver end of the terrestrial link. For instance the RSS expected at the receiver end is 69.3 dB when a transmitting power of 8.5 kW is used. However, the actual RSS fall below this level indicating that there is signal attenuation as a result of atmospheric or environmental losses. The attenuation of the signal level was calculated and the effect is observed in all the measured values of signal strength. Some of the results are shown in Figures 4.4a and 4.4b. Taking the month of February which is a typical dry month for an example, it is seen that the average clear-air attenuation fluctuates between -2 dB to 2.3 dB.
Considering the clear-air attenuation for a typical wet month (July), average attenuation fluctuates between 0 dB and -2.9 dB. One of the factors that contribute to this clear-air attenuation is the k-factor (effective-earth radius factor) fading. Diffraction or k-type fading in line-of-sight links result due to the variation of the effective earth radius factor which also arises because of the time-varying nature of the primary tropospheric parameters of temperature, pressure and relative humidity.

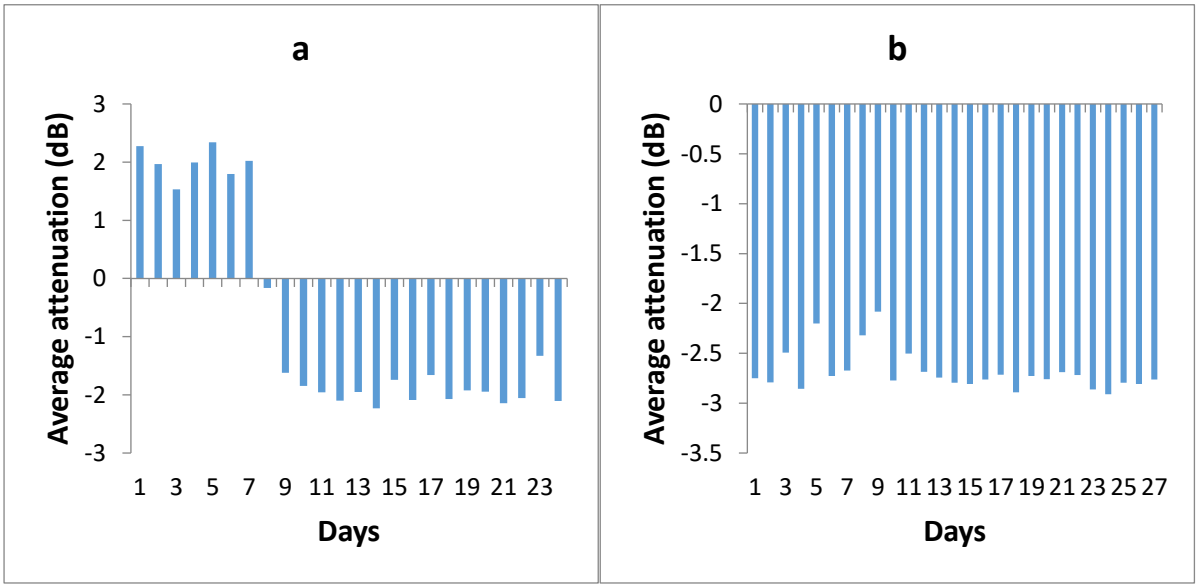

Figure 4.4: Clear air attenuation for a typical dry month (a) and a typical wet month (b)

4.5 Modelling of Field Strength using ITU-R model

The received signal strength was converted to field strength. Subsequently the diffraction values were modelled using the procedure in Recommendation ITU-R P.526-12. The step-by-step calculation of this procedure is given from equation 11-15c. This recommendation uses antenna heights and range to predict path losses due to diffraction over the earth's curvature. Free space field strength for the link was also calculated using equation 5, and assuming that free space loss along the path is classified as enhanced signals. Figure 4.5 gives comparisons between the predicted field strength, the free space field strength and the measured field strength. From the Figure, it is observed that ITU-R model underestimated the received field strength for the radio link. The differences between the predicted and the measured field strength values are notably large, hence no correlation whatsoever exists between the measured field strength and the ITU-R predicted field strength. This observation indicates that some refractive effects are prevalent all the time. Since the majority of the data lie between the free space and diffraction threshold values, this indicates that refractive effects (atmospheric effects) are able to increase the received field strength well beyond the diffraction level and this enhancement in field strength provided by the atmosphere is sufficient to reach the free space threshold as seen in some cases in the figure. For this FM link, 206 (12.46%) out of the measured 1,639 data correspond to enhanced field strength. One of the factors or type of refractive condition responsible for this type of enhanced field strength is ducting. This anomalous effect allows radio signals to reach distant receivers that would not propagate beyond the radio horizon under normal atmospheric conditions.

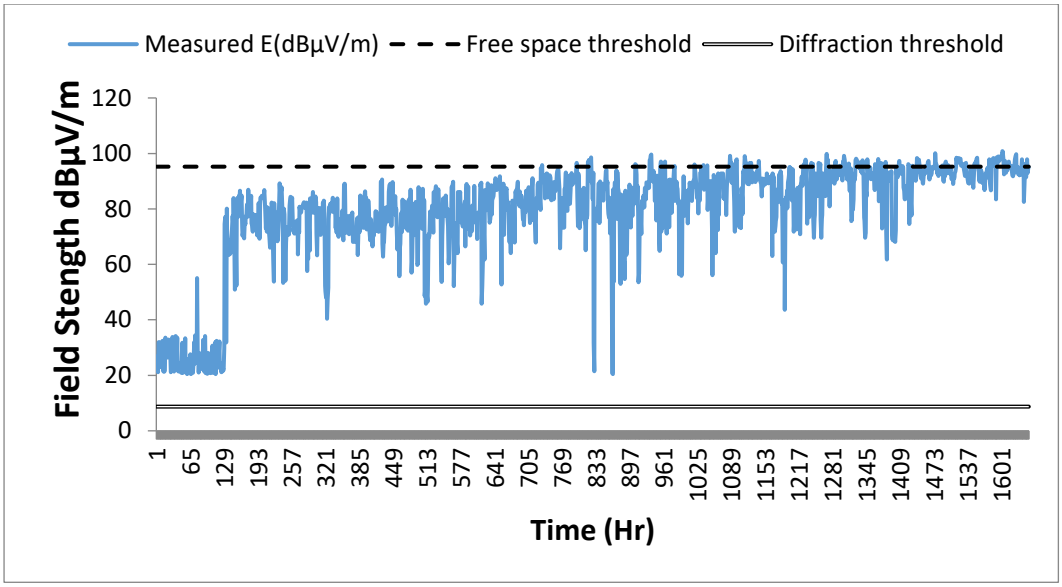

Figure 4.5: Comparison of measured Field Strength with ITU-R Models of Free-Space and diffraction values for Search FM (92.3 MHz) Link.

5. Conclusion

Very high frequency (VHF) measurements have been carried out for a point-to-area network situated in Minna. Measurement carried out reveal the effects of weather on the received signal strength (RSS) as low values were recorded during the daytime and during the dry season while peak values were recorded at night times and during the wet season. The received signal strength was converted to field strength and the field strength was modelled using the procedure in Recommendation ITU-R P.526-12. From the result, it was observed that ITU-R model underestimated the received field strength for the radio link. The experimental results obtained are required for engineers planning to design an efficient radio communication system in this part of the world since preliminary calculations including the expected signal strength at the receiver are very necessary for such design.

References

Aboaba, O. A., & Jegede O. O. (2001). Correlation studies of of VHF radiowave propagation and radiometeorological conditions. *Proc. Of the 11th International Conf. on Antennas and Propagation – ICAP2001, IEEE Conf., No. 480, Vol.1, UMIST, Manchester, UK, pp. 170-171.*

Barringer, M. H. & Springer, K. D. (1999). Radio Wave Propagation, *National Association of Broadcasters Engineering Handbook, 9th edition. Retrieved online from http://maisonthenezay.fr/Maintenance_HF/NAB.html on 2nd April, 2014*.

Collin R. E. (1985). Antennas and Radiowave Propagation. *McGraw-Hill international editions, Electrical Engineering series, Singapore, pp. 339, 402, 409.*

Freeman R. L. (1997). Radio System Design for Telecommunications. *2nd Edition, John Wiley & Sons Inc.*

Hall, M. P. M. & Barclay, L. W. (1991). Radiowave Propagation. *Peter Peregrinus Ltd., England, ISBN 0 86341 156 8, pp. 8, 75, 114, 173, 177.*

ITU-R. (2009). Method for point-to-area predictions for terrestrial services in the frequency range 30 MHz to 3000 MHz. *Recommendation P.1546-4, ITU-R P Sers., Int. Telecomm, Union, Geneva.*.

ITU-R. (2012). Propagation by Diffraction. *Recommendation P.526-12, ITU-R P Sers., Int. Telecomm, Union, Geneva.*

Middleton, J. (2003). The Propagation aspects of Broadcasting at VHF and UHF. *Propagation of Radiowaves, 2nd ed., The Institute of Electrical Engineers, London, UK, 2003, pp 253-255.*

Paris, D. T. & Hurd, F. K. (1969). Basic Electromagnetic Theory. *McGraw Hill, New York ISBN -0 048470-8.*

Prasad, M. V. S. N., Rao, R. T., Ahmad I., & Paul K.M. (2006). Investigation of VHF signals in bands I and II in southern India and model comparisons. *Indian Journ. of Radio and Space Physics, vol. 35, pp. 198-205.*

Roda, G. (1988). Troposcatter Radio Links. *Artech House Inc., Chapter 1,3,4 and 6.*

PROSPECTS AND CHALLENGES OF METAL CASTING TOWARDS ECONOMIC DEVELOPMENT IN NIGER STATE

Mohammed A. S. [1*]Nasiru A. G.[2]Attahiru I.[3]James B. M.[4]
[1,2,3]Science Equipment and Development Institute, Minna, Niger State, Nigeria
[4]Department of Mechanical Engineering, Federal Polytechnic Bida, Niger State, Nigeria
*abdulshab@yahoo.com **GSM:** +2348035864119.

Abstract
This study investigated the prospects and challenges in metal casting towards economic development in Niger State. The study was a survey research in which data was collected with the use of a 31 items questionnaire on a population of 120 respondents purposively sampled from Minna, Bida, Suleja and Kontagora which forms the four major towns in Niger State. The questionnaire was validated and pilot tested to establish a reliability index of 0.91 using Cronbach Alpha statistics. The research questions were answered using mean and standard Deviation on a 5-point scale and z-test used to test the hypotheses at 0.05 alpha level. Findings of the study revealed among others that the prospects of metal casting in the economic development of Niger State are numerous and ranges from creation of employment opportunity, production of domestic items, industrial items, automotive spare parts as well as wealth creation. It was also discovered that numerous challenges also hinders full utilization of the numerous prospects in Metal casting. The study recommended among others: that there should be regular review of the curriculum to capture current trends in foundry technology especially metal casting; extensive awareness should be created on the importance of metal casting occupation to economic development; strengthening collaborative effort and school-industry partnership to enhance funding and supply of adequate training facilities to foundry workshops in institutions and training centers to enhance effective teaching of metal casting skills.

Keyword: Metal casting, Economic development, prospect, challenges.

Introduction

Economic development is a term that economists, politicians, and others have used frequently since the 20th Century. The concept, however, has been in existence in West Africa for centuries. According to Michael (2015), economic development refers to economic growth accompanied by changes in output distribution and economic structure. Economic development is concerned with quality improvements, the introduction of new goods and services, risk mitigation and the dynamics of innovation and entrepreneurship (Ohimain, 2013). Economic development is the development of economic wealth of countries, regions or communities for the well-being of their inhabitants. From a policy perspective, economic development can be defined as efforts that seek to improve the economic well-being and quality of life for a community by creating and/or retaining jobs and supporting or growing incomes and the tax base (Salmon, 2016). Economic development typically refers to improvements in a variety of indicators such as literacy rates, life expectancy and poverty rates. Economic development has direct relationship with the economic growth. While economic development is a policy intervention endeavour which aimed at economic and social well-being of people, economic growth is a phenomenon of market productivity and rise in Gross Domestic Product (GDP). GDP is a specific measure of economic welfare that does not take into account important aspects such as leisure time, environmental quality, freedom, or social justice. Economic growth of any specific measure is not a sufficient definition of economic development. Consequently, as Collier, Soludo and Pattillo (2008) point out, economic growth is one aspect of the process of economic development. This is because economic growth is specific to

GDP level while economic development is broader than GDP, as it encompasses other issues that borders on total wellbeing of citizens of a country.

Economic development typically involves improvements in a variety of indicators such as literacy rates, life expectancy, and poverty rates. Due to the fact that GDP alone does not take into account other aspects such as leisure time, environmental quality, freedom, or social justice; alternative measures of economic well-being have been proposed. Essentially, a country's economic development is related to its human development, which encompasses, among other things, health and education. The Nigerian economy has grossly underperformed relative to her enormous resource endowment and her peer nations. It has the 6th largest gas reserves and the 8th largest crude oil reserves in the world. It is endowed in commercial quantities with about 37 solid mineral types and has a population of over 170 million people. Yet economic performance has been rather weak and does not reflect these endowments. Compared with the emerging Asian countries, notably, Thailand, Malaysia , China, India and Indonesia that were far behind Nigeria in terms of GDP per capita in 1970s, these countries have transformed their economies and are not only miles ahead of Nigeria, but are also major players on the global economic arena through industrial activities. Nigeria's economic position in recent times has been challenges and struggle for survival. The sudden fall in government revenue and subsequent drift into economic recession is a serious concern to all. This has inspired an aggressive discourse on economic diversification to attain sustainable improved economic base in Niger State through metal casting which is an aspect of Foundry technology. Foundry according to Beeley (2001), is a factory where molten metal is poured into moulds to make desired objects of various shapes. It can also be referred to as a place equipped for carrying out metal casting. Casting is a manufacturing process that involves pouring a liquid content into a hollow mould until the content cools and solidifies to form the desired shape (Kumar, 2008). Therefore metal casting is a manufacturing process in which hot liquid metal is poured or forced into a mould after which the liquid metal cools and solidifies to form a piece of metallic object. The small scale foundries through metal casting, cast products such as corn mill plates, cooking pots, automotive parts, manhole covers, and construction equipment items among others. The products are sold both locally and internationally and serve as profitability ventures, important job creation avenues, and major contributor to the nation's economy. According to the National Board for Technical Education (NBTE, 2001), Metal casting is an aspect of Foundry Technology offered as a core course in Mechanical Engineering in tertiary institutions in Nigeria. Below is a typical founry process flow chart of foundry activities in a foundry shop or industry.

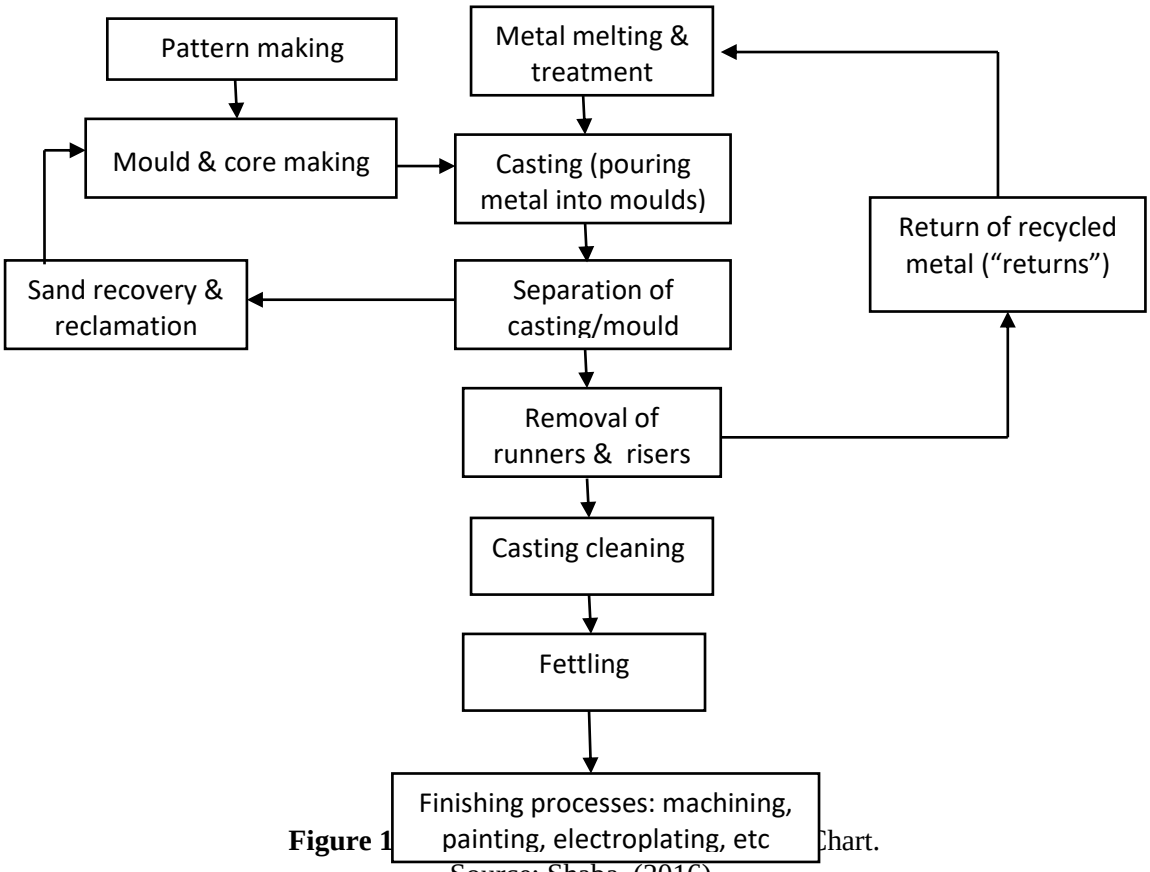

Figure 1 Chart.
Source: Shaba, (2016).

The foundry process leads to production of domestic household utensils and other products as well as industrial products like spare parts for automobiles and other machineries and equipment. Metal casting is an important arm of technological development and the role it can play in the economic development of Niger State due to its high prospects cannot be over- emphasized. Metal casting operations have the potentials for jobs creation for entrepreneurs, reduction in high rate of unemployment and economic empowerment for the state through increased commercial activities, taxation, among others. Studies have shown that, metal casting is the bedrock of world industrialization. It was also unveiled that the world economy rested on the stability of metal casting which is a major activity in foundry technology and steel industries, and is a major feeder to the industrial sectors of the world economy (Alfa , 2013).

Certain economic advantages are inherent in the metal casting process. These often form the basis for choosing metal casting over other shaping processes, such as machining, forging, stamping, rolling and extruding (Collier, Soludo & Pattillo, 2008). There are many advantages associated with metal casting that increases its prospects and chances of economic development. This include the possibility to produce intricate shapes where machining, forging and fabrication operation processes are minimized, possibility to cast both ferrous and non-ferrous materials, tools required are very simple, inexpensive and locally available for the small scale enterprise. Size and weight of any product is never a limitation for the casting process and also, certain parts, e.g. turbine blades, can only be produced through casting process (Ola, Usman., Odunaike, Kollere, Ajiboye & Adeleke (2009),

While setting up of bigger foundries is desirable in view of various technological and cost factors, the small-scale foundry units in Niger State also have several economic advantages, social benefits and prospects. Notably are the following: comparatively less capital investment (as sophisticated infrastructures are not mandatorily required for starting); quicker turnover; utilization of local raw-materials; meeting local demands; more effective management control; easier modification for alternative products in case of change in demand; as well as facilitates the development of indigenous technology (Mohammed & Yusuf, 2004).

The small jobbing foundry shop can be found, scattered all over the country. The purpose of a small-scale foundry is to provide basic services to industry and agriculture, or any sector of the economy that requires small quantities of high quality castings and very rapidly. The small-scale foundry can also substitute locally produced goods for imported ones, thereby saving some foreign exchange. The existence of a small-scale foundry will also permit the direct substitution of imported castings products or equipment. Small-scale foundries promote the establishment of other metal-forming or metal working activities.

Collectively, the small-scale foundry industry that carry out metal casting greatly helps in the creation of an industrial atmosphere, promotes industrialization; technological self-reliance; stimulation of indigenous entrepreneurship; transformation of traditional industry; creation of employment; dispersal of industry; economic diversification as well as utilization of resources (Ohimain & Jenakumo, 2013).

Despite the numerous prospects in metal casting to economic development, Niger State government has not paid special attention to this industry and as a result, the industry is faced with many challenges. They

include quality of cast products as compared to their foreign counterparts, lack of proper quality control procedures resulting in lots of reworks during the manufacturing processes of the various components produced and improper foundry waste management among others. These include quality issues due to lack of technical know-how, access to funding from both government and private financial institutions. Therefore these challenges need to be surmounted if the prospects are to be substantially exploited in order to achieve economic development in this sector. Hence this study investigated the prospects and challenges of metal casting towards economic development in Niger State.

Purpose of the Study

The general purpose of the study was to investigate the prospects and challenges in metal casting towards economic development in Niger State. The study specifically:

1. Determine the prospects of metal casting in the economic development of Niger State.
2. Determine the challenges in metal casting in Niger State.

Research Questions

The following research questions were formulated to guide this study:

1. What are the prospects of metal casting in the economic development of Niger State?
2. What are the challenges in metal casting in Niger State?

Hypotheses

The null hypotheses below tested at 0.05 level of significance guided the study:

H_{01}: There is no significant difference between the mean responses of highly experienced and less experienced metal casting workers on the prospects of metal casting in the economic development of Niger State.

H_{02}: There is no significant difference between the mean responses of highly experienced and less experienced metal casting workers on the challenges in metal casting in Niger State.

Methodology

The study adopted descriptive survey research design to investigate the prospects and challenges in metal casting towards economic development in Niger State. Descriptive survey research design was chosen because it is effective in seeking peoples view about a particular issue that concerns them through the use of questionnaire (Uzoagulu, 2011). Descriptive survey design was therefore considered suitable since the study sought information from a sample that was drawn from a population using questionnaire. A purposive sampling technique was used to select the study areas which are: Minna, Bida, Suleja and Kontagora which forms the four major towns in Niger State. The total population used for the study was 120 purposively sampled respondents comprising of 80 highly experienced metal casting workers and 40 less experienced metal casting workers evenly selected across the study area.

A 31 item questionnaire structured on a 5-point rating scale response option was used to collect data from the respondents. The questionnaire was structured to indicate the degree to which respondents agree to each item as Strongly Agree (SA), Agree (A), Strongly Disagree (SD), Disagree (D) and Undecided(UD).The response category was assigned numerical values as 5,4,3,,2,1.The questionnaire was validated by three

lecturers; two selected from Federal University of Technology, Minna and one from Federal Polytechnic, Bida. Corrections were made appropriately before it was administered. The validated instrument was pilot tested at Kaduna State and the reliability index of 0.91 was established using Cronbach Alpha statistics. The Mean and Standard Deviation (SD) were used to answer the research questions while z-test statistics was used to test the hypotheses at 0.05 level of significance. Decision on the hypotheses was based on comparing p-value with alpha level (0.05). For the purpose of decision making on the items, the researchers used a cutoff point of real limit of numbers applicable to the five point rating scale as : Strongly Agree (4.50-5.00), Agree (3.50-4.49), Strongly Disagree (2.50-3.49), Disagree (1.50-2.49) and Undecided (0.50-1.49).

Results

Research Question 1

What are the prospects of metal casting in the economic development of Niger State?

Table 1: Mean Responses and Standard Deviation of the Respondents on the prospects of metal casting in the economic development of Niger State.
N1=80,N2=40,Total N=120

S/N	Items	$\bar{x}_1$	$\bar{x}_2$	$\bar{x}_A$	SD_1	SD_2	SD_A	Decision
1	Casting of domestic items like cooking pots, spoons etc can contribute to economic development of the State.	4.51	4.62	4.57	.94	.84	0.89	SA
2	Metal casting is necessary in developing small and medium enterprises (SMEs)	4.65	4.71	4.68	.76	1.10	0.93	SA
3	Metal casting processes e.g pottery, blacksmith, metal sand casting, etc are lucrative and therefore, its potentials ought to be exploited.	4.35	3.97	4.16	.81	1.14	0.98	A
4	Welding/Fabrication processes of production is popular than metal casting because it is easier to establish but metal casting is more viable economically.	3.95	4.10	4.03	.77	.75	0.76	A
5	There are other options of manufacturing metal products in the State that are easier to set up but not necessarily enough to develop the economy of the State more than metal casting.	4.35	4.37	4.36	.81	.78	0.80	A
6	The practical lessons in the institutions offering metal casting courses can increase the number of technicians and craftsmen in metal casting thereby, improve on the economy in the state.	4.83	4.52	4.69	.94	.90	0.92	SA
7	There are many products that can be produced with minimal capital from metal casting operations for our local consumptions/uses.	4.03	3.91	3.97	.76	.78	0.77	A
8	Metal casting foundries could improve economic growth at the grassroot levels.	4.23	4.25	4.24	.69	.67	0.68	A

9	Employment opportunities to the teeming youth could be realized through effective metal casting operations.	4.20	3.98	4.09	1.01	1.01	0.89	A
10	Export of metal casting products to neighbouring African countries could boost the economy of the State.	4.20	4.26	4.23	.71	.68	0.70	A
11	Formal exhibitions at Trade Fairs of metal casting products may encourage the public to engage in the trade which can increase empowerment of the individuals and government.	4.16	4.30	4.23	.94	.72	0.83	A
12	Metal casting has the ability to cast spare parts for our automobiles' maintenance.	4.03	4.10	4.07	.76	.75	0.76	A
13	Locally produced metal cast products are cheaper and therefore, more affordable to the less privileged.	4.66	4.59	4.63	.81	.78	0.80	SA
14	Metal casting process has wider range of producing products with limitless shapes, sizes and weights.	3.95	4.05	4.00	.77	.86	0.82	A
15	All types of metals (non-ferrous, ferrous and alloys) can be cast according to desires and functions.	4.35	3.90	4.13	.81	1.24	0.93	A

Key: N1=Number of Highly Experienced Metal Casting Workers (HEMCW), N2= Number of Less Experienced Metal Casting Workers (LEMCW), $\bar{x}_1$= Mean of HEMCW, $\bar{x}_2$=Mean of LEMCW, $\bar{x}_A$ =Average mean of both groups, SA=Strongly Agreed, A=Agreed.

Table 1 reveals that the prospects items with average mean scores between 4.51- 4.83 are Strongly Agreed to by both group of respondents while the prospects with average mean scores between 3.97- 4.36 are Agreed to by both group of respondents. This implies that the highly experienced and less experienced metal casting workers agreed to the items as possible prospects of metal casting in the economic development of Niger State. The standard deviation of the items ranged from 0.68-0.98. This implies that the respondents were not far from the mean and did not differ much from each other in their responses.

Research Question 2

What are the challenges in metal casting in Niger State?

Table 2: Mean Responses and Standard Deviation of the Respondents on the challenges in metal casting in Niger State.
N1=80,N2=40,Total N=120

S/N	Items	$\bar{x}_1$	$\bar{x}_2$	$\bar{x}_A$	SD_1	SD_2	SD_A	Decision
1	Metal casting is very expensive for the poor man to engage in as a business enterprise.	3.11	2.52	2.82	1.01	.83	0.92	SD

2	There has been very low awareness of the economic importance in metal casting in Niger State by the public/government.	3.90	3.55	3.73	.71	.68	0.70	A
3	Metal casting is cumbersome in nature and therefore, many graduates in Foundry Technology do not have interest to engage in it.	3.08	2.67	2.88	.69	.67	0.68	SD
4	Products from metal casting are very crude and not beautiful/ attractive to the public due to lack of modern finishing facilities.	3.96	4.23	4.10	.78	.68	0.73	A
5	People in Niger State are not business oriented and need to be sensitized on metal casting and its prospects.	4.21	4.49	4.35	1.00	.54	0.77	A
6	Government is paying less attention to metal casting in Niger State as a sector which can improve her economic development.	4.35	4.00	4.18	.64	.75	0.70	A
7	Low level of technical education and high level of illiteracy among metal casting workers in Niger State.	3.93	4.32	4.13	.92	.63	0.78	A
8	The state government inconsistent economic development policy do not favour metal casting as a profession.	3.98	4.06	4.02	.96	.75	0.86	A
9	The traditional practice of metal casting in the State is not recognized as a means of contributing to the economic growth of the State.	4.02	4.03	4.03	1.05	.76	0.91	A
10	Metal casting is viewed by the public as a dirty man profession.	4.41	4.03	4.22	.59	.74	0.67	A
11	Unequal availability of raw materials and power supply necessary for the effective metal casting operations is inadequate..	4.15	4.17	4.16	.95	.90	0.93	A
12	The present high exchange rate of dollar is having negative impact on the metal casting operations since interested prospective entrepreneurs cannot import the necessary machines/equipment.	4.22	4.17	4.20	.69	.99	0.84	A
13	Products of metal casting operations do not meet the international standard and therefore, are not patronized in high percentage to increase the economy.	2.98	3.13	3.06	.81	1.02	0.92	SD
14	Lack of feasibility survey in the area of prospects that abound in metal casting may constitute a major hindrance to the growth of economic development in the state.	3.25	2.88	3.07	.88	.84	0.86	SD
15	Metal casting operations are mainly carried out in the urban settlements and needs to spread to rural communities.	3.88	3.98	3.93	.81	.78	0.80	A
16	Inadequate funding leading to non-availability of modern foundry shops in	4.32	3.62	3.97	.67	1.08	0.88	A

	our schools/training centres constitutes major set-back in the establishment of metal casting enterprises in the State.

Key: SD=Strongly Disgreed, A=Agreed.

Table 2 reveals that the items on challenges with average mean scores between 2.82- 3.07 are Strongly Disagreed to by both group of respondents while the challenges with average mean scores between 3.97- 4.35 are Agreed to by both group of respondents. This implies that the highly experienced and less experienced metal casting workers strongly disagreed to item 1, 3, 13 and 14 as challenges in metal casting in Niger State. The remaining items with mean scores ranging from 3.73 to 4.35 were Agreed to as challenges of metal casting in the economic development of Niger State. The standard deviation of the items ranged from 0.68-0.98. This implies that the respondents were not far from the mean and did not differ much from each other in their responses.

Hypotheses Testing

Hypothesis 1: There is no significant difference between the mean responses of highly experienced and less experienced metal casting workers on the prospects of metal casting in the economic development of Niger State.

Table 3: Z-test analysis of the mean ratings of highly experienced and less experienced metal casting workers on the prospects of metal casting in the economic development of Niger State.

Group	N	$\bar{x}$	SD	Df	z-value	p-value, Sig. (2-tailed)	Alpha Level	Decision
HEMCW	80	4.17	0.84	118	2.240	0.251	0.05	Upheld
LEMCW	40	4.10	0.91					

*Significant at p≤0.05.

Key: p-value=probability value calculated by the computer.

Table 3 shows the p-value, Sig. (2-tailed) (0.251) is higher than 0.05, which implies that there is no significant difference in the mean responses of the respondents. Therefore the null hypothesis regarding the prospects of metal casting in the economic development of Niger State is upheld.

Hypothesis 2: There is no significant difference between the mean responses of highly experienced and less experienced metal casting workers on the challenges in metal casting in Niger State.

Table 4: : Z-test analysis of the mean ratings of highly experienced and less experienced metal casting workers on the challenges in metal casting in Niger State.

Group	N	$\bar{x}$	SD	Df	z-value	p-value, Sig. (2-tailed)	Alpha Level	Decision
HEMCW	80	4.13	0.916	118	2.427	0.151	0.05	Upheld
LEMCW	40	4.06	0.922					

*Significant at p≤0.05.

Table 4 shows the p-value, Sig. (2-tailed) (0.151) is higher than 0.05, which implies that there is no significant difference in the mean responses of the respondents. Therefore the null hypothesis regarding the challenges in metal casting in Niger State is upheld.

Summary of Findings of the Study

Based on the data collected and analyzed, the following findings were made:

1. The prospects of metal casting in the economic development of Niger State are numerous and ranges from creating employment opportunity, avenue for income generation, production of home items for domestic uses, avenue for manufacturing automotive spare parts and metal products, source of small and medium scale enterprises among others.
2. Several challenges confront metal casting in Niger State which include : low awareness on the economic importance of metal casting, crude nature of metal casting activity, negligence of government to foundry craft practice at small scale production, high exchange rate, uneven availability of raw materials, erratic power supply, non availability of standard equipment for large scale metal casting operations, low level of technical education and high level of illiteracy among metal casting workers in Niger State among others.
3. There is no significant difference in the mean responses of highly experienced and less experienced metal casting workers on the prospects of metal casting in the economic development of Niger State.
4. There is no significant difference in the mean responses of highly experienced and less experienced metal casting workers on the challenges in metal casting in Niger State.

Discussion

Concerning the prospects of metal casting in the economic development of Niger State, Table 1 reveals that the prospects items with average mean scores between 4.51- 4.83 are Strongly Agreed to by both groups of respondents while the prospects with average mean scores between 3.97- 4.36 are Agreed to by both groups of respondents. The findings from analysis of research question one shows that the prospects of metal casting in the economic development of Niger State are numerous and ranges from creating employment opportunity, avenue for income generation, production of home items for domestic uses, avenue for manufacturing automotive spare parts and metal products, source of small and medium scale enterprises among others. This implies that the highly experienced and less experienced metal casting workers agreed to the items as possible prospects of metal casting in the economic development of Niger State. The standard deviation of the items ranged from 0.68-0.98. This implies that the respondents were not far from the mean and did not differ much from each other in their responses.

With regard to the numerous prospects in metal casting to economic development, Yakubu (2014) in a similar study found out that Small Scale Foundries (SSFs) have been in existence for several years in Niger State. The SSFs or small scale industry has created several jobs for the people of Niger State and to some extent has minimized the burden on government to find ways of disposing scrap metals generated within the country. Anyakwo and Obot (2011) in a similar study found out that the industry has assisted greatly in recycling of scrap metals. While scrap metals are still being exported, the quantity exported has decreased as a result of recycling by foundry men in producing various parts. However, Niger State government has not paid special attention to this industry. Nevertheless, Mohammed (2008) found out that individuals and private investors are heavily involved in producing several thousands of tonnes of castings, annually generating revenue for the government through taxation as well as helping with metal waste disposal.

The small scale foundries through metal casting, cast products such as corn mill plates, cooking pots, automotive parts, manhole covers, and construction equipment items among others. The products are sold both locally and internationally to neighbouring countries. It goes without saying that SSFs in Niger state serve as the threshold of industrial development. SSFs are profitability ventures, important job creation avenues, and major contributor to the nation's economy. However, the industry is faced with many challenges. They include quality of cast products as compared to their foreign counterparts, lack of proper quality control procedures resulting in lots of reworks during the manufacturing processes of the various components produced and improper foundry waste management among others. These include quality issues due to lack of technical know-how, access to funding from both government and private financial institutions and foundry waste management.

With regards to the challenges in metal casting in Niger State, Table 2 reveals that the items on challenges with average mean scores between 2.82- 3.07 are Strongly Disagreed to by both groups of respondents while the challenges with average mean scores between 3.97- 4.35 are Agreed to by both groups of respondents. The result revealed that, several challenges confront metal casting in Niger State and include : low awareness on the economic importance of metal casting, crude nature of metal casting activity, negligence of government to foundry craft practice at small scale production, high exchange rate, uneven availability of raw materials, erratic power supply, non availability of standard equipment for large scale metal casting operations, low level of technical education and high level of illiteracy among metal casting workers in Niger State among others. There is also a serious challenge of inadequate funding leading to non-availability of modern foundry shops in our schools/training centres which constitutes major set-back in the establishment of metal casting enterprises in the State. The standard deviation of the items ranged from 0.68-0.98. This implies that the respondents were not far from the mean and did not differ much from each other in their responses.

The strong disagreement of highly experienced and less experienced metal casting workers to item 1, 3, 13 and 14 as challenges in metal casting in Niger State could be due to the fact that those assumed challenges do not currently affect the metal casting activities in the state. This could be attributed to the fact put forward by Ola et al (2009) who stated that the metal casting operations are not complicated, tools required for small scale metal casting shop are very simple, inexpensive and locally available for the small scale enterprises. Moreso that most foundry products are consumed in Nigeria and thus, the products are not really confronted with challenges posed by foreign customers. Also observation by the researchers show that metal casting shops are not concentrated only in one area but are scattered across both urban and rural settlements.

To buttress the existence of challenges, Yakubu (2014) in a study on competency in Metalwork technology, lamented on the educational challenges when he found out that in Niger State, most of the foundry units are owned and managed by individual families and over 70% of these metal casting workers or foundry men and women have not acquired adequate technical education needed in understanding new trends in metal casting technology used in foundries. According to the authors, the high level of illiteracy suggests the

difficulties foundry men could face when it comes to adaptation to new trends in the foundry industry. Andrews, Gikunoo, Kyei-Fram, and Sarfo (2012) in a study on source of fuel for foundry men found out that some metal casting workers are aware of the new trends in technology. However, they are constrained by lack of technical know-how and funding opportunities. This translates to defects in cast products such as misruns, cold shots, blowholes and rough finishing. Similarly Ohimain (2013) in a study on the challenges to domestic iron and steel production in Nigeria found out that the low educational level of metal casting workers has consequential effect on them which led to poor accounting skills as well as poor book keeping skills. Ohimain narrated that with no accounting skills, foundry men also lack proper bookkeeping and hence financial management is a major concern. Lack of proper bookkeeping also hinders their chances of getting financial support from private financial institutions.

Another major challenge is the uneven availability of raw materials, erratic power supply, non availability of standard equipment for large scale metal casting operations in Niger state. In line with this, Mohammed (2008) in a study on iron and steel production found that almost all the raw materials used by foundry men are obtained locally. For ferrous castings, the materials range from discarded vehicle engine blocks, rims of trucks, shafts, cast-iron corn mill plates and general cast iron products. For non ferrous castings, sources of raw material include copper products and aluminium scraps from aluminium dealers. Most times metal scrap dealers prefer to export their metal scrap to foreign industries and large scale industries who pays more than what local foundry men are willing to pay for the same quantity. This leads to metal scraps supply shortages to the SSFs affecting smooth operation of foundries. This sometimes lead to shortage in availability of raw materials for metal casting by small scale foundry operators and owners.

Also Adebimpe and Akande (2011) in a study on engineering economy analysis on the production of iron ore found that most local small scale foundries do not have documented process to evaluate, review and select suppliers for their raw materials. This affects reproducibility of products since chemical composition of the melt would differ from one charge to another. The authors added that metal scraps supplied are left in an open space and are not labelled and could cause a problem of charging ferrous and nonferrous metal scraps into copula furnace, if careful monitoring system is not put in place. Metal scraps are sorted based on experience by foundry men and are quantified by visual inspection when charging into the copula furnace. Another major challenge found out by Ohimain and Jenakumo (2013) is the access to quality foundry coke. Coke is used by foundrymen as a source of fuel in the melting of metal scraps in copula furnaces. Several towns in Minna does not have coal deposits and therefore does not mine coal. Importation of foundry coke is one challenging and cost involving option for these small scale foundries in Niger State.

On the hypotheses, the study found out that there was no significant difference in the mean ratings of the responses of the highly experienced and less experienced metal casting workers on the prospects of metal casting in the economic development of Niger State. There was also no significant difference in the mean ratings of the responses of the highly experienced and less experienced metal casting workers on the challenges in metal casting in Niger State. This implies that both highly experienced and less experienced metal casting workers did not differ significantly in their opinion on the prospects of metal casting in the economic

development of Niger State as well as on the challenges in metal casting in Niger State. This implies that even as several prospects abound in metal casting for the economic development of Niger State, there are still challenges acting as impediments towards taking full advantage of metal casting opportunities in Niger State. Therefore the null hypotheses (Ho_1 and Ho_2,) were upheld.

Conclusion

Based on the findings of the study, it is concluded that prospects of metal casting in the economic development of Niger State are numerous and ranges from creating employment opportunity, avenue for income generation, production of home items for domestic uses, avenue for manufacturing automotive spare parts and metal products, source of small and medium scale enterprises among others. This implies that the highly experienced and less experienced metal casting workers agreed to the items as possible prospects of metal casting in the economic development of Niger State. However, the industry is faced with many challenges. They include quality of cast products, low level of education by metal casting workers, lack of proper quality control procedures resulting in lots of reworks during the manufacturing processes of the various components produced and improper foundry waste management among others. These include quality issues due to lack of technical know-how, access to funding from both government and private financial institutions and foundry waste management. Taking advantage of the prospects in metal casting and controlling the challenges will go a long way to enhance economic development and industrialization of Niger State.

Recommendations

The following recommendations were made based on the findings of the study:

1. Niger State Government and the appropriate ministry as well as other stakeholders should collaborate to fund and supply adequate training facilities to foundry workshops in institutions and training centers to enhance effective teaching of metal casting skills.

2. Extensive awareness should be created on the importance of metal casting occupation to economic development of Niger State.

3. Establishing partnership with schools and employers of labour in foundry industries to enhance funding.

4. Periodic training and retraining of metal casting workers, foundry students and prospective investors in foundry trade on the new trends in foundry technology.

5. Organizing workshops, seminars and conferences and free access to virtual library resources should be employed to improve metal casting trade.

6 Developing training curriculum to capture current trends in foundry technology especially metal casting.

References

Adebimpe, R.A. & Akande, J.M. (2011). Engineering economy analysis on the production of iron ore in Nigeria. *Geomaterials Journals*, 1(1), 14 – 20.

Alpha, A.A (2013). Development of self-instructional manual for sand casting technology in the polytechnics in north central states of Nigeria. Unpublished PhD thesis, Department of Industrial Technical Education, Faculty of Vocational and Technical Education, University of Nigeria, Nsukka.

Andrews, A., Gikunoo, E., Kyei-Fram, B.K. & Sarfo, R. (2012). Charaterization of spent prebakedaluminium carbon anode as a source of fuel for foundrymen, *Journal of Emerging Trends in Educational Research and Policy Studies*, 5 (8),153-154..

Anyakwo, C.N. & Obot, O.W. (2011). Laboratory studies on phosphorous removal from Nigerias' Agbaja iron ore by Bacillus subtillis. *Journal of Minerals and Materials Characterization and Engineering*, 10(9), 817 – 825.

Beeley, P.R. (2001). *Foundry Technology*. Oxford: Butterworth-Heinemann.

Collier, P., Soludo, C.C. & Pattillo, C. (2008). *Economic policy options for a prosperous Nigeria*. Palgrave: Macmillian.

Kumar, B. (2008). *Introduction to manufacturing technology*. New Delhi: Goswami publishers.

Michael,K (2015). Economic Development and Growth in Nigeria. Retrieved on 18th February, 2017 from www.economic/dev.com

Mohammed, S.A. (2002). Nigerian steel industry-historical development. Abuja: African Iron and Steel Development Association (AISDA) publication.

Mohammed, S.A. and Yusuf, H. A. (2004). Ajaokuta Steel Company Ltd. African Iron and Steel Development Association conference held in Abuja, Nigeria on 6th April.

Mohammed, S.A. (2008). Privatization of the iron and steel industry in Africa. Paper presented at the 8th International Arab Iron and Steel Conference, held at Doha, Qatar 17th – 19th march.

National Board for Technical Education (NBTE) (2001). *Curriculum and Course Specification for National Diploma in Mechanical Engineering*. Kaduna: NBTE.

Ohimain, E. I. (2013). The challenge of domestic iron and steel production in Nigeria. *Greener Journal of Business and Management Studies*,3 (5), 231-240.

Ohimain, E. I. & Jenakumo, C. B. (2013). Scrap metal recycling and valorization in Bayelsa State, Nigeria. *Journal of Materials Science*, 119(1), 137 - 147.

Ola, S.A., Usman, G.A., Odunaike, A.A., Kollere, S.M., Ajiboye, P.O. & Adeleke, A.O. (2009). Pilot scale froth flotation studies to upgrade Nigerian Itakpe Sinter Grade iron ore to mixres-grade super-concentrate. *Journal of Minerals and Materials Characterization and Engineering*, 8(5), 405 – 416.

Salmon, I. (2016).*What is economic development*. New York: Salmon valley business and innovation center.

Shaba, M.A. (2016). Effect of task instruction sheets on foundry students' achievement, interest and retention in polytechnics of north central, Nigeria. Unpublished PhD thesis, Department of Industrial Technical Education,, Faculty of Vocational and Technical Education, University of Nigeria, Nsukka.

Uzoagulu, A.E. (2011). *Practical guide to writing research project reports in tertiary institutions.* Enugu: John Jacobs Classic Publishers Limited.

Yakubu, B. (2014). The Need for Competency in Metal Work Technology in Nigerian Technical *Journal of Emerging Trends in Educational Research and Policy Studies*, 5 (8),153-154.

RAIN ATTENUATION PREDICTION FOR SATELLITE COMMUNICATION AT Ku-BAND IN NORTH CENTRAL NIGERIA

K. C. Igwe[1*], O. D. Oyedum[1], M.O. Ajewole[2] and A. A. Aibinu[3]

[1]Department of Physics, Federal University of Technology, Minna, Niger State

[2]Department of Physics, Federal University of Technology, Akure, Ondo State

[3]Department of Mechatronics Engineering, Federal University of Technology, Minna, Niger State

[1]*Corresponding author: k.igwe@futminna.edu.ng, +2348036382092

Abstract

Prediction of rain attenuation for earth-space links in North Central Nigeria at Ku band is investigated using five of the best performing rain attenuation models: The ITU-R P.618 model, the Bryant model, the Simple Attenuation Model (SAM), the Garcia-Lopez model and the Svjatogor model. Two elevation angles are considered, 55^o and 23^o. The results obtained showed that the ITU-R, Garcia-Lopez and Bryant models performed best in this region. Also, attenuation ranges from 14 dB to 16 dB at 55^{o}elevation angle while it ranges from 20 dB to 22 dB at 23^o elevation angle at exceedance time percentage of 0.01% in all the stations implying that 99.99% (about 53 minute outage in a year) availability of signal is possible at 55^{o}elevation angle but not at 23^o elevation angle.

Key words: Rain Rate, Rain Attenuation, Ku band, elevation angle

1. Introduction

In the design of satellite-to-earth links operating at frequencies above 10 GHz, atmospheric effects play a major role. This is because raindrops normally absorb and scatter radio waves thereby causing signal attenuation and reduction of the system availability and reliability. The severity of rain impairment increases with frequency and also varies with regional locations (Choi *et al*., 1997). Rain attenuation depends on temperature, terminal velocity, size distribution and shape of the raindrops. Although, attenuation due to rain can be accurately measured by the use of satellite beacon signals and radiometers, since such propagation experiments are carried out only in very few places and for a limited number of frequencies and link geometry in the world, results obtained cannot be directly applied to all locations. Hence, various attenuation models based on empirical facts and the use of available meteorological data have been developed to provide enough inputs for system margin calculations in every region of the world (COST 225, 2002). This implies that accurate prediction of rain-induced attenuation on propagation paths is imperative when planning both microwave and terrestrial line-of-sight system links (Salonen and Poiares-Baptista, 1997).

Rainfall effect is more severe in tropical regions which are characterised by high rainfall intensity and the presence of large raindrops (Ojo *et al*., 2008; Moupfouma and Martin, 1995). High rainfall intensity is difficult to be recorded and measured experimentally, as well as highly variable from year to year. In systems design, it is the highest rainfall rates that are of great interest. Also, short integration time rainfall is the most essential input parameter in the prediction models for rain attenuation (Salonen and Poiares-Baptista, 1997).

Two broad classes of rain attenuation prediction on any microwave link exists: The analytical models which are based on physical laws governing electromagnetic wave propagation, and which attempt to reproduce the actual physical behaviour in the attenuation process; and the empirical models which are based on measurement databases from stations in different climatic zones within a given region. When a physical approach is used, not all the input parameters needed for the analysis are available. Therefore, empirical method is the most used methodology (Crane, 2003; Ramachandran and Kumar, 2005; Dutton, and Dougherty, 1979).

In Nigeria, the Nigerian Communication Satellite (NIGCOMSAT-1R) which was launched in 2011 and other satellite outfits like INTELSAT, EUTELSAT, ASTRA, NSS7 and SIRIUS which are linked to various digital television stations like DStv, HiTv, Multi Tv and MyTv Africa operate on Ku band. Therefore, knowledge of the degree of rain-induced degradation in different locations is very important, so as to guide satellite engineers and scientists on improving the quality of local communication networks (Isikwue *et al*., 2013).

For earth-space link design procedure, the margin for rain-induced attenuation must be estimated. It is therefore very important to calculate cumulative percentage of time yearly when rain attenuation on both the downlink and uplink exceeded 0.1% and 0.01% which correspond to about 9 hours per year and about 1 hour per year respectively (Ojo, 2009).

2. Literature Review

The point rainfall rate (mm/h) which is the main input parameter used for the prediction of rain attenuation is estimated from the mean annual rainfall accumulation by using Chebil's model. This model is expressed as:

$$R_{0.01}(mm/h) = \alpha M^{\beta} \quad (1)$$

where $R_{0.01}$ is the point rain intensity exceeded at time percentage of 0.01%, M is the mean annual accumulation of rain while α and β are regression coefficients given as 12.2903 and 0.2973 respectively. This simple approach by Chebil is more suitable for the estimation of point rainfall rate since it uses average annual rainfall accumulation, especially for the type of data used in this research. This rain rate model has been widely used for the prediction of rainfall intensity all over the world (Ajayi *et al*., 1996; Emiliani *et al*., 2004; Ojo *et al*., 2009; Obiyemi *et al*., 2014).

There are different rain attenuation models employed for the prediction of rain-induced attenuation for Satellite to earth communication. Five amongst the best models are selected and used for the estimation in this work. These are the globally accepted ITU-R P.618 model (ITU-R, 2009), the Bryant model (Bryant *et al.*, 1999), the Simple Attenuation Model (Stutzman and Dishman, 1984)), the Garcia-Lopez model (Garcia-Lopez *et al*., 1988) and the Svjatogor model (COST 225, 2002). Only the ITU-R model is explained in detail here because of space constraint.

The ITU-R P. 618-9 Model

This model uses rain rate at 0.01% probability level for the estimation of attenuation and then applies an adjustment factor for the predicted rain attenuation depth for other probabilities.

The steps required for the analysis are given below:
Step 1: Determine the rain height, H_R as:

$$H_R = h_o + 0.36 \text{ km} \quad (2)$$

where h_o is the 0°C isotherm height above mean sea level of the location

Step 2: Determine the slant path length L_s, below the rain height from:

$$L_S = \frac{H_R - H_S}{Sin\ \theta} \quad (3)$$

where θ is the elevation angle and H_S is the height of the location above sea level.

Step 3: Obtain the horizontal projection, L_G, of the slant path length from:

$$L_G = L_S \text{Cos } \theta \quad (4)$$

Step 4: Obtain the point rainfall rate, $R_{0.01}$ (mm/h) exceeded for 0.01% of an average year from one-minute integration rain rate data for the location

Step 5: Obtain the Specific attenuation, $\gamma_{R0.01}$ (dB/km) for 0.01% of time as given by:

$$\gamma_{R_{0.01}} = k\, R_{0.01}^{\alpha} \quad (5)$$

where parameters k and α are determined as functions of frequency in GHz as given in ITU-R P.838-3 (ITU-R, 2005).

Step 6: Calculate the horizontal reduction factor, $r_{h0.01}$ for 0.01% of time using

$$r_{h0.01} = \frac{1}{1+0.78\sqrt{(\frac{L_{G*}\gamma_{R_{0.01}}}{f})} - 0.38[1-\exp(-2L_G)]} \quad (6)$$

where f is the frequency in GHz

Step 7: Calculate the vertical adjustment factor, $v_{0.01}$ (km):

$$L_R = \frac{L_G r_{0.01}}{\cos\theta}, for \rho > \theta \quad (7a)$$

Otherwise,

$$L_R = \frac{H_R - H_S}{\sin\theta}, for\ \rho \leq \theta \quad (7b)$$

where $$\rho = \tan^{-1}(\frac{H_R - H_S}{L_G r_{h0.01}}) \quad (7c)$$

therefore, $$v_{0.01} = \frac{1}{1+\sqrt{\sin\theta}[31\left(1-\exp\left(-\frac{\theta}{[1+\sigma]}\right)\right)\frac{\sqrt{L_G\,\gamma_{R0.01}}}{f^2} - 0.45]} \quad (7d)$$

where $\sigma = 36 - |\varphi|, for\ |\varphi| < 36°$ or $\sigma = 0, for\ |\varphi| \geq 36°$

φ is the latitude of the station

Step 8: The effective path length $L_{eff}(km)$ through rain is calculated as:

$$L_E = L_R v_{0.01} \quad (8)$$

Step 9: The predicted rain attenuation exceeded for 0.01% of an average year is obtained from:

$$A_{0.01} = \gamma_{R0.01} L_E \quad (9)$$

Step 10: The attenuation for other percentage exceedances are thus obtained using the expression below

$$A_p(dB) = A_{0.01}(\frac{p}{0.01})^{-[0.655+0.033\ln(p)-0.045\ln(A_{0.01})-zsin\theta(1-p)]} \quad (10)$$

where p is the percentage probability of interest, and z is given by

$$if\ p \geq 1\%,\ z = 0 \quad (10a)$$

$$if\ p < 1\%, \quad z = 0 \quad \text{if } |\varphi| \geq 36° \quad (10b)$$

$$z = -0.005(|\varphi| - 36) for\ \theta \geq 25°\ and\ |\varphi| < 36° \quad (10c)$$

$$z = -0.005(|\varphi| - 36) + 1.8 - 4.25sin\theta, for\ \theta < 25°\ and\ |\varphi| < 36°. \quad (10d)$$

3. Methodology

The daily rainfall data used for this research work was acquired from the Nigerian Meteorological Agency (NIMET). The rainfall data was measured for a period of 33 years (January 1983 to December 2015) in the study area. The instrument employed in the data measurement is the Casella tipping bucket rain gauge (Figure 1).

The Casella rain gauge is a reliable transducer designed as a stand-alone sensor for operation within an existing logging system or data acquisition system. The body and funnel are made of aluminium alloy with an accurately machined septum ring at the top giving an aperture of 400 cm^2 and it is about 18 inches in height. Rain collects on one side of the bucket, which then tips when a predetermined volume of water has been collected. The tipping action discharges the collected water and repositions the opposite side of the bucket under the discharge nozzle ready for filling.

Figure 1: The Casella rain gauge

4. Results and Discussion

The rainfall analyses from the long-term daily rainfall data for the North Central States of Nigeria are presented. The data include non-rainy days and rainy days for the period of 33 years (January 1983 to December 2015). Relevant information for the understudied stations is shown in Table 1.

Table 1: Station Characteristics for North Central Region

Station	Latitude (ºN)	Longitude (ºE)	Elevation (m)	Average rainfall per annum (mm)
Minna	9.54	6.54	249	1201
Abuja	9	7.28	334	1457
Markudi	7.7	8.5	142	1179
Lokoja	7.47	6.44	204	1229
Ilorin	8.32	4.34	304	1232
Jos	9.58	8.57	1110	1239
Lafia	8.5	8.47	403	1339

Rainfall rate Analysis

The point rainfall rate, $R_{0.01}$ computed from equation 1 for the North Central region are 103.2 mm/h for Minna, 109.4 mm/h for Abuja, 103.9 mm/h for Lokoja, 102.7 mm/h for Makurdi, 104.2 mm/h for Jos, 104 mm/h for Ilorin and 106.7 mm/h for Lafia.

Rain Attenuation Prediction

The point rainfall rate predictions by Chebil model were used as initial input to predict the cumulative distribution of rain attenuation. The five rain attenuation models already mentioned in section two were used. The cumulative distributions of the rain-induced attenuation obtained at different percentages of time were compared for each of the station. 12.675 GHz, which is the Ku band high power downlink frequency, was used. Two elevation angles were considered, 55° and 23°.

The ITU-R model is the most widely accepted method for the estimation of rain attenuation on satellite communication system all over the world, hence the developed models were compared against it for reliability, especially when measured data are not available (Abayomi and Khamis, 2012). Results from experimental data has shown that the ITU-R rain attenuation prediction model which was derived based on lognormal distribution agrees closely with measured values (Choi *et al*., 1997; Emiliani *et al*, 2004; Mandeep and Allnut, 2007; Panchal and Joshi, 2016). This model uses rain rate at 0.01% probability level for the estimation of attenuation and then applies an adjustment factor for the predicted rain attenuation depth for other probabilities. As a result of this global acceptability of the ITU-R model, comparisons carried out in this work are based on the model.

Tables 2 and 3 give brief descriptions of the topographic and climatic features along with the geometrical parameters relevant to satellite links at Ku frequency band.

Table 2: Topographic, Climatic and Geometric features of Links to Satellites at 55° Elevation Angle and 12.675 GHz

Station	Latitude (ºN)	Longitude (ºE)	Elevation (km)	Rain Height (km)	Slant Path Length, LS (km)	Horizontal Projection, LG (km)	Effective Path Length, LE (km)
Minna	9.54	6.54	0.249	4.79	5.54	3.18	3.01
Abuja	9	7.2	0.334	4.76	5.40	3.10	2.88
Lokoja	7.8	6.73	0.204	4.75	5.55	3.18	3.03
Makurdi	7.7	8.5	0.142	4.76	5.64	3.23	3.07
Jos	9.87	8.9	1.11	4.76	4.45	2.55	2.69
Ilorin	8.48	4.58	0.304	4.78	5.46	3.13	2.99
Lafia	8.5	8.47	0.403	4.77	5.33	3.06	2.91

Table 3: Topographic, Climatic and Geometric features of Links to Satellites at 23° Elevation Angle and 12.675 GHz

Station	Latitude (ºN)	Longitude (ºE)	Elevation (km)	Rain Height (km)	Slant Path Length, LS (km)	Horizontal Projection, LG (km)	Effective Path Length, LE (km)
Minna	9.54	6.54	0.249	4.79	11.61	10.69	4.15
Abuja	9	7.2	0.334	4.76	11.33	10.43	3.98
Lokoja	7.8	6.73	0.204	4.75	11.63	10.71	4.20
Makurdi	7.7	8.5	0.142	4.76	11.82	10.88	4.27
Jos	9.87	8.9	1.11	4.76	9.33	8.59	3.74
Ilorin	8.48	4.58	0.304	4.78	11.46	10.54	4.15
Lafia	8.5	8.47	0.403	4.77	11.18	10.29	4.04

The cumulative distribution of the rain induced attenuation obtained for the Ku-band at 55° elevation angle for the stations using the different models were compared. Figures 2a and 2b show the result of the comparison for each of the stations. The Garcia-Lopez and Bryant models predicted closely with the ITU-R model. The SAM and Svjatogor models did not predict correctly as they recorded lower attenuation values. Attenuation values were virtually the same in all the stations since they are all under the same rain zone (the middle belt region of the country). For instance, the rain attenuation predicted by the ITU-R model for 0.001% unavailability of time which is important for internet multimedia applications is 25 dB for Minna, Abuja, Lokoja, Makurdi, Ilorin and Lafia while it is 23 dB for Jos. At this same percentage of time, Garcia-Lopez model predicted 23 dB for Minna, Lokoja, Makurdi, Ilorin, Jos, Lafia and 24 dB for Abuja while Bryant model predicted 24 dB for Minna, Abuja, Makurdi, 23 dB for Lokoja, Ilorin, Lafia and 20 dB for Jos. At 0.01%, the ITU-R model predicted 16 dB for all the stations except for Jos that had 14 dB. Garcia-Lopez model predicted 15 dB for the other stations and 14 dB for Jos while Bryant model predicted 15 dB for every other station except for Jos that recorded 12 dB. At 0.1% which corresponds to an average-year propagation objective (99.9 availability of time), the rain attenuation exceeded using ITU-R model is 7 dB for Minna, 6 dB for the other stations and 5 dB for Jos. The Garcia-Lopez model at this percentage of time predicted 6 dB for Minna, Makurdi, Jos, Ilorin and 7 dB for Abuja, Lokoja and Lafia. At this same percentage of time, the Bryant model predicted 7 dB for the other stations except for Jos that recorded 5 dB. The prediction from the other two models, the Simple attenuation model and the Svjatogor model were not at all close to the aforementioned predictions. These predictions were far lower as observed from the figures, for instance, the SAM predicted between 5 and 7 dB while the Svjatogor model predicted between 8 and 16 dB for the stations at 0.001%.

Figures 3a and 3b show the cumulative distribution of the rain induced attenuation for Ku-band at elevation angle of 23°. It is observed from these figures that there is significant increase in rain attenuation. This is because of the longer path length of the rain region at this lower elevation angle. Therefore, these high attenuation values imply that satellite links with lower elevation angles will suffer more rain attenuation than the ones with higher elevation angles.

From the results obtained, it can be concluded that the ITU-R, the Garcia-Lopez and the Bryant models can satisfactorily be used to predict rain attenuation in this region of Nigeria. Also, at 55ºelevation angle, attenuation generally ranges from 14 dB to 16 dB while it ranges from 20 dB to 22 dB at 23º elevation angle at time percentage of 0.01% in all the stations. These results reveal that at Ku band, 99.99% (about 53 minute outage in a year) availability of signal is possible at 55ºelevation angle since rain attenuation is less than 20 dB but impossible at 23º elevation angle since attenuation here is ≥ 20 dB. Therefore, there will be signal fade

out at 23º elevation angle during rainfall in all the stations. This deduction is based on the fact that most satellites operating at 10 GHz and above are designed to withstand propagation losses that are ≤ 20 dB on its link because of limited carrier power at the output of the transmission amplifier which is about 150 W and minimal battery power onboard the spacecraft (Ippolito, 1986).

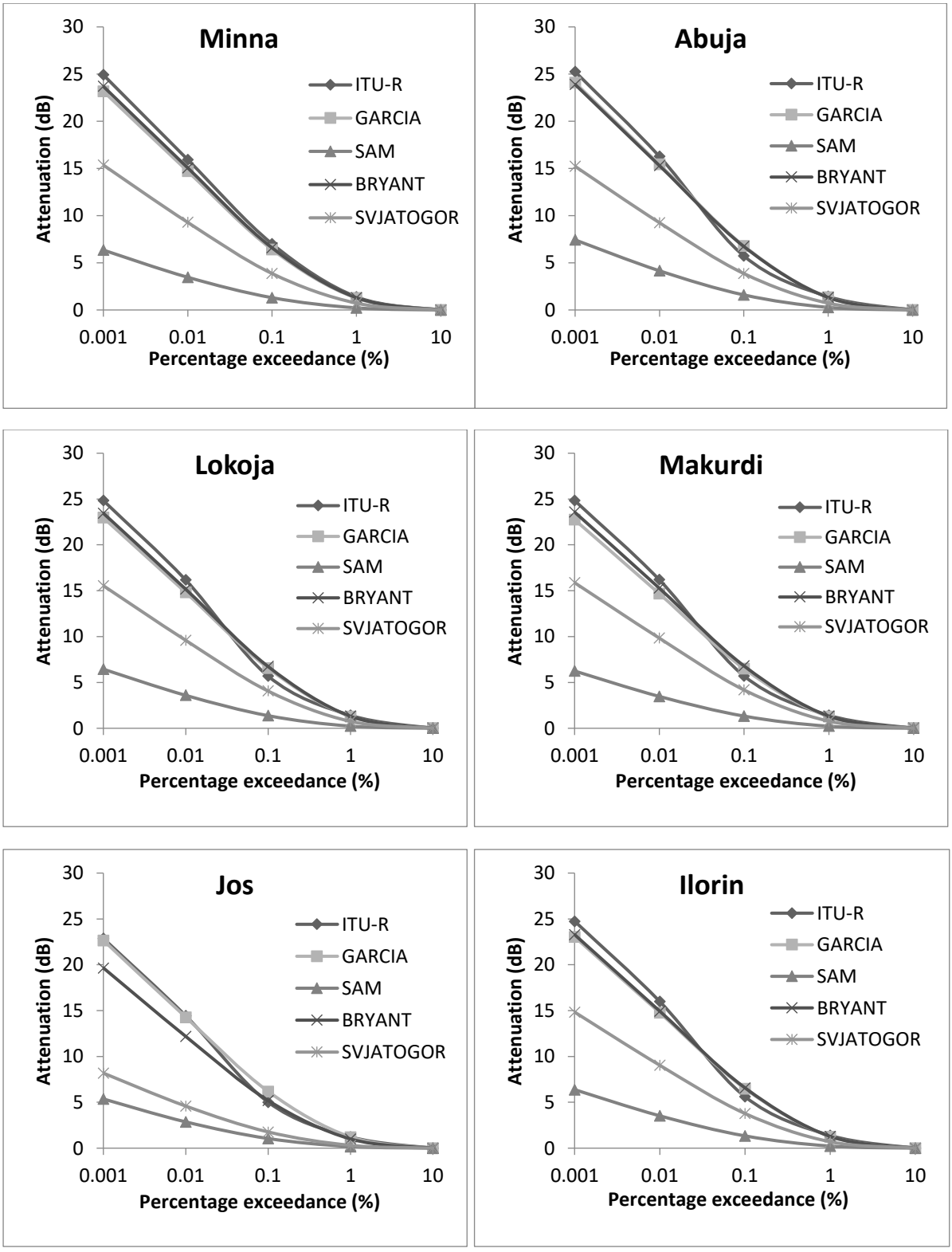

Figure 2a: Comparison of cumulative distribution of rain attenuation models at 55° elevation angle in Minna, Abuja, Lokoja, Makurdi, Jos and Ilorin.

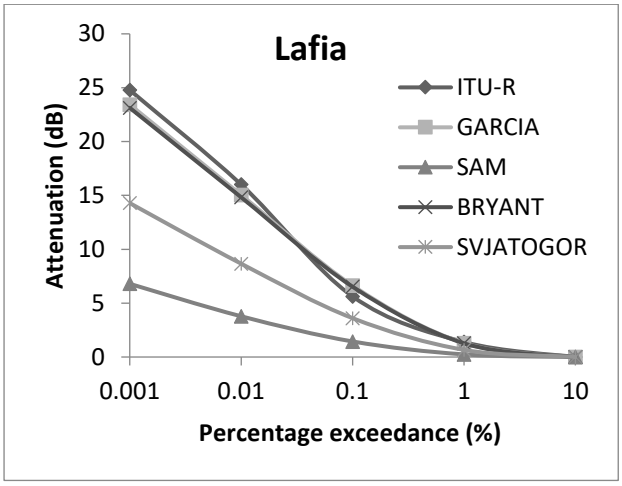

Figure 2b: Comparison of cumulative distribution of rain attenuation models at 55° elevation angle in Lafia

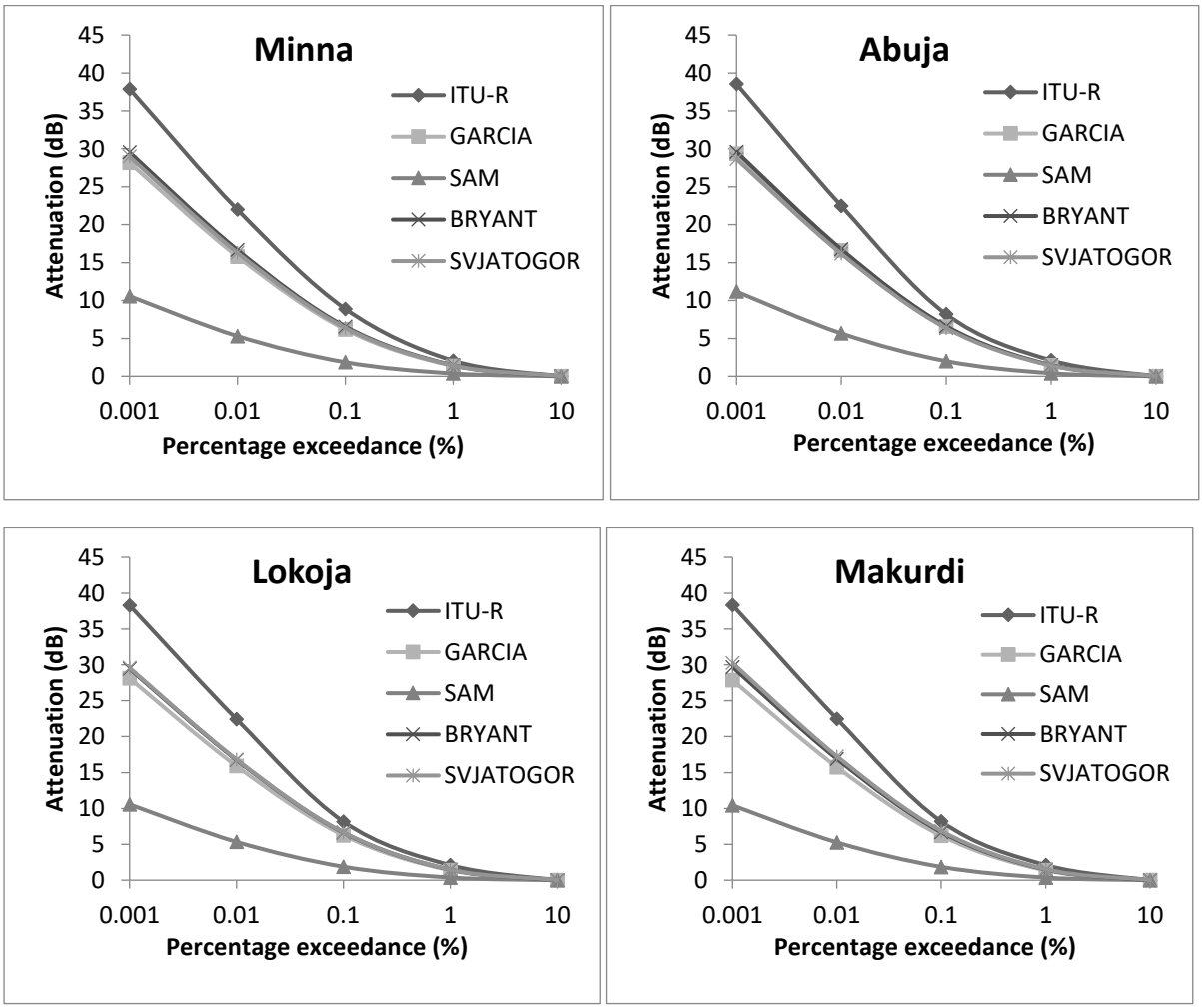

Figure 3a: Comparison of cumulative distribution of rain attenuation models at 23° elevation angle in Minna, Abuja, lokoja and Makurdi.

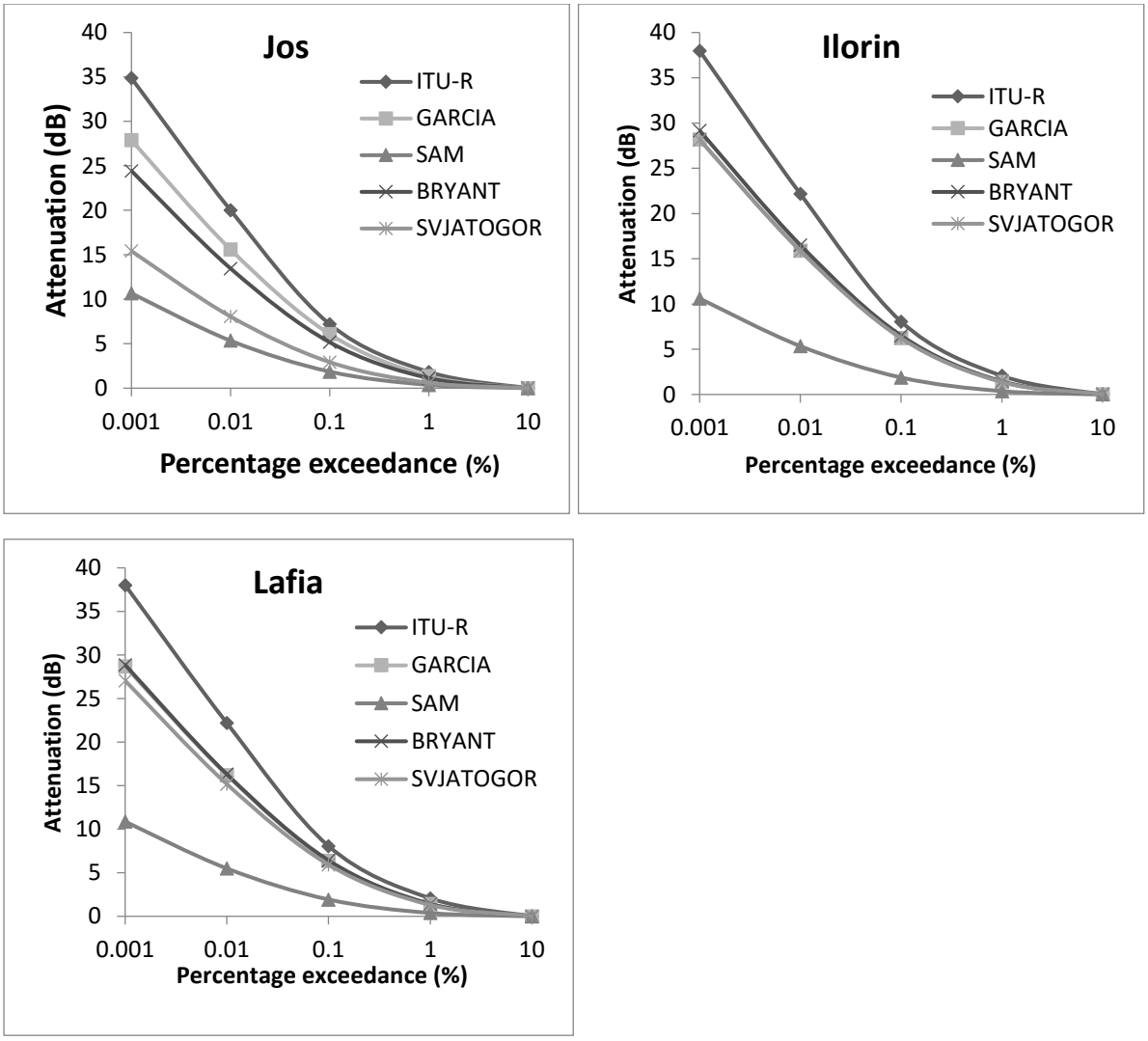

Figure 3b: Comparison of cumulative distribution of rain attenuation models at 23° elevation angle in Jos, Ilorin and Lafia.

5. Conclusion

The prediction of rain attenuation and its effects on satellite communication at Ku band for the North Central region of Nigeria has been investigated for satellite links operating at 55° and 23° elevation angles. This predictions were made using five different rain attenuation models and the results obtained has shown that the ITU model, the Garcia-Lopez model and the Bryant model can satisfactorily be used to predict rain attenuation in this part of Nigeria. From the values of attenuation predicted at time percentage of 0.01% unavailability which is equivalent to 99.99% (about 53 minute outage in a year), availability of signal is possible at 55°elevation angle but impossible at 23° elevation angle thereby implying signal fade out at 23° elevation angle during rainfall in all the stations.

References

Abayomi, Y.I.O. and Khamis N.H.H. (2012). Rain Attenuation Modelling and Mitigation in the Tropics: Brief Review. *International Journal of Electrical and Computer Engineering, vol. 2(6), 748-757.*

Ajayi, G.O., Feng, S., Radicella, S.M. and Reddy, B.M. (1996). Handbook on Radio Propagation Related to Satellite Communication in Tropical and Subtropical Countries. *ICTP, Trieste, Italy, 7-14.*

Bryant G.H., Adimula I., Riva C. and Brussard G. (2001). Rain Attenuation Statistics from Rain Column, Diameters and Heights. *International Journal of Satellite Communications, vol 19, 263-283*

Choi, Y.S., Lee, J.H., and Kim, J.M. (1997). Rain Attenuation Measurements of the KoreaSat Beacon Signal on 12 GHz. *CLIMPARA '98, Ottawa, Canada, 208-211.*

COST 225 (2002). Radiowave Propagation Modelling for SatCom services at Ku-band and above. *Final Report. European Space Agency, the Netherlands, 74, 79, 85-86, 96-97.*

Crane, R. K. (2003). Rain attenuation models: Attenuation by Clouds and Rain. *Propagation Handbook for Wireless Communication System Design, 225-280. CRC Press, USA.*

Dutton, E. J. & Dougherty, H. T. (1979). Year-to-Year Variability of Rainfall for Microwave Applications in the USA. *IEEE Trans. Communication, vol. 28, 829-832.*

Emiliani, L. D., Agudelo, E., Gutierrez, E., Restrepo, J. and Fradique-Mendez, C. (2004). Development of Rain-Attenuation and Rain-Rate Maps for Satellite System Design in the Ku- and Ka-bands in Columbia. *IEEE Antenna and Propag. Mag. vol. 46(6),54-68.*

Garcia-Lopez, J.A., Hernando, J.M. and Selga, J. (1988). Simple Rain Attenuation Method for Satellite Radio Links. Year-to-Year Variability of Rainfall for Microwave Applications in the USA. *IEEE Transactions on Antennas and Propagation, vol. 36(3), 444-448.*

Ippolito, I.J. (1986). Radiowave Propagation in Satellite Communications. *Van Nostrand Reinhold Company Publishers, New York.*

Isikwue, B. C., Ikoyo, A. H. & Utah, E. U. (2013). Analysis of Rainfall Rates and Attenuations for Line-of-sight EHF/SHF Radio Communication Links over Markurdi, Nigeria. *Research Journal of Earth and Planetary Sciences, vol. 3(2), 60-74. Retrieved from http://www.globalresearchjournals.org/journal/rjeps on 23/07/14.*

ITU-R. (2005). Specific Attenuation Model for Rain for use in Prediction Methods *Recommendation P.838-3, ITU-R P Sers., Int. Telecomm, Union, Geneva.*

ITU-R (2007). Propagation Data and Prediction Methods Required for the Design of Earth–Space Telecommunication Systems. *Recommendation P.618-9, ITU-R P Sers., Int.*

Mandeep, J.S. and Allnut, J.E. (2007). Rain Attenuation Predictions at Ku-band in South East Asia Countries. *Progress in Electromagnetics, Res., PIERS, vol. 76, 65-74.*

Moupfouma, F. and Martin, L. (1995). Modelling of the Rainfall Rate Cumulative Distribution for the Design of Satellite and Terrestrial Communication Systems. *International Journal of Satellite Communication, vol. 13(2), 105-115.*

Obiyemi, O.O., Ibiyemi, T.S. and Akande, S.O. (2014). Rainfall Variability and Impact on Communication Infrastructure in Nigeria. *Journal of Telecommunications, vol. 25(1), 6-11.*

Ojo, J. S., Ajewole, M. O. and Sarkar, S. K. (2008). Rain Rate and Rain Attenuation Prediction for Satellite Communication in Ku and Ka Bands over Nigeria. *Progress in Electromagnetics Research B, vol.5, 207-223*

Ojo, J.S. (2009). Distribution of Rainfall Rates of Short Integration Time and Their Applications to Microwave Propagation over Nigeria. *Unpublished Ph.D thesis, Federal University of Technology, Akure, Nigeria, 112.*

Ojo, J.S., Ajewole, M.O. and Emiliani L.D. (2009). One-minute Rain Rate Contour Maps for Microwave-Communication-System Planning in a Tropical Country: Nigeria. *IEEE Antennas and Propagation Magazine, vol. 51, 82-89.*

Panchal, P. and Joshi R. (2016). Performance Analysis and Simulation of Rain Attenuation Models at 12-40 GHz Band for an Earth Space Path over Indian Cities. *7th International Conference on Communication, Computing and Virtualization, ScienceDirect, Elsevier Journals, vol. 79, 801-808.*

Ramachandran, V. and Kumar, V. (2005). Invariance of Accumulation Time Factor of Ku-band Signals in the Tropics. *Journal of Electromagnetic Waves and Applications, vol. 19(11), 1501-1509.*

Salonen, E. T. and Poiares-Baptista, J. P. V. (1997). A new global rainfall rate model. *Proceedings of 10th International Conference on Antenna and Propagation (pub N 14-176-436), pp.182-185.*

Stutzman, W.L. and Dishman, (1984). Correction to a simple Model for the Estimation of Rain-induced Attenuation along Earth-Space paths at Millimeter Wavelengths *Radio Science, vol. 19, 946.*

THE IMPACT OF SYSTEM PERTURBATION ON STABILIZATION OF THE GROWTH OF TWO POLITICL PARTIES

BAZUAYE FRANK ETIN-OSA

DEPARTMENT OF MATHEMATICS AND STATISTICS, UNIVERSITY OF PORTHARCOURT, PORTHARCOURT, RIVERS STATE.

Email: febazuaye@yahoo.com

ABSTRACT

Qualitative characterization of the perturbation of the growth of two political parties which are stochastic in nature requires a strong numerical tool for its analysis. We have therefore in this study utilized MATLAB standard solvers for ordinary differential equations ODE 45, to investigate the impact of system perturbation otherwise called random fluctuation on the stabilization of two interacting political parties in a developing democracy and to evaluate the qualitative characterization of interacting political parties due to 0.01, 0.10, 1.00, 5.00 and 10.00, representing low, average and high random noise system perturbation. The result indicates that as the system perturbation increases, the level of de-stabilization of the entire political system increases.

Keywords: *System perturbation, de-stabilization, political parties, stabilization, qualitative characterization*.

Introduction

Addressing the challenges of de-stabilization, it is important to investigate the impact of system perturbation driving factors such as failure in election, cross carpeting by political gladiators, political instability, can actually affect the potential and motivation of people in the political activities and bring about a non- participatory democracy As it can seen in Huckfeldt and Kohfeld. (1992).Although, we have agreed that in a deterministic sense, the parameterization of Arvind (2012) steady state solution is stable. However, what is the extent of the per capital recruitment rate η_1 of party Q and the per capital recruitment rate η_2 of party R system perturbation has on the stabilization? This is a neglected aspect of modeling two interacting political parties , which remains an open research question since the activities of political parties are dynamical in nature , Arato (2003),.

MATHEMATICAL FORMULATION

Following Arvind (2012), the modeling equation which is a dynamical system,is given by

$$\frac{dP}{dt} = \varphi m - \eta_1 P\frac{Q}{M} - \eta_2 P\frac{R}{M} - \varphi P$$

$$\frac{dQ}{dt} = \eta_1 P\frac{Q}{M} - \gamma_1 Q\frac{R}{M} - \gamma_2 R\frac{Q}{M} - \varphi Q \quad (1)$$

$$\frac{dR}{dt} = \eta_2 P\frac{R}{M} + \gamma_1 Q\frac{R}{M} - \gamma_2 R\frac{Q}{M} - \varphi R$$

With the conditions the initial conditions $P(0) > 0$, $Q(0) \geq 0$, $R(0) \geq 0$.

At the steady state solution $\frac{dM}{dt} = 0$

This is an extended Lotka-Volterra multi-substitution model as in Morris and David (2003).

METHOD OF SOLUTION

The numerical simulation we are proposing for the solution of this complex class of problem (1) is the use of **MATLAB** standard solvers for ordinary differential equations **ODE** 45,to investigate the impact of system perturbation. The philosophy behind this method is to know the impact of varying the level of perturbation on the solution trajectory values.

Following Arvind (2012) and Ekaka-a (2009), we consider the following precise deterministic parameter values;

$$\eta_1 = 0.0417,\ \eta_2 = 0.0278,\ \gamma_1 = 0.0236,\ \gamma_2 = 0.0097,$$

The major method of analysis is based on the implementation of the MATLAB ODE 45 solver scheme which is a Robust Runge-kutta scheme and evaluates the qualitative characterization of interacting political parties due to 0.01, 0.1, 1, 5.0 and 10.0 random noise and observes the qualitative behavior on the solution trajectory.

The full results of applying this method are presented and discussed next.

RESULTS AND DISCUSSION

It can be observed from Table 1 to Table 5 that as the system perturbation increases, the level of de-stabilization of the entire system increases. So, it is cleared from this novel contribution that as the independent variable t tends to infinity, the solution trajectory due to a random system perturbation generally outweighs the solution trajectory without a random system perturbation. On the basis of this systematic analysis, we have observed that a random noise system perturbation has the potential to de-stabilize the deterministic dynamical system that describes the interaction between two political parties in developing democracies like Nigeria.

Table 1: Evaluating the qualitative characterization of interacting political parties due to 0.01 random noise system perturbation using ODE 45

Example	RS	$\eta_1(4)$	$\eta_1 rn$	$\eta_2(4)$	$\eta_2 rn$
1	1	1.43651711325650	1 .0609576567136	1 0.7980529152492	2.48821529715523
2	2	1.43651711325650	1.05790549566056	10.7980529152492	2.48781481084994
3	3	1.43651711325650	1.06625404474447	10.7980529152492	2.49029570275644
4	4	1.43651711325650	1.05680699689741	1 0.7980529152492	2.48828934088830
5	5	1.43651711325650	1.05991760322433	10.7980529152492	2.48305162621826
6	6	1.43651711325650	1.06133475898536	10.7980529152492	2.48289274320012
7	7	1.43651711325650	1.06085914104013	1 0.7980529152492	2.48365162051966
8	8	1.43651711325650	1.06127674399038	10.7980529152492	2.48701821842759
9	9	1.43651711325650	1.05824156275381	10.7980529152492	2.48131002946453
10	10	1.43651711325650	1.05739994984151	10.7980529152492	2.48395500010629

When the value of random noise perturbation is 0.01, the numerical simulation random noise value ranges from the value of 1.05824156275381 to 1.06625404474447 and 2.48131002946453 to 2.49029570275644 for the intrinsic growth rates $\eta_1 rn$ and $\eta_2 rn$ respectively of the interacting two political parties.

Table 2: Evaluating the qualitative characterization of interacting political parties due to 0.1 random noise system perturbation using ODE 45

Example	RS	$\eta_1(4)$	$\eta_1 rn$	$\eta_2(4)$	$\eta_2 rn$
1	1	1.43651711325650	1 .2278527712168	1 0.7980529152492	2.62400631245802
2	2	1.43651711325650	1.17524014827114	10.7980529152492	2.69697672824029
3	3	1.43651711325650	1.25026500565991	10.7980529152492	2.63107198302351
4	4	1.43651711325650	1.22984058004148	1 0.7980529152492	2.69833190689295
5	5	1.43651711325650	1.21890869254285	10.7980529152492	2.65872818385740
6	6	1.43651711325650	1.18967112729009	10.7980529152492	2.67038812676433
7	7	1.43651711325650	1.19737145125192	1 0.7980529152492	2.69471287056911
8	8	1.43651711325650	1.16667083134789	10.7980529152492	2.70316472749864
9	9	1.43651711325650	1.21272231323964	10.7980529152492	2.68372387701938
10	10	1.43651711325650	1.16461465308184	10.7980529152492	2.71849117110819

When the value of random noise perturbation is 0.1, the numerical simulation random noise value ranges from the value of 1.16461465308184 to 1.25026500565991 and 2.62400631245802 to 2.71849117110819 for the intrinsic growth rates $\eta_1 rn$ and $\eta_2 rn$ respectively of the interacting two political parties.

Table 3: Evaluating the qualitative characterization of interacting political parties due to 1.0 random noise system perturbation using ODE45

Example	RS	$\eta_1(4)$	$\eta_1 rn$	$\eta_2(4)$	$\eta_2 rn$
1	1	1.43651711325650	2.5462969084112	1 0.7980529152492	4.48334765667066
2	2	1.43651711325650	2.5374269585154	10.7980529152492	4.41568117876753
3	3	1.43651711325650	2.5802537978094	10.7980529152492	4.59931999407648
4	4	1.43651711325650	2.4309617589688	1 0.7980529152492	4.56505670388324
5	5	1.43651711325650	2.5053024168849	10.7980529152492	4.57407583642139
6	6	1.43651711325650	2.6270813291340	10.7980529152492	4.76683233496164

7	7	1.43651711325650	2.5189851694690	1 0.7980529152492	4.55790894565828
8	8	1.43651711325650	2.5644207874087	10.7980529152492	4.48189851234733
9	9	1.43651711325650	2.3973594428491	10.7980529152492	4.44695160895281
10	10	1.43651711325650	2.5133940503448	10.7980529152492	4.58050523700687

Similarly, when the value of random noise perturbation is 1.0, the numerical simulation

Random noise value ranges from the value of 2.3973594428491 to 2.6270813291340 and 4.41568117876753 to 4.76683233496164 for the intrinsic growth rates $\eta_1 rn$ and $\eta_2 rn$ respectively of the interacting two political parties.

Table 4: Evaluating the qualitative characterization of interacting political parties due to 1.0 random noise system perturbation using ODE45

Example	RS	$\eta_1(4)$	$\eta_1 rn$	$\eta_2(4)$	$\eta_2 rn$
1	1	1.43651711325650	6.3016067016574	10.7980529152492	13.3789554796706
2	2	1.43651711325650	6.378955479670	10.7980529152492	13.2439302145988
3	3	1.43651711325650	6.7633452903934	10.7980529152492	13.4420359648161
4	4	1.43651711325650	6.5814343554167	10.7980529152492	14.2039463727159
5	5	1.43651711325650	6.6064496058526	10.7980529152492	14.3230790042630
6	6	1.43651711325650	6.4026092488267	10.7980529152492	14.6951902151518
7	7	1.43651711325650	6.6843117554080	10.7980529152492	13.0967679462801
8	8	1.43651711325650	6.6336612871534	10.7980529152492	13.1949554862764
9	9	1.43651711325650	6.8926304345713	10.7980529152492	14.1384515328078
10	10	1.43651711325650	6.8509580132006	10.7980529152492	14.2899380729331

When the value of random noise perturbation is 1.0, the numerical simulation

Random noise value ranges from the value of 6.3016067016574 to 6.8926304345713 and 13.1949554862764 to 14.6951902151518 for the intrinsic growth rates $\eta_1 rn$ and $\eta_2 rn$ respectively of the interacting two political parties.

Table 5: Evaluating the qualitative characterization of interacting political parties due to 10.0 random noise system perturbation using ODE45

Example	RS	$\eta_1(4)$	$\eta_1 rn$	$\eta_2(4)$	$\eta_2 rn$
1	1	1.43651711325650	8.8840468198663	10.7980529152492	26.9016524675767
2	2	1.43651711325650	9.3016792483179	10.7980529152492	26.4605476780696
3	3	1.43651711325650	8.8141689814512	10.7980529152492	25.5261725024278
4	4	1.43651711325650	9.9403227931174	10.7980529152492	25.6636555375322
5	5	1.43651711325650	9.5961209073984	10.7980529152492	25.9218805979897
6	6	1.43651711325650	8.9128463048855	10.7980529152492	25.5802604455235
7	7	1.43651711325650	9.2914952824882	10.7980529152492	25.7037420305581
8	8	1.43651711325650	9.3784420158988	10.7980529152492	26.7615214099693
9	9	1.43651711325650	9.3819929912604	10.7980529152492	27.8023554675845
10	10	1.43651711325650	9.8893213894481	10.7980529152492	25.1545358969362

Lastly, when the value of random noise perturbation is 10.0, the numerical simulation Random noise value ranges from the value of 8.8141689814512 to9.9403227931174 and 25.1545358969362 to 27.8023554675845 for the intrinsic growth rates $\eta_1 rn$ and $\eta_2 rn$ respectively of the interacting two political parties.

Conclusion.

This paper has presented a novel contribution to knowledge by successfully utilizing numerical simulation technique to re-enforce the fact that a reduction in the factors that cause the de-stabilization of survival of political parties in a developing democracy, will lead to a robust and growth of parties.

From the analysis carried out, we would recommend a reduction in the factors that brings about fluctuation and cause de-stabilization. For example, lack of internal democracy, fail electoral promises, imposition of candidates, etc can have negative implications in the growth and survival of political parties

In a future analysis, we will like to study the impact of system perturbation on the growth rates, intra-competition coefficient, inter-competition coefficients on each of the political parties and no the entire system as we have proposed in this study.

REFERENCES

1. Arvind K.M (2012). A simple mathematical model for the spread of two political parties. *Journal of Nonlinear analysis modeling and control*. 17(3), 343-354.
2. Arato, M. (2003). A famous nonlinear stochastic equation; Lotka-Volterra model with diffusion. *Journal of Mathematical and computer modeling*. 38(7/9), 709-726.

3 Ekaka-a E.N. (2009). Computational and Mathematical modeling of plant species interactions in a harsh climate. Ph.D Thesis, Department of Mathematics, the University of Liverpool and the University of Chester, United Kingdom.

4 Huckfeldt, C.W, Kohfeld. (1992). Electoral stability and the decline of class in democratic politics. *Journal of Mathematical Computational Modeling*. 16(8-9)223-239

5 Morris, S.A., David Pratt (2003). Analysis of the Lotka –Volterra competition equations as a technological substitution model. *Technological forecasting and change*. 70: 103-133.

COMPUTATIONAL ANALYSIS OF STABILIZATION OF A MATHEMATICAL MODEL OF TWO DOMINANT POLITICAL PARTIES IN A DEVELOPING DEMOCRACY.

[1]BAZUAYE FRANK ETIN-OSA AND [2]BAZUAYE EJIRO PEACE

1. DEPARTMENT OF MATHEMATICS AND STATISTICS, UNIVERSITY OF PORTHARCOURT, PORTHARCOURT, RIVERS STATE.
2. EDO STATE UNUVERSAL BASIC EDUCATION BOARD, BENIN CITY EDO STATE.

Email: febazuaye@yahoo.com

ABSTRACT

This paper focuses on computational analysis of Stabilization of a Mathematical model of two dominant political parties. In contrast to Arvind and Khan, who developed the model without investigating the impact of varying the initial state of political parties on the solution trajectory, we have developed a sound numerical algorithm to analyze the impact of change on the initial data on the behavior of the democratic process which is a rare contribution to knowledge. We have utilized two Matlab standard solvers for ordinary differential equations ODE 45 and ODE 23 to handle these formidable mathematical problems. Our findings indicate that as the initial data varies, the dynamical system describing the interaction between two political parties is stabilized over a period of eight years. As duration increases, the system gets de-stabilized.

Keywords: *dominant political parties, qualitative characterization, stabilization.*

Introduction

The essential components of democracy are competitive elections. It is a process by which people choose an individual or group of persons to hold public office. This process is the normal mechanism by which offices are filled in a democratic society.

The constitution and electoral act of Nigeria (2010), provides the right of individual to vote and be voted for provided he or she reaches the acceptable age. In most democratic societies, the voting system is a single vote which means voter can only vote for one candidate in the particular elective position and the candidate that receives the highest number of *votes* shall be declared *elected* by the electoral body.

It is pertinent to note that due to faulty nature and foundation of the political parties without a clear cut political ideology in these developing democracies like Nigeria, shifting or what is popularly known as " cross carpeting" of individuals from one political party to the other has become a common trend . Khan (2000), conducted a research on the growth of political parties and voters. Calderon etal (2005), worked on the epidemiological approach to the spread of political third parties. However, most of the modeling use statistical approach in the analysis of the rate of shifting of political allegiance. Naresh (2005) considered, using interacting models to model HIV-TB co-infection in a variable size. The non-linear differential equation with time delay was used. However, Huckfeldt and Kohfeld (1992) presented two Mathematical models which are linear and non-linear Mathematical models in line with Morris and David (2003), regarding the stability of the electoral process.

The propose study is concerned with the Numerical simulation of the impart of the perturbation on the growth of two political parties. The idea is to determine the most sensitive parameter for growth in the given model. Certainly, this approach has not been considered anywhere in literature.

Mathematical Model.

Arvind (2012), Poitoriusand Utterback, (1997), consider M total population which is assumed to be constant. M is divided into groups; (i) The electorates P (ii) members of political party Q (iii) Members of political party R. Also, we assumed that individual enters the voting class at the attainment of age 18 years and at the rate of φM where φ is the rate at which individual enter or leave the voting system, with φP , φQ and φR represents those that leave the political system from each class respectively, as a result of incapacitation or death. Also, it is also assumed that each electorate can either join party Q or R on the basis of political interest or any other personal conviction. Let ℓ_1 be the average number of contacts of members of political party Q with electorates per unit time and λ_1 be the probability of convincement per contact on electorate with a member of party Q, while the per capital recruitment rate of party Q is $\eta_1 = \ell_1 \lambda_1$. So, the individual P may decide to join party Q at a rate $\eta_1 (Q/M)$

Similarly, let the per capital recruitment rate η_2 of party R as $\eta_2 = \ell_2 \lambda_2$, where ℓ_2 is the mean number of contacts of members of party R The electorates P may decide to join party R at a rate $\eta_2(R/M)$ In addition, let γ_1 and γ_2 be the capital recruitment from party Q to party R and from party R to party Q respectively. So, member of party Q leaves the party at the rate $\eta_1 Q(R/M)$ and join party R at the same rate. Also, members of party R leaves the party at the rate $\eta_2 R(Q/M)$ and join party Q at the same rate.

So, the modeling equation which is dynamical in nature as is in Arato,(2003) which considered a dynamical system which is corresponds to the simplest Markov chain and the Arvind (2012) model given as

$$\frac{dP}{dt} = \varphi m - \eta_1 P\frac{Q}{M} - \eta_2 P\frac{R}{M} - \varphi P$$

$$\frac{dQ}{dt} = \eta_1 P\frac{Q}{M} - \gamma_1 Q\frac{R}{M} - \gamma_2 R\frac{Q}{M} - \varphi Q \qquad (2.1)$$

$$\frac{dR}{dt} = \eta_2 P\frac{R}{M} + \gamma_1 Q\frac{R}{M} - \gamma_2 R\frac{Q}{M} - \varphi R$$

With the conditions the initial conditions $P(0) > 0$, $Q(0) \geq 0,\quad R(0) \geq 0.$

At the steady state solution $\frac{dM}{dt} = 0$

Method of solution

The numerical simulation we are proposing for the solution of this complex class of problem (2.1) is achievable with the use of Mathematical software is called the Matlab. The philosophy behind this method is to know the impact of varying initial data on the solution trajectory values.

Arvind (2012) considered the following precise deterministic parameters values as $\eta_1 = 0.0417,\ \eta_2 = 0.0278,\ \gamma_1 = 0.0236,\ \gamma_2 = 0.0097.$

The next step is to carry out computational simulation using matlab software's ; ODE45 and ODE23 to consider the impact of varying initial conditions on the solution trajectory values of the two political parties under eight years and sixteen years.

The detailed discussions and analysis are presented in the section below

RESULTS

The research has shown that the stabilization of two political parties can respond to changing initial party strategy on membership drive of political parties. The stabilization is affected adversely after sixteen years as the solution trajectory values become de-stabilized.

DISCUSSIONS

Again following Arvind (2012), the per capital recruitment rate η_1 of party $Q = 0.0417$

the per capital recruitment rate η_2 of party $R = 0.0278$.

The values of the solution trajectories are given in the tables 1 to 4 below.

Table 1: Evaluating the impact of changing initial data on stabilization for 8 years simulation period using ODE45

Eg	Initial condition	η_1	η_2	Q_{1e}	R_{2e}
1	(0.01, 0.02)	0.0417	0.0278	0.007557297632842	0.017642341756936
2	(0.02, 0.04)	0.0417	0.0278	0.015050367156161	0.035308566937593
3	(0.04, 0.08)	0.0417	0.0278	0.029845014032697	0.070712208514602
4	(0.08, 0.16)	0.0417	0.0278	0.058676653958718	0.141801055013298

5	(0.16, 0.32)	0.0417	0.0278	0.113375369055825	0.285079572992890
6	(0.32, 0.64)	0.0417	0.0278	0.211435032369505	0.575839587279911
7	(0.64, 1.28)	0.0417	0.0278	0.366228879808967	1.172623274761353
8	(1.28, 2.56)	0.0417	0.0278	0.540229574175969	2.415836799751757
9	(2.56, 5.12)	0.0417	0.0278	0.540132512740862	5.026626551929935
10	(5.12, 10.24)	0.0417	0.0278	0.080303514262245	10.394339569501064

Table 2: Evaluating the impact of changing initial data on stabilization for 16 years simulation period, using ODE45

Eg	Initial condition	η_1	η_2	Q_{1e}	R_{2e}
1	(0.01, 0.02)	0.0417	0.0278	0.005396174283832	0.015559835168472
2	(0.02, 0.04)	0.0417	0.0278	0.010682958406090	0.031156123337382
3	(0.04, 0.08)	0.0417	0.0278	0.020932539092233	0.062456553875352
4	(0.08, 0.16)	0.0417	0.0278	0.040164779872114	0.125478392115949
5	(0.16, 0.32)	0.0417	0.0278	0.073789906462362	0.253123925099135
6	(0.32, 0.64)	0.0417	0.0278	0.123442894629622	0.514190904780361
7	(0.64, 1.28)	0.0417	0.0278	0.165290031345259	1.054807447746521
8	(1.28, 2.56)	0.0417	0.0278	0.103291037139079	2.180207284657063

9	(2.56, 5.12)	0.0417	0.0278	-0.198941987099984	4.468853721493098
10	(5.12, 10.24)	0.0417	0.0278	-0.581965808042562	8.914626850183225

We can observed from Table 1 that as the first co-ordinate of the initial data ranging from 0.01 to 5.12 while the second co-ordinate is ranging from 0.02 to 10.24, we have observed that the converging points ranging from 0.007557297632842 to 0.080303514262245 for Q_{1e} co-ordinate while the converging points for R_{2e} co-ordinate ranges from 0.015559835168472to 10.394339569501064 under eight years.

However, is a different scenario under sixteen years. Table 2 shows that with the first co-ordinate of the initial data ranging from 0.01 to 5.12, the second co-ordinate is ranging from 0.02 to 10.24, we have observed that the converging points ranging from 0.005396174283832 to -0.581965808042562 for Q_{1e} co-ordinate while the converging points for R_{2e} coordinate ranges from 0.015559835168472to 8.914626850183225 under sixteen years.

Table 3: Evaluating the impact of changing initial data on stabilization for 8 years simulation period using ODE23

Eg	Initial condition	η_1	η_2	Q_{1e}	R_{2e}
1	(0.01, 0.02)	0.0417	0.0278	0.007557297450394	0.017642341579574
2	(0.02, 0.04)	0.0417	0.0278	0.015050366792210	0.035308566603801
3	(0.04, 0.08)	0.0417	0.0278	0.029845013310890	0.070712207932630
4	(0.08, 0.16)	0.0417	0.0278	0.058676652555004	0.141801054209269

5	(0.16, 0.32)	0.0417	0.0278	0.113375366470919	0.285079573007056
6	(0.32, 0.64)	0.0417	0.0278	0.211435027216748	0.575839596090450
7	(0.64, 1.28)	0.0417	0.0278	0.366228828755320	1.172623363492501
8	(1.28, 2.56)	0.0417	0.0278	0.540228141406535	2.415837936597692
9	(2.56, 5.12)	0.0417	0.0278	0.540100422999977	5.026643813665331
10	(5.12, 10.24)	0.0417	0.0278	0.079817020255558	10.394565109969625

Table 4: Evaluating the impact of changing initial data on stabilization for 16 years simulation period, using ODE23

Example	Initial condition	η_1	η_2	Q_{1e}	R_{2e}
1	(0.01, 0.02)	0.0417	0.0278	0.005396171895421	0 .0155598328366
2	(0.02, 0.04)	0.0417	0.0278	0.010682953631349	0.03115611891808
3	(0.04, 0.08)	0.0417	0.0278	0.020932529573322	0.06245654603760
4	(0.08, 0.16)	0.0417	0.0278	0.040164761088405	0.12547838065901
5	(0.16, 0.32)	0.0417	0.0278	0.073789870069224	0.2531239213151
6	(0.32, 0.64)	0.0417	0.0278	0.123442808904518	0 .5141910017180
7	(0.64, .28)	0.0417	0.0278	0.165289255329873	1.05480847225578
8	(1.28, 2.56)	0.0417	0.0278	0.103275072728338	0 .1802189483654

9	(2.56, 5.12)	0.0417	0.0278	-0.199157789853338	0 .4689680326295
10	(5.12,10.24)	0.0417	0.0278	-0.582704398819191	0 .9149804575602

The same argument holds for Table 3 and Table 4 using ODE23

It can be observed from Table 3 that as the first co-ordinate of the initial data ranging from 0.01 to 5.12 while the second co-ordinate is ranging from 0.02 to 10.24, we have observed that the converging points ranging from 0.007557297450394 to 0.079817020255558 for Q_{1e} co-ordinate while the converging points for R_{2e} co-ordinate ranges from 0.017642341579574 to 10.394565109969625 under eight years. Also, this is different under sixteen year's duration. Table 4 shows that with the first co-ordinate of the initial data ranging from 0.01 to 5.12, the second co-ordinate is ranging from 0.02 to 10.24, we have observed that the converging points ranging from 0.015559832836603 to -0.582704398819191 for Q_{1e} co-ordinate while the converging points for R_{2e} co-ordinate ranges from 0.015559832836603to 8.914980457560219 under sixteen years.

In summary, as the initial data varies, the dynamical system describing the interaction between political parties is said to be stabilized over a period of eight years. As duration increases, the system get de-stabilized which is a true reflection of political parties in a growing democracies in the World.

Our present analysis has extended the recent contribution of Arvind (2012), who did not look at the impact of changing the initial data on stabilization in the context of two political parties in a developing democracy.

Conclusion.

The novel contribution of this present analysis that is briefly stated as follows: By using a numerical approach , we have established the fact that the stabilization of two political parties can respond to changing initial party strategy on membership drive of political parties. This is a key contribution which has not been seen anywhere else. We will expect this present contribution to be used when the dynamical that defines the interaction process is subject to disturbance known as a system perturbation. This challenging problem will be the subject of our next investigation.

REFERENCES

3. Arvind K.M (2012). A simple mathematical model for the spread of two political parties. *Journal of Nonlinear analysis modeling and control*. 17(3), 343-354.

4. Arato, M. (2003). A famous nonlinear stochastic equation; Lotka-Volterra model with diffusion. *Journal of Mathematical and computer modeling.* 38(7/9), 709-726.

6 Ekaka-a E.N. (2009) Computational and Mathematical modeling of plant species interactions in a harsh climate. Ph.D Thesis, Department of Mathematics, the University of Liverpool and the University of Chester, United Kingdom.

7 Huckfeldt, C.W,Kohfeld. (1992). Electoral stability and the decline of class in democratic Politics. *Mathematical Computing and Modeling.* 16(8-9)223-239

8 Morris, S.A., David Pratt (2003). Analysis of the Lotka –Volterra competition equations as a technological substitution model. *Technological forecasting and change*. 70: 103-133.

9 Poitorius, C.W.I. Utterback, J.M. (1997) Multi-mode interactions among Technologies. *Research Policy*. 26(1),67-84 .

DELINEATING THE LINEAMENTS WITHIN THE MAJOR STRUCTURES AROUND EASTERN PART OF LOWER BENUE BASIN FROM 2009 AEROMAGNETIC DATA

Adetona A.A Salako K.A.,and Rafiu A.,A.

DepartmentofPhysics, Federal University of Technology, Minna, Niger State ,Nigeria

E-mail/Mobile: tonabass@gmail.com;kasalako2012@gmail.com;a.abbass@futminna.edu.

+234-08036915982

ABSTRACT

The study area falls within the Eastern part of Lower Benue Basin and bounded by latitude 7º00´N and 9º00´N.and longitude 6.30ºE and 9º30E, total area of 110 km by 440 km. Magnetic susceptibility in the area ranges from -689 nT to 613 nT, positive magnetic anomalies were observed at the Northern end of the area above Kwalla and Wamba in Plateau and Nassarawa states respectively while susceptibility are generally low below Wamba down to Akira and Katsina-Ala in Benue state. The IGRF filtered residual data for the study area was reduced to the pole (RTP) before being subjected to Vertical Derivative, Source Parameter Imaging and CET grid analysis all these were aimed at estimating depth to magnetic rocks and delineate the lineaments within the area. The first vertical derivative that sharpens the edges of the anomalies reveals that the Northern part of the study area consist of basement rock outcrops with various degrees of deformations as seen from the distortion to the magnetic signatures which represents the Granite Gneiss at Kwalla and the Migmatite Gneiss at Wamba, similar features were obtained around Akwana, Gboko and Katsina-Ala which depict weathered porphyriticHomblede Granite. Depth to magnetic rocks estimates within the study area is generally shallow though some noticeable depths in the range 3 – 3.5 kilometers were obtained around Akira just above river Benue and below Akwana on latitude 7º30´N. The phase symmetry from CET mapped the geologic boundaries the equally coincide with ridges within the area as thick pink bands enclosing major magnetic highs, these features are predominant within the outcrop basement rocks, valleys where observe within regions long wavelength anomalies where obtained on thr 1VD map around Makurdi, Lafia and Akira. Lineament map obtained from CET shows linear structures that trend in the NW-SE and E-W directions these could be interpreted as veins that are host for minerals within the area, they are predominant around Kwalla in Plateau state and Wamba in Nassarawa state also in Katsina-Ala and Gboko in Benue state.

Keyword:- Centre for Exploration Targeting (CET), Source Parameter Imaging (SPI), International Geomagnetic Reference Field (IGRF)

1.0 INTRODUCTION

1.1 LOCATION AND EXTENT OF THE STUDY AREA

The study area is located within the Eastern part of Lower Benue Trough, it include the basement complexes bounding it at the Eastern and Northern edges. Figure:1 The area is bounded by Latitude 9.0^0N to 9.5^0N and Longitude 7.0^0E to 8.5^0E. The physiological feature recognized in the area are the river Benue, Eight aeromagnetic maps covered the study area and are numbered, (210, 211, 231, 232, 251, 252, 2271 and 272), A total area of 24,200 square kilometers. The study area touches three states majorly, which are Nassarawa and Plateau at the upper part and Benue States at the lower part. Figure:1

.1.2 REVIEW OF GEOLOGY

Sedimentation in the Lower Benue Trough commenced with the marine Albian*Asu River Group*, although some pyroclastics of Aptian – Early Albian ages have been sparingly reported (Petters, S. W. 1977). The Asu River Group in the Lower Benue Trough comprises the shales, limestones and sandstone lenses of the Abakaliki Formationin the Abakaliki area and the Mfamosing Limestonein the Calabar Flank (Ojoh K. A. 1992) The marine Cenomanian – Turonian*Nkalagu Formation* (black shales, limestones and siltsones) and the interfingering regressive sandstones of the *Agala*and Agbani Formationsrest on the Asu River Group. Mid-Santonian deformation in the Benue Trough displaced the major depositional axis westward which led to the formation of the Anambra Basin. Post-deformational sedimentation in the Lower Benue Trough,therefore, constitutes the Anambra Basin. Sedimentation in the Anambra Basin thus commenced with the Campanian-Maastrichtian marine and paralicshales of the Enuguand NkporoFormations,overlain by the coal measures of the Mamu Formation. The fluviodeltaic sandstones of the Ajaliand OwelliFormationslie on the Mamu Formation and constitute its lateral equivalents in most places. In the Paleocene, the marine shales of the Imo and NsukkaFormations were deposited, overlain by the tidal Nanka Sandstoneof Eocene age.Down dip, towards the Niger Delta, the Akata Shaleand the Agbada Formationconstitute the Paleogene equivalents of the AnambraBasin The Basin Formation and the Imo Shale mark the onset of another transgression in the Anambra during the aleocene. In the Anambra Basin, they are only locally expected to reach maturity levels for hydrocarbon expulsion. The Enugu and the NkporoShales represent the brackish marsh and fossiliferous pro-delta facies of the Late Campanian-Early Maastrichtian depositional cycle(Ugbor Desmond O 2007**)**. Deposition of the sediments of the Nkporo/Enugu Formations reflects a funnel-shaped shallow marine setting that graded into channeled low-energy marshes. The coal-bearing Mamu Formation and the Ajali Sandstone accumulated during this epoch of overall regression of the Nkporo cycle. The Mamu Formation occurs as a narrow strip trending north–south from the Calabar Flank, swinging west around the Ankpa plateau and terminating at Idah near the River Niger .

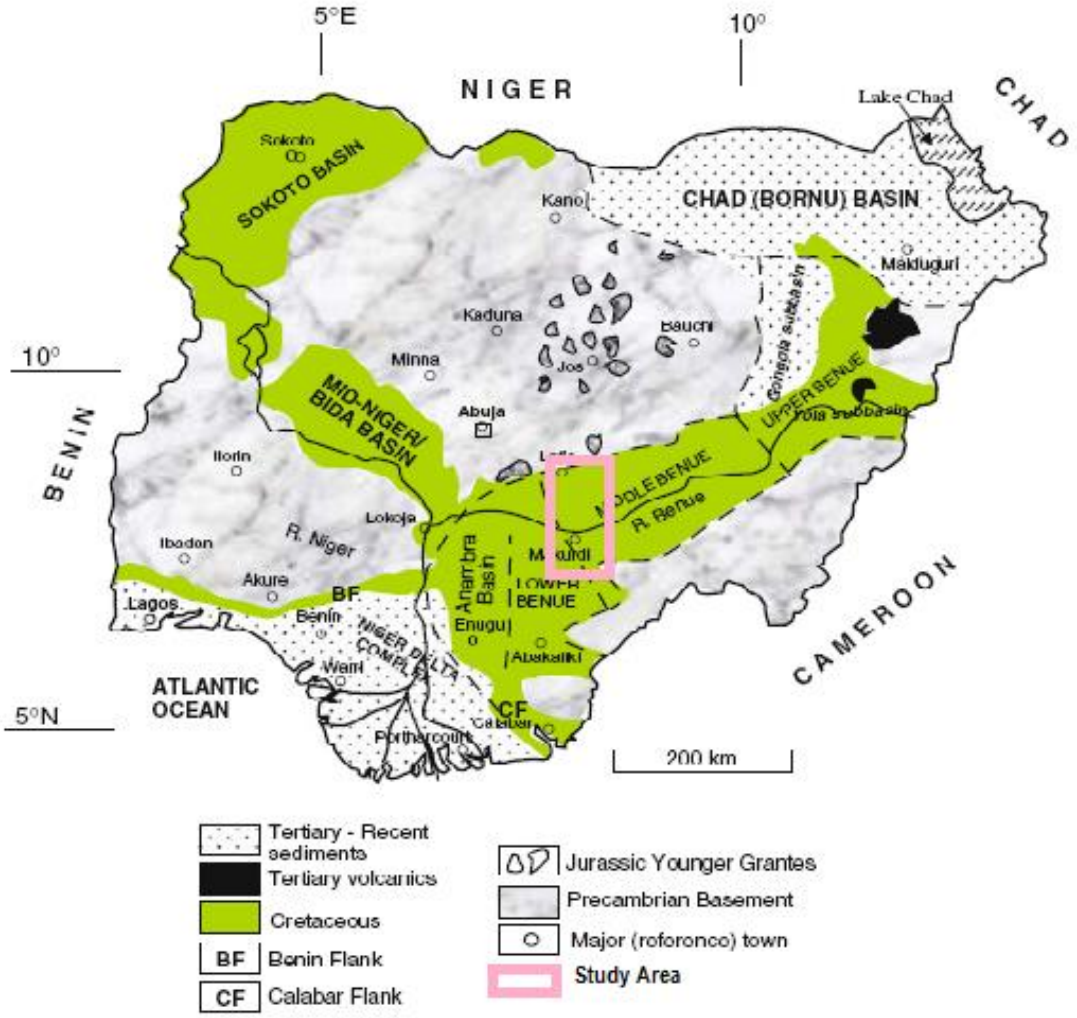

Fig. 1. Geological sketch map of Nigeria showing the major geological components; Basement, Younger Granites, and Sedimentary Basins

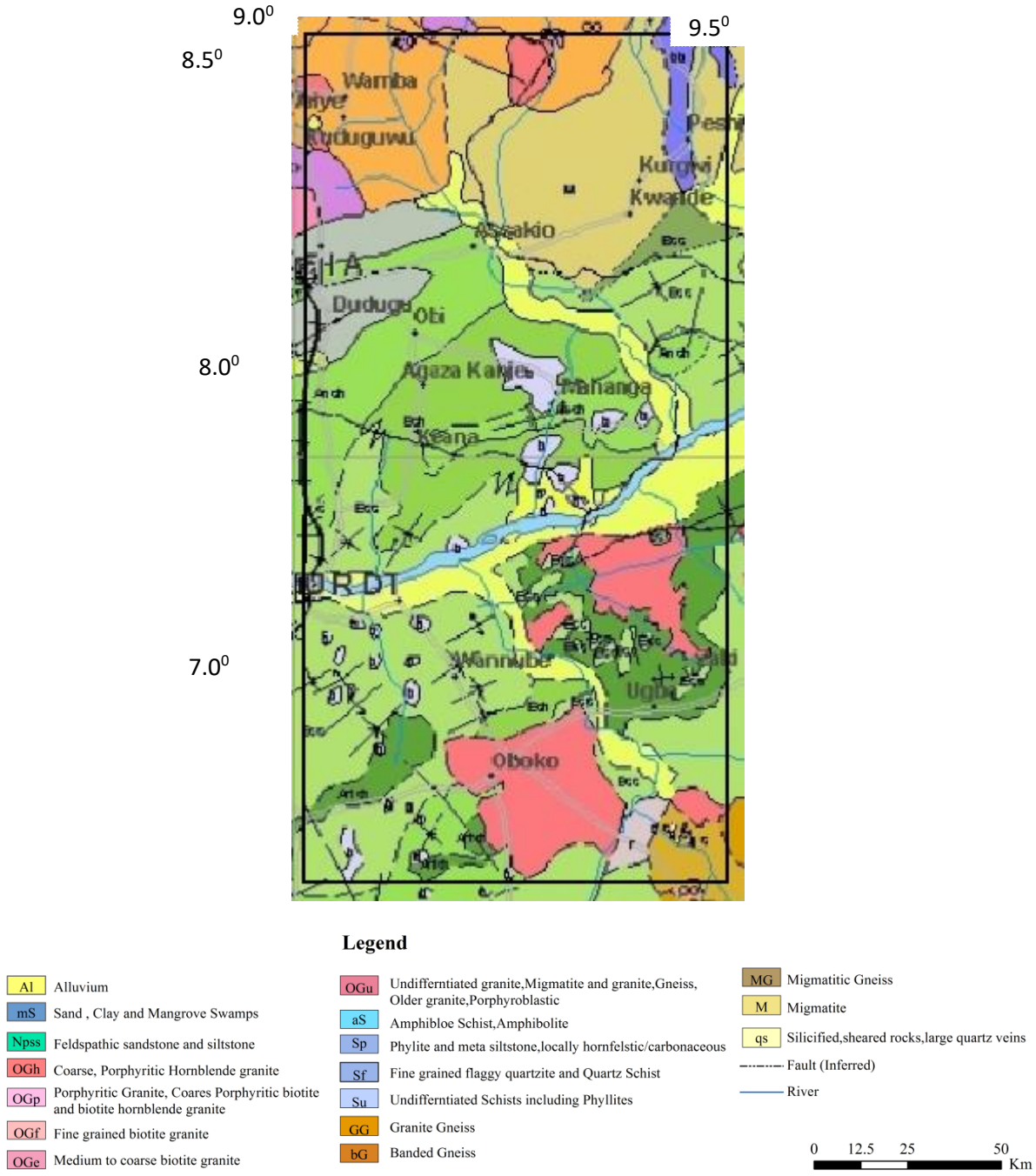

Figure: 2 geology map of the study area Adopted from geology map of Nigeria by NGSA

3.0 METHODOLOGY

In this research four main analytical processes will be required to obtained the final lineament map these are:-

1. Reduction of the TMI to Pole
2. Compute the Horizontal Derivative of the Field
3. Compute the Source Parameter Imaging
4. Compute the CET for the Field

2.1 Theory of method

Magnetic Pole Reduction

Reduction to the pole is using in low magnetic latitudes to change an anomaly to its equivalent as would be observed at the north magnetic pole. This transformation simplifies the interpretation and visualization of anomalies from low magnetic latitudes.

The reduction to the pole is:

$$L(\theta) = \frac{1}{(\sin I_a + i\cos I.\cos(D-\theta))^2}$$

Where, I = geomagnetic inclination I_a = Inclination for amplitude correction (never less than I) D = geomagnetic declination

Parameter:

I_a Inclination to use for the amplitude correction. Default is ± 20. ($I_a = 20$, if $I > 0$; $I_a = (-20)$, if $I < 0$). If I_a is specified to be less then I , it is set to I.

Reduction to the pole has amplitude component (the sin (I) term) and a phase component (the icos (I) cos (D – 0) term). When reducing to the pole from equatorial latitudes, North-South feature can blow-up due to the strong amplitude correction (the sin (I) term) that is applied when D – 0 is π/2 (i.e. a magnetic east-west wavenuber).

Horizontal Gradient (HG)

Horizontal gradient is a simple approach to locate linear structures such as contacts and faults from potential field data. For magnetic field *M(x,y)*, the horizontal gradient magnitude *HG(x,y)* is given by (Cordell and Grauch, 1982, 1985)

$$HG(x,y) = \sqrt{\left(\frac{\partial M}{\partial x}\right)^2 + \left(\frac{\partial M}{\partial y}\right)^2} \qquad (1)$$

This function peak over magnetic contacts under certain assumptions: (1) the magnetic field and source magnetization are vertical, (2) the contact is vertical and (3) the sources are thick (Phillips, 2000). Violation of the first two assumption leads to shift of the peaks away from the contact location. Violation of the third assumption leads to secondary peaks parallel to the contacts. In order to partially satisfy the first two assumptions, the method was applied to the regional component of the reduced to the pole magnetic data. When these assumptions are satisfied, the method is effective in detecting lineaments that may correspond to basement faults and contacts. Moreover, the method is less susceptible to noise in the data, because it only requires calculation of the two first-order horizontal derivatives of the magnetic field

SOURCE PARAMETER IMAGING

The basics are that for vertical contacts, the peaks of the local wave number define the inverse of depth. In other words

$$Depth = \frac{1}{K_{\max}} = \frac{1}{\left(\sqrt{\left(\frac{\partial Tilt}{\partial x}\right)^2 + \left(\frac{\partial Tilt}{\partial y}\right)^2}\right)_{\max}} \quad 2$$

$$Tilt = \arctan\left(\frac{\frac{\partial T}{\partial z}}{\left(\sqrt{\left(\frac{\partial T}{\partial x}\right)^2 + \left(\frac{\partial T}{\partial y}\right)^2}\right)}\right) = \arctan\left(\frac{\partial T / \partial z}{HGRAD}\right) \quad 3$$

The Source Parameter Imaging (SPI) method calculates source parameters from gridded magnetic data. The method assumes either a 2-D sloping contact or a 2-D dipping thin-sheet model and is based on the complex analytic signal. Solution grids show the edge locations, depths, dips, and susceptibility contrasts. The estimate of the depth is independent of the magnetic inclination, declination, dip, strike and any remanent magnetization. Image processing of the source-parameter grids enhances detail and provides maps that facilitate interpretation by non-specialists. [10].

Estimation of source parameters can be performed on gridded magnetic data. This has two advantages. First, this eliminates errors caused by survey lines that are not oriented perpendicular to strike. Second, there is no dependence on a user-selected window or operator size, which other techniques like the Naudy [8].and Euler methods require. In addition, grids of the output quantities can be generated, and subsequently image processed to enhance detail and provide structural information that otherwise may not be evident.

The Centre for Exploration Targeting (CET) Grid Analysis Plug-In For Structures

The aim of structural analysis is to:

1. Locate the contact between the basement at the north and western part and the sedimentary region of the study area
2. Locate the extent and position of the outcrops and intrusive bodies (into basement and sedimentary formations) within the study area
3. Detect fracture or any fault that may exist within the area
4. Interpret entire the lineaments detected.

Starting with the **Standard deviation** that provides an estimate of the local variations in the data. At each location in the grid, it calculates the standard deviation of the data values within the local neighborhood. Features of significance often exhibit high variability with respect to the background signal. For a window containing N cells, whose mean value is μ, the standard deviation σ of the cell values x_i is given by:

$$\sigma = \sqrt{\frac{1}{N}\sum_{i=1}^{N}\left(x_{i-\mu}\right)^2} \qquad 4$$

When interpreting the output, values which approach zero indicate very little variation, whereas large values indicate high variation. [11]. The next stage is to apply **Phase Symmetry;** this property is useful in detecting line-like features through identifying axes of symmetry. It is also known that the symmetry of a signal is closely related to the periodicity of its spatial frequency. Consequently, it is natural to utilize a frequency-based approach to detect axes of symmetry. This plug-in implements the phase symmetry algorithm developed by [12].

The result from phase symmetry is passed through **Amplitude Thresholding,** in conjunction with non-maximal suppression (NMS). The NMS is useful for finding ridges since low values are suppressed whilst points of local maxima are preserved, it also takes into account the local feature orientation so that the continuity of features is maximized and can be used to remove noise and highlight linear features

Finally **Skeleton to Vectors** is applied. The Skeleton to Vectors plug-in is for vectorising the skeletonised structures from the skeletonisation plug-in via a line fitting method described below. This vectorised data can then be used as input to the structural complexity map plug-ins. For each structure in the grid, a line is formed between its start and end points. If the structure deviates from this line by more than a specified tolerance the structure is divided into two at the point of maximum deviation and the line fitting process is repeated on these two new structure segments. This process is continued recursively until no structure segment deviates from its corresponding line segment by more than the specified tolerance. These line segments form the vectorised representation of the structures within the grid [13].

4.0 RESULTS AND DISCUSSION

The IGRF corrected TMI map Figure 3, the positive anomaly belts a shown around the western edge of the map which are the old granites rocks of the Eastern parts of Nigeria and the northern edge that represent the young granitic rocks of the central part of Nigeria, Magnetic susceptibility in the area ranges from -689 nT to 613 nT, positive magnetic anomalies were observed at the Northern end of the area above Kwalla and Wamba in Plateau and Nassarawa states respectively while susceptibility are generally low below Wamba down to Akira and Katsina-Ala in Benue state. Other regions showing positive or high susceptibility are Gboko, around Akwana from latitude $7^0.45'$ N to 8.0^0 N and around Makurdi in Benue state.

The horizontal derivative of the field shown in figure 4 enables us to locate and map the major anomalies within the study area as it is illustrated in the degree of distortion to the magnetic signatures. Rock type at the western portion of the study area is identified as Undifferentiated Older granite, mainly porphyritic granite granitized gneiss with porphyroblastic granite. Rock type at the Northern portion is identified as Biotite gneiss

False bedded sandstone, coal, sandstone and shale are the lithologic units at the surface within the sedimentary basin. River Alluvium deposition identified along the river channel above and below the river Benue. Undifferentiated granite mainly porphyritic granite granitized gneiss with porphyroblastic granite covers Oboko, Kotonkarfi, Dunduga and Kwalla in Kogi Nasarawa State. Akwana, Lafia and Makurdi in Benue State are covered by False bedded sandstone (Ajali Formation).

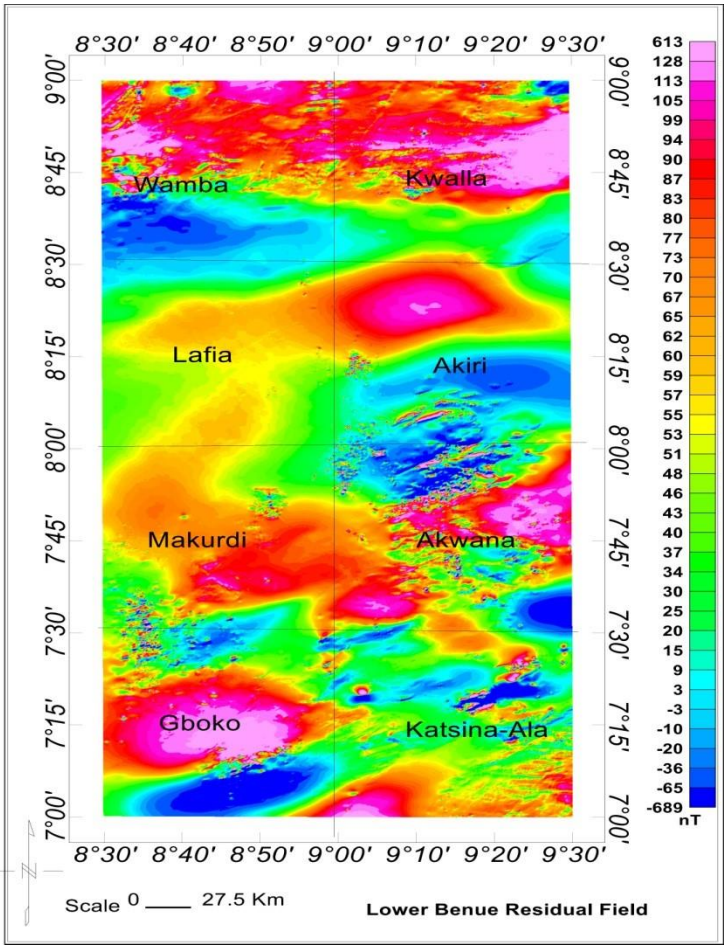

Figure: 3. IGRF Filtered Total Magnetic Intensity of the Study Area.

Computing the Source Parameter Imaging of the field gives us a fair ideal of the thickness of overburden within the study area which will help in estimating the depth of the anomaly investigated. Result of the SPI I figure 5 shows that the depth to magnetic source rocks in the area is generally shallow, though isolated depths to the tune of 3 km are observed just bellow Kwande and on Akira between latitude 8.13^0 to 8.30^0, other points of note ate on attitude 7.30^0, bellow Kwana and just bellow Gboko at the South-western corner of the study area. Shallow sedimentation in the range of 40 to 180 meters dominates the Northern end of the study area around Kwalla in Plateau state and Wamba in Nassarawa state, equally shollow sedimentation is observed on Akwana and bellow Katsina-Ala.

RESULT FROM CET GRID ANALYSIS

The plug-in produces two main images (figures 5 and 6) in its analysis the firs help us delineate the major geologic boundaries between major lithology or rocks within the study area, these contacts that coincide with the ridges identified in the same area are identified as thick pink bands.

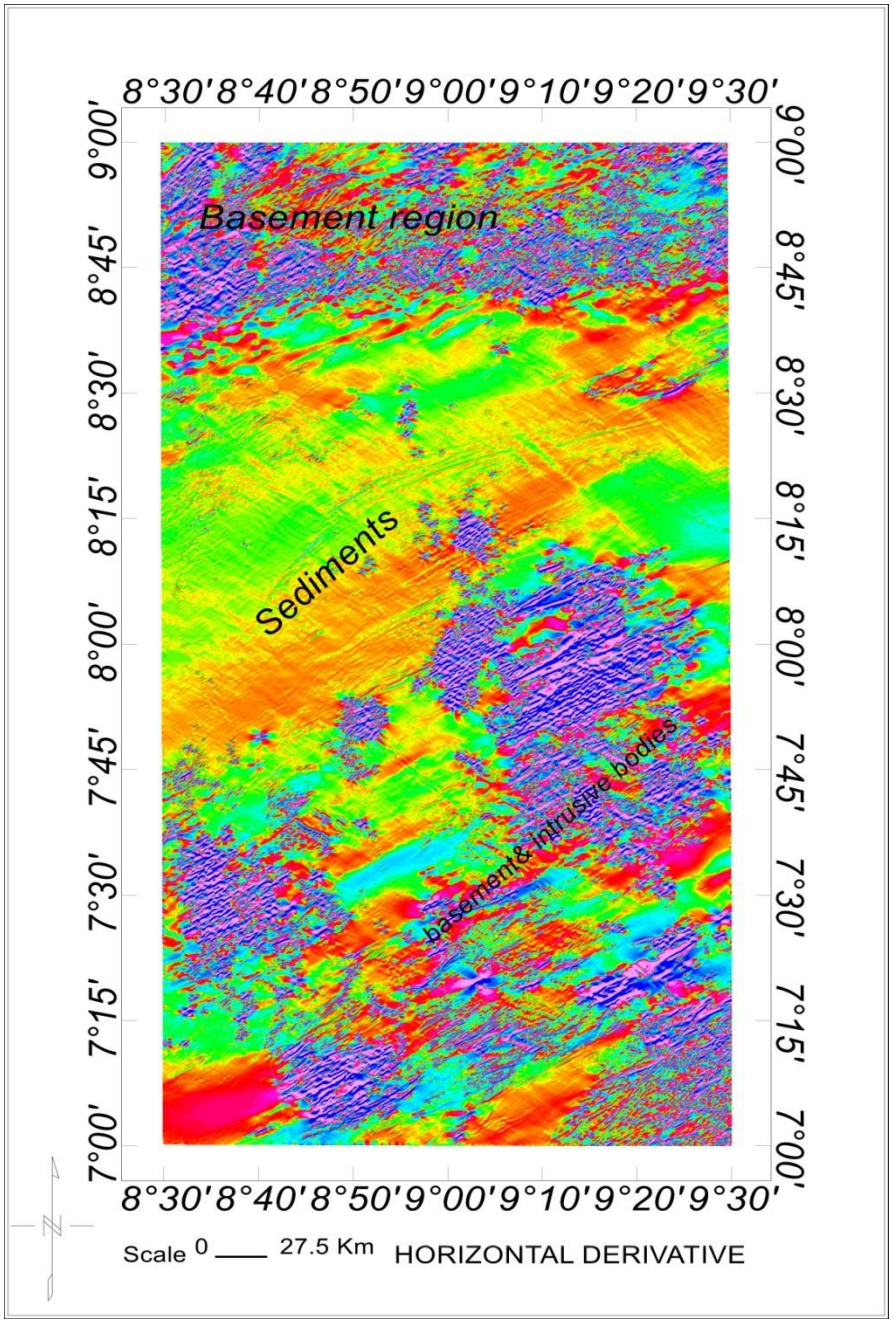

Figure: 4. Horizontal Derivative of the Study Area.

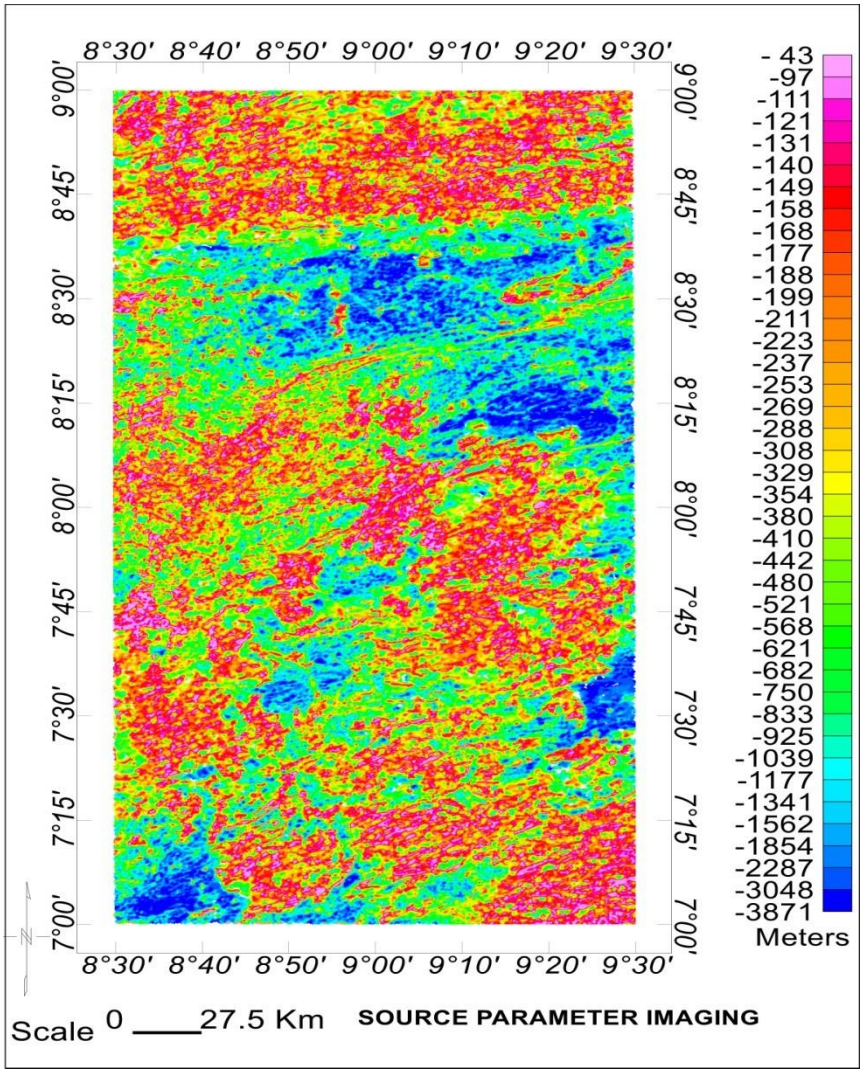

Figure: 5. Source Parameter Imaging of the Study area.

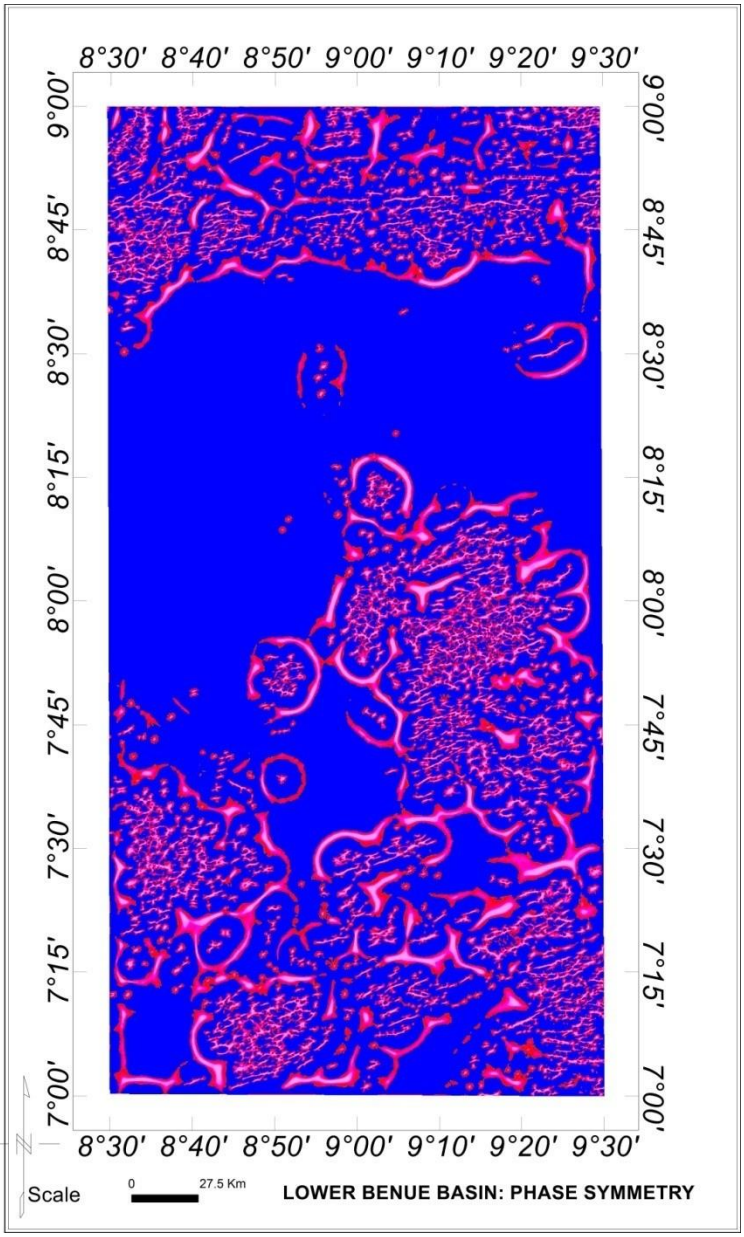

Figure: 6. Phase Symmetry From CET for the Study area.

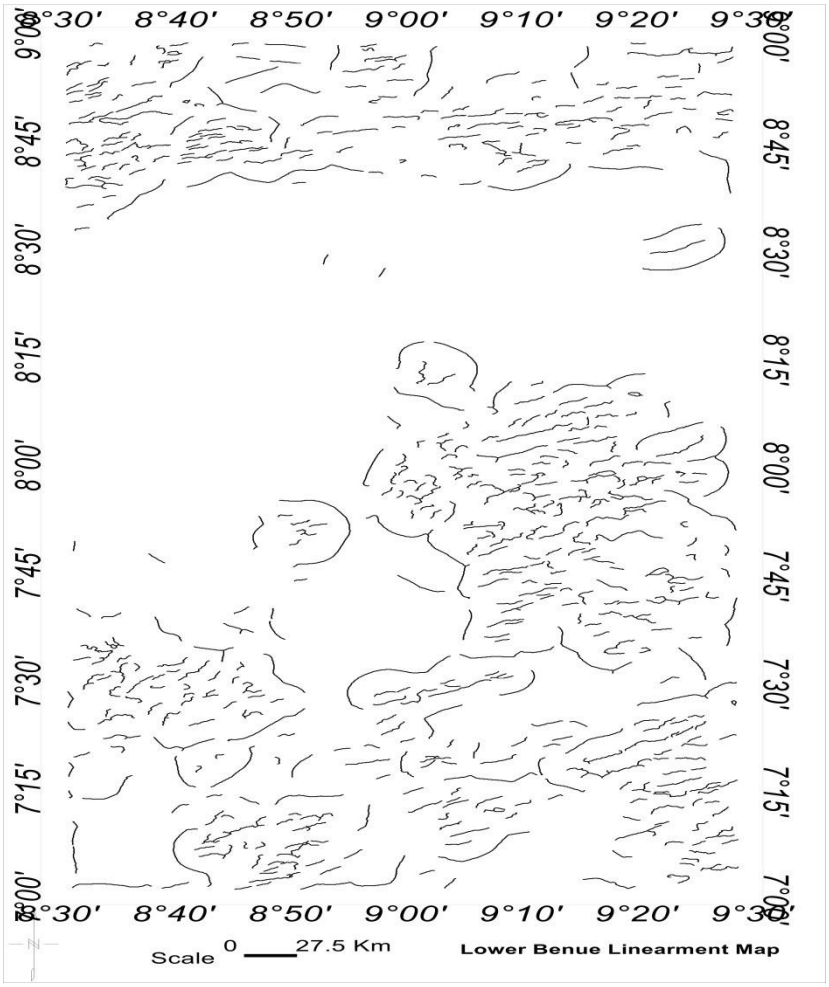

Figure: 7. Lineament Map of the Study area

These are observed all over the study area except on Lafia and makurdi sheets, and between Akiri and Kwala, where average sedimentation is average and plane valleys where observed. The second image from the CET analysis shows the linear structures desired referred to as lineament map as shown on figure 6, most of these features are located within the basement or outcrop regions and areas where sedimentation is generally very shallow or regions where magnetic rocks intrude into the sedimentary formation. It is observed that most of these lineaments are trending in the NE-SW and E-W directions which can be traced to the origin of the Basin sa the shear stress created when the American plate separated from the African plate. They are observed within the Northern and Southern ends of the study area. These lineaments depicting faults, fractures and contacts represent veins of mineralization within the study area.

CONCLUSIONS

The IGRF Total Magnetic Intensity data was reduced to the pole so as to reduced the effect of angle o f inclination n and declination and to remove the due to dipolar nature in magnetic data in order to obtain perfect symmetry and place the magnetic signature directly above the causative body. The result is mapped as shown in figure 3. The result is further subjected to Horizontal Derivative which reveal two main regions, the first showing short wavelength magnetic signatures that are a mixture of both high and low susceptibity which is the characteristic features of basement/ outcrop and regions of intrusive bodies at shallow depth this are at the Northern end of the study area and just below the river Benue (Western end) and the extreme South-Easter corner of the study area. Secondly are regions with long wavelength magnetic signatures which represents

regions of relatively high sedimentation, these occurs on Makurdi, Lafia and upper part of Akira sheets. Depth estimates are generally low except isolated cases that ranges from 3 to 3,8 km . linear structures dominate the Northern end the Southern part of the area, these are structures that are host to mineral deposits.

RECOMMENDATION

Magnetic method is majorly reconnaissance method when it comes to mineral exploration and equally based on the size of the area of study 24,200 square kilometers it is therefore recommended that regions that have been delineated to consist of lineament be investigated using either Resistivity of VLF methods to ascertain the economic viability of the mineral deposits

. REFERENCES

1. A. Spector and F. S. Grant, "Statistical methods for interpreting aeromagnetic data," *Geophysics*, vol. 35, pp. 293–302, 1970.
2. Barbosa, V. C. F., Silva, J. B. C., and Medeiros, W. E. (1999) Stability analysis and improvement of structural index estimation in Euler deconvolution: *Geophysics,* 64, 48–60.
3. B. K. Bhattacharyya, "Continuous spectrum of the total magnetic field anomaly due to a rectangular prismatic body," *Geophysics*, vol. 31, pp. 91–121, 1996.
4. Benkhelil, J. (1989) The origin and evolution of the Cretaceous Benue Trough, Nigeria. J Afr EarthSci 8:251–282
5. J. B. Thurston and R. S. Smith, "Automatic conversion of magnetic data to depth,dip, and susceptibility contrast using the SPI method," *Geophysics*, vol. 62, no. 3, pp. 807–813, 1997.
6. Nabighian, M.N., 1974. Additional comment on the analytic signal of two dimensional magnetic bodies with polygonal cross-section. Geophysics, 39, 85-92.
7. Nabighian, M.N., 1972. The analytic signal of two dimensional magnetic bodies with polygonal cross-section: its properties and use for automated anomaly interpretation. Geophysics, 37, 507-517.
8. Reid, A.B., Allsop, J. M., Granser, H., Millet, A. J., and Somerton, I. W. (1990) Magnetic interpretation in three dimensions using Euler deconvolution: *Geophysics,* 55, p. 80-91.
9. Petters S. W., Ekweozor C. M. (1982) Petroleum geology of the Benue Trough and South-EasternChad Basin, Nigeria. AAPG Bull 66:1141–1149
10. Peter Kovesi, P. (1997) "Symmetry and asymmetry From local phase", AI'97, Tenth Australian. Joint Conference on Artificial Intelligence. 2 - 4 December 1997.
11. Peter Kovesi, "Image features from phase congruency", *Videre: Journal of Computer Vision Research*, Summer 1991, Volume 1, Number 3, The MIT Press.
12. S. W. Petters, "Mid Cretaceous Paleoenvironments and biostratigraphy of the BenueTrough, Nigeria," *Geological Society of America Bulletin*, vol. 89, pp. 151–154, 1977.

OPTIMIZATION OF BIODIESEL PRODUCTION CATALYSED BY CALCIUM OXIDE OBTAINED FROM WASTE EGG SHELL USING SURFACE RESPONSE METHODOLOGY

Bankole MT[1,3], *Tijani JO[1,3], Abdulkareem AS[1,2] and Lawal MA[1]

[1]Department of Chemistry, Federal University of Technology Minna, P.M.B. 65, Niger State, Nigeria

[2]Department of Chemical Engineering, Federal University of Technology Minna, P.M.B. 65, Niger State, Nigeria

[3]Nanotechnology Research Group, Center for Genetic Engineering and Biotechnology, Federal University of Technology Minna, P.M.B. 65, Niger State, Nigeria

[1,3] jimohtijani@futminna.edu.ng

* Corresponding author

Abstract

This study focused on the optimization of biodiesel production via the transesterification process of groundnut oil catalysed by CaO prepared from waste egg shells. The prepared solid calcium oxide catalyst was characterised for its morphologies, crystallinity and specific surface areas by High Resolution Scanning Electron Microscope (HRSEM), X-ray diffraction (XRD) and Brunauer– Emmett–Teller (BET). The effects of temperature, reaction time and stirring speed on the biodiesel yields using central composite designs were investigated. The XRD and HRSEM analysis revealed the formation of a highly crystalline CaO with agglomerated honey comb web morphology. The optimum applied experimental condition to obtain the highest biodiesel yield of 92.83% using highly active CaO catalyst were temperature (60 ºC), reaction time (3 hrs) and stirring speed (600 rpm). The reaction time and temperature are inversely proportional and exerted greater influence on the yield of biodiesel than the stirring speed. It can be deduce from various analysis conducted that the waste egg shell can be utilized as a catalyst for biodiesel production.

Keywords: Biodiesel, calcium oxide, Egg shell, groundnut oil, optimisation

1. Introduction

There is a growing concerns for an alternative renewable energy sources to petroleum fuels across the globe as a result of increasing demand for fossil fuels characterized with high cost, inadequate supply, non-renewability and negative environmental impact on human and other ecological species (Leandro *et al.*, 2017). The issue of environmental pollution specifically land deterioration and degradation caused by the exploration and exploitation processes of fossil fuels has become worrisome (Leandro *et al.*, 2017; Niju *et al.*, 2014). In addition, high cost of conventional chemicals used as catalyst in the production of biodiesel remains a hurdle, which invariably contributed to high production cost of diesel engines (Bello and Daniel, 2015). Thus, the production of a cleaner-burning alternative fuel similar to petroleum diesel is considered necessary. Biodiesel is a biodegradable, environmental friendly, renewable and non-toxic fuel with low emission profile compared to petrol diesel mostly used for diesel engines (Ellabban *et al.*, 2014). Biodiesel production involving the use of edible or non-edible oils feedstock including animal fats, fish oil can be achieved using transesterification process catalysed by either homogeneous or heterogeneous catalysts. Homogenous catalysts include NaOH, KOH, while heterogeneous catalysts are CaO, MgO, and hydrotalcite amongst others (Abdulkareem *et al.*, 2012; Niju *et al.*, 2014; Renita *et al.*, 2016). Transesterification process involves the application of homogeneous alkali based catalyst which transformed the feedstock within shorter reaction time into high quality biodiesel at a relatively low temperature (Jazie *et al.*, 2013). Invariably, the homogeneous process mostly results to higher yields provided the content of free fatty acids (FFAs) in the used feedstock is less than 1 %, compared to the heterogeneous catalytic transesterification (Karmakar *et al.*, 2010). The homogeneous catalytic process has some inherent shortcomings such as the post-separation issues of the applied catalyst after reaction, non-reusability nature, purification problems,

generation of excessive wastewater, as well as high energy consumption (Niju *et al.*, 2014; Sharma and Singh, 2010). In order to solve the highlighted problems stated above, heterogeneous catalyst was discovered and researchers have utilised this catalyst type for biodiesel production (Alamu *et al.*, 2010). Heterogeneous catalyst are preferable to homogeneous due to the ease of catalyst recovery and purification, production of less wastewater, reusability potentials, and less consumption of energy (Ramezani *et al.*, 2010). In spite of the several benefits associated with the use of heterogeneous catalysts for biodiesel production, proper identification of a solid based catalyst that will enhance the transesterification process and obtain high yield biodiessel under mild reaction conditions constitutes a problem (Ojolo *et al.*, 2011).

Among the solid base catalyst, alkaline earth metal oxides such as calcium oxide (CaO) of high basicity are considered appropriate heterogeneous catalyst to catalyse feedstock conversion to biodiesel (Mohadi *et al.*, 2016; Navajas *et al.*, 2013; Renita *et al.*, 2016). For instance, Nakatani *et al.*, (2009) obtained 73.8% biodiesel yield during the transesterification of soybean oil catalysed by 25% weight CaO obtained from oyster shells over reaction time of 5 hrs. Niju *et al.*, (2014) employed 8% white bivalve clam shell as catalyst for the conversion waste frying oil of biodiesel and reported biodiesel yield of 95.84% within 3 hrs reaction time. In this study, Ground nut (Arachis hypogeal, L) which belongs to the leguminosae family was used as a feedstock to produce Biodiessel due to its availability and abundance in Nigeria. Groundnut oil is otherwise categorised as the oleic-linoleic acid oil containing a comparatively significant amount of unsaturated fatty acids namely the monounsaturated oleic acid as well as the polyunsaturated linoleic acid (Suleiman *et al.*, 2012). In addition, indiscriminate dumping of waste eggshell constitutes an environmental nuisance and conversion of the waste eggshells with catalytic activity can mediate transesterification reaction and aids in abatement of environmental pollution (Wei *et al.*, 2009).

In spite of several research work done on waste eggshell catalysts for biodiesel production, the survey of literature reveals that there is scanty information on the influence of process parameters such as stirring speed, stirring time and reaction temperature on the yield of biodiesel from groundnut oil catalysed by CaO prepared from waste egg shells. Therefore, this present study is focused on the application of surface response methodology in the optimisation of aforementioned process parameters on the yield of biodiesel from groundnut oil catalysed by CaO obtained from waste egg shells. The result obtained in this study was compared with commercially available NaOH, KOH, MgO and CaO for the transesterification of groundnut oil. The morphologies, mineralogical phases and surface areas of the prepared CaO were characterized by High Resolution Scanning Electron Microscopy (HRSEM), X-ray diffraction (XRD) and Brunauer–Emmett–Teller (BET).

2. Methodology

2.1 Materials

The groundnut oil was bought from Bosso market, Minna metropolis. Waste chicken eggs were randomly collected from different location in Kure market, Minna Niger state. All other chemicals were of analytical grade (AR), methanol (99.9%), alcoholic KOH (>85%) and potassium iodide (99.9%) supplied by Sigma-Aldrich. The reagents were used as supplied without further purification.

2.2. Sample Pre-treatment

The collected Ground nut oil was filtered using filter paper (0.7µm) to remove suspended particles and kept in the water bath at 110^{o}C for 4 hrs to get rid of the moisture. The waste egg shells (70 g) were washed with distilled water to remove impurities and dried in an oven at 110 ^{o}C for about 8 hrs. The dried egg shells were ground to fine powder and sieved using a 200 µm mesh sieve and were used as a raw material in the production of catalyst.

2.3. Physico-chemical characterisation of ground nut oil

The physico-chemical characterisation of the ground nut oil was carried out using standard methods to determine the following parameters: free fatty acid value, saponification value, viscosity and iodine value (Association of Official Analytical Chemists, 2012).

2.4. Catalyst preparation

The solid metal oxide catalyst (CaO) was prepared using calcination of the waste egg shells. The fine powdered dried egg shells of approximately 30 g placed in a quartz boat were calcined in a muffle furnace under static air conditions at 900 ^{o}C for 4 hrs decompose the calcium species in the egg shell into CaO particle as shown in equation 1.

$$CaCO_3 \rightarrow CaO + CO_2 \quad (1)$$

The calcium based oxides from the egg shells were refluxed in distilled water at 50 ºC for 6 h and thereafter filtered and then dried in oven at 120 ºC for 6 hrs. Again, the solid particle was dehydrated by performing calcination at 600 ºC for 3 hrs to transform the hydroxide material to oxide form. The calcium oxide obtained after decomposition was used as the catalyst for transesterification reaction.

2.4.1. Characterization of the prepared CaO

The mineralogical phase of synthesized solid metal oxide (CaO) was determined by powder X-ray diffraction (XRD; PW 1800 diffractometer, Philips, Netherlands) analysis performed on a Bruker AXS D8 Advance with Cu-Kα radiation. A portion of the solid metal oxides were sprinkled on a de-greased glass slide and diffractograms were recorded between diffraction angles of 200 and 800. The morphology of the synthesised materials was examined using Zeiss Auriga HRSEM. A mass of 0.05 mg powdered sample was sprinkled on carbon adhesive tape and sputter coated with Au-Pd using Quorum T15OT for 5 minutes prior to analysis. The microscope was operated with electron high tension (EHT) of 5 kV for imaging. For BET N_2 adsorption, about 100 mg of the dry powder sample in a sample tube was first degassed at 90º C for 4 hours to remove residual water and other volatile components that were likely to block the pores. The BET surface area and average pore volume distributions were obtained from the plot of volume adsorbed (cm3/g STP) versus relative pressure. The N_2 adsorption-desorption isotherms were collected at -196º C using Brunauer-Emmett-Teller (BET; NOVA 4200e, Quantachrome Instruments, USA).

2.4.2. Optimization of biodiesel yield using Response surface methodology

Surface response methodology was applied to optimise the biodiesel production and to check the influence of process parameters such as stirring speed, stirring time and temperature of the transesterification process on the yield of the biodiesel. A 2^3 Central Composite Design (CCD) of experiment was used where three factors each at lower and upper levels) were chosen. The factors are temperature (°C), time (hours) and stirring speed (rpm). The range of temperature, reaction time and stirring speed were chosen as follows; 60 ºC – 80 ºC, 1hr - 3hrs and 200 rpm – 600 rpm. Six centre points were considered, plus four low points and four high points and six alpha points making a total of twenty experimental runs carried out. The details are presented in Table 1.

Table 1: Influence of process parameters on Biodiesel yield using surface response methodology

Run	Factor 1 Temperature (ºC)	Factor 2 Time (hour)	Factor 3 Stirring speed(rpm)	Response yield (%)
1	70	3.68	400.00	15.35
2	80	1	600.00	25.20
3	70	2	400.00	50.12
4	70	2	63.64	25.20
5	60	1	600.00	69.03
6	70	0.32	400.00	30.45
7	70	2	736.36	55.35
8	70	2	400.00	50.52
9	60	3	200.00	90.12
10	53.18	2	400.00	85.04
11	80	3	600.00	14.78
12	80	1	200.00	31.95
13	86.82	2	400.00	10.75
14	70	2	400.00	50.43
15	60	1	200.00	64.85
16	70	2	400.00	50.32
17	60	2	400.00	85.75

18	80	3	200.00	18.98
19	70	2	400.00	50.82
20	60	3	600.00	92.83

2.4.3. Transesterification procedures

Approximately, 2 g of CaO (catalyst) was added to 19.2 ml of methanol in a conical flask and stirred vigorously separately at a speed of (200, 400 and 600 rpm) on a magnetic stirrer until the CaO dissolved. Furthermore, the transesterification reaction was carried out in a 250 ml conical flask equipped with a thermometer and magnetic stirrer. 80 ml of groundnut oil was put into the conical flask and heated to 70 ^{o}C. Thereafter, the catalyst solution was gently poured into the conical flask containing the oil. The temperature of the system was maintained individually at (60, 70 and 80 ^{o}C), stirring speed of (200, 400 and 600 rpm) and the reaction was monitored for (1hr, 2 and 3 hrs). After the completion of the reaction, the product settled for 24 hours and the catalyst and the transesterification product was separated using a separating funnel. The clear upper layer containing the Fatty Acid Methyl Esters (FAME) was biodiesel while the lower dense layer was the glycerol. The biodiesel was screened using filter paper (0.7µm) in order to remove suspended particles (catalyst) and further washed with warm distilled water to remove glycerol and impurities. Thereafter, the biodiesel was immersed in water bath at 110^{o}C to evaporate the residual methanol. The quantity of biodiesel yield for each run was determined using the following formula

$$Biodiessel\ yield\ = \frac{Volume\ of\ biodiessel\ produced}{Volume\ of\ Oil\ used} \times 100\% \qquad (3)$$

2.4.4. Characterisation of the biodiesel yields

The highest and lowest yield of biodiesel produced were characterised for its kinematic viscosity at 40^{o}C, specific gravity, flash point, acid value, saponification value, iodine value pour point, cloud point and smoke point in accordance with the ASTM protocols. While the Cetane number was determined according to the equation 4 proposed by Alamu *et al.,* (2010).

$$Cetane\ number\ (CN) = CI - 1.5 \qquad (4)$$

$$Where\ Cetane\ index\ (CI) = \frac{46.3+5458}{SV} - 0.225\ IV \qquad (5)$$

Where SV= saponification value of the biodiesel and IV= Iodine value of biodiesel

3.0. Results and Discussion

3.1. Groundnut oil characterisation

The composition of groundnut oil was determined as explained in section 2.3 and the characterisation result is shown in Table 2.

Table 2: Physico-chemical properties of groundnut oil

S/No	Parameters	Obtained values
1	Saponification value (mgKOH/g)	193. 2
2	Acid value(mgKOH/g)	4.58
3	Iodine value(mgI_2/g)	84.24

4	Specific gravity(g/cm^3)	0.94
5	Free fatty acid value (FFA) (%)	2.29
6	Kinematic viscosity @ 40^{o}C	38.50
7	Pour point (^{o}C)	6
8	Flash point (^{o}C)	178

According to Table 2, the FFA of the groundnut oil was determined to be 2.29% and high FFA above 1% reduce the efficiency of homogeneous catalyst and affects the biodiesel yield (Wanodya and Budiman, 2013). On the contrary, studies have shown that heterogeneous catalysts could catalyse oil with FFA in the range of 6% - 15% without any pretreatment (Bello and Daniel, 2015). In the same vein, Bello and Agge, (2012) found that groundnut oil with FFA >3% produced more than 90% biodiesel under the following reaction conditions (temperature 60 ^{o}C, reaction time 3 hrs, catalyst weight of 2%). This shows the ground nut oil used in this study is a useful feedstock for biodiesel production. Furthermore, the specific gravity of the oil was determined to be 0.94, which shows that water is heavier than the oil. The iodine value of 84.24 mgI_2/g is an indication of low level of saturation. The saponification value indicates the ability of the oil to form soap during transesterification process. High saponification value suggests the presence of fatty acid that could be transformed into soap and hence low yield of biodiesel. The saponification value of the groundnut oil was 193.2 mg/KOH, which means the oil has a tendency of soap formation.

3.2. X-ray Diffraction analysis of the calcined eggshells

The XRD pattern of the calcined eggshell at 900^{o}C for 4 hours is display in Figure 1. As shown in Figure 1, the presence of intense and sharp diffraction peak at 2 Θ = 34.2^o, 47.4^o, 53.7^o, 55.6^o, 63.9^o, and 74.3^o with a crystal plane of (200), with a corresponding crystal planes (200), (220), (311), (221), (222) and (210) were assigned to CaO. The diffraction peak of low intensity observed at 2 Θ = 29.4^o in the XRD pattern indicates the formation of $Ca(OH)_2$. The presence of $Ca(OH)_2$ in the XRD spectra is an indication of interaction of CaO with water vapour on the air, which further show that the CaO is highly hydroscopic in nature. The observed peaks are similar with those reported by Wei *et al.*, (2009) and Sharma and Singh, (2010) under similar conditions although with different type of eggshells. This further demonstrates that the difference in the composition eggshell did not affect the mineralogical phase present in the calcined sample. Therefore, the same calcination process can be used to obtain CaO catalyst regardless of type of eggshell (Navajas *et al.*, 2013).

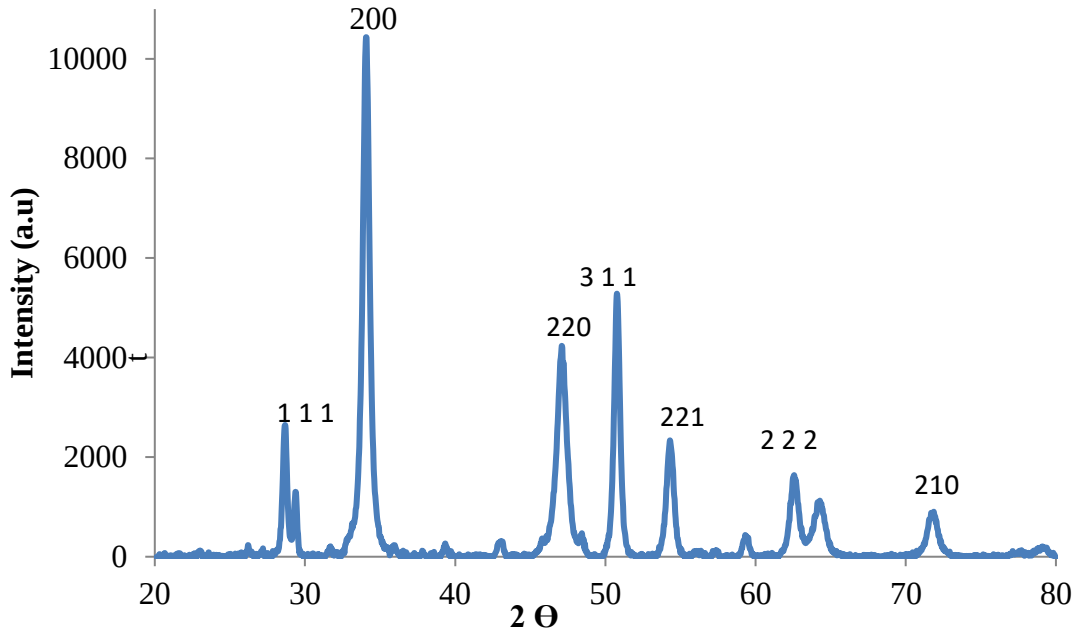

Figure 1: XRD spectrum of the calcined calcium oxide particles at 900 ºC

3.3 HRSEM analysis of the prepared CaO

Figure 2 shows the low and high magnification images of the CaO catalyst obtained from the calcination of egg shells at 900 ºC.

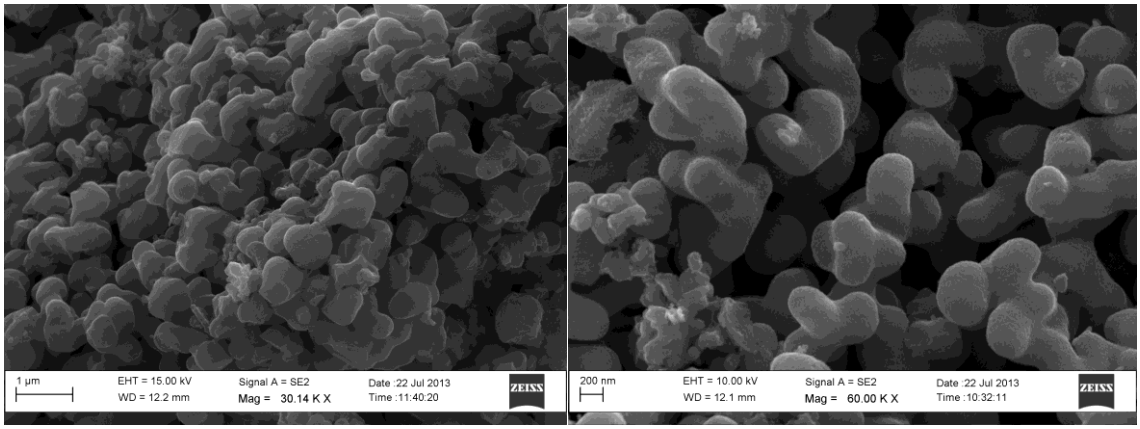

Figure 2: HRSEM micrographs of the calcined calcium oxide particles at (a) low magnification (b) high magnification

Figure 2 demonstrates the presence of agglomerated homogeneously distributed honey comb web- like morphology. The porous honey comb-like morphology is similar to the shape of CaO obtained from egg shells after calcination at 900 ºC for 2.5 hrs (Niju et al., 2014).

3.4. BET surface area of the CaO obtained from waste egg shells

Table 3 shows the specific surface area of the prepared CaO in comparison with the commercial CaO.

Table 3. Specific surface area of the as-prepared CaO and commercial CaO

Parameters	As-prepared CaO	Commercial CaO
BET surface area (m^2 g^{-1})	4.041	3.012
Pore volume (cm^3 g^{-1})	1.356	1.216

According to Table 3, it can be noticed that the surface area of as-prepared CaO in this study is slightly higher than that of commercial CaO. This implies that the catalytic activity of CaO prepared in this study will be higher than that of commercial CaO. The value obtained is closely related to what was reported by Niju et al., (2014).

3.5. Statistical analysis from RSM

The following parameters such as temperature, reaction time and stirring speed were chosen as independent variable in the production of biodiesel catalysed by CaO from waste egg shells with biodiesel yield as a dependent variable. A set of 20 experiments were carried out as shown in Table 1. The model was statistically significant with 95% confident level and all three independent variables exhibited positive effects on the biodiesel yield. The model was assessed with coefficient of determination (R^2=0.9563). Based on the CCD design and result of experiments (Table 1), regression analysis generated the following quadratic regression model data (based on the coded factors)

$$R_1 = 50.07 - 25.69X_1 + 0.021X_2 - 2.72X_3 - 9.06X_1X_2 - 2.23X_1X_3C + 0.14X_2X_3 + 0.42X_1^2 - 8.4X_2^2 + 6.53X_3^2 \quad (6)$$

Where R_1 indicates the yield of biodiesel (%); X_1 temperature (^oC); X_2 reaction time (hour); and X_3 stirring speed (rpm). The equation was used to analyse the response yield by multiple regression through the least square method. Using the above results, different effects of the independent variables on the response were studied by plotting a three-dimensional response surface based on the model equation.

3.5.1. Interaction of time and temperature

The optimum biodiesel yield from groundnut oil catalysed by CaO obtained from waste eggshell was 92.53% at a temperature of 60 ºC, for 3 hours and with stirring speed of 600 rpm as shown in Table 1. The interaction of reaction time and applied temperature is shown in figure 3. As shown in Table 1, it was observed that the highest yield of biodiesel was observed at reaction time of 3 hrs (92%) at optimum temperature of (60 ºC). The value obtained is closely related to 96% yield reported under similar condition (3 hrs at 60 ºC) by Jazie *et al.*, (2013), though with a rapeseed oil using eggshell as catalyst. In the same vein, Ramezani *et al.*, (2010) also reported 87.30% yield of biodiesel using homogeneous catalyst (KOH) under similar condition (2 hrs, at 65 ºC) with castor oil. With continuous increase in reaction time (>3 hrs) (Figure 3), the yield decreases due to loss of solvent in the reaction medium. Conversely, increase in the applied temperature with other conditions constant; corresponded to decrease in biodiesel yield. Specifically, at temperature of 60 ºC, a reasonable yield of biodiesel (50.12%) was obtained at time (2hrs), while 30% yield of biodiesel was obtained at temperature of 80 ºC. This suggests that the biodiesel yield decrease with increasing temperature. Thus, the reaction time and temperature are inversely proportional and increase in one of the parameters beyond optimal value corresponds to decrease in the yield of biodiesel.

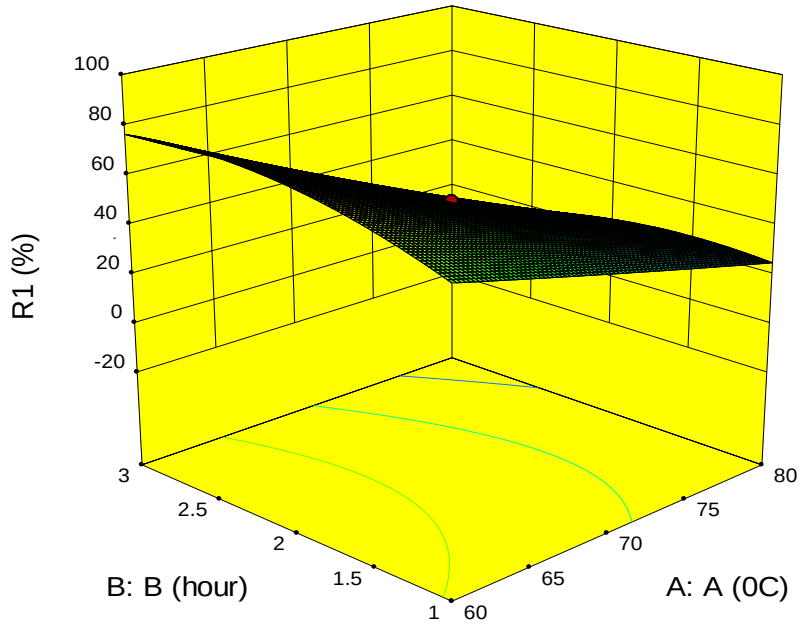

Figure 3: Interaction of time and temperature, where A-axis represents the temperature and B-axis depicts reaction time

3.5.2. Interaction of time and stirring speed

Figure 4 shows the influence of interaction of reaction time and stirring speed on the biodiesel yields. It can be observed that an increase in reaction time (1-3 hrs) is directly proportional to the biodiesel yield whereas and an increase in the stirring speed (200 rpm-600 rpm) had little effect on the biodiesel yield. This implies that the stirring speed did not follow a specific trend and exert no significant effect on the yield of biodiesel. In figure 4, the optimal yield of biodiesel was obtained at 3 hrs with a corresponding stirring speed of 600 rpm. However, there is no much disparity in the biodiesel yield obtained using either a stirring speed of 400 rpm or 600 rpm. According to Table 1 and Figure 4, when the reaction time was 1 hour, temperature (60 ºC) and stirring speed of 600 rpm (experimental runs 5), the yield of biodiesel was 69.03%, while at same

temperature and reaction time with stirring speed of 200 rpm (experimental runs 15), the yield of biodiesel was found to be 64.85%. The yield obtained at experimental runs 5 is slightly higher than that of experimental runs 15 due to difference in the stirring speed. This suggests effective interaction between the catalyst, oil and methanol at 600 rpm and slow diffusion reaction at 200 rpm. Furthermore, when the stirring speed was 200 rpm at constant reaction time of 3 hrs, (experimental runs 9 and 18) with different applied temperature of 60 ºC and 80 ºC, the yield of biodiesel was 90.12% and 18.98%. Similarly, when the stirring speed was 200 rpm, reaction time 1 hr, under the same temperature (experimental runs 9 and 18), and the biodiesel yields were 31.95% and 64.85%. This means under the same stirring speed, the biodiesel yields fluctuate possibly due to different in the applied temperature and reaction time.

Also, there were no much differences in the yield of biodiesel when the stirring speed was 400 rpm and even 600 rpm. When the stirring speed was 400 rpm irrespective of the temperature and reaction time, the yield of biodiesel were 15.35%(experimental runs 1), 50.12% (experimental runs 6), 50.52% (experimental runs 8), 85.04% (experimental run 10), 31.95%(experimental run 12), 10.75% (experimental run 13), 50.43% (experimental run 14). This again shows that the variation of stirring speed on the yield of biodiesel did not follow a specific pattern. It was found that the yield of biodiesel reported by Fadhil *et al.*, (2016) slight higher than what was obtained in this study. The possible reason may be ascribed to differences in the stirring speed and catalyst types.

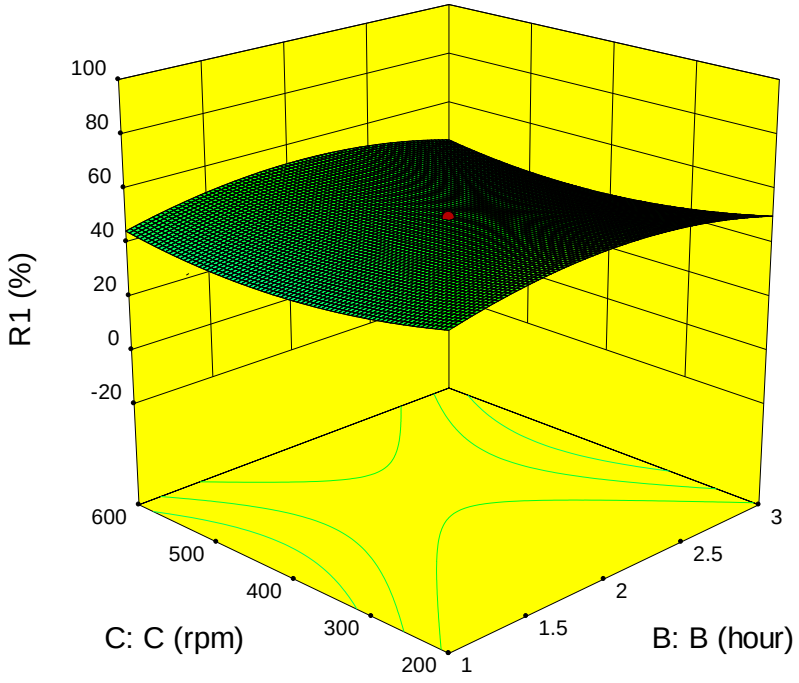

Figure 4: Effect of reaction time and stirring speed on the biodiesel yield, with C-axis stands for stirring speed while D-axis depicts

In summary, the highest biodiesel yield catalysed by CaO obtained from waste egg shells was 92.83% at runs 20 under the following reaction condition; temperature (60^0C), reaction time (3 hrs) and stirring speed (600 rpm). While the least yield of 15.32% of was obtained at experimental runs 1 under the following condition of temperature (70^0C), reaction time (3.68hrs) and stirring speed of 400 rpm. This implies that the optimal conditions to obtain greater yield of biodiesel are: stirring speed (200 rpm), reaction time (2 hrs) and temperature (60 ºC). The statistical analysis of the experimental range revealed the order of significance of the independent variable as temperature > reaction time > stirring speed.

3.6. Characterisation of the prepared biodiesel properties

Table 4 shows basic properties of the prepared biodiesel in comparison with ASTM standards D6751

Table 4. Comparison of prepared biodiesel properties with ASTM standard

Properties	**Values obtained Prepared biodiesel**	**ASTM D6751**
Specific gravity (g/cm^3)	0.91	0.86 - 0.90
Kinematic viscosity @ 40ºC	6.0	1.9 - 6.0
Flash point (ºC)	135	100-170
Pour point (ºC)	6.0	
Iodine value (mgI_2/g)	68.9	120
Cloud point (ºC)		
	8.5	-3 to12
Cetane number (min)	62.35	47

Key: ASTM= American Standard for Testing and Measurement

According to Table 4, the specific gravity of the biodiesel produced is 0.91 which fall within the ASTM standards range of 0.86 - 0.90. Also, the biodiesel flash point was 135 ºC which is slightly higher than the ASTM limit of 130 ºC. This signifies that the biodiesel could easily ignite into flame, though blending with conventional diesel is recommended to reduce the value. The biodiesel cloud point of 8.5ºC which is less

than the ASTM value of 9 ºC, implies that the biodiesel from groundnut oil could fit into regions with lower temperature. Kinematic viscosity is considered very important in the monitoring and performance evaluation of fuel injection system particularly at low temperatures. It can be observed that the viscosity of biodiesel fall within the range of ASTM and thus confirming the suitability of the prepared biodiesel as fuels in diesel engines. Cetane number is referring to the ignition delay time of a fuel when injected inside the combustion chamber or sometimes defined as the times it takes white smoke after start up, drivability before warm up and intensity of diesel knock at idle. The cetane number of the biodiesel was found to be 61.27, which fall within the ASTM limit of 47 min and hence compatible with diesel engines.

Table 5: Comparison of the biodiesel yield results of the previous and present study

Catalyst	**Conditions of biodiesel production**	**Biodiesel yield (%)**	**Reference**
NaOH	No optimization however catalyst dosage (0.7 g)	91.98	Ojolo *et al.*, 2011
NaOH	Reaction temperature (40^{o}C), reaction time (1 hr 30 min), stirring speed (not studied), catalyst concentration (0.5wt %)	99	Abdulkareem *et al.*, 2012
NaOH	Reaction temperature (60^{o}C), reaction time (1 hr), stirring speed (600 rpm), catalyst concentration (1 wt%)	68.7	Bello and Agge, 2012
KOH	Reaction temperature (60^{o}C), reaction time (2 hrs), stirring speed (600 rpm), catalyst concentration (2.4 wt%)	75.22	Bello and Daniel, 2015

CaO from waste egg shells	Reaction temperature (60°C), reaction time (3 hrs), stirring speed (600 rpm), catalyst concentration (2.5wt %)	92.83	This study

As shown in Table 5, it can be noticed that with the biodiesel yield obtained in this study based on surface response methodology competes favourably with the values reported in the literature. In some cases, the solid CaO catalyst exhibited higher catalytic activity than the commercial homogeneous catalysts such as KOH, NaOH. Conversely, the biodiesel yield reported by Abdulkareem *et al.,* (2012) and Muthu and Viruthagiri, (2015) is slightly greater than the observed yield in this study. The differences may be attributed to the longer reaction time used by Abdulkareem *et al.,* (2012) during the biodiesel production and higher catalyst concentration employed by Muthu and Viruthagiri, (2015) compared to reaction time of 3 hrs and 2.5 wt% catalyst concentration used in this study. Previous studies have shown that higher biodiesel yield is a function of reaction time and catalyst concentration.

4. Conclusion

In summary, CaO was obtained from waste egg shells via calcination process and subsequently utilised as a solid heterogeneous catalyst for the production of biodiesel from groundnut oil. Based on this study, the following conclusions were drawn. Groundnut oil served as a useful feedstock for biodiesel production. The XRD and HRSEM analysis demonstrated the formation of highly crystalline CaO resembling aggregated honey comb web. The optimum applied experimental conditioned to obtain high biodiesel yield of 92.83% using CaO of excellent catalytic activity were temperature (60 ^{0}C), reaction time (3 hrs) and stirring speed (600 rpm). The reaction time and temperature are inversely proportional to the yield of biodiesel and the order of contribution to biodiesel yield was as follows: temperature > reaction time > stirring speed. This study revealed CaO prepared from waste egg shells can serve as a substitute to commercially available homogeneous or heterogeneous solid catalyst. Finally, this study demonstrated for the first time that application of surface response methodology involving interactions of process parameters aids in the transformation of groundnut oil to biodiesel using CaO catalyst prepared from waste egg shell.

References

Abdulkareem A.S, Jimoh A, Afolabi A.S, Odigure J.O and Odili O.C. (2012). Production and Characterization of Biofuel from Refined Groundnut Oil. Energy Conservation, Book Chapter Published by INTECH, Chapter 8, Pp. 197-220.

Alamu, O.J, Waheed, M.A. and Jekayinfa, S.O. (2010). Biodiesel production from Nigerian palm kernel oil: effect of KOH concentration on yield. *Energy Sustainable Development*. Vol. 11 (3), 77-82.

Bello E.I and Daniel, F (2015). Optimization of Groundnut Oil Biodiesel Production and Characterization. *Applied Science Reports*, Vol. 9 (3), 172-180

Bello EI and Agge M. (2012). Biodiesel Production from Ground Nut Oil. *Journal of Emerging Trends in Engineering and Applied Sciences*, Vol.3 (2), 276-280.

AOAC. (2012). Official Methods of Analysis of AOAC international. 19th edition. AOAC 54 International, Gaithersburg, Maryland, US

Ellabban O, Haitham A and Blaaberg, F. (2014). Renewable energy resources:current status, future prospects and their enabling technology. *Reviews*, Vol. 39, 748-764.

Fadhil, A.B., Aziz, A.M. and Al-Tamer, M.H (2016). Biodiesel production from silybum marianum L seed oil with high FFA content using sulphonated carbon catalyst for esterifcation and base catalyst for tranesterification. *Energy Conversation Management*, Vol.108:255-65

Jazie A., Pramanik H. and Sinha, S.S.K. (2013). Eggshell as Eco-Friendly Catalyst For Transesterification of Rapeseed Oil: Optimization for Biodiesel Production. *International Journal of Sustainable Development and Green Economics*, Vol. 2, 2315-4721.

Karmakar A., Karmakar S. and Mukherje S. (2010). Properties of various plants and animals

feedstocks for biodiesel production. *Bioresource Technology*, Vol.101, 7201-7210.

Leandro MC, Juan AC, Enrique RC, Célio LC,1 and Rodrigo SV (2017). Relevance of the Physicochemical Properties of Calcined Quail Eggshell (CaO) as a Catalyst for Biodiesel Production. *Journal of Chemistry*, Vol, Article ID 5679512, 12 pages

Lee H.V., Yunus R., Juan J.C. and Taufiq-yap Y.H. (2011). Process optimization design for jatropha-based biodiesel production using response surface methodology. *Fuel Processing*, Vol.92, 2420-2428.

Mohadi R, Anggraini K, Riyanti F, Lesbani A (2016). Preparation Calcium Oxide (CaO) from Chicken Eggshells. *Journal of Environment*, Vol.1(2): 32-35

Muthu K and Viruthagiri T (2015). Optimization and production of biodiesel using calcium oxide as a heterogeneous catalyst. *Int. J. Chem. Sci*, Vol.13(3): 1357-1364

Navajas A, Issariyakul T, Aramendi G, Gandia L.M, Dalai A.K. (2013). Development of egg shell derived catalyst for transesterification of used cooking oil for biodiesel production. *Asia-Pac. J. Chem. Eng*. Vol. 8, 742–748

Nakatani N, Takamori H, Takeda K, Sakugawa H. (2009). Transesterification of soybean oil using combusted oyster shell waste as a catalyst. *Bioresources Technology*, Vol. 100,1510–1513.

Niju S, Meera S, Begum KM, Anantharaman N. (2014). Modification of egg shell and its application in biodiesel production. *Journal of Saudi Chemical Society*, Vol. 5, 702–6.

Ojolo SJ, Adelaja AO, Sobamowo GM (2011). Production of Bio-Diesel from Palm Kernel Oil and Groundnut Oil. *Advanced Materials Research*, Vol. 367, 501-506

Ramezani K., Rowshanzamir S. and Eikani, M.H. (2010). Castor oil transesterification reaction: a kinetic study and optimization of parameters. *Energy*. Vol. 35, 4142-8

Renita A, Chowdhury P.P, Sultana P, Phukan P, Hannan A (2016). Utilization of waste eggshells for production of renewable catalyst for transesterification. *International Journal of Pharmacy and Pharmaceutical Sciences*, Vol 8(7), 143-146

Sharma Y.C. and Singh B. (2010). Development of biodiesel: current scenario. *Renewable and Sustainable Energy Reviews*, Vol.13, 1646-1651.

Suleiman M.M, Bello A.U., Itumoh J.E, Bello K , Bello A.M and Arzika A.T. (2012). Physicochemical properties of some commercial groundnut oil products sold in Sokoto metropolis, Northwest Nigeria. *Journal of Biological Science and Bioconservation*, 4: 23-34

Wei Z, Xu C, Li B. (2009). Application of waste eggshell as a low cost solid catalyst for biodiesel production. *Bioresources Technology*, Vol.100, 2883-5.

LEARNING ABOUT R&D ORGANIZATIONS IN NIGERIA: PLACING THE RESEARCH OFFICER AT THE CENTRE OF INNOVATION EXPERIENCE

M. K. Idris[1*] I. Zakari [2], M. Salisu [3]

[1,2,3]Scientific Equipment Development Institute, Minna. Niger State, Nigeria.
* Juma2i@yahoo.com, 08075756727

Abstract

Nigerian's economy depends heavily on developed indigenous technologies expected from R&D organizations. The main aim of this paper is to examine and place Nigeria's research officers' experiences in the light of delivering innovative products and services. Four case examples were used to examine and position the research officers which are: Bernard O. *et al.* (2014) of Scientific Equipment Development Institute (SEDI) Minna that design and locally develop porcelain insulator; Ibrahim A. M. D. *et al.* (2016) locally design and develop crude oil refinery in chemical engineering department, Ahmadu Bello University (ABU) Zaria; formidable team of GOLDFIRE NIG. LTD that assist organizations to offer themselves to the receiving public using the offerings of present marketing tools and The National Agency for Food and Drug Administration and Control (NAFDAC) zero tolerance to counterfeit drugs, by enforcement and implementation of the Mobile Authentication Service (MAS) by pharmaceutical companies nationwide, able introduced since 2010 by then NAFDAC's Director-General, Dr. Paul Orhii. Critical analysis exposes challenges that include lack of training & retraining, lack instrumentation, inadequate funding, constraints in dissolution of outputs, lack genuine collaboration and troubled research environment. It also reveals how Nigeria's research officers undertake their research adventures and two basic R&D structures do exist in Nigeria with case examples 2&3 as a model staffed primarily by engineers. Meanwhile case examples 1&4 illustrate the other model composed of industrial scientist to facilitate development of products. Recommendations were made to alleviate the challenges for better performance.

Keywords: engineers, R&D organizations, R&D structures, research officer, scientist

1. INTRODUCTION

The future for the Nigerian economy heavily depends on its ability to acquire and apply technology indigenously to produce goods, processes, devices and provide services. These indigenous technologies are expected from R&D activities undertaken from National Innovation System (NIS) composed of ministries,

departments and agencies, tertiary institutions, research institutions/centres, financial institutions, the industry, civil society organisations individual researchers, inventors and traditional knowledge. The new approach to R&D is now coined as responsible research and innovation which is an approach that anticipates and assesses potential implications and societal expectations with regard to research and innovation, with the aim to foster the design of inclusive and sustainable research and innovation (Nicoleta, 2015). Responsible Research and Innovation (RRI) implies that societal actors (researchers, citizens, policy makers, business, third sector organisations, etc.) work together during the whole research and innovation process in order to better align both the process and its outcomes with the values, needs and expectations of society. Scientific form of research relies on application of scientific method in harnessing curiosity, which makes practical application possible. This form of research has brought about what is today referred to as Science Technology & Innovation (STI) the hallmark of practical human civilization that has presently make developed countries like US, China, Japan, Germany etc. to enhance its per capital output which by implication guarantee sound economies of their individual countries. Nigeria is not left behind in this endeavour as it identified that with establishment of Cocoa Research Institute (CRIN) Ibadan under degree 33 of 1964, today there are several public research institutes in Nigeria trying to achieve dedicated mandates e.g. mother ministries like Science and Technology. Agriculture, Education, Health e.t.c. several tertiary institutions from University, Polytechnic and Monotechnics with research institutes/centres such as RMRDC, NARICT, FIIRO, NOTAP, NASENI, SEDI-M among others (Idris, 2015). However Nigeria's Federal Executive Council (FEC) believes that research must utilize our universities and also research must be linked to the private sector. So they agreed that there is a need to rationalize some of the agencies and also see which of those research agencies could be better placed under the auspices of existing universities to perform better. They further believe research centres should also concentrate on new ideas, new technologies, new researches, and the application of result of research also should be driven by industry in order for this to come to fruition. The council also set up a committee which is to be chaired by the minister of national planning to again look at the section of the report that has to do with research agencies, institutes and research centres spread across the country Channels Television **(2013)**. As well articulated the assessment of then FEC may look, the reality of how to achieve the feet on R&D mandates as expected, is hinged on the research officers in R&D organizations. The main aim of

this paper is to examine and place the research officers' experience in Nigeria on the light of delivering the research and innovation deliverables to enhance per capital output of Nigeria for sound economy.

Research Officer Duties and Requirements

Defining who research officer is paramount as a basis to place the personnel in R&D organization as pivot that drive the essence of that corporate existence. The phenomena called research officer can be adjudge as a scientist, who would plan and carry out experiments and investigations to broaden scientific knowledge in a range of areas, from life sciences to industrial processes https://nationalcareersservice.direct.gov.uk/job-profiles/research-scientist (2013). If you have an enquiring mind, and would like to be at the forefront of scientific discovery, this could be the career for you. As a research scientist you may work in industry, research and development (R&D) for a university research department, in government labs or for defense companies. The officer can work in one of the subject areas covered by scientific research, such as life sciences; earth sciences; medical science; physical sciences; industrial science; research and development in the textiles industry among others[4]. The nature of the work will depend on your specialization, but may include:

- drawing up research proposals and applying for funding
- planning and carrying out experiments
- keeping accurate records of results
- analysing results and data
- presenting findings in scientific journals, books or at conferences
- carrying out fieldwork (collecting samples and monitoring environmental factors)
- developing new products or ways of applying new discoveries
- improving manufacturing production methods
- testing products or materials
- teaching or lecturing

Expectedly will work in a team with other scientists, technicians and support staff, in a typical organization https://nationalcareersservice.direct.gov.uk/job-profiles/research-scientist (2013).

Research Officer at work in Nigeria

According to Savage and Skerry (1990) the ultimate outcome of technological activity is the solution derived from the problem-solving activity undertaken by humans through the use of technological processes and resources[5]. This is evident in the formulation of the various mandates of the research institutes, university research departments, industry and government labs in Nigeria as the research officers depending on specialization, tried to be on course.

Case example 1

Bernard, Ndayako and Bashir. (2014) design and locally develop porcelain insulator. The principal researcher in this project is Bernard Oche the sectional head (Ceramics) with team of scientist and engineers at Scientific Equipment Development Institute Minna, Nigeria.

Special formulation of ceramic body for porcelain insulator was undertaken by the research team and the raw materials sourced locally comprises of plastic clay, feldspar, kaolin, talc, water, soda ash, sodium silicate, quartz sand etc., were charged into the ball mill for slip production after undergoing beneficiation process. The slip obtained was sieved then stored in the storage tanks for maturity for readily flowable suspensions called slurry or slip as produced. The suspension was then poured into already made porous plaster moulds where capillary forces suck the water into the moulds from the slip. After a sufficient thickness of deposit has been obtained, the excess slip wash-drained and the moulds opened to reveal free standing clay pieces of

porcelain that was dried, glazed and fired in a klin at 1,200˚C. After the production of electrical porcelain the procedure to obtain mancap standard certification from Standard Organization of Nigeria (SON) was initiated but could not succeed as SON lack the capability to undertake the require test which includes:

1. Dielectric test
2. Flash over voltage
3. Any other possible electrical test

Alternatively SON insists on field test of the porcelain insulator in the six geo-political zones of the country which is presently being look into[6].

Case example 2

(Ibrahim A. M. D. *et al.*, 2016) locally design and develop crude oil refinery. The team leader of the project, Professor Ibrahim Ali Muhammad Dabo is of Chemical Engineering, Ahmadu Bello University Zaria.

The idea of the mini refinery was conceived about 15 years back, but work commenced fully in the year 2011. With the cooperation of the university management, a special security team was deployed to the site of the refinery. Since the commencement of the work in 2011, movement around the area was restricted and findings showed that they kept the project a secret in order to avoid unnecessary distractions[7]. Initially to construct a 1,000 barrel-capacity refinery with more than 80 per cent of the materials used for the construction of the refinery were sourced locally where the controls were sourced from Hong Kong. No expatriate was hired from abroad, all those that were engaged in this project are Nigerians and due to lack of funding ended up with a refinery with capacity to process one barrel of crude oil per day. Beside the land and fencing that ABU provided, the project cost only about N20 million[7]. After the successful completion of the work and the first test-run of the refinery, the developers said it would be used mainly for the training of students, although the department had the manpower to build a refinery that would be bigger than that of Kaduna (capacity of 110,000 BPSD) if it had government support https://gistgalleria.wordpress.com/2016/11/14/abu-zaria-builds-one-barrel-per-day-refinery/.(2017)

Case example 3

GOLDFIRE NIG. LTD. is a Graphics Communications company in Nigeria. It primary focus is on the primary elements that assist organizations to offer themselves to the receiving public using the offerings of present marketing tools.

The company is transforming the concept of Signage and signage related products in Nigeria. The company has within its years of operation, been involved in diverse and ambitious signage projects all over the length and breadth of this country[8]. Goldfire has also manufactured and installed signage elements outside the shores of Nigeria; In Ghana, Republic of Benin, Cote d'ivoire & Burkina Faso. With it collaboration with sister company Liquidfire Engineering Services with core operation in the design and fabrication of secured ATM Kiosks, mobile kiosks, Portacabins e.t.c., which are used for site offices, schools, event halls, temporary and permanent structures, health centres and many more uses. The companies are both base in Ijora, Lagos State, Nigeria http://goldfirenigeria.com/about-us/(2016)

Figure I: Images of some innovative branding by GOLDFIRE http://goldfirenigeria.com/about-us/(2016)

The two sister companies have developed a brand re-positioning process, (through the establishment of business relationship with likeminded organizations) that encompasses a complete process, ranging from ideas development, to brand conceptualization, actual signage manufacture and presentation, and finally to installation/roll-out logistics. They do not only manufacture quality signages, but we carry out premium exclusive nationwide installation for major brands in the petroleum, marketing, banking and hotels &amp leisure sectors in Nigeria http://goldfirenigeria.com/about-us/(2016).

Case example 4

The National Agency for Food and Drug Administration and Control (NAFDAC) on zero tolerance to counterfeit drugs, by enforcement and implementation of the Mobile Authentication Service (MAS) by pharmaceutical companies nationwide.

The enforcement operation which started in Abuja on Wednesday, 2nd July, 2014 under the auspices of the Pharmacovigilance and Post Marketing Surveillance Directorate of NAFDAC was geared towards mopping up from circulation all anti-malarial and anti-biotic medicines that do not carry on their labels, the MAS scratch and text authentication codes which were introduced since 2010 by NAFDAC's Director-General, Dr. Paul Orhii to save consumers from the menace of fake drugs[9]. The scratch and text service (MAS) has put the power of detecting counterfeit drugs in the hands of over 100million mobile phone users in the country, with international community full of commendation for Nigeria for pioneering the use of cutting-edge technologies in combating counterfeit medicines http://www.nafdac.gov.ng/index.php/component/content/category/187-nafdac-innovations (2014).

Diffusion of innovations in Nigeria

A professor of communication studies Everett Rogers argues that diffusion is the process by which an innovation is communicated over time among the participants in a social system. Rogers proposes that four main elements influence the spread of a new idea: the innovation itself, communication channels, time, and a social system where descriptions of the categories have remained similar throughout his editions of papers on this theory as shown in the figure 1

Figure 2: Categories in the process of innovation decisions Sociological theory of diffusion (2014)

There are two basic R&D structures that have emerged in companies throughout the commerce spectrum for which Nigeria is not an exception. One R&D model is a department that is staffed primarily by engineers who develop new products, a task that typically involves extensive research which is institutionalized by the case example 2 and 3 mentioned above. The examples clearly show the knowledge and persuasion of the research deliverables i.e local crude oil refining capability and signage/branding expertise respectively. GOLDFIRE NIG. LTD. not being a government research organization makes decision faster in terms of showcasing and winning customers to contribute efficiently to science and technology innovation in Nigeria, making the implementation and confirmation possible. The research officers in this organization are inspire to continue to innovate in accordance to local operating environment which is confirmed by catchment area the company is able conquered such as Nigeria, Ghana, Republic of Benin, Cote d'ivoire & BurkinaFaso. Interestingly, this R&D organization help to saves the country the importation of this particular innovation and guarantee continuity, employment opportunity and consequently contribute to per capital output of Nigeria by operating in Nigeria and exporting its expertise to the neighboring countries. Chemical Engineering department of Ahmadu Bello University Zaria which is a government research organization in the pool of universities in Nigeria, makes its innovation of developing local construction of the refinery with 80 per cent of the materials used sourced locally with remaining 20% which are the controls sourced from Hong Kong as a unique research output. The knowledge of this innovation may be good enough but the persuasion may be in doubt to either get the government or university authorities to take decisive action on this very laudable project. Although since November, 2016 when the result of the innovation is made public, the pending decision to implement and confirm this research output reside with government in need of local refining capacity with a readymade market to diffuse the deliverable. The hope is that the research output will not go the of Professor Idris Bugaje led project, the present director-general of the National Research Institute for Chemical Technology (NARICT), who supervised a PhD student in the same department in ABU to construct a water treatment plant using moringa seeds, but that breakthrough is yet to be fully utilized. Also, results of many researches in the university are yet to be utilized. The other model involves a department composed of industrial scientists or researchers, all tasked with applied research in technical, scientific or industrial fields, which is aimed at the facilitation of the development of future products or the improvement of current products and/or operating procedures which is illustrated by the case example 1 and 4 aforementioned. Scientific Equipment Development Institute (SEDI) Minna, Nigeria through its research officers came up with an outstanding innovative product (local production of porcelain insulator) but has not gone to the next stage of decision process due to inefficiency of Standard Organization of Nigeria (SON) to have instrumentation in order to confirm the knowledge locally. This will aid in the persuasion for decision to be made for implementation and confirmation to diffuse it into the market to improve per capital output. Meanwhile the other case example that fit into this model is that NAFDAC innovative product of Mobile Authentication Service (MAS). For a government laboratory the organization use this deliverable to prevent making Nigeria a dumping ground all sort of anti-malarial and anti-biotic medicines that do not carry on their labels, which do not only prevent fake drugs being use by Nigerian populace but in the long run create opportunity for pharmaceutical companies to manufacture this drugs locally that will contribute substantially to per capital output.

Challenges

Employers in both government and non government R&D organizations seek motivated individuals with good research, information, organizational, numerical, analytical, communication, interpersonal and teamwork skills for their corporate fulfillment. Knowledge and experience of social research methods, statistical techniques, social policy and specialist computer software including databases is usually required. To achieve all this attribute in a research officer requires deliberate policy for which in Nigeria's terrain is face with challenges as follows:

Training and re-training: Research officer is a principal investigator with all aspects of the development and implementation of a research program. This task entails a variety of functions, including collecting and processing field data for the fulfillment of the survey components. These requirements need special training tailored towards knowing basics in pool of knowledge not minding specialized degrees in field of study so as to be equipped. Therefore accomplished research officers should be made trainers in universities to catch them young and retraining to shaping their knowledge when employed in R&D organization, which is missing as it make research officers to be deficient and lack the basics in the field work. This was shown in the example cases that no enough young research officers communicating their innovations.

Lack of instrumentation: The case example 1 illustrated the frustration of research officers in the course of innovations as it has to follow lay down standard procedures. The procedures can only be confirm using instrumentation which presently have to be imported, that make it capital intensive and where there available expertise and accessories are missing making them not usable.

Inadequate funding: The case example 2 indicated that research officers in Nigeria have no enough accessibility to funds not minding how laudable the projects are. This makes the R&D corridors in the country inactive that allow continuous production of what is available and the snatched without stiff completion by imported innovative technologies causing capital flight and brain drain.

Constraints' in dissolution of research output into market: out of the four case examples only example 3 and 4 are dissolute attributed to being private organization driven and the strategic importance of the rampant health conditions Nigerians found themselves respectively. The decision makers do not consider the other priority as it can easily be imported but losing out in contributing to per capital output of Nigeria for sound economy.

Lack of genuine collaborations: Case example 3 proves the enormous benefits accruable in collaborating to achieve common corporate objectives. The research officers in these organizations require the expertise of each other in order to come out with sound research outputs that can penetrate the market.

Creation of enabling environment: None of the case examples is borne out of deliberate effort made by government to bring together innovators by the establishment of avenues such as technological parks. This has the tendency to provide a fertile ground for small and medium scale enterprises (SMEs) that the Nigeria economy urgently need to fuel and get out of recession.

Conclusion

This research work reveals that:

1. **The four (4) case examples taken shows in clear terms how Nigeria's research officers in R&D organizations undertake their research adventures to actualize individual corporate mandates.**
2. **Case examples 2&3 shows indecision and confirmation respectively in terms of decision on the innovation processes. Although the R&D model of the two examples is same, the fact that case example 2 is public and case example 3 is private driven make all the difference.**
3. **Comparable, the two basic R&D structures do exist in Nigeria with case examples 2&3 as a model staffed primarily by engineers. Meanwhile case examples 1&4 illustrate the other model composed of industrial scientist to facilitate development of products.**
4. **Research officers in Nigeria's terrain is face with challenges that include but not restricted to training/retraining; lack of instrumentations; inadequate funding; constraints in dissolution of**

research outputs into the market; lack of genuine collaborations and non availability of enabling environment.

Recommendations

1. **The basic knowledge of R&D should be introduce as a course as early as first semester in the final year degree program, while in the same vain R&D organizations should endeavor to give new employees orientations.**
2. **R&D organizations should be made to target local development of instrumentations to enhance their availability and avoid capital flight.**
3. **As it is obtainable in nations where STI are taken with sense of relevance, research funds are made a budgetary provision as a matter of necessity.**
4. **Strategic plan be made by government to bridge the gap between innovators and entrepreneurs through enabling laws and avenues like grand exhibitions to attract them to each other.**
5. **The R&D organizations must allow MoUs between them by using each other's strength of expertise for the mutual benefits of both parties.**
6. **Establish technological parks in strategic areas in the Nation that will be more efficient than the present incubation centers to encourage SMEs to strive.**

References

1. nicoleta susanu @NicoletaSusanu, EuropeanUnion #horizon2020#brussels (accessed May 16, 2015).

2. Idris M. K. (2014) challenges facing research institutes in Nigeria: a case study of Sedi – Minna. Presented at the Quarterly lecture series of NIGERIAN SOCIETY OF ENGINEERS MINNA BRANCH. On 27th march 2014 at NSE Minna branch office.

3. Channels Television **(2013)** Nigeria Insists On Scrapping Research Institutes, Other Federal Agencies Posted by: Channels Television Posted date**: June 26, 2013** In: Current**,** Headlines

4. https://nationalcareersservice.direct.gov.uk/job-profiles/research-scientist last updated: 07 December 2016 (accessed Feb. 13, 2017).

5. Savage, E., & Skerry, L. (1990). A conceptual framework for technology education. Reston, VA: International Technology Education Association.

6. Bernard O., Ndayako M. and Bashir K. (2014) Research and Publication Committee, Scientific Equipment Development Institute Minna. Technical paper presentation series, held

on 20/10/16.

7. https://gistgalleria.wordpress.com/2016/11/14/abu-zaria-builds-one-barrel-per-day-refinery/ Source: Daily Trust (accessed Feb. 20, 2017).

8. http://goldfirenigeria.com/about-us/ Posted date: Monday, 14 July 2014 14:22

9. http://www.nafdac.gov.ng/index.php/component/content/category/187-nafdac-innovations (accessed Feb. 20, 2017).

CONTAMINATION RISK ASSESSMENT OF PHYSICO-CHEMICAL AND HEAVY METAL DISTRIBUTION IN WATER AND SEDIMENTS OF NEW CALABAR RIVER, EASTERN NIGER DELTA, NIGERIA

[1]Nwankwoala, H.O.,[1]Angaya, Y.B., [2*]Amadi, A.N. and Ameh, I.M.
[1]Department of Geology, University of Port Harcourt, Nigeria
[2]Department of Geology, Federal University of Technology, Minna, Nigeria
*Corresponding Author: nwankwoala_ho@yahoo.com or geoama76@gmail.com

Abstract
This study is aimed at assessing geo-environmental risk of physic-chemical and heavy metal distribution in water and sediments of New Calabar River, Eastern Niger Delta. Seven (7) river sediments and twelve (12) surface water samples were collected for the study. Heavy metals (Mn, Pb, Zn, Fe, Mg, Cd, Cr, and Cu) were tested for in both river sediment and surface water. Heavy metals were analysed in river sediments, so as to determine their Contamination Factor (CF), Pollution Load Index (PLI) and Geo-accumulation Index (I_{GEO}) within the study area. W.H.O. limits were also used in evaluating Pollution Index (P_I) of heavy metals in surface water. The Pollution Load Index (PLI) level of river sediments ranged from 5.12-33.26; considering the fact that only PLI values <1 was considered unpolluted; all samples analyzed showed high pollution levels. Of all the heavy metals, Cu, Mg, Cr and Mn had moderate to considerable CF levels, while the others were of low levels. I_{GEO} levels were all <1, indicating low levels. For surface water, Pb and Zn had the worst Pollution Index values, with Pb having P_I values ranging 10-211. There was considerable contribution of pollutants from human activities into the river. Discharge from municipal storm water into the river, and the continued corrosion of sea vessels abandoned along the river flow path have been established. It is recommended that regulatory bodies responsible for protecting the environment pay adequate attention to this stretch of the river.

Keywords:*Risk assessment, contamination, heavy metal, pollution index, New Calabar River, Eastern Niger Delta, Nigeria*

1. Introduction

Heavy metal pollution is prevalent in the environment and it usually results from numerous activities and sources such as discharge of untreated effluent from industries, foundry waste, paints, auto-mobile fumes, mining cuttings, and rock weathering (Don-Pedro *et al*., 2004). The major concern with regards heavy metals is their hazardous acute toxicity and ability to bio-accumulate in the human tissue (Otitoloju and Don-Pedro, 2002). Heavy metals are considered to be the most common environmental pollutants, and their occurrence in waters and biota indicate the presence of natural or anthropogenic sources (Mohiuddin*et al*, 2015). Solid wastes can contribute to forms of pollution that are hazardous to human health. Leachate generated from within the waste heap is a source of inorganic and organic hazardous substances that can migrate with the flow of storm water to contaminate both surface and groundwater (Leton, 2013).Akaninwor*et al* (2006) dwelt on pollution by microbial agents, which were most likely caused by the discharge of industrial effluent by Indo-Food Company (Dufil Prima Foods). The study was centred around five (5) sampling stations for surface water of the New Calabar River.Onuoha and Ifeanacho (2015) went further by studying the effect of effluent from Indomie Food Comapany (Dufil Prima Foods) on the biochemical parameters of Tilapia fish from the New Calabar River in which Potassium ion (K^+), Chloride ion (Cl^-), Sodium ion (Na^+), Urea and Creatinine concentrations were measured in the blood, liver, gills and muscles of fishes.

Theodore and Chikwuogwo (2014) studied human and ecological threats to water and sediment of the New Calabar River, using the ChrysicthysNigrodigitus species fish as a biomarker for the quality of the environment.Uzukwu*et al* (2014) investigated the physical characteristics and physico-chemical qualities of the Upper Reach of the New Calabar River, around Aluu. The highest recorded depth at the middle of the river was 9.20m, while its width during the spring high and low tide were 174 and 110m, respectively. The measured cross-sectional area and average flow velocity of the river were 797.13 m^2 and 0.374 m sec^{-l}, respectively. The physico-chemical parameters analysed showed that the river water had an acidic pH value (5.12-7.43).Mmom and Chukwu-Okeah (2011) assessed the impact of sand dredging activity on channel morphology, and the

broader implications on biological resource conservation along parts of New Calabar River. Abu and Egenonu (2008) investigated the incidence of environmental pollutants on bacterial strains isolated from the New Calabar River and ascertained the possible effects of those suspected pollutants on antibiotic resistance and patterns.

The New CalabarRiver and its tributaries are all located in Rivers State. It is a low lying deltaic river which rises at approximately latitude 5˚10'N and longitudes 6˚50'E near Elele-Alimini and flows Southward for roughly 150km before its discharge into the Atlantic Ocean at about latitude 4˚20'N and longitudes 7˚00'E (Francis and Elenwo, 2012). It occupies a low relief region, ranging from 0-50m above sea level at the low zone, to 50-100 above sea level at its source. The soil of the river basin consists of clays, silt and sand, with high organic matter (Theodore and Chikwuogwo, 2014). The river is unidirectional in the upper reach and tidal in the lower reach. Its upstream reach is fresh water with tropical lowland, dense rainforest through secondary forest/farmland vegetation. The downstream reach is however brackish and consist of Mangrove swamp forest.As human population increases geometrically, so also does the need for development that meets the needs of the populace increases. Development in the form of urbanisation and industrialisation, if not checked, has the potential of negatively altering the quality of the environment. In order to maintain the delicate relationship between human development and the quality of the environment, there is need for constant monitoring and evaluation of human activities that have the potential of altering the quality of the environment within which such activities occur.

2. Literature Review

2.1 The Study Area

This study was carried out in Obio-Akpor Local Government Area of Rivers State (Fig. 1), between the months of February and April 2016. Obio-Akpor alongside the Port Harcourt Local Government Area forms the Port Harcourt Urban Area (the metropolis). Rivers State is located in the South-South geopolitical zone of Nigeria and the eastern sector of the oil-rich Niger Delta region of the country. Port Harcourt doubles as the Capital City of Rivers State, and also the largest city in the State. The Port Harcourt urban area has a total population figure of 1, 382, 592 (2006 Census). Obio-Akpor Local Government Area is one of the eight (8) Local Government Areas that forms the Greater Port Harcourt urban area, namely: Port Harcourt, Okrika, Obio-Akpor, Ikwerre, Oyigbo-Bolo, Tai and Eleme Local Government Areas respectively. As at 2012, the Greater Port Harcourt urban area had an estimated total population of 1,947,000 (Nigerian Administrative Division: City Population). This made it the 5th largest urban area in Nigeria; only after Lagos, Kano, Ibadan and Abuja. Port Harcourt has a tropical monsoon climate; having a lengthy and mostly heavy rainy seasons and very short dry seasons. December and January are the only months that truly qualify as dry season months, with December averaging 20mm of rain (Chinda, 1998). The city's heaviest precipitation is usually recorded in the month of September (averaging 367m of rain). The average annual temperature value in the city is typically between 25˚C-28˚C (Nwankwoala, *et al.*,2016). The most dominant economic activity in the study area is centred on the Petroleum Industry. Many Multi-National companies that are into Production and Servicing operations in the Petroleum Industry operate in the State. Rivers State does not only host Multi-National Oil Companies, it also hosts two (2) oil refining facilities. Due to its strategic location, Rivers State is among the richest states in Nigeria; in terms of Gross Domestic Product and revenue derived from Foreign Exchange earnings of the Oil Industry. The State has crude oil as its principal export earner. The major cash crops cultivated are rubber, oil palm products, raffia, coconut and jute. Others that cultivated for food are melon, vegetable, pineapple, banana, mango and plantain (Rivers State Government: People and Culture). The locals however in engage in fishing, hunting, lumbering and petty trading.

2.2 Geology of the Study Area

Port Harcourt is located within the oil-rich Niger Delta sedimentary basin. Generally, the basin consists primarily of regressive sediments which are of Tertiary age. The detailed geology of the lithostratigraphic subdivision of the Niger Delta basin was given by Short &Stauble (1967). The Niger Delta basin is one of the most prolific hydrocarbon systems in the world. The delta was formed at the site of a rift triple junction that is related to the opening of the Southern Atlantic; starting in the late Jurassic, continuing into the Cretaceous. The coastal sedimentary basins of Nigeria have witnessed three depositional cycles. The first depositional cycle began with a marine incursion in the middle Cretaceous, which was terminated by a mild folding phase in the Santonian. The second cycle is identified by events leading to the growth of a Proto-Niger Delta during

the late Cretaceous, ending in a major marine transgression in the Paleocene. The third cycle stretched from Eocene to Recent, marking the continuous growth of the main Niger Delta. A threefold subdivision is established for the lithostratigraphic units of the Niger Delta subsurface. These units occur throughout the Niger Delta basin; with ages ranging from early Tertiary to Recent. They are related to the present outcrops and environment of deposition (Short and Stauble, 1967). The Benin flank is regarded as the northern boundary of the Niger Delta; which is an east-north-east trending hinge line which lies south of the West African basement massif. The basin's north-eastern boundary is defined by outcrops of the Cretaceous on the Abakaliki High and also further east-south-east by the Calabar Flank (a hinge line bordering the adjacent Precambrian).The Tertiary portion of the basin is subdivided into three distinct formations, representing a prograding (regressive) depositional facies which are distinguished by their sand-shale ratio.

(1) The Akata Formation**:** This formation lies at the base of the basin, which is of marine origin; composed of low density, high pressure shallow marine to deep water thick shale sequence (Shield, 1978). Beginning in the Paleocene and through to the Recent, the Akata Formation formed during lowstands, when terrestrial organic matter and clays were transported to deep water areas that are characterized by low energy conditions and anoxic settings. The formation underlies the entire stretch of the delta and it's typically over-pressured. During the development of the delta, the deep sea sands of the upper Akata were most likely deposited by turbidity currents.

(2) The Agbada Formation: This consists of paralicsiliciclastics over 3700 meters thick and represents the actual deltaic portion of the sequence. The formation is entirely an alternating sequence of deltaic (fluvial, coastal, fluvio-marine) sands and marine shale. In the lower Agbada Formation, shale and sandstone beds were deposited in equal proportion. However, the upper coastal portion is mostly sand with minor shale interbeds (USGS, 2009).

(3) The Benin Formation:This formation consists of freshwater continental (fluviatile) deposits, comprising of alluvial and upper coastal sands and gravel with occasional clay layers. The formation has a thickness of 2100 meters at the basin center (Weber and Daukaru, 1975).

3. Methods of Study

Standard field sampling techniques were adopted for the sample collection exercise. The sampling exercise for the work was carried out on two different trips, which were weeks apart. The first sampling trip was aimed at obtaining sample from the effluent fallout point along the New Calabar River. The second sampling trip involved sampling both surface water and river sediment also along the New Calabar River. Due to the riverine nature of the sampling locations, transportation from one location to the next was achieved by the use of a paddling boat.

3.1 Effluent Fall-out Area Sampling

At the fallout point, sample was collected in the capped, transparent, sterilized polyethylene container; which was already labelled prior to sampling. The sample container was sealed-off in an air-tight way, immediately after sampling. The sealing of the sample container was done so as to avoid aerobic reaction or contamination by atmospheric agents (which could be biotic or abiotic).

3.2 Surface Water and River Sediment Sampling

The sampling exercise for surface water and river sediment started off with sampling for river sediments first. This approach to sampling was adopted due to a time sensitive phenomena typical of that part of the New Calabar River. The New Calabar River, around the Choba bridge axis of the East-west road is usually in a regressive position at its banks in the early hours of the day. Towards noon, the level of water at the bank of the river starts rising, thereby flooding portions of its banks that were earlier exposed in the morning hours. As such, river sediment sampling at those sites were only possible in the early hours of the morning. The sediments collected were a mixture of sandy, muddy and clayey sediments. Table 1 shows the coordinates and elevation of sampling locations while Figure 1 is the map of study area showing sampling points.The flow direction of the river influenced the decision to start sampling for surface water at the farthest location of sampling river sediment. The sampling of surface water from the farthest location, then moving up towards the take-off point ensures adherence to the best sampling technique for surface water. This choice ensured the

movement of the boat while sampling was to guide against the flow direction of the river. This made sampling of surface water from an undisturbed flow, possible.

Table 1: GPS Coordinates and Elevation of sampling locations

RIVER SEDIMENT			
S/N	Sample ID	GPS Coordinates	Elevation
1	SD. L_1	N 04.89621˚ E 006.90061˚	1m
2	SD. L_2	N 04.88980˚ E 006.89907˚	2m
3	SD. L_3	N 04.88925˚ E 006.89564˚	4m
4	SD. L_4	N 04.88671˚ E 006. 89471˚	0m
5	SD. L_5	N 04.88392˚ E 006.89209˚	4m
6	SD. L_6	N 04˚ 52’ 50.6” E 006˚ 53’ 49.8”	2m
7	SD. L_7	N 04.86988˚ E 006.90355˚	3m
SURFACE WATER			
S/N	Sample ID	GPS Coordinates	Elevation
1	SW. L_1	N 04.86821˚ E 006.90381˚	3m
2	SW. L_2	N 04.87057˚ E 006.90191˚	3m
3	SW. L_3	N 04.87315˚ E 006.90018˚	3m
4	SW. L_4	N 04˚ 52’ 34.3” E 006˚ 53’ 55.45”	2m
5	SW. L_5	N 04˚ 52’ 43.7” E 006˚ 53’ 50.7”	3m
6	SW. L_6	N 04˚ 52’ 51.0” E 006˚ 53’ 45.1”	2m
7	SW. L_7	N 04˚ 52’ 57.9” E 006˚ 53’ 40.4”	2m
8	SW. L_8	N 04˚ 53’ 2.62” E 006˚ 53’ 33.1”	3m
9	SW. L_9	N 04˚ 53’ 11.6” E 006˚ 53’ 34.9”	3m
10	SW. L_{10}	N 04˚ 53’ 17.6” E 006˚ 53’ 40.9”	2m
11	SW. L_{11}	N 04˚ 53’ 20.6” E 006˚ 53’ 49.0”	3m
12	SW. L_{12}	N 04˚ 52’ 28.7” E 006˚ 53’ 55.0”	3m
EFFLUENT FALL-OUT AREA			
S/N	Sample ID	GPS Coordinates	Elevation
1	EF	Latitude: 04^0 53’ 18.2”	3m
		Longitude: 006^0 53’ 48.8”	

Note: RS= River Sediment, SW= Surface Water, EF= Effluent Fall-out area, L= Sampling Location

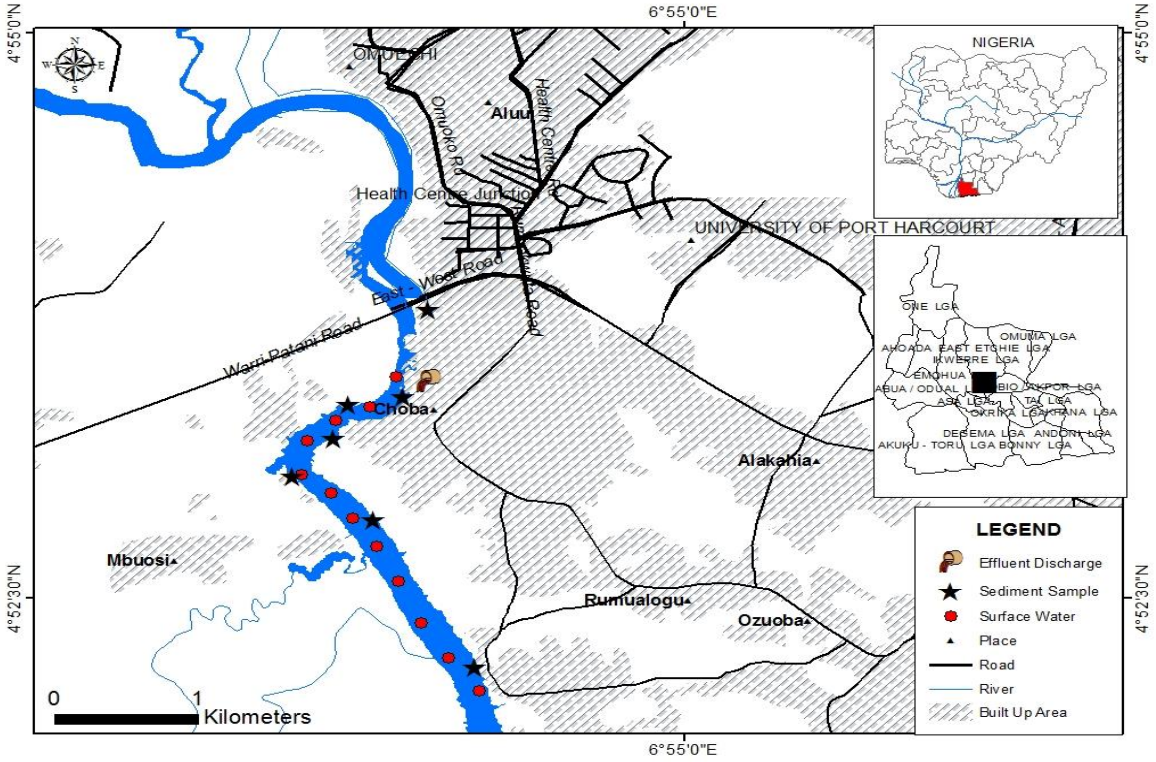

Fig. 1: Map of study area showing sampling points

4. Results and Discussion

4.1 River Sediments and Surface Water

Results from analysis of samples of river sediment and surface water portray a trend of concentration of certain chemical elements which suggests the possibility site specific pollution. As seen from several graphical plots below, the variation of concentrations of parameters across sampling locations were random and only showed a progressively increasing trend between locations 3, 4 and 5 of river sediments. Of particular interest were the levels of Oil and Grease in river sediments from those three locations. In all the heavy metals tested in the sediments, the highest concentrations were all detected between those locations. The river sediments were acidic, with pH values ranging 5.4 - 6.4. Table 2 shows the analytical results of river sediments while Table 3 shows the analytical results of surface water of New Calabar River.

Table 2:Analytical Results of River Sediments in mg/kg

Sample ID	Mn	Fe	Pb	Zn	Cr	Cd	Cu	PO_4	NO_3	SO_4	Mg	TOC (%)	pH	Oil and Grease
SD. L1	10.30	975.0	8.01	25.20	1.71	4.11	23.00	2.32	1.72	1.04	1.17	0.78	5.7	1.43
SD. L2	7.88	218.0	7.42	21.40	1.93	7.50	14.10	1.06	2.11	1.21	1.18	1.76	6.4	1.60
SD. L3	12.60	800.0	15.00	17.20	2.70	5.01	25.10	1.91	3.75	1.76	3.11	5.27	5.8	18.4
SD. L4	8.10	873.0	6.04	27.10	1.83	5.01	21.30	1.52	2.57	0.89	1.21	0.39	5.4	24.5
SD. L5	5.65	477.0	16.50	33.20	2.31	7.82	19.00	1.04	2.34	0.98	2.31	1.37	6.3	23.7
SD. L6	7.38	564.0	14.50	31.10	2.12	4.91	15.30	1.13	1.32	0.56	1.31	0.04	5.7	1.04
SD. L7	6.73	645.0	10.30	25.60	1.87	5.22	13.60	1.43	1.28	0.34	1.02	0.35	5.4	1.02
Minimum	5.65	218.0	6.04	17.20	1.71	4.11	13.60	1.04	1.28	0.34	1.02	0.04	5.4	1.02
Maximum	12.60	975.0	16.50	33.20	2.70	7.82	25.10	2.32	3.75	1.76	3.11	5.27	6.4	24.5
Mean	8.37	650.3	11.11	25.82	2.06	5.65	18.77	1.48	2.15	0.96	1.61	1.42	5.8	10.24
DPR Standard (2002)	_	_	35	_	20	100	0.3	_	_	_	_	_	_	_

Table 3:AnalyticalResults of Surface Water of New Calabar River in mg/l

Sample ID	Mn	Cr	Pb	Cd	Fe	Zn	DO	BOD	COD	PO_4	SO_4	NO_3	TDS	EC (µS/cm)	pH	Oil and Grease
SW. L1	1.24	0.21	0.10	<0.001	2.54	1.08	1.14	2.30	5.01	0.56	0.82	0.09	23.00	5.02	5.7	0.02
SW. L2	1.55	0.01	1.09	0.01	3.60	2.53	2.15	2.98	4.02	0.87	0.73	0.27	28.00	6.74	5.6	0.01
SW. L3	2.38	0.001	0.45	0.01	1.30	0.58	1.57	2.50	4.82	0.82	0.56	0.07	33.40	2.38	6.2	<0.01
SW. L4	2.01	0.05	1.87	<0.001	4.16	1.10	2.38	3.22	3.56	0.96	0.89	0.08	25.60	8.87	5.9	0.02
SW. L5	2.16	<0.001	0.20	0.01	0.97	1.51	1.37	4.10	5.09	0.72	0.67	0.04	37.30	7.07	6.3	0.01
SW. L6	1.85	0.65	2.00	0.03	2.43	1.24	3.13	4.01	4.22	0.55	1.01	0.06	25.20	8.97	5.7	0.01
SW. L7	1.72	0.44	0.10	<0.001	0.27	1.76	2.09	2.89	5.10	0.87	1.03	0.11	33.40	5.02	6.2	<0.01
SW. L8	1.53	0.03	1.30	0.08	0.90	1.80	3.28	4.29	4.77	0.98	0.92	0.24	23.20	8.66	5.8	0.01
SW. L9	2.52	0.10	0.46	<0.001	2.17	0.90	1.49	2.78	3.22	0.59	0.87	0.61	35.30	3.07	5.9	0.02
SW. L10	1.36	0.07	1.55	<0.001	3.40	1.21	1.45	2.36	3.58	0.90	0.76	0.52	24.40	6.88	5.8	0.03
SW. L11	1.38	<0.001	2.11	<0.001	1.25	1.31	1.49	2.15	2.32	0.53	0.64	0.11	27.80	4.12	5.9	<0.01
SW. L12	1.20	<0.001	1.12	<0.001	1.01	1.26	1.18	2.64	3.01	0.61	0.72	0.08	21.20	4.31	6.0	0.01
Minimum	1.20	<0.001	0.10	<0.001	0.27	0.58	1.14	2.15	2.32	0.53	0.56	0.04	21.20	2.38	5.6	<0.01
Maximum	2.52	0.65	2.11	0.08	3.60	2.53	3.28	4.29	5.10	0.98	1.03	0.61	37.30	8.97	6.3	0.03
Mean	1.74	0.13	1.03	0.01	2.00	1.35	1.89	3.02	4.06	0.75	0.80	0.19	28.15	5.93	5.9	0.01
WHO Limits (2011)	0.4	0.05	0.01	0.003	3.00	3.00	N/A	N/A	N/A	N/A	N/A	50	N/A	N/A	N/A	N/A

The surface water showed the most random set of concentrations of the two, which could be attributed to the mobile state of the medium of sampling. The Dissolved Oxygen (DO) range from 1.14mg/l – 3.28mg/l with a mean of 1.89mg/l while the BOD range from 2.15mg/l to 4.29mg/l with a mean of 3.02mg/l. The Chemical Oxygen Demand (COD) range from 2.32mg/l – 5.10mg/l with a mean of 4.06. The amount of Dissolved Oxygen (DO) in the samples, as compared to Biochemical Oxygen Demand (BOD) and Chemical Oxygen Demand (COD) shows a slight pollution of the river water, which would require some time to achieve self-purification. Heavy metal concentrations in the surface water sample were objectionable when compared to the W.H.O. permissible limits for drinking water. Those heavy metals are a great concern for the quality of fish consumed from the river. The pH reading for all the surface water samples were also found to be acidic like those of the river sediments; having pH values ranging from 5.6 - 6.2.

Because the quality of the surface water only gives the momentary quality of the environment, the quality of the river sediment which gives a more definite detail of the quality of the environment is of more importance in interpreting changes in the quality of the environment. Results from sampling and analysis of the river sediment and surface water shows that the chemistry of the two varies distinctly from one location to the other and that certain locations could have been sites of localised pollution (Table 4). Table 5 shows the Pollution Index (P_I) values of sampled surface water while Table 6 shows the contamination factor values for river sediments.

Table 4: Water quality according to pollution index value (GB/T 14848-1993)

Water Quality	Very good	Good	Moderate	Bad	Worst
Pollution Index	<0.80	0.80-2.50	2.50-4.25	4.25-7.20	>7.20

Table 5: Pollution Index (P_I) values of sampled surface water

Sample Locations	Mn	Cr	Pb	Cd	Fe	Zn
SW. L1	3.10	4.20	10.00	0.00	0.84	21.60
SW. L2	3.80	0.20	109.00	3.30	1.20	50.60
SW. L3	5.90	0.00	45.00	3.30	0.43	11.60
SW. L4	5.00	1.00	187.00	0.00	1.30	22.00
SW. L5	5.40	0.00	20.00	3.30	0.32	30.20
SW. L6	4.60	13.00	200.00	10.00	0.81	24.80
SW. L7	4.30	8.80	10.00	0.00	0.09	35.20
SW. L8	3.80	0.00	130.00	26.60	0.30	36.00
SW. L9	6.30	2.00	46.00	0.00	0.72	18.00
SW. L10	3.40	1.40	155.00	0.00	1.10	24.20
SW. L11	3.40	0.00	211.00	0.00	0.41	26.20
SW. L12	3.00	0.00	112.00	0.00	0.33	25.20

Table 6: Contamination factor values for river sediments

Sample Locations	Mn	Fe	Pb	Zn	Cr	Cd	Cu
SD. L1	1.53	1.51	0.77	0.98	0.91	0.78	1.69
SD. L2	1.17	0.33	0.72	0.83	1.03	1.43	1.04
SD. L3	1.87	1.24	1.45	0.67	1.44	0.95	1.84
SD. L4	1.20	1.35	0.58	1.05	0.97	0.95	1.56
SD. L5	0.84	0.74	1.60	1.29	1.23	1.49	1.39
SD. L6	1.09	0.87	1.40	1.21	1.13	0.94	1.12
SD. L7	1.00	1.00	1.10	1.00	1.00	1.00	1.00

Pollution indices for heavy metals in surface water were of significant proportion in most of the locations (Table 4). Manganese (Mn) had pollution index value ranging 3.0 – 5.9, which when compared to the standards, had moderate to bad levels of pollution. Chromium (Cr) pollution levels were slightly insignificant in most of the sampling locations, except for locations 6 and 7 which had pollution index values of 13 and 8.8 respectively. Of all the heavy metals, Lead (Pb) recorded the most chronic levels of pollution across all the sampling locations; having pollution index values ranging from 10 – 211. Next to Lead (Pb) is Zinc (Zn) which also recorded the chronic levels of pollution; ranging 11.6 – 50.6. On the other hand, Iron (Fe) recorded the least levels of pollution of all the other heavy metals, across all the sampling locations; recording 1.3 as its highest pollution index value. Cadmium (Cd) pollution index levels were insignificant in almost all the sampling locations; with locations 6 and 8 recording pollution index levels 10 and 26.6 respectively.

Majority of metals were however of moderate contamination factor levels. Based on the Pollution Load Index, all the sampled locations were found to be polluted; with locations 3 and 5 being the most polluted. Figure 2 is the plot of pH levels in river sediments while Figure 3 is the plot of pH levels in surface water. Figure 4 shows pollution load index and figure 5 shows heavy metal concentration.

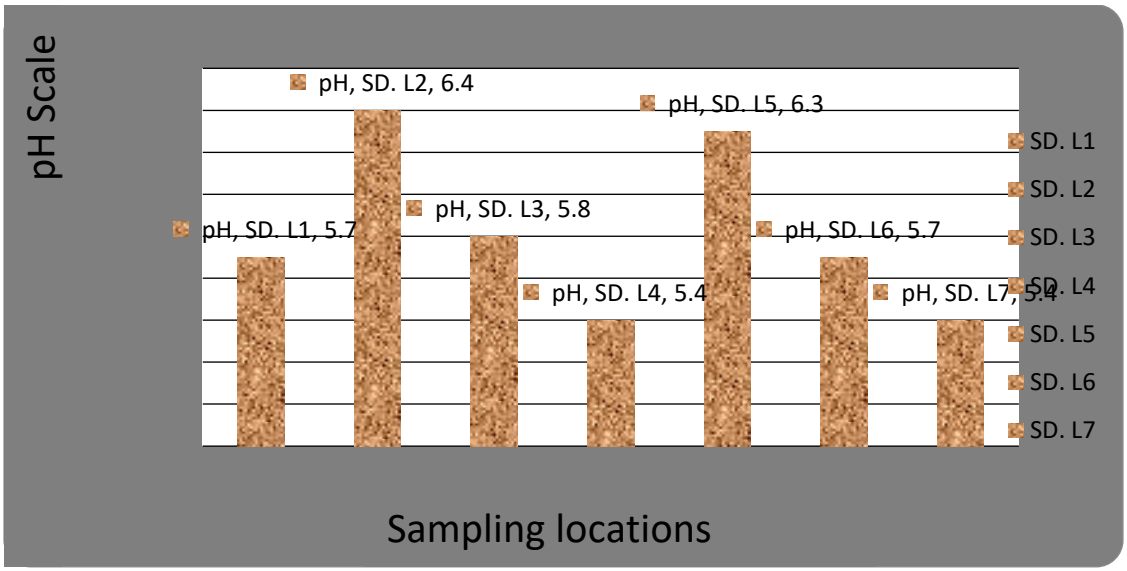

Fig. 2: Plot of pH levels in river sediments

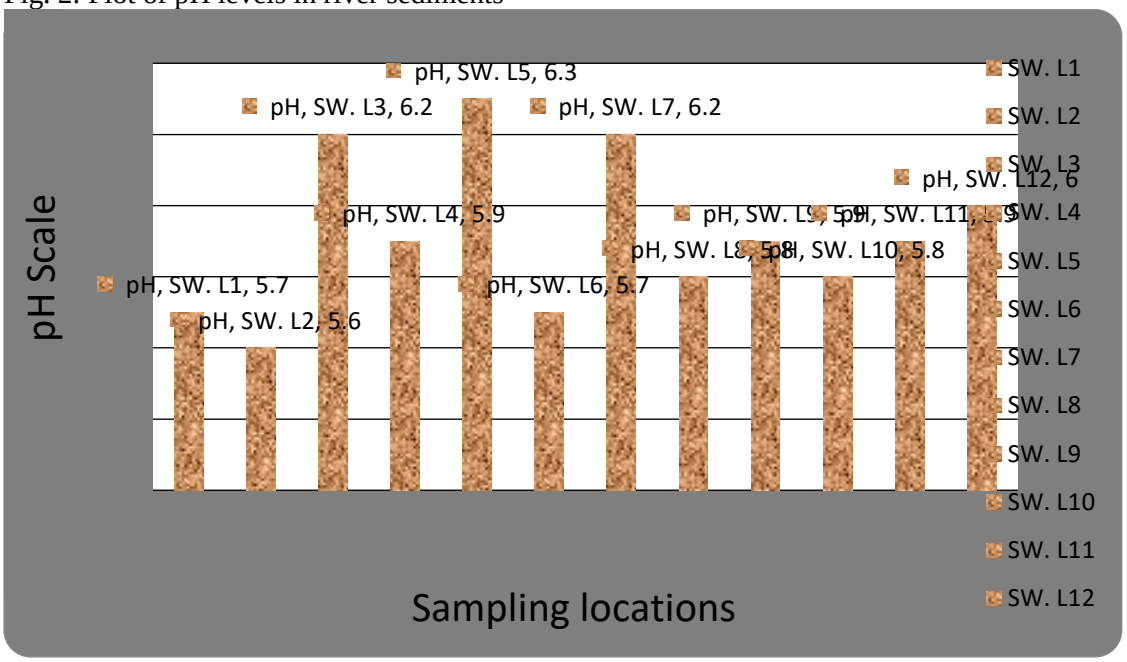

Fig.3: Plot of pH levels in surface water

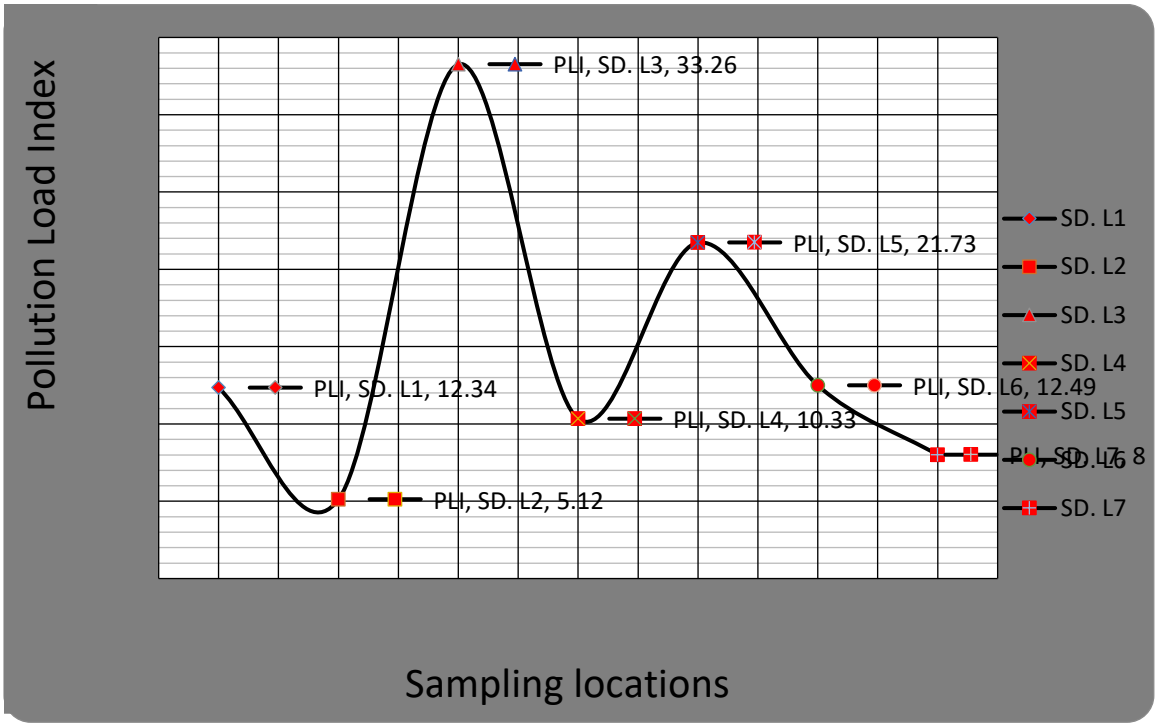

Fig. 4: Plot of pollution load index across all sampling locations

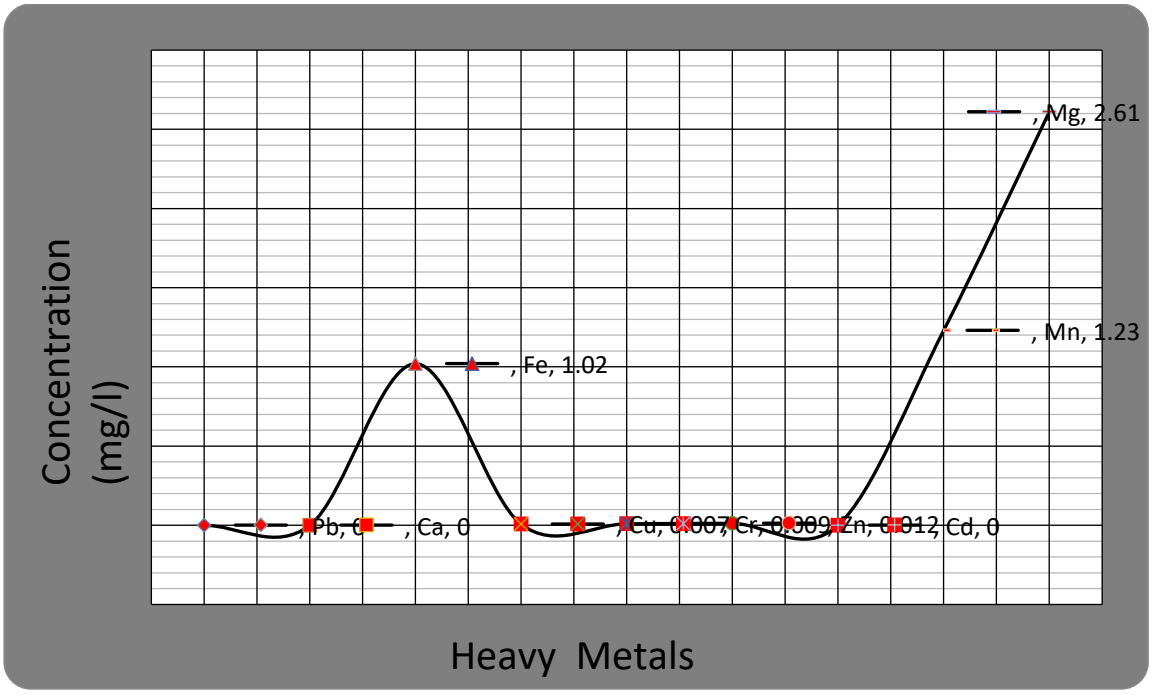

Fig. 5: Plot of Heavy metals concentration

5. Conclusion

The outcome of the analysis of the sampled surface water shows slight pollution of the samples based on some pollution indicator parameters. All the samples tested were found to be acidic; having pH values ranging 5.6-6.2. Aside from chromium and cadmium, all the heavy metals had significant concentrations in all the twelve samples analysed.The Pollution Load Index (PLI) level of river sediments ranged from 5.12-33.26;

considering the fact that only PLI values <1 was considered unpolluted; all samples analysed showed high pollution levels. Of all the heavy metals, Cu, Mg, Cr and Mn had moderate to considerable CF levels, while the others were of low levels. I_{GEO} levels were all <1, indicating low levels. For surface water, Pb and Zn had the worst Pollution Index values, with Pb having P_I values ranging 10-211. There was considerable contribution of pollutants from human activities into the river.It is recommended that authorities responsible for maintenance of environmental quality within Rivers State take seriously the findings of this study, so as to mitigate the potential short and long term effects of the on-going activities on the New Calabar River.

References

Akaninwor, J.O. and Egwin, O. (2006). Effect of Indo Food (Indomie) Industrial Effluent Dicharge On Physicochemical properties of New Calabar River in Choba, Rivers State. *J. Nig. Environ. Soc. (JNES), 3(3), 195–204.*

Chinda, A.C. (1998). The effect of industrial activities on the periphyton community at the upper reaches of the New Calabarriver, Niger Delta, Nigeria. *Waste Res. M. 32(4), 1137–1143.*

Chinese Quality Standard Code for Groundwater (1993).Pollution Index Categorization. *Code: GB/T14848-1993.*

Don-Pedro K.N., Oyewo E. O., Otitoloju A.A. (2004). Trend of heavy metal concentrations in Lagos lagoon ecosystem, Nigeria. *West Afr. J. Appl. Ecol., 5(2), 23-29.*

Francis A. and Elewuo U. (2012). Aspects of the biology of trap caught Chrysichthysnigrodigitatus (Lacepede: 1803) from the New Calabar River, Nigeria. *International Journal of Fisheries and Aquaculture Vol. 4(6), 99-104*.

Muller G. (1969). Index of geoaccumulation in sediments of the Rhine River. *Geology Journal*, 2 (3), 109–118.

Leton T.G. (2013). Engineering with a Human Face.University of Port Harcourt Inaugural Lecture Series No. 101.Delivered 28th February, 2013. ISSN: 1119-9849©2013.

Mohiuddin K. M., Alam M. M., Istiaq A. and Chowdhury A. K. (2015). Heavy metal pollution load in sediment samples of the Burigangariver in Bangladesh. *Journal of Bangladesh Agricultural University*, 13(2), 229–238.

National Population Commission (NPC) (2006).National Demographic Census Data for Rivers State (2006).

National Water Policy (2004).The Federal Ministry of Water Resources.Federal Republic of Nigeria pp 1-28.

Nigerian Administrative Division (2016).City Population. Retrieved 14/11/2016 URL: http://www.citypopulation.de/php/nigeria-admin.php

Otitoloju A. A. and Don-Pedro K. N. (2002). Bioaccumulation of heavy metals (Zn, Pb, Cu, and Cd) by tympanotonusfuscatus var. radula (I) exposed to sublethal concentrations of the test metal compounds in laboratory bioassay. *West Afr. J. Appl. Ecol.* 3(1), 17-29.

Rivers State Government (2016).People and Culture. Retrieved 14/11/2016 URL: http://riversstate.net.ng/people-and-culture/

Short K.C.and Stauble A.J. (1967). Outline geology of Niger Delta. *Am. Assoc. of Petr. Geol. Bull.*, 51(1), 761 – 779.

Theodore A. A. and Chikwuogwo W. P. (2014).Integrated Risk Assessment using ChrysichthysNigrodigitatus: A Case Study of New Calabar River Basin. *International Journal of Environment and Pollution Research.* 2(3),42-69.

Uzukwu P.U., Leton T.G. and Jamabo N.A. (2014).Survey of the Physical Characteristics of the Upper Reach of the New Calabar River, Niger Delta, Nigeria.*Trends in Applied Science Research*, 9(1), 494-502. URL: http://scialert.net/abstract/?doi=tasr.2014.494.502

WHO (2011) Guidelines for Drinking-water Quality, 4th Edition (2011).WHO Library Cataloguing-in-Publication Data.ISBN 978 92 4 1548151.

HYDROGEOCHEMICAL INVESTIGATION OF SURFACE AND GROUNDWATER QUALITY AROUND ANGUWAN MAIGIRU MINING SITES, NIGER STATE, NORTHCENTRAL NIGERIA

MUSA, A., Amadi, A. N., Ebieme, E. E. and Ameh, I. M.
Department of Geology, Federal University of Technology, Minna, Nigeria

*Corresponding Author's Email Address: an.amadi@futminna.edu.ng or geoama76@gmail.com
Phone No.: +234-80377-29977

Abstract
An investigation of surface and groundwater quality was carried out in Anguwan Maigiru, Madaka District of Rafi Local Government of Niger State, North-Central Nigeria. This was aimed at evaluating the quality status of surface and groundwater in the study area. The geological mapping revealed that the area is dominantly underlain by schist and granite. The physical parameters of the collected water samples were determined on site using the appropriate techniques while the chemical analysis was done at Regional Water Quality Laboratory Minna and the National Geosciences Research Laboratory Kaduna. A wide range and standard deviation was observed in the following groundwater quality parameter: Total dissolved solid (54.00-1123.00), electrical conductivity (35.00-1696.00), pH (5.54-10.60), sodium (5.00-471.00), iron (0.10-95.60), zinc (0.03-6.14), copper (0.03-3.13), chromium (0.05-0.36), manganese (0.06-1.36) and lead (0.00-11.00) are signatures that the water sources in the area are deteriorated by enrichment of these parameters. The Piper and Stiff plots show that the water samples analyzed had Na-HCO_3-Cl as the most dominant water type with minor mixed Ca-Na-Cl and Ca-Cl types. Gibbs plot illustrates that majority of the groundwater samples fall within the rock source dominance which suggests that the weathering of rocks primarily controls the major ion chemistry of groundwater in this area. The result of water quality analyses indicates that the surface and groundwater in the area are polluted and unsuitable for drinking and domestic purposes. The study attributed the poor condition of the water sources in the area to long term environmental abuse in the area arising from artisanal and illegal mining. Shallow hand-dug wells should be discouraged and alternative source of groundwater should be provided for the inhabitants. Residents of the area should build their houses miles away from mine site to prevent contamination and inhalation of toxic metals and waste from mine site should be treated before disposal into nearby surface water or farmlands and regulatory agencies should ensure that global minimum mining standard is maintained in every mining site in Nigeria.

Keywords: Hydrogeochemical Assessment, Surface and Groundwater Quality, Anguwan Maigiru Mining Sites, Niger State, Northcentral Nigeria

1. Introduction

Globally, there is an increasing awareness that water will be one of the most critical natural resources in future. Considering the four basic needs of man water, food, shelter and good health, water is the pivot on which the other variables revolves. Potable and safe drinking water is a necessary requirement for the health and productive life of humans in any society. In terms of economic activities such as commerce, tourism and industry, water is an indispensable input. It is essential requirements for civilization and industrial development of any nation. Therefore, a continuous monitoring of its quality is very essential in order to quantify the level of pollution arising from geogenic and anthropogenic sources as well as to avoid water borne diseases traceable common with contaminated water. Polluted water is a major cause of epidemic and chronic diseases in human being (Okiongbo and Douglas, 2013; Amadi *et al*., 2016).

2. Literature Review

Amadi, (2011) worked on the geochemical assessment of Aladimma dumpsite on the nearby soil and shallow groundwater. The concentrations of all the parameters analyzed were higher in soil than in groundwater and these may be attributed to the high affinity between organic matter content of soils and element. Ige and Olasehinde, (2011) carried out preliminary assessment of water quality in Ayede-Ekiti, Southwestern Nigeria., it was found that sodium and chloride are the most dominant ions of the total chemical budget. The hydrochemical characteristics of the water revealed that, the cationic concentrations is in the order of $(Na^{+}+K^{+}) > Ca^{2+} > Mg^{2+}$ for both wells and surface waters, while the anionic concentrations is in the order of $Cl^{-} > HCO_3^{-} > SO_4^{2-}$. Amadi *et al*., (2010) carried out research on coastal plain-sand aquifer of Owerri using factor analysis for characterization of groundwater chemistry. The study revealed five factors which correspond to five possible sources of pollution of groundwater in the area. Olatunji *et al*. (2005) carried out hydrochemical evaluation of groundwater resources in shallow coastal aquifers around Ikorodu area, southwestern Nigeria. Over 120 groundwater samples from hand dug wells and boreholes were sampled and analyzed for their physicochemical properties. The general hydrochemical character of the water revealed that the cationic concentration of the water to be Na>Ca>Mg while the anionic concentration of the water is $Cl>SO_4>HCO_3$. The dominant water type in the area is $Na+K/Cl+SO_4$ type. The water samples analysed showed that the groundwater of the area is affected more by the impact of Lagoon water.

Ali, (2004) carried out research on hydrochemical identification and salinity problem of ground-water in WadiYalamlam basin, western Saudi Arabia. He integrates hydrochemical, hydrogeological and recharge estimation analyses to identify the process/processes, that led to the aquifer salinity. The results of chemical analysis indicate that the groundwater salinity is highly variable and inconsistent along the course of the Wadi. This variability is probably due to the local hydrogeological conditions and to the intensive evaporation of effluent surface irrigation water that led to the precipitation of evaporites. Elueze *et al*., (2001) researched on hydrochemical assessment of surface water in part of Southeastern Nigeria. The application of R-mode factor analysis suggests that the main component of the water characteristics is related to hydrological, lithological and environmental controls while the water facies for the area is sodium-bicarbonate. Hanaa *et al*. (2000) investigated possible relationships between chemical toxicity of high concentrations of heavy metals and incidence of clinic diseases in Great Cairo city of Egypt. They associated high concentrations of Pb and Cd with renal failure, high concentrations of Cu and Mn to liver cirrhosis. They reported the presence of these metals in the urine of patients suffering chronic health effects like cancer, birth defects, organ damage, disorders of the nervous system and nervousness as well as damage to immune system. Nkotagu, (1996) determined the groundwater geochemistry in a Tanzania. He concluded that the chemical character of the groundwater in this area is due to the dissolution of amphiboles, sodic feldspars, cation exchange and salt leaching while the nitrate content of the groundwater in Dodoma was attributed to the nitrification process of the sewage effluents.

3. Methodology

3.1 Water Sampling and Laboratory Analysis

The water samples were collected in the month of November, 2015 and a total of 30 water samples comprising of (10 surface water, 12 boreholes, 4 hand dug well and 4 mine pits) were collected across the entire study area. The coordinate of each sampled location were obtained using the GPS (GARMIN-76) version (Fig. 3). The water samples were collected in pre-cleaned one litre plastic bottles. Two water samples were collected at each location for cation and anion analyses. Two drops of concentrated nitric acid (HNO_3) were added to one of the samples for the determination of major cations and heavy metals while the water samples in the second bottle were for the determination of the anions. The physical parameters measured in-situ on the field included temperature (T), pH, electrical conductivity (EC) and total dissolved solid (TDS) using appropriate techniques in accordance with the American Public Health Association standards (APHA, 2005). For the purposes of quality control, the water samples were duplicated and analyzed at the Department of Water Resources, Aquaculture and Fisheries Technology, Federal University of Technology Minna and National Geosciences Laboratory Kaduna while the control samples were analyzed at Federal Ministry of Water Resources Regional Laboratory, Minna.

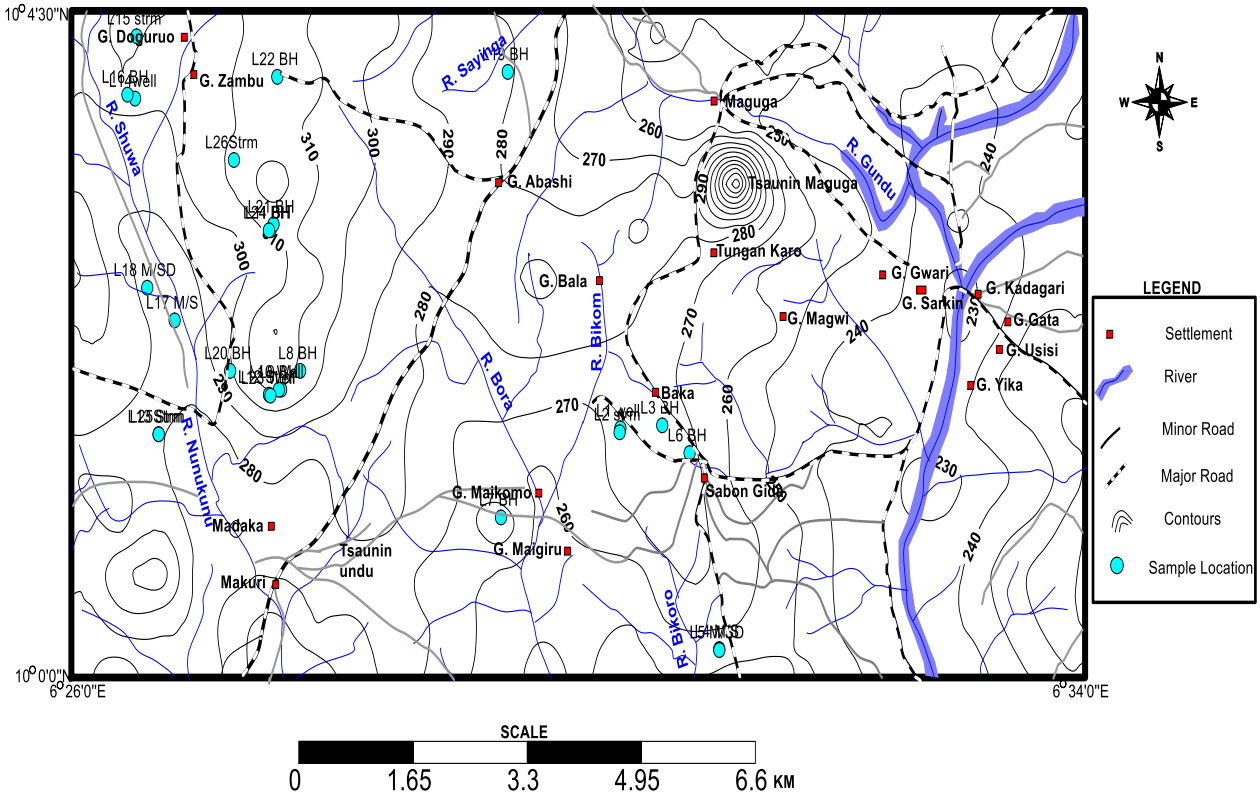

Fig. 3: Fact Map of the Study Area showing Sample Locations

4. Results and Discussion

4.1 Geological Mapping

Results of the geological mapping of the study area reveals schist and granite as the rock types that make up the local geology of the area (Fig. 2). The granite outcrops are common and well exposed in M adaka, Tsaunin-Undu, Baka and Sabon-Gida. They are light in colour and generally fine to medium grained containing feldspars, biotites and quartz as the major minerals. The schist strike NE–SW and dip 45ºW along a stream channel in Angwan-Sarkin area. The schist is well foliated are largely deformed and weathered. They are potential sites for gold mineralization based on the structural configuration while the granite is characterized by dominant pegmatitic and quartz vein in granites (Ajibade *et al.*, 2008).

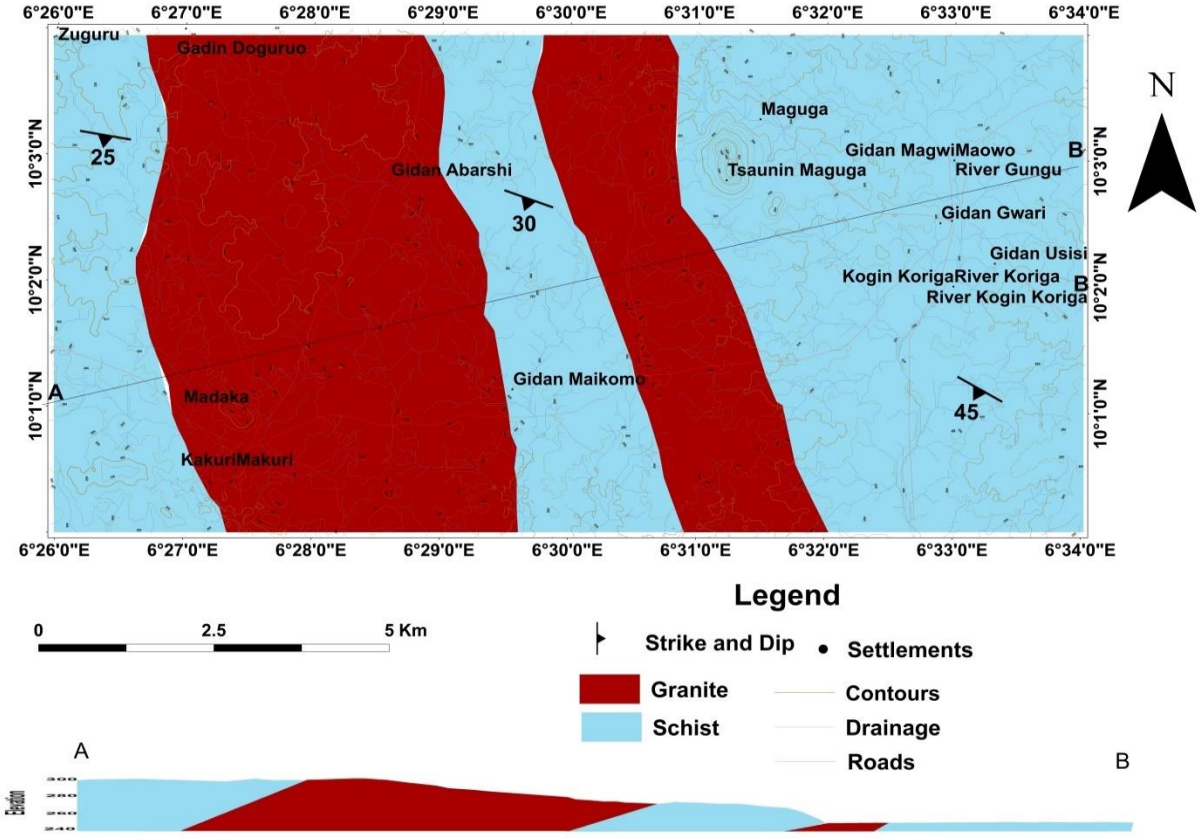

Fig. 2: Geological and Cross Sectional Map of the Study Area

4.2 Physical Parameters

The results of the laboratory analysis of the surface and groundwater are contained in Tables 1 and 2 respectively and discussed accordingly. Water pH is an indicator of the water quality and extent of pollution. The pH of the surface water ranged from 5.69 to 7.54 with a mean value of 6.67 (Table 1) while groundwater pH varied from 5.54 to 10.60 with an average value of 6.54 (Table 2). The mean pH values for both surface and groundwater fall within the permissible limit of 6.5 to 8.5 postulated by World Health organization (WHO, 2010) and Nigerian Standard for Drinking Water Quality (NSDWQ, 2007).

Slightly low pH enhances ionic exchange and mobility of metals in different media. It is a measure of the degree of hotness or coldness of a medium and it effects the various reactions that take place in the water body. The temperature values of the surface water ranged from 22.20 to 30.20 ºC and a mean value of 26.02 ºC while

temperature of the groundwater varied from 25.50 to 32.90 ^{o}C with an average temperature of 29.45 ^{o}C. Water temperature is a crucial aspect of aquatic habitat, as aquatic organisms are adapted to live within a certain temperature range. As the upper and lower temperature limits are approached, the organism becomes more susceptible to diseases.

Total dissolved solid (TDS) is a good water quality indicator used to describe the amount of dissolved solutes in water. The concentration of TDS in surface water varied from 40.00 – 153.00 mg/l and a mean value of 94.75 mg/l (Table 1) while the concentration of TDS in groundwater ranged between 44.00 – 1123 mg/l with an average value of 347.41 mg/l (Table 2). The concentration of TDS for surface water is falls within the acceptable limit of 500.00mg/l (NSDWQ, 2007; WHO, 2010). However, the concentrations of groundwater in some locations exceed the maximum permissible limit. The high TDS values may be a reflection of anthropogenic interference with the surface water body and an indicator of pollution. Water containing more than 500 mg/l of TDS is considered undesirable for domestic use.

The electrical conductivity (EC) is a valuable indicator of the amount of material dissolved in water and the concentration in surface water ranged from 56.00 – 205.00 µs/cm with a mean value of 131.50 µs/cm while the concentration of EC varied between 35.00 – 1696.00 with an average value of 579.64 µs/cm. The concentrations of EC in surface water are far below the maximum permissible limit of 1000.00 µs/cm (WHO, 2010). However, many of the groundwater samples had values exceeding the permissible limit which is an indication that the groundwater contained more solutes than surface water. The observed wide range and deviation in TDS and EC values in groundwater may be attributed to weathering and bedrock dissolution as well as application of agro-chemicals on farm lands and mining. Turbidity value in surface water ranged from 11.80 – 714.00 NTU with a mean value of 158.84 NTU while the concentration of turbidity in groundwater varied between 1.52 – 460.00 NTU with an average value of 46.30 NTU. The values of turbidity in both surface and groundwater exceed the maximum allowable limit of 5.00 NTU (NSDWQ, 2007). The high turbidity in the water in the area is a major confirmation that the water sources in the area contained a lot of suspended substances materials. Turbidity in water reduces the transparency and visibility of the water (Okunlola *et al*. 2016).

Table 1: Table Statistical Summary of Surface water samples in the study area

Parameters (mg/L)	Minimum	Maximum	Mean	Standard Deviation
pH	5.69	7.54	6.67	0.69
Turbidity	11.80	714.00	158.84	239.74
Hardness	23.00	85.00	48.50	22.11
TDS	40.00	153.00	94.75	41.56
EC	56.00	206.00	131.50	58.76

BOD	3.00	9.00	6.25	1.90
COD	7.40	13.80	10.42	1.54
DO	3.00	12.50	7.05	3.58
Temperature	22.20	30.20	26.02	2.46
Alkalinity	11.00	36.00	21.75	8.29
E.coli	0.00	48.00	20.87	18.86
F.cocci	0.00	53.00	27.37	19.36
Chloride	8.00	62.00	20.65	17.46
Sulphate	0.00	63.50	42.08	20.86
Nitrate	0.30	23.89	10.12	10.30
Carbonate	10.80	50.00	21.88	16.28
Bicarbonate	2.00	29.00	12.43	9.65
Phospahe	0.61	0.11	0.72	0.48
Nitrite	0.04	0.03	0.07	0.05
Fluorite	0.00	0.35	0.10	0.15
Sodium	8.00	108	53.01	40.80
Potassium	3.00	39.60	12.02	12.53
Calcium	6.46	30.70	14.91	9.38
Magnesium	2.32	13.60	7.65	4.81
Iron	0.18	7.23	2.65	2.36
Copper	0.01	1.36	0.45	0.47
Arsenic	0.00	0.02	0.01	0.01
Nickel	0.00	0.03	0.02	0.01
Cobalt	0.00	0.04	0.01	0.01
Cadmium	0.00	0.01	0.00	0.00
Mercury	0.00	0.01	0.00	0.00
Lead	0.00	0.41	0.08	0.14
Manganese	0.21	0.92	0.52	0.27
Zinc	0.03	6.14	1.73	1.97

Table 2: Statistical Summary of Groundwater samples in the study area

Parameters (mg/L)	Minimum	Maximum	Mean	Standard Deviation
pH	5.54	10.60	6.54	1.15
Turbidity	1.52	460.00	46.301	112.82
Hardness	27.00	400.00	136.12	118.33
TDS	44.00	1123	347.41	344.80
EC	35.00	1696	550.82	579.64
BOD	3.00	8.00	5.59	1.46
COD	7.50	14.00	10.84	1.96
DO	2.28	7.77	5.19	1.50
Temperature	25.50	32.90	29.45	2.39
Alkalinity	8.00	58.00	35.18	16.00
E.coli	0.00	97.00	10.65	25.85

F.cocci	0.00	102.00	11.53	26.18
Chloride	7.80	367.00	82.79	108.38
Sulphate	0.00	179.00	62.89	45.26
Nitrate	0.15	178.20	25.55	44.86
Carbonate	25.40	80.00	35.65	13.23
Bicarbonate	0.50	43.00	18.79	14.88
Phospahe	0.11	0.81	0.33	0.21
Nitrite	0.01	0.16	0.07	0.05
Fluorite	0.00	1.16	0.54	0.46
Sodium	5.00	471.00	86.47	105.87
Potassium	2.00	61.50	15.55	19.90
Calcium	5.23	129.40	37.28	33.84
Magnesium	2.00	75.80	20.40	19.30
Iron	0.10	95.60	6.80	22.94
Copper	0.03	3.13	0.51	0.78
Arsenic	0.00	0.02	0.00	0.00
Nickel	0.00	0.14	0.02	0.04
Cobalt	0.00	0.01	0.00	0.00
Cadmium	0.00	0.01	0.00	0.00
Mercury	0.00	0.01	0.00	0.00
Lead	0.00	11.00	0.65	2.67
Manganese	0.06	1.36	0.24	0.31
Zinc	0.03	6.14	1.86	1.97

4.3 Bacteriological Parameters

The bacteriological analyses results in Tables 1 and 2 for surface and groundwater respectively show high bacteria count. The concentration of E.coli in surface water ranged from 0.00 – 48.00 cfu/ml with an average value of 20.87 cfu/ml while the concentration of E.coli in groundwater varied between 0.00 – 97.00 cfu/ml with a mean value of 10.65 cfu/ml. These values are higher than the recommended value of 0.00 cfu/ml (NSDWQ, 2007). Similarly, the concentration of faecalcocci ranged from 0.00 – 53.00 cfu/ml with a mean value of 27.37 cfu/ml while the concentration in groundwater varied between 0.00 – 102.00 cfu/ml with an average value of 11.53 cfu/ml as against the postulated value of 0.00 cfu/ml (WHO, 2010). They presence in water is an indication of faecal contamination arising from animal and human faeces being in contact with water. The mean value of E.coli and faecalcocci are higher in surface water compared to groundwater due to direct defecation on the river by the villagers. Studies have revealed that water pollution through faecal contamination is responsible for most water borne diseases such as meningitis, cholera and diarrhea as well as morbidity and mortality among children (Olasehinde *et al*. 2015). It also causes acute renal failure and haemolytic anaemia in adults (WHO, 2010).

4.4 Chemical Parameters

The concentration of chloride ranged between 8.00 – 62.00 mg/l with a mean value of 20.65 mg/l for surface water and 7.80 – 367.00 mg/l with an average value of 82.79 mg/l for groundwater. The value of chloride in the surface water fall below the maximum permissible limit of 250 mg/l (NSDWQ, 2007 and WHO, 2010) while the groundwater values in most locations exceeds the permissible value. High chloride values may not constitute health hazard to human beings, but it does produce salty taste, corrode metal pipes and harm non-halophytic plants. The sulphate level in the surface water ranged between 0.00 – 63.50 mg/l with an average value of 42.08 mg/l (Table 1) and 0.00 – 179.00 mg/l with a mean value of 82.89 mg/l for the groundwater (Table 2).

The sulphide concentration in surface is within the acceptable limits of 100.00 mg/l (NSDWQ, 2007) while the groundwater samples have values higher than the acceptable limit. High sulphate and chloride concentration in water may be naturally induced as a result of bedrock dissolution and chemical weathering or due to anthropogenic influence coming from fertilizer application and mining activities (Dan-Hassan *et al*. 2012). The concentration of total hardness in surface water varied from 23.00 – 85.00 mg/l with a mean value of 48.50 mg/l while in groundwater the value of total hardness varied from 27.00 – 400.00 mg/l with an average value of 136.12 mg/l. The more dissolved and suspended material in water the more the hardness of the water. Groundwater is always in constant contact with the host rock through which it migrates and this explains why its concentration is higher than the surface water. The alkalinity content in surface water is in the order of 11.00 – 36.00 mg/l and a mean value of 21.75 mg/l while in groundwater, the concentration ranged from 8.00 – 58.00 mg/l with an average value of 35.18 mg/l (Tables 1 and 2). Water from shallow aquifers in basement complex is characterized by high alkalinity and this explains why the groundwater concentration is higher compared to surface water.

Biochemical Oxygen Demand (BOD) values ranged from 3.00 – 9.00 mg/l with a mean value of 6.25 mg/l for surface water and 3.00 – 8.00 mg/l with an average value of 5.59 mg/l for groundwater samples. Biochemical Oxygen Demand determines the relative oxygen necessary for biological oxidation of waste waters, effluents and polluted waters. It is the only test available to determine the amount of oxygen required by bacterial while stabilizing decomposable organic matter. It measures the biodegradable organic carbon and under certain conditions, the oxidizable nitrogen present in a water sample. The study of BOD gives an idea of the oxidizable matter actually present in a water sample and this allows pollution load evaluation to be established. The chemical oxygen demand provides a measure of the oxygen equivalent of the portion of organic matter in a sample that is susceptible to oxidation by strong chemical oxidant. It determines the quantity of oxygen required for the oxidation of the inorganic and organic matter in a water sample under controlled condition of oxidizing, temperature and time.

Chemical oxygen demand (COD) test measures the total organic carbon, with the exception of certain aromatics such as benzene, which are not completely oxidized in the reaction. The concentration of COD in the surface water varied from 7.4 – 13.80 mg/l with an average value of 10.42 mg/l (Table 1) and 7.50 – 14.00

with a mean value of 10.84 mg/l (Table 2). The concentration of dissolved oxygen (DO) in surface water ranged between 3.00 – 12.50 mg/l with an average value of 7.05 mg/l while the concentration in groundwater varied from 2.28 – 7.77 mg/l with a mean value of 5.19 mg/l. The DO, BOD and COD measure the water oxygen available for aquatic organisms and their concentration is very important for the survival of aquatic lives.

The concentration of sodium in surface water varied from 8.00 – 108.00 mg/l with a mean value of 53.01 mg/l (Table 1) and 5.00 – 471.00 mg/l with an average value of 86.47 mg/l (Table 2). The mean concentration of sodium in both surface and groundwater are below the maximum permissible value of 250.00 mg/l (NSDQW, 2007) though few locations of the groundwater samples have higher values. Studies have shown a direct relationship between hypertension and high sodium level in drinking water. Calcium content in the surface water ranged between 6.46 – 30.70 mg/l with a mean value of 14.91 mg/l while calcium concentration in the groundwater varied from 5.23 – 129.40 mg/l with an average value of 37.28 mg/l. This values fall within the allowable limits of 200.00 mg/l for a potable water. Calcium is needed by the body for good tooth and bone development. Magnesium concentration in both surface water (2.32 – 13.60) and groundwater (2.00 – 75.80) are far within the allowable limits of 100.00 mg/l (NSDWQ, 2007).

Magnesium in water is better absorbed than dietary magnesium. Epidemiological data in man and experimental data in rats have demonstrated that the intake of water containing sufficient amount of magnesium may prevent arterial hypertension and nervous disturbances. The concentration of potassium in surface water varied from 3.00 – 39.60 mg/l with a mean value of 12.02 mg/l (Table 1) and between 2.00 – 61.50 mg/l with an average value of 15.55 mg/l for the groundwater samples (Table 2).

The concentration of nitrate in surface water ranged between 0.03 – 23.89 mg/l and a mean value of 10.12 mg/l and between 0.15 – 178.20 mg/l with an average value of 25.55 mg/l for the groundwater samples. Nitrate values in the surface water are within the permissible limit of 50.00 mg/l while in groundwater, some locations were higher than the maximum permissible limit of 50.00 mg/l by (WHO, 2010; NSDWQ, 2007). High nitrate level in drinking water causes infant methaemoglobinaemia (blue-baby syndrome), gastric cancer, metabolic disorder and livestock poisoning. The sources of nitrate in the groundwater can be attributed to anthropogenic activities such as on-site sanitation, waste dumpsites and fertilizer application (Dan-Hassan *et al.*, 2012). The mean concentration of phosphate, carbonate and bicarbonate in surface water are 12.02 mg/l, 21.88 mg/l and 12.43 mg/l respectively while in groundwater, their respective mean values are 0.33 mg/l, 35.65 mg/l and 18.79 mg/l. These concentrations are below their permissible limit. The observed concentrations in the major cations and anions are signatures of rock-water interactions.

4.5 Heavy Metals

They are metallic chemical elements that have a relatively high density and are toxic or poisonous at low concentrations. Like all other chemical elements have distinguishing physical and chemical characteristics, properties such as density, valency, redox potentials and solubility makes them unique. From an environmental

standpoint, heavy metals are recognized in terms of their toxicity and health effects (Nikoladis *et al.*, 2008). In spite of some of these elements having physiological functions in plants and animal, they have been shown to be harmful beyond certain concentrations (USEPA, 1997). The concentration of iron varied from 0.08 – 7.23 mg/l with a mean concentration of 2.65 mg/l in surface water (Table 1) while the concentration in groundwater varied between 0.10 – 95.60 mg/l with an average value of 6.80 mg/l (Table 2) as against the acceptable value of 0.30 mg/l (NSDWQ, 2007). The implication of the high iron content is that the water from the well will have taste, colour and other aesthetic problems such as hemochromatosis.

The concentration of lead in surface water ranged between 0.00 – 0.41 mg/l with a mean value of 0.08 mg/l while lead concentration in groundwater varied from 0.00- 11.00 mg/l with a mean value of 0.65 mg/l as against the permissible value of 0.01 mg/l (NSDWQ, 2007). Lead is potentially hazardous to most form of life and is considered toxic to organisms. Lead is bio-accumulated by benthic foraminifera, freshwater plants, invertebrates and fish. The chronic effect of lead on man includes neurological disorders, especially in the foetus and in children, synthesis of hemoglobin, gastrointestinal tract, kidney diseases and impaired performance in IQ test. Lead is however used in batteries, petrol additives, alloys, cable sheathing, pigments, rolled and extruded products (WHO, 2010). The concentration of copper in the surface water ranged from 0.01 – 1.36 mg/l with an average value of 0.45 mg/l while the concentration in 0.03 – 3.13 mg/l with an average value of 0.51 mg/l as against the maximum permissible limit of 1.00mg/l (NSDWQ, 2007). Copper is an essential substance to human life, but in high concentration, it can cause anemia, liver and kidney damage, stomach and intestinal irritation. Copper normally occurs in drinking water from copper pipes, weathering of products made from copper as well as from mining and additives used to control weed (Vasanthavigar *et al*., 2010).

Zinc concentration in surface water ranged from 0.04 – 5.30 mg/l and an average value of 1.82 mg/l (Table 1) while the concentration in groundwater varied from 0.03 – 6.14 mg/l and an average value of 1.73 mg/l (Table 2). High zinc concentration could be a problem in aquatic ecosystem. Zinc is unusual in that it has low toxicity to man, but relatively high toxicity in fish or livestock watering. The maximum concentration of cadmium, cobalt and mercury in groundwater were 0.01 mg/l as against their maximum permissible limit of 0.003 mg/l, 0.001 mg/l and 0.001 mg/l respectively (NSDWQ, 2007). Also, the maximum concentration of cadmium, cobalt and mercury in surface water are 0.01 mg/l, 0.04 mg/l and 0.01 mg/l respectively. They observed high concentration of these metals can be linked with the mining and farming activities going on in the area. Several renal dysfunction and damage to the bone structure, a syndrome known as itai-itai disease, have been associated with long-term exposure to cadmium through water (USEPA, 1997). Cobalt has also been used as a treatment for anemia, as it causes red blood cell production (Mohanty *et al*. 2001). Acute toxicity of cobalt may be observed as effects on the lungs, including asthma, pneumonia, and wheezing (Adams *et al.*, 2008). High concentration of mercury in drinking water causes severe respiratory irritation, digestive disturbances and damage to developing fetus, brain and kidney (Singh *et al*. 2008).

The concentration of nickel in surface water ranged between 0.00 – 0.03 mg/l mg/l with an average value of 0.02 mg/l (Table 1) while the concentration in groundwater varied from 0.00 – 0.14 mg/l with a mean value of 0.02 mg/l (Table 2) as against the maximum allowable value of 0.02 mg/l (WHO, 2010). Nickel is a very abundant element in the environment, and is found primarily combined with oxides and sulphides. The most common adverse health effect of nickel in humans is an allergic reaction. People can become sensitive to nickel when things containing it are in direct contact with the skin, when they eat nickel in food, drink it in water, or breathe dust containing it (Aktar *et al.*, 2010). Once a person is sensitized to nickel, further contact with it will produce a reaction. The most common reaction is a skin rash at the site of contact. Less frequently, allergic people have asthma attacks following exposure to nickel (Lohani *et al*. 2008). Lung effects, including chronic bronchitis and reduced lung function, have been observed in workers who breathed large amounts of nickel (Edet and Okereke, 1997; Kraft *et al.*, 2006).

The concentration of arsenic ranged between 0.00 – 0.02 mg/l for both surface and groundwater. Arsenic is the most common cause of acute heavy metal poisoning in adults and can be released into the environment through mining as a pathfinder element to gold. When arsenic enters the environment, it does not evaporate, rather it can be absorbed in the soil through pesticides application on farm lands, infiltrate into groundwater system or surface water via run off (Karbassi *et al*., 2008; Amadi *et al*. 2013). The concentration of manganese ranged from 0.21 – 0.92 mg/l with an average value of 0.52 mg/l for surface water (Table 1) and between 0.06 – 1.36 mg/l with a mean value of 1.73 mg/l (Table 2). Some locations in both surface and groundwater have values higher than the WHO and NSDWQ acceptable limit of 0.2 mg/l. Manganese is essential for plants and animals, and are used in products such as batteries, glass and fireworks (Aboud and Nandini, 2009). Manganese compounds are used in fertilizer, fungicides and as livestock feeding supplements (Huang and Lin, 2003). Fluoride concentration in surface water ranged from 0.00 – 0.35 mg/l with a mean value of 0.10 mg/l while in groundwater, the fluoride content varied between 0.00 – 1.16 mg/l with an average value of 0.54 mg/l. These values fall below the permissible limit of 1.5 mg/l (NSDWQ, 2007). The high fluoride content in water causes dental and skeletal fluorosis (Amadi *et al*., 2014, Aminu and Amadi, 2014).

4.6 Hydrogeochemical Facies

The evolution of hydrochemical parameters of groundwater can be understood by plotting the major cations and anions in pictorial form as demonstrated in Piper diagram (Fig. 3) and Durov diagram (Fig. 4). They are used to determine the water type and their possible source. For the purpose of plotting, Na and K ions are combined together as well as HCO_3 and CO_3 ions. The diagrams show that the dominant water type in the area is Na-HCO_3-Cl followed by Ca-Na-Cl and Ca-Cl types. From the plot, it was observed that the concentration of alkali metals (Na and K) exceed the alkaline earth (Ca and Mg).

Futhermore, Gibbs plot (Fig. 5) was employed in this study to elucidate the concept and role of rock water interaction in water quality studies. The results revealed that majority of the water

samples fall within the rock source dominance which suggests that weathering of rocks primarily controls the chemistry of groundwater in the area while precipitation is the main source of groundwater recharge. The wet and dry climatic conditions of the area encourage chemical weathering of rock which enhances ionic dissolution of soluble mineral component of the rocks thereby altering the chemistry of water in the study area.

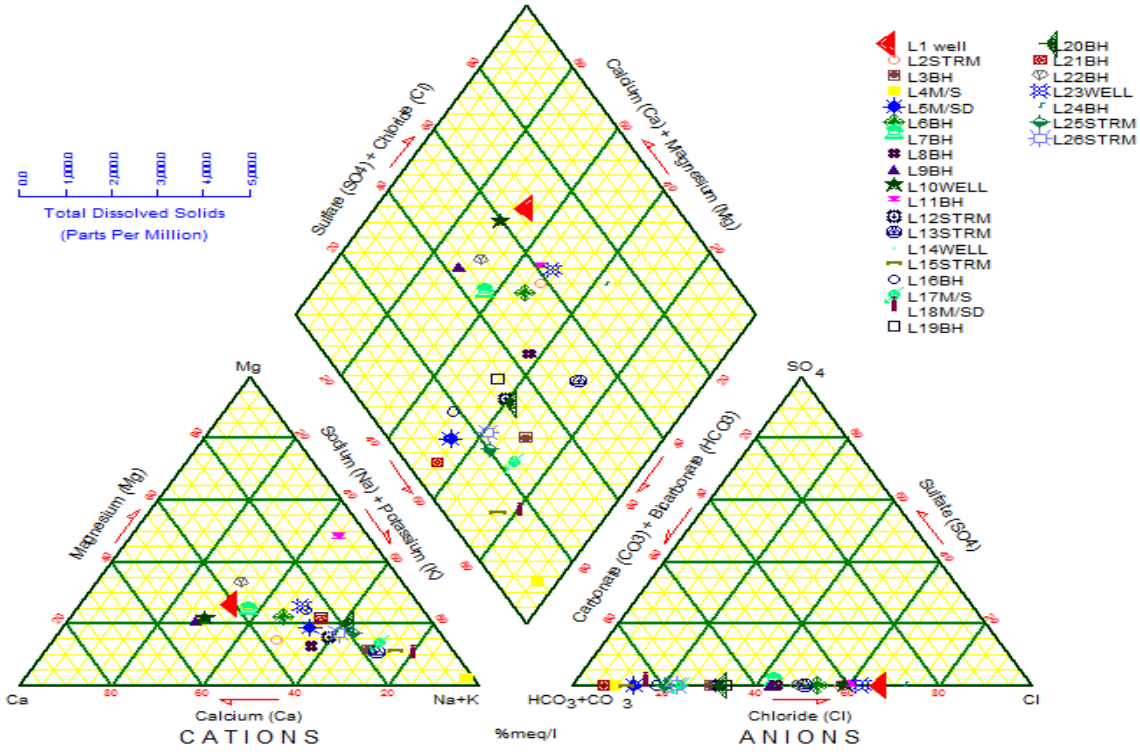

Fig. 3: Piper's Trilinear Diagram for the Study Area

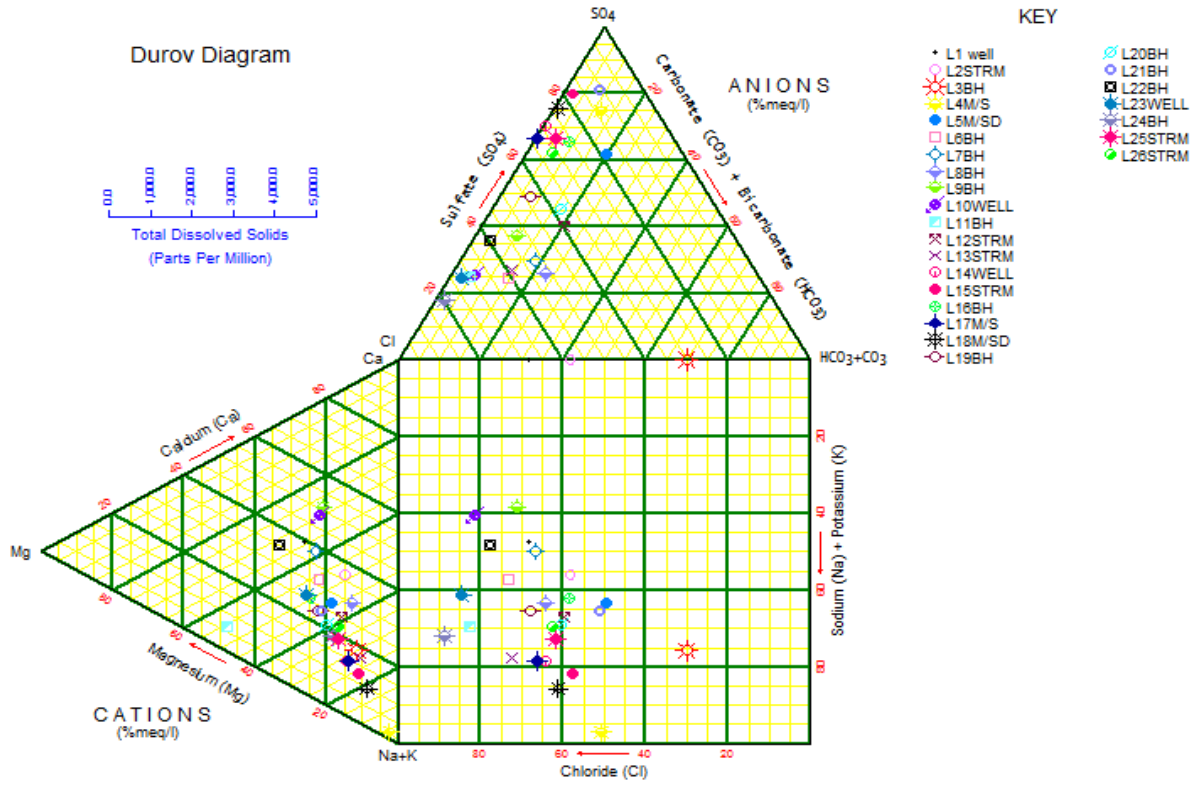

Fig. 4: Durov diagram for the Study Area

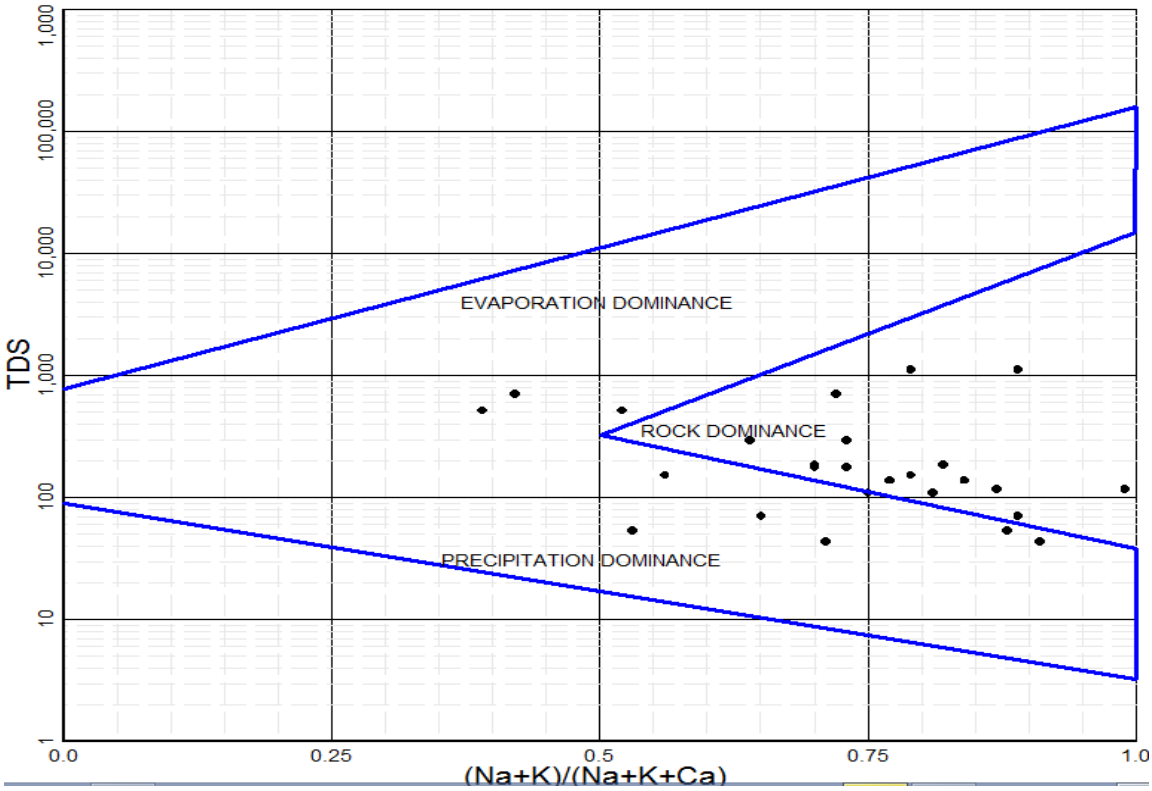

Fig. 5: Gibbs plot for the Study Area

5. Conclusion

The hydrogeochemical evaluation of surface and groundwater quality around Anguwan Maigiru area of Madaka district, Northcentral Nigeria was studied in this work. Results of the field geological mapping of the study area revealed two rock types in the area which are schist and granite, with minor units such as pegmatite as well as quartz veins which are known to host gold mineralization. Results of the water analysis were interpreted by comparing it with the Nigeria Standards for Drinking Water Quality and World Health Organization water quality guideline. The water is poor bacteriologically due to presence of pathogens. The concentration of major cations and anions analysed for both surface and groundwater samples were within the WHO permissible limits and their source in the water is traced to natural geological process of rock weathering. However, the concentration of some trace elements such as Fe, Zn, Cr, Mn and Pb were slightly higher the recommended maximum permissible limits of WHO and NSDWQ which is an evidence of pollution. The results of the laboratory analysis of the rock samples (Schist and granite) indicate that the rocks were highly enriched with these heavy metals. Their presence in groundwater may be attributed to natural process of rock weathering and bedrock dissolution. The excavation of rock boulder as well as the crushing and milling by artisanal gold miners creates a pathway for water pollution via anthropogenic interference. The Piper and Durov diagrams confirmed that the dominant water type in the area is Na-HCO_3-Cl while Gibbs plot established the weathering is the main process controlling the water chemistry in the area. Good hygiene and standard mining procedures are recommended for the area.

References

Aboud, S. J. and Nandini, N. (2009). Heavy metal analysis and sediment quality values in urban lakes. *American Journal of Environmental Science*, 5(6), 678-687.

Adams, R. H., Guzmán-Osorio, F. J. and Zavala, C. J. (2008). Water repellency in oil contaminated sandy and clayey soils. *International Journal of Environmental Science and Technology, 5*(4), 445-454.

Ajibade, A. C., Anyanwu. N. P. C., Okoro, A. U. (2008). The Geology of Minna Area (explanation of 1:250,000 Sheet 42 (Minna). *Nigeria Geolo. Surv. Agency, Bull. No. 43, 112p.*

Aktar, M. W., Paramasivam. M., Ganguly, M., Purkait, S., and Sengupta, D. (2010). Assessment and occurrence of various heavy metals in surface water of Ganga river around Kolkata: a study for toxicity and ecological impact. *Environmental Monitoring and Assessment,*160(2), 207-213. doi.10.1007/s10661-008-0688-5.

Ali, S. M. (2004). Evaluation Of Groundwater Resources In WadiYalamlam and WadiAdam Basins, Makkah-Al-MukarramahArea Ritrieved from https://www.researchgate.net/publication /237478981.

Amadi, A. N., Ameh, I. M., Ezeagu, G. G., Angwa, E. M., and Omanayin, Y. A. (2014). Bacteriological and physico-chemical analysis of well Water from villages in Edati, Niger State, North-central Nigeria. *International Journal of Engineering Research and Development,* 10(3), 10-16. e-ISSN: 2278-067X, p-ISSN: 2278-800X, www.ijerd.com.

Amadi A. N., Dan-Hassan M. A., Okoye N. O., Ejiofor I. C. and Aminu T. (2013). Studies on Pollution Hazards of Shallow Hand-Dug Wells in Erena and Environs, North-Central Nigeria. *Environment and Natural Resources Research,* 3(2), 69-77. doi:10.5539/enrr.v3n2p69.

Amadi, A. N. (2011). Assessing the Effects of Aladimma Dumpsite on Soil and Groundwater Using Water Quality Index and Factor Analysis. *Australian Journal of Basic and Applied Sciences,* 5(11), 763-770.

Amadi, A. N., Yisa, J., Okoye, N. O. and Okunlola, I. A. (2010). Multivariate statistical evaluation of the hydrochemical facies in Aba, Southeastern Nigeria. *International Journal of Biology and Physical Sciences,* 15(3), 326-337.

Amadi, A. N., Obaje, N. G., Goki, N. G., Abubakar K. U., Shaibu, I. and Nwakife, C. N. (2016). Studies on Water Quality in Suleja, Niger State for Domestic and Irrigational Purposes. *Nasara Scientifique: Journal of Natural and Applied Sciences,* 5(1), 16-29.

APHA, (2005). Standards methods for the examination of water and wastewater. 19th Edition *American Water Works Association,* Washington DC.

Dan-Hassan, M.A., Olasehinde, P.I., Amadi, A.N., Yisa, J. and Jacob, J.O. (2012). Spatial and Temporal Distribution of Nitrate Pollution in Groundwater of Abuja, Nigeria. *International Journal of Chemistry* 4(3), 39-48.

Edet, A.E. and Okereke, C.S. (1997). Assessment of Hydrogeological Conditions in Basement Aquifers of the Precambrian Oban Massif, Southeastern Nigeria. *Journal of Applied Geophysics*, 36(1), 95-204.

Elueze, A.A, Ephraim, B.E & Nton, M.E (2001), Hydrogeochemicalassessment of the surface water in part of Southeastern Nigeria, *Mineral Wealth,* 119(1), 45-58.

Hanaa, M., Salem A., Eweida E. and Azza F. (2000). 'Heavy metals in Drinking Water and their Environmental Impact on Human Health', *ICEHM* 542- 556.

Ige, O.O. and Olasehinde, P.I. (2011). Preliminary assessment of water quality in Ayede-Ekiti, Southwestern Nigeria. *Journal of Geology and Mining Research* 3(6), 147-152.

Karbassi, A. R., Monavari, S. M., Nabi-Bidhendi, G. R., Nouri, J. and Nematpour, K. (2008). Metal pollution assessment of sediment and water in the Shur River. *Environmental Monitoring and Assessment,* 147(2), 107-116.

Kraft, C., Tumpling, W. and Zachmann, D. W. (2006). The effects of mining in Northern Romania on the heavy metal distribution in sediments of the rivers Szamos and Tisza, Hungary. *Acta Hidrochim, Hydrobiology*, 34(1), 257-264.

Lohani, M. B., Singh, S., Rupainwar, D. C. and Dhar, D. N. (2008). Seasonal variations of heavy metal contamination in river Gomti of Lucknow city region. *Environmental Monitoring and Assessment*, 147(3), 253-263.

Mohanty, J. K. Misra, S. K. and Nayak, B. B., (2001). Sequential leaching of trace elements in coal: A case study from Talcher coalfield, Orissa. *Indian Journal of Geology and. Sociology,* 58(1), 441-447.

Nkotagu, H. (1996).The groundwater geochemistry in a semi-arid, fractured crystalline basement area of Dodoma, Tanzania. *Journal African Earth Science*, 23(1), 593-605.

Nikolaidis, C., Mandalos P. and Vantarakis, A. (2008). Impact of intensive agricultural practices on drinking water quality in the EVROS Region (NE GREECE) by GIS analysis. *Environmental Monitoring and Assessment.* 143(2), 43-50.

NSDWQ, (2007). Nigerian Standard for Drinking Water Quality. Nigerian Industrial Standard, NIS:554, 1-14.

Okiongbo, K. S. and Douglas, R. (2013). Hydrogeochemical analysis and evaluation of groundwater quality in Yenagoa city and environs, Southern Nigeria. *Ife Journal of Science*, 15(2), 209-222.

Okunlola, I. A., Amadi, A. N., Olashinde, P. I., Maspalma, S. S. and Okoye, N. O. (2016). Quality Assessment of Groundwater from Shallow Aquifers in Hong Area, Adamawa State, Northeastern Nigeria. *Ife Journal of Science*, 18(1), 267-283.

Olatunji, A.S., Abimbola, A.F., Oloruntola, M.O. and Odewade, A.A. (2005).Hydrogeochemical evaluation of groundwater resources in shallow coastal aquifer around Ikorodu area, southwesternNigeria. *Water Resources*, 16(1), 65-71.

Olasehinde P. I., Amadi A. N., Dan-Hassan M. A. and Jimoh M. O. (2015). Statistical Assessment of Groundwater Quality in Ogbomosho, Southwest Nigeria. American *Journal of Mining and Metallurgy*, 3(1), 21-28, doi:10.12691/ajmm-3-1-4.

Singh, A. K., Mondal, G. C., Kumar S., Singh, T. B., Tewary, B. K. and Sinha, A. (2008). Major ion chemistry, weathering processes and water quality assessment in upper catchment of Damodar River basin. *Indian Environmental Geology*, 54(4), 745-758.

Vasanthavigar, M., Srinivasamoorthy, K., Vijayaraghavan, K. and Rajivaganthi, R. (2010). Hydrochemical Assessment of Groundwater in Thirumanimuttar Sub-basin–Implication of Water Quality Degradation by Anthropogenic Activities. *Recent Trends in Water Research: Hydrogeochemical and Hydrological Perspectives*, 99p.

United States Environmental Protection Agency (USEPA, 1997). A citizen's guide to bioremediation. Office of solid waste and emergency response, technology innovations office. Technology fact sheet. clu-in.org/products/citguide/biorem.htm.

World Health Organisation, (2010). Assessment of fresh water quality–Global environmental monitoring system (GEMS). *A report on the related environmental monitoring*, World Health Organization, Geneva, 357-362.

MODELLING ECONOMIC GROWTH IN SUB-SAHARAN AFRICA: A PANEL DATA APPROACH

I.S. Onotu®, G. I. Sule, O.M. Adetutu ,A. O. Bello, F.A Oguntolu*

Department of Statistics, Federal University of Technology, Minna.

Department of Mathematics, Federal University of Technology, Minna.*

idris.onotu@futminna.edu.ng®

gentlegiss@gmail.com

ola.adetutu@futminna.edu.ng

oyedele.bello@futminna.edu.ng

festus.tolu@futminna.edu.ng

ABSTRACT

The debate on the effectiveness of macro-economic variables as a tool for promoting growth and development remains inconclusive given conflicting results of recent studies. Thus, the controversy is yet to be settled. Against this background, this study sought to fit a model to best predict economic growth in sub-Saharan Africa considering Government revenue, Trade Openness, Urbanization and Fiscal Freedom as the predictor variables and hence further explains the combined effect of the variables on economic growth. The study made use of secondary data of sub-Saharan African Countries in panel least squares. The hypotheses were linearly tested while adopting the panel data estimation under fixed-effect assumptions. Findings reveal that all the variables except fiscal freedom has a positive and significant effect on the economic growth of sub-Saharan Africa when the countries were pooled together. Only government revenue has a negative and insignificant effect on the economic growth of the countries in the fixed-effect model which considers the heterogeneity and individuality of the countries. The study therefore recommends that Governments of sub-Saharan Africa countries should engage in critical check on the revenue generated. Improving and strengthening the fiscal freedom so as to attract inflows of investors in order to boost the economic growth and improving the standard of living of the citizens is also recommended.

Keywords: macro-economic, government revenue, trade openness, urbanization, fiscal freedom, and Gross domestic product, panel estimation, heterogeneity, fixed effect

1. INTRODUCTION

Studies has provided insights into why there is difference in the growth rate of the economy of states over time and that the level at which an economy will grow, is also determined by the choices a government makes in her tax and expenditures. Studies on the growth of an economy and its drivers have received attention among scholars but with differing evidences. Abata, et al., (2012), observed that the expansion of a country's potential Gross Domestic Product (GDP) or output represents its Economic growth.

Ulku(2004) emphasized that variation in the 48 countries of the region are extremely high, they vary in size and the economic history, with many small countries and giants such as Nigeria. In sub-Saharan Africa, the social and economic situation, remains delicate and susceptible to domestic and external shocks The ventures in sub-Saharan Africa has remained subdued, and efforts to diversify economic structures and boost growth has been limited (Nkurunziza and Bates, 2004). More so, there have been severe setbacks in development efforts of countries that have recently emerged from civil wars whereas fresh armed conflicts have erupted in other parts of the continent. Adverse conditions, such as poor weather conditions and decline in trade including conflicts, have led to loss in the drive of economy of this region over the last two decades (Ulku, 2004; Nkurunziza and Bates, 2004).
Therefore, the countries in this region are faced with key challenges such as raising economic growth, curbing poverty, reducing conflicts, also trying to integrate itself into the growing world economy. Although, growth in the economy is still not high enough (Nkurunziza and Bates, 2004) to cause an actual change in the prevailing poverty and enable these countries to compete with other developing countries.

2. LITERATURE REVIEW

Ullah and Rauf (2013) noted that whenever there is increase in real GDP of a country it will boosts up the overall output and we called it economic growth. The economic growth is helpful to increase the incomes of the society, help the nation to bring the unemployment at low level and also helpful in the deliveries of public services.
Fadare (2010) noted that growth in economy has long been considered an important aspect of policy making in economy with a substantial body of research dedicated to explaining how this aspect can be achieved.
Khorravi & Karimi (2010) observed that economic growth is largely linked to labour and capital as factors of production. The development of the endogenous growth theory has encouraged specialists to question the role of other factors in explaining the economic growth phenomenon.

Economic growth in sub-Saharan Africa

According to Andersan and Tarp (2003), there is weak evidence of growth-led finance using market size as the indicator of stock market development. In summary, the picture that emerges from the different econometric studies is blurred. In cross-section studies there is a positive correlation between financial development and growth, but in the poorest countries the correlation is negative. In individual-country studies, different causal patterns between financial development and economic growth are characteristic. In some countries, finance seems to lead growth, while there is reverse causality or no clear causal link elsewhere. Moreover, conclusions are very sensitive to the type of estimator used and slight changes in nuisance parameters often change the results.
Research and development (R&D) is another important determinant of economic growth. It plays a major role in economic progress by way of increasing productivity and growth (Artelaris *et al.*, 2007) since the increased use of technology enables introduction of new and superior products and processes. This role has been stressed by various endogenous growth models with the strong relation between R&D and economic growth being empirically affirmed by many studies.
Economic policies and macroeconomic conditions have also attracted much attention as determinants of economic performance. This is because they can set the framework within which economic growth takes place (Barro and Sala-i-Martin, 1995). Economic policies can influence several aspects of an economy through investment in human capital and infrastructure, improvement of political and legal institutions. In addition, a stable macroeconomic environment may favour growth through the reduction of uncertainty, whereas

macroeconomic instability may have a negative impact on growth through its effects on productivity and investment.

Openness to trade has also been used extensively in the economic growth literature as a major determinant of growth performance (Artelaris *et al.*, 2007). Openness affects economic growth through several channels such as exploitation of comparative advantage, technology transfer and diffusion of knowledge, increasing scale economies and exposure to competition. Openness is usually measured by the ratio of exports to GDP (Dollar and Kraay, 2000). It has been found that economies that are more open to trade and capital flows have higher GDP per capita and grow faster.

Foreign Direct Investment (FDI) has recently played a crucial role of internationalizing economic activity and as a primary source of technology transfer and economic growth. The empirical literature examining the impact of FDI on growth has provided more-or-less consistent findings affirming a significant positive link between the two (Lensink and Morrissey, 2006).

3. METHODOLOGY

Nature and Data Sources

The nature of the data used for this study was a cross-sectional and time series data which is a secondary source of data collected from International Monetary Fund (IMF) and World Bank Data websites of selected sub-Saharan Africa countries spanning from 2003 to 2012.

Given the wide geographical location of African continent, studying countries of African continent though not impossible could be cumbersome. While this could be technically possible at least within the context of this work, a sample was considered ideal to be used for this study which include: Nigeria, South Africa, Burkina faso, Egypt, Uganda, Ethiopia, Ghana, Kenya, Tunisia, Angola, Morocco, Cote d'Ivoire, Mali, Benin, Madagascar, Namibia, Seychelles, Sierra Leone, Togo.

Model Specification

Many research work has been carried out on the use of pooled OLS and other economic models such as random effects and fixed effect model on the impact on many micro and macro-economic theory and policies. Research conducted by Tina Vuko and Marko Cular (2014) who used pooled cross-sectional model to establish dependencies of audit opinion, leverage, profitability, audit effort, absolute level of total accruals, company size and audit committee on Audit delay or reporting. In order to test our hypotheses on the impact of the macro-economic variables on economic growth, we estimate the following pooled cross-sectional regression:

$$EG_{it} = \alpha + \beta GR_{it} + \gamma OT_{it} + \delta UR_{it} + \theta FF_{it} + \epsilon_{it}$$

Where EG = economic growth (dependent variable), GR = government revenue, OT = degree of openness to trade, UR = urbanization, FF = fiscal freedom, *i* denotes the different sub-Saharan African countries in the sample and t denotes the time dimension. While ϵ_{it} is the random error for country *i* and year t.

However before proceeding on fitting such model, the panel diagnostics tool of Hausman, H statistic which is a unit scalar from a positive definite matrix and distributed as chi-square distribution would be used to identify whether fixed effect model or random effect model is best for this research work, while also running a background check on the model diagnostics to ensure conformance with assumptions such as normality, heteroscedasticity among others.

Techniques of Analysis

The economic pooled cross-sectional model was proposed for this research work among others to establish whether or not relationship exist between the dependent variable and the stated set of predictors variables which are measured on continuous scale, the parameters estimates are expected to be linear while it is also expected that the predictors (independent variables) be as independent/uncorrelated as much as possible, should this assumption fail, multicollinearity set in which renders the results inconsistent and inaccurate.

Panel Data Estimation

Panel data or longitudinal data sets are defined as one that combine time series and cross sections, in other words panel data sets are repeated measurements at different points in time on the same unit such as an individual, household, industry, firm or, in this case, country. Estimations based on panel data sets can therefore capture variation in cross sectional units over time. However, modelling in this setting requires more complex stochastic specifications. The main focus of the analysis when using panel data is the heteroscedasticity across cross-sectional units (Greene (2002); Wooldridge (2002))

4. EMPIRICAL RESULTS AND DISCUSSION

Table 1 presents a descriptive statistics on all the variables of interest. Economic growth (per capita GDP) of the selected Sub-Saharan African countries has a mean value of 2.9833 per capita GDP with minimum and maximum being 2.1324 and 4.1544 respectively. Government revenue stands at an average of 20.7855% of GDP with maximum of 57.7875% and crashed with a minimum of 4.9996%. Openness to trade has a mean value of 0.7624% share of GDP with maximum value at 2.1731% and minimum of 0.3073%. The Urbanization rate stands at an average of 39.6803% with maximum and minimum value being 77.9880% and 12.4830% respectively. While Fiscal freedom as a mean value of 73.4591 with maximum and minimum value being 95.0000 and 49.7000 respectively.

Table 1. Descriptive statistics for the economic variables.

Variables					
Statistics	**EG**	**GR**	**OT**	**UR**	**FF**
• Mean	2.9833	20.7855	0.7624	39.6803	73.4591
• Median	2.7812	17.0051	0.6569	39.4480	74.8000
• Minimum	2.1324	4.9996	0.3073	12.4830	49.7000
• Maximum	4.1544	57.7875	2.1731	77.9880	95.0000
• Std.dev.	0.4875	9.9836	0.3588	14.2073	9.8494
• Coefficient of variation	0.1634	0.4803	0.4707	0.3580	0.1341
• Skewness	0.6553	0.9318	1.7300	0.0058	-0.5448
• Excess kurtosis	-0.5646	0.4597	3.5538	-0.5079	-0.1837

Apart from the first moment statistics, the results of other statistics are also evident from the table. Kurtosis measures the peakedness or flatness of the distribution of the series. The statistic for excess kurtosis shows that economic growth, urbanization and fiscal freedom are platykurtic (flat-topped relative to the normal), while government revenue, openness to trade are leptokurtic (peaked relative to the normal). Skewness is a measure of asymmetry of the distribution of the series around the mean. The statistic for skewness shows that all variables except fiscal freedom are positively skewed, implying that this distributions have long right tails.

Table 2 presents the ranking for each country with respect to the economic variables. This is interpreted from the top to the least country respectively. The result reveals that Angola has the highest mean government revenue of 40.010% of GDP and ranking 1st, while Nigeria has a mean of 9.643% of GDP and ranks 18th and the least ranked country was Sierra leone with a mean of 9.553% of GDP and ranks 19th. Also, Seychelles has the highest mean of openness to trade of 1.886% share of GDP and ranks 1st, Nigeria has a mean openness to trade of 0.570% share of GDP and ranks 13th, while Benin has a mean openness to trade of 0.451% of GDP and ranks 19th least among the countries selected. Also, Seychelles mean economic growth rate over this period is 4.085% per capita GDP and ranks 1st, Nigeria has a mean economic growth rate of 2.942% per capita GDP and ranks 10th and Ethiopia is least ranked, that is 19th, with a mean growth rate of 2.292% per capita GDP. It can be seen from the table that Tunisia has is ranked 1st with 65.499% urbanization rate in this region, Nigeria ranked 10th with a mean urbanization of 41.277% and Uganda grows with a mean urbanization rate of 13.767% and ranks 19th. Finally, Angola has a mean fiscal freedom of 84.757 and ranks 1st, Nigeria has a mean fiscal freedom of 83.960 and ranks 2nd while the least ranked is Togo with a mean fiscal freedom of 56.180.

Table 2 Descriptive Statistics of the Economic Variables. Mean, Standard deviation in bracket and the Rank of each Country in relation to the Variables.

Countries	*GR*	*Rank*	*OT*	*Rank*	*EG*	*Rank*	*UR*	*Rank*	*FF*	*Rank*
Nigeria	9.643 (3.039)	18th	0.570 (0.107)	13th	2.942 (0.068)	10th	41.277 (2.657)	10th	83.960 (0.721)	2nd
South Africa	29.522 (1.594)	4th	0.599 (0.068)	12th	3.738 (0.029)	2nd	60.875 (1.624)	2nd	69.460 (0.698)	12th
Egypt	25.242 (2.274)	7th	0.558 (0.098)	15th	3.143 (0.046)	9th	43.021 (0.044)	8th	80.270 (12.510)	6th
Uganda	12.761 (1.480)	15th	0.494 (0.103)	17th	2.549 (0.052)	16th	13.767 (0.885)	19th	80.590 (0.152)	5th
Ghana	18.178 (3.679)	8th	0.838 (0.154)	8th	2.751 (0.063)	11th	49.010 (2.060)	5th	80.910 (4.347)	4th
Kenya	17.212 (1.595)	10th	0.566 (0.040)	14th	2.743 (0.032)	12th	22.629 (1.150)	17th	79.290 (2.964)	7th
Tunisia	28.334 (2.211)	6th	0.985 (0.105)	4th	3.545 (0.041)	4th	65.499 (0.539)	1st	74.000 (3.603)	9th
Angola	40.010 (10.389)	1st	1.186 (0.125)	2nd	3.330 (0.109)	6th	42.473 (12.643)	9th	84.757 (5.960)	1st
Morocco	32.624 (2.478)	3rd	0.752 (0.097)	9th	3.333 (0.045)	5th	56.429 (1.509)	3rd	65.160 (2.571)	16th
Cote d'ivoire	15.738 (1.292)	13.5th	0.900 (0.042)	6.5th	2.994 (0.009)	7.5th	48.703 (2.220)	6.5th	60.620 (12.336)	17.5th
Burkina faso	15.738 (1.292)	13.5th	0.900 (0.042)	6.5th	2.994 (0.009)	7.5th	48.703 (2.220)	6.5th	60.620 (12.336)	17.5th
Mali	16.770 (0.782)	11th	0.646 (0.048)	11th	2.671 (0.023)	14th	34.032 (2.372)	15th	66.880 (4.576)	13th
Benin	17.636 (1.276)	9th	0.451 (0.050)	19th	2.737 (0.009)	13th	40.927 (1.134)	11th	65.460 (9.814)	14th
Ethiopia	10.470 (1.496)	17th	0.453 (0.038)	18th	2.292 (0.102)	19th	16.516 (0.982)	18th	74.320 (3.115)	9th

Madagascar	11.424 (1.262)	16th	0.735 (0.083)	10th	2.445 (0.017)	18th	30.408 (1.831)	16th	81.720 (4.961)	3rd
Namibia	28.577 (3.331)	5th	1.013 (0.153)	3rd	3.589 (0.043)	3rd	39.133 (3.015)	12th	66.780 (1.786)	15th
Seychelles	38.584 (4.922)	2nd	1.886 (0.217)	1st	4.085 (0.049)	1st	51.700 (0.767)	4th	73.325 (5.527)	11th
Sierra leone	9.553 (1.283)	19th	0.518 (0.170)	16th	2.540 (0.037)	17th	37.551 (0.851)	13th	76.660 (4.692)	8th
Togo	16.628 (1.240)	12th	0.949 (0.047)	5th	2.584 (0.007)	15th	36.362 (1.422)	14th	56.180 (6.642)	19th

Having described the characteristics of the data, we begin by checking the correlation between these variables (Table 3) and running a multicollinearity diagnostic check (Table 4) using the variance inflation factor and tolerance rate to determine if multicollinearity is present or not.

It is observed that government revenue shows a positive and significant relationship with the degree of openness to trade, economic growth, and urbanization which is put to about 61%, 79% and 55% respectively indicating that as government revenue increases, these economic variables also increases significantly. While it has a negative but not significant relationship with fiscal freedom, meaning as government revenue increases, fiscal freedom decreases but not at a significant rate and vice versa. The degree of openness to trade has a positive and significant relationship with economic growth and urbanization, indicating that as degree of openness is increased, economic growth and urbanization increases significantly, while it has a negative and significant relationship with fiscal freedom. Also, the results obtained indicates that economic growth has a positive and significant relationship with urbanization, implying that as economic growth increases, the urbanization rate increases significantly, but a negative and not significant relationship with fiscal freedom. Lastly, urbanization has a negative and significant relationship with fiscal freedom, revealing that as urbanization rate increases, fiscal freedom decrease significantly.

Table 3 Correlation coefficient matrix with p-values in bracket

	GR	***OT***	***EG***	***UR***	***FF***
GR	1.000				
OT	0.608*** (0.000)	1.000			
EG	0.788*** (0.000)	0.664*** (0.000)	1.000		
UR	0.546*** (0.000)	0.440*** (0.000)	0.724*** (0.000)	1.000	
FF	-0.078 (0.298)	-0.158*** (0.034)	-0.106 (0.159)	-0.236*** (0.001)	1.000

***** corresponds to statistically significant at 5%.**

Table 4 Multico-llinearity diagnostic test

Factor/ Variable	*Multicollinearity Diagnostic Test*	
	Tolerance rate	*Variance Influence Factor (VIF)*
GR	0.612	1.633
OT	0.696	1.437
UR	0.653	1.531
FF	0.933	1.072

Multicollinearity is a serious case if tolerance rate < 0.4, and VIF > 10.

Table 4 above shows the testing of multicollinearity using Tolerance rate and VIF. There is serious case of multicollinearity whenever the tolerance rate is less than 0.4 and the VIF is greater than 10. Hence, since the result of the test shows that no tolerance rate is less than 0.4 and no VIF is greater than 10, we conclude that the model fitted does not suffer from the problem of multicollinearity.

5. CONCLUSION

This study has attempted to fit a parsimonious model that best predict economic growth of the sub-Saharan Africa using the Pooled OLS model which pools the countries together and considers them the same, thereby minimizing error that may arise between them. This study further attempts to ascertain the combined effect of the macroeconomic variables - Government revenue (GR), Urbanization (UR), Openness to trade (OT) and Fiscal freedom (FF) on Economic growth (EG). The study also fitted a Fixed Effect model to best explain the unobserved effect present in this countries that is, in terms of the individuality and heterogeneity of each of the country. We found out that Government revenue, Urbanization, Openness to international trade have a positive and significant effect on the economic growth of the region while that of Fiscal freedom was positive. Implying that Government revenue has a negative impact on the economic growth which contradicts the theory of having a positive impact on economic growth.

Some key recommendations made from the findings of this study were first, improving and strengthening the components of economic freedom (fiscal freedom) will certainly create a more pleasant investment climate favorable for businesses to flourish. Since a business environment consistent with economic freedom can foster economic growth in order to attract inflows of investors. Secondly, Openness to trade is another important predictor for driving growth but must be cautiously allowed in order not to discourage indigenous manufacturers. Thirdly, excessive and unnecessary spending of the generated revenue by the governments of these countries should be drastically reduced and continuity in government projects should be encouraged.

References

Abata, M. A., Kehinde, J. S. and Bolarinwa, S. A. (2012). Fiscal/Monetary Policy and Economic Growth in Nigeria: A Theoretical Exploration. International Journal of Academic Research in Economics and Management Sciences, 1(5), 75 – 88.

Andersen, T. & Tarp, F. (2003). Financial Liberalization, Financial Development and Economic Growth in LDCs. *Journal of International Development*, 15, 189-209.

Artelaris, P., Arvanitidis P. and Petrakos G. (2007). "Theoretical and methodological study on dynamic growth regions and factors explaining their growth performance" Paper presented at the 2nd Workshop of DYNREG in Athens, 9-10 March.

Barro R. J. and Sala-i-Martin X. (1995). "Economic Growth", New York: McGraw-Hill.

Dollar D. and Kraay A. (2000). "Trade, Growth and Poverty," The World Bank Development

Research Group, Washington, (mimeo).

Fadare, S.O. (2010). Recent Banking Sector Reforms and Economic Growth in Nigeria. Middle Eastern Finance and Economics. 8: 1450-2889.

Hulya Ulku, (2004). R&D, Innovation, and Economic Growth: An Empirical Analysis.

Khosravi, A. and Karimi, M. S. (2010). To Investigate the Relationship between Monetary Policy, Fiscal Policy and Economic Growth in Iran: Autoregressive Distributed Lag Approach to Cointegration. *American Journal of Applied Sciences,* 7(3), 420 - 424.

Lensink W. and Morrissey O. (2006). "'Foreign Direct Investment: Flows, Volatility and the Impact on Growth", Review of International Economics, 14, 3, 478-493.

Nkurunziza, J. D. & Bates, R. H. (2004). *Political institutions and economic growth in Africa* (Center for International Development Working Paper, No. 98). Harvard University.

Ullah, F. and Rauf, A. (2013). Impacts of Macroeconomic Variables on Economic Growth: A Panel Data Analysis of Selected Asian Countries, *GE-International Journal of Engineering Research available on line at* www.gejournal.net

THE ALGEBRAIC STRUCTURE OF AN IMPLICIT RUNGE-KUTTA TYPE METHOD

R. Muhammad[1*] Y. A Yahaya[2] A.S Abdulkareem[3].

[3]Department of Chemical Engineering, Federal University of Technology, Minna.

[1&2]Department of Mathematics/Statistics , Federal University of Technology, Minna.

[1]r.muhd@futminna.edu.ng

[2]yusuphyahaya@futminna.edu.ng

[3]kasaka2003@futminna.edu.ng

[*]Corresponding author

Abstract

In this paper, the theory of linear transformation (Homomorphism) and monomorphism is applied to a first order Runge-Kutta Type Method illustrated in a Butcher Table and the extended second order Runge- Kutta Type Methods in order to substantiate their uniform order and error constant.

Keywords:,linear transformation, implicit, runge-kutta type

1. Introduction

A function T between two vector spaces $T: V \rightarrow W$ that preserves the operations of addition if v_1 and $v_2 \epsilon V$ then

$$T(v_1 + v_2) = T(v_1) + T(v_2) \quad (1)$$

And scalar multiplication if $v\epsilon V$ and $r\epsilon R$, then

$$T(r.v) = rT(v) \quad (2)$$

is a homomorphism or linear Transformation, Agam (2013).

A homomorphism that is one to one or a mono is called a monomorphism.

The monomorphism Transformation preserves its algebraic structure and the order of the Domain into its Range.

Butcher and Hojjati (2005) extended the general linear method to the case in which second derivative as well as first derivative can be calculated. They constructed methods of third and fourth order which are A-stable, possess the Runge-Kutta stability property and have a diagonally implicit structure for efficient implementation. However, they concentrated on only linear problems for which it is possible to compute accurate starting methods, the general purpose starting methods for non-linear problems were not developed. Okunuga, Sofoluwe , Ehigie and Akanbi (2012) presented a direct integration of second order ordinary differential equation using only Explicit Runge-Kutta Nystrom (RKN) method with higher derivative. They derived and tested various numerical schemes on standard problems. Due to the limitations of Explicit Runge-Kutta (ERK) in handling stiff problems, the extension to higher order Explicit Runge-Kutta Nystrom

(RKN) was considered and results obtained showed an improvement over conventional Explicit Runge-Kutta schemes. The Implicit Runge-Kutta scheme was however not considered. Yahaya and Adegboye (2013) derived an implicit 6-stage block Runge-Kutta Type Method for direct integration of second order (special or general), third order (special or general) as well as first order initial value problem and boundary value problems. The theory of Nystrom was adopted in the reformulation of the methods. The convergence and stability analysis of the method were conducted and the region of absolute stability plotted. The method was A-stable, possessed the Runge-Kutta stability property, had an implicit structure for efficient implementation and produced simultaneously approximation of the solution of both linear and non linear initial value problem. Numerical results were obtained to illustrate the performance and comparisons made to some standard known. The step number was restricted to 4.

2. Methodology

Let T be a linear transformation which is continuously differentiable on a set of ordered three- tuple vector $\in \mathbb{R}^3$ as follows

$$V_i = (x + c_i h, y + \sum_{j=1}^{s} a_{ij}\, T(v_j), y' + \sum_{j=1}^{s} a_{ij} T'(v_j)) \in \mathbb{R}^3 \quad (3)$$

$$T(V_i) = h(y' + \sum_{j=1}^{s} a_{ij} T'(v_j)) \quad (4)$$

and

$$T'(v_i) = hf\left(x + c_i h, y + \sum_{j=1}^{s} a_{ij}\, T(v_j), y' + \sum_{j=1}^{s} a_{ij} T'(v_j)\right) = hm_i \quad (5)$$

$$i.e\ m_i = f\left(x + c_i h, y + \sum_{j=1}^{s} a_{ij}\, T(v_j), y' + \sum_{j=1}^{s} a_{ij} T'(v_j)\right) \quad (6)$$

Then the Transformation $T: \mathbb{R}^3 \to \mathbb{R}$ is a well defined monomorphism:

Proof

Let $u, v \in \mathbb{R}$ defined by

$$U = (x + c_i h, y_1 + \sum_{j=1}^{s} a_{ij}\, T(u_j), y_1' + \sum_{j=1}^{s} a_{ij} T'(u_j)) \quad (7)$$

$$V = (x + c_i h, y_2 + \sum_{j=1}^{s} a_{ij}\, T(v_j), y_2' + \sum_{j=1}^{s} a_{ij} T'(v_j)) \quad (8)$$

$$T(U + V) = h(y_1' + y_2' + \sum_{j=1}^{s} a_{ij}\, (T'(u_j) + T'(v_j)) \quad (9)$$

By the definition of T on $\mathbb{R}^3$

$$= h\left(y_1' + \sum_{j=1}^{s} a_{ij} T'(u_j)\right) + h(y_2' + \sum_{j=1}^{s} a_{ij} T'(v_j)) \quad (10)$$

$$T(U + V) = T(U) + T(V) \quad (11)$$

$$T(k.U) = k.T(U) \quad (12)$$

Hence T is a homomorphism

Now we show that $T$is $1-1$

Let $u, v \epsilon \mathbb{R}^3$ with

$T(u) = T(v)$ (13)

By definition of T

$\Rightarrow h(y_1' + \sum_{j=1}^{s} a_{ij}\, T'(u_j)) = h(y_2' + \sum_{j=1}^{s} a_{ij}\, T'(v_j))$ (14)

Since

$T(u) = T(v)$ then $T(u_j) = T(v_j)$ and $T'(u_j) = T'(v_j)$ (15)

$y_1 = y_2$ and $x_1 + c_i h = x_2 + c_i h\ i{:}e\ x_1 = x_2$ (16)

Hence $U = V$ (17)

Thus T is $1-1 \Leftrightarrow$ a monomorphism from $\mathbb{R}^3 \to \mathbb{R}$

Remark: The necessity for the above proposition is to ensure that the algebraic structure and the order does not change during the transformation. We consider for the case K=1.

Consider the Butcher Table 3.1 and Table 3.2

Table 3.1: The Butcher Table for K=1

0	0	0	0
$\frac{1}{2}$	0	$\frac{3}{4}$	$\frac{-1}{4}$
1	0	1	0
	0	1	0

Table 3.2: The Butcher Table for second order for K=1

0	0	0	0	0	0	0
$\frac{1}{2}$	0	$\frac{3}{4}$	$\frac{-1}{4}$	0	$\frac{5}{16}$	$\frac{-3}{16}$
1	0	1	0	0	$\frac{3}{4}$	$\frac{-1}{4}$
	0	1	0	0	$\frac{3}{4}$	$\frac{-1}{4}$

The table 3.1 satisfies the Runge-Kutta conditions for solution of first order ode since

$(i) \quad \sum_{j=1}^{s} a_{ij} = c_i$ (18)

$(ii) \quad \sum_{j=1}^{s} b_j = 1$ (19)

We consider the general second order differential equation in the form

$y'' = f(x, y, y'), y(x_0) = y_0 \quad y'(x_0) = \quad y_0'$ (20)

$y'' = f(v), \qquad v = (x, y, y')$ (21)

$T(V_i) = T\left(x + c_i h, y + \sum_{j=1}^{3} a_{ij} T(V_j), y' + \sum_{j=1}^{3} a_{ij} T'(V_j)\right)$ (22)

$= h\,(y' + \sum_{j=1}^{3} a_{ij}\, T'(V_j)) = h\,(y' + \sum_{j=1}^{3} a_{ij}\, hm_j)$ (23)

$T(V_1) = h(y' + 0hm_1 + 0hm_2 + 0hm_3)$ (24)

$T(V_2) = h(\left(y' + 0hm_1 + \frac{3}{4}hm_2 - \frac{1}{4}hm_3\right))$ (25)

$T(V_3) = h(y' + 0hm_1 + hm_2 + 0hm_3)$ (26)

Also

$m_i = T'(V_j) = f\left(x + c_i h, y + \sum_{j=1}^{s} a_{ij} T(V_j), y' + \sum_{j=1}^{s} a_{ij} T'(V_j)\right)$ (27)

$m_1 = f(x + 0h, y + 0 + 0 + 0)$ (28)

$m_2 = f(x + \frac{1}{2}h, y + \frac{1}{2}hy' + \frac{5}{16}h^2 m_2 - \frac{3}{16}h^2 m_3, y' + \frac{3}{4}hm_2 - \frac{1}{4}hm_3)$ (29)

$m_3 = f(x + h, y + hy' + \frac{3}{4}h^2 m_2 - \frac{1}{4}h^2 m_3, y' + hm_2\ )$ (30)

The direct method for solving $y'' = f(x, y, y')$ is now

$y_{n+1} = y_n + b_1 T(V_1) + b_2 T(V_2) + b_3 T(V_3)$ (31)

$y_{n+1} = y_n + 0T(V_1) + T(V_2) + 0T(V_3)$ (32)

$y_{n+1} = y_n + T(V_2)$ (33)

$y_{n+1} = y_n + h\left(y_n' + \frac{3}{4}hm_2 - \frac{1}{4}hm_3\right)$ (34)

$y_{n+1} = y_n + hy_n' + \frac{h^2}{4}(3m_2 - m_3)$ (35)

$y_{n+1}' = y_n' + b_1 T'(V_1) + b_2 T'(V_2) + b_3 T'(V_3)$ (36)

$y_{n+1}' = y_n' + 0hm_1 + hm_2 + 0hm_3$ (37)

$y_{n+1}' = y_n' + hm_2$ (38)

3. Results and Discussion

We made use of the coefficients of the Butcher table of the first order RKTM to prove to the second order RKTM. Equation (35) and (38) satisfy the Runge-Kutta consistency conditions of second and first order respectively. This further shows that it is a monomorphism.

4. Conclusion

This research work established the reason behind uniform order and error constant of the first order Runge-kutta type method and the extended second order Runge-kutta type method. Also why the algebraic structure and the order of the two methods are preserved and not changed during the transformation.

References

Adegboye, Z.A (2013), Construction and implementation of some reformulated block implicit linear multistep method into Runge-Kutta type method for initial value problems of general second and third order ordinary differential equations. Unpublished doctoral dissertation, Nigerian Defence Academy, Kaduna .

Agam, A.S (2012), A sixth order multiply implicit Runge-Kutta method for the solution of first and second order ordinary differential equations. Unpublished doctoral dissertation, Nigerian Defence Academy, Kaduna .

Butcher, J.C (2008), *Numerical methods for ordinary differential equations.* John Wiley & Sons. C ,463.

Butcher, J.C & Hojjati, G. (2005). Second derivative methods with Runge-Kutta stability. *Numerical Algorithms*, Vol.40, 415-429.

Chollom J.P.,Olatun-bosun I.O, & Omagu S. (2012). A class of A-stable block explicit methods for the solutions of ordinary differential equations. *Research Journal of Mathematics and Statistics,* Vol. *4(2),*52-56.

Kendall, E. A (1989). *An introduction to numerical analysis*, (2nd ed), John Wiley & Sons.367.

Okunuga, S.A, Sofulowe, A.B, Ehigie, J.O, & Akanbi, M.A. (2012). Fifth order 2-stage explicit runge kutta nystrom (erkn) method for the direct integration of second order ode. *Scientific Research and Essays*, Vol. *7(2),* 134-144.

Yahaya Y.A. and Adegboye Z.A. (2013). Derivation of an implicit six stage block runge- kutta type method for direct integration of boundary value problems in second order ode using the quade type multistep method. *Abacus*, Vol.*40(2)*, 123-132.

Yahaya, Y.A. & Ajibade, M.T. (2012). A reformulation of a two-step hybrid linear multistep method (lmm) into a 3-stage runge-kutta type (rkt) method for solution of ordinary differential equation. *Book of Readings of the 4th Annual National Conference of the School of Science and Science Education, Federal University of Technology Minna, Nigeria,* Vol. *2(4), 193-198.*

Yahaya, Y.A. & Badmus, A.M. (2009). A class of collocation methods for general second order ordinary differential equations. *African Journalof Mathematics and Computer Science Research 2(4),* 69-72.

CHARACTERIZATION AND ANTIBIOGRAM OF BACTERIA ISOLATED FROM SURGICAL WOUNDS OF PATIENTS ATTENDING IBRAHIM BADAMASI BABANGIDA SPECIALIST HOSPITAL MINNA, NIGER STATE.

ABUBAKAR, I[1]; ENOCH, G.N[1].; MAIKAI, S.S[1]; ABDULLAHI, M.Y[1].; USMAN, A[2]; and TANKO, J.D.[3];

[1]Department of Biological Science, Niger state Polytechnic**,** Zungeru, Niger State, Nigeria
[2]School of Physical Science, Department of Statistics, Federal University of Technology, Minna, Nigeria
[3]Department of Microbiology, Kaduna State University, Kaduna, Kaduna State, Nigeria

Corresponding e-mail:-eedreez98@yahoo.com

Abstract

Surgical wounds are one of the major sources to the establishments of infections by bacteria pathogens creating a medium through which these pathogens can access the internal tissues, Post-operation wound infections is discovered to pose a major challenges in the field of surgery couple with the current spread of multi-drug resistant bacteria pathogens. The study was aimed at determining the proximate bacteria isolated from surgical wound of patients attending Ibrahim Badamasi Babagida specialist hospital Minna, Niger state. Fifty (50) samples were collected from the patient using sterile swab stick, inoculated on the prepared nutrient agar, incubated and identified morphologically, using biochemical characterization and investigating the antibiotic sensitivity of bacteria by Gram staining biochemical test, culturing and use of sensitivity test discs. The result for the proximate analysis indicated that thirty samples were contaminated with Gram positive and Gram negative bacteria. Three (3) proximate bacteria were Gram negative bacteria which include *Pseudomonas aeruginosa*, *Escherichia coli* and *Klebsiella ozaenae*. While four (4) other proximate bacteria were Gram positive which include *Staphylococcus aureus*, *Streptococcus pyogenes*, *Streptococcus agalactiae* and *Clostridium perfringens*. The result revealed that *Staphylococcus aureus* has the highest prevalence of 14 samples (46.67%) followed by *Pseudomonas aeruginosa* of 6 samples (20%), both *Streptococcus agalactiae* and *Streptococcus pyogenes* has prevalence of 3 samples (10%) each, *Escherichia coli* of 2 samples (6.67%), finally *Clostridium perfringens* and *Klebsiella ozaenae* of 1 sample (3.33%) each. From the susceptibility analysis *Klebsiella ozaenae* and *Clostridium perfringens* were the Gram positive and Gram negative isolate having the highest percentage of the sensitivity and resistance to the antibiotic disc respectively. Thus due to high resistance of organisms to antibiotics, rational uses of sensitivity disc was used for the determination.

Key words: Proximate analysis, antibiotic, sensitivity disc, susceptibility analysis.

Introduction

The skin is one of the major impediments to the establishment of infections by bacteria pathogens in internal tissues (first line of defense) meanwhile wounds results in physical disruption of the skin, creating a medium through which these pathogens can access the internal tissues (Mehta *et al*., 2007). The most common underlying event for all wound is trauma. Trauma may be accidentally (accidents) or intentionally (hospital-acquired wounds) induced never the less, wound infections are grouped according to how they are acquired. The current spread of multi-drug resistant bacteria pathogens has added a new dimension to the problem of wound infections. Infection at the site of surgery has been recognized as an issue probably for as long as man has been incising tissues to alleviate the symptoms of disease and injury. Historically, surgical interventions were nearly always associated with infection, patient mortality being accepted as almost inevitability. Developments in infection control, surgical techniques, antibiotics and our understanding of the body's

response to bacterial infection have all resulted in surgery being a safer undertaking (Bouchillon *et al.*, 2004). However, post operation wound infections still remains an issue. Most surgical wounds are contaminated by both pathogens and body commensalism ranging from bacteria and fungi to other parasites. The common Gram positive organisms are the β hemolytic streptococcus, *Streptococcus pyogenes* and *Staphylococcus aureus*. The Gram negative aerobic rod is *Pseudomonas aeruginosa*. The facultative anaerobes include enterobacter species and *Aspergillus* species (Mulu *et al.*, 2012), but the development of infection in the site depends greatly on the complex interaction of many factors such as microbial virulence (Bowler *et al*., 2001), patient risk factor like diabetes, citrate smoking, obesity and coincident remote site infection or colonization (Altekruse *et al.*, 2009) and operation-like risk factors including prolonged hospital stay before surgery, duration of the operation, tissue trauma, poor homeostasis and foreign materials in the wound. Post-operation wound infections have been found to pose a major problem in the field of surgery. It may occur as a primary wound infection following surgical operation from sources in the ward or as secondary wound infection due to some other complications (Masaadeh and Jaran, 2009). In fact, most post-operative wound infections are hospital acquired (nosocomial infection) and varies from one hospital to another (Gupt *et al.*, 2000). Antimicrobial resistance among pathogens of wound infections has become more challenging due to wide spread of bacteria resistance to antibiotics and to greater incidence of infections caused by bacteria (Akinjogunla *et al*., 2011). The pattern of antimicrobial susceptibility of bacteria is a worldwide change, especially in developing countries making antimicrobial agent increasingly less effective infections with multiple drug resistant pathogens whether in hospital or in the community increase morbidity, decrease treatment success, reduce hospital turn-over rate and increase cost of patient care (Alebachew *et al*., 2013). High incident was recorded as children surgical patients in Nigeria reported high surgical wound infection. Thus, this research study is conducted to determine the prevalence and antibiotic susceptibility pattern of bacteria isolated from surgical wounds of patients attending Ibrahim Badamasi Babagida Specialist Hospital Minna, Niger State, Nigeria by isolation and morphological identification of bacteria isolated from such surgical wounds at the same time identifying and investigating the antibiotic sensitivity of bacteria by Gram staining biochemical test, culturing and use of sensitivity test discs.

Methodology

Sample collection

Fifty (50) sterile and well labeled swab stick was aseptically used to collect surgical wound sample from patient attending Ibrahim Badamasi Babangida Specialist Hospital Minna, Niger state that has undergone surgical operations such as appendietis and prostrate operation. The wound sample was collected in the morning before the dressing of the wound. After collection, the swab stick were appropriately labeled with the patients identifiers which includes the patient names, hospital number, date and time of sample collection, specimen type and test requested. The entire specimens were delivered to the laboratory as soon as possible after each collection. Drops of physiological saline were added into the swab stick and were tightly sealed

with masking tape at the edge to avoid contamination. The samples were transported at room temperature and were refrigerated.

Serial dilution

Sterile test tubes were arranged in a test rack and labeled accordingly with the use of masking tape. Nine miles of distilled water was transferred to the first test tube and then serially diluting into the remaining 4 test tube for each sample. Each tube was a 10 fold dilution starting from the undiluted tubes. 1ml of the wound sample was added to the first test tube and was shocked thoroughly. 1ml of the undiluted solution from the test tube was drown with a sterile pipette and was transferred to the test tube labeled 1:10 containing 9ml of the diluted liquid and was mixed thoroughly. The solution was being diluted by a factor of 10. For the second serial dilution, 1ml of solution from test tube labeled 1:10 was from the tube and was added to 9ml of diluted liquid in the tube 1:100 and was mixed, before adding 1ml of 1:100 to 1:1000, this process was repeated to the fourth and fifth test tubes respectively for each of the samples. The final dilution ratio in a serial dilution was calculated and the concentration of the solution following the dilution was also calculated.

Inoculation of sample on media

Sterile nutrient Agar was prepared according to the manufacturer instruction, after sterilizing the media. It was poured into a sterile petri dish and allowed to solidify. Wire loop was flamed to red and was allowed to cooled the sterile wire loop was dipped into the swab stick and was smeared on the prepared plate. This was done repeatedly for the remaining plates and the plates were incubated at 37^{O}C for 24- 48 hours. And the growth on the plate were observes after incubation.

Morphology characteristics

After incubation, bacterial grown on the slide media was a visible as of the microorganism originated from a single mother cell. The key future of the colonies was the criteria for identification. The colonies describe the size, shape, texture, elevation, pigmentation and effect on the growth medium. Different bacteria colonies were grouped into forms (such as circular, irregular, filamentous, rhizoid). Elevation (such as raised, convex, flat, unboned, criteria) margin (such as entire, undulant, filiform curled, ligate) (Hegger *et al*., 2002)

Characterization and Identification of Bacteria Isolates

Single colonies were selected from each cultured plate and the isolates were subsequently characterized and identified by Gram staining and the biochemical tests conducted as described by Idris and Abubakar, (2016). The biochemical tests conducted include; IMViC [Indole, Methyl Red, Voges Proskauer test and Citrate utilization test] (Amenu *et al.*, 2011; Verma *et al*, 2013). Isolates were purified, identified based on the morphological, physiological and the biochemical characteristics as described in Bergey's Manual of Determinative Bacteriology.

Result

Fifty wound swabs were analyzed within the period of two month, May to June 2016. Table 1 shows the biochemical result of the isolated bacteria species, which revealed that only thirty out of the fifty wound sample that was analysis showed the presence of bacterial. Out of the 30 samples that showed the presences of bacteria three proximate bacteria were Gram negative bacteria which include *Pseudomonas aeruginosa*, *Escherichia coli* and *Klebsiella ozaenae*. While four (4) other proximate bacteria were Gram positive which include *Staphylococcus aureus*, *Streptococcus pyogenes*, *Streptococcus agalactiae* and *Clostridium perfringens*. Table 2, shows the colony forming units (cfu/mL) count of the isolate bacteria from plate count of the dilution factor. This revealed that sample 28 has the highest mean (cfu/ml) of $9.9x10^{-6}$ followed by sample 12 which has a mean of $9.2x10^{-6}$ while sample 4 has the least mean (cfu/ml) of $1.2x10^{-6}$. The percentage occurrence of the different bacteria isolated as presented in Table 3 below indicated that *Staphylococcus aureus* was the most predominant with 14 (46.67%) isolates, this is followed by *P. aeruginosa* with 6 (20%) isolates. *Clostridium perfringens and Klebsiella ozaenae* which occurred least with 1 (3.33%) isolates. Table 4 and 5 shows the percentage susceptibility of both Gram negative and Gram positive which revealed that *E. coli* showed high susceptibility to Septrin (90%), Augmentin (90%), Tarivid (80%) and Nalidixicacid (70%). *Klebsiella ozanae* exhibited 100% susceptibility to all the antibiotics, but showed 0% resistance to Septrin, Gentamycin and Ciprofloxacin *Klebsiella ozaenae* and *Pseudomonas aeruginosa* isolates were also susceptible to Reflacine and Ciprofloxacin by 100%. *Pseudomonas aeruginosa* showed susceptibility to most of the antibiotics, but resisted Ciprofloxacin (75%), Augmentin (75%) and Streptomycin (35%), *Staphylococcus aureus* isolated is highly susceptible to Rifampicin (96%), Streptomycin (92%) and Levofloxacin (88%). In the case of *Streptococcus pyogene,* the isolate exhibited 100% susceptibility to Ciprofloxacin, Chloramphenicol and Levofloxacin and strongly resisted to Amoxil (75%). *Clostridium perferinges* is strongly resisted to Gentamycin with 100% and sensistive to ciproflox, Norfloxacin.

Table 1. Characterization and possible identification of biochemical isolates from surgical wounds

s/n	Isolate	Shape	Gram rxn	Motility	Catalase	Coagulase	Oxidase	Indole	Mathylred	VP	Probable Bacteria
1	001	Cocci	+	-	+	+	-	-	-	-	*S. aureus*
2	002	Nil	Nil	Nil	Nil	Nil	Nil	Nil	Nil	Nil	Nil
3	003	Rod	-	-	-	-	-	-	-	-	*P. aeruginosa*
4	004	Nil	Nil	Nil	Nil	Nil	Nil	Nil	Nil	Nil	Nil
5	005	Rod	-	-	-	-	-	-	-	-	*P. aeruginosa*
6	006	Cocci	+								*S. agalactiae*
7	007	Cocci	+	-	+	+	-	-	-	-	*S. aureus*
8	008	Nil	Nil	Nil	Nil	Nil	Nil	Nil	Nil	Nil	Nil
9	009	Nil	Nil	Nil	Nil	Nil	Nil	Nil	Nil	Nil	Nil
10	010	Cocci	+	-	-	-	-	-	-	-	*S. pyogene*
11	011	Cocci	+	-	+	+	-	-	-	-	*S. aureus*
12	012	Nil	Nil	Nil	Nil	Nil	Nil	Nil	Nil	Nil	Nil
13	013	Cocci	+	-	+	+	-	-	-	-	*S. aureus*
14	014	Cocci	+	-	+	+	-	-	-	-	*S. aureus*

15	015	Rod	-	+	+	-	-	+	+	+	*E. coli*
16	016	Nil	Nil	Nil	Nil	Nil	Nil	Nil	Nil	Nil	Nil
17	017	Rod	+	-	-	-	-	-	-	-	*C. perferinges*
18	018	Cocci	+	-	-	-	-	-	-	-	*S. agalactiae*
19	019	Nil	Nil	Nil	Nil	Nil	Nil	Nil	Nil	Nil	Nil
20	020	Nil	Nil	Nil	Nil	Nil	Nil	Nil	Nil	Nil	Nil
21	021	Cocci	+	-	+	+	-	-	-	-	*S. aureus*
22	022	Nil	Nil	Nil	Nil	Nil	Nil	Nil	Nil	Nil	Nil
23	023	Rod	-	-	-	-	-	-	-	-	*P. aeruginosa*
24	024	Cocci	+	-	+	+	-	-	-	-	*S. aureus*
25	025	Cocci	+	-	+	+	-	-	-	-	*S. aureus*
26	026	Cocci	+	-	+	+	-	-	-	-	*S. aureus*
27	027	Nil	Nil	Nil	Nil	Nil	Nil	Nil	Nil	Nil	Nil
28	028	Nil	Nil	Nil	Nil	Nil	Nil	Nil	Nil	Nil	Nil
29	029	Cocci	+	-	-	-	-	-	-	-	*S. agalactiae*
30	030	Nil	Nil	Nil	Nil	Nil	Nil	Nil	Nil	Nil	Nil
31	031	Nil	Nil	Nil	Nil	Nil	Nil	Nil	Nil	Nil	Nil
32	032	Rod	-	-	-	-	-	-	-	-	*P. aeruginosa*
33	033	Nil	Nil	Nil	Nil	Nil	Nil	Nil	Nil	Nil	Nil
34	034	Cocci	+	-	+	+	-	-	-	-	*S. aureus*
35	035	Rod	-	-	-	-	-	-	-	-	*P. aeruginosa*
36	036	Cocci	+	-	-	-	-	-	-	-	*S. pyogenes*
37	037	Cocci	+	-	+	+	-	-	-	-	*S. aureus*
38	038	Nil	Nil	Nil	Nil	Nil	Nil	Nil	Nil	Nil	Nil
39	039	Nil	Nil	Nil	Nil	Nil	Nil	Nil	Nil	Nil	Nil
40	040	Rod	-	+	+	-	-	+	+	+	*E. coli*
41	041	Cocci	+	-	+	+	-	-	-	-	*S. aureus*
42	042	Nil	Nil	Nil	Nil	Nil	Nil	Nil	Nil	Nil	Nil
43	043	Rod	-	-	-	-	-	-	-	-	*P. aeruginosa*
44	044	Nil	Nil	Nil	Nil	Nil	Nil	Nil	Nil	Nil	Nil
45	045	Cocci	+	-	-	-	-	-	-	-	*S. pyogenes*
46	046	Nil	Nil	Nil	Nil	Nil	Nil	Nil	Nil	Nil	Nil
47	047	Cocci	+	-	+	+	-	-	-	-	*S. aureus*
48	048	Nil	Nil	Nil	Nil	Nil	Nil	Nil	Nil	Nil	Nil
49	049	Rod	-	-	-	-	-	-	-	-	*Kleb. Sp*
50	050	Cocci	+	-	+	+	-	-	-	-	*S. aureus*

Table 2. Colony forming unit counts of the isolate bacteria from plate count of the dilution factor

s/n	Samples	Ranges of CFU/mL	Mean CFU/mL
1	001	$32x10^{-3} – 29x10^{-4}$	$1.5x10^{-6}$
2	003	$20x10^{-3} – 14x10^{-4}$	$1.7x10^{-6}$
3	005	$43x10^{-3} – 14x10^{-4}$	$3.8x10^{-6}$
4	006	$15x10^{-3} – 9x10^{-4}$	$1.2x10^{-6}$
5	007	$110x10^{-3} – 85x10^{-4}$	$2.0x10^{-6}$
6	010	$51x10^{-3} – 28x10^{-4}$	$3.9x10^{-6}$
7	011	$81x10^{-3} – 46x10^{-4}$	$1.3x10^{-6}$
8	013	$8x10^{-3} – 5x10^{-4}$	$6.5x10^{-6}$
9	014	$14x10^{-3} – 11x10^{-4}$	$1.3x10^{-6}$
10	015	$23x10^{-3} – 20x10^{-4}$	$2.2x10^{-6}$
11	017	$41x10^{-3} – 31x10^{-4}$	$3.6x10^{-6}$

12	018	$105x10^{-3} – 81 x10^{-4}$	$9.3x10^{-6}$
13	021	$31x10^{-3} – 30 x10^{-4}$	$3.1x10^{-6}$
14	023	$29x10^{-3} – 23 x10^{-4}$	$2.6x10^{-6}$
15	024	$15x10^{-3} – 30 x10^{-4}$	$1.3x10^{-6}$
16	025	$16x10^{-3} – 12 x10^{-4}$	$1.4x10^{-6}$
17	026	$52x10^{-3} – 33 x10^{-4}$	$4.3x10^{-6}$
18	029	$80x10^{-3} – 50 x10^{-4}$	$6.5x10^{-6}$
19	032	$40 x10^{-3} – 50 x10^{-4}$	$3.7x10^{-6}$
20	034	$17 x10^{-3} – 9 x10^{-4}$	$1.3x10^{-6}$
21	035	$32 x10^{-3} – 25 x10^{-4}$	$2.9x10^{-6}$
22	036	$27 x10^{-3} – 16 x10^{-4}$	$2.2x10^{-6}$
23	037	$21 x10^{-3} – 18 x10^{-4}$	$3.9x10^{-6}$
24	040	$50 x10^{-3} – 37 x10^{-4}$	$4.4x10^{-6}$
25	041	$66 x10^{-3} – 50 x10^{-4}$	$5.8x10^{-6}$
26	043	$44 x10^{-3} – 40 x10^{-4}$	$4.2x10^{-6}$
27	045	$12 x10^{-3} – 16 x10^{-4}$	$1.4x10^{-6}$
28	047	$104 x10^{-3} – 94 x10^{-4}$	$9.9x10^{-6}$
29	049	$61 x10^{-3} – 52 x10^{-4}$	$5.7x10^{-6}$
30	050	$70 x10^{-3} – 63 x10^{-4}$	$6.7x10^{-6}$

Table 3: Percentage occurrence of the bacteria isolates from surgical wounds of patients attending Ibrahim Badamasi Babangida Specialist Hospital Minna, Niger State

Bacteria	**Total number**	**Percentage (%)**
Staphylococcus aureus	14	46.67
Pseudomonas aeruginosa	6	20.00
Streptococcus pyogenes	3	10.00
Streptococcus agalactiae	3	10.00
Escherichia coli	2	6.67
Clostridium perferinges	1	3.33
Klebsiella ozanae	1	3.33
Total	30	100

Table 4: percentage of susceptibility of Gram negative isolate to some antibiotics

Antibiotic	*Pseudomonas aeruginosa* n=6	*Escherichia coli* n=2	*Klebsiella ozanae* n=1
Tarivid	87.5 (12.5)	80 (20)	100 (0)
Reflacine	75 (25)	70 (30)	100 (0)
Ciprofloxacin	25 (75)	40 (60)	0 (100)
Augmentin	25 (75)	90 (10)	90 (10)

Streptomycin	37.5 (12.5)	60 (40)	50 (50)
Gentamycin	50 (50)	30 (70)	100 (0)
Ceporex	87.5 (12.5)	50 (50)	20(80)
Nalidixic acid	75 (25)	70 (30)	95 (5)
Septrin	50 (50)	90 (10)	100(0)
Amplicin	75 (25)	50 (50)	0 (100)

Key: Numbers outside bracket = susceptible percentages

Number inside bracket = resistance percentages

Table 5: percentage of susceptibility of Gram positive isolate to some antibiotics

Antibiotic	*Staphylococcus aureus* n=16	*Streptococcus pyogene* n=3	*Streptococcus agalactiae* n=3	*Clostridium perferinges* n=1
Ciprofloxacin	65 (35)	100 (0)	20 (80)	100 (0)
Norfloxacin	69 (30.9)	50 (50)	60 (40)	100 (0)
Gentamycin	19.3 (80.7)	75 (25)	50 (50)	0 (100)
Amoxil	38.4 (61.5)	50 (50)	100 (0)	90 (10)
Streptomycin	92.4 (7.6)	75 (25)	100 (0)	40 (60)
Erythromycin	96 (3.8)	73 (27)	90 (10)	50 (50)
Chlorophenicol	18 (82)	52 (58)	37.5 (62.5)	25 (75)
Ampiclox	23.1 (76.9)	75 (25)	80 (20)	87.5 (12.5)
Levofloxacin	88 (12)	100 (0)	50 (50)	25 (75)
Rifampicin	57.6 (42.3)	25 (75)	25 (75)	60 (40)

Key: Numbers outside bracket = susceptible percentages

Number inside bracket = resistance percentages

Discussion

The present study is in agreement with the report of Basu *et al.*, (2009) who carried out isolation on surgical wounds. The predominant bacteria isolates were *S. aureus* 14 (46.67%), *P. aeruginosa* 6 (20.00 %), *S. pyogenes* 3 (10.00%), *Streptococcus perfringens* 3 (10.00%), *E coli* 2 (6.67%), *Clostridium perfringens* 1 (3.33%) *and Klebsiella ozaenae* 1 (3.33%). The high prevalence of *S. aureus* infection may be because it is an endogenous microbial flora. Infection with these bacteria may also be due to contamination from the environment eg contamination of surgical instruments. With the disruption of natural skin barrier *S. aureus* which is a common bacterium on surfaces, easily find their way into wounds. Similarly high percentage of microbial growth was reported in India (86-100%) and Pakistan (98%) Ethiopia and different parts of the world showed that *S. aureus* and *E coli* were the most frequent isolates (Bhatt *et al.,* 2006). The present study

recalls that out of the 50 sample collected 30 sample were reactive to one of the bacteria, this finding is supported by investigation of Abraham and Wamisho *et al.*, (2009), who reported that the surgical wound infections are one of the most important and potentially serious complications that occur in the acute period, following injury. Massanandhand *et al*., (2009) demonstrated that the infection complications are considered a major cause of morbidity and mortality and the type and amount of bacteria on and in the injured tissues influence wound healing. Most of the isolates discovered in the study had mixed with other bacterial species and some of these have shown to be resistant to many antibiotics and this indicates the high contamination of surgical wounds in our hospitals. The reasons for high prevalence may be due to factors associated with acquisition of nosocomial pathogens in patient with recurrent or long-term hospitalization, complicating illnesses, prior administration of antimicrobial agents, or the immunosuppressive effects of burn trauma (Bhatt and Lakhey, 2006). The result of percentage prevalence of the bacteria isolates from this finding also showed that the rate of isolation of Gram positive bacteria 30 (54.54%) was more than Gram negative bacteria 25 (45.45%). This finding is in contrast with Basu *et al.,* (2009), who reported that the rate of Gram negative bacterial isolation from burn wound was more than twice that of Gram positive and it was noticed that *Klebsiella sp* was the pathogen less isolated constituting 33.3% followed by *P. aeruginosa* (23.33%) and *S. aureus* (15.33%). Resistance to some antibiotic was very low. The percentage susceptibility result showed that *Staphylococcus aureus* isolates is highly susceptible to Rifampcin (96%), Streptomycin (92%), and Levofloxacin (88%). In the case of *streptococcus pyogenes,* the isolates exhibited 100% susceptibility to Ciprofloxacin, Chloramphenicol and Levofloxacin and strongly resisted Amoxil (75%). *E coli* showed high susceptibility to septrin (90%), Augmentin (90%), Tarivid (80%) and Nalidixic acid (70%). *Pseudomonas aeruginosa* showed susceptibility to most of the antibiotics, but resisted Ciprofloxacin (75%), Augmentin (75%) and Streptomycin (63%). This might be as a result of inappropriate use of antimicrobial agents (antibiotic) and the intrinsic ability of the isolate to survive in their environment. This work disagrees with the study done in Ethiopia with average susceptibility of *S. aureus* and *Streptococcus* sp isolates (0%) and *E coli isolates* (4.5%) (Abraham & Wamisho, 2009). The result of antibiotic susceptibility showed that Streptococcus pyogenes strongly resisted Amoxil (75%). P. aeruginosa and Klebsiella ozaenae were found to be highly resistant to Gentamicin and Ciprofloxacin. High resistance of the isolate to antibiotics may be due to practicing self-medication, lack of diagnostic laboratory services or unavailability of guideline regarding the selection of drugs thereby which lead to inappropriate use of antibiotics. This finding is supported by the investigation of Raja and Shearer, (2006), who reported that more than 72% of the Gram-negative isolates of surgical wounds were resistant to Gentamycin, a commonly used antibiotic against Gram-positive infections.

Conclusion

Wound infection rate remains high and antibiotic resistance is steadily increasing. Most of the patients had been admitted for at least 8 days. This suggests that most infections were hospital acquired. *Staphylococcus aureus* and *Pseudomonas aeruginosa* were the main causes of infections. This is because *Staphylococcus aureus* is the main flora on the skin and in the environment while *Pseudomonas aeruginosa* versatile

characteristics allow it to be found in a variety of conditions and plates. Antibiotics were widely used however this correlated negatively with the rate of wound infection due to wrong choice of drug and dosage.

Recommendation

1. Due to high resistance of the organisms to antibiotic, sensitivity test should be regularly carried out to enhance rational use of antibiotic choice should be made based on the sensitivity patterns, ability to penetrate tissue, low toxicity and no allergic reactions. The prescribed antibiotics should have the dose and duration clearly indicated and upon administration, it should be clearly marked on the patient's treatment sheet.
2. Treatment guideline for use of antibiotics should be formulated based on the hospital formulary and the sensitivity patterns. This should be reviewed occasionally to ensure rational use of antibiotics
3. Prolonged hospitalization should be avoided to reduce the risk of hospital acquired infections.

REFERENCES

Abraham, Y. & Wamisho, B.L. (2009). Microbial susceptibility of bacterial isolated from open fracture wounds presenting to the err of black-lion hospital, Addis Ababa University, Ethiopia. *Africa Journal of Microbial Research.* 3(12): 939-951'

Akinjogunla, M.J., Inam, J.I. & Aseel, M.H. (2011). Bacterial isolation from burn wound infection and studying their susceptibility. *Kufa Journal for Veterinary Medical Sciences* 2(1): 121-131.

Alebachew, O.E., Sogebi, A.O. & Fatugase, O.M. (2013). Rates and risk factors associated with surgical site infections in a tertiary care center in South-Western Nigeria. *International Journal Tropic Health* 3(1): 25-36

Altekruse, S. F., McGlynn, K. A., & Reichman, M. E. (2009). Hepatocellular carcinoma incidence, mortality, and survival trends in the United States from 1975 to 2005. *Journal of clinical oncology*, *27*(9), 1485-1491.

Amenu, D., Belachew, T., & Araya, F. (2011). Surgical site infection rate and risk factors among obstretic cases of Jimma University specialized hospital, Southwest Ethiopia. *Ethiopia Journal of Health Science* 21(2): 91-100.

Basu, S., Ramchuran, P.T., Bali, S.T., Gulat, I.A. & Shukla, V. (2009). A prospective, descriptive study to identify the microbiological profile of chronic wounds in outpatient. *Ostomy Wound Manage,* 55(1): 14-20.

Bhatt, C, & Lakhey, M. (2006). The discribution of pathogens causing wound infection and their antibiotic susceptibility pattern. *Journal of Nepal Health Research Council* 5(1): 22-26

Bouchillon, S.K., Johnson, B.M. & Hoban, D.J. (2004). Determining incidence of extended spectrum beta-lactamase producing Enterobacteriaceae, Vancomycin resistance *Enterococcus faecium* and methicilin-resistant *Stahylococcus aureus* in 38 centers from 17 countries: the PEARLS study 2001-2002. International Journal of Antimicrobial Agents 24(2): 119-124

Bowler, P. G., Duerden, B. I., & Armstrong, D. G. (2001). Wound microbiology and associated approaches to wound management. *Clinical microbiology reviews*, *14*(2), 244-269.

George, T.V. (2005). Diagnostic value of clinic features at presentation to identify serious infections. *Medical Microbiology:* 13th ed. Indiana University Press, 398.

Gupta, R., Sinnett, D. & Carpenter, R. (2000). Antibiotic prophylaxis for post-operative wound infection in clean elective breast. *Eur. Journal of Surg.* 26(4): 363-366

Heggers, J. P., Hawkins, H.P., Vitlarreal, C. and Herndson, D.N. (2002). Treatment of infections in burns. Total burn care. 13th ed. D.N. Herndason, Saunders, London England. 120-167

Idris, A. & Abubakar, U (2016). Phytochemical and antibacterial investigation of moringa (*Moringa oleifera*) leaf extract on selected bacterial pathogens. *Journal of Microbiology and Antimicrobials* 8(5), 28-33.

Masaadeh, H. A., & Jaran, A. S. (2009). Incident of Pseudomonas aeruginosa in post-operative wound infection. *Am J Infect Dis*, *5*(1), 1-6.

Massanandhand, J.B., Cannon, C.I. & Pier, G.B. (2009). Establishment of *Pseudomonas aeruginosa* infection. Lessons from a versatile Opportunist. *Journal of Microbes and infection* 2: 1051-1060.

Mehta, R. L., Kellum, J. A., Shah, S. V., Molitoris, B. A., Ronco, C., Warnock, D. G., & Levin, A. (2007). Acute Kidney Injury Network: report of an initiative to improve outcomes in acute kidney injury. *Critical care*, *11*(2), R31.

Mulu, W., Kibru, G., Beyene, G., & Damtie, M. (2012). Postoperative nosocomial infections and antimicrobial resistance pattern of bacteria isolates among patients admitted at Felege Hiwot Referral Hospital, Bahirdar, Ethiopia. *Ethiopian journal of health sciences*, *22*(1), 7-18

Raja, H.A. and Shearer, C.A. (2006). Jahnula species from North and Cental America, including three new species. Mycologia 98: 312-332

Verma, M., Zakhartsev, M., Reuss, M. & Westerhoff, H.V. (2013). 'Domino' Systems Biology and the 'A' of ATP. *Biochim Biophys Acta* 1827 (1): 19-29.

DETERMINATION OF DEPTH TO MAGNETIC SOURCE OVER PART OF MONGUNU AND ENVIRON USING SOURCE PARAMETER IMAGING FROM HIGH RESOLUTION AEROMAGNETIC DATA

Salako K. A., Adeagbo Y. A., Adewumi T., Adetona A. A., Rafiu A. A., and Alkali, A.

Department of Physics, Federal University of Technology, Minna, Niger State, Nigeria

E-mail/Mobile: kasalako2012@gmail.com ; a.abbass@futminna.edu.+*234-07030096000*

Abstract

This study focuses on determination of sedimentary thickness using Source Parameter Imaging (SPI) to interpret high resolution aeromagnetic data over part of Mongunu and environ northeast Nigeria for possible hydrocarbon presence. The study area is covered by four aeromagnetic data sheets: 45 (Dubumbali), 46 (Monguno), 67 (Masu) and 68 (Marte), bounded by latitude 12^0 N - 13^0 N and longitudes 13^0 E - 14^0 E with an estimated total area of 12,100 km^2. Polynomial fitting method was adopted for the regional-residual separation of the total magnetic intensity. The pre-processed grids dx, dy and dz from residual grid were used as input grids to calculate the depth to magnetic source point (SPI). The result of the study shows a minimum sedimentary thickness of 1.5 km and this could be found at the extreme south-eastern part of the study area which correspond to Marte town and maximum sedimentary thickness of 3.50 km which could also be found at the Southwestern part of the study area around Masu town. The maximum sedimentary thickness of 3.50 km around Masu town, southwestern part of the study area may be sufficient for the presence of hydrocarbon maturation and accumulation in the study area.

Keywords: Sedimentary thickness, Source Parameter Imaging, Aeromagnetic data, Polynomial fitting and Hydrocarbon

INTRODUCTION

The continuous search for mineral and petroleum (hydrocarbon) deposit has been a major challenge that will continue to be faced not only in Nigeria but also all over the world. Nigeria is a country that is blessed with lots of mineral resources, but yet to explore most of these resources. Nigeria is being faced with some economical challenges, political challenges, and reliance on some specific mineral deposit leading to the negligence in some others, which may yield large economic potentials to the country at large.

Considering the fact that the hydrocarbon (petroleum) which presently has been a great source of revenue generator for the country. These resources will not always be there forever, holding to the fact that it is a source of energy that is non-renewable in nature, and might one day in the nearest future get exhausted, as a result of continuous exploitation. To that effect, attention needs to be shifted to other basins (sedimentary basins) which have some of the geological potentials of having some useful minerals, be it solid minerals or hydrocarbons.

Recently, some countries have been discovering petroleum from their inland basins, which are similar to that of Nigeria's inland basin in terms of time. Subsequently the Nigerian government through the Nigeria National Petroleum Co-operation (NNPC) and other oil companies deem it necessary to run heavy investments in the inland basins, which have being prospected for hydrocarbon and other minerals. This till today remains exclusive (Salako and Udensi, 2013). Such a Basin is the Benue Trough, which comprises of, Upper, Middle and Lower Benue Troughs and has the prospect of not just hydrocarbon deposit but also some economic minerals. Never the less, effort and money is still been pumped into the research carried out, based on reconnaissance for minerals and hydrocarbon being prospected in the area (Salako, 2014).

The geophysical method that is being employed in this work is the magnetic method, using aeromagnetic data to study the depth to basement estimation over Lafia area, located at the middle Benue Trough. This study is aimed at determining the sedimentary thicknesses in the study area and depths to different magnetic source using the high resolution aeromagnetic data obtained from the airborne magnetic survey in Nigeria carried out between the year 2005 and 2009 by Nigerian Geological Survey Agency. Image processing of the source parameter grids enhances details and provides maps that help interpretation even by non-specialist (Nwosu, 2014). The method assumes either a 2-D sloping contact or a 2-D dipping thin-sheet model and is based on the complex analytic signal.

Location and Geology of the Study Area

The study area is part of Bornu Basin North Eastern, Nigeria is bounded by latitude 12^0 N - 13^0 N and longitudes 13^0 E - 14^0 E with an estimated total area of 12,100 km^2 (Figure 1a). The study area is endowed with rock mineral base resources such as clay, salt, limestone, kaolin, iron ore, uranium and mica. Petroleum is prospected intensively on the shore of the Lake Chad. Commercial activity is very significant in the state. The study area is connected to other neighbouring states and neighbouring countries by air, road and rail which makes commercial activities easier in the area.

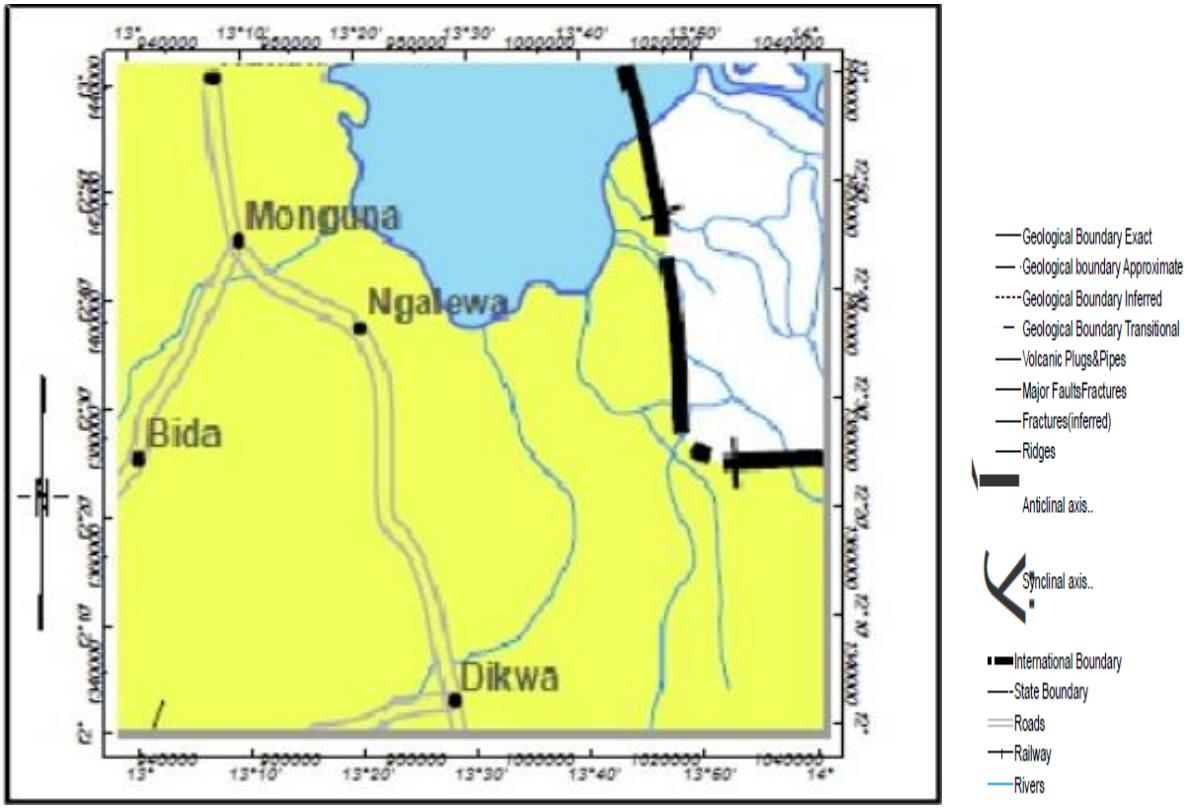

Figure 1a: Extracted Geologic map of the study Area (Adapted from NGSA, 2006)

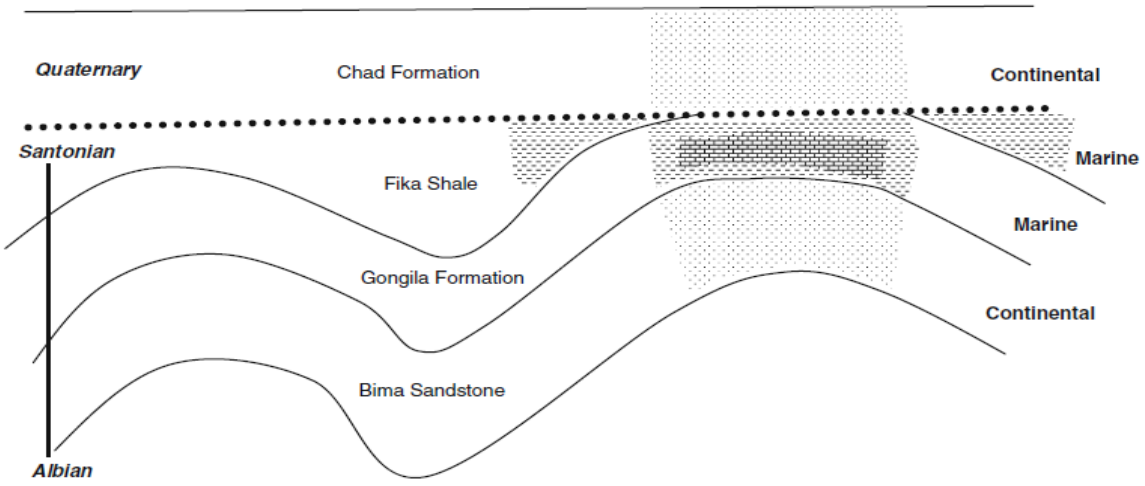

Figure 1b: Generalised Stratigraphic Sequence of Bornu Basin, Nigeria (Adapted from Obaje, 2004).

Geologically, the Bornu basin has been explained as a broad sediment-filled broad depression straddling North-eastern Nigeria and adjoining parts of the Republic of Chad (Obaje, 2004). The sedimentary rocks of the area have a cumulative thickness of over 3.6 km and rocks consist of thick basal continental sequence overlaid by transitional beds followed by a thick succession of Quaternary Limnic, fluviatile and eolian sand and clays (Lawal *et al.*, 2014). The stratigraphy sequence shows that Chad (Figure1b), Kerri-Kerri and Gombe

Formations have an average thickness of 130 to 400 m. Below this formations are the Fika shale with a dark grey to black in colour, with an average thickness of 430 m. Others are Gongila and Bima Formations with an average thickness of 320 m and 3,500 m, respectively (Odebode, 2010).

Materials and Method

Four high resolution aeromagnetic maps (HRAM) were acquired, assembled and interpreted. These maps were obtained as part of the nationwide airborne survey carried out and sponsored by the Nigerian Geological Survey Agency between the year 2005 and 2009. The airborne survey was carried out for the Nigerian Geological Survey Agency by Fugro airways services, the surveys was flown at 500 m line spacing and at an average flight elevation of 80 m along NW – SE direction, and published in form of grid (digital form) on 30` by 30` sheets. The maps are on a scale of 1:100,000 and half-degree sheets contoured mostly at 10 nT intervals. The geomagnetic gradient was removed from the data using the International geomagnetic Reference Field (IGRF) 2005. The total area covered was about 12,100 km^2. The actual magnetic intensity value of 33,000 nT which was reduced for handling and must be added to the value of magnetic intensity value before plotting so as to get the actual value of the magnetic intensity at any point. The four maps (sheets): 45 (Dubumbali), 46 (Monguno), 67 (Masu) and 68 (Marte). covering the study area were combined and re-gridded to obtain the super map of the study area using Oasis Montaj (Figure 2). The total intensity map (TMI) or super map was subjected to regional/residual separation using polynomial fitting method of order 1. The residual map (Figure 3) obtained shows both positive and negative magnetic intensity values which ranges from -120.0 nT to 90.3 nT.

The pre-processed grids dx, dy and dz from residual grid was used as an input grid to calculate the source parameter imaging. This process was carried out using the algorithm in the Oasis Montaj software. SPI method makes the task of interpreting magnetic data significantly easier as shown by the SP images generated from residual field data of the studied area (Figure 4a). The result of the SPI shows that the maximum sedimentary is more pronounced at the Masu eastern part of the study area and this agrees with the analytic signal map (Figure 4b) produced from this study area.

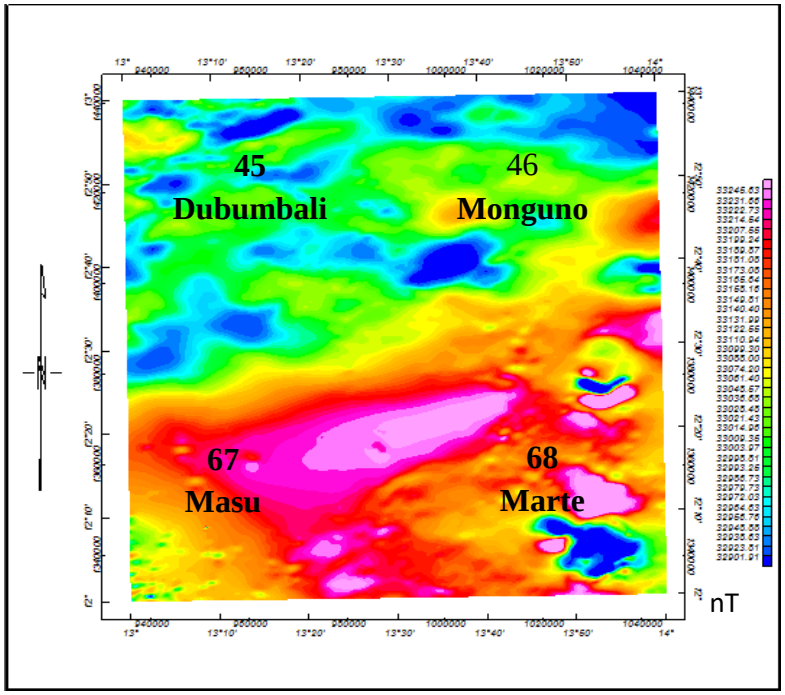

Figure 2: Total Magnetic Intensity (TMI) map of the study area

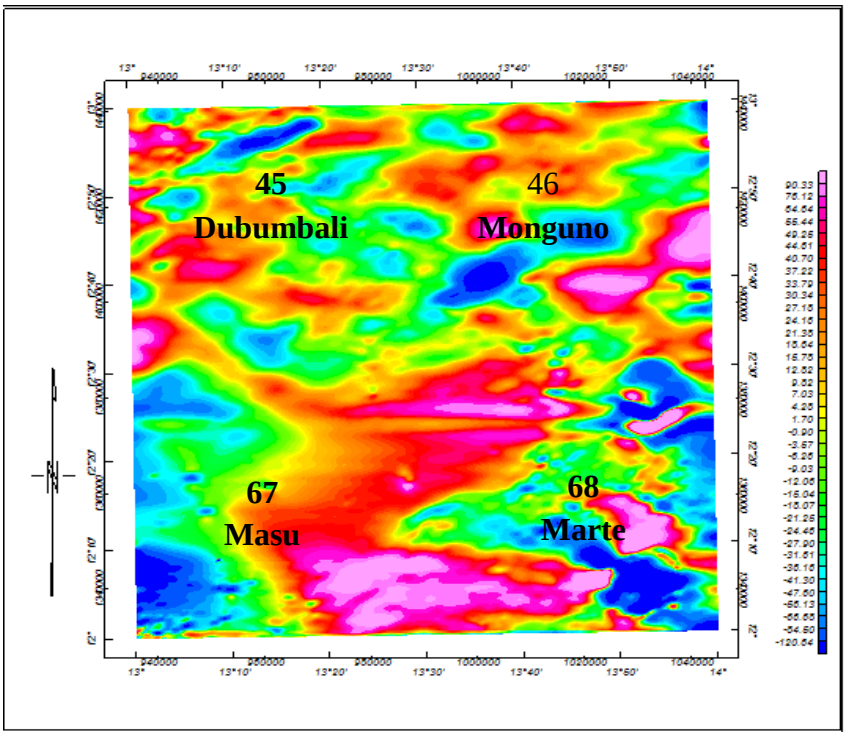

Figure 3: Residual Map of the Study Area

Estimation of Depth to magnetic Source Using SPI™

The Source Parameter Imaging (SPI™) is a technique using an extension of the complex analytical signal to estimate magnetic depths. This technique developed by Thurston and Smith (1997) and Thurston *et al*. (1999,

2002) sometimes referred to as the local wavenumber method is a profile or grid-based method for estimating magnetic source depths, and for some source geometries the dip and susceptibility contrast. The method utilizes the relationship between source depth and the local wavenumber (k) of the observed field, which can be calculated for any point within a grid of data via horizontal and vertical gradients Thurston and Smith, (1997). The depth is displayed as an image. The original SPI^{TM} method (Thurston and Smith, 1997) works for two models: a dipping thin dike and a sloping contact. The local wavenumber has maxima located over isolated contacts, and depths can be estimated without assumptions about the thickness of the source bodies (Smith *et al.*, 1998). Solution grids using the SPI technique show the edge locations, depths, dips and susceptibility contrasts. The local wavenumber map more closely resembles geology than either the magnetic map or its derivatives. The SPI method requires first- and second-order derivatives and is thus susceptible to both noise in the data and to interference effects.

In 1997, Thurston and Smith developed source parameter imaging and used it to estimate the depth from the local wavenumber of the analytical signal. The analytical signal $A_1(x, z)$ is defined by Nabighian (1972) as:

$$A_1(x,z) = \frac{\partial M(x,z)}{\partial x} - j\frac{\partial M(x,z)}{\partial z}, \quad (1)$$

where M(x,y) is the magnitude of the anomalous total magnetic field, j is the imaginary number, z and are Cartesian coordinates for the vertical direction and horizontal direction respectively. Nabighian (1972) reveal that horizontal and vertical derivatives comprising the real and imaginary parts of the 2D analytical signal are related as follows:

$$\frac{\partial M(x,z)}{\partial x} \Leftrightarrow \frac{\partial M(x,z)}{\partial z}, \quad (2)$$

where $\Leftrightarrow$ denotes a Hilbert transformation pair. The local wave number k_1 is defined by Thurston and Smith (1997) to be

$$k_1 = \frac{\partial}{\partial x}\tan^{-1}\left[\frac{\frac{\partial M}{\partial z}}{\frac{\partial M}{\partial x}}\right], \quad (3)$$

The concept of an analytic signal comprising second-order derivatives of the total field, if used in a way similar to that used by Hsu *et al.* (1996), the Hilbert transform and the vertical-derivative operators are linear, so the vertical of (2) will give the Hilbert transform pair,

$$\frac{\partial^2 M(x,z)}{\partial z\,\partial x} - \frac{\partial^2 M(x,z)}{\partial^2 z}, \quad (4)$$

Thus the analytic signal could be defined based on second-order derivatives, $A_2(x, z)$, where

$$A_2(x,z) = \frac{\partial^2 M(x,z)}{\partial z\,\partial x} - j\frac{\partial^2 M(x,z)}{\partial^2 z}, \quad (5)$$

This gives rise to a second-order local wave number k_2, where

$$k_2 = \frac{\partial}{\partial x}\tan^{-1}\left[\frac{\frac{\partial^2 M}{\partial^2 z}}{\frac{\partial^2 M}{\partial z\,\partial x}}\right], \quad (6)$$

The first and second order local wave numbers are used to determine the most appropriate model and a depth estimate independent of any assumptions about a model.

Nabigbian (1972) gives the expression for the vertical and horizontal gradient of a sloping contact model as:

$$\frac{\partial M}{\partial x} = 2KFcsin\ d\,\frac{h_c\cos(2I-d-90)+xsin(2I-d-90)}{{h_c}^2+x^2}, \quad (7)$$

$$\frac{\partial M}{\partial z} = 2KFcsin\ d\,\frac{x\cos(2I-d-90)+h_c sin(2I-d-90)}{{h_c}^2+x^2}, \quad (8)$$

where K is the susceptibility contrast at the contact, F is the magnitude of the earth's magnetic field (the inducing field), $c = 1 - cos^2 isin^2\alpha$,$\alpha$is the angle between the positive x-axis and magnetic north, *i* is the ambient-field inclination, $tanI = sini/cos\alpha$d is the dip (measured from the positive x-axis), *hc* is the depth to the top of the contact and all trigonometric arguments are in degrees. The coordinate system has been defined such that the origin of the profile line (x = 0) is directly over the edge.

The expression for the magnetic-field anomaly due to a dipping thin sheet is

$$M(x,z) = 2KF_{cw}\,\frac{h_1\sin(2I-d)+xcos(2I-d)}{{h_c}^2+x^2}, \quad (9)$$

Reford (1964), where w is the thickness and h_1 the depth to the top of the thin sheet. The expression for the magnetic-field anomaly due to a long horizontal cylinder is

$$M(x,z) = 2KFS\,\frac{sini}{sinr}\,\frac{({h_h}^2-x^2)\cos(2I-180)+2xh_h\sin(2I-180)}{({h_c}^2+x^2)^2}, \quad (10)$$

Murthy and Mishra, S is the cross-sectional area and h_h is the depth to the centre of the horizontal cylinder.

Substituting (7), (8), (9) and (10) into the first- and second- order (i.e. (3) and (6) respectively) local wavenumbers, we obtain, after some simplification, a remarkable result as:

$$k_1 = \frac{(n_k+1)h_k}{{h_k}^2+x^2}, \quad (11)$$

and

$$k_2 = \frac{(n_k+2)h_k}{{h_k}^2+x^2}, \quad (12)$$

where n_k is the SPI structural index (subscript k = c, t or h), and n_c =0 n_t = 1 and n_h = 2 for the contact, thin sheet and horizontal cylinder models, respectively. From (11) and (12) above, it is evident that the first- and

second- order local wave number are independent of the susceptibility contrast, the dip of the source and the inclination, declination, and the strength of the earth's magnetic field.

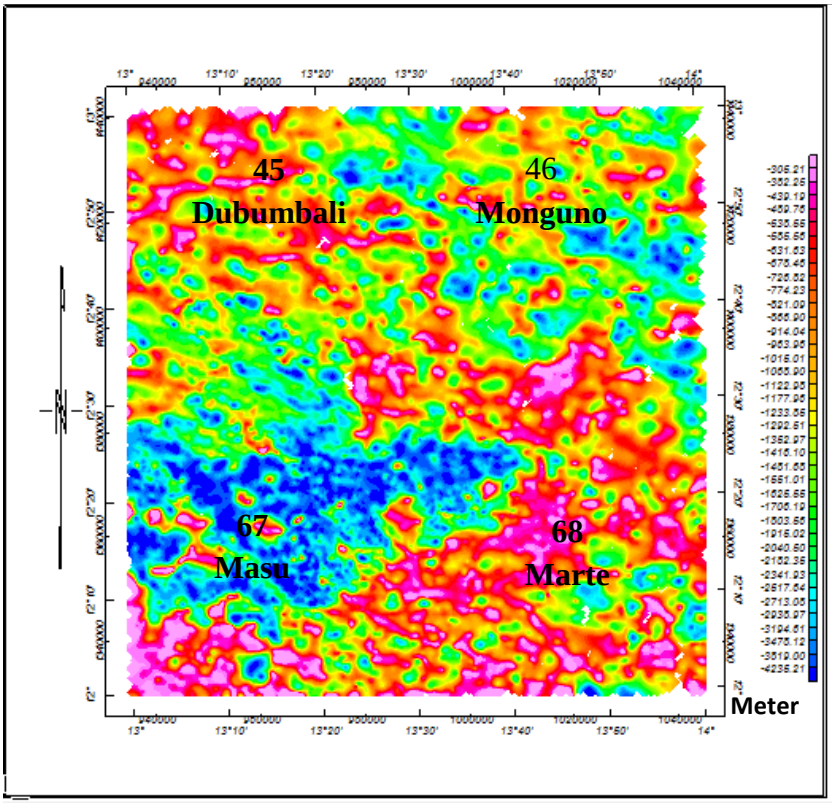

Figure 4a: Source Parameter imaging Map

Result and Discussion

The result of source parameter imaging of the aeromagnetic data of the study area (Mongunu and Environ), Figure 4a, has revealed two magnetic depth source; maximum depth (deep blue coloured) ranges from 1910.2 m and 3203 m with an average depth of 3511 m (3.50 km) and the minimum depth (light green and orange coloured) ranges from 165 m and 1421 m with an average depth of 1503.5 m (1.50 km). The deep blue colour represent areas with deep lying magnetic bodies hence with thicker sedimentary cover with an average depth of 3.50 km could be viewed as the magnetic basement depth of the studied area which might favour hydrocarbon maturation and accumulation. This result was corroborated with the result of the analytical signal (Figure 4b) where the least magnetic amplitude observed at the south-eastern part of the area agreed with the area of highest sedimentary thickness in Figure 4a. The maximum depth to magnetic basement is more pronounced around the western part of the study area which corresponds to Masu town. This result also agreed with other workers in the area like, Lawal *et al*, (2014), Okonkwo *et al.* (2012) , Lawal *et al.* (2007), Isogun (2005) and Nwankwo *et al*, (2013) Salako and Udensi (2013) Nur (2001), Likasson *et al.* (2005) and Salako

(2014). The minimum depth to magnetic basement depicted with orange colour at the extreme south-eastern part of the study area might be as a result of intrusion into the sedimentary basin.

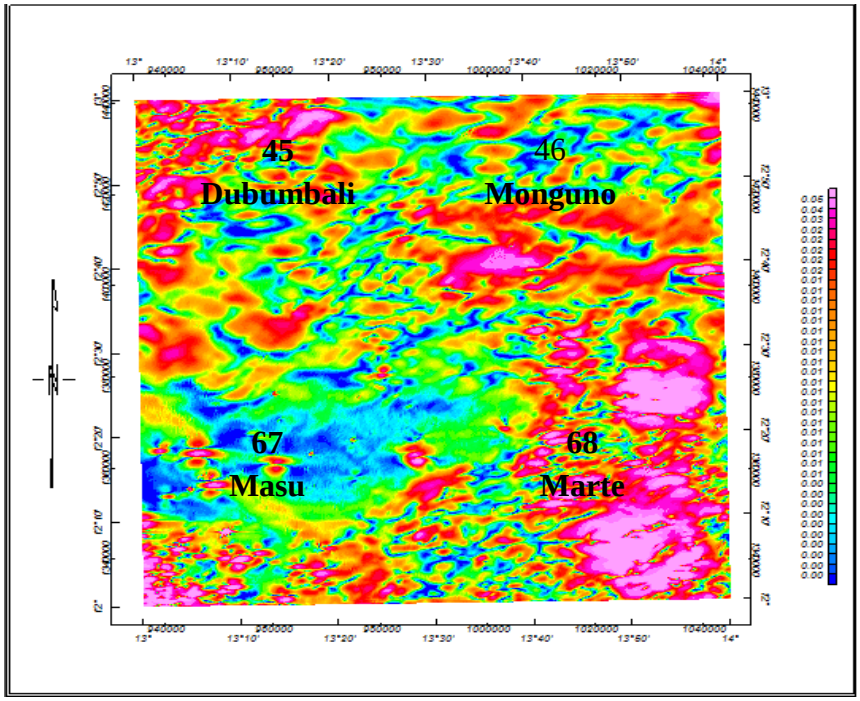

Figure 4b: Analytic Signal Map of the Study Area

Conclusion

The result acquired from this research work agrees with those of the other researchers who have used other depth estimating techniques and the previous old data, however, this could be more reliable and precise due to the nature of high resolution of the 2009 data over than the 1970s data in terms of terrain clearance, and line spacing. The old map requires digitization which is stressful and could introduce error unlike the 2009 data that is in digitized form, different errors have been corrected using improved software and technique. The SPI have estimated depth comparable with that from spectral and other technique and this depth values over part of Mongunu and environ particularly Masu town is an indication that hydrocarbon prospecting should be intensified in this area since the sediment over the area are sufficient for hydrocarbon maturation and accumulation.

References

Isogun, M. A. (2005): Quantitative interpretation of aeromagnetic data of Chad Basin, Bornu State, Nigeria. *Unpublished. M.sc. Thesis*, O.A.U Ile- Ife.

Lawal, T.*O* and Nwankwo L.I, wavelet analysis of high resolution aeromagnetic data over part of Chad Basin, Nigeria. *Ilorin Journal of Science*, 2014(1) pp 110-120.

Lawal, K. M, Umego, M. N. and Ojo, S. B. (2007): Depth-to-Basement Mapping using Fractal Technique: Application to the Chad Basin Northeastern Nigeria. *Nigerian Journal of Physics, 19(1).*

Likkasson, O. K., Ajayi, C. O. & Shemang, E. M. (2005). Some structural features of the Middle Benue Trough, Nigeria, modeled from aeromagnetic anomaly data. *Science Forum, Journal of Pure and Applied Science, 8,* 100 – 125.

Nabighian, M. N., (1972), the analytic signal of two-dimensional magnetic bodies with polygonal cross-section -Its properties and use for automated anomaly interpretation: *Geophysics,* **37,** 507 517.

Nabighian, M. N. (1984): Toward a three-dimensional automatic interpretation of potential field data via generalized Hilbert transforms - Fundamental relations: *Geophysics*, 49**,** 780-786.

Nigeria Geological Survey Agency (2006). Geological map of Nigeria.

Nur, A. (2000). Analysis of aeromagnetic data over the Yola arm of the Upper Benue Trough, Nigeria. *Journal of Mining and Geolog.,* 36, 77 – 84.

Nwankwo, L. I., Olasehinde, P. I. & Akoshile, C.O. (2011): A new technique for estimation of upper limit of Digitization Spacing of Aeromagnetic Maps. *Nigerian Journal of Physics*. **22** (1), 74-79.

Nwankwo, C. N., Ekine, A. S., Nwosu, L. I. (2009). Estimation of heat flow variation in the Chad Basin Nigeria. *Journal Applied Sciences and Environment*, 13(1), 73 – 80.

Nwosu O.B. (2014). Determination of magnetic basement depth over parts of middle Benue trough by source parameter imaging (SPI) techniques using HRAM. *International Journal of Scientific and Technology Research,* 3(1).

Obaje, N.G., Geology and Mineral of Nigeria (Germany: Springer Verlag, 2009)

Obaje, N, Wehner H., Scheeder G., Abubakar M., and Jauro A., Hydrocarbon prospectively of Nigeria's inland basins: from the viewpoint of organic geochemistry and organic petrology. *AAPG bulletin*, 88(3), 2004, 325 – 353.

Odebode, M.O. (2010): A handout on Geology of Boron (Chad) Basin, Northeastern Nigeria.

Okonkwo, C. C., Onwuemesi, A. G., Anakwuba, E. K., Chinwuko, A. I., Ikumbur, B. E. & Usman, A. O. (2012): Aeromagnetic Interpretation over Maiduguri and Environs of Southern Chad Basin, Nigeria. *Journal of Earth Sciences and Geotechnical Engineering*, **2** (3), 77-93.

Okosun, E. A. (1995). Review of Geology of Bornu Basin. *Journal of mining and Geology*, 31(2), 113 – 172.

Oteze, G. E, Foyose, E. A. (1988) Regional developments in the hydrogeology of the Chad Basin. *Water Res* 1:9–29.

Salako, (2014), Depth to basement determination using Source parameter imaging (SPI) of aeromagnetic data: An application to upper Benue trough and Borno basin, Northeast, Nigeria. *Academic Research International*, vol. 5(3).

Salako K.A. & Udensi E. E. (2013). Spectral depth analysis of upper Benue Trough and Bornu Basin, northeast Nigeria using aeromagnetic data. *International Journal of Science and Research (IJSR) 2(8)*pp 48 – 55

Spector, A., Grant, F.S., (1970). Statistical models for interpretation of aeromagnetic data. *Geophysics*, 35, 293–302.

Sunday, J. (2012). Estimation of Magnetic Source depths from Aeromagnetic data of Maiduguri using gradient Inversion, *M.Sc Thesis, Department of Physics, University of Ilorin*.

Summonu, L. (1988). Interpretation of Data from Middle Niger Basin, Nigeria. M.Sc. *Thesis. University of Ibadan.*

Telford, W.M, L.P. Geldart, & R.E. Sheriff, (1990) *Applied Geophysics*, 2nd ed., Cambridge University Press, Cambridge, 1990, p.770.

Thurston, J. B., & Smith, R. S. (1997). Automatic conversion of magnetic data to depth, dip, and susceptibility contrast using the SPI™ method. *Geophysics, 62*, 807-813.

Thurston, J.B, Smith, R.S. and Guillon, J. C. (1999): Model-independent depth estimation with the SPITM method: 69thAnnual International Meeting, SEG, *Expanded Abstracts*, 403–406.

Thurston, J.B, Smith, R.S. and Guillon, J. C. (2000): A multi-model method for depth estimation from magnetic data: *Geophysics*, 67, 555–561.

STRUCTURAL AND THERMOLUMINESCENCE STUDIES OF EUROPIUM DOPED TRIPOTASSIUM SODIUM DISULPHATE

Fatima Talatu Mahmud, Jolayemi Joel Bukola, Olarinoye Oyeleke and Kasim Uthman Isah[1]*

[1]Department of Physics, Federal university of Technology, Minna, Nigeria

[1]kasim309@futminna.edu.ng

* Corresponding author

Abstract

Nanocrystalline Eu^{3+}-doped $K_3Na(SO_4)_2$ and undoped phosphors were prepared by chemical co-precipitation method. Structural and TL properties of the phosphors were studied. The Eu^{3+}-doped $K_3Na(SO_4)_2$ and undoped phosphor were characterised by X-ray diffraction (XRD) and High Resolution Scanning Electron Microscope (HRSEM). XRD patterns confirmed that the phosphor is crystalline and single phase hexagonal structure which did not change after doping with Eu^{3+}. The average crystallite size of the undoped phosphor increased from 49 nm to a maximum of 56 nm for 0.1mol % doping concentration. Slight variation was observed in the lattice parameters which affects the unit cell volume and causes lattice distortion. Microstructural investigation revealed that grain size decreased from 4.08µm to 2.03µm for undoped and maximum dopant concentration respectively. TL studies showed that TL intensity was optimized by 0.1mol % of Eu but quenches with respect to neutron radiation of higher dose. The phosphor has the potential of being used as a dosimeter for low neutron dose.

Keywords: chemical co-precipitation, dosimeter, phosphors, thermoluminescence, tripotassium sodium disulphate

1. Introduction

The unique luminescent (photo-, chemi-, electrochemi-, tribo-, electro-, radio- and thermo-luminescent) properties of phosphors and the sensitivity of these materials make them highly attractive and to find practical applications in many areas such as lamps, cathode-ray tubes, X-ray and ionizing radiation detection, etc. (Shionoya, 2007). Several studies have indicated that the thermoluminescence (TL) property of these materials is quite intriguing owing to their potential use in dosimetry of ionizing radiations for estimations of doses of these high-energy ionizing radiations as the energy absorbed during irradiation (Dhoble *et al*., 2007; Dhoble *et al*., 1993; Sahare *et al*., 2007). Many phosphor materials including $K_3Na(SO_4)_2$:Eu (Dhoble *et al*., 2001), Zn(BO2)2:Dy (Li *et al*., 2008), $Li_2B_4O_7$:Mn (Annalakshmi *et al*., 2011) and $CdSiO_3$:Ni (Manjunatha *et al*., 2011) have been reported to possess good TL properties but most of these phosphors are limited in use as TLDs which could be as a result of low sensitivity with inability to detect the low irradiation doses or as a result of saturation at a certain dose (Sahare *et al*., 2007). In this study, chemical co-precipitation method is employed to synthesise $K_3Na(SO_4)_2$:Eu phosphor, the structural and TL characteristics of the phosphor are also investigated.

2. Literature Review

Recent studies have revealed that $K_3Na(SO_4)_2$:Eu has very interesting characteristics such as high sensitivity which is more sensitive than the widely used CaSO4:Dy TL dosimeter (TLD) (Dhoble *et al*., 2001), saturation at very high doses (as high as 70 kGy) and low fading (Sahare *et al*., 2007; Natarajan *et al*., 2002). The type and method of doping with rare-earth impurities especially europium (Eu) as activator are reported to have a crucial influence on the TL glow curve characteristics of the phosphors for the use in TLD (Dhoble

et al., 1993; Dhoble, 2000; Shinde *et al*., 1999). Many preparation methods such as combustion, sol–gel, precipitation, conventional solid state technique, spray, and fume pyrolysis, etc. have been reportedly employed to achieve a modified structure and incorporation of impurities at different sites in order to improve the TL characteristics of these phosphors (Sahare *et al*., 2007; Manjunatha *et al*., 2011).

3. Methodology

Analytic grade of K_2SO_4, Na_2SO_4 and $EuCl_3$ with high purity was obtained from recognised chemical supplier. K_2SO_4 and Na_2SO_4 in the ratio 3:1 molar proportion were dissolved in 300 ml of triply distilled de-ionized water. Subsequently, $EuCl_3$ salt in three different molar proportion (0.1 %, 0.3 %,0.5%) was added to the solution. The compound $K_3Na(SO_4)_2$; Eu in its nanocystalline was then be obtained by co-precipitating it out by decreasing the solubility on adding absolute ethanol (225 ml) drop-wise to the solution with continuous stirring. After precipitating the required amount, it was filtered out and washed several times with ethanol and dried in an oven at about 343 K for 4 hours. Prepared samples were then annealed at 678K for 2 hours to have higher sensitivity. X-ray Diffractometer (D8 Advance, BRUKER AXS, 40 kV, 40 mA). Cu-k_α radiation in the 2θ range 20^0 to 90^0 with scan step and acquisition time of 0.034^0 and 88.98 seconds respectively were used. For TL studies, the prepared phosphor was exposed to neutrons dose of 25, 50 and 70 kGy. TL glow curve was recorded on a TL/OSL-system Reader (Riso, DA-15, 1.5 kV), by taking 2 mg of sample each time. They were recorded under nitrogen atmosphere at a heating rate of 1 ℃/s.

4. Results and Discussion

4.1 Structural Studies

Typical X-ray diffraction (XRD) patterns of undoped and Eu^{3+}-doped $K_3Na(SO_4)_2$ phosphors are shown in Figure 1. The prominent peaks and in the XRD diffractogram corresponds to the hexagonal phase of $K_3Na(SO_4)_2$ and matches well with JCPDS file no: 00-020-0928 data. However, XRD peaks associated with crystalline were observed in the diffractogram, though with negligible low intensity as indicated by asterisks in the spectrogram. Furthermore, from the spectra, the structural phase of doped and undoped $K_3Na(SO_4)_2$ seems to be consistent as all have identical peaks implying that Eu^{3+} is soluble in $K_3Na(SO_4)_2$ up to the range of concentration studied.

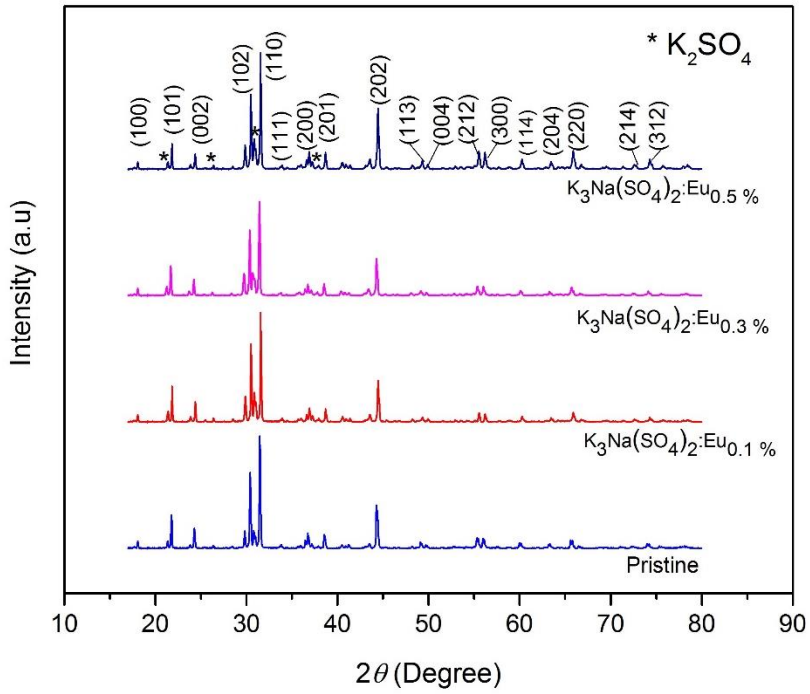

Figure 1. XRD patterns of undoped and Eu^{3+}-doped $K_3Na(SO_4)_2$ phosphors

Average crystallite size (D) and lattice strain of the doped and undoped K3Na(SO4)2 were calculated from full width at half maxima (FWHM) of the most intense XRD peak using Equation (1) and (2) (Vidya and Lakshminarasappa, 2013).

$$D = \frac{0.9\lambda}{\beta \cos\theta} \quad (1)$$

$$\varepsilon = \frac{\beta}{4 \tan\theta} \quad (2)$$

Where β is the FWHM of the diffraction peak in radians, θ is the Bragg diffraction angle of the XRD peak, λ is the wavelength of the X-ray used, ε is the microstrain and is the average crystallite size in nanometers. The crystallite sizes were determined for the most prominent peak (110), the values are given in Table 1.

Table 1: Calculated lattice strain, lattice parameters and cell volume of undoped and Eu^{3+}-doped $K_3Na(SO_4)_2$ phosphors

Phosphor	*D(nm)*	*ε*	*a* (Å)	c (Å)	V(Å)^3
$K_3Na(SO_4)_2$	48.67	2.09 x 10^{-4}	5.6773	7.3198	235.9341
$K_3Na(SO_4)_2$:$Eu_{0.1mol\%}$	56.87	2.24 x 10^{-3}	5.6715	7.31165	235.1855
$K_3Na(SO_4)_2$:$Eu_{0.3mol\ \%}$	51.24	2.58 x 10^{-3}	5.6657	7.3135	234.7685

$K_3Na(SO_4)_2$:$Eu_{0.5mol\,\%}$	52.36	2.43 x 10^{-3}	5.6637	7.2992	234.1400

$$a = \sqrt{\frac{1}{3}} \times \frac{\lambda}{sin\theta} \quad (3)$$

$$c = \frac{\lambda}{\sin\theta} \quad (4)$$

$$V = a^2 c \quad (5)$$

4.2 Thermoluminescence (TL) Studies

TL studies of undoped and Eu^{3+}-doped $K_3Na(SO_4)_2$ phosphor (Figure 2). The TL glow curve of the undoped phosphor consist of only a simple single TL peak located at 457 ℃. However, upon addition of different concentration of Eu^{3+} the TL peak position shifts to higher temperatures of about 482, 497 and 477 ℃ for $K_3Na(SO_4)_2$:$Eu^{3+}_{0.1\,\%}$, $K_3Na(SO_4)_2$:$Eu^{3+}_{0.3\,\%}$ and $K_3Na(SO_4)_2$:$Eu^{3+}_{0.5\,\%}$ respectively.

$K_3Na(SO_4)_2$:$Eu^{3+}_{0.1\,\%}$ phosphor has the highest TL intensity and the TL intensity decreases with increase in Eu doping. The optimum value of Eu^{3+} concentration is found to be 0.1 mol %. Similar observation has been reported by Sahare *et al.* (2007). Figure 3 shows the response of the phosphor under neutron irradiation doses of 25, 50, and 75 KGy respectively.

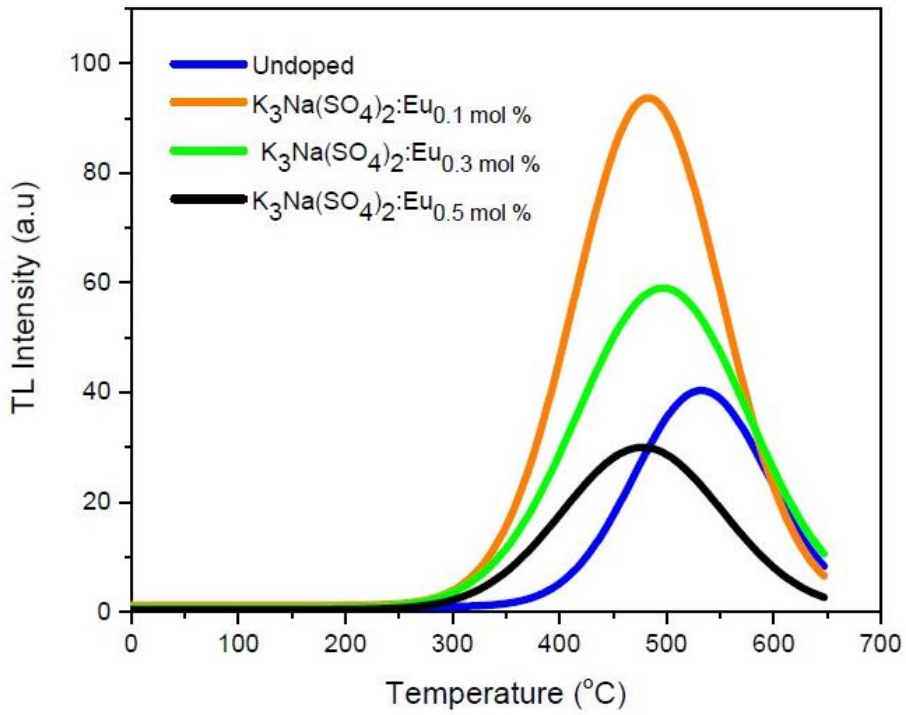

Figure 2. TL glow curve of undoped and Eu^{3+} doped $K_3Na(SO_4)_2$ phosphor exposed to neutron dose of 50 kGy

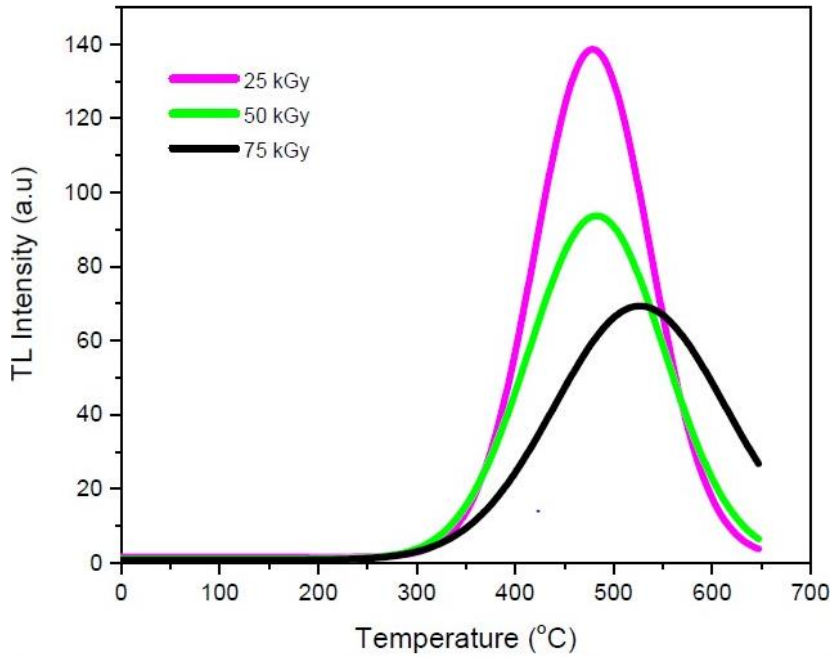

Figure 3. TL glow curve of $K_3Na(SO_4)_2:Eu^{3+}_{0.1\ \%}$ phosphor exposed to different neutron dose

It is observed that the TL intensity decreases with increasing dose, which suggests that the number of traps responsible for these glow peaks were getting less populated with increase in irradiation dose.

4.2.1 Dose Response

From figure 4, TL response is in contradiction with the TL response observed with other types of radiation (Sahare *et al.*, 2007).

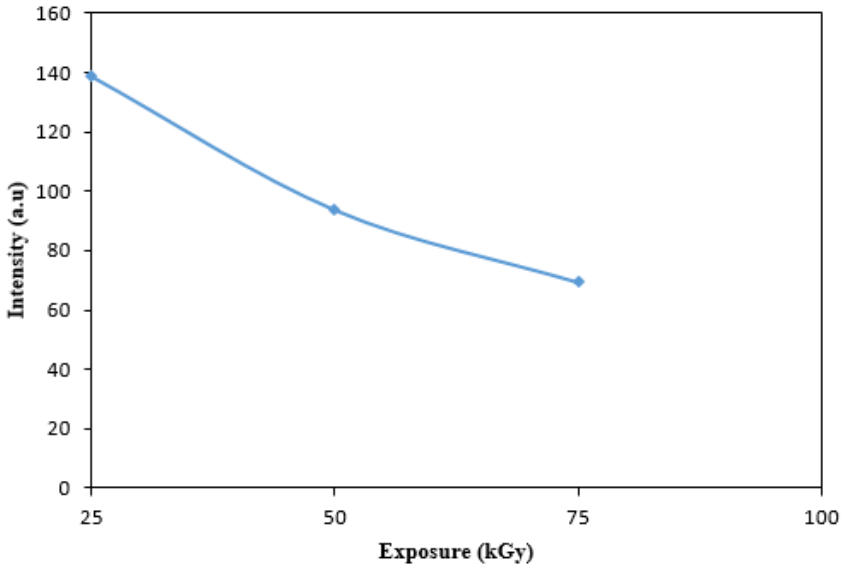

Figure 4. TL response curve of $K_3Na(SO_4)_2:Eu^{3+}_{0.1\ \%}$ exposed to different irradiation dose.

This implies that neuron irradiation has a quenching effect on the material. In other words, the dose range studied are beyond the linear range of the phosphor. From application point of view, this material may not be useful for high dose of neutron radiation. Therefore, further investigation on the TL properties with respect to lower dose of neutron should be carried out.

4.3 Determination of Kinetic Parameters

TL glow curve is a characteristic of the different trap levels that lie in the band gap of a material. The traps are characterised by certain physical parameters which include trap depth (*E*), frequency factor (*s*) and order of kinetics (*b*). To understand the nature of traps formed in $K_3Na(SO_4)_2$:$Eu^{3+}_{0.1\ \%}$ under irradiation with different neutron dose, *E* was calculated using Chen's set of empirical formulae for glow curve shape (Equation 6) (Chen and Kirsh, 1981). The order of kinetics strongly depends on the geometrical form factor (μ_g) (Vidya and Lakshminarasappa, 2014a). To determine order of kinetics, the geometrical form factor which involves T_1 and T_2 (temperature corresponding to the half of the intensities on either side of the maximum), was calculated using Equation 7 (Sahare *et al.*, 2007; Azorin, 1986). A typical diagram showing the different quantities used in TL glow-curve shape method while determining kinetic parameters is shown in Figure 5.

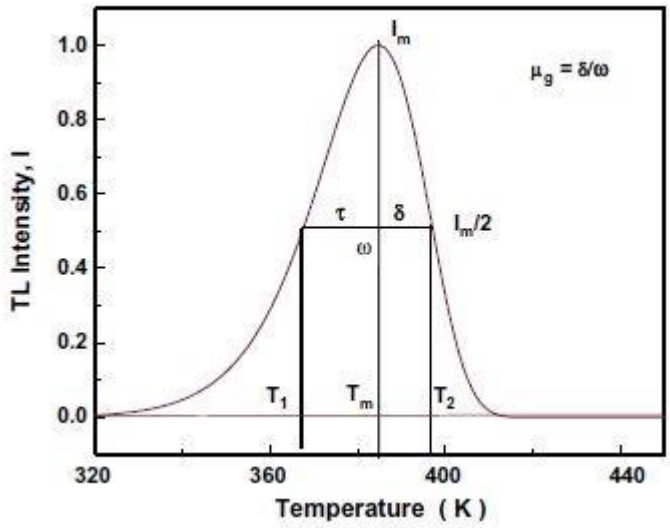

Figure 5. Representative diagram of different quantities used in glow-curve shape method

$$E_\alpha = C_\alpha\left(\frac{kT_m^2}{\alpha}\right) - b_\alpha(2kT_m), \tag{6}$$

With $\alpha = \tau, \delta, \omega$; $\tau = T_m - T_1$, $\delta = T_2 - T_m$, $\omega = T_2 - T_1$,

Where T_1 and T_2 is the temperature corresponding to half the intensity on either side of the peak maximum, T_m is the temperature of the peak maximum intensity, *k* is Boltzmann's constant (8.6×10^{-5} eVK^{-1}).

$$c_\tau = 1.51 + 3.0(\mu_g - 0.420);\ b_\tau = 1.58 + 4.2(\mu_g - 0.42)$$

$$c_\delta = 0.976 + 7.3(\mu_g - 0.420);\ b_\delta = 0$$

$$c_\omega = 2.52 + 10.2(\mu_g - 0.42),\ b_\omega = 1.$$

$$\mu_g = \frac{T_2 - T_m}{T_2 - T_1} \tag{7}$$

Theoretically, the form factor which ranges between 0.37 and 0.52, is close to 0.42 for first order kinetics and 0.52 for second order kinetics (Chen, 1969); other values are considered as general order kinetics (Vidya and Lakshminarasappa, 2014b). In the present study, the form factor of $K_3Na(SO_4)_2:Eu^{3+}_{0.1\ \%}$ irradiated with different dose is 0.5, suggesting that the peaks obeys second order kinetics (Table 2). This suggests that the TL emission involves retrapping of charges (Vidya and Lakshminarasappa, 2013). Furthermore, the order of kinetics could also be determined using Equations (8) (Puppalwar and Dhoble, 2012).

$$\gamma = \frac{\delta}{\tau} = \frac{(T_2 - T_m)}{(T_m - T_1)} \tag{8}$$

For first order kinetics, the parameter ranges from 0.7 to 0.9 and from 1.05 to 1.20 for second order kinetics. The parameter for the glow peaks ranges from 1.00 to 1.02, which suggests that the peaks obeys second order kinetics.

Table 2: kinetics parameters of K3Na(SO4)2: phosphor

Dose (kGy)	μ_g	γ	b	Activation Energy (eV)			Frequency factor (s^{-1})	
				E_τ (eV)	E_δ (eV)	E_ω(eV)	E_{ave}(eV)	
25	0.50	1.01	2	0.34	0.44	0.39	0.4	2.3 x 10^2
50	0.50	1.02	2	0.36	0.40	0.34	0.37	2.3 x 10^2
75	0.50	1.00	2	0.23	0.36	0.30	0.3	7.19

The calculated trapping parameters of $K_3Na(SO_4)_2:Eu^{3+}_{0.1\ \%}$ irradiated with different dose is presented in Table 2 as well. The near constant value of the activation energy as a function of dose is an indication that the shift in the energy level induced by defect clustering is as a result of change in the peak temperature. However, the activation energy has been calculated using the Halperin and Braner; and Lushchik equations for second order of kinetics (Equations 9 and 10) (Strauss and Hajek, 2007) and presented in Table 3.

Table 3: Comparison of average trap depth (activation energy, E_{av}) of $K_3Na(SO_4)_2:Eu^{3+}_{0.1\ \%}$ phosphor from different formulae

Dose (kGy)	Trap Depth (eV)

	Chen's	Halperin and Braner	Lushchik
25	0.4	0.35	0.48
50	0.37	0.29	0.42
75	0.3	0.24	0.40

$$E = 1.81\frac{kT_m^2}{\tau} - 4kT_m \quad (9)$$

$$\tau = T_m - T_1$$

$$E = 1.71\frac{kT_m^2}{\delta} \quad (10)$$

$$\delta = T_2 - T_1$$

$$s = \left(\frac{\beta E}{kT_m^2}\right)\left[\frac{\exp\left(E/T_m\right)}{1+(b-1)\left(2kT_m/E\right)}\right] \quad (11)$$

The calculated trap depth (activation energy) by these glow curve method shows close agreement with the value of trap depth obtained by other formulae. The frequency factor has been calculated using Equation 11 (Vidya and Lakshminarasappa, 2014b) and also presented in Table 2. It is important to note that the frequency factor decreased as dose increases.

5. Conclusion

Nanocrystalline undoped and Eu^{3+}-doped $K_3Na(SO_4)_2$ phosphor were prepared by chemical co-precipitation method the structure and TL properties were studied after neutron exposure. The XRD study indicates the formation of single phase $K_3Na(SO_4)_2$. The crystallinity improved with increased dopant concentration as evident from increase in crystallite size. Slight change was observed in the lattice parameters which affect the unit cell volume and causes lattice distortion. Similarly, the grains were inhomogeneous and the size decreased with Eu concentration. TL studies which is a fundamental characteristics of the phosphor revealed that the TL intensity optimized by 0.1 mol % of Eu quenches with respect to neutron dose, thus implying that the dose range are beyond the linear range of the phosphor. Therefore, this phosphor may stand a chance of being used as a dosimeter for low neutron dose.

References

Annalakshmi, O., Jose, M. T., & Amarendra, G. (2011). Dosimetric characteristics of manganese doped lithium tetraborate: An improved TL phosphor. *Radiation Measurements*, Vol. 46, 669-675.

Chen, R. (1969). Glow Curves with General Order Kinetics. *Journal of The Electrochemical Society*, Vol. 116(9), 1254-1257.

Chen, R., & Kirsh, Y. (1981). *Analysis of Thermally Stimulated Processes.* New York, US: Pergamon.

Dhoble, S. J. (2000). Preparation and characterization ofthe $Sr_5(PO_4)_3Cl:Eu^{2+}$ phosphor. *Journal of Physics D: Applied Physics,* Vol. 33, 158–161.

Dhoble, S. J., Moharil, S. V., & Rao, T. K. (2001). Correlated ESR, PL and TL studies on $K_3Na(SO_4)_2$: Eu thermoluminescence dosimetry phosphor. *Journal of Luminescence,* Vol. 93, 43–49.

Dhoble, S. J., Moharil, S. V., & Rao, T. K. (2007). Correlated ESR, PL and TL studies on $Sr_5(PO_4)_3Cl$:Euthermoluminescence dosimetry phosphor. *Journal of Luminescence, 126,* 383–386.

Dhoble, S. J., Moharil, S. V., Dhopt, S. M., Muthal, P. L., & Kondawa, V. K. (1993). Preparation and Characterizationof the $K_3Na(SO_4)_2$: Eu Phosphor. *Physica Status Solidi (a),* Vol. 135, 289-297.

Li, J., Zhang, C., Tang, Q., Hao, J., Zhang, Y., Su, Q., & Wang, S. (2008). Photoluminescence and thermoluminescence properties of dysprosium doped zinc metaborate phosphors. *Journal of Rare Earths,* Vol. 26(2), 203-206.

Manjunatha, C., Sunitha, D. V., Nagabhushana, H., Sharma, S. C., Ashoka, S., Rao, J. L., Nagabhushana, B. M., Chakradhar, R. P. S. (2011). *Materials Research Bulletin,* Vol. 47, 2306–2314.

Natarajan, V., Seshagiri, T. K., Kadam, R. M., & Sastry, M. D. (2002). SO4−–SO3− radical pair formation in Ce doped and Ce, U co-doped $K_3Na(SO_4)_2$: EPR evidence and its role in TSL. *Radiation Measurements,* Vol. 35, 361 – 368.

Puppalwar, S. P., & Dhoble, S. J. (2012). Determination of kinetic parameters of TL of Eu-doped $LiNaF_2$. *Indian Journal of Pure and Applied Physics,* Vol. 50, 855-858.

Sahare, P. D., Ranjan, R., Salah, N., & Lochab, S. P. (2007). K3Na(SO4)2 :Eu nanoparticles for highdose of ionizing radiation. *Journal of Physics D: Applied Physics,* Vol. 40, 759–764.

Shinde, S. S., Rao, T. K., Sanaye, S. S., & Bhatt, B. C. (1999). TL and ESR Characteristics of BaSo4:Eu Co-Doped with Na/P: Influence of Method of Preparation. *Radiation Protection Dosimetry,* Vol. 84(1-4), 215-218. doi:10.1093/oxfordjournals.rpd.a032721

Shionoya, S. (2007). Introduction to the handbook. In W. M. Yen, S. Shionoya, & H. Yamamoto, *Phosphor Handbook* (pp. 3-8). Boca Raton, USA: Taylor & Francis Group, LLC.

Strauss, L., & Hajek, M. (2007). *Review of methods for the determination of the kinetic parameters of thermoluminiscence dosimeters.* Wien, Austria: Atomic institute of the Austrian Universities.

Vidya, Y. S., & Lakshminarasappa, B. N. (2013). Preparation, Characterization, and Luminescence Properties of Orthorhombic Sodium Sulphate. *Physics Research International,* Vol. 641631, 1-7. doi:10.1155/2013/641631

Vidya, Y. S., & Lakshminarasappa, B. N. (2014a). Influence of Rare Earth Doping on Microstructure and Luminescence Behaviour of Sodium Sulphate. *Indian Journal of Materials Science,* Vol. 675417, 1- 8. doi:10.1155/2014/675417

Vidya, Y. S., & Lakshminarasappa, B. N. (2014b). Synthesis, Characterization and Thermoluminescence Studies of LiNaSO4:Eu3+nanophosphor. *Journal of Luminescence and Applications,* Vol. 1(2), 40-60. doi:10.7726/jla.2014.1005

HUMAN ACTIVITIES AND NATURAL HAZARDS IN AREAS OF NORTHERN NIGERIA

Abdulkadir A[1]., Abubakar A.S[1]., Jibrin A.[2] Emigilati M.A[1]., Abubakar A[1]. and T.I Yahaya[1]

[1]Department of Geography, Federal University of Technology, PMB 65, Minna, Nigeria. Email: abuzaishatu@futminna.edu.ng

[2]Department of Geography, Ahmadu Bello University, Zaria, Nigeria

In Nigeria like most part of the world, anthropogenic activities and human interventions with the natural environment have continued to escalate both natural and human-induced hazards. These usually altered the natural equilibrium leading to alterations of the natural processes that threaten sustainable livelihood across the country. This study examines role of climate change using temperature record (1951-2014) over Kano, Maiduguri, and Sokoto to determine spatiotemporal changes and its potential impact. Shiroro hydrologic record for thirty seven years (1975-2012) were collected and analyzed in addition, hand dug well and borehole water samples were collected around Kuyi waste dump site to determine the impact of waste on the water quality. Furthermore 300 structured questionnaires were administered to the residents of Gurmana downstream settlement for the purpose of generating their responses arising from flooding and its related problems. The result affirmed temperature changes between 1950 - 1981 and 1982 – 2014; it reveals positive changes in April mean, maximum and minimum temperature values of between 0.4 to1.5°C across the study area. Similarly, the observed oscillation and positive trend of inflow and outflow from shiroro reservoir constitute a major and unprecedented shift in stream flow across the downstream communities. Thus, intensifying seasonal rainfall related hazards that threatens livelihood of the exposed and vulnerable community. Specifically, over 70% of the community population strongly agree that flood poses a great threat to their farmlands also; poverty is major factor intensifying vulnerability as about 45% of the population still live in mud houses with thatch roofs. Furthermore, urbanisation has continued to aggravate waste management challenges leading to increase concentration of pollutants that pose direct/indirect health threat to women and children. The pH values for hand dug well is 6.20 and boreholes are between 6.83 and 7.18, the hand dug well is below SON (2007)standard, Magnesium (Mg) and conductivity is generally above SON,(2007) standard value which is 100. It's crucial to understand the physical phenomena and human-induced hazards that intensify natural disaster which can cause human life disruption, loss of life, property damage, socio- economic disruption and environmental degradation. Hence, there is need for systematic development and application of policies, strategies and adoption of best practices to minimize risk, vulnerability and exposure as pathway towards disaster risk reduction.

Introduction

Human activities in Nigeria such as deforestation, emission of greenhouse gases, mining and dam constructions generally affect both natural and human-induced hazards thereby threatening the sustainable livelihood across the country. The increased human activities in recent times have continued to aggravate environmental degradation which pose great threats to sustainable livelihood, escalate natural hazard and struggle for survival. Stephen and Tobi (2014) rightly observed that Nigeria's population and economy are linked to climate sensitive activities including rain-fed agriculture. Our environment today is being degraded, polluted and destroyed at higher rate and pace by human interaction thereby altering the natural balance through emission of green house gases leading to pollution (air, water, land, and food). It is fundamental to note that the state of our environment influence or is influenced by our behaviour and thus, it's crucial for all to either nurture it for enhance and sustainable livelihood or ill-treat and destroy it for future uncertainty.

Temperatures values are generally rising in recent times; thermal comfort is reducing across most locations across the country, particularly in northern Nigeria due to its latitudinal location. Each of the past several decades has been significantly warmer than the previous one (Taalas 2016 and Hansen et.al 2010). This trend has negative impact on thermal comfort, water, vegetation and agricultural resource also, in extreme cases it leads to outbreak of epidemics like meningitis. Africa's climate seems destined to change, with far-reaching implications for water resources and agriculture (Bette et.al 2014). As it is apparent that future temperature will be associated with more extreme and increase variability hence, there is need to understand these changes at micro-levels and the human activities that are exacerbating the intensity of the changes for enhance adaptation and mitigation. Many prevalent human diseases are linked to climate fluctuations, from cardiovascular mortality and respiratory illnesses due to heat waves, to altered transmission of infectious diseases and malnutrition from crop failures (Jonathan et,al 2005). Consequently, it is fundamental to understand these changes in order to identify and develop adaptation measures as well as strategies for the attainment of sustainable livelihood.

Flood is common phenomena in Nigeria that usually affects the riverine communities. This crop up when the flow rate exceeds the carrying capacity of the river channel, particularly at the lower course of the river and low-lying parts of flood plain. The flood plain areas are national assert across the globe but are highly vulnerable areas in Nigeria because emphasis are mainly reactive rather than being proactive. Nott (2006), correctly points out that a flood event is not considered to be a natural hazard unless it threatens human life and/or property. Furthermore, floods constitutes a major hazard in Nigeria because of the high human population densities that inhabit these vulnerable areas, lack of capacity and adverse human activities (lack/ blockage of drainages, building on water ways and poor planning) which are aggravating flood hazard and disaster in most urban centres' across the country. Okori et.al (2009) affirmed that disasters arising from human-induced and natural hazards are growing global threats affecting millions of people annually, with devastating impacts on vulnerable communities.

Similarly, man's unguarded development initiative and ineffective waste management in urban centre across the country have continued to accelerate environmental degradation and outbreaks of epidemics. Illegal dump site and illegal dumping of waste is a common problem particularly in peri-urban areas thereby threatening society safety and security. Generally, illegal dumping of waste can cause serious environmental problem by polluting the environment with toxic substance in the dumped waste. In Minna like any other urban area in Nigeria, enormous amounts of solid waste are generated, collected and dumped at Minna Solid Waste Dumpsite nearer Kuyi Village near Maikukele, Bosso Local Government Headquarter in Niger State. This could have negative impact on the available resource particularly land, water, air and vegetation which may as well lead to outbreak of disease. The most common method of solid waste disposal practice in Nigeria is open dumpsite or land filling.

Further, technology and urbanization has been significantly escalating the emission of Green House Gases (GHGs) such as Carbondixiode (CO_2) in most urban areas across the country. Christopher *et.al* (2014) stated that Cities are major sources of Green House Gas (GHG) emissions and the effects of mass urbanization upon the environment have now become clear. Concentration of GHGs in the atmosphere is aggravting changes in the world's climate which is a prime factor that determine economic livelihood across the country. Our planet is sending a powerful message to world leaders to sign and implement the Paris Agreement on climate change and cut greenhouse gases now before we pass the point of no return (Taalas, 2016). Similarly, deforestation of forest cover which sequesters and store more carbon than any other terrestrial ecosystem is on increase due to intensification of human thereby escalating the CO_2 concentrations in the atmosphere.

Generally, these changes coupled with increase human activities are aggravating the intensity of natural hazard which could be disastrous. ICSU (2007) defined natural hazard as a potentially damaging physical event, phenomenon, or human activity that can cause loss of life or injury, damage to property, social and economic disruption, or environmental degradation. Similarly, UNISDR (2009) define hazard as a dangerous phenomenon, substance, human activity or condition that may cause loss of life, injury or other health impacts, property damage, loss of livelihoods and services, social and economic disruption, or environmental damage. These hazards commonly result to disaster across the study area thereby leading to destruction of live and properties. More than 90 per cent of natural disaster related deaths are to be found in developing countries (ISDR 2003). Climate change and human activities are increasingly threatening both sustainable development and poverty-reduction initiatives in northern Nigeria. UNISDR (2004) stated that sustainable development is generally recognised as the optimum way to harmonise humankind's interactions with and dependence on our environment to the ultimate benefit of both (UNISDR 2004). Thus, it's crucial for institution and relevant stakeholders to identify and take proactive measures that can help in the mitigation of hazards thereby reducing disasters. As well as, improving living standards and opportunities for more fruitful livelihood across the vulnerable areas.

Study Area

Generally, Northern Nigeria is located between Longitudes 3^0 to 15^0 East of the Greenwich meridian and Latitudes 9^0 and 14^0 North of the Equator (Fig.1). The climate of Northern Nigeria is influenced basically by two air masses - The Tropical Maritime air mass (South West trade winds) and the tropical continental air mass (North East trade wind). The boundary zone between these two air masses is called Inter-Tropical Discontinuity (ITD) (Adejuwon, 2012). This area has three distinct seasons: The hot dry season from March to May, and the warm rainy season from June to September, and a cool dry season from November to February with an average relative humidity of 36% during the dry season and 79% during the wet season (Yamusa, *et.al* 2015). The seasonal and latitudinal variations affect diurnal and seasonal temperature ranges, the highest maximum air temperature is recorded in the northern part usually areas north of latitude 9° and occur in March /April and minimum temperatures are recorded in December/January North of latitude 9°N. Kano, Sokoto

Maiduguri and Minna are headquarters of four states among the nineteen states in northern Nigeria. Minna solid waste dumps site is an example of open dump site operated by Niger State Environmental Protection Agency (NISEPA) which is approximately 03km to Kuyi Village at the opposite side of the main road.

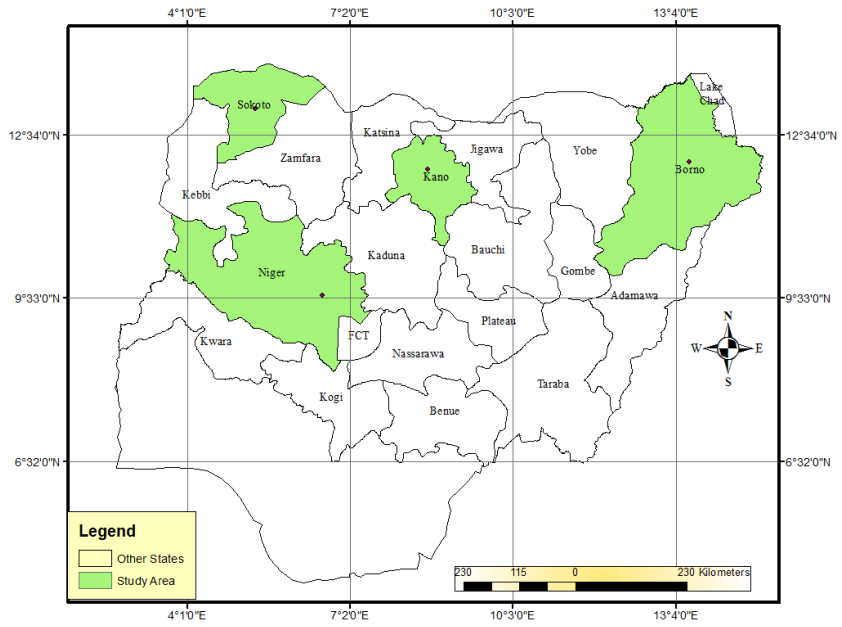

Fig.1 Location of the Study Area

Material and Method

This study examines the human activities, temperature changes and other natural event aggravating natural hazards in northern Nigeria. Maximum and minimum temperature records of three selected globally reference meteorological weather stations were sourced from Geography Department, Federal University of Technology, Minna. Specifically temperature records of Kano, Maiduguri, and Sokoto were used to investigate spatio-temporal temperature changes in northern Nigeria between 1951- 2014. Descriptive and inferential statistics were used to summarize, analyze and visualize the spatiotemporal changes across the study area. In addition, Gasman CO_2 sensor device was used to determine carbon dioxide emission at various locations within Minna and its environs. The mean values were plotted graphically to visualized human activities and carbon dioxide emission within Minna and its environs.

Similarly, hydrologic record of the Shiroro dam area was collected for 37 years (1975-2012), summarized and analyzed using inferential statistic to visualized trend in the hydrological parameters. Furthermore, 300 questionnaires were administered to residents of Gurmana downstream settlement of the dam in order to examine the community flood risk perception and its impact. The entire data was analyzed using IMB Statistical Packages for Social Sciences (SPSS) 21

Finally, groundwater quality of settlement close to dumpsite in Minna was investigated to determine the impact on hand-dug well and borehole water samples in Kuyi village. The analysis of heavy metal and other chemical elements concentrations such as Mg, Pb, Cu, Cr, Ni, Zn, Cd, Na, Mn, Ca, Cl, in groundwater sampled was conducted using atomic absorption spectrophotometer, conductivity and pH were determined. Also, the values were compared to Nigeria Industrial Standard (NIS, 2007).

Results and Discussion

The result reveals the spatio-temporal variability and gradual temperature changes in mean temperature values across the study area (fig. 2). In addition, Pearson correlation analysis shows that there are strong positive corrections between the temperature values of the three locations; Maiduguri and Kano .69, Sokoto and Maiduguri .62 and Kano and Sokoto correlation coefficient is .51.

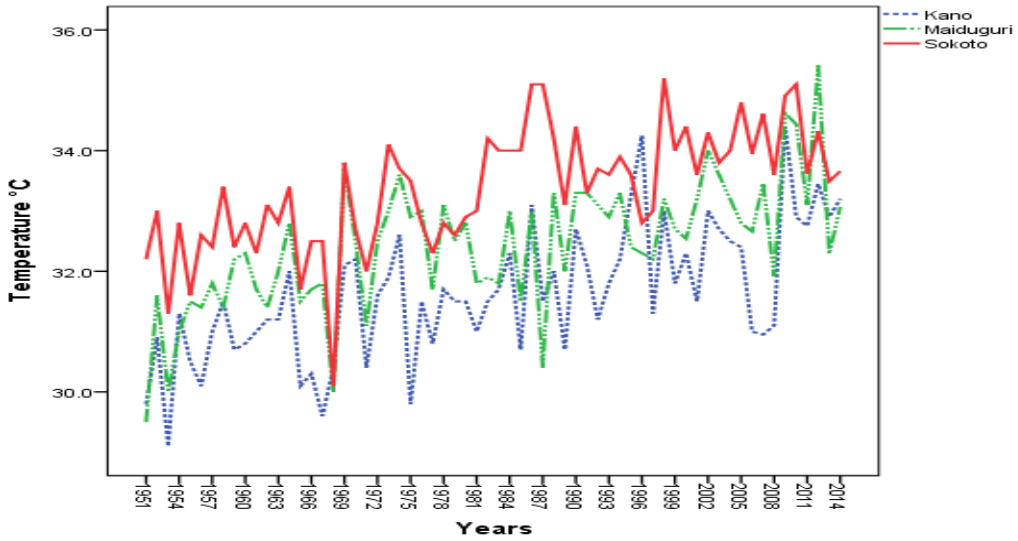

Fig.2 Mean Temperature Value (1951-2014)

The differences in mean temperature values between 1951 to 1982 and 1983 -2014 confirmed the observed gradual temperature changes (Table 1). It indicates that temperature changes are .99 in Maiduguri, Sokoto 1.28 and Kano 1.2. This is in agreement with IPCC (2007) projection that by 2050, average temperatures in Africa are predicted to increase by 1.5 to 3°C, and will continue further upwards beyond this time. Carlowicz (2010) stated that one-degree global change is significant because it takes a vast amount of heat to warm all the oceans, atmosphere, and land by that much. By implication, this percentage seems small but could have adverse impact on man and the physical environment. In addition, the decadal rate of change is higher in Sokoto and Kano (.41 and .39) than Maiduguri (.32) and this affirm decadal changes in mean temperature values across the zone where agriculture is primary occupation. Oladipo (2008) concluded that large rural population that is directly depending on the natural resources for their subsistence and livelihood which are climate-sensitive are highly vulnerable.

Table 1: Mean Temperature changes between 1951-1982 and 1983-2014.

Station	Annual Mean Temperature	Decadal Rate of Change
Maiduguri	.99	. 32
Sokoto	1.28	. 41
Kano	1.2	. 39

Similarly, the January mean minimum and maximum temperature values also unveils the spatio-temporal variability and gradual changes in January mean temperature values which is one of the coldest month in the region. The mean minimum and maximum temperature values across the study area are generally characterized by high variability as well, the figure signals gradual temperature changes (figure 3 & 4). The mean minimum temperature changes is apparent than the maximum values which is an indication of decline in temperature range and a warmer temperature trend.

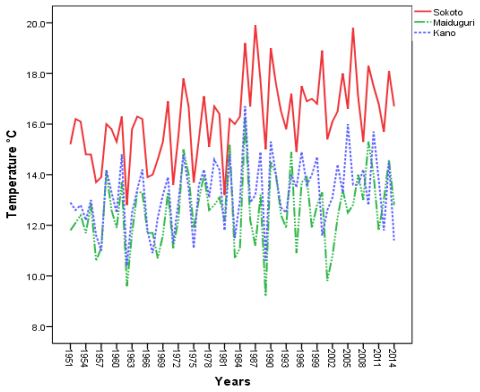

Fig.3 January Minimum Temperature

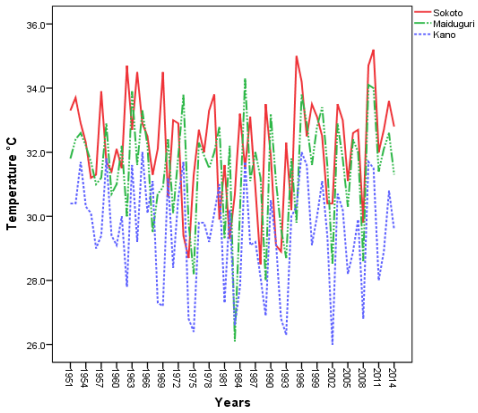

Fig.4 January Maximum Temperature

The April mean minimum and maximum temperature values also shows the variability and gradual changes typical of temperature values across the study area (Figure 5 & 6). The figures signal a warmer temperature across the study area. IPCC (2007) reported that by 2020, between 75 and 250 million people in Africa are projected to be exposed to increased water stress due to climate change. As high temperature values aggravate aridity, moisture stress and reduced thermal comfort as already apparent in the study area.

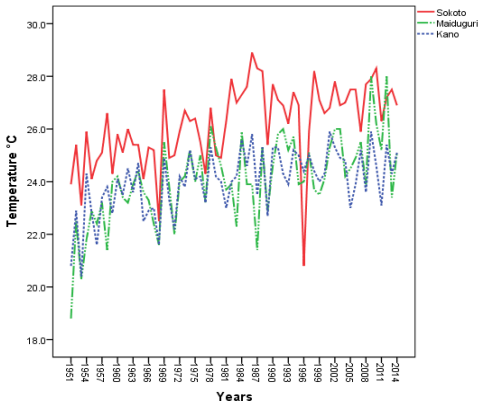

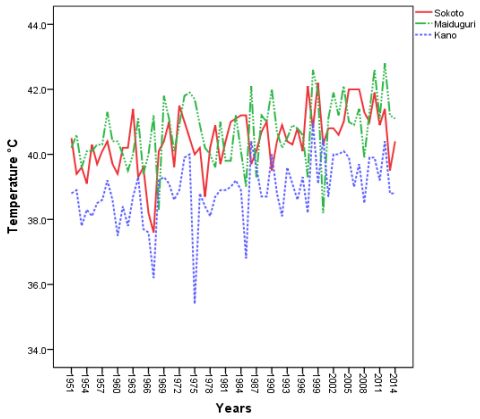

Fig.5 April Minimum Temperature

Fig.6 April Maximum Temperature

The observed changes in minimum and maximum temperature values were confirmed between 1951 - 1982 and 1983 – 2014 as evident in January and April values (Table 2). Positive changes in April mean maximum and minimum temperature values were between 0.4 and 1.5°C across the study area. The negative changes in range (-0.4 to -1.5) is an indication of warmer temperature since the margin between maximum and minimum temperature is declining. FAO (2008) forecasted that for each 1°C rise in average temperature, dry land farm profits in Africa will drop by nearly 10%. These increments in average temperature values will certainly aggravate moisture stress and environmental stress in a region where large proportion of the population are dependent on environmental resource. Consequently, these have continued to aggravate poverty, famine as well as food, socio-economic and political insecurity across the region. Furthermore, Nick et.al (2005) indicated that the most vulnerable nations are those situated in sub-Saharan Africa and those that have recently experienced conflict.

Table 2: Temperature changes between 1951-1982 and 1983-2014.

Stations	Jan max	Jan min	Jan mean	Jan range	April max	April min	April range
Maiduguri	-0.1	0.2	0.1	-0.3	0.6	1.4	-0.8
Sokoto	0.2	1.4	0.5	-1.7	0.4	1.5	-1.5
Kano	-0.6	0.8	0.1	-1.3	0.8	1.2	-0.4

Similarly, there was increasing carbon emission with increase human activities; from 200 at the outskirt to 600 and 700 ppm at central areas and location of small scale industries (Figure7). The alarming rate of change we are now witnessing in our climate conditions as a result of greenhouse gas emissions is unprecedented in

modern records (WMO 2015). As the over reliance on fossil fuel; increase use of automobile in recent time is escalating emission of GHGs across the country.

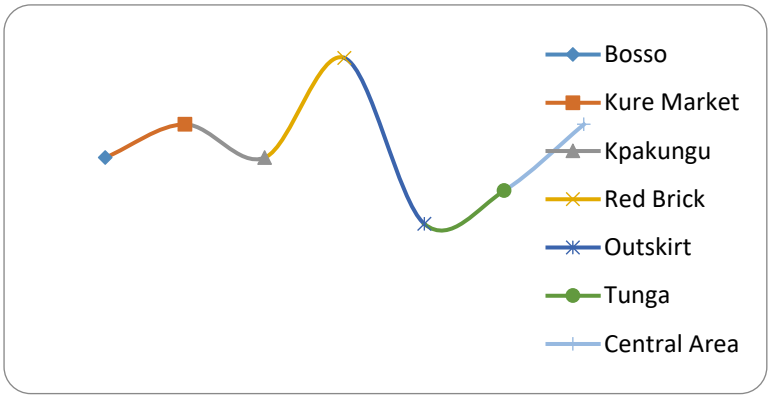

Figure 7: Carbondioxde Emission at Various Locations in Minna

By implication, the ongoing population growth, urbanization and socio-economic development signal higher rate of emission and significant impact on future climate. While climate change is now considered by many to be the most pressing challenge facing the human society today, total anthropogenic GHG emissions have continued to increase (Kevin, 2014). He added that about 78% of the total GHG emission increase from 1970 to 2010 was due to CO2 emissions from fossil fuel combustion and industrial processes. This trend is hazardous to human livelihood particularly in a region where large proportion depends on environmental resources coupled with low capacity will certainly escalating vulnerability. Consequently, Akinwande (2014) identified carbon tax as policy instruments canvassed for the reduction of greenhouse gases (GHGs). Implementing this will reduce emission, mitigate climate change, and enhance sustainable livelihood and resilience to climate change as well as climate-related hazard.

The annual inflow and outflow is generally characterized by variability and positive trend in recent trend which is aggravating flooding downstream (Figure 8). These oscillation and positive trend of inflow and outflow from Shiroro reservoir constitute a major a major environmental hazard downstream across the riverine communities. Changes in extreme weather and climate events are among the most serious challenges societies faced with living in a changing climate (John *et al.*, 2016). Thus, intensifying seasonal climate related hazards that threaten livelihood of the exposed and vulnerable community. Specifically, over 70% of the riverine community strongly agree that floods pose a great threat to them and their farmlands. Families living nearer to the river seem to have fewer opportunities to engage in multiple economic activities which make them more vulnerable to natural disasters and may keep them trapped in a poverty cycle (Brouwer, *et al*.2007).

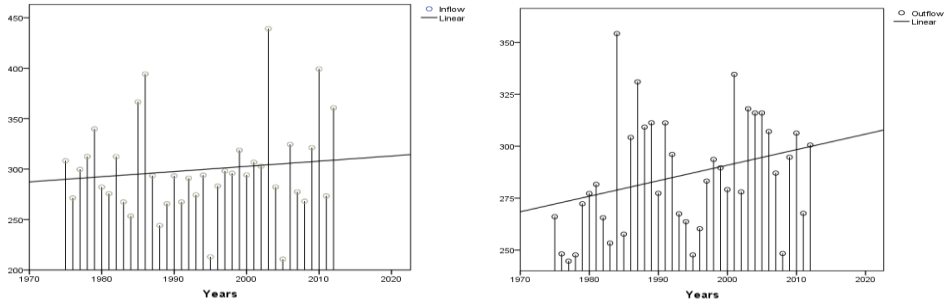

Figure 8: Annual Inflow and Outflow into and from Shiroro Dam (m^3/s)

Furthermore, questionnaire analysis shows that poverty is the major factor that increases the local vulnerability since about 45% of the population still live in mud houses with thatch roofs and 92% are mainly farmers. Correspondingly, about 82% of the respondents strongly agree that flood is an annual phenomenon that poses a great threat to their farmlands and livelihood. Thus, the high level of perception and awareness of the recurring hazards does not deny the community from being at risk because of the exposure of the physical structures, economic resources (farm land) and even live and property that could be injury or damage. Africa's climate seems destined to change, with far-reaching implications for water resources and agriculture (Bette et.al). These in addition to their low capacity to respond and adapt to extreme weather conditions whether (dry or wet) affects' and threaten rural livelihood and the country at large. Malte (2015) concludes that impacts of extreme weather events are relevant for regional economies.

Furthermore, rapid rate of urbanisation in most cities and towns have continued to exacerbate waste management challenges leading to increased concentrations of pollutants that pose direct/indirect health threat to women and children in particular. pH values for a Hand-dug Well (HDW) is 6.20 while that of boreholes are between 6.83 and 7.18; the hand-dug well is below Nigeria Industrial Standard (NIS, 2007) standard (Table 3). This indicates that heavy metal in the HDW has no impact on boreholes. Magnesium (Mg) and conductivity is generally above NIS standard value and this could be due to impact of dump site on the surrounding community. Hunter *et al*. (2009) stated that any level of conductivity above standard value can determine health risk and brain damages. This is an indication that open dumpsite are not only unfriendly, unsightly, unsanitary, and generally smelly but could cause pollutions of all kinds and capable of threatening human health and the physical environment.

Table 3: Physiochemical parameter for water samples from kuyi dumpsite.

Chemical Parameter for water samples	**HDW**	**BW1**	**BW2**	**SIN (2007)**
P^H	6.20	7.18	6.83	6.5 – 8.5
Chloride (Cl)	20.84	12.90	16.18	250

Copper(Cu)	0.12	0.11	0.20	1
Chromium(C r)	0.03	0.01	0.01	0.05
Hardness(as Ca)	17.00	28.00	24.00	150
Lead (Pb)	0.00	0.00	0.01	0.0
Magnesium (Mg)	10.36	16.80	14.40	0.20
Manganese (Mn)	0.08	0.00	0.00	0.2
Conductivity	191	307	265	100
Nitrate (NO_3)	1.26	1.73	2.21	50
Zinc (Zn)	0.00	0.00	2.17	3
Sodium (Na)	6.0	5.10	26.0	200

Hand Dung Water (HDW) and (BW) Borehole Water.

Conclusion

This study shows that it is crucial to understand physical phenomena and human-induced hazards that increase the impact of natural hazard on society, which could cause loss of human life, property damages, socio-economic disruption and environmental degradation. Since, in most cities across the country, the emphasis is always on deriving the maximum benefit from the environment without thinking about the possible impact from such activities that may harm man and his livelihood. Thus, human activities are hazardous to livelihood and are always disastrous in extreme cases when people's lives and livelihoods are destroyed. By indication, these indicate the need to identify these activities, there impact and preventive measures for minimizing the effect of natural phenomenon. Above all, this will minimize human induced potential hazard and its harmful effects on people and economic livelihood. Consequently, there is an urgent need for a systematic development and application of policies, strategies and the adoption of best practices as an indispensable pathway towards a more effective disaster risk reduction.

References

Adejuwon J. O. (2012), Rainfall seasonality in the Niger Delta Belt, Nigeria. *Journal of Geography and Regional Planning* Vol. 5(2), pp. 51-60, DOI: 10.5897/JGRP11.096 ISSN 2070-1845.

Akinwande G. (2014), The Prospects and Challenges of the Proposed Carbon Tax Regime in South Africa: Lessons From The Nigerian Experience. *Journal of Sustainable Development Law and Policy* (2014) Vol3 (1), 177-188

Bette L. Otto-Bliesner, James M. Russell, Peter U. Clark, Zhengyu Liu, Jonathan T. Overpeck, Bronwen Konecky, Peter deMenocal, Sharon E. Nicholson, Feng He, Zhengyao Lu (2014), Greenhouse Gases May Influence Africa's Rainfall and Future Climate . ATMOSNEWS, December 4, 2014

Brouwer, R., Akter, S.,Brander, L. and Haque, E. (2007), Socio-economic Vulnerability and Adaptation to Environmental Risk: A case study of Climate Change and Flooding in Bangladesh. *Journal of Environment*, 27 (2), 313- 319

CE PLAN

FAO (2008), Water for Agriculture and Energy in Africa: The Challenges of Climate Change'. Ministerial Conference on Water for Agriculture and Energy in Africa: The Challenges of Climate Change. Sirte, Libyan Arab Jamahiriya.

Hansen, J., R. Ruedy, M. Sato, and K. Lo (2010), Global surface temperature change. *Reviews of Geophysics*, Vol. 48, 1-27

Hazards and

Hunter, P.R. Zmirou-Navier D, Hartemann P. (2009), Estimating the impact on health of poor reliability of drinking water interventions in developing countries. *Science of the total Environment* Vol.407, 2621-2626

ICSU (2007), Natural and Human-induced Hazards and Disasters in sub-Saharan Africa. ICSU Regional Office for Africa Science Plan Science plan approved by the ICSU Regional Committee for Africa, on 5–6 March 2007 in the Seychelles.

IPCC (2007), Summary for Policy Makers; Chapter 11 of the 4th IPCC Report on Regional Climate

ISDR (2003), Living with Risk: A Global Review of Disaster Reduction Initiatives − Preliminary Version. Geneva, July 2002, Prepared as an inter−agency effort coordinated by the ISDR Secretariat with special support from the Government of Japan, the World Meteorological Organization and the Asian Disaster Reduction Center (Kobe, Japan).

John E.H., David E., Kristie L.E., Akio K. And Martin P. (2016), Introduction to the special issue: Observed and projected changes in weather and climate extremes. *Weather and Climate Extremes* Vol.11, 1-3

Jonathan A. P., Diarmid C., Tracey H. & Jonathan A. F. (2005), Impact of regional climate change on human health. *Nature* Vol.438, 310-317.

Kevin C. U. (2014), Solving Africa's Energy Challenges by 2025. A Paper Presented at the Africa Progress Panel (APP) in preparation for the 2015 edition of the Africa Progress Report held at Geneva, 30 October 2014

Malte J. (2015), Economics of extreme weather events: Terminology and regional impact models. *Weather and Climate Extremes*. Vol.10, 29–39

Nick B., Neil W. Adger P. and Mick K.(2005), The Determinants of Vulnerability and Adaptive Capacity at the National Level and the Implications for Adaptation. *Global Environmental Change* Vol.15,151–163

NIS (2007), Nigerian Industrial Standards NIS 554: 2007, Nigerian Standard for Drinking Water. Approved by Standard Organization Nigeria (SON), ICS 13.060.20, pp: 1-30.

Nott, J. (2006), Extreme Events: A Physical Reconstruction and Risk Assessment.Cambridge University Press. New York.

Okori, W., Obua, J. and Baryamureeba V. (2009), Famine Disaster Causes and Management Based on Local Community's Perception in Northern Uganda. *Research Journal of Social Sciences*, Vol. 4: 21-32,

Oladipo, E. (2008), Climate change and sustainable livelihoods: greening options for Nigeria. Report of the first national environmental summit on the theme: Greening the Environment for Sustainable Development (pp 83-95).

Petteri Taalas (2016), Global climate breaks new records January to June 2016. WMO Report Geneva, 21 July 2016. http://public.wmo.int/en/media/press-release/global-climate-breaks-new-records-january-june-2016 (Access 13 march, 12017)

Stephen, B. O. and Tobi, E. M. (2014), Rainfall Distribution and Change Detection Across Climatic Zones in Nigeria. *Weather and Climate Extremes.* Vol. 5-6, 1–6

UNISDR (2004), Environmental Protection & Disaster Risk Reduction- A Community Leader's Guide. *Africa Educational Series*, Volume 2, (2)

United Nations International Strategy for Disaster Reduction (UNISDR) (2009), UNISDR terminology on disaster risk reduction, UN/ISDR, Geneva

WMO (2015), The WMO Statement on the Status of the Climate in 2015 http://public.wmo.int/en/media/press-release/state-of-climate-record-heat-and-weather-extremes (Access 16 march, 12017)

Yamusa A. M., Abubakar I. U., Falaki A. M., (2015), Rainfall variability and crop production in the North-western semi-arid zone of Nigeria. *Journal of Soil Science and Environmental Management*. Vol. 6(5). Pp 125-131.

LITHOFACIES CHARACTERIZATION OF MIXED-AEOLIAN-FLUVIAL DEPOSITS: EXAMPLE FROM THE PERMO-TRIASSIC OF THE CHESHIRE BASIN, NE UNITED KINGDOM

A. I. Goro[1] N. M. Waziri[2] A. L. Yola[3]

[1&2]Department of Geology, Federal University of Technology, Minna, Nigeria

[3]Department of Earth, Ocean and Ecological Sciences,

University of Liverpool, UK

[3]isahgoro@futminna.edu.ng

* Corresponding author

Abstract

In order to improve prediction of accurate facies definitions (which has implications for fluid flow properties) in Triassic red-bed mixed fluvial and aeolian deposits, a study has been undertaken to assess the variability in lithofacies at outcrop scale from Burton Point and Helsby Forest Farm in the Cheshire Basin, England. Outcrop studies using the concept of Discrete Genetic Intervals from the fluvial Chester Pebble Beds at Burton Point demonstrated that the fluvial facies consists of amalgamated channel bars deposited within braided stream system. Reservoir heterogeneity is expected to results from decrease in bed thickness and fining upwards within beds, to fining upwards within cross strata. The Kinnerton Formation exposed at Burton Point and Helsby Forest Farm show that the Aeolian facies could be divided into moderate to high angle planar crossed stratified aeolian dune slip-face deposits (A1), horizontal to near horizontal dune base and dry interdune sub-facies (A2, B1), wavy laminated horizontal to near horizontal wet interdune deposits (B2) and interdune hollow fill mudstones (B3). Based on the grain size and sorting, the lithofacies A1 is expected to have the best reservoir quality sandstones while the B3 lithofacies may prevent vertical flow of fluid especially at well-scale. This study suggests that detailed outcrop studies is essential for more accurate definition of the lithofacies type, which is particularly important in interpreting depositional environments as well as reservoir studies.

Keywords: Cheshire Basin, aeolian, characterization, Permo-Triassic, lithofacies

1. Introduction

Production histories for many mature fields containing aeolian sandstone reservoirs such as in the southern gas basin of the North Sea (e.g. Heward, 1991) and in the Permian to Jurassic aeolian sequences in the western USA (e.g. Linquist, 1988) show that treating aeolian deposits as simple and homogeneous reservoirs is an over simplification (North and Prosser, 1993). Poor recoveries have also been recorded in most fluvial facies (e.g. the Bartlesville Sandstone which has been a major oil producer in Oklahoma, USA for more than 90 years. This is due to complex reservoir architecture inherent in fluvial as well as aeolian deposits which is very difficult to properly characterise with conventional subsurface information alone (Ye, 1977).

In arid regions, it is common for fluvial and aeolian deposits to be intermixed, with the result that the overall succession has all the complexities of aeolian and fluvial processes, plus the complexities produced at the junction between the two, and by the reworking of one by the other (North and Prosser, 1993). This phenomenon is seen in almost all Triassic continental red beds. Triassic red beds form oil and gas reservoirs in different parts of the world. For example the Sherwood Sandstone Group in Wytch Farm oil field, Wessex basin UK, and in Essaoura basin, Morocco. This study offers a detailed description of selected well exposed ancient aeolian and fluvial deposits exposures from Cheshire basin UK with the intension of

illustrating the usefulness of detailed outcrop characterisation of Permo- Triassic red beds. The objectives are to document reservoir heterogeneities at different architectural scales using the concept of Discrete Genetic Intervals and their subdivision into several different smaller scale elements and to assess their implication for reservoir studies.

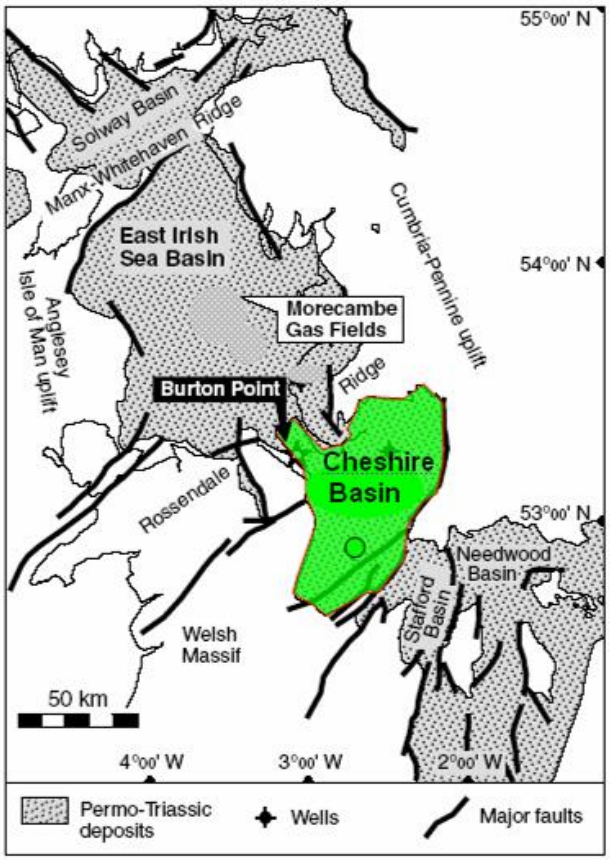

Figure 1. Location map of Cheshire Basin showing the position of Burton Point. From Stanistreet and Stollhofen, 2000.

2. Literature Review

The Cheshire basin, North East England is a faulted and folded half graben filled with Permo-Triassic deposits of largely continental origin (Chadwick, 1977). Most of the work on the area prior to the work of Thompson (1969; 1970) were focused more on the stratigraphy rather than sedimentology of the area. The influence of aeolian activity in the sandstones had been recognised by early workers. For example Wedd et al. (1923) referred to various parts of the Sherwood Group to be deposited in desert while by Taylor *et al*., (1963) suggested deposition by ephemeral sheet flood under predominantly arid conditions. Thompson (1969) described in detail and interpreted the Sherwood Sandstone Group outcrops around Frosham in the north-western part of Cheshire Basin as being the product of aeolian dune migration and ascribed them to the "Frosham Member" of the then Keuper Sandstone (later re-named the Helsby Formation). Further description and interpretation of lithofacies within the Keuper Sandstone led Thompson (1970) to identify low to moderate sinuosity fluvial deposits. The Triassic Stratigraphy of this area broadly follow the principle laid down by Warrington (1980) as shown in Figure 2.

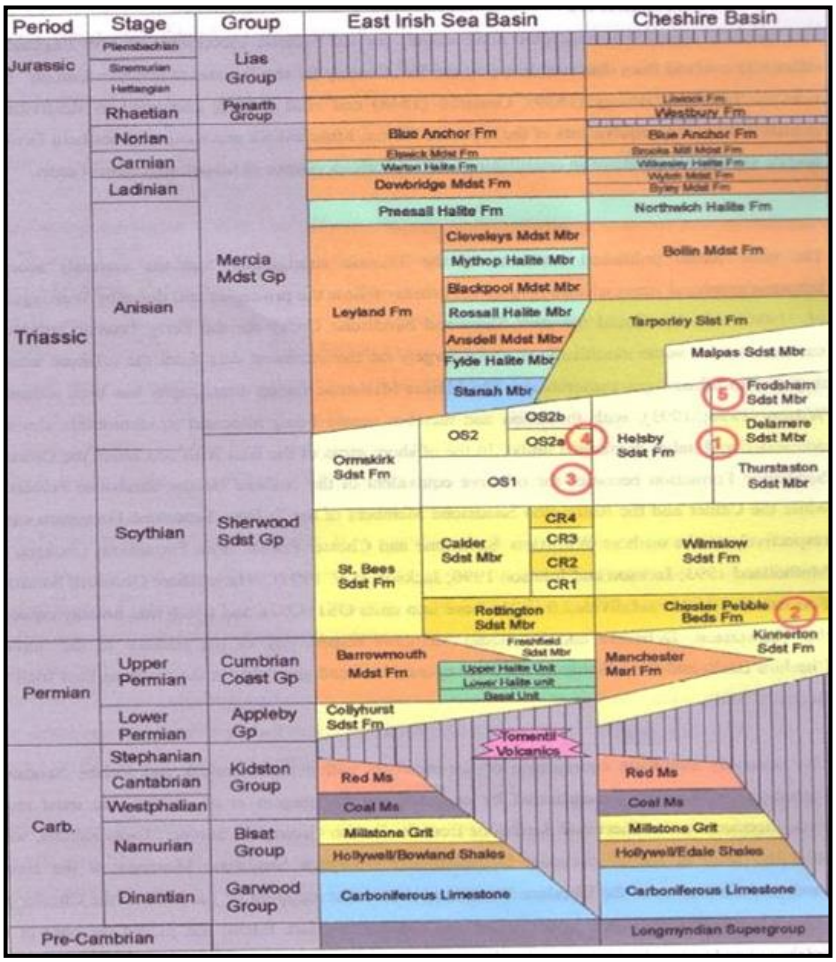

Table 1. Stratigraphy of NW England and the Irish Sea (after Warrington *et al.*, 1980)

3. Methodology

The research work involved field outcrop studies at two selected areas where both aeolian and fluvial facies are well exposed. The localities visited include Burton Point and Heldsby Forest Pack in Cheshire Basin, North West England. The work concentrated on the upper Permian Kinnerton Formation and lower Triassic Chester Formation. The concept of Discrete Genetic Intervals (DGI) developed by Kerr and Jiric (1990) which is of importance to reservoir geologist and engineers in the oil industries was employed in making a detailed investigation of the architectural elements of the studied aeolian and fluvial systems. In this approach, four hierarchy of architectural elements, each of which may influence fluid flow (e.g. Mial 1985, 1996; Mial and Tyler, 1991; Jordan and Pryo, 1992) are described. The hierarchies are:

1. Level 1: Multi-storey Discrete Genetic Intervals (MDGI) - This describes the stacking pattern of multiple DGIs. It is the largest rock volume of hierarchical reservoir architecture and shows vertical and lateral relationship between the stacked DGIs.

2. Level 2: Discrete Genetic Intervals (DGI) - This represents a brief episode of sedimentation that deposited a genetically related 3-D volume of sedimentary rock. The DGI is the fundamental sub surface mapping unit from an oil development point of view. For example the relation between meandering channels and the associated flood plain deposits.

3. Level 3: Facies within DGIs which are associated with the processes acting within the DGIs. This deal with variability within individual fills such as within meandering channel.

4. Level 4: Deals with variability of sub facies within the established facies

4. Results and Discussion

4.1 Results

4.1.1 Aeolian Systems

Two distinct Discrete Genetic Intervals are observed. They are Aeolian Dune (Facies A) and Interdune Deposits (Facies B) which are distinguished based on the nature of their cross bedding. Two sub-facies are recognized in the Facies A and are denoted by A1 & A2. The Facies B can be divided into three sub-facies B1, B2 and B3 based on their structure and position relative to Facies A.

4.1.1.1 Aeolian Dune Facies

4.1.1.1.1 Facies A1 - this sub-facies show moderate to high angle planar cross stratification (Fig. 2). The sandstones are medium to coarse grained and exhibit fine grain size differentiated laminae. The facies is interpreted as grain fall laminae deposited on slip face of aeolian dune form (Hunter, 1977; Kocurek, 1996; Spalletti *et al.*, 2010).

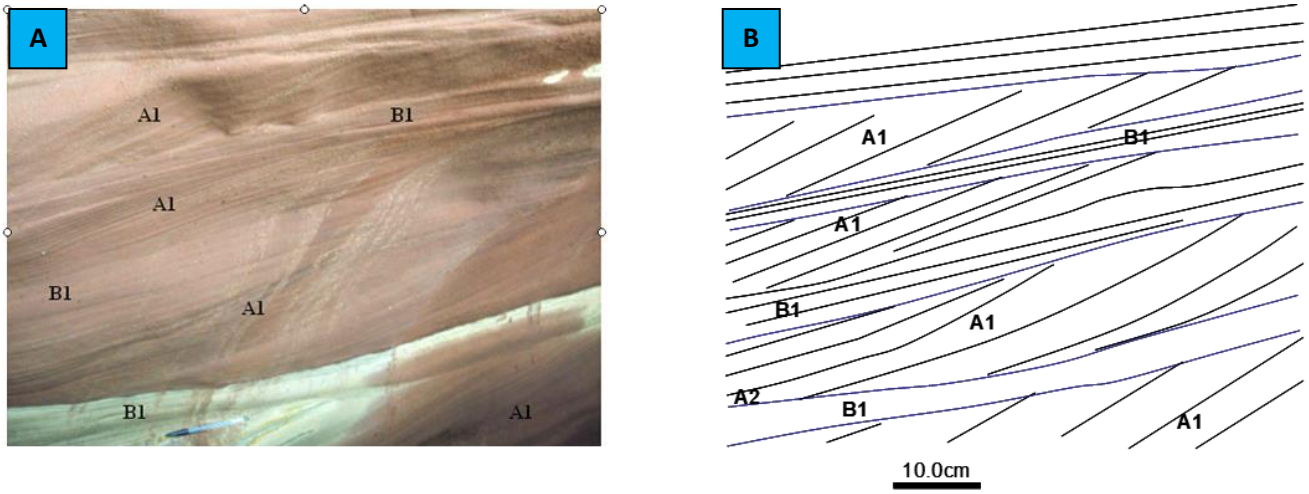

Figure 2. Outcrop Photo from Burton Point showing [A] interbedded aeolian dune face (A1), aeolian dune base (A2) and dry interdune (B1) deposits; [B] Interpreted sketch of [A] showing internal geometry.

4.1.1.1.2 Facies A2 – the sub-facies is characterized by horizontal to near horizontal laminae (Fig. 3). It consists of fine to coarse grained sandstones with more abundant thin dark argillaceous material. It commonly occur at the lower parts of Facies A1 (Fig. 3). This sub-facies is inferred to be deposited as aeolian dune toe deposits or dry Interdune deposits (Hunter, 1977; Kocurek, 1996; Nardi *et al.*, 2008).

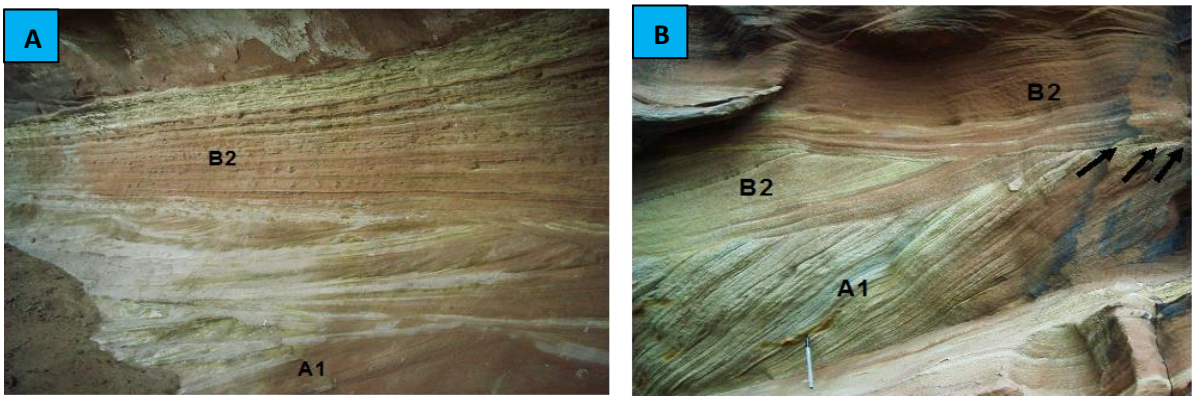

Figure 3. Outcrop photos Burton Point showing [A] Parallel wavy laminae of facies B2, intertonguing relationship between A2 and B2; [B] lateral interconnection of facies B2 and erosional truncation of facies A1 by B2 (arrows).

4.1.1.2 Interdune Facies

4.1.1.2.1 Facies B1 – this sub-facies comprises of fine to coarse sandstones having horizontal or near horizontal laminae with occasional concentration of coarse to very coarse grains. The sub-facies is interpreted as dry interdune deposit (Kocurek, 1996).

4.1.1.2.2 Facies B2- this sub-facies consists of fine grained sandstone with irregular to aligned concentration of coarse sands. They are characterised by parallel wavy laminae (Fig. 3A). They often exhibit centimetre scale lateral and vertical interfingring with the dune strata of facies A1 (Fig. 3A). Facies B2 may be interpreted as product of deposition within interdune areas where water table was periodically at sediment surface or wet (Kocurek, 1996).

4.1.1.2.3 Facies B3 – this sub-facies is composed of bright red mudstones with minor silt and fine sand fractions (Fig. 4). Horizontal bedding and desiccation cracks are the main structures. The facies are interpreted as representing deposition within confined Interdune hollows (Kocurek, 1996).

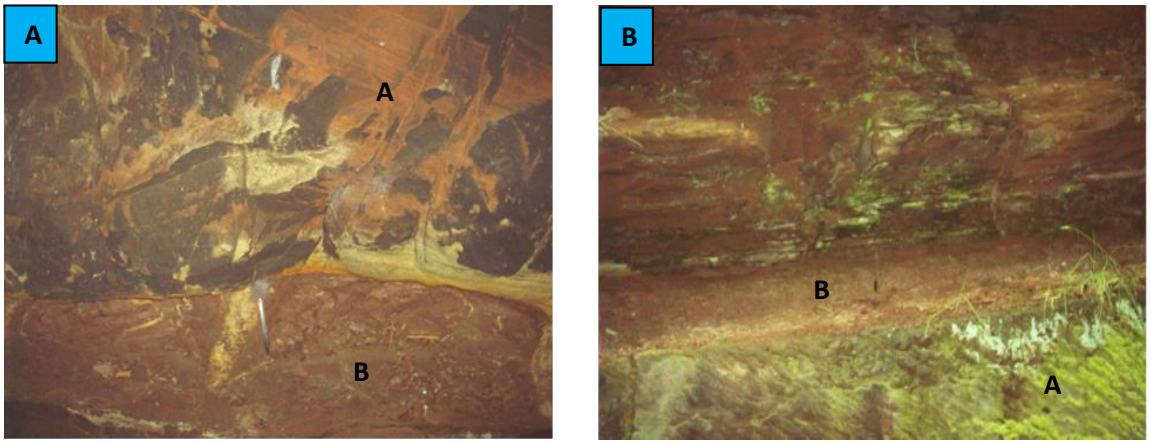

Figure 4. Outcrop photos from Heldsby Forest Farm showing [A] parallel laminated bright red coloured mudstone of B3; [B] a variety of B2 consisting of silty mudstone.

4.1.2 Fluvial Systems

Four levels of reservoir heterogeneity was observed on well exposed outcrop of fluvial deposit at Burton Point. Figure 5A shows a panoramic view of part of this deposit while Figure 5B is an interpreted sketch of the internal configuration.

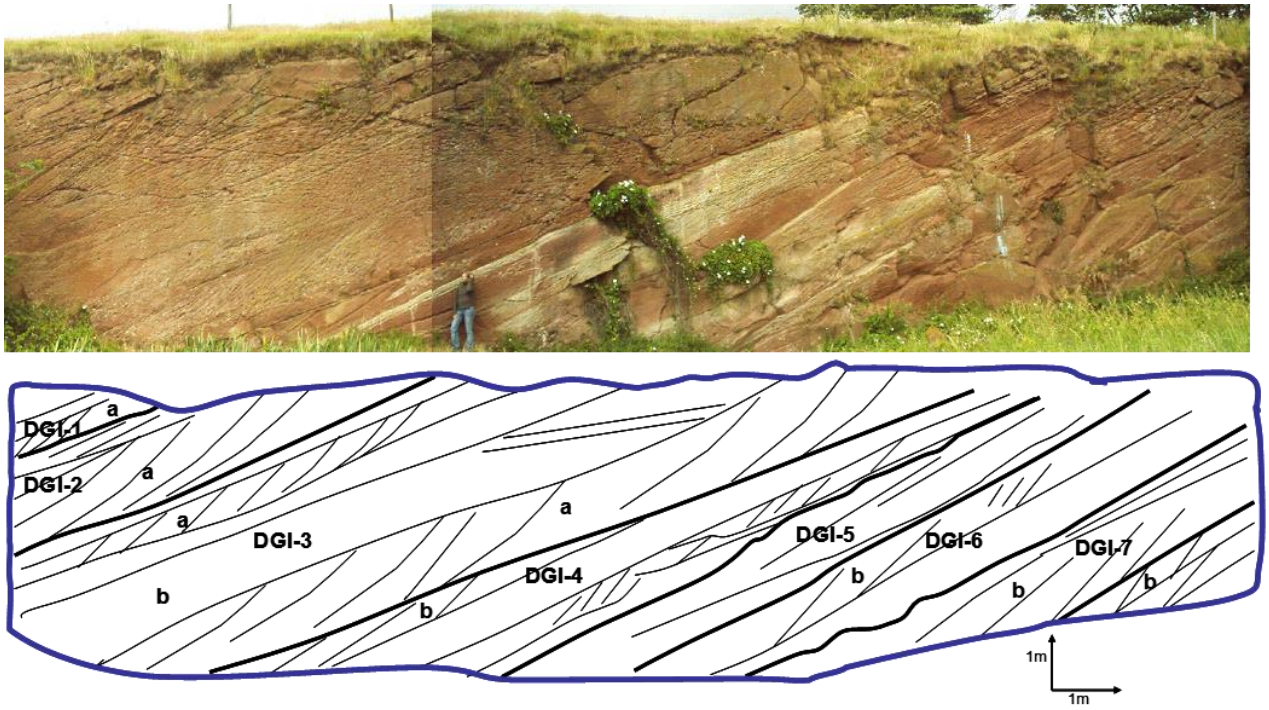

Figure 6. [A] Outcrop photo of part of a typical fluvial deposits. [B] Interpreted sketch of [A] showing the internal geometry of the deposit. DGI 1 to DGI 7 are discrete genetic interval characterised by basal lags and reduction in bed thickness within each. a & b are facies within the DGIs indicating trough cross bedding and planar cross bedding respectively.

1) Level 1: Multi-storey Discrete Genetic Intervals (MDGI) – seven DGIs are picked on the area covered by the picture. The DGIs are vertically superimposed, they are recognised by the presence of basal lags (fig.4.3)

and decrease in the thickness of bed size toward their tops. The DGIs are interpreted as channel bars and the stacking of sand bars is indicative of deposition within braided channel system. The occurrence of this deposit within an area dominated by aeolian sand systems is suggestive of deposition in perennial streams within stabilized aeolian system.

2) Level 2: Individual Discrete Genetic Intervals – A single DGI has the following features:

- Basal lag
- Grain size fines upwards
- Thickness of bed sets within DGI decrease upwards
- The lower parts of DGIs are characterised by trough cross beds with pebble lags along the cross beds
- DGI 3 has concentration of coarse and pebbly material from the central part down to the base.
- Beds become horizontal to near horizontal towards the top of the DGIs

3) Level 3: Facies within DGIs – Three different facies are observed within individual DGIs, they are:

1. Facies **a** – Medium to very coarse grains with pebbles. Characterised by trough cross bedding usually occurring towards the lower parts of DGIs
2. Facies **b** – Medium to coarse grains with pebble. Characterised by planar cross stratification with scattered pebbles towards the base.
3. Facies **c** – More or less parallel bedding towards the top of DGIs.

4) Level 4: Variability within cross beds – Centimetre scale fining upward of grains are observed on the cross beds.

4.2 Discussion

Processes operating in aeolian systems can be defined in terms of three end members: dry, wet and stabilizing systems (Kocurek and Havholm, 1993). In the dry aeolian system the water table has no effect on the substrate and no stabilizing factors occur so that deposition, bye pass and erosion along the substrate are controlled by the aerodynamic conditions only (Kocurek and Havholm, 1993). Such system are characterized by set of dune strata interbedded with dry interdune strata of limited thickness (Mountny, 2000). Facies A1 and B1 of this work clearly demonstrate this characteristics (Fig. 2 & 3). Hunter (1977) explained the processes operating on the slip-face of an aeolian dune as illustrated in Figure 7.

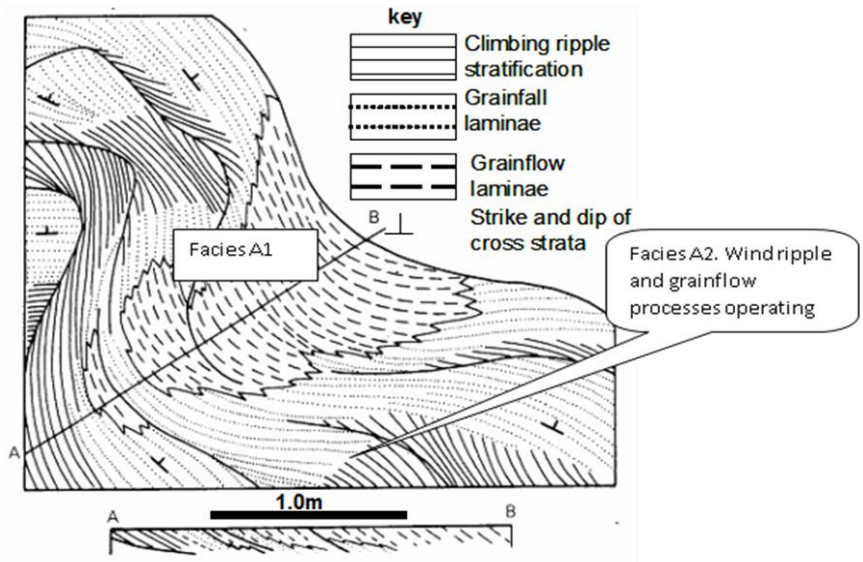

Figure 7. Model for processes operating from top to the base of an aeolian dune slipface depositing grainfall and grainflow strata. Note the absence of grainflow towards the base. (Modified from Hunter, 1977).

Wet aeolian systems are those where the water table or its capillary fringe intersect the accumulation surface so that both the aerodynamic configuration and the moisture content of the substrate determines whether the accumulation surface is depositional, bye pass or erosional (Kocurek and Havholm, 1993). These systems exhibit a variety of sedimentary structures ranging from sub aqueous current and wave ripples, wavy laminae and contorted bedding (wet surface condition) through adhesion structures, bioturbation structures and desiccation cracks (damp surface condition), to wind ripple laminae associated with dry surface conditions (Mountny, 2000). The diagram below is a summary model of Facies B2 and how they are related to Facies A1 and Facies A2 based on the studied interval.

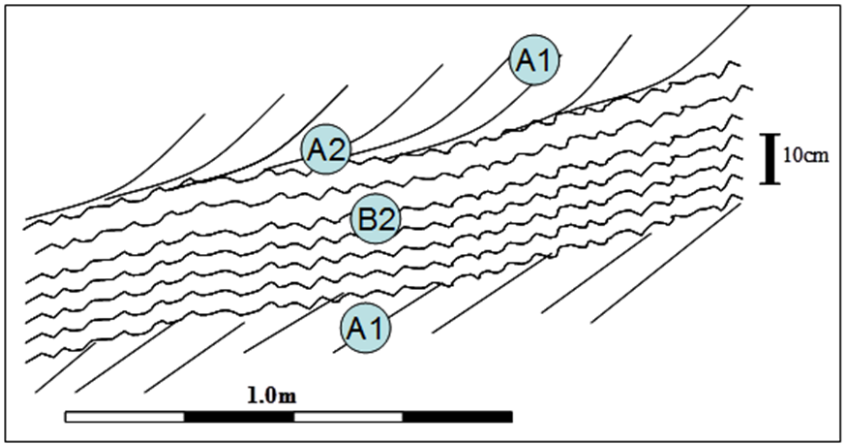

Figure 8. Model of wet interdune – dune relationship as observed in the study interval. A1 = dune slip-face facies, A2 = dune base facies and B2 = wet interdune facies.

Stabilised aeolian systems are those in which surface factors periodically stabilise the substrate and restrict aeolian transport while the system remain active overall (Kocurek and Havholm, 1993). Stabilizing agents include an elevated water table, development of desert crust, cements, soils, regs (serir), vegetation and mud

drapes (Mountny, 2000). A spectrum from subaqueos environments to sabkhas to wet aeolian interdune to dry aeolian interdune systems can occur within stabilizing systems depending on sediment supply and time or space (Kocurek and Havholm, 1993). The fluvial facies described from the outcrop show characteristic similar to braided river deposits (e.g. Boggs, 2005) with individual DGIs representing channel bars and associated channel floor deposits. They commonly occur as ephemeral streams. Areas surrounding the aeolian dune field are commonly characterized by the presence of mixed aeolian and fluvial facies to form sand-sheet complex (e.g. Boggs, 2005. The proposed depositional model that can be used to explain the vertical and lateral relationship of the identified facies is shown in Figure 9, below.

4.2.1 Implications

The gain size (medium to coarse) as well as good sorting displayed by the aeolian dune facies (A1) makes it a more favourable reservoir interval than the dune toe facies (A2). This is due to the presence of dark argillaceous laminae which serves to reduce permeability in the facies A2. This implies that the reservoir performance is expected to reduce at the lower parts of aeolian dune sandstones where facies A2 are developed. Within the interdune units the dry interdune (B1) and wet interdune (B2) are expected to constitute the reservoir units. Their interfingring with the aeolian dune facies may increase connectivity of the sandstones but the presence of confine interdune hollow mudstone (B3) is anticipated to compartmentalize the reservoir when individual well-scale heterogeneity is considered.

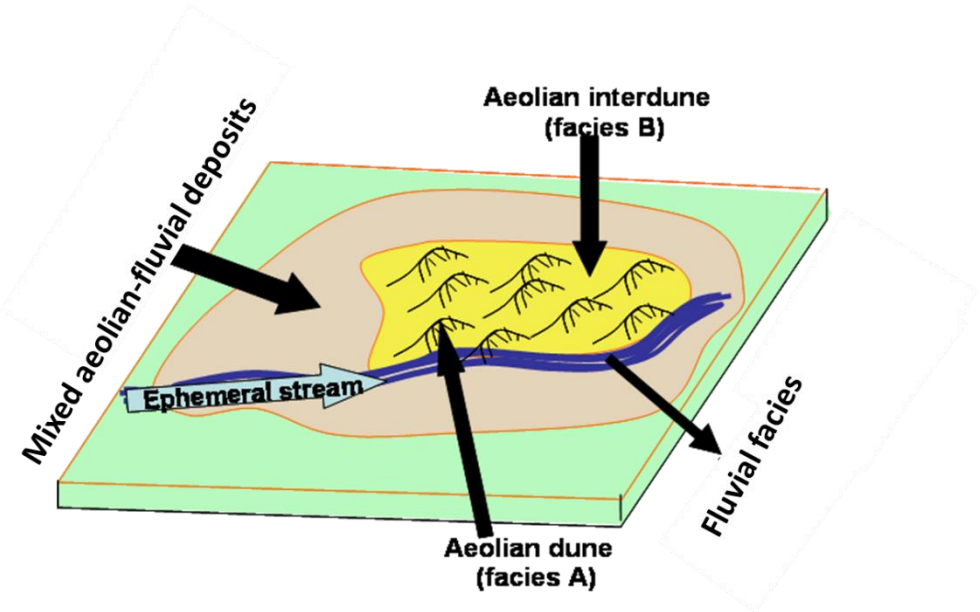

Figure 9. Aerial distribution and stratigraphic relationship between the identified lithofacies.

The fluvial facies are expected to serve as good reservoir units due to the amalgamated nature of the Discrete Genetic Interval (DGI) and the absence of floodplain mudstone intervals, but the poorer sorting may reduce the reservoir performance. Within each DGI, the porosity and permeability is expected to reduce upwards as a result of the fining-up grain size. Amalgamation of the DGIs invokes good reservoir thickness and vertical connectivity at well and even inter-well scale. Horizontal connectivity is also expected to be good due to lack of mudstone intervals within this facies.

The results of this study give insight into reservoir heterogeneity on outcrop scale using the concept of Discrete Genetic Intervals which from the oil development point of view is the fundamental subsurface mapping unit. This allows prediction of reservoir heterogeneity at individual well-scale to inter-well-scale. It provides information at even laminae scale which are often not accessible in well data. These could lead to successful prediction of large scale architectural reservoir heterogeneity and the smallest scale variability in an area dominated by mixed-fluvial and aeolian facies with implications at exploration through development to production stages.

4. Conclusion

This study demonstrates that it is possible to distinguish between aeolian and fluvial facies from the Permo-Triassic red beds exposed on Burton Point and Helsby Forest Farm in Cheshire basin, NE England. Four hierarchical levels of reservoir architecture was recognized based on the outcrop study of the fluvial facies. They are as follows in order of descending rock volume: multi-storey discrete genetic intervals which consists of amalgamated channel bars within braided stream system; discrete genetic intervals which are made-up of the channel bars within which there is upwards decrease in thickness of bed sets; bed sets within the channel bars where fining upwards of grain size occurs; and cross stratification within the bed sets where fining upwards of the grain size occur.

Lithofacies analysis of the aeolian facies provided insight into reservoir heterogeneity within the aeolian deposits. Four facies are recognised including aeolian dune and interdune facies. The aeolian facies can be divided into aeolian dune slip-face sub-facies and dune base sub-facies while the interdune facies are divided into dry and wet interdune as well as hollow fill sub-facies. The variability within these facies corresponds to the position of the facies within the aeolian system. The aeolian dune facies are related to dry aeolian systems while the damp and wet interdune facies are related to the wet aeolian system and the fluvial facies are related to stabilized aeolian system.

The aeolian dune facies are expected to be the best reservoir intervals followed by the interdune sandstones while the interdune hollow fills are expected to compartmentalize the reservoirs of the aeolian intervals. The amalgamated channel bar deposits of probable braided river origin are expected to serve as the reservoirs in the fluvial facies. Both lateral and vertical connectivity are envisaged in this facies due to lack of flood plain mudstone intervals. Accurate identification of the lithofacies as well as sub-facies using outcrop data is important for better prediction of reservoir heterogeneities in mixed aeolian and fluvial facies that commonly occur in desert environment.

References

Chadwick, R.A., 1997. Fault analysis of the Cheshire Basin, NW England. In Meadows, N.S., Trueblood, S.P., Hardman, M. and Cowan, G. (eds.) *Petroleum geology of the Irish Sea and adjacent areas*, Geological Society Special Publication, 124, 297-313.

Heward, A. P. 1991. Inside Auk--the anatomy of an eolian oil reservoir. *In:* MIALL, A. D. & TYLER, N. (eds) *The three-dimensional facies architecture of terrigenous clastic sediments and its implications for Hydrocarbon discovery and recovery.* SEPM Concepts in Sedimentology and Palaeontology, 3, Tulsa, 44-56.

Hunter, R.E., 1977. Terminology of cross-stratified sedimentary layers and climbing ripple structures. *Journal of Sedimentary Petrology*, **47**, 697-706

Jordan, D.W., and Pryo, W.A., 1992, Hierarchical levels of heterogeneity in Mississippi River meander belt and application to reservoir systems: AAPG Bulletin, v.76, p. 1601-1624.

Kerr, D.R., and Jiric, L.A. 1990, Fluvial architechture and resrervoir compartmentalization in the Oligocene middle Frio Formation, south Texas: Gulf Coast Association of Geological Soceities Transactions, v.40, p.373-380.

Kocurek, G. and Havholm, K.G., 1993. Eolian Sequence Stratigraphy - A Conceptual Framework. In Weimer, P. and Possamentier, H.W. (eds.) *Siciliclastic Sequence Stratigraphy*. American Association of Petroleum Geologists Memoir, **58**, pp 393-409.

Kocurek, G., 1996. Desert aeolian systems. In: Reading, H.G. (ed.). Sedimentary Environments: Processes, Facies and Stratigraphy. Oxford, Blackwell Science, 3rd edition, 125-153.

Lindquist, S.J., 1988. Practical Characterization Of Eolian Reservoirs For Development - Nugget Sandstone, Utah Wyoming Thrust Belt. *Sedimentary Geology*, **56**, pp 315-339.

Mountney, N., Howell, J., 2000. Aeolian architecture, bedform climbing and preservation space in the Cretaceous Etjo Formation, NW Namibia. Sedimentology, 47, 825-849.

Miall, A.D., 1985, Architectural-elements analysis: a new method of facies analysis applied to fluvial deposits: Earth Science Review, v.22, p. 261-308.

Miall, A. D. & Tyler, N. (eds) 1991. The three dimensional facies architecture of terrigenous clastic sediments and its implications for hydrocarbon discovery and recovery. SEPM Concepts in Sedimentology and Palaeontology, 3, Tulsa.

Nardi Dias, K.D., Scherer, M.S., 2008. Cross-bedding set thickness and stratigraphic architecture of aeolian systems: An example from the Upper Permian Pirambóia Formation (Paraná Basin), southern Brazil. Journal of South American Earth Sciences, 25, 405-415.

Spalletti, L. A., Limarino, C. O. and Colombo Pinol, F., 2010. Internal anatomy of an erg sequence from the aeolian-fluvial system of the De La Cuesta Formation (Paganzo Basin, northwestern Argentina) Geologica Acta, Vol. 8, 4 3 1 - 4 4 7.

Thompson, D.B., 1969. Dome Shaped Aeolian Dunes in the Frodsham Member of the So-Called 'Keuper' Sandstone Formation [Scythian - ?Anisan: Triassic] at Frodsham, Cheshire (England). *Sedimentary Geology*, **3**, pp 263-289.

Thompson, D.B. (1970) The stratigraphy of the so-called Keuper Sandstone Formation (Scythian-(?) Anisian) in the Permo-Triassic Cheshire Basin. Quatern. J. Geol. Soc. London, 126, 151–181.

Taylor, B.J., Price, R.H. & Trotter, F.M. (1963). Geology of the country around Stockport and Knutsford (Sheet 98, England and Wales). Memoirs of the Geological Survey of Great Britain. London: 183pp.

Warringtogn.,, Audley-Charlmes.G, ., Elliottr, .E., Evansw, .B., Ivimey-Coohk., C ., Kentp, .G., Robinson, P.L., Shottonf,. W. &Taylorf,. M. (1980) A correlation of Triassic rocks in the British Isles. *Special Rep. geol. Soc.Land. No. IS*, 78 pp.

Wedd, G. B., Smith, B., Simmons, W. C., and Wary, D. A. 1923. The geology of Liverpool, Mem. Geol. Surv. Eng. and Wales.

Ye, L., D. Kerr, K. Yang, 1997, *Facies architecture of the Bluejacket Sandstone in the Eufaula Lake Area, Oklahoma: implication for reservoir characterization of the subsurface Bartleville Sandston,* In R. Scatzinger and J. Jordan, eds., Resevoir Characterization-Recent Advances, AAPG Memoir 71, 29-44.

TOXICITIES OF *DICHROSTACHYS CINEREA (*L.) AGAINST *ARTEMIA SALINA* AS SOURCE OF TREATMENT OF SWELLINGS AND TUMOURS

, G.abriel Femi. Ibikunle[1*], Simeon Okwute[2] and Emmanuel Ogbadoyi[3].

[1]Department of Chemistry, Federal University Technology Minna Nigeria.

[2]Department of Chemistry's, University of Abuja, Nigeria. Department of Biochemistry Federal University of Technology, Minna, Nigeria.

febikunle@yahoo.com

* Corresponding author

Abstract

The therapeutic use of natural products to cure and maintain good health has persisted since prehistoric time. Dichrostachys cinerea (L.) Wight & Arn belongs to family of Mimosaceae. It is commonly known as "Vidathalai' in Tamil, Kara-yoruba, Ekannanko-Nupe and Cow-thorn. Earlier folklore the whole plant has been used for antidiarrheal activity in Indian traditional medicine while in Nigeria the root is for anti-cancer. The present study was carried out to ascertain the ethno medicinal use of the plant for the treatment of cancer using Artemia salina toxicities as a bio guide. About 1000 gram of the powdered root bark of the plant material was cold extracted five times for six days with methanol (1L x 6 days). The extract was concentrated, coded DCo and yielded 7.7%. The crude extracts DCo reconstituted with 100ml of distilled water and successively partitioned into n-hexane, Chloroform, Ethyl acetate and aqueous fractions and coded as DC1, DC2, DC3 and DC4 respectively and then bio assayed against Artemia salina (shrimp nauplii). The bioassay revealed that the DCo had LD_{50} and LD_{90} of 37.90±6.26 and 142.53±21.43 µg/ml respectively at 24h. The partition fraction DC3 with the LD_{50} and LD_{90} of 20.00 and 60.55µg/ml at 24 hours respectively was more toxic than the crude indicating that the active constituent reside in Ethyl acetate fraction. The activities in the DC2 were slightly lower than DC3 which had LD_{50} and LD_{90} of 50.85 and 256.85µg/ml respectively. The DC4 had no activities while DC1 had no weight for bio testing. Conclusively it could be deduce that the ethno medicinal use of the root is justified and the improvement in toxicity effect is a finger point to the fact that the crude effect was not synergy but there might be particular compound/s responsible for the activities.

Keywords: *Dichrostachys cinerea, ,Artemia salina*, antidiarrheal, anti-cancer

1. Introduction

Cancer' is an overall term applied to malignant diseases characterized by rapid and uncontrolled abnormal cells formation which may mass together to form a growth or proliferate throughout the body, and it may progress until it causes death. The price of drugs for cancer treatment has been part of the debate over health care cost for several years. The cost is estimated as $100,000.00 per year. For example Gleevec use for treatment of chronic myeloids leukemia came to market 2001 at a cost of $30,000.00 per year in USA and has since gone up three times the price. Even though Gleevec has faced competition from five other drugs, the new drugs are even more expensive, Iclusing cost between $105,000.00 to $125,000.00(Danzon and Taylor 2009)

Dichrostachys cinerea (L.) Wight & Arn belongs to Mimosaceae,is commonly known as "Vidathalai' in Tamil, Kara-yoruba, Ekannanko-Nupe and Cow-thorn. Earlier folklore the whole plant has been used for antidiarrhoeal activity in Indian traditional medicine while in Nigeria the root is for anti-cancer. The ethanolic extract of leaf, bark and root of the plant showed significant antidiarrhoeal activity by both the tested models. (Jayakumari *et al*., 2011, Mann *et al*. (2003),)

Compounds isolated (tannins) from *D. cinerea* and assayed against *Staphylococcus aureus, Shigella boydii, Shigella flexneri, Escherichia coli* and *Pseudomonas aeruginosa* using the agar diffusion method. Tannins exhibited antibacterial activities against all the tested microorganisms (Banso and Adeyemo, 2007).

Lethality of substances to brine shrimp nauplii has been linked to the probable ability of such compounds/substances to kill cancer cells (antitumor activity), possibly pesticide and antibacterial activity. Thus in-vivo lethality in this simple zoologic organism can be used as a convenient monitor for screening and fractionation in the discovering and monitoring of bioactive natural products. BST been used as preliminary in vitro antitumor assay as a safe, rapid, practical, and economic method for the determination of the bioactive synthetic compounds (Amara,*et al*., 2008) as well as plant products (Meyer *et al*., 1982; McLaughlin *et al*., 1991; Ali *et al*., 2013). There is positive correlation between brine shrimp toxicity (BST) and human carcinoma cytotoxicity. It was observed that ED50 values for cytotoxicity are generally about one-tenth the LC50 values found in the brine shrimp simple test (MacLaughin *et al*., 1991, McLaughlin and Roger, 1998). The brine shrimp assay has been established as a safe, practical, and economic method for the determination of the bioactivity of synthetic compounds as well as plant products (Meyer *et al*., 1982; McLaughlin *et al*., 1991; Ali *et al*., 2013). The significant correlation between the brine shrimp assay and *in vitro* growth inhibition of human solid tumor cell lines demonstrated by the National Cancer Institute (NCI, USA) is very significant. The aim and objectives of this research is to determine the toxicities of this plant extract to BST as preliminary confirmation of the plant for managements of cancer

2. Methodology

2.1 Materials

The roots were collected from Minna, Niger State of Nigeria in December, 2013. It was authenticated by Dr. Abdullahi Mann. It was allowed to dry, powdered and stored until required for use. All solvents and chemicals used in this work were of standard grade. Thin layer chromatography (TLC) was carried out using pre-coated siloica gel 60 F254 on aluminium sheets produced by Merck KGA 64271 Damstadt Germany. The TLC were viewed under UV Lamp (254+366) and using iodine vapour. Samples of brine shrimps (*Artemia salina)* were obtained from USA.

2.2 EXPERIMENTAL

2.2.1 List of Apparatus: Materials and Solvents

Equipment used was rotary evaporator, a Vacuum pump, incubator, microscope, UV lamp (254 and 366 nm), Mettler Analytical balance, Micropipette, autoclave, Petri dish and spray gun. In addition, a Vacuum Liquid Chromatographic (VLC) apparatus made up of a Buchner funnel attached to a vacuum pump and Swab stick were used. Glass wares used were chromatographic tanks, set of vails, measuring cylinders, graduated pipettes (µL), pasteur pipette. Others materials were Silica gel (60 - 120 mesh) for column, factory precoated Silica gel thin layer chromatographic plates GF_{254} (0.25 mm) and PTLC spreader for preparative thin layer chromatographic and preparative thin layer chromatographic plates 20cm x 20cm . Solvents used were Methanol, Petroleum ether, Ethylacetate, Chloroform, n-butanol and Dimethyl sulphoxide (DMSO) and they were all of analytical grade.

*2.2.2. Methanolic extract and their fractions***.**

About **1000g, gram each** the powdered plant root material was cold extracted five times for six days with methanol (1L x 6 days). The extracts were bulked and concentrated *in-vacuo*. The methanolic extract was coded as , DC_o, yielded 7.11, percent (Tables3).

2.2.3 Partitioning Process

The crude extracts were dissolved in the 100ml of distilled water and successively partitioned using one liter separating funnel into n-hexane , Chloroform, Ethyl acetate and aqueous fractions. The partition fractions

were coded as, DC1, DC2, DC3 and DC4, for, *Dischrostachys cinnerea*, respectively. Their weights were recorded in the table1.

2.3. Artemia salina cyst bioassay

2.3.1 Material for the Bioassay

The following material used for the bioassay**;** *Artemia salina* cyst (egg), 1000ml conical flask, Sea water, aerator, capillary tubes, 60 watt bulbs and 48 hours supplied source of electicity.

2.3.2. Preparation of shrimp nauplii

For the cytotoxicity bioassay, *Artemia salina* cyst (egg) started by batch hatching with sea water obtained from institute of oceanography Lagos. The 2.0g egg were placed in 800ml sea water (salt solution 38g/l NaCl) in 1L conical flask under 60 watt bulbs with aerator and aeration stone connected with rubber capillary. The aeration and the illumination were done for complete 48h for the hatching of the *Artemia salina* cyst (egg) into shrimp nauplii. The hatched were left under aeration and the illumination for another 48hours before the cytotoxicity bioassay.

2.3.3. Preparation of sample for Cytotoxicity bioassay of shrimp nauplii

20mg of extract was dissolved in 2ml of the solvent that is sea water to give 1000 µg/ml, take 0.2ml from1000 to 1,8ml solvent to give 100ppm and 0.2ml from 100ppm to 1.8ml solvent to give 10ppm 0.2ml from 10ppm to 1.8ml solvent to give 0.10ppm)) (positive controls if was carried out.

3. Results and Discussion

The result of the crude weight and successive partitioning fractions were presented in table 1 and 2. Also, the results of the Preliminary biological-Screenings of Crude methanolic (DC_o) extra from the plants and the partition fractions DC1, DC2, DC3 and DC4 against *A. salina* were presented on the Tables 3.

Table 1: The table showing weight of five plants crude methanolic extraction and their percentages.

Name of samples	DC
The weight of sample extracted (g)	**1000.00**
Initial volume of Methanol added ml	**1500**
Successive addition of methanol in ml	**8x1000**
The weight of Methanol crude Extract (g)	**71.1**
% of the crude extract	**7.11**
Code for the crude extract	**DCo**

Key Dichrostachys cinerea = DC , *Dichrostachys cinerea* =crude DC_0

Table 2: The of Partition fraction of DCo.

The weight of crude partitioned (g)	71.1	n-hexane	$CHCl_3$	EtOAc	Aq
Volume of water added (ml)	100				
volume of n-hexane added 3x100 ml		0.2970g			
volume of chloroform added 7x100ml			47.72		
volume of Ethyl acetate added 12x100ml				0.78	
The weight of each fractions (g)		0.2970	47.72	0.78	21.10
% of the partition fractions		0.417	67.12	1.41.	29.68
Code of fractions		DC1	DC2	DC3	DC4

Key n-hexane –DC1, Chloroform = DC_2, ethyl acetate = DC_3 Aqueous = DC_4

Table 3: The result of bioassay of partition fractions of DC into n-hexane, chloroform , Ethyl acetate and aqueous fractions

Name of fractions	LD50 µg/ml	LD90 µg/ml
D0	37.90^{bc} ± 6.26	142.53^{abc} ± 21.43
D1	Non toxic	Non toxic
DC 2	50.85±6.48	1214.48±±1712.
DC 3	20.02±1.49	60.55±6.20
DC 4	1.09E5±1.1E5	2.71E7±4.5E7

.

The crude methanolic extract (DC_o) of this plant root bark extract had 7.11% Table1and it had LD_{50} and LD_{90} of 37.90±6.26 and 142.53±21.54 respectively at 24h Table 3. When crude extracts under investigation using BST assay showed preliminary screening result of LC50 ≤ 50 µg/ml was considered insignificant presence of antitumor compounds as described by Hostettmann *et al.*, 1995, Ferreira et al., 2007 and Meyer et al., 1982 was further investigated. At the end of 24 hours BST assay, showed the LD_{50} of the crude extract (DC_o) was ≤50µg/ml. The partitioning of the crude (DC_o) into n-hexane (DC_1), Chloroform (DC_2), ethyl acetate (DC_3) and aqueous (DC_4) revealed that $DC_1$was not active and the activities were in DC_3 and DC_2. The activities were in order of $DC_3 \geq DC_2$ .There was an improvement in the toxicity in DC_3 but reduction in activities of DC_2 in comparison to the crude. The reason might be due to spill effect of the active constituent from the DC_3. The BST revealed that toxicity reside in Ethyl acetate fraction (DC_3) with the LD_{50} and LD_{90}

of 20.00 and 60.55µg/ml at 24 hours respectively. The activity in the DC2 at 24h LD_{50} and LD_{90} of 50.85 and 256.85 µg/ml respectively was lower than crude (DC_0 37.90±6.26 and 142.53±21.54). The DC4 and DC1 lost their activities. The result revealed that the major active constituents were fairly polar. Furthermore, the result of BST has justified the root might has anti- cancer constituent and the anti-cancer in it got increased in concentration as the purification continued (table 3). This is possibly revealing that the activities were not based on synergy. It is noteworthy that for the development of the drug in addition to its toxicity, the % weight of the crude extract (7.11) and of the active partition fraction (1.41%) table 1 & 2. It was observed that the weight of the active fraction was very small in comparison to the actual weight extracted. Therefore if the fraction passes other pharmacological test e.g. cell line test, the fraction could be compounded as drug in line with ethno medicinal practice.

4. Conclusion

The plant crude extract and the partition fractions proved toxic to brine shrimp nauplii and the BST increased with purification justifying ethno medicinal use of the root for the management of inflammation and cancer.

References

Ali Mirzaei 1, Nooshin Mirzaei1, Mehdi Ghavamizadeh (2013). Antioxidant Activity and Cytotoxicity of *Dorema aucheri* by *Artemia urmiana:* a Brine Shrimp Lethality Test**.** *Life Science Journal* **10**(12s

Amara, A. A., El-Masry, M. H., and Bogdady, H. H. (2008). Plant crude extracts could be the solution: Extracts showing i*n vivo* antitumorigenic Activity. *Pakistan Journal of Pharmaceutica Science.* **21(2):**159-171.

Banso, A.* and Adeyemo, S.O 2007Evaluation of antibacterial properties of tannins isolated from Dichrostachys cinerea African Journal of Biotechnology Vol. 6 (15), pp. 1785-1787,

Ferreira ICFR, Baptista M, Vilas-boas, Barros L(2007;). Free radical scavenging capacity and reducing power of wild edible mushrooms from northeast Portugal; Individual cap and stipe activity. Food Chem. 100:1511-16.

Hostettmann, K., Marston, A. and Hostettmann, M. (2010). Preparatitive Chromatography Techniques; Applications in Natural Product Isolation 2nd edition page 6.printed by Springer Berlin.

Hostettmann, K., Marston, A. and Woffender, J. L. (1995). Strategy in the search for new biologically active plant constituents in photochemistry of plants used in traditional medicine (eds. Hostettmann,K ,marston,A maillard M and hamburger). Pp 17-45

Mclaughlin Jerry L., Chang CJ and Smith DL. (1991). Bench Top Bioassays for the discovery of bioactive Natural products: An update (Atta Ur-Rahman Ed), Studies in Natural product Chemistry. Elsevier Science publisher By B.V Amsterdam. 9:388-409. .

Mclaughlin, Jerry L., Rogers, L., Lingling and Anderson, E. Jone (1998). The use of biological assays to evaluate botanicals. *Drug information Journal.* **32:**513-524.

Meyer, B. N., Ferrigni, N. R., Putnam, J. E., Jacobsen, L. B. and Nichols, D. E. (1982). Brine shrimp: A convenient general bioassay for active plant constituents. Journal of Planta Medica. **45:**3134-143.

Jayakumari, S., srinivasa rao, g. h., Anbu, j. and ravichandiran, v. (2011) Antidiarrhoeal activity of *dichrostachys cinerea* (l.) Wight & arn *International Journal of Pharmacy and Pharmaceutical Sciences*. **3(3):**61-63

Patricia, M. Danzon and Erin Taylor (2013). Drug Pricing and Value in Oncology. *Drug information journal*. **47:** 226 -234.

Mann Abdullahi, Muhammad Gbate and Abdulkadir NdaUmar (2003) . Medicinal and Economic Plants Of Nupe Land. Jube- Evans Book & Publications.

APPLICATION OF ENVIRONMENTAL ISOTOPES IN ELUCIDATING GROUNDWATER RECHARGE IN ABUJA, NORTH-CENTRAL NIGERIA

[1]**Dan-Hassan, M.A.,** [2]**Amadi, A.N.** [3]**Olasehinde, P.I.,** [2]**Okoye, N.O. and** [2]**Ameh, I.M.**

[1]Rural Water Supply & Sanitation Department, FCT Water Board, Abuja, Nigeria

[2]Department of Geology, Federal University of Technology, Minna, Nigeria

[3]Department of Geophysics, University of Ilorin, Ilorin, Nigeria

*Corresponding Author's emails: geoama76@gmail.com, or an.amadi@futminna.edu.ng

Phone Number: +234-8037729977

ABSTRACT

The study area covers an area of about 5,000Km^2 in the central part of the Federal Capital Territory, Abuja, Nigeria, stretching along a NE–SW axis, cutting across geological, geomorphological and geopolitical boundaries of the territory. The aquifer systems in the study area are formed by weathered and fractured basement except in the southwestern part, which is formed by the sandstones of the Bida Basin. Eleven groundwater and one rain water samples were collected and analyzed for stable isotopes of deuterium (^{2}H) and Oxygen-18 (^{18}O) and radioactive isotope of tritium (^{3}H), according to standard methods. Results of isotope analyses revealed that the measured δ ^{2}H values of the groundwater samples range from -17.1 to -14.3‰ while that of δ ^{18}O range from -3.53 to -2.59‰. The δ ^{2}H and δ ^{18}O diagram shows that the water types originated from precipitation as the samples plot around the Global Meteoric Water Line (GMWL) with a deuterium excess in the range of 10 $\pm$ 2.7. This indicates similar recharge conditions and an isotopic enrichment by evaporation. Tritium (^{3}H) concentration for the groundwater samples varies from 2.3 to 5.0 TU with a mean of 3.56TU while that of the only rainwater sample was 4.85 TU. Applying qualitative age categorization, the range of tritium values depicts active recharge and recent groundwater.

Key words*: Environmental Isotopes, Groundwater, Recharge, Abuja, Nigeria*

1. Introduction

The availability of clean fresh water is one of the great issues facing mankind today, in some ways the greatest, because problems associated with it affect the lives of many millions of people (Geyh, 2000). Since in many areas of the world relevant long-term data on water resources are missing, the traditional and isotope methods in combination with mathematical modelling often answer pressing questions about groundwater origin, chemical reactions, fluxes, ages and mixing processes occurring in reservoirs, naturally and caused by man. Only on this basis can relevant strategies for exploration, exploitation and protection of subsurface waters be developed (Seiler, 2000).

Water isotope hydrology addresses the application of isotopes that form water molecules. These are the oxygen (^{16}O, ^{17}O, ^{18}O) and hydrogen (^{1}H, ^{2}H, ^{3}H) isotopes. These isotopes (unlike other tracers of "water" such as Cl^-, which are still widely used) are ideal tracers of water sources and movement because they are constituents of the water molecule (Akiti, 2000).

The changes in chemical composition of meteoric water recharging the aquifer will depend on factors such as soil-water interaction, residence time, congruent and incongruent dissolution of mineral assemblages, sea water intrusions and anthropogenic impacts. These factors would give rise to different water chemistry and hence different aquifer characteristics (Dapaah-Siakwan and Gyau-Boakye, 2000; Helstrup *et al*., 2007; Edmunds and Shand, 2008).

In groundwater catchments where barrier boundaries and inputs are well defined, interpretation of environmental isotopes record of precipitation, surface water and groundwater, coupled with available information on hydrochemical characteristics of groundwater will provide a detail picture of the groundwater system (Kendal and McDonnell, 1988).

Furthermore, hydrogeochemical and isotopic methods have been successful as economical ways to study local and regional groundwater systems, for example to determine groundwater interactions in the arid and semi arid environments (Schurch and Vuataz, 2000); to identify sources of groundwater (Abd El Samie and Sadek, 2001; Matter *et al*., 2006; Plummer *et al*., 2004; Stimson *et al*., 2001); to evaluate the quantity of groundwater recharge (Abu-Jaber and Wafa, 1996; Mc Conville, 1999,; Negrel *et al*., 2003; Wood and Sanford, 1995); and to research the interaction of different waters such as deep and shallow groundwater (Dassi *et al*., 2005), surface and groundwater (Negrel *et al*., 2003; Amadi *et al.,* 2014), and the replenishment of groundwater (Kendall and Mc Donnell, 1998; Zhang *et al*., 2005; Al-Charideh and Katta, 2016).

Hydrological and hydrogeological information as well as groundwater monitoring data are available for some parts of Nigeria (Alao and Ige, 2003; Adelana and Olasehinde, 2005; Adelana *et al*., 2008; Amadi *et al*., 2015). These have formed the main input to clarify the hydrogeological systems in most regions of the country. Most of the isotope studies in Nigeria have been related to the evaluation of recharge mechanism especially in the semi-arid areas of northern Nigeria (Geyh and Wirth, 1980; Oteze, 1989; Onugba *et al*., 1989, Mbonu and Travi, 1994,; Tijani *et al*., 1996; Goni and Edmunds, 2001; Adelena *et al*., 2002; Tijani, 2008).

The increasing usage of water for drinking and industrial purposes has geared up the interest of hydrogeological investigations in natural recharge and movement of fossil groundwater in the last four decades (Adelana and Olasehinde, 2004). In one of the pioneering isotopic research in northwestern Nigeria, Geyh and Wirth (1980) conducted groundwater dating of the confined aquifer of the Gwandu formation with the aim of determining the groundwater velocity to estimate the rate of recharge and confirm the direction of flow.

In the Federal Capital Territory, Abuja, hydrogeochemical methods have been used to determine groundwater quality. There is no comprehensive monitoring network of the groundwater systems to evaluate its past, current and future status for sustainable groundwater management and this is what the present study attempt to address through isotope technique. The objectives of the study are to determine the recharge sources, estimate age and evaluate isotopic signatures of groundwater in the central portion of the Federal Capital Territory, Abuja.

2. The Study Area

2.1 Physical Setting

The territory was created in 1978, following the decision to relocate the nation's capital away from Lagos in the southern coastal area to a more central location within Nigeria, devoid of domination by any of the major ethnic groups (Figure 1). The factors considered for the location of the "new" capital were justified by the Federal Government in Decree No. 6 of 1976 (FCT Handbook, 1994).

The area of study is located in the central part of the Federal Capital Territory, Abuja, Nigeria (Figure 2), stretching from the northeast to the southwest of the territory, along a diagonal axis. The Federal Capital Territory lies approximately between longitudes 6^0 46' and 7^0 37'E and latitudes 8^0 21' and 9^0 18' N. The study area covers an area of about 5,000 km^2 of the 8000 km^2 of the territory. The Federal Capital Territory is bounded by Nasarawa State to the east, Kaduna State to the north, Niger State to the west and Kogi State to the south (Figures 1.1 and 1.2).

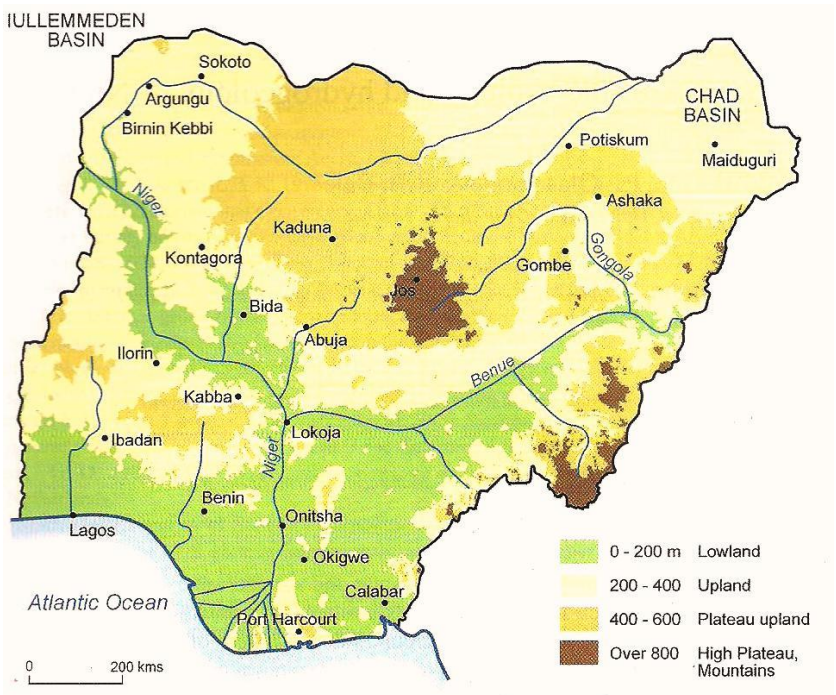

Figure 1: Map of Nigeria showing location of Abuja

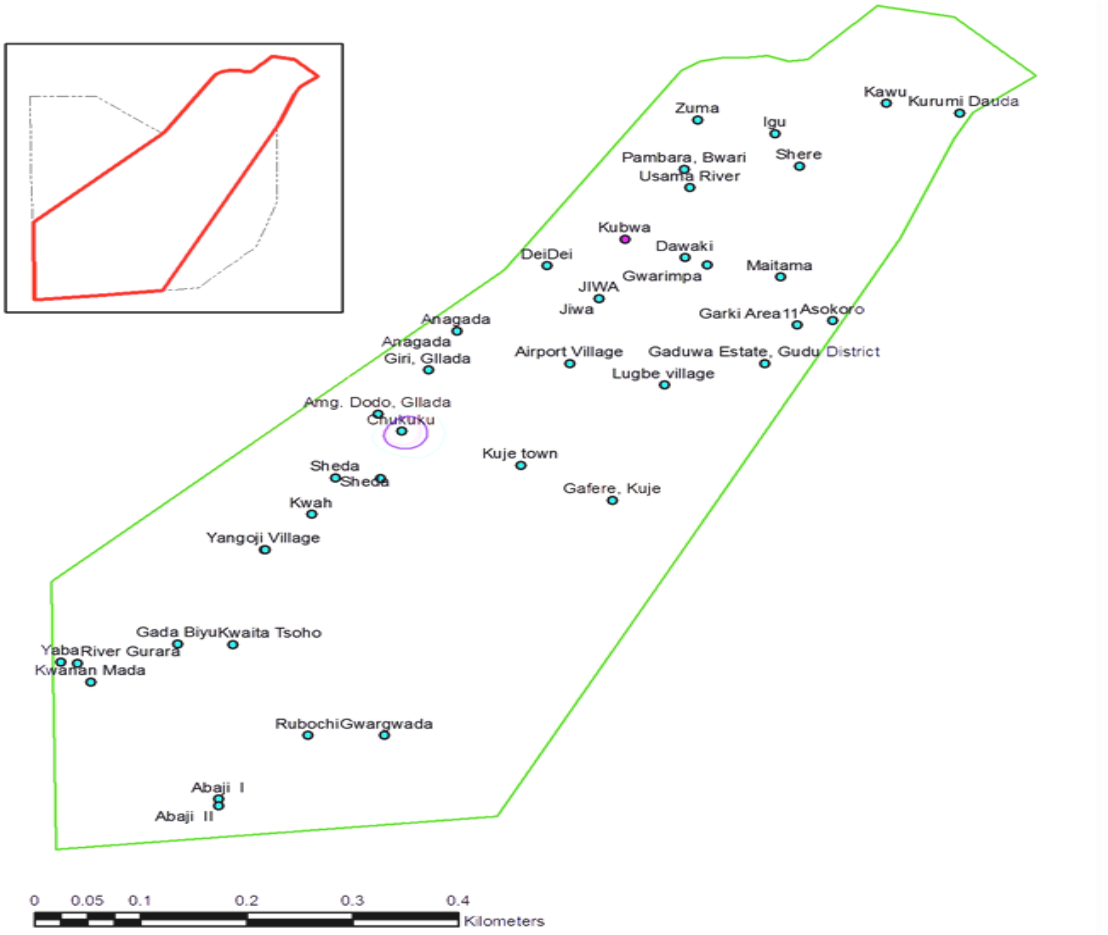

Figure 2: Map of the study area within the FCT showing sampling locations

The topography of the FCT is varied with the lowest elevations in the Territory found in the extreme south-west at the floodplains of the River Gurara (76 m above sea level). From here, the land rises irregularly eastwards, northwards and northwestwards. The highest part of the territory is in the northeast where there are many peaks above 760 metres above sea level.

Hills occur as clusters and long ranges all over the Territory. The most prominent of these include the Gawu range in the northwest, the Bwari-Aso range in the northeast, Idon Kasa to the northwest of Kuje, Wuna range in the north of Gwagwalada and the Wasa-Sukuku range running across the centre of the Territory from Wasa in the east to Kwali in the west (ABU, 1978).

The rivers take their origin from the hills in the northeast and flow southwesterly to join the south flowing River Gurara. The two major rivers are the River Gurara and River Usuma, which join at Nyimbo village to form a tributary of River Niger in the south.

2.2 Climate, Rainfall and Vegetation

The FCT records its highest temperature during the dry season months (November - March), which are generally cloudless. Extreme maximum temperatures occur everywhere in the vicinity of the Territory in these months and vary from 37^0C in the southwest to about 30^0C in the northeast. During the rainy season, the maximum temperature drops to about 27^0C due to the dense cloud cover. Human sensibility to these temperatures is greatly affected by the relative humidity (Yaya, 2006).

The Federal Capital Territory exemplified its character as between the zone of double rainfall maximum to the south and that of a single maximum to the north (Yaya, 2006). The rainy season starts from March on the southern boundary of the Territory and around April in the northern limits. The rains taper off around October in the north and November in the south. Thus, the duration of the rainy season is between 190 days in the north and 240 days in the southern parts of the Territory. The annual total rainfall is in the range of 1100 mm to 1600 mm (CIWAT, 2010).

Two major types of vegetation, namely, forest and savanna, are found within the FCT. The forest is predominantly of woody plants, from which grasses are virtually absent. Two types of forest have been identified on the basis of both topographical locations and differences in characteristics including physiognomy and floristic composition. They are rain forest and riparian vegetation complex (FCT Handbook, 1994).

2.3 Synopsis of the Geology

The description of the geology of the study area has variously been attempted in the works of Truswell and Cope (1963); Oyawoye (1972); Mc Curry (1970, 1976); Turner (1971); ABU (1978); Alagbe (1979) and Adelana *et al*. (2008). The study area is underlain by Precambrian rocks of the Nigerian Basement Complex, which cover about 85% of the land surface and sedimentary rocks, which cover about 15% of the territory in the southwestern part (Figure 3).

The major lithologic units found are:

(a) The Older granites
(b) The Metasediments (schist, phyllite and quartzite)
(c) The Migmatite-Gneiss Complex
(d) The Nupe Sandstones of the Bida Basin

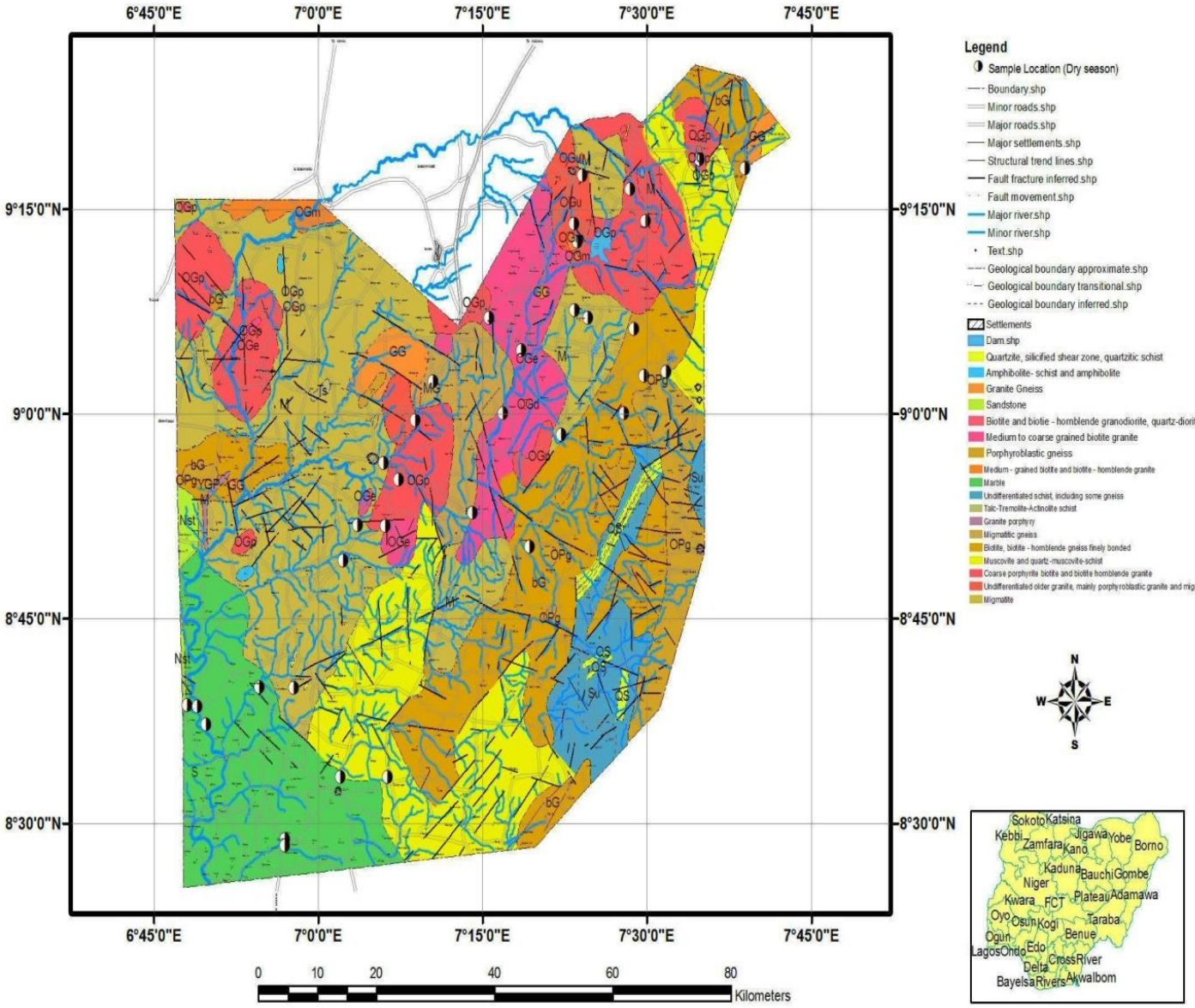

Figure 3: Geological map of FCT, Abuja, showing sample locations (Geological map modified after NGSA, 2004)

3. Materials and Methods

Eleven groundwater samples were collected at the peak of dry season (April, 2009) while one rainwater sample was collected in October, 2009, for isotope analyses using standard methods. The analyses were conducted at Activation Laboratories, Canada. For the determination of oxygen-18 and deuterium, stable isotope ratio mass spectrometer, Finnigan MAT 251 was used. Oxygen isotopes ($\delta^{18}O$) are determined by conventional CO_2 - H_2O equilibration method (Epstein and Mayeda, 1953). CO_2 is added to a vessel containing a surplus of the water sample. The vessel is sealed and emerges to facilitate CO_2 - H_2O equilibration. Equilibration time is 48

hours, long enough to equilibrate. The equilibrated sample is extracted on a vacuum line and cryogenically purified. Isotopic data are reported in the standard deviation from V-SMOW (Vienna Standard Mean Ocean Water). The CO_2 - H_2O equilibration factor is 1.0412. External reproducibility is $\pm$ 0.014‰.

Deuterium isotopes (δ^2H) are determined on 3 µl quantities of water using the uranium reduction method (Actlabs, 2010). Water samples are aliquoted with a microsyringe and ejected into a finger on a gas extraction line. The finger is heated to ensure evaporation of all the water. The water is reduced over hot uranium metal (750ºC) and the resulting H gas collected on charcoal at -19.6 ºC. Data are corrected for $^3H^+$ production in the ion source and reported in the standard delta notation as per mil deviation from V-SMOW. External reproducibility is $\pm$2.3‰ (1σ) based on repeat analysis of Cambrian Formation Water Standard (CFW) (Actlabs, 2010).

Radioactive Isotope (Tritium) Analysis

Tritium measurements (counts per minute {cpm}) are converted directly into absolute concentrations. A Canberra – Packard Pico-fluor LLT (low level tritium) is used, which has a high carrying capacity for water with high efficiency and low background characteristics. The laboratory standard is NBS-4361 tritium reference material diluted with background water which is then calibrated to NB-4926C. The background water is from a well with radiocarbon activity older than 3500 years and a conductivity of less than 300 µmho (Actlabs, 2010).

4. Results and Discussion

For the present study, a total of eleven ground water samples and one rain water sample were collected and analyzed for stable (^{18}O and ^2H) and radioactive (^3H) isotopes. The results of the stable isotopic composition, in δ - notation, are presented in Table 1. Values are reported in per mill (‰) with reference to V – SMOW (Vienna Standard Mean Ocean Water). External reproducibility is $\pm$ 0.14‰ for $\delta^{18}O$ and $\pm$ 2.3‰ for δ^2H.

Table 1: Results of physical properties and environmental isotope measurements in the study area

S/N	Locality	Long.	Lat.	Elev. (m)	Date	Depth (m)	pH	T ºC	D.O. mg/l	E.C. µS/m	TDS g/l	δ^2H	$\delta^{18}O$	d-ex δ	^3H (TU)

1	Zuma	07^0 24.09’	09^0 17.48’	590	10.04.09	24.8	6.1	26.9	4.6	110	70	-15.3	-3.36	12.25	2.3
3	Kawu	07^0 34.77’	09^0 18.66’	736	10.04.09	42.5	6.0	27.7	5.4	90	50	-15.5	-3.29	11.47	3.3
6	Pambara	07^0 23.33’	09^0 13.95’	520	10.04.09	41.2	6.4	28.6	7.1	31	200	-14.3	-3.24	12.26	4.0
9	Anagada	07^0 10.45’	09^0 02.38’	319	10.04.09	24.7	6.7	29.6	6.71	240	140	-16.9	-3.53	12.04	4.2
15	Gaduwa estate	07^0 27.91’	09^0 00.05’	397	12.04.09	17	5.5	28.2	6.2	160	100	-15.0	-3.15	10.83	3.1
18	Gafere, kuje	07^0 19.29’	08^0 50.77’	340	12.04.09	39.9	6.3	29.7	6.7	160	90	-15.0	-3.25	11.65	3.7
20	Yangoji	06^0 59.60’	08^0 46.73’	176	12.04 09	30.5	6.7	30.5	4.0	300	190	-16.5	-2.91	7.36	2.5
26	Gada biyu	06^0 54.63’	08^0 39.99’	82	13.04.09	8.5	5.1	29.5	5.3	320	200	-17.4	-3.26	9.33	3.6
27	Kwanan mada	06^0 49.75’	08^0 37.25’	86	13.04.09	50.5	5.5	30.5	5.9	30	20	-15.0	-3.13	10.66	3.5
30	Abaji 1	06^0 56.97’	08^0 28.87’	150	13.04.09	60	5.1	28.6	6.5	10	10	-17.4	-3.37	10.23	5.0

34	Maitama	07^0 28.79’	09^0 06.23’	533	15.04.09	42.5	6.7	28.3	6.0	100	60	-16.4	-2.59	4.83	4.0
R18	RainwaterGaduwa	07^0 27.91’	09^0 00.05’	397	18.10.09	-	6.5	22.7	8.5	10	10	12.3	1.23	2.21	4.85

Long.= Longitude, Lat.= Latitude, T= Temperature, E.C.= Electrical conductivity, TDS= Total dissolved solids, ^2H= deuterium, ^{18}O= Oxygen-18, d-ex= Deuterium excess, ^3H= Tritium, TU= Tritium Unit, S/N= Sample Number, all groundwater samples from boreholes except Gada biyu (hand-dug well).

Limited number of sampling for isotope analysis was done due to accessibility and cost. Groundwater samples were collected in April, 2009 at the peak of the dry season while rainwater sample was collected in October, 2009. Data interpreted were compared with the isotope measurements from precipitation in Kano for the period 1961-1973 (Onugba *et al*., 1990). The relationship between $\delta\,^{18}O$ and $\delta\,^2H$ is plotted (Figure 4) alongside with the global meteoric water line (GMWL). Such a plot usually reveals indication about recharge source(s) of groundwater system as well as possible evaporation effect (Tijani and Abimbola, 2003; Al-Charideh and Kattaa, 2016). The measured $\delta\,^2H$ values of the analysed groundwater samples range from – 17.4 to – 14.3‰ with an average value of –15.88 ‰ while that of $\delta\,^{18}O$ range from – 3.53 to – 2.59 ‰ with an average of – 3.18 ‰ (Table 1). It can be observed that the stable isotope composition of groundwater in the study area are depleted in both oxygen – 18 and deuterium values with respect to the standard while $\delta\,^{18}O$ and $\delta\,^2H$ for rainwater are 1.23 and 12.3 ‰, respectively, compared to that of seawater ($\delta\,^2H = 0$ ‰ and $\delta\,^{18}O = 0$ ‰) and also plotted close to the GMWL as defined by the equation:

$$\delta\,^2H = 8 \times \delta\,^{18}O + 10 \qquad \text{----------(1)}$$

The values of deuterium excess (d-excess), calculated from the relation:

$$d = \delta\,^2H - 8\,\delta\,^{18}O \qquad \text{---------- (2)}$$

are generally in the range of 10 ± 2.7‰, i.e. close to 10 (Table 1). Exception to this, however, is the sample from Maitama with relatively lower deuterium excess value of 4.83‰ compared to other samples which may be attributed to the local geology of the area as well as evaporation effect. The deuterium excess reflects the conditions that lead to kinetic isotope fractionation between water and vapour during primary evaporation in

the oceans (Dansgaard, 1964). This number also shows the extent of deviation of a given sample from the meteoric water line (Gibrilla *et al*., 2010). The low deuterium excess observed in this location is probably related to enrichment due to kinetic evaporation as well as the influence of rock-water interaction. The influence of other physical factors such as density – duration of rainfall (amount effect) and latitude – altitude effects could also be significant.

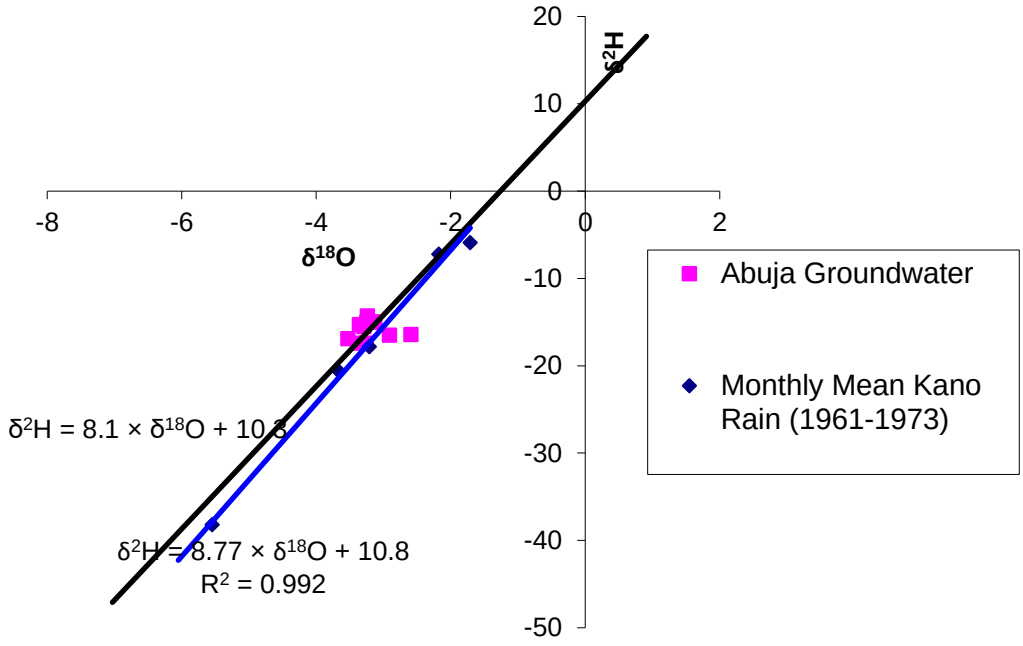

Figure 4: A plot of δ ^{18}O vs δ ^{2}H for Abuja groundwater samples (present study) and monthly mean of precipitation for kano (Onugba *et al*., 1990).

4.1 Stable Isotopes in Precipitation and Groundwater

Isotopes in precipitation have been measured monthly for samples collected at Kano Airport (N 12.05^0, E 8.53^0, altitude 476 m a.s.l.) by the International Atomic Energy Agency (IAEA) from 1961 to 1973 (Onugba *et al*., 1990). Kano has one season rainfall (May – September: >50 mm/month) with temperature range from 21.3 to 30.9^{0}C); and relatively dry period (November – April: <0.1 – 11 mm/month).

Figure 5 shows the plot of δ^2H and δ^{18}O values for groundwater and rain water samples in the study area with the long-term mean of monthly precipitation at Kano, north-central Nigeria. The plot of δ^2H and δ^{18}O for

meteoric water in Kano is the closest isotopic measurement in Nigeria that can be compared to Abuja groundwater as shown in the Figure 5. The isotopic composition of the studied groundwater is low in δ^2H and $\delta^{18}O$. However, these depleted values plot around the Global Meteoric Water Line (GMWL), which suggest that the groundwater in the area is recharged from meteoric source. In Table 2, the data for annual weighted mean values for δ^2H and $\delta^{18}O$, the corresponding annual precipitation and mean temperature for the period 1961 – 1973 at Kano are presented. The long-term (1967 – 1973) weighted mean values of $\delta^{18}O$ and δ^2H for rainfall are – 3.3 and – 17.9%o, respectively (Onugba *et al*., 1990). The weighted monthly mean of $\delta^{18}O$ and δ^2H are – 3.19% and - 15.9% respectively. The local meteoric water line (LMWL) obtained using the average monthly precipitation measured at Kano Airport is not significantly different from the Global Meteoric Water line ($\delta^2H = 8.1 \times \delta^{18}O + 10.3$) as earlier shown in Figure 4. The findings further confirmed that the groundwater in the area is of meteoric source.

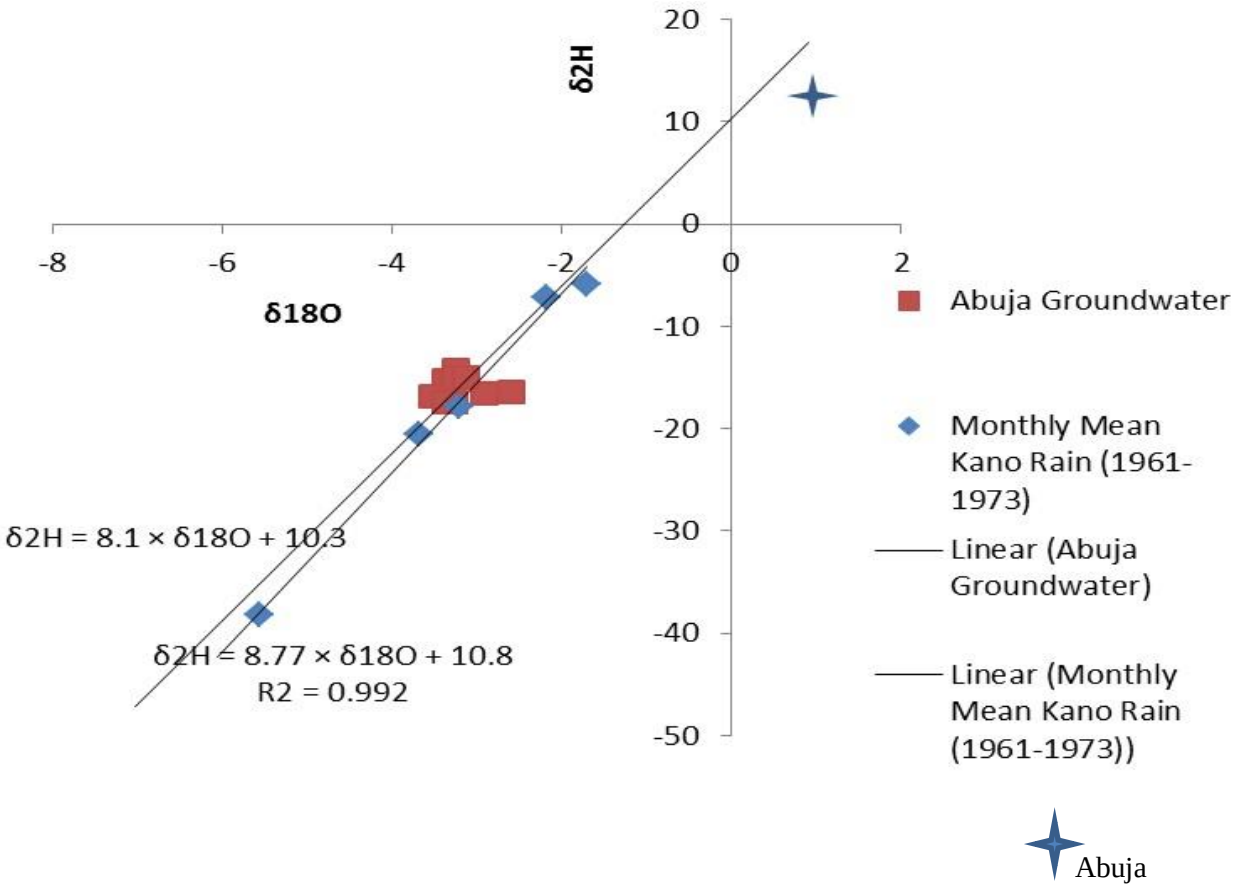

Figure 5: Plot of Oxygen-18 vs Deuterium for the groundwater and rainwater samples (note the isotopically enriched rainwater sample

Table 2: Annual weighted mean values for δ^2H and $\delta^{18}O$, the corresponding annual precipitation (P) and mean temperature (T) for the period 1961 – 1973 at Kano, Nigeria

Year	$\delta^{18}O$ (‰)	% of P	δ^2H (‰)	% of P	P (mm)	T (°C)
1961	-5.99	100.0	-37.58	100.0	770	25.5
1962	-3.40	91.0	-25.62	91.0	1140	26.2
1963	-5.53	98.9	-41.17	98.9	698	26.1
1964	-3.83	99.7	-20.84	99.7	659	26.2
1965	-1.14	100.0	-8.10	100.0	944	26.0
1966	-2.39	79.2	-18.57	67.3	792	26.2
1971	-7.32	74.5	-	-	693	25.6
1972	-2.22	99.1	-7.12	46.1	589	26.2
1973	-0.79	18.0	-2.32	18.0	416	27.0
Max	-0.79	100.0	-2.32	100.0	1140	27.0
Min	-7.32	18.0	-41.17	18.0	416	25.5
Range	6.53	82.0	38.85	82.0	724	1.5
Std. dev.	2.25	26.7	14.20	31.1	207	0.4
Median	-3.40	98.9	-19.71	94.9	698	26.2

Source: (Onugba *et al*., 1990)

However, all these data plot around the Global Meteoric Water Line and showed relatively higher deuterium excess, d (calculated from the equation defined by Dansgaard, 1964). The local values of the weighted yearly means, as well as the long-term average from 1961 – 1973, plot almost on the global meteoric water line (GMWL) following the relation:

$$\delta\ ^{2}H = 8.77 \times \delta^{18}O + 10.8 \qquad \text{----------(3)}$$

Both slope and D – excess are comparable to the Global Meteoric Water Line. The fact that the groundwater samples plot around the GMWL can be explained by fairly low precipitation and moderately high evaporation occasioned by the vegetation and climate of the area which results to subsequently less depleted isotopic groundwater.

The d–excess calculated from the weighted average values is 10.3%o, thereby indicating relatively lower deuterium content in the groundwater regime in the area. The mean isotopic concentration of the rain water from which the groundwater was derived suggests that the mean $\delta^{18}O$ of rainfall events resulting in recharge is about – 3.3%o VSMOW (IAEA, 1979).

4.2 Radioactive Tritium Isotope Profile

Tritium values from 11 groundwater samples (Table 3) vary from 2.3 to 5.0 TU with a mean of 3.56 TU while that of the rain water sample from the study area is 4.85TU. The apparent qualitative age of groundwater is considered to be the amount of time determined from an age-dating tracer that has elapsed from the time water lost contact with the atmosphere. Therefore, the groundwater could be classified as a mixture of recent water with old groundwater and groundwater that has been subjected to radioactive decay.

With respect to the concentration profile of tritium as shown in Table 3, it might be postulated that groundwater in the study area have a narrow range of tritium values (2.3 – 5.0 TU). This narrow range of tritium enrichment should reflect the effect of recharge inputs from rainwater. The tritium value for the rainwater sample is 4.85 TU. This incidentally lies within the range of tritium values for the groundwater and thus indicates groundwater with evidence of mixing with meteoric water. This is clearly an indication of recent groundwater system dominated by recharge from recent precipitation.

Furthermore, this indicates the importance of direct recharge water contribution to groundwater storage through the fractures and faults that tend to control the surface drainage network in the basement rock area. The sandstone formation in the sedimentary area is characterized by highly porous and permeable sandy horizons, which provide direct and easy access to percolating rainwater. Table 3 shows the summary of

isotopic compositions along with hydrochemical water type and geology. The range of tritium concentration from both the basement and sedimentary aquifers varies narrowly, with samples from the basement aquifers having tritium concentration varying from 2.3 – 4.2 TU while those from the sedimentary aquifer have tritium concentration from 3.5 – 5.0 TU. The overlap and similarity in tritium concentration (Table 3) in both the basement and sedimentary aquifers probably indicate similar recharge sources for the aquifers. Applying the qualitative age categorization proposed by Clark and Fritz (1997), the range of tritium values depicts active recharge and mixture of sub-modern and recent groundwater.

Therefore, taking the conventional wisdom that elevated tritium (^3H) content in groundwater points to active recharge (Diop and Tijani, 2008) and that the chemistry of groundwater of the study area is marked by mixed spatial distribution of tritium content (Table 3), probably resulting from varied rainfall pattern and amount across the area. Groundwater undergoing evaporation will have a positive correlation between $\delta^{18}O$ and conductivity. In the diagram of $\delta^{18}O$ versus conductivity (Figure 6), it was observed that a negative correlation was obtained with $R^2 = 0.005$. In addition, an increase in electrical conductivity (EC) values takes place without significant changes in isotopic composition (Figure 7), which may be due to mineralization. The groundwater samples show a relative enrichment of the heavier isotopes without a simultaneous increase in EC, thus confirming that the groundwater appears to be recharged by moderately high evaporated isotopically enriched water on the surface or in the unsaturated zone.

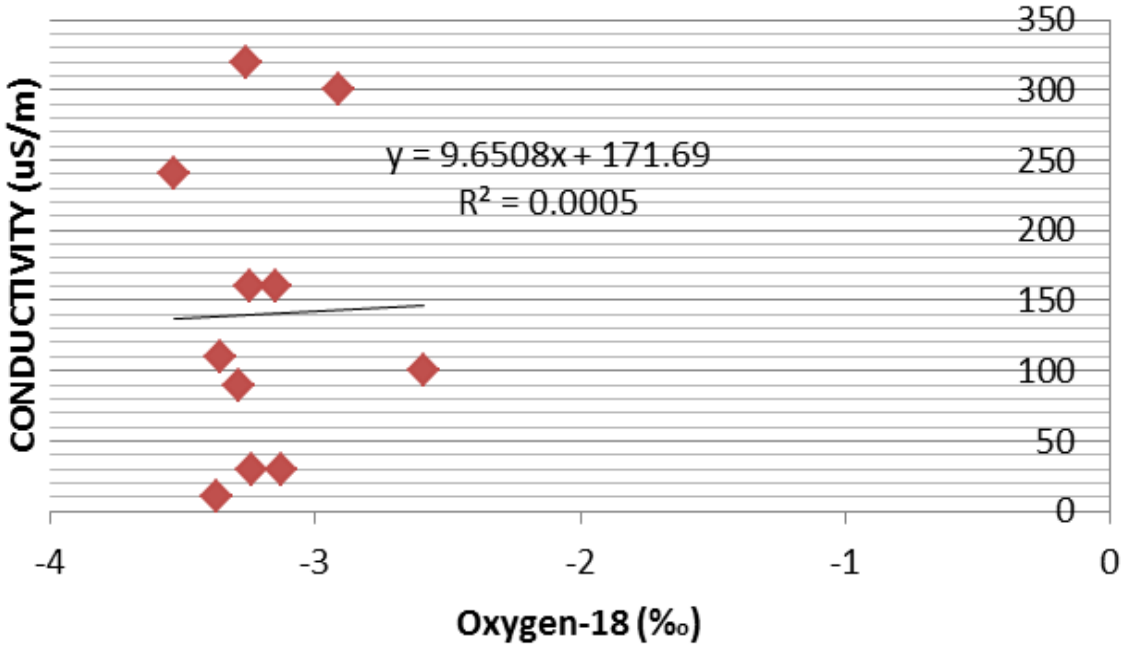

Figure 6: A plot of electrical conductivity (EC) versus Oxygen-18

Table 3: Summary of the Geology and Isotopic Composition in the study area

Sample No.	Locality	Long.	Lat.	$\delta^{2}H$ ‰	$\delta^{18}O$ ‰	d-excess, ‰	^{3}H (TU)	Geology
1	Zuma	07^{0} 24.09’	09^{0} 17.48’	-15.3	-3.36	12.25	2.3	Granite
3	Kawu	07^{0} 34.77’	09^{0} 18.66’	-15.5	-3.29	11.47	3.3	Granite
6	Pambara	07^{0} 23.33’	09^{0} 13.95’	-14.3	-3.24	12.26	4.0	Granite
9	Anagada	07^{0} 10.45’	09^{0} 02.38’	-16.9	-3.53	12.04	4.2	Granite
15	Gaduwa estate	07^{0} 27.91’	09^{0} 00.05’	-15.0	-3.15	10.83	3.1	Mig/gneiss
18	Gafere, kuje	07^{0} 19.29’	08^{0} 50.77’	-15.0	-3.25	11.65	3.7	Mig/gneiss
20	Yangoji	06^{0} 59.60’	08^{0} 46.73’	-16.5	-2.91	7.36	2.5	Mig/gneiss
26	Gada biyu	06^{0} 54.63’	08^{0} 39.99’	-17.4	-3.26	9.33	3.6	Metasediments
27	Kwanan mada	06^{0} 49.75’	08^{0} 37.25’	-15.0	-3.13	10.66	3.5	Sandstone
30	Abaji 1	06^{0} 56.97’	08^{0} 28.87’	-17.4	-3.37	10.23	5.0	Sandstone
34	Maitama	07^{0} 28.79’	09^{0} 06.23’	-16.4	-2.59	4.83	4.0	Granite

R18	Rainwater Gaduwa	07^0 27.91'	09^0 00.05'	12.3	1.23	2.21	4.85	---

Long.= Longitude, Lat.= Latitude, ^2H= deuterium, ^{18}O= Oxygen-18, d-excess= Deuterium excess, ^3H= Tritium, TU= Tritium Unit, all groundwater samples from boreholes except Gada biyu (hand-dug well), Mig/gneiss= Migmatite-gneiss.

4.3 Deuterium Excess (d-excess)

The deuterium excess (d-excess) reflects the conditions that lead to kinetic isotope fractionation between water and vapour during primary evaporation in the oceans (Dansgaard, 1964). This number also shows the extent of deviation of a given sample from the Global Meteoric Water Line (Gibrilla *et al.*, 2010). The groundwater deuterium excess values range from 4.83 to 12.26 ‰, while that of the only rain water sample was 2.21 ‰. As the $\delta^{18}O$ increases (becomes more enriched), the deuterium excess in all the samples decreases gradually (Figure 7). This observation can be partly attributed to the dilution of the groundwater with rainfall, which could increase the d-excess (Tijani and Abimbola, 2003; Yuan and Miyamoto, 2008).

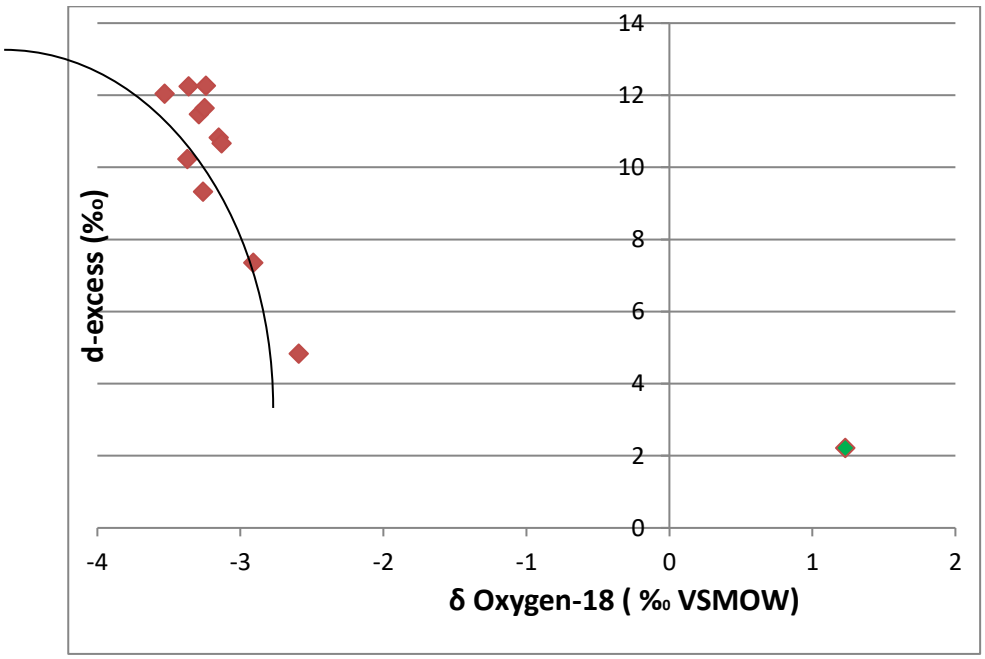

Figure 7. A plot of deuterium-excess (d-excess) versus Oxygen-18 ($\delta^{18}O$).

5. Conclusion and Recommendation

The results of stable isotope analysis (Table 3) carried out on the sampled groundwater revealed $\delta^{18}O$ values as varying from -3.53 to -2.59 %o, with an average of -3.18%o. The $\delta^{2}H$ values range from -17.4 to -14.3%o, with an average of -15.88%o. The negative values of oxygen-18 (^{18}O) and deuterium (^{2}H) are indicative of depletion of oxygen-18 and deuterium relative to the Vienna Standard Mean Ocean Water (VSMOW). The stable isotope composition relative to the Global Meteoric Water Line (GMWL) reveals important information on the groundwater recharge pattern. The plot of $\delta^{2}H$%o against $\delta^{18}O$%o of the analysed samples indicate a cluster around the GMWL given by the equation (Craig, 1961): $\delta^{2}H = 8\ \delta^{18}O + 10$.

The narrow variation in the tritium content of sampled groundwater could be a reflection of similar recharge sources for both the aquifers of the basement complex and sedimentary formations. The range of tritium content (2.3 – 5.0 TU) depicts active recharge and mixture of sub-modern and recent groundwater. Despite the spatial heterogeneity of geological and climatic conditions in the study area, this would probably suggest that the groundwater of the study area has received significant contribution from rainwater, which is responsible for the apparent tritium enrichment in the groundwater. The major possible recharge pathways in the study area are through topsoil and the loose, unconsolidated formation. Another possible recharge pathway is by direct infiltration through joints, fractures and faults in the Basement Complex parts of the study area.

References

Abu-Jaber, N. S. & Wafa, N. A. (1996). Hydrochemistry of aquifers in the Southern dead sea area, Southern Jordan. *Environmental Geology,* 28, 213 – 222.

Abd El Samie, S. G. & Sadek, M. A. (2001). Groundwater recharge and flow in the lower Cretaceous Nubian sandstone aquifer in the Sinai Peninsula, using isotopic techniques and hydrochemistry. *Hydrogeology Journal*, 9, 378 – 389.

A.B.U. (1978). Ahmadu Bello University (ABU) *Geoscience investigation of the Federal Capital Territory,Phase I (Federal Capital City)*. Unpublished technical report.

Actlabs (2010). *Activation laboratories international schedule of services and fees*. Retrieved March 2, 2010, from http://www.actlabs.com

Adelana, S. M. A. & Olasehinde, P. I. (2005). Characterisation of Groundwater flow in fractured/weathered hard rock using hydrogeochemical and isotopic investigations. In: Proceedings of XXXIII International Association of Hydrogeologists (IAH)Congress: *Groundwater flow understanding: from local to regional scales*. Zacatecas, Mexico, 11 – 15 October, 2004.

Adelana, S. M. A., Olasehinde, P. I. & Vrbka, P. (2002). Groundwater recharge in the Cretaceous and tertiary sediment aquifers of northwestern Nigeria, using hydrochemical and isotopic techniques. In: D. Martinez and H. Massone (eds.). *Groundwater and human development* (pp. 907– 915), Bocanegra, Mar de Plata, Argentina.

Adelana, S. M. A. & Olasehinde, P. I. (2003). Hydrochemical and environmental isotope properties of shallow groundwater of the Basement rock aquifer in Offa, SW Nigeria. In: J. Krasny, Z. Hrkal & J. Bruthans (Eds.) *Groundwater in fractured rocks* (pp. 189 – 190). IAH Publication.

Adelana, S. M. A., Olasehinde, P. I., Vrbka, P.; Edet, A. G. & Goni, I. B. (2008). An overview of the Geology and Hydrogeology of Nigeria. In: S. M. .A. Adelana and A. M. Mc Donald (Eds.), *Applied groundwater studies in Africa*. IAH Selected papers in Hydrogeology, Vol. 13. Leiden, Netherlands. CRC Press/Balkema.

Akiti, T. T. (1986). *Environmental isotope study of groundwater in crystalline rocks of the Accra plains*. 4th Working meeting on isotopes in nature, proceedings of an advisory group meeting, IAEA, Vienna.

Alagbe, S. A. (1979). *The geology of Jidu-Gidan Anfani-Karumo district of FCT with emphasis on the relationship of porphyroblastic and non-porphyroblastic rocks*. Unpublished B.Sc. Project report, Ahmadu Bello Univerisity, Zaria, Nigeria.

Alao, D. A. & Ige, O. O. (2003). Preliminary assessment of pollution of Asa River in Ilorin metropolis using physiochemical indices. *Water Resources*, 14, 25 – 30.

Al-Charideh, A. & Katta, B. (2016). Isotope hydrology of deep groundwater in Syria: renewable and non-renewable groundwater and paleoclimatic impact. Hydrogeology Journal, Vol. 24, No. 1, p. 79 – 98. DOI 10.1007/s 10040-015-1324-4

Amadi, A. N., Olasehinde, P. I. and Nwankwoala, H. O., (2014). Hydrogeochemistry and statistical analysis of Benin Formation in Eastern Niger Delta, Nigeria. *International Research Journal of Pure and Applied Chemistry,* 4(3), 327 – 338.

Amadi, A.N., Tukur Aminu., Okunlola, I. A., Olasehinde, P. I. and Jimoh M.O., (2015). Lithologic Influence on the Hydrogeochemical Characteristics of Groundwater in Zango, North-west Nigeria. *Natural Resources and Conservation,* 3(1), 11–18.

CIWAT, (2010). *Water supply master plan of Abuja, Nigeria*. Unpub. Technical Report by CIWAT Nigeria Limited, submitted to FCT Water Board, Abuja, Nigeria.

Clark, I. & Fritz, P. (1997). *Environmental isotopes in hydrogeology*. New York, Lewis Publishers, CRC Press.

Dansgaard, W. (1964). Stable isotopes in precipitation. *Tellus,* 16, 436 – 468.

Dapaah-Siakwan, S. & Gyau-Boakye, P. (2000). Hydrochemical framework and borehole yields in Ghana. *Journal of Hydrology*, 8, 845 – 852.

Dassi, I.; Zouari, K.; Seiler, K. P.; Faye, S. & Kamel, S. (2005). Flow exchange between the deep and shallow groundwaters in the Sheitla synclinal basin (Tunisia): an isotopic approach. *Environmental Geology*, 47, 501 – 511.

Diop, S. & Tijani, M. N. (2008). Assessing the basement aquifers of eastern Senegal. *Hydrogeology Journal*, 16, (7), 1349 – 1369.

Edmund, W. M. & Shand, P. (2008). Groundwater baseline quality. In: W. M. Edmund and P. Shand (Eds.), *Natural groundwater quality* (pp. 1 – 21). Malden, Blackwell Publishing Ltd.

Epstein, S. & Mayeda, T. (1953). Variations of 18O content of waters from natural sources. *Geochimica et Cosmochimica Acta* 4, 213 – 224.

FCT Handbook (1994). *Federal Capital Territory, Abuja: Background, history and progress*. Abuja, Garkida Press Limited, Nigeria.

Geyh, M. A. (2000). Groundwater: saturated and unsaturated zone. In: W. G. Mook (Ed.), *Environmental Isotopes in the Hydrological Cycle. Principles and Applications*. UNESCO-IHP Technical document in Hydrology (pp. 151 – 200) Paris, UNESCO.

Geyh, M. A. & Wirth, K. (1980). ^{14}C-ages of confined groundwater from the Gwandu aquifer, Sokoto Basin, Northern Nigeria. *Journal of Hydrology*, 48, 281 – 288.

Gibrilla, A.; Osae, S.; Akiti, T. T.; Adomako, D.; Ganyaglo, S. Y.; Bam, E. P. K. & Hadisu, A. (2010). Origin of dissolve ions in groundwater in the northern Densu river basin of Ghana using stable isotopes of ^{18}O and ^{2}H. *Journal of Water Resources and Protection*, 2, 199 - 208. doi:10.4236/jwarp.2010.212121

Goni, I. B. & Edmunds, W. M. (2001). *The use of unsaturated zone solutes and deuterium profiles in the study of groundwater recharge in the semi-arid zone of Nigeria*. Isotope based assessment of groundwater renewal in water scarce region. IAEA-Technical document, 1246:85 – 99.

Helstrup, T.; Jorgensen, N. O. & Bonoeng-Yakubu, B. (2007). Investigation of hydrochemical characteristics of groundwater from the Cretaceous – Eocene Limestone aquifer in southern Ghana and southern Togo, using hierarchical cluster analysis. *Journal of Hydrology*, 15, (5), 977 – 989, doi: 10.1007/S/10040-007-0165-1

IAEA. (1979). Environmental isotope data. No. 6: World survey of isotope concentrations in precipitation, 1972- 1975. Technical report series, 192, Vienna, IAEA.

Kendall, C. & McDonell, J. J. (1988). *Isotope in catchment hydrology*. Amsterdam, Elsevier North Holland Publishing Company.

Kendall, C. & Mc Donell, J. J. (1988). *Isotope tracers in catchment hydrology*. USGS. Amsterdam, Elsevier Science. B. V.

Matter, J. M.; Waber, H. N.; Loew, S. & Matter, A. (2006). Recharge areas and geochemical evolution of groundwater in an alluvial aquifer system in the Sultanate of Oman. *Hydrogeology Journal*, 14, 203 – 224.

Mbonu, M. & Travi, Y. (1994). Labelling of precipitation by stable isotopes ^{18}O, ^{2}H) over the Jos Plateau and the surrounding plains (northcentral Nigeria). *Journal of African Earth Sciences*, 19, 91 – 98.

Mc Conville, C. (1999). *Using stable isotopes to estimate groundwater recharge in a temperate zone*. Unpublished Ph.D. Thesis, Civil Engineering Department, Queens University, Belfast.

Mc Curry, M. C. (1970). *The geology of degree sheet 21 (Zaria)*. Unpublished M.Sc. Thesis, Ahmadu Bello University, Zaria, Nigeria.

Mc Curry, M. C. (1976). A general review of geology of the Precambrian to lower Paleozoic rocks of northern Nigeria: a review. In: C. A. Kogbe (Ed.), *Geology of Nigeria* (pp. 15 – 38), 2nd edition, Ibadan, RockView Nig. Ltd.

Negrel, P.; Petelet-Giraud, E; Babier, J. & Gautier, E. (2003). Surface water groundwater interactions in an alluvial plain: chemical and isotopic systematics. *Journal of Hydrology*, 277, 248 – 267.

Nigerian Geological Survey Agency (NGSA) (2004). *Geological Map of Nigeria*. NGSA, Federal Ministry of Solid Minerals Development, Nigeria, NGSA.

Onugba, A.; Blavoux, B. & Dray, M. (1990). *The environmental isotopes in monthly precipitation at Kano, Nigeria, from 1961 – 1973*. Proceedings of 1st biennial National hydrology symposium, Maiduguri, Nigeria, pp. 67 – 88.

Onugba, A.; Blavoux, B.; Guirand, R. & De Rooy, C. (1989). Results of preliminary Hydrochemical and environmental isotope study of the groundwater in Gongola State (N. E. Nigeria). *WaterResources*, 1, (2), 147 – 153.

Oteze, G. E. (1989). Environmental isotope hydrology of the main Rima aquifer waters (Sokoto basin), Northwest Nigeria. *Journal of Mining and Geology*, 25, (1 and 2), 205 – 210.

Oyawoye, M. O. (1972). The Basement Complex of Nigeria. In: T. F. J. Dessavagie & A. J. Whiteman (Eds.), *African Geology* (pp. 66 – 102), Ibadan, University of Ibadan Press.

Plummer, L. N.; Bexfield, L. M. ; Anderholm, S. K.; Sanford, W. E. & Busenberg, E. (2004). Hydrogeochemical tracers in the middle Rio Grande Basin, USA: 1.Conceptualisation of groundwater flow. *Hydrogeology Journal*, 12, 359 – 388.

Schurch, M. & Vuataz, F. D. (2000). Groundwater components in the alluvial aquifer of the alpine Rhone River valleys, Bois de Finges area, Wallis canton, Switzerland. *Hydrogeology Journal*, 8, 549 – 563.

Seiler, K. (2000). Man's impact on groundwater systems. In: W. G. Mook (Ed.), *Environmental Isotopes in the Hydrological Cycle: Principles and applications,* 5 (39), 109), technical document in hydrology, UNESCO-IHP.

Stimson, J.; Frape, S.; Drimme, R. & Ruodolph, D. (2001). Isotopic and geochemical evidence of regional scale anisotropy and interconnectivity of an alluvial fan system. Cochobamba valley, Bolivia. *Applied Geochemistry*. 16, 1097 – 1114.

Tijani, M. N. (2008) Hydrochemical and stable isotopes compositions of saline groundwaters in the Benue Trough, Nigeria. In: S. M.A. Adelana & A. M. Mac Donald (Eds.), *Applied groundwater studies in Africa* (pp. 351 – 369), IAH selected papers on hydrogeology, Series 13, Netherlands, CRC Press/Balkema.

Tijani, M. N. & Abimbola, A. F. (2003). Groundwater chemistry and isotope studies of weathered basement aquifer: a case study of Oke-ogun area, S. W. Nigeria. *African Geosciences Review*, 10, (4), 373 – 387.

Tijani, M. N.; Loehnert, E. P. & Uma, K. O. (1996). Origin of the saline groundwaters in the Ogoja area, Lower benue Trough, Nigeria. *Journal of African Earth Sciences*, 23, (2), 237 – 252.

Truswell J. F. & Cope, R. N. (1963). *The geology of parts of Niger and Zaria Provinces, Northern Nigeria*. Geological Survey of Nigeria, Bulletin, No. 29, 38pp.

Turner, D. C. (1971). The Precambrian and LowerPaleozoic basement of Nigeria. In: UNESCO Report*: Tectonics of Africa*, Earth Sciences, 6, 255 – 260.

Wood, W. W. & Sanford, W. E. (1995). Chemical and isotopic methods for quantifying groundwater recharge in a regional semi-arid environment. *Groundwater*, 33, 458 – 468.

Yaya, O. O. (2006). *Impact of urbanization on the quality of groundwater resources of the Federal Capital Territory, Abuja, Nigeria*. Unpub. research proposal report for a Ph.D. degree research project, Department of Geology, University of Benin, Nigeria.

Yuan, F. & Miyamoto, S. (2008). Characteristics of Oxygen-18 and Deuterium composition in waters from Pecos River in American Southwest. *Chemical Geology*, 255, (3 and 4), 220 – 230.

Zhang, Y.; Wu, Y.; Su, J.; Wen, X. & Liu, F. (2005). Groundwater replenishment analysis by using natural isotopes in Ejina Basin, Northwestern China. *Environmental Geology*, 48, 6 – 14.

Zouari, K.; Chkir, N. & Ouda, B. (2003). *Paleoclimatic variation in Meknassi basin (central Tunisia) during Holocene period using multidisplinary approaches* (pp. 80 – 88), Vienna, IAEA.

EFFECT OF SALT APPLICATIONS ON WATER ABSORPTION CAPACITY (WAC) OF MUSHROOM VARIETIES OBTAINED IN AKURE, NIGERIA

[1*]Abulude, Francis Olawale and [2]Ndamitso, Mohammad Mohammad

[1]Science and Education Development Institute, Akure, Ondo State, Nigeria

[2]Department of Chemistry, Federal University of Technology, Minna, Niger State, Nigeria.

*Corresponding author: sedinst@yahoo.com

ABSTRACT

This work was researched to study the effect of different salts concentrations on the WAC of mushroom varieties obtained in Akure, Nigeria. From the results obtained, The WAC of all samples in water differed significantly ($p < 0.05$) with *Chlorophyllum molybditis* having the highest while *Pleurotus ostreatus* the lowest while, the WAC of the fungus in the different salts at different concentrations differed significantly ($p < 0.05$) in the order of CH_3COONa >Na_2SO_4> $NaNO_3$> $NaNO_2$> NaCl. Our results compare favourably with other research works on food formulations. It was noticed that WAC value of samples decreased as the concentration of the salts increased which may be depended on the type of salt and effects of salt with the cation and anion species involved. In conclusion, it was observed that WAC concentrations were influenced by the different salts concentrations. Therefore formulations involving the use of mushroom will have to take into consideration different salts concentrations.

KEYWORDS: fungi, Water Absorption capacity, salt concentrations, functional properties, Akure

INTRODUCTION

Edible mushrooms have for a long time been recognized not only as a delicacy, but also for their use as food in man's diets (Ndamitso and Abulude, 2013; Abulude *et al*., 2004)). They have been found to be rich sources of protein, lipids, amino acids, glycogen, vitamins and mineral salts (Okwulehie and Odunze, 2004). According to Adeyeye *et al*. (2008), the mineral salts contents of mushrooms are superior to those of meat and fish and nearly twice those of most common vegetables. These fungi have also been mentioned for their medicinal values (Selvi *et al*., 2007; Abulude, 2013).

Nigeria is a country of many tribes among which are the Hausas in the North, Yorubas in the South West, Urhobo in the Mid – West and the Ibos in the East and each of these tribes has recognized mushrooms for many years using a number of them for various economic and medicinal purposes (Ukoima *et al*., 2009).

Besides the edible mushrooms, the natives have also recognized some poisonous or none edible ones which include *Coprinus africans* popularly known as Ajeimutin; *Phallus aurantiacus, Phallus industiatus, phallus rubicundus* and *Mutinus bambustnus*, collectively called Akufodewa; *Celtis zenkeri* which is known as Asa-ita and *Coprinus enphemerus* which is referred to as Olu-gbongaga.

Although the nutritional and medicinal values of mushrooms have long been recognized (Manzi *et al*., 2001; Kettawan *et al*., 2011), in the past, their consumption has mainly been confined to rural Nigeria. However, in recent times, their consumption has assumed greater importance in the diets of both rural and urban dwellers. For example, they are being marketed along major highways and urban centres where the trade now booms. It is conceivable that the increased demand for mushrooms is predicated upon the phenomenal

rise in the costs of the conventional sources of animal protein sources like the beef, pork, chicken, fish and eggs.

The ultimate success of utilizing plant proteins as ingredients depends largely upon the beneficial qualities they impact to foods which by extension depend largely on their functional properties. The functional properties of plant protein have been reported to be dependent upon the chemical characteristics inherent in the seed (Aremu *et al*., 2009). The effects significant of salts have been reported in food formulation (Ogungbemile *et al*., 2009). The relative effects cations and anions are influenced by the intensity of their surface charge which is influenced by the atomic radii. At this salt concentration, electrostatic interactions are of little importance with regards to the amount of water bounds of protein because competition of the ions and proteins for water becomes predominant (Ogungbemile *et al*., 2009). In this study, mushroom species would be prepared with different salts concentrations and the effects of the salts concentrations on the functional properties would be studied.

Objective of the Study

To determine the effects of different concentrations of NaCl, Na_2SO_4, CH_3COONa, $NaNO_2$ and $NaNO_3$ on the Water Absorption Capacity of mushroom varieties consumed in South West of Nigeria.

MATERIALS AND METHODS

Source of Materials and Sample Pre-treatment

The mushrooms; *Lentinus subnudus* Berk (M_1), *Chlorophyllum molybditis* (M_2), *Volvariella esculenta* (M_3), *Coprinus tramentarius* (M_4), *Pleurotus ostreatus* Jacq (M_5), *Termitomyces microcarpus* (M_6) and *Pleurotus pulmonarius* (M_7) were collected from Federal College of Agriculture campus, Akure, Ondo State, Southwest part of Nigeria. The bad or rotten samples were sorted out. The samples were oven dried at 65^oC for 72 hours and were then pounded into powdered form using porcelain pestle and mortar. The milled samples were then sieved with a 2mm mesh sized sieve and stored in waterproof polyethylene bags at room temperature for further analysis.

Determination of Water Absorption Capacity (WAC)

The water absorption capacity was determined using the modified method of Ogungbemile *et al*., (2009). One gram of sample was taken in triplicates in test tubes and mixed with 10cm^3 of distilled water on a mixer and kept at room temperature for 30 minutes. It was later centrifuged for 30 minutes and the volume of the supernatant taken using a 10 cm^3 graduated cylinder. The density of water was assumed to be 1g/cm^3. The excess water absorbed by the flour in each case was expressed as the percentage water bound by 100g sample.

Statistical analysis

Data obtained were generated in triplicates and analyzed using Mean, Standard deviation and one-way analysis of variance with Duncan Multiple Range test at 95% confidence or $p < 0.05$.

RESULTS AND DISCUSSION

The results for WAC in water are presented in Table 1. The WAC of all samples in water differed significantly ($p < 0.05$) with *Chlorophyllum molybditis* having the highest while *Pleurotus ostreatus* the lowest. The results for WAC in *Chlorophyllum molybditis* are presented in Table 2. The WAC of the fungus in the different salts at different concentrations differed significantly ($p < 0.05$) in the order of $CH_3COONa > Na_2SO_4 > NaNO_3 > NaNO_2 >$ NaCl. The WAC of *V. esculenta* in the different salt concentrations differed significantly ($p < 0.05$). Table 3 showed the strength of the different concentration from the highest to the lowest. *V. esculenta* - $CH_3COONa > NaNO_3 > NaNO_2 > Na_2SO_4 >$ NaCl. Same observations were obtained in Tables 4 – 8 (As the concentrations of the different salts increases, there were decreases in WAC).

Water Absorption Capacity (WAC) values of the samples were as shown in Tables 1 – 8. These varied from 180.48±20.08% (*Pleurotus ostreatus*) to 430.48±20.46 % (*Coprinus tramentarius*) for all salts. The lowest value in this work was lower than that reported for the three species of mushrooms by Aremu *et al.,* (2009) but the highest value obtained in this work was highest the 390.00±5.00% reported for *Ganoderma spp*. These values were also higher than that reported for Lima bean flours by Aremu *et al.* (2009). These tables showed decrease in WAC of samples as the concentration of the salts increased which is depended on the type of salt. This may be due to the fact that effects of salt vary with the cation and anion species involved (Ogungbemile *et al*., 2009). The higher water absorption capacity of mushroom spieces compared to Bambara groundnuts flour 221.83 and 281.35% recorded by Eltayeb *et al*. (2011) may be due to the higher polar amino acid residues of proteins having an affinity for water molecules (Yusuf *et al*., 2008). The major chemical compositions that enhance the water absorption capacity of flours are proteins and carbohydrates, since these constituents contain hydrophilic parts, such as polar or charged side chains (Lawal and Adebowale, 2004).

The ultimate success of utilizing plant proteins as ingredients depend largely upon the beneficial qualities they impact to foods which depend largely on their functional properties (Ndamitso and Abulude, 2014). Functional properties are intrinsic physico-chemical characteristics which affect the behaviour of properties in food systems during processing, manufacturing, storage and preparation (Abdel Rahman *et al*., 2011) Nutritional and functional qualities of protein are largely determined by its amino acid content and nitrogen solubility (Eltayeb *et al*., 2011). The critical functional properties necessary in protein ingredients include gelation, emulsion and foam formation, which are important for function of proteins in food systems. Other paramount functionalities are proteins solubility, water and fat absorption capacity (Abdel Rahman *et al*., 2011). These characteristics are influenced by salt concentration during food formulation in modern food industry (Andualem and Gessesse, 2013*)*.

Table 1: The Results of Water Absorption Capacity (WAC) of Selected Varieties of Mushrooms in Water (%)

Samples	WAC
M_1	340.24±20.10[c]
M_2	380.38±19.87[d]
M_3	380.42±20.03[d]
M_4	260.28±20.02[b]
M_5	180.48±20.08[a]
M_6	200.22±20.20[a]
M_7	260.24±19.74[b]

All values were expressed as averages of triplicate determinations ± the standard deviations and values bearing the same superscripts in the same row are significantly not different ($p < 0.05$).

Table 2: Water Absorption Capacity of *Chlorophyllum molybditis* In Different Salts Concentrations (%)

Concentration of different Salts	$NaNO_2$	$NaNO_3$	CH_3COONa	NaCl	Na_2SO_4

2	340.44±19.95[a]	420.55±2.05[c]	240.82±20.10[ab]	280.56±20.00[a]	320.35±19.90[b]
4	320.54±20.15[a]	240.21±19.85[a]	240.11±20.00[ab]	280.35±19.95[a]	300.35±20.00[ab]
6	340.61±20.00[a]	280.49±20.10[b]	240.73±20.00[ab]	280.45±19.95[a]	280.50±20.10[a]
8	340.36±20.05[a]	300.50±20.00[b]	280.43±20.00[a]	240.38±20.00[a]	300.55±20.00[ab]
10	326.98±23.15[a]	293.79±23.01[b]	247.08±23.11[ab]	260.38±19.98[a]	287.08±22.97[ab]
12	340.39±20.07[a]	287.06±23.11[b]	240.38±22.15[ab]	253.88±22.88[a]	293.78±23.05[ab]

All values were expressed as averages of triplicate determinations ± the standard deviations and values bearing the same superscripts in the same row are significantly not different ($p < 0.05$).

Table 3: The Results of Water Absorption Capacity of *V. esculenta* In Different Salts Concentrations (%)

Concentration of different salts	Salts				
	$NaNO_2$	$NaNO_3$	CH_3COONa	NaCl	Na_2SO_4
2	463.55±11.74[c]	480.36±20.15[b]	510.28±19.72[b]	300.28±19.83[c]	430.48±20.46[ab]
4	440.34±19.84[c]	400.48±20.18[a]	460.15±19.82[ab]	280.38±19.73[bc]	428.42±20.07[ab]
6	433.11±19.83[ab]	360.13±20.19[a]	460.29±20.28[ab]	260.19±19.72[ab]	410.26±20.10[a]
8	430.39±19.81[ab]	384.20±18.74[a]	460.25±19.85[ab]	252.45±19.62[bc]	400.16±19.86[a]
10	401.88±23.32[b]	315.12±23.01[a]	460.45±29.73[a]	242.22±17.76[ab]	400.52±10.18[a]

12	361.99±17.83[a]	311.95±22.31[a]	410.45±29.73[a]	200.35±19.97[a]	400.59±19.50[a]

All values were expressed as averages of triplicate determinations ± the standard deviations and values bearing the same superscripts in the same row are significantly not different ($p < 0.05$).

Table 4: The Results of Water Absorption Capacity of *C. tramentarius* In Different Salts Concentrations (%)

Concentration of different Salts				Salts		
		$NaNO_2$	$NaNO_3$	CH_3COONa	NaCl	Na_2SO_4
	2	460.11±20.16[d]	460.44±19.75[b]	460.25±20.38[a]	325.11±15.53[d]	440.22±19.67[c]
	4	400.19±20.29[ab]	443.52±20.18[a]	440.36±20.19[b]	300.82±18.73[bcd]	420.45±19.68[bc]
	6	400.35±20.28[ab]	440.09±20.13[b]	401.86±22.27[a]	285.26±19.72[abc]	380.36±19.71[ab]
	8	400.11±20.04[a]	440.42±19.82[b]	441.95±20.10[b]	260.22±19.82[a]	400.35±19.72[abc]
	10	420.34±20.15[bc]	440.53±19.84[b]	440.63±20.01[b]	280.43±19.84[ab]	420.48±10.18[bc]
	12	460.34±20.15[d]	400.48±19.95[a]	440.65±19.80[b]	320.43±20.05[cd]	360.59±19.50[a]

All values were expressed as averages of triplicate determinations ± the standard deviations and values bearing the same superscripts in the same row are significantly not different ($p < 0.05$).

Table 5: The Results of Water Absorption Capacity of *P. ostreatus* In Different Salt Concentrations (%)

Concentration of different Salts				Salts		
		$NaNO_2$	$NaNO_3$	CH_3COONa	NaCl	Na_2SO_4
	2	340.51±20.10[b]	340.42±20.07[ab]	240.48±20.38[b]	293.11±15.53[b]	231.29±20.67[b]
	4	235.19±20.29[a]	280.56±19.93[b]	224.356±15.19[a]	260.81±19.73[a]	200.48±19.68[a]
	6	201.35±20.28[a]	205.11±18.83[a]	220.35±22.27[a]	281.26±19.72[a]	225.21±18.71[a]
	8	320.38±19.93[b]	213.77±19.82[a]	220.40±19.95[a]	260.38±19.89[a]	200.36±20.06[a]
	10	320.32±20.15[b]	200.53±19.84[a]	200.49±20.01[a]	260.36±19.98[a]	200.29±10.18[a]
	12	200.52±20.15[a]	200.48±19.95[a]	233.84±19.80[a]	280.48±19.77[a]	187.12±19.50[a]

All values were expressed as averages of triplicate determinations ± the standard deviations and values bearing the same superscripts in the same row are significantly not different ($p < 0.05$).

Table 6: The Results of Water Absorption Capacity of *T. microcarpus* In Different Salts Concentrations (%)

Concentration of different Salts	$NaNO_2$	$NaNO_3$	Salts CH_3COONa	NaCl	Na_2SO_4

	2	345.51±20.00^{ab}	420.30±19.95^{c}	280.40±19.90^{c}	280.48±20.53^{b}	350.51±20.67^{b}
	4	320.31±19.89^{a}	240.34±20.03^{a}	243.05±15.19^{ab}	280.81±19.73^{b}	300.41±19.68^{ab}
	6	340.45±20.18^{a}	280.41±19.83^{b}	277.35±22.27^{c}	280.26±19.72^{b}	300.42±18.71^{ab}
	8	340.38±19.93^{a}	300.48±20.82^{b}	240.45±19.95^{a}	240.38±19.89^{a}	300.49±20.06^{ab}
	10	320.37±20.16^{a}	300.35±19.84^{b}	240.35±19.93^{ab}	260.55±19.98^{ab}	280.39±20.18^{a}
	12	340.31±20.00^{a}	280.35±20.05^{b}	260.39±19.80^{b}	260.36±20.77^{ab}	300.39±19.50^{ab}

All values were expressed as averages of triplicate determinations ± the standard deviations and values bearing the same superscripts in the same row are significantly not different ($p < 0.05$).

Table 7: The Results of Water Absorption Capacity of *P. pulmonarius* In Different Salts Concentrations (%)

Concentration of different Salts		$NaNO_2$	$NaNO_3$	CH_3COONa	NaCl	Na_2SO_4
	2	360.04±19.90^{a}	360.54±20.95^{ab}	400.41±19.90^{ab}	280.48±20.53^{ab}	380.22±20.67^{b}
	4	340.40±20.00^{a}	240.34±20.03^{a}	360.25±15.19^{a}	280.81±19.73^{ab}	360.25±19.68^{ab}
	6	380.58±19.18^{bc}	340.45±20.83^{a}	360.42±22.27^{a}	280.26±19.72^{ab}	340.58±18.71^{a}
	8	353.71±19.93^{ab}	326.95±20.82^{a}	280.35±19.95^{a}	240.38±19.89^{ab}	340.38±20.06^{a}

10	360.04±19.16^{ab}	340.55±19.94^{a}	260.56±19.93^{a}	260.55±19.98^{a}	380.22±20.18^{b}
12	362.49±23.57^{ab}	330.49±20.05^{a}	310.19±19.80^{a}	260.36±20.77^{b}	360.12±19.50^{ab}

All values were expressed as averages of triplicate determinations ± the standard deviations and values bearing the same superscripts in the same row are significantly not different ($p < 0.05$).

Table 8: The Results of Water Absorption Capacity of *V. subnudus* In Different Salts Concentrations (%)

	Salts				
Conc. of Salts	$NaNO_2$	$NaNO_3$	CH_3COONa	NaCl	Na_2SO_4
2	330.37±19.94^{c}	270.27±20.17^{ab}	300.52±19.90^{b}	300.41±20.53^{ab}	300.38±19.67^{c}
4	320.33±20.00^{a}	260.48±20.03^{a}	250.15±20.19^{a}	289.37±20.73^{b}	300.34±20.68^{c}
6	300.19±19.18^{bc}	240.34±20.17^{b}	240.39±19.27^{a}	260.23±19.72^{a}	280.19±20.71^{bc}
8	320.23±19.99^{ab}	300.22±19.82^{a}	240.35±19.95^{a}	260.34±20.17^{a}	260.44±20.06^{ab}
10	300.52±19.90^{ab}	240.37±19.99^{a}	260.29±19.93^{a}	280.51±19.98^{ab}	280.33±20.00^{bc}
12	300.55±20.57^{ab}	240.23±20.05^{a}	260.19±19.80^{a}	280.47±19.85^{ab}	280.28±19.50^{bc}

All values were expressed as averages of triplicate determinations ± the standard deviations and values bearing the same superscripts in the same row are significantly not different ($p < 0.05$).

CONCLUSION

The results showed that WAC concentrations were influenced by the different salts concentrations. Therefore formulations involving the use of these organisms will have to take into consideration the effects of different salts concentrations in order to achieve the maximum goal.

REFERENCES

Abulude F.O, Adeyeye E.I. and Asaolu S. S. (2004). Metal levels in Mushrooms consumed in Southwestern Nigeria. *Advances in Food Sciences*. 26 (4): 155 – 158.

Abulude, F. O (2013). Functional properties of selected mushroom varieties obtained in Akure, Southwest Nigeria as affected by different salts concentrations. Unpublished M. Tech Thesis. Federal University of Technology, Minna, Niger State, Nigeria.

Abdel Rahman S. M. Eltayeb, Ali O. Ali, Azza A. Abou-Arab and Ferial M. Abu-Salem (2011). Chemical composition and functional properties of flour and protein isolate extracted from Bambara groundnut (*Vigna subterranean*). African Journal of Food Science Vol. 5(2), pp. 82 – 90

Adeyeye, E.I., Adubiaro, H.A. and Awodola, O.J. (2008). Comparability of chemical composition and functional properties of shell and flesh of *Penaecus notabilis*. *Pakistan Journal of Nutrition*, 7 (6), 741 – 747.

Aremu, M O., Basuk, Gyan, S. D., Goyal, A., Bhowmik, P. K. and Datta Banik, S. (2009). Proximate composition and functional properties of mushroom flours from *Ganoderma spp*, *Omphalotus olearius* (DC) sing and *Hebeloma mesphaeum* (Pers) Quels used in Nassarawa State, Nigeria. *Malaysian of Journal Nutrition*, 15 (2), 233-241.

Andualem B and Gessesse A (2013). Effects of Salt (NaCl) Concentrations on the Functional Properties of Defatted Brebra (*Millettia ferruginea*) Seed Flour. Middle-East Journal of Scientific Research 13 (7): 889-897. DOI: 10.5829/idosi.mejsr.2013.13.7.2791.

Eltayeb, Abdel Rahman S. M., Ali, O. Ali, Abou-Arab, Azza A. and Abu-Salem, Ferial M. (2011). Chemical composition and functional properties of flour and protein isolate extracted from Bambara groundnut (*Vigna subterranean*). *African Journal of Food Science*, 5(2), 82 – 90.

Kattawan, A., Chanlekha, K., Kongkachuichai, R., and Chaaroensiri, R. (2011). Effects of cooking on antioxidant activities and polyphenol content of edible mushrooms commonly consumed in Thailand. *Pakistan Journal of Nutrition*, 10 (11), 1094-1103.

Lawal OS and Adebowale KO (2004). Effect of acetylation and succinylation on solubility profile, water absorption capacity, oil absorption capacity and emulsifying properties of muncuna bean (*Mucuna pruiens*) protein concentrate. Nahrung/Food, 48(2): 129-136.

Manzi, P., Aguzzi, A., and Pizzoferrato., L. (2001). Nutritive value of mushrooms widely consumed in Italy. *Food Chemistry*, 73, 321 – 325.

Ndamitso M. and Abulude F. (2013). Nutritional assessment of some mushroom species,

Electronic Journal of Polish Agricultural Universities (EJPAU) 16(4), #11. Available

Online: http://www.ejpau.media.pl/volume16/issue4/art-11.html

Ndamitso, M.M and Abulude, F. O (2014). Effect of different salt concentrations on protein solubility of mushroom varieties obtained in Akure, Nigeria. *American Journal of Food and Nutrition.* Vol. 2, No. 1, 7-10.

Ogungbenle, H.N., Oshodi, A. A. and Oladimeji, M.O. (2009). The proximate and effect of salt applications on some functional properties of Quinoa (*Chenopodium quinoa*) flour. *Pakistan Journal of Nutrition*, 8 (1), 49 – 52.

Okwulehie, I.C. and Odunze, E.T. (2004): Evaluation of the Myco-chemical and Mineral Composition of Some Tropical Edible Mushroom. *Journal of Sustainable Agriculture and Environment*, 6 (1), 63-70.

Selvi, S., Uma, Devi P., Suja, S., Murugan, S. and Chinnarswamy, P. (2007). Comparison of non-enzymic antioxidant status of fresh and dried form of *Pleurotus florida* and *Calocybe indica. Pakistan Journal of Nutrition*, 6 (5), 468-471.

Ukoima, H.N., Ogbonnaya, L. O., Arikpo, G. E. and Ikpe, F. N. (2009). Cultural studies of mycelia of *Volvariella volvacea*, *Pleurotus tuber-regium* and *Pleurotus sajor caju* on different culture media. *Pakistan Journal of Nutrition,* 8 (7), 1052-1054.

Yusuf AA, Ayedun H and Sanni LO (2008). Chemical composition and functional properties of raw and roasted Nigerian benniseed (*Sesamum indicum*) and Bambara groundnut ((*Vigna ubterranean*). Food Chem., 111: 277-282.

CHARACTERISATION, PERFORMANCE EVALUATION AND MODELLING OF SINGLE-CRYSTAL PHOTOVOLTAIC MODULE IN MINNA, NIGERIA

[1]Ezenwora Joel Aghaegunam,* [2]Oyedum David Onyedi and [3]Ugwuoke Paulinus Ekene
[1, 2]Department of Physics, Federal University of Technology, Minna, Nigeria.
[3]National Centre for Energy Research and Development, University of Nigeria, Nsukka.
[1]aghaegbunam@yahoo.com
[2]oyedumod@yahoo.com
[3]peugwuoke@yahoo.com
*corresponding author

Abstract
The performance response of single-crystal silicon Photovoltaic (PV) module to atmospheric parameters of solar irradiance, temperature, wind speed and relative humidity, was investigated in local environment (Minna, Nigeria), using Campbell Scientific CR1000 software-based data acquisition system. The PV module under test and meteorological sensors were installed on a metal support structure at the same test plane. The data monitoring was from 08.00 to 18.00 hours (sunrise to sunset) each day continuously for a period of one year, from December 2014 to November 2015. Maximum value of module efficiency of 5.86% for the single-crystal module was recorded at irradiance of 375 W/m^2. At 1000 W/m^2 the efficiency reduced to 3.30 %, as against manufacturer's specification of 46 % for the module. The maximum power output achieved for the module at irradiance of 1000 W/m^2 was 0.711 W representing 7.11 % of the manufacturer's power specification for the module. Accordingly, Module Performance Ratio (MPR) for the PV module is 0.07. The rate of variation of module response variables with irradiance and temperature was determined using a linear statistical model given as $Y = a + bHg + c\,Tmod$. The coefficient of determination for the fits for the performance variables are: 82.8 %, 92.6 %, 81.0 % and 90.7 % for the open-circuit voltage, short-circuit current, power and maximum power respectively. The overall lack of fit tests for these performance variables is significant at probability, P value of 0.000, signifying good fits.

Keywords - Ambient, Module, Photovoltaic, Single-Crystal, Statistical-model

1.0 Introduction

The need to characterise and evaluate the performance of photovoltaic modules in order to ensure optimal performance and technical quality in photovoltaic power systems has been pointed out (Almonacid *et al*., 2009). Standard Test Condition (STC) hardly occur outdoors, therefore the effect of deviation of meteorological parameters from STC together with the fact that PV modules with actual power smaller than the nominal value can still be found in the market lend credence to this. Essentially, PV power system design involves electrically-matching power components and ultimately, the power supply to the load. STC are easily recreated in a factory, and allow for consistent comparisons of products, but need to be modified to estimate output under common outdoor operating conditions. Module output power reduces as module temperature increases. The rate of decrease of output power with temperature for a particular locality ought to be understood and the loss factor for each module type in every location established. These loss factors need to be documented and applied in order to effectively estimate system output and sizing before installation. This will lead to the design and installation of efficient PV power system that is reliable, dependable and durable. In developed world such as the United States of America (USA) which is a lead actor in PV research, there have been efforts to conduct outdoor tests of modules and array performance since 1976 through the Sandia National Laboratory (California Energy Commission, 2001). The US has effectively

established and documented loss factors for all losses affecting PV power systems for all PV module types and for every location.

Realistic outdoor performance analysis of various types of modules is needed in developing countries such as Nigeria, in order to be able to effectively design and size arrays for different applications and sites. It is no longer news that Nigeria is an energy resource rich country, blessed with both fossil fuel reserves such as crude oil, natural gas, coal, and renewable energy resources like solar, wind, biomass, biogas and hydropower resources. It is also true that despite the abundance of these energy resources in Nigeria, the country is in short supply of electrical power. There is supply-demand gap particularly in view of the growing energy demand in the domestic, commercial and industrial sectors of the economy, and the reason for this is not farfetched. The National energy supply is at present almost entirely dependent on fossil fuels, firewood (which are depleting fast) and hydropower. The capacity utilisation of hydropower plants over the recent years has been reduced at about 30% only (Umar, 1999). According to Umar (1999), Grid power generation capacity in Nigeria as at 1990s was about 1,800 MW or 31% of the installed capacity and according to Okafor and Joe-Uzuegbu (2010), less than 40% of the 150 million Nigerians in the country were supplied electricity from the national grid in the urban centres while in the rural centres, where about 70% of the population live, the availability of electricity dropped to 15%. Nigeria with an annual population growth rate of about 2.8% (according to 2006 population census), the total Electricity generation capacity as at 2010 stood at less than 4000 MW with per capita consumption of 0.03 kW. With these figures, the level of shortage in Electricity supply becomes evident, resulting in consistent unreliability and epileptic nature of electricity supply in the country.

While the initial capital investment may be higher, PV power system provides electrical power at less cost than electricity from generator, based on life-cycle cost. Because it has an added advantage of requiring little maintenance, low running costs and being environmentally friendly. PV power is the most reliable source of electricity ever invented and it is portable, easily installed, and virtually maintenance-free (Midwest Renewable Energy Association Fact Sheet, 2013). Therefore, this study was carried out to determine the realistic outdoor performance of single-crystal silicon PV module in Minna environment for effective design and sizing of PV power system.

2.0 Methodology

2.1 Monitoring Stage

The performance response of single-crystal silicon PV module to ambient weather parameters; solar irradiance, temperature, wind speed and relative humidity, was monitored in Minna environment, using CR1000 software-based data logging system with computer interface. The PV module under test, and meteorological sensors, were installed on support structure at the same test plane, at about three metres of height, so as to ensure adequate exposure to insolation and enough wind speed, since wind speed is proportional to height (Ugwuoke, 2005). The elevation equally ensures that the system is free from any shading from shrubs and also protected from damage or interference by intruders. Also, the whole experimental set up was secured in an area of about four metres in diameter. The modules were tilted at approximately 10^{o} (since Minna is on latitude $09^{o}37'$ N) to horizontal and south-facing to ensure maximum insolation (Strong and Scheller, 1991; Ugwuoke *et al*., 2005).

The data monitoring was from 08.00 to 18.00 hours local time, each day continuously for a period of one year, spanning from December 2014 to November 2015, so as to cover the two distinct and well

defined climate seasons of the area. The experiment was carried out near Physics Department, Federal University of Technology, Minna (latitude 09°37' N, longitude 06°32' E and 249 metres above sea level). The sensors were connected directly to the CR1000 Campbell Scientific data logger, while the module was connected to the logger via electronic load specifically designed for the module. The logger was programmed to scan the load current from 0 to 1 A at intervals of 50 mA every 5 minutes, and average values of short-circuit current, I_{sc}, open-circuit voltage, V_{oc}, current at maximum power, I_{max}, voltage at maximum power, V_{max}, power and maximum power obtained from the module together with the ambient parameters are recorded and logged. Data download at the data acquisition site was performed every 7 days to ensure effective and close monitoring of the data acquisition system (DAS). At the end of each month and where necessary, hourly, daily and monthly averages of each of the parameters - solar (global) irradiance, solar insolation, wind speed, ambient and module temperatures, and the output response variables (open-circuit voltage, V_{oc}, short-circuit current, I_{sc}, voltage at maximum power, V_{max} , current at maximum power, I_{max}, efficiency, Eff and fill factor, FF) of the photovoltaic module was obtained. The global solar radiation was monitored using Li-200SA M200 Pyranometer, manufactured by LI-COR Inc. USA, with calibration of 94.62 microamperes per 1000 W/m^2. The ambient temperature and relative humidity were monitored using HC2S3-L Rotronic HygroClip2 Temperature/Relative Humidity probe, manufactured in Switzerland. Wind speed was monitored using 03002-L RM Young Wind Sentry Set. And module temperature was monitored using 110PV-L Surface-Mount Temperature probe. All sensors are installed in the CR1000 Campbell Scientific data logger with measurement and control module. Table 1 shows the manufacturer's specifications at STC of the module investigated while Plate I shows the data acquisition set up.

Table 1: Manufacturer's Specifications at STC and Measured Dimensions of the Solar Module

Cell Technology	No of Cells per Module	Max. Rated Power (W)	Max. Rated Voltage (V)	Max. Rated Current (A)	Open-Circuit Voltage (V)	Short-Circuit Current (A)	Module Dimensions (m x m)	Cell Dimensions (m x m)	Total Surface Area of Cells(m^2)	Model/ Make	Eff (%)
Single-Crystal Module	72 Cells of 4 parallel and 18 series	10	17.4	0.57	21.6	0.65	0.29 x 0.16	0.025 x 0.012	0.0216	SLP 10-12 /China	46*

*Module efficiency was calculated because it was not included in the manufacturer's specifications

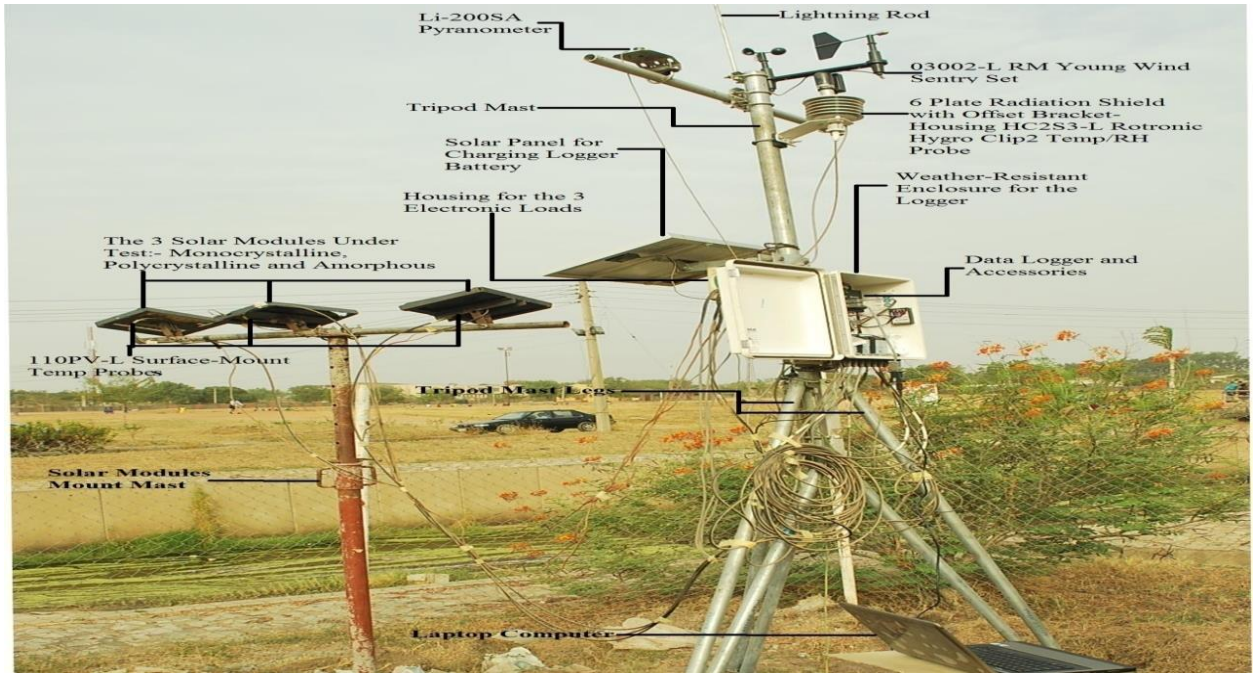

Plate I: The Experimental Set up (Near Physics Department, FUT Minna)

2.2 Data Analysis

Performance response of the module to ambient weather parameters was investigated in terms of open-circuit voltage, V_{oc}, short-circuit current, I_{sc}, voltage at maximum power, V_{max} , current at maximum power, I_{max} , efficiency, Eff and fill factor, FF. Fill Factor, FF, Efficiency, Eff, and Module Performance Ratio (MPR) were evaluated using the following expressions:

Fill Factor, $FF = I_{max}V_{max}/I_{sc}V_{oc}$ (1)

Efficiency, $Eff = I_{max}V_{max}/P_{in} = I_{sc}V_{oc}FF/P_{in} = I_{sc}V_{oc}FF/AE_e$ (2)

Module Performance Ratio (MPR) = Effective Efficiency/Efficiency at STC (3)

Statistical analysis was carried out with the aid of statistical package; Minitab 17 to determine the rate of variation of module response variables with irradiance and temperature, and linear statistical models for prediction of performance variables are presented. Multiple regression models, analysis of variance (ANOVA) and correlation between the variables were considered with the aim of establishing the statistical significant relationship between the variables and the goodness of fit of the models for the research study. The regression equation is;

$Y = a + bH_g + c\,T_{mod}$, (4)

where Y is the output response parameter being predicted, H_g is global radiation (solar irradiance) and T_{mod} is module temperature. The coefficients b and c are the rates of variation of output variables with respect to irradiance and module temperature, respectively while a is intercept on the Y axis.

The I-V curves were produced by plotting current against voltage produced by the logger in scanning the electronic load current from 0 to 1 A at intervals of 50 mA. The maximum power point, P_{max}, which is the operating point of the module, was equally recorded by the logger.

3.0 Results and Discussion

The output characteristics of the single-crystal silicon PV module as a function of global irradiance are shown in Figure 1. This output characteristics is expressed in the form of I-V curves.

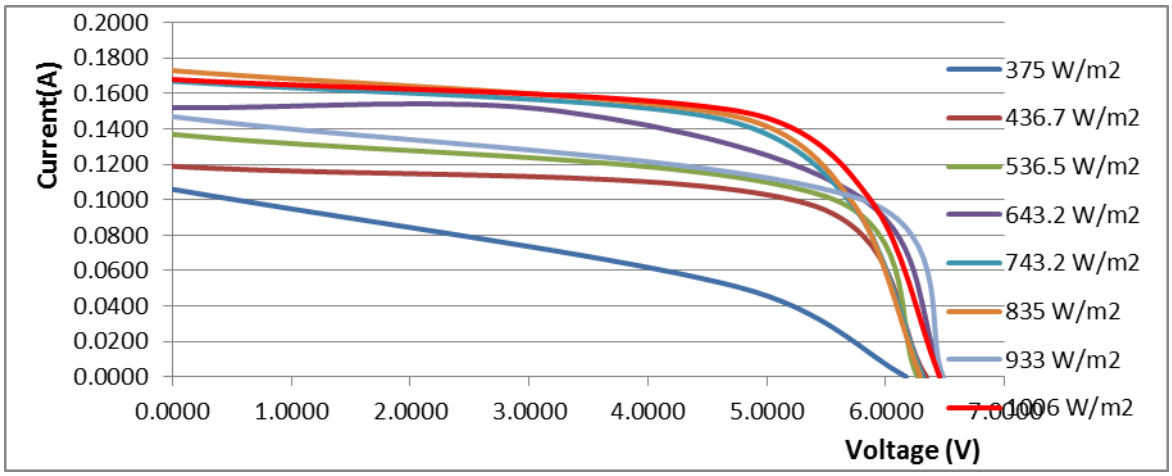

Figure1: I-V Characteristics for the single-crystal silicon module as a function of global irradiance.

Open-circuit voltage, V_{oc}, is seen to increase slowly with increase irradiance. Its increase is not commensurate with increase in irradiance and this explains the bunching of the I-V characteristics curves along voltage axis compared to relative regular spacing along the current axis. This is due to high temperature associated with increase in irradiance which has adverse effect on the open-circuit voltage. On the contrast, the short-circuit current increased generally with irradiance. This contrast in open-circuit voltage and short-circuit current is more glaring in Figures 2 and 3 where these performance variables are compared with module temperature at various irradiance levels.

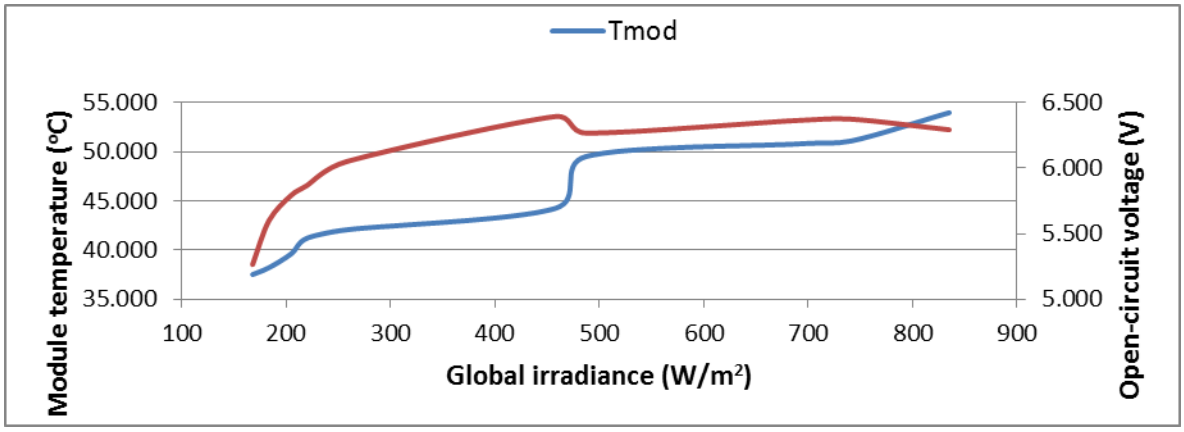

Figure 2: Variation of open-circuit voltage and module temperature as a function of global irradiance for the single-crystal module.

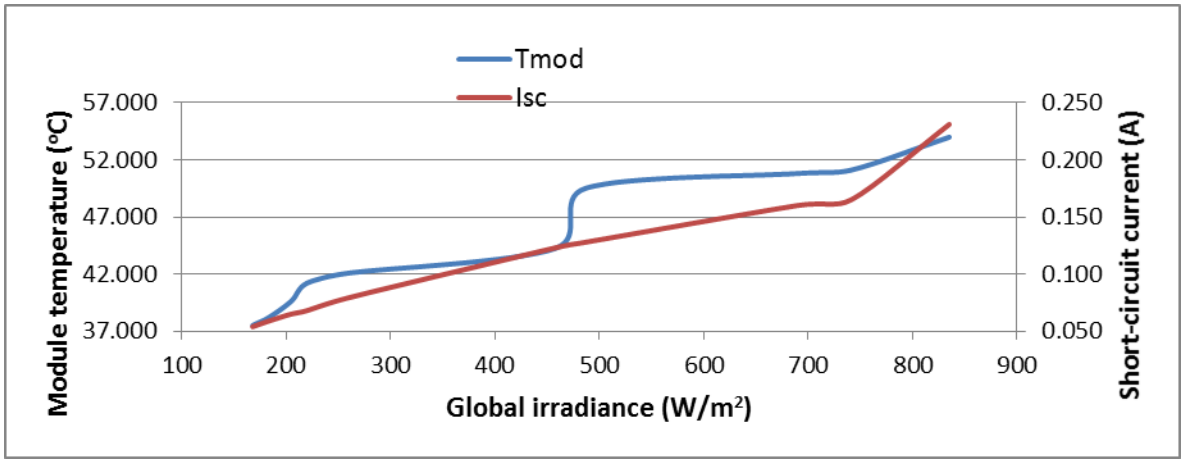

Figure 3: Variation of short-circuit current and module temperature as a function of global irradiance for the single-crystal module.

It is obvious then that the open-circuit voltage does not increase steadily with module temperature and solar irradiance as against short-circuit current that increased linearly. This result is in agreement with Ugwuoke and Okeke (2012) and other researchers in the field.

The relationship of maximum power point (MPP) and efficiency to temperature variations was investigated and shown in Figures 4 and 5 respectively.

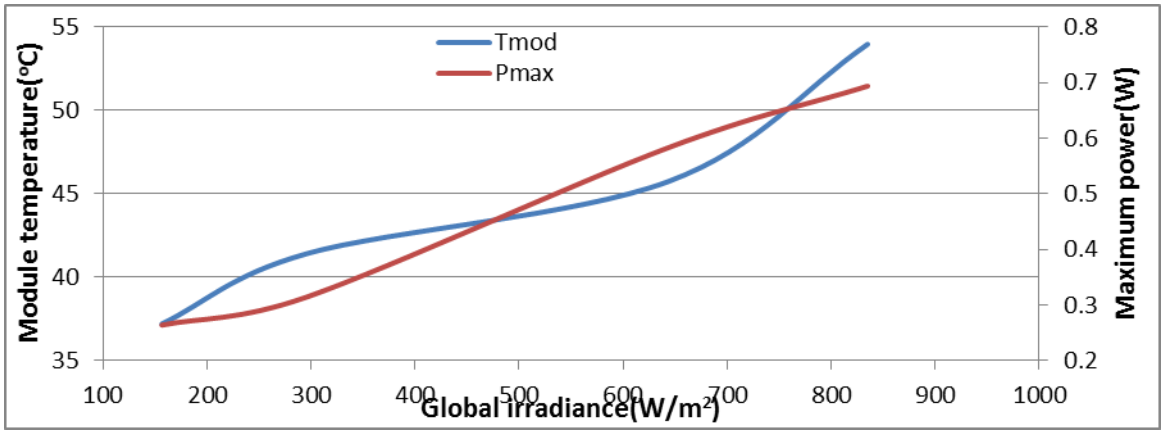

Figure 4: Variation of Maximum Power Point (MPP) and module temperature at different levels of irradiance for the single-crystal module

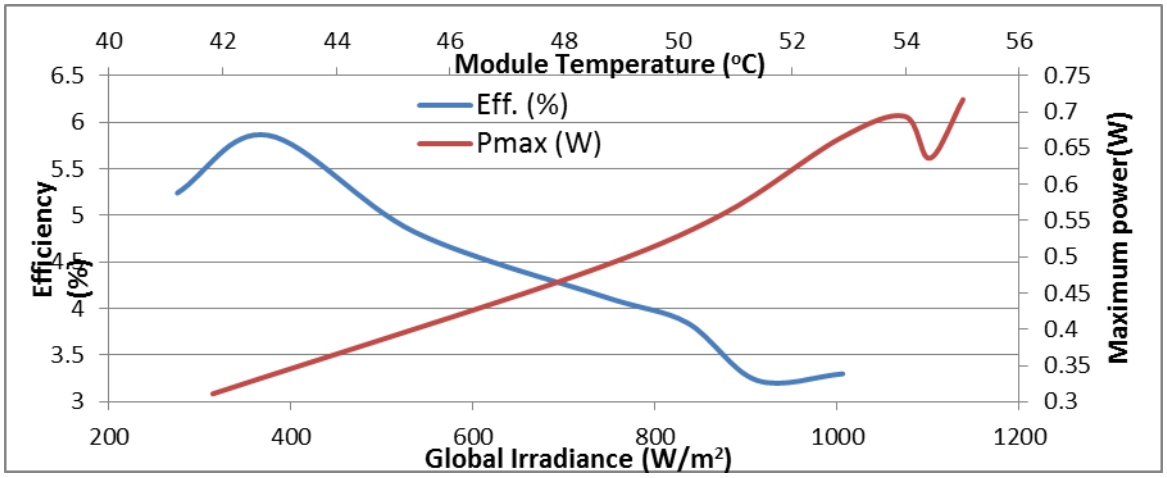

Figure 5: Variation of efficiency and maximum power point as a function of global irradiance and module temperature for the single-crystal module

It was observed that the maximum power, like the short-circuit current, increased steadily with increased solar irradiance and module temperature for the single-crystal, suggesting that maximum power is more correlated to current than voltage for the measured range of solar irradiance. As shown in these Figures the maximum power point increases with increase in solar irradiance of about 900 W/m^2. This explains the inclusion of Maximum Power Point Tracker (MPPT) in some photovoltaic power system components. Maximum power point and efficiency show symmetrical structure at irradiance of about 650 W/m^2. This is in agreement with some earlier works (Bajpai and Gupta, 1986; Ugwuoke, 2005).

Monthly hourly averages of open-circuit voltage, short-circuit current, power output and maximum power were investigated and the plots for a typical dry season month (January) and a typical rainy season month (August) are shown in Figures 6 to 9.

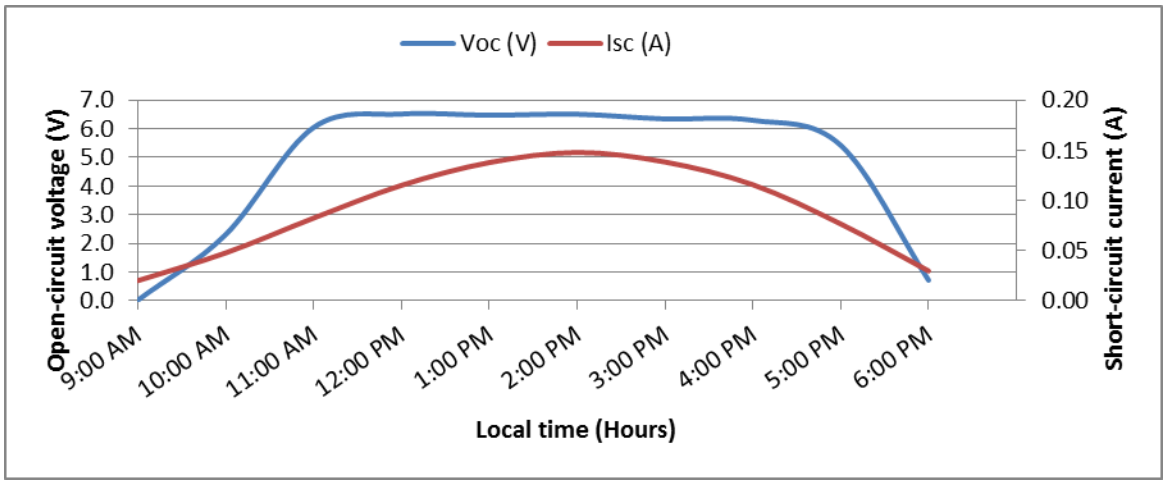

Figure 6: Hourly average variation of open-circuit voltage and short-circuit current of the single-crystal silicon module as a function of time for the month of January 2015

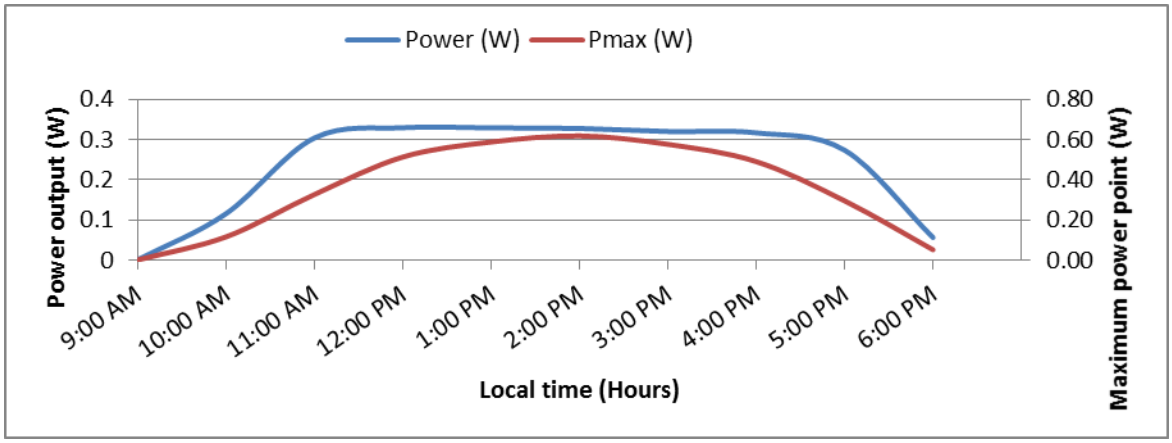

Figure 7: Hourly average variation of power and maximum power of single-crystal silicon module as a function of time for the month of January 2015

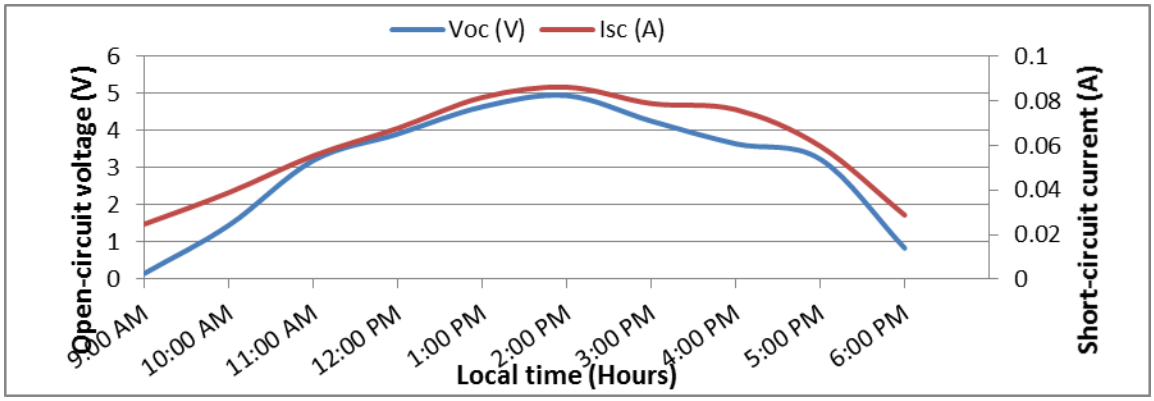

Figure 8: Hourly average variation of open-circuit voltage and short-circuit current of single-crystal silicon module as a function of time for the month of August 2015

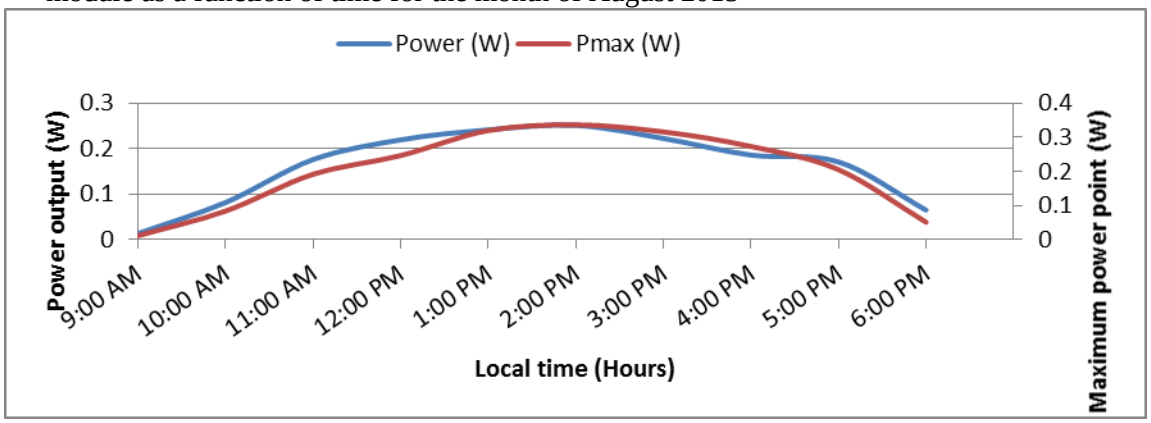

Figure 9: Hourly average variation of power and maximum power of single-crystal silicon module as a function of time for the month of August 2015

It was observed that open-circuit voltage peaks earlier in the day than short-circuit current for the single-crystal. The open-circuit voltage peaks at local noon time for the typical dry season month of January and then for the typical rainy season month of August, open-circuit voltage peaks at 2:00 pm local time. On the other hand the short-circuit current maintains a steady peak time of 2:00 pm local time for the two seasons. This is in the afternoon time when the module temperature is high, confirming that short-circuit current has a linear relationship with module temperature and solar irradiance. It is equally observed that power output peak time coincides with open-circuit voltage peak time and maximum power peak time coincides with short-circuit current peak time for the single-crystal silicon module. Thus, confirming earlier suggestion that current is more correlated to maximum power than voltage and the well known fact that output voltage and power of crystalline silicon photovoltaic modules decreases at high temperatures as their module temperature increases. This is further alluded to by the shape of the curves of these performance variables as seen in the Figures.

Hourly average values of the module performance variables and ambient parameters for the one year duration of this study are shown in Tables 2.

Table 2: Annual hourly averages of ambient parameters and performance variables for the single-crystal silicon module

T (Hours)	H_g (W/m^2)	T_a (^oC)	T_{mod} (^oC)	V_{oc} (V)	I_{sc} (A)	Power (W)	P_{max} (W)	RH (%)	WS (m/s)
9:00 AM	258	26.5	28.2	0.58	0.030	0.032	0.031	65.3	1.99

10:00 AM	427	27.8	32.2	3.13	0.057	0.163	0.176	61.8	2.18
11:00 AM	569	29.1	36.1	5.27	0.085	0.269	0.330	54.5	2.17
12:00 PM	666	30.3	39.6	5.69	0.109	0.289	0.443	53.2	2.08
1:00 PM	708	31.3	42.3	5.90	0.124	0.299	0.502	51.5	2.02
2:00 PM	696	32.2	43.9	5.95	0.130	0.301	0.521	48.8	1.93
3:00 PM	608	32.7	43.5	5.67	0.120	0.290	0.484	47.3	1.87
4:00 PM	482	33.0	42.1	5.41	0.101	0.276	0.408	45.7	1.82
5:00 PM	309	32.9	38.9	4.33	0.068	0.224	0.246	44.9	1.71
6:00 PM	139	31.9	33.8	0.80	0.030	0.057	0.053	46.2	1.59

The monthly average values of solar irradiance, wind speed and relative humidity together with open-circuit voltage, short-circuit current, maximum power and module temperature for the single-crystal module is presented in Table 3.

Table 3: Monthly average values of ambient parameters and performance variables

Month	H_g (W/m^2)	WS (m/s)	RH (%)	V_{oc} (V)	I_{sc} (A)	P_{max} (W)	T_{mod} (^oC)
Dec 14	509.5	1.68	32.08	4.621	0.088	0.343	38.01
Jan 15	529.8	1.99	25.97	4.620	0.091	0.352	36.54
Feb 15	529.6	1.59	32.06	4.282	0.085	0.311	41.66
Mar 15	537.6	1.88	33.14	4.272	0.084	0.311	41.57
Apr 15	569.0	1.70	31.99	4.683	0.095	0.354	42.96
May 15	509.9	1.81	55.87	4.499	0.085	0.319	38.54
Jun 15	424.3	1.74	71.40	3.695	0.069	0.244	34.33
Jul 15	415.7	1.68	73.14	3.533	0.070	0.243	34.29
Aug 15	326.4	1.45	81.08	3.020	0.060	0.195	31.90
Sep 15	415.8	1.47	74.15	3.936	0.080	0.283	35.42
Oct 15	479.9	1.39	70.18	4.621	0.097	0.358	38.96
Nov 15	557.9	1.41	35.34	5.144	0.116	0.441	42.48

It was observed here that wind speed peaked in the month of January, during the dry season of the study area, normally characterised by strong North-East trade wind and favours open-circuit voltage more than short-circuit current (amidst other factors). Also it is observed that module temperature recorded relatively low value, vis-a-vis their irradiance levels during this month. This is because high wind speed leads to increased rate of heat transfer from the module to the ambient resulting in the low module temperature. Relative humidity peaked in the month of August, which is the peak of rainy season of the study area and leads to lowest insolation level also witnessed in this month because increased water content in the atmosphere gives rise to cloudy weather which results in the absorption and scattering of sun's rays. Other factors being equal, high relative humidity brings about low module temperature which would normally favour open-circuit voltage more than short-circuit current. However, with such high value of relative humidity as recorded in August, its effect becomes domineering and results in very low insolation level that dictates the results of other parameters as is shown in the Table. This explains the lowest recorded values of all the performance variables for the module.

The performance of the single-crystal photovoltaic module at different levels of solar irradiance (global irradiance) for the period studied were summarised in Table 4. Fill factor and efficiency at the different levels of irradiance for the module were also computed and inserted.

Table 4: Summary of performance response for the module at different irradiance levels

Irradiance (W/m^2)	V_{oc} (V)	I_{sc} (A)	P_{max} (W)	V_{max} (V)	I_{max} (A)	FF	Eff (%)
276	6.12	0.083	0.311	6.12	0.051	0.615	5.24
375	6.17	0.106	0.475	4.74	0.100	0.725	5.86
437	6.34	0.119	0.523	5.33	0.098	0.693	5.55
537	6.27	0.137	0.558	5.49	0.102	0.651	4.82
643	6.48	0.152	0.583	5.82	0.100	0.592	4.20
743	6.31	0.167	0.663	4.51	0.147	0.629	4.13
835	6.29	0.173	0.694	4.68	0.148	0.638	3.85
912	6.26	0.158	0.636	4.27	0.149	0.643	3.23
933	6.48	0.147	0.578	5.81	0.100	0.609	2.88
1000	6.51	0.160	0.711	4.69	0.152	0.684	3.30

T_{mod} = 45.34°C

MPR = 0.07

Pmax (%) = 7.11%

For comparison between the outdoor module performance and the Standard Test Condition (STC) specifications, module performance ratio (MPR), module temperature and maximum power at 1000 W/m^2 are equally presented. The maximum power output achieved for the module at 1000 W/m^2 was 0.711 W representing 7.11 % of the manufacturer's power specifications for the single-crystal photovoltaic module. Module efficiency is seen to decrease steadily as solar irradiance increased with maximum value of 5.86 % at irradiance of 375 W/m^2. This maximum value then decreased steadily with increased irradiance and at 1000 W/m^2 the efficiency reduced to 3.30 % as against manufacturer's specification of 46 %. Open-circuit voltage at 1000 W/m^2 was 6.51 V as against manufacturer's specification of 21.6 V, while the short-circuit current was 0.160 A as against manufacturer's specification of 0.65 A. Maximum current, I_{max} recorded 0.152 A, as against STC value of 0.57 A. Therefore, module performance ratio for the PV module under investigation is 0.07 and it was equally observed here that the module did not record module temperature of 25 °C at 1000 W/m^2 solar irradiance as usually assumed for STC condition, rather, as seen in Table 4, the module temperature is well beyond 25 °C in the local environment. It is then quite clear and obvious, given the enormous margin of deviation of the outdoor characterised values from the manufacturer's STC specifications, that STC data is suspect; it is only handy in making comparison among solar modules. Designing with manufacturer's STC data will produce an unreliable and defective PV power system. In addition, over specified modules are flooding our local market.

3.1 Results of Statistical Analysis and Models

Models for V_{oc}, I_{sc}, P and P_{max} were analysed in this section.
The regression equation for V_{oc} is

$$V_{oc} = -3.40 + 0.00672\, H_g + 0.115\, T_{mod}, \quad (5)$$

where H_g is solar (global) irradiance and T_{mod} is module temperature

Table 5: Predictor coefficient for the independent variables and the T-test value for equation 5

Predictor	Coefficient	SE Coefficient	T-test	P-value	VIF
Constant	-3.3952	0.5943	-5.71	0.000	
H_g	0.0067167	0.0006281	10.69	0.000	2.0
T_{mod}	0.11520	0.02029	5.68	0.000	2.0

From Table 5 the coefficient of H_g and T_{mod} are statistically significant since the P-value =0.000 is less than 0.05(5%) level of significance and from equation 5, V_{oc} – axis has an intercept of -3.40, and for every unit increase in H_g there is an increase of 0.00672, also for every unit increase in T_{mod}, there is a positive increase of 0.115 in the model.

Table 6: Regression Analysis of variance (ANOVA) of the model for equation 5

Source	Degree of freedom	Sum squares	Mean square	F-test	P-value
Regression	2	388.05	194.02	234.11	0.000
Residual Error	97	80.39	0.83		
Total	99	468.44			

S = 0.910367 R-Sq = 82.8% R-Sq (adj) = 82.5%

From Table 6, since the P-value = 0.000 is less than 5% (0.05) level of significance; it can be concluded that there is statistical significant difference in the contributions of the variables H_g and T_{mod} in the model. This is further explained by the coefficient of determination R^2= 82.8% that is 82.8% of the variable was explained by the model, while only 17.2% was unexplained. The model in equation 5 is a good model. Overall lack of fit test is significant at P = 0.000. Scatter plot of Voc versus H_g and T_{mod} is shown in Figure 10 below.

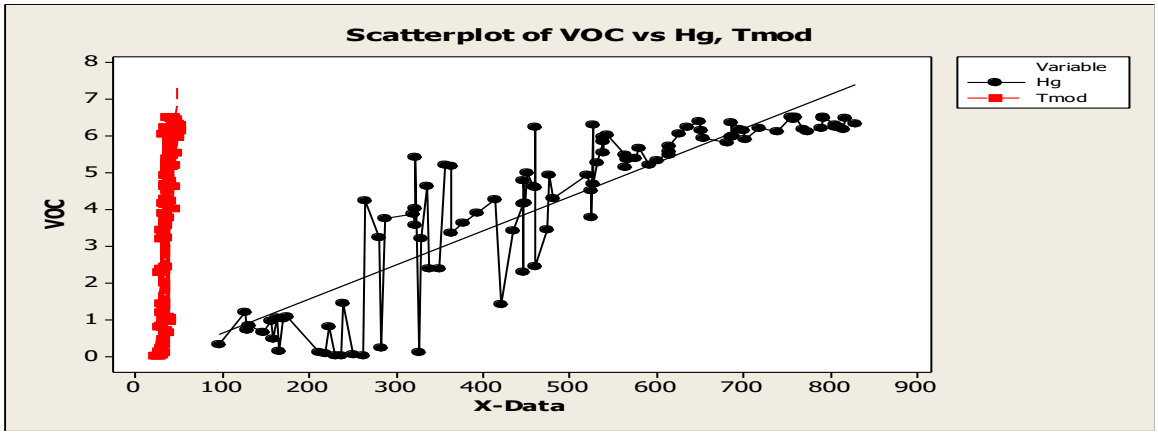

Figure 10: Scatter plot of V_{oc} versus H_g and T_{mod} for the single-crystal module

The regression equation for I_{sc} is

$$I_{sc} = - 0.0616 + 0.000115\ H_g + 0.00233\ T_{mod}, \quad (6)$$

Table 7: Predictor coefficient for the independent variables and the T-test value for equation 6

Predictor	Coefficient	SE Coefficient	T-test	P-value	VIF
Constant	-0.061650	0.006686	-9.22	0.000	
H_g	0.00011516	0.00000707	16.30	0.000	2.0
T_{mod}	0.0023272	0.0002283	10.20	0.000	2.0

From Table 7 the coefficient of H_g and T_{mod} are statistically significant since the P-value = 0.000 is less than 0.05 (5%) level of significance. And from equation 6, I_{sc} – axis has an intercept of -0.0616, and for every unit increase in H_g there is an increase of 0.000115; also for every unit increase in T_{mod}, there is a positive increase of 0.00233 in the model.

Table 8: Regression Analysis of variance (ANOVA) of the model for equation 6

Source	Degree of freedom	Sum of Square	Mean Square	F-test	P-value
Regression	2	0.127732	0.063866	608.81	0.000
Residual Error	97	0.010176	0.000105		
Total	99	0.137907			

S = 0.0106970 R-Sq = 92.6% R-Sq (adj) = 92.5%

From Table 8, since the P-value = 0.000 is less than 5% (0.05) level of significance; it can be concluded that there is statistically significant difference in the contributions of the variables H_g and T_{mod} in the model. This is further explained by the coefficient of determination R^2= 92.6% that is 92.6% of the variable was explained by the model, while only 7.4% was unexplained. The model in equation 6 is a good model and no evidence of lack of fit since P <= 0.1000. The scatter plot of I_{sc} versus H_g and T_{mod} is shown in Figure 11.

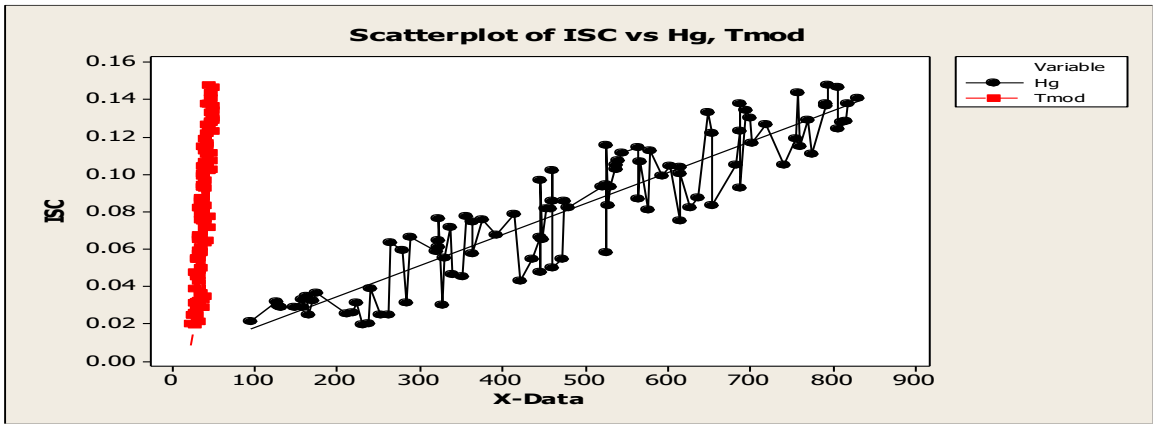

Figure 11: Scatter plot of I_{sc} versus H_g and T_{mod} for the single-crystal module

The regression equation for P is

$$P = - 0.156 + 0.000320\ H_g + 0.00577\ T_{mod}, \quad (7)$$

Table 9: Predictor coefficient for the independent variables and the T-test value for equation 7

Predictor	Coefficient	SE Coefficient	T-test	P-value	VIF
Constant	-0.15632	0.03068	-5.10	0.000	
H_g	0.00032004	0.00003242	9.87	0.000	2.0
T_{mod}	0.005772	0.001047	5.51	0.000	2.0

From Table 9, the coefficient of H_g and T_{mod} are statistically significant since the P-value =0.000 is less than 0.05 (5%) level of significance. And from equation 7, P – axis has an intercept of -0.156, and for every unit increase in H_g there is an increase of 0.000320, also for every unit increase in T_{mod}, there is a positive increase of 0.00577 in the model.

Table 10: Regression Analysis of variance (ANOVA) of the model for equation 7

Source	Degree of freedom	Sum of Squares	Mean Square	F-test	P-value
Regression	2	0.91065	0.45532	206.14	0.000
Residual Error	97	0.21425	0.00221		
Total	99	1.12490			

S = 0.0469974 R-Sq = 81.0% R-Sq (adj) = 80.6%

From Table 10, since the P-value = 0.000 is less than 5% (0.05) level of significance; it can be concluded that there is statistically significant difference in the contributions of the variables H_g and T_{mod} in the model. This is further explained by the coefficient of determination R^2= 81.0% that is 81.0% of the variable was explained by the model, while only 19.0% was unexplained. The model in equation 7 is a good model. Overall lack of fit test is significant at P = 0.000.

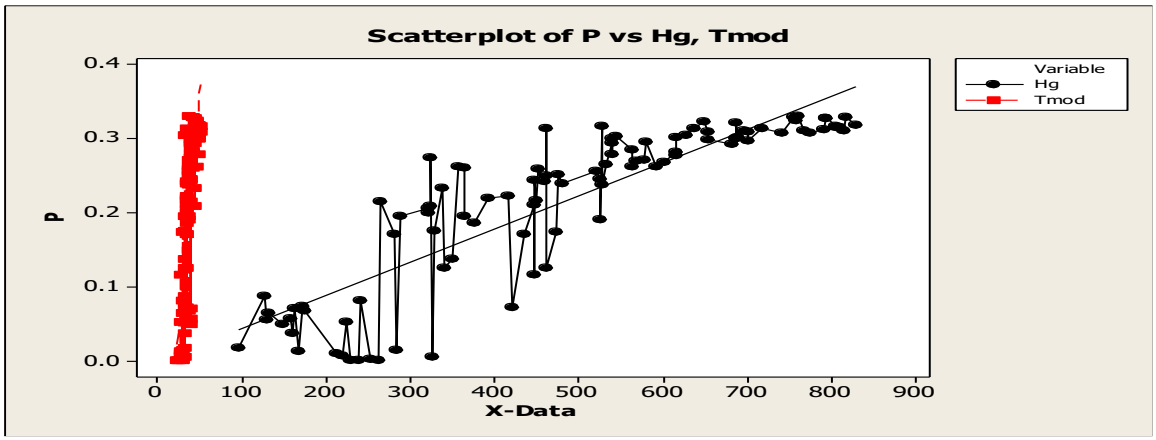

Figure 12 Scatter plot of P versus H_g and T_{mod} for the single-crystal module

The regression equation for P_{max} is

$$P_{max} = - 0.389 + 0.000579\, H_g + 0.0110\, T_{mod}, \quad (8)$$

Table 11: Predictor coefficient for the independent variables and the T-test value for equation 8

Predictor	Coefficient	SE Coefficient	T-test	P-value	VIF
Constant	-0.38915	0.03737	-10.41	0.000	
H_g	0.00057864	0.00003949	14.65	0.000	2.0
T_{mod}	0.011029	0.001276	8.65	0.000	2.0

From Table 11 the coefficient of H_g and T_{mod} are statistically significant since the P-value = 0.000 is less than 0.05(5%) level of significance. From equation 8, P_{max}– axis has an intercept of -0.389, and for every unit increase in Hg there is an increase of 0.000579; also for every unit increase in T_{mod}, there is a positive increase of 0.011029 in the model.

Table 12: Regression Analysis of variance (ANOVA) of the model for equation 8

Source	Degree of freedom	Sum of Squares	Mean Square	F-test	P-value
Regression	2	3.0922	1.5461	471.85	0.000
Residual Error	97	0.3178	0.0033		
Total	99	3.4101			

S = 0.0572423 R-Sq = 90.7% R-Sq (adj) = 90.5%

From Table 12, since the P-value = 0.000 is less than 5% (0.05) level of significance; it can be concluded that there is statistically significant difference in the contributions of the variables H_g and T_{mod} in the model. This is further explained by the coefficient of determination R^2 = 90.7% that is 90.7% of the variable was explained by the model, while only 9.3% was unexplained. The model in equation 8 is a good model. No evidence of lack of fit since P = 0.000.

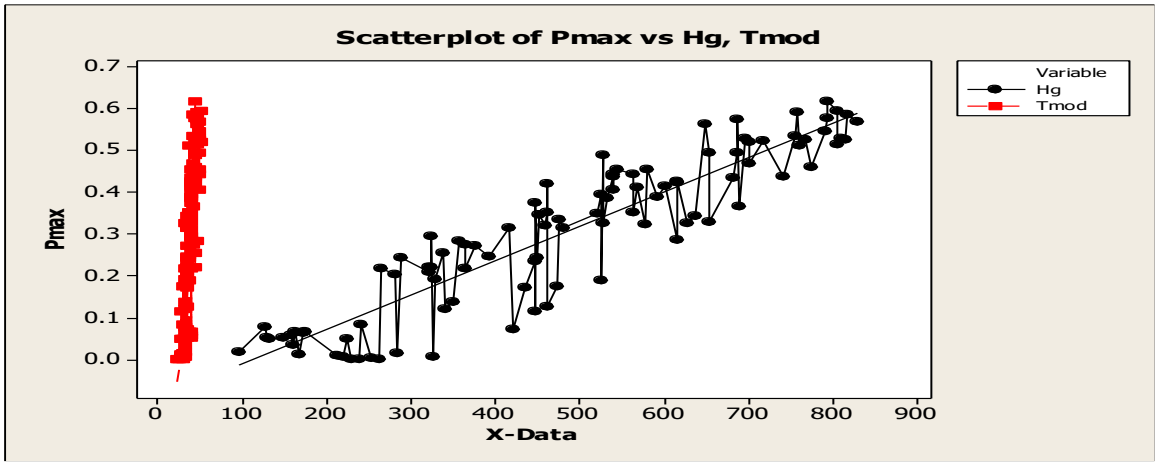

Figure 13 Scatter plot of P_{max} versus H_g and T_{mod} for the single-crystal module

The correlation between the variables T_{mod}, H_g, T_a, RH and WS were computed and the analysis is shown in Table 13.

Table 13: Correlation Matrix of single-crystal Module: T_{mod}, H_g, T_a, RH, and WS

	T_{mod}	H_g	T_a	RH
H_g	0.709 0.000			
T_a	0.261 0.009	0.077 0.444		
RH	-0.477	-0.290	0.080	

	0.000	0.003	0.430	
WS	-0.092	0.419	-0.059	-0.353
	0.365	0.000	0.557	0.000

Cell Contents: Pearson correlation
P-Value

From Table 13, the correlation between T_{mod} and H_g is 0.71 which is substantially high, show a high positive linear relationship between the variable T_{mod} and H_g, furthermore there is significant relationship in the variables at 5% level of significant with P-value = 0.000. However, there are low correlation among T_a and T_{mod} of 0.26, T_a and H_g of 0.08, RH and T_{mod} of -0.48, RH and H_g of -0.3, RH and T_a of 0.08. Similarly, there are low correlation between WS and T_{mod} of -0.09, WS and H_g 0.42, WS and T_a of -0.06, WS and RH of -0.35.

3.2 Comparison between Measured and Predicted Performance Variables

The predicted performance variables at different levels of irradiance and module temperature were plotted with the measured variables for the single-crystal silicon module and presented in Figures 14 – 17. Here it is seen that the predicted short-circuit current shows exact profile with the measured short-circuit current. This again confirms that output current of the PV module has linear relationship with solar irradiance and module temperature while output voltage and power have non-linear relationship with these ambient parameters.

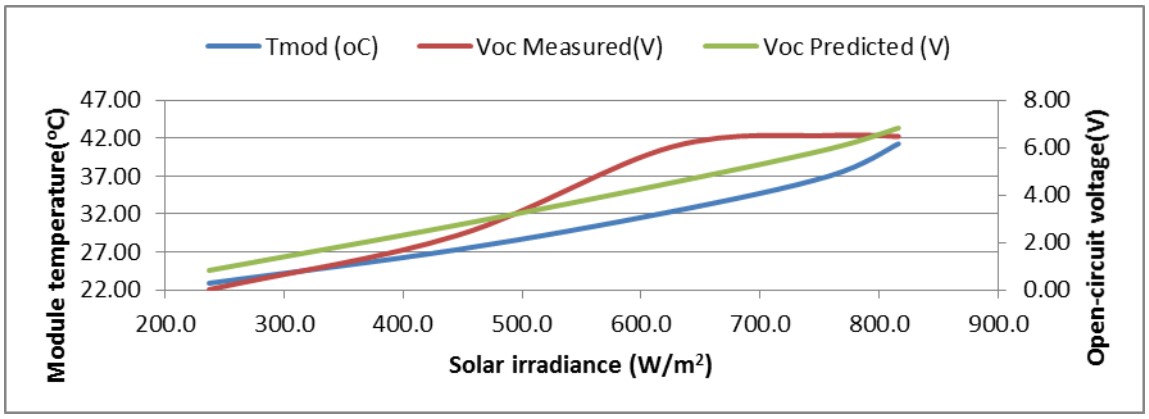

Figure 14: Measured and predicted open-circuit voltage with module temperature as a function of solar irradiance for the single module

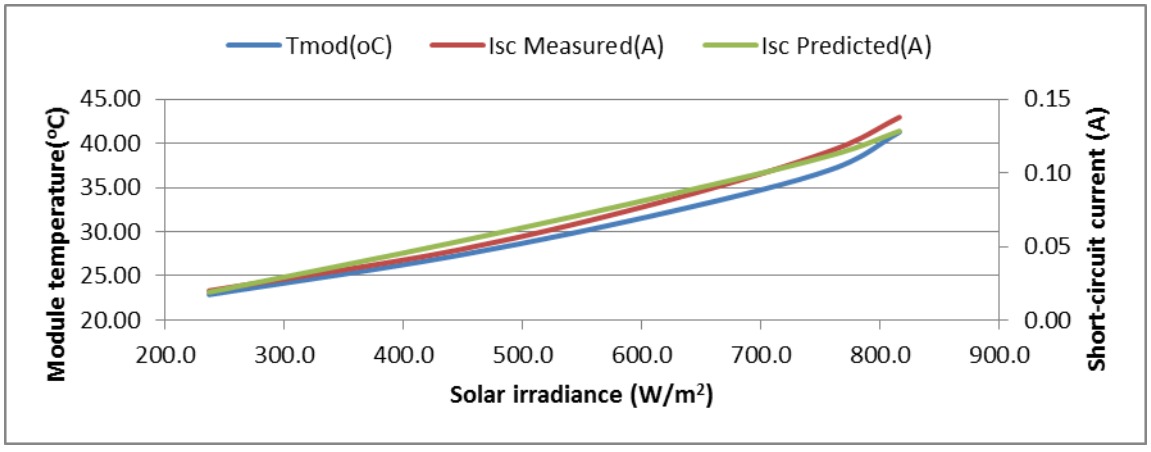

Figure 15: Measured and predicted short-circuit current with module temperature as a function of solar irradiance for the single-crystal module

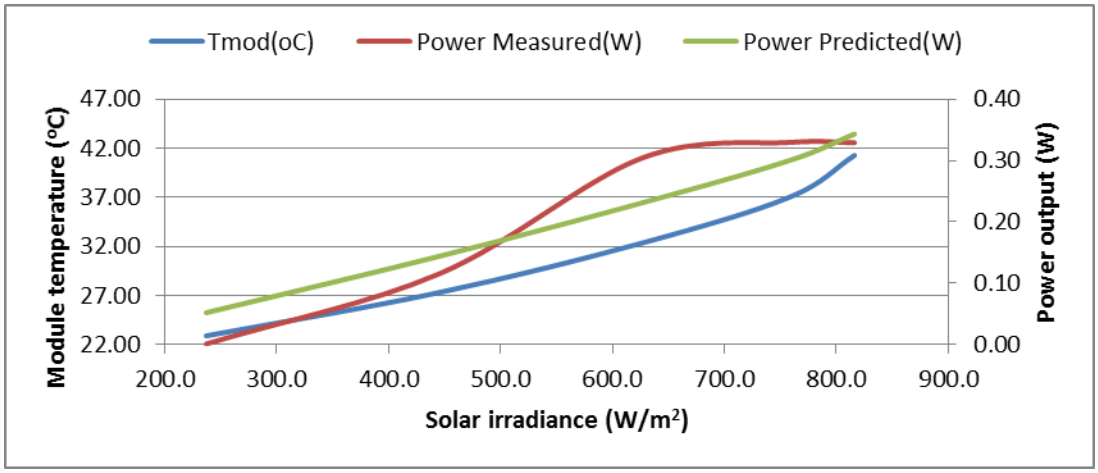

Figure 16: Measured and predicted power output with module temperature as a function of solar irradiance for the single-crystal module

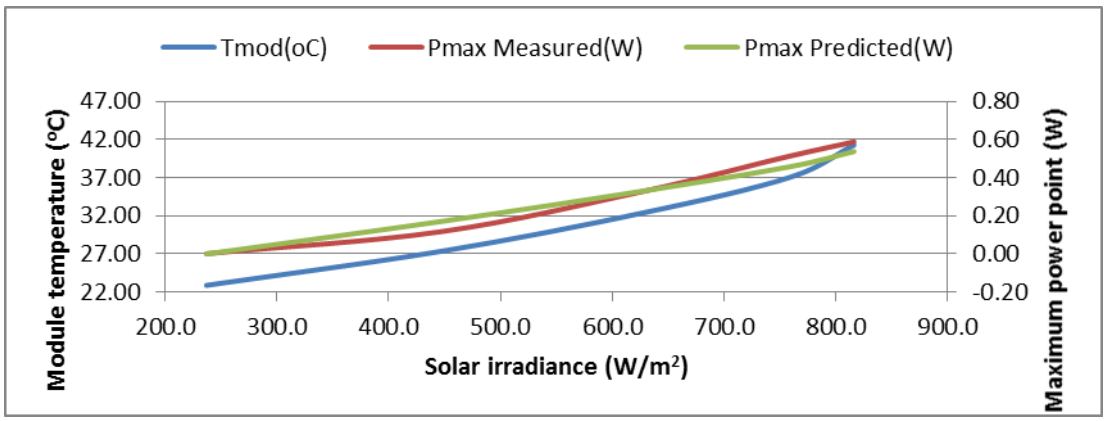

Figure 17: Measured and predicted maximum power with module temperature as a function of solar irradiance for the single-crystal module

4.0 Conclusion

The outdoor characterisation and performance evaluation of the single-crystal photovoltaic module in Minna local environment reveals that actual values of performance variables of the module differ greatly from the manufacturer's specifications. The magnitude of the difference between STC specification and the realistic outdoor performance, in this particular study, points to the fact that over specified modules are entering our local market. The maximum power output achieved for the module at irradiance of 1000 W/m^2 was 0.711 W representing 7.11 % of the manufacturer's power specification. While maximum efficiency peaked at irradiance of 375 W/m^2 with efficiency value of 5.86 %. This maximum value then dropped steadily with increase in irradiance and, at 1000 W/m^2, reduced to 3.30 % as against manufacturer's specifications of 46 %. Similarly, it was observed that the module did not record 25^{o}C module temperature at irradiance of 1000 W/m^2 as used in STC specifications by the manufacturer. Module temperature was therefore observed to have significant influence on the general performance of the module. In addition to the temperature effects on the performance of the module, some non-intrinsic effects like module mismatch, dust and ohmic losses can contribute to some fraction of the observed reduction in output performances (Causi *et al.*, 1995; Ugwuoke *et al.*, 2012).

The prediction models at different levels of irradiance and module temperature for the performance variables resulting from this work are all good, judging by statistical index, and are as follows:

$V_{oc} = - 3.40 + 0.00672\ H_g + 0.115\ T_{mod}$,

$I_{sc} = - 0.0616 + 0.000115\ H_g + 0.00233\ T_{mod}$,

$P = - 0.156 + 0.000320\ H_g + 0.00577\ T_{mod}$,

$P_{max} = - 0.389 + 0.000579\ H_g + 0.0110\ T_{mod}$,

4.1 Recommendation/Suggestion

It is recommended that outdoor characterisation and performance evaluation of all commercially available PV modules be carried out in every location of developing countries where this is lacking. Results should be collated, adopted and installers of PV power systems made to abide by the regulations thereof to ensure technical quality. Also government should put adequate mechanism in place to checkmate over specified PV modules and dumping.

References

Almonacid, F., Rus, C., Hontoria, L., Fuentes, M. and Nofuentes, G. (2009). Characterisation of Single-Crystalline Modules by Artificial Neural Networks, *Journal of Renewable Energy*, 34 (4): 941-949.

Bajpai, S.C. & Gupta, R.C. (1986). Effects of Temperature Changes on the Performance of Single-crystalline Solar Cells. *Nigerian Journal of Solar Energy*, 5: 35-41.

California Energy Commission: Energy Development Division. (2001). A Guide to PV System Design and Installation, California, USA.

Causi Li, S., Messana, C., Noviella, G., Paretta, A. & Sarno, A. (1995). Performance Analysis of Single Crystal Silicon Modules in Real Operating Conditions. *In Proceedings of 13th European Photovoltaic Solar Energy Conference (EUPVSEC)*, Nice, France, pp 11-14.

Midwest Renewable Energy Association Fact Sheet: Off Grid PV Systems (2013). Accessed from www.doe.erec@nciinc.com, on 13th May, 2013.

Okafor, E.N.C. & Joe-Uzuegbu, C.K.A. (2010). Challenges to Development of Renewable Energy for Electric Power Sector in Nigeria. *International Journal of Academic Research*, 2 (2), 211-216.

Strong, S.J. & Scheller, W.G. (1991). "*The Photovoltiac Room*". 2nd ed. Sustainability Press, Chap. 2, Massachusetts, pp 5-7.

Ugwuoke, P.E. & Okeke, C.E. (2012). Performance Assessment of Three Different PV Modules as a Response of Solar Insolation in South Eastern Nigeria, *International Journal of Applied Science and Technology*, 2 (3), 319-327.

Ugwuoke, P.E., (2005). Characterisation and Performance Evaluation of Crystalline and Amorphous Photovoltaic Modules in Nsukka Under Field Conditions. PhD Thesis, Department of Physics and Astronomy, University of Nigeria, Nsukka, 3-39.

Ugwuoke, P.E., Ezema F.I. & Okeke C.E. (2005). Performance Response of Single-crystalline PV Modules to Some Atmospheric Parameters at Nsukka, *Nigerian Journal of Space Research*. 3 (2), 183-190.

Umar I.H. (1999). Research and Development and Energy Crisis in Nigeria. *In Proceedings of 1999 Technology Summit*, Abuja, Nigeria, pp 39-42.

INTEGRATED GEOSCIENCES PROSPECTING FOR GOLD MINERALIZATION IN KWAKUTI, NORTHERN NIGERIA

Ejepu, S. J.*, Olasehinde, P. I., Unuevho, C. I., Ako, T. A., Bassagi, M. and Abdullahi, D. S.
Department of Geology, School of Physical Sciences, Federal University of Technology, Minna, Niger State, Nigeria.
*Corresponding Author: ejepu.jude@futminna.edu.ng. Tel: +2348034065079

Abstract
Geoscience prospecting for gold mineralisation was conducted in Kwakuti town located within Latitudes 9.362500°N to 9.387500ºN and Longitudes 6.920833ºE to 6.945833°E in northern Nigeria. The deployed geosciences techniques comprise surface geological mapping, analysis of SRTM DEM using *ArcGIS* software, processing and analysis of aeromagnetic total magnetic field intensity data using *Oasis Montaj* software and X-ray fluorescence analysis of soil samples. Migmatites and gneiss dominate the rock outcrops in the area. The migmatites occupy high elevations on the north-eastern and eastern portion of the area, where they display low magnetic field intensity values. The schist occupies moderate to low elevation areas and they display high magnetic field intensity values. The migmatites are dotted with quartz veins which constitute the gold mineralisation zone. Oval shaped high magnetic anomalous zones within the schist indicate basic intrusive into the schist. First derivative map of the magnetic field intensity data reveal NE-SW trending lineaments. They likely conducted hydrothermal fluids from the basic intrusive into the migmatites on the northeast, where gold mineralisation occurred by metasomatic ionic exchange. Spatial concentration of TiO_2 and MnO_2 are highest within the oval shaped high magnetic anomalous zones in the southern portion of the study area. This strengthens the inference that basic intrusive underlie the area. Gold concentration distribution pattern in the area is skewed NE-SW, thereby suggesting that the NE-SW structures control the mineralisation. Mining activities will be more efficient if directed along the NE-SW structural trend.
Keywords: Aeromagnetic data, Aero-radiometric data, Geologic mapping, Gold mineralisation, SRTM DEM, X-ray fluorescence.

1. Introduction

Lithologic units, lithologic boundaries, fractures and mineral accumulations are more accurately identified and delineated using the combination of surface geological mapping, remotely sensed radar data, geophysical data, and geochemical data on subsurface samples.

Aeromagnetic geophysical prospecting employs high magnetic susceptibility contrast between basement rocks to identify and map different lithologic units, geological structures and mineral accumulations within basement terrains (Kearey *et al*., 2002, Osinowo *et al.*, 2013).

The introduction of several computer software and improved digital mechanisms for data acquisition has expanded the scope of aeromagnetic applications. The combination of surface geological mapping, remotely sensed radar data, geophysical data, and geochemical data on subsurface samples were analysed using *Oasis Montage* to delineate different lithologic units, structures and gold mineralisation within part of Sheet 185NW Paiko (1: 50,000).

2.0 Location, geomorphological and geological setting of the area

The study area lies within Latitudes 9.362500°N to 9.387500ºN and Longitudes 6.920833ºE to 6.945833°E of Paiko Sheet 185NE (1: 50,000 Paiko). The tenement is located in Kwakuti community (Paikoro Local Government area of Niger State), a few kilometres off Suleja - Minna express way.

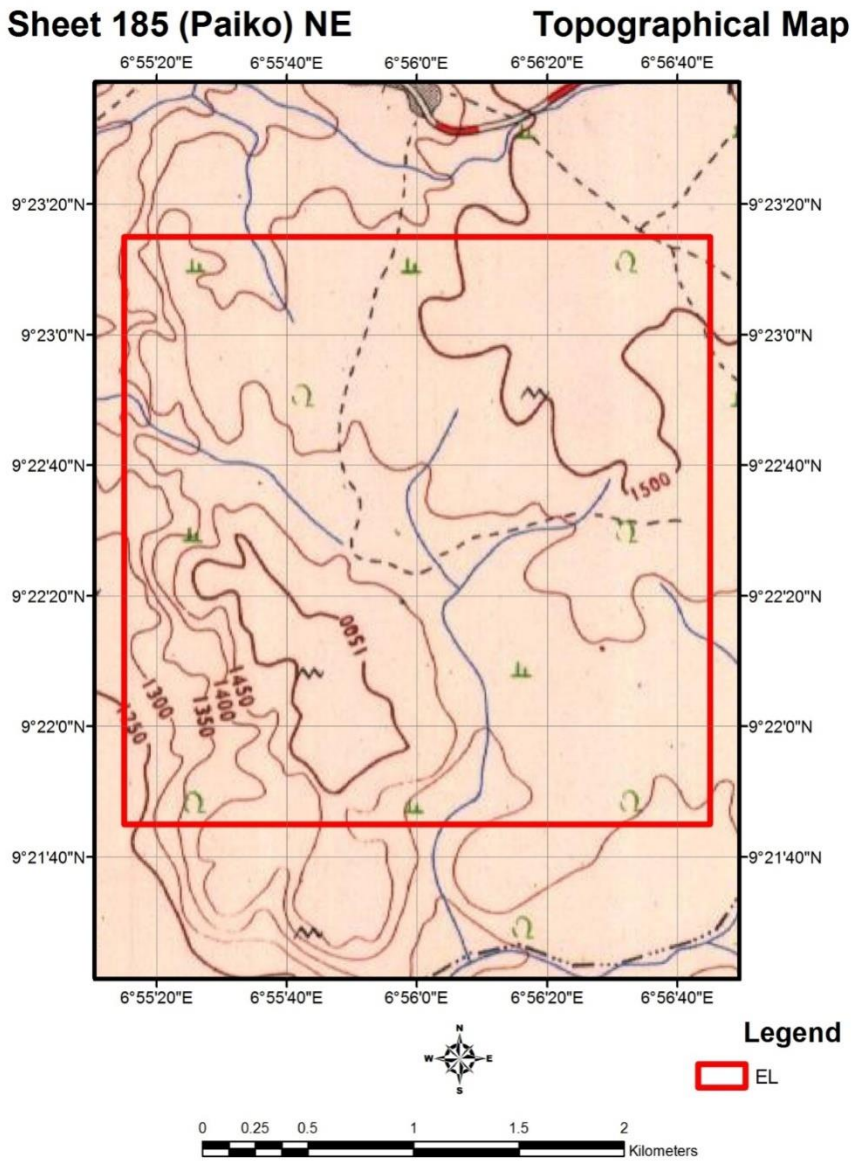

Figure 1: Topographic map showing boundary Layout of the study area

The area is characterized generally by undulating geomorphology. There are zones of low flat terrain that are dotted with a few hills, and display structurally controlled drainage of trellis pattern.

The area is an integral part of schist belt that hosts gold mineralization in Nigeria. The dominant rocks are the migmatites and schist. Pegmatite dykes occur within the schist while the migmatites outcrop over larger surface area than the schist. Feldspar, quartz and muscovite are major constituents within the schist. All the outcropping lithologic units in the area are transverse by quartz veins. The area is highly mineralized with gold occurring within pegmatite schist, quartz veins and in alluvium.

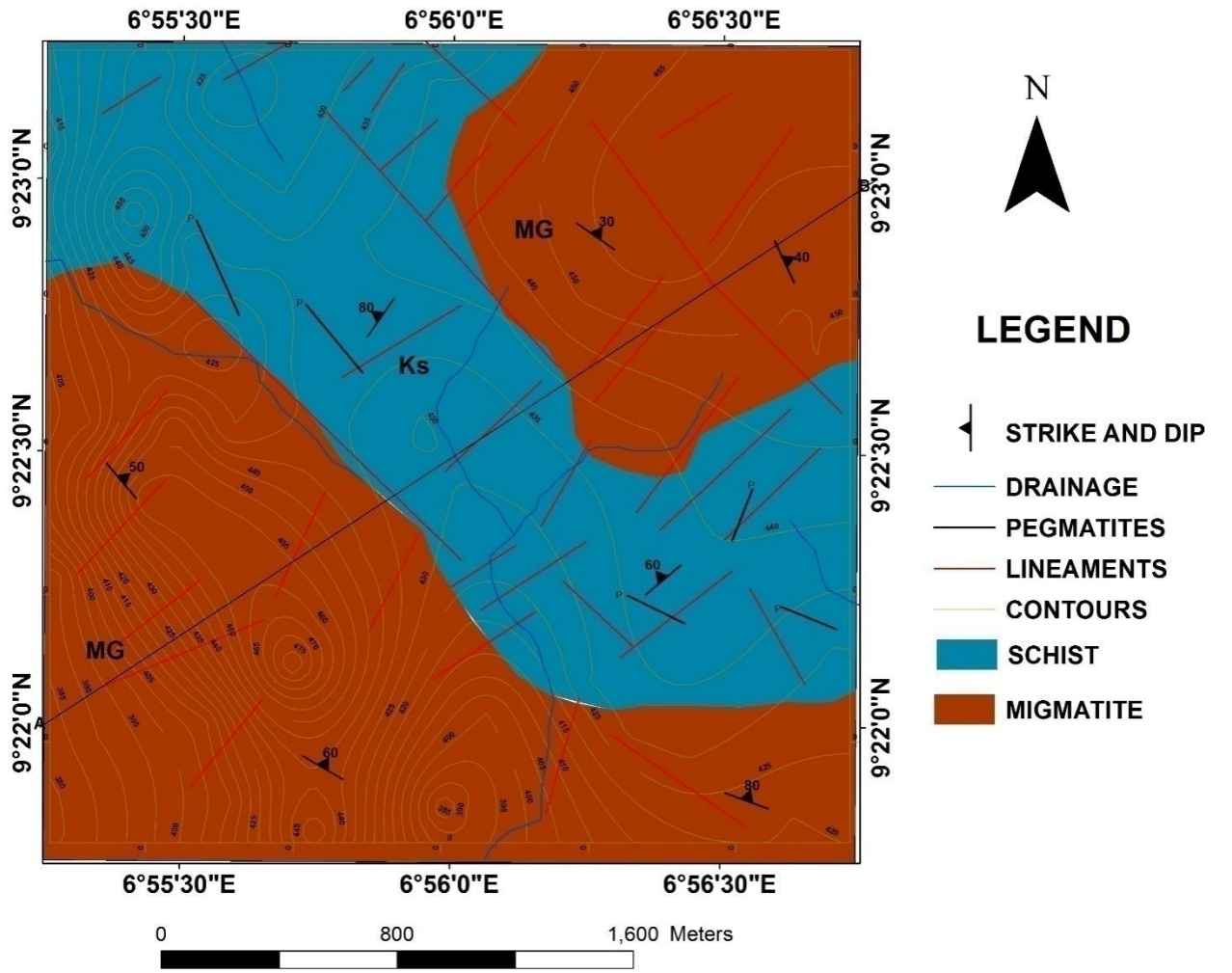

Figure 2: Geologic map of the study area. Some fault lines are digitized from published geologic map. (Source: Nigerian Geological Survey Agency (NGSA), 2009).

The structural elements in the study area include joints, faults, foliations and minor folds. The migmatites and schist generally trend NE-SW. The quartz veins are found trending NE-SW and in some areas. The quartz veins are seen be of great importance in our study because they host there are cases of gold infillings within them. Most of these structural elements do not appear on the map due to the scale of the map. Dolerite dykes are seen cutting across some of the outcrops. Fracturing may be as a result of thermo tectonic deformational events mostly of the Eburnean and Pan-African Orogeny (Oluyide, 1988). The dominant NE-SW structural trend coheres with the tectonic grain of the schist belt (Olasehinde *et al.*, 2013; Ejepu et al., 2015).

3.0 Methodology

Primary mineralization in Nigeria are mostly lithologically and structurally controlled (Ajakaiye *et al*., 1991). Structures include faults, shear zones (lineaments), pegmatites, quartz and quartzite veins. The methodology for this study was therefore structured to capture the general trends of surface and subsurface structures which control primary gold mineralization in the area. The exercise comprised surface geological mapping, lithologic and structural analysis of remote sensing images, pitting and sample collection. Soil samples were collected in the neighbourhood of stream channels and analysed using X-ray fluorescence.

3.1 Geologic mapping

Geological mapping exercise was carried out by locating areas of good outcrop exposures. Mapping was done using a topographic map on a scale of 12,500. Areas of geological interest were studied and tracked with the aid of a GPS device. Captured spatial data were tied to UTM, WGS 84 Zone 32N system. Data collected from the field were downloaded into the computer and developed into useful information with ArcGIS software. The success of the remote sensing and geological studies conducted on the area led to delineating regions with

high geological confidence of gold deposit occurrence. Faults and joints were investigated and strike and dip and of the fracture set were recorded using compass clinometers. Ground-truthing was also done on information extracted from remote sensing.

3.2 Aeromagnetic data processing and interpretation

The aeromagnetic data was obtained from NGSA. The data was acquired along a series of NE-SW tie lines direction with a flight line spacing of 500 m and terrain clearance of 80 m. The average magnetic inclination and declination across the survey is -5.49° and -1.99°, respectively. The data was gridded using the minimum curvature gridding method (Briggs, 1974). The micro-leveled magnetic data covering the study area was windowed out using the vertices coordinates in Oasis Montaj software. The total magnetic intensity field has been IGRF (International Geomagnetic Reference Field, 2009) corrected and super-regional field of 32000nT was deducted from the raw data. The airborne magnetic data were processed in *Oasis montaj* software, while information extraction and interpretation was done using *ArcGIS* software. The magnetic data was initially subjected to Reduction to the Magnetic Equator (RTE) and was further processed to investigate the presence of buried structures that might be relevant in the mineral exploration study. Directional and normalised derivatives were calculated to accentuate near surface structures from which lineaments were identified and delineated. These include First vertical, total horizontal and tilt derivatives, analytic signal. Source Parameter Imaging algorithm was applied to the RTE magnetic data to model depth to causative bodies.

3.2.1 Reduction to Magnetic Equator (RTE)

Due to the inherent problem of low latitude anomaly shift, the magnetic grid was reduced to the equator and then inverted (Geosoft Inc., 2014). This was done with the aim of making magnetic anomalies to centre on their respective causative bodies.

3.2.2 First Vertical Derivative (1VD)

MAGMAP was used to calculate the first vertical derivative of the magnetic data. This enhancement sharpens up anomalies over bodies and tends to reduce anomaly complexity, allowing a clearer imaging of the causative structures (Geosoft Inc., 2014). The transformation can be noisy since it will amplify short wavelength noise.

3.2.3 Total Horizontal Derivative and Tilt Derivative

The Total Horizontal Derivative and the tilt derivative are both useful in mapping shallow to near surface basement structures (Geosoft Inc., 2014). These enhancements are also designed to image faults and contact features. They complement the results of the vertical derivative processing.

3.2.4 Analytic Signal

The analytic signal processing generates a maximum directly over discrete magnetic bodies, as well as over their edges. The width of a maximum, or ridge, is an indicator of the depth to the contact. This transformation is often useful at low magnetic latitudes because of the inherent problems with RTP at such low latitudes (Geosoft Inc., 2014).

3.3 Radiometric data processing and interpretation

Airborne gamma-ray data are used as an aid to lithological mapping. Often, there is a good correlation between patterns in the radiometric data and unweathered rocks (Milligan & Gunn, 1997). This information complements magnetic, electromagnetic and geochemical data normally acquired during mineral exploration programs. This technique is cost-effective and rapid for geochemical mapping of the radioactive elements such as potassium, uranium and thorium. Radiometric surveys detect and map natural radioactive emanations, called gamma rays, from rocks and soils. Gamma-ray spectrometry (GRS) can be very helpful in mapping surface geology. The method provides estimates of apparent surface concentrations of the most common naturally occurring radioactive elements comprising potassium (K), equivalent uranium (eU), and equivalent thorium (eTh). The use of the method for geological mapping is based on the assumption that absolute and relative concentrations of these radio elements vary measurably and significantly with lithology.

3.4 Pitting

Locations for pitting were chosen from analysis of aeromagnetic map. Seven pits were dug to ascertain spatial extent of subsurface mineral occurrence. This is aimed at delineating or establishing a target size which is an area which is more mineralized.

3.5 Geochemical analysis

Stream sediments were collected based on the anomalous regions from the geophysical surveys. The site for the sampling coincided in drainage channels and samples were taken at about 0.3 m from the surface the stream. The samples were put in a plastic bag and then properly labelled and sent to the laboratory for analysis. X-ray fluorescence was performed on the samples for both major oxides and trace elements. Samples were prepared using pulverisation and palletisation methods. The selection of filters was guided by a given periodic table used for elemental analysis. Time of measurement for each sample was 100 seconds and the medium used was air throughout.

4.0 Results

4.1 Field investigations

Figure 2 is a digital elevation model of the study area. It reveals high elevation regions on the north-eastern and eastern portions of the area. Low elevation regions dominate the south-western and western portions.

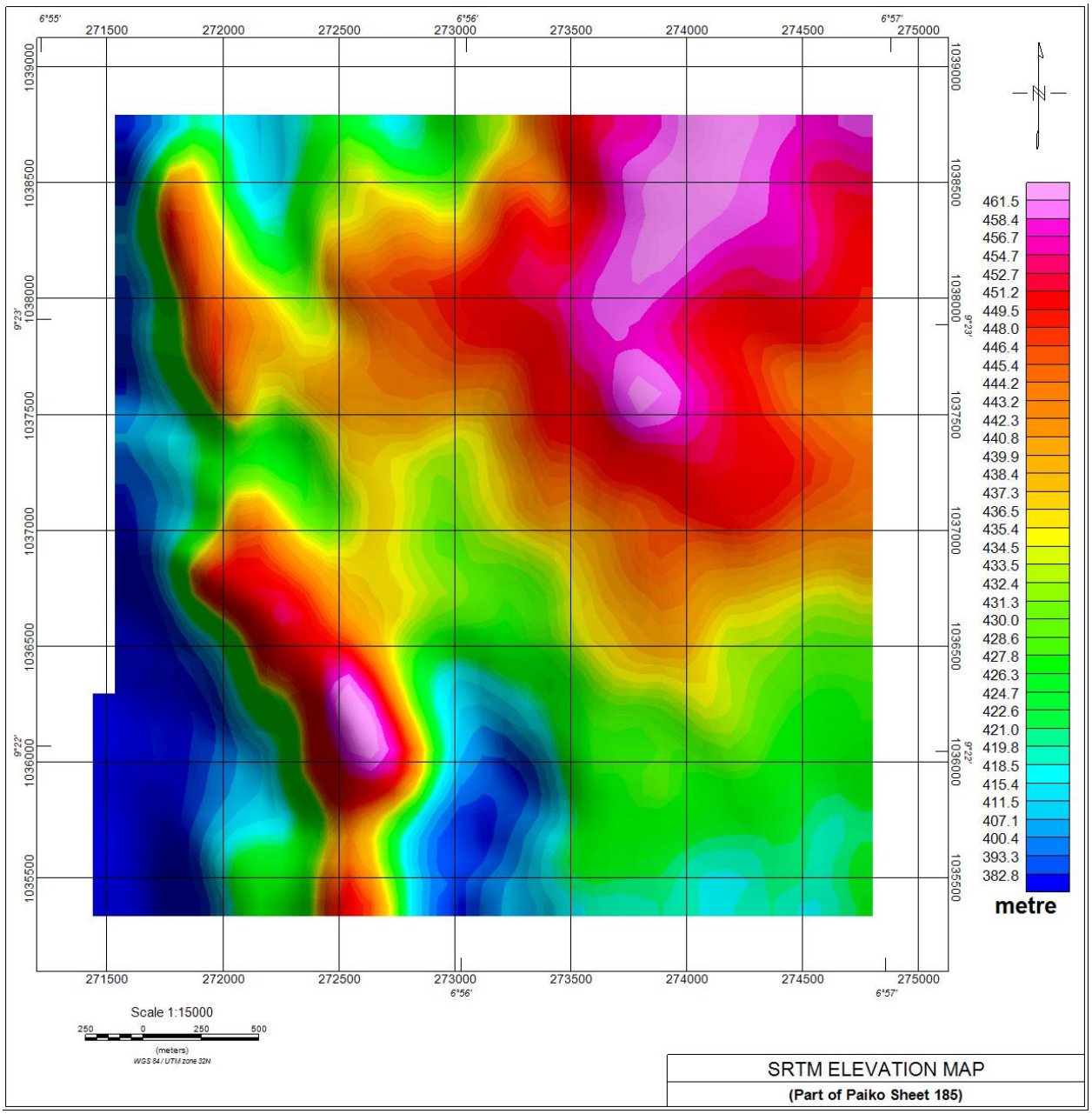

Figure 3: SRTM elevation map.

4.2 Geophysical data processing and interpretation

Figure 4 is the reduced to Equator (RTE) map generated from the total intensity magnetic anomaly (TIMA) data for the study area. The blocked region is the region covered by SRTM elevation map of figure 3. The map reveals that magnetic field intensity values that range from 40 to 67nT characterise the rocks in the study area. The high elevations regions (Figure 3) coincide with very low magnetic regions (figure 4), and are underlain with migmatites and dykes. Areas of moderate elevation are associated with high magnetic anomaly corresponding to schistose rocks.

Contact zones recorded low magnetic anomaly. This is an indication of demagnetization of magnetite minerals to hematite minerals with low magnetic response as a result of hydrothermal fluid flow through fractures and faults (Wilford *et al*, 1997). This is as a result of severe shearing and faulting at the contact zones. This prospective fault-bounded contact between the schists and the migmatites may potentially hosts mineralization zones in the area.

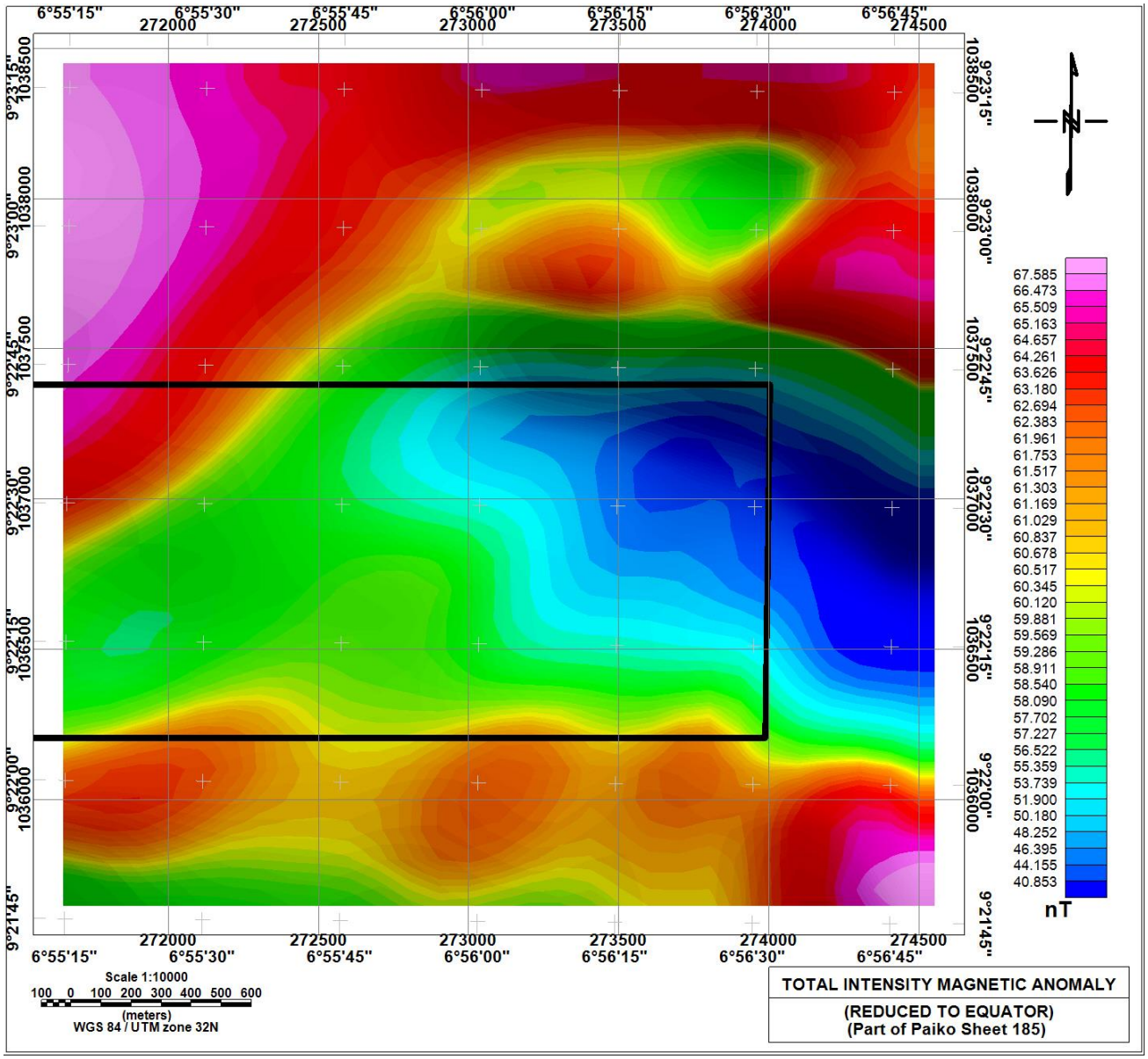

Figure 4: Reduce-to-Equator total intensity magnetic anomaly map. Map was produced using Geosoft Oasis montaj. Black outline represents coverage where samples were taken for geochemical analysis.

4.2.1 First Vertical Derivative (FVD)

The FVD map reveals NE-SW trending lineaments. Oval shaped anomalies with high total magnetic intensity values in the southern portion of figure 5 may indicate basic intrusives into the schist.
The quartz veins are hosted mainly in migmatites and are closely associated with the gold mineralization. The NE-SW trending lineaments are likely fractures that conducted hydrothermal fluids from basic intrusive into migmatites on the northeast.

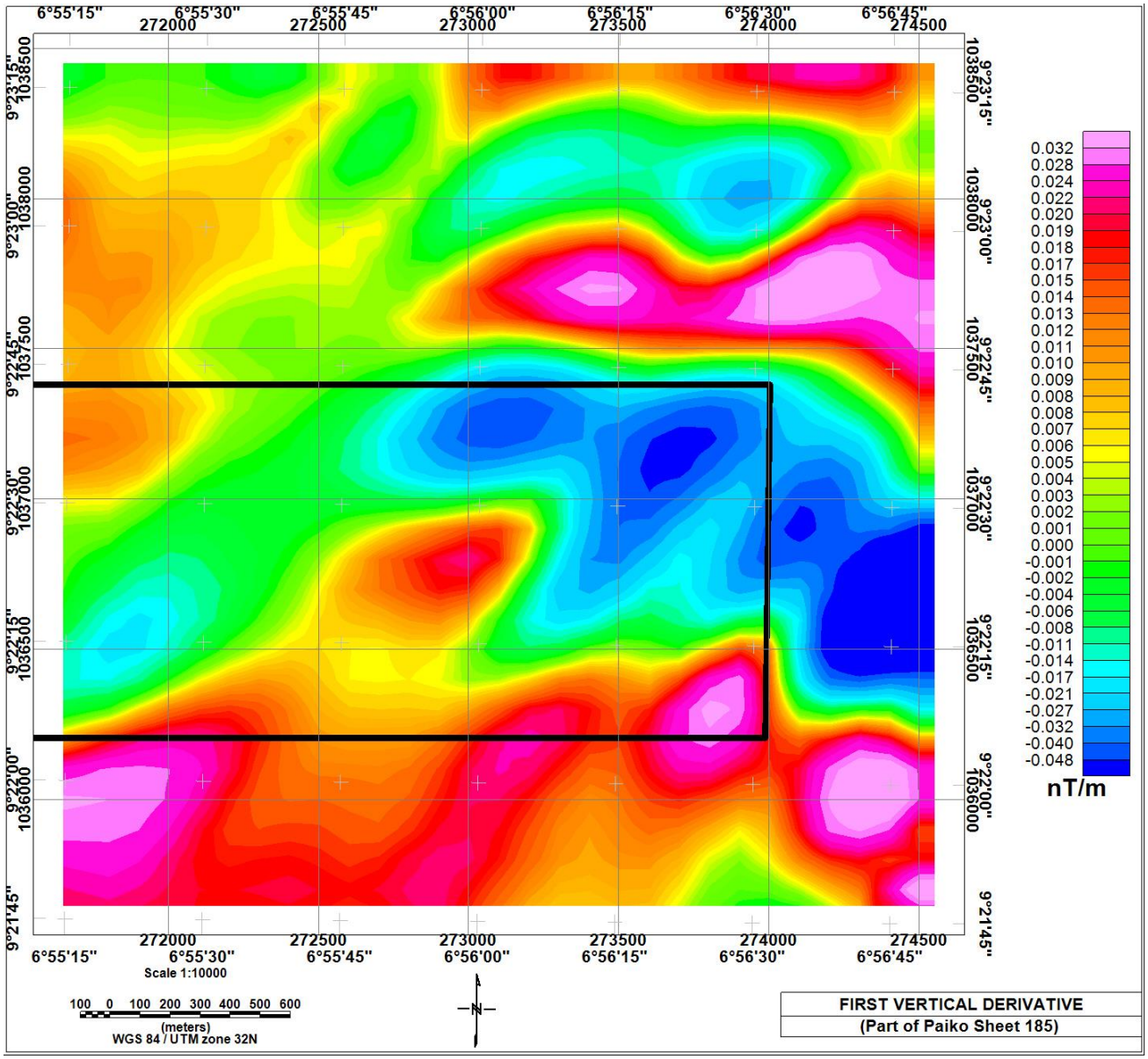

Figure 5: First vertical derivative (FVD) map. Map was produced using Geosoft Oasis montaj. Black outline represents coverage where samples were taken for geochemical analysis.

4.2.2 Tilt Derivative map (TDR)

The NE-SW trending lineaments are also revealed in the TDR map (figure 6). The map also reveals NW-SE trending lineaments on its north-eastern portion. Both lineaments constitute a conjugate fracture system. Since the NE-SW trending lineaments run through the schist and migmatites, they seem to control the mineralisation in the area.

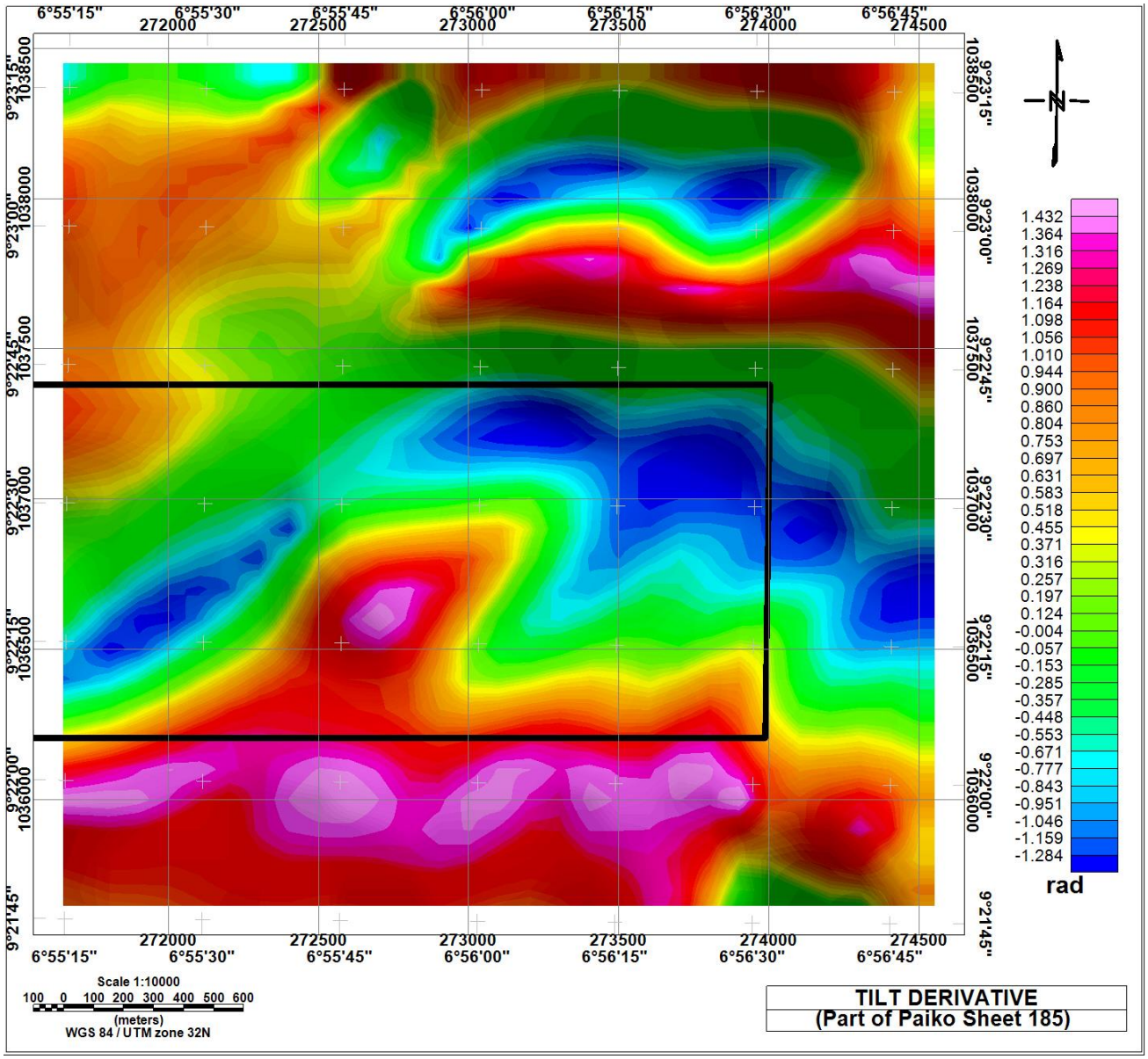

Figure 6: Tilt Derivative map. Map was produced using Geosoft Oasis montaj. Black outline represents coverage where samples were taken for geochemical analysis.

4.2.3 Analytic Signal (AS)

The NW-SE trending lineaments are indicated on the AS map (figure 7). It also revealed high magnetic anomaly zones in the north-eastern portion. The lineaments and the high magnetic anomaly

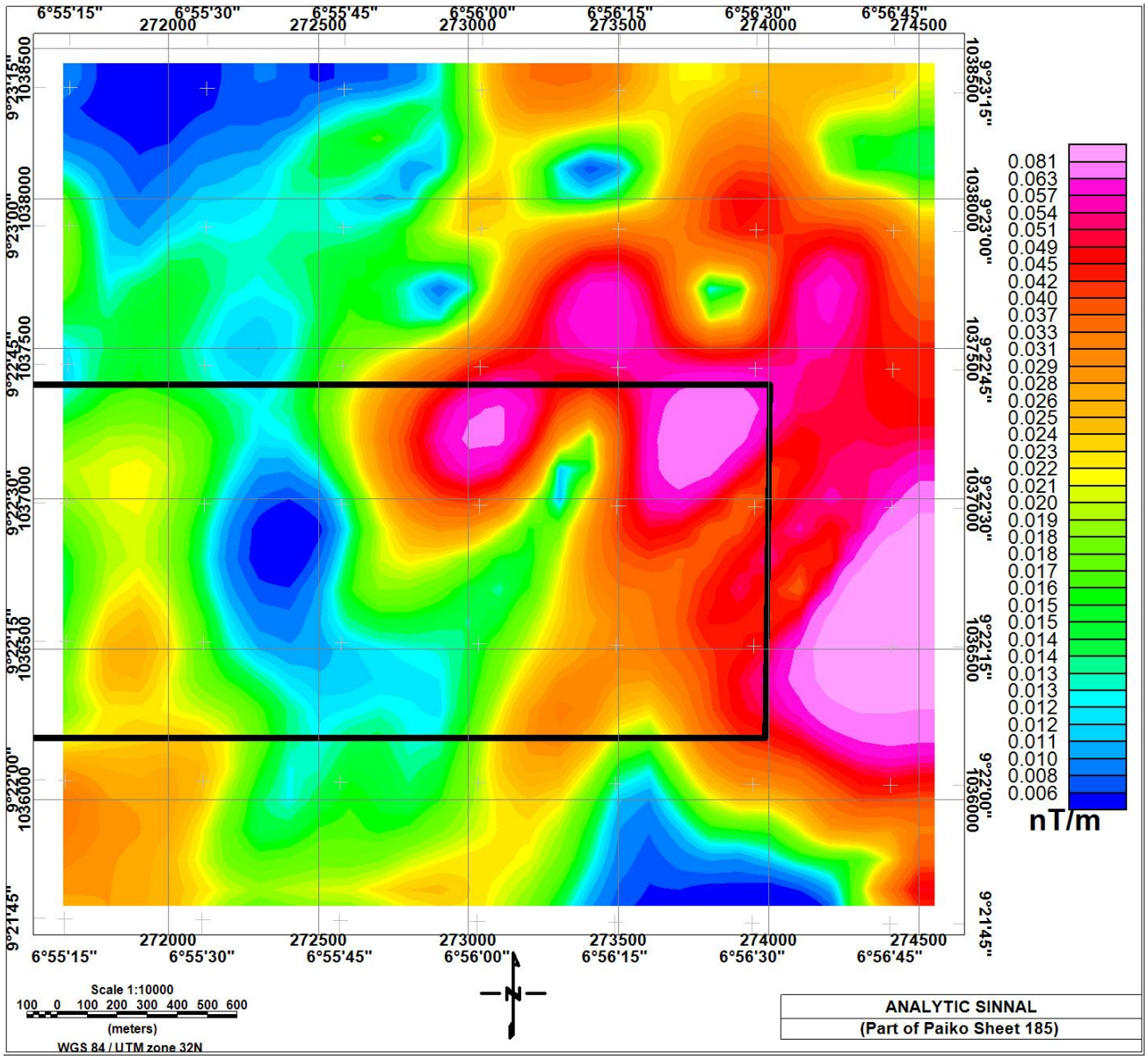

Figure 7: Analytic signal map. Map was produced using Geosoft Oasis montaj. Black outline represents coverage where samples were taken for geochemical analysis.

Figure 8 is a map showing the composite lineaments obtained from the different processing of the total magnetic field intensity data, and the lineaments determined from surface geological mapping exercise. The dominant lineaments are the conjugate NW-SE and NE-SW fractures.

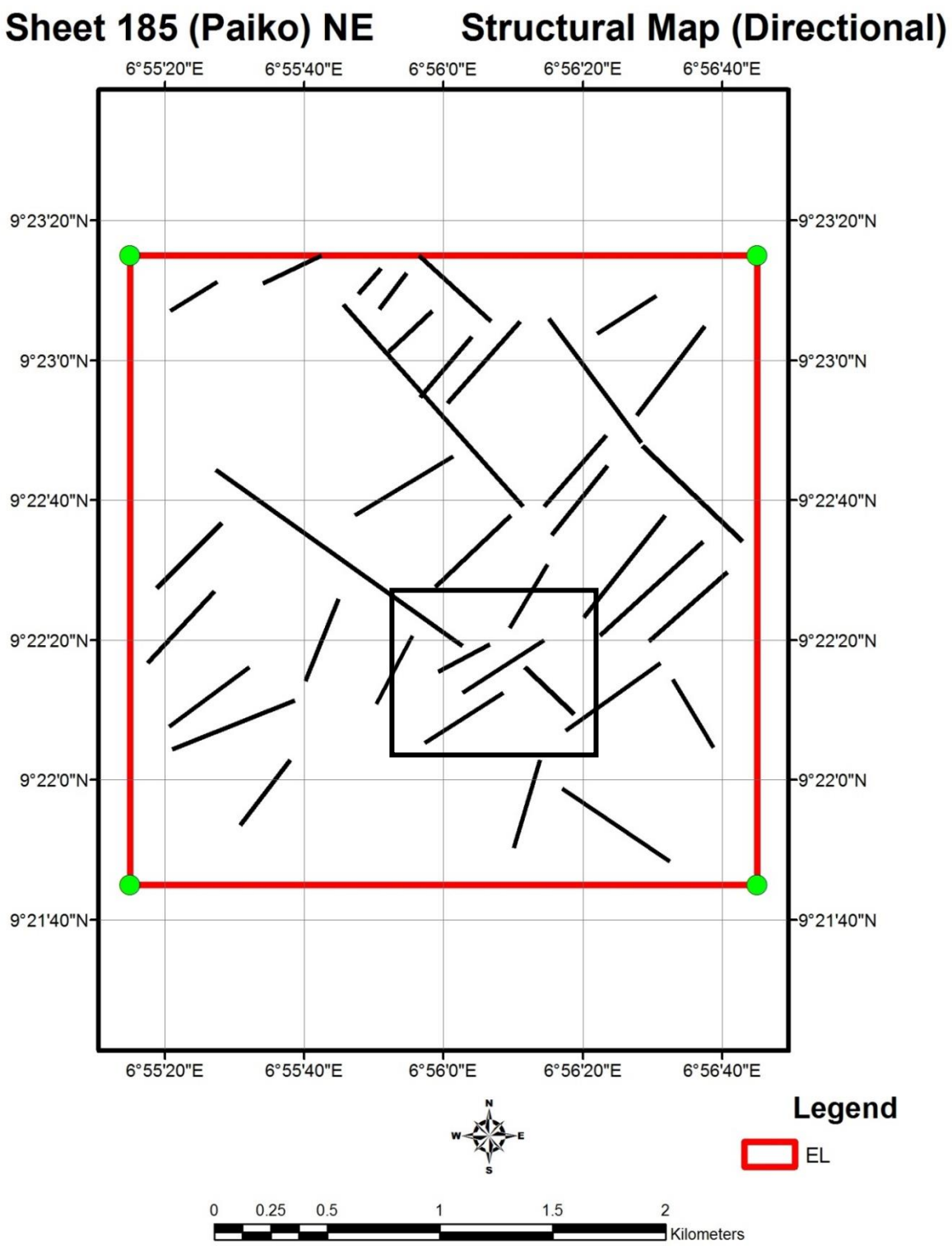

Figure 8: Lineament map of the study area. Some mapped surface structures are also represented.

4.3 Ternary Image

The ternary image (**Figure 9**) comprises of colours generated from the relative intensities of the three components and represents subtle variations in the ratios of the three bands with K assigned to red, U to blue and Th to green. The composite image presents strong spatial correlations with the known geologic units and the most prominent features in the K, Th, and U images. The most notable units in the ternary image are the mafic and magnetite rich migmatite formations which are represented in cyan and also notable in both U and

Th maps. In addition, the migmatite with high K concentration and some traces of U are given a magenta colour. This strong correlation is based on the fact that the migmatite are made up of the potash-rich (high K concentration) regolith which come in the form of muscovite and biotite as well as the mineral constituents of the pegmatite dykes (Wilford et al, 1997).

The K, Th and U map show that the schist recorded weak anomaly of K and Th but strong U anomaly. A long denudation period of weathering has probably depleted most of the U concentration of migmatites within the western portion of the ternary map. The dark regions which occur within faulted zones and in some areas at the contact zones of the rock formation can be attributed to the low concentration of the K, Th and U. The light yellow zones in the ternary image are indications of high concentration of K, Th but low U concentrations.

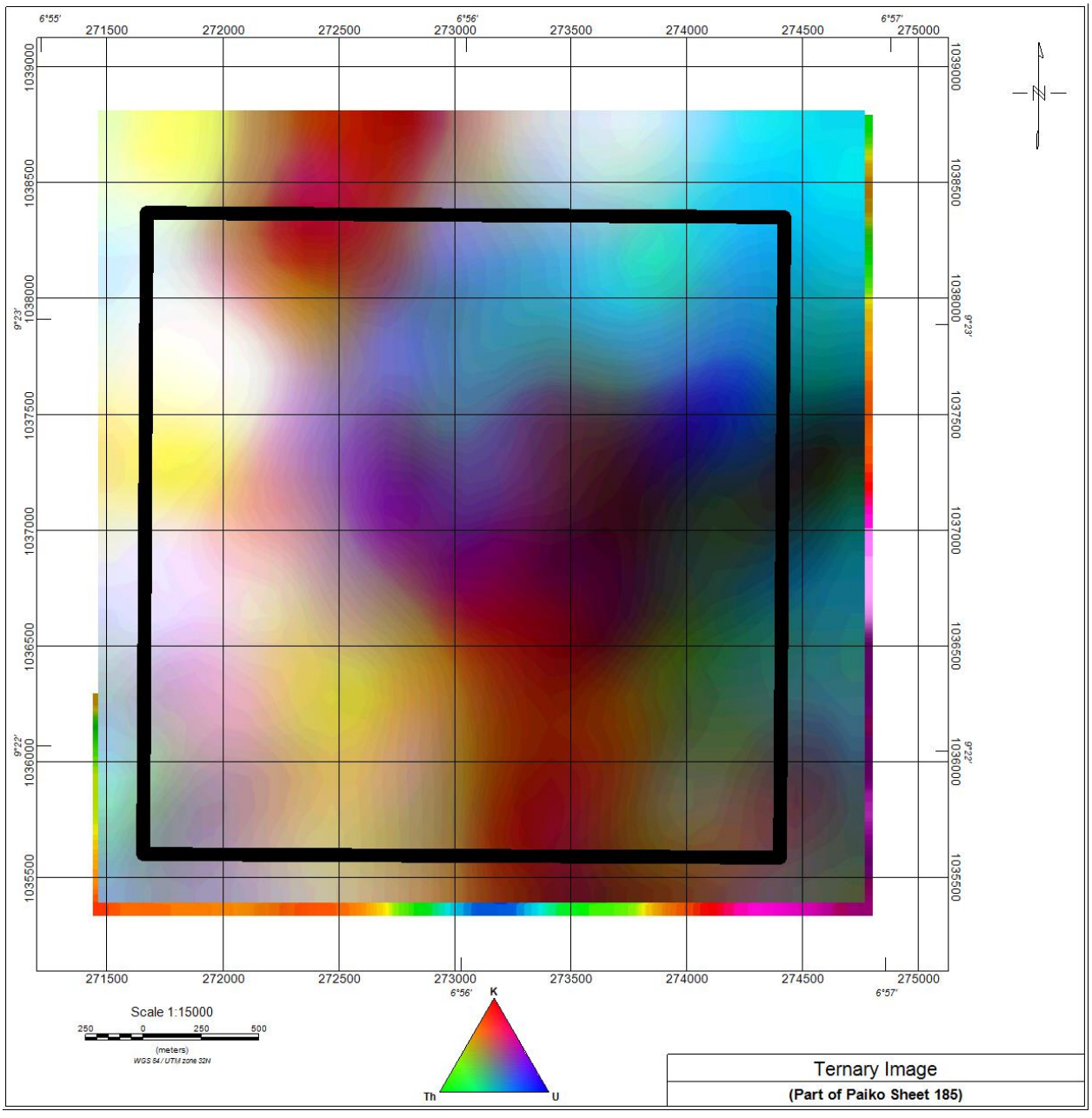

Figure 9: Ternary Image Map produced from equivalent potassium, thorium and uranium concentrations. Map was produced using Geosoft Oasis montaj.

4.4 Pitting and geochemical analyses

The geographic coordinates of the sampled pits are presented as table 1.

Table 1: Geographic coordinates of the pits.

PIT NUMBER	LONGITUDE (E)	LATITUDE (N)
01	6°56′03.0″	9°22′05.3″
02	6°55′23.7″	9°22′11.9″
03	6°55′09.3″	9°22′24.4″
04	6°55′16.8″	9°22′33.4″
05	6°55′26.3″	9°22′40.4″
06	6°55′34.9″	9°22′37.2″
07	6°56′31.6″	9°22′43.3″

The concentration of the major oxides in percentage is given in table 2

Table 2: Major oxides (%)

The determined trace elements and rare earth elements are shown in table 3.

SAMPLE ID	SiO2 (%)	Al2O3 (%)	SO3 (%)	P2O5 (%)	Na2O (%)	K2O (%)	CaO (%)	MgO (%)	TiO2 (%)	Fe2O3 (%)	MnO (%)	H_2O^+ (%)
LOC. 1	54.20	14.08	-	-	1.04	8.26	1.20	0.24	4.83	10.40	0.06	5.68
LOC. 2	69.80	8.41	-	-	0.02	2.40	4.95	0.54	6.22	5.12	0.22	2.30
LOC. 3	48.10	19.00	-	-	0.41	4.24	0.78	-	1.86	18.10	0.16	7.33
LOC. 4	65.80	7.98	-	-	0.32	2.70	2.89	1.04	2.84	10.42	0.075	5.93
LOC. 5	59.70	18.00	-	-	1.02	5.51	0.47	-	2.55	7.99	0.035	4.72
LOC. 6	60.00	13.21	-	-	1.04	7.09	1.68	0.02	1.68	9.00	0.12	6.14
LOC. 7	56.20	18.34	-	-	1.54	5.34	1.90	0.03	3.03	8.84	0.14	4.60

Table 3: Trace elements/Rare Earth metals (ppm)

ELEMENTS (ppm)	LOC. 1	LOC. 2	LOC. 3	LOC.4	LOC. 5	LOC. 6	LOC. 7
Ag	3.040	1.606	3.346	1.354	1.628	2.252	1.790
As	0.008	<0.001	5.001	<0.001	0.900	<0.001	<0.001
Au	2.940	0.872	3.588	2.018	2.620	0.296	1.954
Bi	1.240	2.140	1.483	3.025	3.312	0.895	0.864
Cd	<0.001	<0.001	<0.001	<0.001	<0.001	<0.001	<0.001
Ce	<0.001	<0.001	<0.001	<0.001	<0.001	<0.001	<0.001
Co	<0.001	<0.001	<0.001	<0.001	<0.001	<0.001	<0.001
Cr	0.880	0.083	0.630	2.400	1.420	0.635	0.782
Cs	<0.001	<0.001	<0.001	<0.001	<0.001	<0.001	<0.001
Cu	0.100	0.130	0.220	0.044	0.120	0.053	0.055
Eu	0.480	0.540	0.530	0.170	0.200	0.230	0.420
Ga	0.010	<0.001	4.001	<0.001	<0.001	0.801	<0.001
Ge	<0.001	<0.001	<0.001	<0.001	<0.001	<0.001	<0.001
Mo	<0.001	<0.001	<0.001	<0.001	<0.001	<0.001	<0.001
Nb	<0.001	<0.001	<0.001	<0.001	<0.001	<0.001	<0.001
Ni	<0.001	<0.001	<0.001	<0.001	<0.001	<0.001	<0.001
Os	<0.001	<0.001	<0.001	<0.001	<0.001	<0.001	<0.001
Pb	0.180	0.084	10.087	<0.001	0.690	<0.001	<0.001
Re	0.100	0.070	0.200	0.700	0.042	0.130	0.120
Sr	0.018	0.110	0.140	0.290	<0.001	0.970	0.010
Ta	<0.001	<0.001	<0.001	<0.001	<0.001	<0.001	<0.001
Th	<0.001	<0.001	<0.001	<0.001	<0.001	<0.001	<0.001
Tl	<0.001	<0.001	<0.001	<0.001	<0.001	<0.001	<0.001
U	<0.001	<0.001	<0.001	<0.001	<0.001	<0.001	<0.001
V	0.702	0.512	<0.001	0.680	0.730	0.850	0.500
W	<0.001	<0.001	<0.001	<0.001	<0.001	<0.001	<0.001
Zn	0.840	1.470	0.180	2.000	1.700	0.370	1.002
Zr	48.00	25.000	6.500	1.200	1.770	0.288	0.2985

The spatial distribution of TiO_2, and MnO_2 are shown in figures 9 and 10 respectively. The highest concentration of these oxides is in the south-western portion of the area. This supports the interpretation that oval shaped high anomalies in the FVD map (figure 5) are basic intrusive. Figure 11 shows the spatial distribution of gold in the area. The NE-SW alignment of the concentration pattern supports the interpretation that the NE-SW fractures conducted hydrothermal fluids from basic intrusive in the SW to migmatites in the NE.

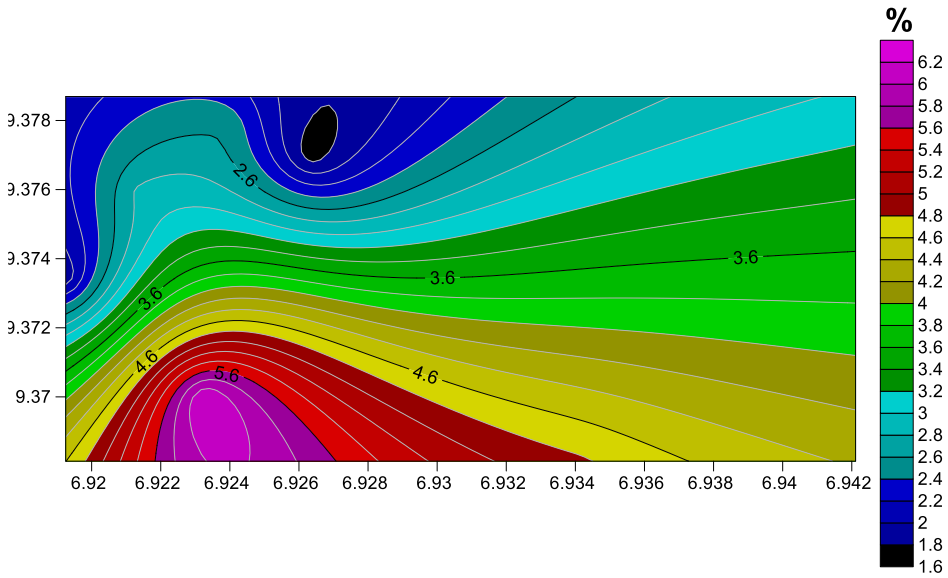

Figure 10: Contour plot of geochemical distribution of TiO_2 (in %) for Pit samples in the area.

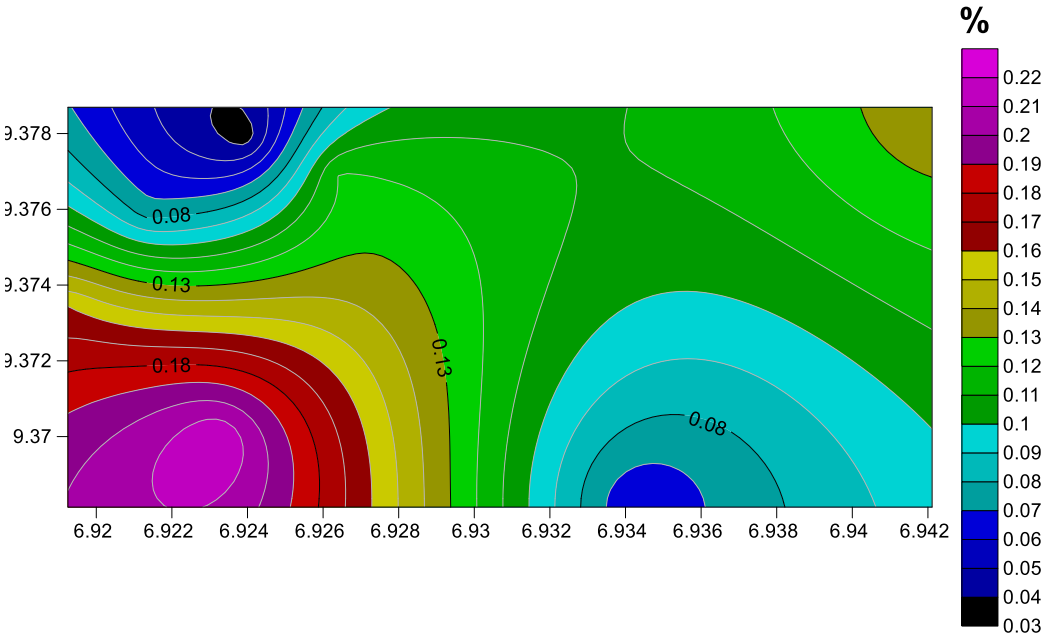

Figure 11: Contour plot of geochemical distribution of MnO (in %) for Pit samples in the area.

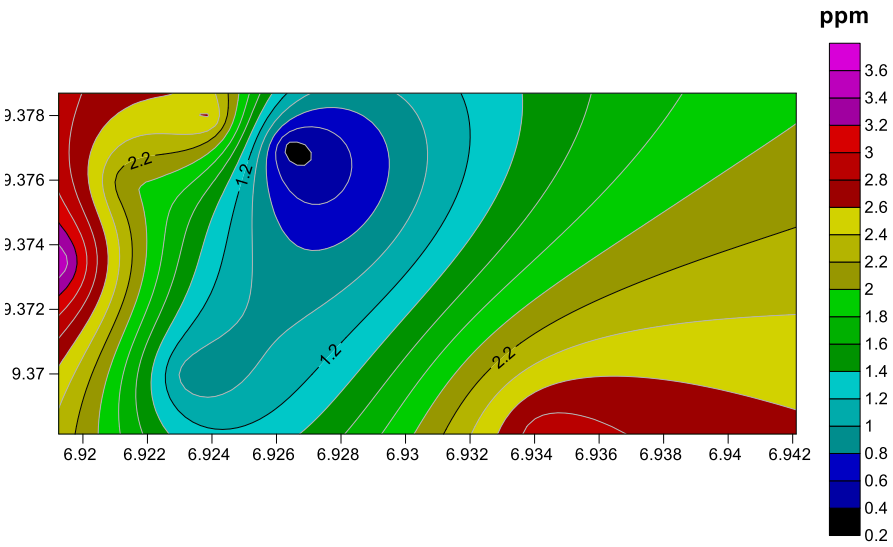

Figure 12: Contour plot of geochemical distribution of Au (ppm) for Pit samples in the area.

5.0 Conclusion and Recommendation

The area has undergone a pronounced tectonic activity resulting in shearing and fracturing. A common feature of the rare-metal pegmatites and veins in Nigeria is their close proximity to major and subsidiary fault structures. So, the sheared zone and fractures are potential channels for mineralization fluids. The observed zonation in the magnetic data and the potassic alteration in the ternary image are indication of hydrothermal alteration associated with mineralization. Often this alteration signature may be broad and laterally extensive providing a larger exploration target. The contacts between different geological units, the intersections between linear features, sheared and fractured zones are potential traps for minerals and therefore give a significant exploration vectors.

The locations of core drilling will be determined based on recommended sites from the detailed geophysical and geochemical form of exploration. The core samples should advisably be analysed in a world class laboratory in other to ascertain the grade.
It is recommended that fire assay geochemical analysis be performed on the soil samples that have been taken from various anomalous regions in the prospect area.

References

Abedi, M. & Norouzi, G. H. (2012). Integration of various geophysical data with geological and geochemical data to determine additional drilling for copper exploration. *Journal of Applied Geophysics*, 83**,** 35-45.

Abedi, M., Gholami, A. & Norouzi, G. H. (2013). A stable downward continuation of airborne magnetic data: A case study for mineral prospectivity mapping in Central Iran. *Computers & Geosciences*, 52**,** 269-280.

Abu El-Ata, A. S., EI-Khafeef, A. A., Ghoneimi, A. E., AbdAlnabi, S. H. & Al-Badani, M. A. (2013). Applications of aeromagnetic data to detect the Basement Tectonics of Eastern Yemen region. *Egyptian Journal of Petroleum*, 22**,**277-292.

Ajakaiye, D. E., Hall, D. H., Ashiekaa, J. A., & Udensi, E. E. (1991). Magnetic anomalies in the Nigerian continental mass based on aeromagnetic surveys. *Tectonophysics*, 192(1), 211-230.

Briggs, I. C. (1974). Machine contouring using minimum curvature. *Geophysics*, *39*(1), 39-48.

Ejepu, S. J., Olasehinde, P. I., Omar D. M., Abdullahi, D. S, Adebowale, T. A., & Ochimana, A. (2015). Integration of Geology, Remote Sensing and Geographic Information System in assessing groundwater potential of Paiko Sheet 185 North-Central Nigeria. *Journal of Information, Education, Science and Technology*. 2(1), 145 – 155.

Geosoft (2014). GM-SYS Gravity & Magnetic Modelling Software, Users Guide, v.4.10, Northwest Geophysical Associates, Inc., P.O. Box 1063, Corvallis, Oregon 97339-1063 USA, 2006.

Hirdes, W., Senger, R., Adjei, J., Efa, E., Loh, G. and Tetty, A. (1993) Explanatory Notes for the Geological Map of Southwest Ghana 1: 100,000, Sheet Wiawso (0603d), Asafo (0603c), Kukuom (0603b), Goaso (0603a), Sunyani(0703d) and Berekum (0703c). Geologisches Jahrbuch Reine B, Band B 83, Hannover, 139 p.

Kearey, P., Brooks, M. & Hill, I. (2002). *An introduction to geophysical exploration*, John Wiley & Sons.

Keating, P. B. (1995) A simple Technique to Identify Magnetic Anomalies Due to Kimberlite Pipes. *Exploration and Mining Geology*, **4**, 121-125.

Milligan, P.R. and Gunn P.J. (1997) Enhancement and Presentation of Airborne Geophysical. *AGSO, Journal of Australian Geology and Geophysics*, **17**, 64-74.

Olasehinde P. I., Ejepu S. J. & Alabi A. A. (2013). Fracture Detection in a Hard Rock Terrain Using Radial Geoelectric Sounding Techniques. *Water Resources Journal* 23(1&2), 1-19.

Oluyide, P.O. (1988). Structural trends in the Nigerian Basement Complex. In: Precambrian Geology of Nigeria. *Geological Survey of Nigeria*, pp. 93 - 98.

Osinowo, O. O., Akanji, A. O. & Olayinka, A. I. (2013). Application of High Resolution Aeromagnetic Data for Basement Topography Mapping of Siluko and Environs, South-western Nigeria. *Journal of African Earth Sciences*.

Reynolds, R.L., Rosenbaum, J.G., Hudson, M.R. and Fishman, N.S. (1990) Rock Magnetism, the Distribution of Magnetic Minerals in the Earth's Crust and Aeromagnetic Anomalies. *US Geological Survey Bulletin*, **1924**, 24-45.

Wilford, J.R., Bierwirth, P.N. and Craig, M.A. (1997) Application of Airborne Gamma-Ray Spectrometry in Soil/Regolith Mapping and Applied Geomorphology. *AGSO, Journal of Australian Geology and Geophysics*, **17**, 201-216.

ENHANCING ECONOMIC PRODUCTIVITY OF UPLAND RICE IN EKITI STATE THROUGH A FREQUENCY SWEEP AND MANUAL FREQUENCY-SELECT ULTRASONIC BIRD PEST CONTROL DEVICE

Ibrahim, A.G.[1*], Alabadan, B.A.[2], Olaniyan, A.M.[3], Fayose, T.S.[4], Okonji, C.J.[5], Oloye, A.O.[6], Fakayode, S.B.[7], Ajayi, E.S.[8], Ajiboye, A.T.[9]

[1]Department of Physics, Federal University of Technology, Minna

[2-6]Department of Agricultural and Bio Resources Engineering, Federal University, Oye, Ekiti State

[7]Department of Agricultural Economics and Extension, Federal University, Oye, Ekiti State

[8]Department of Crop Science and Horticulture, Federal University, Oye, Ekiti State

[9]Department of Computer Engineering, University of Ilorin, Kwara State.

*Corresponding Author: ibrahimaku@futminna.edu.com

ABSTRACT

The economic Productivity of upland rice in Ekiti State is threatened by weaver bird pest infestation. In this work, the outcome of an intensive field survey consisting of ultrasonic broadcast was used to generate design considerations for an ultrasound device designed to scare weaver birds away from rice farms. The device which transmits ultrasound signal at 20, 25, 35 and 45 kHz has two modes of operation: the auto-frequency mode, which is able to sweep between all available frequencies at fifteen seconds interval and the manual frequency-select mode, which is able to switch between selected frequencies of interest at same interval. The design comprises of the power supply, oscillator, frequency selection, amplification, microcontroller, LCD and the ultrasonic transducer sections along with their respective specifications, design calculations and circuit diagrams. The design which is fortified to delay habituation when implemented will guarantee reasonable horizontal ultrasound spread to deter weaver birds away from rice farms, thereby maximizing the productivity of upland rice in Ekiti State.

Keywords: Design consideration, integrated circuit (IC), Ultrasound, weaver birds.

1. Introduction

Ekiti State, south-west Nigeria is known for the cultivation of arable crops such as rice, yam, cowpea and cassava to mention just a few (Adeboboye, 2017). The main occupation of the people is agriculture and it provides income and employment for more than 75% of the people. The food sufficiency in the area is however being threatened by the activities of pests, prominent is that of the notorious weaver birds (*Ploceus cucullatus*) attacking rice farms (Bright, 1988, Bright *et al.*, 2007). Rice (*Oryza sativa*), is one of the most staple food in several homes of Ekiti people (Akande, 2003, and USAID, 2008). Available pest control methods in the area include: use of scarecrow, tapes, mechanical devices, hunting, screaming, chemicals and juju to mention just a few (Bright *et al*., 2007 and Bright *et al*., 2009). All these control methods has proved to be less effective due to habituation. In this research, an attempt was made to solve the weaver bird pest problem of the area electronically using ultrasound as a scaring parameter.

2.Literature Review

In line with earlier recommendation (Ibrahim *et al*., 2013), that ultrasonic pest control devices should not be deployed to location without an extensive field survey carried out to determine the effective ultrasonic frequency, crop stage(s) prone to attack, period of the year and period of the day of attack and other interesting factors needed to formulate effective design parameters. A robust field studies was conducted in Niger State, Nigeria (Ibrahim, 2015). The study among others carried out an ultrasonic broadcast using a collection of independent equipment in weaver birds infected farms. Analysis of data collected at tree homes pointed to the put-to-flight frequency and the stay-away frequency for weaver birds as 35 kHz respectively. Also of interest is their equivalent in farms determined to be 25 kHz (Ibrahim *et al*., 2016). The outcome of the survey have been adopted in addition to other studies in the study area as the preliminary study which served as precursor for the development of specific design consideration for an ultrasonic device that effectively tackled the weaver bird pest menace in the area. The bird pest problem bedeviling rice farms in neighboring Ekiti State,

is the same weaver birds which have been effectively tackled using ultrasound (Ibrahim *et al.*, 2013b). Both Niger and Ekiti State may slightly vary in location but to a large extent, shares similar geographical entity and will not result in emergence of variation within same specie. It is still within the confine of the concept of specificity (Ibrahim *et al*., 2013a) to adopt the outcome of field study (Ibrahim *et al.*, 2016) with little moderation to suit the new study area. An ultrasound device developed through this process will effectively deter the pests away from farms for a longer period by delaying the onset of habituation.

3. Methodology

The block diagram in Figure 1 shows the constituent sections and the direction of signal flow intended for the ultrasound pest control device.

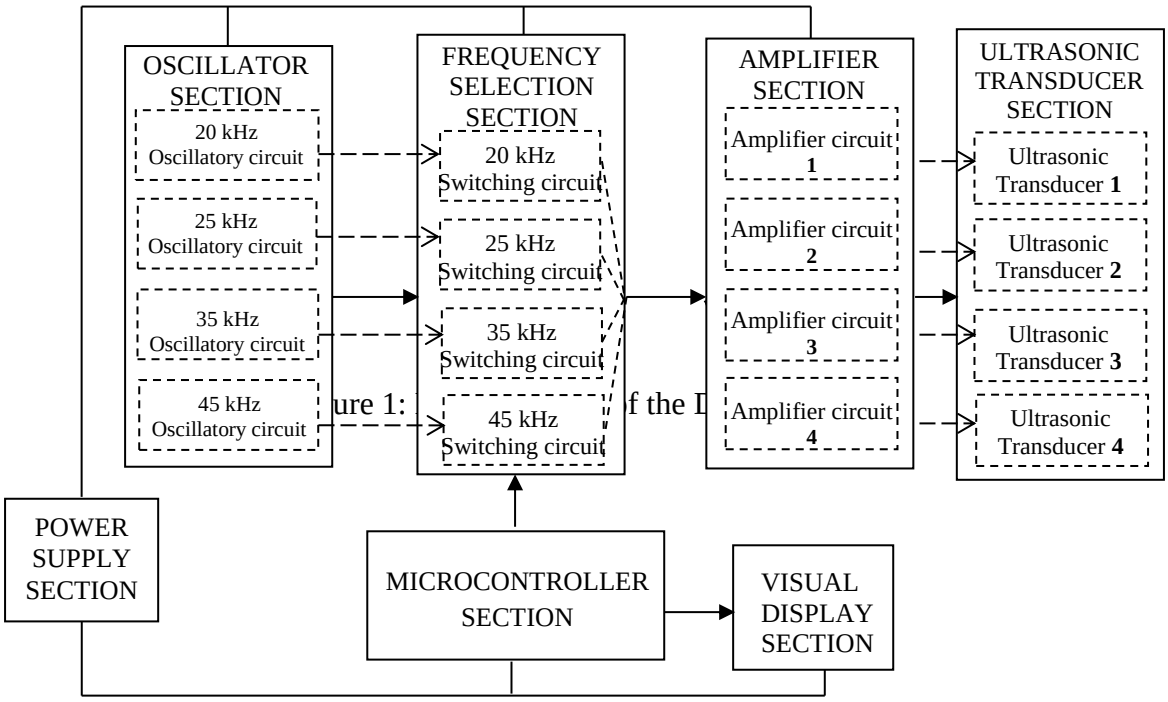

ure 1: f the D

Each sectional design shall be discussed sequentially.

3.1 Power Supply Section

The power system designed for the device is a 5 V power supply system since all components used in this design can be adequately powered using 5 V DC. The ultrasonic device is a part of an integrated system consisting of three bird scaring devices. The entire system has a central power system which is made up of a solar powered inverter and to which all constituent devices shall be connected. The output of the central power system is AC, therefore, the 5 V power supply will convert the 230 V alternating current (AC) output of the central power system into 5 V direct current (DC) required by the ultrasound device.

A simple and conventional 5 V power supply consisting of a 230 – 9 V step down transformer, a bridge rectifier, a filter and a regulator was designed. The transformer steps down the 230 V of the inverter to 9 V AC and is made available at the secondary terminal. This is 4 V above the 5 V required, but necessary to compensate for the drain from the rectifier. The rectifier which is made up of four IN 4007 diodes is connected to the transformers secondary terminal and will only permit a one directional current (DC) at its output. Each of the two diodes conducting at a time will drain 0.7 V. Therefore, a total of 1.4 V is drained from the 9 V. The filtering to obtain the smoothest DC is done via a 10 µF capacitor (C_1). It let AC current pass through and block DC, by so doing will remove any ripple of AC left over in the system. The regulating IC denoted in this work as IC_1 is the 7805 voltage regulator. It will peg the output at 5 V. Regulators need at least 2 V more than their output voltage as input in order to make up for the dropout voltage. Of the 9 V stepped down, 1.4 V was

drained by the rectifier, leaving 7.6 V, enough for the dropout voltage. Pin 1 is the regulators input, the common (pin 2) of the voltage regulator is grounded. The output (Pin 3) of the voltage regulator is again filtered by another 10µF capacitor (C_2), and then the 5 V output is taken. This 5 V output will be fed into the power line for all succeeding sections to tap from. The power supply circuit is furnished with an electric fan and a heat sink fitted to the 7805 IC to prevent overheating.

3.2 Oscillatory Section

The desired frequency of ultrasound transmission is generated from the oscillatory section. The effective ultrasound frequencies for scaring weaver birds as obtained during the field surrey were 25 and 35 kHz (Ibrahim *et al*., 2016). However, in order to moderate the frequencies and adapt it to Ekiti State, two more frequencies were introduced, 20 kHz (below the targeted frequencies) and 45 kHz (above the targeted frequencies). Therefore, four oscillatory circuits were designed, the 20 kHz, 25 kHz, 35 kHz and 45 kHz oscillatory circuits. Each of these circuits comprises of the oscillator and its auxiliary circuit. For this work, the 555 Timer IC (IC_2) connected in astable mode was used as the oscillator and together with resistors and capacitor shown in Figure 2 will generate the frequency.

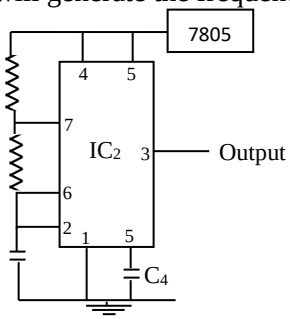

Figure 2: 555 Timer in Astable Mode

The magnitude of ultrasound frequency generated by the oscillator is in accordance with the design equation (Tony, 2009);

$$F = \frac{1}{(0.693 \text{ X } C_3 \text{ X } (R_1 + 2R_2)} \quad (1)$$

where F is the desired frequency of ultrasound, C_3 is the timing capacitor and R_1 and R_2, the timing resistors. F the operating frequency is decided, it is usual to make R_1 about 1 kΩ because this helps to give the output pulses a duty cycle close to 50%. Choices are made for the values of R_1 and C_3 respectively. R_2 can now be calculated using equation (1). The values of R_1 and R_2 must be within practical limits. The design equation of equation (1) will be modified to obtain the respective frequency of operation for each of the oscillatory circuit.

3.2.1The 20 kHz Oscillatory circuit

The design equation and circuit is same as in equation (1) and Figure 2 respectively. After deciding the operating frequency (20 kHz), R_1 was made 1 kΩ and a choice made for the values of C_3 as 10 nF. R_2 can now be calculated using equation (1) to give 3 kΩ. The values of R_1 and R_2 are within practical limits.

3.2.2 For the 25 kHz Oscillatory circuit

$$F = \frac{1}{(0.693 \text{ X } C_5 \text{ X } (R_3 + 2R_4)} \quad (2)$$

Choices were made for the values of R_3 and C_5 as 1.5 kΩ and 10 nF respectively. R_4 can now be calculated using equation (2) to give 2.14 kΩ.

3.2.3 The 35 kHz Oscillatory circuit

$$F = \frac{1}{(0.693 \text{ X } C_7 \text{ X } (R_5 + 2R_6)} \quad (3)$$

With F as 35 kHz, the values of R_5 and C_7 were again chosen as 1.5 kΩ and 10 nF respectively. R_6 was subsequently calculated using equation (3) to obtain 1.3 kΩ.

3.2.4 The 45 kHz Oscillatory circuit

$$F = \frac{1}{(0.693 \text{ X } C_9 \text{ X } (R_7 + 2R_8)} \quad (4)$$

R_7 and C_9 were chosen as 1.5 kΩ and 7 nF respectively. R_8 was subsequently calculated using equation (4) to obtain 1.5 kΩ.

3.3 Frequency Selection Section

Being a multi-frequency device, there is need for a mechanism to select which of the frequency is transmitted at a particular time. This role is played by the frequency selection circuit. It switches ON the output of a particular oscillatory circuit over a period of time while switching OFF others. By so doing, a measure of variability is introduced into the ultrasound signal while controlling the birds both on the farm and at home (Ibrahim *et al*., 2013a). This is also necessary to delay habituation to ultrasound by the weaver birds as stated in the design considerations. As they try to get familiar to a particular frequency, it switches over to the next. Two modes of operation will be considered, the frequency sweep mode and the manual frequency-selection mode. In the frequency sweep mode, it starts by selecting the 20 kHz sound; it switches over to 25 kHz and followed by 35 kHz and 45 kHz. The cycle of frequency selection continues uninterrupted until the frequency sweep mode is disabled. In the manual frequency-selection mode, a choice is made on a frequency or frequencies of interest, only the selected frequency or frequencies is/are transmitted over the period of time.

Four independent frequency selection circuits were designed, 20 kHz frequency selection circuit to select the output of the 20 kHz oscillatory circuit when activated, the 25 kHz frequency selection circuit to select the output of the 25 kHz oscillatory circuit whenever it is activated, the 35 kHz frequency selection circuit to select the output of 35 kHz oscillator when activated and the 45 kHz frequency selection circuit to select the output of the 45 kHz oscillatory circuit. The major component in each frequency selection circuit is the 5 V **Single Pole Double Throw (SPDT)** relay. The relay is interfaced to a source of trigger using a transistor whose role is to drive the relay. Figure 3 shows one of the frequency selection circuits. Three others were designed to select the three other frequencies.

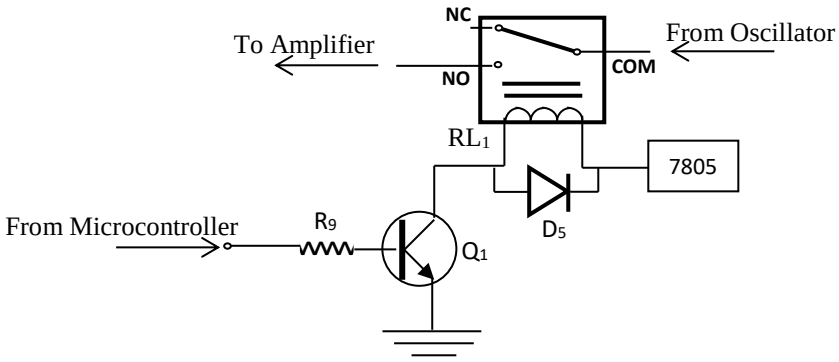

Figure 3: Frequency Selection Section

To activate the network to select a desired frequency, an external source of trigger is required. This is provided by the microcontroller's electronic communication with the base of the transistor. By sending pulses from a particular pin to trigger a particular transistor for certain duration of time, the microcontroller regulates the activity of the section. The control program to do this is written and stored in port 3 (pin 11 to pin 14) location of the microcontroller. Pulse duration of 15 seconds was programmed; it takes one minute to switch ON and OFF all the four frequencies. This is enough to create an unpredictable, noticeable ultrasound frequency change required to delay habituation.

The microcontroller on its own cannot source enough current to energies the coil wounded on the relays soft iron core. Hence a transistor which can amplify the current to operate the relay is needed. A high current transistor BC547 (Q_1) was considered. The normally open (NO) and common (COM) terminals of the four relays were connected from the output of the respective oscillatory circuit (after pin 3 of IC_2 to IC_5). By so doing the ultrasound frequency of that particular oscillatory circuit is switched ON and OFF as desired by a user. Transistors are easily damaged as a result of back emf generated in the relay coil, for this reason fast switching diodes, 1N4148 denoted by D_5 to D_8 were used to prevent reverse current flow, when the transistor is switched OFF. The resistor R_9, usually 1 kΩ was used to provide biasing to the transistor. When the

microcontroller goes high, the transistor BC547 turns ON and current flows through the relay's coil, an electromagnetic field is produced which attract the armature, and causing the COM and NO contact to get connected, and letting out the oscillatory frequency output tied to it.

3.4 Microcontroller Section

The AT89C52 microcontroller (IC_6) is an 8-bit microcontroller with an endurance of 1000 Write/Erase cycles (Kushagra, 2012). It was considered for this work due to its low power requirement of 5V and high recommendation for use in electronic control. Once connected to factory specification using R_{13} (10 K) and C_{10} (10 µF) as shown in Figure 4 and programmed, it faithfully executes inputted instruction, up to a maximum of thirty two instructions.

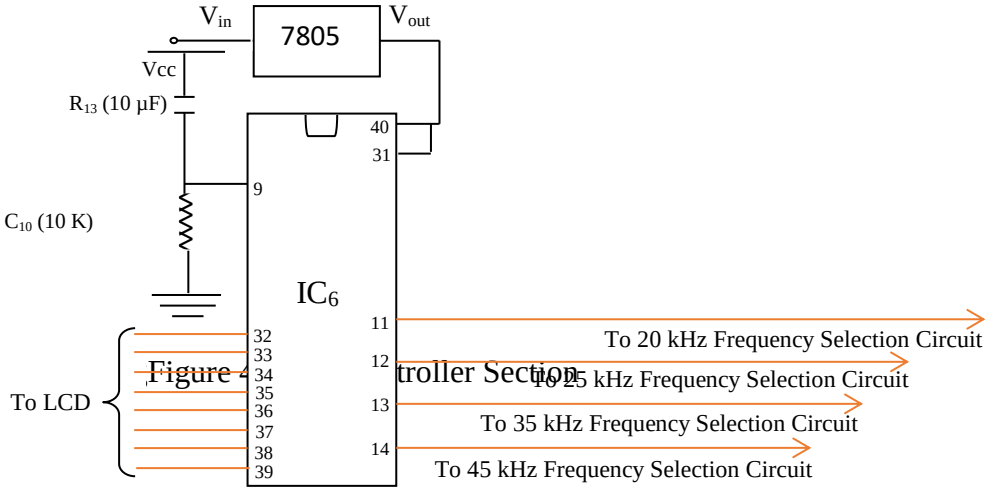

Figure 4 troller Section

In this work, the microcontroller will be used to control two sections of the device. These are: the frequency selection section, and the visual display section. The program to be executed was first written in Assembly Language and stored in specific locations for the respective sections. The program to control the frequency selection is stored in port 3 (pin 11 to pin 14) location while that to control the LCD is stored in port 0 (pin 32 to pin 39) location. Once operational, it automatically exercises control over these sections either by triggering them into operation or enabling them to execute instructions as commanded.

3.5 Visual Display Section

This section permits interaction between the device and a user by visually displaying the current ultrasound frequency being transmitted by the device. In view of the number of data to be displayed, a 16 x 2 Liquid Crystal Display was considered. The LCD will be connected to factory specification as shown in Figure 5.

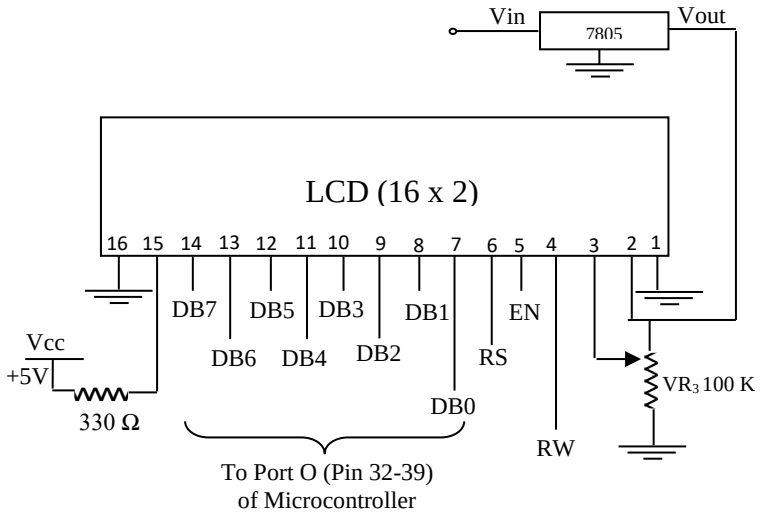

Figure 5: Liquid Crystal Display

The information to be displayed on the LCD is programmed into a memory location (port 0) in the microcontroller and will be executed whenever that pin controlling the location is triggered. The information to be displayed are: “the current frequency is 20 kHz”, “the current frequency is 25 kHz”, “the current frequency is 35 kHz”, “the current frequency is 45 kHz” and “Hello” as an initializing comment. To achieve this, Pin 7 to pin 14 (DBO to DB7) of the LCD is connected to port 0 (pins 32 to 39) of the microcontroller. Through this means, the microcontroller alerts the LCD of its communication with the frequency selection unit where it displays the current selected ultrasound frequency.

3.6 Amplifier Section

Ultrasound signal are easily attenuated in air. For this reason, the design consideration “high penetrative power” was emphasized (Ibrahim *et al.,* 2014). For it to effective on target weaver birds, it should penetrate to a longer distance and at a high intensity. To achieve this, an amplifier of high gain is needed in all the four directions of transmission. For this design, LM 324 (IC_7) was considered appropriate for its gain and space economy. The IC is composed of quad (four) operational amplifiers (op amp) combined in a single chip as shown in Figure 6.

.

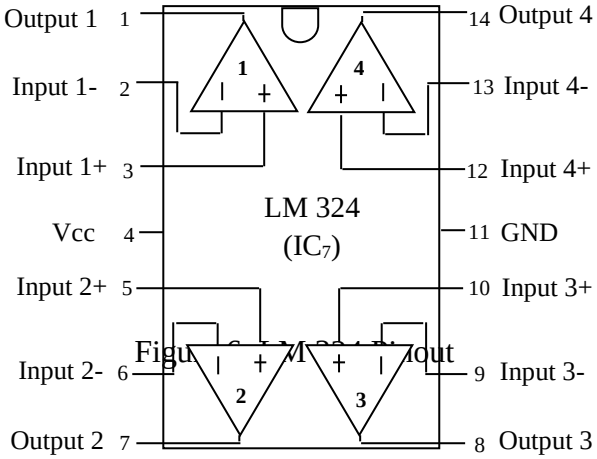

Figure 6: LM 324 Pinout

The gain of each op amp in the IC can be improved upon by external add-on parts. Such was considered as shown in Figure 7 on op amp 1.

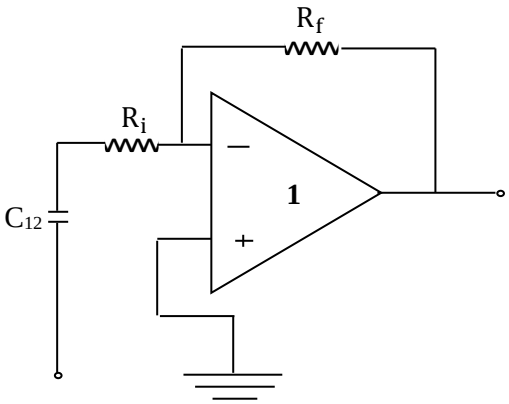

Figure 7: External connection to each Op Amp of LM 324

A feedback loop was connected on the inverting input. The Gain (A_v) of the op amp in this mode is given by;

$$A_v = \frac{R_f}{R_i} \qquad (5)$$

where R_i and R_f are the input and feedback resistors respectively. To avoid diminishing gain encountered at very high frequencies, a gain of 500 was considered. A choice of 1.5 kΩ was made for R_i, and R_f was calculated using equation (5) as 750 kΩ. Same inverting gain was implemented on the three other op amps. By so doing, each of the operational amplifiers in the IC will amplify by this factor of 500 in a particular direction to result in a four directional and amplified transmission. The capacitors C_{11} to C_{14} blocks noise from entering each respective amplifier.

3.7 Ultrasonic Transducer Section

The signal so generated to this point is purely electrical in nature, it needs to be converted to sound energy in order to be sensed and appreciated by the weaver birds. To do this, an ultrasonic transducer is required. An ultrasonic transducer converts ultrasonic frequency signal (electrical energy) into ultrasound (sound energy) **(**Britanica, 2010**)**. The overall objective does not end with conversion to ultrasound, but transmitting the converted ultrasound. To achieve this objective, an ultrasonic twitter with frequency responds high enough to take care of the lowest and highest designed frequencies is required. Table 1 shows the specification of the ultrasonic twitter used due to its broadcast ability.

Table 1: **Specification of ultrasonic tweeter**

SPECIFICATION	DETAILS
Frequency	4-50 kHz
Sensitivity	95 dB 2.83 V/1M
Power	75/300W
Impedance	4-8 Ω
Size	6 x 3 cm
Net Weight	135 g

Four of such twitters were used in this design, each oriented 90º to each other. This arrangement is to guarantee 360º horizontal spread. A capacitor of adequate capacitance is required to couple each of the output of the four amplifiers to their respective ultrasonic twitter. Thus, C_{15} to C_{17} of 220 µF each served as coupling capacitors

4. Results and Discussion

The individual sections designed in this work when integrated forms the overall design for the frequency sweep and manual frequency-select ultrasonic bird pest control device developed to deter weaver birds from rice farms in Ekiti State. The overall circuit diagram showing two of the oscillatory circuits: the 20 and 25 kHz oscillatory circuit, their corresponding frequency selection circuit, two amplifier connections and transmitting in only two of the four perpendicular directions is shown in Figure 8.

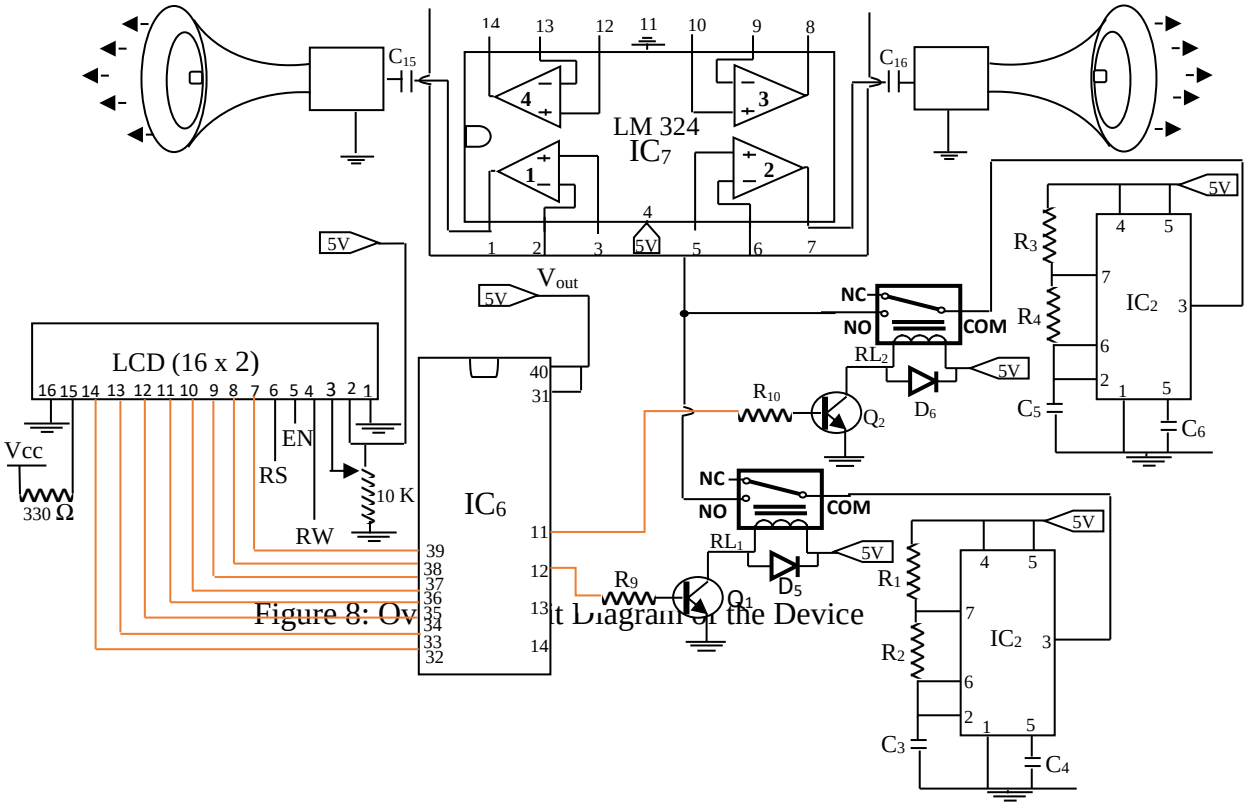

Figure 8: Ov[illegible]t Diagram of the Device

When the device is powered, 5 V DC is made available to all the sections. The oscillatory circuits generate their respective frequencies and await further instructions. The mode of operation whether manual frequency-select or frequency sweep is selected. When in manual frequency-select mode and a frequency is selected by activating the corresponding pin of the microcontroller (with the aid of switch when implemented), it triggers the corresponding frequency selection arm, sending current to toggle the relay for a period of fifteen seconds. The operation of the relay within this period will connect the ultrasound frequency signal generated by the oscillatory circuit into all the individual operational amplifiers of LM 324 for magnification by a multiple of five hundred. The ultrasonic twitters connected to each operational amplifier will convert the hitherto ultrasound electrical signal generated, selected and amplified into ultrasound and broadcast same in their respective directions. When more than one frequency is selected, the microcontroller as programmed will first trigger the lowest frequency into being transmitted. The selected frequency is disconnected after fifteen seconds and the next higher frequency is selected for another fifteen seconds. After running through all the frequencies, it continues the cycle over again until the selection is altered or switched off.

In the sweep frequency mode, all the frequencies from the 20 kHz to 45 kHz are transmitted sequentially for fifteen seconds each, in a continuous cycle. For each frequency selected by the microcontroller as instructed by the user, the LCD is instantly alerted to display programmed information on the selected frequency. By so doing, a user is kept informed about the frequency selections and changes all through the operation.

5. Conclusion

As presented, a specific ultrasonic device designed for weaver birds in Ekiti State is in place. If implemented and tested in whichever mode of operation, there is a guarantee of a high intensity ultrasound capable of penetrating the environment to constantly discomfort weaver birds away from the vicinity of broadcast. The composition of four transmission frequencies changing intermittently at few seconds interval and introduction of variable resistors in the oscillating circuit creates unpredictable variability needed to delay habituation. It prolongs the device's effective period beyond the period of rice vulnerability. With the weaver birds effectively

controlled, rice will yield to its maximum potential. Rice farmers will enjoy bountiful harvest, smiling to the bank and encouraged to cultivate more rice until Ekiti becomes rice sufficient. By so doing, the economic productivity of Ekiti upland rice is enhanced.

Acknowledgement
This research was made possible with the support of the Tertiary Education Trust Fund and the Federal University, Oye, Ekiti State.

References

Adeboye, T. (2012). The Sun Newspaper of 18 October 2012 (http://www.ekiti.com/AboutEkiti/agric.htm,

Akande, T. (2003). "The Rice Sector in Nigeria" United Nation Crop Project (UNCP) Country Agricultural Project on Trade Liberalization in Agricultural Sector and the Environment. Geneva pp 10.

Bright, E.O. (1988). Species Composition of Weaver Bird pests of Rice in Badeggi, Niger State, Nigeria. *Int. Rice Res. Newsl.* 13(6): pp 43.

Bright, E., Manu, S. and Tiamiyu, S. (2007). Empirical Study of Bird Damage in Ofada Rice Production in South West Nigeria. DFID Funded Monograph Series # 33 pp 6, 13, 29.

Bright, E.O, Tologbonse, E.B and Ogunyemi, S. (2009). Farmers' Perceptions and Management Practices of Weaver Bird Pests in Niger State, Nigeria. *Production Agriculture and Technology*5(1):pp 1-13.

Encyclopædia Britannica (2010). Ultrasonic Transducer. Ultimate Reference Suite Chicago.

Ibrahim, A.G., Oyedum, O.D., Awojoyogbe, O.B., Okeke, S.S.N. (2013). Electronic Pest Control Devices: Their Necessity, Controversies and Design Considerations. The International Journal of Engineering and Sciences (IJES), 2(9), 2013, pp 26-30.

Ibrahim, A.G., Oyedum, O.D., Awojoyogbe, O.B., Okeke, S.S.N. (2013). Design, Construction and Characterisation of an Ultrasonic Device for the Control of Birds in Farms. A paper presented at the National Institute of Physics Conference held in March 2013 in Abuja, Nigeria.

Ibrahim, A.G., Oyedum, O.D., Awojoyogbe, O.B., Okeke, S.S.N. (2014). Developmental Features and Implementation Challenges of Electronic Pest Control Devices in Developing Countries. International Journal of Scientific & Engineering Research (IJSER),5(2), 2014, pp 411- 416.

Ibrahim, A.G., 2015. Development and Performance Evaluation of a Solar Powered Ultrasonic Device for the Control of Weaver Birds in Farms. A Ph.D Thesis, Department of Physics, Federal University of Technology, Minna, Nigeria.

Ibrahim, A.G., Oyedum, O.D., Awojoyogbe, O.B., Ezenwora, J.A and Aje, J.D., (2016). Pest and Environmental Specific Application of Ultrasound in Pest Control. Advances in Multidisciplinary and Scientific Research, 2(4) 189 – 200.

Kushagra, S. (2012). www.engineersgarage.com
LM 324 Datasheet National Semi conductor www.alldatasheet.com

Tony, V. (2009). LM555 and LM556 Timer Circuits**,** Doctronics Williams Lab**,** Retrieved 15/7/ 2010 from http://www.matni.com/Arabic/Elec.../NE555%20DETAILS/555.html

USAID MARKET (2008). Improved Packages of Practices for Rice Production, United State Agency for International Development funded Maximising Agricultural Revenue and Key Enterprises in Targetted Sites. Pp. 16.

A MATHEMATICAL MODEL OF YELLOW FEVER DISEASE DYNAMICS INCORPORATING SPECIAL SATURATION INTERACTIONS FUNCTIONS

N. I. Akinwande*[1], S. Abdulrahman[2], T. T. Ashezua[3] and S. A. Somma[1]

[1]Department of Mathematics, Federal University of Technology, Minna, Nigeria

[2]Department of Mathematics, Federal University Birnin Kebbi, Nigeria

[3]Department of Mathematics/Statistics/Computer Science, Federal University of Agriculture, Makurdi, Nigeria

*Corresponding email: aninuola@yahoo.com, aninuola@gmail.com, sam.abu@futminna.edu.ng

Abstract

We proposed an Mathematical Model of Yellow Fever Disease Dynamics Incorporating Special Saturation Process functions, obtained the equilibrium states of the model equations and analyzed same for stability. Conditions for the elimination of the disease in the population are obtained as constraint inequalities on the parameters using the basic reproduction number R_0. Graphical simulations are presented using some demographic and epidemiological data.

Keywords: Basic Reproduction Number, Equilibrium States, Saturation Process, Stability

1. Introduction

We present a model of five ordinary differential equations representing the dynamics of Yellow Fever Infection in a host population of humans enabled by vector populations of mosquitoes which facilitate the transmission of the causative virus. We obtain the Disease Free Equilibrium state and analyze same for stability using the Reproduction number.

In the urban Yellow Fever infection dynamics, the virus incubation period in the host is from 3 to 6 days after an effective interacting bite of a virus carrying vector. The host is humans while the vector is the *aedes egypti* specie of mosquitoes. The Yellow Fever infection is characterized by the sudden onset of fever, chills, intense headache, lumbosacral and generalized muscular pain, nausea, vomiting and lethargy. All these result in a short remission of the fever, and the development of haemorrhagic signs, jaundice, bleeding from the nose and gums, black vomit and stool, anuria (failure to pass urine), hypertension, shock and death within 10 days if not treated, (Tomori, 1988). It is worthy of note that after surviving a Yellow Fever infection, the host will have a life-long immunity. Also, the infant have natural immunity for the first nine months of birth so all the offspring of the host are born as susceptible. The dynamics of Yellow Fever though has some similarity with Malaria yet has its own peculiarity as outlined above.

According to Monath (1989), Van der *et al.* (1999), Figueiredo (2000), Souza (2010) and Auguste *et al.* (2010), Yellow fever virus (YFV) is the prototype species for the genus *Flavivirus*. Historically, YFV is one of the most important human arboviral pathogens. It continues to cause large sporadic epidemics in Africa but typically emerges as epizootics among nonhuman primates in South America with or without associated human cases. Several phylogenetic studies have shown that YFV is locally maintained during these interepizootic periods in Peru, Bryant *et al.* (2003), Brazil, Vasconcelos *et al.* (2004), and Auguste *et al.* (2010). Yellow fever virus

undergoes regionally independent evolution within some countries, (Bryant *et al.* 2003). The sporadic emergence of YFV in the Americas has been strongly associated with infection of red howler monkeys *Alouatt aseniculus*, which are particularly susceptible to disease, (Auguste *et al.* 2015).

In section 3, the notations and definitions of parameters and variables together with the set of the model equations are presented. In section three, we obtain the Disease Free Equilibrium state of the model equations, obtained the Reproduction number and analyze the state for stability or otherwise. The concluding remark is presented in section 5.

2. Literature Review

Yellow fever virus (YFV) is mainly transmitted through the bite of the yellow fever mosquito *Aedes aegypti*, but other mosquitoes such as the tiger mosquito (*Aedes albopictus*) can also serve as a vector for this virus. Like other Arboviruses which are transmitted via mosquitoes, the yellow fever virus is taken up by a female mosquito when it ingests the blood of an infected human or other primate. Viruses reach the stomach of the mosquito, and if the virus concentration is high enough, the virus can infect epithelial cells and replicate there, (Fontenille *et al*. 1997).

Akinwande (1996), formulated a model of yellow fever epidemics, which involves the interactions of two principal communities; hosts (humans) and Vectors *(aedes aegypti* mosquitoes). The host community was divided into three compartments of Susceptible $S(t)$, Infected $I(t)$ and Recovered $R(t)$ while the vector community was partitioned into two compartments of Susceptible $N(t)$ and Infective or virus carriers $M(t)$ where $t \geq 0$ is the time. He analyzed the local stability of the model using Jacobian matrix and implicit function.

Fernandez *et al.* (2013), formulated a model and incorporated the biology of the urban vector of yellow fever, the mosquito *Aedes aegypti*, the stages of the disease in the host (humans). From the epidemiological point of view, the mosquito follows a SEI sequence (Susceptible, Exposed, Infective). In their, model the adult populations are subdivided according to their status with respect to the virus. They assumed that there is no vertical transmission of the virus and eggs, larvae, pupae and non parous adults are always susceptible. The humans are subdivided in sub-populations according to their status with respect to the illness as: susceptible (S), exposed (E), infective (I), in remission (r), toxic (T) and recovered (R).

Hui-Ming *et al.* (2008), considered an epidemic model of a vector-borne disease which has direct mode of transmission in addition to the vector-mediated transmission. The incidence term is assumed to be of the bilinear mass-action form. They include both a baseline ordinary differential equation (ODE) version of the model, and, a differential-delay model with a discrete time delay. The delay in the differential-delay model accounts for the incubation time the vectors need to become infectious. They studied the effect of that delay on the stability of the equilibria.

3. Methodology

3.1 Model Formulation

At time instant $t \geq 0$ the host community is separated into three disjoint compartments namely Susceptible $S(t)$, the Infected $I(t)$ and Recovered/Immune $R(t)$ while the vector community is partitioned into two compartments namely virus carriers $M(t)$ and non-virus carriers $N(t)$.

An effective bite among the interacting compartments is defined as the bite that results in the transmission of virus; essentially between $N(t)$ and $I(t)$ on one hand and $M(t)$ and $S(t)$ on the other. Using the method adopted by Sowunmi (1987), we construct the interaction functions as follow:

3.2 Construction of Virus Transmission Interaction Saturation Functions

Let

p = the probability that a member of the Susceptible hosts $S(t)$ is effectively bitten by a virus carrier member from the $M(t)$ compartment.

q = the probability that a member of the Infected hosts $I(t)$ is effectively bitten by a non-virus carrier member from the $N(t)$ compartment.

$$(1-p)^{-1} = a \ , \ (1-q)^{-1} = b \ ; \ 0 \le p, q \le 1 \text{ and } 1 \le a, b < \infty . \tag{3.1}$$

Thus $1-p$ is the probability that no effective bite takes place between $S(t)$ and $M(t)$ while

$1-q$ is the probability that no effective bite takes place between $I(t)$ and $N(t)$.

Then

$(1-p)^{M(t)}$ gives the proportion of the susceptible host members who are not bitten effectively at time $t \ge 0$, and

$(1-q)^{I(t)}$ gives the proportion of the non-vector carrier members which did not bite effectively at time $t \ge 0$.

Let

$$(1-p)^{M(t)} = \exp[-\alpha_1 M(t)], \ \alpha_1 = \log a \tag{3.2}$$

The proportion of the susceptible class who are effectively bitten at time $t \ge 0$ will be given by

$$B(\alpha_{1,} M(t)) = 1 - \exp[-\alpha_1 M(t)] \tag{3.3}$$

Also

$$(1-q)^{I(t)} = \exp[-\alpha_2 I(t)], \ \alpha_2 = \log b \tag{3.4}$$

the proportion of the non-virus carrier class which effectively bite at time $t \ge 0$ will be given by

$$B(\alpha_{2,} I(t)) = 1 - \exp[-\alpha_2 I(t)] \tag{3.5}$$

The virus transmission interaction function between $S(t)$ and $M(t)$ is thus given by

$$f_1(S,M) = B(\alpha_{1,}M(t))S(t) = (1-\exp[-\alpha_1 M(t)])S(t) \quad (3.6)$$

And between $N(t)$ and $I(t)$ is given by

$$f_2(N,I) = B(\alpha_{2,}I(t))N(t) = (1-\exp[-\alpha_2 I(t)])N(t) \quad (3.7)$$

These functions are saturation functions, we have that

$$f_1(S,0) = f_1(0,M) = 0$$

$$f_2(I,0) = f_2(0,N) = 0$$

Also

$f_1(S,M) \to S$, as $M \to \infty$

$f_2(I,N) \to N$, as $I \to \infty$

3.3 Definition of Parameters & Variables

β_1 = natural per capita birth rate for the host population.

μ_1 = natural per capita death rate for the host population.

γ = per capita immunization rate

α = per capita recovery rate

δ = per capita death rate from infection in the host population.

w = per capita loss of immunity rate in the Recovered/Immune host compartment.

β_2 = natural per capita birth rate for the vector population.

μ_2 = natural per capita death rate for the vector population.

θ = proportion of the infants/eggs of $M(t)$ with virus

$S(t)$ = Susceptible host compartment.

$I(t)$ = Infected host compartment.

$R(t)$ = Recovered/Immune host compartment.

$N(t)$ = Non-Virus-Carrying vector compartment.

$M(t)$ = Virus-Carrying vector compartment.

t = time

3.4 The Model Equations

$$\frac{dS(t)}{dt} = \beta_1 - \left(\mu_1 + \gamma + B(\alpha_1, M(t))\right)S(t) + wR(t) \tag{3.8}$$

$$\frac{dI(t)}{dt} = B(\alpha_1, M(t))S(t) - \left(\mu_1 + \delta + \alpha\right)I(t) \tag{3.9}$$

$$\frac{dR(t)}{dt} = \alpha I(t) + \gamma S(t) - \left(\mu_1 + w\right)R(t) \tag{3.10}$$

$$\frac{dN(t)}{dt} = \theta\beta_2 + \mu_2 M(t) - B(\alpha_2, I(t))N(t) \tag{3.11}$$

$$\frac{dM(t)}{dt} = (1-\theta)\beta_2 - \mu_2 M(t) + B(\alpha_2, I(t))N(t) \tag{3.12}$$

$$B(\alpha_1, M(t)) = 1 - \exp(-\alpha_1 M(t)) \tag{3.13}$$

$$B(\alpha_2, I(t)) = 1 - \exp(-\alpha_2 I(t)) \tag{3.14}$$

3.5 Computation of the Reproduction Number

In this section we compute the Reproduction number for the system of equations (3.8) – (3.14).

The basic reproduction number is the average number of secondary infections caused by a single infectious individual during his/her entire infectious life time. Applying next generation matrix operator to compute the Basic Reproduction Number of the model as used by Diekmann *et al*, (1990) and improved by Driessche and Watmough (2002). The basic reproduction number is obtained by dividing the whole population into n compartments in which there are $m < n$ infected compartments. Let x_i, $i = 1, 2, 3, \ldots, m$ be the numbers of infected individuals in the i^{th} infected compartment at time t. The largest eigenvalue or spectral radius of FV^{-1} is the basic reproduction number of the model.

At equilibrium state let

$$S(t) = x,\ R(t) = y,\ I(t) = z,\ N(t) = p,\ M(t) = q \tag{3.15}$$

Now, R_0 is the spectral radius (highest eigen value) of FV^{-1}, where F (infection terms) and V (transition terms) are Jacobian matrix obtained from the infected classes of the model equations, i.e. equations (3.9) and (3.12).

Thus,

$$F = \begin{pmatrix} 0 & x\alpha_1 e^{-\alpha_1 q} \\ p\alpha_2 e^{-\alpha_2 z} & 0 \end{pmatrix} \tag{3.16}$$

And

$$V = \begin{pmatrix} (\mu_1 + \delta + \alpha) & 0 \\ 0 & \mu_2 \end{pmatrix} \tag{3.17}$$

So that,

$$V^{-1} = \frac{1}{\mu_2(\mu_1 + \delta + \alpha)} \begin{pmatrix} \mu_2 & 0 \\ 0 & (\mu_1 + \delta + \alpha) \end{pmatrix} \tag{3.18}$$

i.e.

$$V^{-1} = \begin{pmatrix} \frac{1}{(\mu_1 + \delta + \alpha)} & 0 \\ 0 & \frac{1}{\mu_2} \end{pmatrix} \tag{3.19}$$

Then,

$$FV^{-1} = \begin{pmatrix} 0 & x\alpha_1 e^{-\alpha_1 q} \\ p\alpha_2 e^{-\alpha_2 z} & 0 \end{pmatrix} \begin{pmatrix} \frac{1}{(\mu_1 + \delta + \alpha)} & 0 \\ 0 & \frac{1}{\mu_2} \end{pmatrix} \tag{3.20}$$

i.e.

$$FV^{-1} = \begin{pmatrix} 0 & \frac{x\alpha_1 e^{-\alpha_1 q}}{\mu_2} \\ \frac{p\alpha_2 e^{-\alpha_2 z}}{(\mu_1 + \delta + \alpha)} & 0 \end{pmatrix} \tag{3.21}$$

Now, to get the eigenvalues, we have

$$\left| FV^{-1} - \lambda \right| = 0$$

i.e.

$$\begin{vmatrix} 0 - \lambda & \frac{x\alpha_1 e^{-\alpha_1 q}}{\mu_2} \\ \frac{p\alpha_2 e^{-\alpha_2 z}}{(\mu_1 + \delta + \alpha)} & 0 - \lambda \end{vmatrix} = 0 \tag{3.22}$$

which gives

$$\lambda = \pm \sqrt{\frac{x\alpha_1 e^{-\alpha_1 q} p\alpha_2 e^{-\alpha_2 z}}{\mu_2 (\mu_1 + \delta + \alpha)}} \tag{3.23}$$

Thus, Reproduction number R_o is given by the highest eigenvalue, i.e.

$$R_0 = \sqrt{\frac{x\alpha_1 e^{-\alpha_1 q} p\alpha_2 e^{-\alpha_2 z}}{\mu_2(\mu_1 + \delta + \alpha)}} \tag{3.24}$$

Setting $z = q = 0$ in (3.15) at Disease Free State, we have

$$R_0 = \sqrt{\frac{xp\alpha_1\alpha_2}{\mu_2(\mu_1 + \delta + \alpha)}} \tag{3.25}$$

If $R_o < 1$ we have that

$$\alpha_1 < \frac{\mu_2(\mu_1 + \delta + \alpha)}{xp\alpha_2} = \alpha_{1\max} \tag{3.26}$$

The inequality (3.17) gives an upper bound on the susceptible hosts infection per capita which guarantees the stability of the Disease Free State resulting in the imminent removal of the infection from the population.

4 Results and Discussion

4.1 Graphical Profiles

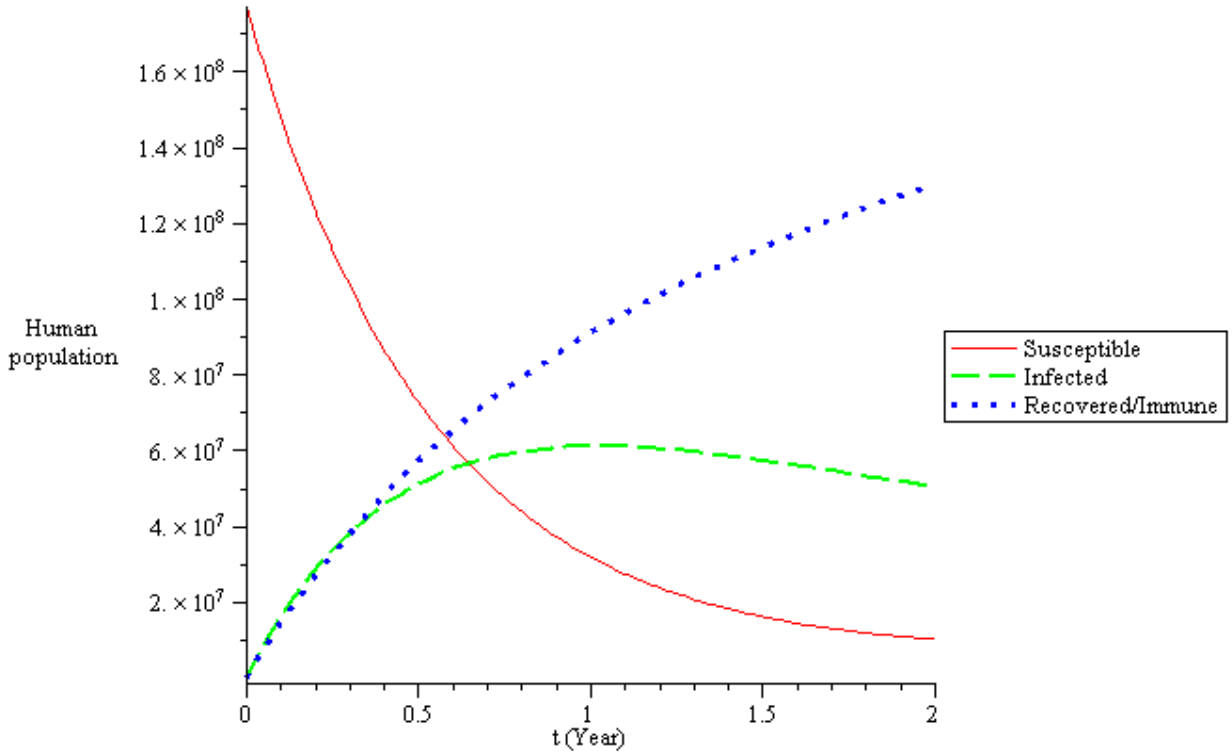

Figure 4.1: Effect of High Immunization Rate γ

Figure 4.1, is the effect of high immunization rate on the entire human population. It was observed that, the susceptible population decreases while the recovered/immune increases, this is because the susceptible individuals that are successfully immunized moved to recovered class. The increase of infected population was not high because only few susceptible were infected.

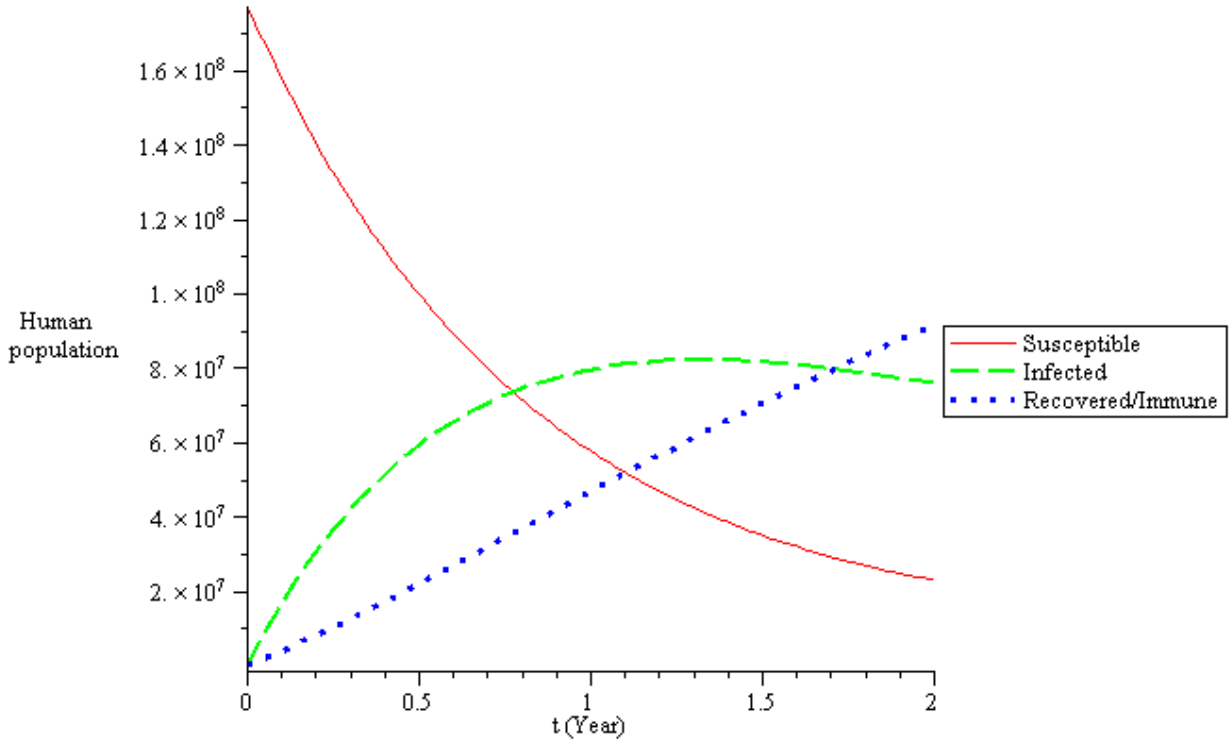

Figure 4.2: Effect of Low Immunization Rate γ

Figure 4.2, is the effect of low immunization rate on the entire human population. It was observed that, the susceptible population decreases while the recovered/immune increases. But the decrease and increase on susceptible and recovered are not the same as that of high immunization rate. It was also shown that, the increase of infected population was high compare to that of figure 4.1, this is because only more susceptible were infected with low immunization rate.

5 Conclusion

The basic reproduction number R_0 was computed and used to determine an upper bound for the biting/infection rate α_1 . For the effective control of the disease, the biting/infection rate $\alpha_1 < \alpha_{1\max}$. The effect of high and low immunization rate γ on the entire human population was presented graphically, and it was observed that with high immunization rate the susceptible human population decreases and the recovered/immune population increases. Therefore the immunization rate γ should be kept high in order to eliminate the disease from the population.

References

Akinwande, N. I., (1996), A Mathematical Model of Yellow Fever Epidemics, AfrickaMathematika, 6: 50-59.

Auguste A. J, Lemey P, Pybus O. G., Suchard M. A., Salas R. A., Adesiyun A. A., (2010). Yellow Fever Virus Maintenance in Trinidad and its Dispersal throughout the Americas.*Journalof Virology;* 84(19): 9967–9977.

Auguste A. J., Lemey P., Bergren N. A., Giambalvo D., Moncada M., Morón D., Rosa Hernandez, Hernandez R., Navarro J., and Weaver S. C., (2015). Enzootic Transmission of Yellow Fever Virus, Venezuela, *Emerging Infectious Disease;* 21(1): 99-102.

Bryant J, Wang H, Cabezas C, Ramirez G, Watts D, and Russell K, (2003). Enzootic Transmission of Yellow Fever Virus in Peru.*Emerging Infectious Disease*, 9(8): 926–933.

Diekmann, O.; Heesterbeek, J. A. P. & Metz, J. A. J. (1990)."On the Definition and the Computation of the Basic Reproduction Ratio R_0 in Models for Infectious Diseases in Heterogeneous Populations".*Journal of Mathematical Biology*, 28 (4): 365–382.

Driessche Van Den, P. &Watmough, J. (2002)."Reproduction Numbers and Sub-threshold Endemic Equilibria for Compartmental Models of Disease Transmission".*Mathematical Biosciences*180 (1–2): 29–48.

Fernandez M L, Otero M, Schweigmann N and Solari H G, (2013), A Mathematically Assisted Reconstruction of the Initial Focus of the Yellow Fever Outbreak in Buenos Aires (1871). Papers in Physics, vol. 5, art. 050002.

Figueiredo LT, (2000). The Brazilian Flaviviruses.*Microbes and Infections;* 2(13):1643–1649.

Fontenille D, Diallo M, Mondo M, Ndiaye M, and Thonnon J., (1997). "First Evidence of Natural Vertical Transmission of Yellow Fever Virus in *Aedesaegypti*, its Epidemic vector". *Transactions of the Royal Society of Tropical Medicine and Hygiene***91** (5): 533–5. doi:10.1016/S0035-9203(97)90013-4

Hui-Ming W., Xue-Zhi L., and Maia M., (2008). An Epidemic Model of a Vector-borne Disease with Direct Transmission and Time Delay, *Journal of Mathematical Analysis and Applications*; 342(2): 895-908.

Monath TP, (1989). Yellow Fever. In: Monath TP, editor. The arboviruses: Ecology and Epidemiology. Boca Raton (FL): CRC Press.; 5: 139–231.

Souza R P, Foster P G, Sallum M A, Coimbra T L, Maeda A Y, Silveira V R, Moreno E S, Silva F G, Rocco I M, Suzuki A, Ferreira I B, Oshiro F M, Petrella S M, Pereira L E, Katz G, Tengan C H, Siciliano M M and Santos C L, (2010). Detection of a New Yellow Fever Virus Lineage within the South American Genotype I in Brazil.*Journal of Medical Virology*; 82(1):175–185.

Sowunmi, C. O. A. (1987). On a Set of Sufficient Conditions for the Exponential Asymptotic Stability of Equilibrium States of a Female Dominant Model; *J. Nig. Math Soc.* 6, 59 – 69.

Tomori, O. (1988), Mathematical Modeling and Disease Epidemics; *Proceedings of the International Workshop on Biomathematics, University of Ibadan, Ibadan, Nigeria;* 9-22.

Van der Stuyft P, Gianella A, Pirard M, Cespedes J, Lora J, Peredo C, (1999) Urbanisation of Yellow Fever in Santa Cruz, Bolivia. *The Lancet;* 353(1964):1558–1562.

Vasconcelos P F, Bryant J E, da Rosa T P, TeshR B, Rodrigues S G, Barrett AD, (2004). Genetic Divergence and Dispersal of Yellow Fever Virus, Brazil.*Emerging Infectious Disease;* 10(9): 1578–1584.

PATH LOSS MODELS FOR TERRESTRIAL BROADCAST IN VHF BAND IN MINNA CITY, NIGER STATE, NIGERIA

Moses Abiodun Stephen*[1], Oyedum Onyedi David[2], Ajewole Moses Oludare[3]
[1,2]Department of Physics, Federal University of Technology Minna, P.M.B. 65 Minna, Niger State, Nigeria
[3]Department of Physics, The Federal University of Technology Akure, P.M.B. 704 Akure, Ondo State, Nigeria
[1]abiodun.moses@futminna.edu.ng*
[2]oyedumod@yahoo.com
[3]oludare.ajewole@futa.edu.ng

* Corresponding author

Abstract

Propagation models are required for proper planning of a network and for accurate interference estimation, or else, it could result in networks with high co-channel interference and a waste of power. This research work aims to adapt a propagation model that is best suitable for Minna city in Niger State, Nigeria. This is done by optimisation of some existing empirical propagation models - Free space, Hata, CCIR and Ericsson path loss models, to suit Minna city using a VHF television signals of Nigeria Television Authority (NTA) Minna, channel 10. The station transmits at 210.25 MHz for video signal. The signal levels of the transmitted signal were measured along five radial routes from the transmitting station with a digital signal level meter and Global Positioning System (GPS) was used to measure the corresponding distances. Data processing and computation were carried out using SPSS and Microsoft software applications. The results show that the Ericsson Model gives more accurate prediction for path loss in Minna city after general modification with the correction factor of -38.72 and Root Mean Square Error of 6.34 dB.

Keywords: Path loss, Propagation models, Signal level, VHF

1. Introduction

Wireless communication involves transfer of information between two antennas (transmitter and receiver) by means of radio wave. Consequently, the interaction between the radio wave and the objects that surround these two antennas severely affect the signal resulting to path loss.

There are numerous path loss prediction models but none of these models can be generalised for all environments and localities, instead, they are suitable for some specific areas, terrain and climate. However, path loss model's parameters can be adjusted according to the specific environment to obtain minimal error between predicted and measured signal strength (Ayeni *et al*., 2015).

Path loss models are used in network planning, for conducting feasibility studies and in the course of initial deployment. Furthermore, they are important for predicting coverage area, interference estimation and frequency assignments which are basic elements for network planning process in terrestrial broadcast systems (Mardeni and Pey, 2012). Propagation models can be divided into three types of models, namely: the empirical models, deterministic models and semi-deterministic models (Mardeni and Kwan, 2010).

The empirical approach relies on fitting curves or analytical expressions to sets of measured data and has the advantage of implicitly taking into account all factors (known and unknown). Therefore, it does not explain a system but are based on observations and measurements alone (Shahajahan and Abdulla, 2009). Some situations are not possible to be explained by mathematical model, so some data are used to predict the behaviour approximately.

Empirical models were employed in this research work. Free space, Hata, CCIR and Ericsson path loss models were modified and generalised to suit Minna city in Niger State, Nigeria, using VHF television

signal of Nigeria Television Authority (NTA), Minna, channel 10. This station transmits at a frequency of 210.25 MHz for video signal and 215.25 for audio signal.

2. Path Loss Models

Path loss means attenuation of radio waves between transmitter and receiver in radio communication system. The effects of reflection, refraction, diffraction, absorption, as well as free space loss between the transmitter and the receiver could lead to path loss (Mardeni and Kwan, 2010). There are many empirical path loss models for radio communication systems but attention will be given to the prediction models by free space, Hata, CCIR and Ericsson model because these models have been widely accepted and therefore will be used to evaluate the propagation measurement results.

2.1 Free Space Propagation Model

In free space, radio wave is not reflected or absorbed but as the power spread over a greater area, the signal attenuate. Free space propagation between transmitting and receiving antennas may be assumed when both antennas are sufficiently high, so that only the direct signal gets to the receiving antenna. If the transmitting antenna gain is G_t and the transmitter power is W_t , power density P_r at distance d can be expressed as (Kurniawan, 1997):

$$P_r = \frac{W_t G_t}{4\pi d^2} \tag{1}$$

Received power W_r at distance d with a receiving antenna gain G_r is therefore

$$W_r = \frac{W_t G_t}{4\pi d^2} \cdot \frac{\lambda^2 G_r}{4\pi} \tag{2}$$

or $\frac{W_r}{W_t} = G_t G_r \left(\frac{\lambda}{4\pi d}\right)^2$

$$= G_t G_r \left(\frac{c}{4\pi d f}\right)^2 \tag{3}$$

where:

G_t: transmitting antenna gain
G_r: receiving antenna gain
d: distance
c: speed of propagation (3 x 10^8 m/s)
f: carrier frequency.

For isotropic transmitting and receiving antennas, $G_t = G_r = 1$ and if distance d is expressed in km and carrier frequency f in MHz, the ratio between W_r and W_t in dB can be expressed as:

$$L_f = 32.45 + 20\log_{10} f + 20\log_{10} d \tag{4}$$

where L_f (dB) is free space loss between two isotropic antennas.

2.2 Hata's Propagation Model

Hata model was derived from Okumura field strength curves and various path loss equations for different types of environment were predicted. For Hata model, distance from the base station ranges from 1 km to 20 km, mobile antenna height is between 1 m and 10 m, base station antenna height is between 30 m and 200 m and carrier frequency is between 150 MHz and 1500 MHz (Nadir,, 2011). Furthermore, Hata's model is classified into urban area, suburban and open space models (Mardeni and Kwan, 2010):

Path loss for Hata model is defined as:

$$L_p = A + B \log_{10} d \quad \text{(urban area)} \tag{5}$$

$$L_p = A + B \log_{10} d - C \quad \text{(Suburban area)} \tag{6}$$

$$L_p = A + B \log_{10} d - D \quad \text{(rural area)} \tag{7}$$

where:

$$A = 69.55 + 26.16 \log_{10}(f_c) - 13.82 \log_{10}(h_b) - a(h_m) \tag{8}$$

$$B = 44.9 - 6.55 \log_{10}(h_b) \tag{9}$$

$$C = 5.4 + 2[\log_{10}(\tfrac{f_c}{28})]^2 - 19.33 \log_{10}(f_c) \tag{10}$$

The parameter $a(h_m)$ is a "correction factor"

For medium or small city:

$$\mathrm{a(h_m)} = [1.1 \log_{10}(\mathrm{f_c}) - 0.7]\mathrm{h_m} - [1.56 \log_{10}(\mathrm{f_c}) - 0.8] \tag{11}$$

For large city:

$$a(h_m) = 8.23[\log_{10}(1.54 h_m)]^2 - 1.1 \quad \text{for} \quad f_c \leq 200\ MHz \tag{12}$$

$$a(h_m) = 3.2[\log_{10}(11.75 h_m)]^2 - 4.97 \quad \text{for} \quad f_c \geq 400\ MHz \tag{13}$$

where:

h_m is mobile antenna height above local terrain height (m)
d is distance between the mobile antenna and the base station antenna
h_b is base station antenna height above local terrain height (m) and
f_c is carrier frequency (MHz)

2.3 CCIR Path Loss Model

The *Comit´e International des Radio-Communication* (CCIR), now International Telecommunication Union - Radiocommunication Sector (ITU-R) published an empirical formula for the combined effects of free space path loss and terrain induced path loss given as (Lee and Miller, 1998):

$$L_{CCIR} = 69.55 + 26.16 \log_{10}(f_{MHz}) - 13.82 \log_{10} h_b - a(h_m) + [44.9 - 6.55 \log_{10} h_b] \log_{10}(d_{km}) - B \tag{14}$$

where h_b and h_m are base station and mobile antenna heights in meters respectively, d_{km} is the link distance in kilometers, f_{MHz} is the frequency in megahertz,

$$\mathrm{a(h_m)} = [1.1 \log_{10}(\mathrm{f_{MHz}}) - 0.7]\mathrm{h_m} - [1.56 \log_{10}(\mathrm{f_{MHz}}) - 0.8] \tag{15}$$

$$B = 30 - 25 \log_{10}(\%\ of\ areas\ covered\ by\ buildings) \tag{16}$$

This formula is the Hata model for medium-small city propagation conditions with a correction factor, B.

2.4 Ericsson Model

Ericsson model is a modified Hata model that gives allowance for changing the parameters according to the propagation environment. Path loss according to this model is given by (Milanovic *et al*., 2007):

$$L_E = a_o + a_1.\log_{10}(d) + a_2.\log_{10}(h_b) + a_3.\log_{10}(h_b).\log_{10}(d) - 3.2[\log_{10}(11.75h_r)^2)] + g(f) \quad (17)$$

where $g(f)$ is defined by:

$$g(f) = 44.49\log_{10}(f) - 4.78(\log_{10}(f))^2 \quad (18)$$

and

f : frequency (MHz)
h_b: transmission antenna height (m)
h_r: receiver antenna height (m)

The default values of a_o, a_1, a_2 *and* a_3 are 36.2, 30.2, 12.0 and 0.1 respectively for urban terrain.

3. Study Area

Minna is a capital city of Niger State in North Central Nigeria (Figure 1), the most populous black nation in the world with estimated population of 304,113 in 2007 (http://en.wikipedia.org/wiki/Minna, 2016). Minna is surrounded by granite hills to the north and to the east while the west and the southern parts of the town extend on a lowly plain. The city has a moderate weather, with lows of 24ºC and highs of 30ºC in the dry season, around the month of April. More also, it has a tall grassland vegetation and woody area close to river valleys (http://www.world66.com/africa/nigeria/minna/, 2016).

Figure 1: Location of Minna (9º36'50"N, 6º33'25"E) in Nigeria (http://en.wikipedia.org/wiki/Niger_State, 2016)

4. Data Collection and Analysis

The effective radiating power of the transmitter of the television station during the period of this work was 7.5 kW and the transmitting antenna was mounted on a mast of height 150 m. The signal level of the transmitted video signal was measured along five radial routes from the transmitting station and the routes are designated Route A, Route B, Route C, Route D and Route E as shown in Figure 2. A dipole antenna of 1.5 m high above ground surface was connected to a Digital Signal Level Meter - GE-5499, to measure the signal levels of the transmitted signal from the station along these routes. Each signal level corresponding distance, elevation

above the mean sea level and location (Longitude and Latitude) were also measured using Global Positioning System (GPS 72 – Personal Navigator).

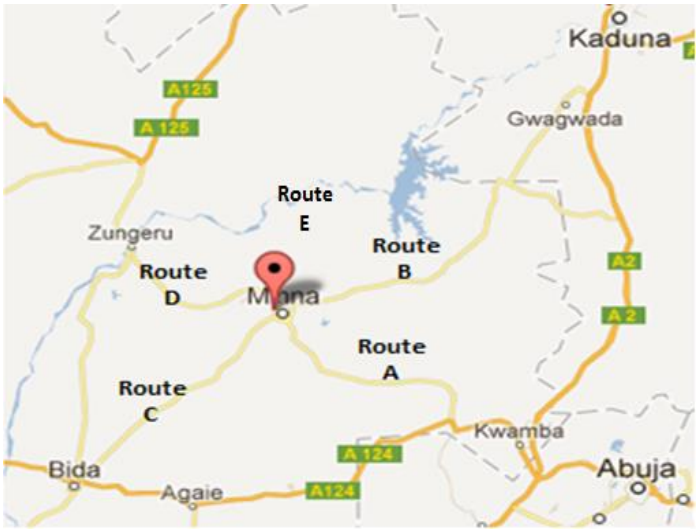

Figure 2: The routes along which measurements were taken (http://www.geodata.us/weather/place.php?usaf=651230&uban=99999&c=Nigeria&y=2011, 2016)

Data processing and computation were carried out using SPSS and Microsoft software applications. From the measured signal level, the path loss for each route was obtained and the corresponding path loss as predicted by Free space, Hata, CCIR and Ericsson models were also estimated. The Root Mean Square Error or Deviation (RMSE) for each model along all the routes was determined. Similarly, the Mean Prediction Error (MPE) was estimated and used as a correction factor to modify each model to obtain the least RMSE. To generalise each model for all the routes in Minna, instead of having a number of correction factors for a single model for a city, as a result of different routes considered, the average values of the MPE of the five radial routes were obtained and used as the correction factors to generalise the path loss models.

5. Results

The path loss models and the measured path loss for each route are shown in Figure 3 to Figure 7. All the models follow the same trend for all the routes. The Free space model has the lowest path loss prediction while Ericson model has the highest path loss prediction. At this frequency (210.25 MHz), the path loss predicted by Hata model for large city and Hata model for small city have almost the same values, consequently, the two graphs overlapped.

The RMSE of all the path loss models for each route are shown in Table 1. Hata model for suburban environment has the least error for route A, B, C and E (6.01 dB, 7.17 dB, 5.70 dB and 5.04 dB respectively) while Hata model for large city has the least error (5.82 dB) for route D. Each route has different path loss because of the irregular elevation of the surface of the ground. The ground elevation is high in some parts of the city and low in some other parts, moreover, there are also hills in some part of the city (Ajewole *et al*., 2013).

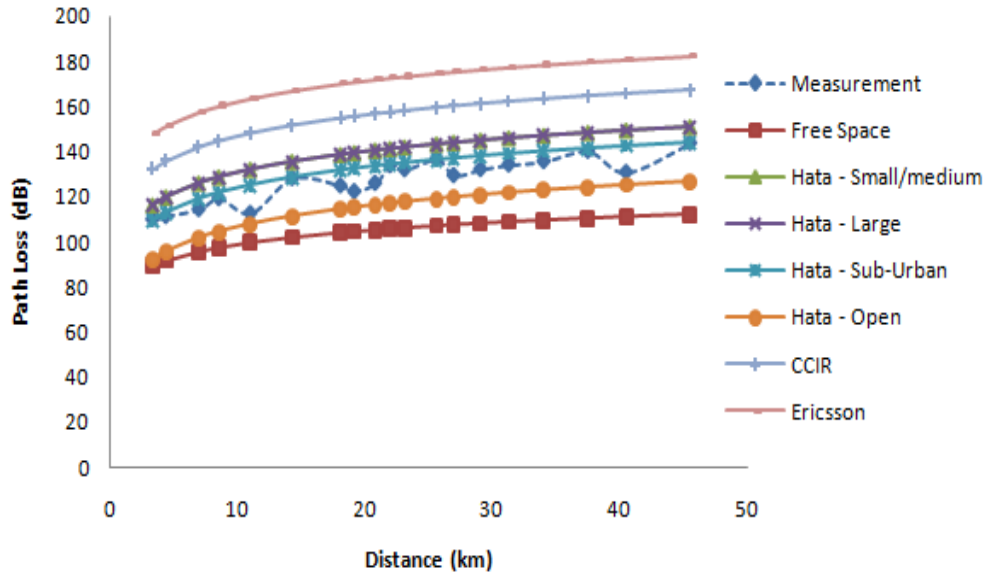

Figure 3: Path loss models for route A

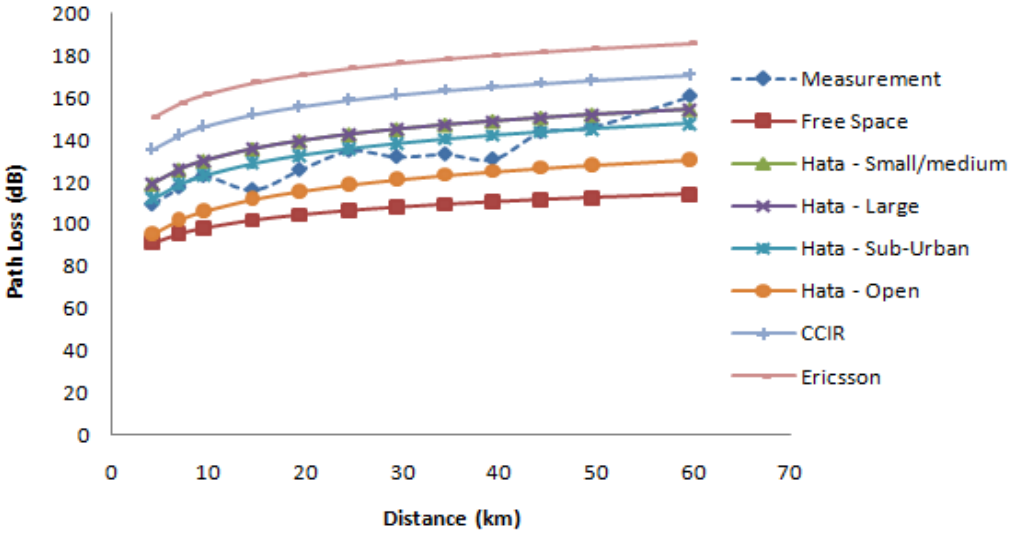

Figure 4: Path loss models for route B

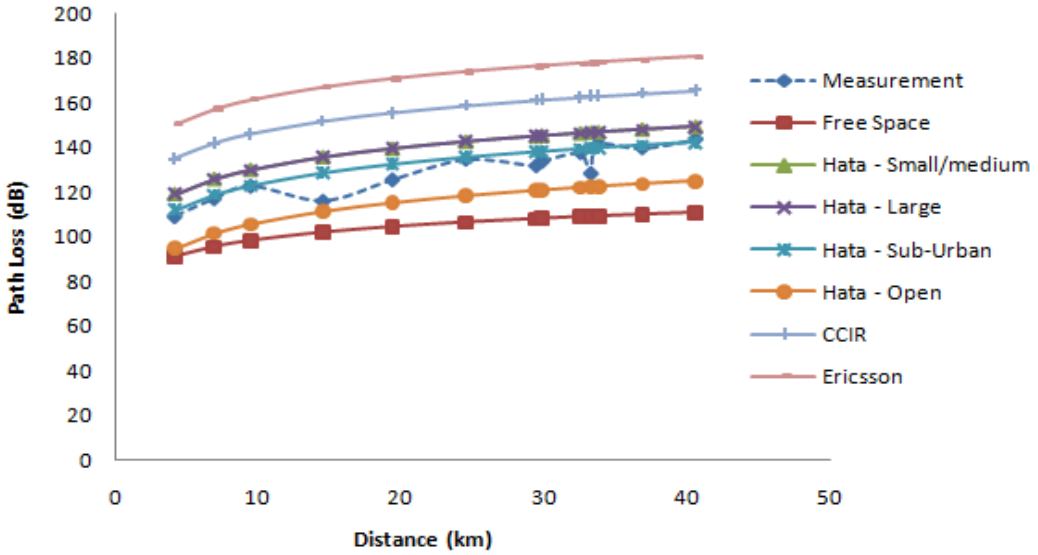

Figure 5: Path loss models for route C

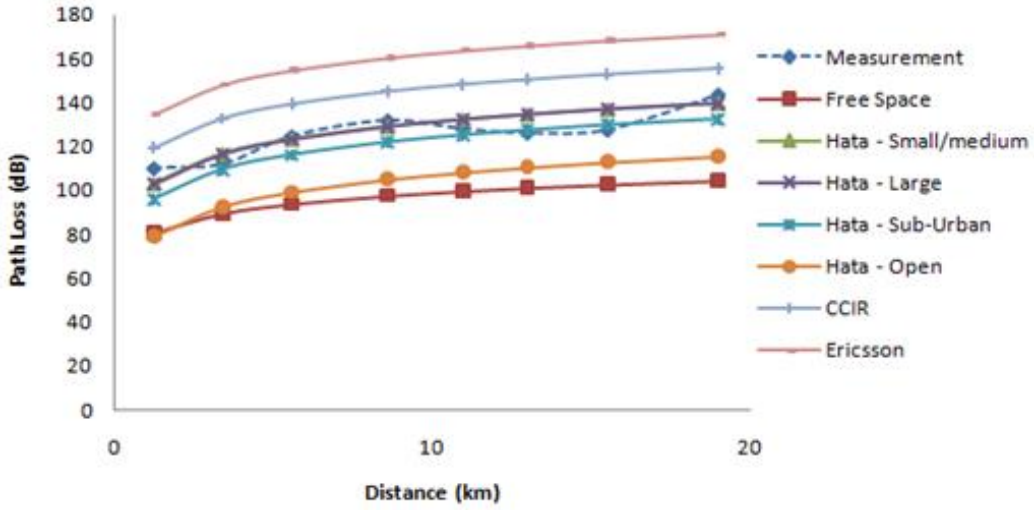

Figure 6: Path loss models for route D

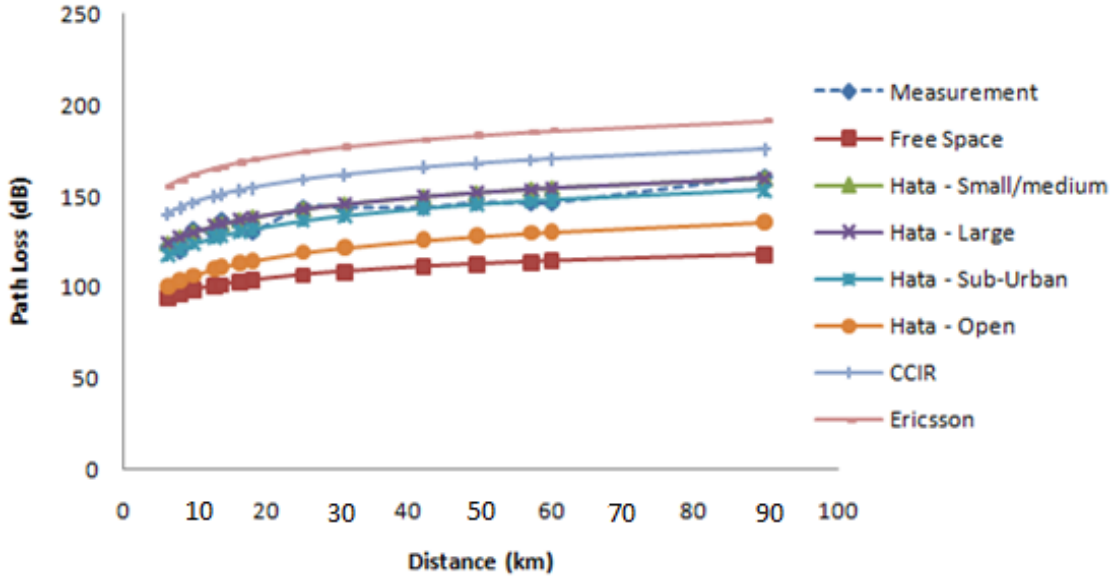

Figure 7: Path loss models for route E

Table 1: Root Mean Square Error of the Path Loss Models

	Free Space	Hata (Small/medium)	Hata (Large)	Hata (Sub-Urban)	Hata (Open)	CCIR	Ericsson
Route A	23.76	12.10	12.08	6.01	13.31	27.86	42.95
Route B	26.88	11.90	11.86	7.17	15.60	26.89	41.78
Route C	25.19	11.50	11.46	5.70	14.17	27.13	42.19
Route D	29.75	5.83	5.82	8.01	23.56	18.32	33.18
Route E	32.60	5.22	5.19	5.04	20.90	20.08	35.09

5.1 Modified Path Loss Models

Table 2 shows the correction factors used for the modified path loss and Figure 8 to Figure 12 show the modified path loss models for all the routes. After the modification, all the Hata models and CCIR model become the same, hence, the graphs overlapped and have the same RMSE.

The RMSE of all the path loss models for each route are shown in Table 3. Ericsson model has the least error for route A and E (3.95 dB and 3.76 dB respectively). Likewise, Hata and CCIR models have the least error for routes B and C (6.5 dB and 4.31 dB respectively) and Free space model has the least RMSE for route D (5.19 dB).

Table 2: Correction Factors used for the Modified and the Generalised Path Loss

	Free Space	**Hata (Small/medium)**	**Hata (Large)**	**Hata (Sub-Urban)**	**Hata (Open)**	**CCIR**	**Ericsson**
Route A	23.30	-11.40	-11.40	-4.52	12.70	-27.58	-42.77
Route B	25.60	-9.96	-9.93	-3.03	14.19	-26.09	-41.27
Route C	24.60	-10.70	-10.60	-3.73	13.49	-26.79	-41.97
Route D	29.29	-1.29	-1.25	5.64	22.86	-17.42	-32.70
Route E	32.25	-3.59	-3.56	3.34	20.56	-19.72	-34.89
AVERAGE	27.01	-7.39	-7.35	-0.46	16.76	-23.52	-38.72

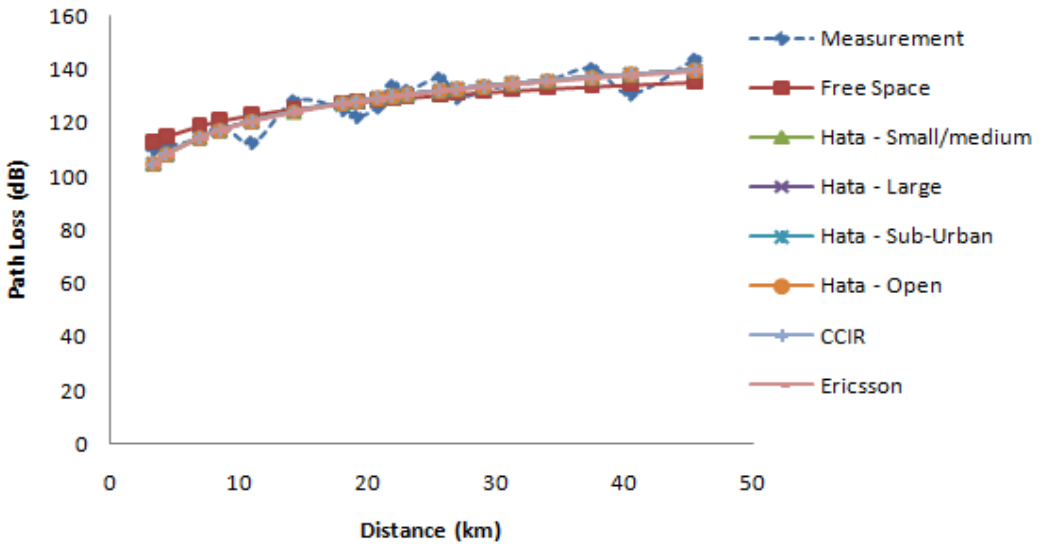

Figure 8: Path loss models for route A

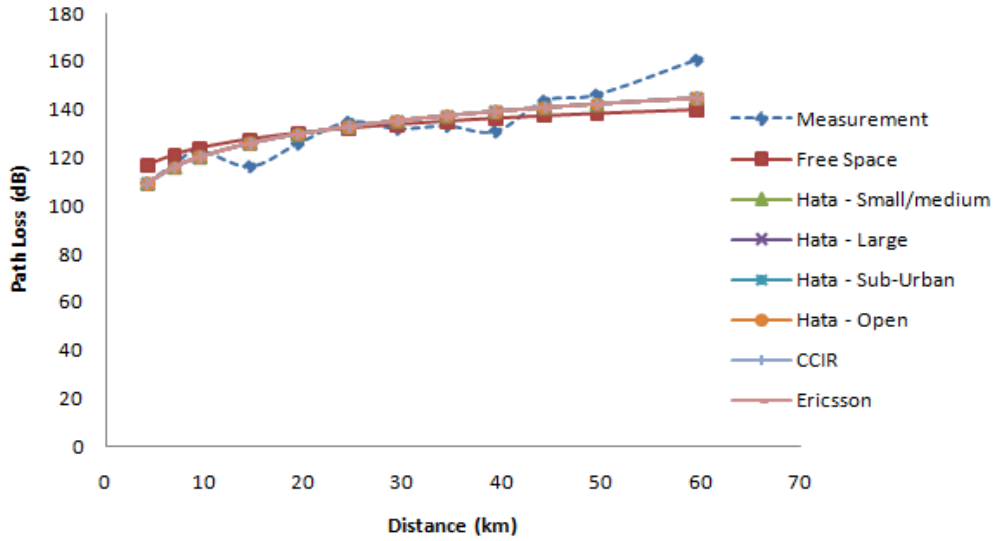

Figure 9: Path loss models for route B

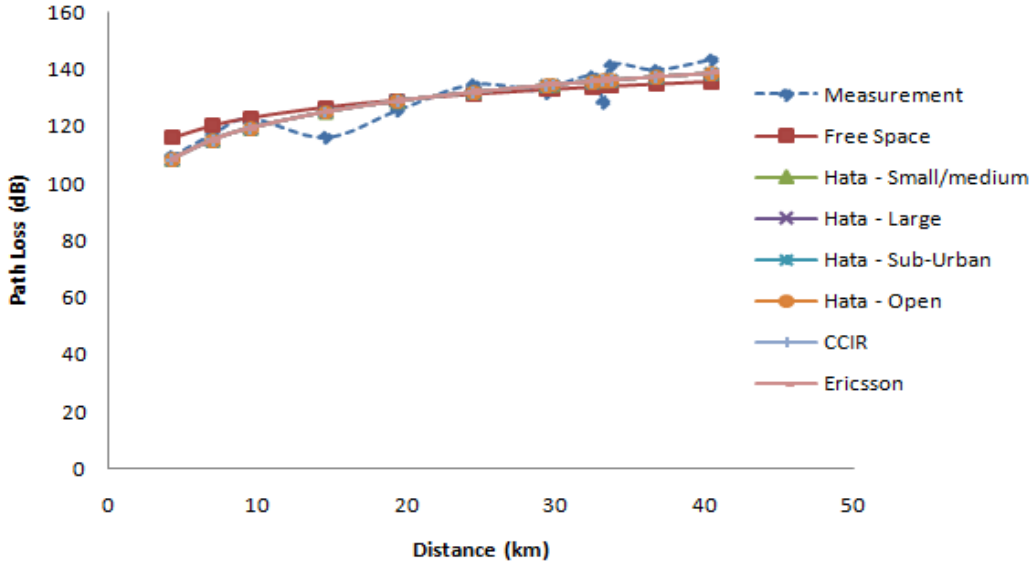

Figure 10: Path loss models for route C

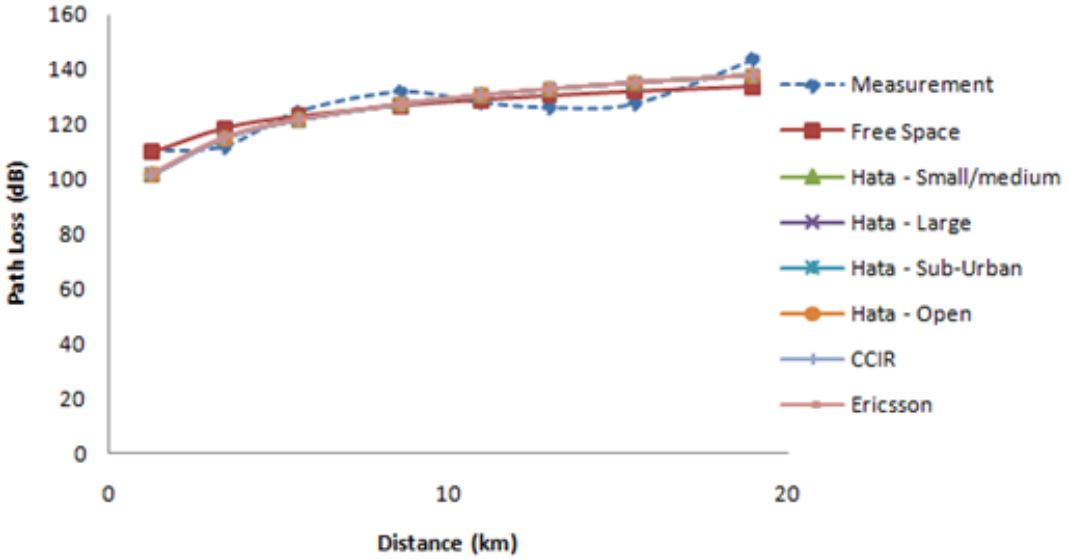

Figure 11: Path loss models for route D

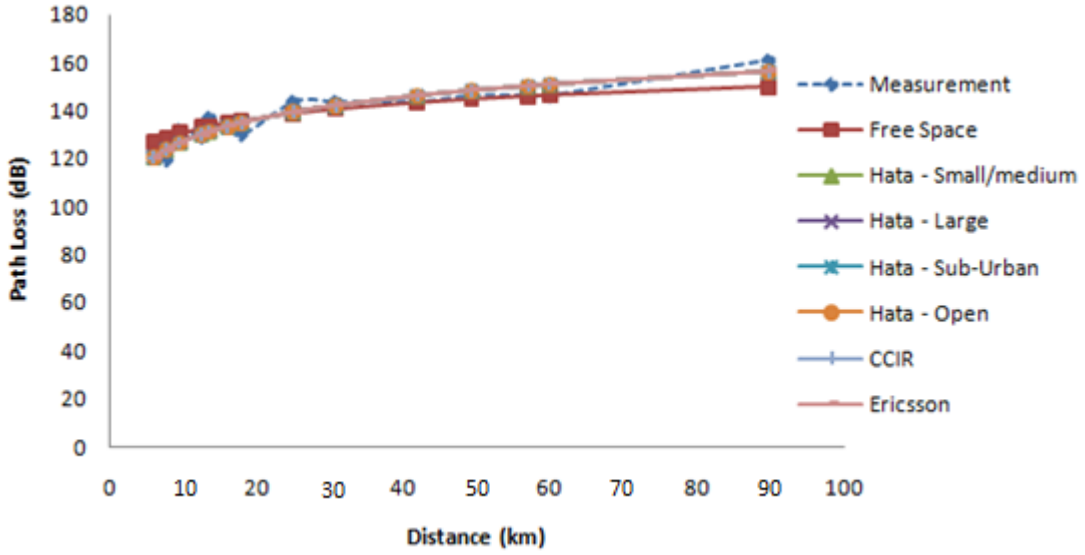

Figure 12: Path loss models for route E

Table 3: Root Mean Square Error of the Modified Path Loss

	Free Space	Hata (Small/medium)	Hata (Large)	Hata (Sub-Urban)	Hata (Open)	CCIR	Ericsson
Route A	4.64	3.96	3.96	3.96	3.96	3.96	3.95
Route B	8.20	6.50	6.50	6.50	6.50	6.50	6.52
Route C	5.43	4.31	4.31	4.31	4.31	4.31	4.32
Route D	5.19	5.69	5.69	5.69	5.69	5.69	5.65
Route E	4.73	3.78	3.78	3.78	3.78	3.78	3.76

5.2 Generalised Path Loss Models

The average values of the MPE of all the routes obtained are used as the correction factors to generalise the path loss model for each model as shown in Figure 13 to Figure 17. The RMSE of the path loss models for each route are shown in Table 4. For route A and route C, Ericsson model has the least error (5.66 dB and 5.4 dB respectively). For route B and route E, Hata and CCIR models has the least errors (6.99 dB and 5.36 dB respectively) while Free space model has the least error (5.67 dB) for route D. The average values of the RMSE of the generalized path loss models for the five radial routes considered are taken as the RMSE values for all the routes in Minna city. Consequently, Ericsson model has the least average RMSE value (6.34 dB).

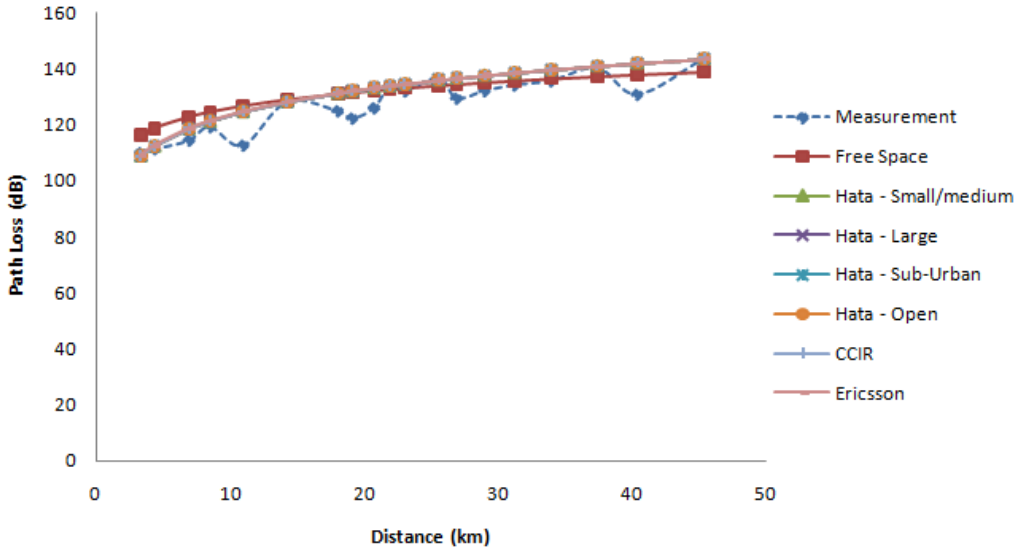

Figure 13: Path loss models for route A

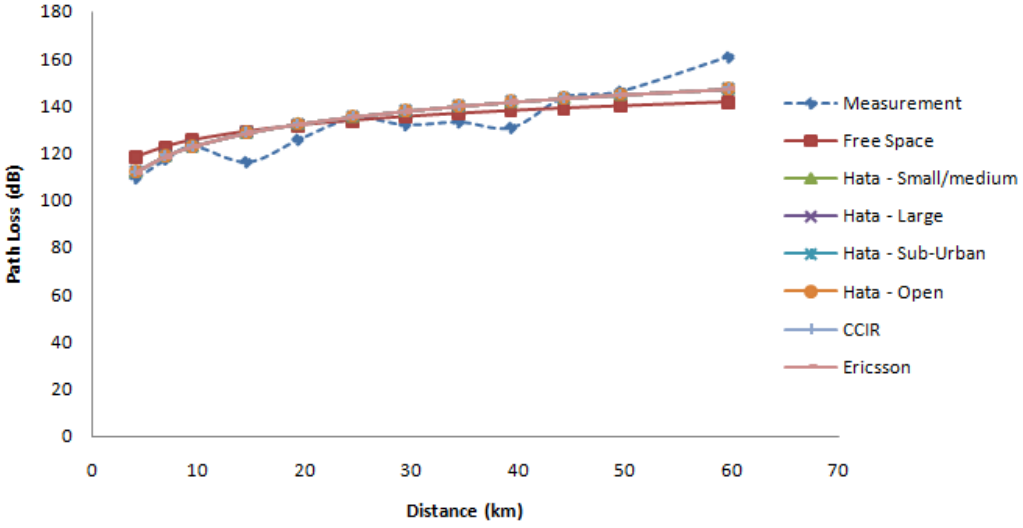

Figure 14: Path loss models for route B

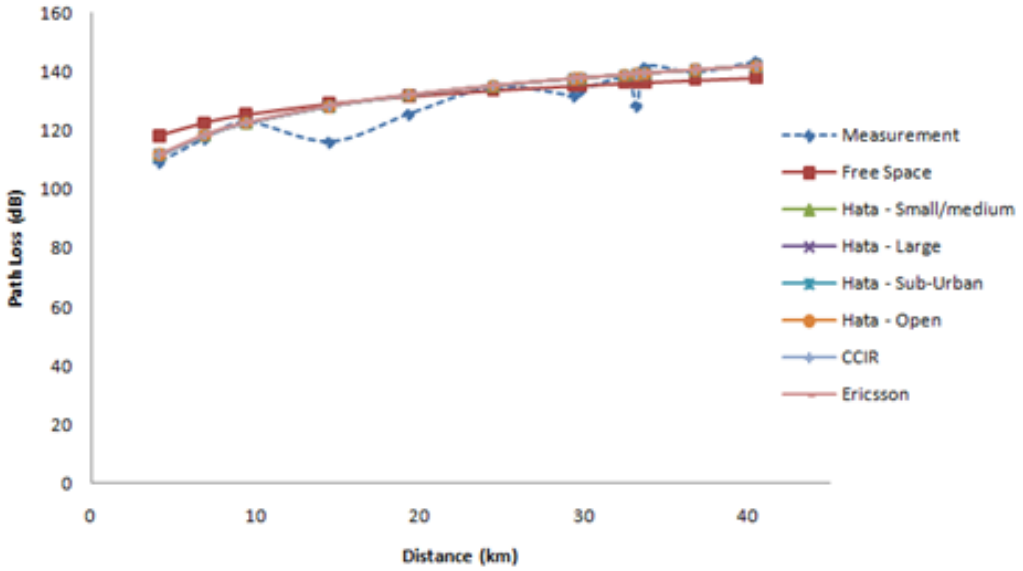

Figure 15: Path loss models for route C

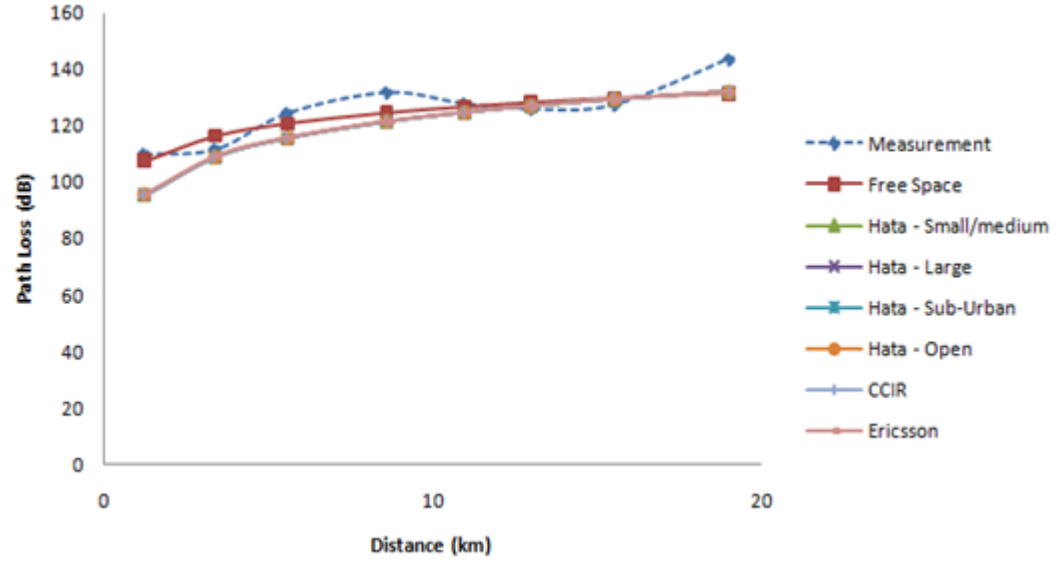

Figure 16: Path loss models for route D

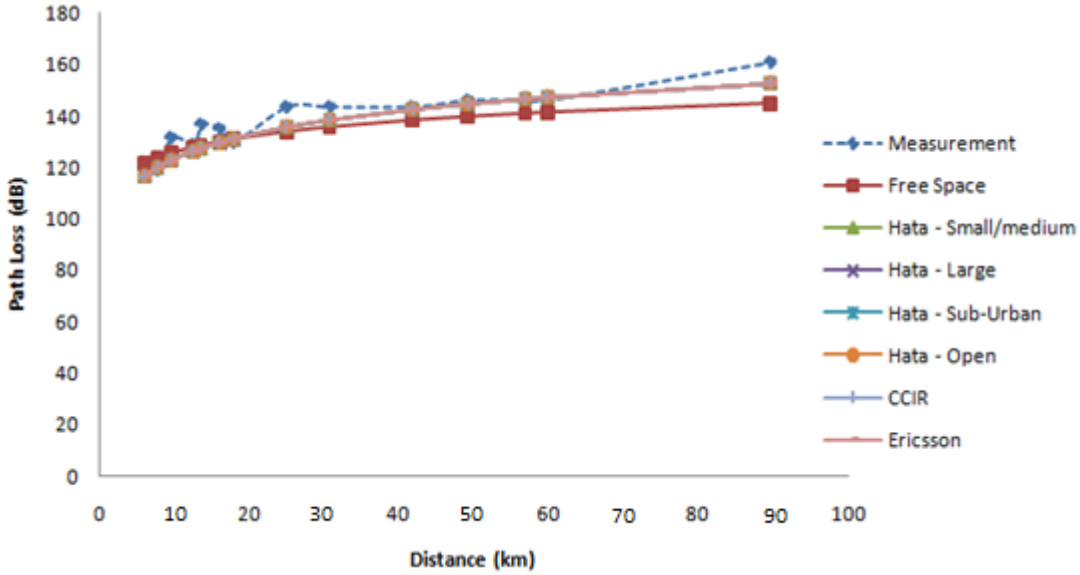

Figure 17: Path loss models for route E

Table 4: Root Mean Square Error of the Generalised Path Loss

	Free Space	Hata (Small/medium)	Hata (Large)	Hata (Sub-Urban)	Hata (Open)	CCIR	Ericsson
Route A	5.94	5.67	5.67	5.67	5.67	5.67	5.66
Route B	8.32	6.99	6.99	6.99	6.99	6.99	7
Route C	5.94	5.41	5.41	5.41	5.41	5.41	5.4
Route D	5.67	8.34	8.34	8.34	8.34	8.34	8.25
Route E	7.07	5.36	5.36	5.36	5.36	5.36	5.37
AVERAGE	6.59	6.35	6.35	6.35	6.35	6.35	6.34

6. Summary and Conclusion

The generalized path loss models for Minna city with least RMSE were obtained by using the average values of the MPE of the five radial routes considered, as the correction factors for each model. The average values of the RMSE of the generalized path loss models for the five radial routes are taken as the RMSE values of all the routes in Minna city.

The correction factors used for all the path loss models considered are: 27.01 (Free space), -7.39 (Hata - small/medium city), -7.35 (Hata - large city), -0.46 (Hata - suburban), 16.76 (Hata - open area), -23.52 (CCIR) and -38.72 (Ericsson models) with average RMSE of 6.59 for Free space, 6.34 for Ericsson models and all the Hata models and CCIR model have the same average RMSE, 6.35, because they all become the same after modification.

Ericsson model gives the least RMSE for Minna city. Therefore, the generalized Ericson model for urban environment gives more accurate prediction for path loss in Minna city compared to other models considered.

References

Ajewole, M. O., Oyedum, O. D., Adediji, A. T., Moses, A. S. and Eiche, J. O. (2013), Spatial Variability of VHF/UHF Electric Field Strength in Niger State, Nigeria. International Journal of Digital Information and Wireless Communications (IJDIWC) 3(3): 26-34**.** *The Society of Digital Information and Wireless Communications*.

Ayeni, A.A., Faruk, N., Surajudeen-Bakinde, N. T., Okanlawon, R. A. and Adediran, Y. A. (2015), Spatial Spectrum Utilization Efficiency Metric for Spectrum Sharing System. International Journal of Digital Information and Wireless Communications (IJDIWC) 5(1): 44-51. *The Society of Digital Information and Wireless Communications*.

Kurniawan, A. (1997), Prediction of Mobile Radio Propagation by Regression Analysis of Signal Measurements. *Magazine of Electrical Engineering (Indonesian: Majalah Ilmiah Teknik Elektro)*, vol. 3, no. 1, pp. 11-21.

Lee, J.S. and Miller, L.E. (1998), CDMA Systems Engineering Handbook. Boston: Artech House.

Mardeni, R. and Kwan, K.F. (2010), Optimization of Hata Propagation Prediction Model in Suburban Area in Malaysia. *Progress in Electromagnetics Research* C, Vol. 13, 91-106.

Mardeni, R. and Pey, L.Y. (2012), Path Loss Model Optimization for Urban Outdoor Coverage Using Code Division Multiple Access (CDMA) System at 822 MHZ. *Modern Applied Science* Vol. 6, No. 1.

Milanovic, J., Rimac-Drlje and Bejuk, K. (2007), Comparison of Propagation Model Accuracy for WiMAX on 3.5GHz. *14th IEEE International Conference on Electronic Circuits and Systems, Morocco,* pp. 111-114.

Minna Travel Guide, taken from http://www.world66.com/africa/nigeria/minna/

Minna, taken from http://en.wikipedia.org/wiki/Minna

Nadir, Z. (2011), Seasonal Path Loss Modeling at 900 MHz for OMAN. 2011 International Conference on Telecommunication Technology and Applications. Proc. of CSIT vol.5 *IACSIT Press*, Singapore.

Niger State, taken from http://en.wikipedia.org/wiki/Niger_State

Shahajahan, M. and Abdulla Hes-Shafi, A.Q.M. (2012), Analysis of Propagation Models for WiMAX at 3.5 GHz. Thesis presented as part of Degree of Master of Science in The Department of Electrical Engineering, Blekinge Institute of Technology, Karlskrona, Sweden, (2009), http://btu.se/fou/cuppsats.nsf/all/a9f238eea5e811bdc125763c003cd3ca/$file/Thesis_final_report.pdf.

Weather in Minna, Nigeria 2011, map, taken from http://www.geodata.us/weather/place.php?usaf=651230&uban=99999&c=Nigeria&y=2011

INFLUENCE OF HOSPITAL INFORMATION MANAGEMENT SYSTEM ON PATIENT CARE MANAGEMENT IN RIFT VALLEY PROVINCIAL GENERAL HOSPITAL

Willys Ochenge Okindo[1]

Information Technology Department

Directorate of Information and Communication Technology

Kenyatta University

Email: willysokindo@gmail.com

Dr. John Kandiri[2]

Computing and Information Technology (CIT) Department

School of Engineering and Technology

Kenyatta University

Email: jkandiri@gmail.com

Abstract

Information systems (IS) have revolutionized organizations and institutions on how they process, manage and execute their functions, and one of such systems is the Hospital Information Management System (HIMS), that is used to manage information required by health professionals and management staff to execute their duties effectively and; however there is insufficient knowledge on the extent of use of the system, influence of the system on clinical decision making, continuity of care , and the privacy and security of patient information on patient care management. **Method:** The study involved sixty-two participants participated and completed a questionnaire on the extent of use of the system, influence of the system on clinical decision making, continuity of care, and the privacy and security of patient information on patient care management. **Results:** extent of use, privacy and security, continuity of care, clinical decision making had significant variability influence on patient care management with (R^2= 0.582). Privacy and security, continuity of care, and Clinical decision making were statistically significant ($p<0.05$) while extent of use was statistically insignificant ($p<0.132$). This further revealed that Privacy and Security, Clinical Decisions were the better predictors of Patient care management (beta = 0.565) and (beta = 0.513) respectively. **Conclusion:** The system has significant influence on patient care management however there was a general belief that users are resistant to the adoption of information systems, but from the results revealed that the medical staff have adopted the use of the systems for service delivery. More studies need to be done on the extent of use and addressing the challenges the system is facing in supporting implementation of internal protocols, monitoring and follow-up of patients.

Keywords: Hospital Information Management System, Hospital Information System, Information Systems, Patient Care Management

Introduction

The rapid and continuous growth of Information Technology globally has led to governments and institutions to recognize IT as a powerful tool to improve productivity and service delivery. This triggered expeditious adoption of Information Systems in all aspects of society by the government and organizations to effectively and efficiently manage their core roles and this has not left the hospitals behind, they are either using or are planning to implement IS in some capacity. In aligning itself with this noble global idea, Kenya embarked on the process of automation of the government owned referral hospitals with a hospital information management system to manage the increasing volume and variety of health information that had resulted to challenges in delivering of patient care when using conventional information systems like paper-based medical records that could be effortlessly misplaced causing serious problems such as repetitive diagnostic tests, delays in the care planning or delayed patient discharges hence the adoption of the system to improve the process of patient care through the generation of electronic health records (Samireh a., 2012). Similarly related to HIMS, is an electronic health record (EHR) system that enables hospitals to store and retrieve detailed patient information to be used by health care providers, and patients, during a patient's hospitalization, over time, and across care settings. One of the modules embedded in this systems is a clinical decision support systems that has the ability to help clinicians to provide safe and effective diagnosis compared to relying on memory and paper-based systems (Sharon Silow-Carroll, Jennifer N. Edwards, 2014).

The purpose of this study was to establish the influence of the hospital information management system on patient care management in Rift Valley provincial General Hospital. Studies have been done on the extent of use on the HIMS and one notable study on the extent of use, perceptions, and knowledge of a hospital information system by staff physicians in a Jordanian hospital (Hayajneh, Hayajneh, & Matalka, 2006). The study aimed to describe physicians' use, perceptions, and knowledge regarding the implemented HIS. In their findings, they discovered that staff physicians use the system and their experience to access of information was improved as a result of the HIS. They specifically base their study on describing the extent to which staff physicians use the system, their knowledge of the system capabilities and their perceptions of system's impact on certain aspects of hospital operation and the results showed that physicians are

not completely aware of all features of the HIS. However, they also found out that the HIS had the capability in meeting its intended objectives in relation to the laboratory application ranging from access speed, accurate results, and effectiveness of communication (Hayajneh et al., 2006). Similarly, (Khalifa, 2014) argues in their study to identify, analyze and evaluate technical human challenges of implementing hospital information systems in Saudi Arabia, he points out a summary of challenges hindering the extent to which systems are implemented and adopted among many others as human challenges; those related to the healthcare professionals and their beliefs, nature of work and time constraints as well as technical challenges; those related to software and hardware of hospital information systems are the major barriers and challenges in the way of successful implementation of these systems in Saudi Arabia. The researcher goes ahead and recommends that increasing the awareness, training resources and adding hospital information system training to the undergraduate and postgraduate medical and nursing education in order to reduce the challenges realized in his research.

On the other hand a lot of research has been done on Clinical decision making that is concerned with a balance of experience, knowledge and information gathering using suitable assessment tools, your colleagues and evidence-based practice to guide you in coming up to conclusions. (Sharon Silow-Carroll, Jennifer N. Edwards, 2014) postulate that postulate that the leading hospitals find the Electronic health record (EHR) system living up to their expectations by helping them improve health care quality and safety. Communication among providers has been improved by the use of EHR system, led to better-coordinated care, and promoted patients' participation. Clinical guidelines entrenched in the EHR promote consistent use of evidence-based care while automated systems help to detect and prevent errors. However, they fail to establish how clinical decision making through the system has influenced patient care management.

Continuity of care is another major service that the system can facilitate efficiently to enhance patient care management to improve on service delivery by the care givers or health facility. It involves sharing, coordinating, and integrating of medical data among different health service providers to support patient care across multiple facilities and care settings simultaneously (Schlossman M.David, 2013) . A study by (Bayliss et al., 2015) asserted that an integrated system with a shared electronic health record provides informational continuity and measures of interpersonal continuity of care are less likely to serve as proxies for medical knowledge about the patient, and more likely to reflect the benefits of the

patient-clinician relationship. More so they argue that an integrated delivery system with high informational continuity, greater continuity of care is independently associated with lower hospital utilization for seniors with multiple chronic medical conditions.

The privacy and security feature on any HIMS provides resources to assist healthcare organizations, service consumers and business associates with their privacy and security initiatives. The system must ensure that patient information stored is accessible by authorized individuals only is not compromised, stolen or accessed by unauthorized persons (Lee Kim, 2013). For example some studies found out that larger percentages (48 percent vs. 41 percent) of the physicians believe that the system did not help in protecting the confidentiality of patient information while fifty one percent of the physicians observed that the system venerable to unauthorized access of patient information (Hayajneh et al., 2006). Their findings indicate that the HIS was in general effective in improving access to information but at the same time it could not guarantee the confidentiality and security of patient information and they suggest further study and analysis to find the causes of the phenomenon and identify solutions to information security.

Methodology

The study was carried out in Nakuru County and it was narrowed down to Rift Valley General Hospital a Level 5 referral hospital. The hospital serves approximately 3.6 million people and it provides all major services including antenatal care, antiretroviral therapy, basic emergency obstetric care, theater operations, comprehensive emergency obstetric care, curative in-patient services, curative outpatient services, family planning, HIV counseling and testing, home based care, immunization, radiology services. The target population for this study was purposively selected for the study namely the top level management staffs, doctors, nurses and support staffs that access the system and a sample size of sixty-five respondents were purposively selected to participate in the study using structured questionnaires.

Results

The regression analysis on all the variables revealed an R-square 0.582 indicating that the four variables accounted for 58.2 percent of the variability in Patient care management. This represented a fairly good fit which depicted a relative significant influence of extent of use, privacy and security, continuity of care, clinical decisions on Patient care

management. The remaining 41.8 percent could have been due to chance, error or other factors. The other factors that were observed were unavailability of enough medical staff members, enough drugs, and hospital facilities which also affected on ability to offer optimum patient care management. It was also established that extent of use, privacy and security, continuity of care, clinical decision making had significant variability influence on patient care management with (R^2= 0.582) and they were all statistically significant ($p<0.05$) while extent of use was statistically insignificant ($p<0.132$). This further revealed that Privacy and Security, Clinical Decisions were the better predictors of Patient care management (beta = 0.565) and (beta = 0.513) respectively.

Discussion

The main findings showed that majority of the respondents seemed to agree that the introduction, adoption and implementation of the system on most of the departments had improved the quality of patient care management in the hospital and it was easier to use and interact with in providing services. However, they also seemed to agree with (Khalifa, 2014) who observed in their study findings that human challenges ranging from personal beliefs, nature of work that affected on the use and acceptance of the system. Other observed factors were related with level of knowledge on technology use. To mitigate this observation, the hospital had scheduled refresher trainings to improve the user ability to use and acceptance of the system use. Another key finding was that the system did not support implementation of internal protocols and this was attributed to the fact that the system is still in implementation stage.

The medical staff who interacted regularly with the clinical decision making module concurred with (Sharon Silow-Carroll, Jennifer N. Edwards, 2014), (Schlossman M.David, 2013) and (Bayliss et al., 2015) that the system had influenced patient care management, majority of the respondents were agreed that HIMS had helped in reducing diagnostic errors that could have otherwise led to misdiagnosis of patients as well as quicker informed decision making leading to faster action taking. Although the system was still in its implementation stage, the research also showed that it had significantly improved the quality of care as well as integrating evidence based knowledge into care delivery. This was important since it helped the care givers an opportunity to compare variety of information for informed decisions.

Hospitals and other health care providers have had a long time challenge of providing continuity of care. Continuity of care is defined as the sharing, coordinating, and integrating of medical information among different health care providers

to support patient care across multiple points in time and multiple care settings (Schlossman M.David, 2013), (Rewar, 2012). The demand in keeping track of patients with manageable diseases (Diabetes, HIV/Aids, Cancer, Acute heart conditions and strokes etc) who are increasing rapidly necessitated the need to have systems in place to be able to address the challenge of tacking and transferring the patients across the health care givers. The study found out that the system supported and improved access to care and the ease to share information. This was due to the ability of the system to be accessed online and allowing the sharing of information easily making it possible to offer quality care over a period of time to patients with manageable diseases. This kind of care provides an important opportunity to ensure high quality services, patient safety, and patient-centered care.

We can all agree that the most important attribute of any System is to ensure that it has got security features to protect and safeguard the data stored as well as ensure availability and integrity of patient information at any one given time. This are all attributed to the level of privacy and security. Privacy of information involves ensuring that patient information stored is accessible by only authorized individuals only while Security on information involves ensuring that patient data is not compromised, stolen or accessed by unauthorized persons. It is the ability of the system to make to owners of the information satisfied with the security features in place to ensure they have total control of who should access their information, at what time and for how long. This is a concern for any organization or institution that seeks to adopt and implement any system; this is supported by a study that was done in Tanzania that focused on challenges affecting e-healthcare adoption, (Omary, Lupiana, Mtenzi, & Wu, 2010) where they pointed out that systems are venerable to security intrusion and other threats which negatively affect their adoption and implementation. This study sought to determine if the HIMS was trusted to protect on the patient data and information. Though the finding in this paper showed that the system had improved the accuracy of the stored patient information as well as availability and confidentiality of the patient information, there was still some level of reservation as to what extent it can be trusted with patient data. The findings also revealed that there was an average response to the security of patient information hence required more attention to ensure that the patient information is not accessed by any unauthorized persons. This seemed to be consistently in agreement with (Hayajneh et al., 2006) who on their study on the Extent of Use, Perceptions, and Knowledge of a Hospital Information System by Staff Physicians stated that the physicians believed that the system did not help in protecting the confidentiality of private patient information and it allows for easy access to patient information to unauthorized individuals.

Conclusion

This study found out that the Hospital Information Management System has a significant influence on patient care management in Rift Valley Provincial General Hospital. There is a general belief that users are resistant to adoption and use of information systems and use of computers but results from this research contradicts this misconception and reveals that the medical staff have accepted the use of the systems on a daily basis to provide services. From the research, the results shows that the system has not significantly helped in reducing health care costs while their also existed a number of respondents that felt that the system had improved on the efficiency of services provided and patient satisfaction. In general, the research findings show that the HIMS was generally effective in improving Patient care management. However there seems to be a challenging in the system in supporting monitoring and follow-up of patient as well as integrating and supporting the implementation of internal protocols.

REFERENCES

Accurate Info, S. (n.d.). *Accurate Info Soft Pvt. Ltd.* Retrieved 03 24, 2016, from Accurate Info Soft Pvt. Ltd.: www.acsonnet.com/aperp.doc

Adekeye, A. (2010). Adoption of Management Information Systems (Mis) In Lautech Teaching Hospital Library. *Ozean Journal of Social Sciences 3(1), 2010* , 318-27.

Adomavicius, G., Bockstedt, J. C., Alok, G., & Robert, K. J. (2005, March 3). Technology roles in an ecosystem model of technology evolution. Minneapolis, MN 55455, University of Minnesota, USA.

AIMTech. (2012). *Evaluation of information systems*. Retrieved 03 24, 2016, from Adaptation Information Management and Technology: http://lubswww.leeds.ac.uk/aimtech/research-areas/evaluation-of-information-systems/

Ajzen, F. a. (1975). *Beliefs, attitudes, intentions, and behaviors.* Reading, MA: Addison-Wesley.

Ammenwerth, E., Kutscha, U., Mahler, C., Eichstadter, R., Haux, R., & Ansgar, K. (2001). Nursing process documentation systems in clinical routine–prerequisites and experiences. *International Journal of Medical Informatics, 64* , 187-200.

Argyris, C. (1982). Organizational learning and management information systems. *SIGMIS Database* , 3-11.

Bayliss, E. A., Ellis, J. L., Shoup, J. A., McQuillan, D., & Steiner, J. (2015). Effect of Continuity of Care on Hospital Utilization for Seniors With Multiple Medical Conditions in an Integrated Health Care System. *The Annals of Family Medicine* (2), 123-129.

Care, S. (2014). *Care Management Software.* Retrieved 03 23, 2016, from Sandlot Solutions: http://www.sandlotsolutions.com/turning-health-data-into-information/care-management-software

Chandrasekhar, S. (2010, June 05). *Resources.* Retrieved August 13, 2015, from Mainstay Development Consultants: http://mainstayin.com/Research%20prespective%20on%20Hospt.%20mgt.pdf

Clifford, G. D., Blaya, J. A., Hall-Clifford, R., & Hamish, F. S. (2008, June 11). *Medical information systems.* Retrieved August 11, 2015, from Biomedical Engineering Online: http://www.biomedical-engineering-online.com/content/7/1/18#

Dan, S. (1997 , Feb 27). *Hospital Information Systems*. Retrieved 09 01, 2015, from CSAIL: http://groups.csail.mit.edu/medg/courses/6872/96/notes/sheldon.html

Davis, F. D., Bagozzi, P. R., & Warshaw, P. R. (1989, August 01). User acceptance of computer technology: A comparison of two theoretical models. (1003, Ed.) *Management Science , 35*, p. 982.

Fichman, R. G., Rajiv, K., & Ranjani, K. (2011, September 03). The Role of Information Systems in Healthcare: Current Research and Future Trends. *Information Systems Research 22(3)* , pp. 419–428.

Goodell S, B. T.-M. (2009). *Care Management of Patients with Complex Health Care Needs.* Retrieved 03 23, 2016, from Robert Wood Johnson Foundation: http://www.rwjf.org/en/library/research/2009/12/care-management-of-patients-with-complex-health-care-needs.html

Hannah, V., & Sethuraman, K. (2008). Healthcare Information Systems (Vols. 1). *United States of America: Information Science Reference* , vols1.

Hayajneh, Y., Hayajneh, W., & Matalka, I. (2006). Extent of Use, Perceptions, and Knowledge of a Hospital Information System by Staff Physicians. *The 1st Jordanian European International Medical Informatics and Biomedical Engineering Symposium* .

(2013). Bill of Rights. In M. o. Health, *Patients Charter 2013* (pp. 3-6). Nairobi: Minstry of Health.

HIMSS. (2013). *HIMSS*. Retrieved 03 23, 2016, from Healthcare Information and Management Systems Society: http://www.himss.org/library/healthcare-privacy-security

Kadida, J. (2015, June 03). *Lecturer sues Aga Khan for misdiagnosis*. Retrieved August 12, 2015, from The-star.co.ke: http://www.the-star.co.ke/news/lecturer-sues-aga-khan-misdiagnosis

Khalifa, M. (2014). Technical and Human Challenges of Implementing Hospital Information Systems in Saudi Arabia. *Journal of Health Informatics in Developing Countries , 8* (1), 12-25.

Kihuba, E., David, G., Stephen, M., & Mercy, M. (n.d.). *Assessing the ability of health information systems in hospitals to support evidence-informed decisions in Kenya.* Retrieved July 01, 2015, from National Center for Biotechnology Information: http://www.ncbi.nlm.nih.gov/pmc/articles/PMC4119289/

Kimama, F. (2011). *Challenges facing the implementation of hospital management.* Nairobi: Nairobi University.

Konthari, C. (2004). *Research Methodology.* Mumbai: New Age nternational (P) Limited.

Lee Kim. (2013). Privacy & Security | HIMSS. Retrieved January 26, 2017, from http://www.himss.org/library/healthcare-privacy-security

Lee, T.-T. (2004). Evaluation of Computerized Nursing Care Plan:Instrument Development. *Journal of Professional Nursing* , 230-238.

Lesly, A. (2012, 08 20). *Clinical Decision Making*. Retrieved 03 23, 2016, from Effective Practitioners: http://www.effectivepractitioner.nes.scot.nhs.uk/resources/video-podcast-library/clinical-decision-making.aspx

Lucy, T. (2004). *Management Information Systems.* Croatia: Thomson Learning.

Masoud Mohammadian, R. J. (2008). Healthcare Information Systems (Vols. 2). *United States of America: Information Science Reference* , 890-905.

Mugenda, O. (1999). *Research Methods.* Nairobi: Acts Press.

Mutai, K. (2004). *How to write Quality Research Proposal: A Complete and Simplified Recipe.* New Delhi: Thelley Publishers.

Omary, Z., Lupiana, D., Mtenzi, F., & Wu, B. (2010). Analysis of the Challenges Affecting E-healthcare Adoption in Developing Countries : A Case of Tanzania Analysis of the Challenges Affecting E-healthcare Adoption in Developing Countries : A Case of Tanzania. *International Journal of Information Studies*, *2*(1), 38–50.

Pennell, U., & Eric, F. M. (2013, August 21). *Hospital Information Systems (HIS)*. Retrieved August 12, 2015, from EMR Consultants.com: http://www.emrconsultant.com/emr-education-center/emr-selection-and-implementation/hospital-information-systems-his/

Qasim, Z., & Sayyed Wasim, H. B. (2011). *A Plan for Implementation of Hospital Information.* Sweden: Linnaeus University.

Rahimi, M. T. (2014, May 4). Malaria or flu? A case report of misdiagnosis. *Asian Pacific Journal of Tropical Biomedicine* , 56-58.

Richard, E. (2011, April 03). *The Most Important Effects Of Information Technology On The Society* . Retrieved from Hi-Tech Platform: http://hitechplatform.blogspot.co.ke/2011/04/most-important-effects-of-information.html

Schlossman, D. M. (2013, September 09). *Continuity of Care in the United States.* Retrieved November 24, 2015, from HIMSS - Healthcare Information and Management Systems: http://www.himss.org/News/NewsDetail.aspx?ItemNumber=22261

Sharon, S.-C., Edwards, J. N., & Rodin, D. (2012, July 02). *Using Electronic Health Records to Improve Quality: The Experiences of Leading Hospitals.* Retrieved August 11, 2015, from The Commonwealth Fund: http://www.commonwealthfund.org//1608_silowcarroll_using_ehrs_improve_quality.pdf

Silow-Carroll, S., Edwards, J. N., & Rodin, D. (2012, July). Using electronic health records to improve. *The Experiences of Leading Hospitals* , 1-40.

Srit, A. (2000, 04 01). *Healthcare Information Management System(HIMS)*. Retrieved 09 01, 2015, from SRIT: http://www.renaissance-it.com/corporate_overview.php

Steve, G., & Nilmini, W. (2008). Healthcare Information Systems (Vols. 1). *United States of America: Information Science Reference* , Vols 1.

Takhti, H. K., Abdul Rahman, D. A., Samireh Abedini, S. A., & Abedini, S. (2012). Impact of Hospital Information Systems on patient care: Nurses'. *Canadian Journal of Nursing Informatics* , Vol 4.

Technology, E. (2006, OCtober 03). *Theory of reasoned action*. Retrieved 09 01, 2015, from Edutechwiki: http://edutechwiki.unige.ch/en/Theory_of_reasoned_action

Venkatesh, Morris, M. G., & Davis, G. B. (2003). Toward a Unified View. *User Acceptance of Information Technology* , pp. 425–478.

Venkatesh, V., Thong, J. Y., & Xu, X. (2012, March 13). Consumer acceptance and Use of Information: Extending the Unified Theory. *MIS Quarterly Vol. 36 No. 1* , pp. 157-178.

Winter, A., Bott, Buchauer, & W., H. (2001). Strategic information management plans; the basis for systematic information. *International Journal of Medical Informatics* , 99–109.

SPECTRAL DEPTH ANALYSIS OF PARTS OF BIDA BASIN, NORTH CENTRAL NIGERIA, USING AEROMAGNETIC DATA

[1]*Alkali, A., Salako, K. A., and Udensi, E. E.*
[1]*Department of Physics, Federal University of Technology Minna, Nigeria*
aisha.alkali@futminna.edu.ng
s.kazeem@futminna.edu.ng
eeudensi @yahoo.com

Abstract

Spectral depth analysis of aeromagnetic data covering latitude 8.50^0N to 10.00^0N and longitudes 5.00^0E to 6.00^0E which corresponds to part of central Bida Basin, North Central Nigeria, was carried out for the purpose of investigating the sedimentary thickness beneath the subsurface. The study area was covered by six aeromagnetic maps. The aeromagnetic maps were digitized on a 37 by 37 grid and later compiled to produce a combined aeromagnetic data file for the area. The data file comprised 1369 data points. The polynomial fitting method was applied in the regional-residual separation. The residual map was later sub-divided into 16 spectral sections. The result of the study shows that the first layer depth was 1.8km while the second layer depth was 2.85 km with an average thickness of 2.0km. The maximum depth of 2.8km could be found at the South- Eastern part while the minimum depth of 1.8km could be found at North–Western part. Several depressions or variations in thickness have been observed in some parts of Bida Basin, particularly around Egbako and Pategi areas. These deeper sections of the Bida sedimentary basin identified in this study might be possible potentials sites for hydrocarbon deposits and is therefore recommended to be subjected to further geophysical method like seismic reflection/refraction, so as to ascertain its hydrocarbon potential.

Keywords: Aeromagnetic data, Spectral, Depth, Sedimentary depth, First and Second layer depth

1. Introduction

Up to 90% of Nigeria economy depends on crude oil from the south, but this has greatly affect the potential stability of the country, as this (Crude oil) is today only found in the southern part of the country, in order to resolve the political in-balance there is need to explore our inlands basin in the country for possible presence of crude oil resources, of which Bida Basin is one of those Basins being suspected to have high hydrocarbon potential as reported recently in the media. This study will be very useful on a reconnaissance basis for oil. The Spectral analysis of aeromagnetic fields over the area would differentiate and characterize regions of sedimentary thickening from those of uplifted or shallow basement and also to determine the depths to the magnetic sources. The results could be used to suggest whether or not the study area has the potential for oil/gas concentration. This study area is bounded by latitude 8.50^0N to 10.00^0N and longitudes 5.00^0E to 6.00^0E located within the North Central part of Bida Basin, Nigeria (Figure 1). It is covered by 6 aeromagnetic maps. The data from each digitized map is stored in a 37 by 57 coding sheet and later compiled to produce a combined aeromagnetic data file for the area.

2. Geology of the Study Area.

The study area covers extensively the central part of Bida Basin (Northern part of Bida Basin). Map of Nigeria shows the location of the study Area and the geological map of the area, Figure 1 and Figure 2. The study area covers Fashe, Akerre, Mokwa, Egbako, Lafiagi and Pategi. All the rocks in the study area belong either to the upper Cretaceous or to the Precambrian rocks of the Basement complex (Russ, 1957; Adeleye, 1973 and 1976; Udensi *et al.*, 2003). The Nupe sandstones consist of slightly cemented fine to coarse-grained sandstones and siltstones with interbedded thin beds of carbonaceous shales and clays. The Nupe sandstones appear to lie directly on the Basement (Adeleye, 1976).

3. Materials and Method

The aeromagnetic dataset used for the study was obtained from the Nigerian Geological Survey Agency between 1974 and 1980. The magnetic data were collected at a nominal flight altitude of 154.2m along approximately N-S flight lines spaced at 2 km apart. The study area is covered by six aeromagnetic maps of total-field intensity in ½ º by ½ º sheets. These are numbers 161, 162, 181, 182, 203 and 204 on a scale of 1:100, 000. The magnetic values were plotted at 10nT (nano Tesla) interval. The actual magnetic values were reduced by 25,000 gammas before plotting the contour maps. This means that the value of 25,000 gammas should be added to the contour values so as to obtain the actual magnetic field at a given point. A correction based on the international Geomagnetic Reference Field, IGRF, and epoch date

January 1, 1974 was included in all the maps. The data used were digitized on a 19 by 19 grid systems and later compiled to produce a combined aeromagnetic data file for the area (Figure 3a). The data file comprised 1369 data points. The polynomial fitting method was applied in the regional-residual separation. The residual map (Figure 4) was later sub-divided into 16 spectral sections.

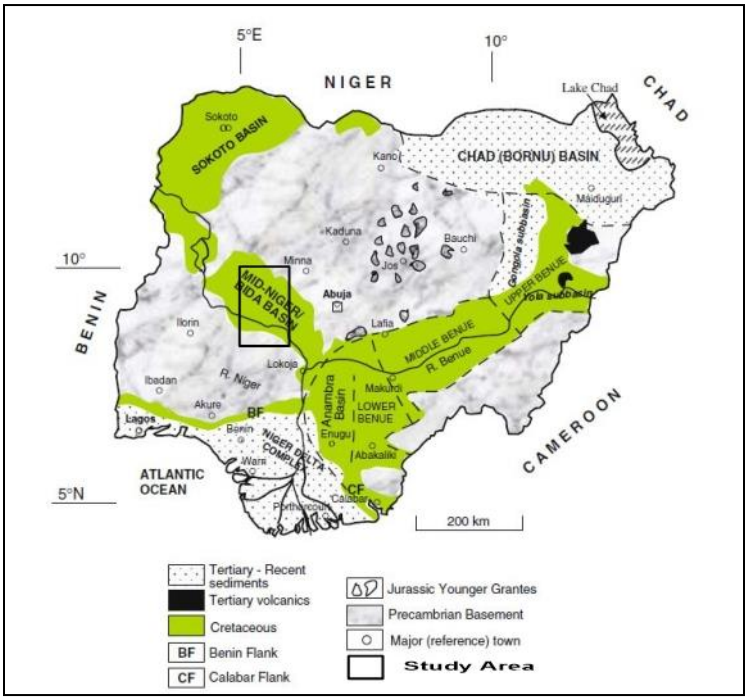

Figure 1: Location of the Study Area on Generalized Geological Map of Nigeria (Adopted from Obaje, 2009)

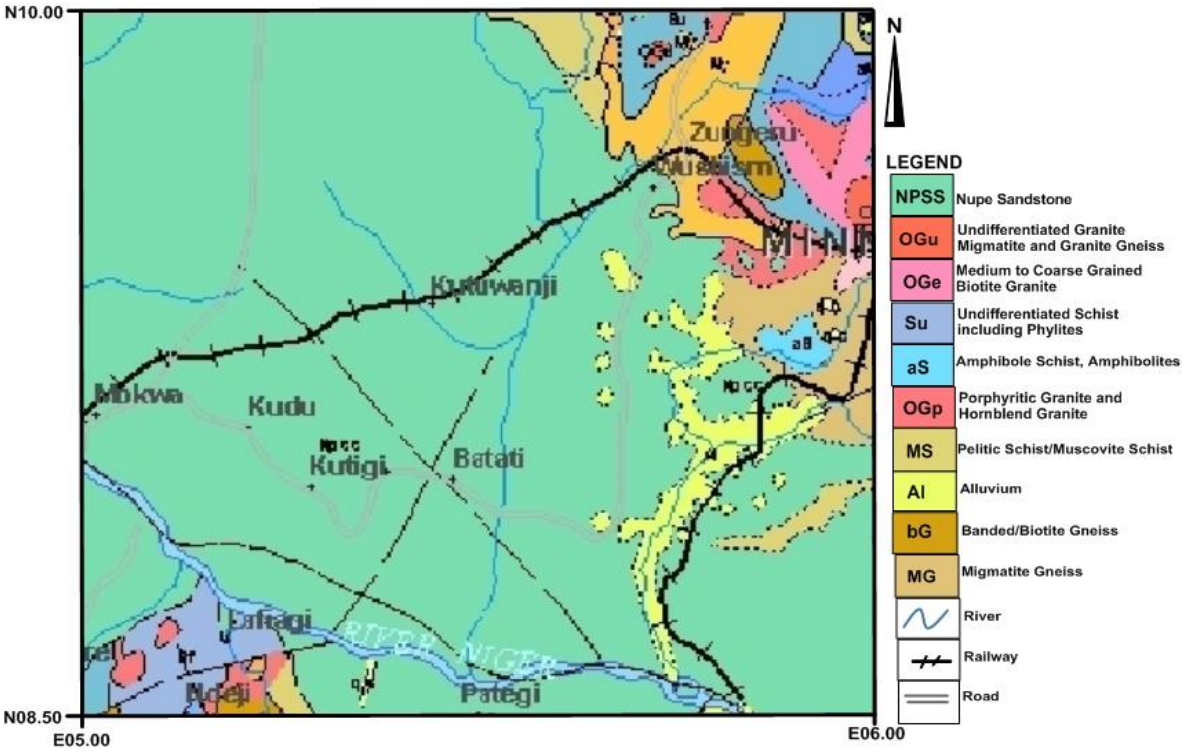

Figure 2: Geological Map of the Study Area (Adapted from Nigeria Geological

Survey Agency, 2006)

4. Spectral Analysis

The Fourier transform of the potential field due to a prismatic body has a broad spectrum whose peak location is a function of the depth to the top and bottom surfaces and whose amplitude is determined by its density or magnetization.The peak wave- number (ω') can be related to the geometry of the body according to the following expression.

$$\omega' = \frac{In\left(h_b/h_t\right)}{h_b - h_t} \qquad (1)$$

where,

ω' is the peak wave-number expressed in radian /ground

h_t is the depth to the top

h_b is the depth to the bottom.

For a bottomless prism, the spectrum peak at the zero wave – number, is given according to the expression:

$$f(\omega) = e^{-H\omega} \qquad (2)$$

where ω is the angular wave - number expressed in radians/ground ₋ unit and h is the depth to the top of the prism. (Bhattacharyya, 1996) for a prism with top and bottom surface, the spectrum is:

$$f(\omega) = e^{-h_t\omega} - e^{-h_b\omega} \qquad (3)$$

where h_t and h_b are the depths to top and bottom surface respectively. As the prism bottom moves closer to the observation point at surface, the peak moves to a higher wave number. When looking at the spectrum, it is important to note that the amplitude of a deep prism does not exceed the amplitude of the same prism at shallow depth at any wavenumber. The effect of increasing the depth is to shift the peak to lower wavenumbers.

Because of this characteristic, there is no way to separate theeffect of deep sources from shallow sources of the same type by using wavenumber filters. The sources can only be distinguished if the deep sources have greater amplitude or if the shallow sources have less depth extent. When considering a line that is long enough to include many sources, the log spectrum of this data can be used to determine the depth to the top of a statistical ensemble of sources using the relationship.

$$LogE(k) = 4\pi hk \qquad (4)$$

where *h* is the depth in ground – units and k is the wavenumber in cycles / ground – unit. The depth of an'ensemble' of source can be determined by measuring theslope of the energy

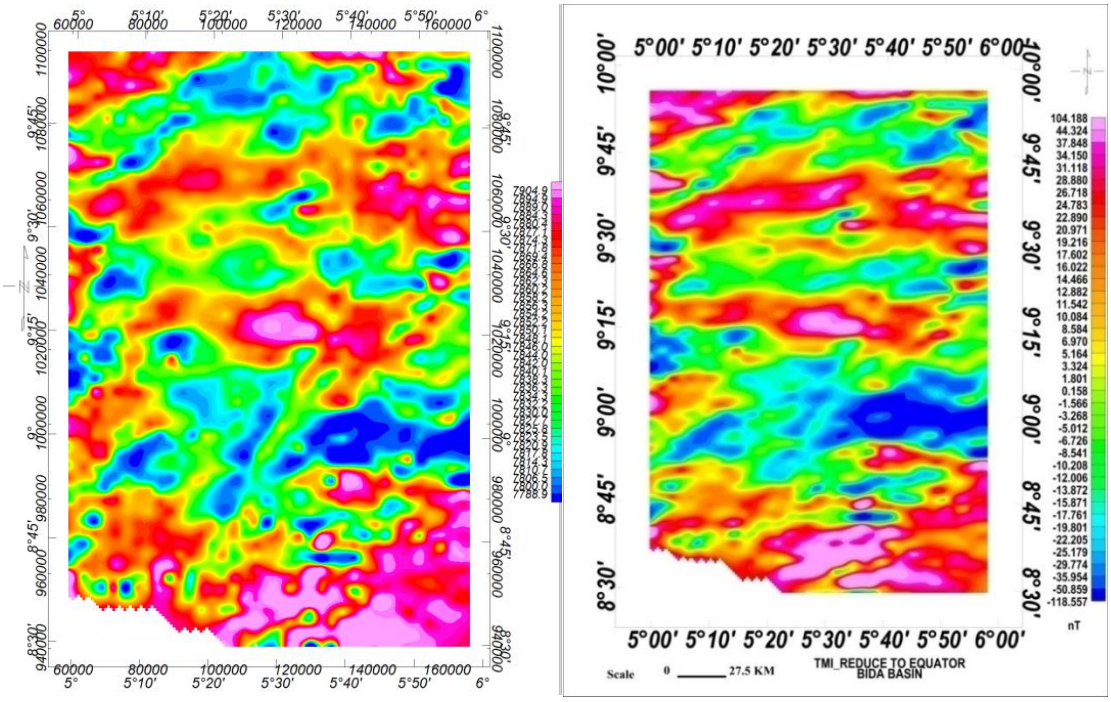

(a) **(b)**

Figure 3: (a) Total Magnetic Intensity Map of the Study Area after 25,000nT have been Removed (b) TMI Reduced to Equator Map of the Study Area

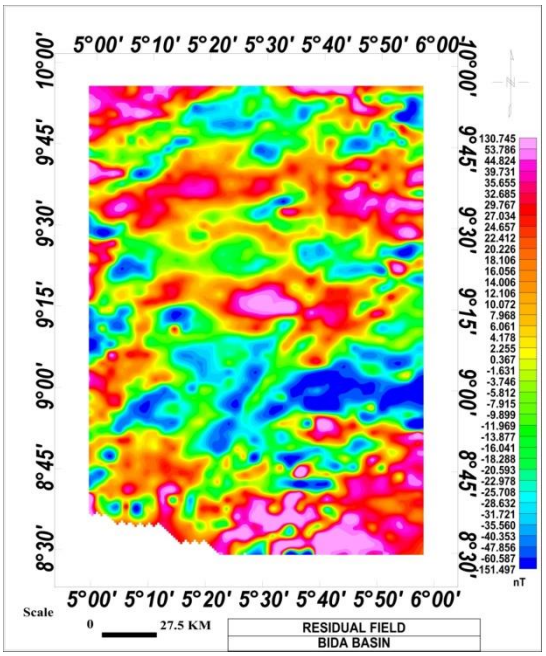

Figure 4: Residual Field Map of the Study Area

(power) spectrum and dividing by 4π. A typical energy spectrum for magnetic data may exhibit three parts – a deep source component, a shallow source component and a noise component and a noise component. The residual map of the study area was divided into sixteen (16) blocks of overlapping magnetic sections. The divisions of residual data/map into 16 spectral sections was done with Oasis Montaj and the spectral energies were plotted within it,*. SPC file obtained were later exported into the Microsoft Excel worksheets one after the other until the total number of 16 spectral (*SPC) energy files were exported. The Microsoft Excel worksheets file obtained was later used as an input file into a spectral program plot (SPP) developed with Matlab. The total numbers of 16 spectral energies were plotted in Matlab with the

developed program. Atypical plot of energy against frequency (wavenumber) is as shown in Figure 4. From the slopes of the plot, the first and second magnetic source depth was respectively estimated using the relations below:

$$Z = -\frac{m}{4\pi} \qquad (5)$$

where m and z is the slope and the depth respectively

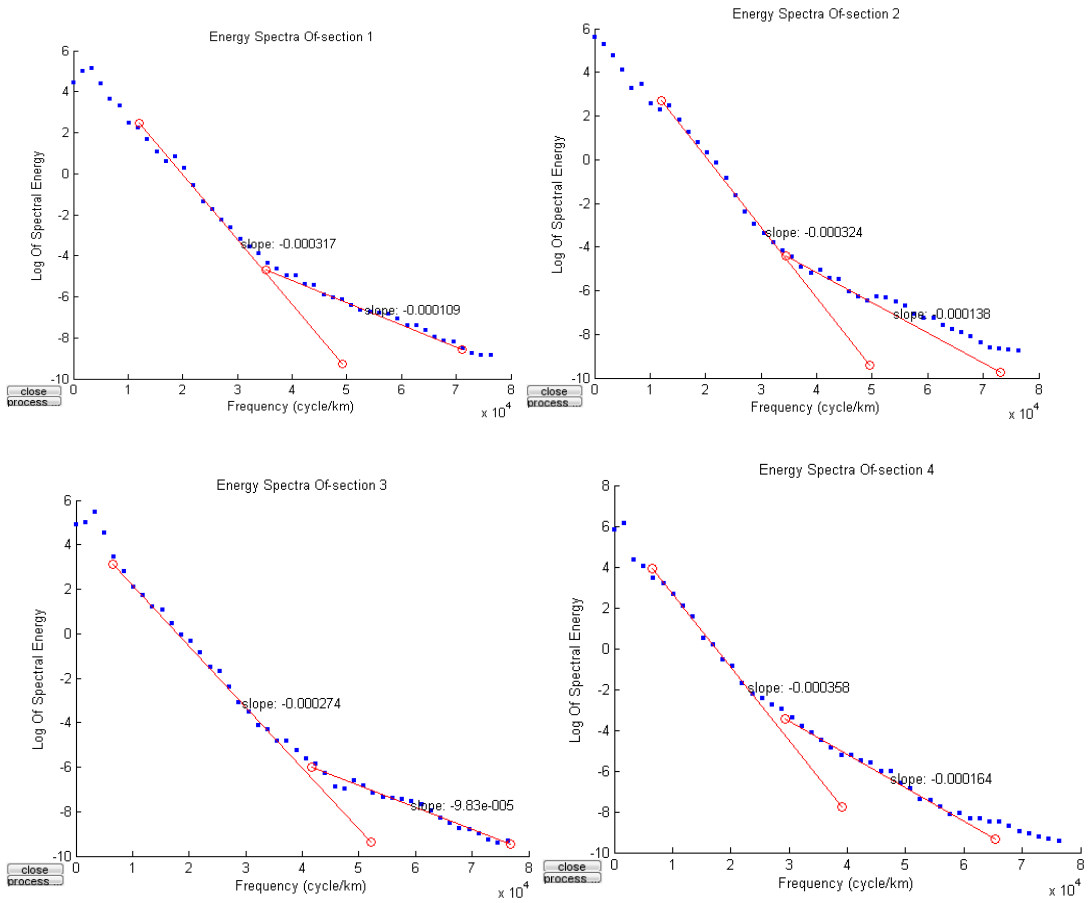

Figure5: Atypical plot of energy spectrum against frequency for sections 1-4

The coordinates of each spectral block were obtained by summing the values of the bounding latitude and longitude and averaging it. This was used in plotting the spectral energy against frequency as presented in Figure 5.

5. RESULTS

Equation (5) shows the relationship between the depth (h) to the basement and the decay slopes (m) of the energy spectrum. Table 1 shows the estimated magnetic sources for both the shallow source (depth 1) and deeper sources (depth 2). The primary sources that account for the first layer depth derived from the statistical spectral analysis are the magnetic rocks that intrude the sedimentary formation.The Second layer depth may be attributed to magnetic rocks that are emplaced or intruded into the basement underlying the sedimentary basin. Intra basement features like fractures and faults are other sources of the second layer depth.Result of spectral analysis of the aeromagnetic data over the Bida area revealed two depth source models.

The first layer (h1) varies from a thickness of1.8 km to 2.85 km with an average thickness of 2.0km. The maximum depth of 2.85km could be found at the South- Eastern part while the minimum depth of 1.8km could be found at North–Eastern part of Figures5a and 5b.Figure 5(b) is the 3D view of the depth to basement within the subsurface, the map is contoured with the depth values inverted by multiplying the depth values in Figure 5a by (-1).Several depressions or variations in thickness have been observed in some parts of Bida Basin, particularly around Egbako, Pategi and Mokwa areas. The highest sedimentary thickness observed from Figure 5b is the depression seen at the south-eastern part of the study area which corresponds to Egbako and Pategi areas. These areas correspond to areas with highest magnetic values

of total magnetic intensity (TMI) map of Figure 3 and residual map of Figure 4. These deeper sections of the Bida sedimentary basin identified in this study might be possible potentials sites for hydrocarbon deposits and is therefore recommended to be subjected to further investigations.

The spectral depth value of 2.8 km agreedat large with the views of Kogbe (1989) thatthe total thickness of Cretaceous sediments in the eastern portion of southern Nigeria basins is about 3.3km.Similarly, Udensi and Osazuwa (2003) got the depth estimate of about 3.3 km for the entire Bida Basin.

Table 1: Estimated depth to the shallow (depth 1) magnetic sources and deep (depth 2) magnetic sources in km

S/ No	Spectral Section	Longitude	Latitude	M1	M2	h_1(km)	h_2(km)
1	SPT1	5.25	8.75	-0.000317	-0.000109	2.521	0.867
2	SPT2	5.75	8.75	-0.000324	-0.000138	2.577	1.097
3	SPT3	5.25	9.25	-0.000274	-0.000146	2.179	1.161
4	SPT4	5.75	9.25	-0.000358	-0.000164	2.847	1.304
5	SPT5	5.25	9.75	-0.000288	-0.000172	2.290	1.368
6	SPT6	5.75	9.75	-0.000278	-0.000148	2.211	1.177
7	SPT7	5.5	8.75	-0.000277	-0.000153	2.203	1.217
8	SPT8	5.5	9.25	-0.000255	-0.000159	2.028	1.264
9	SPT9	5.5	9.75	-0.000231	-0.000143	1.837	1.137
10	SPT10	5.25	9.0	-0.000261	-0.000158	2.076	1.256
11	SPT11	5.25	9.5	-0.000258	-0.000148	2.052	1.177
12	SPT12	5.75	9.0	-0.000291	-0.000162	2.314	1.288
13	SPT13	5.75	9.5	-0.000228	-0.000178	1.813	1.415
14	SPT14	5.5	9.0	-0.000251	-0.000162	1.996	1.288
15	SPT15	5.5	9.5	0.000269	-0.000143	2.139	1.137
16	SPT16	5.5	9.25	-0.000283	-0.000165	2.251	1.312

M_1 and M_2 are slopes of the first and second of the plot while Z_1 and Z_2 are first and second depths respectively (Table 1).

6. Summary and Conclusion

Presence of hydrocarbon and its potential is enhanced by the thickness of the sediments of the basin, and also by the kind of geological structure existing within the basement that forms traps for oil and gas.The highest sedimentary thickness obtained with spectral analysis is 2.8 km, located at the south-eastern part of the study area around Egbako and Pategi. This thickness may be sufficient for hydrocarbon (gas) presence in the area.

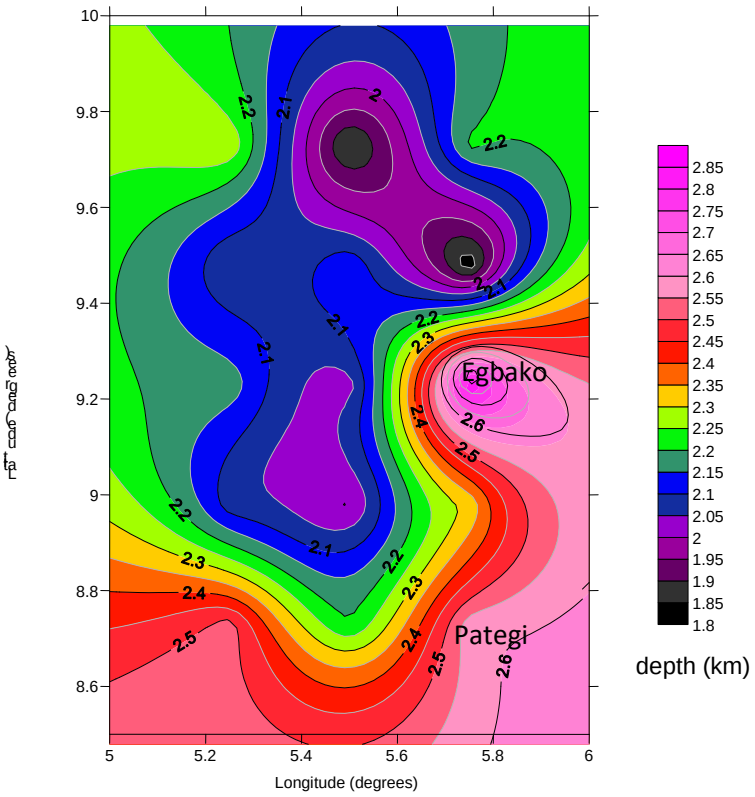
Egbako
Pategi
Longitude (degrees)
depth (km)

(a)

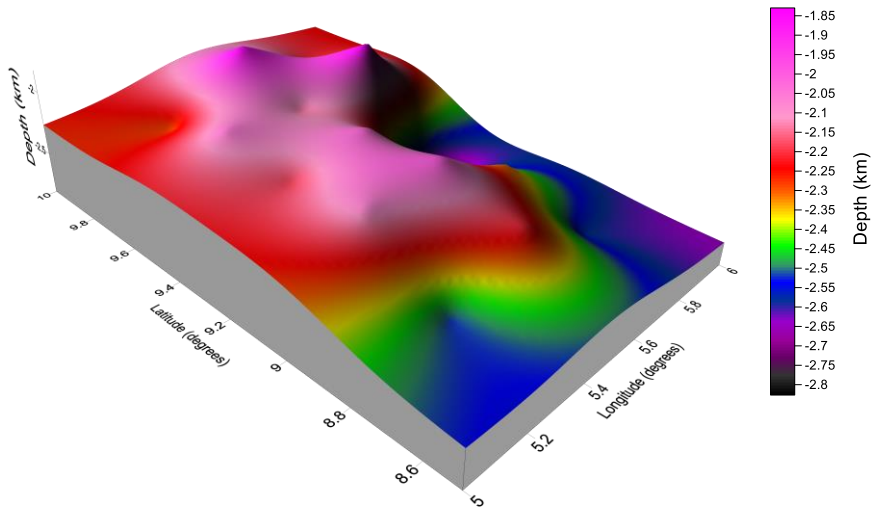
Latitude (degrees)
Longitude (degrees)
Depth (km)

(b)

Figure 5: **(a)** Contour map of first layer magnetic source contour interval is 0.05km **(b)** 3D of deeper magnetic sources

References

Adeleye, D.R. (1973). Origin of Ironstones: An Example from Middle Niger Valley, *Nigerian Journal of Sedimentary Petrology, 43, 709-727.*

Adeleye, D.R. (1976). The Geology of Middle Niger Basin. In: C.A.Kogbe (editor), *Geology of Nigeria,* Elizabethan, Lagos, pp. 283-287

Bhattacharyya, B.K. (1966). A method for computing the total magnetization vector and the dimensions of a rectangular block-shaped body from magnetic anomalies.*Geophysics, 31, 74-96*

Obaje, N.G. (2009) *Geology and Mineral resource of Nigeria* Berlin: Springer-Verlag Heidelberg, Pp. 221.

Kogbe, C. A. (1989(b)): The Cretaceous and Paleogene Sediments of Southern Nigeria. In: Kogbe C. A. (Ed.) Geology of Nigeria(2nd Ed.). Rock View (Nig.) Ltd, 325-334.

Russ, W. (1957).The Geology of part of Niger, Zaria and Sokoto Province.*Geological Survey of Nigeria Bulletin, 27, 1-42.*

Spector, A. and Grant, F.S. (1970): Statistical Models for interpretation aeromagnetic data Geophysics (35)293 302

Udensi, E.E, Osazuwa, I.B., and Daniyan, M.A. (2003). Trend Analysis of the Total Magnetic Field over the Bida Basin, Nigeria. Nigerian Journal of Physics 15(1), 143-151

DETERMINATION OF THE DEPTH TO MOHOROVICIC DISCONTINUITY IN THE MINNA AREA IN NIGERIA, USING BOUGUER GRAVITY DATA

[1]Peter, E. Aaron, *Alkali, A., and Udensi, E. E.*

[1]*Department of Physics, Federal University of Technology Minna, Nigeria*

aisha.alkali@futminna.edu.ng

eeudensi @yahoo.com

Abstract

The present study deals with the determination of depth to Mohorovicic discontinuity beneath the Minna area, Nigeria using Bouguer gravity data. The Empirical relation, Power Spectral analysis and 2–D modeling techniques were used on the Bouguer gravity data covering the study area. Three Empirical relations were used to mathematically compute the Mohorovicic depth for the area. From Spectral analysis carried out on the gravity data, depth to major density boundaries was obtained which are the Basement depth, Conrad discontinuity and Moho discontinuity. The Moho depth results obtained from Empirical analysis and spectral analysis, summed and averaged were used on straight line equation to obtain the relationship between the Moho depth H_C in kilometer. Two 2-D gravity models along two profiles trending NW–SE and N-S direction were constructed with the available geological and geophysical information to obtain a correlated Moho depth for the study area. The obtained result from the model indicates that the average density of the upper mantle is 3.2 g/cm^3 underlying the Migmatitic-Gniess, lower crust of average density 2.8 g/cm^3. The considerable Moho depth range of 30 to 47 km and Conrad depth range of 4 to 24 km obtained for the study area gives an indication that the tectonic stability of the area is further enhanced.

Keywords: Empirical analysis, Power Spectral analysis and 2–D modeling techniques Basement depth, Conrad discontinuity and Moho discontinuity

1. Introduction

The crustal thickness of the Earth varies from place to place and it is necessary to know the crustal thickness of the area which indicates the thickness of the Lithosphere and the stability in terms of tectonic movement. The area with high crustal thickness gives an indication of stability of that area. Previous work on the study area was limited to the use of empirical method. This study will use empirical relationship and Spectral analysis to ascertain the crustal thickness of the study area. The aim is to determine the crustal thickness within parts of minna batholith using bouguer gravity data. The study area is located in Niger state Nigeria, whose Capital is Minna and the study area is located between longitudes 6.0^0 - 7.0^oE and Latitude 9.5^0- 10.5^0N. It possesses the focal segment of the Nigeria basement complex. The area contains meta-sedimentary and meta-volcanic rocks which have experienced polyphase disfigurement and changeability. In these rocks, there are intrusions of granitic rocks of pan – African age. The three different rock groups that make up the complex, migmatite-gneiss, the low – grade schist belt and the older granites are well represented in the area (Trustwell and Cope 1963; Ajibade 1980). The gravity is a potential field; it is a force that acts at a distance which involves the measuring of the acceleration due to the earth's gravitational field. Variations in gravitational field result from density lateral variations of subsurface rocks within the portion where the measurement is observed (Mariita, 2007). The aim of studying elaborate gravity data is to obtain appreciable knowledge level of subsurface geology. The Moho demarcates the boundary between crust and mantle (Lewis, 1983). The boundary separation between the crust and the mantle (Moho) which interfaces lies at a depth ranging from 30 to 50 km on the continents and about 7km beneath the oceanic crust. Mohorovicic discovered the discontinuity between the surface of the crust and mantle. Depth to Moho can be evaluated by seismic or the gravimetric strategy (Coch and Ludman, 1991).

2. Geology of the Area

The area of study is part of north-central Nigeria Precambrian basement complex rocks. The lithologic units include granites, gneisses, migmatites and meta-sediment (Adeleye, 1976). Three rocks type exist in minna comprises of the: granites, schists, and gneiss with quartzite intrusion. The granites belong to the older granite suites occurring as Minna batholith of several high, the texture and colour of these granites vary from medium to coarse grained and light to dark

colour. The area has witnessed fracturing and joint values. The Batholith is a massive body intrusive igneous rocks created during the cooling of magma crystallising beneath the Earth's surface. Magmatic intruitions in them is notcontinuous but rather repeated (multiple individual plutons). This cool and solidified magma becomes exposed after some time as a result of erosion (Udensi, 1984).). Figure 1 (Map of Nigeria) shows the location of the Study Area and Figure 2 is the geological map of the area.

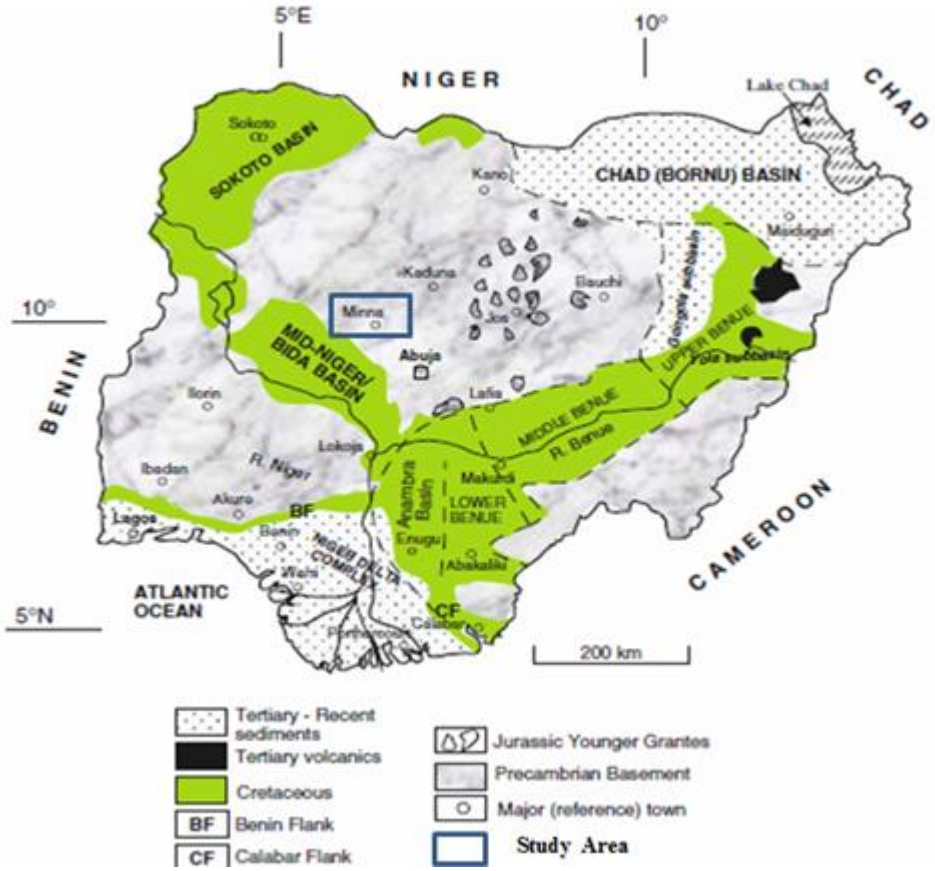

Figure 1: Map of Nigeria showing the study area (Obaje *et al.*, 2009).

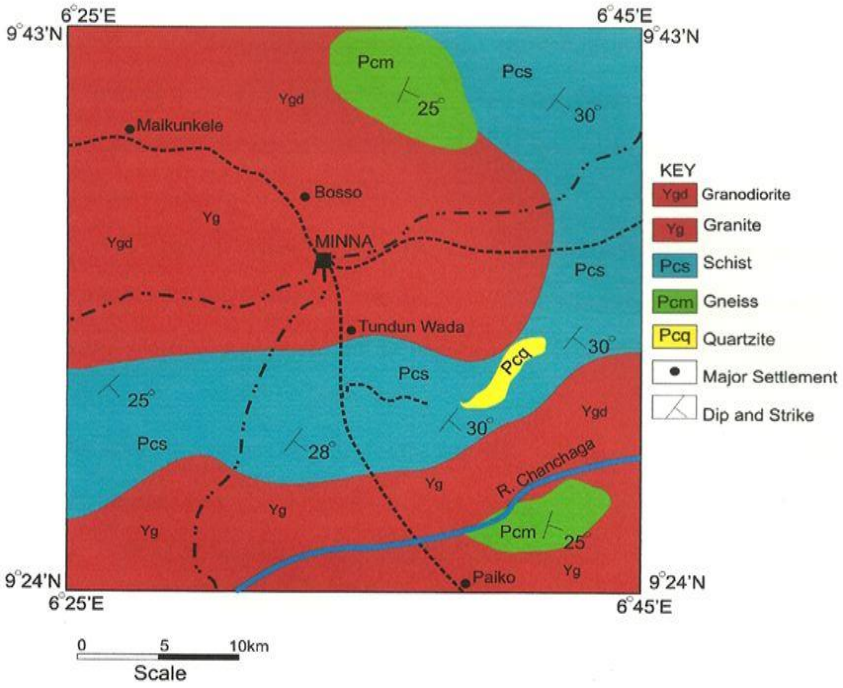

Figure 2: Geology Map showing Location of the Study Area (Alabi A.A., 2011)

3. Materials and Method

Materials

The Bouguer gravity anomaly map of the study area was prepare from the gravity data which was acquired from the Nigeria Geological Survey Agency (NGSA) for this research. About 957 gravity data point was used to prepare a complete Bouguer anomaly map.

Equipment

Materials used for this research study including the following

- Gravity data of the study area
- Oasis Montaj software
- Surfer 10 software
- Excel software
- Work station (Laptop)

Methods

This study basically integrate the use of three different methods to determine the crustal thickness of the study area.

I. The Empirical Relation
II. The Spectral Analysis
III. 2- D Modeling

DETERMINATION OF THE MOHO DEPTH

Empirical Relation

The available data set comprises of Bouguer gravity data anomaly of the study area will be gridded at an interval of 10 km. The Bouguer gravity anomaly data values will be substituted into the following empirical relation below, which will aid in calculating the crustal thickness of the study area using Demeniskaya (1958), Woollard (1959), Woollard and Strange (1962).

The outcome of the below process will be useful for the determination of the crustal thickness, deducing the geological history of an area, and also essentially in tectonic study (Udensi, 2000).

The empirical relation equations are as follow:

$$H_D = 35(1 - TANH(0.037BG)) \quad (1.1)$$

$$H_W = 32.0 - 0.08BG \quad (1.2)$$

$$H_{WS} = \frac{40.50 - 32.50TANH((BG+75)}{275} \quad (1.3)$$

Where H_D, H_W and H_{WS} are in km and BG is mGal. The average of value estimated from the computed relation at any given location is the crustal thickness at that particular location (Raid *et al.*, 1981).
The data are inputted into the Microsoft excel package in the form of X,Y and Z, the excel package was used to estimate the depth to Moho using the above equation 1.1, 1.2, and 1.3.
Thereafter, the average values estimated from the relation H_D H_W and H_{WS} is the depth to Moho of the study area.

The Power Spectral

Power spectrum analysis (Dimri 1992; Blakely 1995). Power spectral analysis estimates the mean depth of the interfaces considering the log power of the Bouguer gravity spectrum as a function of wave number / frequency. This assumes that the distribution of sources or the scaling natures of the sources are uncorrelated, (Spector and Grant, 1970; Pilkington *et al* 1994; Maus and Dimri (1992). The gravity anomaly spectrum due to layered source is separated into multiple segments in frequency domain that can be interpreted in terms of mean depth of the interface. The half of the slope of the segments gives the mean depth of the interfaces. The method is used to map geological structure from the observed gravity data at the surface.

Two Dimensional Modeling (2-D)

The 2 – D gravity modeling is an essential tool to study the crustal structure and usually the final stage in gravity interpretation. Gravity data reveal a regular relationship between crustal structure, crustal composition (density) and the surface elevation. Bouguer anomalies are enough to give evidence of changes in mass distributions in the lower and the upper mantle, for any regional scale (Tealeb, A and S. Raid, 1986).

The modeling technique commonly involues using a residual gravity anomaly, in this technique the interpreter must use a density contrast between the body of interest and the surrounding material, in the process of modeling Bouguer gravity anomalies the density of the body is used (Mariita, 2007).

The model system is based on the geology of the area and the geophysical data obtained from the gravity data. The gravimetric model will be performed using the GM, sys program, which is hosted by the interface of Oasis Montaj 6.4.2. Gravity modeling is considered an important tool to study the crustal structures. This method is straight forward, which is by means of trial and error method, varying the body geometry allow to obtain a good fitting between theoretical and observed anomalies. (Tealeb, A and S. Raid, 1986).

5. RESULTS AND DISCUSSION

Empirical Method

Table 5.1 show some of the result obtained from the calculated depth to Moho, the empirical relation used was developed by Demenitskaya (1958), Woollard (1959) and Woollard and Strange (1962). The average values obtained from the three relation at any given location is the crustal thickness at that location. The values obtained were interpolated into the excel spread sheet, which was used to produce contour crustal thickness map of the study area. Figures 3, 4, 5 and 6 respectively are the result from Demenitskaya (1958), Woollard (1959), Woollard and Strange and the average crustal thickness, using Surfer 10 software package. (Raid *et al.*, 1981).

Table 5 .1 Sample Results of the Calculated Empirical Relations

H_D (Km)	H_W (Km)	H_{WS} (Km)	Average
57.02008	33.60	34.08530	41.56846
57.02008	33.60	34.08530	41.56846
57.02008	33.60	34.08530	41.56846
55.80530	33.48	33.91510	41.06681
55.38199	33.44	33.85840	40.89349
56.21940	33.52	33.97181	41.23707
57.78435	33.68	34.19896	41.88777

Key: H_D, H_W and H_{WS} are the crustal thicknesses using Demenistskaya, Woollard, Woollard and Strange in Kilometre respectively.

Demenistskaya Relation

Figure 3 shows the map of Demenistskaya relation. The crustal thickness values ranges from 53.5 to 67.5 km with an increase of 0.5 km interval. The maximum value 67.5 km is at the south west part of the map, the minimum value 53.5 km is at the South western and South Eastern part of the map.

Woollard Relation

Figure 4 represent the map of Woollard relation, whose values ranges from 33.2 to 35.6 km with an increase of 0.1 km interval. The highest value 35.6 km is at South western, the lowest value 33.2 km at the North western and South Eastern region of the map.

Woollard and Strange Relation

Figure 5 shows the map of Woollard and Strange relation, the values ranges from 33.6 to 37 km increasing in the trend of 0.2 km interval. The maximum value 37 km at South Western part and the minimum value of 33.6 km at South Eastern part of the map.

Average Empirical Relation

Figure 6 show the average empirical relation developed by Demenistskaya (1958), Woollard (1959) and Woollard and Strange (1962). The average empirical map showed that the crustal thickness of the study area ranges from 40 to 47 km with an increase of 0.5 km interval. The thickness varies from maximum value of 47 km to a minimum value of 40 km. The maximum depth is located at the South Western, its minimum Moho depth is located at North West, South Western and South Eastern part of the map.

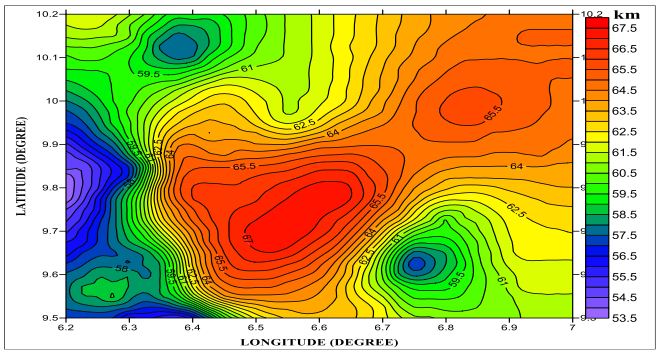

Figure 3: Contour Map of Demenistskaya relation of the Study Area. Contour Interval of 1 km. The legend shows Values of the Moho depth in the study Area.

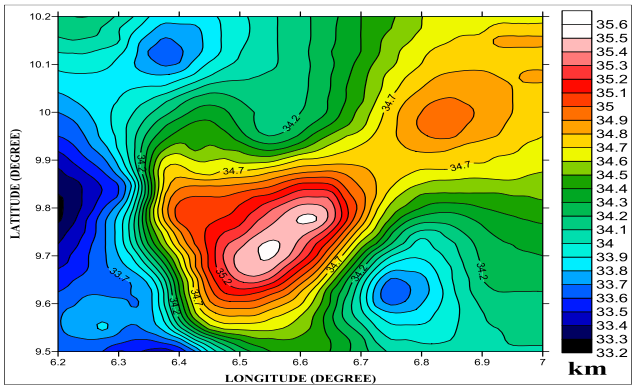

Figure 4: Contour Map of Woollard relation of the Study Area. Contour Interval is 0.1 km. The Legend shows Values of the Moho depth in the study Area

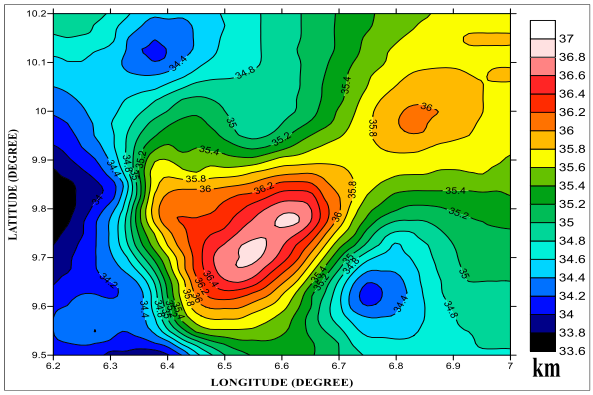

Figure 5: Contour Map of Woollard and Strange relation of the Study Area. Contour Interval is 0.2 km. The Legend shows Values of the Moho depth in the study Area

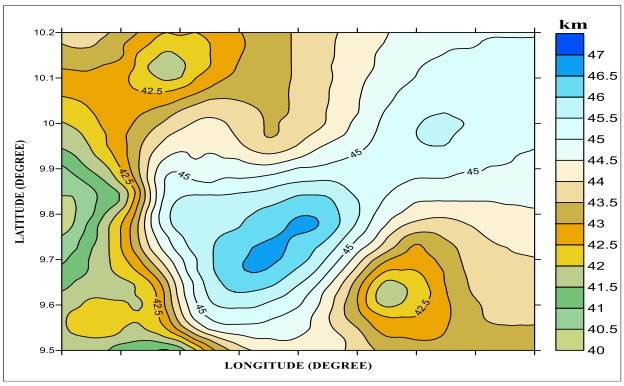

Figure 6: Contour Map of Average Crustal Thickness of the Study Area using the empirical relation. Contour Interval is 0.5 km. The Legend shows Values of the Moho depth in the study Area

Power Spectral Analysis

Table 5.2 which shows the three (3) line segment represent slope 1, 2, and 3. M_1, M_2, and M_3 are the corresponding slopes of each of the segment. The values generated from each of the slopes, are used to estimate the H_1 which is attributed to the shallowest depth sources from crystalline rock (basement interface/ intrusion), H_2 is associated to the average depth to conrad discontinuity which may correspond to the depth variation between the upper and lower crust and the last level H_3 is attributed to the average depth of the seated Moho discontinuity.

Table 5.2 Representing Spectral Plot Values and the corresponding Depth of the Study Area

SECTION	M_1	M_2	M_3	H_1	H_2	H_3
A	0.000151	0.000682	0.00137	4.5981	20.7674	41.7174
B	0.00016	0.000785	0.00124	4.8721	23.9038	37.7588
C	0.000172	0.000653	0.000608	5.2375	19.8843	18.5140
D	0.000159	0.000798	0.00119	4.8417	24.2996	36.2363
E	0.00175	0.000414	0.00139	5.3289	12.6066	54.2022
F	0.00175	0.000275	0.00116	5.3289	8.4044	35.0255
G	0.000205	0.000265	0.00132	6.2424	8.0694	40.1949
H	0.000156	0.000608	0.00159	4.7503	18.5140	48.4166
I	0.000154	0.000789	0.00128	4.6894	24.0256	38.9768

Where M_1, M_2, and M_3 values are linear gradient and H_1, is the depth to the seated features.H_2, is the Conrad depth and H_3 is the Moho depth (in Kilomtre)

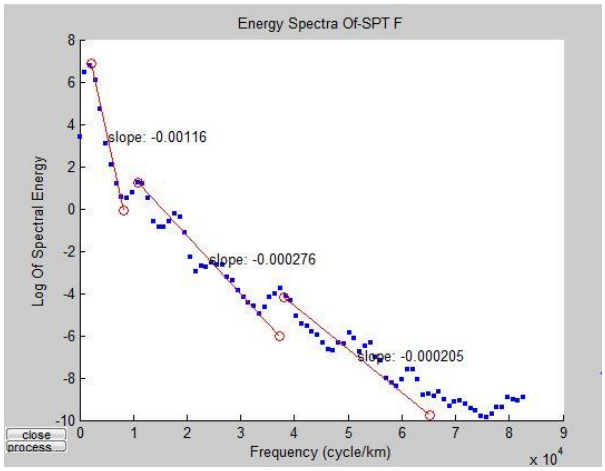

Figure 7: Typical plot of energy spectrum against frequency of section

Analysis of the Moho Depth

Figure 8 represent the Moho depth map, the depth range from 18 to 48 km. The minimum depth value of 18 km is located at of North West region, while the maximum depth value of 46km is located at North Eastern part of the map. The values vary at 2 km interval with an increases down North -West and a decrease in the south Eastern part of the study area.

Analysis of the Conrad depth

Figure 9 represent the Conrad depth, the depth which ranges from a minimum of 8 km to a maximum of 25 km, the maximum value 25 km is located at the North Eastern and minimum value 8 km is located at Northern and Western part of the map with a steady increase down West to Southern region of the map.

Analysis of the Basement Depth

Figure 10 represent the Basement depth, the depth which ranges from a minimum 4.5 km and 6.3 km. The maximum value 6.3 km is located at the Western region and minimum value 4.5 km is located at the North East and South West of the map.

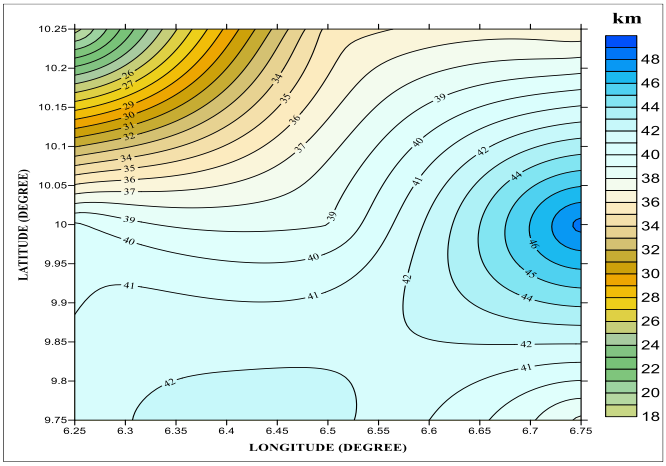

Figure 8: Contour map of Moho Depth of the Study Area. Contour interval of 2 km depth shown at the Legend

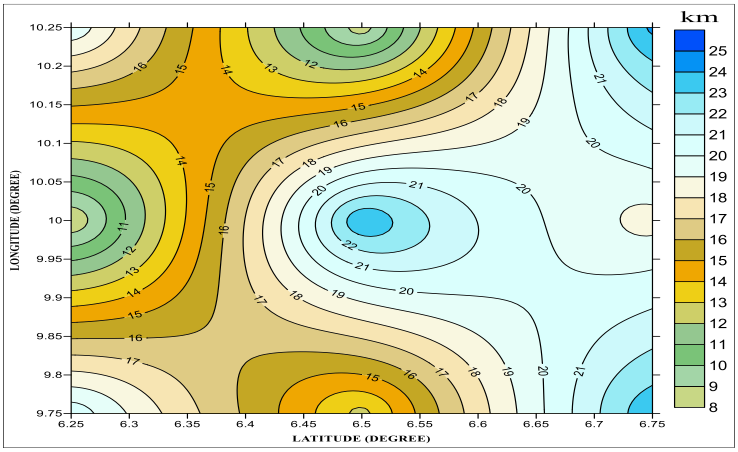

Figure 9: Contour map of Conrad Depth of the Study Area. Contour interval

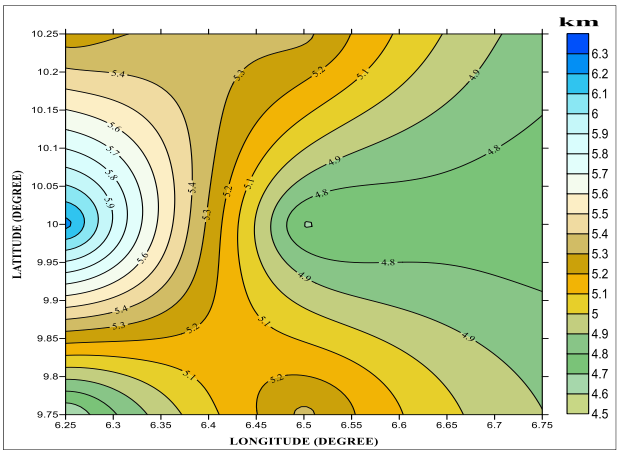

Figure 10: Contour Map of Average Crustal Thickness of the Study Area using the empirical relation. Contour Interval is 0.5 km. The Legend shows Values of the Moho depth in the study Area.

Crustal Thickness Map of the Study Area

Figure 11: Shows the Crustal thickness of the study area, the area has a maximum depth of 47 km, it increases down North – East and North - South region of the area. The minimum depth of 33 km, which has a contour interval of 1 km. The results obtained from the methods used shows no significant different.

2- D Modeling Analysis

In the present study, two gravitational Profile (AA^{l} and BB^{l}) as shown in Figure 12 and 13, were selected to be investigated with 2- D Modeling approach.

PROFILE AA^{l}

The model profile of A (Figure 12) extends about 105 km long. The profile is distinguished by an Anomaly that ranges between -46 to 0 mGal. The model contains the Zungeru- Birnin Gwari Schist, sand, soil, clay, Batholith, Kushaka Schist, older granite and Migmatite – Gnesis complex. The Zungeru – Birnin Gwari Schist has a density of 2.73 gm/cm^3, the Batholith has a density of 2.65 gm/cm^3, Clay has a density of 2.35 gm/cm^3, Sand has a density of 2.19 gm/cm^3, Soil has a density of 2.27 gm/cm^3, the Kushaka Schist has a density of 2.72 gm/cm^3 and the older Granite has a density of 2.65 gm/cm^3. From the profile, the crustal thickness ranges between 32 and 47 km, the minimum value is 32 km and the maximum value is 47 km. In addition, the average density of the mantle is 2.8 gm/cm^3.

PROFILE BB'

Figure 13 represent the model profile B which cut across the study area in the direction, and extend about 110 km. The profile has an anomaly that ranges between -42 to -26 mGal. Profile B contain older granite with density of 2.65 gm/cm^3, sand with a density of 2.19 gm/cm^3, Kushaka schist has a density of 2.72 gm/cm^3, Batholith has a density of 2.35 gm/cm^3, Migmatite has a density of 2.8 gm/cm^3 and the Mantle has a density of 3.2 gm/cm^3. From the profile, the Crustal thickness has a minimum value of 30 km and a maximum value of 46 km.

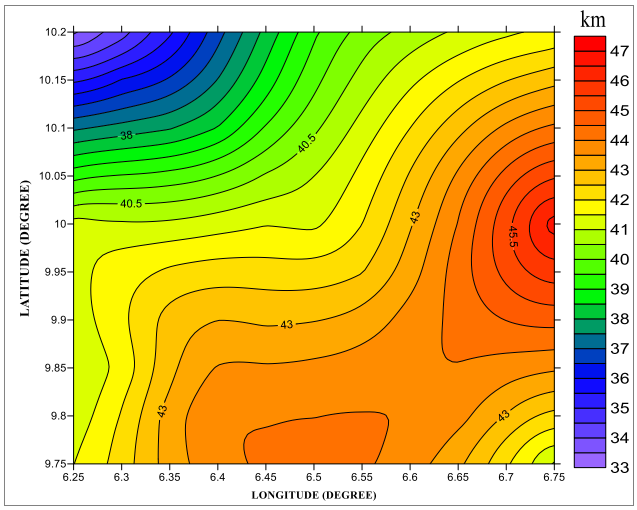

Figure 11: Contour Map of Crustal Thickness of the Study Area. Contour 1 km interval depth shown at the Legend

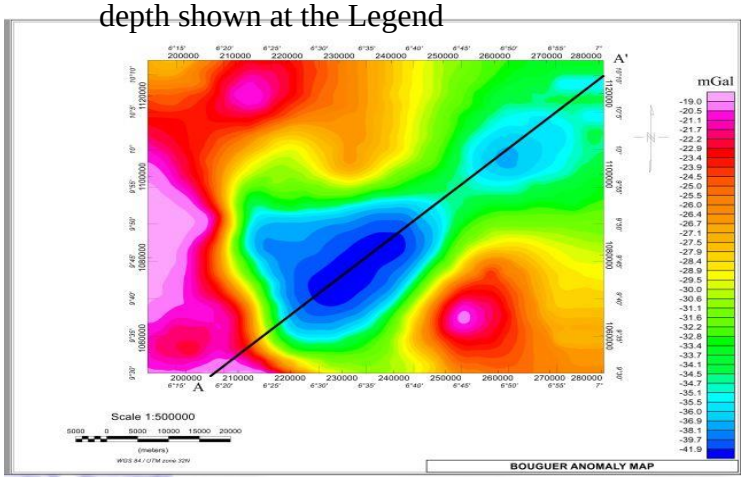

Figure 12: Bouguer gravity Map of the Study Area showing Profile AA[1]

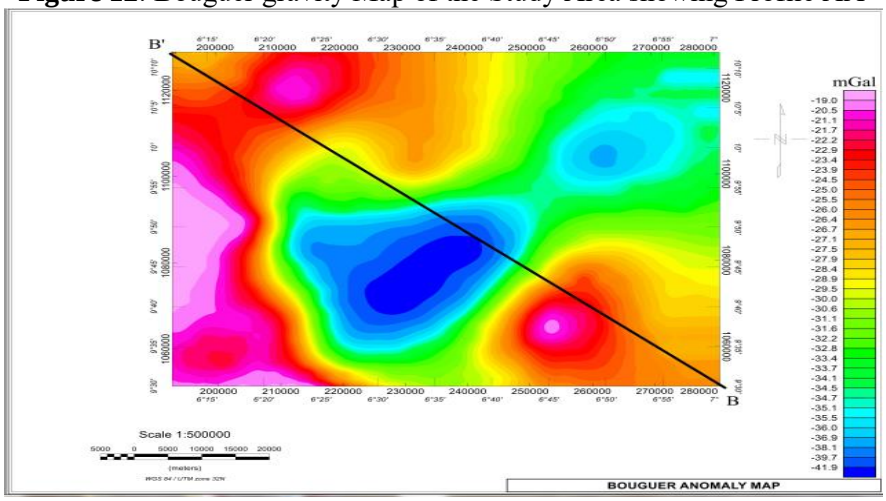

Figure 13: Bouguer gravity Map of the Study Area showing Profile BB[1]

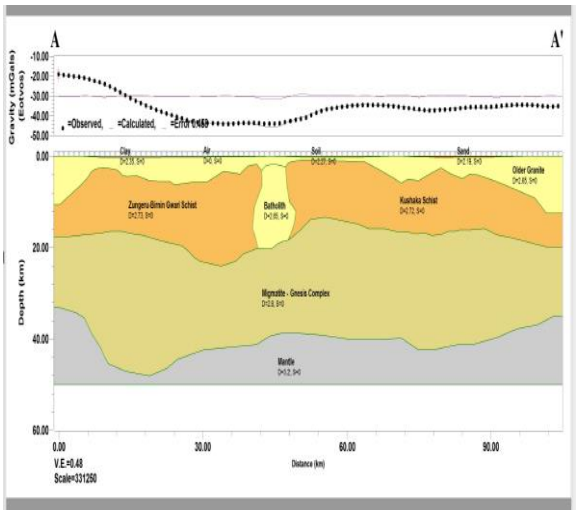

Figure 14: Gravity Model along Bouguer gravity Profile AA[1]

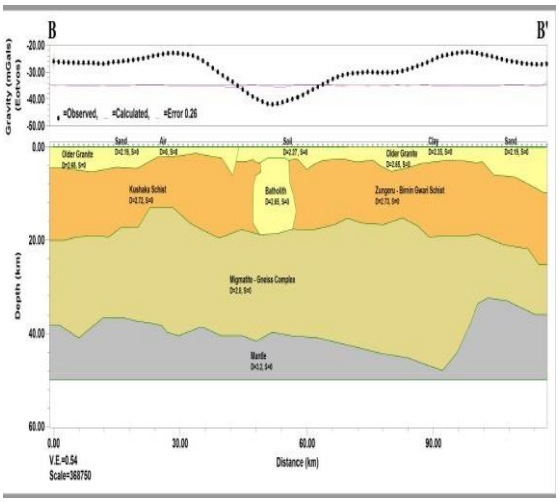

Figure 15: Gravity Model along Bouguer gravity Profile BB[1]

Tectonic Stability of the Study Area

Tectonically, Nigeria like other African Countries lies within a plate. Therefore, stable and Diastrophic activities, unlike other countries like Japan that lies in plate boundaries where tectonic activities is predominant, such country, no matter how large or small their moho depth is, will always be unstable obtaining a considerable moho depth. From the 2 –D modeling of the study area revealed depth of 35 to 48.5 km which has improve the stability of the area.

6.0 Summary and Conclusion

The empirical relation and power spectral analysis methods were employed for the estimation of the crustal thickness of the study area. From the power spectral analysis technique, shows a corresponding average depth of three level basement, conrad and the moho discontinuities within 4.5 to 6.2, 18.5 to 24.29 and 35 to 48.5 respectively. The result from the empirical relation revealed that the average depth 47km is in close correlation to the moho depth.

Two gravity profiles have been investigated with 2- D modeling to explain the shape and variation of the crust along these profiles. The results of these models are summarised in two maps (Figure 14 and 15) respectively.

The Moho discontinuity occures at a depth of 30.0 km and 47 km. The density model used indicate that the average densities of different rock layers and schist formation in the study area: Zungeru – Birnin Gwari schist has a density of 2.73 gm/cm^3, Kushaka schist has a density of 2.72 gm/cm^3, older Granite has a density of 2.65 gm/cm^3, Batholith has a density of 2.35 gm/cm^3, Migmatite has a density of 2.8 gm/cm^3, soil has a density of 2.27 gm/cm^3, and sand has a density of 2.19 gm/cm^3. The average density of the Mantle from the two profiles is 2.8 to 3.2 gm/cm^3. The computed results show that the crustal thickness of Minna area has a maximum depth of 47 km, it increase down North – East and North South region and a minimum depth of 33 km.

The result obtained correspond to the research result of Udensi, (2000) within the study area using empirical relation formula to estimate the crustal thickness

REFERENCES

Adeleye, (1976).“The Geology of the Middle Niger Basin: In the Geology of Nigeria, Education Kogbe. Elizabeth Press, Lagos, 283 – 287.

Ajibade, A. C. (1980) Geotectonic Evolution of the Zungeru Region. Ph.D Thesis University College of Wales

Alabi A.A (2011) Geology and Environmental Impact Assessment and Benefit of Granitic Rocks of Minna Area, Northwest Nigeria Doi: http://dx.doi.org/10-4314/ejesm.v4i4.5

Blakely, R. J (1996). Potential theory in Gravity and Magnetic applications, Cambridge University Press

Coch, N.K., and Ludman, A., (1991). Earth Dynamics and Plate Tectonics, Physical Geology, Macmillian Publishing Company, New York, page 678

Demenistskaya, R. M (1958) Planetary Structure and their Reflection in Bouguer Anomalies Survey Geology Bull

Dimri, V.P. (1992). Deconvolution and inverse Theory (Elsevier Science Publishers, Amsterdam London New York Tokyo)

Lewis, B. T. (1983). The process of Formation of Ocean Crust; Science, 220, 151 – 157 Doi: 10.1126/science.220.4593.151.

Mariita, N.O., (2007). The Gravity Method: Presented at Short Course II on Surface Exploration for Geothermal Resources, Organised by United Nations University- Geothermal Training Programme 2- 17

Obaje, N.G., (2009). Geology and Mineral Resources of Nigeria, Longon: Springer Dordrecht Heidelberg Page 5 – 14

Pilkington, M., Gregotski, M. E., & Todoeschuck, J. P. (1994), Using Fractal Crust Magnetization Models in Magnetic Interpretation, Geophys. Prospect42**,** 677–692.

Raid, S. Refai E and Ghalib, M. (1981), Bouguer Anomalies and Crustal Structure in the Eastern Mediterranean Technolophysics 71, page. 253 – 286.

Spector, A. and Grant, F. S. (1970). Statistical models for Interpreting Aeromagnetic data. Geophysics 35, 293–302.

Trustwell, J. F and Cope, R. N. (1963). The Geology of Parts of Niger and Zaria Province Northern Nigeria. Publish by Geological Survey of Nigeria

Tealeb A., and Raid S. (1986). Regional tectonics of Sinai Peninsula interpreted from Gravity and Deep Seismic data proceedings Fifth Annual meeting of Egyptian Geophysical Society, Cairo, 18 - 49

Udensi, E. E. (2000). Estimation of crustal thickness of Minna: Preliminary investigation. Journal of Science, Technology and Mathematics Education (JOSTMED)

Woollard, G.P (1959) Crustal Structure from Gravity and Seismic Measurement, Journal Geophysics Reserves 69: 1521 - 44

Woollard, G. P and Strange, W. E. (1962). "Gravity Anomalies and Crust of Earths in the Pacific Basin" Monograph 6: 60 – 80.

DETERMINATION OF COVERAGE AREA OF VHF TELEVISION SIGNAL IN BENUE STATE, NIGERIA

Moses Abiodun Stephen*[1], Oyedum Onyedi David[2], Ajewole Moses Oludare[3]
[1,2]Department of Physics, Federal University of Technology Minna, P.M.B. 65 Minna, Niger State, Nigeria
[3]Department of Physics, The Federal University of Technology Akure, P.M.B. 704 Akure, Ondo State, Nigeria
[1]abiodun.moses@futminna.edu.ng*
[2]oyedumod@yahoo.com
[3]oludare.ajewole@futa.edu.ng

* Corresponding author

Abstract

This study investigates the coverage areas of VHF television signal in Benue State, Nigeria, by quantitatively measuring the electric field strength of the signals. The signal levels of the transmitter of Nigeria Television Authority (NTA), Makurdi, Channel 10, on a frequency of 210.25 MHz were measured along several radial routes with the transmitting stations at focus. The distances, elevations above the sea level and locations (longitude and latitude) where every signal level was taken were also measured. The signal levels were taken using Digital Signal Level Meter GE-5499 while other measurements were done with GPS 72 – Personal Navigator. Measurements were taken along all the accessible radial routes in the state until all the signals faded away completely. From the data obtained, Surfer 12 software application was used to draw the contour maps of the signal levels of the areas covered by the transmitting station. The results obtained showed that the present configuration of the transmitter of the television station does not give an optimum coverage of the state. Only 6.13% of the entire land mass of the state has the television signal coverage, consequently, greater percentage of Benue State is out of the television signal coverage. So, there is need to have repeaters stations at some intervals to ensure reception of the television signals throughout the state.

Keywords: coverage areas, electric field strength, transmitter, VHF

1. Introduction

At broadcast frequencies in the VHF band (30 – 300 MHz), propagation is usually by direct wave. Therefore, in these frequency bands, height of the antenna, curvature of the earth surface and weather conditions influence wave propagation. The degree to which these factors affect propagation depends primarily on the frequency of the wave and the polarization (Hall, 1991). The electric field strength at a given distance from the transmitter is attenuated by these parameters, with the result that radio services in the VHF band are limited to distances close to the transmitter. The present trend in broadcasting is to use widespread broadcast transmitter of medium or VHF or UHF range of frequencies to serve areas not far away from the transmitter.

Coverage areas of broadcast stations are usually classified into primary, secondary and fringe areas. The size of each of these areas depends on the transmitter power, the directivity of the aerial, the ground conductivity and the frequency of propagation. The coverage area decreases with increase in frequency and reduction in the ground conductivity (Ajayi and Owolabi, 1975).

The primary coverage area is defined as a region about a transmitting station in which the signal strength is adequate to override ordinary interference in the locality at all times. The primary coverage area corresponds to the area in which the electric field strength is at least 60 dBμV. The quality of service enjoyed in this area can be regarded as Grade A1. The appropriate value of the electric field strength for this quality of service is dependent on the physical features of the environment and manmade noise in the locality. The relevant electric field strength also depends on whether the locality is rural, industrial or urban. The secondary coverage area is a region where the electric field strength is often sufficient to be useful but is insufficient to overcome interference completely at all times. The service provided in this area may be adequate in rural areas where the noise level is low. The secondary coverage area corresponds to the area in which the electric field strength is at least 30 dBμV but less than 60 dBμV. The quality of service enjoyed in this area can be regarded as Grade B1. The fringe service area can be regarded as that in which the electric field strength can be useful

for some periods, but its service can neither be guaranteed nor be protected against interference. This is an area in which the electric field strength is greater than 0 dBμV but less than 30 dBμV. Such an area may be said to enjoy Grade B2 service (Ajayi and Owolabi, 1979).

This study investigated the coverage areas of the Nigeria Television Authority, Makurdi Zonal Network Centre (NTA Makurdi, Channel 10), with broadcasting frequency of 210.25 MHz, by means of quantitative measurement of the electric field strength signals.

1.0

2. Theoretical Background

The attenuation experienced by a radio wave is the result of absorption and scattering. At wavelengths greater than a few centimeters, absorption by atmospheric gases is generally thought to be negligibly small except where very long distances are concerned. However, cloud and rain attenuation have to be considered at wavelengths less than 10 cm, and are particularly pronounced in the vicinity of 1 and 3 cm.

It is helpful to recall that when an incident electromagnetic wave passes over an object whose dielectric properties differ from those of the surrounding medium, some of the energy from the wave is;

(a) absorbed by the object and heats the absorbing material (this is called true absorption), and
(b) some of the energy is scattered, the scattering is generally smaller and more isotropic in direction (Bean and Dutton, 1968).

2.1 Radio Propagation at VHF Band

Radio reception of broadcast services at VHF is almost entirely dependent on the space wave because, except for reflections due to the rare Sporadic E (Es) and trans-equatorial (TE) ionospheric effects, transmissions at f > 30 MHz ordinarily pass through the ionosphere without being reflected back to the earth. The height of transmitting antenna (usually > λ) and high attenuation of the surface wave normally render it negligible, except for diffraction over and around obstacles which may occur when the space wave encounters obstructions such as buildings, hills, etc. (Oyedum, 1999).

Diffraction allows short-range reception into built-up areas, though mobile systems are subject to screening by hills and to multipath effects caused by scatter or reflections off obstacles. In general the precise prediction of signal level is not possible, and it is necessary to specify the deviation from the calculable median expressed for a given percentage of locations and percentage of time (Hall, 1991).

In clear air the radio refractive index of the troposphere is slightly greater than unity (typically about 1.0003). The way in which refractive index changes with height has much consequence for radio-wave propagation at frequencies greater than about 30 MHz. Above 30 MHz the wavelength is comparable with the distance over which variations of refractive index occur in the troposphere. The tropospheric refractive index variations are due to changes of temperature, pressure and humidity. The refractive index of the troposphere generally decreases with height. This leads to a slight downwards refraction of radio rays, which can be very important for communication at VHF, UHF and SHF. If the rate of refractive index decreases with height is sufficiently large and extends over a sufficient height interval and horizontal extent, it may give rise to atmospheric ducts which guide radio energy far beyond the normal horizon. Normal duct heights are such that complete trapping within them occurs only at centimeter wavelengths, but partial trapping (and very rarely total trapping) may also be found at the shorter metric wavelengths.

If over a large horizontal area, the refractive index decreases with height abruptly, this may lead to partial reflection of radio energy. Both ducting and partial-reflection mechanism may cause multipath interference on line-of-sight or inter-path interference on beyond-horizon links. Randomly distributed small-scale spatial fluctuations of refractive index about the local mean value cause weak signal levels always to be present at large distance beyond the horizon. This is due to tropospheric scattering from the irregularities, and such scattering may be used to provide radio communication over hundred kilometers of line-of-sight paths. These refractive index fluctuations may cause significant scintillation (rapid

fading) which is large in magnitude for longer range or higher frequency. For two terrestrial radio terminals within line of sight, there may often be a ground reflected ray in addition to the direct ray. There may also be a reflected ray (or more than one) from layers of abrupt change of refractive index with height. According to their relative phase, the "multipath" contributions may give rise to slow signal enhancement or fading.

The effect of obstacles such as hills, building or trees on a radio wave depends on its wavelength. Such obstacles cause reflection (and multipath), diffraction and absorption. In a built-up area this results in an incalculable field with wide variations. The losses caused by absorption and scattering increase with frequency, until, at frequencies above UHF, walls or masonry more than about 20 cm thick may be regarded as opaque, together with buildings (except those of very light construction) and good land which is visually opaque (Hall, 1991).

2.2 Area Coverage

A traditional broadcast system comprises several receivers which receive signals from a single, fixed base station. In most cases the base station is centrally located within the area to be served and is connected to the control room via a radio link. A straightforward approach to the problem of providing coverage over very large areas would therefore be to erect a very high tower somewhere near the centre of the required coverage area and install a powerful transmitter. This technique is used by the broadcasting authorities; their transmitting masts may be over 300 m high and they radiate signals of many kilowatts. Broadcasting always aims to deliver a strong signal to many receivers all tuned to the same broadcast.

If a single high mast were situated in the middle of a territory with sufficient transmitter power to cover large area, then that frequency would not be reusable anywhere close to the coverage area. For traditional broadcast services, if the area is too large to be economically covered by one base station or if geographical conditions produce difficulties, an alternative is to have a large number of low-power transmitters radiating from short masts, each covering a small territory but permitting reuse of the frequencies assigned to them many times in a defined geographical area. This is the basis of the 'cellular radio' approach to area coverage and is extremely effective (Appleby and Garrett, 1985; Department of Trade and Industry, 1985). In this case the transmitters are all operated at nominally the same frequency so that whatever the location of the receiver within the overall coverage area, it is within range of at least one of the base stations and its receiver does not have to be retuned. This method of operation is well established and is known as quasi-synchronous or simulcasts operation. It exploits the fact that although a transmission frequency cannot be used for another service close to the desired coverage area because of interference, it can be reused for the same service (Dernikas, 1999).

3. Study Area

Benue State is a state in north central Nigeria and the capital is Makurdi. Benue State lies within the lower river Benue trough in the middle belt region of Nigeria. Benue State lies between latitude 6.42°N and 8.13°N and longitude 7.78°E and 10°E (Figure 1) and shares boundaries with Nassarawa, Taraba, Cross-River, Enugu and Kogi. It also shares a boundary with the Republic of Cameroun. The total land mass of Benue State is about 33,955 square kilometers and has a population of 4,780,389 (2006 census).

Benue State experiences two distinct seasons, the rainy season and the dry season. The annual rainfall ranges from 100 mm to 200 mm. The rainy season starts in April to October, while the dry season starts in November to March. The temperature varies between 23ºC to 37 °C in the year. However, the south eastern part of the state close the Obudu-Cameroun Mountain varies, it has a cooler climate similar to that of the Jos Plateau. The western and southern part of the state has rain forest vegetation which consists of tall grasses and tall trees while the eastern and northern parts has Guinea savannah vegetation which are mixed trees and grasses that are of average height. (http://benuestate.gov.ng/wp/historical-background/, 2013)

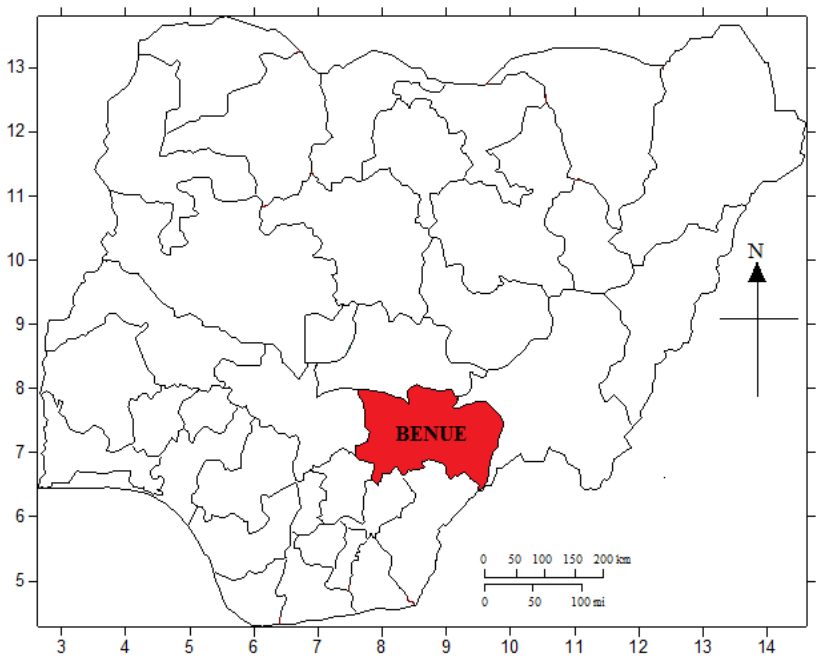

Figure 1: Location of Benue State in Nigeria

4. Methodology

NTA Makurdi, Channel 10 has 5 kW transmitter, Rohde and Schwarz (Germany product). The video carrier frequency of the station was 210.25 MHz and the audio carrier frequency was 215.75 MHz. The output power of the transmitter was constant at 1.1 kW all through the period of this work. The mast on which the transmitting antenna was mounted was 150 m. The signal levels of the television station was taken along four radial routes from the transmitting station as shown in Figure 2, using Digital Signal Level Meter GE-5499. The signal level corresponding distances, elevations above the sea level and locations were also measured using GPS 72 – Personal Navigator. Measurements were taken (at distances further from each transmitter) along these radials until all the signals faded away completely.

From the data obtained, Surfer 12 software application was used to draw the contour maps around the transmitting stations for signal levels to determine the coverage areas around the state. The coverage areas are divided into three different areas based on the following classification of electric field strength E:

i. Primary Coverage Areas, E > 60 dBµV
ii. Secondary Coverage Areas, 60 dBµV > E > 30 dBµV
iii. Fringe Coverage Areas , 60 dBµV > E > 0 dBµV

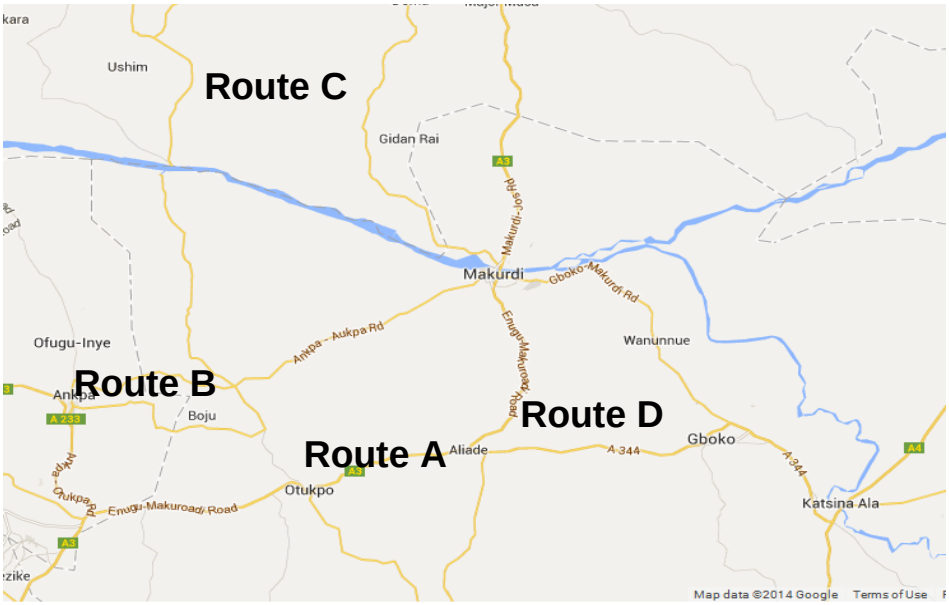

Figure 2: The routes along which measurements were taken in Makurdi **(**http://www.viewphotos.org/nigeria/flat-map-of-Makurdi-145.html, 2013**)**

5. Results and Discussion

Figure 3 shows the contour map for signal levels around the transmitting station and the coverage area in Benue State. Tables 1 and 2 show the television signal coverage area as percentages of the total land mass of the state and that of the Local Government Areas.

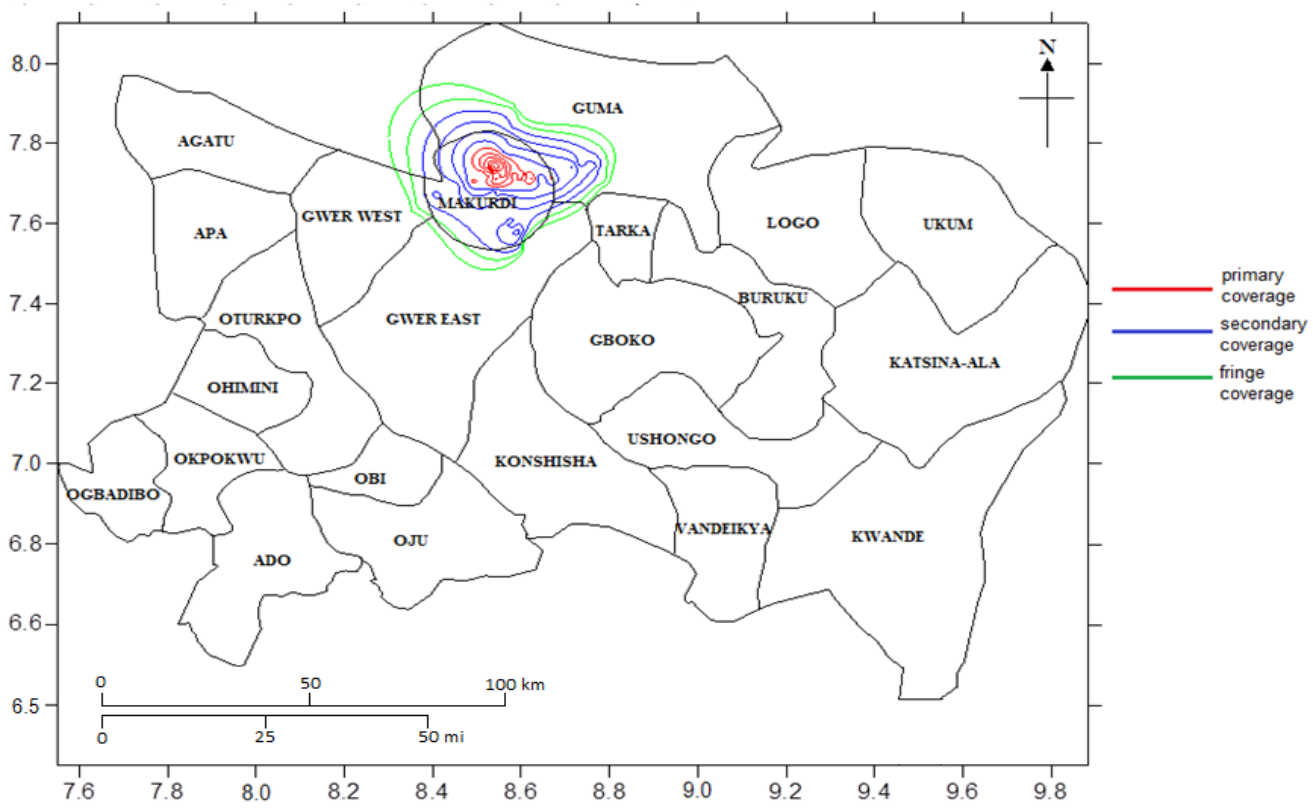

Figure 3: Coverage Area of the NTA Zonal Network Makurdi, Channel 10 in Benue State

Table 1: Percentage of the Coverage Areas of NTA Makurdi relative to the total land mass of Benue State

Station	Primary coverage (%)	Secondary coverage (%)	Fringe coverage (%)	Total coverage (%)
NTA Makurdi, Channel 10	0.39	3.07	2.67	6.13

Table 2: Percentage of the Local Government Areas Covered by NTA Makurdi in Benue State

L.G.A	Primary coverage (%)	Secondary coverage (%)	Fringe coverage (%)	Total coverage (%)
Makurdi	11.43	80.00	8.57	100
Guma	-	11.29	13.71	25.00
Gwer-West	-	-	6.25	6.25
Gwer-East	-	-	4.55	4.55
Outside the State	-	-	7.14	7.14

The field strength measurements of the transmitting station shows that 0.39% of the entire land mass of Benue State has the television signal strong enough to override ordinary interference in the locality at all times, which comprise the primary coverage area. About 3.07% of the state also enjoys good television signal of the station, but not strong enough to overcome interference completely at all times, thus within the secondary coverage area. The service provided in this area may be adequate in rural areas where the noise level is low. Also, 2.67% of the state is in fringe service areas of the television coverage. In such areas, the service can neither be guaranteed nor protected against interference, and antennas with high antenna gain and heights higher than the surrounding buildings and obstacles are needed to receive good signals.

6. Conclusion

In conclusion, only 6.13% of the entire land mass of Benue State has the television signals coverage. More than 93% of the state does not receive television signals from the television station. Thus, the present configuration of the transmitter does not give optimal coverage of the total land mass of Benue State. So, installation of repeater stations at certain intervals of distance to provide reception of television signals for the entire state is necessary.

Although 7.14% of the coverage area enters into Nasarawa State, the television station may not constitute potential interference to any of the television stations in Nasarawa States because of the shape of the boundary between the two states. Hence, the station operates in compliance with the Nigeria Broadcasting Commission (NBC) regulations.

References

Hall, M.P.M. (1991), Overview of Radio wave propagation, Peter Peregrines Ltd., London, United Kingdom pp 9-16)

Ajayi, G .O. and Owolabi, I. E. (1975), Medium Wave Propagation Curves (for use in medium wave transmission planning and designed), Technical Report of the Radio wave propagation Research Group Department of Electronic and Electrical Engineering, University of Ife, Nigeria.

Ajayi, G. O. and Owolabi, I. E. (1979), Coverage Area of the 10KW, 702 KHz Medium Wave Transmitter at Minna and Feasibility Studies for full Radio Coverage of Niger State, Technical Report of the Electrical Communication Consultancy Unit (ECCU), Department of Electrical and Electronics Engineering, University of Ife, Nigeria.

Bean, B. R. and Dutton, E. J., (1968), Radio Meteorology, Dover Publications, Inc. New York, 261-270.

Oyedum, O. D. (1999), VHF/UHF. Broadcast Service and Interference, *Journal of Science, Technology and Mathematics Education (JOSTMED),* Vol. 2 No. 2, 87-94.

Appleby, M.S. and Garrett, J. (1985), Cell net cellular radio network. *Br. Telecommun. Engng*. 4, 62-9

Department of Trade and Industry (1985), A Guide to the Total Access Communication System. DTI, London

Dernikas, D. (1999), Performance evaluation of the TETRA radio interface employing diversity reception in adverse conditions. PhD thesis, University of Bradford.

Flat map Makurdi - Benue-State, Retrieved from http://www.viewphotos.org/nigeria/flat-map-of-Makurdi-145.html, 2013

Government of Benue State – Historical Background, Retrieved from http://benuestate.gov.ng/wp/historical-background/, 2013

ANALYSIS OF DROUGHT DYNAMICS IN BIDA ENVIRONS, NIGER STATE, NIGERIA

Yahaya, T.I.and Okesola, M. S.
Department of Geography,
Federal University of Technology, Minna,
Niger State, Nigeria.

Mobile Phone Number:
+0248035955888
E-mail address:
iyandatayo@futminna.edu.ng

Abstract

Drought is a weather related natural disaster. It cause may be due to insufficient rainfall, or prolong dry spells and or lack of rainfall. Crop production in Bida environs is rain fed and it is characterized by drought incidences, the attributes which is reducing the Farmers' zeal for crops farming because of the resultant wastage of capital. The Study analyzed Drought dynamics in Bida environs. A data set of 51 years (1965-2015) of monthly rainfall, and two types of comparable drought index; the Rainfall Anomaly index (RAI) and Standardized Precipitation Anomaly taking the average as normal were used to investigate the fluctuating pattern and intensity of drought. Result shows that drought occurrences of the area are highly variable from year to year. The RAI shows that there was drought of varying degrees in 21 years out of 51 years of the studied period, with the peak value of -4.6 in 1972. The SPA also corroborated the occurrence of erratic dry spells at the planting season with the worst in the year 2015. The crux of the problems as claimed by the Farmers is their inability to determine the best time of farming input from planting to fertilizer application which also usually result to multiple inputs and thus waste of resources as a result of this fluctuations. Since Drought is beyond the Farmers control, suggestion was made that NiMet be encouraged to provide timely and accurate weather and drought forecast on her part, while farmers be informed through all effective means, accept and plan their crop production activities with it on their own part to reduce risk and loss due to this natural event of potential hazard.

Key words:, Drought, Rainfall Anomaly Index, Dry spell, Standardized Precipitation Anomaly.

Introduction

Drought is a weather related natural disaster. It is a very less understood and complex phenomenon. The causes of this natural phenomenon may be due to insufficient rainfall, rainfall variability or prolong dry spell. Drought has been ranked as the third most costly geophysical phenomena (Haas, 1978). This is because of its devastating impact on food production and the socio-economic activities of any country it affect. Drought however is a creeping phenomenon with insidious characteristics (Shuaibu and Oladipo,1993). This imply that drought do not just occur without an underlining factors.

Large area of northern Nigeria falling within the sahel and sudan ecological zone between latitude 9^0N and 14^0N are prone to recurrent drought in one way or the other and the probability of drought at the onset and toward the end of the raining season is usually very high in northern Nigeria (Abubakar, and Yamusa, 2013) "Over the years a consistent shift in the climate and weather condition in Nigeria has become noticeable. This may be attributed to the general change in the global climate conditions as a result of global warming, for instance the onset of the raining season on the average is expected to commence in northern Nigeria between late March and April, but the current weather condition show a deviation from this trend particularly in the year 2015" (Babs Iwalewa 2015).

Agricultural crops production in Bida and environs still depends largely on rain water. Amongst the several problems facing agriculture in Bida and environs is large-inter annual variability of rainfall with dry spells within the rainfall regime.

In reality, it is not only lack of rain or its insufficiency and the consequent drought that determines agricultural crop yields and productions, other agro-climatic parameters such as temperature, soil moisture and soil fertility also count. However, it is only rainfall characteristics, a function of drought occurrences that is mostly noticeable or apparent to farmers' understanding and hence an important factor that dictate their decisions on agricultural planning.

Bida and particularly the immediate environs' habitants are predominantly Farmers. Very large percentage of the able population relies or depends on agricultural sector for survival and each years at the onset of the rainfall also set to make a significant impact for an expected bountiful harvest but at the end, majority are still being disappointed as a result of prolong and erratic dry spells. It is important to monitor drought because droughts is one of the most costly natural hazard on year -to- year basis, their impacts are significant and wide spread, affecting many sector of and People at any all-time (IDMP 2016). Threat to food security which may result to hunger and poverty among the farmers who solely depends on agricultural resources for livelihoods may occur in a severe drought.

The aim of this study is to assess the drought dynamic, with a specific objective of analyzing the temporal variations of drought in the study area. This will serve a great benefits in reducing loses and vulnerability due to drought incidences.

Study Area

Bida is located at about 87km southwest of Minna, capital of Niger State. It lies within latitude 09^{o}05'N - 09^{o}083'Nand longitude 06^{o}01E - 06^{o}017E. It has a population of188, 181(2009National Population Census). However, with the addition of the population of the people of the immediate neighborhood and the increasing population over time, the study area's population may now be over 300000 comprises of the native tribe- the Nupes, which make the bulk of the population, and other major ethnic groups; the Hausa, Yoruba, Igbo and other minority tribes. The town is known for its traditional craft, notably metal and brass wares, but agricultural activities constitute major occupation especially in the neighborhood.

The typical climate of the area is Tropical Monsoon type. It is marked with distinct dry and wet seasons, the raining season which is the crop production regime, spans from April to October with the maximum rainfall in the month of September and the mean annual rainfall of about 1150mm (NiMet Bida, 2015). The dry season spans from November to March, the driest period is within the month of January which record the lowest relative humidity. The season is hottest in the month of March which records a maximum temperature of above 38^{o}c and coldest in the months of December through early part of January with average minimum temperature of about 21^{o}c, and lowest mean relative humidity and occasional negative dew point temperature. The closest major river of micro-climatic impact is the downstream tributary of river Kaduna at Wuya, about 25 kilometers along Bida- Mokwa Road. The vegetation is more of characteristic of southern guinea savanna (Physical setting, Niger State, 2003). It is cover by expanse of annual grasses interspersed with

tall dense species and weeds and sparsely distributed within are Shrubs and Trees, of various species and economic values which includes Shear butter, Mango, Locust bean Trees etc.

The soil

The soil is typical of ferruginous tropical soil types which are formed from the basement complex or sedimentary rocks over varying period of time (Physical setting- Niger State, 2003). The surface soils are loamy- sand, alluvial deposit and sand stones.

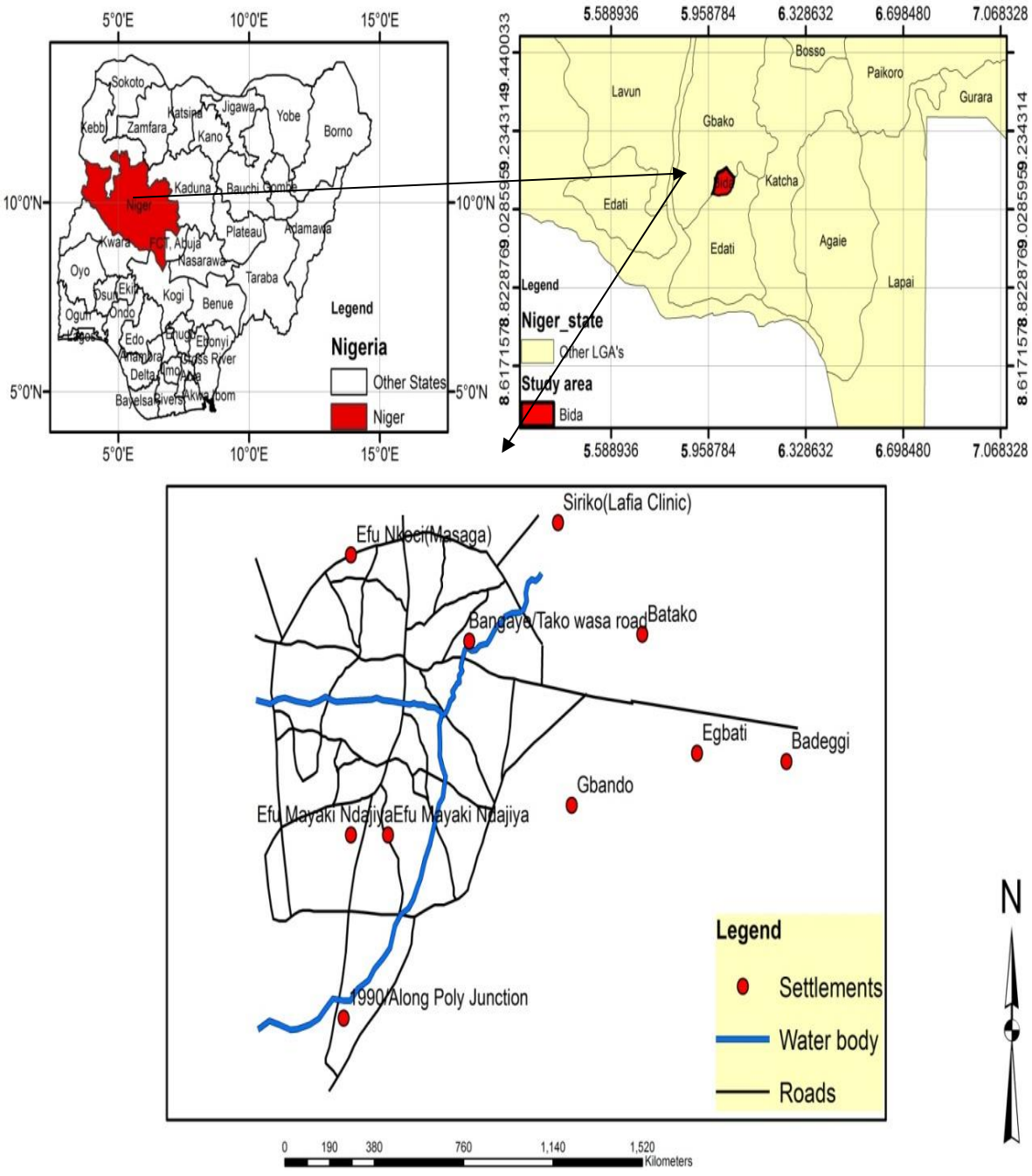

Figure

1: The Study Area (Bida and its Environs, Niger State, Nigeria)
Source: Remote Sensing and GIS Laboratory, Federal University of Technology, Minna (2016)

Materials and Methods

The study utilized secondary data. This is the rainfall data of the study area for consecutive 51 years (1965-2015) obtained from the archive of the Nigerian Meteorological Agency,Bida Aerodrome. The conventional rain gauge used for the measurement is located at 142.3m above mean sea level (MSL) and has been unchanged for those years there by provided a good tool of comparison in assessing the rainfall trend and its variability in determining the Drought incidences without positional bias. Rainfall Anomaly Index and Standardized Precipitation Index were employed for the analysis.

Rainfall Anomaly Index (RAI).

The rainfall anomaly index developed by Van-Rooy (1965) was used to evaluate the annual rainfall variability. It employed the use of rainfall measurement of the area for a period of 51 years (1965-2015). The rainfall data for those years were arranged in descending order of magnitude with the highest rainfall values ranked first and the lowest rainfall values ranked last. Also, the average values of the ten highest rainfall measurements connoting the maximal average of the first ten extrema and the average values of the ten lowest rainfall measurements connoting the minimal average of the last ten extrema for the period understudy were computed respectively.

The values of these respective ten extrema represent the positive and negative anomalies respectively based on the average rainfall values of the ten extreme as, with the upper been the positive and the lower been the negative. These were used to calculate the Rainfall Anomalies for both positive and negative anomalies for all the years involved. The technique is given by the equations (i) and (ii):

$$\text{RAI} = +3\left[\frac{R_{t-}M_{Rt}}{M_{H10-}M_{Rt}}\right], \text{ for positive RAI} \ldots\ldots\ldots\ldots\ldots\ldots\ldots\ldots\ldots\ldots\ldots\text{(i)}$$

$$\text{RAI} = -3\left[\frac{R_{t-}M_{Rt}}{M_{L10-}M_{Rt}}\right], \text{ for negative RAI} \quad \ldots\ldots\ldots\ldots\ldots\ldots\ldots\ldots\ldots\ldots\text{...(ii)}$$

Where:RAI = the annual Rainfall Anomaly Index for a particular year.

Rt = total annual rainfall for a particular year.

M_{Rt} = long term mean rainfall of the years under study.

M_{H10} = mean value of the 10 highest (ranked) rainfall.

M_{L10} = mean value of the 10 lowest (ranked) rainfall

+/-3 = constant for both positive and negative anomalies respectively.

Standardized Precipitation Index (SPI) for the months of April and May.

Standardized Precipitation Index developed by Mckee *et al* (1965) and as employed by Akeh *et al* (2000) normally used to compute the number of standard deviation a value is above or below the mean of the data set. It gives meaningful information about each data point or value and where it falls relative to the mean of the distribution.
This is obtained using equation (iii):

$x_s = \frac{x - x_m}{x_{sd}}$ ……(iii)

Where:
x_s= standardised anomaly
x = rainfall variable
x_m= average of all the sampled rainfall $= \frac{\sum x}{N}$
N = number of the variable sampled.
x_{sd}= standard deviation of all the rainfall sampled $= \frac{\sqrt{\Sigma(x - x_m)^2}}{N}$

The positive SPI values are indicative of absence of drought while the negative values showed the occurrence of drought (Akeh*et al*., 2000). The rainfall values of the months of April and May of the years for this study was used to calculate the rainfall anomaly; this was because these months are crucial in the seasonal planting regime.

Results and Discussion

Rainfall Anomaly Index

The careful observation of the RAI shows that there were some degrees of slight drought of less than -1 in relative to the mean in 1976, 1977, 1981, 1986, 1987, 1990, 1999, 2008 and 2011. For 1979 and 2006, the deficit was between -1 and -2 while in 1965, 1972, 1982, 1983, 1992, 1994, 1998, 2002, 2003, and 2014 was in moderate of higher than -2 to this negative side with the peak value of -4.6 in 1972 indicating the greatest drought year among the studied years. In this context, 21 out of the 51 years used in the study which is about 41% of the time period had some levels of drought.

The temporal variability of drought is conspicuous from the annual RAI. The patterns of fluctuation can be adjudged erratic as the there was no period of consecutive five years other than between 1966 and 1971 without water deficit. Some other years were characterized by moderate intermittent drought which means that farmers will find it difficult on their own to literally know the trends of occurrence, and plan made based on immediate past year may be fruitless, thus scientific drought forecast will be the better and reliable technique of guide to greater yield.

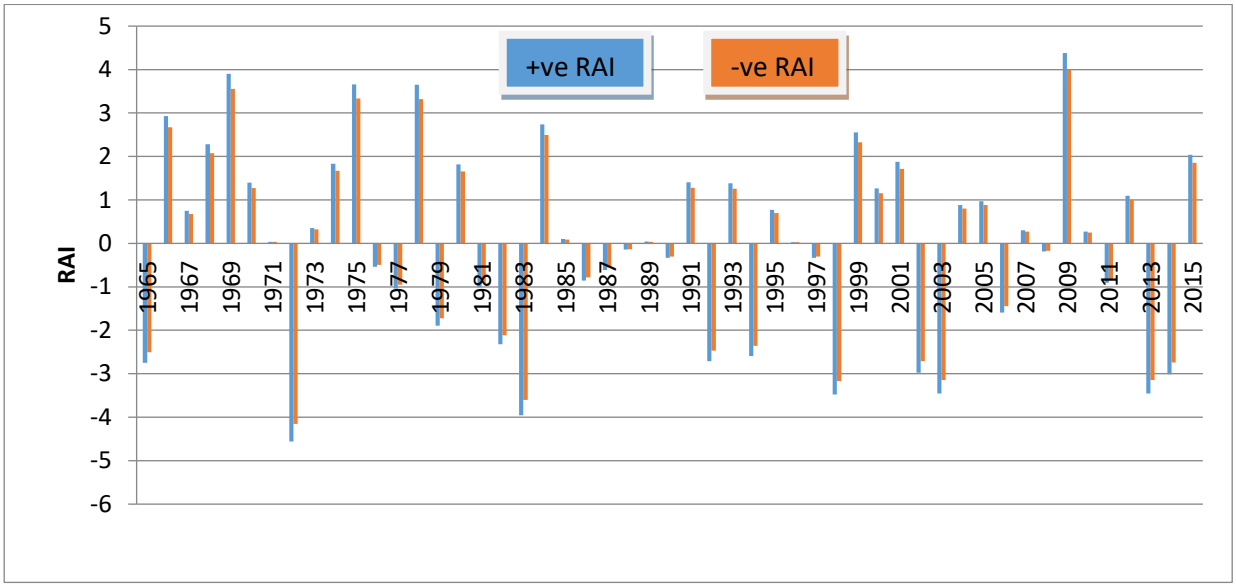

Figure 2: Annual Rainfall Anomaly Index
Source: Author's computation (2016)

Table 1: Rainfall Anomaly Index

S/N	Years	Deviation from mean(X-mX)	Positive. RAI	Negative. RAI
1	1965	-189.98	-2.7475	-2.50215
2	1966	202.7196	2.931739	2.669935
3	1967	51.61961	0.746525	0.67986
4	1968	157.5196	2.278055	2.074625
5	1969	269.7196	3.900696	3.552364
6	1970	96.51961	1.39587	1.271219
7	1971	2.719608	0.039331	0.035819
8	1972	-315.38	-4.56104	-4.15374
9	1973	24.31961	0.351711	0.320303
10	1974	126.8196	1.83407	1.670288
11	1975	252.9196	3.657734	3.331098
12	1976	-37.4804	-0.54204	-0.49364
13	1977	-71.9804	-1.04098	-0.94802
14	1978	252.3196	3.649056	3.323196
15	1979	-130.88	-1.8928	-1.72377
16	1980	125.7196	1.818162	1.6558
17	1981	-69.6804	-1.00772	-0.91773
18	1982	-160.28	-2.31798	-2.11099
19	1983	-273.48	-3.95508	-3.6019
20	1984	189.3196	2.737948	2.493449
21	1985	6.819608	0.098625	0.089818
22	1986	-59.1804	-0.85587	-0.77944

23	1987	-42.1804	-0.61001	-0.55554
24	1988	-9.98039	-0.14434	-0.13145
25	1989	2.919608	0.042223	0.038453
26	1990	-23.1804	-0.33524	-0.3053
27	1991	97.31961	1.40744	1.281756
28	1992	-187.28	-2.70846	-2.46659
29	1993	95.51961	1.381408	1.258049
30	1994	-179.28	-2.59276	-2.36123
31	1995	53.21961	0.769664	0.700933
32	1996	2.019608	0.029208	0.026599
33	1997	-23.0804	-0.33379	-0.30398
34	1998	-240.48	-3.47784	-3.16727
35	1999	176.4196	2.551388	2.323549
36	2000	87.61961	1.267158	1.154001
37	2001	129.9196	1.878903	1.711117
38	2002	-205.98	-2.9789	-2.71288
39	2003	-238.78	-3.45325	-3.14488
40	2004	60.81961	0.879576	0.80103
41	2005	67.21961	0.972133	0.885321
42	2006	-109.88	-1.58909	-1.44719
43	2007	20.61961	0.298202	0.271572
44	2008	-12.7804	-0.18483	-0.16833
45	2009	302.7196	4.377943	3.986993
46	2010	18.91961	0.273616	0.249182
47	2011	-62.5804	-0.90504	-0.82422
48	2012	75.81961	1.096506	0.998588
49	2013	-238.98	-3.45614	-3.14751
50	2014	-208.18	-3.01071	-2.74186
51	2015	140.8196	2.036539	1.854676

Source: Author's computation(2016)

Inter-annual variability of rainfall for the months of April and May

A synoptic view of Figure 3 gave a clear pattern of the deviation from mean of the values of rainfall for the months of April and May with years; 1965, 1967, 1973, 1977, 1988, 1993, 2000, 2001 and 2003 recorded a rainfall deficit of bellow 50mm from the mean, while 1982, 2002, 2008, and 2015 deviated above minus 100mm with the highest in 2015 of minus 151.1mm amount to 74.2% deviation to the negative side of the mean. This suggested a drought period in the crop sowing regime which usually is the month of April through the month of May. The year 2015 as a typical example amongst the studied years, it had a good annual rainfall value of 1296.0mm but have a deficit rainfall value of 151.1mm in the earlier 61 days (April and May) of the growing season. This lead to crop wilt, dried off, crop lose and multiple planting. This in part accounted for non-optimum production of maize and melon (Egusi) in the study area in that year.

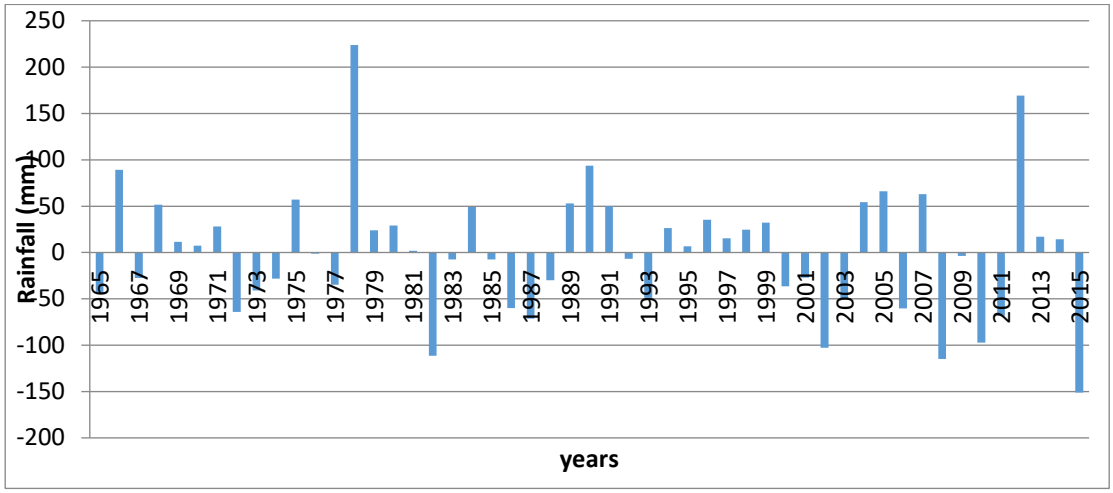

Figure 3: Patterns of Rainfall deviation from mean for the months April and May
Source: Author's computation (2016)

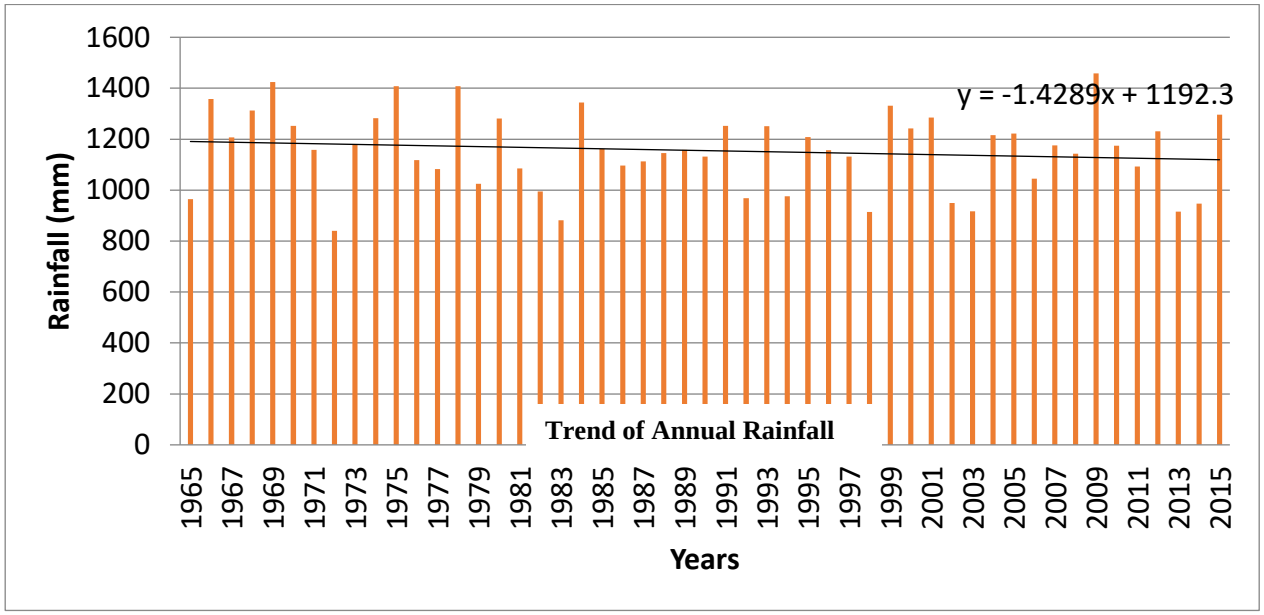

Figure 4: Patterns of Annual Rainfall
Source: Author's computation (2016)

Comparison of patterns of mean rainfall deviations for the months of April and May (Figure 2) and the trend of annual rainfall (Figure 3) shows that there were some years of high annual rainfall of above 1200mm but with drought at the early growing phase of Crops. This occurred in the years: 1967, 1973, 1974, 1985, 1993, 2000, 2001, 2010, and recently the year 2015. This stressed further the fact that, there may be optimum annual rainfall but yet characterized by intermittent drought within the Crop growing season, sufficient enough to affect Crop production negatively.

Standardized Precipitation Index

The patterns of rainfall values indicated the occurrence of some levels of anomalies to the two sides. To the negative side, constituting dry spells in different degrees were years: 1965, 1967, 1972 – 1974, 1977, 1982, 1986 – 1988, 1993, 2000 – 2003, 2006, 2008, 2010, 2011, and 2015 been the worst drought s year at the early season – April and May.

Table 2: Standardized Precipitation Anomaly for the months of April and May.

Year	Sum Rainfall: April and May(mm)	Deviation from mean	SPI for April and May
1965	160.1	-43.7	-0.6
1966	293.1	89.3	1.3
1967	176.3	-27.5	-0.4
1968	255.5	51.7	0.8
1969	215.4	11.6	0.2
1970	211.0	7.2	0.1
1971	231.9	28.1	0.4
1972	139.7	-64.1	-1.0
1973	162.8	-41.0	-0.6
1974	175.5	-28.3	-0.4
1975	260.8	57	0.8
1976	202.4	-1.4	0.0
1977	169.2	-34.6	-0.5
1978	427.6	223.8	3.3
1979	227.7	23.9	0.4
1980	233.0	29.2	0.4
1981	205.7	1.9	0.0
1982	92.3	-111.5	-1.7
1983	196.4	-7.4	-0.1
1984	252.9	49.1	0.7
1985	196.2	-7.6	-0.1
1986	143.7	-60.1	-0.9
1987	132.6	-71.2	-1.1
1988	173.8	-30.0	-0.4
1989	256.6	52.8	0.8
1990	297.6	93.8	1.4
1991	253.5	49.7	0.7
1992	196.9	-6.9	-0.1
1993	155.0	-48.8	-0.7
1994	230.1	26.3	0-4
1995	210.6	6.8	0.1
1996	239.0	35.2	0-5
1997	219.1	15.3	0.2

1998	228.4	24.6	0.4
1999	236.0	32.2	0.5
2000	167.2	-36.6	-0.5
2001	176.6	-27.2	-0.4
2002	101.0	-102.8	-1.5
2003	154.6	-49.2	-0.7
2004	258.1	54.3	0.8
2005	270.0	66.2	1.0
2006	143.6	-60.2	-0.9
2007	266.8	63	0.9
2008	88.9	-114.9	-1.7
2009	200.1	-3.7	-0.1
2010	106.5	-97.3	-1.4
2011	135.6	-68.2	-1.0
2012	373.1	169.3	2.5
2013	221.0	17.2	0.3
2014	217.9	14.1	0.2
1015	52.7	-151.1	-2.2
Sum	**10392.1**		
Mean	**203.8**		

Source: Author's computation (2016)

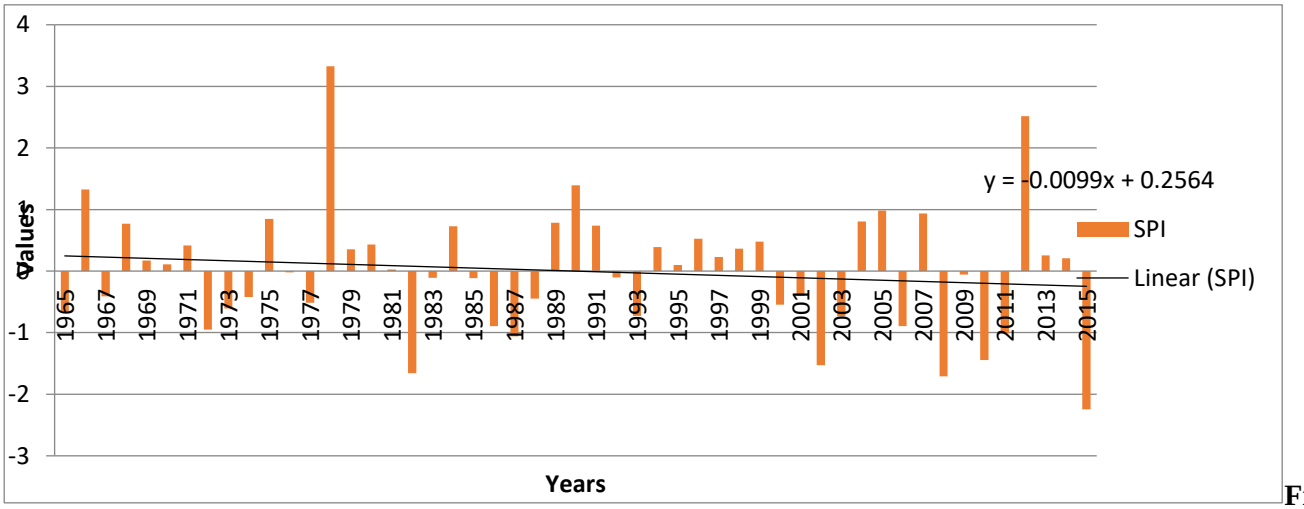

Figure 5: Standardized Precipitation Index (April and May)
Source: Author's computation (2016)

Conclusion and Recomendations

The overall analysis shows that drought is not an alien phenomenon in the study area. The drought characteristic of the area in terms of intensity is not too high to have caused untold level of damages and lose of capital. The temporal pattern of occurrence is that which is causing significant crop failure, resulting to loss of capital, particularly at the onset of the season where the farmers have to plant and replant before rainfall steadiness.

There are some years which recorded early sufficient rainy days that could be taken to be onset of rain by the farmers, and thereafter dry spell for up to a month. This happened recently in the year 2015, and it's perhaps one of the factors that accounted for individual low production of maize and melon in the study area in that said year.

Crop productions in this micro climatic zone rely mainly on rain fed. Drought intensity, temporality or perpetuity may come under the influence of the unarguable climate change phenomenon, it is therefore important to be constantly acquainted with the patterns the rainfall of the area will take. Irrigation scheme is not readily feasible to these set of farmers, also drought is a natural phenomenon not readily preventable, while the exact patterns of drought may as well be tricky and difficult to predict. However the assertion that "Prevention is better than cure" seem to be the only feasible option applicable now, therefore crop production planning based on available weather and drought forecast will still serve no small measure to reduce crop failure.

Specific measure to achieve this is to fund well the Nigerian Meteorological Agency (NiMet) which has the statutory function of providing information about weather and climate. This will enable her to better achieve her mandate of monitoring, forecasting and issuance of early warning of drought fore stakeholders' consumption using both meteorological and satellite based indicators.

Also, information dissemination on drought forecast should be improved through social media and in local languages of the area and also through improved Agriculture Extension Workers which is very necessary for effective communication that will enhance questions, answers, feedback and direct guidance as to the best time of impute and suitable crop varieties to plant.

Also, all other related research institutes should collaborate with NiMet in any other areas necessary that can help her to provide qualitative drought predictions.

National Cereal Research Institute (NCRI) Badeggi Niger state, should not cease in finding improved, suitable and drought resistant varieties are made to be known and be available to farmers at affordable prices.

Drought insurance Scheme should be established and farmers to be sufficiently convinced about its importance and its roles it can be made to provide a bail out to farmers who drought is genuinely the culprit for his lose.

References

Abubakar, I.U., and Yamusa, M.A. (2013) Recurrence of Drought in Nigeria: Causes, Effect, and Mitigation. *International Journal of Agriculture and Food Science Technology. ISSN 2249 – 3050, vol.4 No. 3.* Pp. 169 – 180. http://www.riplication.com/ijafst.

Ake, I.E., Nnoli, N., Gbuyiro, S., Ikekhua, F..&Ogunbo, S. (2000).*Meteorological Early Warning System (EWS) for Drought Preparedness and Drought Management in Nigeria*. Publication of Nigerian Meteorological services, Lagos Nigeria.

Babs Iwalewa (2015). *Drought in Norther Nigeria and Stability of Food Price in 2015.*

Daily Trus,t 28th May 2015. *www.dailytrust.com.ng*

Haas, J.E. (1978). Strategies in the Event of Drought in N.J. Rosenberg (ed), *North American Drought*, West View Press, Boulder, 103-122.

Intergrated Drought Management Program-IDMP (2016). *Handbook of Drought Indices*. www.droughtmanagement.info

Nigerian Meteorological Agency-NiMet (2015).Register of Rainfall Bida, Niger State. Nigerian Meteorological Agency (NiMet), Oshodi, Lagos, Nigeria.

Physical Setting, Niger State (2003). www.onlinenigeria.com/nigerstate/? Retrieved June 2016..

Shuaibu, U.G. &Oladipo, E.O. (1993).A Bhalme – Morley Type Meteorological Drought Intensity Index for Northern Nigeria.*The Zaria Geographer*, 14, 18-27.

AN OVERVIEW ON CU_2ZNSNS_4 - BASED THIN FILMS FOR SOLAR CELL APPLICATION

Kasim Ibrahim Mohammed[1*] Kasim Uthman Isah[1], Uno Esang Uno[1] and Abdullahi Mann[2]

[2]Department of Chemistry, Federal University of Technology, Minna, Nigeria

[1]Department of Physics, Federal university of Technology, Minna, Nigeria

[1]kasim309@futminna.edu.ng

[1]kasimzabbo@nigerpoly.edu.ng

* Corresponding author

Abstract

Cu_2ZnSnS_4 is a compound semiconductor material made of copper, zinc, tin and sulphur, which are sufficiently abundant elements, none of them is harmful to the environment in the used amounts. Although it is a comparatively new material, there are already promising results that indicate that it could be used as a solar cell absorber material. This paper is aimed at reviewing the various methods that have being used in depositing the Cu_2ZnSnS_4 thin films with a view of choosing the best method to be used to get the best thin films for solar cell application.

Keywords: Cu_2ZnSnS_4, thin fims, solar cell,

1. Introduction

Pollution of the earth and shortage of energy sources have been the bottle-neck of survival and development for human beings since the start of the 21st century. Therefore, lowering energy consumption and protecting the environment have gradually gained attention from countries all over the world (Jiang and Yan, 2015).

In order to keep sustainable development, governments, research institutes, and industries have been working on the problems caused by the shortage of available energy sources (Husser *et al*., 2007). It is well known that the best way is to exploit renewable energy resources. Solar energy is considered to be the most economic and effective among all available renewable energy resources. Solar energy is inexhaustible and it has already been theoretically and experimentally proved that the earth would not be polluted at all if solar energy was utilized effectively (Jiang and Yan, 2015). To encourage and promote the direct utilization of solar energy, developed countries have been legislating and deploying solar initiatives (Husser *et al*., 2007). Joint Research Centre (Europe) predicted that energy directly harvested from sunlight would be 20% of total energy consumption in 2050, and this value could be over 50% in 2100. Solar energy will be widely utilized in industry, agriculture and daily life (Jiang and Yan, 2015).

Photovoltaic (PV) systems have recently attracted much attention due to their inherent advantages. Firstly, PV systems are capable of directly translating sunlight into electrical energy. The theoretical conversion efficiency of PV systems is relatively higher than other power generators (Ito, 2015). Secondly, PV systems do not necessarily contain movable parts and as such system wear induced by mechanical movement is avoided. PV systems can work continuously free from maintenance longer than other power generation technologies (Jiang and Yan, 2015).

There are three main types of thin film PV technologies, CdTe, $CuIn_xGa_{1-x}S(Se)_2$ (CIGS), and thin film Si, which gained 14%, 9%, and 6% of PV market share in 2010, respectively. Nevertheless, Si thin film solar cell (TFSC) has been relatively underdeveloped due to low efficiency and instability from the Staebler-Wronski effect. For the other two thin film technologies, there are restrictions on the usage of heavy metals such as cadmium, the limitation in

supplies for indium and tellurium, and the wide fluctuation in prices of indium and tellurium. These render the combined production capacity of the existing CdTe and CIGS technologies at a small scale lower than 100 GW per year. This is only a small fraction of energy consumption projection for 2050 which is expected to be 27 TW.

Recently, quaternary compound Cu_2ZnSnS_4 (CZTS) has been intensively examined as an alternative PV material due to its similarity in material properties with CIGS and the relative abundance of raw materials (Washio *et al*., 2015). CZTS thin film solar cells being an earth abundant material are non-toxic, low cost and belong to the second generation PV, in which the active bulk-material, used as absorber layer in the standard PV technology is replaced by a thin film, with typical thickness of micron. The huge reduction of the active material requirement respect to the standard technology allows a large decrease of the device costs (Chopra *et al*., 2004).

With a high absorption coefficient ($> 10^4$ cm^{-1}) and a desirable bandgap (~1.45 eV), CZTS thin film has been considered an excellent PV material. Theoretical calculations have shown that conversion efficiency as high as 32% was possible for CZTS TFSCs with a CZTS layer of several micrometers (Ito and Nakazawa, 1988). Wadia *et al*. (2009) also calculated the minimum cost of raw materials for the existing PV technologies and the emerging PV technologies and the results shows that the cost of raw material for CZTS PV technology is much lower than that of the three existing thin film PV technologies. This paper is therefore targeted at reviewing the existing technologies of CZTS thin films fabrication for solar cell application.

2. CZTS Thin Film Deposition Techniques

The increasing awareness of CZTS as a potentially ideal candidate for photovoltaic absorber material is mainly due to the abundance and variety of routes that have been developed for thin-film deposition. To determine the most promising technique for the fabrication of thin film solar cells, the overriding criteria are that the deposition can be completed at low cost while maintaining high deposition or processing rate with high yield and reproducibility. There exists a wide variety of vacuum and non-vacuum based techniques. For each of these deposition techniques, one key barrier toward a reliable and low-cost process is the complexity for preparing single phase films. A second common theme generally encountered is the challenge of compositional control during deposition of the film. Despite these challenges, reasonably successful film deposition and device fabrication has been demonstrated for CZTS using both vacuum and non-vacuum deposition techniques.

a. Evaporation

Evaporation is a well-known technique in the development of thin film solar cells. Based on the success of evaporated CIGS materials, initially evaporation was selected as the principal deposition technique for CZTS thin films too. Katagiri *et al*. (2005) deposited CZTS thin films using electron beam (EB) evaporation followed by sulfurization. They deposited precursors, Cu/Sn/Zn stacked layers ('Zn' on bottom of stack), by EB evaporation. In order to obtain CZTS films they sulfurized precursors at 500°C in N_2+ H_2S (5 %) atmosphere. The films obtained were p-type with a bandgap of 1.45 eV and absorption coefficient greater than 10^4 cm^{-1}. Grain size of the films is extremely large (~3 µm) compared with the film thickness of 1.9 µm. They obtained very high value of resistivity of the order of 10^4 Ω.cm. In another report during the same year they reported an even high value for resistivity of the order of 10^5 Ω.cm, by increasing the hold time for sulfurization (Katagiri *et al*., 2007).

Yeon *et al*. (2015) reported the preparation of CZTS using ZnS as precursor for 'Zn', while precursors for 'Sn' and 'Cu' were same as earlier work. Use of ZnS instead of 'Zn' increased the adhesion of the CZTS film and they could bring down the resistivity to 3.9×10^2 Ω.cm. In another report Katagiri *et al*., (2005) tried different thickness of precursor layers and found that resistivity of the films decreased from 10^4 to 10^{-2} Ω.cm, when Cu/(Zn+Sn) ratio increased from 0.9 to 1.1.

CZTS thin films were also prepared by varying Cu/(Zn+Sn) ratio from 0.49 to 1.18 (Katagiri *et al*., 2005). They reported that the band gap energy increased and the absorption of the tail region decreased with increase in Cu/(Zn+Sn) ratio up to 0.9. For CZTS films whose Cu/(Zn+Sn) ratio was over 0.94, absorption of the tail region was extremely elevated due to the presence of binary phases of 'Cu' and 'S'. They concluded that CZTS films with Cu/(Zn+Sn) ratio from 0.8 to 0.9 are suitable as absorbers. (Katagiri *et al.*, 2005) discovered that the ordering of precursors can improve the surface morphology of the films and with the fabricated films using the modified precursor with the stacking order of Sn/Cu/ZnS the SEM micrographs was found to have a surface morphology much improved using the new order of precursors.

Tanaka *et al*. (2006) prepared CZTS thin films by co-evaporation of elemental sources. Larger and densely packed grains were formed as substrate temperature increased. Chen *et al.* (2009) deposited CZTS films on 'Si' substrates by multisource evaporation. They confirmed the tetragonal structure of films from RHEED patterns. Broad emissions at ~ 1.45 eV and 1.31 eV were observed in the PL spectrum measured at 13 K. The peak at ~1.45 eV was assigned to the donor–acceptor pair transition. Multistage evaporation technique is used for the deposition of CZTS thin films (Weber *et al*., 2010). They investigated two different stage sequences: Sample A using Cu_2SnS_3as precursor to react with Zn-S and Sample B using ZnS as precursor to react with Cu-Sn-S. Both sequence results in formation of CZTS, while SEM micrographs reveal that films of sample type B are denser and have larger crystallites than for sample type A. Tanaka *et al*. (2011), prepared a near stoichiometric single phased polycrystalline CZTS thin films by fast coevapouration process. They showed that Cu-rich growth conditions lead to the segregation of a CuS secondary phase. Nearly stoichiometric CZTS thin films were prepared by sulphurisation of simultaneously evapourated Cu/Zn/Sn metal alloy films.

Gutay *et al*. (2012) deposited Sn/Cu/ZnS precursors, by evaporation, on soda lime glass at room temperature, and then polycrystalline thin films of CZTS were produced by sulphurising the precursors in a sulphur atmosphere at 550 ^{o}C for 3 hour. Carrier concentration, resistivity and mobility of the deposited film were found to be 6.98×10^{16} cm^{-3}, 6.96 Ω.cm and 12.9 $cm^2.V^{-1}.s^{-1}$ respectively.

b. Sputtering

Sputtering has been extensively used by researchers to deposit high quality thin films. Various sputtering technologies such as argon beam, ion beam, DC, RF, hybrid and reactive magnetron sputtering have been employed for the deposition of CZTS thin films. In the case of CZTS thin films, there are two different approaches: a single step without sulfurization and a two-step, deposition of metallic precursors Cu–Zn–Sn/Cu–Zn–Sn–Cu or Cu–ZnS–SnS, followed by a sulfurization (Ito, 2015).

The first reported CZTS material was made by argon beam sputtering, using pressed and sintered targets produced from synthesized powders (Ito, 2015). A sharp peak resulting from (112) plane of the stannite type CZTS appeared for the film deposited at 90^{o}C. Hall Effect measurement estimated that deposited film had mobility lower than 0.1 $cm^2.V^{-1}.s^{-1}$ and carrier concentration higher than $5\times10^{19}cm^{-3}$.

Shin *et al*. (2013) deposited CZTS thin films using RF magnetron sputtering technique without substrate heating. Effects of sputtering power and annealing temperature on the properties of CZTS thin films were checked. It was found that the atomic ratio of the thin films deposited between 50W and 100W was appropriate. The as-deposited films were amorphous and annealed in the atmosphere of 'Ar'+'S'. With the increase of annealing temperature crystallinity of CZTS thin films was improved and sheet resistance decreased rapidly.

Tanaka *et al*. (2005) for the first time used vacuum based hybrid sputtering to deposit CZTS thin films on a quartz glass substrate. Films were fabricated by the sequential deposition of metal elements and annealing in 'S' flux, varying the substrate temperature from 300 to 500 ^{o}C. Film thickness decreased with increase in substrate temperature. Single

phase, stoichiometric CZTS film with stannite structure was obtained at 400 ^{o}C. However, composition of the thin films became Zn-poor at and above 450 ^{o}C. Resistivity, carrier concentration and Hall mobility of the films at 400 ^{o}C were 0.13 Ω.cm, 8×10^{18} $cm^{-3}$and 6 $cm^2.V^{-1}.s^{-1}$ respectively.

Yeon *et al*. (2015) successfully prepared CZTS thin films through sulfurization of ion beam sputtered precursors. Their results show that electrical and optical properties of the prepared films have strong dependence on atomic ratio of the constituents. By optimizing the precursor preparation conditions they obtained low resistivity of ~ 0.156 Ω.cm.

Katagiri *et al*. (2007) after doing extensive pioneering work on CZTS employing evaporation based approaches, they deposited sputtered CZTS thin films using targets of 'Cu', ZnS and SnS simultaneously by RF sources. The finished precursor was automatically transferred to the annealing chamber without being exposed to atmosphere and annealed at 580 ^{O}C for 3 hours in an atmosphere of N_2+H_2S (20%). The deposited film was 2.5 µm thick and having a band gap value of 1.45 eV. The film was Cu-poor and slightly Zn-rich and S-rich (Cu/Zn+Sn: 0.87, Zn/Sn: 1.15, S/metal: 1.17).

Fernandes *et al*. (2009) reported preparation of CZTS thin films using sulphurisation of (DC magnetron) sputtered Cu/Zn/Sn precursor layers. They got CZTS films having a thickness of 1.5µm and with the preferential growth orientation along (112) plane. They confirmed the existence of CZTS from the presence of Raman peaks at 338-339 cm^{-1}, 288 cm^{-1} and 256–257 cm^{-1}. In another report, the effect of changing precursor's deposition on the morphological and structural properties of CZTS films was studied and the result indicates that the best precursor sequence for the CZTS growth was found to be Mo/Zn/Sn/Cu. The 'Cu' layer on top reduces the loss of 'Zn' and 'Sn'. This allows for a better composition control of the CZTS (Fernandes *et al*., 2011).

c. Pulsed Laser Deposition (PLD)

First report on CZTS prepared using pulsed laser deposition (PLD) was in 2006. Washio *et al*. (2012) deposited CZTS thin films epitaxially on GaP substrates using PLD. The band gap of the films was found to be 1.5 eV and films were nearly stoichiometric. Wadia *et al*. (2009) prepared CZTS thin films using PLD. Film was Sn- rich and the band gap was 1.5 eV. In another report, Vigil *et al.* (2008) prepared CZTS precursor using PLD and then annealed in N_2+H_2S (5 %) atmosphere.

Sugimoto *et al*. (2011) prepared polycrystalline CZTS thin films through PLD at room temperature. Study of laser incident energy revealed that structural, morphological and optical properties were improved up to incident energy of 2.5 J/cm^2. Shin *et al.* (2013) deposited CZTS thin films on heated Mo-coated glass substrates using PLD. Band gap of the films varied from 1.53 to 1.98 eV depending on substrate temperature. From EDAX results, all the films were Cu-rich and S-deficient. Recently, Scragg *et al*. (2008) reported the growth of CZTS thin films by reactive PLD in H_2S atmosphere and further annealed in N_2 atmosphere. The films were close to stoichiometric and as prepared films had a band gap of 1.27 eV which increased up to 1.5 eV upon annealing.

d. Electrodeposition

Electrodeposition is the application of metallic coatings to metallic or other conductive surfaces by electrochemical processes. It is a low cost preparation technique used for the deposition of different semiconductor thin films. It has been extensively used for fabrication of CdTe as well as CIGS absorber layers. CZTS thin films can be prepared using this technique either by sequential electroplating of precursors or by single step electrodeposition of precursors, followed by sulfurization/annealing. Feasibility of this new technique for depositing CZTS thin films was first studied by Scragg *et al.* 2008. The deposition process consists of the electrodeposition of metallic precursors followed by annealing in sulphur vapour. Polycrystalline films of about 1µm thickness with grain size in the range 0.2–0.5 µm could be deposited. In another report on electrodeposited CZTS films by photo-electrochemical methods, it was shown that the films were p-type with doping densities of the order of 10^{16} cm^{-3} and a band gap of 1.49 eV (Scragg *et al*., 2008). In another report, solar cell with 3.2% efficiency using electrodeposited CZTS absorber layer was prepared

(Scragg *et al*., 2011). Lin *et al.* (20015) prepared CZTS thin films by sulphurising precursors deposited by electroplating. The precursors (Cu/Sn/Zn stacked layers) were deposited using electroplating sequentially onto 'Mo' coated glass substrates. Aqueous solutions containing copper sulphate for 'Cu' plating, tin sulphate for 'Sn' plating and zinc sulphate for 'Zn' plating were used as the electrolytes. X-ray diffraction peaks attributable to CZTS were detected in thin films sulphurised at temperatures above 400 ^{o}C. Li *et al*. (2015) deposited CZTS thin films on 'Ag' substrates by the electrochemical atomic layer epitaxy (EC-ALE) method. Chan *et al*. (2009) deposited CZTS thin films by ionic liquid electrodeposition technique. Sulphurisation of the stacked layers was achieved in elemental sulphur vapour at 450 °C for 2 hours. In another report, Chan *et al*. (2010) reported the preparation of kesterite CZTS using the same technique.

Kato *et al*. (2012) synthesized CZTS thin films by sequentially electrodepositing layers of 'Cu', 'Sn', and 'Zn' from unstirred baths and subsequently annealing the stacked precursors in sulphur atmosphere. Control of the flux of ions to the deposition surface allowed uniform layers of material to be deposited and this also resulted in films of uniform composition. Ennaoui *et al*. (2009) fabricated CZTS absorbers by solid-state reaction in H_2S atmosphere of electrodeposited Cu–Zn–Sn precursors. The ternary alloys were deposited in one step from a cyanide-free alkaline electrolyte containing Cu (II), Zn (II) and Sn (IV) metal salts on 'Mo' coated glass substrates.

Katagiri *et al*. (2008) deposited CZTS thin films on 'Mo' coated and ITO coated glass plates. The polycrystalline CZTS thin films with kesterite crystal structure were obtained after annealing as-deposited thin films at 550^{o}C in 'Ar' atmosphere for 1 hour. The deposited films were nearly stoichiometric and photoactive. In another report, Katagiri *et al*. (2008) studied effect of complexing agent on properties of electrodeposited CZTS thin films. Film prepared without complexing agent showed well covered surface morphology on the substrate with some cracks on the surface whereas those prepared using complexing agent, exhibited uneven and slightly porous films with some over grown particles on the surface of the films.

Kondrotas *et al.* (2015) showed that surface morphology of electrodeposited CZTS was greatly influenced by change in the pH of the 'Zn' electroplating solution. At a pH of 9, an irregular hollow column type CZTS was formed, resulting in the highest CZTS electrode photocurrent. Jiang *et al*. (2015) characterised electrodeposited CZTS layers using in depth resolved Raman scattering and auger electron spectroscopy. Jiang *et al*. (2015) employed two different techniques for the electrodeposition of CZTS layers: a potentiostatic method and a pulsed potential electrodeposition method. Near stoichiometric CZTS thin films were prepared using potentiostatic deposition method. The samples deposited through pulsed potential methods showed wire-like CZTS nanostructures. Husser *et al.* (2007) employed single step electrodeposition process for the preparation of CZTS layer followed by post annealing treatment at 550 ^{o}C for 60 min in the atmosphere of N_2+H_2S (5%).

e. Hydrothermal Deposition Method

Hydrothermal method is another non-vacuum method that does not require any expensive precursors or equipment and can be readily adopted for industrial production processes. It possesses remarkable reliability and selectivity as well as high efficiency at low temperature.

Hydrothermal and solvothermal methods have been developed to prepare CZTS nanoparticles. The hydrothermal method is defined as a method that uses water as a solvent in a sealed reaction container when the temperature is raised above 100 °C, while a solvothermal method uses an organic solvent in the precursor solution (Habib, 2012).

The organic solvents such as ethylene glycol and oleylamine used in the solvothermal method are toxic and harmful to the environment. Thus, it is desirable to develop a suitable hydrothermal method for fabrication of CZTS material, because of its low environmental impact.

Hydrothermal synthesis is usually undertaken in an autoclave, normally consisting of a stainless steel shell with a Teflon liner. The function of an autoclave is to withstand the internal pressures developed during the hydrothermal process, while the inert liner is used to protect the stainless steel outer shell from the corrosive reagents used in material synthesis (Habib, 2012).

Hydrothermal synthesis of CZTS nanocrystals was firstly reported by Wang *et al*. (2011) by dissolving copper (I) chloride (CuCl), zinc chloride ($ZnCl_2$), tin (IV) chloride pentahydrate ($SnCl_4 \cdot 5H_2O$) and thiourea in water followed by hydrothermal treatment at 200 °C for 30 h.

Agglomerate plate-like nanocrystals with average diameters ranging from 5 - 7 nm were observed. The bandgap of the material was found to be 1.7 eV. Binary products such as ZnS and SnS_2 were found in the hydrothermal product when the reaction temperature and duration were reduced. They concluded that a reaction temperature above 200 °C was necessary to produce CZTS without impurities. However, Emovon *et al*. (2011) used lower reaction temperature (180 °C) and duration (16 h) in a hydrothermal synthesis to produce pure phase CZTS material. They have also suggested that the hydrothermal method is a better route to yield pure phase CZTS compared to the solvothermal synthesis approach which uses ethylenediamine (EN) as solvent in the precursor solution. Metal ions are suspected to have complex with thiourea to form metal-thiourea complexes prior to hydrothermal reaction. During the hydrothermal treatment, hydrogen sulphide (H_2S) is produced through decomposition of thiourea, which then acts as the sulphur source for the formation of binary sulphide products. The reaction of the binary sulphides leads to the formation of CZTS.

With the introduction of ethylenediamine (EN) (volume ratio of EN : water = 1 : 9) in water, Liu *et al*. (2010) synthesised CZTS nanoparticles. In their experiment, hydrothermal treatment was carried out at 180 °C for 24 h and thiourea was used as the sulphur source. However, the XRD pattern shows impurities in the final product which were not identified by the authors. Irregular sphere shape and nearly monodispersed CZTS nanocrystals with sizes in the range of 5 ± 0.5 nm were resolved using TEM. The same group has also reported bandgap tuneable hydrotropic CZTS nanocrystals by employing the same precursor solution and hydrothermal treatment. CZTS nanocrystal size was found to vary from 3 - 10.5 nm when the reaction duration was extended from 6 - 48 h. Peak broadening and blue shift (~2 cm^{-1}) in the Raman scattering spectrum of the CZTS nanocrystals were detected when the size of the nanocrystals decreased. These asymmetric broadening and shift of Raman bands are attributed to the broadening of the phonon momentum based on the Heisenberg uncertainty principle. A similar blue shift in the bandgap measurement of the CZTS nanocrystals (from 1.48 - 1.89 eV) was also observed with the reduction in nanocrystals size, which is caused by optical quantum confinement. EN was proposed to play an important role in increasing the hydrophilism. EN also acts as a capping ligand which binds to the nanocrystal surface to reduce the growth of CZTS crystals. Unique CZTS microspheres (sizes: 4 - 8 μm) were synthesised through the utilization of hydrothermal conditions at 190 °C for 24 h in the presence of citric acid with metal chlorides and thiourea.

In this hydrothermal reaction, citric acid played an important role in reducing the segregation. In the meantime, citric acid also helped the formation of the microspheres structure of CZTS by controlling the crystal growth. A possible nucleation-dissolution-recrystallisation growth mechanism has been proposed based on the time-dependent investigation of the hydrothermal product. The photoresponse of the as-deposited CZTS films was found to increase with the increment of citric acid concentration in the reaction system. In a separate study, Jiang *et al*. (2012) reported a metastable orthorhombic phase of CZTS using thiocarbamide as the sulphur source and a solvent mixture of water and EN (volume ratio = 1 : 1). The hydrothermal reaction was performed at 200 °C for 24 h. The crystal phase was found to gradually transform from kesterite to orthorhombic structure with the increase of the concentration of EN. The orthorhombic CZTS transformed to kesterite CZTS through a heat treatment at 500 °C for 2 h. The electrical properties of the orthorhombic CZTS were evaluated and the CZTS film was discovered to perform as a photoresistor.

The inorganic sulphur source approach was introduced by Jiang & Yan (2015) who substituted the commonly used thiourea or thioacetamide with sodium sulphide nonahydrate ($Na_2S{\cdot}9H_2O$) in the hydrothermal reaction. A CZTS material was obtained by hydrothermally treating the precursor solution containing the corresponding metal chlorides and Na_2S at 230 °C for 24 h. However, the authors failed to obtain pure phase CZTS materials. Impurities of Cu_2SnS_3 and $Cu_{2-x}S$ were found to coexist in the final synthesised product. Two reaction routes were proposed in this system: (i) Direct formation of ternary and binary products, Cu_2SnS_3 and ZnS, respectively, leading to the formation of CZTS; (ii) Formation of CZTS through binary products, Cu_2S, SnS_2 and ZnS. Although the size distribution of the resulting CZTS products and the homogeneity of the deposited film in terms of surface coverage were poor, the heat treated CZTS film (at 450 °C for 1 h under N_2 flow) exhibited remarkable photocurrent and voltage under light illumination in a photoelectrochemical measurement.

Chopra *et al*. (2004) synthesized nanocrystalline CZTS powder through hydrothermal process, using thiourea as sulphur precursor. They got kesterite CZTS of particle size 4-5nm. High-temperature thermal annealing treatments are needed for the as-deposited nanocrystal films to form large grains, which are crucial for high performance thin film solar cells. Based on the experience with CIGS and CIS film deposition for solar cells, films with micrometer sized grains in the absorber layer can produce cells with high power conversion efficiencies. The current progress in CZTS nanocrystal based solar cells have demonstrated that without a grain-growing thermal treatment process, solar cells are generally unable to generate 1% efficiency.

Hence, even though kesterite crystal structure nanocrystals have been formed in the as-deposited films, thermal annealing cannot be omitted. To make CZTS thin films from the nanocrystals, CZTS nanocrystals are generally dispersed in a solvent or a mixture of solvent and binder before being subjected to film deposition. The CZTS slurry or paste with suitable rheological properties must be prepared to create a uniform layer with homogenous film thickness. The nanocrystal coatings are normally accomplished by either repeating spin coating or doctor-blading to achieve 1 to 2 μm of film thickness, which is the typical absorber layer thickness for thin film solar cells. The as-deposited films then undergo soft baking at a temperature around 300 °C, followed by a high temperature annealing at 500 to 580 °C for a designed duration. Although CZTS nanocrystals already contain the necessary amount of chalcogen (sulphur in most cases), the thermal annealing process of the nanocrystal films still requires the presence of chalcogen vapour. Under high vacuum conditions, the CZTS phase decomposes at temperature above 550 °C due to the volatilisation of SnS and elemental sulphur (Weber *et al*., 2010). The decomposition rate largely varies depending on the temperature, total pressure of the annealing chamber, and the partial pressure of the volatile products. Therefore, in order to prevent the loss of CZTS phase and the formation of undesired phases, an atmospheric base pressure and a chalcogen source are normally applied in the thermal annealing process. Continuous supply of sulphur (sulphurisation) or selenium (selenisation) is a reasonable option to prevent the decomposition of CZTS and CZTSe.

f. Screen Printing Method

Zhou *et al*. (2010) reported a simple and low cost screen printing approach for the preparation of CZTS absorber layers. Microparticles of CZTS prepared using wet ball milling and sintering methods, were dispersed in isopropanol. Separately, ethyl cellulose was dissolved in isopropanol. The screen printable paste was then made by mixing both solutions with small quantity of terpinol and deposited onto 'Mo' coated polyimide substrates. Band gap, sheet resistance, carrier concentration, and Hall mobility of the screen printed CZTS layers were 1.49eV, $2.42\times10^3\ \Omega$/cm, $3.81\times10^{18}\ cm^{-3}$, and 12.61 $cm^2.V^{-1}.s^{-1}$ respectively.

g. Chemical Bath Deposition Method

Chalapathi *et al.* (2015) deposited SnS and ZnS on 'Mo' coated SLG substrates through chemical bath deposition (CBD) in which 'Cu' ions were incorporated into the precursor films via ion exchange technique. These CZTS

precursor films were then annealed in H_2S atmosphere at 500 ^oC. They could produce compositionally uniform microcrystalline CZTS with kesterite structure and band gap of 1.45 eV.

h. Successive Ionic Layer Adsorption and Reaction (SILAR) Deposition Method

Bag *et al.* (2012) reported a novel chemical successive ionic layer adsorption and reaction (SILAR) technique for CZTS thin film formation by sequential reaction on SLG substrate surface. Films were then annealed in vacuum at 400^{o}C. X-ray diffraction studies showed formation of kesterite structure of CZTS films. Sugimoto *et al*. (2011) reported fabrication of CZTS thin film based solar cells using similar approach. CZTS thin films were formed by sequential immersion of substrate into the solutions of cationic and anionic precursors. As deposited films were dried in oven at 60 ^{o}C for 30 min and reported an efficiency of 1.85 % on a solar cell based on CZTS prepared from SILAR technique. Nagoya *et al*. (2010) prepared CZTS films by sulphurising (Cu, Sn) S/ZnS structured precursors prepared by combination of the successive ionic layer absorption and reaction method and the chemical bath deposition method, respectively.

i. Sol-Gel Deposition Method

Sol-gel is one of the catalysts preparation methods of CZTS thin films; it is a homogeneous process resulting in continuous transformation of a solution into hydrated solid precursor. This method has several promising advantages over the conventional techniques. It offers better control of the texture, composition, homogeneity and structural properties of the final solids.

Tanaka *et al*. (2007), for the first time, prepared CZTS thin films by sulphurising precursors deposited by sol-gel method. They prepared films by annealing oxyhydrate precursors deposited by the sol-gel method in an N_2+H_2S atmosphere. The films showed XRD peaks attributed to CZTS and had almost stoichiometric chemical composition and a direct band gap of 1.49 eV. Tanaka *et al.* (2008) deposited CZTS thin films on SLG by annealing the prepared CZT precursors deposited by sol-gel in N_2+H_2S atmosphere. They improve transmittance in IR region and eliminated voids in the CZTS films by pre-annealing the precursors in air or in N_2+H_2 (5 %) atmosphere before annealing of precursors in H_2S contained atmosphere. Tanaka *et al*. (2009) reported fabrication of CZTS-based thin film solar cell using sol-gel method. They used CZTS films prepared over 'Mo' coated glass substrates by sulphurising precursors deposited by sol-gel technique as the absorber layer.

Zhang *et al.* (2009) prepared CZTS films by sol-gel spin coating deposition. They avoided usual sulphurisation process. Film with a nearly stoichiometric composition was prepared at synthesizing temperature of 280^{o}C. Absorption coefficient and the optical energy gap of the deposited films were 2.9×10^4 cm^{-1} and 1.5 eV respectively. Tanaka *et al.* (2011) studied the properties of CZTS thin films deposited by sol–gel sulphurisation. They found that as Cu/(Zn+Sn) ratio of the sol–gel solution decreased, the grains in the CZTS thin films became larger. Band gap of the films shifted to higher energies as Cu/(Zn+Sn) ratio of the CZTS film decreased.

In another report, the effect of H_2S concentration used for sulphurisation was studied. CZTS thin film prepared with an H_2S concentration of 3% had grains in the order of 1µm in size, which were larger than those of films prepared at other H_2S concentrations (Maeda *et al*., 2011). In another report, Wang *et al.* (2011) prepared CZTS thin films by spin-coating the sol-gel precursor followed by annealing in a nitrogen atmosphere. Band gap and absorption coefficient of the films were 1.51 eV and 10^4 cm^{-1} respectively. Zhou *et al*. (2010) deposited sol-gel processed CZTS thin films without sulphurisation. The grain size was up to 1µm and the Cu/(Zn+Sn) and Zn/Sn ratios were 0.93 and 1.07 respectively.

Spray pyrolysis is a sol-gel process in which a thin film is deposited by spraying a solution on to a pre-heated substrate, where the constituents react to form the required chemical compound. It is the one of the most popular technique due to

its simplicity, cost-effectiveness and ability to control the structure at molecular level. There is virtually no restriction on substrate material and its surface, any support having high temperature tolerance will be a suitable substrate.

The first report on spray deposited CZTS was by Nakayama and Ito (1996). They deposited polycrystalline stannite CZTS films on glass substrates. As deposited films were sulphur deficient while it becomes stoichiometric on annealing at 550 ^{o}C in an 'Ar' flow containing H_2S. Stoichiometric film showed resistivity of $2 \times 10^2\ \Omega$.cm. Madarasz *et al*. (2001) prepared CZTS thin films on glass substrates by varying substrate temperature from 225 ^{o}C to 350 ^{o}C. The XRD profiles correspond to the zincblende superstructure of the stannite type CZTS. Kamoun *et al*. (2007) reported preparation of CZTS thin films by varying substrate temperature from 280 ^{o}C to 360 ^{o}C. They prepared films by spraying precursor solution for duration of 30 and 60 min. All the films exhibited kesterite structure with preferential orientation along the (112) direction. Annealing at 550 ^{o}C showed an improvement in optical properties.

Tanaka *et al*. (2011) studied effect of substrate temperature on the properties of CZTS thin films prepared using chemical spray pyrolysis technique. Films deposited at T_s = 290 ^{o}C were found to contain Cu_2SnS_3 and Cu_xS as the secondary phases while at T_s = 330 ^{o}C, Cu_xS was found to be the secondary phase. At T_s = 450 ^{o}C, ZnS appears as the secondary phase. Polycrystalline CZTS thin films, with amorphous ZnS being present to a small extent, could be obtained in the substrate temperature range 370 – 410 ^{o}C. In another report, Aberman, (2013) studied the effect of starting solution pH on the properties of spray deposited films. Polycrystalline, non-stoichiometric CZTS thin films with kesterite structure could be obtained when solution pH is 3.0. Films deposited from a solution having pH = 4.5, contain CuxS and ZnS along with CZTS. Films deposited with solution pH = 5.5 contain only binary sulfides. Nagoya *et al.* (2010) studied effect of copper salt and thiourea concentrations on the formation of CZTS thin films. Near-stoichiometric CZTS films with kesterite structure could be obtained with solution containing 0.009 M copper salt, 0.0045 M zinc salt, 0.005 M tin salt and 0.05 M thiourea.

For citations, the format of surname and year of publication: Oseghale (2016) or (Oseghale, 2016) is preferred for single authors. Double authors should read: Musa and Adediji (2002) or (Musa and Adediji, 2002). Multiple authors should read: Oseghale *et al*. (2016) or (Oseghale *et al.*, 2016).

3. Record efficiencies and other performance parameters of thin film solar cells using CZTS absorber

S/N	Method of CZTS preparation	η (%)	V_{oc} (mV)	I_{sc} (mA/cm^2)	FF (%)	Refernce
1	DC-sputtering	…	265	0.1	…	(Ito and Nakazawa, 1988)
2	DC-sputtering	4.59	545	15.44	55	(Ito, 2015)
3	RF-sputtering	6.77	610	17.9	62	(Katagiri *et al.*, 2008)
4	Co-evaporation	4.1	541	13	60	(Ito, 2015)
5	EB-evaporation	4.53	629	12.53	58	(Kato *et al*., 2005)
6	Thermal evaporation	8.4	661	19.5	66	(Shin *et al*., 2013)
7	Pulsed laser deposition	4.13	700	10.1	59	(Lin *et al*., 2015)
8	Sol-gel (spray pyrolysis)	0.49	173	10.1	28.2	(Scragg *et al*., 2008)

9	Sol-gel (spin coating)	2.03	575	9.69	36	(Tanaka *et al*., 2011)
10	Screen printing	0.49	386	4.76	27	(Zhou *et al*., 2010)
11	CBD	0.16	210	2.4	…	(Wang *et al*., 2011)
12	SILAR	0.396	280	0.63	62	(Sigimoto *et al*., 2011)
13	Hydrothermal	12.6	513	35.2	69.8	(Wang *et al*., 2013)
13	CVD	6.03	658	16.5	55	(Washio *et al*., 2012)
14	Electrodeposition	7.3	567	22	58	(Habib *et al*., 2012)

4. Conclusion

In spite of the great potentials associated with the CZTS based solar cells, from the literature survey, its practical energy conversion efficiency is still far from its theoretical estimate. The major factor usually reported as cause fir the low energy conversion efficiency is the quality of the CZTS absorber layer. The choice of hydrothermal method of deposition of the CZTS absorber layer can be used addressing this challenge. Hydrothermal is a low cost and environmentally friendly method, which uses water-based precursor solutions to prepare CZTS materials. Its advantage over other methods lies in the ability to generate homogenous nucleation and growth of nano-crystals.

This review also realised that the replacement of CdS with In_2S_3 yielded better properties due to the toxicity of Cd and the hazardous waste and bye product generated by the deposition process (Chemical Bath Deposition CBD) which requires special handling. Also CdS has relatively narrow bandgap of 2.4 eV, which absorbs some of the incoming photons in the low energy wavelength region (300-520 nm) which leads to optical losses and photon current losses. This leads to limitation in short circuit current (I_{SC}). In_2S_3 is an organic compound semiconductor material with good stability for photochemical solar cell application. It also has a wider band gap (2.8 eV) and photoconductive behavior (Husser *et al*., 2007).

References

Abermann, S. (2013). Non-vacuum processed next generation thin film photvoltaics: Towards marketable efficiency and production of CZTS-based solar cells. *Solar Energy* (94) 56-59

Ahn, D., Brag, H. O. & Zhika, D. (2010). *The physics of solar cells*. Imperial college press. 29-37

Anderson, D. (2006). *A summary of thin film deposition techniques*, Rochester-New York:Consolidated Vacuum Corporation

Babu, M., Farinella, R. & Spano, T. (2010). Electrochemical deposition of CZTS thin films on flexible substrates. *Advanced Materials*. (44) 105-110

Bag, S., Gunawan, O., Gokmen, T., Zhu, Y., Todora, T. K. & Mitzi, D. B. (2012). Low band gap liquid-processed CZTS solar cell with 10.1% efficiency. *Energy Environmental Sciences* (5) 7060-7065

Chalapathi, U., Uthanna, S. & Raja, S. (2015). Growth of Cu_2ZnSnS_4 thin films by a two stage process-Effect of incorporating of sulfur at the precursor stage. *Solar Energy Materials and Solar Cells* (132) 476-484

Chen, J., Taoufik, S. T., Benamar, E. B. & Ulyashin, A. (2009). Deposition time effect on the physical properties of Cu_2ZnSnS_4 (CZTS) thin films obtained by Electrodeposition route onto Mo-coated glass substrates. *Energy Procedia*. (84) 127-133

Chen, J., Chen, Q., Ni, Y., Wang, T., Jia, Z., Dou, X. & Zhuang, S. (2010). Facile fabrication of Cu_2ZnSnS_4 thin films based on a novel metal-salt precursor printing route. *Material Letters*. (143) 185-187

Chen, J., Zhuang, S., Wang, T. & Ni, Y. (2012). A review of pulsed laser deposition CZTS thin films for solar cell applications. *Journal of Alloys and Compounds*. (619) 109-121

Chopra, K. L., Paulson, P. D. & Dutta, V. (2004). Thin film solar cell: an overview. *Programmed Photovolt: Research Application*, 12, 69-92

Dittrich, T. (2015). *Materials concepts for solar cells*. Imperial College Press. 35, 42, 57, 343

Emovon, I., Kareem, B. & Adeyeri M. K. (2011). Power generation in Nigeria: Problems and solution. *Proceedings of the International Conference of the Nigerian Association for Energy Economics NAEE*, Abuja 234-237

Ennaoui, A., Lux-Steiner, M., Weber, A., Abou-Ras, D., Kotschau, I., Schock, H. W., Schurr, R., Holzing, A., Jost, S., Hock, R., Vob, T., Schulze, J. & Kirbs A. (2009). Cu_2ZnSnS_4 thin film solar cells from electroplated precursors: Novel low-cost perspective. *Thin solid films*. (517) 2511-2514

Fernandes, M., Cao, L., Zhang, B. L. & Jiang, J. C. (2009). One step deposition of CZTS thin films for solar cells. *Solar Energy Materials and Solar Cells*. (117) 81-86

Fernandes, M., Cao, L., Zhang, B. L. & Jiang, J. C. (2011). CZTS stoichiometry effects on band gap energy. *Journal of Alloys and Compounds*. (582) 528-534

Friedlmeier, S. A., Vanalakar, G. L., Patil, P. S. & Kim, J. H. (1997). A review on pulsed laser deposition CZTS thin films for solar cell applications. *Journal of Alloys and Compounds*. (619) 109-121

Green, J., Jiang, J., Yang, P., Peng, C., Huang, Z., Zuo, S. & Chu, J. (1998). A 5.5% efficient co-electrodeposited ZnO/CdS/Cu_2ZnSnZ_4/Mo thin film solar cell. *Solar Energy Materials and Solar Cells*. (125) 20-26

Green, M. A., Emery, K. & Hishikawa, Y. (2010). *Solar cell efficiency tables (version 36)*. John Wiley & Sons, Ltd. 5(18) 346-352

Gutay, M., Raadik, T., Raudoja J. & Krustok, J. (2012). Growth and characterization of CZTS photovoltaic thin films by Electrodeposition and sulfurization. *Journal of Alloys and Compounds*. (410) 31-36

Habib, S. L., Idris, N. A., Ladan, M. J. & Mohammed, A. G. (2012). Unlocking Nigeria's solar PV and CSP potentials for sustainable electricity development. *International Journal of Scientific and Engineering Research* 3(5) 2010-2012

Husser, P., Watt, G. & Kaizuka, I. (2007). CZTS- based solar cells using non-vacuum methods. *Proceedings of 17th international PVSEC* 1110-1113

Ito, K. (2015). *Copper Zinc Tin Sulfide-Based thin film solar cells*. John Wiley and Sons Ltd. 93-199

Ito, K. & Nakazawa, T. (1988). Electrical and optical properties of stannite-type quaternary semiconductor thin films. *Japanese Journal of Applied Physics* 27(11) 2094-2097

Jiang, M. & Yan, X. (2015). Cu_2ZnSnS_4 thin film solar cells: Present status and future prospects. *Solar Cells – Research and Application Perspectives* (108) 107-117

Jiang, C. S., Repins, I. C., Montinho, H. R., Ramanathan, K. & Aljassinn M. M. (2015). Investigation of micro-electric properties of CZTS thin films using scanning probe microscopy. *Solar Energy Materials and Solar Cells* (132) 342-347

Katagiri, H., Yamada, S., Pawar, H. S. & Woo, J. (2005). Structural, morphological, compositional and optical properties of single step electrodeposited CZTS thin films for solar cell application. *Current Applied Physics*. (14) 254-258

Katagiri, H., Jimbo, K., Maw, W. S., Oishi, K., Yamazaki, M., Araki, H. & Takeuchi, A. (2007). Development of CZTS-based thin film solar cells. *Thin Solid Films*. (517) 2455-2460

Katagiri, H., Jimbo, K., Yamada, S., Kamimura, T., Maw, W. S., Fukano, T., Ito, T. & Motohiro, T. (2008). Enhanced conversion efficiencies of CZTS-based thin film solar cells by using preferential etching technique. *Applied Physics Express* (4) 412-415

Kato, T., Hiroi, H., Sakai, N., Muraoka, S. & Sugimoto, H. (2012). Characterization of front and back interfaces on CZTS thin-film solar cells. *In Proceeding of the 27th EU-PVSEC* 123-128

Kondrotas, R., Juskenas, R., Nanjokaitis, A., Selskis, A., Giraitis, R., Mockus, Z., Kanapec, K., Aite, S.,… Sancedo, E. (2015).Characterization of Cu_2ZnSnS_4 solar cells prepared from electrically co-deposited Cu-Zn-Sn alloy. *Solar Energy Materials and Solar Cells* (132) 21-28

Li, J., Zhang, Y., Wang, H., Wu, L., Wang, J., Zhou, Z., He, Q. & Sun, Y. (2015). On the growth process of $Cu_2ZnSn(S,Se)_4$ absorber layer formed by selenizing Cu-ZnS-SnS precursors and its photovoltaic performance. *Solar Energy Materials and Solar Cells* (132) 363-371

Lide, G., Raadik, T., Raudoja, J. & Krustok, J. (1999). Photoluminescence study of defect clusters in Cu_2ZnSnS_4 polycrstals. *Current Applied Physics*. (14) 447-450

Lin, X., Jaison, K., Ahmed, E., Marther, C. & Steiner, L. (2015). $Cu_2ZnSn(S,Se)_4$ thin film absorbers based on ZnS, SnS and Cu_3SnS_4 nanoparticles inks. Enhanced solar cells performance by using a two-step annealing process. *Solar Energy Materials and Solar Cells* (132) 221-229

Liu, S., Walsh, A., Gong, X. G. & Wei, S. H. (2010). Classification of lattice defects in kesterite Cu_2ZnSnS_4 and $Cu_2ZnSnSe_4$ earth-abundant solar cell absorbers. *Advanced Materials*. (25) 11522-11539

Malerba, C. (2014). An investigation into the stoichiometry effect on CZTS microstructure and optoelectronic properties. *Solar Energy Materials and Solar Cells* (97) 433-438

Maeda, G., Keskenler, E. F., Aydin, S. & Dogan, B. (2011). Fabrication and characterization of Al/Cu_2ZnSnS_4/n-Si/Al heterojunction photodiodes. *Physica Status Solidi*. (211) 580-586

Nagoya, K. V., Pawara, S. M., Shinb, S. W., Moona, J. H. & Kima, P. S. (2010). Electrosynthesis of CZTS films by sulfurization of CZT precursor: effect of soft annealing treatment. *Applied Surface Science*. (238) 74-80

Nakayama, N. & Ito, K. (1996). Sprayed films of stannite Cu_2ZnSnS_4. *Applied Surface Science*. (92) 171-175

Nwulu, N. I. & Agboola, O. P. (2011). Utilizing renewable energy resources to solve Nigeria's electricity generation problem. *International Journal of Thermal and Environmental Engineering* 3(1) 15-20

Olekseyuk, Y., Cui, S., Jiang, J & Chu, S. Z. (2004). Synthesis and characterization of co-electroplated CZTS thin films as potential photovoltaic material. *Solar Energy Materials and Solar Cells*. (95) 2136-2140

Persson, H., Shen, X., Wang, W., Pi, J., Hao, Y. & Shi, X. (2008). Synthesis of CZTS films from co-electrodeposited Cu-Zn-Sn precursors and their microstructural and optical properties. *Applied Surface Science*. (282) 765-769

Persson, H. Strong, G. & Bull, K. (2010). *Characterization of thin films methodology*. European Materials Society. 42-61

Poortmans, J. & Arkhipove, V. (2013). *Thin film solar cells: Fabrication, Characterization and Application*. John Wiley and Sons. 451, 432, & 445

Price, D. B., Mitzi, O., Gunawan, T. k. & Wang, K. (1999). The path towards a high performance solution-processed kesterite CZTS. *Solar Energy Materials and Solar Cells.* (95) 1421-1436

Repin, X., Steiner, L., Kornhuber, K. & Levcenko, S. (2011). Structural and optical properties of Cu_2ZnSnS_4 thin film absorbers from ZnS and Cu_3SnS_4 nanoparticle precursors. *Thin Solid Films*. (35) 10-13

Scragg, J. J. (2010). *Copper Zinc Tin Sulfide thin films for photovoltaics: Synthesis and Characterisation by electrochemical methods*. Springer Books Ltd. 36-46

Scragg, J. J., Dale, P. J., Peter, L. M., Zoppi, G. & Forbes, I. (2011). New routes to sustainable photovoltaics: evaluation of Cu_2ZnSnS_4 as an alternative absorber material. *Physica Status Solidi Basic Research* (245) 1772-1778

Schurr, S., Jovina, D. & Rajesh, L. (2009). The influence of deposition temperature in the photovoltaic of sprayed deposition CZTS thin films. *Solar Energy*. (106) 166-170

Shin, B., Gunawa, O., Zhu, Y., Bajarczuk, N. A. Chey, S. J. & Guha, S. (2013). Thin film solar cell with 8.4% power conversion efficiency using an earth-abundant Cu_2ZnSnS_4 absorber. *Programmed Photovoltaic Research Application.* (21) 72-76

Sugimoto, H., Hiroi, H., Sakai, N., Muraoka, S. & Katou, T. (2011). Over 8% efficiency Cu_2ZnSnS_4 submodules with ultra-thin absorber. *IEEE Photovoltaic Specialist Conference* 2997

Tanaka, K., Livreri, P. & Sunseri, C. (2005). A review of CZTS thin film deposition methods. *Energy Procedia*. (43) 104-109

Tanaka, T., Kasaki, D., Nishio, M., Guo, Q. & Ogawa, H. (2006). Fabrication of Cu_2ZnSnS_4 thin films by co-evaporation. *Physica Status Solidi*. (3) 2844-2847

Tanaka, K., Moritake, N. & Uchiki, H. (2007). Preparation of Cu_2ZnSnS_4 thin films by sulfurizing sol-gel deposited precursors. *Solar Energy Materials and Solar Cells*. (91) 1199-1201

Tanaka, K., Kasaki, D., Nishio, M. & Ogawa, H. (2009). Pneumatically sprayed CZTS films under Ar and Ar-H_2 atmosphere. *Journal of Physics D: Applied Physics*. (47) 24-29

Tanaka, K., Kato, M. & Uchiki, H. (2011). Effects of chlorine and carbon on Cu_2ZnSnS_4 thin film solar cells prepared by spray pyrolysis deposition. *Journal of Alloys and Compounds*. (616) 492-497

Vigil, G. O., Courel, M., Rodrignez, E. M., Olarte, J. D., Frutis, A. M. & Sancedo, E. (2015). Electrical properties of sprayed CZTS thin films and its relation with secondary phase formation and solar cell performance. *Solar Energy Materials and Solar Cells* (132) 476-484

Wadia, C., Alivisatos, A. P. & Kammen, D. (2009). CZTS-based solar cell from sol-gel spin coating and its characterization. *Evironment Science and Technology* (43) 2072-2077

Wang, K., Mitzi, D. B., Barkhouse, R. & Aaron, D. (2011). Prospects and performance limitations for Cu-Zn-Sn-S-Se photovoltaic technology. *Philadelvia Transnational Royal Society* (371) 1-22

Wang, K., Mitzi, D. B., Barkhouse, R. & Aaron, D. (2013). Solution processed stannite CZTS thin films for solar cell application. *Materials Letters*. (76) 87-99

Walsh, T., Shinj, T., Tajima, S., Fukano, T., Motohiro, T., Jumbo, K. & Katagari, H. (2012). 6% efficiency Cu_2ZnSns_4-based thin film solar cells using oxide precursors by open atmosphere type CVD. *Journal of Materials Chemistry* (22) 4021-4024

Washio, T., Shinj, T., Tajima, S., Fukano, T., Motohiro, T., Jumbo, K. & Katagari, H. (2015). Study of optical and structural properties of CZTS thins films grown by co-evapouration and spray pyrolysis. *Iopscience* (65) 141-145

Weber, R., Ishino, K., Moritake, R. & Minemoto, T. (2010). Improvement of CZTS thin film morphology using Cu-Zn-Sn-O precursor grown from sputtering. *Current Applied Physics*. (13) 1861-1870

Wu, E., Kavalakkat, J. & Lin, X. (2007). $Cu_2ZnSn(S,Se)_4$ thin film absorbers based on ZnS, SnS and Cu_3SnS_4 nanoparticle inks: Enhanced solar cells performance by using a two-step annealing process. *Solar Energy Materials and Solar Cells*. (132) 221-229

Wurfel, P. (2009). *Physics of solar cells: from basic principles to advanced concepts*. John Wiley and Sons. 71-94

Yeon, H. J., Mohauty, B. C., Denk, H.Y., Lee, S. M. & Yong, S. C. (2015). Single elementary target-sputtered $Cu_2ZnSnSe_4$ thin film solar cells. *Solar Energy Materials and Solar Cells* (132) 136-141

Zhang, X. G. & Shae, A. (2009). Defect physics of kesterite thin film cell absorber Cu_2ZnSnS_4. *Applied Physics Letters*. (96) 23-28

Zhou, M., Valdes, M., Hillie, M. & Vasquez, D. (2005). Electrodeposition Cu_2ZnSnS_4 thin films. *Electrodeposited Acta*. (128) 393-399

Zhou, Z., Wang, Y., Xu, D. & Zhang, Y. (2010). Fabrication of Cu_2ZnSnS_4 screen printed layers for solar cells. *Solar Energy Materials and Solar Cells*. (94) 2025-2042

EFFECT OF IMPROVISED INSTRUCTIONAL MATERIALS ON PERFORMANCE OF SENIOR SECONDARY SCHOOL PHYSICS STUDENTS ON PROPERTIES OF WAVES IN SULEJA METROPOLIS OF NIGER STATE

Fadipe Bayo Michael[1]* Gana Celina Shitnan[2]
[1]Department of Science Education, College of Education, Veritas University, Bwari-Abuja.
[2]Department of Science Education, School of Science and Technology Education, Federal University of Technology, Minna.
[1]fadipe.mike@gmail.com
[2]gana.celina@futminna.edu.ng

Abstract
The paper was an investigation conducted on the "Effects of Improvised Instructional Materials on Performance of Secondary School Physics Students on Properties of Waves in Suleja Metropolis". The research design employed was the quasi experimental research design. The sample size for the study was 120 students from four secondary schools randomly selected from a population of 20 secondary schools offering physics in Suleja metropolis. One objective, one research question and one null hypothesis guided this research study. A physics achievement test (PAT) drawn from past question papers of West African Examination Council (WAEC), National Examinational Council of Nigeria (NECO) and Unified Tertiary Matriculation Examination (UTME) was used to generate data for the study. The instrument was validated by experts in science education and a reliability coefficient of 0.79 was obtained after a trial testing of the instrument in a school different from the school where the experiment was conducted .The statistical tools used for the study were mean and standard deviation to answer the research question and t-test to test the hypothesis. The result obtained indicated that the use of improvised instructional material improved the learning and performance of students in physics, a p-value of 0.03 was obtained. It is therefore concluded that improvised instructional materials are effective in enhancing learning of physics. Based on the findings of the study, it was recommended that all sectors, government, philanthropist, schools administration should embrace and encourage the improvisation of instructional materials and its used in physics.

Key Words*: improvisation, student academic performance, waves.*

Introduction

The federal government of Nigeria is actively involved in providing quality education to the citizens of the country. This of course is in realization that no country can develop in any dimension unless quality education is provided to her citizens. As such, the federal government assumed the responsibility for improving the standard at all levels of education by encouraging the use of quality educational techniques such as the use of improvised material, computer assisted instruction, the use of cloud based technology and so on. Improvisation in sciences dates back to the genesis of experimental sciences when the earliest pioneering scientists had originate both their ideas and the methods needed to empirically demonstrate and authenticate their validity (Soyibo, 2000). Improvisation in science technology and mathematics education is the preparation and use of materials and equipment obtainable from the local environment for the enhancement of the effectiveness of teaching and learning science and technology and mathematics(Soyibo, 2000). According to Igwe (2003), improvisation is the making or inventing of a piece of science teaching equipment in emergency. It is an essential part of laboratory management for the purpose of maximizing the use of the available resources. Improvisation of instructional materials simply means making or constructing of substitute instructional materials from available materials when the real equipment is not available (NERDC 1987). Ango (2000) went further to explain that improvisation rightly conceived means substituting something in place of another to serve a unique function, altering the shape, size or the look of a thing to serve a function other than that originally used for or intended for. The literatures reviewed during this study shows that improvised materials improve the teaching and learning of science subjects and that necessitate the researcher to improvised and apply in teaching of physics. Physics is a science subject which is activity oriented and the suggested method for teaching it is, guided discovery method which is resource

based. This suggests that the mastery of physics concept cannot be fully achieved without the use of instructional learning material. The teaching of physics without learning material will certainly result to poor performance of the course also, a professionally qualified science teacher no matter how well trained would be might not be able to practice effectively , if the school setting lacks the equipment and materials necessary for the teacher to translate his/her competence into reality(Frenzer,1992).

Bassey (2002) opined that science is resource intensive; furthermore, in a period of economic recession, it will be very difficult to adequately find some of the electronic gadgets and equipment for physics in schools. A situation that is further compounded by the galloping inflation in the country and often un-relatedness of some of the imported sophisticated materials and equipment; hence, the need to produce materials locally. Researchers reported that, there were inadequate resources for the teaching of science subjects in secondary schools in Nigeria. They further stated that where there were still resources at all, they are not usually in good conditions, while the few that were in good conditions were not enough to go round those who needed them(Ogunleye,2000; Okonkwo,2000; Mkpanang,2005& Obioha,2006). Hence, there is need for improvisation.

Orasanya (2008), Adebimpe (1997) and Aguisiobo (1998) noted that improvisation demands adventure, creativity, curiosity and perseverance on the part of the teacher. The author added that such skills are only realizable through well planned training programme on improvisation. There have been several studies on instructional materials and academic achievements for instance; Isola (2010) conducted a research on the effects of instructional resources on students' performance in West Africa School Certificate Examination (WASCE) in Kwara state. The researcher correlated material resources with academic achievement of students in ten subjects. Data were collected from the subject teachers in relation to the resources employed in teaching. The achievements of student in WASCE for the past five years were related to the resources available for teaching each of the subjects. The researcher concluded that material resources have a significant effect on students' achievement in each of the subjects. The gains of using improvised materials in teaching and learning include the following among others: Effect of Instructional Materials on Learning

- Helps learner to remember for longer time.
- Helps learner to read pictures and models with skill.
- It stimulates interest in learning.
- Sharpens perception and ability of learners.
- Add enjoyment to learning.
- Permit learner to learn through personal experiences.
- Provides multi-sensory avenue for learning.
- Help learners to have critical approach to what they are learning.

Influence of Instructional Materials on Learning Habits

- It influence attitude.
- Can help change behaviour.
- Leads to experimentation and innovation.
- Promotes emotional feelings towards what is being learned.
- Promote better understanding.
- Helps to teach habit.

Effects of Instructional Materials on Teachers

- Helps teachers to reach slow learners.
- Teachers can learn from instructional materials.
- Permit teachers to reach more learners.
- Helps teachers to become more skillful.
- Help teachers to have better control of the class.

- Help teachers to organize their work/teaching better.

Teaching materials help focus the learner's attention on the lesson and so shift educational activities from the teacher to the learner. These foster understanding and help learners remember what they have learned. It also helps in development of skills and attitude in learners. The poor performance of students in physics at the final Senior Secondary School Certificate Examination (SSCE); research revealed that in 2005, the percentage of students that passed physics was 41.50%, from records obtained; there has been a declined in the level of performance of students in physics especially in external examinations such as West Africa Examination Council (WAEC), National Examinational Council (NECO) and the Unified Tertiary Matriculation Examination (UTME).For instance percentage score of WAEC result in physics for 2005 – 2009 are as follows , in the year 2005 , the students that enrolled for physics were 344,411 and only 41.50 percent passed physics; in the year 2006 , the students that enrolled for physics were 345,225 and only 43.84 percent passed physics ; in the year 2007 , the students that enrolled for physics were 427,390 and only 58.05 percent passed physics ; in the year 2008 , the students that enrolled for physics were 424,693 and only 48.26 percent passed physics and in the year 2009 , the students that enrolled for physics were 429,174 and only 43.56 percent passed physics(Source: WAEC Office Yaba, Lagos). From this source, it is clear that the students' performance in physics dropped seriously from 2007 – 2009, and the overall performance is not encouraging, if not 2007 that had a performance percentage above 50, all other years reviewed showed a performance percentage below 50. This is very poor for a nation like Nigeria that is tending towards self-dependent in technological development. More so, research has shown that there are no improvised instructional materials on the area under study. In schools where such materials are available, they are only in chart forms or diagrams, no concrete models. The researcher used concrete improvised instructional materials to bridge the gap between charts and diagrams. Based on the fore going the researchers sought to investigate the effect of improvised instructional materials on performance of senior secondary school physics students on properties of waves in Suleja metropolis of Niger state.

.

Methodology

The research design adopted was the quasi experimental research design in which the pretest – post-test control group design was used. The two groups were drawn from a homogenous or the same population. The population for the study comprised of all the twenty senior secondary schools offering physics in Suleja metropolis. The researchers targeted the senior secondary two (SSII) students.

A three stage sampling technique was employed in selecting the sample. A purposive sampling technique was first employed to select the four sampled senior secondary schools because the schools offer physics and are close to the researchers reach in this recession. Secondly, a simple random sampling technique was used to assign the four schools selected to experimental group and control group respectively. Finally, an intact class each of 30 (thirty) students were randomly selected from each of the sampled school, making a total of 120 (one hundred and twenty) students in all.

Physics achievement test (PAT) was developed from past West Africa Examination Council (WAEC), National Examination Council (NECO) and Unified Tertiary Matriculation Examination (UTME), examination question papers which covered the topic treated from (1988 – 2011). The improvised instructional material was designed and constructed by the researcher using metallic materials which are readily available and affordable as well. Although the items used were drawn from internationally and nationally validated question papers. The items were still subjected to expert validation by physics professionals from Federal University of Technology, Minna. The reliability coefficient of the instrument was 0.79. The researcher used the research assistance to administer the questions to ensure fairness and objectivity and to reduce teacher's variableness.

Physics achievement test (PAT) was used to obtain pretest and post-test data for the research study. The experimental and control groups were pretested before the administration of the treatment. The result was collected and analyzed to determine their entry behaviour. The second test which is post-test was administered to the two groups after the treatment. The mean score and standard deviation was used to answer research question while ANCOVA statistical analysis was used to test the hypothesis using the 13.0 version of Statistical Package for Social Sciences (SPSS). The hypothesis was tested at 0.05 alpha of significant level of probability.

Objective of the Study

The objective of the study is to determine the effect of improvised instructional materials on senior secondary school physics students' performance when taught wave properties in Suleja metropolis.

Research Question

What is the mean performance score of the experimental and the control group when taught wave properties in Suleja metropolis?

Research Hypothesis

H_0 – There is no significant difference in the mean performance scores of students taught physics with improvised instructional materials and those students taught without improvised instructional materials.

Results and Discussion

Table 1: Mean and Standard Deviation of Physics Students Exposed to Improvised Instructional Material and those Exposed to Lecture Method

		Pre-test		Posttest		
Groups	**N**	**Mean**	**SD**	**Mean**	**SD**	**Mean Gain**
Experimental	60	47.12	6.856	94.24	3.108	
Control	60	46.22	6,327	82.44	3.914	

Table1. Shows that the mean score of the experimental group before treatment is 47.12 and that of the control group is 46.22 with only a marginal difference of 0.90 which is not significant. Based on the above, it can be deduced that the experimental and the control group are equivalent in terms of entering knowledge of the subject physics before the treatment and therefore the group was considered okay for the study. The posttest result shows that the mean score of experimental group after treatment is 94.24 and that of the control group is 82 .44.The mean gain is 11.80 in favour of the experimental group.

Table 2.0: ANCOVA Result of Physics- Students Scores of Experimental and Control Groups Exposed to Improvised Instructional Material and those Exposed to Lecture Method

Source	**Sum of Squares**	**df**	**Mean Squares**	**F-value**	**P-value**
Corrected Model	101846.000	2	50923.000	145.30	.000
Intercept	2793.311	1	2793.311	796.75	.000
Pretest(covariate)	2.082	1	2.082	0.59	.442
Treatment	1333.455	1	1333.455	380.35	.030
Error	581.976	117	3.506		
Total	930248.000	120			
Corrected Total	102427.979	119			

Significant at ≥ 0.05 probability level

The result in table 2.0 shows the result of experimental and control group. The p-value was significant at 0.05 level of significance (F-value = 380.35, $p < 0.05=.03$). Therefore, the hypothesis which states that, there is no significant

difference in the mean performance scores of students taught physics with improvised instructional materials and those taught without improvised materials is hereby rejected.

Students found it difficult to pass physics in the Senior Secondary Certificate Examination (SSCE) because the teaching of physics have been rendered abstract due to the fact that teachers no longer exploit the natural environment and they no longer apply innovative ideas to teach the subject(Ugwu,2000). These facts is being supported by the findings of IGS (2000), who noted that science teachings and learning can only be meaningful and effective if backed up by the necessary resources to enrich instruction.

The result in Table 2.0 revealed that the student taught physics properties of waves with improvised instructional materials might performed better than those taught without instructional materials. This shows that the use of improvised instructional materials contributed positively to the learning achievement of students in physics. The result is in agreement to previous findings of Ango (1990) and Ngoka (1992) as well as the findings of Dawodu (2007), Ayodele (2001), Cirfat, Zumyil and Tongjura (2006) who noted that there was significant difference in the performance of students expose to a particular treatment. It is also supported by findings of Nsofor (2004) who noted that students learn more from science lesson when they are taught with learning or teaching materials. The result is contrary to the findings of Delialogle and Yoldrin (2008), Serger and Verhoven, Nwa, Chukwu et al (2006) among others who noted that there was no significance difference between the performance of the experimental group and control group when diagrams, instrumental models and styles were administered on different group of students.

This research work also revealed that students taught with improvised instructional materials participated more actively than those taught without instructional materials as revealed from the p-value score of .030 which is significant. This is supported by the findings of Pine and West (1986) and Nwachukwu et al (2007), Alazi (1990) and Azubuike (1999), Wasaagu (2000), Olumotumi and Fenso (2000), Adeniyi (2001), Nsofor (2004) who all noted that using teaching materials help students to show more interest in teaching and learning. They also noted that facilities motivates the student and also help them to recall easily.

Conclusion

In conclusion, the researcher discovered and concludes that improvised instructional materials will enhance, stimulate and motivate the teaching of physics in schools and colleges. Based on the findings of the researcher, the following conclusions were drawn;

- Improvised instructional materials are effective in enhancing learning.
- Improvised instructional materials motivate and stimulate learning.
- Improvised instructional materials help to improve teaching skills.

Recommendations

Based on the finding available as a result of this study, the following recommendations are made;

1. The physics teacher should always endeavor to improvise instructional materials for effective teaching and learning.
2. Government, philanthropist, non-governmental organizations should come to the aid of the schools and colleges that offer physics by providing a befitting laboratory for improvised instructional materials.
3. Government and school administration should make funds available to teachers to encourage improvisation of instructional materials.
4. Physics teachers should be encouraged to attend conferences, seminars and workshops to improve their competence in the use of improvised materials for teaching physics.
5. Physics teachers and laboratory attendance should be trained and retrained on how to produce improvised instructional materials.

References

Ango, M. L. (1990). Basic Science Laboratory in Jos. Ehindero Publishers Ltd. Jos, Plateau State. Pp. 15 – 20.

Dawodu, F.A.A. (2007). Repositioning Polytechnic Education for Sustainable Development Knowledge Review. A Multi-Diplomacy Journal. 15 (2), 133 – 139.

Demirel, O. (2004) Planning and Evaluation in Instruction. Art of Teaching, Pegem Publication. Pp. 16 – 24.

Federal Ministry of Education (2004). National Policy on Education in Lagos, Nigeria. Educational Research and Development Press, Lagos, Nigeria. Pp. 10 – 15.

Gana, E. S. (1973). Ideals and Techniques for Producing and Utilizing Visual International Materials, Paper Presented at a Workshop for Post-Primary School Teachers at Federal University of Technology, Minna. Pp. 13 – 15.

Gambari, (2004). The Development of Computer Aided Instruction (CAI) Software for Individualized Instruction in Physics in Senior Secondary Schools in Niger State. M. Tech. Thesis Submitted to The Department of Science and Science Education, University of Technology, Minna. Pp. 15 – 20.

Owolabi, OT (1999). Prevalent of Errors in Physics Practical among Pre-Science Students of College of Education in Nigeria. Journal of Educational Research and Evaluation. 3 (2): 915.

Owolabi OT (2003). Design and Validation of Error Correcting Instructional Package (ECIP) for Secondary School Practical, Unpublished Ph.D. Dissertation, University Of Ado-Ekiti, Nigeria.

Ugwu AN (2008). Current Issues in Implementation of Senior Secondary School Science Curriculum in Nigeria. Proceedings of The 49th Science Teachers Association Of Nigeria (STAN) Annual Conference. Pp. 19 – 25.

Gbodi, B. E. & Laleye A. M. (2006). Effect of Video-Trapped Instruction on Learning of Integrate Science. Journal of Research in Communication and Teaching. 1 (1), Pp. 10 – 19.

Ibitoye, S. J. (1996). Gender Differences and Achievement in Secondary School Agricultural

Science in Kwara State. The Nigeria Teacher Today. 6 (1), 52 – 56.

PALEOENVIRONMENTAL AND PALEOCLIMATIC RECONSTRUCTION OF OM-4 AND OM-A WELLS, NIGER DELTA, NIGERIA

[*1]Taiwo, O. M., [1]Okosun, E. A., [1]Onoduku U. S.
[1]Department of Geology, Federal University of Technology, Minna
***Corresponding Author: opeyemifasola@gmail.com/+2347061691639**

Abstract
Palynological studies have been carried out on 100 ditch cuttings samples penetrated by OM-4 and OM-A wells in the Niger Delta, Nigeria, with the aim of reconstructing the paleoenvironment and paleoclimate of the interval studied which ranged from 8200 – 11400 ft each in both wells. The palynomorphs yielded 51 and 44 species in OM-4 and OM-A wells respectively. The succession studied yielded rich terrestrial components of the palynomorph assemblage which gave zero to low PMI values in both wells, suggesting a paralic environment. Also, the abundance of mangrove swamp species such as *Zonocostites ramonae, Acrostichum aureum, Botryococcus braunii* and *Psilatricolporites crassus* in both wells (which are brackish water indicators) denotes an environment of deposition with higher terrestrial influences, indicated a paralic environment of deposition. The palynomorph distribution was also used to interprete the depositional climatic conditions and on the basis of changes in the vegetation shown in the nature of distribution of the paleoclimatic zones were established. Four zones in OM-4 well and five zones in OM-A well. These zones showed a variation between dry and wet climates.

Keywords: Paleoenvironment, paleoclimate, Palynomorphs, Miocene

Introduction

Palynology involves the study of acid resistant microfossils with organic walled microfossils, which are spores, pollen and dinoflagellates, **t**hey are the products of continental vegetation, and might best be considered as a biogenous component of fine-grained detrital or terrigenous marine sediment. Palynomorphs undergo rapid diversification, they are considerably resistant to geologic obliteration and acids, easy to process, numerous and are good facies indicators. These characteristics give them stratigraphic value and have made palynological research applicable in numerous present day studies. These applications include;

i. Paleoenvironmental studies; this entails how information from present day studies of modern organisms can be used to infer environmental conditions in the past and also predict future environmental conditions, since the distribution organisms generally, are controlled by a combination of physical conditions of the surrounding area including terrain, vegetation structure, rainfall, sea level rise or fall and temperature.
ii. Paleoclimatic reconstruction; this is based on the fact that changes in climate are most evidently reflected in the vegetation since the manner in which vegetation is distributed is dependent on the prevalent climatic conditions. Thus, reconstructing vegetation helps to reconstruct past climates (Ivanor *et al*., 2007).
iii. Paleoecology: certain individuals or assemblages of plants are known to be characteristic of specific ecological zones and the occurrence of their fossils serves as ecological indicator species in sediments.
iv. Well correlation in hydrocarbon exploration
v. Depositional environment studies amongst many other uses.

This study focuses on the use of palynomorphs for paleoenvironmental and paleoclimatic reconstruction of the studied interval.

Description of the Study Area

The Niger Delta lies between latitude 4^0 and 6^0 N and longitudes 3' and 9' E in the southern part of Nigeria. The studied OM-4 and OM-A wells are located on the onshore part of the Niger Delta, on latitude 4.63^0 N and longitude 6.8^0 N and 4.627^0 E and 6.786^0 E respectively (Figure 1). OM-4 well lies in the Central depobelt while OM-A well lies within the coastal swamp depobelt.

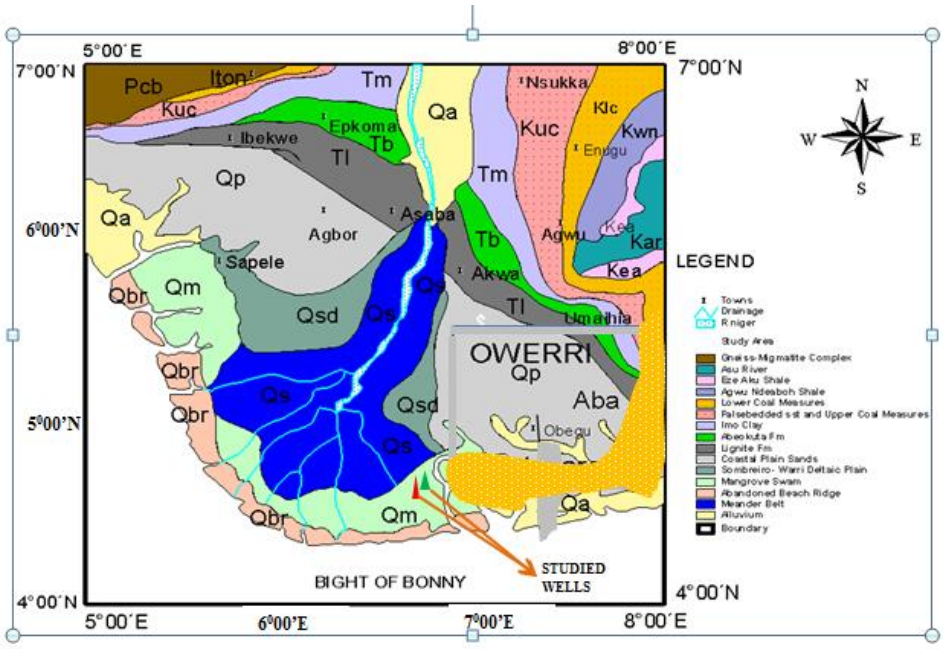

x

Figure 1: Geological map of Niger Delta showing the location of the studied wells (Modified after Knox and Omotasola, 1990)

Methodology

A constant weight (30g) of each sample was initially given a hot hydrochloric acid (HCl) treatment to remove carbonates prior to complete digestion in hydrofluoric acid (HF) under a fume cupboard to remove silicates. Gentle agitation of the acid/sample mixture was carried out to aid acid digestion. The sample was then washed with over a 5micron mesh polypropylene sieve under running water to facilitate the complete removal of silt and clay particles. A spatula was used to scoop the organic-rich fraction and strewn mounted on the slides and made to dry on a hot plate by heating it up to 40^o C. Two to three drops of loctite impruv were used as the mounting medium and cured over ultraviolet (UV) light. The palynomorphs were counted on each of the two slides per sample. The slides were viewed under the National binocular microscope in the laboratory of Mosunmolu Nigeria Limited, Lagos, Nigeria. Forms observed were identified and named using palynological albums as well as descriptions of previous workers (Adegoke *et al*., 1986; Evamy *et al*.,

1978; Germeeraad et al., 1968). The identified species were noted, counted and recorded on the analysis sheet using the tally system. The process was repeated for all the slides. The results were inputted into the stratabug software to prepare the palynomorphs distribution chart.

Results

Palynomorph Distribution

The distribution of palynomorphs, (pollen, spores, dinoflagellates and algae) in the studied section varied from one depth to another in diversity and abundance. Pollen and spore preservation was fair in both wells with total species count of fifty-one and forty-four in OM-4 and OM-A wells. Dinoflagellates were poorly represented with 2 species each, found in both wells. Figures 2 and 3 show palynomorph distribution chart from samples analysed, plotted using the stratabug software for OM-4 and OM-A wells respectively. The lists of the forms of palynomorphs as recovered from the ditch cuttings from both wells as plotted on the charts are listed below:

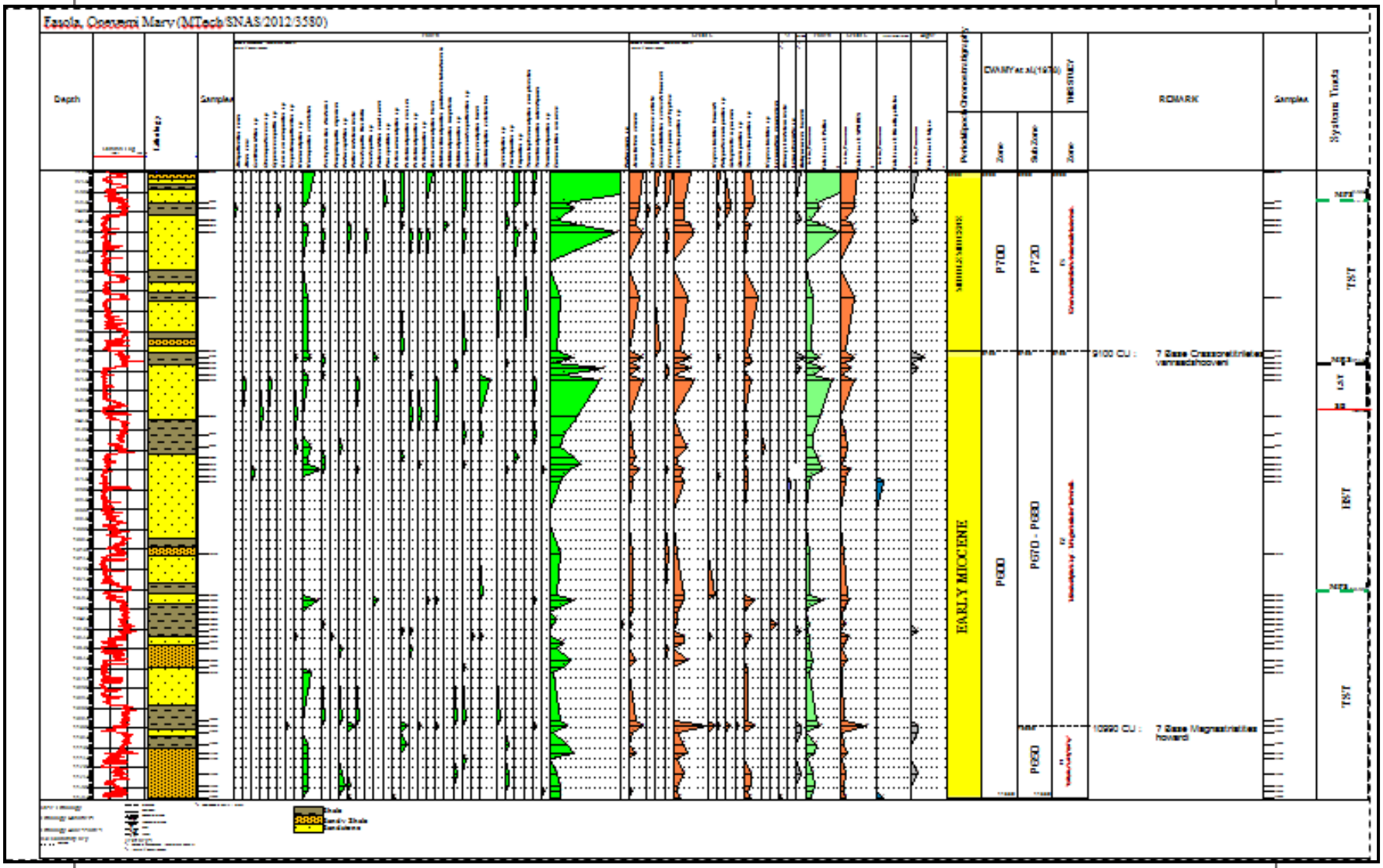
Depth
Samples
Chronostratigraphy
Zone
Sub Zone
REMARK
Samples
System Tracts
EARLY MIOCENE
P700
P720
P600
P670 - P680
P650
TST
HST
TST

Figure 2: Palynomorph distribution chart for OM-4 well

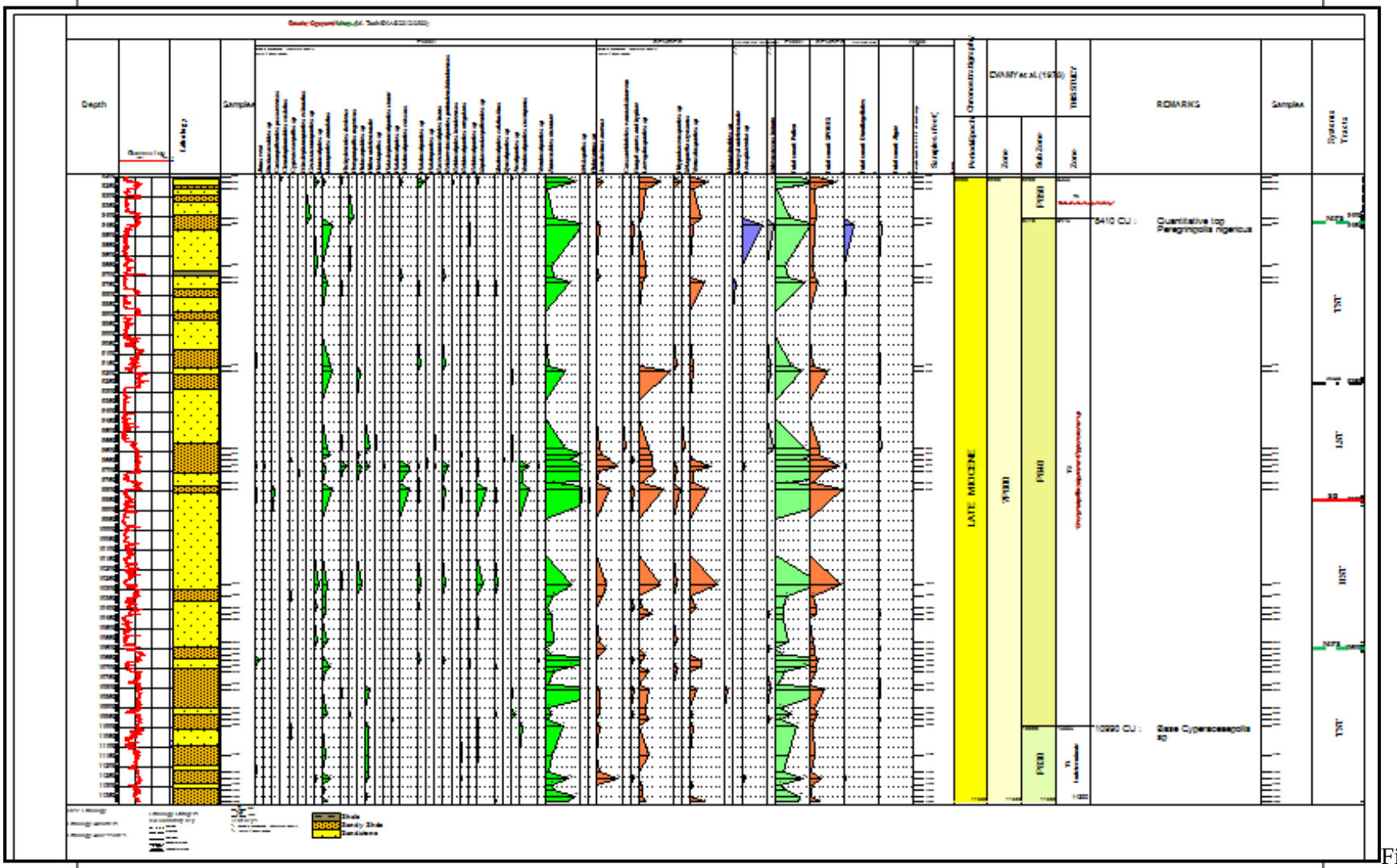

Figure

3: Palynomorph distribution chart for OM-A well.

From Figures 2 and 3, it can be seen that the most abundant palynomorphs were of the pollen family, which accounts for about 71% of the total palynomorph assemblage in OM-4 well (Figure 4) and 75% in OM-A well (Figure 5), the second most abundant group are the spores, with 23% and 18% of all palynomorphs in both wells respectively. Both OM-4 and OM-A wells are characterised by very low counts of marine palynomorphs (dinoflagellates) with 4% and 5% in both wells respectively. Algaes were rare, comprising about 2% in both wells (Figures 4 and 5).

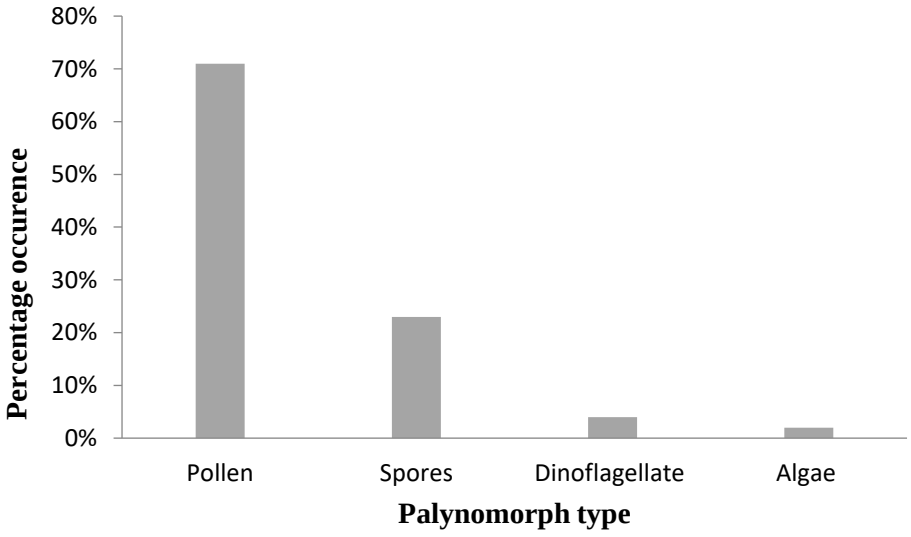

Figure 4: Percentage palynomorph distribution in OM-4 well

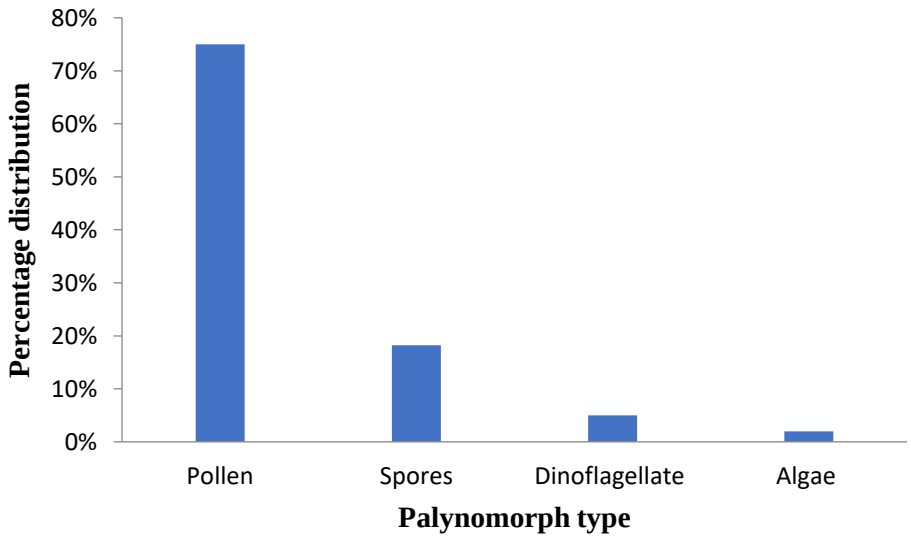

Figure 5: Percentage palynomorph distribution in OM-A wells

Paleoenvironmental Analysis

This is concerned with the use of microfossils (microflora and fauna) to infer environmental conditions in the past (Culver *et al*, 2011). Information on the palynological assemblage is useful in reconstructing paleoenvironment. (Van Bergen *et a1*., 1990; Petters and Edet, 1996; Ojo and Akande, 2004), this is because changes in the environment are reflected in palynologic assemblages (Oloto, 1989; Ojo and Akande, 2004). The tools adopted in establishing the paleoenvironment for this study are: PMI, environment markers and dominant species group

Palynological Marine Index (PMI) of OM-4 and OM-A wells

This index was proposed by (Helenes *et al.*, 1998) to interprete environments of deposition, using the PMI formula: PMI = (Rm/Rt + 1)100, with Rm being the number of marine palynomorphs which include dinoflagellates, acritarchs and foraminiferal test linings and Rt, the number of terrestrial palynomorphs (pollens and spores). In this study, Rm and Rt were expressed as the number of species per sample. High PMI values were interpreted to indicate normal marine depositional conditions, low values as brackish and nil values as fresh water (Helenes *et al.*, 1998). In relations to the classification by (Helenes *et al*., 1998), this study adopts 0% as nil PMI values indicating freshwater, 1-50% as low PMI values indicating brackish and 51-100% as high PMI values indicating marine environment.

PMI values for OM-4 well were generally nil with most depth recording 0.0% PMI values (Table 2, Figure 6), this indicates a fresh water environment. However, at few depths 9160 ft, 9760 ft, 10510 ft, 10990 ft, 11020 ft, 11230 ft and 11350 ft, low PMI values of 14.0%, 20%, 33.3%, 6.7%, 25%, 12.5% and 16.7% were obtained respectively (Table 1, Figure 6) denoting a brackish environment. In OM-A well, most depths also had PMI values of 0.0% (Table 2, Figure 7), representing freshwater environment. Depths with low PMI values include 8440ft (14.3%), 9160 – 9670ft (14.3%), 10610 ft (50%), 10810 – 10780 ft (10 – 50%), 10960 ft (20%) and 11260 ft (12.5%) as seen in Table 2, Figure 7. These depths indicate brackish water environment. From the PMI values, it is can be inferred that sediments were deposited in a paralic environment.

Table 1: PMI values for OM-4 well

Marine Diversity Rm	Terrestrial Diversity Rt	PMI (Rm/Rt+1)X100	Depth
0	13	0	8200
0	11	0	8350
0	13	0	8380
0	4	0	8440
0	11	0	8470
0	15	0	8500
0	7	0	8830
0	7	0	9100
1	9	10	9130
1	6	14.3	9160
0	0	0	9190
0	6	0	9220
0	11	0	9250
0	6	0	9430
Rm Marine Diversity	Rt Terrestrial Diversity	PMI (Rm/Rt+1)X100	Depth
0	7	0	9590
0	8	0	9640
0	7	0	9670
0	11	0	9700
0	6	0	9730
1	4	20	9760
1	2	33.3	10510
0	8	0	10540
0	3	0	10570
0	4	0	10600
0	3	0	10660
0	3	0	10690
0	3	0	10720
0	9	0	10960
1	14	6.7	10990
1	3	25	11020
1	7	12.5	11230
0	7	0	11290
0	7	0	11320
1	5	16.7	11350

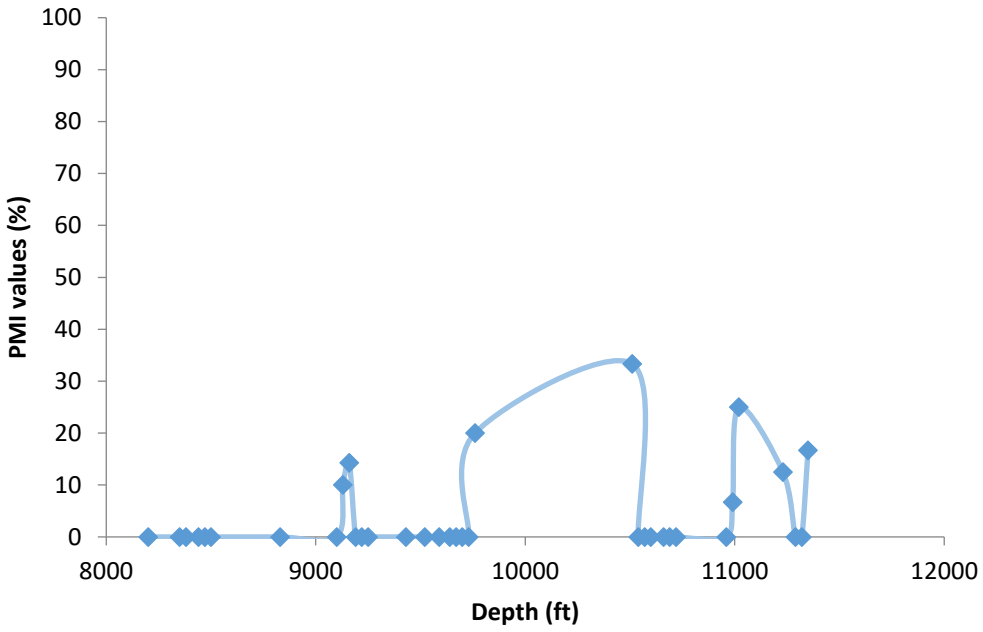

Figure 6: PMI plot for OM-4 well

Table 2: PMI values for OM-A well

Marine Diversity Rm	Terrestrial Diversity Rt	PMI (Rm/Rt+1)X100	Depth
0	6	0	8200
0	12	0	8230
0	3	0	8260
Rm Marine Diversity	Rt Terrestrial Diversity	PMI (Rm/Rt+1)X100	Depth
1	6	14.3	8440
0	4	0	8650
0	6	0	8710
0	8	0	8740
1	6	14.3	9160
1	6	14.3	9190
1	11	8.3	9580
0	7	0	9610
1	10	9.1	9640
1	20	4.8	9670
0	13	0	9700
0	5	0	9760
0	17	0	9790
0	13	0	10270
0	4	0	10330
0	7	0	10390
0	3	0	10450
0	2	0	10480
0	5	0	10570

1	1	50	10600
0	4	0	10630
0	6	0	10690
0	4	0	10720
1	1	50	10780
1	9	10	10810
0	4	0	10900
0	9	0	10930
1	4	20	10960
0	7	0	10990
0	6	0	11140
0	4	0	11230
1	7	12.5	11260
0	3	0	11290
0	3	0	11320
0	3	0	11350
0	5	0	11380

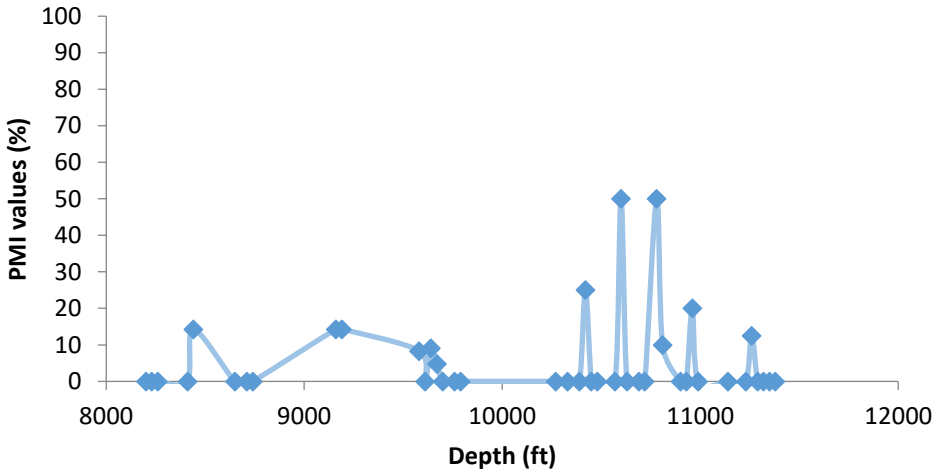

Figure 7: PMI plot for OM-A well

Marker Species and dominant species groups for paleoenvironmental studies.

Generally, the freshwater swamp species which include *Laevigatosporites* sp, *Peregrinipollis nigericus, Racemonocolpites hians, Retitricolporites irregularis, Striatricolpites catatumbus, Crassoretitriletes vanraadshooveni* and *Magnastriates* sp, were observed to be well represented in terms of diversity in both wells (Figures 2, 3, 8 and 9). These species were observed to occur at depths with 0.0% PMI values (although not restricted to only those depths), hence, confirming those depth intervals to have been deposited in a freshwater environment. Generally, of the all the palynomorphs recovered from both wells (OM-4 and OM-A), *Zonocostites ramonae* was the most abundant species accounting for about 48% in OM-4 well and 52% in

OM-A well, next to it is *Laevigatosporites* sp with about 19% in OM-4 well and 15% in OM-A well, *Acrostichum aureum* 12%, *Verrucatosporites* sp 7%, *Monoporites annulatus* 5% and other palynomorphs accounting for about 9% in both wells respectively (Figures 6 and 7).

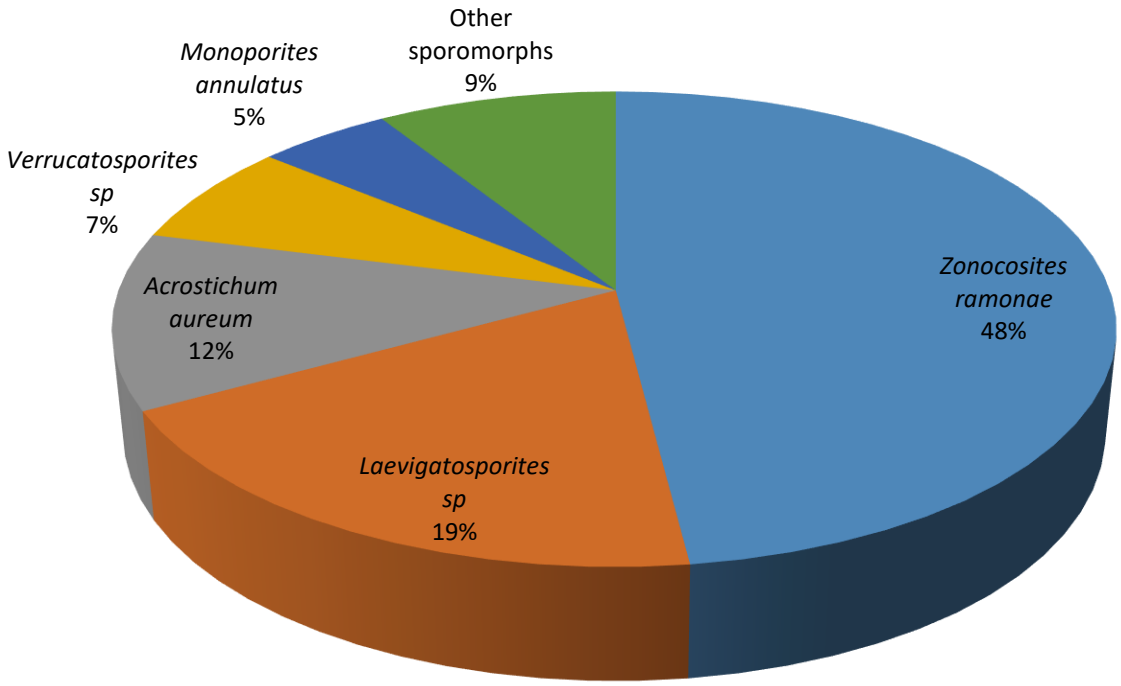

Figure 8: Percentage palynomorph species abundance in OM-4 well

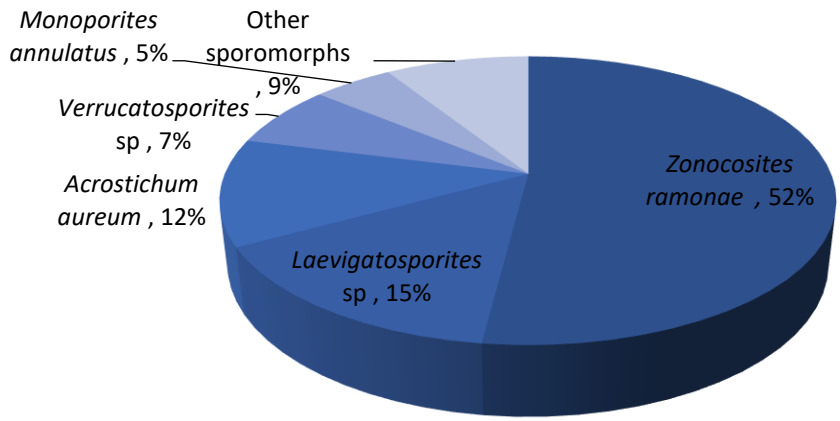

Figure 9: Percentage palynomorph species abundance in OM-A well

In both wells, high percentages of mangrove species (brackish water indicators) which includes *Zonocostites ramonae, Acrostichum aureum, Psilatricolporites crassus, Verrucatosporites* sp and *Botryococcus braunii* (Ige, 2009; Sowunmi, 1981; Jennifer *et al.,* 2012; Oboh *et al.*, 1996), were recorded (Figures 8 & 9). Also depths intervals with low PMI values showed an assemblage of at least two mangrove swamp species. For instance, in OM-A well, at 8440 ft with PMI value of 14.3% (Table 3), *Zonocostites ramonae, Acrostichum aureum,* and *Botryococcus braunii* were present at that depth. Although, the presence of these species was not limited to the depths with low PMI values, their presence at such depths had higher population than the freshwater species. These mangrove species were generally most abundant in terms of population in both wells especially *Zonocostites ramonae* and *Acrostichum aureum* (Figures 8 & 9). The presence of these Mangrove swamp species further confirms that the depths with low PMI values were deposited in a brackish environment. The major palynomorph groups that were used in the paleoenvironmental studies are pollen, spores and dinocyts, representing the terrestrial and marine influences (Soronnandi-Ononiwu *et al*., 2014). From Figures 4 and 5, it can be seen that pollen and spores accounted for 71% and 23% in OM-4 well and 75% and 18% in OM-A well respectively, compared to the low counts of marine influences (dinoflagellates) which had 4% and 5% in OM-4 and OM-A wells respectively, indicating an environment with greater terrestrial influences. Shrank (1994) has suggested that palynomorph assemblages with higher content of pollen from land indicates terrestrial influence and vice versa, hence the succession of sediments in OM-4 and OM-A wells show it is strongly dominated by terrestrial palynomorph, denoting a generally continental environment. The presence of marine influences denotes an environment prone to marine interactions, hence, suggesting a paralic environment. Moreover, the nature of the sediments is also an important factor in the distribution of the palynomorphs. Being allochthonous sediments, generally the siliciclastic sediments deposited in marine environments show higher abundances of terrestrial than marine palynomorphs (Traverse and Ginsburg, 1966; Groot and Groot, 1966; Lana, 1997).

From the PMI values, dominat species group and presence of marker species, sediments within both wells were deposited in a paralic environment denoting a fluvial to coastal environment.

Paleoclimatic Studies

Paleoclimate is the study of changes in climate. This study employs the use of palynomorphs to carry out paleoclimatic studies, this is because, changes in climate are most evidently reflected in the vegetation since the vegetation of any area is an integral and important of an ecosystem and are responsive to change in the ecosystem (Ivanor, *et al*., 2007). The palynomorph distribution charts of both wells (Figures 3 and 4), show the important taxa of the wells which are also ecologically significant. These taxa have been used to delineate the wells ecologically and to interprete the depositional climatic conditions. On the basis of observed changes in vegetation, which was reflected in pollen distribution, a total of nine (9) paleoclimatic zones have been recognized; 4 zones in OM-4 well and 5 zones in OM-A well.

Paleoclimate of OM-4 well

Dry climates

Of the four paleoclimatic zones established in this well, two zones (Zones A and C) showed dry climates.

Zone A (11350-9700 ft) shows a consistent general reduction in percentage occurrence of *Zonocostites ramonae* and other mangrove species such as *Psilatricolporites crassus* as seen in Figure 2. Sparse distribution of rain forest species such as *Pachydermites diederixi* and *Sapotaceoidaepollenites* sp suggests a dry condition during deposition of the sediments. The presence and relative increase in the distribution of *Monoporites annulatus* (Poaceae) (Morley, 1995), indicates the thriving of open vegetation in the area. The reduction in percentage distribution of *Zonocostites ramonae* in this zone is relative in comparism to its distribution in other zones; hence the zone may not represent an extremely dry climate, but suggests a drier condition since there are evidences of sparse distribution of the forest species. The reduction in percentage of *Zonocostites ramonae* may be as a result of a drop in the level of the sea since mangrove swamps species respond to changes in the sea level hence are pointers of sea level fluctuation. According to (Ige, 2011; Sowunmi, 1981; Lexine and Vergnaud- Grazzini, 1993), high value of *Rhizopora* (*Zonocostites ramonae*) represent rise in sea level and vice versa. The presence of *Podocarpus* sp. is significant as it represents a cool montane climate (Knapp, 1971).

Zone C (9150-8680 ft) showed a fall in the number of *Zonocostites ramonae* in this zone coupled with the sparse occurrence of savanna and the forest species may denote the prevalence of a more adverse climatic condition. A reduced but relatively stable sea level might have dominated in this zone. Although there was a drop in the general distribution of species, mangrove swamp species; *Zonocostites ramonae* and *Psilatricolporites crassus* still dominated the entire zone, still denotes a wet climate although not as in zone B.

Wet climates

Two zones (B and D) had wet climates. Zone B (9700-9150 ft) showed gradual upward rise in the number of *Zonocostites ramonae* suggests a gradual increase in the sea level and the setting in of a wetter climate

compared to Zone A (Figure 10). Fresh water swamp species such as *Striatricolpites catatumbus* and rain forest species such as *Pachydermites diederixi* were represented in higher percentage than in the preceeding zone although they are generally sparsely distributed compared to the mangrove swamp species. This confirms a gradual change from a drier climatic condition to the wetter one with gradual sea level rise.

Zone D (8650-8200 ft) displayed good representation of *Zonocostites ramonae* with an initial gradual increase in its percentage. This suggests a rise in sea level. Although within the zone, there was evidence of a local fluctuation in sea level shown by a drop in *Zonocostites ramonae* with corresponding presence of charred gramineae cuticle, fungal spores and hyphae and other savanna species, showing about the same percentages, suggests the prevalence of an open vegetation condition indicating a relatively drier climate.
Following this stage was the sharp rise in distribution of *Zonocostites ramonae.* This zone records the peak of its occurrence in the entire section denoting rise in sea level and a wet climate.

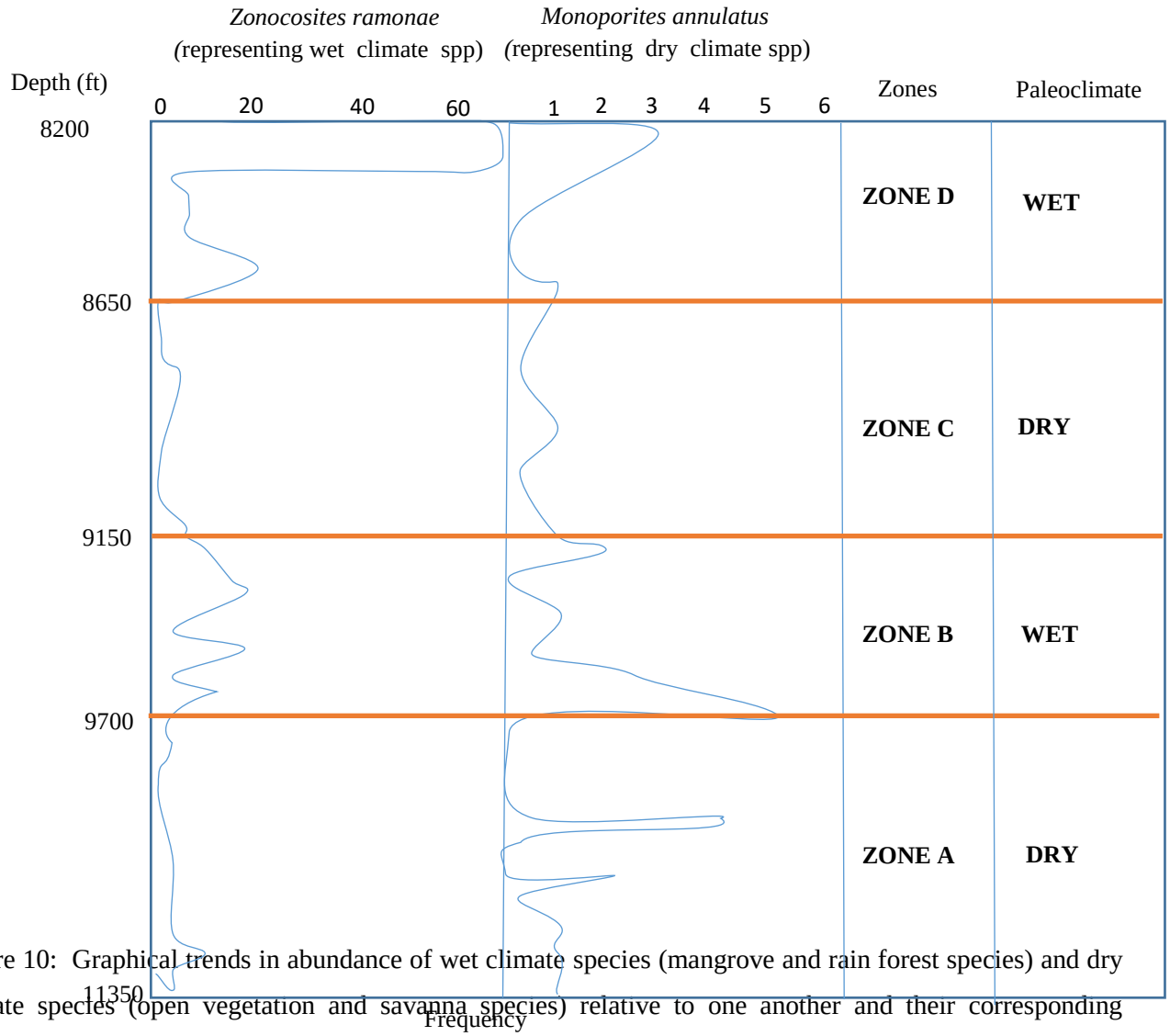

Figure 10: Graphical trends in abundance of wet climate species (mangrove and rain forest species) and dry climate species (open vegetation and savanna species) relative to one another and their corresponding paleoclimatic zones for OM-4 well.

Generally, within this zone, there was prevalence of wet climate, besides the local adverse condition between 8440 ft and 8350 ft of the zone. The presence of rain forest, fresh water swamp species and savanna species suggests that all the vegetation throve in the zone but was dominated by the mangrove swamp forest vegetation.

Paleoclimate of OM-A well

Wet climates

Three zones (A, B and D) showed wet climates. Zone A (11350-10900 ft) shows consistent fluctuation in the percentage of *Zonocostites ramonae* within it. This rise and drop in its percentage maybe due to gradual oscillation in sea level (Ige, 2009). The zone generally shows high percentages of mangrove species (*Zonocostites ramonae)* and presence of few rain forest species such as *Pachydermites diederixi* and *Sapotaceoidaepollenites* sp. denoting wet climate with sea level fluctuations (Germeraad *et al.*, 1968; Morley, 1991, 1995).

Zone B (10900-10630 ft) showed that mangrove swamp forest vegetation flourished at that time. Abundance of *Zonocostites ramonae* suggests an increase in sea level with local fluctuations. Presence of *Pachydermites diederixi* and absence of poaceae species confirms the prevalence of a wetter climate.

Zone D (9900-9580 ft) showed mangrove swamp forest vegetation to be well established as represented by the peak occurences of *Zonocostites ramonae* and *Psilatricolporites crassus*. This suggests that mangrove swamps throve and expanded along the coast (Ige, 2009). This high value of *Zonocostites ramonae* indicates sea level rise. Presence of rain forest taxon in the zone such as *Bombacacidites* sp, *Ctenolophonidites coastatus* and absence of *Cyperacaceaepollis* sp (Figure 3), confirms a prevalent wet and warm climate in the zone (Sowunmi, 1981).

ZONE E (9580-8200 ft)

This zone shows consistent fluctuation in the percentage of *Zonocostites ramonae*, ranging from reduction, at the bottom of the zone to complete absence at the top of the zone. This fluctuation may have resulted from continuous rise and drop in sea level with its rise resulting in the increase in *Zonocosites Ramonae* and vice versa. This fluctuation in sea level results to both wet and dry climatic conditions occurring within the zone. Peaks of Poaceae (*Monoporite annulatus*) which indicates a drier climate (Ige, 2009), was observed in this zone (Figure 11), suggesting the existence of open vegetation. Reduced percentages of *Pachydermites diederixi* and *Sapotaceoidaepollenites* sp confirms this zone has a drier climatic condition compared to the preceding zone.

Dry climate

ZONE C (10630- 9900 ft)

This zone was the only zone marked as dry. This is due to the upward reduction in the occurrence of *Zonocosites ramonae* to its complete absence indicates a fall in sea level (Figure 11). Sparse distribution of

Rain forest fossils such as *Sapotaceoidaepollenites* sp (Morley, 1991) and savanna fossils suggest the prevalence of an adverse climatic condition. The absence of *Podocarpus* sp which suggests a cool and moist climate indicates the presence of a drier climate (Knapp, 1971).

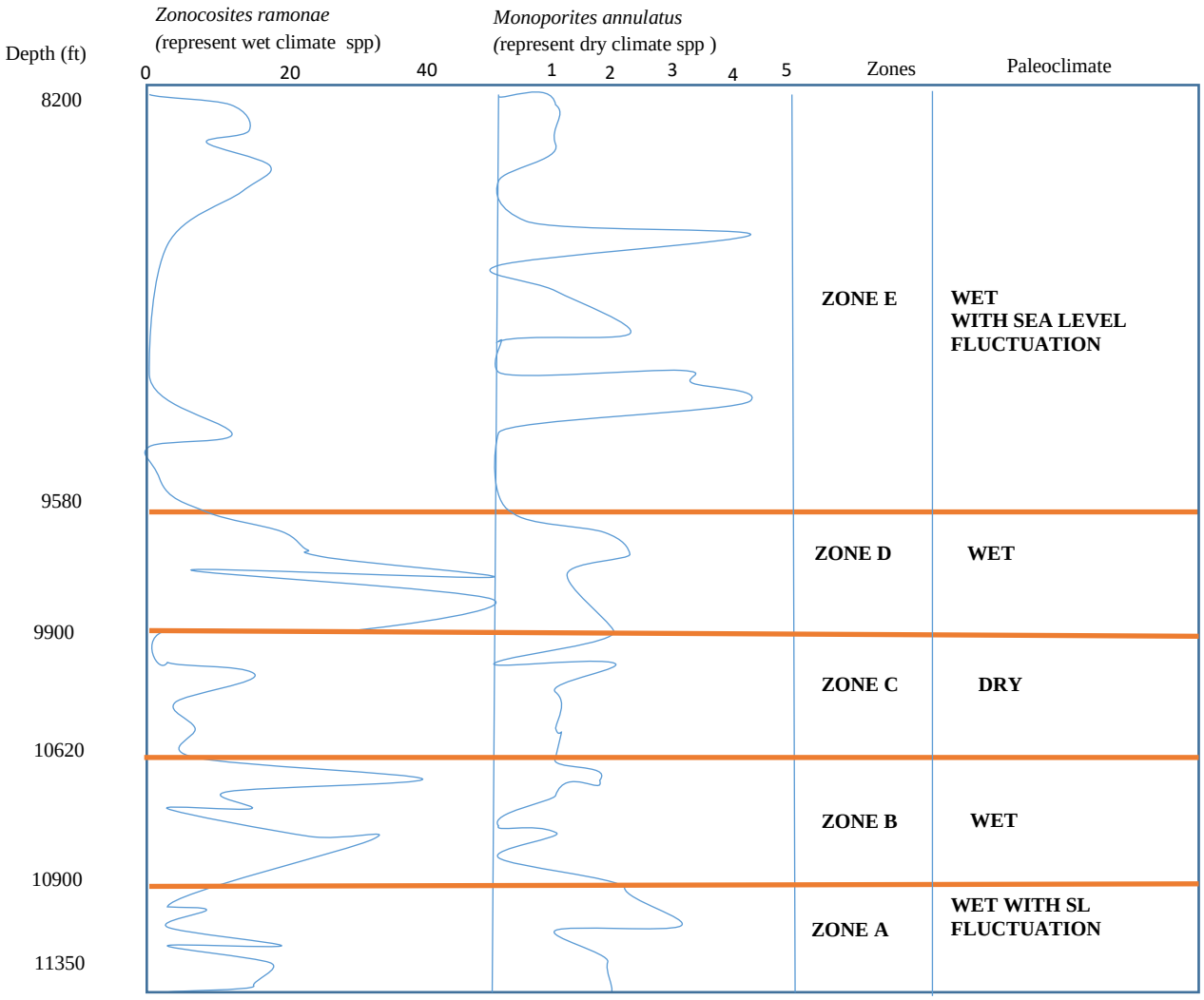

Figure 11: Graphical trends in abundance of *Zonocostites ramonae* representing wet climate species (mangrove and rain forest species) and *Monoporites annulatus* representing dry climate species (open vegetation and savanna species) relative to one another and their corresponding zones for OM-A well.

CONCLUSION

Zero to low PMI values in both wells denotes an environment of deposition with higher terrestrial influences, indicated a paralic environment of deposition. Presence of mangrove swamp species such *Zonocostites ramonae, Acrostichum aureum, Botryococcus braunii* and *Psilatricolporites crassus* in both wells (which are brackish water indicators), as well as the poor yield of nannofossils in both wells confirmed a paralic environment of deposition.

The palynomorph distribution was used to interprete the depositional climatic conditions. On the basis of changes in the vegetation shown in the nature of distribution of the palynomorphs, a total of nine (9) zones were recognized; four zones in OM-4 well and five zones in OM-A well. In OM-4 well, the four zones

established were observed to show a variation between dry and wet climates, with zone A indicating the only dry climate in the zone. Although zones B, C and D indicated wet climates, zone B was wetter than zone C as it showed more mangrove and rainforest species compared to zone C. Zone D showed a predominantly wet climate with peak percentages of mangrove species as well as other rain forest species within the zone. The five zones identified in OM-A well showed a predominantly wet climate in four zones (Zones A, B, D and E) and dry climate in one zone (zone C).

ACKNOWLEDGEMENTS

The authors are grateful to Chevron Nigeria Plc for supplying the ditch cuttings used for this study. The assistance of the staff members of Mosunmolu Nigeria Limited in slide preparation is appreciated.

REFERENCES

Adegoke, O. S., Jan Du Chene, R. E., Agumanu, A. E., & Ajayi, P. O. (1986). Palynology and Age of the Kerri-Kerri Formation, Nigeria. *Revista Espanola De Micropaleontologi*, X(2), 267-285.

Culver, S. J., Farrel, K. M., Mallinson, D. J., Horton, B. P., Willard, D. A., Debra, A.,… Hillier, C. (2011). Micropaleontologic Record of Quartenary Paleoenvironments in Central Albermarle Embayment, North Carolina, U.S.A. *Paleogeography, Paleoclimatology, Paleoecology,* 305, 227-245.

Doust, H., & Omatasola, E. (1990). Niger Delta Divergent/passive Margin Basins. *American Association of Petroleum Geologist Memoir,* 48, 239-248.

Evamy B. D., Haremboure J., Kamerling, P., Knapp, W. A., Molloy, F. A., & Rowlands, P. H. (1978). Hydrocarbon habitat of Tertiary Niger Delta. *American Association of Petroleum Geologists Bulletin,* 62, 1-39.

Germeraad, J. H., Hopping, C. A., & Muller, J. (1968). Palynology of Tertiary sediments from Tropical areas. *Revised Palaeobotany and Palynology*, 6, 189-198.

Groot, J. J., & Groot, C. R. (1966). Marine palynology: Possibilities, Limitations, Problems. *Marine Geology,* 4, 387-395.

Helenes, J., de-Guerra, C., & Vásquez, J. (1998). Palynology and chronostratigraphy of the Upper Cretaceous in the subsurface of the Barinas area, western Venezuela. *The American Association of Petroleum Geologists Bulletin,* 82, 1308-1328.

Ige, O. E. (2009). A Late Tertiary Pollen record from Niger Delta, Nigeria. *International Journal of Botany*, 5, 203-215.

Ige, O. E. (2011). Vegetation and Climatic History of the Late Tertiary Niger Delta, Nigeria, based on Pollen record. *Resources Journal Botany,* 6, 21-30.

Ivanor, D. A., Asharf, A. R., & Mosbrugger, V. (2007). Late Oligocene and Miocene climate and vegetation in the eastern parathys area (Northeast Bulgaria) based on pollen data. *Palaeogeography, Paleaoclimatology, Palaeoecolology, 255*, 342-360.

Knapp, W. A. (1971). A Montane Pollen Species from the Upper Tertiary of the Niger Delta. *Journal of Mining and Geology*, 6, 23-29.

Knox, G. J., & Omatasola, E. (1990). Development of the Cenezoic Niger delta in terms of the Escalator Regression Model and impact on Hydrocarbon Distribution. *Proceedings of KNGMG Symposium Coastal Lowlands, Geology and Geotechnology*, 27-31.

Lana, M. C. (1997). Bacia de Sergipe-Alagoas- uma hipótese de evolução tectono-sedimentar. In G. P. R. Gabaglia & E. J. Milani (Eds.), *Origen e Evolução de Bacias Sedimentares* (pp. 311-332). Portugal, Rio de Janeiro.

Lexine, A. M., & Vergnaud-Grazzini, C. (1993). Evidence of Forest Extensiuon in West Africa since 22000BP: A Pollen record from Eastern Tropical Atlantic. *Quatenary Science Reviews* 12, 203-210.

Morley, R. J. (1991). Tertiary stratigraphic palynology in South East Asia: Current status and new directions. *Geologic Society Malaysia Bulletin*, 28, 1-36.

Ojo, O. J., & Akande, S. O. (2004). Palynological and Palaeoenvironmental studies of Gombe Formation, Gongola Basin, Nigeria. *Journal of Mining and Geology*, 40, 143- 149.

Okada, H., & Bukry, D. (1980). Supplementary modification and introduction of code numbers to the low latitude coccolith biostratigraphic zonation. *Marine Micropaleontology, 5*(2), 321-325.

Oloto, I. N. (1989). Maastrichtian dinoflagellate cyst assemblage from the Nkporo Shale on the Benin flank of the Niger Delta. *Review of Palaeobotany and Palynology*, 57, 173-186.

Petters, S. W., & Edet, J. J. (1996). Shallow Shelf and Anoxic facies in the Late Campananian – Early Maastrichtian of South Western Nigeria. *Geologie de'l Afrique et de L'Atlantique sud*, 219-233.

Schrank, E. (1994). Palynology of the Yessoma Formation in nNrthern Somalie. A study of the Pollen, Spores and Associated Phytoplankton from the Late Cretaceous Palmae Province. *Paleontographica,* B(2), 63 – 112.

Soronnandi-Ononiwu, G. C., Omoboriowo, A. O., Yikarebogha, Y., & Chiaghanam O. I. (2014). Palynology and Paleoenviromental Study Of Akukwa-1 Well, Niger Delta and Anambra Basins, Nigeria. *International Journal of Scientific and Technology Research 3*(2), 297-304.

Sowunmi, M. A. (1981). Aspects of Late Quaternary vegetational changes in West Africa. *Journal of Biogeography*, 8, 457-474.

Traverse, A., & Ginsburg, R. N. (1966). Palynology of the surface sediments of Great Bahama Banks, as related to water movements and sedimentation. *Marine Geology* 4, 417-459.

Van Bergren, P., Janssen, N., Alferink, J., & Kerp, J. (1990). Recognition of the Organic Matter types in Standard Palynological slides. In W. J. J. Fermont & J. W. Weegink (Eds), *Proceedings of the International symposium on Organic Petrology (*pp. 45), Madedel.

EFFECT OF SOME WEATHER ELEMENTS ON HUMAN THERMAL COMFORT IN BIDA, NIGER STATE, NIGERIA

Ojoye, S[1], Adebowale, M[1] Adenle, A.A[1], and Bassey S. S[2]
*[1]Department of Geography, Federal University of Technology, Minna, Niger State
[2]Department of Geography and Regional Planning, University of Uyo, Uyo, Akwa Ibom State, Nigeria
dejyojo@futminna.edu.ng,
ade.ademola@futminna.edu.ng sundaybasi@gmail.com
+2348030589944

Abstract

Atmospheric conditions such as relative humidity, temperature, wind, solar radiation, air pollution and precipitation greatly affect living creatures. There is always a certain limit beyond which these conditions are no longer tolerable by them. Whenever the limit is exceeded, stress, discomfort and disaster, are inevitable. Proper study on the evaluation of human comfort is yet to be given much needed attention in many parts of Nigeria in general and Niger state in particular. The effect of climatic variables on human comfort has become a major concern affecting the well-being of people of the people of Bida. This study examined the trend in temperature and relative humidity in relation with human comfort in Bida. The objectives of the study includes; examination of the trend and variation of temperature and relative humidity in the study area; assessment of the effect of temperature and relative humidity on human comfort and examination of the proportions of stressed and unstressed peoples. To achieve these, Monthly data of Temperature, Relative Humidity and Vapour pressure for eleven years (2004-2014) was obtained from Nigerian Meteorological Agency (NiMET) office, Bida which was used to calculate the Relative Strain Index(*RSI*) and Discomfort Index (DI). The results showed that there is an increase in temperature and relative humidity over the years under study with the values reaching its peak in 2011 and the variation was well marked. The discomfort levelwas well pronounced in the months of March, April, and May while the heat stress becomes moderate in the months of January, July, August, September and December. At all these months, 80% of humans and animals are not comfortable due to hot and humid weather condition. Tree planting is encouraged as it helps in the absorption of Carbon-dioxide and lessen ozone emanations from vehicles. The review of the master plan of Bida is recommended to cater for well-defined environment through adequate spacing of structures that will allow free flow of low level winds that support atmospheric thermal reduction. It was also recommended that education and awareness of daily weather conditions in the area be given utmost priority.

1.0 Introduction

Bida is found in the tropics, where the climate is seasonally damp and very humid. The town experiences consistently high temperatures all year round. Since temperature varies only slightly, rainfall distribution over space and time becomes the single most important factor in differentiating the seasons and climatic regions. Nigeria in general and Bida town in particular have two major seasons, the dry and wet season, the lengths of which vary from north to south.(NFC 2003).The extent to which the thermal environment challenges the body's thermo-regulatory mechanisms is referred to as the environment heat or thermal stress (Ojoye and Yahaya, 2008).

The concept of the heat stress index as well as heat exposure assessment plays a fundamental role in integrating knowledge of human responses to the heat in a way which can be used to specify safe working conditions (Pourmahabadian *et.al.,* 2008). The physiological sensation of human and animal comfort is influenced by heat stress. In hot regions and seasons, discomfort level is raised by heat stress as well as increase in mortality rate among the aged and those who constantly suffer from malnutrition (Okpara, 2007).

There is no particular temperature and humidity condition at which everyone is comfortable. People are comfortable at a range of temperatures and humidity. American Society of Heating, Refrigeration, and Air Conditioning Engineers(ASHRAE, 2015) concluded that there is a range of combined temperatures and humidity that provides comfort to most people, hence most people are comfortable at higher temperatures if there is a lower humidity, as the temperature drops, higher humidity levels are still within the comfort zone..

Atmospheric conditions which include relative humidity, temperature, wind, solar radiation, air pollution and precipitation greatly affect living creatures including human beings. There is always a certain limit beyond which these conditions are no longer tolerable by them. Pauli and Rizzi, (2005) found that whenever this limit is exceeded, disaster and stress is inevitable as hospitals record showed an increase in the number of people admitted during days with high temperature (Pauli and Rizzi, 2006).

According to Ojoye and Yahaya (2008) which affirm that proper study on the evaluation of human comfort is yet to be given much needed attention in many parts of this country. Hence, Bida, Niger state in particular has been so much vulnerable to thermal stress due to prolong and intense daylight heating of the surfaces experienced over the years, longer dry seasons and thermally built up environment that affects peoples comfort.The effect of climatic variables on human comfort has become a major concern affecting the living standards in Bida. This however has made it difficult for people moving from one part of the country to another to acclimatize. It is obvious, that people want to live in thermal environments in which they feel comfortable. If the temperature drops due to changes in diurnal weather variations or season, people want to stay in warmer environments and if it rises, they want to stay in cooler environments accordingly.

Bida town is so vulnerable to stress as a result of variation in climatic elements such as temperature, relative humidity, vapour pressure and so on which has resulted to human discomfort due to prolong

and intense daylight heating of the surface over a long period of time. Exposure to hot and cold conditions can result in a spectrum of outcomes that range from mild discomfort to life-threatening medical conditions. Thermal discomfort is at the mild end of the spectrum and is distinguished from the more severe effects of heat and cold stress by the absence of significant potential for adverse medical outcomes. Most of the people living in this place experience several thermally related difficulties such as skin cancer and diseases outbreak, continuous aridity and small and large scale changes in climate as a result of excessive or insufficient heat received from the Sun. The aim of this study is therefore to assess the effects of some weather elements on the human comfort of the people of Bida town in Niger state. The aim was achieved through the following objectives; examination of the trend and variation in temperature and relative humidity in the area; to assess the effect of temperature and relative humidity on human comfort and to examine the proportion of stressed and unstressed people.

2.0 Review of Literature

The relationship between man and climate is reciprocal in the sense that man responds to variation in climate by insulating buildings, heating and air-conditioning. Man's aim is to be comfortable despite the climate, and this gives rise to the notion of thermal comfort. Thermal comfort has been studied since the start of 20th century, and improvements in building techniques, as well as discoveries in central heating and air conditioning systems have led to improved comfort in indoors, even in the hottest and coldest climates (Brager and de Dear, 1998).

According to ASHRAE, 2004 thermal comfort is a subjective response, and is defined as the 'state of mind that expresses satisfaction with existing environment, making it difficult to assign it a specific numerical value. The state of mind is widely driven by perception and expectation of the occupants. So, the same thermal environment may be perceived differently by different occupants, or different occupants may perceive the same thermal comfort sensation for different thermal environments (de Dear, Brager, 2002). Bangladesh is widely recognized as one of the most climate vulnerable countries in the world (United National Development Programme, 2007). This growing concern about climate change is imposing additional future threat to the

functionality of existing built environment and design of future buildings. Studies shows that, 85% of the rural dwelling units in Bangladesh are very basic shelters, and do not provide adequate protection from wind, rain, flood, and other climatic forces (Hassan, Ullah, Gomes, 2000). There has been no thermal comfort study in rural areas. Previous research has all concentrated on the urban situations. Numerous recent studies on vernacular buildings conclude that bioclimatism is an integral part of vernacular rural architecture and a deciding parameter towards achieving sustainability of modern architecture (Plemenka, 1982).

In Nigeria, recent studies have shown that heat induced mortality resulting from meningitis has increased in the north and middle belt of Nigeria (Greenwood, 1999; Mohammed *et al.*, 2000; Greenwood, 2006). Sawa and Buhari (2011) also predicted that meningitis and measles would increase by 6 and 19 persons per thousand, respectively, for every 1 ◦C increase in temperature in their study on Zaria, in northern Nigeria. Although records of mortality and hospital treatments are fraught with uncertainties in many developing countries (Kwast *et al.*, 1986; Williams and Boren, 2008), we know that urbanization in Nigeria, as in most developing countries, is rapid, and the explosion of urban population has not been matched by a change in social, economic and technological development (United Nations population Fund, 2007; WHO, 2011). Public infrastructure, social and health services have been neglected, and urban planning and zoning have been slow or stagnant in many cases. Consequently, there is the preponderance of large proportion of urban dwellers living and working under conditions that make them vulnerable to effects of climate. These are often poor people, and a sizeable proportion of the Nigerian population is in this category (Adepoju, 1982). Certain urban characteristics, including structure and geometry can affect the pattern of movement and distribution of the air and solar radiation, with important implications for thermal comfort (Jonsson, 2004; Candido *et al.*, 2010; Krueger *et al.*, 2011). Thus, the research attempted to analyse the thermal sensation, and perception of occupants living in naturally ventilated typical rural houses in Bida region of Niger State, Nigeria.

3.0 The Study Area

Bida is an ancient Nupe town, the headquarters of Nupe ethnic group in North -central Nigeria with a population of about 188,181 persons (NPC,2006, 2010). The town lies within latitude 09^0 0380”N to 09^0 06’40”N and longitude 06^0 0’0”E to 06^0 02’42”E. It is about 20km away from tributary of River Kaduna called River Wuya along Mokwa-Bida road and 84km south–east of Minna, Niger state capital (Adebunmi, 2002).

It is located in middle Niger Basin that can also be referred to as Bida basin, also known as the Nupe sandstone formation, which consist of plains with ironstone capped hills or mesas. The scenery is fairly uniform since lithology and dock structure are not greatly variable. An important feature of thescenery is the existence of large areas of Fadama. The northern edge of the town consists of a broken off Plateau. The town is drained by Chiken and Musa rivers, with Landzun which flows right across the heart of the town. The importance of these rivers is that they provide good irrigation opportunities for the inhabitants. Thus they are of both economic and social importance (Abubakar, 2003).

Being an ancient town one could still see the remnant of its former glory (City wall) here and there embracing the wide expanse of Bida. This ancient city wall estimated to measure more than 19 kilometers in circumference. Before it was demolished this wall had ten gates. Bida a traditional once walled city is situated on a gentle slope of the river Landzun which runs through its heart in a given swath of Fadama (Abubakar, 2003).Bida has a mean annual rainfall of 1227mm with the highest mean monthly rainfall in September with 248mm. The rainy season starts on average between the 5th and 15th April and last just over 200 days. The mean monthly temperature is highest in March at 31 and lowest in August (Abubakar, 2003).

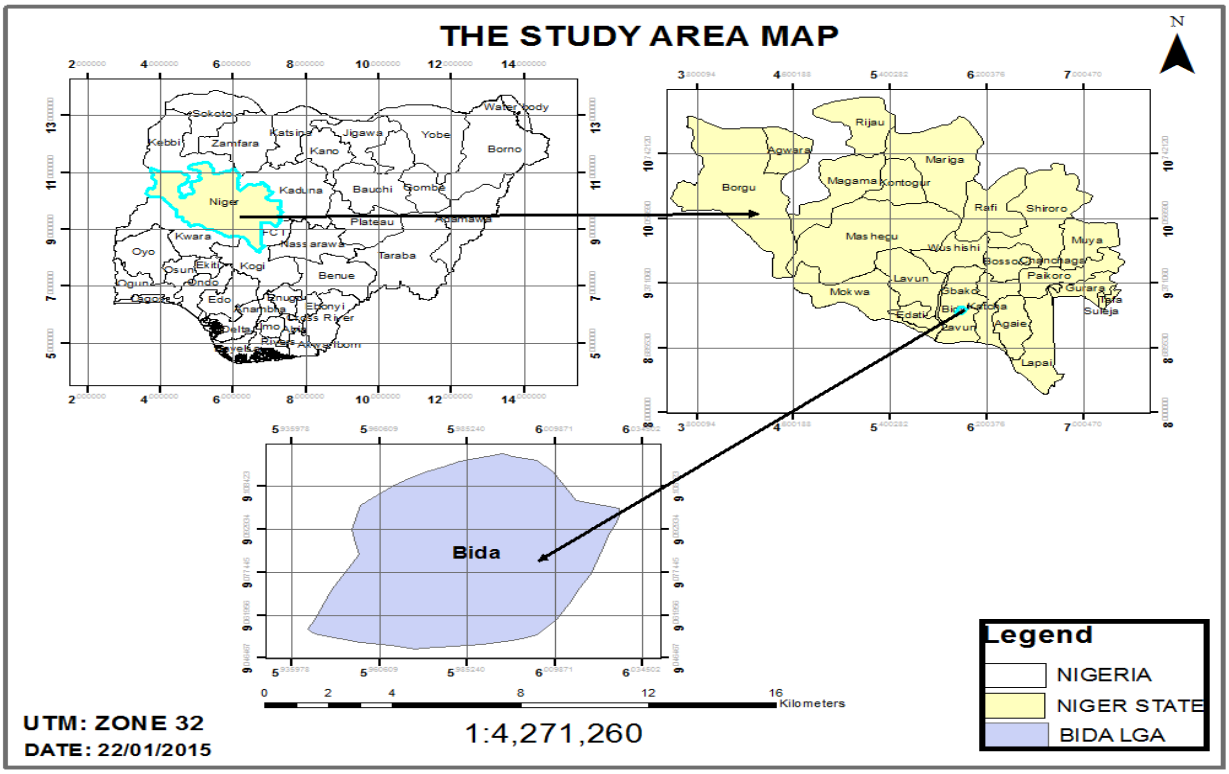

Figure 1, Bida **Source:** Author's work (2015)

4.0 Materials and Methods

The data used for this work were obtained from crucial primary and secondary sources. The primary data used was in form of an extensive personal field work carried out with a view to obtain a clear picture of an inventory condition and present thermal perception and identifying their ways of combating its negative effects.The secondary data used while embarking on this research work include; Weather data, journals, maps, past project works and relevant literatures, thesis etc.The dry and wet bulb temperature, vapour pressure and relative humidity data for a period of eleven years (2004-2014) were obtained from the Nigerian Meteorological Agency, (NiMET) Bida. The mean annual values were computed for the period under consideration.

Methods

Trend analysis and some indices were employed in analyzing the results using suitable charts in order to provide thoroughmonthly mean variations in human comfort of climatic conditions of Bida over the past eleven years (2004 to 2014). Temperature, relative humidity and vapour pressure data were fitted into the various analysis and indices.

Relative Strain Index: was used to examine the proportion of stressed and unstressed people. Relative Strain Index (RSI) is used to determine proportion of persons unstressed or distressed. RSI have been found to be readily suitable for Nigeria(Unger, 1999, Alessandro and de Garin, 2003) RSI take into account the effects of clothing insulation and net radiation. RSI for a "standard man" (i.e. healthy 25-year old male, un-acclimatized to heat, in business clothing) under specified conditions (i.e. internal heat production = 100Wm-^{2}, wind speed = 1ms-^{1} and no direct solar radiation) is given by the following

$$RSI = (t - 21) / (58 - e)1 \text{..} 1$$

Where:

't' is the air temperature (°C)

'e' is the vapour pressure (kPa)

Table 1: The Relative Strain Index (RSI) classification

RSI	Proportion of Persons unstressed/distressed (%)

0.10	100 unstressed
0.20	75 unstressed
0.30	0 unstressed
0.40	75 distressed
0.50	100 distressed

Source: Adapted fromKyle (2008)

Human Thermal Comfort Index (HTCI): was used to assess the effect of temperature and relative humidity on human comfort**.** Bio-climatological indices are standard models used in determining heat stress quality within few kilometers of a given area. The microclimate of any area using human thermal comfort index (HTCI) is characterized with the levels of comfort to which it occurs at a particular time. Models develop for this often provides Physiological Equivalent Temperature (PET) in degrees centigrade. However through several applications, the Discomfort Index (DI) or scale has been successfully long time in use and observed to be one of the most suitable indices for Tropical Climate Zones among the known ones. Thom from the US weather Bureau development (2006) made use of such index in the study of heat stress within confines. The index is based only on two major weather parameters as expressed mathematically in the following equation:

$$DI = 0.4(Td + Tw) + 4.8 \quad \text{.....2}$$

Where $\boldsymbol{DI} = DiscomfortIndex in ℃$ $\boldsymbol{Td} = drybulbtemperature in ℃$

$$\boldsymbol{Tw} = Wetbulbtemperature in ℃$$

Thus, the levels of risk correspond to given heat stress were classified according to the temperature discomfort index ($\boldsymbol{DI}$) values as in Table 2.

Table 2: Classification of thermal environment according to ranges of discomfort Index

S/n	Di classification	Temperature discomfort index (di) in ^{o}c	Heat stress indications

1	No discomfort	DI<23	Safe
2	Under 50% population feels discomfort	23 ≤DI < 25	Heat fatigue is possible with prolonged exposure and activity
3	Over 50% population feels discomfort	25 ≤ DI < 27	Sunstroke and exhaustion are possible with prolonged exposure and activity
4	Most of population suffers discomfort	27 ≤ DI < 29	Sunstroke and exhaustion are at high-risk
5	Everyone feels severe stress	29 ≤ DI > 31	Sunstroke and heat Cramps are possible
6	State of medical emergency	DI ≥ 31	Sunstroke, heatstroke and heat confusion, or delirium is possible

Source: Adapted from Thom (2006)

5.0 Results and Discussion

Trend and Variation in Temperature and Relative Humidity in the Area

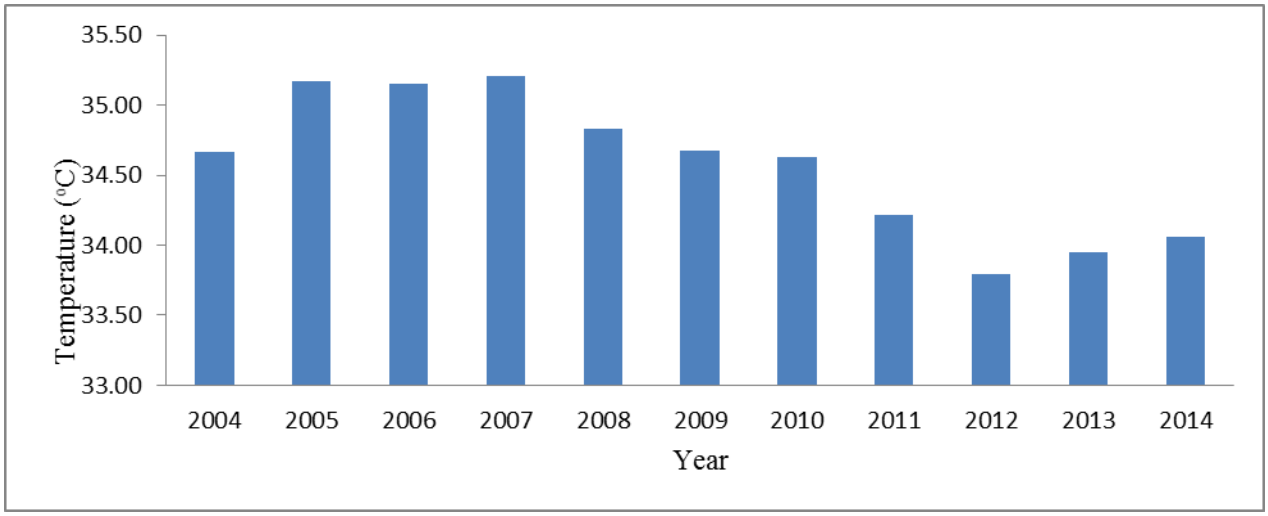

Figure 2: Mean Annual Temperature Distributions in Bida **Source:** NiMET Bida (2015)

Figure 2 indicate the pattern of average annual temperature between the periods of study 2004-2014 the lowest temperature observed was in the year 2012, while the highest temperature observed was in 2007. It is seen that temperature decreased between 2007 and 2012 and later started increasing.

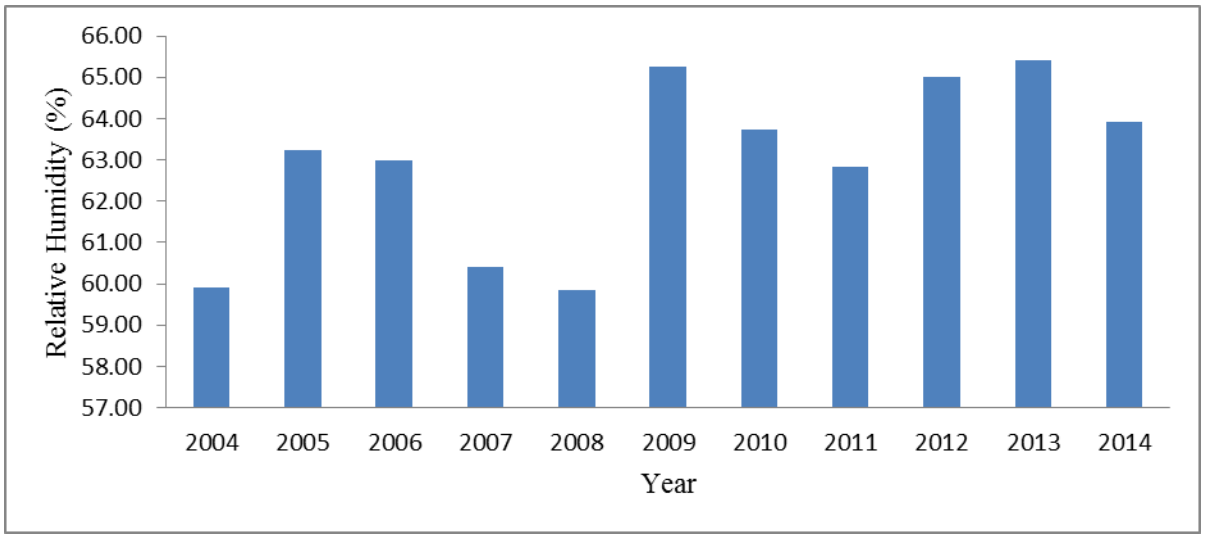

Figure 3: Average Annual Relative humidity in Bida **Source:** NiMET Bida (2015)

Figure 3 reflects the pattern of average annual relative humidity between the periods of study (2004-2014) the lowest relative humidity observed was in the year 2008, while the highest relative humidity observed was in 2013. It is seen that relative humidity decreased between 2005 and 2008 and later increased sharply till 2009 when it started decreasing till the year 2011, before it started increasing again till 2013 when it began to decrease till 2014.

Effect of temperature and relative humidity on human comfort

Table 3: Discomfort Index (DI) January to December (2004 -2014) in Bida

	Discomfort Index $(DI) = 0.4(Td + Tw) + 4.8$											
Years	JAN	FEB	MAR	APR	MAY	JUN	JUL	AUG	SEP	OCT	NOV	**DEC**
2004	27.60	29.60	31.04	30.48	28.00	27.04	26.60	26.00	26.48	27.60	29.88	**27.60**
2005	27.40	31.40	31.88	30.80	28.80	27.28	26.72	26.60	26.96	27.36	28.04	**27.60**
2006	29.08	30.80	31.04	31.24	28.28	27.64	27.16	26.24	26.68	27.80	27.52	**26.84**
2007	27.00	30.08	31.12	30.20	28.84	27.04	26.96	26.32	26.72	27.60	28.24	**27.84**
2008	26.76	29.20	31.36	30.28	29.04	27.52	26.40	26.20	26.44	27.36	27.92	**27.80**
2009	28.12	30.20	31.56	29.60	28.76	27.12	26.96	26.44	26.48	26.88	27.48	**27.32**
2010	27.96	30.48	31.32	31.20	29.20	27.60	26.32	26.28	26.56	27.16	29.40	**26.60**
2011	26.68	29.96	30.92	30.20	28.44	27.16	26.76	26.28	26.48	26.88	27.32	**26.44**
2012	28.16	29.92	30.92	29.60	27.16	26.72	25.84	25.84	25.92	26.92	28.16	**27.44**
2013	28.24	29.68	31.16	29.56	27.72	26.56	25.76	25.84	26.00	27.20	28.20	**27.48**
2014	28.00	29.64	30.68	29.28	27.96	27.20	26.80	26.04	26.20	27.08	28.00	**27.32**
Mean($\bar{x}$)	27.73	30.09	31.18	30.22	28.38	27.17	26.57	26.19	26.45	27.26	28.20	**27.30**

Source: Author's Computation (2015)

The mean monthly analysis of Discomfort Index (DI) for eleven years (2004 - 2014) obtained in Bida is presented in figure 4

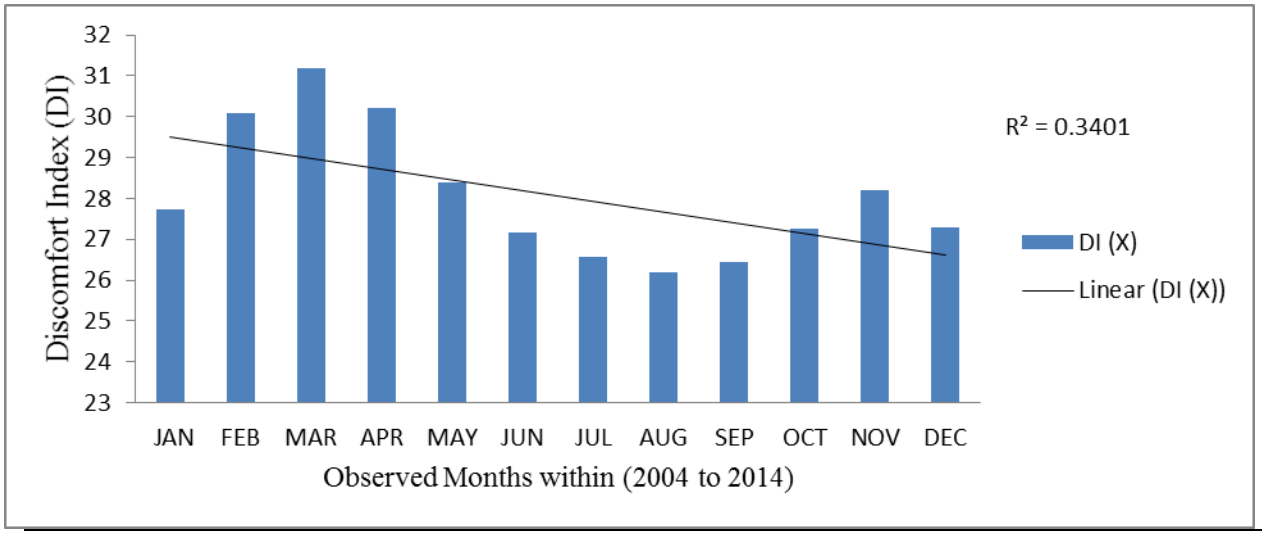

Figure 4: Monthly Mean Variations of Discomfort Index in Bida for the period (2004 - 2014)

Figure 4 shows that generally the environment of Bida, Niger State, human thermal stress increases from January to April and begins to attain maximum comfort through the months of June, July, August, and September, respectively while October, November and December are a little bit environmental harsh. There is a level of significance between the monthly mean of Discomfort Index and the months of the years observed($R^2 = 0.34$). However, the chart reveals what is likely to experience in Bida at any month of staying. Over 50% of population are likely to feel discomfort in the months of August, September and July respectively as their indexes fall between the range ($25 \leq DI < 27$) such that the environment could exposed them to the effects of sunstroke and heat exhaustions with prolong activity resulting into illness with fever, rheumatism, Eczema and often loss of consciousness among other risks are attached While the environmental level of exposure in the

months of June, October, December, January, November, and May (27 ≤ DI < 29) could to be a little bit at high risk compared to the aforementioned months and most of population suffers discomfort. Lastly, the months of February, and April produce the highest environmental discomfort respectively in Bida with Discomfort index of ranges (29 ≤ DI < 31) such that everyone feels severe stress; and the health implications which could be Sunstroke and heat cramps (painful involuntary muscular contraction, mental bar with bent ends for holding masonry). However, the month of March in Bida has discomfort index exceeding (DI ≥ 31) resulting into state of medical emergency for the period of eleven years of case study (2004 to 2014).

The proportion of stressed and unstressed people

The result in table 4 provides the monthly mean variation in proportions to the human thermal percentage of persons unstressed and distressed for the periods of eleven years (2004 to 2014) in Bida.

Table 4: Showing the Relative Strain Index (RSI) result for the months of January to December within (2004 to 2014) in Bida

Relative Strain Index$(RSI) = (t-21) / (58-e)$												
Years	JAN	FEB	MAR	APR	MAY	JUN	JUL	AUG	SEP	OCT	NOV	**DEC**
2004	0.33	0.37	0.42	0.50	0.44	0.39	0.34	0.31	0.35	0.42	0.45	**0.38**
2005	0.30	0.46	0.52	0.52	0.48	0.39	0.36	0.33	0.38	0.41	0.42	**0.37**
2006	0.42	0.46	0.47	0.51	0.45	0.42	0.38	0.32	0.37	0.45	0.37	**0.32**
2007	0.29	0.40	0.44	0.53	0.50	0.39	0.37	0.34	0.38	0.44	0.46	**0.38**
2008	0.28	0.35	0.49	0.50	0.48	0.40	0.34	0.33	0.34	0.41	0.40	**0.37**
2009	0.36	0.45	0.48	0.51	0.48	0.40	0.37	0.35	0.35	0.38	0.39	**0.36**
2010	0.36	0.45	0.45	0.53	0.50	0.41	0.33	0.33	0.34	0.38	0.44	**0.34**
2011	0.30	0.43	0.48	0.47	0.47	0.38	0.35	0.32	0.35	0.38	0.39	**0.31**
2012	0.37	0.43	0.42	0.48	0.39	0.36	0.29	0.28	0.32	0.46	0.45	**0.35**
2013	0.35	0.41	0.51	0.48	0.42	0.35	0.29	0.29	0.33	0.40	0.45	**0.35**
2014	0.36	0.38	0.47	0.48	0.43	0.39	0.35	0.30	0.33	0.40	0.42	**0.35**
Mean($\bar{x}$)	0.34	0.42	0.47	0.50	0.46	0.39	0.34	0.32	0.35	0.41	0.42	**0.35**

Source: Author's computation (2015)

The monthly mean analysis of eleven years RSI obtained through the result for the months of January to December are presented in figure 5 in graphical representation.

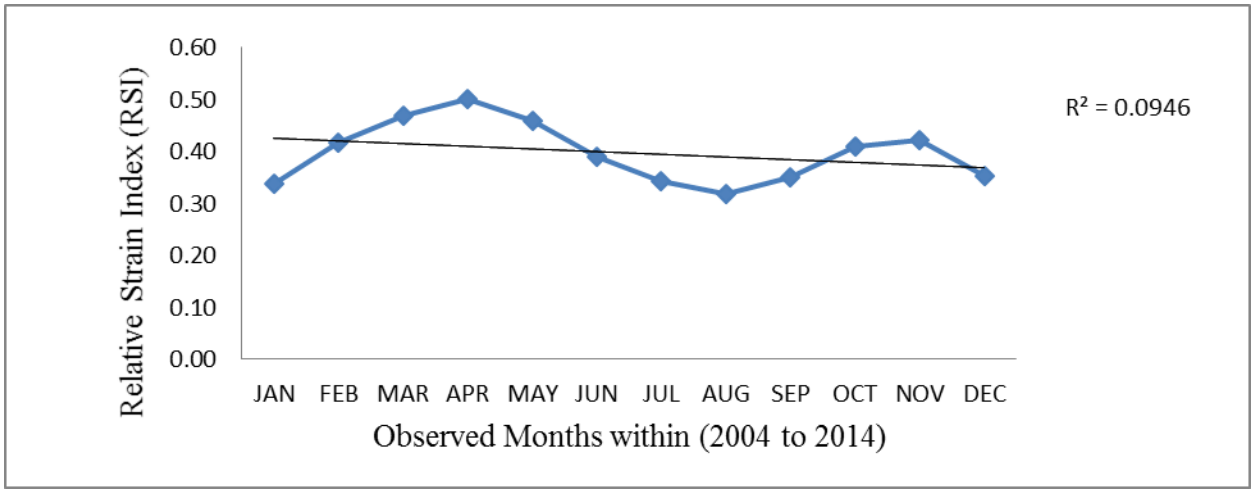

Figure 5: Monthly mean variations of Relative Strain Index (RSI) in Bida (2004 - 2014).

Figure 5 depicts an outcome of the mean monthly variation in human thermal discomfort. The Relative Strain Index (RSI) is proportional to the percentage of person(s) unstressed and distressed for the period of eleven years (2004 - 2014) in Bida Niger State. The chart however, shows a regression between the monthly mean variations in human thermal perception and the Relative Strain Index (RSI) with a high level of significance$R^2 = 0.09$.

The result obtained through the chart is interpreted as follows; note that value above 0.30 stress has started, but since the months of January, July, August, September and December falls within the RSI indication of about 0.34 where value less than 20% of the entire populations in Bida are stressed such could be as a result of decreases in the amount of vapour pressure moderate air temperature. In the months of February, June, October and November there is a greater increase in the degree of human discomfort since the RSI is about 0.40 in which almost 75% of persons were distressed, correlating with an increase in the amount of vapour pressure and air temperature. Furthermore, the months of March, April and May further increase in discomfort proportion to 100% while the months of produced the highest thermal discomfort with a very strong RSI of about 0.50 to which 100% of population in Bida were distressed. It also marks the months with the highest amount of vapour pressure and air temperature over the past eleven years of case study.

6.0 Conclusion and Recommendations

Thermal stress is known to reduce mental and physical efficiency of man. It therefore deserves more close study. Having achieved the aim of this work by adopting suitable Human Thermal Model (HTM) which include the Relative Strain Index (RSI) and Discomfort Index (DI) for heat stress evaluation in an attempt to keep environmental alertness and to offer use in regulating the needed measures to our thermally build up society. The main conclusion is that proportions of human thermal stress/comfort and related diseases in an environment are largely influenced by the degrees of air temperature, relative humidity and the vapour pressure amount at any particular time.

Finally, the bio-meteorological studies of this type are invaluable for societal concerned and support environmental health practitioners. Such studies are prerequisites to analysis both spatial and temporal pattern of diseases that are associated with human thermal comfort such as cerebral spinal meningitis and measles. This type of study will assist in timely intervention to avert and manage the consequence of the outbreaks of such diseases so as to achieve health Sustainable Development Goal (SDG) in the country.

Thermal human comfort can be characterized as a state of mental which communicates fulfillment with the thermal environment. Because of extensive varieties from individual to individual, it is hard to fulfill everybody thermal conditions within the same thermal environment. An average satisfying temperature that is needed to sustain human comfort is between $25 - 32℃$ as per the National Standard given by the Department of Occupational Safety and Health. However, to keep our environment Thermally Disaster Risk Free (TDRF) or reduction, the following recommendations are offered

I. Also education of migrants to new environment example if someone travelling from Lagos State going to Bida, Niger State needs to be educated of the experiences to encounter before going there. This will thus give such a person a psychological boost to face the strange experience with not much shock. Hence impress this productivity, since he has achieved a psychological thermal comfort even before entering a new place; (know the layer of cloth to wear and type of food to take).

II. Planting of Trees is exceptionally prescribed in other to offer advantages, for example, absorbing carbon dioxide, and different contamination. Trees additionally give shade and lessen ozone emanations from vehicles by planting numerous trees, we can cool the city thermal by roughly 10 degrees to 20 degrees, which will help diminishing ozone and helping groups that are for the most part influenced by the impacts of environmental change and micro-climatic thermal stress.

III. The government must review the master plan of Bida to cater for well defined environment through adequate spacing of structures that will allow free flow of low level winds that support atmospheric thermal reduction.

Finally, further projects or studies should be done for various locations so as to be able to predict their thermal state of health risk.

References

Abubakar, *et al* (2003).Physical setting of Niger State.

Adebunmi S.O (2002). Spectral Analysis of the Residual Magnetic Anomalies over the Lower Bida Basin, Nigeria Unpublished M.Tech. Thesis Federal University of Technology Minna.

Adepoju A.(1982). Population growth and urbanization. In *Population and Development*

Alessandro A, de Gar´ın A. (2003). A study on predictability of human physiological strain in Buenos Aires City. Meteorol. Appl. 10: 263–271

ASHRAE Standard 55. Energy Build; 34(6):549–61.

ASHRAE Standards 55-1992 (1992) Thermal environmental conditions for human occupancy.American Society of Heating, Refrigerating and Air-Conditioning Engineers.

Brager GS, de Dear RJ (1998). Thermal adaptation in the built environment: a literature review. Build ;5(1):

Contemporary Climatology. *In Proceedings of COC/IGU Meeting*. 15–20 August. Masaryk University, Brno, Czech Republic,

de Dear RJ, Brager GS (2002). Thermal comfort in naturally ventilated buildings: revisions to Energy Build; 27:83–96.

Ethiopia. *Stud. Fam. Plan.* **1**: 288–301.

Gaborone, Botswana. *Int. J. Climatol.* **24**: 1307–1322. Kalkstein L, Smoyer K. 1993. The impact of climate change on human health: some international implications. *Experientia* **49**: 969–979.

Hassan M, Ullah, M. S., Gomes., C. D (2000). Rural housing in Bangladesh: An inquiry into housing typology, construction technology and indigenous practices, Village Infrastructure to cope with environment, S M Seraj, R L P Hodgson & K I Ahmed (eds). Pp.51-60.

in Nigeria, Orubulaye IO, Oyeneye OY (eds). Nigeria Institute of Social and Economic Research: Ibadan, Nigeria; 178.

in Zaria, northern Nigeria. *Res. J. Appl. Sci. Eng. Technol.* **3**(5): 399–402.
Jonsson P. (2004). Vegetation as an urban climate control in the subtropical city of
Kwast EB, Rochat RW, Kidane–Mariam W (1986). Maternal mortality in Addis Ababa,
Kyle (2008).Thermal environmental condition for human occupancy. Atlanta: American Society of Heating

Kyle W. 1994. The human bioclimate of Hong Kong. In Brazdil R, Kolar M.
National Population Commission (2010).2006 Population and Housing Census of the Federal Republic of Nigeria, Cross River State Priority Tables, Volume 1.

NFC (2003) Nigeria's First National Communication under The United Nations Framework Convention on Climate Change. The Ministry of Environment of the Federal Republic of Nigeria Abuja. Retrieved from http://unfccc.int/resource/docs/natc/nignc1.pdf last accessed 15 august 2015

NPC, 2006.National Population Estimates. National Population Commission, Nigeria.

Ojoye S and Yahaya T.I (2008). Micro climate analysis and its effect on human comfort**:** A case study of Minna Niger State**.** *Journal of Science, Education and Technology* (2) 27-32

Okpara, J. N., Kolawole, S. M., Gbuyiro, S. O. &Okwara, M. O. (2002): Investigating the Effects of Weather Parameters onthe Human Comfort and Discomfort of Inhabitants of Urban Environments of Akure, In Nigeria. *Journal of Nigerian Meteorological Society*, 3(3): 12-18.
Pauli, F. &Rizzi, L. (2005).A Statistical Approach to the Relationship between Temperature and Health of Local Population. EEE Working Paper Series, Number 22.
Pauli, F. and Rizzi, L. (2006), Statistical analysis of temperature impact on daily hospital admissions: analysis of data from Udine, Italy. Environmetrics, 17: 47–64. doi:10.1002/env.749

Plemenka S (1982). Vernacular architecture: a lesson of the past for the future. Energy
RCC web bulletin.

Sawa B, Buhari B. (2011). Temperature variability and outbreak of meningitis and measles
Thom, K., *et.al*. (2006). "*Zonal Weather analysis and Computational strategies"* from the US Weather Bureau development.

UNDP (United National Development Programme, 2007). Country-in-focus: Bangladesh. UNDP
Unger J. (1999). Comparisons of urban and rural bioclimatological conditions in the case of a central–European city. Int. J. Biometeorol. 43: 139–144

United Nations Population Fund, UNFPA (2007). The state of world population 2007: unleashing the potential of urban growth. UNFPA, USA.

DUALITY OF A LINEAR PROGRAM

NYOR N.[1*], RAUF K.[2] AND OMOEHIN J. O.[3]

[1]Department of Mathematics, Federal University of Technology Minna
[2]Department of Mathematics, University of Ilorin
[3]Department of Mathematics, Federal University Lokoja
[*]Corresponding author: ngutornyor@yahoo.com; 08051087384; 07081491344

Abstract.
In this work, an Integer Programming (IP) problem of an Airline Crew Formulation was considered. It was relaxed to a minimization form of Linear Programming (LP) problem. The duality of the LP in minimization form yielded the maximization form of the LP problem. The results of the IP, LP relaxation and its Dual consistently gave the same objective value of 3183, proving the consistency and the characteristic property of duality.

Key words and phrases: Linear programming (LP), Duality, Airline Crew Formulation, LP relaxation, Minimization, Maximization

1. Introduction

Associated with every linear programming problem is a corresponding "dual" linear programming problem. According to Oliveira and Carravila (1997), duality is a unifying theory that develops the relationships between a given linear program and another related linear program stated in terms of variables with this shadow-price interpretation. The dual problem is constructed from the cost and constraints of the original, or "primal," problem. Being an LP problem, the dual can be solved using the simplex method. However, as we shall see, the solution to the dual can also be obtained from the solution of the primal problem, and vice versa (Taha, 2010). Solving an LP problem through its dual may be simpler in certain cases, and also often provides further insight into the nature of the problem. In this study basic properties of duality and an interpretive example of duality is provided. Duality can be used to improve the performance of the simplex algorithm (leading to the so called "primal-dual" algorithm), as well as to develop non-simplex algorithms for solving LP problems

2. Literature Review

Duality of a Linear Programming (LP) Problem
The dual problem is an LP defined directly and systematically from the primal (or original) LP model. The two problems are so closely related that the optimal solution of one problem automatically provides the optimal solution to the other. In most LP treatments, the dual is defined for various forms of the primal depending on the sense of optimization (maximization or minimization), types of constraints ($\geq$, $\leq$ or =), and orientation of the variables (nonnegative or unrestricted). According to Wikipedia.org, in mathematical optimization theory, duality or the duality principle is the principle that optimization problems may be viewed from either of two perspectives, the primal problem or the dual problem. The solution to the dual problem provides a lower bound to the solution of the primal (minimization) problem. This type of treatment is somewhat confusing, and for this reason we offer a *single* definition that automatically subsumes *all* forms of the primal. Our definition of the dual problem requires expressing the primal problem in the *equation form* (all the constraints are equations with
nonnegative right-hand side and all the variables are nonnegative). This requirement is consistent with the format of the simplex starting tableau. Hence, any results obtained from the primal optimal solution will apply directly to the associated dual problem (Shanno, 2012).

Linear programming problems are optimization problems in which the objective function and the constraints are all linear. In the primal problem, the objective function is a linear combination of *n* variables. There are *m*

constraints, each of which places an upper bound on a linear combination of the *n* variables. The goal is to maximize the value of the objective function subject to the constraints. A *solution* is a vector (a list) of *n* values that achieves the maximum value for the objective function.

In the dual problem, the objective function is a linear combination of the *m* values that are the limits in the *m* constraints from the primal problem. There are *n* dual constraints, each of which places a lower bound on a linear combination of *m* dual variables (Vanderbei, 2007).

Relationship between the primal problem and the dual problem

In the linear case, in the primal problem, from each sub-optimal point that satisfies all the constraints, there is a direction or subspace of directions to move that increases the objective function. Moving in any such direction is said to remove slack between the candidate solution and one or more constraints. An *infeasible* value of the candidate solution is one that exceeds one or more of the constraints.

In the dual problem, the dual vector multiplies the constraints that determine the positions of the constraints in the primal. Varying the dual vector in the dual problem is equivalent to revising the upper bounds in the primal problem. The lowest upper bound is sought. That is, the dual vector is minimized in order to remove slack between the candidate positions of the constraints and the actual optimum. An infeasible value of the dual vector is one that is too low. It sets the candidate positions of one or more of the constraints in a position that excludes the actual optimum.

Economic interpretation

If we interpret our primal LP problem as a classical "Resource Allocation" problem, its dual can be interpreted as a "Resource Valuation" problem.

The weak duality lemma

The weak duality lemma states that a feasible solution to either problem yields a bound on the optimal cost of the other problem. The cost in the dual is never above the cost in the primal. In particular, the optimal cost of the dual is less than or equal to the optimal cost of the primal, that is, "maximum<minimum." Hence, if the cost of one of the problems is unbounded, then the other problem has no feasible solution. In other words, if "minimum= - ∞" or "maximum= +∞, then the feasible set in the other problem must be empty (Vanderbei, 2007).

The Duality Theorem

Duality Theorem states that, if the primal problem (either in symmetric orasymmetric form) has an optimal solution, then so does the dual, and the optimal values of their respective objective functions are equal (Vanderbei, 2007).

LP Relaxation

In mathematics, the linear programming relaxation of a 0 - 1 integer program is the problem that arises by replacing the constraint that each variable must be 0 or 1 by a weaker constraint, that each variable belong to the interval [0,1]. The resulting relaxation is a linear program, hence the name. This relaxation technique transforms an NP-hard optimization problem (integer programming) into a related problem that is solvable in polynomial time (linear programming); the solution to the relaxed linear program can be used to gain information about the solution to
the original integer program.

To formulate this as a 0 - 1 integer program, form an indicator variable x_i for each set S_i, which takes the value 1 when S_i belongs to the chosen subfamily and 0 when it does not. Then a valid cover can be described by an assignment of values to the indicator variables satisfying the constraints

$$x_i \in (0, 1),$$

that is, only the specified indicator variable values are allowed. The linear programming relaxation of the set cover problem describes a fractional cover in which the input sets are assigned weights such that the total weight of the sets containing each element is at least one and the total weight of all sets is minimized. The linear programming relaxation of an integer program may be solved using any standard linear programming technique. If the optimal solution to the linear program happens to have all variables either 0 or 1, it will also be an optimal solution to the original integer program. However, this is generally not true, except for some special cases (e.g., problems with totally uni-modular matrix specifications).

In all cases, though, the solution quality of the linear program is at least as good as that of the integer program, because any integer program solution would also be a valid linear program solution. That is, in a maximization problem, the relaxed program has a value greater than or equal to that of the original program, while in a minimization problem such as the set cover problem the relaxed program has a value smaller than or equal to that of the original program. Thus, the relaxation provides an optimistic bound on the integer program's solution (https://en.wikipedia.org).

3. Methodology

Every Primal Problem:

$$\text{Maximize } \sum_{j=1}^{n} c_j x_j$$

$$\text{subject to } \sum_{j=1}^{n} a_{ij} x_j \le b_i \qquad i = 1,2,\ldots,m$$
$$x_j \ge 0 \qquad j = 1,2,\ldots,n$$

Has a dual

$$\text{Minimize } \sum_{i=1}^{m} b_i y_i$$

$$\text{subject to } \sum_{i=1}^{m} y_i a_{ij} \ge c_j \qquad j = 1,2,\ldots,n$$
$$y_i \ge 0 \qquad i = 1,2,\ldots,m$$

The dual in standard form:

$$\text{-Maximize } \sum_{i=1}^{m} -b_i y_i$$

$$\text{subject to } \sum_{i=1}^{m} -a_{ij} y_i \ge c_j \qquad j = 1,2,\ldots,n$$
$$y_i \ge 0 \qquad i = 1,2,\ldots,m$$

4. An Integer Programming Problem

Consider a formulated IP problem as below (Rauf *et al*., 2016):

Minimize $Z = 128x_1 + 181x_2 + 245x_3 + 280x_4 + 384x_5 + 445x_6 + 146x_7 + 210x_8 + 45x_9+349x_{10}+410x_{11}+168x_{12}+203x_{13}+307x_{14}+368x_{15}+82x_{16}+186x_{17}+247x_{18}+ 136x_{19} + 197x_{20} + 132x_{21} + 216x_{22} + 241x_{23} + 210x_{24} + 197x_{25} + 126x_{26} + 217x_{27} + 249x_{28} + 186x_{29} + 281x_{30} + 186x_{31} + 326x_{32} + 301x_{33} + 292x_{34} + 280x_{35} + 154x_{36}$

Subject to:

$$x_1 + x_2 + x_3 + x_4 + x_5 + x_6 + x_{22} \ge 1$$

$$x_7 + x_8 + x_9 + x_{10} + x_{11} + x_{23} \geq 1$$
$$x_{12} + x_{13} + x_{14} + x_{15} + x_{24} \geq 1$$
$$x_{16} + x_{17} + x_{18} + x_{31} + x_{35} \geq 1$$
$$x_{19} + x_{20} + x_{25} + x_{28} + x_{29} \geq 1$$
$$x_{21} \geq 1$$
$$x_2 + x_3 + x_4 + x_5 + x_6 + x_{22} \geq 1$$
$$x_3 + x_4 + x_5 + x_6 + x_8 + x_9 + x_{10} + x_{11} + x_{23} + x_{32} \geq 1$$
$$x_{33} \geq 1$$
$$x_{30} \geq 1$$
$$x_4 + x_5 + x_6 + x_9 + x_{10} + x_{11} + x_{13} + x_{14} + x_{15} \geq 1$$
$$x_{32} \geq 1$$
$$x_5 + x_6 + x_{10} + x_{11} + x_{14} + x_{15} + x_{17} + x_{18} + x_{31} + x_{36} \geq 1$$
$$x_6 + x_{11} + x_{15} + x_{18} + x_{20} + x_{25} + x_{26} + x_{27} + x_{32} + x_{33} + x_{34} \geq 1$$
$$x_1 + x_{22} + x_{23} + x_{35} \geq 1$$
$$x_2 + x_7 + x_{24} + x_{28} \geq 1$$
$$x_3 + x_8 + x_{12} \geq 1$$
$$x_4 + x_9 + x_{13} + x_{16} + x_{29} \geq 1$$
$$x_5 + x_{10} + x_{14} + x_{17} + x_{19} + x_{21} \geq 1$$
$$x_7 + x_{11} + x_{15} + x_{18} + x_{20} + x_{21} + x_{25} \geq 1$$
$$x_{22} + x_{35} \geq 1$$
$$x_{23} \geq 1$$
$$x_2 + x_{30} + x_{35} \geq 1$$
$$x_{28} \geq 1$$
$$x_{32} + x_{33} \geq 1$$
$$x_{35} \geq 1$$
$$x_{30} \geq 1$$
$$x_{34} \geq 1$$
$$x_{29} + x_{36} \geq 1$$
$$x_{27} \geq 1$$
$$x_{26} \geq 1$$
$$x_j = 0 \text{ or } 1 (j = 1 - 31)$$

3. LP Relaxation of Problem Formulation

The Integer Program in section 2 is relaxed to a Linear Program (LP) of the minimization form as below:

Minimize $Z = 128x_1 + 181x_2 + 245x_3 + 280x_4 + 384x_5 + 445x_6 + 146x_7 + 210x_8 + 245x_9 + 349x_{10} + 410x_{11} + 168x_{12} + 203x_{13} + 307x_{14} + 368x_{15} + 82x_{16} + 186x_{17} + 247x_{18} + 136x_{19} + 197x_{20} + 132x_{21} + 216x_{22} + 241x_{23} + 210x_{24} + 197x_{25} + 126x_{26} + 217x_{27} + 249x_{28} + 186x_{29} + 281x_{30} + 186x_{31} + 326x_{32} + 301x_{33} + 292x_{34} + 280x_{35} + 154x_{36}$

Subject to:

$$x_1 + x_2 + x_3 + x_4 + x_5 + x_6 + x_{22} \geq 1$$
$$x_7 + x_8 + x_9 + x_{10} + x_{11} + x_{23} \geq 1$$
$$x_{12} + x_{13} + x_{14} + x_{15} + x_{24} \geq 1$$
$$x_{16} + x_{17} + x_{18} + x_{31} + x_{35} \geq 1$$
$$x_{19} + x_{20} + x_{25} + x_{28} + x_{29} \geq 1$$
$$x_{21} \geq 1$$
$$x_2 + x_3 + x_4 + x_5 + x_6 + x_{22} \geq 1$$
$$x_3 + x_4 + x_5 + x_6 + x_8 + x_9 + x_{10} + x_{11} + x_{23} + x_{32} \geq 1$$
$$x_{33} \geq 1$$
$$x_{30} \geq 1$$
$$x_4 + x_5 + x_6 + x_9 + x_{10} + x_{11} + x_{13} + x_{14} + x_{15} \geq 1$$
$$x_{32} \geq 1$$
$$x_5 + x_6 + x_{10} + x_{11} + x_{14} + x_{15} + x_{17} + x_{18} + x_{31} + x_{36} \geq 1$$

$$x_6 + x_{11} + x_{15} + x_{18} + x_{20} + x_{25} + x_{26} + x_{27} + x_{32} + x_{33} + x_{34} \geq 1$$
$$x_1 + x_{22} + x_{23} + x_{35} \geq 1$$
$$x_2 + x_7 + x_{24} + x_{28} \geq 1$$
$$x_3 + x_8 + x_{12} \geq 1$$
$$x_4 + x_9 + x_{13} + x_{16} + x_{29} \geq 1$$
$$x_5 + x_{10} + x_{14} + x_{17} + x_{19} + x_{21} \geq 1$$
$$x_7 + x_{11} + x_{15} + x_{18} + x_{20} + x_{21} + x_{25} \geq 1$$
$$x_{22} + x_{35} \geq 1$$
$$x_{23} \geq 1$$
$$x_2 + x_{30} + x_{35} \geq 1$$
$$x_{28} \geq 1$$
$$x_{32} + x_{33} \geq 1$$
$$x_{35} \geq 1$$
$$x_{30} \geq 1$$
$$x_{34} \geq 1$$
$$x_{29} + x_{36} \geq 1$$
$$x_{27} \geq 1$$
$$x_{26} \geq 1$$
(Non-negativity Condition) $x_j \geq 0$; (j = 1, …31)

4. Duality of Problem Formulation

The method of solving a standard minimization problem is called dual method. The dual method converts a standard minimization problem into a standard maximization problem. By the theory of duality, a minimization LP problem can be converted to a maximization LP problem. That is, the dual of the primal LP in minimization form is the corresponding maximization LP problem. Hence, the dual LP problem is stated as follows:

Maximize z = w1 + w2 + w3 + w4 + w5 + w6 + w7 + w8 + w9 + w10 + w11 + w12 + w13 +w14 +w15 +w16 +w17 +w18 +w19 +w20 +w21 +w22 +w23 +w24 +w25 +w26 + w27 + w28 + w29 + w30 + w31 + w32 + w33 + w34 + w35 + w36

subject to:

$$w1 + w15 \leq 128$$
$$w1 + w7 + w16 \leq 181$$
$$w1 + w7 + w8 + w17 \leq 245$$
$$w1 + w7 + w8 + w11 + w17 \leq 280$$
$$w1 + w7 + w8 + w11 + w13 + w19 \leq 384$$
$$w1 + w7 + w8 + w11 + w13 + w14 \leq 445$$
$$w2 + w16 + w20 \leq 146$$
$$w2 + w8 + w17 \leq 210$$
$$w2 + w8 + w11 + w18 \leq 245$$
$$w2 + w8 + w11 + w13 + w19 \leq 349$$
$$w2 + w8 + w11 + w13 + w14 + w20 \leq 410$$
$$w3 + w17 \leq 168$$
$$w3 + w11 + w18 \leq 203$$
$$w3 + w11 + w13 + w19 \leq 307$$
$$w3 + w11 + w13 + w14 + w20 \leq 368$$
$$w4 + w18 \leq 82$$
$$w4 + w13 + w20 \leq 186$$
$$w4 + w13 + w14 + w20 \leq 247$$
$$w15 + w19 \leq 136$$
$$w5 + w14 + w20 \leq 197$$
$$w6 + w20 \leq 132$$

$$w1 + w7 + w15 + w21 \leq 216$$
$$w2 + w8 + w15 + w22 \leq 241$$
$$w3 + w16 + w23 \leq 210$$
$$w5 + w14 + w20 \leq 197$$
$$w14 + w31 \leq 126$$
$$w14 + w30 \leq 217$$
$$w5 + w16 + w24 \leq 249$$
$$w5 + w18 + w29 \leq 186$$
$$w10 + w23 + w27 \leq 281$$
$$w4 + w13 + w19 \leq 186$$
$$w8 + w12 + w14 + w25 \leq 326$$
$$w9 + w14 + w25 \leq 301$$
$$w14 + w28 \leq 292$$
$$w4 + w15 + w21 + w23 + w26 \leq 280$$
$$w13 + w29 \leq 154$$
$$w_j \geq 0; (j = 1, \ldots 31)$$

5. Results and Discussion

Using TORA Software, the result of the IP formulation under section 2 yielded the following result:
Objective Value = 3183

$X_{Variables}$ = { 1 for x_5; x_{12}; x_{21}; x_{23}; x_{26}; x_{27}; x_{28}; x_{29}; x_{30}; x_{32}; x_{33}; x_{34}; x_{35}
0 otherwise.

And the LP relaxation in section 3 gives the same result as in IP in section 2 thus:
Objective value = 3183

$X_{Variables}$ = { 1 for x_5; x_{12}; x_{21}; x_{23}; x_{26}; x_{27}; x_{28}; x_{29}; x_{30}; x_{32}; x_{33}; x_{34}; x_{35}
0 otherwise.

This proves that our relaxed problem from IP to LP maintains its characteristic properties. Note that the problem converged at the 50th iteration.

It can be observed from the dual result below that, the objective value of the dual problem, 3183, is the same with that of its primal. This satisfies the principle of duality which states that; when a standard minimization problem and its dual have solutions, then the maximum value of the function is the same as the minimum value of the function (Saravanan, 2011; Robbert, 2007). Note however that the x combinations differ from the primal result and the dual version converged at the 33rd iteration.

$X_{Variables}$ = { 1 for x_1; x_3; x_4; x_7; x_9; x_{10}; x_{11}; x_{12}; x_{13}; x_{16}; x_{17}; x_{18}; x_{19}; x_{20}; x_{21}; x_{22}; x_{24}; x_{26}; x_{28}; x_{29}; x_{30}; x_{31}
0 otherwise

6. Conclusion

Though both primal and dual problems have the same objective function, the dual problem has given flight combinations that look more acceptable. And since it converged faster at the 33rd iteration than it's primal at 50th iteration, We consider the dual result to be better. It is concluded that, this result is optimal.

References

Oliveira J. F. and Carravila M. A. (1997). Duality in Linear Programming. Addison-Wesley, USA

Rauf K., Nyor N., Kanu R. U. and Omolehin J. O. (2016). An Airline Crew Scheduling for Optimality. .International Journal of Mathematics and Computer Science, 11(2016), no. 2, 187–198

Shanno D. (2012). Who Invented the Interior-Point Method? Documenta Mathematica · Extra Volume ISMP (2012) 55–64

Taha H. A. (2010). Operations research: an Introduction. Pearson Prentice Hall, USA.

Vanderbei R. J. (2007). Linear Programming:Duality. Operations Research and Financial Engineering, Princeton University Princeton, http://www.princeton.edu/_rvdb.

www. https://en.wikipedia.org.

MODELING AND ANALYTICAL SIMULATION OF TROPICAL FRUITS DRYING

Mahmood, Hamza; A.A Mohammed

Department of Mathematics,

Federal University of Technology, Minna, Nigeria.

E-mail.: zicohamzy@yahoo.com

Abstract

A mathematical model capable of predicting the dynamic behavior of the dryer during tropical fruits has been presented. The criteria for the existence and uniqueness of solution of the model were established. The equations were decoupled using parameter expansion method and solved analytically using Eigen functions expansion technique. The results obtained revealed that pecklet number, velocity at the exposed surface and air mass flux play important roles in drying.

***Keywords*:** Drying, tropical fruit, simulation, Eigen Function expansion technique, parameter expansion method

INTRODUCTION

In botany, a fruit is the seed-bearing structure in flowering plants (also known as angiosperms) formed from the ovary after flowering. Fruits are the means by which angiosperms disseminate seeds. Edible fruits, in particular, have propagated with the movements of humans and animals in a symbiotic relationship as a means for seed dispersal and nutrition; in fact, humans and many animals have become dependent on fruits as a source of food. Accordingly, fruits account for a substantial fraction of the world's agricultural output, and some (such as the apple and the pomegranate) have acquired extensive cultural and symbolic meanings. (Wikipedia.org, 2017).

Drying is one of the most important operations in chemical processing. Many food products are dried to increase their life, reduce packaging costs and improve the appearance (Mariem and Mabrouk, 2014) .One of the most important methods for industrial food preservation is drying. Many applications of drying have been successfully applied to minimize biochemical, chemical and microbiological deterioration of food products due to the reduction of the moisture content to the level, which allows safe storage over a long period and brings substantial reduction in weight and volume, minimizing packaging, storage and transportation costs (Zielinska and Markowski, 2010).
Drying process plays an important role in the preservation of agricultural products (Waewsak *et al.*, 2006). It enhances the resistance of high humid products against degradation by decreasing their water activity (Doymaz and Pala, 2003., *et al.*, 2008; Simal *et al.*, 2005).
In many agricultural countries, large quantities of food products are dried to improve shelf life, reduce packaging costs, lower weights, enhance appearance, retain original flavor and maintain nutritional value (Baysal *et al.*, 2003., Demir *et al.*, 2007., *et al.*, 2000., Sokhansanj and Jayas, 1987) Different kind of materials are usually submitted to drying. In some cases the aim is to decrease their transportation costs in some others to preserve materials from deterioration (Maria *et al.*, 2010).

Dried fruit is a good source of nutrients and is filled with vitamins and minerals. It is also rich in natural sugar. You can dry a wide variety of fruits, including grapes (sultanas, currants and raisins), apples (sliced), apricots, pears, peaches, figs, dates, plums (prunes) and bananas (wikihow.com, 2017).

Mathematical Formulation

The modeling of the dryer comprises both material and equipment models. The material model determines the drying kinetics and the equipment model determines the changes of the condition of the drying medium with time and space during drying. The material model together with the equipment model constitutes a complete modeling tool for a batch type tunnel dryer, which is capable of predicting the dynamic behavior of the dryer.

To simplify the model, the following assumptions were made;

1. Moisture movement and heat transfer are one dimensional.
2. No chemical reaction takes place during drying i.e. thermal and chemical properties of material, air and moisture are constant within the range of temperatures considered.
3. The material undergoes shrinkage as drying progresses.
4. Drying air is distributed uniformly through the dryer.
5. Thermal properties of moisture and air are constant;
6. The problem is one dimensional and conduction heat transfer within the bed is negligible;
7. The changes in void fraction or bed porosity are negligible;
8. Sample (product) size is uniform;
9. Product is uniformly distributed in the drying chamber.
10. Initial moisture content concentration is assumed to increase lengthwise

The drying material is considered as a thin slab of thickness L = 2b at a uniform initial temperature T_0 and moisture content M_0. The two sides are exposed to an air flow at temperature Ta and relative humidity RH. If it is considered that material surface shrinks at a
Velocity u(x) towards the center of the material sample, the shrinkage effect can be considered as analogous to convective flow. The shrinkage effect appears explicitly in terms of convective velocity in the heat and mass transfer equations.
Following Karim (2005), the material and equipment models are given by the following equations:

Mass transfer equation for material

$$\frac{\partial M}{\partial t} + u\,\frac{\partial M}{\partial x} = D_{eff}\,\frac{\partial^2 M}{\partial x^2} \tag{1}$$

Heat transfer equation for material

$$\frac{\partial T}{\partial t} + u\frac{\partial T}{\partial x} = \alpha\frac{\partial^2 T}{\partial x^2} \tag{2}$$

Mass balance for equipment

$$\varepsilon\rho_a\,\frac{\partial Y}{\partial t} + G_0\,\frac{\partial Y}{\partial z} + = -\rho_s(1-\varepsilon)\frac{\partial M}{\partial t} \tag{3}$$

Energy balance for equipment

$$-G_0 c_{pa}\,\frac{\partial T_a}{\partial z} = \varepsilon\rho_a c_{pa}\,\frac{\partial T_a}{\partial t} - h_{fg}\,\frac{\partial M}{\partial t}\,\rho_s(1-\varepsilon) \tag{4}$$

It is necessary to determine the shrinkage velocity in order to solve the governing equations. This study assumes a linear distribution of shrinkage velocity. Thus at any point in the sample, shrinkage velocity can be obtained from the equation below;

$$\frac{\partial^2 u}{\partial x^2} = 0 \tag{5}$$

The initial and boundary conditions are formulated as;

$$
\left.
\begin{array}{llll}
M(x,0)=M_0\,\dfrac{x}{L}(1-\dfrac{x}{L}), & \dfrac{\partial M}{\partial x}\Big|_{x=0}=0, & -D_{eff}\,\dfrac{\partial M}{\partial x}\Big|_{x=b}+uM\Big|_{x=b}=h_m(M-M_e)\Big|_{x=b} & \\
T(x,0)=T_{0,}, & \dfrac{\partial T}{\partial x}\Big|_{x=0}=0, & (K\dfrac{\partial T}{\partial x}-\rho c_p uT)\Big|_{x=b}=h(T_a-T)\Big|_{x=b}-h_m\rho(M-M_e)h_{fg}\Big|_{x=b} & \\
T_a(z,0)=T_0, & \dfrac{\partial T_a}{\partial z}=0 & or & T_a=T_0 \\
Y(z,0)=Y_0, & Y=Y_0 & or & \dfrac{\partial Y}{\partial z}=0 \\
u(0)=0, & u(b)=u_b &
\end{array}
\right\} \quad (6)
$$

Method of Solution

Non-dimensionalization

Here, we non-dimensionalized equations (1) – (4) using the following dimensionless variables:

$$x'=\frac{x}{b}, \qquad t'=\frac{U}{b}, \qquad \phi=\frac{M}{M_0},$$

$$\theta=\frac{T}{T_0}, \qquad \psi=\frac{T_a}{T_0} \qquad \varphi=\frac{Y}{Y_0}, \qquad u'=\frac{u}{U}, \qquad z'=\frac{z}{L}$$

and we obtain

$$\frac{\partial\phi}{\partial t}+u\frac{\partial\phi}{\partial x}=\frac{1}{P_{em}}\frac{\partial^2\phi}{\partial x^2} \quad (7)$$

$$\frac{\partial\theta}{\partial t}+u\frac{\partial\theta}{\partial x}=\frac{1}{P_e}\frac{\partial^2\theta}{\partial x^2} \quad (8)$$

$$\frac{\partial\psi}{\partial t}+G_1\frac{\partial\psi}{\partial z}=\gamma\frac{\partial\phi}{\partial t} \quad (9)$$

$$\frac{\partial\varphi}{\partial t}+G\frac{\partial\varphi}{\partial z}=-\beta\frac{\partial\phi}{\partial t} \quad (10)$$

With Initial and Boundary conditions

$$\phi(x,0)=x(1-x), \qquad \frac{\partial\phi}{\partial x}\Big|_{x=0}=0, \qquad -a\frac{\partial\phi}{\partial x'}\Big|_{x=1}+u'\phi\Big|_{x=1}-(\phi-c)\Big|_{x=1}=0 \quad (11)$$

$$\theta(x,0)=1, \qquad \frac{\partial\theta}{\partial x}\Big|_{x=0}=0, \qquad a_1\frac{\partial\theta}{\partial x}\Big|_{x=1}-b_1u\theta\Big|_{x=1}-d_1(\varphi-c)\Big|_{x=1}-c_1(\varphi-\psi)\Big|_{x=1}=0 \quad (12)$$

$$\psi(z,0) = 0 \tag{13}$$

$$\varphi(z,0) = 0 \tag{14}$$

Where; $P_{em} = \frac{bU}{D_{eff}}$, $P_e = \frac{bU}{\alpha}$, $G = \frac{bG_0}{\varepsilon\rho_a U}, \beta = \frac{\rho_s(1-\varepsilon)M_0}{\varepsilon\rho_a Y_0}$ $G_1 = \frac{bG_0}{\varepsilon\rho_a UL}$ *and* $\gamma = \frac{h_{fg}\rho_s(1-\varepsilon)M_0}{\varepsilon\rho_a c_{pa} T_0}$

Analytical Solution

Here, we solve equations (7) – (14) using parameter-expanding method (where details can be found in He, 2006) and eigenfunctions expansion method (where details can be found in Myint-U and Debnanth, 1987).

$$let\, 0 \prec \delta \prec\prec 1, G = a\delta,\ G_1 = b\delta, d_1 = e\delta\ and\ c_1 = f\delta$$

Such that

$$\left.\begin{aligned}\phi(x,t) &= \phi_0(x,t) + \delta\phi_1(x,t) + h.o.t\\ \theta(x,t) &= \theta_0(x,t) + \delta\theta_1(x,t) + h.o.t\\ \psi(z,t) &= \psi_0(Z,t) + \delta\psi_1(Z,t) + h.o.t\\ \varphi(z,t) &= \varphi_0(Z,t) + \delta\varphi_1(Z,t) + h.o.t\end{aligned}\right\} \tag{15}$$

for

δ^0 :

$$\frac{\partial\phi_0}{\partial t} = \frac{1}{P_{em}}\frac{\partial^2\phi_0}{\partial x^2} \tag{16}$$

$$\phi_0(x,0) = x(1-x), \qquad \frac{\partial\phi_0}{\partial x}\Big|_{x=0} = 0, \qquad -a\frac{\partial\phi_0}{\partial x}\Big|_{x=1} = 0 \tag{17}$$

for

δ^1 :

$$\frac{\partial\phi_1}{\partial t} + x\frac{\partial\phi_0}{\partial x} = \frac{1}{P_{en}}\frac{\partial^2\phi_1}{\partial x^2} \tag{18}$$

$$\phi_1(x,0) = 0, \qquad \frac{\partial\phi_1}{\partial x}\Big|_{x=0} = 0, \qquad -a\frac{\partial\phi_1}{\partial x}\Big|_{x=1} + bx\phi_0\Big|_{x=1} - e(\phi_0 - c)\Big|_{x=1} = 0 \tag{19}$$

for

δ^0 :

$$\frac{\partial\theta_0}{\partial t} = \frac{1}{P_e}\frac{\partial^2\theta_0}{\partial x^2} \tag{20}$$

$$\theta_0(x,0) = 1, \qquad \frac{\partial\theta_0}{\partial x}\Big|_{x=0}, \qquad a_1\frac{\partial\theta_0}{\partial x}\Big|_{x=1} - d_1(\phi_0 - c)\Big|_{x=1} = 0 \tag{21}$$

for

δ^1 :

$$\frac{\partial \theta_1}{\partial t} + x\frac{\partial \theta_0}{\partial x} = \frac{1}{P_e}\frac{\partial^2 \theta_1}{\partial x^2} \tag{22}$$

$$\theta_1(x,0) = 0, \quad \frac{\partial \theta_1}{\partial x}\Big|_{x=0} = 0, \quad a_1\frac{\partial \theta_1}{\partial x}\Big|_{x=1} + b_1 x\theta_0\Big|_{x=1} - d_1(\phi_1)\Big|_{x=1} - f(\theta_0 - \psi_0)\Big|_{x=1} = 0$$

for

δ^0 :

$$\frac{\partial \psi_0}{\partial t} = \gamma\frac{\partial \phi_0}{\partial t} \tag{23}$$

$$\psi_0(z,0) = 0 \tag{24}$$

for

δ^1 :

$$\frac{\partial \psi_1}{\partial t} + b\frac{\partial \psi_0}{\partial z} = \gamma\frac{\partial \phi_1}{\partial t} \tag{25}$$

$$\psi_1(z,0) = 0 \tag{26}$$

for

δ^0 :

$$\frac{\partial \varphi_0}{\partial t} = -\beta\frac{\partial \phi_0}{\partial t} \tag{27}$$

$$\varphi_0(z,0) = 0 \tag{28}$$

for

δ^1 :

$$\frac{\partial \varphi_1}{\partial t} + a\frac{\partial \varphi_0}{\partial z} = -\beta\frac{\partial \phi_1}{\partial t} \tag{29}$$

$$\varphi(z,0) = 0 \tag{30}$$

Using eigenfunctions expansion method and direct integration, we obtain the solution of equations (16) - (30) as

$$\phi_0(x,t) = \frac{1}{3} + \sum_{n=1}^{\infty} Ae^{-rt}\cos n\pi x \tag{31}$$

$$\phi_1(x,t)=\left(\frac{-2Ae^{-rt}}{n\pi r}+\frac{2xt}{3}-\frac{2Axe^{-rt}}{r}\right)+\frac{1}{2}\left(\begin{array}{l}\frac{b}{a}\left(\frac{1}{3}+\sum_{n=1}^{\infty}Ae^{-rt}\cos n\pi x\right)-\\ \frac{e}{a}\left(\frac{1}{3}+\sum_{n=1}^{\infty}Ae^{-rt}\cos n\pi x-c\right)\end{array}\right)x^2 \quad (32)$$

$$\theta_0(x,t)=\frac{2d_1}{a_1}\left(\frac{t}{3}+\frac{Ae^{-rt}(-1)^n}{r}-ct\right)+2+\frac{d_1}{a_1}\left(\frac{1}{3}+\sum_{n=1}^{\infty}Ae^{-rt}(-1)^n-c\right) \quad (33)$$

$$\psi_0(z,t)=1+\gamma\left(\sum_{n=1}^{\infty}A\cos n\pi x\right)-\gamma\left(\sum_{n=1}^{\infty}Are^{-rt}\cos n\pi x\right) \quad (34)$$

$$\theta_1(x,t)=\begin{pmatrix} \frac{2d_1}{a_1}\left(\frac{t^2}{6}+\frac{A(-1)^n e^{-rt}}{r^2}-\frac{rt^2}{2}\right)+ \\ \frac{d_1}{a_1}\left(\frac{t}{3}+A(-1)^n e^{-rt}-t\right)+ \\ \frac{4d_1}{a_1}\left(\frac{t^2}{6}+\frac{A(-1)^n e^{-rt}}{r^2}-\frac{rt^2}{2}\right) \\ +\frac{2d_1}{a_1}\left(\frac{t}{3}+A(-1)^n e^{-rt}-t\right) \end{pmatrix}+\begin{pmatrix} \frac{b_1}{a_1}\begin{pmatrix} \left(\frac{2d_1}{a_1}\left(\frac{t}{3}+\frac{Ae^{-rt}(-1)^n}{r}-ct\right)\right)+2 \\ + \\ \frac{d_1}{a_1}\left(\frac{1}{3}+\sum_{n=1}^{\infty}Ae^{-rt}(-1)^n-c\right) \end{pmatrix}- \\ \frac{d_1}{a_1}\begin{pmatrix} 2x\left(\frac{-Ae^{-rt}}{n\pi r}+\frac{t}{3}-\frac{Ae^{-rt}}{r}\right)+ \\ \frac{1}{2}\begin{pmatrix} \frac{b}{a}\left(\frac{1}{3}+\sum_{n=1}^{\infty}Ae^{-rt}\cos n\pi x\right) \\ -\frac{e}{a}\left(\frac{1}{3}+\sum_{n=1}^{\infty}Ae^{-rt}\cos n\pi x\right) \end{pmatrix}x^2 \end{pmatrix}- \\ \frac{f}{a_1}\begin{pmatrix} \begin{pmatrix} \frac{2d_1}{a_1}\left(\frac{t}{3}+\frac{Ae^{-rt}(-1)^n}{r}-ct\right)+ \\ 2+ \\ \frac{d_1}{a_1}\left(\frac{1}{3}+\sum_{n=1}^{\infty}Ae^{-rt}(-1)^n-c\right) \end{pmatrix} \\ - \\ 1+\gamma\left(\sum_{n=1}^{\infty}A\cos n\pi x\right) \\ -\gamma\left(\sum_{n=1}^{\infty}Are^{-rt}\cos n\pi x\right) \end{pmatrix} \end{pmatrix}$$

(35)

$$\varphi_0(z,t) = 1 - \beta\left(\sum_{n=1}^{\infty} A\cos n\pi x\right) + \beta\left(\sum_{n=1}^{\infty} Ae^{-rt}\cos n\pi x\right) \tag{36}$$

$$\psi_1(z,t) = \gamma\left(\left(\frac{-2Axe^{-rt}}{n\pi r} + \frac{2Axe^{-rt}}{r} + \frac{2xt}{3}\right) + \left(\sum_{n=1}^{\infty}\frac{Abx^2e^{-rt}}{2ar} + \sum_{n=1}^{\infty}\frac{Arx^2ee^{-rt}}{2a}\right)\right) - \gamma\left(\left(\frac{-2Ax}{n\pi r} - \frac{2Ax}{r}\right) + \left(\sum_{n=1}^{\infty}\frac{Abx^2}{2ar} + \sum_{n=1}^{\infty}\frac{Arx^2e}{2a}\right)\right) \tag{37}$$

$$\varphi_1(z,t) = \beta\left(\left(\frac{2Ax}{r} - \frac{2Ax}{n\pi}\right) + \left(\sum_{n=1}^{\infty}\frac{Abx^2}{2ar} + \sum_{n=1}^{\infty}\frac{Arx^2e}{2a}\right)\right) - \beta\left(\left(\frac{2Axe^{-rt}}{r} - \frac{2Axe^{-rt}}{n\pi} + \frac{2xt}{3}\right) + \left(\sum_{n=1}^{\infty}\frac{Abx^2e^{-rt}}{2ar} + \sum_{n=1}^{\infty}\frac{Arx^2ee^{-rt}}{2a}\right)\right) \tag{38}$$

RESULTS AND DISCUSSION

We solve the systems of coupled nonlinear partial differential equations with the material model determining the drying kinetics and the equipment model determining the changes of the condition of the drying medium with time and space during drying analytically. We solved the equations using Eigen functions expansion technique. Analytical solutions of equations were computed for the following parameter values:
The following figures explain the Moisture content of specimen, Air humidity ratio, Temperature of the air and Temperature of material.
The computations were done using computer symbolic algebraic package MAPLE 16.

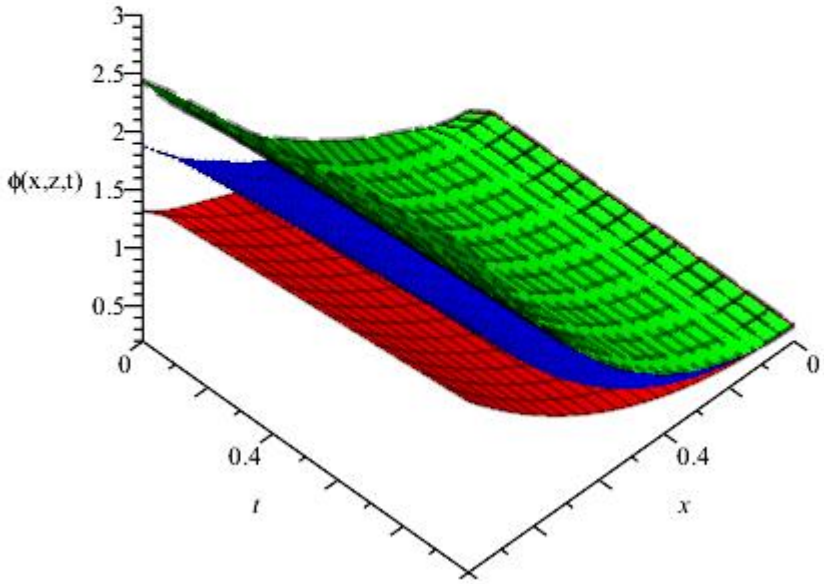

Fig 4.1: Variation of Moisture content of specimen $\phi(x,z,t)$ *with* δ

Figure 4.1 shows the effect of velocity at the exposed surface (δ) on the Moisture content of specimen. It is observed that the Moisture content of specimen increases with distance and decreases with time. Clearly, velocity at the exposed surface enhances Moisture content of specimen.

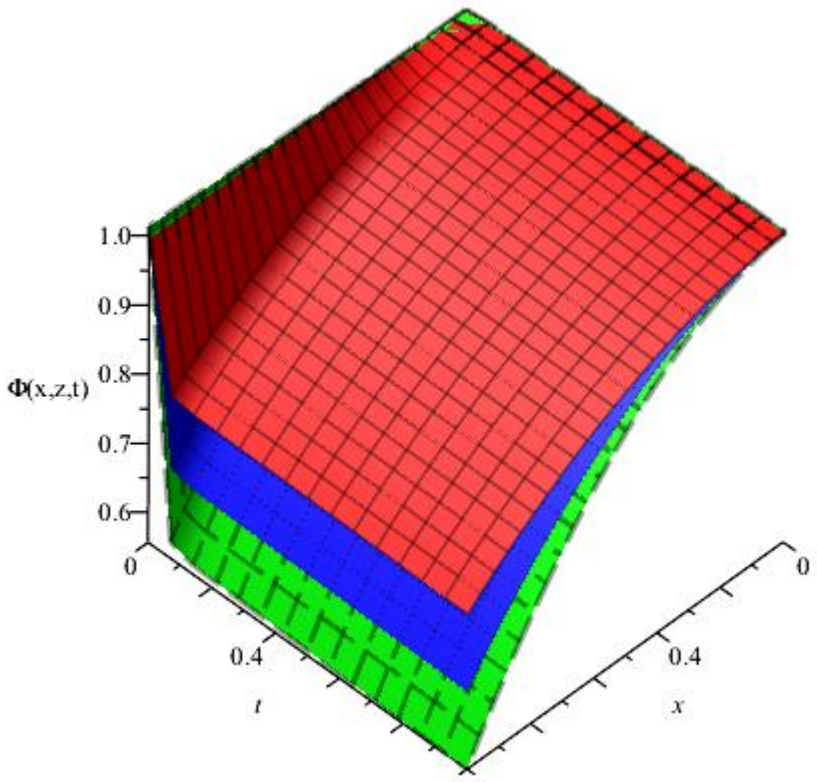

Fig 4.2: Variation of Temperature of the air $\Phi(x,z,t)$ *with* δ

Figure 4.2: Shows the effect of velocity at the exposed surface (δ) on Temperature of the air. It is observed that the Temperature of the air decreases with time and distance. Clearly, the velocity at the exposed surface decreases the Temperature of the air. This is as a result of exchange of heat between the layers

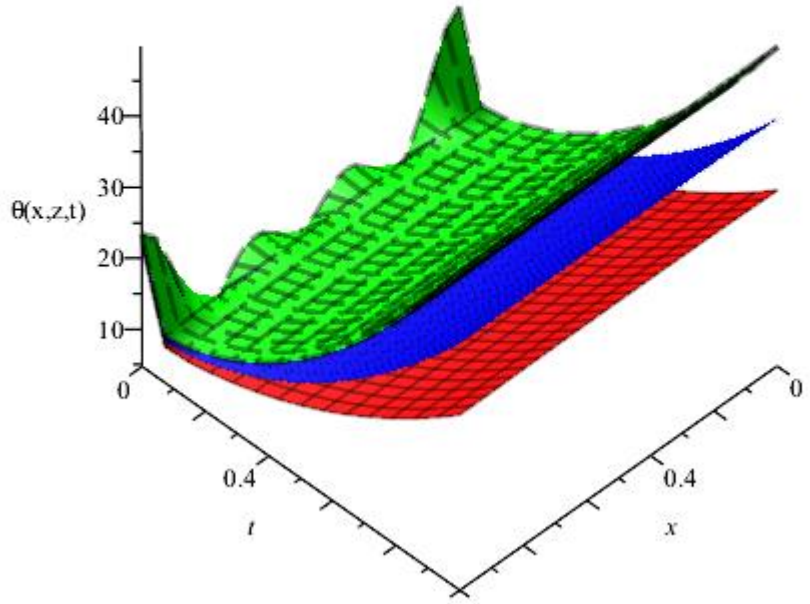

Fig 4.3: Variation of Temperature of material $\theta(x,z,t)$ *with* δ

Figure 4.3 shows the effect of velocity at the exposed surface (δ) on Temperature of material. It is observed that the Temperature of material decreases sharply and later increases time and decreases with distance. Clearly, the velocity at the exposed surface enhances the temperature.

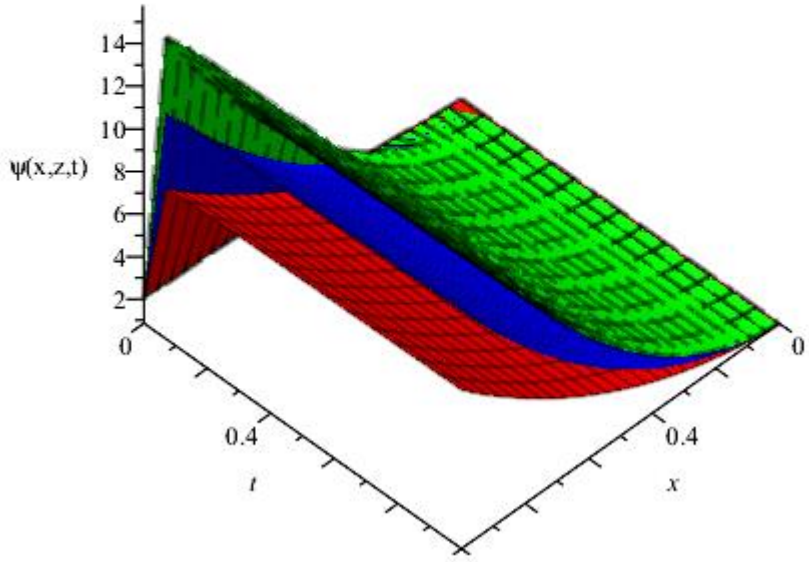

Fig 4.4: Variation of Air humidity ratio $\psi(x,z,t)$ with δ

Figure 4.4: Shows the effect of velocity at the exposed surface (δ) on Air humidity ratio. It is observed that the Air humidity ratio increases with time and distance. Clearly, the velocity at the exposed surface enhances Air humidity ratio.

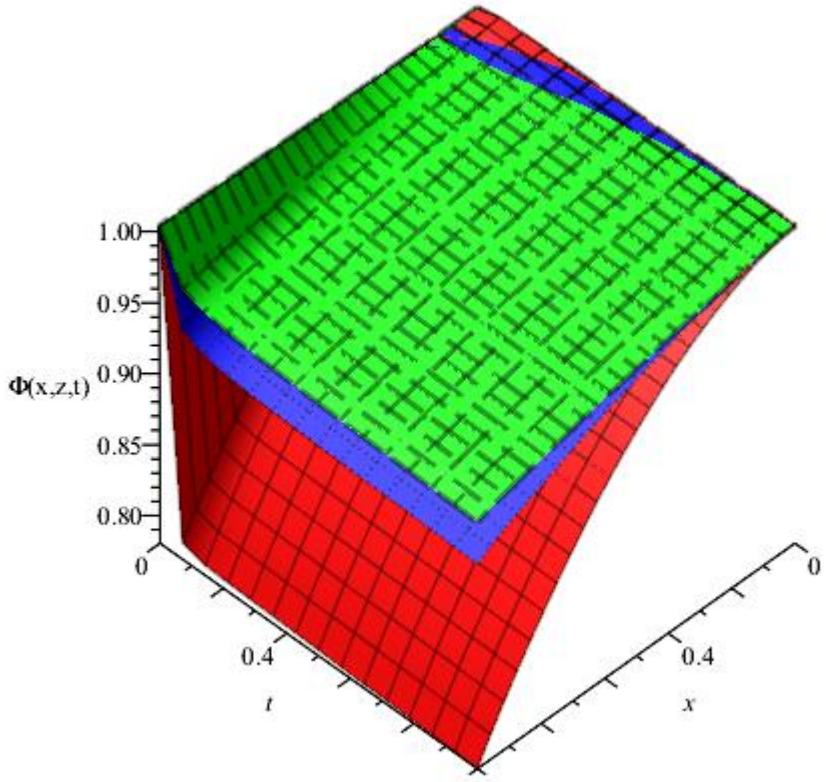

Fig 4.5: Variation of Temperature of the air $\Phi(x,z,t)$ *with* P_{em}

Figure 4.5: Shows the effect of Pecklet mass (P_{em}) on the Air humidity ratio. It is observed that Air humidity ratio decreases with time and decreases with distance. Clearly, Pecklet mass enhances the Air humidity ratio Air

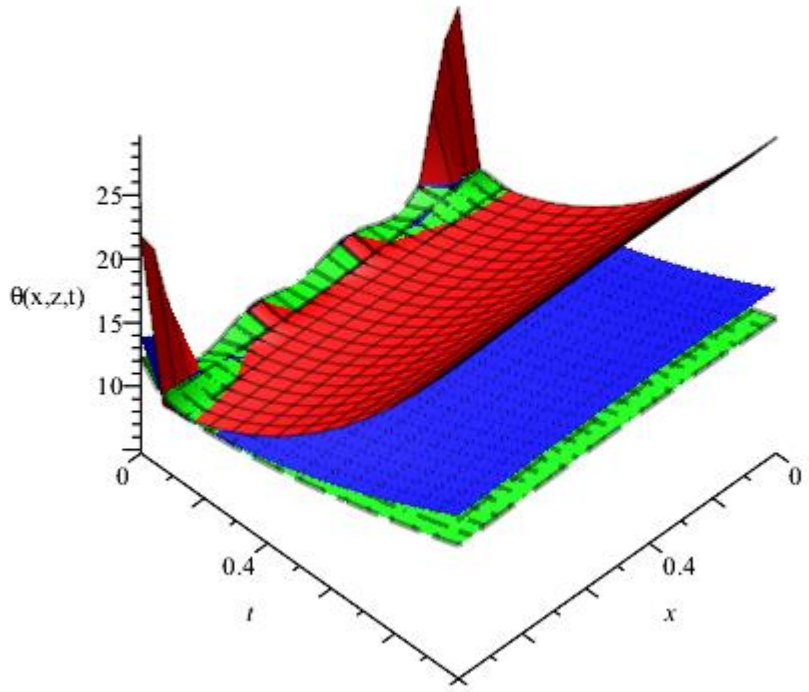

Fig 4.6: Variation of Temperature of material $\theta(x,z,t)$ with P_{em}

Figure 4.6: Shows the effect of Pecklet mass (P_{em}) on the Temperature of material. It is observed the Temperature of material increases with time and decreases with distance. Clearly Pecklet mass enhances Temperature of material

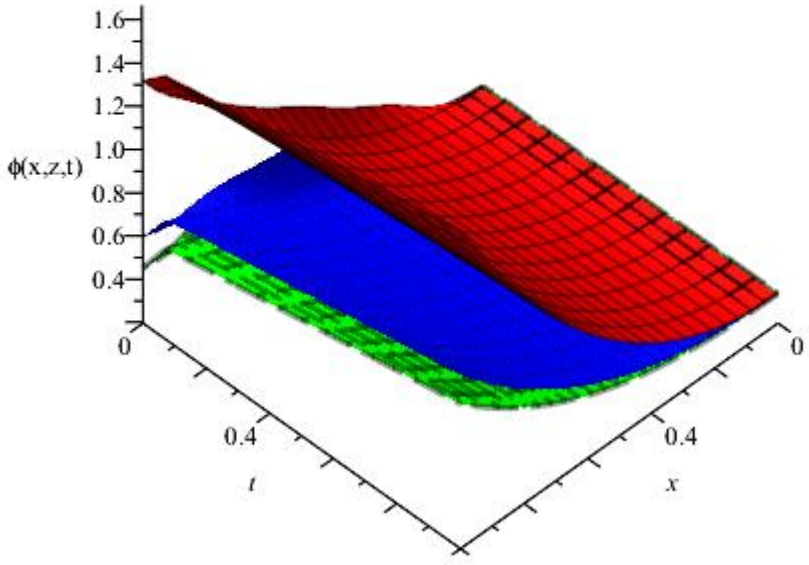

Fig 4.7: Variation of Moisture content of specimen $\phi(x,z,t)$ with G_0

Figure 4.7: Shows the effect of air mass flux (G_0) on Moisture content of specimen. It is observed that Moisture content of specimen increases with time and distance. Clearly, the air mass flux decreases the Moisture content of specimen.

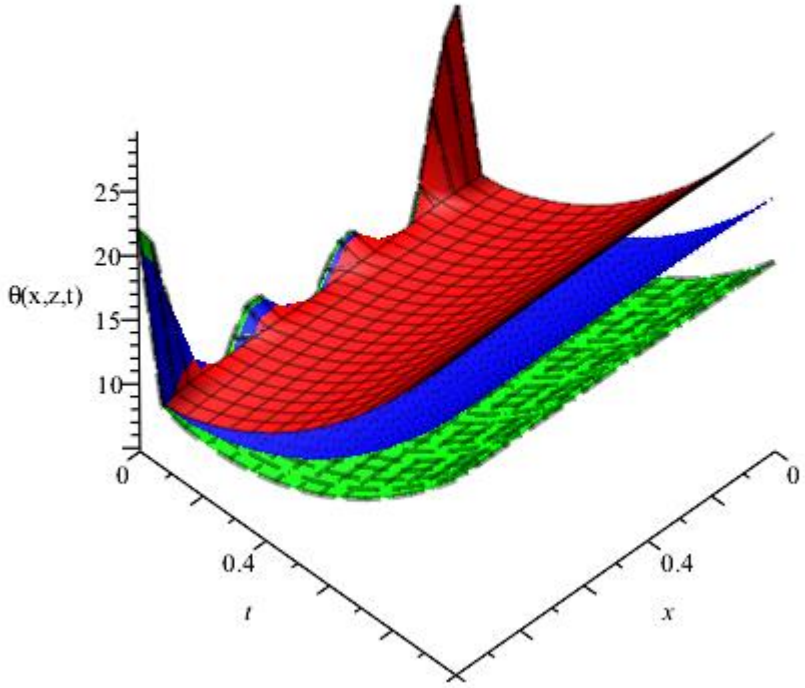

Fig 4.8: Variation of Temperature of material $\theta(x,z,t)$ with G_0

Figure 4.8: Shows the effect of air mass flux (G_0) on Temperature of material. It is observed the Temperature of material increases with time and decreases with distance. Clearly, air mass flux decreases the Temperature of material.

CONCLUSION

In this study, we have formulated mathematical model capable of predicting the dynamic behavior of the dryer during drying. The model derived is capable of predicting the drying rate, temperature and moisture distribution in the material, and temperature and moisture distributions in the drying air along the dryer during drying process. We decoupled the equations using parameter expansion method, the criteria for the existence and uniqueness of solution of the model was established, the results obtained were solved analytically using Eigen functions expansion technique. Finally, graphical summaries of the system responses were provided.

REFERENCES

Abadias, M., Usall, J., Anguera, M., Solson, M. C., & Vinas I. (2008) Microbiological quality of fresh, minimally-processed fruit and vegetables, and sprouts from retail establishments. *International Journal of Food Microbiology*, 123 (1–2) (2008), pp. 121–129

A.G.B. Lima., M.R. Queiroz., and S.A. Nebra, Simultaneous moisture transport and shrinkage during drying solids with ellipsoidal configuration, Chem. Eng. J. 86 (2002) 83–85

Amin, T.G., Shahin, R., & Alireza, K.(2011). Effective Moisture Diffusivity and Activation

Energy of Tomato inThin Layer Dryer during Hot Air Drying. *International Transaction Journal of Engineering, Management* (2011).

Allende A., McEvoy, J.L., Luo, Y., Artes, F., & Wang, C.Y., (2006). Effectiveness of two-sided UV-C treatments in inhibiting natural microflora and extending the shelf-life of minimally processed 'Red Oak Leaf' lettuce Food Microbiology, 23 (3) (2006), pp. 241–249

Azizi, S., & Peyghambarzadeh, S.M., (2010). Effect of Temperature History on Mass Transfer Diffusivity in Convective Drying Process. *World Applied Sciences Journal*, 10(10): 1216- 1224, 2010ISSN 1818-4952

Baysal, T., Ic-ier, F., Ersus., S., & Yildiz, H. (2003). Effects of microwave and infrared drying on the quality of carrot and garlic. *European Food Research Technology*, 218:68-73.

Corbo, M.A., Nobile, D..,Sinigaglia, M. (2006). A novel approach for calculating shelf life of minimally processed vegetable *International Journal of Food Microbiology*, 106 (1) (2006), pp. 69–73

Demir, V., Gunhan, T., & Yagcioglu, A. K.(2007). Mathematical modeling of convection drying of green table olives. *Biosystems Engineering* 98: 47-53.

Donald, G. M.(2012) Department of Food Science University of Guelph Ontario, Canada.

Doymaz, I., & Pala, M. (2003). The thin-layer drying characteristics of corn. *Journal of Food Engineering*, 60 (2): 125-130.

FAO. (2010). Statistical Yearbook 2010 [online]. Available from: http://www.fao.org/ fileadmin/templates/ess/ess_test_folder/Publications/yearbook_2010/c11.xls. Date accessed: 2 January 2012.

FAOSTAT(2011). Available from: http://faostat.fao.org. Date accessed: 18 May 2011.

Froder, H., Martins, C.G., de Souza, K.L.O., Landgraf, M., Franco, B., & Destro, M.T. (2007). Minimally processed vegetable salads: Microbial quality evaluation *Journal of Food Protection*, 70 (5) (2007), pp. 1277–1280.

Giri, S.K. (2007). Microwave-Vacuum Drying of Button Mushroom (Agaricus bisporus), unpublished PhD Thesis, Indian Institute of Technology Kharagpur India.

Giri, S.K., & Prasad, S. Drying kinetics and rehydration characteristics of microwave vacuum and convective hot-air dried mushrooms. *Journal of food Engineering*, 2007,78, 512- 521.

Hadrich, B., Boudhrioua., N., & Kechaou, N.(2008). Drying of Tunisian sardine (Sardinellaaurita) experimental study and three-dimensional transfer modeling of drying kinetics.*Journal of Food Engineering*, 84: 92-100.

Hatamipour, M.S. & Mowla, D. (2002). Shrinkage of carrots during drying in an inert medium fluidized bed. *Journal of Food Engineering*, 55, 247–252.

Harmathy, T.Z.(1998). Simultaneous moisture and heat transfer in porous systems with particular reference to drying, Ind. Eng. Chem. Fundament. 8, 92–103.

Hawlader, M. N. A., Perera, C. O. & Tian, M. 2(006). Properties of modified atmosphere heat pump dried foods. *Journal of Food Engineering*, 74: 392- 401.

Ibrahim, D. (2011). Department of Chemical Engineering, Yildiz Technical University, Esenler, Istanbul, Turkey Scientific Paper, DOI 10.2298/CICEQ101217004D

Karim, M.d .A, & Hawlader, M.N.A. (2005). Mathematical Modelling and Experimental Investigation of Tropical Fruits Drying. *International Journal of Heat and Mass Transfer*, 48,4914–4925.

Lertworasirikul, S., & Tipsuwan, Y. (2008). Moisture content and water activity prediction ofsemi-finished cassava crackers from drying process with artificial neural network. *Journal of Food Engineering*, 84: 65-74.

Litvin, S., Mannheim, C.H., & Miltz, J. (1998).Dehydration of Carrots by a Combination of Freeze Drying, Microwave Heating and Air or Vacuum Drying. *Journal of Food Engineering*, 36, 103- 111

Maria, A., Stefano C., Vincenza C., & Gabriele I.(2010). Transport Phenomena Modeling during Drying of Shrinking Materials. *20th European Symposium on Computer Aided Process Engineering* – ESCAPE20 (2010).

Maskan, M. (2001). Kinetics of color change of kiwifruits during hot air and microwave drying. *Journal of Food Engineering* 48: 169-175.

Mayor, L., & Sereno A.M. (2004). Modelling Shrinkage during Convective Drying of Food Materials. *Journal of Food Engineering*, 61 373–386.
Munde, A.V., Agrawal, Y.C., & Shrikande, V.J. (1988).Process development for multistage dehydration of onion flakes. *Journal of Agricultural Engineering*, 25 (1), 19-24.
Nicoleti, J. F., Telis-Romero, J., & Telis, V. R. N. (2001). Air-drying of fresh and osmotically pretreated pineapple slices: fixed air temperature versus fixed temperature drying kinetics.Drying Technology 19: 2175-2191.
Parish, M.E., Beuchat, L.R., Suslow, T.V., Harris, L.J., Garret, E.H., & Farber, J.N.(2003). Methods to reduce/eliminate pathogens from fresh and fresh-cut produce. *Comprehensive Reviews in Food Science and Food Safety*, 2 (2003), pp. 161–173
Paull, R.E., & Duarte, O. (2011). Tropical Fruits (2nd ed.). *CAB International, London*, UK. pp. 1-10.
Pimentel D. (2011). Food for thought: a review of the role of energy in current and evolving agriculture. *Critical Reviews in Plant Sciences* 30:35-44.
Ragaert, P., Verbeke, W., Devlieghere, F., & Debevere, J., (2004). Consumer perception and choice of minimally processed vegetables and packaged fruits Food Quality and Preference, 15 (3) (2004), pp. 259–270
Rayaguru, K., & Routray, W. (2012). Mathematical modeling of thin layer drying kinetics of stone apple slices. *International Food Research Journal* 19(4): 1503-1510 ()
Sachin, V. J., Chung L. L., & Arun S. M. Drying of Foods,Vegetables and Fruits Volume 2 ISBN: 978-981-08-7985-3.
Sana, B. M., & Salah., B. M. (2014). Drying Characteristics of Tomato Slices and Mathematical Modeling. *International Journal of Energy Engineering*, 4(2A): 17-24.
Singh, G.D., Sharma, R., Bawa, A.S., & Saxena, D.C. (2008). Drying and rehydration characteristics of water chestnut (Trapa natans) as a function of drying air temperature. *Journal of Food Engineering*, 87: 213-221
Simal, S., Femenía, A., Llull, P. & Rosselló, C. (2000). Dehydration of aloe Vera: Simulation of drying curves and evaluation of functional properties. *Journal of Food Engineering*, 43:109-114.
Sitesh, K.P., Subodh., D., & Richa, S.(2015). Review of Mathematical Modeling of Thin Layer drying process. ISSN (print): 2393-8374, (online): 2394-0697, Volume-2, Issue- 11, 2015.
Shi, Q., Xue, C., Zhao, Y., Li, Z. & Wang, X. (2008). Drying characteristics of horse mackerel(Trachurus japonicus) dried in a heat pump dehumidifier. *Journal of Food Engineering*, 84:12-20.
Sokhansanj, S., & Jayas, D.S. (1995). Drying of foodstuffs. Handbook of industrial drying. 2nd edition. Edited by Mujumdar, A.S. Marcel Dekker, Inc. NY.
Su, L.J., & Arab, L.(2006). Salad and raw vegetable consumption and nutritional status in the adult US population: Results from the Third National Health and Nutrition Examination Survey *Journal of the American Dietetic Association*, 106 (9) (2006), pp. 1394–1404
Tournas, V.H. (2005). Moulds and yeasts in fresh and minimally processed vegetables, and sprouts *International Journal of Food Microbiology*, 99 (1) (2005), pp. 71–77
Turner, I., & Mujumdar, A.S., (1997).Mathematical Modelling and Numerical Techniques in Drying Technology, MarcelDekker Inc., New York.
Wankhade, P.K., Sapkal, R.S., & Sapkal, V.S.(1998). Drying characteristics of Okra Slices using different drying methods by Comparative Evaluation ISBN: 978-988-19252-4-4.
Warriner, K. (2005). Pathogens in vegetables W. Jongen (Ed.), Improving the safety of fresh fruit and vegetables, Wood head Publishing limited and CRC Press, Cambridge. pp. 3–43
Yaldýz, O., & Ertekýn, C. (2001). Thin layer solar drying of some vegetables. *Drying Technology* 19: 583–596.
Yaldiz, O., Ertekin, C., & Uzun, H.I. (2001). Mathematical Modeling of Thin layer Solar drying of Sultana Grapes. Energy 26(5): 457-465.
Zielinska, M., & Markowski, M. (2010). Air drying characteristics and Effective moisture diffusivity of carrots. *Chemical Engineering Process*, 49: 212–218
http://bijlmakers.com/agriculture/tropical-fruits/
http://www.wisegeek.org/what-is-a-tropical-fruit.htm
https://en.wikipedia.org/wiki/Dried_fruit
http://nchfp.uga.edu/publications/uga/uga_dry_fruit.pdf

https://en.wikipedia.org/wiki/Simulation
http://www.fruitsinfo.com/exotic-fruits.php

EFFECT OF GREEN SPACES ON URBAN HEAT DISTRIBUTION IN BWARI AND ABUJA MUNICIPAL AREA COUNCILS OF THE FEDERAL CAPITAL TERRITORY OF NIGERIA

Odekunle M. O.[1]*, Olusegun S. S.[1],.Adenle A. A[1], Ojoye S.[1], Sule I.[1]and Saidu S[1]
[1]Department of Geography, Federal University of Technology, Minna, Nigeria
[1]odemary@futminna.edu.ng; +2348035957159
*Corresponding author

ABSTRACT

Urban Heat Distribution (UHD) is considered as one of the major problems in the 21st century posed to human beings as a result of industrialization and urbanization, though they tend to improve our material lives and comfort in some ways. Urbanization has resulted in alterations in spatial patterns of urban land use/land cover change; leading to decreases in green spaces. It is necessary to assess the role of green spaces on heat distribution in fast growing cities like Abuja. Developed countries have invested huge resources in developing green spaces as part of the best practices in mitigating urban heat, purifying the air, among others. This study analyzed the effects of green spaces in urban heat distribution (UHD) in FCT, Abuja, Nigeria. The urban temperature was estimated from Landsat Operational Land Imager (OLI) 2015 imagery and *in situ* data. ArcGIS 10.3 was used to generate Normalized Difference Vegetation Index (NDVI) and thermal maps of the study area. Results from the analysis of the thermal band of the satellite images and the *in situ* data revealed that differences in vegetation distribution caused differences in temperature variation. The ratio of temperature between urban heat area and green space areas increased rapidly with increasing distances from the green space boundaries. A comparison of temperature of some selected green areas and non-green areas showed marked differences. The three arms zone, a non-green area had a temperature4.2°C higher than National Arboretum, a green area. Louga Road (non-green area) had a temperature 4.47°C higher than Lobito Crescent Park. Thus green areas had relatively lower temperatures than built up areas and bare sources.This shows the important role played by green spaces in mitigating urban heat in urban central areas. The study also utilized Effective Temperature (ET) in calculating the Human Thermal Comfort Index in the study area to further buttress the mitigating effects of green spaces on urban heat distribution.

Keywords: Green Spaces, Urban Heat Distribution, Effect, Effective Temperature

1.0 Introduction

Increased replacement of the natural green area with urbanised areas has led to significant changes in the local weather conditions. Due to the economic demands, urban populations are constantly growing in size and complexity because more people are migrating from the rural areas to the urban centres. Earlier studies by Akbari (2011), Elsayed (2009), Giannaros and Melas (2012), Senanayake*et al.* (2004) have revealed that the temperature distribution in the urban areas is notably higher than its neighbouring suburban areas. The human induced heat released from vehicles, power plants, air conditioners and other heat sources, dramatic removal of the vegetation cover and increasing of impervious surfaces are major contributors to the formation of Urban Heat Distribution (UHD) (Memon*et al.*, 2008 and Senanayake*et al.*, 2013).

The concept of including green spaces in urban planning is an important feature in the history of urban planning (MacHarg, 1971). Proper understanding of urban heat distribution is important for a variety of reasons. The

radiation absorbed warms the ambient air; increasing the low level stability and consequently preventing the pollution dispersal which results in an increase in pollution concentration. The urban heat distribution adds to the development and self-sustenance of a 'dust-dome' and a 'haze hood' of contaminating particles. It also results in setting up the recirculation of pollutants thus making the pollution problems more serious. With the increasing emphasis on planning for healthier and comfortable physical environments in cities, the need to recognise the role of cities in contributing to and meeting the challenges posed by climate change has become greater. The very presence of a city affects the local climate and as the city changes, so does, its climate. The modified climate adds to the city residents' discomfort and even ill-health (Devi, 2003).

Studies on adequate environmental preferences specifically this kind on the green space interaction with heat distribution are largely conducted in developed countries, but rarely in developing countries. Thus, the main goal of this paper is to understand the effect of urban green spaces on urban heat distribution in developing Nigeria, taking the city of Abuja as a case study. In a capital city, like Abuja, vegetation is crucial for reducing heat islands and creating shade. The benefits are more obvious when trees are abundant and when their canopies are large. It is believed that in Abuja, the temperature on the environment will not be so high if there are patches of trees that are abundant and large. Also, it has been noted that connected and complex shapes of tree canopy are usually perceived as natural landscapes (Lee *et al.*, 2008). These structures are often favoured because they create the feeling of being close to nature and away from the built environment, and thus bring a restorative experience. The study focuses on determining the effect of green spaces on urban heat distribution in the city of Abuja, Nigeria, taking into cognisance the importance of green spaces, and the effect of urban heat distribution on life and environment. The study purpose include to(1) compare heat distribution effect from Green spaces and non-green from satellite images (2)compare heat distribution effect from Green spaces and non-green from Field survey (3) examine the effects of the heat generated the likely comfort of the area.

1.1 Study Area

Abuja is the capital city of Nigeria; it is located in the centre of Nigeria, within the Federal Capital Territory (FCT). The study area covers 275 sq miles (713KM^2), with a population density of 1,235,880 and lies on latitude 8^0 25'N & 9^0 25'N and longitude 6^0 45'E & 7^0 45'E(Figure 1). Abuja is a planned city, and was built mainly in the 1980s. It officially became Nigeria's capital on 12 December 1991, replacing Lagos, though Lagos remains the country's most populous city. Abuja's geography is defined by Aso Rock, a 400-metre monolith left by water erosion. The Presidential Complex, National Assembly, Supreme Court and much of the city extend to the south of the rock. Zuma Rock, a 792-metre monolith, lies just north of the city on the road to Kaduna State.

Abuja, under Köppen climate classification features a tropical wet and dry climate. The FCT experiences three weather conditions annually. This includes a warm, humid rainy season and a blistering dry season. In between the two, there is a brief interlude of harmattan occasioned by the northeast trade wind, with the main feature of dust haze and dryness. The rainy season begins from April and ends in October, when daytime temperatures reach 28 °C (82.4 °F) to 30 °C (86.0 °F) and nighttimes low hover around 22°C (71.6 °F) to 23 °C (73.4 °F). In the dry season, daytime temperatures can soar as high as 40 °C (104.0 °F) and night-time temperatures can dip to 12 °C (53.6 °F). Even the chilliest nights can be followed by daytime temperatures well above 30 °C (86.0 °F). The high altitudes and undulating terrain of the FCT act as a moderating influence on the weather of the territory. Rainfall in the FCT reflects the territory's location on the windward side of the Jos Plateau and the zone of rising air masses with the city receiving frequent rainfall during the rainy season from March to November every year.

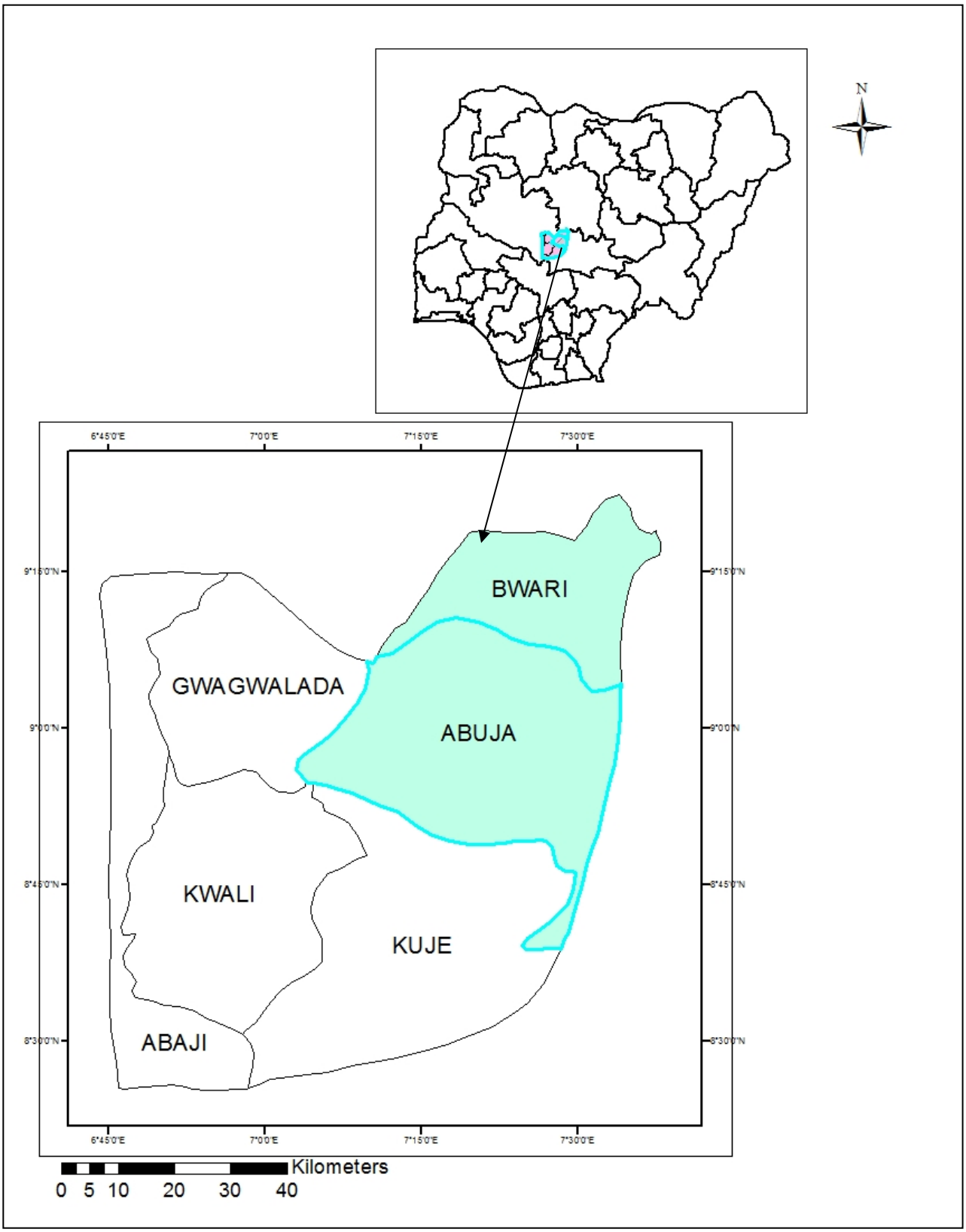

Figure1 Nigeria showing the Study Area Source: Author's Compilation (2017)

2.0 Literature Review

2.1 Urban Heat Distribution

Adinna*et al*. (2009) evaluated the impact of urban heat island effect in the Enugu city of Nigeria and suggested adaptive measures to keep the UHD under control in the city. The study concluded that the use of high dense green vegetation, low absorptive roofing materials and lightening of pavement materials can reduce the effect in Enugu urban settlement. Akbari*et al*. (2001) studied the effect of cool surfaces and trees shades on the UHD. The findings revealed that surfaces with great albedo and urban trees can significantly reverse the heat islands. Tthe cost reduction due to the mitigating measures of UHD was also calculated in the studies. According to Akbari*et al.* (2001), for every 1^0C increase in temperature, the electricity demand may rise by 2-4%. On the other hand, 20% energy used for air conditioning can be saved if mitigation measures are put in place in order to reduce the UHD. Yamamoto (2006) described several mitigation measures for UHD and also gave a description about some mitigation projects in Japan and other countries including the wind paths in Freiburg in Germany and recommended some key mitigation measures such as energy saving buildings and traffic systems, restoring green areas in urban areas and improvement of urban airflow.

2.2 Urban Green Space

Urban forests and trees contribute to a better quality of living environment in cities, for example by improving air quality and consequently the health of urban residents. Using a cross-sectional study design, De Vries*et al.* (2003) tested the hypothesis that people in green areas are healthier than people living in less green areas. The work combined Dutch data on the self-reported health of 17,000 people with land use data on the amount of green space in their living environments. The statistical examination controlled for confounding factors such as age, sex, and socio-economic status. The authors concluded that those living in a greener environment were positively related to all three available health indicators and the association was stronger for housewives and older people. The three health indicators considered by De Vries (2000).were: number of health problems experienced in the previous 14 days; perceived general health measured on a five point scale; and the score on the Dutch version on the General Health Questionnaire.

Currently, vegetal cover removal is one of the most alarming global development challenges. Specifically, it is the most serious long-term environmental issue affecting the world and Nigeria is not left out. Historically, the critical long term development challenge at the attainment of independence in 1960 was how to grow rapidly from a predominantly primary production based economy to an industrialized one with strong inter-sectorial links. The high hopes regarding the possibility of an appreciable progress towards getting self-sustained and rapidly industrialized within a generation or two was heightened by the emergence of the unprecedented large foreign exchange earnings from crude oil and gas exports. But after over four decades, this dream has remained largely unfulfilled in spite of all the development initiatives.

3.0 MATERIALS AND METHODS

3.1 Data

Moderate resolution multispectral and multi-temporal Enhanced Thematic Mapper Plus (ETM+) imageries of Landsatfor the year 2015 covering Abuja was obtainedfrom path 189 and row 54 were downloaded from Global Visualization site. It was used to identify the Green Spaces and Heat Distribution in Abuja and its

environs. The image was used as a guide to identify the sampling points. Twenty-two (22) points were picked within the study area as sampled location for micro temperature data of all the points which form the primary data source used. Their respective locations, relative humidity, wind speed and temperature data were gathered using GPS, hand held thermometer, wind meter and humidity meter.The points were divided into two (2), eleven (11) of which are areas with green spaces and the other eleven(11) are areas without green spaces.Google earth image of the study area was also acquired.

3.2 Methods of Data Analysis

3.2.1 Micro Temperature Data Analysis (from Field work)

A portion was extracted from study area map for more detail study. From the extracted portion, figure 5 represents the NDVI map of the area while figure 6 represents the thermal map of the same area. Samples of different points were taken from both extracted maps based on two criteria as follows:

i. Built-up areas and bare ground (represented by alphabets a-k)
ii. Vegetated (green) spaces (represented by numbers 1-11)

The green spaces are represented by numbers 1-11 on the satellite images and shown on table 4.1 together with their absolute locations, relative humidity, wind speed and temperature; while the built-up/ bare ground areas indicated with alphabets (a-k). The details can be found on tables 4.1 and 4.2. This was necessary to compare the effect of vegetation/green spaces on heat distribution in the study area from field work as the same time estimate the thermal comfort of the area (Blazejczyk*et al.*, 2012)

After collecting the micro temperature data of the twenty two (22) locations, the data collected was tabulated and comparisons were made; some analogies were inferred and used in analysing the tabulated data. The result of the analysis was presented through simple line graphs and histograms with analysing comments. Also the micro temperature data from the locations were used to calculate the Human thermal comfort index of which the value accepted as a suitable comfort index for maximum comfort is (-0.5 to 0.5).

3.2.2 Creation of NDVI Map

Normalised Difference Vegetation Index (NDVI) is an index describing vegetation by showing the difference between near-infrared, which is strongly reflected by vegetation and red light which is absorbed by vegetation. The NDVI map was created in ArcGIS 10.2 environment using the Landsat ETM+ Imageries. Healthy vegetation (chlorophyll) reflects more near-infrared (NIR) and green light compared to other wavelengths and it absorbs more red and blue light. This was why NDVI map was chosen for this study because it uses NIR and Red channels to measure healthy vegetation and identify the locations of green spaces in Abuja and its environs.

The formula for calculating NDVI is:

$$NDVI = \frac{NIR - red}{} \quad \text{……..(i)}$$

3.2.3 Creation of Thermal Map

Heat map also referred to as thermal map of Abuja was created using ArcGIS 10.3. Thermal map is necessary

for identifying the heat distribution in Abuja and its environs. The thermal map was generated using the thermal bands of Landsat Operational Land Imager (OLI) and the NDVI of the study area was calculated. The first step taken was to convert the Digital Numbers (DN) on the imageries to Radiance values using the formula

$L_\lambda = M_L Q_{cal} + A_L$ ……(ii)

where

L_λ = TOA Spectral Radiance (Watts/(m2 * srad *))

M_L = Band-specific multiplicative recalling factors from the metadata (RADIANCE_MULT_BAND_x, where x is the band number)

A_L = Band-specific additive recalling factors from the metadata (RADIANCE_MULT_BAND_x, where x is the band number)

Q_{cal} = Quantized and calibrated standard product pixelvalues (DN)

The Radiance calculated above was then used to generate the Satellite Brightness Temperature with the following formula

$$T = \frac{K_2}{\ln\left(\frac{K_1}{L_\lambda} + 1\right)}$$ ……..……(iii)

T = At-Satellite brightness temperature (K)

L_λ = TOA spectral radiance (Watts/(m2 * srad * µm))

K_1 = Band-specific thermal conversion constant from the metadata (K1_CONSTANT_BAND_x, where x is the band number, 10)

K_2 = Band-specific thermal conversion constant from the metadata (K2_CONSTANT_BAND_x, where x is the band number, 10)

But this gives the temperature on the satellite whereas land surface temperature was needed which lead to step the third step calculated using the following formula:

Land Surface Temperature = BT/1 + w * (BT/p) * in(e))

Where

BT = At Satellite Temperature

w = wavelength of emitted radiance (11.5µm)

p = h * c/s (1.438 * 10^-2 m K)

h = Planck's constant (6.626 * 10^-34 Js)

s = Boltzmann constant (1.38 * 10^-23 J/K)

c = Velocity of light (2.998 * 10^8 m/s

With these processes, the thermal map for Abuja City and its environs was generated so as to know the Heat Distributions in the area.

3.2.4 Thermal Comfort Index

To assess the thermal exposure of the human body, the integral effects of all thermal parameters must be taken into account. To this end, sophisticated bio meteorological indices are available to assess thermal comfort. Examples include the predicted mean vote (PMV), the physiologically equivalent temperature (PET), and the universal thermal comfort index (UTCI), which are based upon models for the human heat budget. Such models use all relevant meteorological parameters as well as physiological factors as input (Fiala*et al*., 2012) More so, Blazejczyk*et al.* (2012) compared several of the thermal comfort estimates from the simple empirical indices with the UTCI. This index has been proposed for use as the standard model to assess human thermal

comfort, and is one of the indices based on a fairly complete description of the human energy balance. It was found that the so-called ET can be regarded as a reasonable proxy for the much more sophisticated UTCI. ET is computed from air temperature, water vapour pressure and wind speed, and these are generally available from meteorological observations. The findings of Blazejczyk*et al.* (2012) were confirmed in an independent analysis based on data from the Dutch city of Rotterdam (Stewart *et al.*, 2012).

Based on the results from the Field survey, ET was used as a thermal comfort index that was considered an alternative exposure indicator. ET was estimated as follows according to (Blazejczyk*et al.*, 2012):

…….(iv)

Where: $ET = 37 - \frac{37 - T_{air}}{0.68 - 0.014RH + \frac{1}{1.76 + 1.4w_s^{0.75}}} - 0.29T_{air}(1 - 0.01RH)$

T_{air} = air temperature (°C)

RH = the relative humidity of the air (%)

W = the average wind speed (m/s).

The ET threshold used to count occurrences of thermal discomfort is shown in Table 1. This table has been used to relate thermal comfort to ET in West Africa (Blazejczyk*et al*., 2012). The situation where value ET ranges between 31-37 °C, conditions are generally perceived as 'warm', which corresponds to strong heat stress in other indices. Hence the number of zones where the maximum ET exceeds 31°C was counted. The perception of heat has typically been derived for daytime conditions.

Table 1: Effective Temperature Rating Table

ET RANGE (^{O}C)	THERMAL COMFORT CLASS
>37	Hot
31-37	Warm
27-31	Comfortable
21-27	Fresh
17-21	Cool
11-17	Cold
1-11	Very cold

Note: ET values are different form air temperature values Source: Blazejczyk*et al.*, 2012

4.0 Results and Discussion

4.1 Green spaces and heat distribution effect from satellite image comparison

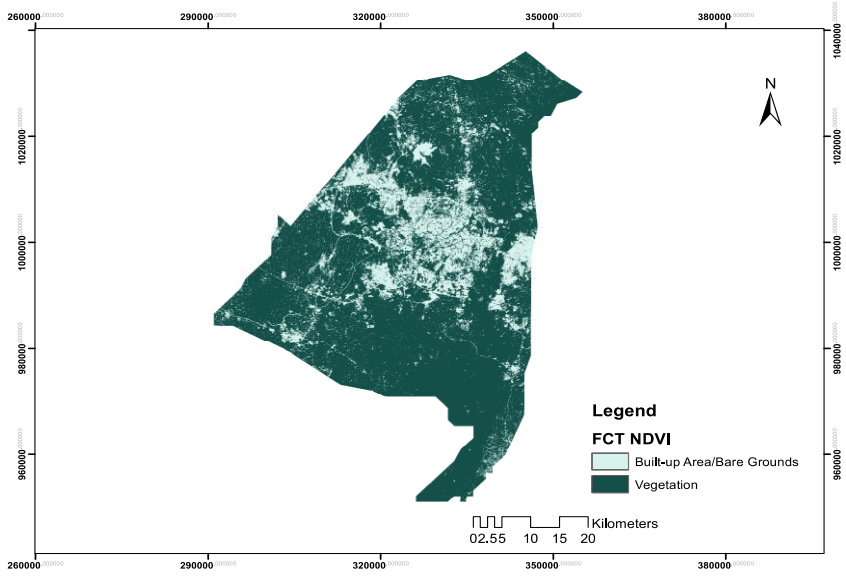

Figure 2: NDVI of the Area (FCT) in 2015 distinguishing Vegetation from built-up/bare ground

Source: Author (2016)

The major vegetation distribution of study area (FCT) Nigeria is shown on figure 2, the image showcases the various green spaces and built up area/bare ground available in the area from which the twenty-two sampled locations were picked and mapped. The dark green represent the green spaces in the area while the white bluish colour is the built up/ bare ground surface of the study area. It was seen that the dark green colour area are more that the built up/bare ground. They are equally found to be more dormant around the built up/bare ground of the study area. (Figure 2)

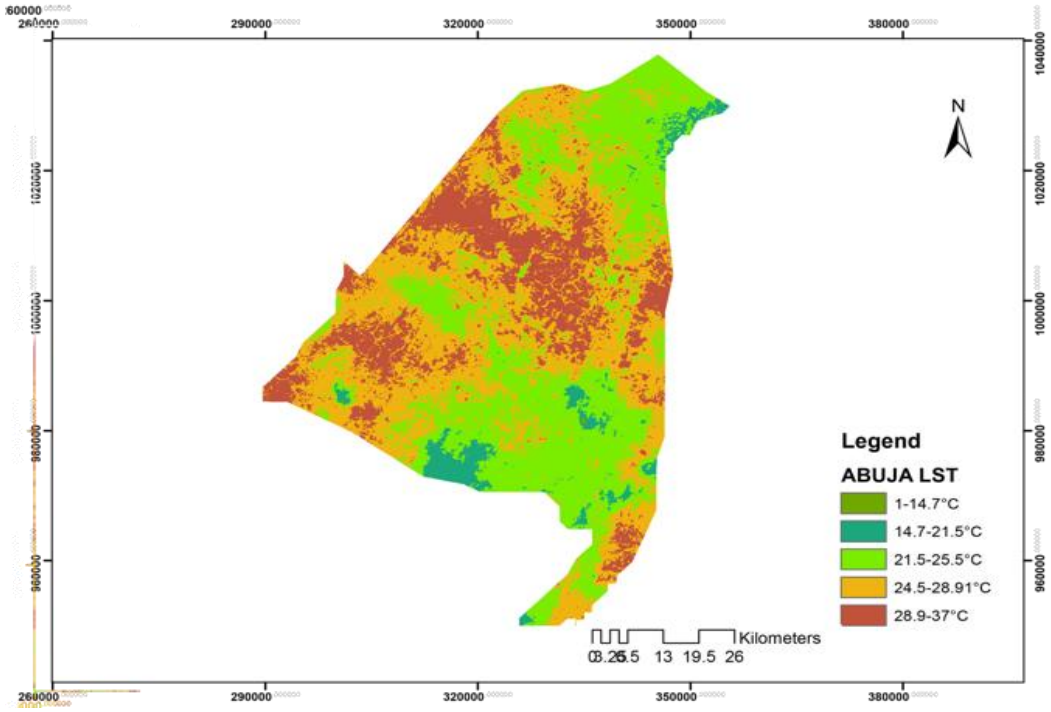

Figure 3: Temperature distribution of the area in 2015 Source: Author (2016)

The major heat distribution of the area is shown on Figure 3, the image showcases the various heat distribution of the study area which correlates with the sampled areas visited during the field survey. From Figure 3, Five (5) different ranges of heat were identified. The lowest temperature range was between 1^0c to 14.7 ^{0}C, which was not too pronounced in the map of heat distribution. This less visibility of this temperate range implies there are no low temperature distributions over the area. The second and third temperature ranges are between 14.7^{0}C to 21.5^{0}C and 21.50C and 25.5^{0}C respectively. These temperature classes are visible at areas at location far away from the centre of the city they represent suburban areas. The moderate temperature ranges these classes connotes that places further away from the city centre have lesser temperature compared with the main city. Temperature ranges, 25.5^{0}C and 28.9^{0}C and 28.9^{0}C and 37.5^{0}C respectively are more dormant at the point representing built up and bare ground surface in Figure 2 which represent the centre of the city the densely urbanized part of the study area. The Google earth image of the area (figure 4) depicts a portion of the built-up/bare ground and vegetation distribution of the area in 2016. Supporting the various effects of green spaces on heat distribution from satellite image comparison.

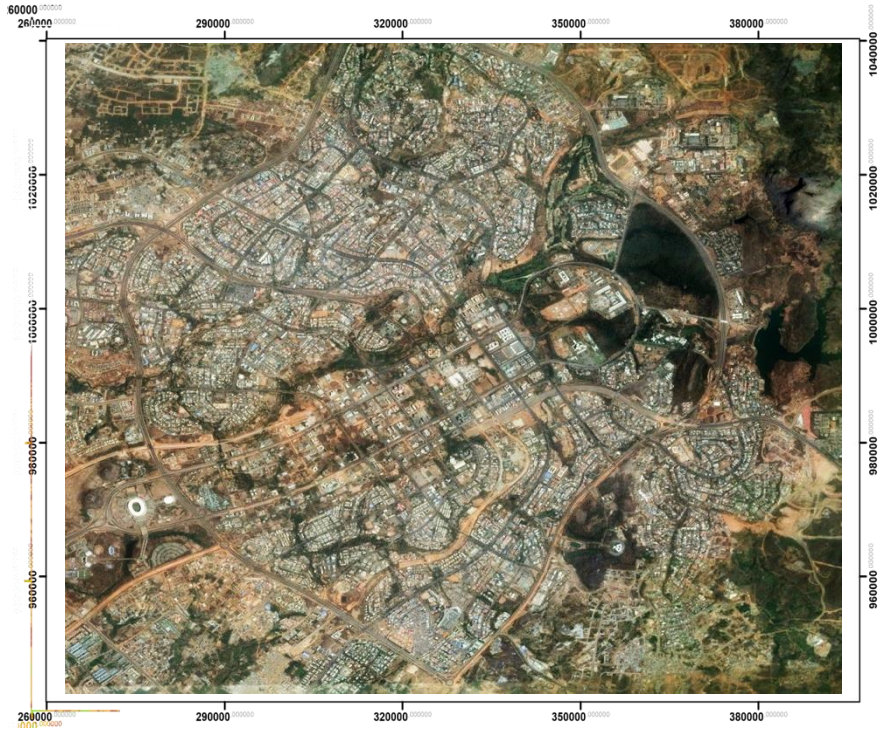

Figure 4: QuickBird image of FCT in 2016 Source: Google Earth 2016

4.2 Green spaces and heat distribution effect from micro field work comparison

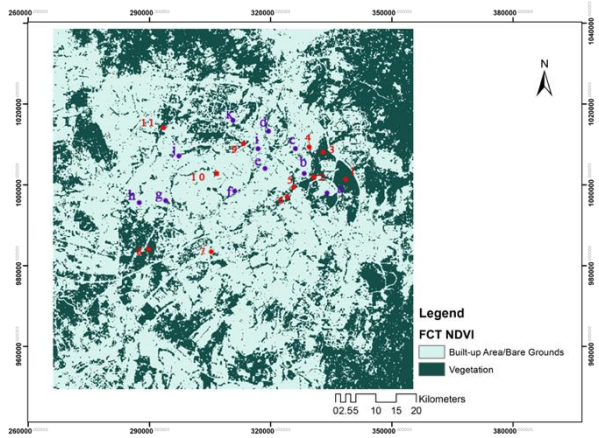

Figure 5: NDVI of an extracted area from Study Area

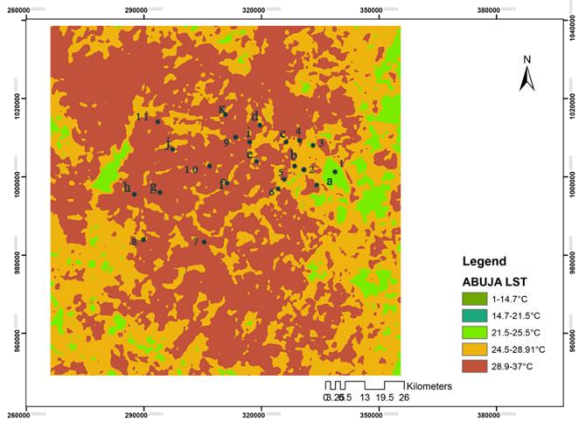

Figure 6: Temperature Distribution of an extracted area from Study Area

Source: Author's field work, 2016

As shown Figures 5 and 6; Tables 2 and 3, it was clear that the sampled green spaces have lower temperature reading than non-green space found in the study area. Comparing points (a) and (1) it was discovered that the temperature readings of point (a) 23.13ºC (non-green space, Three arms zone) is 4.2ºC higher than that of point (1) at 18.93ºC(green space, National Arboretum) . In the same vein, point (e) at 26.67ºC (non-green space, Louga road) is 4.47ºC higher than point (5) at 22.20ºC (green space, Lobito crescent park). Point (k) 24.12ºC (non-green space,Tapeta Street) is 2.14ºC higher than that of point (11) at 21.9ºC(green space,City Park). Details of other the temperature readings comparison between greens pace and non-green are shown see (Tables 2 and Table 3). On a general note, one can conclude that non green spaces mainly which comprises of built up and bare ground generate more heat than green spaces.

S/N	Green Areas	Coordinates		Rel. Humidity (%)	Wind Speed	Temp (ºC)
		Latitude	Longitude			
1	National Arboretum	9.087778	7.517747	89	3.4	18.93
2	Millennium park	9.070692	7.498844	82	3.5	19.23

3	IBB Golf Club	9.085819	7.506431	80	3.1	21.89
4	Maitamaneighbourhood park	9.085492	7.500022	79	2.9	22.10
5	Lobito crescent park	9.070408	7.4948	81	3.1	22.20
6	Durban street neighbourhood park	9.063008	7.438036	81	3.0	19.67
7	Abuja national stadium area	9.029297	7.452111	86	2.8	18.62
8	Nigeria army cemetery	9.026472	7.464519	80	3.2	21.45
9	Wuse rock park	9.069172	7.463728	78	2.8	22.12
10	Julius Berger neighbourhood park	9.068192	7.453742	79	2.5	22.06
11	City Park	9.077469	7.475753	79	2.6	21.98

Table 2 Green Areas with the relative temperatures and coordinates

Source: Author (2016)

Table 3 Built-UpAreas/Bare Ground with the relative temperatures and coordinates

	Non green areas	**Coordinates**		**Rel. Humidity (%)**	**Wind speed**	**Temp (ºC)**
		Latitude	Longitudes			
a	Three arms zone	9.066882	7.509857	75	2.5	23.13
b	Usuma street	9.074694	7.497720	76	2.4	22.89
c	Gana street	9.082284	7.498510	74	2.8	24.67
d	Pope John Paul II street	9.084111	7.494939	77	2.3	25.88
e	Louga road	9.073974	7.488556	73	2.2	26.67
f	4u supermarket	9.072122	7.484564	75	2.7	24.12
g	IdrisGidado street	9.048381	7.445309	76	2.4	24.55

h	Wuye	9.043536	7.440944	73	2.1	27.2
i	Madiana close	9.074827	7.470066	75	2.4	25.98
j	Yaounde street	9.074695	7.456771	73	2.5	26.8
k	Tapeta Street	9.077160	7.482543	74	2.2	24.12

Source: Author's field work, 2016

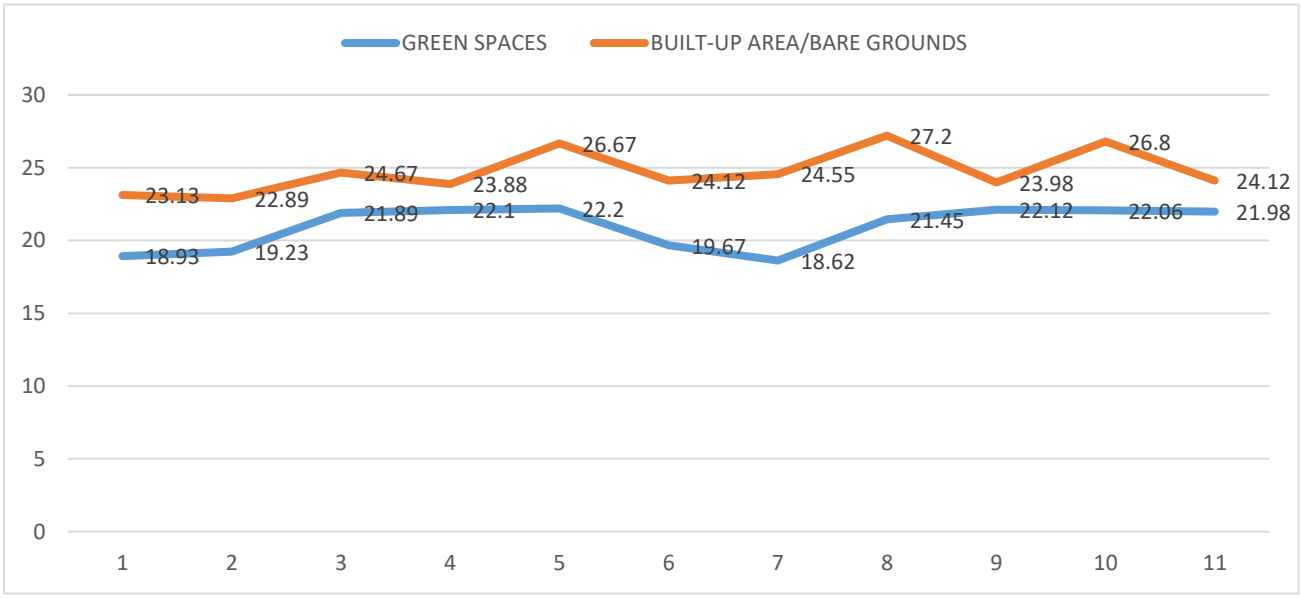

Figure 7 Temperature Graph showing readings from green spaces and Built-up Areas/Bare Grounds (Non green Spaces). Source: Author (2016)

Figure 7 show a clear indication of lower temperature from the line graph in green spaces as compared to Non Green spaces such as the built-up/bare ground areas. The gap between the lines is an indicator of the temperature difference between them. The wider the gap, the more the temperature difference, and the smaller the gap, the less the temperature difference between these points. Figure 7 depicting the temperature gap, proves that non green spaces have effect on temperature /heat distribution.

4.3 Thermal Comfort Index

Table 4 Thermal Comfort results for the selected green spaces.

Location	Efficient temperature (ET)	Thermal comfort index
National Arboretum	31.39	0.39
Millennium park	31.38	0.38
IBB Golf Club	31.59	0.59
Maitama neighbourhood park	31.46	0.46
Lobito crescent park	31.71	0.71
Durban street neighbourhood park	31.08	0.08
Abuja national stadium area	30.83	-0.16
Nigeria army cemetery	31.56	0.56
Wuse rock park	31.35	0.35
Julius Berger neighbourhood park	31.15	0.15
City Park	31.2	0.21

Source: Authors (2016)

The Thermal comfort Indices of the selected green spaces are shown on tables 4. The highest comfort is experience at Lobito Crescent Park with 0.71index value. IBB Golf Club, Nigeria army cemetery and Maitama Neighbourhood Park also have fairly high thermal comfort index of 0.59, 0.56 and 0.46 respectively while National Arboretum and Millennium parks also have thermal indices of 0.39 and 0.38 values. These identified areas have a thermal comfort class between warm and hot because of their high ET and thermal index. Other areas like Julius Berger neighbourhood park, City Park and Durban street neighbourhood park as well as Abuja national stadium area have extremely low 0.21,0.15, 0.08, -0.16 respectively. These areas have a thermal comfort class between cool and cold because of their low ET and thermal index.

Table 5 Thermal Comfort results for the selected non green spaces (Built-up Areas/Bare Grounds).

Location	Efficient temperature (et)	Thermal comfort index
Three arms zone	31.22	0.21
Usuma street	31.13	0.13
Gana street	31.68	0.68
Pope john paul ii street	31.83	0.83
Louga road	31.71	0.70
4u supermarket	31.57	0.56
IdrisGidado street	31.52	0.52
Wuye	31.77	0.77
Madiana close	31.79	0.79
Yaounde street	31.91	0.90
Tapeta Street	31.51	0.51

Source: Authors (2016)

The Thermal comfort Indices for non-green space (Built-up/Bare ground areas)is shown table5.The highest comfort is experience by virtually all the selected areas with the exception of three arms zone and UsumaStreet having low thermal comfort index of 0.21 and 0.31 respectively. The areas with high values is expected to have a thermal comfort class between warm and hot because of their high ET and thermal index while areas with low values will have a thermal comfort class between cool and cold. The summary of the

Table 6 Thermal Comfort indices for both Green Spaces and non-green spaces (Built-up Area/Bare Grounds)

Thermal Comfort Indices (Green Spaces)	Thermal Comfort Indices Diff (Built-up/Bare Ground)
0.39	0.21
0.38	0.13
0.59	0.68
0.46	0.83
0.71	0.70
0.08	0.56
-0.16	0.52
0.56	0.77
0.35	0.79
0.15	0.90
0.21	0.51

Source: Authors (2016)

KEY

Within Acceptable Range

Manageable

Ideal

Out of acceptable range

Table 6 shows the results obtained from the calculated thermal comfort indices based on the formula earlier mentioned under methodology. The table was colour coded to show the points that comply with the ET (Efficient Temperature) value needed and the ones that do not comply divided into four ranges starting with places within acceptable range, ideal, manageable and places termed as out of acceptable range.

For Green Spaces(Table 6)**,**National Arboretum, Millennium park and Wuse rock park have within the acceptable thermal comfort indices, while Maitamaneighbourhood park,Durban street neighbourhood park, Abuja national stadium area and Julius Berger neighbourhood park as well as City Park recorded an ideal thermal comfort index. While IBB Golf Club and Lobito Crescent Park have manageable thermal comfort index range but Lobito Crescent Park has a thermal index outside the acceptable index. For non-Green spaces(Table 6)**,**,three arms zone,andUsumaStreet have an ideal thermal comfort index;4u supermarket, IdrisGidado street and Tapeta Street have a manageable thermal comfort index; while other areas have thermal index exceeding the acceptable range.

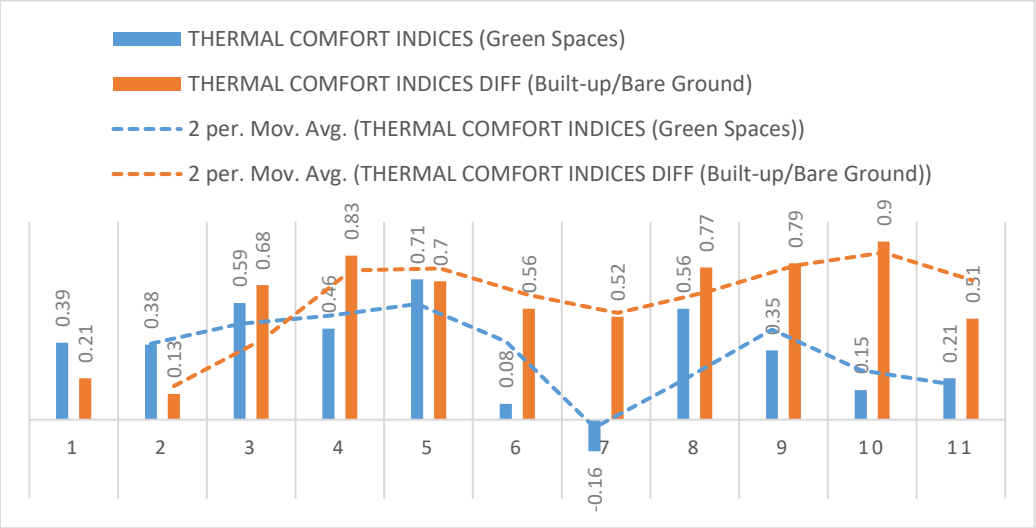

Figure 8: Thermal Comfort Index chat showing results from green spaces and Built-up Areas/Bare Grounds (Non green Spaces). Source: Author (2016)

Figure 8 gives a graphical view of the results displayed in table 4.4; the chart also featured trend lines (Moving Averages) that shows how each variable rise and fall from one zone to another.

4.5 Discussion of Results

The NDVI Map of Study Area (FCT) is indicated with figure 2 from Landsat Operational Land Imager (OLI) ETM+ imagery of Abuja. The image shows the major vegetation distribution of the area and the built-up areas/bare grounds. Figure 3 is the thermal Map of Study Area (FCT) in 2015. The image shows the different heat distributions in Federal Capital Territory (FCT). In contrast to the method used by Qiu*et al.* (2001), who used mono-window algorithm to generate the LST (Land Surface Temperature) map. The mono-window algorithm requires three parameters; emissivity, transmittance and effective mean atmospheric temperature (Sobrino*et al.*, 2004). The atmospheric water vapour content and the near surface air temperature were used to calculate the air transmittance and effective mean atmospheric temperature (Liu and Zhang, 2011). The third parameter is emissivity was calculated from NDVI. This study used DN (Digital Number) to calculate the band radiance, also the radiance generated was in-turn used to generate the temperature at the satellite level followed by the generation of the land surface emissivity which also made use of the already generated NDVI (Normalised Difference Vegetation Index) followed by the land surface temperature (LST).

Figures5 and 6show the comparison of the extracted NDVI map of Study Area and the Thermal Map of the same area. The figures reveal that there is an inverse relationship between temperature and vegetation from the maps (NDVI and Thermal maps).This is evident from the 22 points that were surveyed (11 points with green spaces and 11 points with built-up area/bare grounds). The analysis also shows that areas with more vegetation cover have lower air temperature compared to areas with no vegetation (built-up areas). figure 7 clearly indicates this and also shows the graphical representation of the air temperature readings derived from the different points, it was discovered from the line graph that the areas with vegetation cover tend to have a lower temperature with an average of 3-4ºC compared to build-up area/bare grounds.

On the other hand Table 6 shows the Thermal Comfort Indices of both Green Spaces and Built-up Area/Bare Grounds, the table was colour coded to show the areas that comply with the ET (Efficient Temperature) rating of the thermal comfort index and areas that does not comply, Green represents ideal results, Blue represents areas within acceptable range, Orange represents areas with manageable results while red indicates areas that are not within acceptable range, it was noticed from the results obtained that out of the (11) areas selected in the green zone; three (3) zones did not fall within acceptable value, the three zones have values 0.59, 0.71 and 0.56 which falls short of the ±0.5 acceptable value. This is as a result of the green spaces in the zone not being more than one hectare (1ha) and it consists of mostly lawn and shrubs, it is known that areas that tend to have an appreciable effect on human thermal comfort are areas with dense population of trees, because the canopies help mitigate the effect of urban heat distribution among other things. Also, for the Buil-up areas, it was noticed that Nine (9) out of Eleven (11) locations fall short of the acceptable values, while Two (2) of the points fall within the acceptable regions with values; 0.21 and 0.13 respectively, this difference is due to the fact that the two locations with the acceptable values are in close proximity to major green areas in the study area.

The above results further confirmed the effect of Green Spaces on Heat Distribution, it is more evident now that green spaces helps reduce heat, therefore an inverse relationship exists between green spaces and heat distribution, i.e. the more the green space the lower the temperature distribution of a particular area.

5. Conclusion

Through the NDVI and thermal satellite imageries of FCT Abuja, 2015, it was noted that there is a strong relationship between the vegetation distribution and Heat distribution in FCT, 22 points were picked based on two criterion, (i) Areas with Vegetation, (ii) Built-up areas/Bare Grounds. Comparing the results obtained from FCT NDVI map and Thermal Map, it was noted that the 11 points with high NDVI value (vegetation cover) are relatively cooler (lower in temperature) on the thermal map while the 11 points that represents Built-up area/Bare Grounds (non vegetated area) i.e. Low NDVI values are hotter (have a high temperature).

Also, the micro temperature data taken from the 22 points during the ground survey wasfound to correlate with the result from the satellite imagery, temperature readings taken from those locations shows a significant temperature difference between the 11 areas with vegetation cover and the 11 areas with built-up area/Bare grounds, it was noted that the areas with vegetation is significantly lower in temperature than the built-up areas by an average of 4^{o}C. The result of the 22 points that was investigated was used to calculate the Human thermal comfort in FCT Abuja Using the Effective Temperature (ET) Profile and discovered that the areas with low vegetation cover has a significantly low thermal comfort index compared to the non-vegetated areas.

This research has come up with the following recommendations:

1. Selective planting of trees: Mature trees promote cooling through their evapotranspiration capacity and the area of shade they provide. Therefore, tree planting should be encouraged to reduce the effect of urban heat island and help reduce the heat distribution in the area.
2. Vegetation around buildings: Walls of building are one of the main causes of temperature increase in the urban areas; therefore having vegetation around buildings can go a long way in reducing the temperature of the area, reducing the rate at which the walls get heated up. Various plant species provide heat and pollution-mitigating capacities, and compact multi-layering of diverse plant species can help improve overall resilience to drought, heat and pollution. Among plant types, trees have an

exceptional ability to capture and filter multiple air pollutants, including ground-level ozone, sulphur dioxide, nitrogen oxides and particulate matter. Trees are also significantly associated with improved thermal comfort and relief from heat stress at the street level and neighbourhood scale, particularly during hot seasons and times of day.

3. Green roofs: Green roofs is one of the best ways to reduce the heat of an area because, a green roof has a higher albedo compared to dark roofs, and the higher the albedo the higher the spectral reflectance of the object and the higher the reflectance, the lower the heat accumulation, therefore the use of green roofs should be encouraged to help reduce the heat. Implementing these measures will not only help to reduce the energy demand but will also provide healthy environmental benefits such as reduced mortality due to heat stroke, less CO_2 emission, increased thermal comfort, reduced air pollution and hence less lung diseases.

REFERENCES

Akbari, H. (2011). Cool Roofs and Pavements to Cool the World: An Integrated Mitigation/Adaptation Strategy for Cities. In *Resilient Cities 2011: 2nd World Congresson Cities and Adaptation to Climate Change*. Montreal, Canada.

Elsayed, I. S. M. (2009).A Study on the Urban Heat Island of the City of Kuala Lumpur, Malaysia.In *IASTED International conference on Environmental Management andEngineering*. Alberta, Canada.

Giannaros, T. M., &Melas, D. (2012).*Study of the Urban Heat Island in a Coastal Mediterranean City: The Case Study of Thessaloniki, Greece. Atmospheric Research*, *118*, 103–120. doi:10.1016/j.atmosres.2012.06.006

Senanayake, I. P., Welivitiya, W. D. D. P., &Nadeeka, P. M. (2013). Remote Sensing Based Analysis of Urban Heat Islands with Vegetation Cover in Colombo city, Sri Lanka using Landsat-7 ETM+ data. *Urban Climate*. doi:10.1016/j.uclim.2013.07.004

Wan Mohd, W. M. N., Hashim, S., &Mohd Noor, A. M. (2004). Integrating Satellite Remote Sensing and GIS for Analysing Urban Heat Island. *Built Environment Journal*, *1*(2), 34–44.

Memon, R. A., Leung, D. Y. C., &Chunho, L. (2008).A Review on the Generation, Determination and Mitigation of Urban Heat Island.*Journal of Environmental Sciences(China)*, *20*(1), 120–8. Retrieved from http://www.ncbi.nlm.nih.gov/pubmed/18572534

MacHarg, I. L., 1971, *Design with nature*. New York:Doubleday, Garden City.

Devi, S. S. (2003). *urban heat islands and environmental impact.*Orbit. Nesdis. Noaa. Gov.

Akbari H. and Konopacki S. (2001).*Calculating energy-saving potentials of heat island reduction strategies. Energy Policy,* 33:721-756.

Bretz, S., Akbari, H., and A, R. (1998).*Practical issues for urban solar-reflective materials to mitigate urban heat islands. Atmospheric Environment*, 32:95–101.

Roelofs, J., 1999, Building and designing with nature: Urban design. In: J. Roelofs (Eds.), *Greening cities: Building justand sustainable communities*. New York: Bootstrap Press.

De Vries S (2000). *Regional differences in the demand for and supply of nature-based recreation within The Netherlands. In: Krishnapillay, B, et al. (eds) Forests and Soiety: the role of research. Proceed- ings of the XXI IUFRO World Congress 2000*, Malaysia, 7–12 August. IUFRO/FRIM, Vienna/Kuala Lumpur, Vol. 1, pp 453–464

Fiala, D., Havenith, G., Bröde, P., Kampmann B. and Jendritzky, G., 2012, 'UTCI-Fiala multi-node model of human heat transfer and temperature regulation', Int J Biometerol, 56(3) 429–424.

Blazejczyk, K., Y. Epstein, G. Jendritzky, H. Staiger and B. Tinz, (2012) 'Comparison of UTCI to selected thermal indices', Int J Biometeorol, (56) 515–535.

Stewart H, Owen S, Donovan R, MacKenzie R & Hewitt N (2001) *Trees and sustainable urban air quality. Brochure, Lancaster University and Centre for Ecology and Hydrology, Lancaster*

SIMULATION OF THE EFFECT OF PHYSICAL EXERCISE ON THE TEMPERATURE DISTRIBUTION IN THE PERIPHERAL REGIONS OF HUMAN LIMBS

Olayiwola, R.O[1], Saidu, Y.V[2] & Mahmood, Hamza[1]

[1]Department of Mathematics,

Federal University of Technology, Minna, Nigeria.

[2]Department of Mathematics,

Federal Polytechnic,Bida, Nigeria.

E-mail.: Send2yasav@yahoo.com

ABSTRACT

The paper presents analytical solution to investigate the effect of physical exercise on the temperature distribution in the peripheral regions of Human limbs. The equation governing the phenomena is solved using parameter expanding method and eigenfunction expansion technique. The result obtained revealed that the thermal conductivity, Blood mass flow rate of metabolic heat generation in tissue play a crucial role in the phenomenon.

Key words: Physical Exercise, Temperature, Human limbs.

Introduction

The survival of human body in cold and hot temperature, weather and environmental changes by skin and core temperature regulation. Survival in severe hot and cold environment means adjusting to very high and low temperatures quickly. The body core temperature is maintained at 98.6 degrees or 37 degree C.

Activities like exercise and aerobics cause corresponding increase in energy production and body temperature: vasodilatation of blood vessels increases blood circulation leading to sweating and evaporation, bringing down skin and core temperature.

Earlier experimental investigations were made by Patterson to obtain temperature pries in the SST region under normal physiological and environmental conditions. Some theoretical investigations have been carried out during the last few decades by (Cooper et al., 1972; Chao et al., 1973) In SST region under normal environmental Effect of physical exercise on temperature distribution and physiological conditions.

Many people spend more than half their waking hours sitting down. And activities that don't enhance health account for quite a lot of the remainder. This growing trend may cause more trouble than most people realize.

Observational studies suggest habitual inactivity raises risks for obesity, diabetes, cardiovascular disease, deep-vein thrombosis, and metabolic syndrome (Mitchell *et al*.,2008).

1.0 Mathematical Formulation

Following Kumari and Adlakha (2013), the mathematical model for heat flow in body tissue for a one-dimensional transient state is given below:

$$\rho Cp\frac{\partial T}{\partial t}=\frac{\partial}{\partial x}\left(k\frac{\partial T}{\partial t}\right)+m_b c_b(T_a-T)+S \qquad (1)$$

It is assumed that at time t = 0 the outer surface of the body is perfectly insulated. Thus the initial condition is given by

$$(Tx,0)=T_b \qquad (2)$$

The outer surface of the skin is exposed to the environment and the heat loss from the outer skin surface to the environment takes place by conduction, convection, radiation and evaporation. Therefore, the boundary condition at the outer surface can be written as

$$K\frac{\partial T}{\partial t}=h(T-T_a)+LE, \qquad x=0, \qquad t>0 \qquad (3)$$

The body core which forms the inner boundary is maintained at a uniform temperature. Therefore, the inner boundary condition is prescribed as given below

$$(Tx,t)=T_{b,} \qquad x=b, \qquad t\geq 0 \qquad (4)$$

Where

ρ = Density

C_P =Specific heat capacity with pressure

T = Temperature of the tissue

K =Thermal conductivity

m_b = Blood mass flow rate

C_b =Specific heat of the blood

S = Rate of metabolic heat generation in tissue

T_a =Atmospheric temperature

T_b =Body core temperature

b =Thickness of the skin layer

L =Latent heat

E =Rate of sweat evaporation

h = Heat transfer coefficient

In this study, we consider peripheral regions (SST) of circular shaped human limbs. Therefore, equations 3 & equation 4 can be expressed in polar cylindrical coordinates as:

$$\rho C_p \frac{\partial T}{\partial t} = \frac{1}{r}\frac{\partial}{\partial r}\left(kr\frac{\partial T}{\partial t}\right) + m_b c_b\left(T_a - T\right) + S \qquad (5)$$

Together with initial and boundary conditions:

$$T(r,0) = T_b \qquad ,T(a,t) = T_b \qquad k\frac{\partial T}{\partial r}\Big|_{r=R} = h\left(T - T_a\right) + LE, \qquad (6)$$

$$a < r < R$$

2.0 *Non-dimensionalization*

Here, we Non–dimensionalized equation 3 and equation 4 using the following dimensionless variables

$$\left.\theta = \frac{T - T_b}{T_a - T_b}, \quad r^I = \frac{r}{R}, \quad t^I = \frac{t}{t_0}\right\} \tag{7}$$

We obtain the dimensionless equation together with the initial and boundary conditions as follows

$$\frac{\partial \theta}{\partial t} = \lambda \frac{1}{r} \frac{\partial}{\partial r}\left(r \frac{\partial \theta}{\partial r} \right) + m(\theta - 1) + S \tag{8}$$

$$\theta(r,0) = 0, \qquad \theta(a,t) = 0, \qquad \frac{\partial \theta}{\partial r}\Big|_{r=1} = \alpha(\theta - 1) + \beta \tag{9}$$

Where

$$\alpha = \frac{Rh}{k}, \qquad \beta = \frac{RLE}{K(T_a - T_b)}$$

3.0 *Method of Solution*

Here, we solve equations (8) using parameter-expanding method (where details can be found in He, 2006) and eigenfunctions expansion method (where details can be found in Myint-U and Debnanth, 1987).

Let

$$\theta(r,t) = \theta_0(r,t) + \varepsilon\theta_1(r,t) + \ldots \tag{10}$$

and $\alpha = b\varepsilon$ (11)

Then for order zero, we obtain (12) together with the initial and boundary condition (13)

ε^0 :

$$\frac{\partial \theta_0}{\partial t} = \lambda \frac{\partial^2 \theta_0}{\partial r^2} + m(1-\theta_0) + s \tag{12}$$

$$\theta_0(r,0) = 0, \qquad \theta_0(a,t) = 0, \qquad \left.\frac{\partial \theta_0}{\partial r}\right|_{r=1} = \beta \tag{13}$$

Also for order one, we obtain (14) together with the initial and boundary condition (15)

ε^1 :

$$\frac{\partial \theta_1}{\partial t} = \lambda \frac{\partial^2 \theta_1}{\partial r^2} + \frac{\lambda}{r}\frac{\partial \theta_0}{\partial r} - m\theta_1 \tag{14}$$

$$\theta_1(r,0) = 0, \qquad \theta_1(a,t) = 0, \qquad \left.\frac{\partial \theta_1}{\partial r}\right|_{r=1} - b(\theta_0 - 1)\big|_{r=1} = 0 \tag{15}$$

Using eigenfunctions expansion method and direct integration, we obtain the solution of equations (12) and (14) as

$$\theta_0(x,t) = \sum_{n=1}^{\infty} \frac{\sigma}{c}\left(1-e^{-ct}\right)\sin\left(\frac{2n-1}{2(1-a)}\right)^2 \pi x + \beta x \tag{16}$$

$$\theta_1(x,t) = q(x,t) + xb\left(\beta(1-a) + \sum_{n=1}^{\infty} -\frac{\sigma}{c}(-1)^n\left(1-e^{-ct}\right) - 1\right) \tag{17}$$

Where

$$q(x,t) = \sum_{n=1}^{\infty}\left(B_4\left(1-e^{-ct}\right) + B_5\left(\frac{1}{c}\left(1-e^{-ct}\right) - te^{-ct}\right)\right) * \sin\left(\frac{2n-1}{2(1-a)}\right)\pi x$$

$$B_4 = \left(\frac{2\lambda\beta B_1}{(1-a)c} - \frac{2bmB_2\beta(1-a)}{(1-a)c}\right)$$

$$B_5 = \left(\frac{2bmB_2}{(1-a)} \sum_{n=1}^{\infty} \frac{\sigma}{c} (-1)^n + \frac{2\lambda B_3}{(1-a)} \sum_{n=1}^{\infty} \frac{\sigma}{c} \left(\frac{2n-1}{2(1-a)} \right) \right)$$

Then,

Case 1:

$$m(t) := m[0] + m[0] \cdot \exp(-t) :$$

$$s(t) := s[0] + s[0] \cdot \exp(-t) :$$

Case2:

$$m(t) := m[0] \cdot \left(\cos\left(\frac{\pi \cdot t}{l} \right) \right) :$$

$$s(t) := s[0] \cdot \left(\cos\left(\frac{\pi \cdot t}{l} \right) \right) :$$

4.0 *Results and Discussion*

The system of partial differential equation describing the effect of a physical exercise on the temperature distribution in the peripheral region of human limbs was solved analytically using eigenfunction expansion technique. Analytical solution of equation (3.33) – (3.34) for case one and case two were computed.

The results have been computed for two cases (i) A person was doing exercise initially and stops doing exercise at t=0 (ii) The person does exercise periodically with a period of l i.e he does exercise for period l and takes rest for period l alternatively. Graphs have been plotted between temperature and time for normal conditions and for subjects doing exercise.

For the graph of Case one, we have the following values

$$s_0 = 1, \quad m_0 = 1, \quad \lambda = 0.4, \quad \varepsilon = 0.01, \quad a = 0.8, \quad b = 2, \quad \beta = 2, \quad x = 1/2$$

Maple 16 application has been used to simulate the model on Hp (core i3) laptop with 4gigabite Ram. Figure 1-10

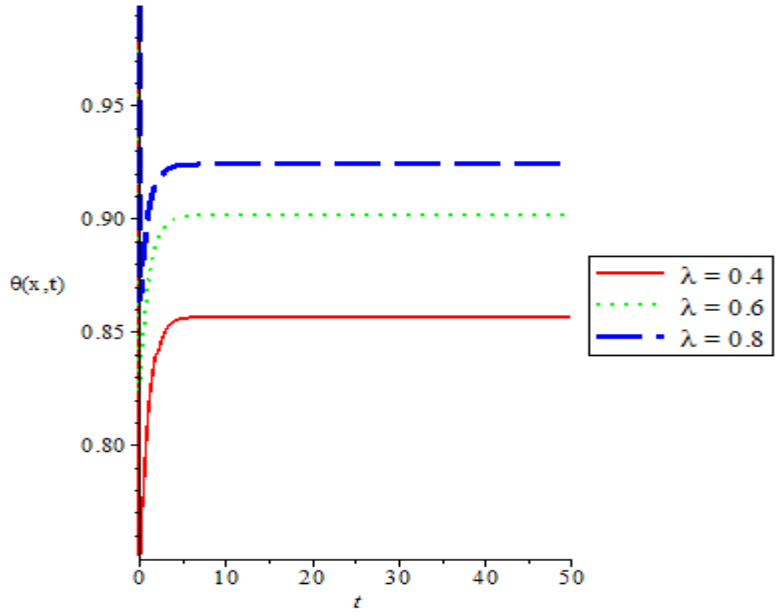

Figure 1: Variation of temperature of the human tissue $\theta(x,t)$ with thermal conductivity λ.

Figure 1, shows the effect of thermal conductivity (λ) on the temperature of the human tissue profile. It is observe that the human tissue temperature increases sharply and later becomes steady with time. Clearly the thermal conductivity enhances the human tissue temperature.

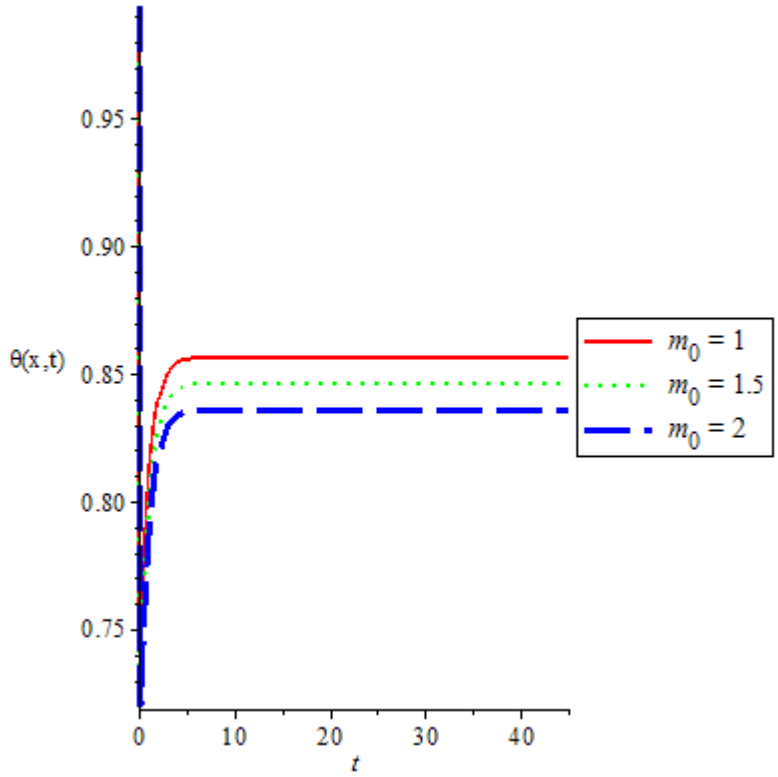

Figure 2: Variation of temperature of the human tissue $\theta(x,t)$ with blood mass flow rate m_o

Figure 2, shows the effect of blood mass flow rate (m_o) on the temperature of the human tissue profile. It is observe that the human tissue temperature increases sharply and later becomes steady with time. Clearly the blood mass flow rate enhances the human tissue temperature.

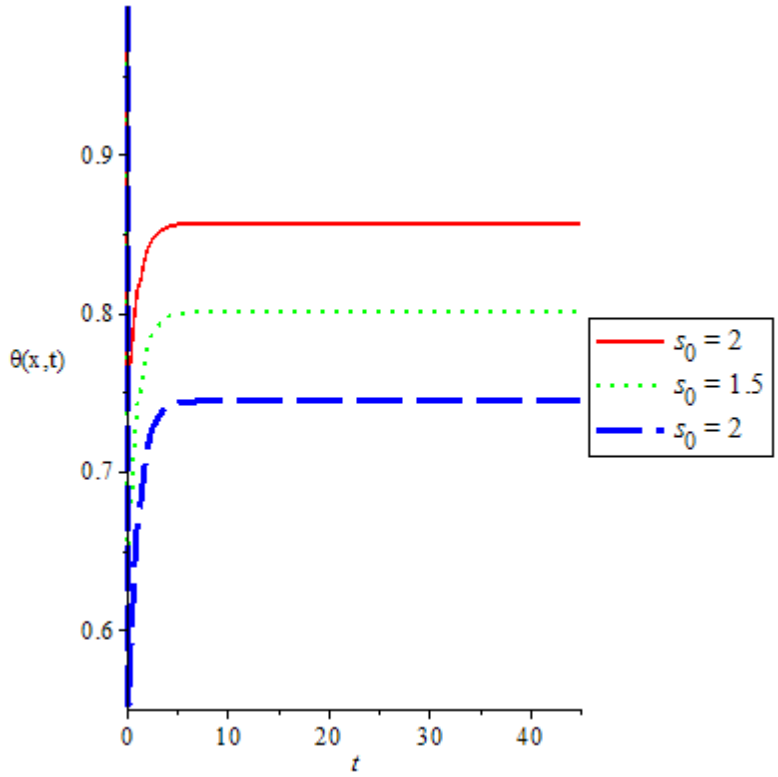

Figure 3: Variation of temperature of the human tissue $\theta(x,t)$ with rate of metabolic heat generation in tissue s_o

Figure 3, shows the effect of rate of metabolic heat generation in tissue (s_o) on the temperature of the human tissue profile. It is observe that the human tissue temperature increases sharply and later becomes steady with time. Clearly the rate of metabolic heat generation in tissue enhances the human tissue temperature.

For the graph of Case two, we have the following values

$s_0 = 1,\ m_0 = 1,\ \lambda = 0.4,\ \varepsilon = 0.01,\ l = 2.5,\ a = 0.8,\ b = 2,\ \beta = 2,\ x = 1/2$

$s_0 = 1,\ m_0 = 1,\ \lambda = 0.4,\ \varepsilon = 0.01,\ l = 5.0,\ a = 0.8,\ b = 2,\ \beta = 2,\ x = 1/2$

$s_0 = 1,\ m_0 = 1,\ \lambda = 0.4,\ \varepsilon = 0.01,\ l = 7.5,\ a = 0.8,\ b = 2,\ \beta = 2,\ x = 1/2$

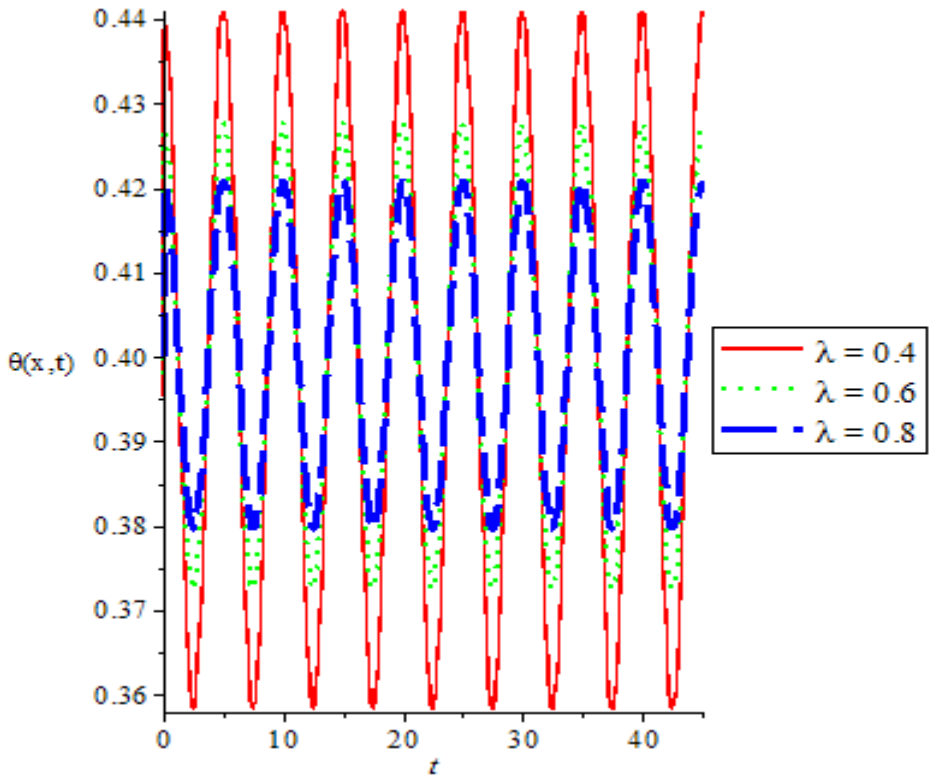

Figure 4: Variation of temperature of the human tissue $\theta(x,t)$ with thermal conductivity (λ).

Figure 4, shows the effect of thermal conductivity (λ) on the temperature of the human tissue profile. It is observe that the human tissue temperature increases sharply when the man does exercise and drop sharply over a period of 2.5 minutes when the man stops exercise. It is observe that, the maximum temperature decreases as thermal conductivity increases, and also the minimum temperature increases as thermal conductivity increases.

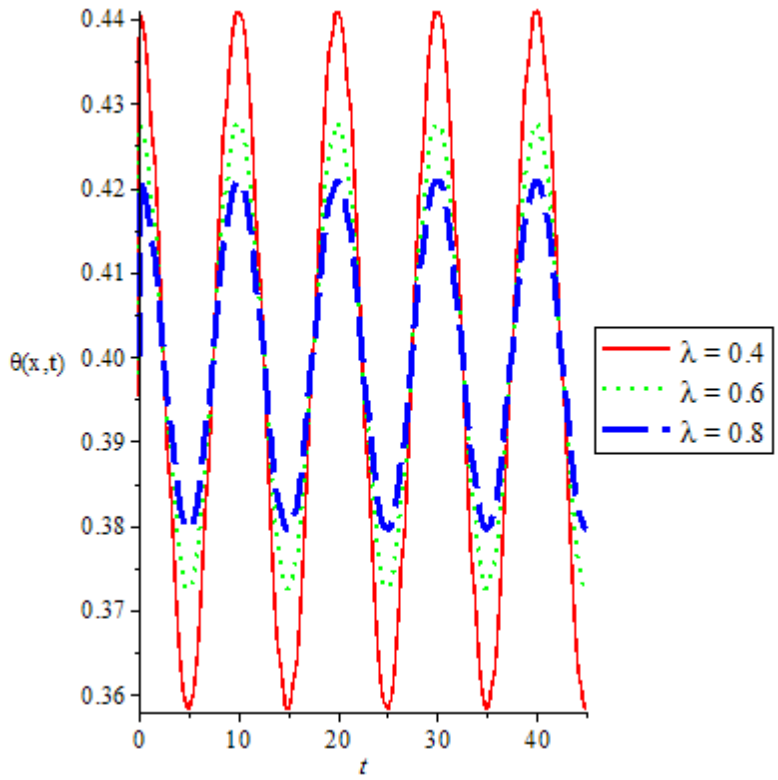

Figure 5: Variation of temperature of the human tissue $\theta(x,t)$ with thermal conductivity (λ).

Figure 5, shows the effect of thermal conductivity (λ) on the temperature of the human tissue profile. It is observe that the human tissue temperature increases sharply when the man does exercise and drop sharply over a period of 5.0 minutes when the man stops exercise. It is observe that, the maximum temperature decreases as thermal conductivity increases, also the minimum temperature increases as thermal conductivity increases.

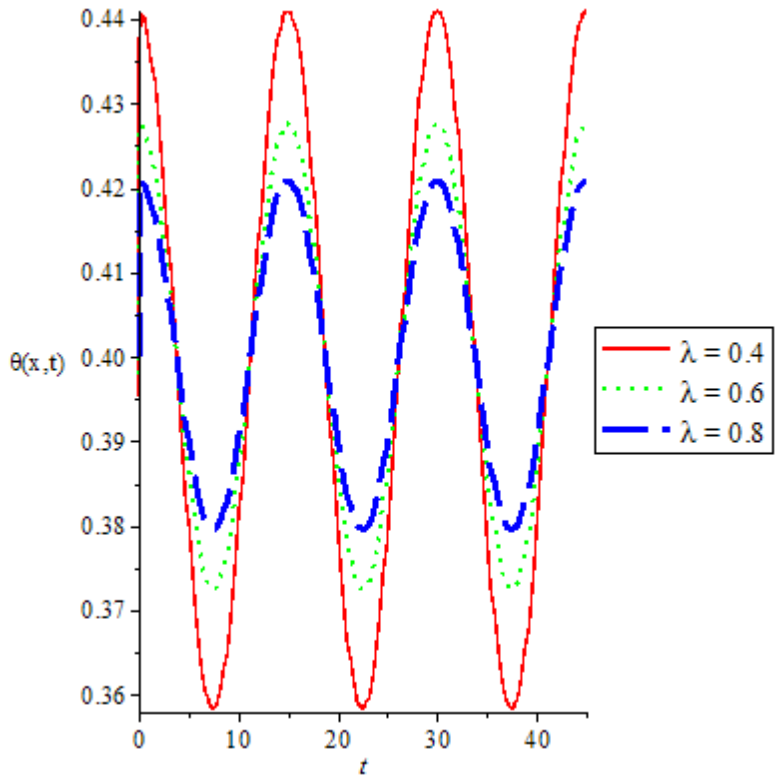

Figure 6: Variation of temperature of the human tissue $\theta(x,t)$ with thermal conductivity (λ).

Figure 6, shows the effect of thermal conductivity (λ) on the temperature of the human tissue profile. It is observed that the human tissue temperature increases sharply when the man does exercise and drop sharply over a period of 7.5 minutes when the man stops exercise. It is observe that, the maximum temperature decreases as thermal conductivity increases, also the minimum temperature increases as thermal conductivity increases.

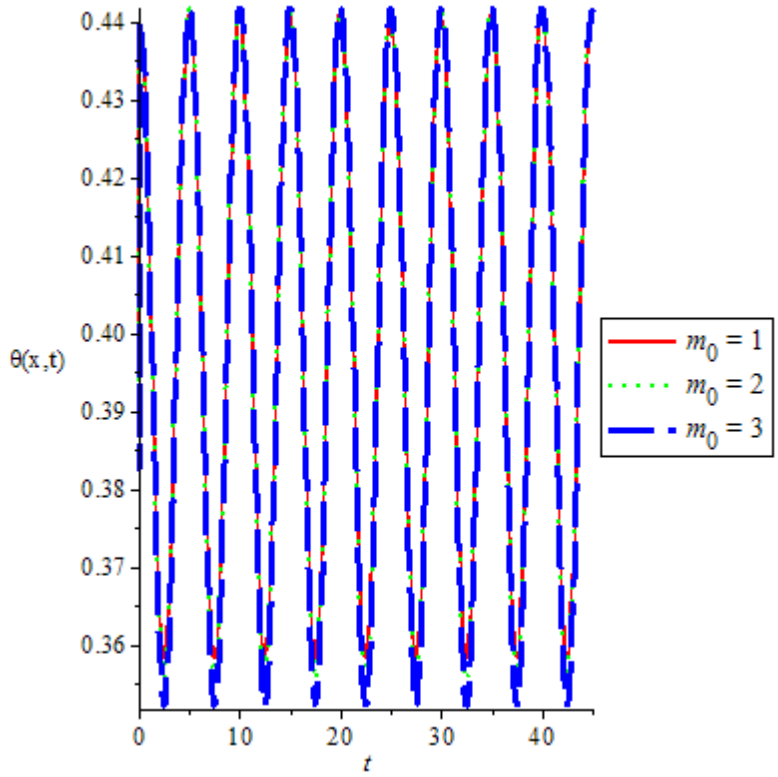

Figure 7: Variation of temperature of the human tissue $\theta(x,t)$ with blood mass flow rate m_0

Figure 7, shows the effect of blood mass flow rate on the temperature of the human tissue profile. It is observed that the human blood mass flow rate increases sharply when the man does exercise and drop sharply over a period of 2.5 minutes when the man stops exercise. It is observed that, the maximum temperature decreases as blood mass flow rates increases, and also the minimum temperature decreases as the blood mass flow rate increases.

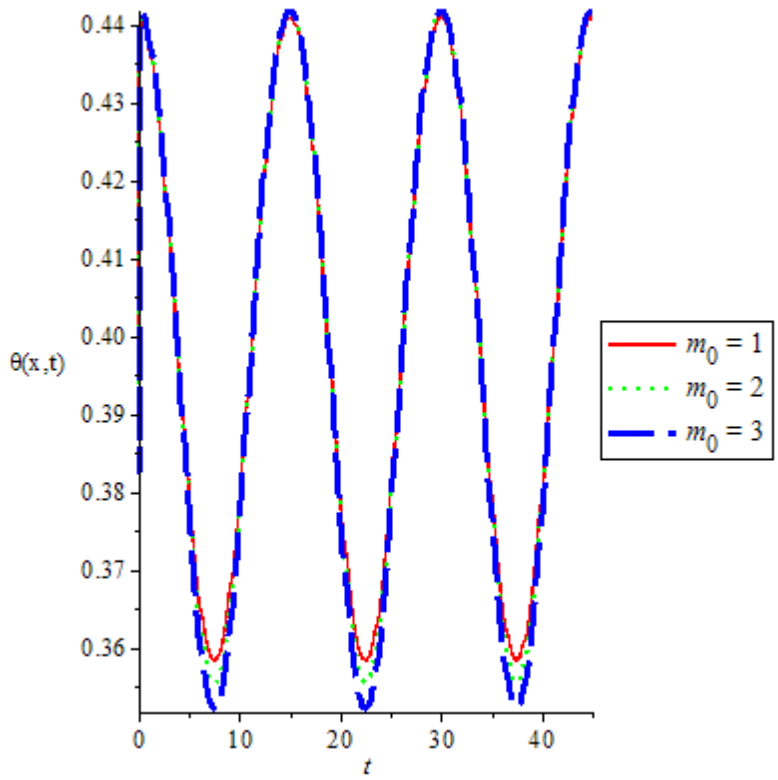

Figure 8: Variation of temperature of the human tissue $\theta(x,t)$ with blood mass flow rate m_0

Figure 8, shows the effect of blood mass flow rate on the temperature of the human tissue profile. It is observed that the human blood mass flow rate increases sharply when the man does exercise and drop sharply over a period of 7.5 minutes when the man stops exercise. It is observed that, the maximum temperature decreases as blood mass flow rates increases, and also the minimum temperature decreases as the blood mass flow rate increases.

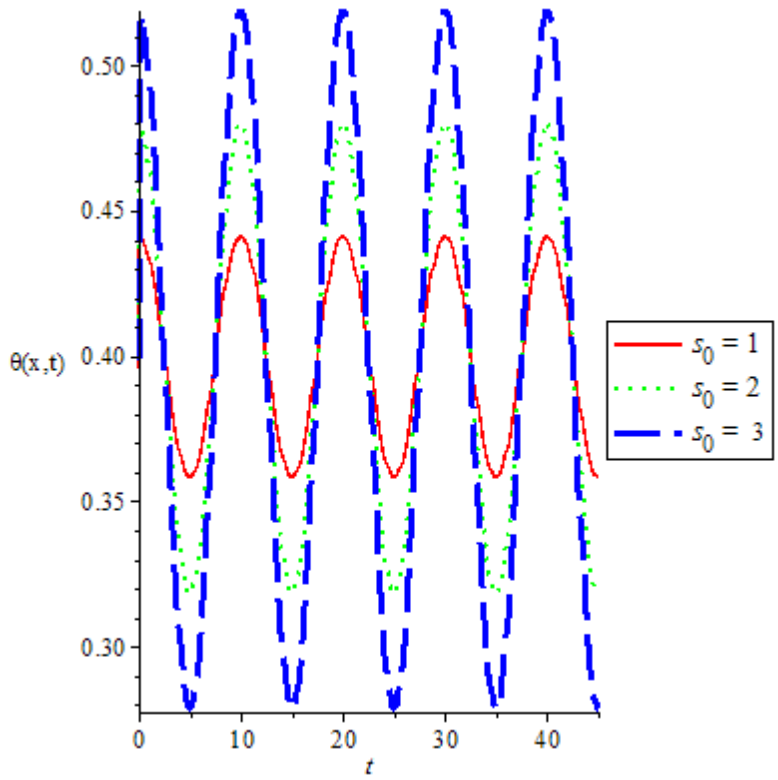

Figure 9: Variation of temperature of the human tissue $\theta(x,t)$ with rate of metabolic heat generation in tissue s_0

Figure 9, shows the effect of rate of metabolic heat generation in tissue on the temperature of the human tissue profile. It is observed that the human rate of metabolic heat generation in tissue increases sharply when the man does exercise and drop sharply over a period of 5.0 minutes when the man stops exercise. It is observed that, the maximum temperature decreases as the rate of metabolic heat generation in tissue increases. Also, the minimum temperature decreases as the rate of metabolic heat generation in tissue increases.

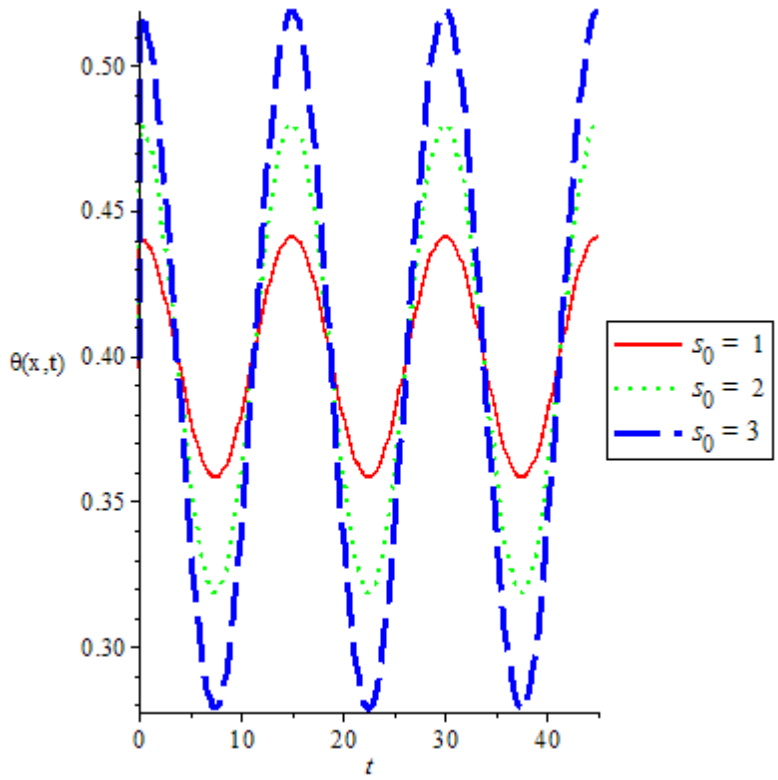

Figure 10: Variation of temperature of the human tissue $\theta(x,t)$ with rate of metabolic heat generation in tissue s_0

Figure 10, shows the effect of rate of metabolic heat generation in tissue on the temperature of the human tissue profile. It is observed that the human rate of metabolic heat generation in tissue increases sharply when the man does exercise and drop sharply over a period of 7.5 minutes when the man stops exercise. It is observed that, the maximum temperature decreases as the rate of metabolic heat generation in tissue increases. Also, the minimum temperature decreases as the rate of metabolic heat generation in tissue increases.

5.0

6.0

7.0 *Conclusion*

The Mathematical model developed for the temperature distribution in SST region of human limbs during exercise was solve analytically using parameter expanding method and eigenfunction expansion technique to

predict the effect of thermal conductivity, blood mass flow rate, and the rate of metabolic heat generation in tissue for a human subject that is involved in doing a physical exercise over a period of time.

Furthermore, the model developed can be used to generate thermal information for developing strategies regarding physical work and rest for sportsmen, military persons and labourers based on their biophysical and demographic characteristics like fitness, age, clothing, sex and so on

References

Bellomo N. and Preziosi L. , Modelling mathematical methods and scientific computation, (CRC Press, Boca Raton, 1995).

Cena & Bates, (1992). Sweat and the Human Body. Heat stress and Heat disorder 12-15

Donald W.T (2013), Apply partial differential equation

(Encyclopedia of science clarified, 2013). The Benefits of Physical Activity Harvard School of Public Health. Retrieve from http://www.hsph.harvard.edu/nutritionsource/staying-active-full-story/ and Exercise as Preventive Medicine The New York Times

(Encyclopedia of science clarified, 2013).Regular physical exercise improving health and wellness Retrieve from http://well.blogs.nytimes.com/2013/10/09/exercise-as-preventive-medicine/?_r=1

Gisolfi, C.V and Mora F. (2000), the hot brain: Survival, Temperature and the Human Body, Massachusetts. MIT Press, 1-13.

Havenith et al., (1990). The effects of hypohydration on Thermoregulation in Heat loss 12-15

He, JH (2006): Some asymptotic methods for strongly nonlinear equations, *Int. J. Modern Phys.* B. 20(10): 1141 – 1199

J.W Mitchell, T.L Galvez, J Hengle, G.E Myers, and K.L Siebecker (2008), Thermal response of human legs during cooling, J.Appl. Physiology. USA,Vol.29(6) 859-865.

K.N Chao, J.G Eisley and W.J Yang , (1973), Heat and water migration in regional skins and Subdermal tissues, Bio-Mech., Symp.ASME69-72.

K.R Pardasani, and N Adlakha (1995), Coaxial circular sector elements to study two-dimensional heat Distribution problem in Dermal regions of human limbs, Int. J of Mathematical and Computer Modelling,Vol.22(9) 127-140.

K.R Pardasani, and N Adlakha (1993), Two-dimensional steady state Temperature Distribution in annular tissue layers of a human or animal body, Indian, J. Pure appl. Math,Vol.24(11) 721-728.

Kumari and Adlakha (2013), One Dimensional Model to Study the Effect of Physical Exercise on Temperature Distribution

K.R Pardasani, and N Adlakha (2000), Exact Solution to a heat flow problem in Peripheral

Patterson, A.M. (1976), Measurement of Temperature Profiles in Human Skin, South African J.Sci,Vol.72 (78-79).

K.R Pardasani, and N Adlakha (1995), A study of thermal effect of epithelial tumor on Temperature Distribution in annular tissue layers of a human body, Proc. Int. Conf. IEEE Engineering in Medicine & Biology, 4.45-4.46.

K.R Pardasani, and N Adlakha (1993), Two-dimensional steady state Temperature Distribution in annular tissue layers of a human or animal body, Indian, J. Pure appl. Math,Vol.24(11) 721-728.

K.R Pardasani, and M Shakya (2005), A two dimensional infinite element model to study Temperature Distribution in human Dermal regions due to tumors, Int. J of Mathematics and Statistics,Vol.1(3) 184-188.

M Agrawal, N Adlakha, and K.R Pardasani (2010), Semi numerical model to study Temperature Distribution in Peripheral Layers of Elliptical and Tapered shaped human limbs, Journal of Mechanics in Medicine and Biology,Vol.10(1) 57-72.

Nose et al., (1988), Research on the water deficit from both the intracellular and extracellular fluid compartments.

Peter et. al, (170) a book on Excursions in modern mathematics.

Unsworth, J. & Duarte, F.J.(1979). Heat diffusion in a solid sphere and Fourier theory Tissue layers with a solid Tumor in the Dermis, Indian, J. Pure appl. Math,Vol.22(8) 679-687.

V.P, Saxena (1983), Temperature distribution in human skin and sub dermal Tissues, J.Theo. Biol.,Vol.102 277-286.

V.P Saxena, and K.R Pardasani (1987), Steady state radial heat flow in skin and underlying tissue layers of Spherical regions of human or animal body, Int.J. Tech,Vol.25(4) 501-505.

Warburton, D.E.R., S. Charlesworth, A. Ivey, L. Nettlefold and S.S.D. Bredin, 'A systematic review of the evidence of Canada's Physical Activity Guidelines for Adults', Int J Behav Nutr Phys Act 2010, 7: 39

Candas et al., (1986). A review of the evidence of Water as the component of the human body. The effects of hypohydration on Thermoregulation 12-14

Sutton et al.,(1972) A review of the evidence of water deficit and magnitude of performance The effects of hypohydration on Thermoregulation 12-14

STUDY OF THE THERMAL DEGRADATION PROFILE OF CHEMICALLY MODIFIED WOOD SAWDUST

Ruth A. Lafia-Araga[1]*, Blessing A. C. Enwere[2], Mohammed A. T. Suleiman[3] and Stephen S. Ochigbo[4].
[1,3&4] Department of Chemistry, School of Physical Sciences, Federal University of Technology, Minna.
[2] Department of Chemistry, federal College of Education, Zuba, FCT, Abuja.
[1] rutharaga@yahoo.ca
[2] chibless2013@gmail.com
[3] smatsule@yahoo.com
[4]stephen_ochigbo@yahoo.com
*corresponding author

Abstract
In this study, *Gmelina arborea* sawdust was chemically modified using, 4% and 8% concentrations of NaOH solution for 30 and 90 minutes soaking times. The influence of this modification on the chemical composition and thermal properties of samples were investigated. Functional groups analysis by Fourier Transform Infrared Spectroscopy (FTIR) showed evidence of reduction in OH and removal of C=O groups associated with the wood polymers after chemical modification. Chemical characterization of samples revealed that the percentage content of hemicellulose decreased from 23.49% in the unmodified sample to 20.80%, 17.55% and 15.15% in samples soaked in 4% NaOH solution for 90 minutes, 8% NaOH for 30 and 90 minutes respectively. The amount of lignin decreased from 25% in unmodified samples to 19.00% when the sample was treated with 8% NaOH for 90 minutes. A moisture content of 9.02% and 2.50% were recorded in unmodified and sample treated with 8% NaOH for 90 minutes respectively. However, the cellulose content increased from 38.10% in unmodified sample to 60.10% when the sample was treated with 8% NaOH for 90 minutes. The percentage weight loss increased as concentration and modification time increased. Thermogravimetric analysis revealed that samples treated with 4% NaOH for 90 minutes presented the highest onset and peak degradation temperatures of 274.04°C and 372.11°C respectively. From these results, it can be concluded that modification with 4% NaOH solution for 90 minutes imparted a significant improvement on the thermal stability of *Gmelina arborea* sawdust.

Keywords: Chemical Modification, FTIR, Lignocellulosics, Thermal Degradation, and Thermogravimetry

1. Introduction

Lignocellulosic materials such as wood, water plants, grass, agricultural residues and other plant substances are natural, three-dimensional polymeric composites that consist of lignin, hemicellulose and cellulose. Wood had played vital roles in different industrial sectors, such as in packaging, as attractive reinforcement material in automobiles as well as in building/engineering applications because of their unique qualities such as light weight, renewability, abundance, non-toxicity, low processing energy/cost, less abrasiveness to plastic processing equipment and useful mechanical properties (Fa´bio *et al.*, 2007).

In spite of the several applications of wood in the construction/furniture industries, it has a number of limitations. This includes thermal instability, biodegradability (low microbial resistance), hygroscopicity (high moisture absorption), poor adhesion with hydrophobic polymer matrix, dimensional instability and the restriction of the processing temperature of wood composites to about 200°C since wood polymers undergoes degradation at higher temperature (Maya and Rajesh, 2008; Sultana *et al.*, 2012).

These limitations of wood are due to the presence of hydroxyl groups (OH) in their three main chemical components; cellulose, lignin and hemicellulose, which are responsible for the basic chemical and physical properties of wood. Several treatment methods have been employed to alleviate these limitations and enhance better performance (Kallakas *et al.*, 2015; Wu *et al., 2016*). Alkalination by soaking in NaOH is one of the modification methods employed in order to checkmate these disadvantages (Hakkou *et al.*, 2005; Korkut and Kocaefe, 2009; Rowell, 2006; Shayesteh and Gregory, 2015; Xiaoli *et al.*, 2015). Reports revealed improved mechanical properties of polymer matrix composites obtained from combining alkaline treated wood saw dust with high density polyethylene (Olakanmi et al., 2015).

The reaction between wood and NaOH solution is as shown below:

Wood- OH + NaOH $\longrightarrow$ Wood – O^-Na^+ + H_2O + [surface impurities]

The thermal properties of composites resulting from alkali treated wood composites were reported to improve over the untreated counterparts (Olakanmi et al., 2015).

The analysis of the thermal degradation profile of chemically modified *Gmelina arborea* wood sawdust will help to determine its thermal stability. Furthermore, it will assist in designing a better process conditions for composite production. An understanding of the degradation temperatures will enable the determination of the processing temperature in order to avoid excessive degradation in the processing equipment, which can lead to poor mechanical properties of the resultant composites.

Therefore this study is aimed at modifying *Gmelina arborea* sawdust with NaOH solutions of different concentrations and time, and to study the effect of alkaline modification on their thermal degradation profile in order to ascertain its potential for use as fillers in polymer matric composites (PMC).

2. Literature Review

Mercerization, the alkaline treatment of natural fibres, is one of the common methods of producing high quality fibres for composites production. Alkaline treatment of natural fibres disrupts the hydrogen bonding in the network structure of the wood polymers, thereby increasing the surface roughness. It reduces fibre diameter, increases aspect ratio, increases the amount of crystalline cellulose and removes natural and artificial impurities, thereby producing a rough surface topography (Kalia et al.,2009). Consequently, there is an increase in the number of reactive sites by increasing the amount of cellulose exposed on the fibre surface thereby increasing the surface roughness. In addition, it affects the degree of polymerization and molecular orientation of cellulose crystallites due to the removal of the binding substances like lignin and hemicellulose (Gassan and Bledzki, 1999).

The type of alkali (KOH, LiOH and NaOH) and its concentration affect the degree of modification. Studies revealed that NaOH treatment results in higher modification than other alkalis (John and Anandjiwala, 2007). Liu *et al*. (2004) studied the effects of alkaline treatment on the structure, morphology and thermal properties of native grass fibres as reinforcements for polymer matrix composites. The authors soaked chopped grass fibre in 5% and 10% solution of NaOH for between 1 and 16 hours. Results revealed that the amount of lignin and hemicellulose reduced with alkali treatment and time. It was also observed that the degradation peak temperature of the grass fibre increased with the treatment and duration, indicating an increase in thermal stability. This was attributed to the removal of hemicellulose with alkaline treatment. The authors concluded that higher concentration of NaOH causes excessive delignification of natural fibres resulting in weaker or damaged fibre.

3. Methodology

3.1 Sample Collection and Preparation

The *Gmelina arborea* sawdust was collected from a sawmill in the timber market in the Federal Capital Territory, Abuja Nigeria, during milling operation. The sample was cleaned manually and dried at 105°C until a constant weight was obtained. Finally, the sample was ground and sieved to obtain particles between 40 and 100 mesh sizes (150-400μm) and kept in a desiccator for further use.

3.2 Modification with NaOH Solution

Modification with NaOH solution was carried out in accordance with the method described by Jayabal *et al.*, (2012) with slight modifications. 2.00 g of sample was soaked in 100 cm^3 of 2% 4%, 6%, 8% and 10% NaOH solution for 30, 60 and 90 minutes respectively. The sample was neutralized with 2% H_2SO_4 to pH of 7 and washed several times with deionized water. The modified sample was dried in an oven at 105°C until a constant weight was achieved. The extent of modification was calculated as percentage weight loss which was measured as the differences between oven dry weight of the sample before modification (W_1) and after modification (W_2) using the formula;

Percentage weight loss = $[(W_1–W_2)/W_1] \times 100$

3.3 Chemical Composition of Samples

Ash content was assessed using ASTM E-1755 (2002) standard while moisture content was determined according to ASTM D-4442 (2002) standard. Extractives free wood were prepared according to ASTM D-1105 (2003) standard. Acid insoluble lignin was determined using ASTM D-1106 (2002) standard. Cellulose and hemicellulose content was determined according to the method described by Rowell *et al*. (2005)

3.4 FTIR Analysis

FTIR-ATR spectra of samples were recorded using the FTIR spectrophotometer (Spotlight 400, Perkin Elmer, USA), combined with a universal ATR accessory at a resolution of 4 cm^{-1} for 64 scans in the range of 650-4,000 cm^{-1}. Samples were pressed against the diamond crystal of the ATR unit. A pressure applicator with a torque knob ensured that the applied pressure was the same for all measurements.

3.5 Thermal Properties

The thermogravimetric (TG) analysis was carried out on between 5 and 7 mg sample in the temperature range of between 50°C and 650°C under a nitrogen atmosphere at a flow rate of 20 cm^3min^{-1} and a heating rate of 10°$Cmin^{-1}$. Continuous records of weight loss versus temperature were obtained and analyzed to determine the following TGA parameters; onset temperature (T_{onset}/°C), peak temperature (T_p/°C), temperature at 50% mass degradation ($T_{50\%}$/°C) and degradation temperature range (°C). Derivative peak temperature (DT_p) was defined as the temperature of the maximum derivative of the weight change with time.

4. Results and Discussion

4.1 Weight loss

The results of weight loss of chemically modified samples are presented in Table 1. At 30 minutes modification, the weight loss (in %) was 6, 8, 10, 13 and 18 for samples modified with 2%, 4%, 6%, 8% and 10% NaOH concentrations respectively. At 60 minutes modification, the weight loss (%) was 10, 13, 16, 18 and 22 in samples treated with 2%, 4%, 6%, 8% and 10% NaOH concntrations respectively. The highest weight loss of 13, 18, 16, 22 and 24% was observed in the samples soaked for 90 minutes when the concentrations of the NaOH solution was 2% , 4%, 6%, 8% and 10% respectively.

Table 3.1: Percentage Weight Loss for NaOH Modified Samples

S/N	Soaking Time (Minutes)	Percentage Weight Loss (%)				
		2% NaOH	4% NaOH	6% NaOH	8% NaOH	10% NaOH
1	30	6	8	10	13	18
2	60	10	13	16	18	22
3	90	13	18	16	22	24

The result agrees with the findings of Liu *et al.* (2004) who investigated the effect of NaOH modification on weight loss of native grass fiber and reported an increase in weight loss as modification duration and NaOH concentration increased. The observed increase in percentage weight loss as the concentration of NaOH solution and modification duration increased is an indication of the dissolution of hemicellulose and lignin. Further increase in NaOH concentration and modification duration could lead to the formation of a weak or damaged sample (Mansour *et al.*, 2011). In addition, treatment with 2% NaOH presents the lowest weight loss, an indication that this concentration of NaOH had a minimal effect on the wood flour. On the other hand, samples immersed in 10% NaOH displayed values that can also be obtained when samples were soaked in 8% solution of NaOH. Samples treated with 6% NaOH did not show any justifiable trend. Therefore, 4% and 8% NaOH concentrations at 30 and 90 minutes soaking durations were chosen as the optinum reaction condition for subsequent analysis of the samples.

4..2 Chemical Composition Analysis

Table 2 presents the percentage composition of unmodified and modified samples. The moisture content decreased with NaOH concentration and soaking time. The highest moisture content of 9.02% was recorded in the unmodified sample, while the lowest (2.50%) was obtained for sample soaked in 8% NaOH solution for 90 minutes. On exposing the samples to NaOH solution, swelling of the sample and formation of hydrophobic ionic groups (Cellulose-O^-Na^+) on the surface of the sample occurred. This could lead to the decrease its moisture absorption capacity, thus leading to the reduction in the observed moisture content of the sample. The decrease could also possibly be attributed to the reduction in number of hydroxyl (OH) groups in the wood sawdust components as well as the partial removal of hemicellulose and lignin by NaOH solution (Akinrinola *et al.*, 2014). Similarly, the unmodified samples presents the highest extractives content (3.10%) than the modified samples. The hemicellulose (24.49%) and lignin (25.00%) contents decreased to 15.15% and 19.00% respectively, after soaking the samples with NaOH solution. Also, from the result, the amount of ash and cellulose showed an increase after modification. The observed increase in percentage content of cellulose in the modified samples could be because of the partial hydrolysis of hemicellulose and the depolymerization of lignin leading to the formation of sugar and phenolic groups which are soluble in water. The hydroxyl groups in cellulose have been converted to alkoxides (Cellulose-O^-Na^+) during modification and to inorganic salt on neutralization with 2% H_2SO_4. However, on rinsing with water, the sodium ion (Na^+) that was linked to cellulose was removed which then led to transformation of native cellulose 1 to cellulose 11 with a new crystalline structure, hence reducing hydrophilicity (Mohammed and Kesava, 2014).

Table 2: Percentage Composition of cell wall Polymers present in Unmodified and Modified Samples

Results are expressed in mean values, ± standard deviations where n=5.

Materials	Moisture content (%)	Ash content (%)	Extractives (%)	Hemicellulose (%)	Cellulose (%)	Lignin (%)
Unmodified	9.02 ± 0.1	0.4 ± 0.02	3.10 ± 0.2	24.49 ± 0.2	38.10 ± 0.1	25.00 ± 0.3
4% NaOH 30 minute	6.40 ± 0.13	2.15 ± 0.05	2.19 ± 0.1	22.93 ± 0.5	42.70 ± 0.6	23.53 ± 1.0
4 % NaOH 90 minute	5.44 ± 0.2	2.40 ± 0.01	1.33 ± 0.2	20.80 ± 0.4	49.90 ± 0.1	21.13 ± 0.1
8% NaOH 30 minute	3.20 ± 0.1	2.83 ± 0.01	0.85 ± 0.4	17.55 ± 0.2	57.50 ± 0.4	19.20 ± 1.5
8 % NaOH 90 minute	2.50 ± 0.5	3.10 ± 0.02	0.63 ± 0.1	15.15 ± 0.3	60.10 ± 0.2	19.00 ± 0.2

4.3 FTIR Analysis

The FTIR spectra of unmodified and modified samples are shown in Figure 1. All the spectra band revealed in the samples are those typical of lignocellulosic materials. The spectra band around 3335 cm^{-1} showed a reduction in intensity to 3320 cm^{-1} after modification, suggesting a reduction in the hydroxyl groups of the three main wood components. Also the characteristic band at 1735 cm^{-1} disappeared in the modified samples, indicating the removal of carbonyl groups C=O in hemicellulose. The vibration peak at 1507 cm^{-1} assigned to the aromatic C=C in-plane benzene stretching of lignin showed a slight shift to 1505 cm^{-1} confirming its partial removal with NaOH solution. The vibration peak at 1265 cm^{-1} belonging to C-O stretching vibration of acetyl groups in hemicellulose and lignin component of the sample showed a remarkable reduction in wave number to 1254 cm^{-1} in the modified samples and decreased in intensity. The spectra peak at 1317 cm^{-1} assigned to CH_2 wagging vibration in cellulose increased to 1320 cm^{-1} in the modified samples confirming the observed increase in the cellulose content. These results indicates that modification with NaOH could lead to a partial removal of hemicellulose and lignin (Bodîrlău and Teaca, 2007; Deepa *et al.*, 2011; Zhu *et al.*, 2015).

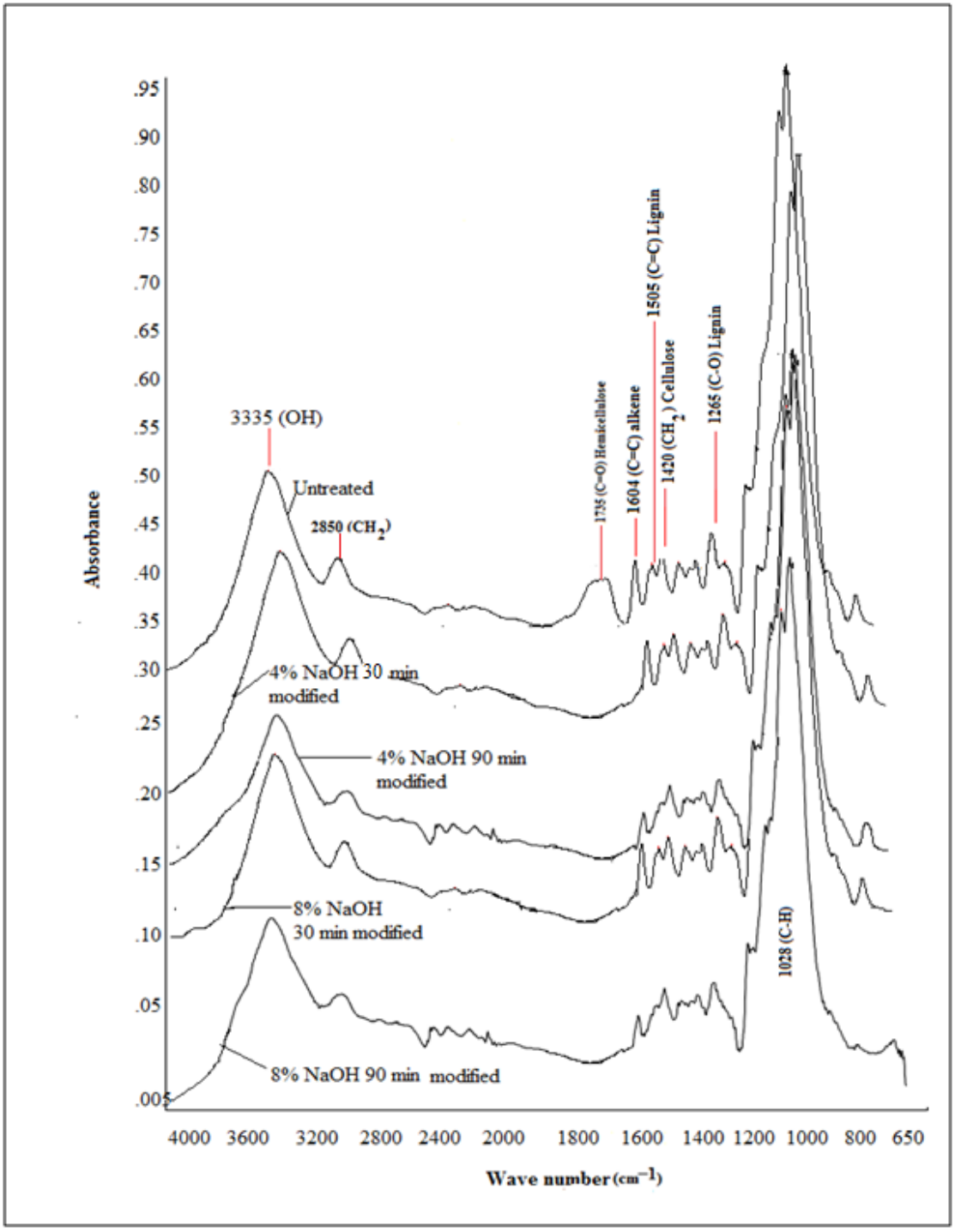

Figure 1: FTIR Spectra of unmodified and modified Sawdust Samples

4.4 Effect of Modification on Thermal Characteristics

The thermogravimetric (TG) and differential thermogravimetric (DTG) curves of samples are shown in Figure 2. Data extracted from these curves are presented in Table 3. There are two main degradation events as shown in the DTG curves. The first event occurred at between 50°C and 150°C. This could be attributed to the evaporation of water and possibly, the volatization of extractives. The results shows that the unmodified sample had the highest percentage weight loss of 1.88% around this temperature region when compared with the modified samples that recorded weight loss as low as 0.132%. The high extractives content in unmodified sample promotes its thermal degradation at lower temperature due to their high volatility and could be responsible for this observation. The second event occurring within the range of 220°C and 400°C, could be

attributed to the degradation of hemicellulose, cellulose, and lignin. It has been observed that lignocellulosic materials, being chemically active, decomposes thermo-chemically in the range of 150°C to 500°C. Hemicellulose degrades between 150°C to 350°C, cellulose between 240°C to 350°C and lignin between 250°C and 500°C (Lafia-Araga *et al*. 2012).

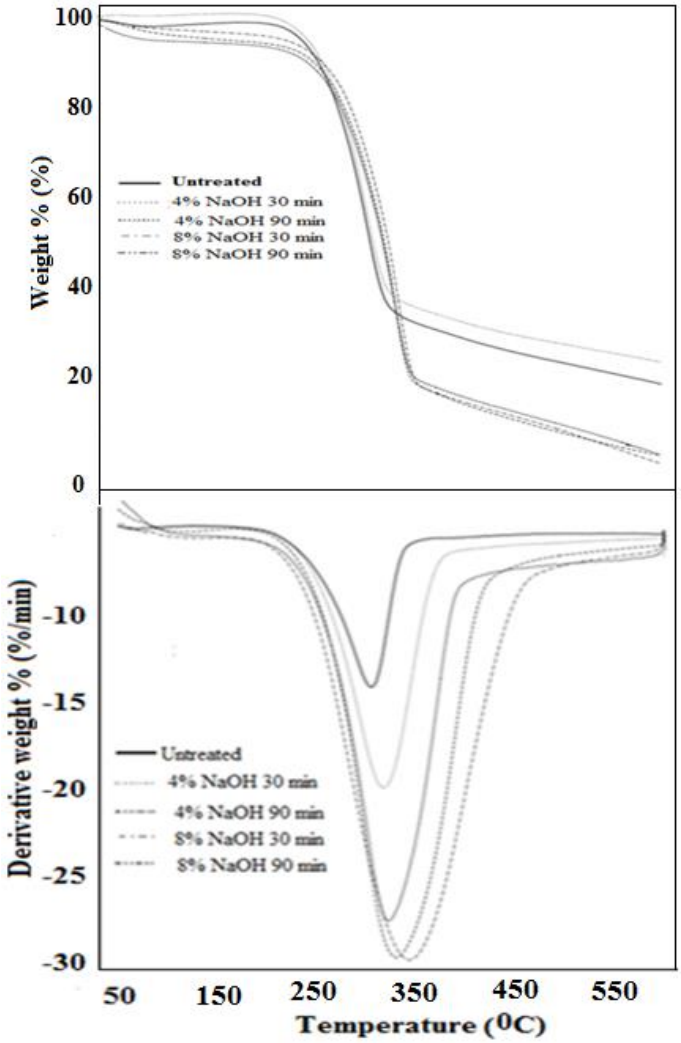

Figure 2: TGA and DTG curves of sawdust samples at 10°Cmin^{-1} heating rate

Although, the samples displayed a general increase in the onset T_{onset} and degradation peak temperatures, T_p, the T_p of the samples increased from 260.20°C in unmodified sample to a highest value of 372.11°C in samples soaked with 4% NaOH solution for 90 minutes. Samples soaked in 4% NaOH solution for 30 minutes has a T_{onset} and T_p of 256.37 and 337.04°C respectively. This improvement in thermal stability may also be as a result of the fact that hemicellulose are removed from the wood flour by alkaline treatment. This is expected to have possibly improved the thermal properties by reducing its heat transfer coefficient (Kotalainen *et al*. 1999; Esteves & Pereira, 2008). The hight T_p value for wood flour treated with 4% NaOH solution for 90 minutes is in agreement with the findings of Olakanmi, *et al*., (2015), who invesgtigated the use of alkaline treated *Daniela oliveri* wood flour as reinforcedment in virgin HDPE and reported that wood flour treated with 4% NaOH solution for 150 minutes produced composites that exhibited the highest T_{onset} and T_p of 375°C and 495°C respectively, indicating the highest thermal stability among the samples. Though samples treated with 8% NaOH for 30 minutes and 90 minutes presented lower values of T_p, there is no observable trend in the T_p of the samples. The lower values at this concentration and soaking time may be due to the depolymerization of the native cellulose resulting in excessive delignification of the wood flour treated with NaOH

concentrations greater than 4% (Olakanmi, *et al*., (2015). This shows that modification with 4%NaOH solution for 90 minutes enhanced the thermal stability of the wood flour used in this study. In general, it has been observed that alkalination of wood flour with NaOH at specified concentration and time has the ability to improve the thermal properties of wood flour (Kelly, *et al.*, 2010; Okoroigwe, 2015). It is therefore necessary to note that samples modified with 4% naOH for 90 minutes can be conveniently compounded with a polymer matrix at temperatures as high as between 250°C and 300°C.

Table 3: Thermal Degradation data for unmodified and samples modified with 4% and 8%NaOH for 30 and 90 minutes

Samples	T_{onset} (°C)	T_p (°C)	$T_{50\%}$ (°C)	Degradation temperature range (°C)	Moisture (%)
Unmodified	230.33	260.20	265.00	220.20-358.12	1.8
4% NaOH 30 min	256.37	337.04	345.33	220.10-401.22	1.57
4% NaOH 90 min	274.04	372.11	361.15	226.22-413.34	0.13
8% NaOH 30 min	267.15	366.10	355.34	226.03-409.23	0.17
8% NaOH 90 min	270.37	367.51	356.21	222.10-411.97	0.30

5. Conclusion

The alkaline modification of *Gmelina arborea* with NaOH solution at different concentrations and durations was successfully carried out. The results revealed an increase in weight loss as the concentration of NaOH and time of soaking increased, indicating the dissolution of hemicellulose and lignin. The moisture, hemicellulose, lignin and extractives content decreased with modification, whereas, the cellulose content showed and appreciable increase with concentration and time. FT-IR spectra showed evidence that modification of wood sawdust by NaOH solution had taken place as the absorption peak at 1735 cm^{-1} assigned to carbonyl group disappeared after modification, suggesting that a dissolution of hemicellulose and lignin in NaOH had occurred. The peak at 3335 cm^{-1} which corresponds to hydroxyl (OH) molecules present in absorbed water and the three main polymeric constituents in the samples showed a reduction in both intensity and absorbance, a possible proof that the OH groups of the wood polymers had decreased. Thermogravimetric assessment of the samples indicates that the T_{onset} and T_p of the samples are higher in the modified wood flour relative to the unmodified counterparts. This indicates that the degradation of hemeicellulose, the component of the wood polymer with the lowest thermal stability, has led to the overall thermal stability of the modified samples.

From the results it can be concluded that chemical modification with 4%NaOH for 90 minutes has resulted in significant improvement in the thermal properties of *Gmelina arborea* sawdust. This study encourages the use of the modified wood sawdust as fillers in polymer matrix composites, as it can be processed conveniently at temperatures between 250°C and 300°C without damage to the thermal properties of the wood flour.

References

Akinrinola, F. S., Darvell, L. I., Jones, J. M., Williams, A., and Fuwape, J. A. (2014). Characterization of selected Nigerian biomass for combustion and pyrolysis applications. *Energy and Fuels*, 28(6), 3821-3832.

ASTM D1106-96(2013), Standard Test Method for Acid-Insoluble Lignin in Wood, ASTM International, West Conshohocken, PA, 2013, www.astm.org

ASTM E1755-01(2015), Standard Test Method for Ash in Biomass, ASTM International, West Conshohocken, PA, 2015, www.astm.org

ASTM D1105-96(2013), Standard Test Method for Preparation of Extractive-Free Wood, ASTM International, West Conshohocken, PA, 2013, www.astm.org

ASTM D4442-16, Standard Test Methods for Direct Moisture Content Measurement of Wood and Wood-Based Materials, ASTM International, West Conshohocken, PA, 2016, www.astm.org

Bodîrlău, R., and Teacă, C. A. (2007). Fourier transforms infrared spectroscopy and thermal analysis of lignocelluloses fillers modified with organic anhydrides. *Romanian Journal of Applied Physics*, Vol. 54(1–2), 93–104.

Deepa, B., Abraham, E., Cherian, B. M., Bismarck, A., Blaker, J. J., Pothan, L. A., Leao, A. L., and Kottaisamy, M. (2011). Structure, morphology and thermal characteristics of Banana nanofiber obtained by steam explosion. *Bioresource Technology*, Vol. 102 (11), 1988-1997.

Esteves B and Pereira H. M.(2008) Wood modification by heat treatment: A review. *BioResources*, Vol. 4(1): 370-404.

Fa´bio, T., Thais, H. D. S., and Kestur, G. S. (2007). Studies on lignocellulosics fiber of Brazil. Part II: Morphology and properties of Brazilian coconut fiber. Composites: Part A, Vol. 38, 1710–1721.

Gassan J and Bledzki A. K. (1999). Alkali treatment of jute fibres: Relationship between structure and mechanical properties. *Journal of Applied Polymer Science*. Vol. 71(4): 623-629.

Hakkou, M., Pétrissans, M., Bakali, I., Gérardin, P., and Zoulalian, A. (2005). Wettability changes and mass loss during heat treatment of wood. *Holzforschung*, Vol. 59(1), 35-37.

Jayabal, S., Sathiyamurthy, S., Loganathan, K. T., and Kalyanasundaram, S. (2012). Effect of soaking time and concentration of NaOH solution on mechanical properties of coir polyester composites. *Bulletin of Material Science, Indian Academy of Sciences*, Vol. 35(4), 567–574.

Kallakas, H., Shamim, M. A., Olutubo, T., Poltimäe, T., Krumme, A., and Kers, J. (2015). Effect of chemical modification of wood flour on the mechanical properties of wood-plastic composites. *Agronomy Research*, Vol. 13(3), 639–653.

Kalia S., Kaith B. S and Kaur I (2009). Pretreatments of natural fibres and their application as reinforcing material in polymer composites - A review. *Polymer Engineering & Science* Vol. 49(7): 1253-1272.

Kelly, C. C., Carvalho, D. R., Mulinari, H. J. C., Maria, O. H. C., and Voorwald, A. C. (2010). Chemical modification effect on the mechanical properties of Hips/Coconut fiber composites. *Bioresource Technology*, Vol. 5(2), 1143-1155.

Korkut, S., and Kocaefe, D. (2009). Effect of heat treatment on wood properties. Duzce University. *Journal of Forestry*, Vol. 5(2), 11-34.

Kotalainen R, Alen R and Arpiainen V. (1999) Changes in the chemical composition of Norway Spruce (Picea abies) at 160°C–260°C under air and nitrogen atmospheres. Paper Timber; 81(5): 384–388.

Lafia-Araga R. A., Hassan A., Yahya R., Rahman N. A., Hornsby P. R and Heidarian J (2012). Thermal and mechanical properties of treated and untreated Red Balau (Shorea dipterocarpaceae)/LDPE composites. *Journal of Reinforced Plastics and Composites* Vol. 31(4): 215-224.

Liu, W., Mohanty, A. K., Drzal, L. T., Askel, P., and Misra, M. (2004). Effects of alkali treatment on the structure, morphology and thermal properties of native grass fibers as reinforcements for polymer matrix composites. *Journal of Materials Sciences*, Vol. 39, 1051–1054.

Mansour, R., Hocine, O., Abdellatif, I., and Noureddine, B. (2011). Effect of chemical treatment on flexure properties of natural fiber-reinforced polyester composite. *Procedia Engineering*, Vol. 56(10), 2092-2097.

Maya, J. J., and Rajesh, D. A. (2008). Recent development in chemical modification and characterization of natural fiber-reinforced composites. *Polymer Composites*, Vol. *29(2): 187-207.*

Mohammed, A. A., and. Kesava, R. V. (2014). Thermal characterization of Neem and Cork wood polyacrylonitrile composites. *Global Journal of Research in Mechanical and Mechanics Engineering*, Vol. 14(3), 234-245.

Okoroigwe, E. (2015). Combustion analysis and devolatilisation kinetics of Gmelina, Mango, neem and tropical Almond woods under oxidative condition. *International Journal of Renewable Energy Research*, Vol. 5(4), 1024-1033.

Olakanmi E.O, Ogunesan, E.A., Vunai, E, Lafia-Araga R.A**,** Doyoyo M and Meijboom R (2015). Mechanism of Fiber/Matrix Bond and Properties of Wood Polymer Composites Produced From Alkaline Treated Daniella oliveri Wood Flour. *Polymer Composites*. DOI 10.1002/pc.23460.

Rowell, R. M. (2006). Acetylation of wood: A journey from analytical technique to commercial reality. *Forest Product Journal*, Vol. 56(9), 4–12.

Rowell R. M., Pettersen R., Han J. S., Rowell J. S and A. Tshabalala M. (2005). *Cell wall chemistry*. In: R. M. Rowell; Editor. Handbook of wood chemistry and wood composites. Boca Raton: CRC Press,. 473.

Shayesteh, H., and Gregory, D. S. (2015). Natural fiber reinforced polyester composites: A literature review. *Journal of Reinforced Plastics and Composites,* Vol. 35, 23-29.

Sultana, S., Nur, H. P., Saha, T., and Saha, M. (2012). Fabrication of raw and oxidized sawdust reinforced low density polyethylene (LDPE) composites and investigation of their physico-mechanical properties. *Bangladesh Journal of Scientific and Industrial Research,* Vol. 47(4), 365-372.

Xiaoli, G., Lan, S., Guozhen, L., Chaoqun, Y., Chun, K. C., and Jianfeng, Y. (2015). Chemical modification of poplar wood in gas and liquid-phase acetylation. *Wood Research,* Vol. 60 (2), 247-254

Zhu, J., Brington, J., Zhu, H., and Abhyankar, H. (2015). Effect of alkali, esterification and silane surface treatments on properties of flax fibers. *Journal of Scientific Research & Reports,* Vol. 4(1), 1-11.

Wu, C-M 1., Lai, W-Y., and Wang, C-Y (2016). Effects of Surface Modification on the Mechanical Properties of Flax/Polypropylene Composites. *Materials*, Vol. 9 (5), 314:1-11.

IN-VITRO ANTIBACTERIAL ACTIVITY – GUIDED ISOLATION AND CHACTERIZATION OF β-SITOSTEROL FROM THE MESOCARP OF THE FRUITS OF Diospyros mespiliformis

Fadipe, L. A[1*], Babayi, H[2], Ogunyemi, O. J[1], Suleiman, B. O[1], Yahaya, J[1], Agada, E. E[1] and Anga, P. I[1]
[1]Department of Chemistry, Federal University of Technology, Minna, Niger State, Nigeria
[2]Department of Microbiology, Federal University of Technology, Minna, Niger State, Nigeria
[1]labsfad@yahoo.com
[2]acadbabayi@yahoo.com
*Corresponding author

Abstract

A phytochemical and antibacterial study of the chloroform extract of the mesocarp of the fruits of *Diospyros mespiliformis* and its fractions led to the isolation of β-sitosterol (a phytosterol) for the first time from the fruits of the plant. The structure of the isolated compound was elucidated using physical parameters, colour reactions, spectroscopic identification and literature search. The isolated compound at 100μg/cm^3 displayed moderate inhibitory activity against tested Gram-positive and Gram-negative organisms in comparison to that exhibited by erythromycin (100 μg/cm^3) against the test organisms.

Keywords: Antibacterial, β-sitosterol, chloroform extract, *Diospyros mespiliformis*, isolation and mesocarp

1. Introduction/Literature Review

Beta-sitosterol,a 4-desmethyl sterol which structurally resembles cholesterol produced in the human body is one of the well-known bioactive plant sterols with several biological and pharmacological activities. It has been isolated and purified from non-polar fractions of diverse plant families and marine sources using different chromatographic methods (Saeidnia *et al*., 2014). *Diospyros mespiliformis* Hochst Ex A. Dc (family: Ebenaceae) isa semi-deciduous woodland, savannah plant commonly called African ebony or Jackal berry (English), Kanya (Hausa), Akawayi (Igbo) and Kanram (Yoruba). It is amedium-sized evergreen tree with dense rounded stem and bell-shaped cream-colored flowers (Belemtougri *et al*., 2006). Bark is grey-black, crown is branchy with dense foliage; leaves are alternate, 4.7 cm and 1.5-5.5 cm in length and width respectively. Fruits are spherical with a fleshy berry, greenish when immature and yellowish /orange yellow when ripe. They contain between 4-6 seeds that are bean-shaped, shiny, smooth and dark brown in colouration (Venter and Venter, 1996; Orwa *et al*., 2009). Ethnomedicinally, the plant is used in the treatment of fever, malaria, wounds, leprosy, syphilis, diarrhea, pneumonia, skin diseases and helps in facilitating delivery (Mohammed *et al*., 2009). Research carried out on various parts of the plant revealed its usefulness as an antimalarial (Etkin, 1997; Adzu and Salawu, 2009), antimicrobial (Lajubutu *et al*., 1995; Adeniyi *et al*., 1996; Esimone *et al*., 2009; Shagal *et al*., 2012; Sadiq *et al*., 2013), antitrypanosomal (Freiburghaus *et al*., 1996), anti-inflammatory, analgesic, antipyretic, sedative (Adzu *et al*., 2002a; 2002b), anticancer (Adeniyi *et al*., 2003) and antiproliferative property (Abba *et al*., 2016). Phytochemical studies of the plant revealed the presence of saponins, steroidal and triterpenoidal compounds, anthraquinones, sugars, alkaloids, tannins and flavonoids (Adeniyi *et al*., 1996; Adzu *et al*., 2009; Shagal *et al*., 2012; Abba *et al*., 2016). Triterpenes, such as, α-amyrin, β-sitosterol, lupeol, betulin, betulinic acid and lupenone were isolated from the stem bark of the plant (Zhong *et al*., 1984; Mohammed *et al*., 2009). From the roots, the isolation and antibacterial activity of diosquinone and plumbagin have been reported (Lajubutu *et al*., 1995); diosquinone was later reported to be active against cancer cell lines (Adeniyi *et al*., 2003). A high presence of C16:0 and C18:2 fatty acids were reported in the oil extracted from the fruit seeds and seeds of the plant (Chivandi *et al*., 2009; Adewuyi and Oderinde, 2014). This study was undertaken to separate, isolate and characterize a phytosterol from the chloroform extract of the mesocarp of *Diospyros mespiliformis* via antibacterial testing of the extract, its fractions and sub-fractions in comparison with a standard antibiotic, erythromycin.

2. Materials and Methods

Plant Material

Fruits of *D. mespiliformis* were collected from Angwan Biri, Bosso Local Government Area, Niger state, Nigeria in September, 2016. Fruits were identified and authenticated by Dr. (Mrs.) Jemilat Ibrahim of the Department of Medicinal Plant Research and Development (MPR&TM) of National Institute for Pharmaceutical Research and Development, Idu (NIPRD) and compared with a voucher specimen already deposited (NIPRD number 5120).

Extraction of Plant Material

The fleshy part of the fruits was separated from the seeds, air-dried and pulverized. 1kg of the dried mesocarp was extracted exhaustively by macerating with chloroform and continuously shaking using a flask shaker for 5 days. Extract was concentrated *in-vacuo* to dryness and coded crude chloroform extract of *D. mespiliformis* mesocarp (D, dark green crystalline mass, 1.72 % yield).

Phytochemical Tests for Phytosterols (Harbone, 1998)

(i) Liebermann-Burchard's test: Little quantity of extract D was dissolved in $CHCl_3$ and a few drops of conc. H_2SO_4 added, followed by addition of 3 drops of Ac_2O. A change in colour from violet-blue to green was taken as positive for the presence of a steroidal nucleus.

(ii) Salkowski's test: To a small quantity of extract D in $CHCl_3$, few drops of conc. H_2SO_4were added down the side. Appearance of a reddish-brown color in the $CHCl_3$ layer was taken as evidence of presence of steroidal nucleus.

(iii) A little quantity of extract D was dissolved in 0.5 cm^3 of dioxane and added to 0.5 cm^3 of a solution of cerric ammonium nitrate (4 g of cerric ammonium nitrate was dissolved on mild heating in 10 cm^3 of 2N HNO_3) and mixture shaken thoroughly. Emergence of a yellow color that gradually changed to red indicates the presence of an alcoholic hydroxyl group.

Antibacterial Testing of Crude Extract, D

The antibacterial activity of extract D was tested against overnight cultures of two Gram positive (*Bacillus subtilis* and *Staphylococcus aureus*) and three Gram negative bacteria (*Escherichia coli*, *Pseudomonas aeruginosa* and *Salmonella typhi*) all obtained from the Department of Microbiology, Federal University of Technology, Minna, Niger State, Nigeria. The viability test for each organism was carried out by resuscitating each microorganism on nutrient agar medium and incubating at 37ºC for 24h. 0.2 cm^3 of stock cultures were transferred to 20 cm^3 of Mueller Hinton broth (MHB) and incubated for 5 h to obtain $1x10^6$cfu/cm^3 and a loopful used for assay. The agar dilution method was adopted for the assay (Fadipe *et al*., 2012). 250 mg of extract D was reconstituted in 1 cm^3 of tween-80 and 4 cm^3 of sterile distilled water was added. 1 cm^3 of reconstituted mixture was then transferred to sterile Petri dishes containing 19 cm^3 of Mueller Hinton agar (MHA) and allowed to set at room temperature. A loopful of each standardized bacterial culture was streaked unto each solidified agar plate. Plates were prepared in duplicates. Plates for standard control (erythromycin; 100 µg/cm^3), extract sterility control (ESC), organism viability control (OVC) and medium sterility control (MSC) were also prepared. All plates were incubated aerobically at 37ºC for 24h and checked for growth/no growth of organisms (Table 1).

Isolation, Characterization and Antibacterial Activity of β-sitosterol

Crude extract, D (8g) was applied to the surface of a prepared flash column packed with 200 g of silica gel (60-120 mesh) by wet method and eluted sequentially with varying proportions of increasing polarity of petroleum ether: $CHCl_3$ (100:0 to 0:100). Similar fractions were pooled based on their thin layer chromatographic profile and concentrated *in-vacuo* to yield 4 major fractions, D1-D4. All chromatograms were visualized under UV light (254 and 366 nm) followed by spraying with a solution of vanillin-sulphuric acid and heating at 120ºC. Fractions were tested for the presence of steroidal nucleus and also screened for their antibacterial potentials in comparison with erythromycin(Table 2).

Fraction D4 (2.5 g) obtained from solvent system, petroleum ether: $CHCl_3$, 1:1 was further purified (silica gel; mesh 230-400, 90 g, flash chromatography) and eluting with varying proportions of hexane: EtOAc gave rise

to a single spotted compound from solvent system hex: EtOAc (19:1) which concentrating *in-vacuo* and re-crystallization from EtOH afforded some cream-coloured flakes, coded D4a. The compound was subjected to physical, chemical and spectral characterization.Melting point was uncorrected and recorded by open capillary method. IR and UV were both recorded in $CHCl_3$ using FTIR 8400 spectrometer and T60 UV-Visible spectrophotometer respectively. ^{1}H-NMR, ^{13}C-NMR and DEPT-135 spectra (Table 3) were taken in $CDCl_3$ on Varian Gemini spectrometer operating at 400 MHz, while, its GC-MS was recorded using GCMS-QP 2010 plus, Shimadzu. Optical rotation was recorded using Rudolph Autopol IV automatic polarimeter. Compound D4a was further screened for its antibacterial potentials in comparison with erythromycin(Table 4).

3. Results and Discussion

The crude chloroform extract of *D. mespiliformis* gave a positive Liebermann-Burchard's, Salkowski's and cerric ammonium tests, an indication that the plant has steroidal compounds that possesses alcoholic –OH group(s). Gram positive *B. subtilis* and Gram negative *P. aeruginosa* were sensitive to the extract at 50 mg/cm^3, while only Gram positive *K. pneumoniae* was not susceptible to erythromycin at100 µg/cm^3 (Table 1). Generally, the antibacterial property of a plant extract is dependent on the quality and quantity of bioactives, such as steroidal compounds and the inter-relationship that exists between them and other bioactives (Maffei-Facino *et al*., 1990; Hili *et al*., 1997). Usually, these bioactives, even in relatively low concentrations could be responsible for the observed activity (Dall'Agnol *et al*., 2003).
Fraction D4 obtained from fractionation of extract D also gave strong positive Liebermann-Burchard's and Salkowski's test. Spraying its chromatogram (PE: EtOAc, 9:1) with a mixture of vanillin-H_2SO_4 revealed reddish-brown spots, typical of steroidal compounds (Saeidnia *et al*., 2014). Antibacterial activity of the 4 major fractions at 25 mg/cm^3 showed that the organisms were not susceptible to fractions D1 and D2, while they were moderately sensitive to fractions D3 and D4 (Table 2). Sometimes, fractionation does not improve the antibacterial potency of a medicinal plant (Okoli and Iroegbu, 2004); furthermore, the better biological activity of crude extract, D, than its fractions, probably reflects a synergistic contribution from a number of constituents present in the extract (Ndip *et al*., 2009) or could be that the activity of D was enhanced at higher concentration (Fadipe *et al*., 2012).

Table 1: Antibacterial activity of test compounds against test bacterial strains

Test bacterial strains	Extract D (50mg/cm^3)	Erythromycin (100µg/cm^3)
B. subtilis	-	+
S. aureus	+	+
E. coli	+	+
K. pneumoniae	+	-
P. aeruginosa	-	+
S. typhi	+	+

+ = activity, - = no activity

Table 2: Antibacterial activity of fractions of extract (D) against test bacterial strains

Test bacterial strains	Activity of fractions (25 mg/cm^3 each) against test bacterial strains			
	D1 (PE:$CHCl_3$ 19:1)	D2 (PE:$CHCl_3$ 9:1)	D3 (PE:$CHCl_3$ 4:1)	D4 (PE:$CHCl_3$ 1:1)
B. subtilis	-	-	+	+
S. aureus	-	-	-	+
E. coli	-	-	-	-
K. pneumoniae	-	-	+	-
P. aeruginosa	-	-	+	-

S. typhi	-	-	-	+

+ = activity, - = no activity, PE = Petroleum ether

Characterization of Compound D4a

Physical Characterization

White crystalline flakes (18 mg) re-crystallized from EtOH; melting point, 136-138^{o}C [lit. 135-137^{o}C] (Ahmed *et al*., 2013); single-spotted in petroleum ether: EtOAc (9:1, R_f 0.33), petroleum ether: EtOAc (4:1, R_f 0.54) and $CHCl_3$: EtOAc (4:1, R_f 0.69). The spot gave no colour under sunlight and UV (254 and 366nm), golden brown (I_2 crystals) and reddish-brown (vanillin-H_2SO_4); colour reactions were typical of a steroidal nucleus (Saeidnia *et al*., 2014). Compound was soluble in $CHCl_3$, EtOAc and Me_2CO, slightly soluble in hexane and petroleum ether, insoluble in MeOH, EtOH and H_2O. GC-MS revealed its molecular weight and molecular formula to be 414gmol^{-1} and $C_{29}H_{50}O$ respectively. Its observed rotation, α at 589 nm was -0.05, while, its optical rotation was calculated to be $[\alpha]^{20}_{D\ (589nm)}$= -100.0 [lit. -100.0], an indication that it is a chiral and levorotatory molecule, possessing several chiral centers (Tripathi *et al*., 2013).

Chemical Characterization

Compound **D4a** gave a positive Salkowskii's, Liebermann-Burchard's and cerric ammonium tests indicating that the compound possesses an alcoholic group on a steroidal nucleus. This is typical of all phytosterols (Chaturvedula and Prakash 2012; Mokua, 2013; Tripathi *et al*., 2013, Rajpoot and Singh, 2014; Saeidnia *et al*., 2014).

Spectral Characterization

IR (ν cm^{-1}): 3431 (O-H stretching), 2945 (CH_3 stretching), 2863 (CH_2 stretching), 1632 (C=C stretching), 1451 (CH_2bending), 1072 (C-O stretching) and 1058 (cycloalkane). These absorption bands are due to energy changes arising from molecular vibrations of the bond stretching and bending (deformation) type. The strong absorption band at 3431 cm^{-1} is as a result of the polarity of an oxygen-hydrogen bond (Furniss *et al*., 1989), while, the broad absorption band at 1072 cm^{-1} is as a result of carbon-oxygen bond stretching of a secondary alcohol (Carey, 2003).

^{1}H-NMR (δ ppm): The obtained peaks in comparison with literature (Table 3) are characteristic of a steroidal system, likely a tetracyclic skeleton (Tripathee *et al*., 2011) A doublet at δ4.66 suggests the presence of a proton at position C-6 (olefinic bond between C-5 and C-6), while proton corresponding to H-3α of a sterol moiety appeared as a triple of doublet of doublets at δ3.35, δ3.28 and δ3.21, as earlier reported by Chaturvedula and Prakash (2012). The shielding of this signal indicates its α-orientation (Kumar *et al*., 2014). The spectrum also displayed double of triplets at δ2.41 and δ2.35 assigned to methylene protons at positions C- 4 and C-7 (neighbors to olefinic proton at C-6). Other triplet and multiplet peaks which appeared up-field were assigned to protons appearing at δ1.67, δ1.49, δ1.53, δ1.48… representing protons on C-8, C-9, C-11 and C-12 to mention a few. Two angular protons resonating as singlet at δ0.72 and δ1.02 are due to quaternary methyl protons at C-18 and C-19 respectively, while; another singlet at δ1.01 was due to primary methyl protons at C-29. Other methyl groups resonating as doublets appearing at δ0.98, δ1.12 and δ1.08 are due to secondary methyl protons at C-21, C-26 and C-27 respectively. The peak integration ratio confirmed that the compound is made up of 50 protons.

^{13}C-NMR (δ ppm): Proton de-coupled carbon-13 NMR spectra revealed a total of 29 signals(Table 3) of which signals at δ150.5 and 109.7 ppm, were assigned to C_5 and C_6 double bonds respectively as in Δ^5spirostene (Agrawal *et al*., 1985), while, a signal at δ78.7 was assigned to a carbon bearing an electronegative β-hydroxyl at position 3 (an oxymethine). Usually, OH at C-3 with a β orientation shows a signal of a carbinolic carbon that appears at 78-79 ppm (Kumar *et al*., 2014). A de-shielded peak at ~46.9ppm was assigned to C-4 because it is a neighbor to C-3 (bears the OH group). Another downfield

peak at ~59.8 ppm was given to C-17 as a result of the alkyl substituents attached to it. Other low-field peaks were assigned to methine carbons, while high-field peaks were given to methyl carbons.

DEPT-135 (δ ppm): Among the 29 carbon resonances obtained, DEPT-135 (Table 3) revealed that three carbon atoms were quaternary (disappeared in the spectrum), nine were methine (above in the spectrum), eleven were methylene (below in the spectrum) and six were methyl (above in the spectrum).

GC-MS (m/z): 414[$C_{29}H_{50}O$, M] $^+$, 396[$C_{29}H_{48}$, M - H_2O] $^+$, 329[$C_{24}H_{41}$, M-C_5H_9O] $^+$, 303[$C_{22}H_{39}$, M-$C_7H_{11}O$] $^+$, 275[$C_{20}H_{35}$, M-$C_9H_{15}O$] $^+$, 273[$C_{20}H_{33}$, M-$C_9H_{13}O$] $^+$, 255 [$C_{19}H_{27}$]$^+$, 231[$C_{17}H_{27}$, M-$C_{12}H_{23}O$] $^+$, 213[$C_{16}H_{21}$] $^+$, 173[$C_{13}H_{17}$] $^+$, 145[$C_{11}H_{13}$] $^+$, 109[C_8H_{13}] $^+$, 81[C_6H_9]$^+$, 57 [C_4H_9] $^+$ and 43[base peak, C_3H_7]$^+$. The GC-MS fragmentation patterns revealed the compound to be a tetracyclic steroidal compound, with characteristic fragment ion peaks at m/z 396, 329, 303, 275 and 273. An intense peak at m/z 396 indicates loss of water from the molecular ion (M^+-18), which is characteristic for dehydration of steroidal compounds (Gangwal *et al*., 2010). Generally, cyclic alcohols like cyclohexanol (2^o alcohol) undergo fragmentation-involving dehydration by complicated pathways (Silverstein *et al.,* 1991). Usually, water is lost by losing an α-H and a β-OH (Furniss *et al*., 1989). Peaks, especially at m/z 329, 303 and 275 are diagnostic peaks for sterols possessing Δ^5 – unsaturation. Such compounds fragment readily by a pathway in which the molecular ion loses the ring bearing OH with other rings to form various carbocations (Carey, 2003). Usually, cleavage is favoured at substituted carbon atoms helping to generate carbocations in which degree of stability is cyclic C^+> 3^oC^+> 2^oC^+ > 1^oC^+> methyl C^+ Peak at m/z 273 is attributable to the loss of R substituents on ring at position C-17. Usually, saturated rings tend to lose alkyl side chains to form a positive charge on the ring fragment. Such cleavage is favoured at alkyl substituted carbon atoms, so that, the more substituted, the more likely is the cleavage (Silverstein *et al*., 1991). Another peak at m/z 255 is likely as a result of loss of the side chain at C-17 and further dehydration of such fragment ion. Another peak at m/z 231 is likely as result of loss of both the ring and R groups at C-17 to form a 3^o carbocation.

A comparative study of the obtained physical, chemical and spectroscopic data of compound **D4a** with those published in literature revealed it to be β-sitosterol, a tetracyclic steroidal compound (Figure 1). The assignments are in good agreement with other published data for the structure of the compound, where it has been isolated and characterized by several authors from different plants (Habib *et al*., 2007; Pateh *et al*., 2008; Patra *et al*., 2010; Ahmed *et al.*, 2010; Kamboj and Saluja, 2011; Tripathee *et al*., 2011; Trivedi and Choudrey, 2011; Chaturvedula and Prakash 2012; Sen *et al*., 2012; Ahmed *et al*., 2013; Mokua, 2013; Tripathi *et al*., 2103, Isah *et al*., 2014; Kumar *et al*., 2014; Rajpoot and Singh, 2014; Saeidnia *et al*., 2014; Kumar *et al*., 2015). This is the first report of the isolation and characterization of β-sitosterol from the mesocarp of *D. mespiliformis*

Table 3: ^{1}H-NMR,^{13}C- NMR and DEPT-135^o spectral data obtained for compound D4a in comparison with literature values*

Position	δ H (ppm)	δ H (ppm)*	δ C (ppm)	δ C (ppm)*	DEPT (ppm)	DEPT (ppm)*
1	1.45 (m)	1.43 (m)	29.8	30.1	29.8 (-CH_2)	29.8 (below)
2	1.55 (m)	1.57 (m)	34.5	35.8	34.5 (-CH_2)	34.5 (below)
3	3.35 (dd)	Triple dds				
	3.28 (dd)					
	3.21 (dd)					
3 (OH)	2.04 (m)	2.00 (m)	79.0	78.7	79.0 (-CH)	79.0 (above)
4	2.41 (t)	2.43 (t)	47.8	46.9	47.8 (-CH_2)	47.8 (below)
5	-	-	150.5	148.9	150.5 (-C-)	150.5 (disappeared)
6	4.66 (d)	4.70 (t)	109.7	110.9	109.7 (-CH)	109.7 (above)
7	2.35 (t)	2.34 (t)	29.7	30.0	29.7 (-CH_2)	29.7 (below)

8	1.70 (m)	1.65 (m)	37.2	37.9	37.2 (-CH)	37.2 (above)
9	1.49 (t)	1.47 (t)	50.4	50.8	50.4 (-CH)	50.4 (above)
10	-	-	40.8	39.8	40.8 (-C-)	40.8 (disappeared)
11	1.53 (t)	1.54 (t)	20.7	20.7	20.7 ($-CH_2$)	20.7 (below)
12	1.48 (t)	1.48 (t)	38.9	38.2	38.9 ($-CH_2$)	38.9 (below)
13	-	-	42.1	42.0	42.1 (-C-)	42.1 (disappeared)
14	1.37 (m)	1.40 (m)	55.2	55.5	55.2 ($-CH_2$)	55.2 (below)
15	1.60 (d)	1.61 (d)	27.4	27.7	27.4 ($-CH_2$)	27.4 (below)
16	1.80 (d)	1.78 (d)	27.1	27.3	27.1 ($-CH_2$)	27.1 (below)
17	1.51 (d)	1.49 (d)	60.2	59.8	60.2 (-CH)	60.2 (above)
18	0.72 (s)	0.71 (s)	18.3	18.7	18.3 ($-CH_3$)	18.3 (above)
19	1.02 (d)	1.06 (s)	19.1	19.0	19.1 ($-CH_3$)	19.1 (above)
20	1.63 (m)	1.64 (m)	37.3	37.1	37.3 (-CH)	37.3 (above)
21	0.98 (d)	1.02 (m)	16.1	16.4	16.1 ($-CH_3$)	16.1 (above)
22	0.97 (m)	1.01 (m)	38.7	38.9	38.7 ($-CH_2$)	38.7 (below)
23	1.08 (m)	1.05 (m)	27.9	27.9	27.9 ($-CH_2$)	27.9 (below)
24	1.60 (t)	1.61 (t)	48.6	48.1	48.6 (-CH)	48.6 (above)
25	1.42 (d)	1.42 (d)	33.8	33.7	33.8 (-CH)	33.8 (above)
26	1.12 (d)	1.11 (d)	15.9	15.6	15.9($-CH_3$)	15.9 (above)
27	1.08 (d)	1.06 (d)	15.4	15.1	15.4 ($-CH_3$)	15.4 (above)
28	1.30 (m)	1.29 (m)	25.2	25.6	25.2 ($-CH_2$)	25.2 (below)
29	1.01 (s)	0.98 (s)	12.3	12.2	12.3 ($-CH_3$)	12.3 (above)

Keys: s=singlet, d=doublet, dd=doublets of doublets, t=triplet, m=multiplet

*ACD/ChemDraw (Product version 15); Pateh *et al*., 2008; Saiednia *et al*, 2014

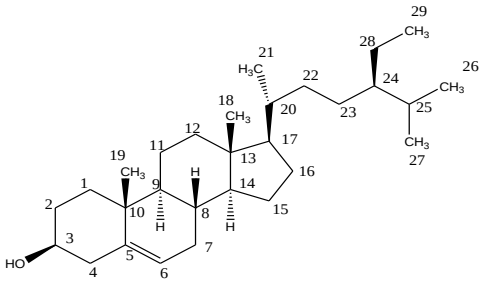

Figure 1: β-Sitosterol/ 24β-Ethylcholesterol/ 22, 23-Dihydrostigmasterol/ 5-Stigmasten-3β-ol/ 24R-Stigmast-5-en-3β-ol/ α-Dihydrofucosterol

Table 4: Antibacterial activity of isolated β-sitosterol (D4a) in comparison with erythromycin against test bacterial strains

Test bacterial strains	Activity of test compounds against test bacterial strains	
	D4a (100 µg/cm^3)	Erythromycin (100 µg/cm^3)
B. subtilis	-	+
S. aureus	+	+
E. coli	+	+

K. pneumoniae	-	-
P. aeruginosa	-	+
S. typhi	+	+

+ = activity, - = no activity

The isolated compound at 100µg/cm^3 displayed moderate antibacterial activity in comparison with erythromycin that was more active against both Gram-positive and Gram-negative organisms tested, except against Gram negative *Pseudomonas aeruginosa* (Table 4). Generally, β-sitosterol has been reported to possess low/moderate antibacterial activity against several bacterial strains (Beltrame *et al*., 2002; Sen *et al*., 2012; Woldeyes *et al*., 2012; Rajpoot and Singh, 2014; Yadav *et al*., 2014).

4. Conclusion

Extraction, fractionation, purification and *in-vitro* antibacterial testing of the chloroform extract of the mesocarp of fruits of *Diospyros mespiliformis* and its fractions led to the isolation, characterization and structural elucidation of β-sitosterol. The phytosterol in comparison with erythromycin (both100 µg/cm^3) exhibited a moderate antibacterial activity against the tested organisms. The isolated compoundprobably acted individually or synergistically with other constituents present in the mesocarp of the fruits of the plant to account for the ethnomedicinal uses of the plant. Further research will focus on the bio-assay guided isolation and characterization of more phytoconstituents from the plant.

5. Acknowledgement

The authors wish to express their unreserved gratitude to Prof. Ermias Dagne and Dr. Mesfin Tadesse both of African Laboratory for Natural Products (ALNAP), Addis Ababa University, Arat Kilo, Ethiopia for helping out with the spectral aspect of this research.

References

Abba, A., Agunu, A., Abubakar, A., Abubakar, U. S. and Jajere, M. U. (2016), Phytochemical screening and antiproliferative effects of methanol extract of stem bark of *Diospyros mespiliformis* Hochst (Ebenaceae) against guinea corn (*Sorghum bicolor*) seeds radicles length, *Bayero Journal of Pure and Applied Sciences*, 9 (1), 1-5

Adeniyi, B. A., Odelola, H. A. and Oso, B. A. (1996), Antimicrobial potentials of *Diospyros mespiliformis* (Ebenaceae), *Afr. J. Med. Sci.*, 25 (3), 221-224

Adeniyi, B. A., Robert, M., Chai, H. and Fong, H. H. S. (2003), *In-vitro* cytotoxicity activity of diosquinone, a naphthoquinone epoxide, *Phytotherapy Research*, 17 (issue 3), 282-284

Adewuyi, A. & Oderinde, R. A. (2014), Fatty acid composition and lipid profile of *Diospyros mespiliformis*, *Albizia lebbeck* and *Caesalpinia pulcherrima* seeds oils from Nigeria, *International Journal of Food Science*,http://dx.doi.org/10.1155/2014/283614

Adzu, B., Amos, S., Dzarma, S., Muazzam, I. and Gamaliel, K. S. (2002a), Pharmacological evidence favouring the folkloric use of *Diospyros mespiliformis* Hochst in the relief of pain and fever, *J. Ethnopharmacol*., 82, 191-195

Adzu, B., Amos, S., Muazzam, I., Inyang, U. S. and Gamaliel, K. S. (2002b), Neuropharmacological screening of *Diospyros mespiliformis* in mice, *J. Ethnopharmacol*., 83, 139-143

Adzu, B. and Salawu, O. A. (2009), Screening *Diospyros mespiliformis* extract for antimalarial potency, *Int. J. Biol. Chem. Sci*., 3 (2), 271-276

Agrawal, P. K., Jain, D. C., Gupta, R. K. and Thakur, R. S. (1985), Carbon-13 NMR spectroscopy of steroidal sapogenins and steroidal saponins, *Phytochemistry Res*., 24 (11), 2476-2496

Ahmed, Y., Sohrab, M. H., Al-Reza, S. M., Tareq, F. S., Hassan, C. M. and Sattar, M. A. (2010), Antimicrobial and cytotoxic constituents from leaves of *Sapium baccatum*, *Food and Chemical Toxicology*, 48 (2), 549-552

Ahmed ,Y., Rahman, S., Akhtar, P., Islam, F., Rahman, M. and Yaakob, Z. (2013). Isolation of steroids from n-hexane extract of the leaves of *Saurauia roxburghii*, *Int. Food Res. Journal*, 20 (5), 2939-2943

Belemtougri, R. G., Constatin, B., Conard, C., Raymond, G. and Sawadogo, L. (2006), Effects of two medicinal plants, *Psidium guajava* L. (Myrtaceae) and *Diospyros mespiliformis* L. (Ebenaceae) leaf extracts on rat skeletal muscle cells in primary culture, *Journal of Zhejiang University*, 7 (1), 56-63

Beltrame, F. L., Pessini, G. L., Doro, D. L., Filho, B. P. D., Bazotte, R. and Cortez, D. A. G. (2002). Evaluation of the antidiabetic and antibacterial activity of *Cissus sicyoides*, *Brazilian Archives of Biology and Technology*, 45 (1), 21-25

Carey, F. A. (2003). *Organic Chemistry*, 5thed, New York: McGraw Hill Higher Education 651, 653

Chaturvedula, V. S. P. and Prakash, I. (2012), Isolation of stigmasterol and β-sitosterol from the dichloromethane extract of *Rubus suavissmus*, *International Current Pharmaceutical Journal*, 1 (9), 239-242

Chivandi, E., Erlwanger, K. H. and Davidson, B. C. (2009), Lipid content and fatty acid profile of the fruit seeds of *Diospyros mespiliformis*, *International Journal of Integrative Biology*, 5 (no 2), 121-124

Dall'Agnol, R., Ferraz, A., Bernardi, A. P., Albring, D., Nor, C., Sarmento, L., Lamb, L., Hass, M., von Poser, G. and Schapoval, E. E. S. (2003), Antimicrobial activity of some *Hypericum* species, *Phytomedicine*, 10, 511-516

Esimone, C. O., Nworu, C. S., Onuigbo, E. B., Omeje, J. U., Nsirim, K. L., Ogbu, J. C., Ngwu, M. I. and Chah, K. F. (2009), Anti-mycobacterial activity of root and leaf extracts of *Anthocleist adjalonensi*s (Loganiaceae) and *Diospyros mespiliformis* (Ebenaceae), *Int. J. Green Pharm*., 3, 201-205

Etkin, N. L. (1997), Antimalarial plants used by Hausa in Northern Nigeria, *Tropical Doctor*, 27, 12-16

Fadipe, A. L., Babayi, H. and Ogunleye, D. (2012), Phytochemical and *in-vitro* antimicrobial screening of the ethanolic extract of *Theobroma coca* seeds and its fractions, *Journal of Science, Technology, Mathematics and Education*, 8 (3), 48-60

Freiburghaus, F., Kaminsky, R, Nkunya, M. H. H. and Brun, R. (1996), Evaluation of African medicinal plants for their *in-vitro* trypanocidal activity, *J. Ethnopharmacol*., 55, 1-11

Furniss, B. S., Hannaford, A. J., Smith, P. W. G. and Tatchell, A. R. (1989), *Vogel's Textbook of Practical Organic Chemistry*, 5th ed, Edinburgh Gate, England: Pearson Education Limited 256, 270, 274, 279, 288

Gangwal, A., Pamar, S. K. and Sheth, N. R. (2010), Triterpenoids, flavonoids and sterols from *Lagenaria siceraria* fruits, *Der Pharmacia letter*, 2 (1), 307-317.

Habib, M. R., Nikkon, F., Rahman, M. E. and Karim, M. R. (2007), Isolation of stigmasterol and beta-sitosterol from methanolic extract of root of bark of *Calotropis gigantean* (Linn), *Pak. J. Biol. Sci*., 10, 4174-4176.

Harbone, J. B. (1998), *Phytochemical Methods: A Guide to Modern Techniques of Plant Analysis*, 3rd ed., Chapman and Hall, Ltd., London, pp. 302

Hili, P., Evans, C. S. and Veness, R. G. (1997), Antimicrobial action of essential oils: The effect of dimethylsulfoxide on the activity of cinnamon oil. *Lett. Appl. Microbiol*., 24, 269-275

Isah, Y., Ndukwe, I. G., Rufai, Y. and Ayo, R. G. (2014), Characterization and microbial activities of β-sitosterol and β-sitosterone mixture isolated from the stem bark of methanol fraction of *Sarcocephalus latifolius* (Smith Bruce), *International Research Journal of Natural Sciences*, 2 (2), 1-13

Kamboj, A. and Saluja, A. K. (2011), Isolation of stigmasterol and β-sitosterol from petroleum ether extract of aerial parts of *Ageratum conyzoides* (Asteraceae), *International J. of Pharmacy and Pharmaceutical Sciences*, 3 (Issue 1), 94-96

Kumar, S., Siddhu, S. K. and Mehta, B. (2014), New triterpenoid compound (Lup-20 (29)-en-3β-3, 27-diol) isolate from extract of *Nigella sativa* (seeds), *J. of Natural Products*,**7,** 113-115

Kumar, U. P., Sreedhar, S. and Purushothaman, E. (2015), Secondary metabolites from the heartwood of *Combretum albidum* G Don., *Int. J. of Pharmacognosy and Phytochemical Research*, 7 (2), 319-324.

Lajubutu, B. A., Pinney, R. J., Roberts, M. F., Odelola, H. A. and Oso, B. A. (1995), Antibacterial activity of diosquinone and plumbagin from the root of *Diospyros mespiliformis* (Hostch) (Ebenaceae), *Phytotherapy Research*, 9 (issue 5), 346-350.

Maffei-Facino, R., Carini, M., Franzoi, L., Pirola, O. and Bosisi, E. (1990), Phytochemical, characterization and radical scavenger activity of flavonoids from *Helichnysum italicum* G. Don (Compositae), *Pharm. Res*., 22, 709-720.

Mohammed, I. E., ElNur, E. E., Choudhary, M. I. and Khan, S. N. (2009), Bioactive products from two Sudanese medicinal plants, *Diospyros mespiliformis* and *Croton zambesicus*, *Res. Nat. Prod*., 3 (4), 198-203.

Mokua, G. N. (2013),Toxicity of individual and blends of pure phytoecdysteroids isolated from *Vitex schiliebenii and Vitex payos* against *Anopheles gambiae* S. S larvae, *World Journal of Organic Chemistry*, 1 (1), 1-5.

Ndip, R. N., Ajonglefac, A, N., Wirna, T., Luma, H. N., Wirmum, C. and Efange, S. M. N. (2009), *In-vitro* antimicrobial activity of *Ageratum conyzoides* (Linn) on clinical isolates of *Helicobacter pylori*, *African Journal of Pharmacy and Pharmacology*, 3 (11), 585-592.

Okoli, A. S. and Iroegbu, C. U. (2004), Evaluation of extracts of *Anthocleist adjalonensis*, *Nauclea latifolia* and *Uvaria afzalii* from cases of non-gonococcal urethritis, *Journal of Ethnopharmacology*, 92 (1), 135-144.

Orwa, C., Mutua, A., Kindt, R., Jamnadass, R. and Simons, A. (2009), Agroforestree database: a tree reference and selection guide version 4.0.Url: http://www.Worldagroforestry.org/af/treedb/

Pateh, U. U., Haruna, A. K., Garba, M., Iliya, I., Sule, I. M., Abubakar, M. S. and Ambi, A, A. (2008), Isolation of stigmasterol, β-sitosterol and 2-hydroxyhexadcanoic acid, methyl ester from the rhizomes of *Stylochiton lancifolius* Pyer and Kotchy (Araceae), *Nigerian J. of Pharmaceutical Sciences*, 7(1), 19-25.

Patra, A., Jha, S., Murthy, P. N., Manik, A. and Dharone, A. (2010), Isolation and characterization of stigmast-5-en-3β-ol (β-sitosterol) from the leaves of *Hygrophila spinosa* T. Anders, *International Journal of Pharma Sciences and Research*, 1 (2) , 95-100.

Rajpoot, S. and Singh, P. (2014), Study of antibacterial activity of β-sitosterol isolated from the leaves of *Nyctanthes arbortristis* Linn. *Indian J of Applied Research*, 4 (issue 9), ISSN-2249-555X.

Sadiq, I. S., Dangoggo, L. G. H., Hassan, L. G. and Manga, S. B. (2013), Bioactive isolation and antifungal screening of leaf and bark of *Diospyros mespiliformis* and *Zizyphus spina-christi*, *International Journal of Traditional and Natural Medicines*, 2 (2): 104-117.

Saeidnia, S., Manayi, A., Gohari, A. R. and Abdollahi, M. (2014), The story of beta-sitosterol: A review, *European Journal of Medicinal Plants, Science Domain International*, 4 (5), 590-609.

Sen, A., Dhavan, P., Shukla, K. K., Singh, S. and Tejovathi G. (2012), Analysis of IR, NMR and antimicrobial activity of β-sitosterol isolated from *Momordica charantia*, *Sci. Secure J. Biotech*., 1 (1), 9-13.

Shagal, M. H., Kubmarawa, D. and Alim, H. (2012), Preliminary phytochemical investigation and antimicrobial evaluation of roots, stem-bark and leaf extracts of *Diospyros mespiliformis*, *Int. J. Biochemistry and Bioinformatics*, 2 (1), 011-015.

Silverstein, R. M., Bassler, G. C. and Morrill, T. C. (1991), *Spectrometric Identification of Organic Compounds*, 5th ed., New York: John Wiley and sons, 19, 26-27.

Tripathee, H. P., Sharma, R. P., Timilsina, Y. P., Pathak, P. and Devkota, K. P (2011), An Assesment of ethnomedicinal use, chemical constituents analysis and bioactivity evaluation on high altitude medicinal plant *Delphinium brunonianum* of Manang District, *Nepal Journal of Science and Technology*, 12, 111-118.

Tripathi, N., Kumar, S., Singh, R., Singh, C. J., Singh, P. and Varshney, V. K. (2013), Phytochemical studies from the roots of *Girardinia heterophylla*, *Oriental Journal of Chemistry*, 29 (3), 1143-1148.

Trivedi, P. C. and Choudhrey, N. (2011), Isolation and characterization of bioactive compound β-Sitosterol from *Withania somnifera* L., *J. Pharmacy Res*., 4, 4252-4253.

Venter, F. and Venter, J. A. (1996), *Making the Most of Indigenous Trees*. Briza Publications, Pretoria

Woldeyes, S., Adana, L., Tariku, Y., Muleta, D. and Begashaw, T. (2012), Evaluation of antibacterial activities of compounds isolated from *Sida rhombifolia* Linn (Malvaceae), *Nat. Prod. Chem. Res.*, 1:101 doi:10.4172/npcr.1000101.

Yadav, A., Bhardwaj, R. & Sharma, R. A. (2014), Isolation, quantification and antimicrobial activities of phytosterols from different parts of *Cassia pumila* Lamk, *Int. J. of Pharmacy*, 4 (1), 86-92.

Zhong, S. M., Waterman, P. G. and Jeffrers, J. A. D. (1984), Naphthoquinone and triterpenes from Africa *Diospyros* species, *Phytochem*istry, 23, 1067-1072.

PEBBLE MORPHOMETRIC ANALYSIS AND DEPOSITIONAL ENVIRONMENT OF THE BASAL CONGLOMERATES OF BIDA SANDSTONE EXPOSED AROUND ZUNGERU, NW NIGERIA

SALIHU, H.D.*[1], GORO, A.I.[1], AKANDE, W.G.[1] & ABDULFATAI, I.A.[1]
[1]*Department of Geology, Federal University of Technology, P.M.B. 65, Minna, Nigeria*
fatai.asema@futminna.edu.ng
waheed.akande@futminna.edu.ng
isahgoro@futminna.edu.ng
salihu.dantata@futminna.edu.ng
*Correspondence Author

ABSTRACT

The basal conglomerate lithofacies of Bida Formation is common along the basin margin where it overlies the rocks of the basement complex in Zungeru area, northwestern Nigeria. The conglomerate lithofacies contains abundant pebbles of vein quartz and the clasts of these pebbles were selected for morphometric study to determine their depositional environment. A total of 190 pebbles were selected from nineteen weathered outcrops for this study. The three mutually perpendicular axes; long, intermediate and short axes were measured and the roundness estimated with the aid of a roundness image set. Form names were obtained using triplot to generate Sneed and Folk diagram. Morphometric parameters such as size, flatness ratio, elongation ratio (ER), maximum projection sphericity index (MPSI), form geometry and oblate-prolate index (OPI) were computed. The bivariate plots of morphometric parameters such as coefficient of flatness versus MPSI, and MPSI versus OPI indicate that the pebbles were deposited in fluvial environment but bivariate plot of roundness versus elongation ratio showed that they were deposited in littoral (marine) environment. The dominance of bladed shape pebbles in the conglomerate lithofacies indicates that the basal conglomerates of Bida Formation exposed in Zungeru area is sourced from the surrounding basement such as schists and gneisses rich in vein quartz fills. It is concluded that these sediments are products of fluvial deposition with some marine influence.

Keywords: Bida basin, Bida Formation, Zungeru, Conglomerate, Morphometric, depositional, bivariate plot, fluvial

1. INTRODUCTION

In detrital sedimentary rocks, the surface characteristics of the grains make up the particle morphology, or form. These forms were acquired by the sedimentary grains during denudation processes such as weathering, erosion and transportation (Benn, 2010; Dumitriu *et al*., 2011).

Variety of shape indices and diagrammatical presentations of pebble shapes have been proposed (e.g. Wentworth, 1922; Krumbein, 1941; Sneed and Folk, 1958; Dobkins and Folk, 1970; Blott and Pye, 2008). Data generated through morphometric analysis can be used to give important insight on sediment source origin, transportation history and sedimentation processes as well as in paleo-environmental determination (e.g. Hurst *et al*., 2010; Tamrakar and Shrestha, 2008; Lindsey *et al*., 2007; Graham and Midgley, 2000; Attal and Lavé, 2006). A variety of Conglomerate lithofacies have been reported in the northern part of Bida basin (Braide, 1992; Okosun *et al.*, 2009) but the one of interest in the present work is the conglomerates that occupy the base of the Bida Formation. This unit overlies the basement complex rocks directly and mostly outcrop near the margins of the basin. Even though their environmental implications were briefly discussed (Braide, 1992; Okosun *et al.*, 2009), information regarding pebble morphometry is lacking on these sediments. The purpose of the study is to analyse the shapes and forms of vein quartz pebbles in the coglomerate lithofacies exposed near Zungeru (NW Nigeria) and use the information to evaluate their depositional environment.

2. LOCATION AND GEOLOGICAL SETTING

The study area falls within latitude N09^{0}46'54" and longitude E006^{0}08'31" on Zungeru Sheet 163NW, northwestern Nigeria. The area is located about 1.5 km SW of Zungeru town. The study area is accessible through major roads like the Minna-Zungeru, Zungeru-Wushishi and the Zungeru-Kontagora in the north, west and southeast respectively. It is also accessible by innumerable minor roads and footpaths. By rail, it is accessible by Zungeru-Minna-Kano rail line to the north and Zungeru-Lagos rail line to the south.

Bida basin, one of the inland basins of Nigeria, is often described in terms of northern and southern Bida portions. Four lithostratigraphic units were recognised in the northern part of the basin (Adeleye, 1974; Adeleye and Dessauvagie, 1972; Figure 1). From the base they include the Bida Formation, the Sakpe Ironstone, the Enagi Siltstone and the Batati Formation. The Lokoja, Patti and Agbaja formations constitute laterally correlatable units from the southern part of the basin (Figure 1).

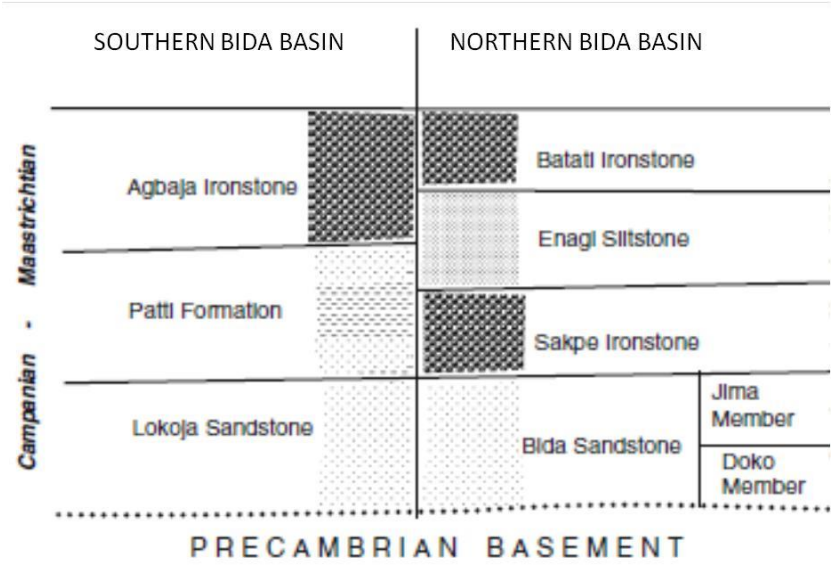

Fig. 1: Generalized stratigraphic subdivisions in the Bida basin (modified after Obaje, 2009).

The studied conglomerate lithofacies overlies the basement directly in Zungeru, Chechehi and Wushishi areas. The typical conglomerate unit is essentially a matrix-gravel mix in which the larger grains are very angular through sub-rounded granule to fine pebble-sized clasts of vein quartz, and in some cases weathered feldspars and clay chips are present. Cobbles and boulders are also common. Lithologies of the matrix vary from fine sand through silt to clay. Textural characters are poor sorting and matrix-support as well as crude bedding to massive appearance (Ajibade *et al*., 2008; Okosun *et al*., 2009).

3. MATERIALS AND METHODS

A total of 190 vein quartz pebbles were selected from 19 different locations of the conglomerates exposures within the study area. Locations of outcrops were obtained using GPS. The study involved the use of vernier calliper to measure the Long (L), Intermediate (I) and Short (S) axes of the selected pebbles following the guidelines of Stratten (1973) and Folk (1980). Morphometric parameters were obtained by adopting the formulas suggested by Luttig (1962) for determining the Flatness Ratio (FR), Coefficient of Flatness and Elongation ratio (ER); and Dobkins and Folk (1970) for evaluating the Oblate-Prolate Index (OPI). Maximum Projection Sphericity Index (MPSI) and Roundness of pebbles were computed according to procedures of Sneed and Folk (1958) and Sames (1966) respectively (Table 1). Tri-plot, an excel spreadsheet developed by Graham and Midgley (2000), was used to produce the Sneed and Folk triangular diagram (form name). Table 1 shows the morphometric parameters used in this work. The following parameters were plotted on a scatter plot, MPSI vs. OP Index (Dobkins and Folk, 1970), Coefficient of flatness vs. MPSI (Stratten, 1973) and Roundness vs. ER (Sames, 1966) to aid identification of the environment of deposition of the pebbles. The pebble samples were collected and measured in batches of ten (10). The dimensions of the vein quartz pebbles are presented on a data sheet for morphometric analysis according to Lambert-Aikhiobare and Olayinka (2009).

Table 1: Various formulas used in computation of the morphometric parameters.

PARAMETERS	FORMULA	AUTHORS
Flatness Ratio (FR)	Short axis/long axis (S/L)	Luttig (1962)
Coefficient of Flatness	S/L × 100	Stratten (1974); Els (1988)
Elongation Ratio (ER)	I/L	Luttig (1962)
Forms	L-I/L-S	Sneed and Folk (1958)
Maximum Projection Sphericity Index (MSPI)	$(S^2/LI)^{1/3}$	Sneed and Folk (1958)
Oblate-Orolate Index (OP)	10(L-I-0.5)/(L-S)/(S/L)	Dobkins and Folk (1970)
Form Names	Triangular Sphericity diagram	Sneed and Folk (1958)
Roundness %	Visual estimationof the pebbles	Sames (1966)

4. RESULTS PRESENTATION AND DISCUSSION

4.1 Results Presentation

4.1.1 Field Observations

The conglomerates directly overlie the precambrian basement complex rocks (Fig. 2a, b) and consists predominantly of vein quartz pebbles whose grain size are in order of millimetres to few centimetres (a maximum of 3.75 cm longest axis recorded) with subordinate amount of metaquarzite and metamorphic rock fragments, mainly schist. The quartz pebbles generally display angular to subrounded shapes while the metaquartzites commonly occur as equant pebbles and the schist pebbles are essentially disc to tabular shaped (Figure 2e and f). Both grain-supported (Figure 2c) and matrix-supported fabrics (Figure 2d) are displayed by the conglomerates but the later predominate. The conglomerate unit is averagely

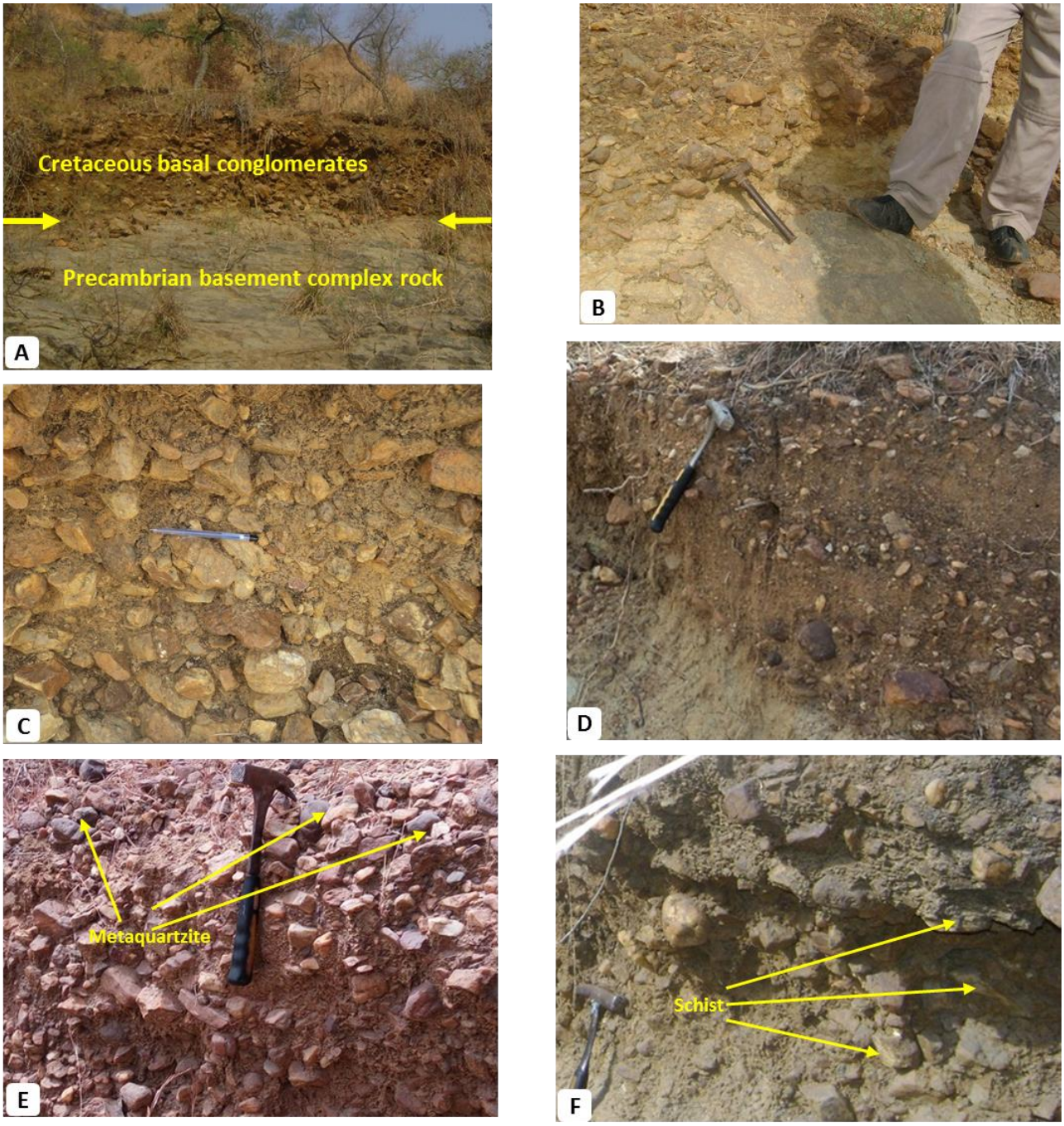

Fig. 3. Outcrop pictures showing typical features of the conglomerates exposed on a stream section near Zungeru NW Nigeria. [A] contact between the conglomerates and the Precambrian basement rocks [B] close-up view of (A); Note: the geologist is standing on the Precambrian basement rocks, [C] grain-support fabric, [D] matrix-support fabric [E] equant/rounded metaquartzite grains, [F] dics shaped schist pebbles

4.1.2 Morphometric Analysis

The results of pebble morphometry are presented in Table 2 while Table 3 shows the summary, i.e. total average, of the calculated pebble morphometric parameters. Scatter plot of MPSI vs. OP-Index is presented in Figure 3 for all samples in all the locations while Figure 4 shows scatter plot of total average (summary) of MPSI vs. OP-index. Figure 5 shows the scatter plot of coefficient of flatness vs. MPSI for all location and Figure 6 shows plot of total average of coefficient of flatness vs. MPSI. Roundness vs. Elongation ratio is presented in Figure 7. Sneed and Folk triangular diagrams for all locations and total average of all the locations

are shown in Figures 8a and 8b respectively. Pebble suites in the study area display coefficient of flatness rangeing from 0.17 - 0.77 (average 0.73) and Elongation ratio of 0.33 - 0.97 (average 0.73), and Form with dominant Bladed shape with 31.05% and compact bladed with 17.37% and the Form takes values from 0.08 - 0.98 with mean of 0.51. The MPSI varies from 0.40 - 0.89 with mean of 0.66; Oblate-Prolate Index (OPI) ranges from -3.56 - 3.85 with mean of 0.66 while roundness ranges from 10 - 90% with a mean value of 51.47%.

Table 2: Summary of total average of pebble morphometric parameters for basal conglomerates of Bida Formation exposed around Zungeru NW Nigeria.

Location	L(cm)	I(cm)	S(cm)	S/L	I/L	S/Lx100	L-I/L-S	MPSI	OPI Index	Form Name	Roundness (%)	Effective radius
1	3.25	2.36	1.53	0.46	0.72	46.45	0.52	0.67	0.68	B	56.00	0.47
2	3.42	2.40	1.64	0.49	0.72	49.34	0.56	0.69	1.06	B	55.00	0.48
3	3.46	2.36	1.32	0.39	0.69	39.47	0.51	0.61	0.88	B	58.00	0.29
4	3.12	2.10	1.19	0.39	0.68	39.45	0.53	0.61	0.81	B	46.00	0.24
5	3.19	2.14	1.22	0.38	0.66	37.86	0.55	0.61	0.99	B	39.00	0.25
6	3.12	2.34	1.35	0.45	0.77	44.62	0.43	0.64	0.46	B	60.00	0.43
7	2.70	1.95	1.04	0.42	0.72	42.06	0.51	0.62	0.20	B	48.00	0.29
8	3.15	2.26	1.34	0.43	0.73	42.76	0.49	0.63	0.68	B	46.00	0.39
9	2.82	1.84	1.22	0.45	0.66	44.97	0.62	0.67	0.83	B	47.00	0.28
10	2.95	1.94	1.16	0.43	0.71	42.69	0.50	0.63	0.15	B	51.00	0.22
11	2.91	2.05	1.22	0.45	0.75	44.68	0.42	0.64	-0.07	B	50.00	0.34
12	2.79	1.89	1.14	0.40	0.68	39.92	0.55	0.61	0.95	B	49.00	0.27
13	2.59	1.80	1.19	0.47	0.72	46.88	0.52	0.67	0.09	B	51.00	0.34
14	3.75	2.91	1.76	0.47	0.78	46.64	0.43	0.65	0.68	B	53.00	0.59
15	3.36	2.72	1.73	0.52	0.82	52.23	0.40	0.70	0.17	CB	56.00	0.60
16	4.35	3.38	2.19	0.51	0.76	51.13	0.51	0.70	1.17	CP	53.00	0.73
17	3.58	2.48	1.93	0.54	0.70	53.74	0.65	0.75	1.62	CB	53.00	0.57
18	3.63	2.82	2.02	0.56	0.78	55.78	0.49	0.74	0.68	CB	61.00	0.67
19	3.10	2.28	1.65	0.54	0.75	53.63	0.53	0.73	0.49	CB	46.00	0.52
Average	3.22	2.32	1.47	0.46	0.73	46.02	0.51	0.66	0.66	B	51.47	0.42

Effective radius = $[(S^*-L)\,(S^*-I)\,(S^*-S)/S^*]^{1/2}$ where $S^* = (L+I+S)/2$.

Table 3: Summary of the Pebble Morphometric Parameters

Morphometric Parameters	**Total Mean Pebble Sets**
Flatnes ratio (F.R)	0.46
Elongation ratio (E.R)	0.73
Maximum Projection Spericity Index (M.P.S.I.)	0.66
Oblate-Prolate Index (O.P.I.)	0.66
Roundness (%)	51.47
Pebble Size (Magnitude)	3.22

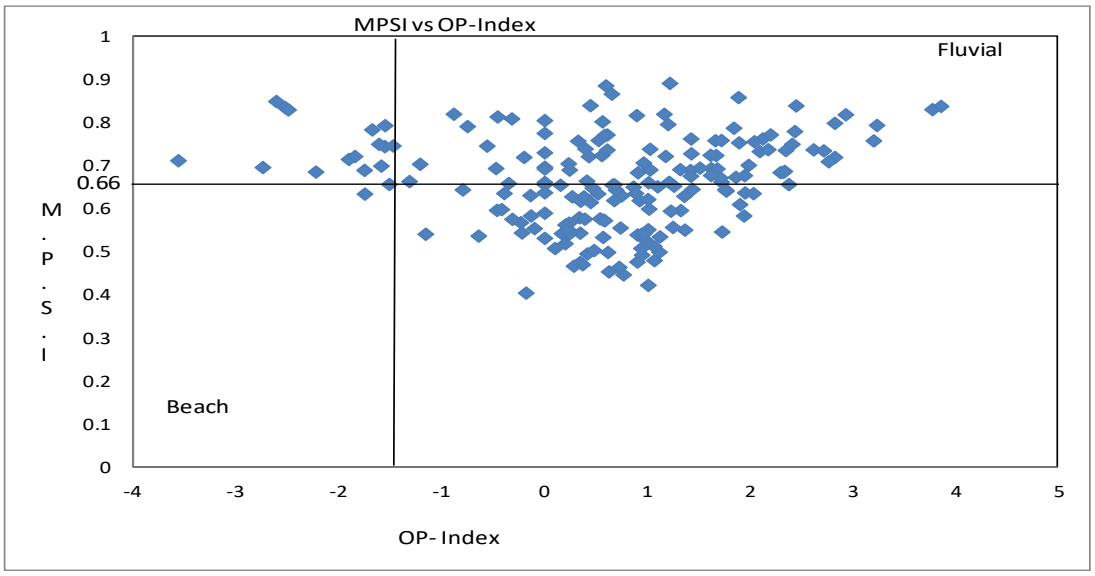

Fig. 3: Scatter Plot of M.P.S.I vs O.P.I for Location 1-19 (raw data).

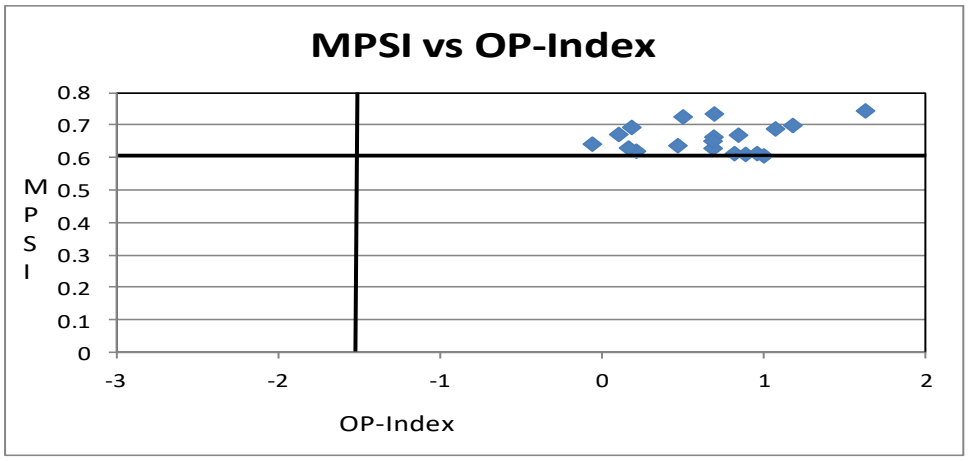

Fig. 4: Scatter Plot of Total Average of M.P.S.I. vs. O.P.-Index for Location 1-19.

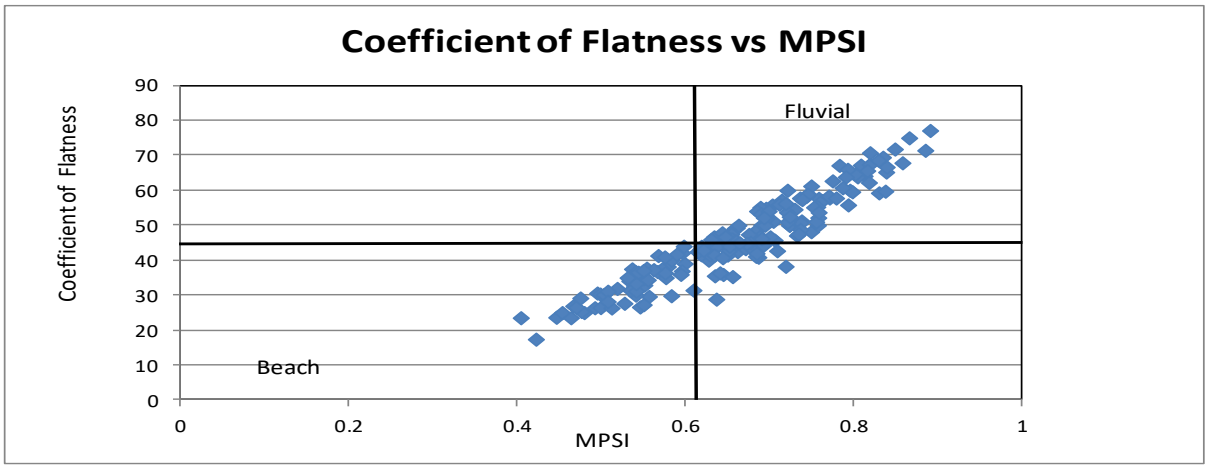

Fig. 5: Scatter Plot of Coefficient of Flatness vs. M.P.S.I for Location 1-19 (raw data).

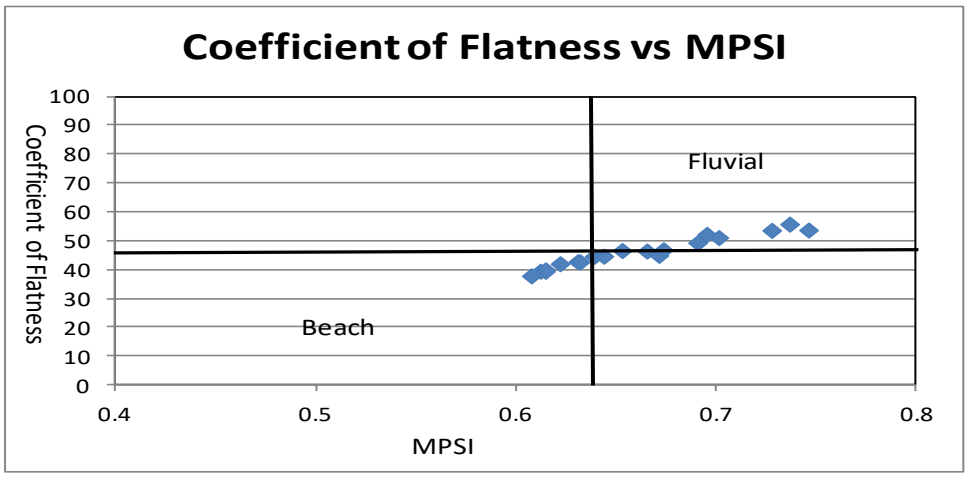

Fig. 6: Scatter Plot of Total Average of Coefficient of Flatness vs. M.P.S.I. for Location 1-19

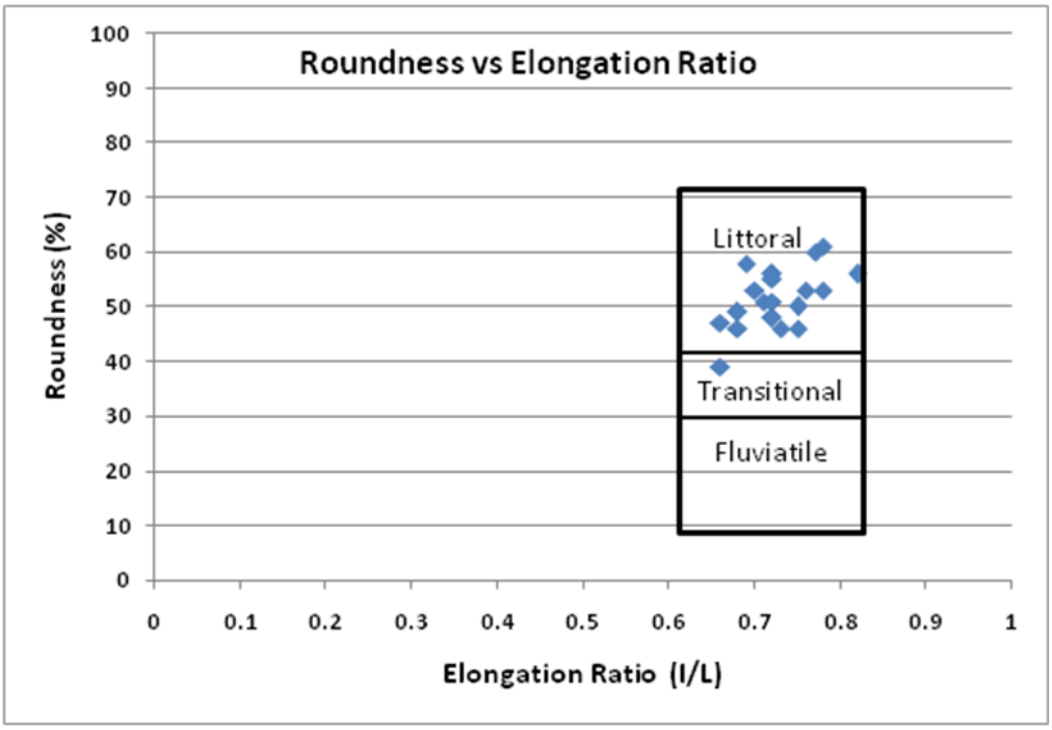

Fig. 7: Scatter Plot of Total Average of Roundness vs. Elongation Ratio for all Locations.

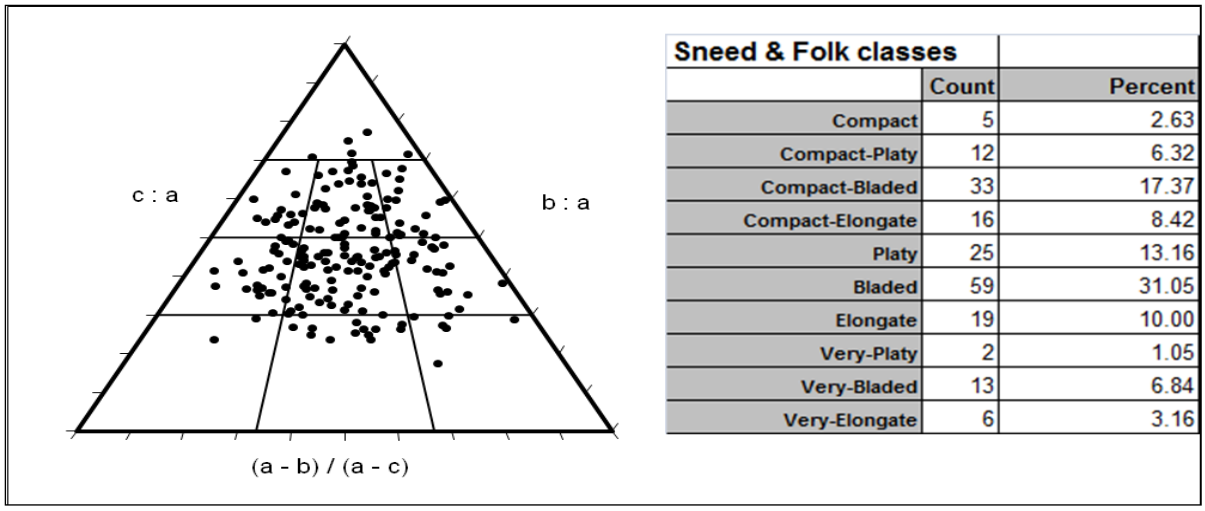

Sneed & Folk classes	Count	Percent
Compact	5	2.63
Compact-Platy	12	6.32
Compact-Bladed	33	17.37
Compact-Elongate	16	8.42
Platy	25	13.16
Bladed	59	31.05
Elongate	19	10.00
Very-Platy	2	1.05
Very-Bladed	13	6.84
Very-Elongate	6	3.16

Fig. 8a: Sneed and Folks Triangular Diagram for basal conglomerates of Bida Formation exposed around Zungeru NW Nigeria (Graham and Midgley, 2000). (Note: Letters a, b and c represent the long, intermediate and short orthogonal axes of each particle respectively).

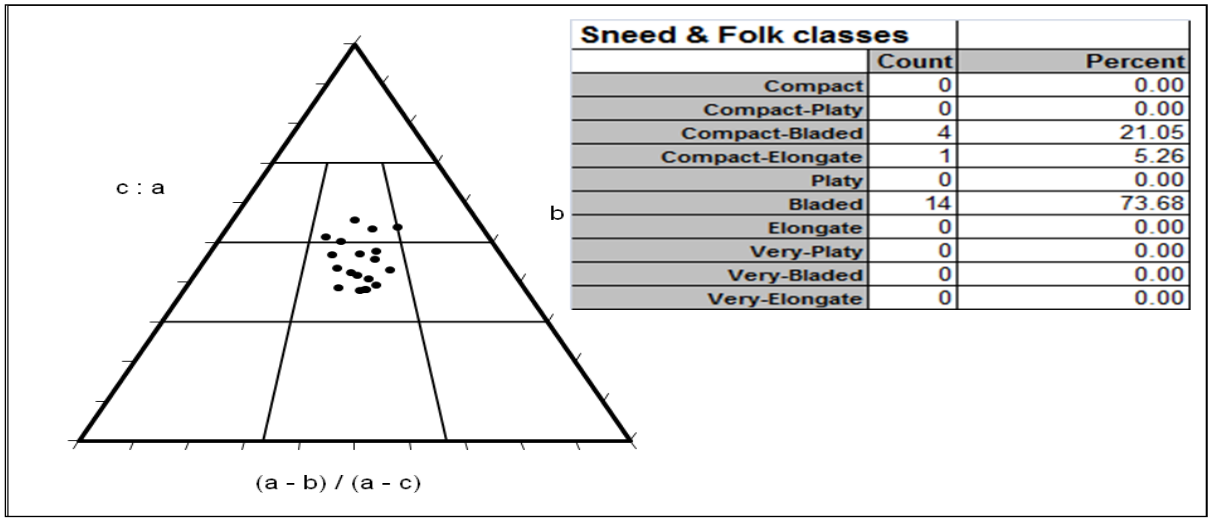

Sneed & Folk classes	Count	Percent
Compact	0	0.00
Compact-Platy	0	0.00
Compact-Bladed	4	21.05
Compact-Elongate	1	5.26
Platy	0	0.00
Bladed	14	73.68
Elongate	0	0.00
Very-Platy	0	0.00
Very-Bladed	0	0.00
Very-Elongate	0	0.00

Fig. 8b: Sneed and folk Diagram for Total Average of Samples (Graham and Midgley, 2000)

4.2 Discussion

The predominance of vein quartz and the presence of metaquartzite classifies the studied interval as a quartzose conglomerate (Boggs, 2009). This type of conglomerate is formed by the destruction of large volume of rocks (mainly metamorphic and some igneous rocks) rich in quartz filled veins (Pettijohn, 1975; Boggs, 2009). It has been suggested that the vein quartz were concentrated by the destruction of the less stable primary igneous or metamorphic rocks. Vein quartz rich conglomerates in the geologic record were commonly concentrated by fluvial processes but wave-reworked examples have been reported (Boggs, 2009).

Dobkins and Folk (1970), Lutig (1962), Sames (1966), Stratten (1974), Els (1988), Illenberger and Redding (1993), Barret (1980) and Nwajide and Hoque (1985) demonstrated the importance of pebble morphometric studies in the determination of paleoenvironment. The following parameters serve independent functions for environmental interpretation; they are coefficient of flatness (FR), Elongation ratio (ER), Maximum Projection Sphericity Index (MPSI), Oblate-Prolate Index (OPI), roundness and form. On the other hand scatter plots of

MPSI vs. OPI, Coefficient of flatness vs. MPSI and roundness vs. ER are used in interpretation as dependent variables.

Nwajide and Hoque (1985) show that the magnitude of the long axis of pebble determines the size. The mean size of pebbles in this study is 3.22 cm (Table 3) which is indicative of fluvial origin (Nwajide and Hoque, 1985).

Dobkin and Folk (1970) suggested that pebble suites with mean MPSI of 0.65 and less indicate beach processes while those with values above 0.65 are shaped by fluvial processes. The mean MPSI value obtained for the study area is 0.66 (Tables 2 and 3) and this is indicative of fluvial process. The mean OPI of 0.66 is also indicative of fluvial transport. Mean coefficient of flatness of 46.02% (Tables 2 and 3) indicates fluvial action as dominant depositional process (Stratten, 1974). The mean form index of 0.51 and Bladed form (B) (Figures 8a & b) indicate fluvial shaping of grain with indication of marine influence for the conglomeratic lithofacies of Bida Formation in Zungeru area. Table 4 shows that 28.42% of pebbles indicate fluvial, 50.53% are non-diagnostic and 21.05% indicates pebble shaped in marine environment, and this also lends credence to marine-influenced fluvial processes.

Turker (2011) emphasized that the shape of the pebbles is largely a reflection of composition and any planes of weakness (such as bedding/lamination, cleavage or jointing) in the rocks from which sediments are sourced. According to him, rocks with a uniform composition and structure, such as many granites, dolerites and thick sandstones will give rise to equant/spherical pebbles; thin-bedded rocks will generally form tabular and disc-shaped clasts; and highly cleaved or schistose rocks, such as slates, schists or some gneisses, will generally form bladed or rod-shaped pebbles. Thus, the larger percentage of bladed shape or form pebbles in this study indicates that the conglomerate sediment in Zungeru is sourced from the surrounding basement, consisting possibly of schists and gneisses.

Table 4: Showing percentage distribution of pebbles.

Fluvial			**Non-diagnostics**				**Marine**		
C	CB	CE	B	E	VE	CP	P	VP	VB
5	33	16	59	19	6	12	25	2	13
28.42%			50.53%				21.05%		

Roundness indicates the extent of travel and abrasion of pebble. The pebble roundness values estimated for this study range from 10 - 90% (angular to well rounded), and the mean roundness of 51.47% (0.515) shows that the pebbles are dominantly sub-rounded which indicates relatively short distance of travel. It also reveals that the pebble might have been transported from the weathering of the basement rocks around the study area (Odumodu and Odumodu, 2012).

Dobkin and Folk (1970) as well as Sames (1966) identified environments of deposition using scatter plots of MPSI vs. OPI (Figures 3 & 4) and Roundness vs. ER (Figure 7). Plots of MPSI vs. OPI (Figures 3 & 4) and plot of coefficient of flatness and MPSI (Figures 5 & 6) indicates fluvial setting with marine influence. The plot of roundness versus ER indicates littoral (marine) environment (Figure 8), possibly suggesting marine influence during the deposition of the sediments.

In this study we introduced a new parameter, '*effective radius'*, which is defined as the radius of an approximate sphere a pebble assumes when all its edges have been abraded and worn out during transportation process. We found that there is a strong positive correlation (r = 0.791) between our effective radius parameter and maximum projection sphericity index (MPSI) of Sneed and Folk (1970). We propose that effective radius parameter could be environment of deposition indicator on the basis of its good correlation with the MSPI. Figure 9 shows the relationship between effective radius parameter and MPSI, and reveals that the minimum MPSI value for the studied vein quartz pebbles is about 0.57, which is 13.6% lower than the average MPSI value (0.66).

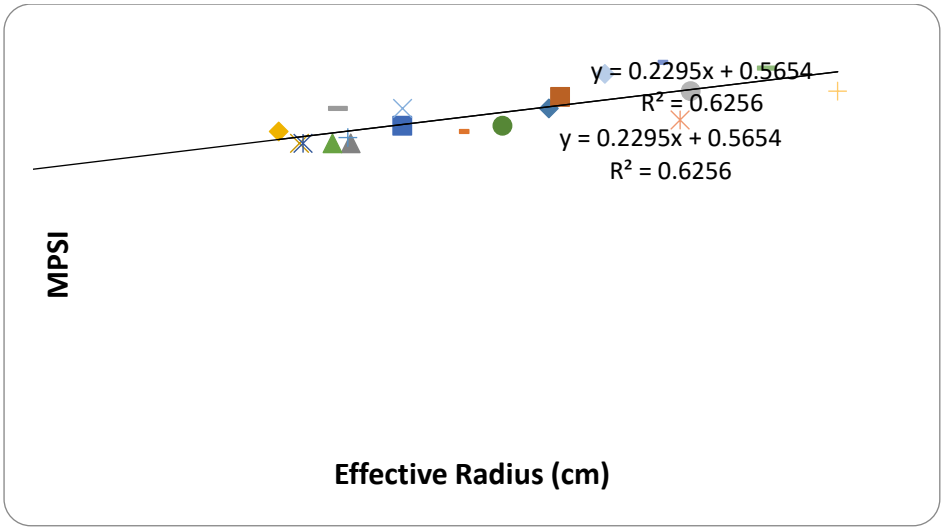

Fig. 9: Relationship between effective radius parameter and MPSI for the studied pebbles

5. CONCLUSIONS

The basal conglomerates of the Bida Formation outcropping in a stream around Zungeru (NW, Nigeria) can be classified as quartzose conglomerate based on the predominance of vein quartz pebbles. The bivariate plots of morphometric parameters such as coefficient of flatness versus MPSI and MPSI versus OPI indicate that the pebbles are deposited by fluvial processes. However, the bivariate plot of roundness versus elongation ratio showed that the vein quartz pebbles were deposited in littoral (marine) environment. The dominance of bladed shape pebbles in this study indicates that the conglomerate sediment in Zungeru is sourced from the surrounding basement such as schists and gneisses. Thus, we concluded that the conglomerate lithofacies of Bida Formation in Zungeru area are products of fluvial deposition with some marine influence.

REFERENCES

Adeleye, D. R. (1974). Sedimentology of the fluvial Bida Sandstones (Cretaceous) Nigeria. *Sedimentary Geology*, 12, 1-24.

Adeleye, D. R. & Desauvagie, T. F. J. (1972). Stratigraphy of the Niger Embayment near Bida, Nigeria. In: T. F. J. Dessauvagie and A. J. Whiteman (eds), *African Geology, University of Ibadan Press*. p. 181-186.

Ajibade, A.C., Anyanwu, N.P.C., Okoro, A.U. and Nwajide, C.S. (2008). The Geology of Minna Area: Explanation of 1:250,000 Sheet 42 (Minna). *Geological Survey of Nigeria Bulletin* 43, 83-100.

Attal, M. and Lavé, J., (2006). Changes of bedload characteristics along the Marsyandi River (central Nepal): Implications for understanding hillslope sediment supply, sediment load evolution along fluvial networks, and denudation in active orogenic belts. In Tectonics, Climate, and Landscape Evolution: *Geological Society of America Special Paper 398*, 143–171.

Barrett, P. J. (1980). The shape of rock particles: a critical review. *Sedimentology*, **27**, 291 – 303.

Benn, D.I. (2010). *Particle morphology of sediments*. http://science.jrank.org/pages/47975/particle-morphology sediments.html">particle morphology of sediments.

Blott, S.J. and Pye, K. (2008). Particle shape: a review and new methods of characterization and classification. *Sedimentology* 55, 31-63.

Boggs Jr., S. (2009). *Petrology of Sedimentary Rocks*. 2nd Edition. Cambridge University Press, 600p.

Braide, S.P. (1992). Alluvia Fan Depositional Model in the Northern Bida Basin. *J. Min. Geol*. 28, 65-73.

Dobkin, J.E. and Folk, R.L. (1970). Shape Development on Tahiti-Nui. *Journal of Sedimentary Petrology*, **40**; 1167-1203.

Dumitriu, D., Niculita, M. and Condorachi, D. (2011). Downstream Variation in the Pebble Morphometry of the Trotuş River, Eastern Carpathians (Romania). *Forum geografic. Studii şi cercetări de geografie şi protecţia mediului*. Vol. 10, issue 1, pp 78-90.

Els, B.G. (1988). Pebble Morphology of an Ancient Conglomerate: The Middelvlei Gold Placer, Witwatersand, South Africa. *Journal of Sedimentary Petrology*, **58**, 894-901.

Folk, R. L. (1980). *Petrology of sedimentary rocks*. Hemphill Publishing Company, Austin, Texas. 184p.

Graham, D. J. and Midgley, N. G. (2000). Graphical Representation of Particles Shape Using Triangular Diagrams: An Excel Spreadsheet Method. *Earth Surface Processes and Landforms*, **25**(13): 1473-1477.

Hurst, S., Johnson, E., Martinez McCoy, Z., Cunningham, D., (2010). The lithology of Ogallala Gravels and Hunter Gatherer Procurement Strategies along the Southern High Plains Eastern Escarpment of Texas, USA. *Geoarchaeology: An International Journal*, 25, 1, 96-121.

Illenberger, W. K. and Reddering, J.S. V. (1993). An evaluation of shape indices as palaeoenvironmental indicators using quartzite and metavolcanic clasts in Upper Cretaceous to Palaeogene beach, river and submarine fan conglomerates – discussion. *Sedimentology*, **40** (5), 1019 –1020.

Krumbein W. C. (1941). Measurement and geologic significance of shape and roundness of sedimentary particles. *Journal of Sedimentary Petrology* **11**, 64–72.

Lambert-Aikhionbare, D.O. and Olayinka, A.I. (Eds.) (2009). *Proceedings of Field Mapping Standardization Workshop*. University Press, Ibadan. 266p.

Lindsey, D.A., Langera, W.H., Van Gosena, B.S., (2007) Using pebble lithology and roundness to interpret gravel provenance in piedmont fluvial systems of the Rocky Mountains, USA. *Sedimentary Geology*, 199, 3-4, 223-232.

Lutig, G. (1962). The Shape of Pebbles in the Continental Fluviatile and Marine Facies. *International Association of Scientific Hydrology Pub.* , **59**, 235-258.

Nwajide, C.S. and Hoque, M. (1982). Pebble Morphometry as an Aid in Environmental Diagnosis: An Example from the Middle Benue Trough, Nigeria. *Journal of Mining and Geology*, **19**, 114-120.

Obaje, N.G. (2009). *Geology and Mineral Resources of Nigeria*. Springer, Heildelberg, 221p.

Odumodu, P.N. and Odumodu, C.F. (2012). Pebble Morphology of the Conglomeritic Arkosic Sandstone Unit of the Ogoja Sandstone, Ogoja, South Eastern, Nigeria. *Journal of Basic Physical Research*, **3**, 40-50.

Okosun, E. A., Goro, A. I., Olobaniyi, S. B., Shekwolo, P. D., and Nwosun, J. E. (2009). stratigraphy of Bida Formation, Bida Basin, Nigeria. *Borno Journal of Geology*, 4.21-37.

Pettijohn, F. J. (1975). *Sedimentary Rock*, 3rd Ed. Haper and Row Pub New York, Pp.195 – 259, 508 – 564.

Sames, C.W. (1966). Morphometric Data of Some Recent Pebble Associations and Their Applications to Ancient Deposits. *Journal of Sedimentary Petrology*, **36**, 126-142.

Sneed, E.D. and Folk, R.L. (1958). Pebbles in Lower Colorado River, Texas: A Study in Particles Morphogenesis. *Journal of Sedimentary Petrology*, **66**, 114-150.

Stratten, J. (1973). Notes on the Application of Shape Parameters to differentiate between Beach and River Deposits in Southern Africa. *Trans. Geol. Soc. S.Africa*, **76**, 59-64.

Tamrakar, N.K. and Shrestha, M.B., (2008). Relationship between fluvial clastic sediment and source rock abundance in Rapti River Basin of Central Nepal Himalayas. *Bol. geol.*, 30, 1, 63-75.

Turker, M. E. (2011). *Sedimentary Rocks in the Field – A Practical Guide*. Ho Printing Singapore Pte Ltd: Singapore. 4th Edition, 275 pp.

Wentworth C. K. (1922). The shape of beach pebbles. *US Geological Survey Professional Paper* **131-C**, 75–83.

A STUDY OF THE EFFECTS OF BAKING MATERIALS AND OVEN TEMPERATURE ON CAKE HEIGHT: SPLIT-PLOT CENTRAL COMPOSITE DESIGN APPROACH

Yisa Yakubu[1], Aliyu Zulihatu Queen[1], Abubakar Usman[1] & Evans O. Patience[2]

[1]Department of Statistics, Federal University of Technology, Minna, Nigeria

yisa.yakubu@futminna.edu.ng

[2]Department of Mathematics and Statistics, The Federal Polytechnic, Bida, Nigeria

patevansjj@gmail.com

Abstract

Most people love a delicious piece of cake. But what is the secret to a good cake? While many may comment on flavor, frostings or other attributes, most people agree on one thing: texture. The texture of the cake needs to be "fluffy". While there are exceptions to the traditional textures, one of the easiest ways to get the right texture of a cake is by having the cake rise to a maximum height. By having the tallest cake with the same amount of starting material, more air is allowed into the cake, thereby creating the "fluffy" texture that people desire. In this work, a central composite design (CCD) experiment within a split-plot structure was conducted to assess the impact of some baking materials on cake height. The experimental factors (cake-baking materials) include oven temperature (factor A), amount of flour (factor B), baking powder (factor C), and amount of milk (factor D) with a fixed amount of other necessary ingredients present. The generated data were analyzed using Design Expert (version 10) statistical package. The restricted maximum likelihood (REML) estimates of the variance components were first obtained and the generalized least squares (GLS) estimator was used to obtain the factor effects estimates. The set of levels of these factors that yields optimum value of the cake height (the stationary point) was then sought using optimization facility of the statistical package. It was observed that each of the linear terms: A, B, C, D, the interaction term: BC and the quadratic terms: A^2, C^2, and D^2 contributes significantly to the height of the cake. The fitted generalized least squares model accounted for 95% of the total variation in the cake height. The estimated optimum cake height was found to be $\hat{y} = 11.047$ at the stationary point: $oven\ temp = 250^oC$, $amount\ of\ flour = 1.5\ cups, baking\ powder = 1.5\ teaspoonfull, and\ milk = 0.75cup.$

Keywords: Cake height, Split-plot CCD, Experiment, Design

Corresponding author: yisa.yakubu@futminna.edu.ng

1. Introduction

Most people love a delicious piece of cake. However, the secret to a good cake as most people often agree is texture. The texture of the cake needs to be "fluffy". While there are exceptions to the traditional textures, one of the easiest ways to get the right texture of a cake is by having the cake rise to a maximum height. By having the tallest cake with the same amount of starting material, more air

is allowed into the cake, thereby creating the "fluffy" texture that people desire. In this work, a study was carried out on the impact of some cake-baking materials on cake height using statistically-designed experimental technique.

Statistically designed experiment is an indispensable technique in the design stage of a product or a process for investigating the effects of several factors on a quality characteristic of interest. These experiments play a key role in the design of new products, improvement of existing ones as well as the design and development of manufacturing processes to produce them, which are the crucial activities in most industrial organizations today. In most industries today, for instance, biotechnology and pharmaceuticals, medical devices, electronics and chemical industries etc., experimental design methodology has resulted in shorter design and development time for new products as well as products that are easier to manufacture, products with higher reliability and enhanced field performance, products that meet or even exceed customer requirements. The tools required for adequate selection of a design and the subsequent fitting and evaluation of the hypothesized model using the data generated by the design, have been developed in an area of experimental design known as **response surface methodology (RSM)**.

Response Surface Methodology is an area of experimental design which consists of a group of mathematical and statistical techniques used in the development of an adequate functional relationship between a response of interest, y, and a number of associated control (or input) variables denoted by $x_1, x_2, \ldots, x_k$ (Myers *et all*, 2009). The most extensive applications of RSM are in the industrial world, particularly in situations where potential influence of several process variables on some quality characteristic of the process is being investigated. RSM is widely used to explore and to optimize response surfaces in these experiments. RSM is sequential in nature and so the experimenter begins with a screening experiment to identify important factors. Follow-up experiments then seek to improve the performance of the response. This process allows the experimenter to learn about the process or system under study as the investigation proceeds. Response Surface Methodology is useful for developing, improving, and optimizing the response variable especially when treatments are from a continuous set of values. One of the most commonly-used response surface design is the second-order design such as the central composite design (CCD) and the Box-Behnken design (BBD), which were introduced, respectively, by Box and Wilson (1951), and Box and Behnken (1960). The variables in these designs are always completely randomized.

The CCD consists of factors with five levels that involve three components. They are:

i. a complete (or a fraction of) 2^k factorial design with factor levels coded as -1, 1 (called the factorial portion),
ii. an axial portion consisting of $2k$ points arranged so that two points are chosen on the coordinate axis of each control variable at a distance of α from the design center,
iii. n_0 center points.

Thus the total number of points in a CCD is $n = 2^k + 2k + n_0$. These three components of the design play important and somewhat different roles.

i. The factorial portion consists of n_f equally-spaced points that contribute to the estimation of linear terms and are the only points that contribute to the estimation of the interaction terms in the model.
ii. The axial portion consists of points lying on the axis of each input variable, and in this portion of the design, the factors are not varying simultaneously but rather in a one-factor-at- a-time array. Thus no information regarding the interaction effect is provided by this portion of the design. However, the axial portion allows for efficient estimation of pure

quadratic terms in the model, and without these points, only the sum of the quadratic terms, i.e., $\sum_{i=1}^{k} \beta_{ii}$, can be estimated.

iii. The center runs provide an internal estimate of error (i.e., the pure error), and efficiently provide information about the existence of curvature in the system. If curvature is found in the system, the addition of axial points allows for efficient estimation of the pure quadratic terms.

This design technique was used in this work but conducted within a split-plot structure.

One difficulty in applying classical response surface designs is that they inherently assume that all factors are equally easy to manipulate, thereby allowing for complete randomization of the experimental run order. In practice most industrial experiments cannot be completely randomized due to the presence of factors with levels that are difficult to change (called hard-to-change (HTC) factors) and those with levels that are easy to change (called easy-to-change (ETC) factors). Thus factors with HTC levels cannot be completely randomized and once an experiment includes such factors, split-plot design approach is used, in which the experimental runs are performed in groups, where, in a group, the levels of the HTC factors are not reset from run to run. This creates dependence among the runs in one group, thereby leading to clusters of correlated errors and responses.

There are two separate randomizations for every split-plot design- whole plot factor levels are randomly assigned to the whole plots using a different randomization for each block; subplot factor levels are randomly assigned within each whole plot using a separate randomization for each whole plot. This leads to two error terms for effects comparison, one for the whole-plot treatments (σ_{γ}^2), and one for the subplot treatments (σ_{ε}^2) as well as the interaction between whole-plot treatments and subplot treatments.

Split-plot central composite designs consist of four different categories of points. These include the factorial portion (f), which consists of n_f equally-spaced points that contribute to the estimation of linear and interaction terms in the model, axial point (whole-plot(α) and subplot(β)), which consists of points lying on the coordinate axis of each input variable, and which allow for efficient estimation of pure quadratic terms in the model and center (c) points, which provide an internal estimate of error (i.e., the pure error), and efficiently provide information about the existence of curvature in the system. If curvature is found in the system, the addition of axial points allows for efficient estimation of the pure quadratic terms.

This work carried out the split-plot central composite design experiment that investigates the effects of oven temperature (factor A), amount of flour (factor B), baking powder (factor C), and amount of milk (factor D) on cake height and then locates the set of levels of these factors that optimizes the predicted cake height (the stationary points). The oven temperature is a HTC factor while the other three are ETC factors. Therefore, the central composite design (CCD) experiment was conducted with a split-plot approach using these factors with a fixed amount of other necessary ingredients present. The generated data were analyzed with the aid of Design Expert (version 10) statistical package using restricted maximum likelihood (REML) approach.

1.1 Statistical model and notations

As stated earlier, the responses from the split-plot experiment are correlated and this violates the assumption of independence of the ordinary least squares or OLS estimator. Therefore generalized least squares or GLS estimates are better since they account for the correlation between these

observations and are generally more precise. The generalized least squares (GLS) model for a split-plot response surface design is

$$\mathbf{y} = \mathbf{X\beta} + \mathbf{Z\gamma} + \boldsymbol{\varepsilon} \qquad \textbf{(1.1)}$$

where **y** is the N x 1 vector of responses, **X** is the N x p overall model matrix, **β** is the p x 1 vector of regression coefficients, **Z** is an N x b incidence matrix assigning observations to each of the b whole plots; γ is the N x 1 vector of whole-plot error terms, ε is the N x 1 vector of subplot error terms. It is assumed that $\gamma_i \sim N(0, \sigma_\gamma^2)$, $\varepsilon_{ij} \sim N(0, \sigma_\varepsilon^2)$, $\mathrm{cov}(\gamma_i, \varepsilon_{ij}) = 0$.

The variance - covariance matrix for the observation vector **y** is

$$\mathrm{Var}(y) = V = \sigma_\varepsilon^2 I_n + \sigma_\gamma^2 ZZ'$$

$$= \sigma_\varepsilon^2 (I_n + dZZ')$$

where $d = \frac{\sigma_\gamma^2}{\sigma_\varepsilon^2}$ gives the relative magnitude of the two variance components. The matrix $\boldsymbol{ZZ}'$ is a block diagonal matrix with diagonal matrices of $J_{n1}, J_{n2}, \ldots, J_{nz}$, where J_{ni} is an n_i x n_i matrix of 1's and n_i is the number of observations in the ith whole-plot.

The diagonal elements of V are the variances of the responses and the off- diagonal elements are the covariances between pairs of responses. The nonzero off-diagonal elements correspond to pairs of responses from within a given whole plot while the zero off-diagonal elements correspond to pairs of runs from two different whole plots.

The generalized least squares (GLS) estimates are calculated from

$$\hat{\beta}_{GLS} = (X'V^{-1}X)^{-1}X'V^{-1}y \qquad (1.2)$$

Thus,

$$\mathrm{Var}(\hat{\beta}_{GLS}) = (X'V^{-1}X)^{-1}$$

$$\hat{y} = X(X'V^{-1}X)^{-1}X'V^{-1}y = Hy$$

where H is the 'hat' matrix.

2. LITERATURE REVIEW

Research works on impact of a split-plot structure on response surface designs began in the 1990s and most of these work focused on two-level fractional factorial designs run as split-plots. Box (1996) explains that completely randomized experiments are often impractical in industry and indicates that split-plot experiments are often very efficient and easier to run.

Bisgaard and Steinberg (1997) look at the design and analysis of prototype experiments. They present examples that use split-plot designs and show clearly how to carry out a two-stage analysis of the data. Bisgaard (2000) uses two-level fractional factorials to construct split-plot designs and gives general expressions for deriving alias structures based on the group structure of the arrays.

Letsinger, Myers and Lentner (1996) is the first paper to exclusively focus on restricted randomization in response surface methodology. The authors describe an experiment from the chemical industry which investigates the effects of five process variables (temperature 1, temperature 2, humidity 1, humidity 2, and pressure) on a certain quality characteristic. They used a modified central composite design but the experimental runs were not completely randomized due to the fact that the levels of temperature 1 and pressure were hard to change. Thus, the split-plot design approach was used in which the levels of the hard-to-change factors were changed as little as possible.

A sequential strategy for designing multi stratum designs, special cases of which are split-plot designs, was presented by Trinca and Gilmour (2001). The authors describe an experiment to investigate the effects of five factors on protein extraction. The factors were the feed position for the inflow of the mixture, the feed flow rate, the gas flow rate, the concentration of protein A and the concentration of protein B, each factor consisting of three levels. The feed position consists of hard-to-change levels and is therefore the whole plot factor. The merit of split-plot approach was fully utilized in this experiment since two experimental runs instead of one could be performed on one single day.

Kowalski (2002) considers split-plot experiments in robust parameter design. He constructs 24-run designs in two ways: using the properties of a balanced incomplete block design and by semifolding a 16 run design.

Vining, Kowalski and Montgomery (2005), hereafter referred to as VKM, show how to modify the standard central composite design (CCD) and Box-Behnken design (BBD) to accommodate a split-plot structure. The authors then establish the general conditions under which the ordinary least squares estimates of the model are equivalent to the generalized least squares estimates and therefore are best linear unbiased.

3. MATERIALS AND METHODS

The materials used for baking all the cakes include flour, baking powder, milk and oven temperature, with fixed amount of other necessary ingredients. Oven temperature was included because the temperature at which the batches are baked strongly impacts cake height. It is a HTC factor since its levels cannot be frequently changed as it takes some time to stabilize, while the other three are ETC factors as their levels can easily be changed during randomization. Each of the factors consists of five (5) levels and these levels were coded using

$$x_i = \frac{2X_i - (X_{il} + X_{ih})}{X_{ih} - X_{il}} \qquad (3.1)$$

Where x_i is the coded level of the ith factor, $i = 1,2, \ldots, k$; X_{il} and X_{ih} are, respectively, the actual low and high levels of the ith factor. The choice of factors, levels and factor ranges are listed in TABLE 3.1.

Table3.1: Choice of factors, levels and ranges

Factor	coded levels				
	-1	-1	0	1	1

Amount of Flour(X_1)	1/2 cup	1/2 cup	1 cup	1.5 cups	1.5 cups
Amt of Baking Powder(X_2)	1/2 teaspoon	1/2 teaspoon	1 teaspoon	1.5 teaspoon	1.5 teaspo
Amount of Milk(X_3)	1/4 cup	1/4 cup	1/2 cup	3/4 cups	3/4 cups
Temperature of Oven(z_1)	150C	150C	200C	250C	250C

For every cake, the butter and sugar were first mixed together in the same Kitchen-aid mixer on the same speed setting. The flour, baking powder and salt were sifted together and added with the specified amount of milk and mixed at the same speed. This was then poured into the cake pan and a spatula was used to scrape all into the pan. All cakes were baked from the same batch of ingredients and the same cake pans were used for each run.

3.1 Performing the Experiment

A four-factor central composite experiment was designed with a split-plot structure in one whole-plot variable and three subplot variables, and with single replication of factorial and axial parts. Each factor consists of five (5) levels: -1, +1, $-\alpha$, $+\alpha$, and 0. At each of the factorial points involving the HTC factor, the subplot runs are the factorial points in the ETC factors. At each of the two axial points that make up whole plots (i.e., $z_1 = -\alpha, +\alpha$), eight replicates of the center of the subplot factors (i.e., $x_1 = 0$, $x_2 = 0$, $x_3 = 0$) were run. Two replicates of the whole-plot center points ($z_1 = 0$) were run, one consisting of the six (6) axial points in the ETC factors while the other containing four(4) replicates of the center of the subplot factors ($x_1 = 0$, $x_2 = 0$, $x_3 = 0$). Thus each of the whole-plot factorial and axial portions of the design is of size eight while the first and second replicates of the whole-plot center portion are, respectively, of size six and four. Thus the resulting split-plot central composite design (CCD) has $n_f = 16$ factorial points, $n_\alpha = 16$ whole-plot axial points, $n_\beta = 6$ subplot axial points and $n_c = 4$ center points. Thus there were $N = 42$ total design points in 6 whole plots as given in Table 3.2. DESIGN-EXPERT (version 10) statistical package was used to create the design layout. The fully-randomized order of runs of the experiment was given in the appendix.

Table 3.2: Design Matrix for **D(1,3)** split-plot CCD

Wp	z1	x1	x2	x3	n
1	−1	±1	±1	±1	8
2	+1	±1	±1	±1	8
3	$-\alpha$	0	0	0	8
4	$+\alpha$	0	0	0	8
5	0	$\pm\beta$	0	0	2
	0	0	$\pm\beta$	0	2

	0	0	0	$\pm\beta$	2
6	0	0	0	0	4

At each setting (level) of the HTC factor (temperature), all possible combinations of the levels of the ETC factors (flour, baking powder and milk) were baked at the same time. This was followed by another (single) run of the oven at the other temperature setting and the process was continued until all the temperature factor levels were completely run. All cakes were baked for 28 minutes to minimize baking time as a nuisance factor. After every run of the oven, its temperature was allowed to stabilize (i.e., cool down to 0^{o}C) before another level was randomly selected for another run. Thus the experiment took us six days to complete. All cakes were measured using the same ruler and measurements were taken in centimeters (cm). No unusual behavior was observed during the experimental runs.

The design consists of two different randomization structure:- temperature factor-levels were randomly and independently assigned to the whole-plots; within each whole plot, the ETC factor level combinations were randomly and independently assigned to the subplots using a different randomization technique. Thus levels of the whole-plot factors were not reset for each run of the subplot factors and this leads to two error terms for effects comparison, one for the whole-plot treatments (σ_{γ}^{2}), and one for the subplot treatments (σ_{ε}^{2}), as well as the interaction between whole-plot treatments and subplot treatments.

3.2 Data Analysis

The generated data were analyzed using Design Expert (version 10) statistical package. **Restricted maximum likelihood** estimation (REML) technique was used to estimate the whole-plot and subplot variance components (σ_{γ}^{2} and σ_{ε}^{2}, respectively). REML estimates for these variance components can be obtained by maximizing the restricted log likelihood function:

$$l_g = -\frac{1}{2}\log|\boldsymbol{V}| - \frac{1}{2}\log\left|\boldsymbol{X'V^{-1}X}\right| - \frac{1}{2}\boldsymbol{r'V^{-1}r} - \frac{n-p}{2}\log(2\pi) \qquad (3.2)$$

Where $\boldsymbol{X}$ and $\boldsymbol{V}$ are as defined in section 1.1 above; $\boldsymbol{r} = \boldsymbol{y} - \boldsymbol{X}(\boldsymbol{X'V^{-1}X})^{-1}\boldsymbol{X'V^{-1}y}$ and p is the number of parameters in $\boldsymbol{\beta}$ **(**Goos and Jones, 2011**).** These estimates were obtained here with the aid of the statistical package.

The Generalized Least Squares (GLS) estimator given in equation (1.2), which is a version of least squares that allows us to account for covariances among the responses, such as might be present in a mixed effects model, was used to estimate the factor effects. The standard errors for the factor effects were then computed as the square root of the diagonal elements of the covariance matrix $(\boldsymbol{X'V^{-1}X})^{-1}$**.**

Optimization facility of the statistical package was then used to obtain the set of levels of the factors that yields optimum value of the cake height (the stationary point).

4. RESULTS AND DISCUSSION

We first looked at the analysis of variance (ANOVA) for our fitted model. This ANOVA confirms the adequacy of our fitted model, as given in the Table below.

TABLE 4.1: ANOVA (REML)

Source	Term df	Error df	F	p-value Prob > F	
Whole-plot	2	27	11	0.0003	significant
a-Oven temperature	*1*	*27*	*8.14*	*0.0082*	
a^2	*1*	*27*	*13.87*	*0.0009*	
Subplot	12	27	42.19	< 0.0001	significant
B-Quantity of flour	*1*	*27*	*355.82*	*< 0.0001*	
C-Amount of baking powder	*1*	*27*	*10.92*	*0.0027*	
D-Amount of milk	*1*	*27*	*17.86*	*0.0002*	
aB	*1*	*27*	*2.27*	*0.1432*	
aC	*1*	*27*	*2.03*	*0.1653*	
aD	*1*	*27*	*0.015*	*0.9036*	
BC	*1*	*27*	*8.37*	*0.0075*	
BD	*1*	*27*	*0.081*	*0.7776*	
CD	*1*	*27*	*0.042*	*0.8401*	
B^2	*1*	*27*	*0.71*	*0.4081*	
C^2	*1*	*27*	*6.97*	*0.0136*	
D^2	*1*	*27*	*6.97*	*0.0136*	

The fourth column of the table gives the computed F-values while the fifth column gives the probability values. From this column we can see that each of the terms: a, B, C, D, BC, a^2, C^2, and D^2 contributed significantly to the goodness-of-fit of the model. That is, each of the oven temperature, amount of flour, amount of baking powder and amount of milk had significant effect on the cake height, with p-values far less than 0.05. Also, the interaction effect of the quantity of flour and amount of baking powder was highly significant; the quadratic effects of the oven temperature, amount of baking powder and quantity of milk were also highly significant. All other terms were not significant.

Next we considered the group (or whole-plot) and residual (or subplot) variance components. These are variations that were not explained by the model in terms of the factors, as given in the Table below.

TABLE4.2: Variance Components

Source	Variance	StdErr	95% CI Low	95% CI High
Group	*0.000*	*0*	*0*	*0*
Residual	*0.38*	*0.1*	*0.24*	*0.7*
Total	0.38			

The group (or whole-plot error) variance is due to resetting of a hard-to-change factor level (in this work, oven temperature). The computed group variance was zero, and this signifies that the whole-plot model explained all of the variation between the whole plots. The residual (or subplot error) variance is due to each of the subplot runs. In this work, the residual variance was 0.38.

This fitted model explains 95% of the total variability in the cake height ($R^2 = 0.95$). Thus only 5% was not accounted for by the model, also, the adjusted R^2 was 0.92 ($Adj.\ R^2 = 0.92$), as given at the bottom of Table 4.3. These statistics signify that the fitted model was good, that is, the model have captured most of the variation in the data.

Then we looked at the computed regression coefficients and variance inflation factors (VIF) as given in Table 4.3 below. The VIF measures how much the variance of the model is inflated by the lack of orthogonality in the design. It indicates the extent to which multicollinearity (correlation among predictors) is present in a regression analysis.

TABLE 4.3: Estimated regression coefficients

Source	Coefficient Estimate	Standard Error	VIF
Intercept	5.727822581	0.19865203	
Whole-plot Terms:			
a-Oven temperature	-0.309375	0.1084569	1
a^2	-0.861391129	0.23130547	1.082949309
Subplot Terms:			
B-Quantity of flour	2.727777778	0.1446092	1
C-Amount of baking powder	0.477777778	0.1446092	1
D-Amount of milk	0.611111111	0.1446092	1
aB	0.23125	0.15338122	1
aC	-0.21875	0.15338122	1
aD	0.01875	0.15338122	1

BC	0.44375	0.15338122	1
BD	-0.04375	0.15338122	1
CD	0.03125	0.15338122	1
B^2	0.303629032	0.36128969	3.566820276
C^2	0.953629032	0.36128969	3.566820276
D^2	0.953629032	0.36128969	3.566820276

$R^2 = 0.95$, Adjusted $R^2 = 0.92$

From the last column of this table, all the VIFs are equal to one except for the last three terms of the model. This indicates that each of the first eleven predictors was orthogonal to (i.e., not correlated with) all the other predictors in the model. Each of the last three predictors has VIF equal to 3.56, which indicates that it was moderately correlated with all the other predictors. Thus there was no case of multicollinearity in the data, and we have the fitted second-order model for the data as:

$$Height = 5.73 - 0.31z_1 + 2.73x_1 + 0.48x_2 + 0.61x_3 + 0.23z_1x_1 - 0.22z_1x_2 + 0.019z_1x_3 + 0.44x_1x_2 - 0.044x_1x_3 + 0.031x_2x_3 - 0.86z_1^2 + 0.30x_1^2 + 0.95x_2^2 + 0.95x_3^2 \quad (4.1)$$

Each of the terms in this model has the same p-value as in Table 4.1. Thus the effects of the terms: a, B, C, D, BC, a^2, C^2, and D^2 were each significant while that of the remaining terms were not significant.

4.1 Diagnostic plots

Here we diagnose the statistical properties of the above fitted model. Figure 4.1 below gives the normal probability plot of the residuals, which indicates whether the residuals follow a normal distribution.

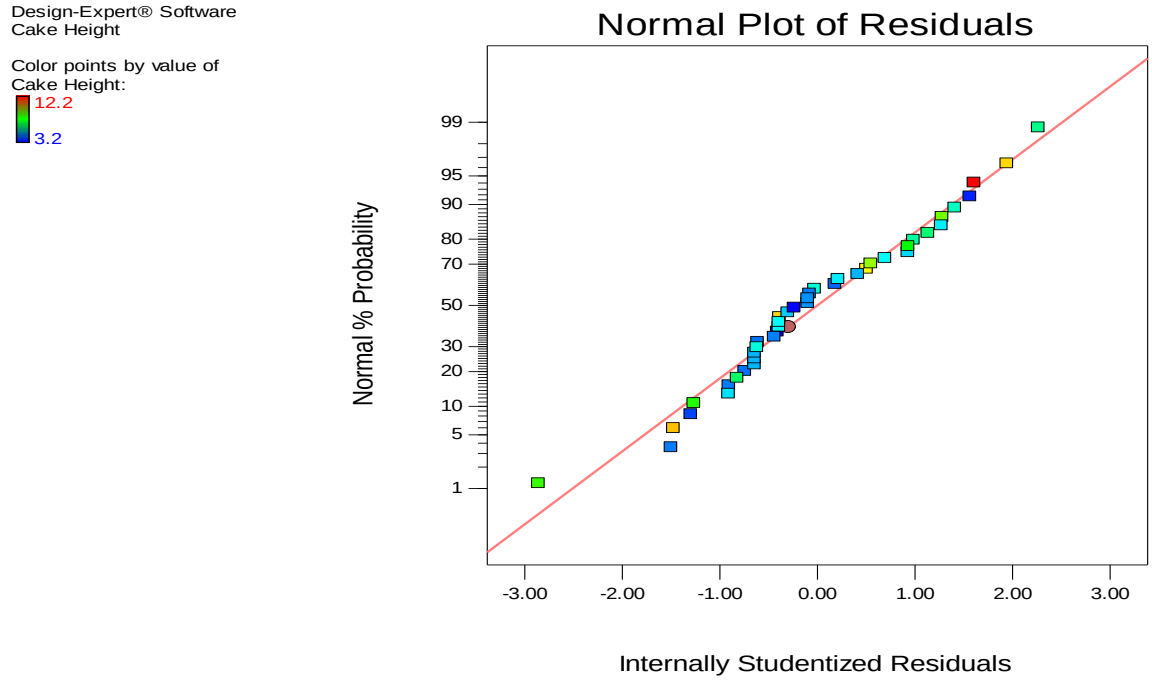

Fig.4.1: Normal probability plot of the residuals

From this plot, all the points fall on the straight line. This indicates that, to some extent, the residuals were normally distributed. Thus there are no problems with our data. next we looked at the plot of the residuals versus the predicted values, as given in figure4.2 below.

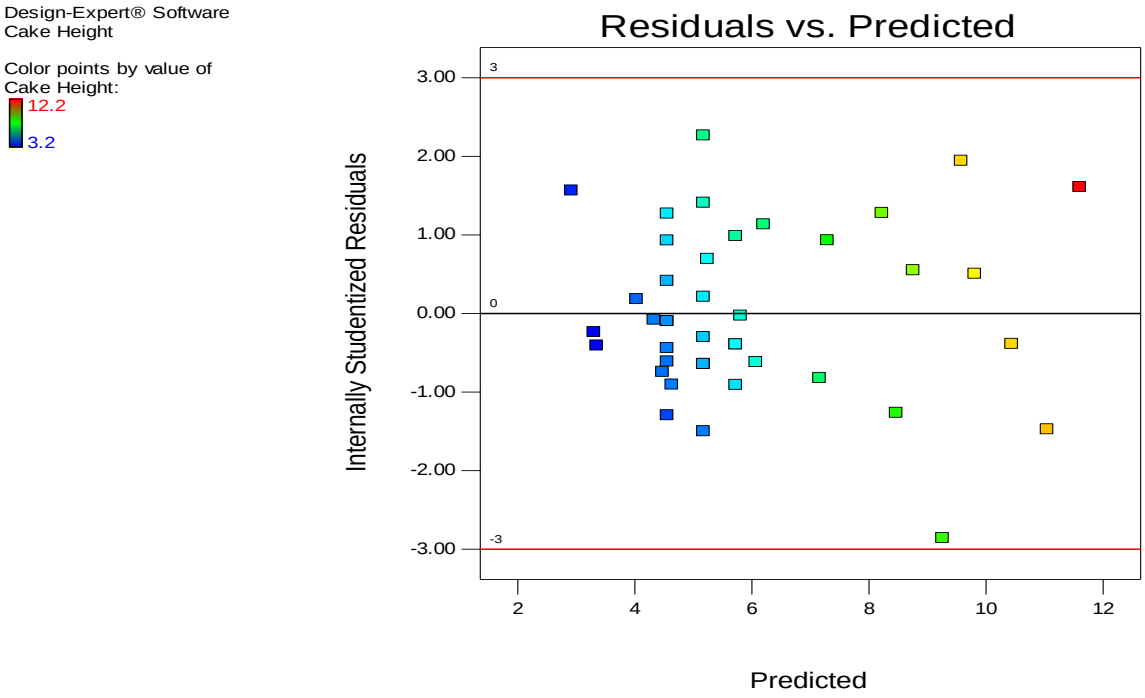

Fig.4.2: Residuals Vs Predicted plot

This plot is a visual check for the assumption of constant variance. As can be directly seen, this plot is a random scatter with a consistent top to bottom range of residuals across the predictions on the X axis. Thus we can conclude here that our model satisfied the constant variance assumption.

Next we looked at the plot of the residuals versus the experimental run order, as given in figure 4.3 below.

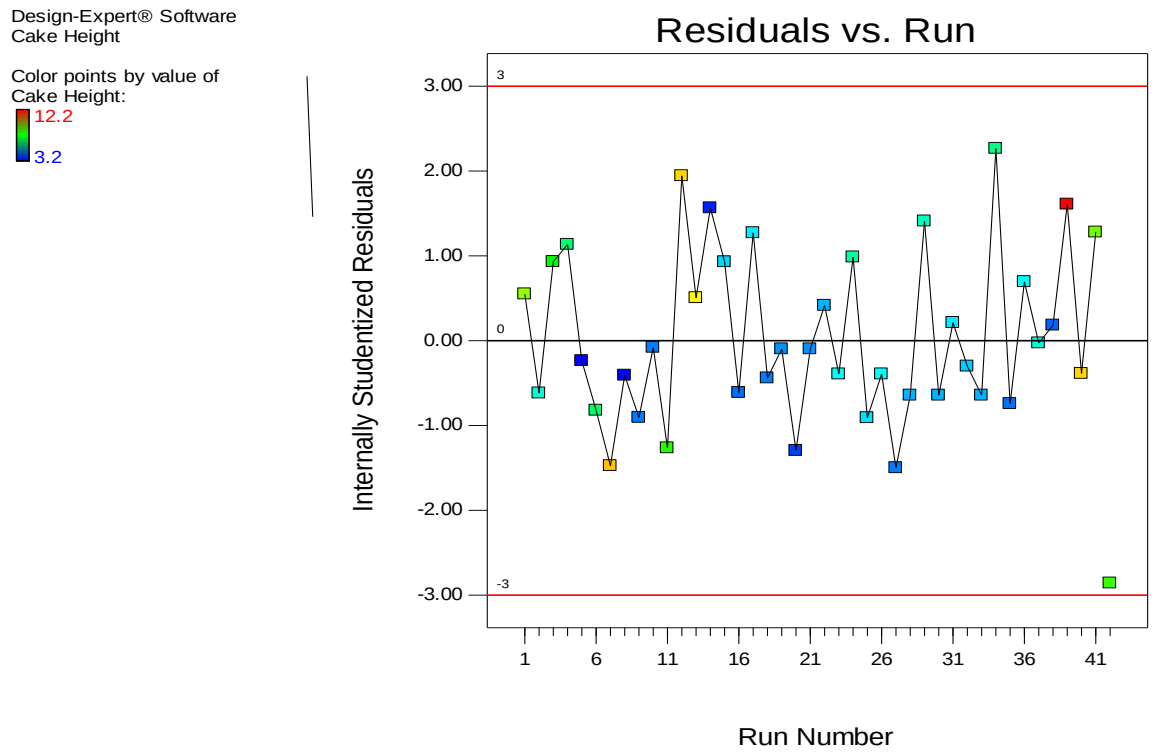

Fig.4.3: Residuals versus experimental run order

This plot provides a check for lurking variables that may have influenced the response during the experiment.

As can be directly observed, the plot showed a random scatter without any trend. Thus there were no any lurking variable in the background.

Lastly, we looked at the plot of the predicted values versus the actual values, as given in the figure 4.4 below.

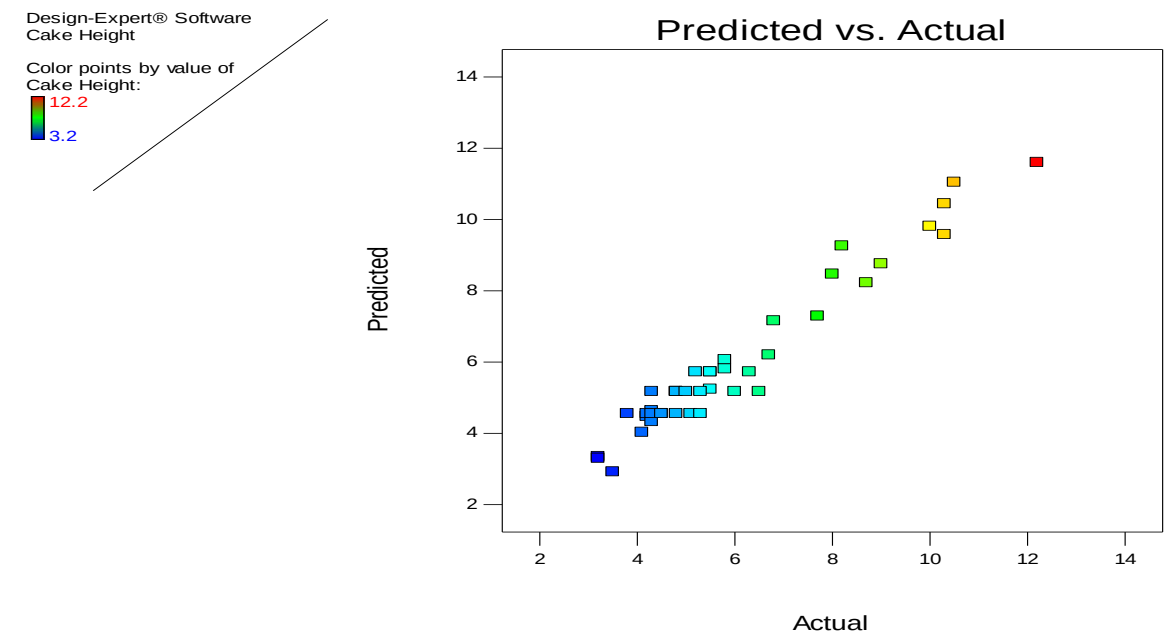

Fig.4.4: predicted versus actual values plot

This graph plots the observed (actual) response values versus the predicted response values. The plot help us to detect observations that that were not well predicted by the model. From this figure, the data points were evenly split by the 45 degree line. Thus our fitted model was okay.

5. Conclusion

This study has investigated the potential effects of baking materials and oven temperature on cake height through the conduct of the response surface experiment within a split-plot structure. By conducting the response surface experiment within the split-plot structure, the number of times the oven temperature has to be reset was reduced by sorting the design into whole-plot groups. Since randomization was restricted by sorting, a restricted maximum likelihood (REML) analysis was applied to obtain the estimates of the variance components and the generalized least squares (GLS) estimator was used to obtain estimates of the effects. The predictors were not linearly correlated and so there was no case of multicollinearity; thus the parameter values were independently estimated. The baking materials considered as well as the oven temperature play significant roles in determining the cake height, which is one of the easiest ways to get the right texture of a cake. The fitted generalized least squares (GLS) model accounted for 95% of the variability in the cake height.

Numerical optimization resulted in the set of the factor levels that will yield optimum value of the cake height. The statistical properties of the fitted model were further diagnosed and these revealed no problems with the data. The conducted split-plot CCD allowed the experimenters to save time and money and run a design which might well have been infeasible if fully randomized.

References

Box, G. E. P. and Behnken, D.W. 1960. Some New Three Level Designs for the Study of Quantitative Variables. *Technometrics* 2: 455-475.

Box,G.E.P. and Wilson,K.B.1951. On the Experimental Attainment of Optimum Conditions. *Journal of Royal Statistical Society*, Series B 13: 1-45.

Cochran, W. G. and Cox, G. M. 1957. *Experimental Designs*. 2nd ed. New York:John Wiley and Sons Inc.

Daniel C. 1976. *Applications of Statistics to industrial Experimentation*, John Wiley and Sons, New York.

Kowalski, S. M. and Potcner, K. J. 2003. How to Recognize a Split-plot Experiment, *Quality Progress* 36:60-66.

Myers, R. H., Montgomery, D. C., Christine M. A. 2009. *Response Surface Methodology, Process And Product Optimization Using Designed Experiments*, New York, Wiley.

Trinca, L.A. and Gilmour,S.G.2000. Multi-Stratum Response Surface Designs. *Technometrics* 43: 25-33.

Vining, G. G., Kowalski, S. M. and Montgomery, D.C. 2005. Response Surface Designs Within a Split-Plot Structure. *Journal of Quality Technology* 37: 115-129.

Appendix

Design matrix and run- order of the data

				Factor 1	Factor 2	Factor 3	Factor 4
Std	Group	Run	Space Type	a:Oven temperature	B:Quantity of flour	C:Amount of baking powder	D:Amount of milk

38	1	1	Axial	0	1	0	0
41	1	2	Axial	0	0	0	-1
42	1	3	Axial	0	0	0	1
39	1	4	Axial	0	0	-1	0
37	1	5	Axial	0	-1	0	0
40	1	6	Axial	0	0	1	0
16	2	7	Factorial	1	1	1	1
9	2	8	Factorial	1	-1	-1	-1
13	2	9	Factorial	1	-1	-1	1
15	2	10	Factorial	1	-1	1	1
10	2	11	Factorial	1	1	-1	-1
14	2	12	Factorial	1	1	-1	1
12	2	13	Factorial	1	1	1	-1
11	2	14	Factorial	1	-1	1	-1
29	3	15	Axial	1	0	0	0
31	3	16	Axial	1	0	0	0
33	3	17	Axial	1	0	0	0
34	3	18	Axial	1	0	0	0
32	3	19	Axial	1	0	0	0
30	3	20	Axial	1	0	0	0
35	3	21	Axial	1	0	0	0
36	3	22	Axial	1	0	0	0
19	4	23	Center	0	0	0	0
17	4	24	Center	0	0	0	0
20	4	25	Center	0	0	0	0
18	4	26	Center	0	0	0	0
22	5	27	Axial	-1	0	0	0
25	5	28	Axial	-1	0	0	0
23	5	29	Axial	-1	0	0	0

24	5	30	Axial	-1	0	0	0
26	5	31	Axial	-1	0	0	0
27	5	32	Axial	-1	0	0	0
21	5	33	Axial	-1	0	0	0
28	5	34	Axial	-1	0	0	0
3	6	35	Factorial	-1	-1	1	-1
5	6	36	Factorial	-1	-1	-1	1
7	6	37	Factorial	-1	-1	1	1
1	6	38	Factorial	-1	-1	-1	-1
8	6	39	Factorial	-1	1	1	1
4	6	40	Factorial	-1	1	1	-1
2	6	41	Factorial	-1	1	-1	-1
6	6	42	Factorial	-1	1	-1	1

MODELING PLATINUM GROUP ELEMENTS (PGE) DEPLETION IN METAMORPHOSED ULTRAMAFIC ROCKS OF THE NYONG SERIES, SOUTHEAST CAMEROON

T. A. Ako [1, 2*], A. Vishiti[3], C. E. Suh[2], A. C. Kedia[2]

[1]Department of Geology, Federal University of Technology, Minna, Nigeria (akoagbor@futminna.edu.ng)

[2] Department of Geology, University of Buea, Cameroon

[3]Department of Mining and Extractive Metallurgy, Institute of Science, Engineering and Technology, Cameroon Christian University, Bali, Cameroon

ABSTRACT

Meta-ultramafic rocks in the Paleoproterozoic Nyong Series (SE Cameroon) which occur as intrusions within the metasedimentary and meta-igneous units have been studied. The aim was to study the concentration of platinum group elements (PGEs) within the layered sequence and suggests models of their depletion relevant to the rocks. Twenty-seven samples of the ultramafic rocks were collected from the different layers of the sequence and analysed for their Ni, Cu, Au and PGE contents. Ni, Cu, Au, Pt and Pd were analysed by ICP-MS while Ir, Os, Rh and Ru were analysed by INAA. Results of the analyses show that the concentrations of Cu, Au, PGE and ΣPGE are very low throughout the cliff face while Ni concentrations are high and variable. The effect of alteration of the rocks has resulted in the low PGE concentration due to remobilization. It is also suggested that the rocks are PGE-depleted due to low degree of partial melting or depleted mantle source and various models have been used to explain this depletion as related to the Nyong Series.

Key words: instrumental neutron activation analysis, ultramafic rocks, PGE depletion model, Poyi Poshi, Nyong Series

1. INTRODUCTION

Platinum group elements (PGEs) belong to Group 8, periods V and VI of the transition metals and they include platinum (Pt), palladium (Pd), rhodium (Rh), Iridium (Ir), Osmium (Os) and ruthenium (Ru). These six chemically similar elements comprise the light platinum elements, (Ru, Rh, Pd) and the heavy platinum elements (Os, Ir and Pt). Together with gold and silver, the PGEs are precious metals and occur rarely in the earth's crust. The average crustal abundance of Pt and Pd is 5 ppb while Rh, Ru and Ir are even rarer with approximately 1 ppb. Due to their similarity in physical and chemical characteristics, the PGEs often occur naturally together and can be mined together as co-products with Pt normally providing the reason behind PGE production levels (Polinares Consortium, 2012). These elements are strongly siderophile and chalcophile (e.g. Brain, 2011; Ranvide *et al*., 2015) and have similar geochemical behaviors during magmatic processes. Traditionally, the PGEs can be subdivided into two groups, the compatible IPGEs which include Os, Ir and Ru and the incompatible PPGEs which are made up of Rh, Pd and Pt (Qing *et al.,* 2012). It has been suggested that the IPGEs are refractory and tend to be retained in the mantle peridotite during partial melting (Brain, 2011; Evans

et al., 2012; Barnes *et al*., 2011). Most economic PGE deposits belong to a continuum of Ni-Cu-PGE sulfide mineralization styles from those that tend to be sulfide-poor and mined mainly for their PGE contents, to those that are sulfide-rich and are mined mainly for their Ni-Cu contents (Keays and Lightfoot, 2002). PGE mineralization in magmatic deposits is formed in three different ways (Holwell and McDonald, 2010). These include (1) fractional separation of PGEs during magma crystallization, (2) PGE concentration in the oxide-ore phase forming segregations, and (3) PGE extraction from magma into immiscible sulfide liquids.

A larger part of the Cameroon basement is made up of ancient crystalline rocks which have been deformed multiple times and re-metamorphosed during various tectonic events resulting in the development of structures which have implications on mineralization. In the Nyong Series these structures are thought to have controlled the emplacement of ultramafic bodies which are potential PGE host rocks. Studying ultramafic rocks across the globe throws more light on mechanisms of PGEs enrichment and this will enhance exploration strategies. This is regardless if the ultramafics are mineralised or barren. This work therefore studies ultramafic rocks and proposes models of PGE depletion in rocks relevant to the Nyong Series.

2. REGIONAL GEOLOGICAL SETTING

The Nyong Series is part of the West Central African Belt (WCAB) of Eburnean age (2400 - 1800 Ma) which has been differentiated into cratons and mobile zones in central African (Bessoles and Lassere, 1980). It corresponds to the WCAB known in Cameroon, Gabon, Central African Republic, Republic of Congo, Democratic Republic of Congo and Angola and extends through the Transamazonian Belt in Brazil (Lerouge *et al.,* 2006; Owona, 2011). The Nyong Series occupies the NW border of the Ntem complex that was remelted during the collision of the São Francisco and Congo cratons (Ledru *et al*., 1994) is dominated by metasedimentary rocks. It comprises of various migmatitic rocks (including biotite gneisses and amphibolites with or without biotite gneisses) quartzites associated with BIFs and pyroxene-garnet-bearing amphibolites (Lerouge *et al*., 2006). The unit which is the NW corner of the Congo craton is a metasedimentary and metaplutonic rock unit that underwent a high grade tectono-metamorphic event at ~ 2050 Ma associated with charnockite formation (Lerouge *et al.,* 2006) and is bordered by the Ntem unit at the SE part, the Pan-African gneiss formations at the north and NE parts and by the Quaternary sedimentary formations at the NW part (Figure 1) (Ebah Abeng *et al.,* 2012). It is a high-grade gneiss unit, which was initially defined as a Neoproterozoic, or palaeoproterozoic- reactivated NW corner of the Archaean Congo craton (Lasserre and Soba, 1976; Feybesse *et al.,* 1986; Lerouge *et al.,* 2006). The unit is made up of a greenstone belt (pyroxenites, amphibole-pyroxenites, peridotites, talcschists, amphibolites and banded iron formations), foliated series (TTG and gneiss), and magmatic rocks (augen metadiorites, granodiorites and syenites) (Shang *et al.,* 2010; Lerouge *et al.,* 2006; Owona *et al*., 2011).

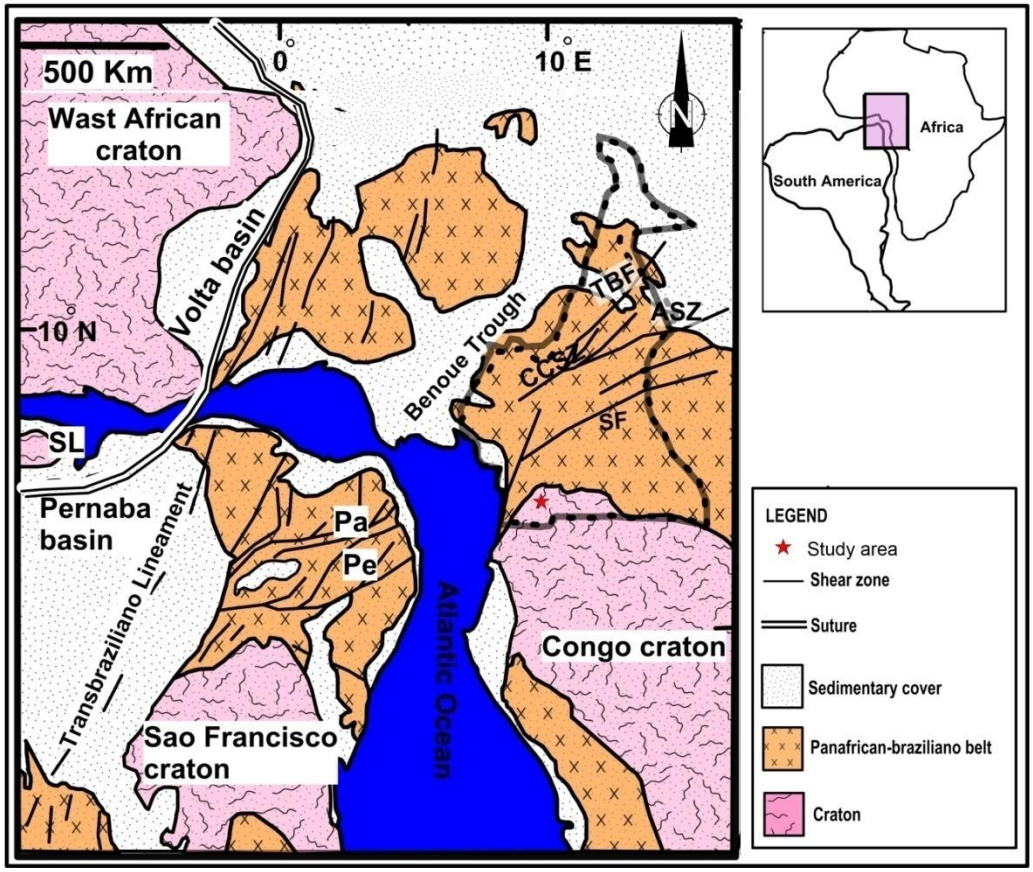

Figure 1: Geological map of the pre-drift Gondwana showing the Congo craton in Cameroon and the northern part of São Francisco craton of Brazil (modified after Ebah Abeng *et al.*, 2012)

This large belt resulted from the collision between the Congo and São Francisco cratons. Most of the WCAB is characterized by tectonic reworking of Archean crust with little addition of juvenile material, particularly in the southern part of the belt (Toteu *et al.*, 1994a). However, this dominant recycling character is diminished northward with the appearance of ~ 2.1 Ga juvenile metasedimentary and meta-plutonic rocks intensively reworked and dismembered in the Pan-African belt north of the Congo craton (Pénaye *et al.*, 2004). The Nyong Series (coined as Nyong Group, e.g. Lerouge *et al.*, 2006; Owona *et al.*, 2011; Owona *et al.*, 2013) in the northwestern corner of the Congo craton in Cameroon is a-well-preserved granulitic unit of the WCAB resting as an Eburnean nappe on the Congo craton (Feybesse *et al.*, 1986; Toteu *et al.*, 1994b).

3. MATERIALS AND METHODS

The field study consisted of systematic mapping and sampling of lithological units of the selected area within the Nyong Series where ultramafic rocks where found. A total of twenty seven ultramafic rock samples were collected during the field work and were later used for the various analyses. Twenty seven metamorphosed ultramafic rock samples were crushed using a jaw crusher with steel plates. The crushed samples were pulverized in a ball mill made up of 99.8% Al_2O_3 at the ACME Analytical Laboratory, Vancouver, Canada. A two-step loss on ignition (LOI) was done in which powders were first heated at 105˙ C in the presence of nitrogen to drive off adsorbed water and then ignited at 1000˙ C in the presence of oxygen to drive off the remaining volatile components.

Nickel (Ni) and copper (Cu) were analysed by ICP-MS while gold (Au), platinum (Pt) and palladium (Pd) were analysed by Ni sulphide fire assay method (code 3B-MS). A 25 g aliquot of each sample was fused at 1000^o C with a suitable amount of flux for the sample matrix with nickel oxide and sulphur added as a carrier. The resulting nickel sulphide button was extracted, ground and partially dissolved in 1MHCl under a high enough f_{H2S} to ensure that the precious metals remain insoluble. The resulting insoluble residues containing the precious metals was dissolved in aqua regia and analysed by ICP-MS. Au, Pt and Pd had detection limits of 2, 3 and 2 ppb respectively.

The remaining PGEs (Ir, Os, Rh and Ru) were determined by nickel-sulphide fire assay followed by Te co-precipitation (code NAA-2). The sample solutions were melted with sodium carbonate and sodium tetraborate in the presence of nickel sulfide melt. After the quenching of each sample, a bead of NiS was broken out of the crucible and digested by concentrated HCl in Telfon vessels using concentrated HCl acid. Tellurium co-precipitation was used to ensure that the insoluble residue to acid digestion retained all Au-PGE. Solutions were filtered in a vacuum after which the precipitate was redissovled in aqua regia and deionized water. The resulting solutions were analysed by instrumental neutron activation analysis (INAA). Details of this method are contained in Savard *et al*. (2010). The detection limits for Ir, Os, Rh and Ru was 1, 10, 5 and 50 ppb respectively. All the analyses were done at Acme Analytical Laboratory, Vancouver, Canada. The accuracy of the analytical results was verified through the analysis of matrix-matched reference materials, and any potential contamination during sample preparation and analysis was monitored via suitable black materials. All analytical data presented in this work passed through quality control tests to ascertain the reliability of the results.

1.0 4. RESULTS AND DISCUSSIONS

2.0 4.1Field Characteristics of the Ultramafic Rocks

The study area is made up of two distinct rock units. These units are the metasedimentary unit which is represented by the talc-tremolite schists and these rocks occur as floats of blocks with fine to medium-grained texture and a meta-igneous unit which is made up of amphibole-pyroxene gneiss, amphibole-garnet gneiss and biotite-garnet gneiss. These units have been intruded by ultramafic rocks

which were sampled for this study. The ultramafic unit investigated is a layered sequence exposed on a cliff face and details of the geology and petrography are contained in Ako *et al*., 2015 and depicted in Figure 2.

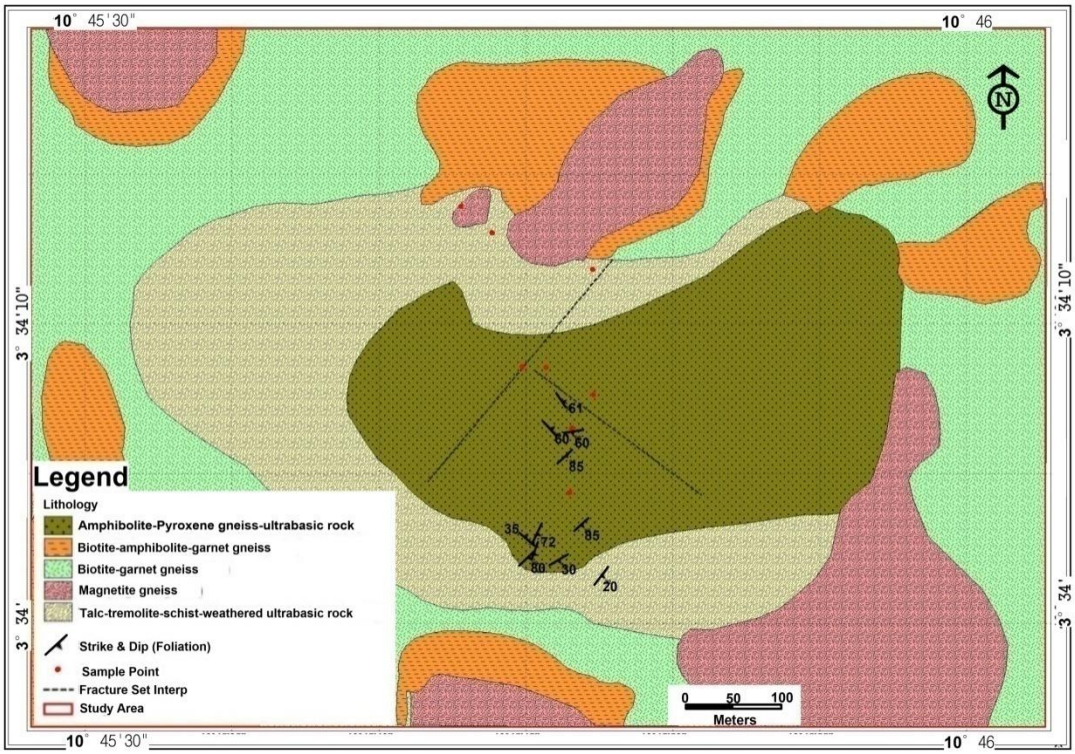

Figure 2: Geological map of the study area showing the various lithologies intruded by the ultramafic rocks (after Ako *et al*., 2015).

4.2 GEOCHEMISTRY

The Ni-Cu-Au- PGE data of the ultramafic rocks of the study area are presented in table 1. The ultramafic rocks of the northern limit of the Nyong Series show very low ΣPGE contents with a very narrow range of 5 – 13 ppb and ΣAu-PGE concentrations from 7.7 to 521.7 ppb. Os, Rh and Ru were all below detection limits in the samples, thus only Pd, Pt and Ir were used for plotting and comparison in the study. Pd (3 to 5 ppb); Ir (< 1 to 7 ppb); Pt (<3 to 8 ppb) and Au (1.3 to 3.9 ppb, except sample ESK 27 which has a concentration of 517.7 ppb) display relatively narrow variations. Cu content in the samples is relatively very low (0.69 to 11.2 ppm, except sample ESK 27 which again has a value of 50 ppm) while Ni contents range from 680 - 2622 ppm.

Table 1: Ni-Cu-Au-PGE contents of the ultramafic rocks in the Nyong Series

Sample No.		ESK 1	ESK2	ESK 3	ESK 4	ESK5	ESK6	ESK 7	ESK 8	ESK 9	ESK 10	ESK 11	ESK 12	ESK 13	ESK 14
(ppb)	d.l														
Pt	3	<3	<3	<3	<3	<3	<3	<3	<3	<3	<3	<3	<3	<3	<3
Pd	2	3.00	3.00	3.00	4.00	3.00	3.00	4.00	3.00	3.00	3.00	3.00	4.00	5.00	5.00
Rh	5	<5	<5	<5	<5	<5	<5	<5	<5	<5	<5	<5	<5	<5	<5
Ir	1	4.00	4.00	7.00	4.00	4.00	5.00	4.00	7.00	2.00	4.00	2.00	2.00	2.00	3.00
Os	10	<10	<10	<10	<10	<10	<10	<10	<10	<10	<10	<10	<10	<10	<10
Ru	50	<50	<50	<50	<50	<50	<50	<50	<50	<50	<50	<50	<50	<50	<50
Ni(ppm)	20	1461	1450	2235	2222	2133	2121	1593	1599	2489	2490	2475	2479	2615	2617
Cu(ppm)	0.1	4.4	4.7	11.2	11	3.9	3.7	7.1	7.3	7.5	7.6	0.7	0.69	3.9	4.1
Au	2	3.7	3.7	2.4	2.7	2.9	2.8	3.8	3	1.3	1.5	3.3	3.8	3.7	3.9
ΣPGE	-	7	7	11	8	7	8	8	10	5	7	5	6	7	8
AU-PGE	-	10.7	10.7	13.4	10.7	9.9	10.8	11.8	13	6.3	8.5	8.3	9.8	10.7	11.9
PPGE	-	7	7	11	8	7	8	8	10	5	7	5	6	7	8
Pd/Ir	-	0.75	0.75	0.43	1	0.75	0.6	1	0.43	1.5	0.75	1.5	2	2.5	1.67

Cu/Ir	-	1.1	1.18	1.6	2.75	0.98	0.78	1.78	1.04	3.75	1.9	0.35	0.35	1.95	1.37
Cu/Pd	-	1.467	1.567	3.733	2.75	1.3	1.233	1.775	2.433	2.5	2.533	0.233	0.173	0.74	0.82
Pt+Pd+Au		6.7	6.7	5.4	6.7	5.9	5.8	7.8	6.00	4.3	4.5	6.3	7.8	8.7	8.9
Pt+Pd+Au/Cu	-	1.52	1.52	0.57	0.61	1.15	1.57	1.11	0.82	0.57	0.59	9	11.3	2.23	2.17
Pt+Pd+Au/CaO	-	134	134	270	670	-	-	390	200	4.58	4.89	42	48.75	870	890

d.l: detection limits

Table 1 (continued)

Sample No.		ESK 15	ESK 16	ESK 17	ESK18	ESK 19	ESK 20	ESK 21	ESK 22	ESK 23	ESK 24	ESK 25	ESK 26	ESK 27
(ppb)	d.l													
Pt	3	<3	<3	<3	<3	<3	<3	<3	<3	<3	<3	<3	8	4
Pd	2	4.00	3.00	4.00	4.00	3.00	4.00	5.00	4.00	4.00	4.00	5.00	5.00	4.00
Rh	5	<5	<5	<5	<5	<5	<5	<5	<5	<5	<5	<5	<5	<5
Ir	1	4.00	4.00	4.00	7.00	4.00	4.00	3.00	4.00	4.00	2.00	2.00	<1	<1
Os	10	<10	<10	<10	<10	<10	<10	<10	<10	<10	<10	<10	<10	<10
Ru	50	<50	<50	<50	<50	<50	<50	<50	<50	<50	<50	<50	<50	<50
Ni(ppm)	20	2009	2010	2188	2179	2110	2115	2619	2622	2506	2510	2456	2462	680
Cu(ppm)	0.1	7.8	7.1	1.5	1.9	1	1.2	3	2.9	8.4	8.2	3.1	3.3	50
Au	2	3.2	3.3	1.6	1.5	2.1	2.1	2.5	2.8	3.4	3.3	2.5	2.7	517.7
ΣPGE	-	8	7	8	11	7	8	8	8	8	6	7	13	8
AU-PGE	-	11.2	10.3	9.6	12.5	9.1	10.1	10.5	10.8	11.4	9.3	9.5	14.7	525.7
PPGE	-	8	7	8	11	7	8	8	8	8	6	7	13	8
Pd/Ir	-	1	0.75	1	0.57	0.75	1	1.67	1	1	2	2.5	-	-
Cu/Ir	-	1.95	1.78	0.38	0.27	0.25	0.3	1	0.73	2.1	4.1	1.55	-	-

Cu/Pd	-	1.95	2.367	0.375	0.475	0.333	0.3	0.6	0.275	2.1	2.05	0.62	0.66	12.5
Pt+Pd+Au	-	7.2	6.3	5.6	5.5	5.1	6.1	7.5	6.8	7.4	7.3	7.5	15.7	525.7
Pt+Pd+Au/Cu	-	0.92	0.89	3.73	5.91	5.1	5.17	2.5	2.35	0.88	0.89	2.42	2.33	10.43
Pt+Pd+Au/CaO	-	56.36	55	56	550	-	-	6.58	6.07	12.13	12.37	107.14	85.56	100.91

d.l: detection limits

Pt + Pd +Au values range from 4.3 to 15.7 ppb (with the exception of sample 27 which show a value of 525.7 ppb) while Cu/Pd ratios vary from 0.17 to 3.73. Ni concentration is very high in the samples with a range of 680 to 2622 ppm (Table 1). The average Pt/Pd ratio (1.4) of the ultramafic rock samples is less than that of the Merensky Reef (2.33). Also, the samples have average Ni/Cu, Pd/Ir and Pt/Ir ratios of 329.8, 1.01 and 0.06, respectively. The Merensky Reef has average Pd/Ir and Pt/Ir ratios of 15.4 and 3.6 , respectively while those of the Platreef are 89.5 and 75.8 respectively (Naldrett, 1989). Maier *et al. (*2008) suggested that the difference in Pt/Pd ratios between the Merensky Reef and the Platreef is either as a result of Pd loss from the Merensky sulfides due to mobilization in late-stage magmatic or hydrothermal melts and/or fluids or enhanced partitioning of Pd relative to Pt into the sulfide melt due to the Platreef magma having a higher oxygen fugacity than the Merensky magma.

3.0 5.3 Models of PGE Depletion in Rocks Relevant to the Nyong Series

The ultramafic rocks in the Nyong Series have very low PGE contents. Os, Rh and Ru are completely absent in the samples. These low PGE data suggest that the potential of these ultramafic rocks to produce exploitable PGE deposits is very low (Ako, 2016). However, there is also the possibility that the Nyong Series ultramafic intrusions are feeder intrusions with the implication that further PGE-rich sulphides were transported into wherever these feeder intrusions deposited them, either as lavas or possibly large-scale gabbro intrusions (e.g. Holwell *et al*., 2012). On the other hand as feeder intrusions, there may be further PGE deposits at depth and the mineralization in the studied ultramafic rock intrusions may simply represent a small fraction of a much large volume of sulphides. This will be related to having a larger body of magma at depth in which both PGE enrichment and sulphide saturation occurred. Huminicki *et al*., 2008 and Kozlu *et al*., 2014, have reported similar situations in which sulphide droplets in intrusion systems such as sills and dykes describe this style of mineralization above areas of PGE mineralization and sulphide saturation.

Generally, the concentration of PGE in magmas is influenced to a large extent by S saturation (Maier *et al*., 2008, Zhou *et al*., 2013 and Iheinfeld and Keays, 2011). However, it is important to seek explanations for the low levels of PGE in the Nyong samples in order to better enhance exploration in this region. Three main reasons are advanced and debated. The Nyong Series rocks have strong total PGE (ΣPGE) depletion and various mechanisms besides alteration (*Ako et al*., 2015) have been advanced to explain this observation including the fact that the parental magma might have been originally poor in PGE. The low PGE abundance may be attributed to melting of a depleted refractory lithospheric mantle source which had previously experienced periodic melt extraction as noted in the Voisey Bay mineralisation in Canada as depicted in model in Figure 3 (Lightfoot *et al*. 2012). Other models ascribe PGE depletion to sulphide segregation from magma at depths which reduced the ΣPGE content or levels in the residual magma due to high K_D (~10^4) of PGE into these sulphides as illustrated in Figure 4 (e.g. Song *et al.*, 2009a and b, Wang *et al.*, 2011, Wei *et al*., 2013). The third scenario relates to PGE depletion due to metal retention in sulphide minerals in the mantle at low

degrees of partial melting (Figure 5) (e.g. Keays, 1995). These scenarios can be evaluated for the ultramafics in the Nyong series of this study.

Pt and Pd are incompatible during mantle partial melting and previous melting will deplete the mantle source in Pt and Pd as suggested by Maier *et al*. (2012). Consequently, subsequent stage melts from a depleted refractory lithospheric mantle will produce PGE-depleted magma. However, previous studies of rocks of the Nyong Series have reported negative ƐNd values (Toteu *et al*., 1994a; Bayiga *et al*., 2011 and Ebah Abeng *et al*., 2012) (Figure 3) indicating the absence of a long-lived depleted mantle source. The fact that ƐNd values are negative show that the mantle has not been depleted of PGE so is a fertile mantle source and has the potential of generating PGE. If these valves were positive then it will show that it has a long-lived depleted source and the result would be a low Pd + Pt values in the primary ultramafic rocks. The higher the ƐNd values, the long-lived depleted mantle source and the lower the values of PGE and vice visa. The Nyong Rocks have negative ƐNd values meaning the mantle is fertile enough to generate PGE (Figure 3). Another reason should thus be accounted for their low PGE contents. It therefore suggests that the primary ultramafic intrusions here were derived largely from an asthenospheric mantle source with minor inputs from metasomatised lithospheric mantle. Therefore the mantle source of the Nyong Series should be fertile in ΣPGE.

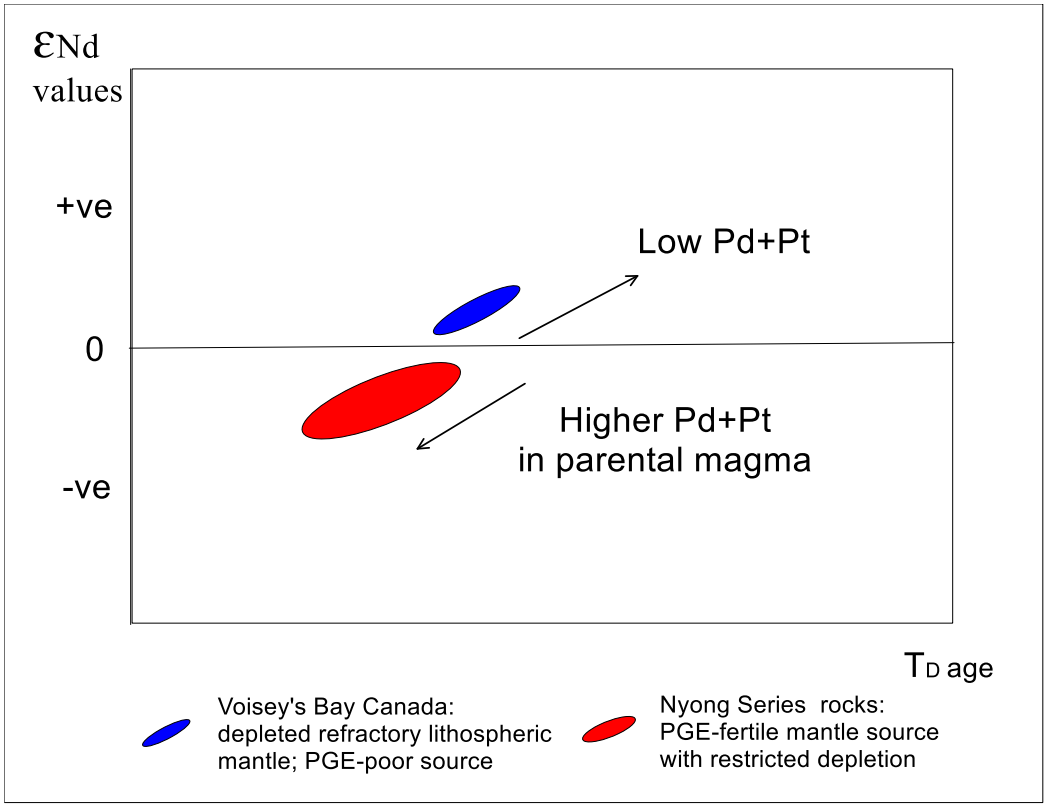

Figure 3: Model depicting low ∑PGE content in the Nyong Series rocks due to the nature of the mantle source

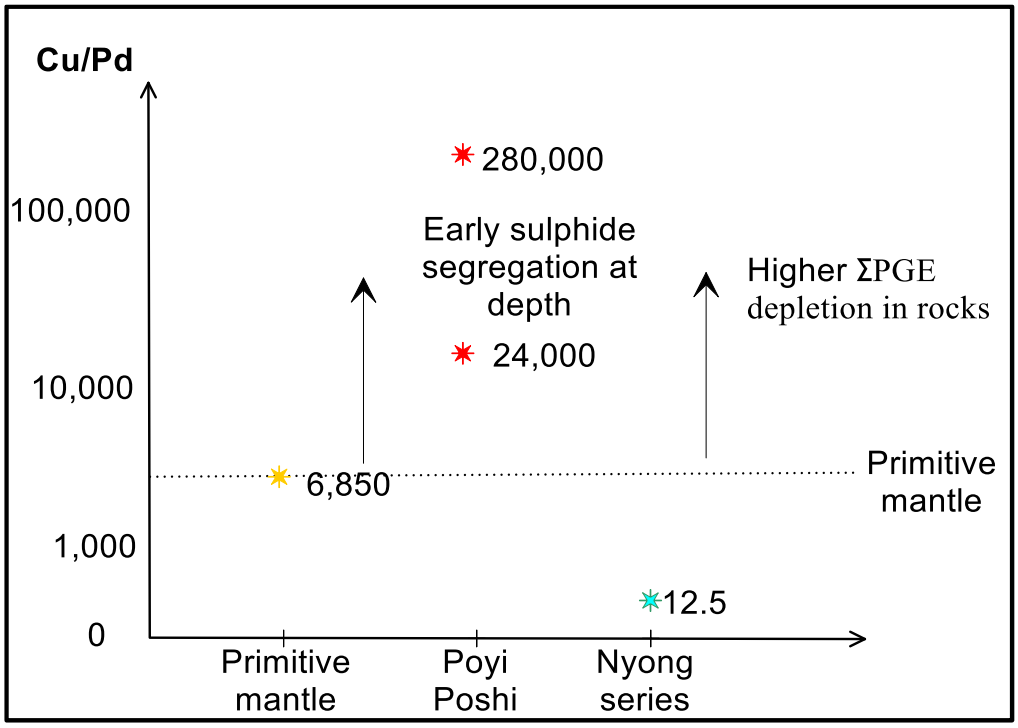

Figure 4: Model illustrating low ∑PGE content in the Nyong Series rocks due to early sulphide segregation at depth

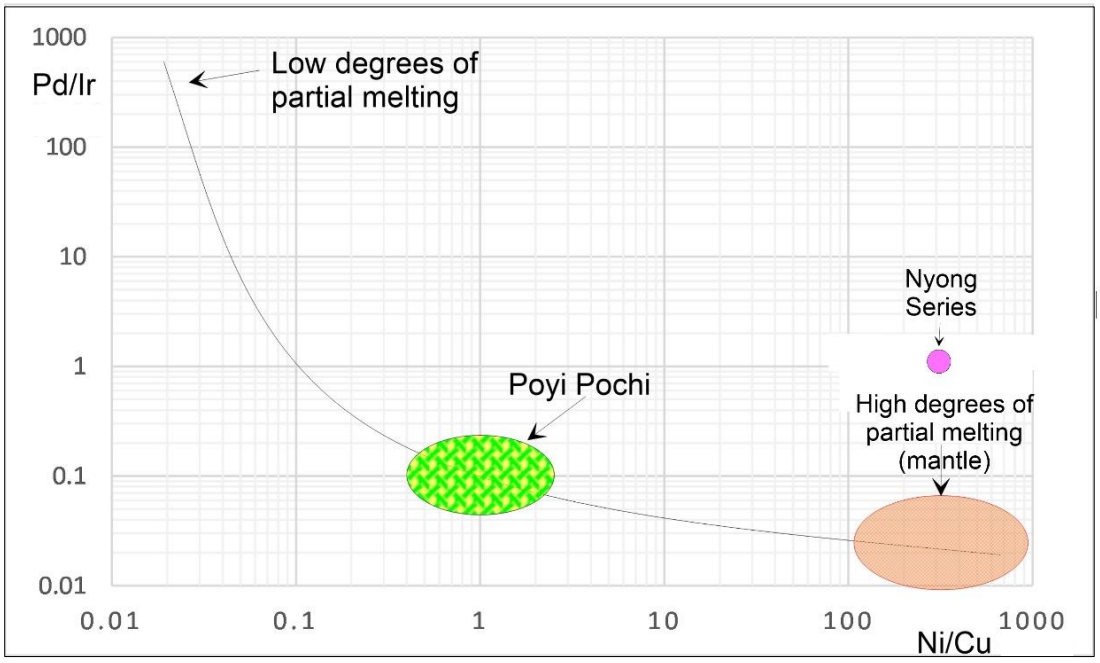

Figure 5: Model showing low ∑PGE content in the ultramafic rocks of the Nyong Series due to sulphide retention in mantle

The Cu/Pd ratios of the samples in this study range from 0.17 to 12.5 compared to the values of 24,000 to 280,000, (that are significantly higher than the primitive mantle values of 6850) of the Poyi Poshi ultramafics, Tarim, NW China (Yang *et al*. 2014). Early sulphide segregation will generally enhance Cu/Pd ratios of the residual magma because Pd has much higher partition coefficient values between sulphide melts and silicate melts than Cu (Figure 4). Consequently, higher Cu/Pd ratios imply parental magmas experienced early sulphide segregation, either in the mantle or during the evolution of magmas en route to the chamber where they crystallized. Unfortunately, primitive olivine is not preserved in the Nyong rocks as the forsterite of these olivines will allow for the evaluation of the primitive nature of these magmas. However, the geotectonic context of the Nyong series suggests that such magmas would have experienced limited fractionation before the emplacement. It is thus unlikely that the magma experienced early sulphide segregation in the deep crust.

Sulphide retention leading to poor PGE in ultramafics can also occur due to low degrees of partial melting (e.g. Lightfoot *et al*., 2012a). Os, Ir, Ru and Ni behave more compatible than Rh, Pt, Pd and Cu during partial melting of the upper mantle and therefore the Pd/Ir ratio and Ni/Cu ratios are sensitive to degrees of partial melting. Usually rocks from high degrees of partial melting have low Ni and Ir contents with low Pd/Ir and high Ni/Cu ratios(Maier *et al*., 2008) whereas basaltic lavas from low degrees of partial melting usually have low Ni and Ir contents, with high Pd/Ir and low Ni/Cu ratios (e.g. Barnes and Maier, 1999).

Pd/Ir ratios of 10 - 24 and Ni/Cu ratios of 0.9 to 1.6 plot in the field of high Mg basaltic rocks indicating a low to moderate degree of partial melting. Keays (1995) estimated that about ~25% is the minimum degree of melting in the mantle (according to Pd/Ir and Ni/Cu ratios of ~ 01 and ~>10, respectively) capable of extracting all the sulphides in the mantle. The Pd/Ir ratio in this study reaches a height of 2.5 and this suggests that sulphide retention in the mantle or at depth seems to be the most likely reason to account for the PGE depletion of the rocks of the Nyong series (Figure 5).

The segregation of sulphides and PGEs from silicate melts is perhaps the most important aspect of Cu-Ni-PGE mineralization, on which several views have been proposed (Barnes *et al.*, 2004). The altered pyroxenites and amphibolites in the northeastern corner of the Nyong Series reveal that coarse-grained olivine and pyroxenes are the dominating minerals in these ultramafics rocks where the matrices of intergranular spaces of the cumulates are occupied by medium-to-fine grained, magnetite and sulphides which could be pyrrhotite and

pentlandite which have been altered to pyrite (Ako *et al*., 2015). The olivine and pyroxenes have been altered to fine grained secondary hydrous silicates such as actinolite, tremolite and chlorite. The presence of these secondary hydrous silicates suggests that if PGE mineralization is present, they are product of dissolution and redeposition during hydrothermal alteration. The change in texture from coarse-grained to fine-grained, and appearance of diverse mineralogy (silicates, sulphides and oxides) subsequent to the olivine crystallization/fractionation, is an important event in the ultramafic rocks in the Nyong Series that could have provided a congenial environment for sulphur saturation conditions in the magma. The behavior of PGE availability in ultramafic rocks and magmatic volatile phases are studied to identify the geochemical controls of the manner they are formed and distributed in the Earth's crust, and to understand the primary mantle-derived magmatic processes (Balaram *et al.,* 2013). The olivine, pyroxene, magnetite and sulphides of Ni, Fe and Cu are the most compatible mineral phases for PGE enrichment in the ultramafic rocks (Keays *et al.,* 1981, Crocket, 2002), and are mainly important and responsible for PGE enrichment in magmatic systems. There are five important factors that have been advocated by some authors (e.g. Holwell and McDonald, 2006; Maier, 2005) for PGE deposits in many ultramafic and associated mafic rocks. These factors include, (i) degree of partial melting of PGE-enriched/fertile mantle, (ii) metasomatism and fractionation of PGE-rich magma, (iii) dissolved sulphur (S), (iv) S-saturation condition during crystallization of magma, and (v) hydrothermal intrusive. These factors may operate together or separately depending on the prevailing geological conditions during their emplacement and formation (Naldrett, 2010). That notwithstanding, the magmatic enrichment of PGEs in ultramafic rocks is primary controlled by the degree of partial melting of the juvenile mantle from which the mafic magma is derived. In general, the generation of mafic and ultramafic magmas typically takes place in the asthenospheric or lithospheric mantle, but contributions of partial or wholesale melts from the crust can also modify the composition of these mantle-derived magmas. The concentration of Ni, Cu, and PGEs in crustal and even in mantle rocks is very low when compared to bulk earth (Barnes and Lightfoot, 2005) because these elements are siderophile (i.e., they prefer to form metals rather than oxides) and thus were concentrated in the core during the early history of the earth.

High MgO, Fe_2O_3t, Ni and low CaO, Na_2O, Al_2O_3, K_2O, TiO, PGEs and V in the ultramafic rocks in the Nyong Series suggest high degree of partial melting from a depleted mantle source that existed during the development of the peridotite magma (Ako, 2016). The observation about the origin of ultramafic magma and the various mechanisms for the fertility of juvenile mantle (Sproule *et al*., 2002), and dissemination of sulphide within the ultramafic complex have been proposed from several areas (Barnes *et al*., 2004; Lesher and Barnes, 2009) showing similar geochemical trend for the ultramafic rocks of the Nyong Series. The low Pd/Ir, Cu/Pd, Pt + Pd + Au, Cu/Ir, Cu/Pd, Pt + Pd +Au/Cu and Pt + Pd +Au/CaO ratios in the rocks (Table 1), and low concentration of both PPGE and IPGE (Table 1) from the study area compared to similar studies in other parts of the world indicate that the ultramafic rocks of the Paleoproterozoic Nyong Series were formed during S-undersaturated condition (Chen and Xia, 2008; Balaram *et al*., 2013). The averages of these ratios indicate that the PGEs and Au could behave differently in the same samples. Despite the high MgO, very low PGEs in

these rocks suggest that the magma is derived from PGE-poor/depleted mantle (Ako, 2016). It has been suggested that the IPGEs are refractory and tend to be retained in the mantle peridotites during partial melting (Brain, 2011; Evans *et al*. 2012; Barnes *et al*., 2011). The low PGE contents in the rocks could be due to sequestration during the magma process (Bockrath *et al.,* 2004) or to extremely very limited hydrothermal mobility (Barnes and Lui, 2012). The low PGE contents might also be caused by an increase in oxygen fugacity (Fonseca *et al.,* 2009). There is a slight positive correlation between Pt and Pd which suggests that Pt is usually associated with Pd (Barnes and Lui, 2012; Godel *et al.,* 2007). Barnes *et al.* (2012) reported that PGE depletion in the silicate melt of the Mount Keith nickel deposit, Yilgarn Craton, Australia, due to sulphide liquid extraction is limited by entrainment of sulphide liquid droplets and continuous equilibrium with the transported silicate magma. Keays *et al.* (2012) also investigated PGE in ultramafic series of the Stillwater Complex, Montana and reported that the rocks contain the highest MgO and lowest Al_2O_3 contents, as all the Al_2O_3 in the peridotites would have been contributed by interstitial magma. These rocks thus have a very low trapped silicate melt component. The small amount of Pd and Pt in the low Al_2O_3 rocks was probably contributed by tiny amounts of cumulus sulphides. Generally, the ultramafic rocks of the Nyong Series have very low PGE-Au contents(except samples ESK 26 and 27)(Table 1) which is similar to what Maier and Barnes (1999a) reported in the ultramafic rocks of the Curaca Valley of Bahia in the NE corner of the Transamazonian belt in Brazil and in other parts of the world. Hugh (1993) reported that in rocks such as ocean-floor basalts PGEs concentrations are so low that some elements are below the limit of detection. This might have been the situation with the Nyong Series ultramafic rocks as their Os, Rh and Ru are below detection limits and are suggested to have formed in the ocean ridge and floor environment (Table 1). In such cases analysis may be limited to the elements Au, Pd, and Ir. The PGE geochemistry can also be used to understand the mechanism responsible for the Ni-Cu and PGE deposits in different geological and tectonic settings (Li and Ripley 2009; Naldrett, 2010; Balaram *et al*., 2013).

The recognition of rocks with strong PGE depletion signatures at the Nyong Series in the context of the depletion signatures recognized at Sudbury, Noril'sk and the Vosiey's Bay (Keays and Lightfoot, 2004; Lightfoot and Keays, 2005 and Lightfoot *et al*., 2012) provides further support to the suggestion that the mineralizing process produces not only the signature of anomalous to economic metal enrichment but also measurable metal depletion signature in different silicate melts. Whether the ultramafic intrusions in the Nyong Series are anomalous with respect to the Sudbury, Noril'sk and Vosiey's Bay intrusions, in so far as the parental magma had anomalously low PGE abundance levels is a key question. Modeling of the PGE content in the ultramafic intrusions in the Nyong Series indicates their parental magmas had the same low PGE contents as the Sudbury, Noril'sk and Vosiey's Bay magmas. It would be an unusual coincidence if these similar features of low PGE concentrations were resulted from different processes.

5. CONCLUSION

Ultramafics in the Nyong Series are altered and metamorphosed resulting in low PGE concentration and despite their high MgO and Ni contents, low PGE contents suggest that the magma is derived from PGE-poor/depleted mantle. Low Cu-Au-PGE content in the rocks suggests melt produced in an oceanic ridge setting capable of forming major Ni sulphide deposits. Natures of the mantle source, sulphide segregation at depth and sulphide retention in the mantle are models proposed for depletion of PGE relevant to the rocks of Nyong Series.

ACKNOWLEDGEMENT

This article is part of the PhD thesis of the first author supervised by Prof. C. E. Suh (CES) at the University of Buea, Cameroon and completed within the research framework of economic geology on the Precambrian Mineral belt of Cameroon supported by University of Buea, Faculty Grants to CES. We gratefully acknowledge funding from the AvH Stiftung, Germany (courtesy of CES) and the Research grant in support of this thesis from the national body of Academic Staff Union of Universities (ASUU, Nigeria).

REFERENCES

Ako, T. A., Vishiti, A., Ateh, K. I., Kedia, A. C. and Suh, C. E. (2015). Mineral Alteration and Chlorite Geothermometry in Platinum Group Element (PGE)-bearing meta-ultramafic rocks from South East Cameroon. *Journal of Geosciences and Geomatics,* **3** (4): 96-108

Balaram, V., Singh, S. P., Satyanarayanan, M. and Anjaiah, K. V. (2013). Platinum group elements geochemistry of ultramafic and associated rocks from Pindar in Madarawa Igneous Complex, Bundlkhand massif, Central India. *Journal of Earth System Sciences*, **122** (1): 79-91.

Barnes, S. J., Fiorentini, M. L. and Fardon, M. C. (2012). Platinum group element and nickel sulphide ore tenors of the Mount Keith nickel deposit, Yilgarn Craton, Australia. *Mineralium Deposita*, **47**: 129-150.

Barnes, S-J. and Lightfoot, P.C. (2005). Formation of magmatic nickel-sulfide ore deposits and processses affecting their copper and platinum-group element contents. In Hedenquist, J. W., Thompson, J.F.H., Goldfarb, R.J. and Richards, J.P. (eds.) *Economic Geology* 100th Anniversary Volume, 179-213.

Barnes, S-J. and Lui, W. (2012). Platinum and palladium mobility in hydrothermal fluids: evidence from komatiites and from thermodynamic modeling. *Ore Geology Reviews*, **44**, 49-58.

Barnes, S-J. and and Maier, W.D. (1999). The fractionation of Ni, Cu, and the noble metals in silicate and sulphide liquids. *Geological Association of Canada Short Course Notes*, **13**: 69–106.

Barnes, S-J., Godel, B. M., Locmelis, M., Fiorinitini, M. L. and Ryan, C. G. (2011). Extremely Ni-rich Fe-Ni sulfide assemblages in Komatiitic dunite at Betheno, Western Australia: results from synchrotron X-ray fluorescence mapping. *Austrialian Journal of Earth Sciences*, **58** (7): 691-709.

Barnes, S-J., Hill, R. E. T., Perring, C. S. and Dowling, S. E. (2004). Lithospherical exploration for Komatiite-associated Ni-sulfide deposits: Stratigies and limitations. *Contributions to Mineralogy and Petrology*, **82**: 259-293

Bayiga, E. C., Bitom, D., Ndjigui, P.-D. and Bilong, P. (2011). Mineralogical and geochemical characterization of weathering products of amphibolites at SW Eséka (Northern border of the Nyong unit, SW Cameroon). *Journal of Geology and Mining Research,* **3** (10): 281-293.

Bessoles, B. and Tromprtte, R. (1980). Géologie de l'Afrique: la chaîne Panafrique "zone mobile d'Afrique Centrale (partie sud) et zone Soudanaise" Mém. B.R.G.M, **92**: 396p.

Bockrath, C., Ballhaus, C. and Holzheid, A. (2004). Fractionation of the platinum-group elements during mantle melting. *Science*, **305**: 1951-1953.

Brain, D. G. (2011). Igneous Petrology of the Ni–Cu–PGE Mineralised Tamrack Intrusion, Aitkin and Carlton Counties, Minnesota. MSc thesis of University of Minnesota (156).

Chen, G. and Xia, B. (2008). Platinum-group elemental geochemistry of mafic and ultramafic rocks from the Xigaze ophiolite, Southern Tibet. *Journal of Asian Earth Sciences*, **32**: 406-422.

Crocket, J. H. (2002). Platinum-group elements in basalts from Maui, Hawai'i: low abundances in alkali basalts: *Canadian Mineralogist*, **40**: 585-610

Ebah Abeng, A. S., Ndjigui, P-D., Beyanu, A. A., Tessontsap, T. and Bilong, P. (2012). Geochemistry of pyroxenites, amphibolites and their weathered products in the Nyong unit, SW Cameroon (NW border of Congo Craton): Implications for Au-PGE exploration. *Journal of Geochemical Exploration*, **114**: 1 – 19.

Evans, D. M., Barrett, F. M., Prichard, H. M. and Fisher, P. C. (2012). Platinum-Palladium gold mineralization in the Nkenja Mafic-Ultramafic body, Ubendian Metamorphic belt, Tanzania. *Mineralium Deposita*, **47**: 175-196.

Feybesse, J. L., Johan, V., Maurizot, P. and Abessol, A. (1986). Evolution tectono-métamorphique libérenne et éburnéenne á la partie NW du craton zaïrọis (SW Cameroon). *Current Research In Africa Journal of Earth Sciences*, Matheis and Schandelmeier (eds) Balkema, Rotterdam: 9 – 12.

Fonseca, R. O. C., Campbell, I. H., O'Neil, H. S. C. and Allen, C. M. (2009). Solubility of Pt in sulfide mattes: Implications for the genesis of PGE-rich horizons in layered intrusions. *Geochimica et Cosmochimica Acta*, **73**: 5768-5777.

Holwell, D. A. and McDonald, I. (2006). Petrology, geochemistry and the mechanisms determining the distribution of platinum-group element and base metal sulphide mineralization in the Platreef at Overysel, nortern Bushveld Complex, South Africa. *Mineralium Deposita*, **41**(6): 575-598.

Holwell, D. A. and McDonald, I. (2010). A review of the behavior of platinum group elements within natural magmatic sulfide ore systems. *Platinum Metals Review*, **54**(1): 26-36.

Holwell, D. A., Abraham-James, T., Keays, R. R. and Boyce, A. J. (2012). The nature and genesis of marginal Cu-PGE-Au sulphide mineralization in Paleogene Macrodykes of the Kangerlussuaq region, East Greenland. *Mineralium Deposita*, **47**: 3-21.

Hugh R. R. (1993). Using geochemical data: Evaluation, Presentation and Interpretation. Pearson Education Limited, Edinburgh Gate (380).

Huminiki, M. A. E., Sylvester, P. J. Lastra, R, Cabri, L. J., Evans-Lamswood, D. and Wilton, D. H. C. (2008). First report of platinum-group minerals from a hornblende gabbro dyke in the vicinity of Southeast Extension Zone of the Voisey's Bay Ni-Cu-Co deposit, Labrador. *Contribution to Mineralogy and Petrology*, **92**: 129-164.

Ihlenfeld, C. and Keays, R. R. (2011). Crustal contamination and PGE mineralization in the Platreef, Bushveld Complex, South Africa: evidence for multiple contamination events and transport of magmatic sulfides. *Mineraliun Deposita*, **46**: 813-832

Keays, R. R., Lightfoot, P. C. and Hamlyn, P. R. (2012). Sulfide saturation history of the Stillwater Complex, Montana: chemostratgraphic variation in Platinum group elements. *Mineralium Deposita*, **47**: 151-173.

Keays, R. R. (1995). The role of komatiite and picritic magmatism and S-saturation in the formation of ore deposits, *Lithos*, **34**: 1-18.

Keays, R. R., Ross, J. R. and Woolrich, P. (1981). Precious metals in volcanic peridotites associated nickel sulfide deposits in Western Australia. II: Distribution within the ores and host rocks at Kambalda. *Economic Geology*, **76**: 1645-1674.

Kozlu, H., Prichard, H. M., Melcher, F., Fisher, P.C., Brough, C. P. and Stueben, D. (2014). Platinum group element (PGE) mineralisation and chromite geochemistry in the Berit ophiolite (Elbistan/Kahramanmaraş), SE Turkey. *Ore Geology Reviews*, **60**: 97-111.

Lasserre, M. and Soba, D. (1976). Age libérien de granodiorites et des gneiss à pyroxene du Cameroon méridional. Bullutin, B.R.G.M. 2è série, section **IV** (I): 17 – 32.

Ledru, P., Johan, V., Milési, J. P. and Tegyey, M. (1994). Makers of the last stages of the Palaeoproterozoic collision: evidence for a 2 Ga continent involving circum- South Atlantic Provinces. *Precambrian Research*, **68**: 169-191).

Lerouge, C., Cocherie, A., Toteu, S. F., Penaye, J., Mile'si. J., Tchameni. R., Nsifa, E. N. Fanning, C. M. and Deloule, E. (2006). Shrimp U-Pb Zircon age for Paleoproterozoic sedimentation and 2.05Ga syntectonic plutonism in the Nyong Group, South-Western Cameroon: consequences for the Eburnean – Transamazonian belt of NE Brazil and Central Africa. *Journal of African Earth Sciences*, **44**(4/5): 413-427.

Lesher, C. M. and Barnes, S-J. (2009). Komatiite-associated Ni-Cu-(PGE) Deposits; In: Magmatic Ni-CuPGE deposits: Genetic models and exploration, edited by Li, C. and Ripley, E. M. Geological Publishing House of China, Beijing, 27-101.

Li, C. and Ripley, E. M. (2009). Sulfur contents at sulfide-liquid or anhydrite saturation in silicate melts: empirical equations and example applications. *Economic Geology*, **104**: 405 – 412.

Lightfoot, P. C. and Keays, R. R. (2005). Siderophile and chalcophile metal variations in flood basalts from the Siberian trap, Noril'sk region: Implication for the origin of the Ni-Cu-PGE sulfide ores. *Economic Geology*, **100**: 439–462.

Lightfoot, P. C., Keays, R. R., Evans-Lambswood, D. and Wheeler, R. (2012). S-saturation history of Nain Plutonic Suite mafic intrusions: origin of the Voisey's Bay deposit, Labrador, Canada. *Mineralium Deposita*, **47**: 23-50.

Maier, W. D. (2005). Platinum-group element deposits and occurrences: Mineralisation styles, genetic concepts and exploration criteria. *Journal African Earth Sciences*, **41**: 165-191.

Maier, W. D. and Barnes, S-J. (1999a). Platinum- group elements in silicate rocks of the lower, critical, and main zones at Union Section, Western Bushveld Complex. *Journal of petrology*, **40**: 1647-1617.

Maier, W. D. and Barnes, S-J. (1999b). The origin of Cu sulphide deposits in the Curaçá valley, Bahia, Brazil; evidence from Cu, Ni, Se and platinum-group elements concentrations. *Bulletin of Society of Economic Geology*, **94**: 165-183.

Maier, W. D., Peltonen, P., McDonald, I., Barnes, S. J., Barnes, S-J., Hatton, C. and Viljoen, F. (2012). The concentration of platinum-group elements and gold in southern African and Karelian kimberlite-hosted mantle xenoliths: implications for noble metal content of the Earth's mantle. *Chemical Geology*, **302-303**: 119-135.

Naldrett, A. J. (1989). Magmatic sulfide deposits. Oxford University Press Monographs on Geology and Geophysics, **14 (**186).

Naldrett, A. J. (2010). Secular Variation of Magmatic Sulfide Deposits and their Source Magmas. *Economic Geology*, **105**: 669 – 688.

Owona, S., Mvondo, J. O., Ekodeck, G. E. (2013). Evidence of quartz, feldspar and amphibole crystal plastic deformation in the Paleoproterozoic Nyong complex shear zones under amphibolites to granulite conditions (West Central African Fold Belt, SW Cameroon). *Journal of Geography and Geology*, **5**(3): 186-201.

Owona, S., Schulz, B., Ratschbacher, L., Ondoa, J. M., Ekodeck, G. E., Tchoua, F. M. and Affaton, P. (2011). Pan-African Metamorphism evolution in the southern Yoaunde Group (Qubannguide Complex, Cameroon) as revealed by EMP-Monazite dating and thermobarometry of garnet metapelites. *Journal of African Earth Sciences*, **59**: 125-139.

Pénaye, J., Toteu, S. F., Tchameni, R., Van Schmus, W. R., Tchakounté, J., Ganwa, A., Minyem, D. and Nsifa, E. N. (2004). The 2.1 Ga West Central African Belt in Cameroon: extension and evolution. *Journal of African Earth Sciences*, **39**: 159-164.

Polinares Consortium (2012). Fact Sheet: Platinum Group Metals. Polinnares working paper no. **35**: 1–16.

Qing, L. Quanlin, H. Liewen, X. Hui, L. Shanqin, N. and Yudong, W. (2012). Different Origins of the Fractionation of Platinum-Group Elements in Raobazhai and Bixi Ling Mafic Rocks from Dabie Orogen, Central China. *Journal of Geological Research*, (**2012)**: 1-11.

Randine, K., Kumar, J. V. and Korakoppa, M. (2015). Platinum-group elements mineralization in the cumulate gabrro of Phenai Mata Complex, Deccan Large Igneous Province, India. *Current Science*, **108** (10): 1796 - 1798.

Savard, D., Barnes, S. J. and Meisel, T. (2010). Comparison between Nickel-Sulfur Fire Assay Te Co-Precipitation and isotope Dilution with High-Pressure Asher acid digestion for the determination of platinum–group elements, rhenium and gold. *Geo-Standards and Geoanalytical Research*, **34** (34): 281-291.

Shang, C. K., Liégois, J-P., Satir, M. and Nsifa, E. N. (2010). Late Archaean high-K granite geochronology of the northern metacratonic margin of the Archaean Congo Craton, Southrn Cameroon: Evidence for Pb-loss due to non-metamorphic causes. *Gondwana Research*, **18**: 337-355.

Song, X. Y., Keays, R. R., Zhou, M. F., Qi, L., IhIenfeld, C. and Xiao, J. F. (2009a) Siderophile and chalcophile elemental constraints on the origin of the Jinchuan Ni–Cu–(PGE) sulfide deposit, NW China. *Geochimica et Cosmochimica Acta*, **73**: 404–424

Song, X. Y., Keays, R. R., Xiao, L., Qi, H. W. and Ihlenfeld, C, (2009b). Platinum-group element geochemistry of the continental flood basalts in the central Emeishan Large Igneous Province, SW China. *Chemical Geology*, **262**: 246 – 261

Sproule, R. A., Lesser, C. M., Ayer, J. A. and Thurston, P. C. (2002). Komatiites and komatiitic basalts of the Abititi greenstone belt: A proposed model for their formation. *Precambrian Research*, **115**: 153-186.

Toteu, F. S., Van Schmus, W. R., Penaye, J. and Nyobé, J. B. (1994b).U-Pb and Sm-Nd evidence for Eburnean and Pan-African high grade metamorphism in cratonic rocks of Southern Cameroon. *Precambrian Research*, **67**: 321-347.

Toteu, S. F., Pénaye, J., Van Schmus, W. R. and Michard, A. (1994a). Preliminary U-PB and Sm-Nd geochronologic data on the North Central Cameroon: Contribution of the Archaean and Paleoproterozoic crust to the edification of an active domain of the Pan-African orogeny. *Canadian Research of Acadamic Sciences*, Paris, **319(**Series II): 1519 – 1524.

Wang, Y. W., Wang, J. B., Wang, L. J., Long, L. L., Liao, Z., Zhang, H.Q. and Tang, P. Z. (2011). Problems of PGE metallogenesis related to mafic–ultramafic complexes in North Xinjiang, China. *Geoscience Frontiers*, **2**: 187–198.

Wei, B., Wang, C. Y., Li, C. S. and Sun, Y. L. (2013). Origin of PGE-depleted Ni-Cu sulfide mineralistion in the Triassic Hongqiling 7 orthopyroxenite intrusion, Central Asian Orogenic Belt, Northern China. *Economic Geology*, **108**: 1813-1831.

Yang, S. H., Zhou, M. F., Lightfoot, P. C., Xu, J. F., Wang, C. Y., Jang, C.Y. and Qu, W. J. (2014). Re-Os isotope and platinum-group element geochemistry of the Pobei Ni-Cu sulfide-bearing mafic-ultramafic complex in the northern part of the Tarim craton. *Mineralium Deposita*, **49** (3): 381-397.

Zhou, M. F., Chen, W. T., Wang, C. Y., Prevec, S. A., Liu, P. P., Howarth, G. H., 2013. Two stages of immiscible liquid separation in the formation of Panzhihua-type Fe–Ti–V oxide deposits, SW China. *Geoscience Frontiers*, **4**: 481–502.

PRELIMINARY INVESTIGATION OF TOTAL ATMOSPHERIC DEPOSITS (TAD) IN AKURE, ONDO STATE, NIGERIA

Francis Olawale Abulude[1,2*], Mohammed Mohammed Ndamitso[2], Yahaya Ahmed Iyaka[2] and Aishatu Abdulkadir[3]
[1]Science and Education Development Institute, Akure, Ondo State, Nigeria
[2]Department of Chemistry, Federal University of Technology, Minna, Niger State, Nigeria
[3]Department of Geography, Federal University of Technology, Minna, Niger State, Nigeria
*Correspondence author:waleabul@outlook.com

Abstract
To evaluate the TAD of Akure, Ondo State, Nigeria, samples were collected monthly for a period of 12 months at 40 designated sites. A sampler fashioned after the Australian model gauge was used for the samples collection. TAD was obtained gravimetrically. The results ranged between 5 and 427 µg/m^2. The results obtained showed that man-made activities in Akure have contributed to air pollution.
Keywords: Air pollution, urbanization, mega cities, gravimetrical, limit

1. Introduction

Air pollution like other pollutions has been a major problem globally due to the effects on living and non-living things (Abulude, 2016). Urbanization and industrialization are part of the activities that cause pollution. Akure is a state capital in Nigeria and so has a steady growth in industrialization and urban development. There is no record of TAD in this town. To allay the fear of air pollution, it will be necessary to conduct this study.

2. Materials and Methods

The aim of the study was to analyze the TAD in Akure, Ondo State, Nigeria. Standard methods used by Onwudiegwu *et al*. (2016) was employed. Eleven locations were identified with a total of 40 sites. The choice of the locations was based on the followings: industrial, high traffic density, road construction, and control. The sampler was placed in each site at a height of 1.5 meters above the ground level. 480 samples were collected at a monthly interval, filtered with Whatman Ashless filter paper and subjected to gravimetrical analytical method for a period of 12 months (July 2015 to June 2016).

3. Results and Discussion

The results (5 to 427 µg/m^2) of this study showed that part of the TAD values recorded exceeded the recommended limit (350 µg/m^2). The highest values were observed in the months of November 2015 to February 2016. During these periods there were scanty or no rainfall. These were confirmed by the results obtained for one of the meteorological parameter (Rainfall). Also, the high values could be as a result of strong wind blown from the areas of the construction sites and high traffic density. The incidence of TAD on the environ had significant effects on the residents due to complaints of low visibility and dust depositions on buildings, vehicles, and crops.
In comparison of this study results with those obtained by Obioh *et al*. (2013) for Nigerian mega cities, it was observed that the values of the cities like Aba (422 - 926 µg/m^2), Maiduguri (37 - 370 µg/m^2) and Kano (61 - 757 µg/m^2) were far above the results of this study. The reasons for the differences could be attributed to the higher traffic densities of the study areas, again Maiduguri and Kano are closer to Saharan desert, which is closer to dust.

4. Conclusion

The results obtained showed that man-made activities in Akure have contributed to TAD. It is expected that the results obtained would serve as a baseline for other research works on TAD within

Akure environ. Also, an awareness would be created on the potential danger of air pollution to the citizenry. Finally, it will assist in clean air programs. Further research is ongoing to determine the metal concentrations in both rainwater and TAD samples obtained in Akure.

Competing interests

We wish to declare that no competing interests in the cause of this study.

References

Abulude F.O (2016) Particulate Matter: An Approach to Air Pollution. *Preprints*. doi:10.20944/preprints201607.0057.v1.

Obioh I.B, Ezeh G.C, Abioye O.E, Alpha A, Ojo E. O, Ganiyu A.K (2013). Atmospheric particulate matter in Nigerian megacities. *Toxcol and Envi Chem* 95, 379 - 385. Doi:10.1080/02772248.2013.790970.

Onwudiegwu C.A, Ezeh G.C, Obioh I.B (2016) Trace Metals in Total Atmospheric Depositions (TAD) of a Nigerian Island. *J Atm Poll* 4, 15-22.

EFFECTS OF PIT LATRINES AND POOR DESIGN OF SANITARY FACILITIES ON GROUNDWATER QUALITY: A CASE STUDY OF MINNA AND BIDA, NORTH-CENTRAL NIGERIA.

Idris-Nda, A. [1], Aliyu, M.B., [2] Salihu, H. D. [1], Jimada, M. A. [3] and Ejepu, S. J. [1]
[1]Department of Geology, Federal University of Technology, Minna
[2]Department of Microbiology, Federal Polytechnic, Bida
[3]Niger State Rural Water Supply and Sanitation (RUWATSAN) Agency, Minna

Abstract

A study on the water quality of groundwater in unconfined shallow aquifers was conducted with the aim of assessing physicochemical and bacteriological contamination of groundwater as a result of poor design of water and sanitation facilities in Minna and Bida, Nigeria. The study was conducted using a grid-based approach on wells and boreholes in households. The water has a high Total Dissolved Solids and Electrical Conductivity indicating high concentration of dissolved and suspended materials. The pH is slightly acidic to basic and mean distance of wells to pit latrines, septic tanks and other waste disposal facilities is 12m. Chemical parameters that occur in high concentrations are sulphates, chlorides, nitrates and sodium. Nitrate and chloride are pollution indicators from sewage in groundwater. Total Coliform count, Faecal Coliforms and Faecal Streptococci are very high and far above the maximum permissible limit. Contamination of deeper sources of water from the dug wells is both lateral and vertical with contamination plume spreading to better planned areas. Sanitation facilities in unplanned areas should be upgraded from pit to Ventilated Improved Pit latrines and with adequate provision of water to pour-flush and septic tank system. Septic tanks and soakaways should be designed to protect groundwater from contamination.

Keywords: pit latrines, VIP latrine, poor sanitation, sewage, groundwater quality

Introduction

Groundwater is the water present beneath Earth's surface in soil pore spaces and in the fractures of rock formations. A unit of rock or an unconsolidated deposit is called an aquifer when it can yield a usable quantity of water. The depth at which soil pore spaces or fractures and voids in rock become completely saturated with water is called the water table. Groundwater is recharged from, and eventually flows to, the surface naturally; natural discharge often occurs at springs and seeps, and can form oases or wetlands. Groundwater is also often withdrawn for agricultural, municipal, and industrial use by constructing and operating extraction wells. Groundwater is often cheaper, more convenient and less vulnerable to pollution than surface water, therefore, it is commonly used for public water supplies.

Polluted groundwater is less visible, but more difficult to clean up, than pollution in rivers and lakes. Groundwater pollution most often results from improper disposal of wastes on land. Major sources include industrial and household chemicals and garbage landfills, excessive fertilizers and pesticides used in agriculture, industrial waste lagoons, tailings and process wastewater from mines, industrial fracking, oil field brine pits, leaking underground oil storage tanks and pipelines, sewage sludge and septic systems.

Groundwater pollution, from pollutants released to the ground that can work their way down into groundwater, can create a contaminant plume within an aquifer. Pollution can occur from landfills, naturally occurring arsenic, on-site sanitation systems or other point sources, such as petrol stations or leaking sewers.

Movement of water and dispersion within the aquifer spreads the pollutant over a wider area, its advancing boundary often called a plume edge, which can then intersect with groundwater wells or daylight into surface water such as seeps and springs, making the water supplies unsafe for humans and wildlife.

A pit latrine is a type of toilet that collects human feces in a hole in the ground. They use either no water or one to three liters per flush with pour-flush pit latrines. When properly built and maintained they can decrease the spread of disease by reducing the amount of human feces in the environment from open defecation. This decreases the transfer of pathogens between feces and food by flies. These pathogens are major causes of infectious diarrhea and intestinal worm infections. Infectious diarrhea resulted in about 700,000 deaths in children under five years old in 2011 and 250 million lost school days (WHO, 2011). Pit latrines are the lowest cost method of separating feces from people.

A pit latrine generally consists of three major parts: a hole in the ground, a slab or floor with a small hole, and a shelter. The shelter is often known as an outhouse. The pit is typically at least 3 meters (10 feet) deep and 1 m (3.2 feet) across. The World Health Organization (2011) recommends they be built a reasonable distance from the house balancing issues of easy access versus that of smell. The distance from groundwater and surface water should be as large as possible to decrease the risk of groundwater pollution. The hole in the slab should not be larger than 25 centimeters (9.8 inches) to prevent children falling in (Reed, 2011). Light should be prevented from entering the pit to reduce access by flies. This may require the use of a lid to cover the hole in the floor when not in use. When the pit fills to within 0.5 meters (1.6 feet) of the top, it should be either emptied or a new pit constructed and the shelter moved or re-built at the new location. Fecal sludge management involves emptying pits as well as transporting, treating and using the collected fecal sludge. If this is not carried out properly, water pollution and public health risks can occur.

Study area

Minna is the capital of Niger State and lies between latitudes 9°32'N and 9°41'N and longitudes 6°28'E and 6°37'E, covering an approximate surface total area of 105km^2. The area is easily accessible through Abuja-Dikko-Lambata-Tegina, Lagos-Mokwa-Bida and Kaduna- Sarkin Pawa roads. It has an annual rainfall of about 2500mm with distinct rainy and dry seasons experienced between April to October and between November to March respectively. It has a mean temperature of 27°C in the rainy season and 35°C at the peak of the dry season with a relative humidity of 87% in the rainy season and 35% in the dry season (Idris, 2000). The area is drained mainly by River Chanchaga, which is a tributary of River Niger, as well as other minor seasonal streams. The geology of the area comprises mainly of rocks belonging to the Precambrian basement complex system of Nigeria (Truswell and Cope, 1963) and is mainly underlain by granites, migmatites, gneisses and schist.

Bida lies on latitude 9°05'08″N and longitude 6°00'36"E at an altitude of 151m with a total surface area of 51 km square. It is located in central Nigeria and is the second largest city in Niger State, one of the 36 federating states in Nigeria, with a population of 224,132 projected to 2015 from the 2006 population census using an annual growth rate of 3.4%. The area is drained mainly by River Landzu which runs in the E-W direction and cuts the town roughly into two. Houses in the area are built close to each other and consist of old buildings that are over 100 years old and more modern ones. The area is underlain by rocks belonging to the Maastrichtian Bida Basin and comprises basically of sandstones, siltstones, mudstones, shale and clay, and is in places capped by the lateritic ironstone.

Groundwater use is mostly restricted to the use of hand dug wells and shallow boreholes all placed within the unconfined aquifer. As a result of the complete failure of the public water supply system attention has turned fully to the use of groundwater as the main source of water supply for the inhabitants (Idris-Nda, 2010).

Sanitary facilities consist of shallow pit latrines and pour flush (locally known as soakaway) and open defecation by children. Waste disposal is by use of open dumps located in open spaces between houses and the drainage systems which have consequently become littered with all kinds of wastes including polythene bags, which are the common packaging materials in the area.

Due to the high population density within a relatively small area, water and sanitation facilities coexist side by side and both are mostly in direct contact with the water table. This situation is likely to have a negative impact on the water quality, owing to the poor design of both water and sanitary facilities.

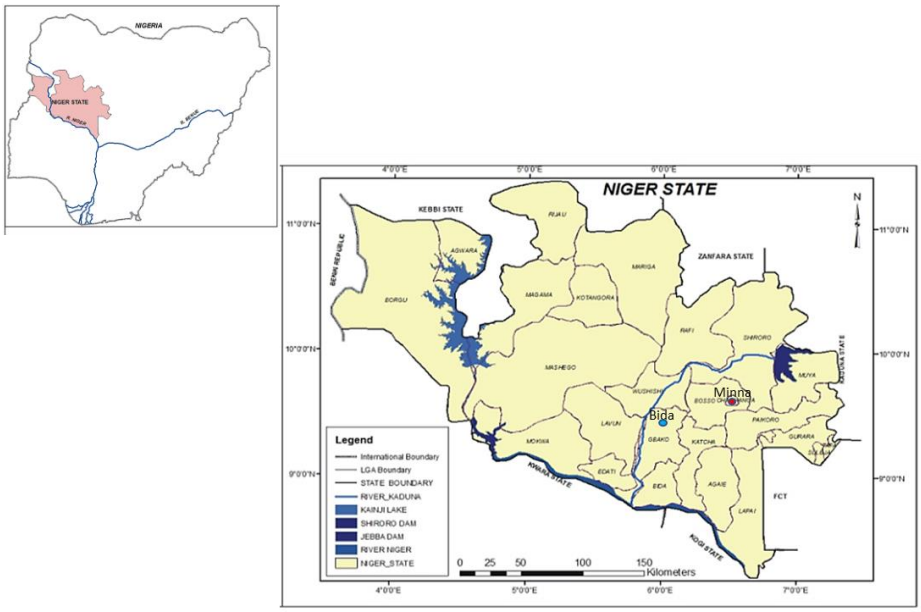

Figure 1: Map of Niger state showing Minna and Bida (inset is map of Nigeria)

Types of Toilets

Off-site sanitation systems

Off-site systems are widely acknowledged as systems that are only suited to developed and affluent areas, whose water resources are plentiful and reliably delivered to household connections in enough quantities. In low income and less developed areas where water is often collected from a stand-post or well, dry (on-site) systems are the only possibilities. Despite this, there are alternatives to conventional sewerage that may sometimes be applicable.

On-site Sanitation Systems

Simple Pit Latrine: On-site sanitation systems are more widely employed in low income and rural areas of the world. Numerous forms have been developed ranging in both price and complexity. A simple pit latrine (figure 2) is perhaps the simplest and the first step among sanitation solution identified by the UN to meet the criteria of the Millennium Development Goals (JMP, 2004). In reality the variance in the standard of these facilities can be great. The JMP distinction is that the latrine should have a superstructure to be

acceptable to users. The simplest form of pit latrine is a hand dug pit that is unlined and covered with a series of wooden logs strapped together allowing the user to defecate into the pit. This system can gradually be improved.

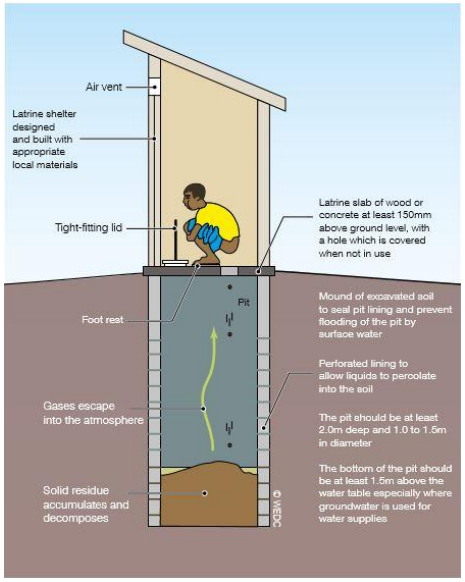

Figure 2: Simple pit latrine (Reed, 2014

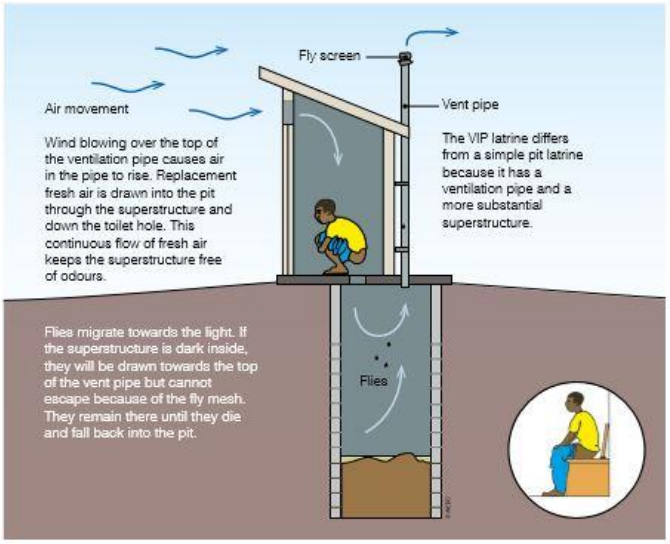

Figure 3: Ventilated improved pit latrine (Reed, 2014)

Raised Latrines: When the groundwater is high or the ground is too rocky to excavate by hand there is a case for using a raised pit latrine (other latrine types can also be raised although it is more common for simple pit latrines to be raised). One major disadvantage is the lack of privacy afforded to the users of the latrines.

Slab type: There are numerous types of slabs that can be used for a latrine, each with different benefits. The purpose of the slab is to hold the weight of the user over the pit, provide a clean surface for the users feet and drain liquids into the squat hole. A variety of materials can be used such as timber, reinforced concrete and un-reinforced concrete slabs in a dome shape to avoid tensile forces. Sanitation platforms (San-plats) are often added onto traditional latrine slabs to provide a clean surface, foot plates and a suitably shaped squat hole.

Ventilated Improved Pit (VIP) Latrine: During the 1980s the VIP latrine (Figure 3) was developed in Zimbabwe. The main drivers for design were to eliminate two unpleasant aspects of using on-site sanitation systems, flies and smell. Furthermore, the reduction of flies can also reduce the transmission of disease. Put simply, the technology facilitates the flow of air through the system. One important aspect is that the inside of the toilet should remain dark as means of attracting flies up a vent pipe where they will eventually die and fall back into the latrine.

Pour-Flush Latrine: Where water is more widely available, or traditionally used for anal cleansing, a pour flush latrine may be appropriate and can bring a number of further benefits on top of simple or VIP latrines. A waterseal is created by a plastic u-bend which prevents bad odour and flies affecting the user (this system is less susceptible to building errors than the VIP system). The system only requires a few litres of water and so should not put a strain on resources.

Offset pits: These are a means of improving the operational nature of a latrine, but may increase the cost of construction and increase the complexity of the system. Two main advantages of employing an offset pit are to make emptying easier without having to disturb the superstructure and they can also enable the toilet to be constructed inside the house.

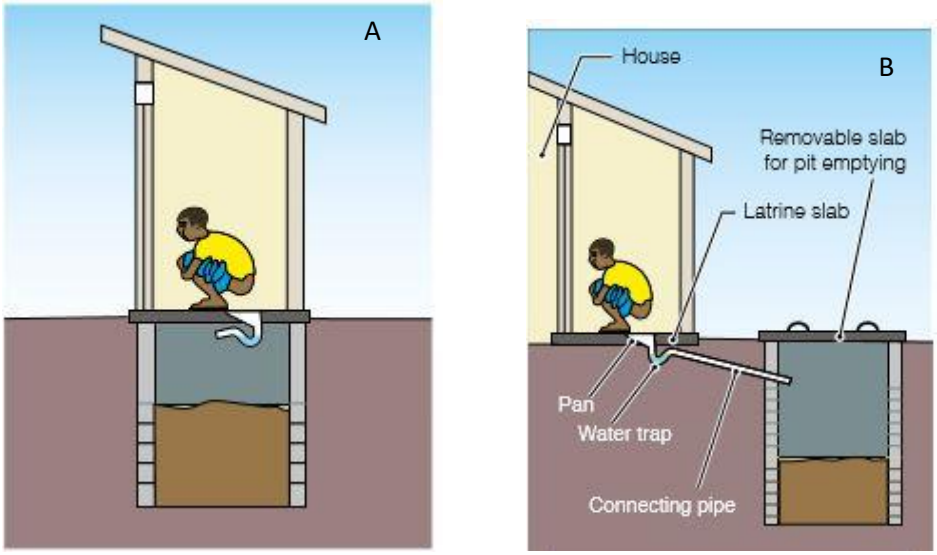

Figure 4: Direct (A) and offset (B) Pour-flush latrine (Reed, 2014)

Single or Double Pit: It is also possible to include a double pit, this involves the need to change the direction of flow between pits. The advantage of a double pit is that the contents of one pit gradually decompose over time whist the other pit used and become safer to remove. The sanitation facility also becomes a more permanent piece of infrastructure as the superstructure never has to be removed. One area for caution is to ensure that the double pits are operated correctly, in some cases it has been observed that incorrect use means the contents of one pit are not safe to remove (Pickford, 1995).

Ecological Sanitation Latrines: Ecological sanitation (ecosan) latrines have been developed employing the concept that human waste contains nutrients that should be returned to the soil and used to grow more food. There are different types of toilet, which treat the waste to some extent prior to using the by-product to increase fertility of land. The types of toilet can be split into dehydrating and composting types with urine diversion often being employed to make the most of the nutrients available.

Aqua-Privy: An aqua-privy function in a similar manner to a septic tank whilst avoiding the need for a consistent water supply to operate a flush toilet. The water will drain off the top and the sludge needs to be emptied on a regular basis. An advantage of the aqua privy is that it reduces odours. However, regular emptying could become an onerous requirement.

Septic Tanks: A septic tank is a water tight tank that typically receives waste from a flush toilet. They are useful in areas with a high water table (due to the sealed nature contamination of the water table is less likely) and when a reliable water supply is present. The system provides some level of treatment to the waste through the separation of solids.

Other Forms of On-Site Sanitation

There are other forms of sanitation which are less used or unsanitary. Borehole latrines are often used in emergency situations but adopted less elsewhere. Unsanitary forms would include overhung latrines which will dispose directly into a watercourse, or bucket latrines where users defecate into a bucket which is routinely emptied.

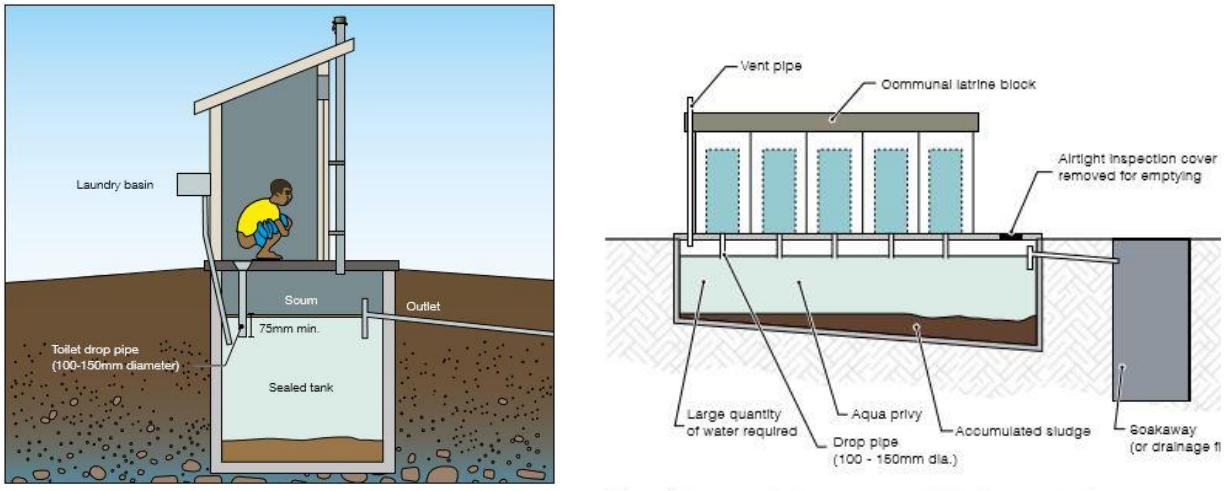

Figure 4: An aqua privy latrine for single and communal uses (Reed, 2014)

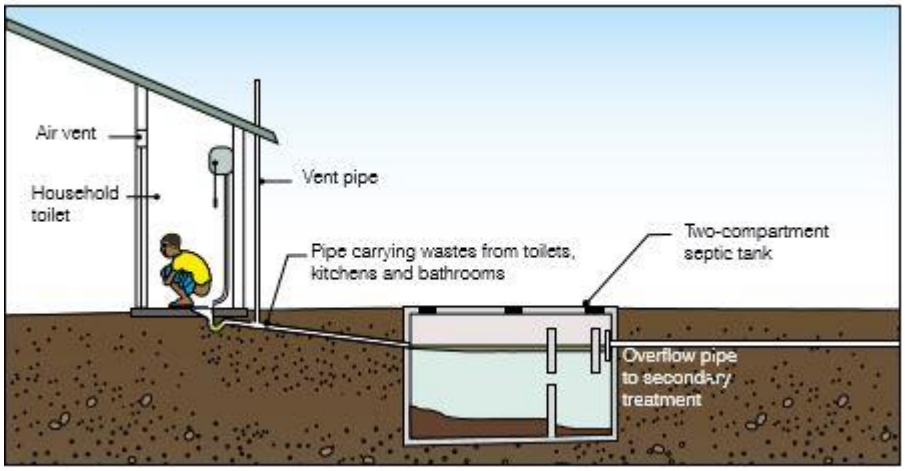

Figure 5: Septic tank system (Reed, 2014)

Groundwater Pollution

An important consideration when employing on-plot sanitation systems is that of groundwater pollution. Due to the nature of on-site systems shallow groundwater can be exposed to the pathogens within faeces and become contaminated. In urban areas this can be particularly problematic especially if shallow groundwater is used for drinking. In general it is possible to reduce this risk by locating a latrine at least 10m horizontally from a groundwater source (Boot, 2008). There is often debate as to the costs associated with alternative sanitation systems as oppose to alternative water sources. An alternative means to reduce the risk of contamination to groundwater is to employ a raised pit latrine.

Aim and objectives

The study is aimed as assessing the effects of poor design and construction of water and sanitation facilities in Minna and Bida, central Nigeria.

The main objectives include:

1. Determine water and sanitation facilities design and proximity in the area
2. Determine the water level and direction of groundwater flow
3. Determine the physicochemical and bacteriological composition of groundwater
4. Propose strategies for effective use and sustainability of water and sanitation facilities

Methodology

In order to meet the objectives of the research work the following methodology was adopted.

- Sampling of wells, boreholes and households in the area was conducted using the grid-based approach. The area was divided into 250m x 250m grids and samples were taken within each alternative grid. Wells, boreholes and sanitary facilities within each grid were carefully recorded and questionnaires administered to respondents within the grid. Coordinates of locations were established using a hand-held Global Positioning System, Etrex Legend H.
- Questionnaires, oral interviews and visual inspection were used to determine water and sanitation facilities in 250 households in each area.
- Depth and water levels of wells and boreholes were determined using a water level dip meter. Some of the installed boreholes were lifted slightly to access the depth and water level.
- 100 water samples were taken in glass and plastic bottles across the area and taken to the laboratory for analysis using standard analytical methods (Atomic Absorption Spectrometry, Titrimetric and Flame Photometry). Physical parameters of pH, Eh, Conductivity, Temperature and Total Dissolved Solids, were taken at the point of sampling. Microbial analysis was conducted using the American Public Health Association (APHA, 2005) standards for the examination of water and wastewater. All other analysis was in conformity with this standard.
- Direction of groundwater flow was determined by using water table elevation contour maps derived from measured results. The differences in water table elevation between wells with the highest and lowest elevations were connected to form a triangle from which the direction of groundwater flow was determined. Vertical flow components were computed from sieved samples using empirical methods. Downward flow component was indicated by the negative hydraulic gradient computed from the water level elevations.

Results and Discussion

Groundwater Occurrence and Use

Groundwater in Minna occurs mostly within the weathered and fractured zones of the rock. Weathering depth ranges mostly between 3 – 10m with most wells relying on this weathered zone for water supplies. Boreholes depend on deeply seated fractures within the rock while well designed boreholes totally exclude water from shallow sources by totally sealing it off. In Bida groundwater occurs in three aquifer levels which are unconfined, semiconfined and confined occurring at 3-60m, 80-150m and >170m respectively (Idris-Nda, 2010). As a result of paucity of water supply from the public service (Niger State Water Board) inhabitants of both areas have turned completely to groundwater as the main source of domestic water supplies for drinking and other utilities. Shallow hand dug wells depend solely on the shallow unconfined aquifers and which tend to dry up in the dry season, for this reason most inhabitants have turned to boreholes as the main source of water supplies. Depth of the boreholes range from 30 to 200m with a mean of 120m. Most of the boreholes have are for commercial activities, selling to water vendors in carts while some are for the production of sachet water commonly called “pure water”. Overdependence on groundwater often leads to over pumping or over drafting resulting into over withdrawal of groundwater and consequent lowering of the water table (dewatering) and pollution from shallow sources of pollutants like pit latrines, septic tanks, wastewater in unlined drains and slaughter houses or abattoirs.

Latrines Types, Design and Use

Common latrines in both areas include; simple pit latrines (both lined and unlined), Ventilated Improved Pit (VIP) latrines, pour flush and septic tanks. Table 1 shows the percentage of the different toilet types in Minna and Bida. The study shows that there are more pit latrines in Bida than in Minna. Pit latrines are found in both areas in older parts of the cities where the houses are older and closer together. The pit latrines have a depth range of 3 – 6m and are mostly in direct contact with the water table especially during rainy season which lasts for about seven months. The septic tank consist of two interconnected chambers, the first chamber is where

the waste is first discharged into and the second chamber contains the sewage which is allowed to drain freely into the surrounding rocks through perforations made in it. The first chamber is cemented while the second is not, they are constructed up to depth ranges of 2 – 3m. The average distance of the sanitary facilities to the water facility in the area is 12.2m. If the local hydrogeological conditions are ignored, pit latrines can cause significant public health risks via contaminated groundwater (Buitenkamp and Richert, 2008).

Table 1: Percentage of latrine types in Minna and Bida

	Minna (%)	Bida (%)
Simple pit latrine	10	30
VIP latrine	5	3
Pour-flush latrine	10	20
Aqua privy	-	-
Septic Tank	75	47

Figure 6: Public water supply in Bida with borehole and septic tank in close proximity

Figure 7: Public water supply borehole close to a large open dump.

Groundwater flow and contaminant transport

Generally, groundwater flows from areas of higher hydraulic head to areas of lower head, dissolved and suspended particles, both chemical and bacteriological are carried by the moving water as it tortuously makes its way to a discharge point. The particles it carries are subjected to processes of advection, sorption, advection, degradation, dispersion and attenuation as the water flows, all aimed at removing the particles thereby purifying the water. However due to the proximity of the contributing sources and rapid groundwater withdrawal due to pumping the particles are forced to move faster and to draw from all other sources within the radius of influence of the pumping well. This leads to more sewage from latrines that are not well planned to move into groundwater thereby increasing pollution level. Figure 1 is the graph of mean water level elevation in the area. Groundwater flow is principally in the SE-NW direction with a minor E-W flow component (Figure 6). Determining flow direction is important for mapping recharge areas and contaminant migration path.

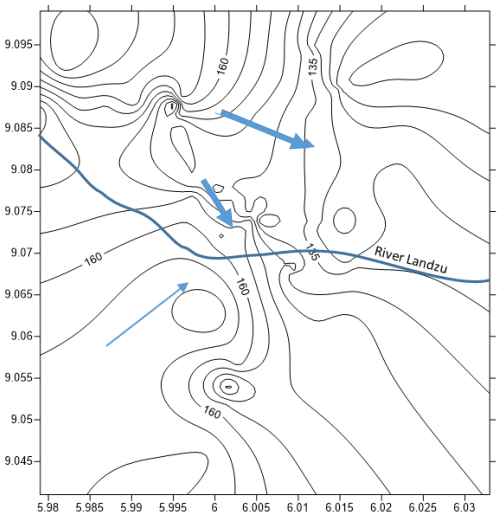

Figure 8: Direction of groundwater flow in Bida (blue arrow).

Physicochemical and bacteriological Composition of Groundwater

Table 2 is the results of the mean values of physical parameters of groundwater in Minna and Bida areas, generally pH is neutral to slightly basic at 6.7 and 8.72 respectively, some areas close to open dumps have pH that trends towards been acidic. Eh (redox potential) which is a measure of the tendency of the solution to either gain or lose electrons and a common measurement for water quality, is -65 and -80 for Minna and Bida respectively, this indicates water that is more in the reduced state with a high tendency to donate electrons. Mean temperature is 29°C, Electrical Conductivity (EC) which is an indication of the dissolved chemical constituents of the water is 905 to 1263µS/cm while Total Dissolved Solids (TDS) which is a measure of the combined content of all inorganic and organic substances contained in the water and is used as an aggregate indicator of the broad presence of a broad array of chemical contaminants, is 458 to 525mg/l. Surface water has the least TDS value of 32mg/l while dug wells have the highest with 385mg/l and boreholes occupy an intermediate position with 148mg/l. Even though the acceptable limits for TDS is 500mg/l some dug wells in the area have concentrations above this limit. Most of the areas have TDS values that exceeds the NDWQS, this is especially more noticeable in Bida. Figure 9 is the map of Bida and Minna showing TDS concentration in both wells and boreholes. Highest values for TDS (>500) and conductivity (>1000) in Minna include; Limawa, Kongila, Sabon Gari, Mobil, Kpakungu, Paida and Unguwan Kaje areas. In Bida areas with high TDS and have higher nitrate concentration include; Gbangbara, Gbangaie, Basakun, Tutuchiba, Lonchita, Forgun, Lalemi, Kabari Gulu, Efu Madami, Nasarafu, Swatamukun, Masagas, Dokozha, Darachita, Banwuya, Bantigi, Eso, Efu Nakodi and Masaba.

TDS concentration is found to be higher in areas that are unplanned and more densely populated than in better planned areas with low population and better sanitary facilities.

Table 2: Results of physical parameters of groundwater in Minna and Bida

Parameter	Mean		NSDWQ
	Minna	Bida	
TDS	454	525	500
Electrical Conductivity (µS/cm)	905	1263	1000
Dissolved Oxygen (mg/l)	6.97	7	
pH	6.75	8.72	6.5-8.5
Eh (mV)	-65.00	-80	
Temperature (°C)	29.5	29.4	Ambient
Turbidity (NTU)	3.65	3.7	5

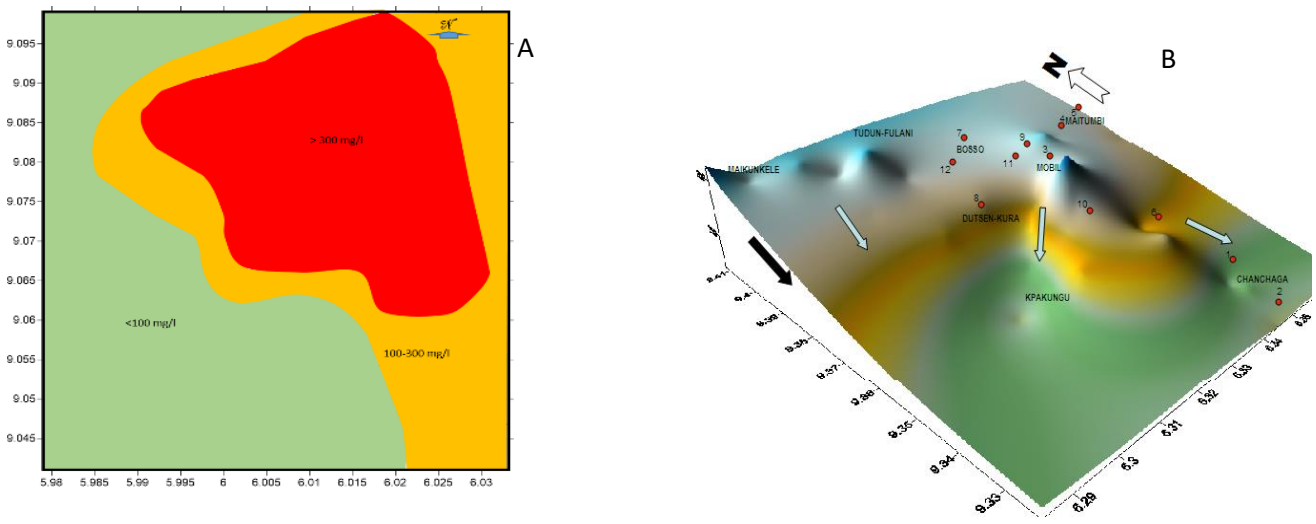

Figure 9: TDS distribution in Bida (A) and Minna (B)

Laboratory analysis of the chemical and bacteriological constituents of the water shows that sulphates, chlorides, nitrates and sodium are the chemical constituents that occur in high concentrations with sulphate and nitrates have values approaching the maximum permissible limits of NDWQS (2007) standards (100 and 50 respectively) for drinking water. Sulphate concentrations range from 230 to 80mg/l while nitrate ranges between 110 and 13mg/l. Chloride concentration ranges between 180 and 20mg/l. Figure 10 shows the major chemical constituents of groundwater while Figure 11 shows the concentrations of heavy metals in the groundwater in parts of Minna and Bida.

Total coliform ranges from 200 to 12cfu/100ml, faecal coliform and faecal streptococci ranges from 80 to 6cfu/100ml and 73 to 1cfu/100ml respectively, NDWQS limit is 0cfu/100ml for all parameters.
Total coliforms count give a general indication of the sanitary condition of a water supply. include bacteria that are found in the soil, in groundwater that has been influenced by surface water, and in human or animal waste. Faecal coliforms are the group of the total coliform that are considered to be present specifically in the gut and faeces of warm-blooded animals. Faecal coliforms are considered an accurate indication of animal or human waste than the total coliforms. Escherichia Coli (E. Coli) is the major species in the faecal coliform group that is

generally not found growing and reproducing in the environment. Consequently, E. Coli is is considered to be the species of coliform bacteria that is the best indicator of faecal pollution and the possible presence of pathogens. Water pollution caused by faecal contamination is a serious problem due to the potential for contracting diseases from pathogens.

Table 3: Results of chemical and bacteriological parameters in groundwater of Minna and Bida

Parameter	**Mean**		**NSDWQ**
	Minna	**Bida**	
Chloride	43.0	78.4	250
Sulphate	60.0	85.2	100
Nitrate	48.0	44.7	50
Bicarbonate	10.0	32.6	
Fluoride	0.5	0.5	1.5
Phosphate	2.0	1.3	
Nitrite	0.1	0.0	0.2
Carbonate	0.0	0.0	
Sodium	45.0	64.4	200
Potassium	32.0	22.6	50
Calcium	21.0	33.8	200
Magnesium	27.0	22.6	20
Iron	0.4	0.3	0.3
Manganese	0.1	0.1	0.2
Chromium	0.2	0.6	0.05
Zinc	1.4	0.8	3.0
Copper	0.7	0.3	1.0
Total Coliforms (cfu/100ml)	30.0	54.5	10
Faecal Coliforms	11.0	13.0	0
Faecal Streptococci	8.0	11.0	0

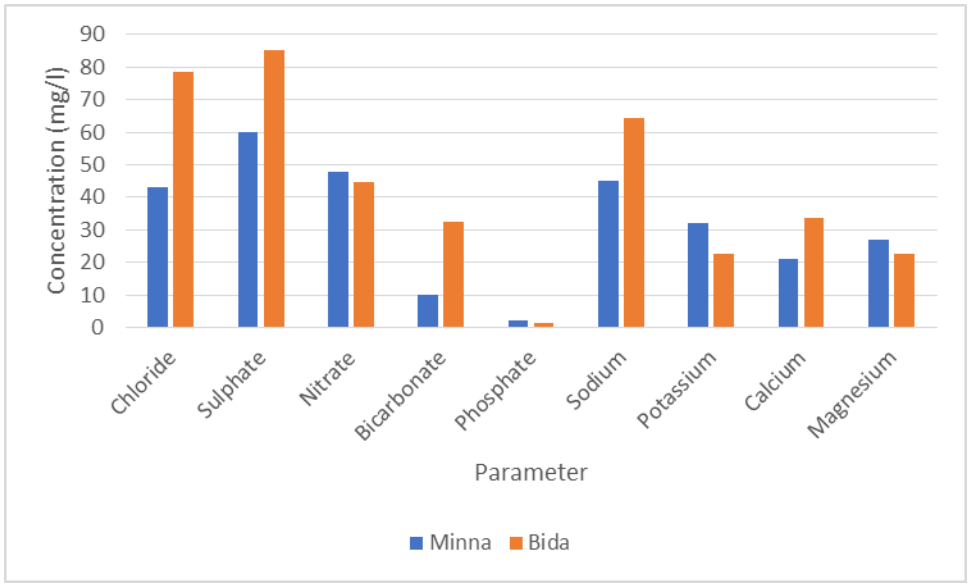

Figure 10: Major chemical constituents in groundwater in parts of Minna and Bida areas

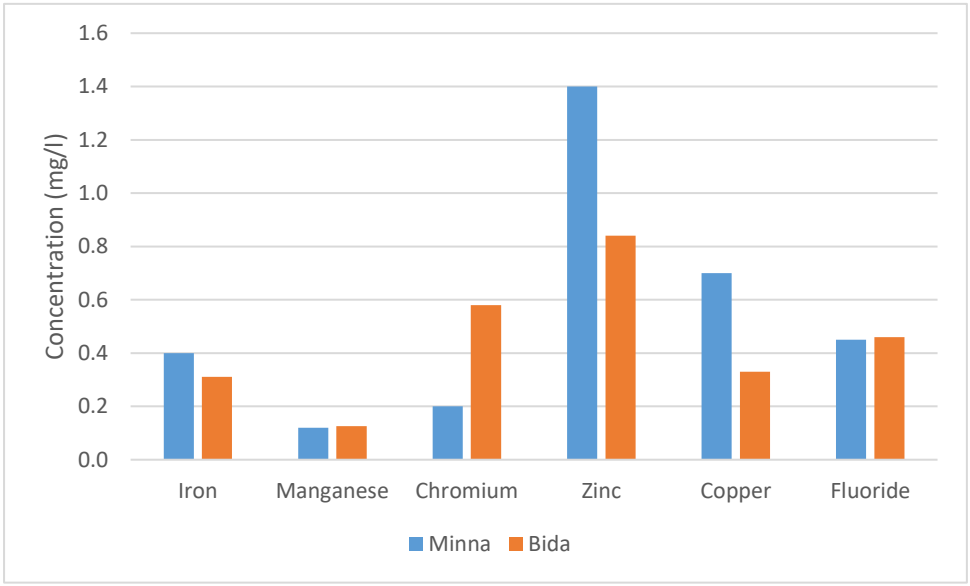

Figure 12: Heavy metal concentration in groundwater of parts of Bida and Minna

Mitigation strategies will involve the following:

i. Upgrading public water supply facilities in Minna and Bida to ensure adequate and sustainable water supply to the teeming populace, this will greatly reduce reliance on groundwater and thereby reducing pollution from sewage.
ii. Improving the present unlined pit latrines by upgrading to the Ventilated Improved Pit (VIP) latrines. As a very general guideline it is recommended that the bottom of the pit latrines should be at least 2 m above groundwater level, and a minimum horizontal distance of 30 m between a pit and a water source is normally recommended to limit exposure to microbial contamination (WEDC, 2012).
iii. Closing down all wells and boreholes placed on shallow aquifer sources and replacing them with well-designed boreholes ones that targets deeper sources of water.
iv. Groundwater development should be monitored and licensed to protect the resource.

v. Routine monitoring of all sources of water in the state should be carried out sustainably in order to identify early on any contaminant(s) that might be potentially detrimental to health.

Conclusions

Common constituents as a result of domestic waste that lead to groundwater contamination and which can be potentially harmful include chloride, copper, nitrate, nitrite and sulphate while bacteriological constituents are mainly coliform bacteria (USGS, 2015). All these parameters are found to be present in concentrations considered above acceptable limits in the groundwater of Minna and Bida. Concentrations are generally higher in hand dug wells than in boreholes but lowest in the surface water, except for turbidity. Bacteriological contamination is found to be particularly high in hand dug wells and poorly designed boreholes. It is therefore advised that secondary treatment with chlorine tablets be carried out on poorly constructed shallow boreholes and hand dug wells before drinking, or such water could be boiled and allowed to cool before using. Transmission of the contaminants was found to be vertically downwards to the deeper water sources and laterally to areas not presently seriously affected. Sanitary systems should be well designed to safeguard groundwater from contamination. The design in Figure 13 is suggested and building supervisors should ensure compliance, present unplanned ones could also be upgraded to comply with the design.

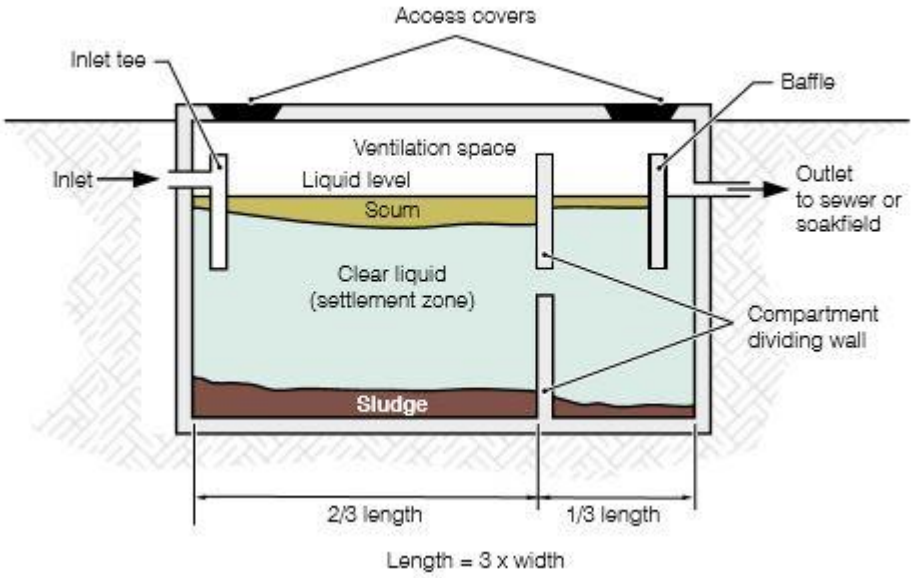

Figure 13: Septic tank design for optimal sanitary condition for groundwater protection (Reed, 2014)

References

APHA, (2005). Standard methods for the examination of water and wastewater. American Public Health Association (21st Ed.) Washington DC, USA.

Buitenkamp, M., Richert, S. A. (2008). Europe's sanitation problem - 20 million Europeans need access to safe and affordable sanitation. Women in Europe for a Common Future (WECF), The Netherlands.

Boot, N. (2008). Types of Toilet and their Suitability. The Schumacher Centre Bourton-on- Dunsmore Rugby, Warwickshire, CV23 9QZ United Kingdom.

Idris-Nda, A. (2010). Hydrogeophysical and Hydrogeochemical characterisation of the Bida Basin aquifer system. Unpb PhD thesis, Federal University of Technology, Minna, Nigeria.

NDWQS (2007). Nigerian Standards for Drinking Water Quality, Nigerian Industrial Standards, Standards Organisation of Nigeria, Abuja, Nigeria.

Reed, B. (2011). Septic Tank and Aqua Privy Design, Guide 30, Edited by Louise Medland and Brian Reed. Water, Engineering and Development Centre School of Civil and Building Engineering Loughborough University Leicestershire LE11 3TU UK.

Reed, B., Brian R. and Scott, R. (2014). Ventilated Improved Pit (VIP) Latrines, Guide 27, Engineering and Development Centre School of Civil and Building Engineering Loughborough University Leicestershire LE11 3TU UK.

Reed, B. and Scott, R. (2014). Simple Pit Latrines, Guide 25, Engineering and Development Centre School of Civil and Building Engineering Loughborough University Leicestershire LE11 3TU UK.

Reed, B., Brian R. and Scott, R. (2014). Pour-flush Latrines, Guide 26, Engineering and Development Centre School of Civil and Building Engineering Loughborough University Leicestershire LE11 3TU UK.

The Sphere Project (2004). Humanitarian Charter and Minimum Standards in Disaster Response, Geneva, Switzerland.

USGS (2015) Water Science School. Groundwater quality. U.S. Department of the Interior, U.S. Geological Survey. http://water.usgs.gov/edu/earthgwquality.html

WEDC. Latrine slabs: an engineer's guide, WEDC Guide 005 (2012). Water, Engineering and Development Centre The John Pickford Building School of Civil and Building Engineering Loughborough University. p. 22. ISBN 978 1 84380 143 6.

WHO (2011). Guidelines for Drinking Water Quality. World Health Organisation, Geneva, Switzerland.

MODELING AND ANALYTICAL SIMULATION OF UNSTEADY HYDROMAGNETIC FREE CONVECTIVE FLOW PAST AN INFINITE VERTICAL PLATE IN POROUS MEDIUM

Okoosi, F.E.; Mohammed A.A.; Olayiwola, R. O.

Department of Mathematics,

Federal University of Technology, Minna, Nigeria.

E-mail.: okoosifunsho@gmail.com

ABSTRACT

The paper considers a review of the two dimensional flow of a viscous incompressible electrically conducting fluid past an infinite vertical porous plate through a porous medium in the presence of uniform transverse magnetic field and constant heat source. This study establishes the criteria for the existence of a unique solution of the equations describing flow by Derrick and Grossman approach and examine the effects of the flow parameters on the Velocity, Temperature and Concentration Profiles.
***Keywords*:** Hydromagnetic, Free Convective flow, Constant heat source, Porous Medium, Self-similar solution and Frobenius method.

INTRODUCTION

Free convection studies have been carried out both theoretically as well as experimentally. In one of the earlier investigations in MHD, Hartmann (1937) investigated experimentally as well as theoretically the hydromagnetic flow between two infinite parallel plates. This work provided fundamental knowledge for development of several MHD devices such as MHD pumps, generators, brakes and flow meters.

Theoretical and experimental investigation of problems of unsteady hydromagnetic natural convection flow of an electrically conducting fluid within porous media has received considerable attention of several researchers during past few decades due to its overwhelming and important applications in science, technology and engineering which includes geophysics, astrophysics, electronics, aeronautics, metallurgy, chemical and petroleum engineering. The importance of this fluid past bodies with different geometries under different condition has endeared investigations by various researchers like Rao *et al*. (2014), in the use of Finite Element Method (FEM) of Solution of heat and mass transfer in MHD flow of a viscous fluid past a vertical plate under oscillatory suction velocity. Gundagani *et al*. (2013), obtained by FEM a numerical solution of the problem of unsteady MHD free convective flow past a vertical porous plate. Sharma *et al*. (2012), investigated the flow of a viscous incompressible electrically conducting fluid along a porous vertical isothermal non-conducting plate with variable suction and internal heat generation in the presence of transverse magnetic field. The governing equations were transformed into ordinary differential equations using similarity parameters and then solved numerically using forth ordered Runge-Kutta method along with shooting technique.. This researchers all solved these problems numerically, but some employed analytical methods and they include: Mohammed *et al*. (2015), Presented an analytical method to describe the heat and mass transfer in the flow of an incompressible viscous fluid past an infinite vertical plate. With the governing equations accounting for the viscous dissipation effect and mass transfer with chemical reaction of constant reaction rate. The couple differential equations were transformed using similarity transformation and solved analytically using iteration perturbation method. It was discovered that the heat transfer rate decreases due to increase of Prandtl (Pr) and Eckert number (Ec). Mass transfer rate decreases due to increase of Schmidt number (Sc) and increase of reaction rate.

Farhad *et al*.(2013), investigated the combined heat and mass effects on unsteady MHD free convection flow of an incompressible viscous fluid passing through a porous medium. The flow in the fluid is caused due to the uniform motion of the plate. Exact solutions were obtained for governing equation using Laplace transform technique. It was observed that the effect of Hartmann number and porosity parameter on velocity are opposite.

The velocity increases with increasing values of permeability parameter, Grashof number (Gr), and dimensionless time (t), while it decreases for larger values of Hartmann number (M) and 'Pr' greater than one.

The temperature and thermal boundary layer decrease owing to the increase in the values of radiation parameter and 'Pr'. The fluid concentration decreases with increasing values of chemical reaction parameter and 'Sc'.

Hamad *et al*. (2011), investigated the unsteady magnetohydrodynamic flow of a nanofluid past an oscillatory moving vertical pearmeable semi-infinite flat plate with constant heat source in a rotating frame of reference. The velocity along the plate (slip velocity) is assumed to oscillate on time with a constant frequency. The analytical solutions of the boundary layer equations are assumed of oscillatory type and they are obtained by using the small perturbation approximations. It was shown that the inclusion of the nanoparticles into the base fluid is capable to change the flow pattern for the problem considered.)

Das *et al*. (2010) – investigated the effect of heat and mass transfer of heat and mass transfer on the unsteady free convection flow of a viscous, electrically conducting incompressible fluid near an infinite vertical plate embedded in porous medium which moves with time dependent velocity under the influence of uniform magnetic field applied normal to the plate. An exact solution of the governing partial differential equation is obtained by using Laplace transform technique. The values chosen, 'Pr' = 7(water) and 'Pr' = 0.71(air). The values of the 'Sc' are chosen to represent the presence of species by hydrogen (0.22), water vapour (0.60), ammonia (0.78) and carbondioxide (0.96). It was observed that the velocity decreases with increasing 'M', 'Pr' but increases with increasing 'Sc', 'Gr', 'K', Grashof mass transfer number. It is observed that the temperature of air is greater than that of water, because thermal conductivity of fluid decrease with increasing 'Pr'. An increase in the 'Sc' leads to an increase in the concentration of air.

Maina *et al*. (2015), considered the analysis of effects of heat transfer on unsteady MHD free convective flow past a vertical porous plate in a porous medium with heat source and constant injection. Crank-Nicolson method (FDM) was used to solve the governing coupled differential equations. The effects of varying the various flow parameters on the velocity, temperature and concentration profiles were presented in form of graphs

MATERIALS AND METHODS

3.1 Mathematical Formulations

Consider the two dimensional flow of a viscous incompressible electrically conducting fluid past an infinite vertical porous plate through a porous medium in presence of uniform transverse magnetic field (B_0) and constant heat source (Q) .

The vertical plate is taken to be the x-axis and y-axis normal to it. All the governing equations will therefore be independent of x-axis because it is infinite. The fluid motion is two dimensional.

The physical sketch and geometry of the problem is shown in figure 1:

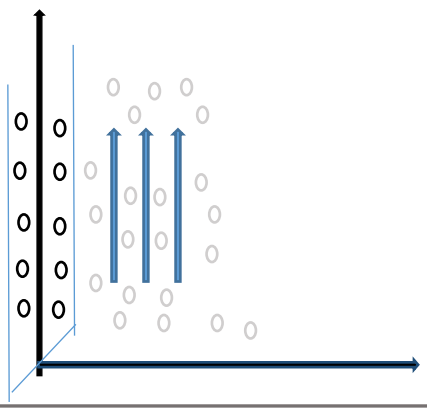

Figure 1: The flow configuration

The surface of the vertical plate is at uniform temperature T_w and concentration C_w. The temperature and concentration for away from the plate are T_∞ *and* C_∞ respectively.

A magnetic field of strength B_0 acts normal to the plate that is, along the y-axis

Following Maina *et al*. (2015) and Mohammed A.A (2015) the governing equations are

Continuity equation

$$\frac{\partial u}{\partial x}+\frac{\partial v}{\partial y}=0 \tag{3.1}$$

Momentum equation

$$\frac{\partial u}{\partial x}+v\frac{\partial u}{\partial y}=\upsilon\frac{\partial^2 u}{\partial y^2}-\frac{\upsilon}{k}u-\frac{\sigma B_0^2 u}{\rho}+\mathrm{g}\,\beta^1(\mathrm{C}-\mathrm{C}_\infty) \tag{3.2}$$

Energy equation

$$\frac{\partial T}{\partial t}+v\frac{\partial T}{\partial y}=\frac{k}{\rho C_p}\frac{\partial^2 T}{\partial y^2}+\frac{\upsilon}{C_p}\left(\frac{\partial u}{\partial y}\right)^2+Q(\mathrm{T}-\mathrm{T}_\infty) \tag{3.3}$$

The equation for species concentrations

$$\frac{\partial C}{\partial t}+v\frac{\partial C}{\partial y}=D_m\frac{\partial^2 C}{\partial y^2} \tag{3.4}$$

With initial and boundary conditions

$$\left.\begin{array}{lll} \mathrm{u}(\mathrm{y},0)=U_\infty & u(0,t)=U_w & u(\infty,t)=0 \\ T(\mathrm{y},0)=\mathrm{T}_\infty & T(0,\mathrm{t})=T_w & T(\infty,t)=T_\infty \\ C(y,0)=\mathrm{C}_\infty & C(0,t)=C_w & C(\infty,t)=C_\infty \end{array}\right\} \tag{3.5}$$

3.2 Coordinate transformation

Here, by means of streamline function **(**Olayiwola, 2015)

$$\eta(y,t) = \int_0^y \rho(s,t)ds \tag{3.6}$$

The coordinate transformation becomes,

$$\frac{\partial}{\partial y} \to \frac{\partial}{\partial \eta}\frac{\partial \eta}{\partial y} = \rho\frac{\partial}{\partial \eta} \tag{3.7}$$

$$\frac{\partial}{\partial t} \to \frac{\partial}{\partial \eta}\frac{\partial \eta}{\partial t} + \frac{\partial}{\partial t} = -\rho v\frac{\partial}{\partial \eta} + \frac{\partial}{\partial t} \tag{3.8}$$

Therefore (3.2) becomes

$$\left(\frac{\partial}{\partial t}\right)u + v\left(\frac{\partial}{\partial y}\right)u = \upsilon\left(\frac{\partial}{\partial y}\right)\left(\frac{\partial}{\partial y}\right)u - \frac{\upsilon}{k}u - \frac{\sigma B_0^2 u}{\rho} + \mathrm{g}\,\beta^1(\mathrm{C} - C_\infty) \tag{3.9}$$

Substituting we have

$$\left(-\rho v\frac{\partial}{\partial \eta} + \frac{\partial}{\partial t}\right)u + v\left(\rho\frac{\partial}{\partial \eta}\right)u = \upsilon\left(\rho\frac{\partial}{\partial \eta}\right)\left(\rho\frac{\partial}{\partial \eta}\right)u - \frac{\upsilon}{k}u - \frac{\sigma B_0^2 u}{\rho} + \mathrm{g}\,\beta^1(\mathrm{C} - C_\infty) \tag{3.10}$$

i.e

$$-\rho v\frac{\partial u}{\partial \eta} + \frac{\partial u}{\partial t} + \rho v\frac{\partial u}{\partial \eta} = \upsilon\rho^2\frac{\partial^2 u}{\partial \eta^2}u - \frac{\upsilon}{k}u - \frac{\sigma B_0^2 u}{\rho} + \mathrm{g}\,\beta^1(\mathrm{C} - C_\infty) \tag{3.11}$$

i.e

$$\frac{\partial u}{\partial t} = \upsilon\rho^2\frac{\partial^2 u}{\partial \eta^2} - \frac{\upsilon u}{k} - \frac{\sigma B_0^2 u}{\rho} + \mathrm{g}\,\beta^1(\mathrm{C} - C_\infty) \tag{3.12}$$

Then (3.3) becomes

$$\left(\frac{\partial}{\partial t}\right)T + \upsilon\left(\frac{\partial}{\partial y}\right)T = \frac{k}{\rho C_p}\left(\frac{\partial}{\partial y}\right)\left(\frac{\partial}{\partial y}\right)T + \frac{\upsilon}{C_p}\left(\left(\frac{\partial}{\partial y}\right)u\right)^2 + Q(\mathrm{T} - \mathrm{T}_\infty) \tag{3.13}$$

i.e.

$$\left(-\rho v\frac{\partial}{\partial \eta} + \frac{\partial}{\partial t}\right)T + v\left(\rho\frac{\partial}{\partial \eta}\right)T = \frac{k}{\rho C_p}\left(\rho\frac{\partial}{\partial \eta}\right)\left(\rho\frac{\partial}{\partial \eta}\right)T + \frac{\upsilon}{C_p}\left(\rho\frac{\partial}{\partial \eta}u\right)^2 + Q(T - T_\infty) \tag{3.14}$$

i.e.

$$-\rho v\frac{\partial}{\partial \eta} + \frac{\partial T}{\partial t} + \rho v\frac{\partial T}{\partial \eta} = \frac{k}{C_p}\rho\frac{\partial^2 T}{\partial \eta^2} + \frac{\upsilon}{C_p}\left(\rho^2\left(\frac{\partial u}{\partial \eta}\right)^2 + Q(\mathrm{T} - \mathrm{T}_\infty)\right) \tag{3.15}$$

i.e.

$$\frac{\partial T}{\partial t} = \frac{k}{C_p}\rho\frac{\partial^2 T}{\partial \eta^2} + \frac{\upsilon}{C_p}\rho^2\left(\frac{\partial u}{\partial \eta}\right)^2 + Q(\mathrm{T}-\mathrm{T}_\infty) \tag{3.16}$$

Also (3.4) becomes

$$\left(\frac{\partial}{\partial t}\right)C + v\left(\frac{\partial}{\partial y}\right)C = D_M\left(\frac{\partial}{\partial y}\right)\left(\frac{\partial}{\partial y}\right)C \tag{3.17}$$

i.e.

$$\left(-\rho v\frac{\partial}{\partial \eta} + \frac{\partial}{\partial t}\right)C + v\left(\rho\frac{\partial}{\partial \eta}\right)C = D_M\left(\rho\frac{\partial}{\partial \eta}\right)\left(\rho\frac{\partial}{\partial \eta}\right)C \tag{3.18}$$

i.e.

$$-\rho v\frac{\partial C}{\partial \eta} + \frac{\partial C}{\partial t} + \rho v\frac{\partial C}{\partial \eta} = D_M\rho^2\frac{\partial^2 C}{\partial \eta^2} \tag{3.19}$$

i.e.

$$\frac{\partial C}{\partial t} = D_M\rho^2\frac{\partial^2 C}{\partial \eta^2} \tag{3.20}$$

After coordinate transformation, the governing equations are

$$\frac{\partial u}{\partial t} = \upsilon\rho^2\frac{\partial^2 u}{\partial \eta^2} - \frac{\upsilon}{k}u - \frac{\sigma B_0^2 u}{\rho} + g\beta'(C - C_\infty) \tag{3.21}$$

$$\frac{\partial T}{\partial t} = \frac{k}{C_p}\rho\frac{\partial^2 T}{\partial \eta^2} + \frac{\upsilon}{C_p}\rho^2\left(\frac{\partial u}{\partial \eta}\right)^2 + Q(T - T_\infty) \tag{3.22}$$

$$\frac{\partial C}{\partial t} = D_M\rho^2\frac{\partial^2 C}{\partial \eta^2} \tag{3.23}$$

With initial and boundary conditions

$$\left.\begin{array}{lll} \mathrm{u}(\eta,0) = U_\infty & u(0,t) = U_w & u(\infty,t) = 0 \\ T(\eta,0) = \mathrm{T}_\infty & T(0,\mathrm{t}) = \mathrm{T}_w & T(\infty,t) = T_\infty \\ C(\eta,0) = \mathrm{C}_\infty & C(0,t) = C_w & C(\infty,t) = C_\infty \end{array}\right\} \tag{3.24}$$

3.3 Non-dimensionalization

3.3.1 To non-dimensionalize the above equations and their respective initial and boundary conditions, the following non dimensional parameters and variables defined as given below have been used.

$$t' = \frac{Dt}{L^2} \ , \ \eta' = \frac{\eta}{L} \ , \ \theta = \frac{T - T_\infty}{T_w - T_\infty} \ , \ \phi = \frac{C - C_\infty}{C_w - C_\infty} \ , \ u' = \frac{u}{U_\infty} \tag{3.25}$$

Where $D = D_m \rho^2$ (3.26)

$$t' = \frac{Dt}{L^2} \Rightarrow t = \frac{t'L^2}{D} \ \ and \ \ \partial t = \frac{L^2}{D}\partial t'$$

$$\eta' = \frac{\eta}{L} \Rightarrow \eta = L\eta' \quad and \ \partial\eta = L\partial\eta'$$

$$u' = \frac{u}{U_\infty} \Rightarrow u = u'U_\infty \ \ and \ \ \partial u = U_\infty \partial u' \tag{3.27}$$

$$\theta = \frac{T - T_\infty}{T_w - T_\infty} \Rightarrow T = \theta(\mathrm{T}_w - \mathrm{T}_\infty) + \mathrm{T}_\infty \ \ and \ \ \partial T = (\mathrm{T}_w - \mathrm{T}_\infty)\partial\theta$$

$$\theta = \frac{C - C_\infty}{C_w - C_\infty} \Rightarrow C = \phi(\mathrm{C}_w - C_\infty) + C_\infty \ \ and \ \ \partial C = (\mathrm{C}_w - C_\infty)\partial\phi$$

Substituting the dimensionless variables (3.21) we have

$$\frac{U_\infty D\partial u'}{L^2\partial t'} = \upsilon\rho^2\left(\frac{\partial}{\partial\eta}\right)\left(\frac{\partial u}{\partial\eta}\right) - \frac{\upsilon}{k}u - \frac{\sigma B_0^2 U_\infty}{\rho} + \mathrm{g}\,\beta'(\mathrm{C} - \mathrm{C}_\infty)$$

$$\frac{U_\infty D\partial u'}{L^2\partial t'} = \upsilon\rho^2\left(\frac{\partial}{L\partial\eta'}\right)\left(\frac{U_\infty\partial u'}{L\partial\eta'}\right) - \frac{\upsilon}{k}u'U_\infty - \frac{\sigma B_0^2 u'U_\infty}{\rho} + \mathrm{g}\,\beta'[\phi(\mathrm{C}_w - C_\infty)] \tag{3.28}$$

$$\frac{U_\infty D\partial u'}{L^2\partial t'} = \frac{\upsilon\rho^2 U_\infty}{L^2}\frac{\partial^2 u'}{\partial\eta'^2} - \frac{\upsilon}{k}u'U_\infty - \frac{\sigma B_0^2 u'U_\infty}{\rho} + \mathrm{g}\,\beta'[\phi(\mathrm{C}_w - C_\infty)]$$

Multiply through by $\frac{L^2}{U_\infty D}$

$$\frac{\partial u'}{\partial t'} = \frac{\upsilon\rho^2}{D}\frac{\partial^2 u'}{\partial\eta'^2} - \frac{\upsilon L^2 u'}{kD} - \frac{L^2\sigma B_0^2 u'}{D\rho} + \frac{\mathrm{g}\,\beta' L^2[\phi(\mathrm{C}_w - C_\infty)]}{U_\infty D} \tag{3.29}$$

Dropping prime we have,

$$\frac{\partial u}{\partial t} = Sc\frac{\partial^2 u}{\partial\eta^2} - \left(M + \frac{1}{kp}\right)u + Gr_\phi\phi \tag{3.30}$$

where

$$M = \frac{\sigma B_0^2 L^2}{D\rho} \ , \ K_p = \frac{kD}{\upsilon L^2} \ , \ Sc = \frac{\upsilon}{D_M} \ , \ Gr_\phi = \frac{g\beta' L^2(\mathrm{C}_w - C_\infty)}{U_\infty D}$$

Substituting in (3.22) we have

$$\frac{(\mathrm{T}_w-\mathrm{T}_\infty)D\partial\theta}{L^2\partial t'}=\frac{k}{\rho C_p}\rho^2\left(\frac{\partial}{\partial\eta}\right)\left(\frac{\partial T}{\partial\eta}\right)+\frac{\upsilon}{C_p}\rho^2\left(\frac{\partial}{\partial\eta}u\right)^2+Q[\theta(\mathrm{T}_w-T_\infty)$$

$$\frac{(\mathrm{T}_w-\mathrm{T}_\infty)D\partial\theta}{L^2\partial t'}=\frac{k}{\rho C_p}\rho^2\left(\frac{\partial}{L\partial\eta'}\right)\left(\frac{(\mathrm{T}_w-\mathrm{T}_\infty)\partial\theta}{L\partial\eta'}\right)+\frac{\upsilon}{C_p}\rho^2\left(\frac{\partial}{L\partial\eta'}u'U_\infty\right)^2+Q[\theta(\mathrm{T}_w-T_\infty) \quad (3.31)$$

$$\frac{(\mathrm{T}_w-\mathrm{T}_\infty)D\partial\theta}{L^2\partial t'}=\frac{k}{\rho C_p}\rho^2\frac{(\mathrm{T}_w-\mathrm{T}_\infty)\partial\theta}{L\partial}+\frac{\upsilon}{C_p}\rho^2\frac{U_\infty^2}{L^2}\left(\frac{\partial u'}{\partial\eta'}\right)^2+Q[\theta(\mathrm{T}_w-T_\infty)$$

Multiplying through by $\dfrac{L^2}{(\mathrm{T}_w-\mathrm{T}_\infty)\mathrm{D}}$

$$\frac{\partial\theta}{\partial t'}=\frac{k\rho^2}{\rho C_p D_M\rho^2}\frac{\partial^2\theta}{\partial\eta'^2}+\frac{\upsilon\rho^2U_\infty^2}{C_pD_M\rho^2(\mathrm{T}_w-\mathrm{T}_\infty)}\left(\frac{\partial u'}{\partial\eta'}\right)^2+\frac{QL^2\theta}{D} \quad (3.32)$$

Dropping prime we have

$$\frac{\partial\theta}{\partial t}=\frac{1}{\mathrm{Pr}}\frac{\partial^2\theta}{\partial\eta^2}+Ec\left(\frac{\partial u}{\partial\eta}\right)^2+q\theta \quad (3.33)$$

Where

$$\mathrm{Pr}=\frac{\rho C_p D_M}{k},\ Ec=\frac{U_\infty^2\upsilon}{C_p\left(T_w-T_\infty\right)D_M},\ q=\frac{QL^2}{D}$$

Substituting the dimensionless in (4.9) we have

$$\frac{\left(C_w-C_\infty\right)D\partial\phi}{L^2\partial t'}=D_M\rho^2\left(\frac{\partial}{\partial\eta}\right)\left(\frac{\partial C}{\partial\eta}\right)$$

$$\frac{\left(C_w-C_\infty\right)D\partial\phi}{L^2\partial t'}=D_M\rho^2\left(\frac{\partial}{L\partial\eta'}\right)\left(\frac{\left(C_w-C_\infty\right)\partial\phi}{L\partial\eta'}\right) \quad (3.34)$$

$$\frac{\left(C_w-C_\infty\right)D\partial\phi}{L^2\partial t'}=\frac{D_M\rho^2\left(C_w-C_\infty\right)}{L}\frac{\partial^2\phi}{\partial\eta'^2}$$

Multiply through by $\dfrac{L^2}{\left(C_w-C_\infty\right)D}$

$$\frac{\partial\phi}{\partial t'}=\frac{D_M\rho^2}{D_M\rho^2}\frac{\partial^2\phi}{\partial\eta'^2} \quad (3.35)$$

Where $D=D_M\rho^2$

Dropping prime

$$\frac{\partial \phi}{\partial t} = \frac{\partial^2 \phi}{\partial \eta'^2} \tag{3.36}$$

3.3.2 Non-dimensionalization of initial and boundary conditions

Given $u(\eta,\theta) = U_\infty \quad u(0,t) = U_w \qquad u(\infty,t) = 0$

But $u = u'U_\infty$

$u(\eta,t) = \mathrm{u}'(\eta,\mathrm{t})U_\infty$

Therefore,

$u(\eta,\theta) = \mathrm{u}'(\eta,0)U_\infty = U_\infty$

$$\Rightarrow u'(\eta,0) = \frac{U_\infty}{U_\infty} = 1$$

$$u'(\eta,0) = 1$$

Dropping the prime

$$u(\eta,0) = 1 \tag{3.37}$$

Similarly

$u(0,t) = u'(0,t)U_\infty = U_w$

$$\Rightarrow u'(0,\mathrm{t}) = \frac{U_w}{U_\infty} = \alpha(\text{say})$$

Dropping prime

$$u(0,t) = \alpha \tag{3.38}$$

Also

$u(\infty,t) = \mathrm{u}'(\infty,\mathrm{t}) = U_\infty = 0$

$$\Rightarrow u'(\infty,t) = 0$$

Dropping prime

$$u(\infty,t) = 0 \tag{3.39}$$

Given $T(\eta,0) = \mathrm{T}_\infty \qquad T(0,t) = T_w \qquad T(\infty,\mathrm{t}) = \mathrm{T}_\infty$

Where

$$T = \theta(T_w - T_\infty) + T_\infty$$

$$T(\eta, t) = \theta(\eta, t)(T_w - T_\infty) + T_\infty$$

i.e.

$$T(\eta, 0) = \theta(\eta, 0)(T_w - T_\infty) + T_\infty = T_\infty$$

$$\Rightarrow \theta(\eta, 0)(T_w - T_\infty) = T_\infty - T_\infty$$

$$\theta(\eta, 0)(T_w - T_\infty) = 0$$

$$\theta(\eta, 0) = 0 \qquad (3.40)$$

Also

$$T(0, t) = \theta(0, t)(T_w - T_\infty) + T_\infty$$

$$\Rightarrow \theta(0, t)(T_w - T_\infty) + T_\infty = T_w$$

$$= \theta(0, t)(T_w - T_\infty) = T_w - T_\infty$$

$$= \theta(0, t) = \frac{T_w - T_\infty}{T_w - T_\infty}$$

$$\theta(0, t) = 1 \qquad (3.41)$$

Similarly

$$T(\infty, t) = \theta(\infty, t)(T_w - T_\infty) + T_\infty$$

$$\Rightarrow \theta(\infty, t)(T_w - T_\infty) + T_\infty = T_\infty$$

$$= \theta(\infty, t)(T_w - T_\infty) = T_\infty - T_\infty$$

$$= \theta(\infty, t)(T_w - T_\infty) = 0$$

$$\theta(\infty, t) = 0 \qquad (3.42)$$

Given $C(\eta, 0) = C_\infty$ $\quad C(0, t) = C_w$ $\quad C(\infty, t) = C_\infty$

Where

$$C = \phi(C_w - C_\infty) + C_\infty$$

$$C(\eta, \mathrm{t}) = \phi(\eta, \mathrm{t})(\mathrm{C}_w - \mathrm{C}_\infty) + \mathrm{C}_\infty$$

i.e.

$$C(\eta, 0) = \phi(\eta, 0)(\mathrm{C}_w - \mathrm{C}_\infty) + \mathrm{C}_\infty = \mathrm{C}_\infty$$

$$\Rightarrow \phi(\eta, 0)(\mathrm{C}_w - \mathrm{C}_\infty) = \mathrm{C}_\infty - \mathrm{C}_\infty$$

$$\phi(\eta, 0)(\mathrm{C}_w - \mathrm{C}_\infty) = 0$$

$$\phi(\eta, 0) = 0 \qquad (3.43)$$

Also

$$C(0, \mathrm{t}) = \phi(0, \mathrm{t})(\mathrm{C}_w - \mathrm{C}_\infty) + \mathrm{C}_\infty$$

$$\Rightarrow \phi(0, \mathrm{t})(\mathrm{C}_w - \mathrm{C}_\infty) + \mathrm{C}_\infty = \mathrm{C}_w$$

$$\Rightarrow \phi(0, \mathrm{t})(\mathrm{C}_w - \mathrm{C}_\infty) = \mathrm{C}_w - \mathrm{C}_\infty$$

$$\phi(0, t) = \frac{\mathrm{C}_w - \mathrm{C}_\infty}{\mathrm{C}_w - \mathrm{C}_\infty}$$

$$\phi(0, t) = 1 \qquad (3.44)$$

Similarly,

$$C(\infty, \mathrm{t}) = \phi(\infty, \mathrm{t})(\mathrm{C}_w - \mathrm{C}_\infty) + \mathrm{C}_\infty$$

$$\Rightarrow \phi(\infty, \mathrm{t})(\mathrm{C}_w - \mathrm{C}_\infty) + \mathrm{C}_\infty = \mathrm{C}_\infty$$

$$\phi(\infty, \mathrm{t})(\mathrm{C}_w - \mathrm{C}_\infty) = \mathrm{C}_\infty - \mathrm{C}_\infty$$

$$\phi(\infty, \mathrm{t})(\mathrm{C}_w - \mathrm{C}_\infty) = 0$$

$$\phi(\infty, \mathrm{t}) = 0 \qquad (3.45)$$

Therefore, the dimensionless equations are:

$$\frac{\partial u}{\partial t} = Sc\frac{\partial^2 v}{\partial \eta^2} - \left(M + \frac{1}{K_p}\right)u + Gr_\phi \phi \qquad (3.46)$$

$$\frac{\partial \theta}{\partial t} = \frac{1}{\Pr}\frac{\partial^2 \theta}{\partial \eta^2} + Ec\left(\frac{\partial u}{\partial \eta}\right)^2 + q\theta \tag{3.47}$$

$$\frac{\partial \phi}{\partial t} = \frac{\partial^2 \phi}{\partial \eta^2} \tag{3.48}$$

With initial and boundary conditions

$$\left.\begin{array}{lll} \mathrm{u}(\eta,0)=1 & u(0,t)=\alpha & u(\infty,t)=0 \\ \theta(\eta,0)=0 & \theta(0,\mathrm{t})=1 & \theta(\infty,t)=0 \\ \phi(\eta,0)=0 & \phi(0,t)=1 & \phi(\infty,t)=0 \end{array}\right\} \tag{3.49}$$

$$h(m) = C_1\left(1+m-\frac{1}{2}m^2+\frac{1}{3}m^3+.\cdots\right)+C_2\left(m-\frac{1}{6}m^3+\frac{5}{24}m^4-\frac{13}{60}m^5+\cdots\right) \tag{3.50}$$

$$f(m) = P_1(1+m+P_2m^2+P_3m^3+P_4m^4+...)+P_5(m+P_6m^3+P_7m^4+P_8m^5+....) \tag{3.51}$$

Taking the first derivative of equation (10.19), we have

$$f'(m) = P_1(1+2P_2m+3P_3m^2+4P_4m^3+...)+P_5(3P_6m^3+4P_7m^3+5P_8m^4+....) \tag{3.52}$$

Where,

$$P_1 = -\frac{B\alpha}{AE-BC}$$

$$P_2 = \frac{\left(M+\frac{1}{K_p}\right)-Sc-2Gr}{2Sc}$$

$$P_3 = \frac{3Sc\left[\left(M+\frac{1}{K_p}\right)-Sca_1-2\,\mathrm{Gr}\right]+\left[\left(M+\frac{1}{K_p}\right)-Sc\right]+\frac{62}{99}Gr}{6Sc}$$

$$P_4 = \left(\frac{5Sc\left[3Sc\left(\left(M+\frac{1}{K_p}\right)-Sc-2\,\mathrm{Gr}\right)\right]+\left[\left(M+\frac{1}{K_p}\right)-Sc\right]+\frac{62}{99}Gr}{24Sc}+\frac{\left[\left(M+\frac{1}{K_p}\right)-Sc-2Gr\right]\left[\left(M+\frac{1}{K_p}\right)-4Sc\right]}{24Sc}+\frac{Gr}{12}\right)$$

$$P_5 = \frac{A\alpha}{AE-BC}$$

$$P_6 = \left(\frac{\left[\left(M + \frac{1}{K_p} \right) - Sc \right] + \frac{62}{99} Gr}{6Sc} \right)$$

$$P_7 = \left(\frac{\left[\left(M + \frac{1}{K_p} \right) - Sc \right] + \frac{62}{99} Gr}{24Sc} + \frac{Gr}{12Sc} \right)$$

$$P_8 = \left(\frac{\left[\left(M + \frac{1}{K_p} \right) - Sc \right] + \frac{62}{99} Gr}{40Sc} + \frac{\left[\left[\left(M + \frac{1}{K_p} \right) - Sc \right] + \frac{62}{99} Gr \right] \left[\left(M + \frac{1}{K_p} \right) - 9Sc \right]}{120Sc} - \frac{2Gr}{660Sc} \right)$$

$$g(m) = q_1 \left(1 + m + q_2 m^2 + q_3 m^3 + q_4 m^4 + \cdots \right) + q_5 \left(m + q_6 m^3 + q_7 m^4 + q_8 m^5 + \cdots \right) \quad (3.53)$$

Where

$$q_1 = \frac{-G}{(FJ - HG)}$$

$$q_2 = \left(\frac{-1 - \Pr q - \Pr Ec(\mathrm{P}_1 + P_5)^2}{2} \right)$$

$$q_3 = \left(\frac{2 + 2\Pr q + 3\mathrm{Ec}(\mathrm{P}_1 + \mathrm{P}_5)^2 - 2\Pr Ec\left((\mathrm{P}_1 + \mathrm{P}_5)^2 + 2\mathrm{P}_1\,\mathrm{P}_2(\mathrm{P}_1 + \mathrm{P}_5) \right)}{6} \right)$$

$$q_4 = \left(\frac{1}{12} \left[\begin{array}{l} -\frac{5}{2}\left[2 + 3\Pr q - \Pr q a_1 + 3Ec\left(P_1 + P_5\right)^2 - 2\Pr Ec\left(\left(P_r + P_5\right)^2 + 2P_1P_2(\mathrm{P}_1 + P_5) \right) \right] \\ -2\left(-1 - \Pr q - Ec\left(P_1 + P_5\right)^2 \right) - \Pr q \left(\frac{-1 - \Pr q - Ec\left(P_1 + P_5\right)^2}{2} \right) - \\ \Pr Ec\left(\left(P_1 + P_5\right)^2 + 8P_1P_2\left(P_1 + P_5\right) + 2P_1^2\left(3P_3 + 2P_2^2\right) + \left(6P_5P_6\left(2P_1 + P_5\right)\right) \right) \end{array} \right] \right)$$

$$q_5 = \frac{F}{(FJ - HG)}$$

$$q_6 = \left(\frac{-(1 - \Pr q) - 2Ec\Pr\left(\left(P_1 + P_5\right)^2 - 2P_1P_2\left(P_1 + P_5\right) \right)}{6} \right)$$

$$q_7 = \left(\frac{\frac{5}{2}\left[-\left(1 + \Pr q\right) - 2Ec\Pr\left(P_1 + P_5\right)^2 + 8P_1P_2\left(P_1 + P_5\right) \right] - Ec\Pr\left(\left(P_1 + P_5\right)^2 + 8P_1P_2\left(P_1 + P_5\right) \right)}{12} \right)$$

$$q_8 = \left(-\frac{1}{20} \times \left[\begin{array}{l} -\frac{9}{4}\left[-\frac{5}{2}\left[-(1+\Pr q) - 2Ec\Pr\left((P_1+P_5)^2 - 2P_1P_2(P_1+P_5) \right) \right] - Ec\Pr\left((P_1+P_5)^2 - 8P_1P_2(P_1+P_5) \right) \right] \\ -\frac{1}{6}\left[-(1+\Pr q) - 2Ec\Pr\left((P_1+P_5)^2 - 2P_1P_2(P_1+P_5) \right) \right](9+\Pr q) - Ec\Pr 4P_1P_2(P_1+P_5) - \\ Ec\Pr\left(8P_1^2P_2^2 + 12P_1P_3(P_1+P_5) + 12P_5P_6(P_1+P_5) \right) - \Pr Ec\left(8P_1P_4(P_1+P_5) + 8P_5P_7(P_1+P_5) + 12P_1P_2(P_1+P_5P_6) \right) \end{array} \right] \right)$$

The computations were done using computer symbolic algebraic package MAPLE.

RESULTS AND DISCUSSION

The method of Derrick and Grossman (1976) was used to prove the uniqueness and existence of solution to the problem. The governing equation (3.2), (3.3), and (3.4) are solved analytically by Self-Similar Solution and Frobenius method, with solutions computed for the values of the following parameters $M = 0.5,\ 2.5,$ and $5.0.$ $Kp = 0.05,\ 0.1,$ and 0.5 $Sc = 0.22,\ 0.69,$ and $0.78,$ $\Pr = 0.71,\ 0.85,$ and $1.00,$ $\mathrm{Ec} = 0.001,\ 0.030,$ and $0.050,$ $q = 0.0001,\ 0.001,$ and $0.01,$ for $Gr = \pm 15,\ \pm 45,$ and ± 75

And constant $\alpha = 1$

We are able to show that the solution is unique for all $t \geq 0$

The results obtained are shown in the figures. The following figures explain the Velocity, Temperature, and Concentration Profiles against different dimensionless parameters, with Grashof number 'Gr' greater than zero (cooling of the plate) and 'Gr' less than zero (heating of the plate).

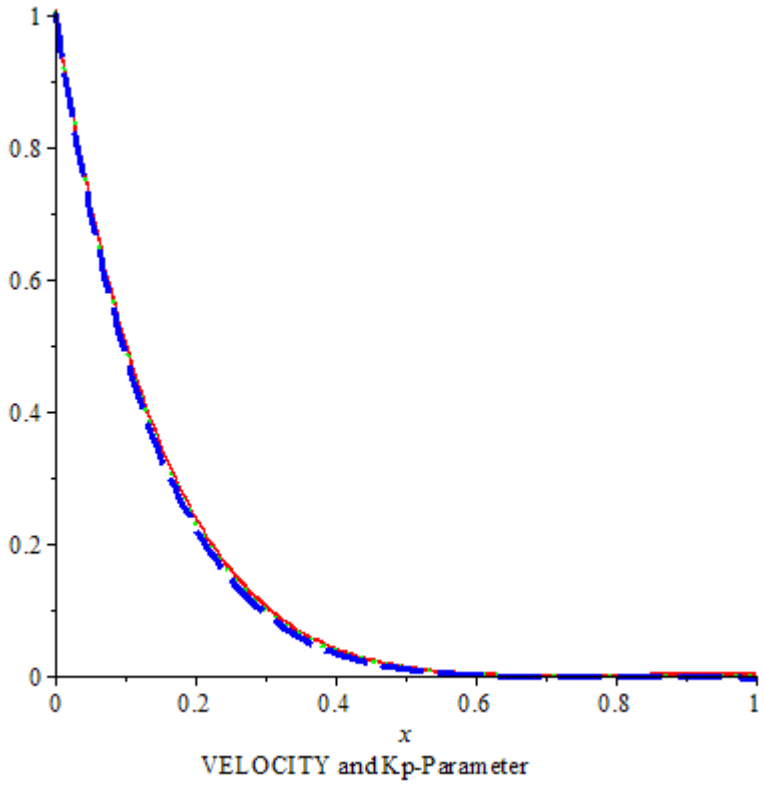

Fig. 2: Variation of velocity with permeability parameter K_P .

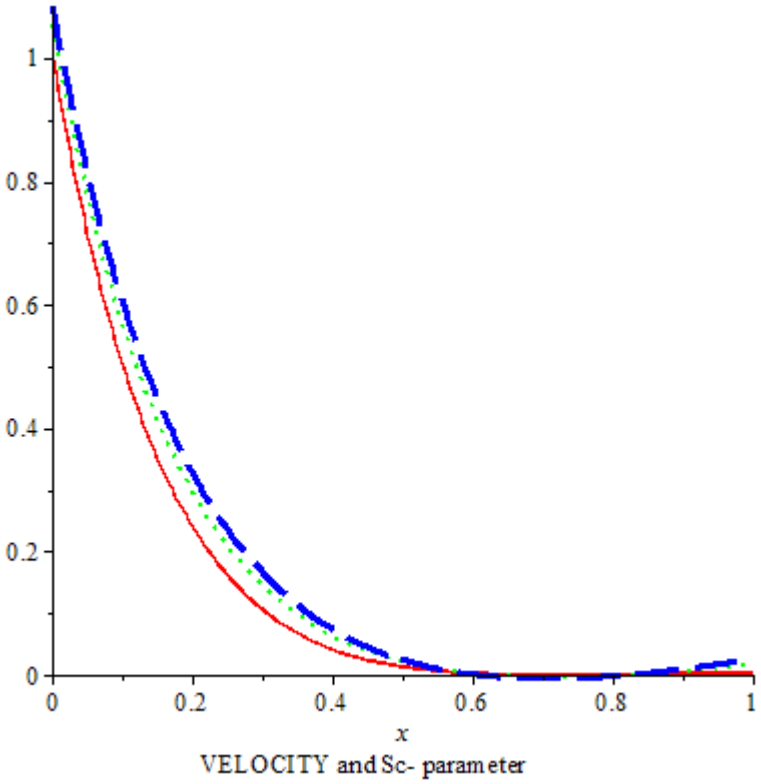

Fig. 3: Variation of velocity with Schimdt number Sc .

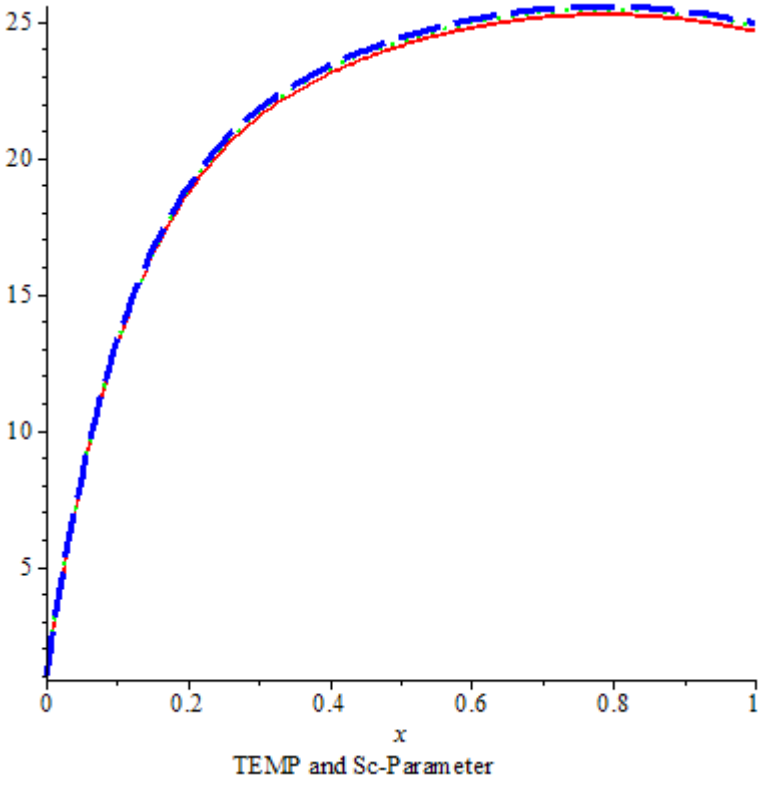

Fig. 4: Variation of Temperature with Schimdt number Sc .

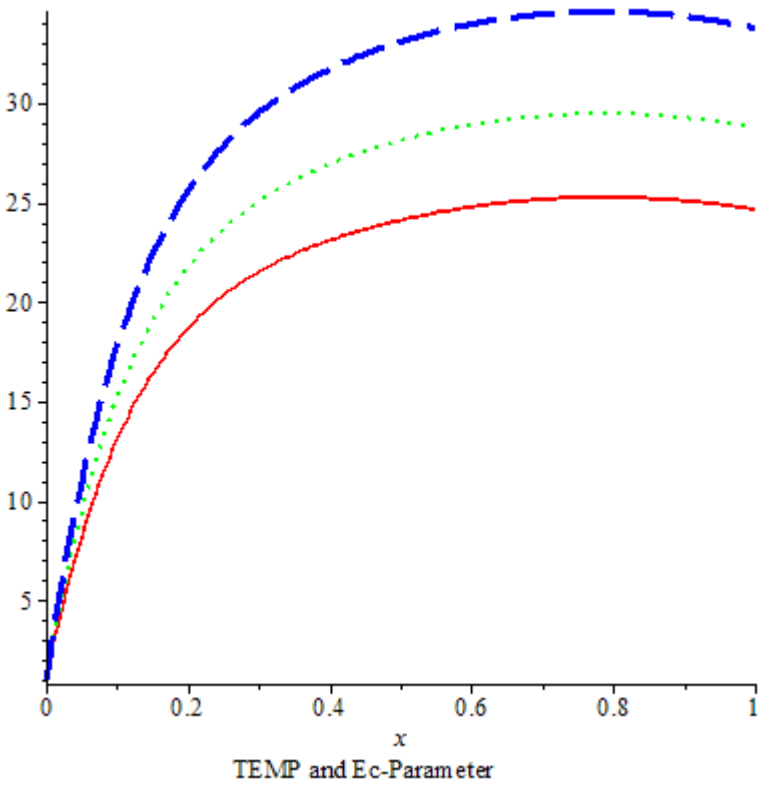

Fig. 5: Variation of Temperature with Eckert number Ec .

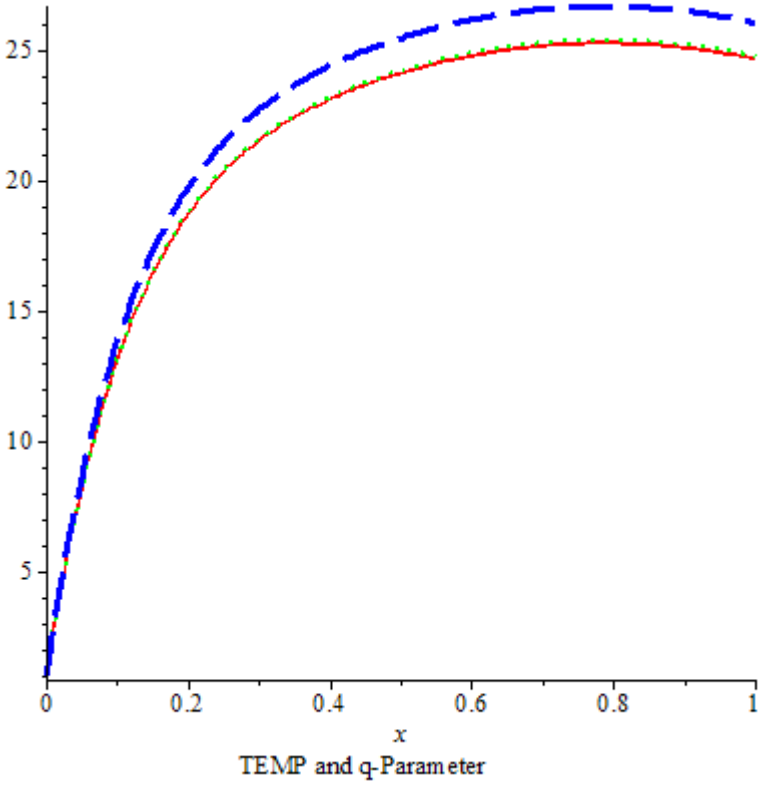

Fig. 5: Variation of Temperature with constant heat source parameter q .

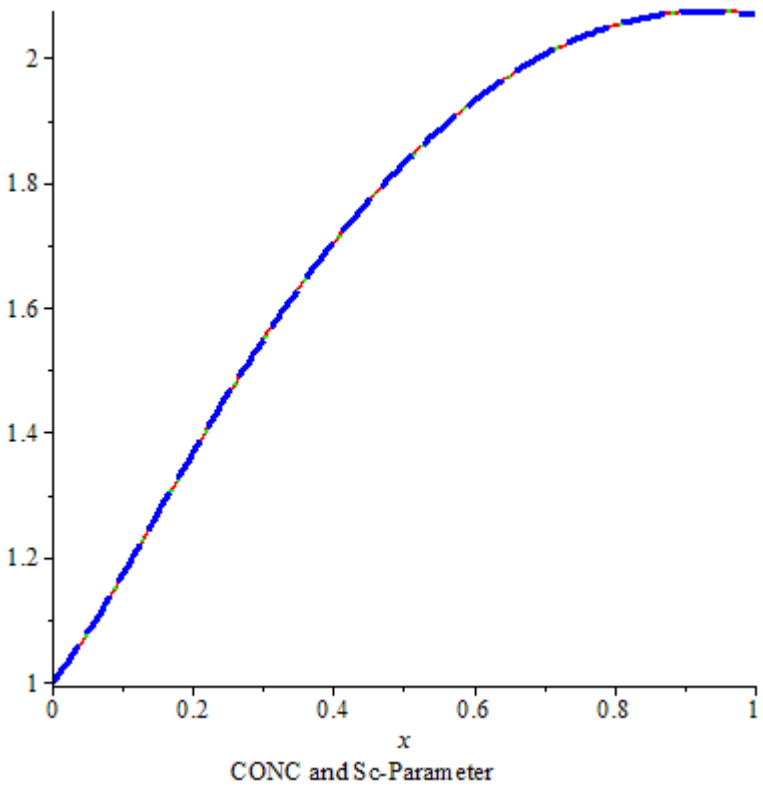

Fig. 5: Variation of Concentration with Schimdt number Sc.

1. Velocity rapidly decreases as the Magnetic parameter increases before maintaining stabilty. Lorentz force is produced when transverse magnetic field is applied to an electrically conducting fluid. The force acts against the flow if the magnetic field is applied in the normal direction as studied presently. The force slows down the motion of the fluid in the boundary layer.
2. It was observed from the figure above that the velocity rapidly **decreases** as the Schmidt number 'Sc' slowly increases before maintaining stabilty. Same as Gundagani M. *et al* (2013)
3. It was observed from the figure above that the velocity rapidly **decreases** as the Prandtl number slowly increases before maintaining stabilty. Same as Gundagani M. *et al* (2013)
4. It was observed from the figure (Gr > 0) above that the Temperature of the flow rapidly increases as Eckert number 'Ec' slowly increase before maintaining stability. Eckert number shows the relation between the kinetic energy in the flow and the enthalpy. It expresses the conversion of kinetic energy into internal energy by workdone against the viscous fluid stresses. Positive Eckert number means cooling of the plate that is, loss of heat from the plate to the fluid. Thus the higher viscous dissipative heat causes a rise in the temperature.
5. It was observed from the figure (Gr < 0) above that the Temperature Rapidly Increases as the heat source parameter 'q' slowly increases before maintaining stability. Increase in heat source creates an increase in the heating effect, thus increase in temperature producing convection currents on the surface of the plate leading to increase in skin friction. There is an increase in skin friction at the wall, with increase in the thickness of the thermal boundary layer and hence a reduction in the rate of heat transfer.
6. Concentration Profile for Gr > 0 with Variation of Concentration 'C' with distance along the plate with different values of Schmidt number and at $\alpha = 1$. It was observed from the figure above that the Concentration rapidly increases as Schmidt number 'Sc' slowly increase before it slowly deeps. Dass K. *et al* (2010).
7. Concentration Profile for Gr > 0 with Variation of Concentration 'C' with distance along the plate with different values of Schmidt number and at $\alpha = 1$. It was observed from the figure above that the

Concentration rapidly increases as Schmidt number 'Sc' slowly increase before it slowly deeps. Dass K. *et al* (2010). Physically Sc, relates the relative thickness of the hydrodynamic layer and mass diffusivity. The increase in Sc, results in presence of heavier fluid which cause a decrease in heat transfer.

Fig. 2 shows the effect of Frank-Kamenetskii number (δ) on the reactive layer temperature profile. It is observed that the reactive layer temperatureincreases significantly with time and decreases with distance. Clearly, the Frank-Kamenetskii number enhances the reactive layer temperature. This is as a result of increase in heat of reaction because the reaction that occurred in this layer is exothermic.

Fig. 3depicts the effect of Frank-Kamenetskii number (δ) on the inert layer temperature profile. It is observed that the inert layer temperatureincreases significantly with time and decreases with distance. Clearly, the Frank-Kamenetskii number enhances the inert layer temperature. This is as a result of exchange of heat between the layers.

Fig. 4presents the effect of frequency factor for polymerization reaction (σ) on the monomer concentration profile. It is observed that the monomer concentration decreases significantly with time and distance. Clearly, the frequency factor for polymerization reactiondecreases the monomer concentration.

Fig. 5displays the effect of frequency factor for decomposition reaction (β) on the initiator concentration profile. It is observed that the initiator concentration decreases significantly with time and distance. Clearly, the frequency factor for decomposition reactiondecreases the initiator concentration.

These curves are in semi quantitative agreement with experiment.

Note that the effects observed in figs. 4 and 5 are of great economic importance, since the major reason for using Frontal Polymerization for polymer synthesis is conversion. For polymer synthesis to be effective there must be rapid conversion without the use of solvent and there mustn't be initiator 'burn out', that is, a situation when all the initiator has decomposed before the monomer has been completely reacted. However, if conversion is low and the product must be purified, those advantages will be non-existent.

CONCLUSION

We have reviewed the mathematical model for the two dimensional flow of a viscous incompressible electrically conducting fluid past an infinite vertical porous plate through a porous medium in presence of uniform transverse magnetic field and constant heat source. The non-dimensional governing equations were solved analytically by coordinate transformation, change of variable method (self-similar solution method), asymptotic expansion method and the Frobenius method. Finally, we have provided the graphical summaries of the system responses.

REFERENCES

https://en.wikipedia.org/wiki/Convection

https://en.wikipedia.org/wiki/Magnetohydrodynamics

Das K., & Jana S (2010)
Heat and mass transfer effects on unsteady MHD free convection flow near a moving vertical plate in porous medium

Farhad A., Ilyas K., Shafie S., & Norzieha M. (2013)
Heat and Mass Transfer with Free Convection MHD Flow Past a Vertical Plate Embedded in a Porous Medium

Gundagani M., Sivaiah S., Ajit P., & Reddy M.C.K., (2013)
Unsteady Magnetohydrodynamic Free Convective Flow Past a Vertical Porous Plate
Hamad M.A.A., & Pop I. (2011) Unsteady MHD Free Convention Flow Past a Vertical Permeable Flat Plate in a Rotating Frame of Reference with contant heat source in a nanofluid 47: 1517-1524 DOI 10.1007/s00231 -011 -0816-6

Ibrahim S.I, (2014)
Unsteady MHD Free Convective Flow Along A Vertical Porous Plate Embedded In A Porous Medium With Heat Generation, Variable Suction And Chemical Reaction Effects

Merle P. & David C.W (2008). Schaum's outline of Fluid Mechanics. New York, McGraw-Hill.

Mohammed, A. A., Olayiwola R. O. & Yisa E.M. (2015). Simulation of Heat and Mass Transfer in the Flow of an Incompressible Viscous Fluid Past an Infinite Vertical Plate:

Mohammed A.A., Olayiwola R.O., Bashir A.U., & Yisa E.M. (2015)
Modeling and Analytical Simulation of Heat and Mass Transfer In The Flow Of An Incompressible Viscous Fluid Past An Infinite Horizontal Wall

Nakayama Y. & Boucher (1999). Introduction to Fluid Mechanics. Oxford Great Britain: Butterworth Heinemann.

Rao J.A., Srinivasa R., & Sivaiah S. (2012). Finite Element Solution of Heat and Mass Transfer in MHD Flow of a Viscous Fluid past a Vertical Plate under Oscillatory Suction Velocity: *Journal of applied fluid Mechanics.* ISSN 1735-3572, ` EISSN 1735-3645. 5(3), 1-10

Reddy T.S., Raju M.C., &Varma S.V.K. (2013)
Unsteady MHD Radiative and Chemically Reactive Free Convection Flow near a Moving Vertical Plate in Porous Medium

Seth G.S., Sharma R & Kumbhakar B (2016)
Heat and Mass Transfer Effects on Unsteady MHD Natural Convection Flow of a Chemically Reactive and Radiating Fluid through a Porous Medium
Past a Moving Vertical Plate with Arbitrary Ramped Temperature.

Sharma P.R., Dadheech I.K & Singh G. (2012)
Heat and Mass Transfer Effects on Unsteady MHD Free Convective Flow Along A Vertical Porous Plate with Internal Heat Generation And Variable Suction. International Journal of Mathematical Archive-3(5), 2012, 2163- 2172

Almeida, AS; Wada, K; Secchi, AR (2008). Simulation of Styrene Polymerization Reactors: Kinetics and Thermodynamic Modeling. *Brazilian Journal of ChemicalEngineering. 25*(2): 337-349.

Ayeni, RO (1982). On the explosion of Chain-thermal Reactions. *J. Austral. Math. Soc. (SeriesB)*. 24: 194-202.

Cardarelli, SA; Golovaty, D; Gross, LK; Gyrya, VT; Zhu, J (2005). A Numerical Study of One-Step Models of Polymerization: Frontal versus Bulk Mode. *ElsevierPhysica D.*206:145–165.

Comissiong, DMG; Gross, LK;Volpert, VA (2006). Frontal polymerization in the presence of an inert material. *Journal of Engineering Mathematics.* 54: 389–402.

He, JH (2006): Some asymptotic methods for strongly nonlinear equations, *Int. J. Modern Phys.* B. 20(10): 1141 – 1199.

Myint-U, T;Debnath, L (1987). Partial Differential Equation for Scientists and Engineers. PTR Prentice – Hall, Englewood Cliffs, New Jersey 07632.

Odian,GG (1991). Principles of Polymerization, 3rd edition. New York, Wiley-Interscience, 768.

Olayiwola, RO;Durojaye, MO;Immam, MS; Shuaib, SE (2013). A Mathematical Study of One-Step Models of Polymerization. *Pacific Journal of Science and Technology*. *14*(2):153- 162. http://www.akamaiuniversity.us/PJST.htm

Washington,RP;Steinbock, O (2003). Frontal Free-Radical Polymerization: Applications toMaterials Synthesis.*Polymer News*, 28: 303–310.

Abrahamwitz, M. &Stegun, I. A. (1972) Handbook of mathematical funtions. *Dover Publications*, New York.

Ali, M. E. (1994). Heat transfer characteristics of a continuous stretching surface, Warme-Undstoffubertragung. 29, 227-234.

Ashokkunar, K., Venna., P.H. & Pravin, V.K (2013). Closed form solutions of heat and mass transfer in the flow of a MHD visco-elastic fluid over a porous stretching. *International journal of applied mechanics and engineering*, *18*(4), 989-1002.

Anuj, K. & Manoj, K. (2013). MHD boundary layer flow past a stretching plate with heat transfer. *International journal of Engineering and Science* 2, 9-13

Ali, M.E (1995) on thermal boundary layer on a power law stretched surface withsuction or injection. *International journal of heat mass flow*. 16, 280-290.

Bank, W.H.H. (1993). Similarity solution of the boundary layer equation for a stretching wall. *Journal of Mechanics theory application*, 2, 375-392.

Bhaskar, K. (2014). Effects of mass transfer on unsteady free convection MHD flow between two heated vertical plates in the presence of transverse magnetic field. *International of Mathematical Engineering and Science.* 1(3), 1-13

Chand K., R. Kumar & Sharma, S (2012). Hydromagnetic oscillatory flow through a porous medium bounded by two vertical plate with heat source and soret effect. *Pelagia research library advance in applied science research* 3 (4), 2169-2178 www.pelaglaresearchlibrary.com Downloaded on 11/12/2014.

Chen C. H. (1998). Laminar mixed convection adjacent to vertical, continuously stretching sheets. Heat and mass transfer, 33, 471-476.

Doma, S.B. (2010) .Two –dimensional fluid past a rectangle plate with variable initial velocity. *Alexandria journal of Mathematics 1*(2), 1-10.

Elbashbeshy E.M.A (1998). Heat transfer over a stretching surface with variable heat flux. *Journal physics D Apply physics*, 31, 1951-1955.

Foraboshci, F.P. & Federico, I.D (2003). Heat transfer in a laminar flow of non- newtonian heat generation fluids. *International Journal*. Heat transfer over a stretching surface with prescribed flux. *Canada Journal of Physics.* 81, 699-705.

He, J.H. (2006). Some asymptotic methods for strongly nonlinear equations. *International journal of modern physics B*, 10 ,1141-1199.

Hossain Md.A, MollaMd, M &Lun Shin, Y (2004). Natural convection flow along a vertical wavy surface with uniformtemperature in presence of heat generation/absorption. *International Journal of Thermal Sciences 43*(2), 157- 163. www.researchgate.net. Downloaded on 11/12/2014

Ibrahim, S.M. (2014). Unsteady MHD convection heat and mass transfer past an infinite vertical plate embedded in a porous medium with radiation and chemical the reaction under influence of dufour and soret effects. *Chemical and process engineering research*. 19, 2014.

Khan,W.A. (2005). Fluid flow around and heat transfer from elliptical cylinders: analytical approach. Journal of thermophysics and heat transfer, (19)2, 1-10

Lakshmi, K.B., Raju, G.S.S., Kishore, P.M &Prasada Rao, N.V.R.V (2013). The study of heat generation and viscous dissipation on MHD and mass diffusion flow past a surface. *IOSR-Journal of Apply Physics*. *5*(4), 17-28.

Olajuwon &Oahimire (2013). Unsteady free convection heat and mass transfer in an MHD micro polar fluid in the presence thermo diffusion and thermal radiation. *International journal of and pure applied mathematics, 84*(2), 15-37.

Omowaye, A.J (2014) Steady Arrhenius laminar free convective MHD flow and heat transfer past a vertical stretching with viscous dissipation. *Journal of Nigeria mathematics society*, 33,259-271.

Sharma, P.R & Singh, G.(2008). Unsteady MHD free convection flow and heat transfer along a vertical porous plate with variable suction and internal heat generation. *International Journal of Applied Mathematics Mechanics*, 4,1-8.
Uwanta&Omokhuale (2012). Viscoelastic fluidflow in a fixed plane with heat and mass transfer. *Research Journal of Mathematics and statistics transfer 4(3)*, 63- 69

Vajravelu, k., Vinayaka, P.K., & Chin-on, N.G (2013). The effect of variable viscosity on the flow and heat transfer of a viscous Ag-water and Cu-water nanofluids journal of hydrodynamics, 25(1), 1-9.

TIME SERIES ANALYSIS OF THE AVERAGE MONTHLY RELATIVE HUMITY IN BIDA, NIGER STATE.

Hillary Okemmiri Uche, B Tech Statistics

Abstract

This work modelled the average monthly relative humidity of Bida. Data were collected from National Cereal Research Institute (NCRI) Badeggi. A preliminary check on the data obtained for this work was conducted to gain insight on the pattern of trend and seasonal components that constitute the monthly relative humidity. The inspection on the data using time plot, revealed that the data has a slight downward trend. Furthermore, the monthly data was also found to be stationary and serially uncorrelated by the Augmented Dickey Fuller test, KPSS of unit root and the Autocorrelation test for serial correlation of the error term respectively. Ljung-Box was utilized for diagnostic procedure. Five models were fitted and based on Akiaike, Schwarz and Hannan-Quinn information criteria, SARIMA $(0,0,0)(2,1,0)_{12}$ was selected as the best model and hence, recommended for forecasting average monthly Relative Humidity of Bida.

Keywords: *Time series, SARIMA model, Relative Humidity, Forecasting*

1.0 GENERAL INTRODUCTION

1.1 **Introduction**

Relative humidity is the amount of moisture in the air compared to what the air can "hold" at that temperature. When the air can't hold all the moisture, then it condenses as dew.

Can a time series model be built for forecasting the magnitude of relative humidity? This is the question this research seek to answer.

When thinking conceptually of water vapor as a gas, it's easy to define relative humidity. Also Relative humidity (RH) can be define as the ratio of the partial water vapor pressure (P_w) to the water vapor saturation pressure (P_{ws}) at a particular temperature.

Relative humidity is strongly temperature dependent. For example, in a room with a RH of 50% and a temperature of 20°C, increasing the temperature of the room to 25°C will decrease the RH to about 37%, even though the partial pressure of the water vapor remains the same. Pressure will also change relative humidity.

A Time Series (TS) is a sequence of observation ordered in time, mostly, these observations are collected at equally discrete time intervals. Shitu and Yaya (2011) defined time series as record of observation measuring certain quantity of interest at regular or irregular interval of time. The observation may be recorded daily, weekly, quarterly, yearly or bi-annually. It is a realization or sample function from a certain stochastic process.

The goal of time series is to identify a model within a given class of flexible model which can reasonably approximately express a time-structure relationship of the process that generated the time series data and also helps to make inference of the process based on the observed realization. **1.2 Stochastic processes**

The theory of stochastic processes plays an important role in the investigation of random phenomena depending on time; a time series is a kind of stochastic process indexed by time.

Climate evolves in time, and a stochastic process (a time-dependent random variable, relative humidity representing a climate variable with not exactly known value) and time series (the observed or sampled process) are central to statistical climate analysis. A wide definition of trend and decomposition of a stochastic process, X, is used to explain the behavior of the stochastic process, as follows:

$X(T) = X_{trend}(T) + X_{out}(T) + S(T).X_{noise}(T)$, …….(2.1)

Where T is continuous time, $X_{trend}(T)$ is the trend process, $X_{out}(T)$ is the outlier process, S (T) is a variability function scaling $X_{noise}(T)$, the noise process. The trend is seen to include all systematic or deterministic, long-term processes such as a linear increase, a step change or a seasonal signal. The trend is described by parameters, for example, the rate of an increase. Outliers are event with an extremely large absolute value and are usually rare. The noise process is assumed to be weakly stationary with zero mean and autocorrelation. Given $X_{noise}(T)$ standard deviation unity enables introduction of S (T) to honor climates definition as not only the mean but also the variability of the state of the atmosphere and other compartments (Briickner 1890; Hann 1901; Koppen 1923). A version of equation (2.1) is written for discrete time, T (i), as

$X(i) = X_{trend}(i) + X_{out}(i) + S(i).X_{noise}(i)$ …….(2.2)

Using the abbreviation X (i) Ξ X (T (i)), etc. However, for unevenly spaced T(i) this is a problematic step because of a possibly non-unique relation between $X_{noise}(T)$ and $X_{noise}(i)$. The observed, discrete time series from process X (i) is the set of size n of paired values t(i) and x(i), compactly written as $\{t(i), x(i)\}_{i=1}^{n}$.

Thus "Climate change" refers to time, and the analysis of modelled or observed time series, such as global surface-air temperature over the past millennium, is an important field for climate analysis. In time past, one of the earliest papers in statistical time series analysis examined a "supposed 26 day period of meteorological phenomena" (Schuster, 1898).

One might possibly view of climate change as a time-dependent random variable that is composed of trend, outliers / extremes and variability / noise (Mudelsee, 2010); this structural approach is also the basis of a presented method (Section 5.3.1). The task of the analysis is to use the data for estimating the parameters describing the trend, variability and other components.

Instrument for Measuring Relative Humidity and Methods

A hygrometer is an instrument used to measure relative humidity. Humidity is the measure of the amount of moisture in the air. A psychrometer is an example of a hygrometer. A psychrometer uses two thermometers to measure relative humidity; one measures the dry-bulb temperature and the other measures the wet-bulb temperature.

2.0 Review of Relevant Literature

There has been much work done on "time series analysis on topics like road accident, petroleum, precipitation temperature, internally generated revenue, health e.t.c in such studies, the time series analysis was used to analyze the data and used also to forecast future events.

Adebanjo (1993): carried out a time series analysis of monthly revenue collection through P.A>Y.E of Ado-Ekiti State, within the period (1986 – 1992). The study concluded that the revenue of the years under study has been on the increase. The study also found out that the monthly revenue of Ado Ekiti have been following a seasonal pattern.

Agbarasim (1996) Studied mean temperature of turned K.e (1987 – 1996). The study used multiplicative model to decompose his data and least-square methods to estimate the trend. It was found that the influence of cyclical and regular components was not pronounced, so forecasting as based also on trend and seasonal factors.

This research will utilize Seasonal Autoregressive Integrated Moving Average

(SARIMA) model, for modelling the RH data. Works too, numbers to mention have utilized this model.

Jahanbakhsh and Baser (2003) used Autoregressive Integrated Moving Average (ARIMA) to study Tabriz monthly average temperature fluctuation from 1959 to 1998 (for 40 years). They showed that monthly average temperature of Tabriz fluctuates around a nonlinear axis with an increasing trend indicating temperature rise. They also used ARIMA (0, 0, 1) $(0, 0, 1)_{12}$ model to forecast Tabriz station monthly average temperature up to 2010.

Jahanbakhsh and Torabi (2004) carried out investigation on temperature and rainfall data changes for different locations in Iran. Apart from SARIMA other forecasting procedures also exist.

Chatfield (1982) found that Holt-Winters, Harrison's method and stepwise auto-regression are roughly equal in accuracy but better than Browns method. Newbold and Granger in Bolarinwa (2005) show that Box-Jenkins method tends to give more accurate result than other simple automatic procedure. They also found that the combination of Holt-winters and stepwise auto-regression gave result almost as accurate but as those given by Box-Jenkins.

Kendall and Ord (1990) reported the study by Markridakis and Hibon, and large scale follow up studies that examined 1001 series, making forecast up to 18 months 9 quarters and 6 years ahead of monthly, quarterly and annual data respectively. The studies concluded that simple methods like exponential smoothing perform just as well as more sophisticated ones.

3.0 Methods

This work, seeks to explore the various statistical and time series tool and techniques that will be employed in the analysis of the data on monthly relative humidity of Bida urban. These tools include the method used in inspecting the data for trend and seasonal components, method used for testing for randomness and stability of the series and the method adapted for forecasting future events

3.1 Method of Data Collection

The information (Data) collected for the analysis of this work is purely secondary source of data that is, already made data. The data on the monthly average relative humidity for the period of fifteen years (2010-2016), were collected from NCRI (National Cereal Research Institute) Badeggi, Niger state.

3.2 Methodology for making the model

3.21 Box-Jenkins method

The Box-Jenkins methodology refers to the set of procedures for identifying, fitting, and checking ARIMA models with time series data. Forecasts follow directly from the form of the fitted model. By Box-Jenkins, a P_{th} order autoregressive model: AR (p), has the general form

$X_t = \alpha + \emptyset_1 X_{t-1} + \emptyset_2 X_{t-2} + \ldots + \emptyset_p X_{t-p} + \varepsilon_t$ ---------- (3.2.1)

Where

X_t , Represents the response variable at time t,

$X_{t-1}, X_{t-2}, \ldots, X_{t-p}$ are the response variables at time lags t-1, t-2, . . . , t-p, respectively.

$\emptyset_1, \emptyset_2, \ldots, \emptyset_3$ are the coefficients to be estimated, and ε_t is the error term at time t.

Also, a q_{th} order moving average model: MA (q), has the general form

$$X_t = \varepsilon_t + \phi_1 \varepsilon_{t-1} + \phi_2 \varepsilon_{t-2} + \ldots - + \phi_q \varepsilon_{t-q} \qquad (3.2.2)$$

Where

X_t Is the response variable at time t,

μ= constant mean of the process,

$\theta_1, \ldots, \theta_p$ are the coefficients to be estimated,

ε_t is the error at time t and

$\varepsilon_{t-1}, \varepsilon_{t-2}, \ldots, \varepsilon_{t-p}$ are the errors in previous time periods that are incorporated in the response Xt.

Autoregressive Moving Average Model: ARMA (p, q), which has the general form

$X_t = \alpha + \emptyset_1 X_{t-1} + \emptyset_2 X_{t-2} + \ldots + \emptyset_p X_{t-p} + \varepsilon_t + \theta_1 \varepsilon_{t-1} + \ldots + \theta_q \varepsilon_{t-q}$

We can use the graph of the sample autocorrelation function (ACF) and the sample partial autocorrelation function (PACF) to determine.

Box-Jenkins forecasting models consist of a four-step iterative process which are; Model Identification, Model Estimation, Model Checking (Goodness of fit) and Model Forecasting.

3.22 Seasonal Time Series model

To deal with series containing seasonal fluctuations like the Relative Humidity, Box-Jenkins recommend the following general model:

$$\emptyset_p(B)\Phi_P(B)(1-B)^d(1-B^s)^D X_t = \theta_q(B)\Theta_Q(B^s)a_t$$

Where *d* is the order of differencing, *s* is the number of seasons per year, and *D* is the order of seasonal differencing. The operator polynomials are

$$\emptyset_p(B) = (1 - \emptyset_1 B - \cdots - \emptyset_p B^p)$$
$$\theta_q(B) = (1 - \theta_1 B - \cdots - \theta_q B^q)$$
$$\Phi_P(B^s) = (1 - \Phi_1 B^s - \cdots - \Phi_P B^{sp})$$
$$\Theta_Q(B^s) = (1 - \Theta_1 B^s - \cdots - \Theta_Q B^{sQ}$$

Note that $(1 - B^s)X_t = X_t - X_{t-s}$

Box-Jenkins explain that the maximum value of *d, D, p, q, P,* and *Q* is two. Hence, these operator polynomials are usually simple expressions. The model will be adopted for this work.

3.3 Model Estimation

Maximum Likelihood Estimation

Once you have guestimated values of *p*, *d*, and *q*, you are ready to estimate the phis and thetas. This study utilize the maximum likelihood estimation process outlined in Box-Jenkins (1976). The maximum likelihood equation is solved by nonlinear function maximization. Backcasting is used to obtain estimates of the initial residuals. The estimation process is calculation intensive and iterative, so it often takes a few seconds to obtain a solution. The probability density function of a shock therefore is given by Mc Cleary *et al.* (1980):

$$\mathbf{P}\,(e_t) = \frac{e^{-e_t^2/2\sigma_e^2}}{\sigma_e\sqrt{2\pi}}$$

The multiplicative constant can be dropped and the probability of the product of multiple shocks can be expressed (Box *et al.*, 1994) as

$$\mathbf{P}\,(a_1, a_2, \ldots, a_n) \propto \sigma_e^{-n}\exp[-(\sum_{t=1}^{n}\frac{e_1^2}{2\sigma_e^2})]$$

Taking the natural log of that function, the analyst can obtain the natural log of the likelihood function, conditional on the choice of the parameters:

$$\mathbf{LL}\,(\varphi, \theta, \sigma_e) = -n\,In\,(\sigma_e) - \frac{\sum e_{t,(\varphi,\theta)}^2}{2\sigma_e^2}$$

3.4 Diagnostic Check

Once a model has been fit, the final step is the diagnostic checking of the model. The checking is carried out by studying the autocorrelation plots of the residuals to see if further structure (large correlation values) can be found. If all the autocorrelations and partial autocorrelations are small, the model is considered adequate and forecasts are generated. If some of the autocorrelations are large, the values of *p* and/or *q* are adjusted and the model is re-estimated.

Ljung Box Q Statistic

The Q statistic at lag k, a test statistic for the null hypothesis is that there is no autocorrelation up to order k and is given as

$$LB = n(n+2)\sum_{i=1}^{k}\left(\frac{\hat{\rho}k}{n-k}\right) \sim \chi^2_{(k)}df \quad \text{----------3.2.1}$$

The Q statistic is often used as a test of whether the series is white noise. This hypothesis is rejected if the probability value of the Q statistic is significant. Thus the series is serially correlated.

The Hypothesis

$$H_0: the\ series\ is\ uncorrelated$$

Vs $$H_0: the\ series\ is\ serialy\ correlated$$

3.5 The criterion for choosing the model

In time series, or generally data analysis, there might be used several proper models for indicating a set of given data. When applying the ARIMA model, Akaike Information Criterion (AIC) has higher accuracy and comparing two ARIMA model for choosing best fitting model provided can be operated better. In this study, for modeling the average monthly Relative Humidity of Bida, there has been used SARIMA model using Gretl, MINITAB software and AIC test. According to this test, any rank with least was selected as the best model.

3.6 Forecasting

One of the most important objectives of time series analysis is to forecast the future behaviour of the series. Forecasting procedure is categorized into three broad categories namely: subjective, univariate and multivariate forecasting. However, most forecasting results are derived from the general theory of linear prediction developed by kolmogorov (1939, 1941); wiener (1949), kalman (1960) whittle (1983) among others. From this work, emphasis is placed on univariate forecasting in a given series by fitting a model to the data

4.0 RESULTS

4.1 Introduction

The Time Series results and graphs of the Average Monthly Relative Humidity data are shown in Tables and Figures below. MINITAB (17.0) and Gretel package was utilize for this work.

4.2 Graphical Representations of Monthly Relative Humidity in Bida.

Fig1: Time plot for relative humidity

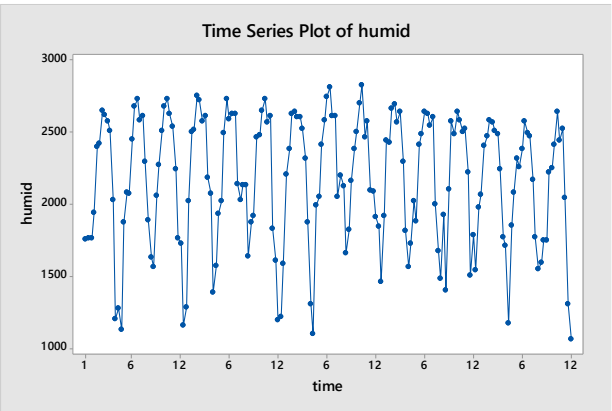

Fig2: Time plot and the fitted regression model line of the relative humidity

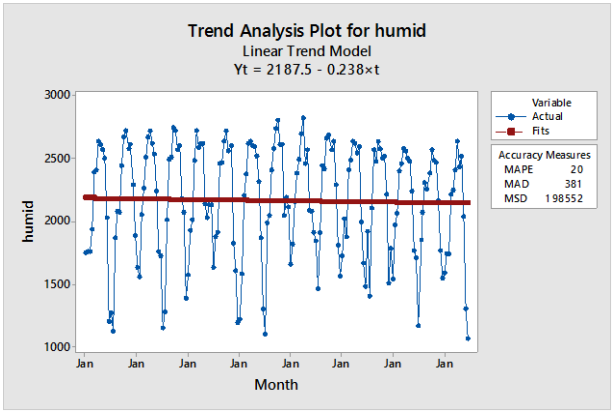

Fig3: Residual plots

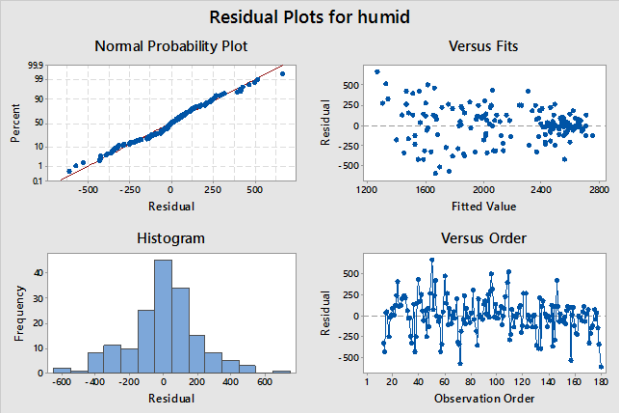

Table4.1 Augmented Dickey-Fuller Test Equation

Null Hypothesis: HUMID has a unit root
Exogenous: Constant
Lag Length: 11 (Automatic - based on AIC, maxlag=13)

		t-Statistic	Prob.*
Augmented Dickey-Fuller test statistic		-2.045302	0.2674
Test critical values:	1% level	-3.469451	
	5% level	-2.878618	
	10% level	-2.575954	

*MacKinnon (1996) one-sided p-values.
Augmented Dickey-Fuller Test Equation
Dependent Variable: D(HUMID)
Method: Least Squares
Date: 08/13/16 Time: 21:53
Sample (adjusted): 13 180
Included observations: 168 after adjustments

Variable	Coefficient	Std. Error	t-Statistic	Prob.
HUMID(-1)	-0.471107	0.230336	-2.045302	0.0425
D(HUMID(-1))	-0.096442	0.223946	-0.430646	0.6673
D(HUMID(-2))	-0.067841	0.207741	-0.326566	0.7444
D(HUMID(-3))	-0.186253	0.191499	-0.972602	0.3323
D(HUMID(-4))	-0.252565	0.170134	-1.484501	0.1397
D(HUMID(-5))	-0.295645	0.152523	-1.938361	0.0544
D(HUMID(-6))	-0.328754	0.136040	-2.416606	0.0168
D(HUMID(-7))	-0.357923	0.119514	-2.994810	0.0032
D(HUMID(-8))	-0.518660	0.104683	-4.954570	0.0000
D(HUMID(-9))	-0.380371	0.096017	-3.961511	0.0001
D(HUMID(-10))	-0.393835	0.088018	-4.474499	0.0000
D(HUMID(-11))	-0.238765	0.079290	-3.011273	0.0030
C	1020.446	501.5722	2.034494	0.0436

R-squared	0.603852	Mean dependent var	-0.839286
Adjusted R-squared	0.573182	S.D. dependent var	314.6062

S.E. of regression	205.5363	Akaike info criterion	13.56335
Sum squared resid	6548003.	Schwarz criterion	13.80508
Log likelihood	-1126.321	Hannan-Quinn criter.	13.66145
F-statistic	19.68896	Durbin-Watson stat	2.037882
Prob(F-statistic)	0.000000		

Table4.2
KPSS test for humid (including trend and seasonals)
T = 180
Lag truncation parameter = 12

	10%	*5%*	*1%*	*t-stat KPSS*	*p-val*
Critical value	0.120	0.148	0.216	0.233595	<0.001

Fig4:ACF and PACF of relative humidity data

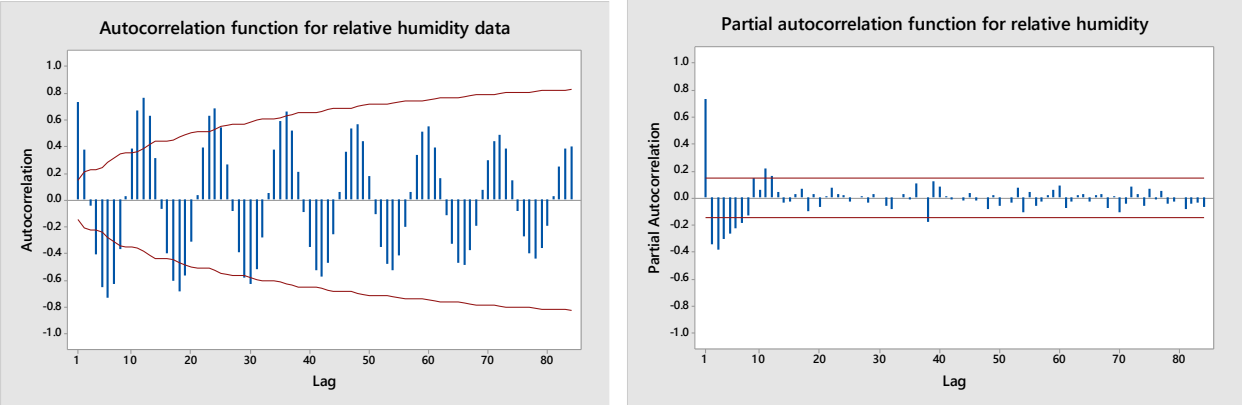

Fig4: Time plot of the differenced series

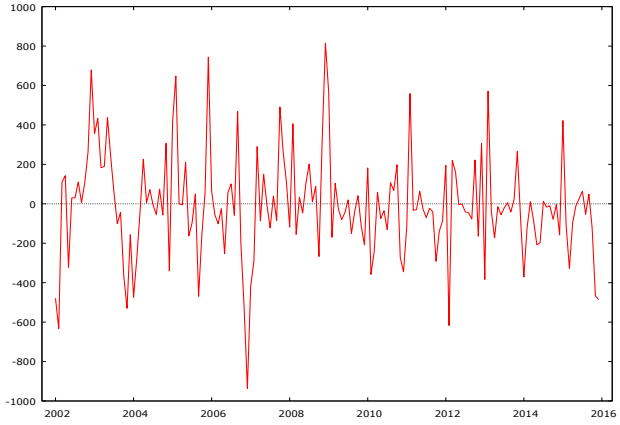

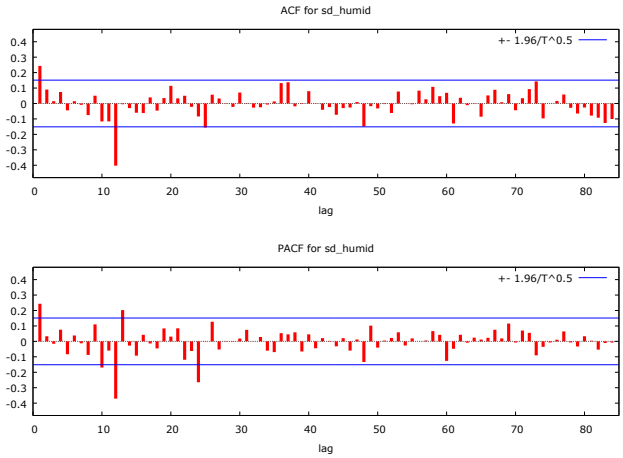

Fig5: ACF and PACF for the differenced series

Table4.3

SARIMA (0,0,0)(1,1,1) Model: humid

Final Estimates of Parameters
Differencing: 0 regular, 1 seasonal of order 12
Number of observations: Original series 180, after differencing 168

Type	***Coeff***	***SE coeff***	***T-value***	***P-value***	***Res SS***	***Res MS***	***DF***
SAR	0.0413	0.0915	0.45	0.653	6661668	40374	165
SMA	0.9104	0.0586	15.53	0.000			
Constant	-4.056	2.225	-1.82	0.070			

Log-likelihood	−1059.672	Akaike criterion	2129.344
Schwarz criterion	2144.594	Hannan-Quinn	2135.538

Modified Box-Pierce (Ljung-Box) Chi-Square statistic

Lag	*Chi-square(χ^2)*	*DF*	*p-value*
12	23.0	9	0.006
24	28.8	21	0.120
36	32.0	33	0.519
48	39.1	45	0.720

Table4.4
SARIMA(0,0,0)(1,1,0) Model: humid
Final Estimates of Parameters
Differencing: 0 regular, 1 seasonal of order 12
Number of observations: Original series 180, after differencing 168

Type	***Coeff***	***SE coeff***	***T-value***	***P-value***	***SSE***	***RMSE***	***DF***
SAR 12	-0.4922	0.0700	-7.04	0.000	8981289	54104	166
Constant	-11.87	17.95	-0.66	0.509			

Log-likelihood	−1067.664	Akaike criterion	2141.329
Schwarz criterion	2150.479	Hannan-Quinn	2145.045

Modified Box-Pierce (Ljung-Box) Chi-Square statistic

Lag	*Chi-square(χ^2)*	*DF*	*p-value*
12	21.2	10	0.020

24	44.8	22	0.003
36	52.9	34	0.021
48	64.1	46	0.040

Table4.5
SARIMA(0,0,0)(0,1,1) Model: humid
Final Estimates of Parameters
Differencing: 0 regular, 1 seasonal of order 12
Number of observations: Original series 180, after differencing 168

Type	*Coeff*	*SE coeff*	*T-value*	*P-value*	*Res SS*	*Res MS*	*DF*
SMA 12	0.9086	0.0504	18.02	0.000	6673786	40202	166
Constant	-4.159	2.698	-1.54	0.125			

Log-likelihood	−1146.033	Akaike criterion	2300.066
Schwarz criterion	2312.562	Hannan-Quinn	2305.138

Modified Box-Pierce (Ljung-Box) Chi-Square statistic

Lag	*Chi-square(χ^2)*	*DF*	*p-value*
12	24.0	10	0.008
24	29.9	22	0.121
36	32.7	34	0.531
48	39.5	46	0.740

Table4.6
SARIMA(0,0,0)(2,1,0) Model: humid
Final Estimates of Parameters
Differencing: 0 regular, 1 seasonal of order 12
Number of observations: Original series 180, after differencing 168

Type	*Coeff*	*SE coeff*	*T-value*	*P-value*	*Res SS*	*Res MS*	*DF*
SAR 12	-0.6636	0.0732	-9.06	0.000	7683842	46569	165
SAR 24	-.04294	0.0739	-5.81	0.000			
Constant	-13.32	16.66	-0.80	0.425			

Log-likelihood	−975.8774	Akaike criterion	1959.755
Schwarz criterion	1971.634	Hannan-Quinn	1964.582

Modified Box-Pierce (Ljung-Box) Chi-Square statistic

Lag	*Chi-square(χ^2)*	*DF*	*p-value*
12	19.9	9	0.019
24	28.3	21	0.131
36	37.9	33	0.254
48	44.5	45	0.493

Table4.7
SARIMA(0,0,0)(0,1,2) Model: humid
Final Estimates of Parameters
Differencing: 0 regular, 1 seasonal of order 12
Number of observations: Original series 180, after differencing 168

Type	*Coeff*	*SE coeff*	*T-value*	*P-value*	*Res SS*	*Res MS*	*DF*
SMA 12	0.8473	0.0811	10.45	0.000	6588335	39929	165
SMzA 24	0.0752	0.0821	0.92	0.361			
Constant	-3.375	2.335	-1.45	0.150			

Log-likelihood	−1145.972	Akaike criterion	2301.943
Schwarz criterion	2317.563	Hannan-Quinn	2308.283

Modified Box-Pierce (Ljung-Box) Chi-Square statistic

Lag	*Chi-square(χ^2)*	*DF*	*p-value*
12	22.0	9	0.009
24	27.9	21	0.141
36	31.5	33	0.539
48	38.2	45	0.752

Table4.8: Goodness-of-Fit Statistics for SARIMA models

	Criterion			***Residuals***	
Models	*Akaike criterion*	*Schwarz criterion*	*Hannan Quinn*	*RMSE*	*SSE*
SARIMA(0,0,0)(1,1,1)	2129.344	2144.594	2135.538	6661668	40374
SARIMA(0,0,0)(1,1,0)	2141.329	2150.479	2145.045	8981289	54104
SARIMA(0,0,0)(0,1,1)	2300.066	2312.562	2305.138	6673786	40202
SARIMA(0,0,0)(2,1,0)	1959.755	1971.634	1964.582	7683842	46569
SARIMA(0,0,0)(0,1,2)	2301.943	2317.563	2308.283	6588335	39929

The estimated models
SARIMA(0,0,0)(1,1,1): $\boldsymbol{X_t = -4.056 + 0.413X_{t-12} + 0.9104\varepsilon_{t-12} + \varepsilon_{t-12}}$
SAIC: 2129.344, SBC: 2144.594, Hannan Quinn: 2135.538
SARIMA (0,0,0)(1,1,0): $\boldsymbol{X_t = -11.87 - 0.4922X_{t-12} + \varepsilon_{t\text{-}12}}$
SAIC: 2141.329, SBC: 2150.479, Hannan Quinn: 2145.045
SARIMA(0,0,0)(0,1,1): $\boldsymbol{X_t = -4.156 + 0.986\varepsilon_{t-12} + \varepsilon_{t-12}}$
SAIC: 2300.066, SBC: 2312.562, Hannan Quinn: 2305.138
SARIMA(0,0,0)(2,1,0): $\boldsymbol{X_t = -13.32 - 0.6636X_{t-12} - 0.04292X_{t-24} + \varepsilon_{t-24}}$

SAIC: 1959.755, SBC:1971.634, Hannan Quinn: 1964.582

SARIMA(0,0,0)(0,1,2): $\boldsymbol{X_t = -3.375 + 0.8473\varepsilon_{t-12} + 0.0752\varepsilon_{t-24} + \varepsilon_{t-24}}$

SAIC: 2301.943, SBC: 2317.563, Hannan Quinn: 2308.283.

Table4.9

Forecasts from SARIMA (0,0,0)(2,1,0) for twelve months of the relative humidity series.

		95% Limits	
Period(year)	**Forecast**	**Lower**	**Upper**
January 2016	1455.96	1032.91	1879.01
February 2016	1853.96	1430.91	2277.01
March 2016	1945.94	1522.89	2368.99
April 2016	2304.31	1881.26	2727.36
May 2016	2329.23	1906.24	2752.34
Jun 2016	2463.02	2039.97	2886.07
July 2016	2575.63	2152.58	2998.68
August 2016	2464.15	2041.10	2887.19
September 2016	2478.46	2055.41	2901.51
October 2016	2142.89	1719.84	2565.94
November 2016	1598.61	1175.56s	2021.66
December 2016	1440.02	1015.96	1863.06

Fig6 : Time Series Plot Including Forecasts For SARIMA(0,0,0)(2,1,0)

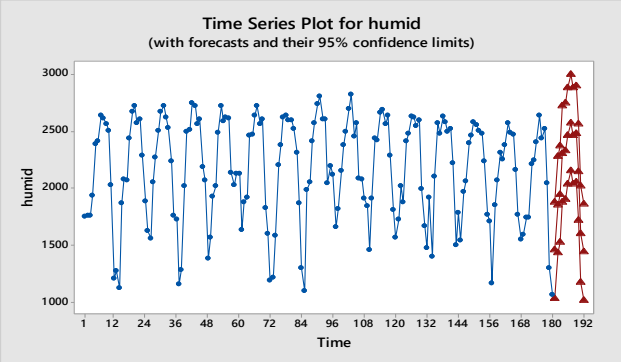

Fig 7: ACF of the model residuals

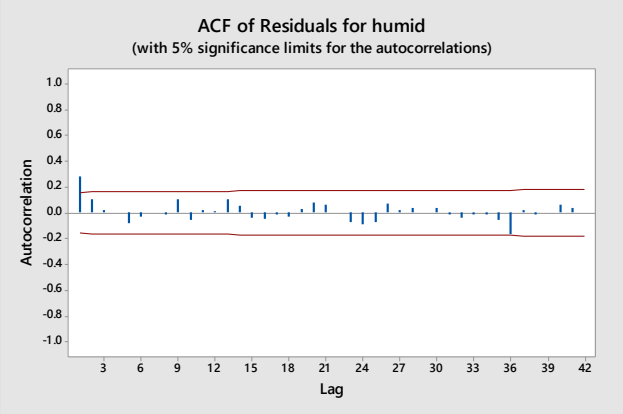

Fig 7: PACF of the model residuals

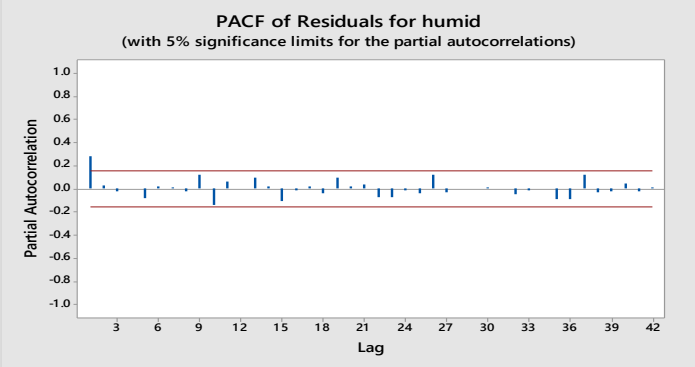

5.1 **Discussion of Results**

The following discussion are deduced from the results of the tables and figures presented in Chapter four. From Fig1 (Time plot of humid) and Fig2 in chapter four above, the pattern shown exhibit a seasonal variation with a slight dawn ward trend. Fig3 shows combination of four plots of residuals of the relative humidity data. The normal probability plot and Histogram from the figure shows that the errors are normally distributed. Also the figure show the scatter plot of the residual versus fitted value and the time plot of the residual versus the observation order.

Dickey and fuller have shown that under the null hypothesis $H0$: $\delta = 0$, the estimated t value of the coefficient is not asymptotically normally distributed but rather follow the (tau) statistic. If the hypothesis is rejected, we can still use the student t's distribution. The DF test of unit root test is estimated in three forms under the null hypothesis. (1) Test for unit root $\nabla y_t = \delta y_{t-1} + \mu_t$ (2) Test for unit root with drift $\nabla y_t = a_0 + \delta y_{t-1} + \mu_t$ (3) Test for unit root with drift and deterministic in time trend $\nabla y_t = a_0 + a_1 t + \delta y_{t-1} + \mu_t$
Each version of the test has its own critical value which depends on the size of the sample. In each case, the null hypothesis is that there is a unit root, δ=0. The test have a low statistical power in that they often cannot distinguish between true unit-root processes (δ= 0) and near unit root test processes (δ is close to zero). This called "near observation equivalence" problem.
The augmented Dickey fuller test is conducted to correct for auto correlation in the error term if it is present in the data. From Test results, presented in the table above, it indicate that the null hypothesis stating that the relative humidity series contain unit root has to be rejected. That is, the p-value is less than conventional significance levels α =0.05 and 0.01 (See tables 4.1 and 4.2)

The autocorrelation plot show how values of the series are correlated with past values of the series. These plots are called autocorrelation functions because they show the degree of correlation with past values of the series as a function of the number of periods in the past (that is, the lag) at which the correlation is computed.
By examining these plots, we can judge whether the series is *stationary* or *nonstationary*. In this case, a visual inspection of the autocorrelation function plot indicates that the relative humidity series exhibit characteristic of no stationary as we increase the lag value, since the ACF decays very slowly. For more formal stationarity tests, is carried out. From fig4 the ACF and PACF show spikes at different levels at lag k making it difficult to determine the order of the seasonal model. The data is serially correlated because the autocorrelation coefficient for lag k=1 is higher than the upper 95% confidence interval limit of the autocorrelation function (See Fig4).
To fit a suitable model to the monthly relative humidity data, we have confirmed the stationarity of the data but the data appears to have seasonal variations and that is why we have seasonally differenced the data to adjust for such variations before proceeding with the model fitting (See Fig5)

From the ACF and PACF plot of the differenced series in chapter four above we can choose plausible models that can best describe the monthly relative humidity data.

A Seasonal Autoregressive Integrated Moving Average (SARIMA) model is appropriate for this work, since the monthly relative humidity data is a seasonal data. Thus, we determine the parameters of the model

We can now build plausible models (five in this case) to describe the monthly relative humidity data. The five models are: SARIMA $(0,0,0)(1,1,1)_{12}$, SARIMA $(0,0,0)(1,1,0)_{12}$, SARIMA $(0,0,0)(0,1,1)_{12}$, SARIMA $(0,0,0)(2,1,0)_{12}$and SARIMA $(0,0,0)(0,1,2)_{12}$

Five models have been fitted and we have selected the best model using the AIC, Schwarz criterion and Hannan-Quinn goodness of fit criterion. The smaller the model's AIC, Schwarz criterion and Hannan-Quinn the better the model. We therefore choose model with the least information criterion: SARIMA $(0,0,0)(2,1,0)_{12}$ (See Fig 6)

The estimated SARIMA(0,0,0)(1,1,1) Model for relative humidity shows that the seasonal autoregressive estimate (SAR) and the constant are not significant at 5% level of significance since the p-value = 0.653 for SAR and 0.070 for the constant is greater than the conventional significance levels α =0.05. While the seasonal moving average is significant at 5% level of significance with p-value <0.0001. The AR model at lag 12 is $\boldsymbol{X_t = -4.056 + 0.413X_{t-12} + \varepsilon_t}$while the MA model at lag 12 is $\boldsymbol{X_t = -4.056 + 0.9104\varepsilon_{t-12} + \varepsilon_{t-12}}$and the general estimated model at lag 12 is:

SARIMA (0,0,0)(1,1,1) is:$\boldsymbol{X_t = -4.056 + 0.413X_{t-12} + 0.9104\varepsilon_{t-12} + \varepsilon_{t-12}}$

The χ^2test statistics for the residuals series indicate whether the residuals are uncorrelated (white noise) or contain additional information that might be utilized by a more complex model. In this case, the test statistics reject the no-autocorrelation hypothesis at a high level of significance. (p=0.006 for the first twelve lags.) This means that the residuals are not white noise, and so the AR(1) model is not a fully an adequate model for this series at lag twelve (See table 4.3)
The estimated SARIMA(0,0,0)(1,1,0) Model for relative humidity shows that the seasonal autoregressive estimate (SAR) is significant at 5% level of significance since the p-value = <0.001. while the constant is not significant with p-value= 0.509 The AR model is $\boldsymbol{X_t = -11.87 - 0.4922X_{t-12} + \varepsilon_{t-12}}$

As stated earlier in table3, the χ^2test statistics for the residuals series indicate whether the residuals are uncorrelated (white noise) or contain additional information that might be utilized by a more complex model. In this case, the test statistics reject the no-autocorrelation hypothesis at a high level of significance. (p=0.020, 0.003, 0.021, 0,040 for all lags.) This means that the residuals are not white noise, and so the AR(1) model is not an adequate model for this series at all specified lag (See table 4.4)
The estimated SARIMA (0, 0, 0)(0,1,1) Model for relative humidity shows that the seasonal moving average (SMA) is significant at both lags 12 and 24 at 5% level of significance with p-value <0.0001. While the constant is not significant with p-value= 0.125 The MA model is$\boldsymbol{X_t = -4.156 + 0.986\varepsilon_{t-12} + \varepsilon_{t-12}}$

Just like table4, the χ^2test statistics for the residuals series indicate whether the residuals are uncorrelated (white noise) or contain additional information that might be utilized by a more complex model. In this case, the test statistics reject the no-autocorrelation hypothesis at a high level of significance. (p=0.008, for the first twelve lags.) This means that the residuals are not white noise, and so the MA(1) model is not fully an adequate model for this series at lag twelve (See table 4.5)

The estimated SARIMA (0,0,0)(2,1,0) Model for relative humidity shows that the seasonal autoregressive estimate (SAR) is significant at both lags 12 and 24, at 5% level of significance since the p-value <0.0001 while the constant is not significant with p-value =0.425. The AR model is $\boldsymbol{X_t = -13.32 - 0.6636X_{t-12} - 0.04292X_{t-24} + \varepsilon_{t-24}}$

Similarly, the χ^2test statistics for the residuals series here, indicate whether the residuals are uncorrelated (white noise) or contain additional information that might be utilized by a more complex model. In this case, the test statistics reject the no-autocorrelation hypothesis at a high level of significance. (p=0.019, for the first twelfth lags.) This means that the residuals are not white noise, at lag 12 and so the AR (2) model is not fully an adequate model for this series at lag twelve (See table 4.6)

The estimated ARIMA(0,0,0)(0,1,2) Model for relative humidity shows that the seasonal moving average (SMA) is significant at lag 12, at 5% level of significance with p-value <0.0001. While at lag 24 the SMA model and the constant are not significant with p-value= 0.361 and 0.150 for the constant. The MA model is$\boldsymbol{X_t = -3.375 + 0.8473\varepsilon_{t-12} + 0.0752\varepsilon_{t-24} + \varepsilon_{t-24}}$

Similarly, the χ^2 test statistics for the residuals series indicate whether the residuals are uncorrelated (white noise) or contain additional information that might be utilized by a more complex model. In this case, the test statistics reject the no-autocorrelation hypothesis at a high level of significance. (p=0.009, for the first twelve lags.) This means that the residuals are not white noise, and so the MA(2) model is not fully an adequate model for this series at lag twelve (see table4.7).

Goodness-of-Fit Statistics for AR(p) Model

The "Constant Estimate" is a function of the mean term MU and the autoregressive parameters. This estimate is computed only for AR or ARMA models, but not for strictly MA models. The "Variance Estimate" is the variance of the residual series, which estimates the relative humidity variance. The item labeled "Std Error Estimate" is the square root of the variance estimate. In general, when comparing candidate models, smaller AIC, SIC and Hannan-Quinn statistics indicate the better fitting model. The section "Estimation Details" of the model estimate base on their AIC, SBC and Hannan-Quinn statistics, is summarized in table8 below.

Summary

From the estimates statement for the models given above we choose SARIMA$(0,0,0)(2,1,0)_{12}$ as the best model Since it possesses the minimum value information criterions. Thus we suggest the model for forecasting relative humidity series.

Conclusion

This research, in the course of modelling average relative humidity of Bida, entertains five models. Out of the models, SARIMA $(0,0,0)(2,1,0)_{12}$ was chosen as the best model on basis of AIC, SIC and H.Q criteria.

Recommendation

Selected SARIMA $(0,0,0)(2,1,0)_{12}$ is recommended for forecasting relative humidity of Bida. The research is also suggested to be extended to other metrological data.

References

Alvisi, S., Franchini, M., & Marinelli, A. (2007). A short-term, pattern-based

Analysis. Newberry Park: Sage, p. 80, 83, 312–318. Data are used with permission of

Andason, D., & Hall, R. (1981). *Introduction to Statistics: An Application*

Approach. Minnesota: West Publish Company.

Association **65,** pp. 332, 1509–1526.

Bartlett, M. S. (1966). *An Introduction to Stochastic Processes*, (2nd Edition). Cambridge, London: Cambridge University Press.

Biometrika **65**(2), 297–303.

Bolarinwa, I.A (2005). A comparism of forecasting Accuracy of three University Methods on meteorological data. *Nigeria journal of applied acts Science (NJAAS), 1, 30-37*

Bougadis, J., Adamowski, K., & Diduch, R. (2005). Short-term municipal water
Bougadis, J., Adamowski, K., &Diduch, R. (2005). Short-term municipal water
Box, G. E. P., & Jenkins, G. M. (1976). *Time Series Analysis: Forecasting and Control*. San Franciso: Holden-Day.
Box, G. E. P., and Pierce, D. A. (1970). ‘‘Distribution of Residual Autocorrelations in Autoregressive-
Box, G. E., Jenkins, G., and Reinsel, (1994). *Time Series Analysis: Forecasting and Control*,
Bruce, J. P., & Clark, R. H. (1966). *Introduction to Hydrometeorology*, Oxford,
C. F. Kettering (1949). 2020 Vision Seeing the Future (1999). World Wide Web URL: http://
Chang, Ih, Tiao, G. C., and Chen, C. (1988). ‘‘Estimation of Time Series Parameters in the
Chatfield, C. (1982). The Analysis Time series an introduction (2nd ed). Nesw York: Chapman and Hall.

MODELLING MEAN SURFACE TEMPERATURE OF NIGERIA, USING GEOSTATISTICAL APPROACH

A. Isah[1] , G. Y. Attah[2], U. Abdullahi[1] and A. Usman[1]

[1]Department of Statistics, Federal University of Technology, Minna

[2]Department of Statistics, Ahmadu Bello University, Zaria

[1]aisah@futminna.edu.ng, [1]u.abdullahi@futminna.edu.ng

Abstract

Understanding spatial variability of mean surface temperature (MST) of Nigeria is necessary for ecological restoration and national planning toward effects of unstable climate conditions. This study aimed to develop MST model derived from two geostatistical procedures and multiple linear regression (MLR) model using measurements of monthly MST in Nigeria. The geostatistical models includes ordinary kriging (OK) developed in two dimensions with isotropy and in three dimensional plane with anisotropy and regression kriging (RK) that employs both correlation with explanatory variables and spatial autocorrelation simultaneously. Six statistics were considered to evaluate the performance of the approaches used. The results revealed that in the fitted MLR model all the predictors are significant and the model explains 62% variability in the MST values. The one-leave-out cross-validation indicates that RK produced less errors compared to OK model with R^2 value of 78%. The OK with zonal anisotropic shows that the spatial continuity in the directions of north and north east are stronger than in the directions of east and south east at a distance of 930 kilometres and 460 kilometres respectively. The kriging weights for OK and RK were similar as shown in the maps.

Keywords: Geostatistical models, multiple linear regression, anisotropy and model performance.

1. Introduction

When we speak of temperature of an object, we often associate this concept with how hot or cool the object feels. Scientifically, temperature is a property of an object that decides the direction of flow of energy of the object when being encountered with another object. Temperature measurements were dated back to 1600 by Galileo and compatriot, Santario. Temperature measuring instruments varies, depending on the size, nature and the position of the body on the planet earth. According to National Aeronautics and Space Administration (NASA) Goddard Institute for Space Studies Scientists (2016)," *the average temperature for 2006 and 2009 tie with 2013, being the seventh warmest years since 1880".* (NASA) further emphasized that the weather pattern will cause drastic change in climate which resultant effect could bring about poor production and

extinction of plants and animals. Therefore, it is necessary for a developing country like Nigeria to have a geostatistical model that is capable of predicting future temperature values at locations where surface temperature readings has not been measured, using data from the surrounding weather stations.

Surface temperature is an important site characteristic used in determining site suitability for agricultural and forest crops (Hudson and Wackernagel, 1994), and it is used in parameterizing the habitat of plant species (Rubio *et al.*, 2002) and in determining the patterns of vegetational zonation (Richardson *et al.*, 2004). Moreover, surface temperature is a factor related to plant productivity, as it is connected with the length of the vegetative period and evapotranspiration.

Different interpolation methods have been used to model the spatial distribution of surface temperature; the most widely used being the inverse distance interpolation weighting, Voronoi tessellation, regression analysis and more recently, geostatistical methods (Hengl, 2009). Lapen and Hayhoe (2003) compared inverse distance weighting to geostatistical methods ordinary kriging (OK) and cokriging, and ordinary kriging with kriging with external drift (OKED)) to spatially model the seasonal and annual temperature and total precipitation normals in the Great Lakes (Ontario, Canada); Hudson and Wackernagel (1994) mapped air temperature of Scotland using ordinary kriging with external drift; and Ishida and Kawashima (1993) used different kriging estimators, specially cokriging estimators, to evaluate the usefulness of these approaches in temperature modelling in Japan. Isah (2011) used multiple linear regression and cokriging procedure for joint modeling and prediction of wind speed and wind in Nigeria.

The main objective of this study is to develop MST model derived from geostatistical and multiple linear regression (MLR) models using four years of measurements of monthly MST in Nigeria.

2. Study Area and Geostatistical methods

2.1 Study area and Data Used

Nigeria with an area of 909,890 square kilometres is situated between Latitude 4^0 and 14^0 North and between Longitude 3^0 and 14^0 East. The longest distance from East to West is about 767 kilometres and from North to South 1,605 kilometres NBS, (2009). Nigeria is also blessed with favourable and varied climatic conditions. NBS (2009) reported eleven climatic conditions in Nigeria of which this study covers four out of the eleven; namely; mean surface temperature, relative humidity, mean radiation and evaporation. Temperature in Nigeria vary according to the seasons of the year as with other lands found in the tropics. Nigeria's seasons are

determined by rainfall with rainy season and dry season being the major seasons in Nigeria (http://www.nigeria-weather.com).

The study covers readings of average surface temperature by Meteorological and Hydrological service stations in Nigeria as contained in annual reports of National Bureau of Statistics (NBS), 2009. The data is used to model mean surface temperature as a function of mean relative humidity, mean radiation, elevation, evaporation, distance of state capitals of Nigeria to Lagos (nearby ocean/sea), longitude and latitude (position of each of the monitoring stations).

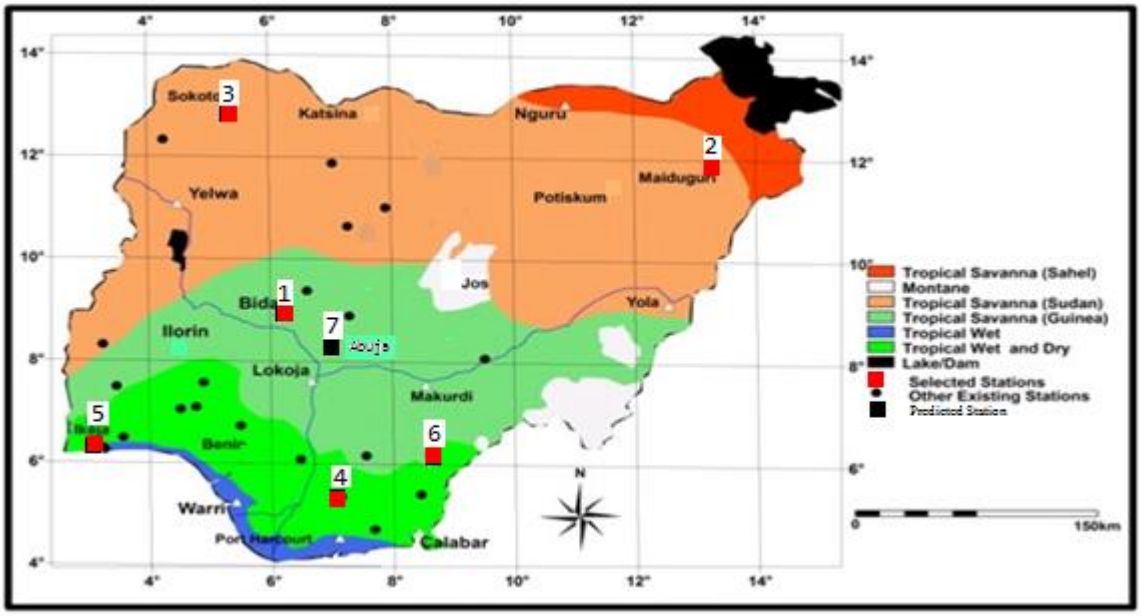

Figure 1: Map of Nigeria showing the locations of meteorological stations

2.2 Geostatistical Methods

Geostatistics is a valuable tool that can be used to characterize spatial, temporal or spatiotemporal phenomena. That is, each data value is associated with a location in space and there is at least an implied connection between the location and the data value. Location here could have two different meanings: One is simply a point in space which only exists in an abstract mathematical sense while the second is an area or volume in space (average value of an observed value).

2.2.1 Experimental Variogram

The experimental variogram measures the average degree of dissimilarity between un-sampled values and a nearby data value and consequently can depict autocorrelation at various distances (Robinson and Metternicht, 2006):

$$2\hat{\gamma}(h) = \frac{1}{N(h)} \sum_{i=1}^{N(h)} [z(x_i) - z(x_i + h)]^2 \quad (1)$$

where $N(h)$ is the number of data pairs with a given class of distance and direction.

If the values at $z(x_i)$ and $z(x_i + h)$ are auto-correlated, the result of equation (1) relative to an uncorrelated pair of point will be small. Using an analysis of the experimental variogram, a suitable model (Gaussian, linear, exponential or spherical) is fitted. This is made using weighted least square and relevant parameters of the covariance structure (range, nugget and sill) are then used in the kriging procedure.

Once the variogram model is estimated, it is used to derive semivariances at all locations and solve the kriging weights. The kriging weights are derived from a statistical model of spatial correlation expressed as semivariograms that characterized the spatial dependency and structure in the data. The OK weights are solved by multiplying the covariance:

$$\lambda_o = c^{-1} v_o \,;\; c(|h| = 0) = c_o + c_1 \quad (2)$$

where c is the covariance matrix derived for $n \times n$ observations and v_o is the vector of covariance's at a new location (Hengl, 2009). The solution to the minimization, constrained by unbiasedness, gives the kriging equations (Hengl, 2009):

$$\Gamma^{-1} * \ell = \lambda \quad (3)$$

$$\begin{bmatrix} c(s_1, s_1) & \cdots & c(s_1, s_n) & 1 \\ \vdots & & & \vdots \\ c(s_n, s_1) & \cdots & c(s_n, s_n) & 1 \\ 1 & \cdots & 1 & 0 \end{bmatrix}^{-1} \begin{bmatrix} c(s_o, s_1) \\ \vdots \\ c(s_0, s_n) \\ 1 \end{bmatrix} = \begin{bmatrix} w_1(s_o) \\ \vdots \\ w_n(s_o) \\ \varphi \end{bmatrix} \quad (4)$$

where φ is the so-called Lagrange multiplier.

2.2.2 Ordinary Kriging (OK)

A standard version of kriging is called ordinary kriging (OK). Here the predictions are based on the model :

$$T(s) = \mu + \varepsilon(s) \quad (5)$$

where μ is the constant stationary function and $\varepsilon(s)$ is the spatially correlated stochastic part of variation.

The ordinary kriging prediction of $T(s)$ at location s_o is given by the following equation:

$$\hat{T}_{OK}(s_o) = \sum_{i=1}^{n} \lambda_i(s_o) T(s_i) \quad (6)$$

where λ_i is an unknown weight for the measured value at the ith location, s_o is the prediction location so that the estimation of error variance in equation (7) is minimised, under the constraint of unbiasedness of the estimator equation (8).

$$\sigma_E^2 = Var[\hat{T}(s_o) - T(s_o)] \quad (7)$$

$$\sum_{i=1}^{n} \lambda_i = 1 \quad (8)$$

2.2.3 Ordinary kriging with Zonal Anisotropy.

When observations are available at all directions and specified distances, the anisotropy may be modelled directly from the directional experimental variogram model (Hengl, 2009). When elevation is included in the kriging system the directional variograms show zonal anisotropy. Both directional variograms were modelled as the sum of an isotropic Gausian variogram and an Exponential variogram for the Z-axis, which constitutes a valid model:

$$\gamma(d) = \gamma_{Gausian}(X, Y, Z) + \gamma_{\text{Exponential}}(Z) \quad (9)$$

Ordinary kriging is carried out calculating the sum variogram for each pair of observations for prediction point. All pairs of locations forming an angle with the horizontal greater than 3.29km were selected to calculate the directional variogram for the Z-axis, whereas those pairs of locations forming an angle with the horizontal smaller than 2.19km, and with elevation difference no greater than 840m, were selected to calculate the XY variogram. For each lag, the vertical component of the distance was averaged across all pairs of observations, both in the XY plane and in the Z direction variogram.

2.2.4 Regression Kriging (RK).

Matheron (1969) proposed that a value of a target variable at some location can be modelled as a sum of deterministic and stochastic components with the model below:

$$Z(s) = m(s) + \varepsilon(s) + \varepsilon' \quad (10)$$

where $m(s)$ is deterministic part, $\varepsilon(s)$ is spatially correlated stochastic component and ε' is the error term, which he called the universal model of spatial variation, that both deterministic and stochastic components of spatial variation can be modelled separately.

Hengl (2009) proposed another approach in which he combined; OK and simple linear regression model (SLR) and called it RK with the predictor:

$$\hat{Z}(s_o) = b_o + b_1 q_1 + \sum_{i=1}^{n} \lambda_i(s_o) e(s_i) \qquad (11)$$

where Z is the target variable at sampled location s_o, b_o is the estimated intercept, b_1 is the regression coefficient, q_1 is the explanatory variable, and $\lambda_i's$ are the kriging weights determined by spatial dependence structure of the residual and $e(s_i)$ is the residual at location s_i.

The regression coefficient b_1 can be estimated from the sample by using: either ordinary least squares (OLS) or Generalized Least Squares (GLS) (Cressie, 1993):

$$\hat{b}_{GLS} = (q^t c^{-1} q) q^t c^{-1} z \qquad (12)$$

where $\hat{b}_{GLS}$ is the vector of estimated regression coefficients, c is the covariance matrix of residuals, q is the matrix of auxiliary variables at sampled locations and z is vectors of measured values of the target variable.

2.2.5 Multiple Linear Regression (MLR) Model

A common regression-based approach to spatial prediction is multiple linear regression (Draper and Smith, 1998; Kutner *et al*., 2004). Here, the predictions are obtained by weighted averaging:

$$\hat{Z}_{GLS}(s_o) = \hat{b}_o + \hat{b}_1 q_1(s_o) + \cdots + \hat{b}_p q_p(s_o) = \sum_{k=0}^{p} \hat{b}_k q_k(s_o) \qquad (13)$$

where $q_k(s_o)$ are the values of the explanatory variables at the target location, *p* is the number of predictors or explanatory variables, and $\hat{b}_k$ are the regression coefficients solved using the

Ordinary Least Squares Hengl (2009):

$$\hat{b} = (q^t q)^{-1} q^t z \qquad (14)$$

where q is the matrix of predictors $(n \times p+1)$ and z is the vector of sampled observations.

3.1 Proposed Mean Surface Temperature (MST) Model

The proposed model is a combination of multiple linear regression (MLR) model as in equation (13) and the second part of RK model in equation (11). The predictors are given by:

$$\hat{T}(S_i) = \sum_{k=0}^{P} b_K q_K(S_i) + \sum_{i=1}^{n} \lambda_i(S_0) e(S_i) \tag{15}$$

where $q_K(S_i)$ are the values of explanatory variables at sampled locations, P is the number of explanatory variables, λ_i is the kriging weights, $e(S_i)$ is the residual at location S_i and b_K is the regression coefficients solved using generalised least squares (GLS) Cressie (1993).

$$\hat{b}_{GLS} = (q^t c^{-1} q) q^t c^{-1} z \tag{16}$$

The mean surface temperature (MST) at the unmonitored locations is given by equation (17)

$$MST(S_o) = b_o + b_1 MRH(S_o) + b_2 LAT(S_o) + b_3 DIST(S_o) + b_4 LONG(S_o)$$

$$+ b_5 ELEV(S_o) + b_6 EVAP(S_o) + b_7 EMRAD(S_o) + \sum_{i=1}^{6} \lambda_i e(S_i) \tag{17}$$

Where MRH mean relative humidity, ELEV denote elevation, MRAD denote mean solar radiation, EVAP denote evaporation and DIST denote distance to the nearby sea or ocean.

3.2 Relationship of Regression Kriging to Multiple Linear Regression

If the residuals show no spatial autocorrelation (pure nugget effect), the Regression Kriging converges to pure MLR equation (13) because the covariance matrix (C) becomes identity matrix (Hengl, 2009):

$$\begin{bmatrix} C_0 + C_1 & \cdots & 0 \\ \vdots & C_0 + C_1 & 0 \\ 0 & 0 & C_0 + C_1 \end{bmatrix} = (C_0 + C_1)\mathrm{I} \tag{18}$$

So the kriging weights in equation (2) at any location predict the mean residual zero. Similarly, the regression kriging variance (20) reduces to the MLR Variance.

$$\hat{\delta}^2_{RK}(S_0) = (C_0 + C_1) - 0 + X_0^t \left(X^t \frac{1}{(C_0 + C_1)} X \right)^{-1} X_0$$

$$\hat{\delta}^2_{RK}(S_0) = (C_0 + C_1) + (C_0 + C_1) X_0^t \left(X^t X\right)^{-1} X_0 \quad (19)$$

And since $(C_0 + C_1)$ = C(0) = MSE, the RK variance reduces to MLR variance (Hengl, 2009):

$$\hat{\delta}^2_{RK}(S_0) = \hat{\delta}^2_{OLS}(S_0) = MSE\left[1 + X_0^t \left(X^t X\right)^{-1} X_0\right] \quad (20)$$

3.3 Relationship of Regression Kriging to Ordinary Kriging

If the target variable shows no correlation with the explanatory variables, the regression kriging model reduces to the ordinary kriging model because the deterministic part is equal to the global mean.

$$\hat{T}(S_0) = \mu_k = \frac{1}{n_k} \sum_{i=1}^{n_k} T(S_i) \quad (21)$$

Also from equations (6) and (11)

$$T_{RK}(S) = \mu + \mathrm{K(S)} = \mathrm{T_{OK}}(S) \quad (22)$$

From the above, it implies that:

$$M(S) + e = \mu \quad (23)$$

3.4 Model Validation

The common validation method in climatological studies has been variously termed as cross validation (Nalder & Wein, 1998). Cross validation (leaving-one-out method) is based on removing one data point at a time and performing the interpolation for the location of the removed point using the remaining samples. At the final step of cross validation, the difference (residual) between observed and predicted values of the point are calculated. The leaving-one-out approach is repeated until every sample has been, in turn, removed (Davis, 1987) and estimates are calculated for each point. The overall performance of each kriging method is calculated using mean prediction error (MPE), mean standard prediction error (MSPE), average kriging standard error (AKSE), Root mean square prediction error (RMSPE), root mean square standardized prediction error (RMSSPE) and R^2:

$$MPE = \frac{1}{N} \sum_{k=1}^{n} \left(T_{OK} - T_{PK}\right) \quad (24)$$

$$MSPE = \frac{1}{N}\sum_{k=1}^{n}\frac{(T_{0K} - T_{PK})}{\delta(K)} \quad (25)$$

$$AKSE = \left[\frac{1}{N}\sum_{k=1}^{n}\delta(K)\right]^{\frac{1}{2}} \quad (26)$$

$$RMSPE = \left[\frac{1}{N}\sum_{k=1}^{n}(T_{OK} - T_{PK})^2\right]^{\frac{1}{2}} \quad (27)$$

$$RMSSPE = \left[\frac{1}{N}\sum_{k=1}^{n}\frac{(T_{OK} - T_{PK})^2}{\delta(k)}\right]^{\frac{1}{2}} \quad (28)$$

$$R^2 = \frac{\sum(T_P - T_m)^2}{\sum(T_O - T_m)^2} \quad (29)$$

where T_P is the predicted values of temperature, T_O is the observed values of temperature, T_m is the mean values of temperature, p is the total number of explanatory variables, n is the sample size, T_{OK} is the observed temperature at location K, T_{PK} is the predicted temperature at location K through ordinary kriging, N is the number of pairs of observed and predicted values and δ(K) is the prediction standard error at location K.

As an indicator of prediction error, the MPE and MSPE values reveal the degree of bias in model prediction and should be close to zero. Assessment of variability in prediction, the RMSPE and AKSE values show the precision of predictions and should be equal to one another. In other words, the RMSPE reveals the level of scatter that a model produces and provides a comparison of the absolute deviation between the predicted and the observed values. The lower the RMSPE values, the better a model is indicated to perform. Over estimation of variability occurs when AKSE > RMSPE and under estimation occurs when AKSE < RMSPE.

4. Results and Discussion

This study used observations from six different locations which was used to carry out all the analysis. The location seven (7) in the study was not monitored, however, the MST was predicted for location (7) using information from the other six (6) locations.

4.1 Preliminary Statistical Analysis

To develop mean surface temperature (MST) model using geostatistics procedures, the MST values were tested for normality by inspection of autocorrelation and histogram plots as in Figure 8. Looking at autocorrelation plot on MST values, it shows that the temperature values are spatially auto correlated and therefore possible to predict the value at one location based on the value sampled from a nearby location. Histogram plot with a normal density superimposed also shows that the MST distribution does not deviate too severely from normality.

4.2 Regression models

The relationship between MST and explanatory variables in the OLS regression models were fitted using equation (13) and the result presented n Table 1. The result shows that MRH and ELEV have negative contributions while, MRAD, EVAP and DIST have positive contributions to the MLR model. Although, the coefficients are significant and explained 62% of variability in the MLR model. A further question of interest is whether any of the observations greatly affect the estimates. The MLR fits to the full dataset and produce a set of four plots: residuals versus fitted values, a Q-Q plot of standardized residuals, a scale-location plot (square roots of standardized residuals versus fitted values, and a plot of residuals versus leverage that adds bands corresponding to Cook's distances figure 2. Cooks distance is a measure of how much the estimate changes as each observation is dropped. It was found that 62, 74 and 99 were outliers and after dropping the three outliers the MLR fitted is given in Table 1:

Table1: Result of Multiple Linear Regression (MLR) model of MST for the Selected Stations

Explanatory variables in MLR model	Estimate	Std. Error	t value	Pr(>|t|)
(Intercept)	27.852	3.941	7.395	1.15e-11
Longitude (decimal degree)	0.114	0.076	-1.696	0.0022
Latitude (decimal degree)	0.033	0.059	-0.385	0.0015
MRH	-0.006	0.020	-0.322	0.0028
MRAD	0.204	0.164	1.684	3.43e-05
ELEV	-0.003	0.001	-4.280	0.0044
EVAP	0.564	0.480	1.175	6.030e-10
DIST	0.001	0.001	1.1917	0.0005

All the variables are significant at *p≤0.05. Adjusted* R-squared: 0.6213, Residual standard error = 1.811, F-statistic: 4.864 on 6 explanatory variables and *p-value*: 0.0001515.

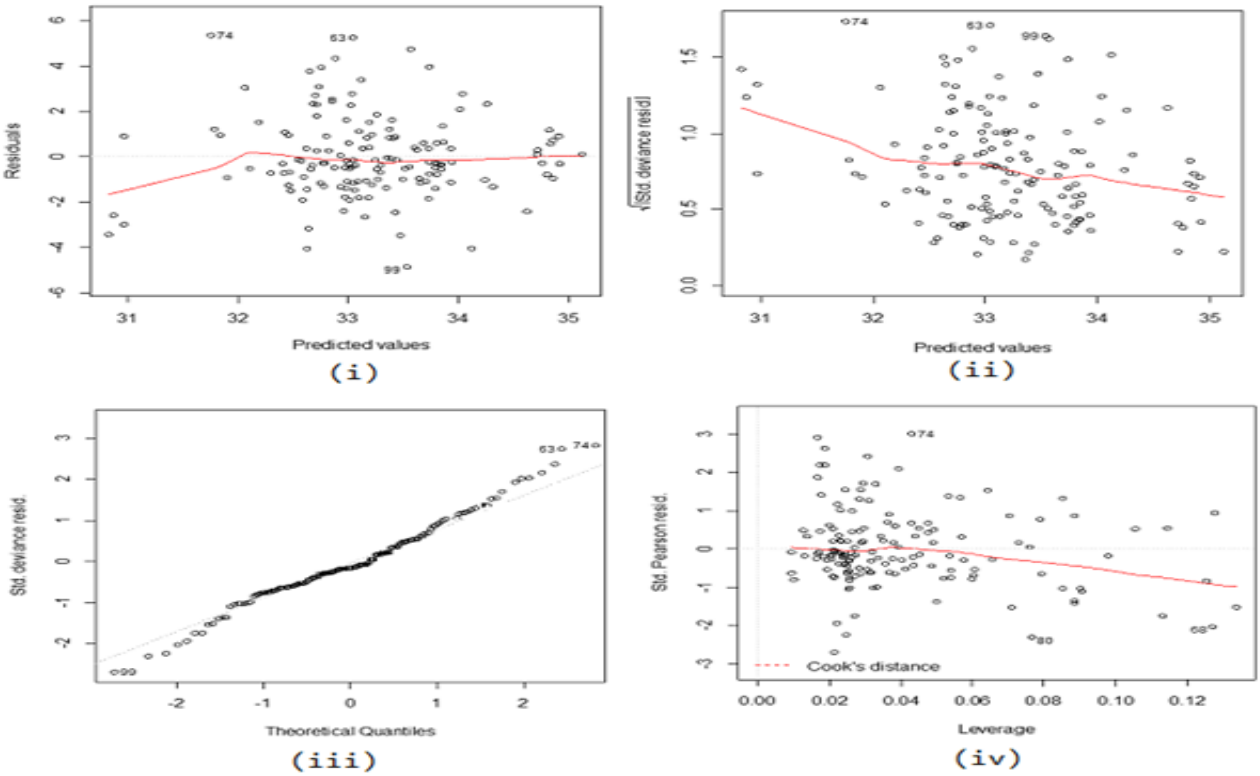

Figure 2: Residual scatter plot of the outliers (i) residuals versus fitted values, (ii) scale location plot (square roots of standardized residuals versus fitted values, (iii) Q-Q plot of standardized residuals, and (iv) plot of residuals versus leverage**.**

4.3 Results of Geostatistical Models

In order to fit the kriging model, it is sufficient to fit the variogram for the residuals. The parameters for the fitted theoretical variogram models are shown in Table 2. The Gaussian model explained the highest variability of (R^2 = 63%) of the fitted isotropic variogram model for MST; while exponential model explained the highest variability of 51% in the MST values of the fitted anisotropic variogram models. The Gaussian and exponential models were therefore chosen as the most reliable models for interpolating MST and used for the final map productions. The two models had the smallest residual sum of squares (RSS), which indicated a tight fit of the models to the MST distributed around 2.03 and 57.4 values respectively.

Table 2: Parameters for the fitted theoretical variogram models for MST

Isotropic Variogram						
Model Type	**Nugget Variance (C_0)**	**Structural Variance Sill(C_0+C)**	**Range (A)**	**Residual SS**	**R^2**	**Proportion (C/[(C_0+C)])**
Linear	0.827	1.906	6.355	3.950	0.277	0.556
Spherical	0.001	1.717	3.470	2.050	0.628	0.999

Exponential	0.001	1.749	4.020		2.260	0.608	0.999
Gaussian	0.062	1.676	2.355		2.030	0.629	0.963
Anisotropic Variogram							
Model Type	**Nugget Variance (C_0)**	**Structural Variance Sill(C_0+C)**	**Range Minor**	**Major**	**Residual SS**	**R^2**	**Proportion (C/[(C_0+C)])**
Linear	1.080	6.251	24.20	75.61	57.80	0.403	0.827
Spherical	0.936	6.106	31.28	72.21	58.40	0.204	0.847
Exponential	1.046	6.217	58.95	206.07	57.40	0.506	0.832
Gaussian	1.358	6.528	21.85	98.62	60.20	0.169	0.792

The fitted experimental variogram of isotropy using Gaussian model, and the four directional variograms in the XYZ plane of anisotropic using exponential model is presented in Table 3. The values of nugget, sill, range, residual sum of square and R^2 with isotropic variogram and with anisotropic variogram are shown in Figures 3 and 4 respectively.

Table 3: Directional variogram with isotropic and anisotropic models for MST

Isotropic Variogram						
Degree	**Nugget Variance (C_0)**	**Structural Variance Sill(C_0+C)**	**Range (A)**		**Residual SS**	**R^2**
	0.001	1.749	1.34		2.26	0.608
Anisotropic Variogram						
Degree	**Nugget Variance (C_0)**	**Structural Variance Sill(C_0+C)**	**Range Minor**	**Major**	**Residual SS**	**R^2**
0^0	1.168	6.338	15.35	15.38	63.60	0.072
45^0	1.245	6.416	11.28	29.80	58.10	0.073
90^0	1.358	6.529	13.77	56.94	60.21	0.069
135^0	0.788	5.959	10.00	10.01	72.90	0.076

In addition, the anisotropic variogram in Figure 4 shows that the spatial continuity in the directions of North with angle 0^0 and North-East with angle 45^0 are stronger than in the directions East with angle 90^0 and South East with angle 135^0. In the North and North East directions, the semivariogram levels off to the sill when it reached a distance of about 930 kilometres. While in the East and South East directions the spatial correlation for the semivariogram are similar except that it levels off earlier at about 460 kilometres.

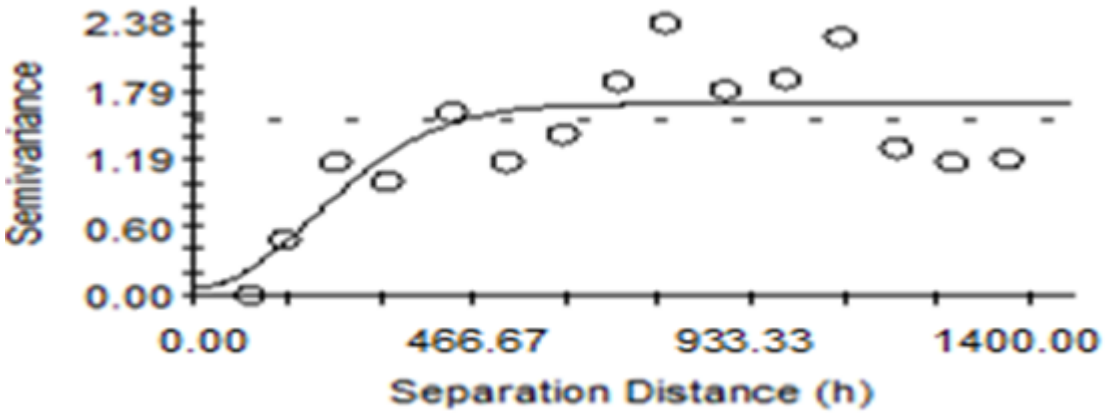

Figure 3: Variogram of fitted isotropic model for MST residuals

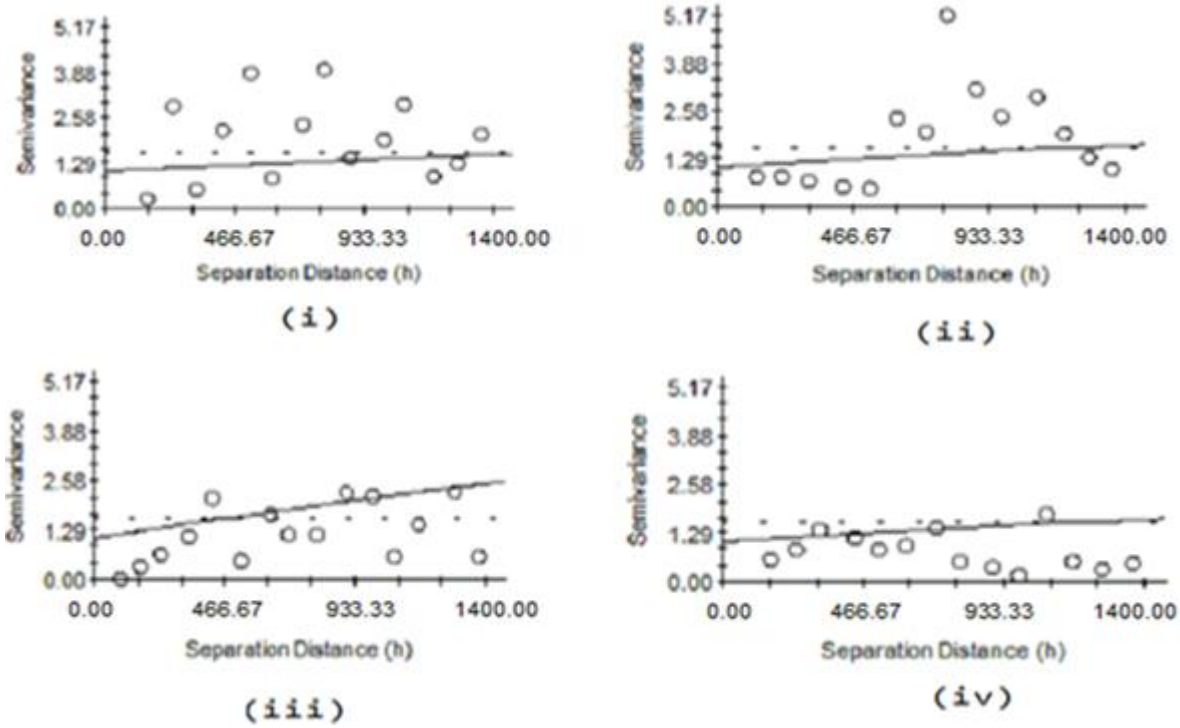

Figure 4: Variogram of fitted anisotropic models of (i) 0^0 (ii) 45^0 (iii) 90^0 and (iv) 135^0 for MST residuals.

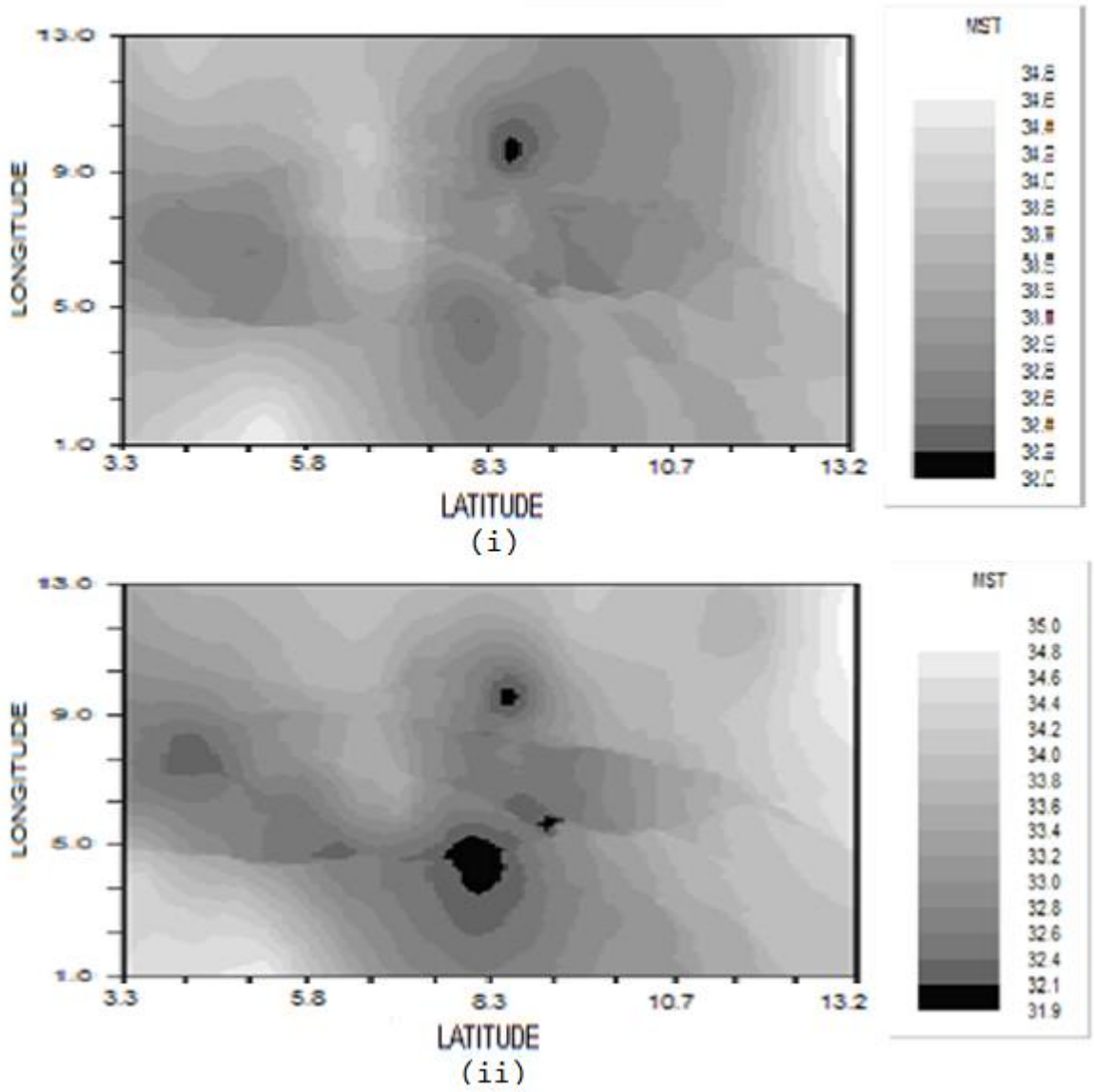

Figure 5: (i) OK and (ii) RK of isotropic variogram using Gaussian model: Spatial prediction of MST

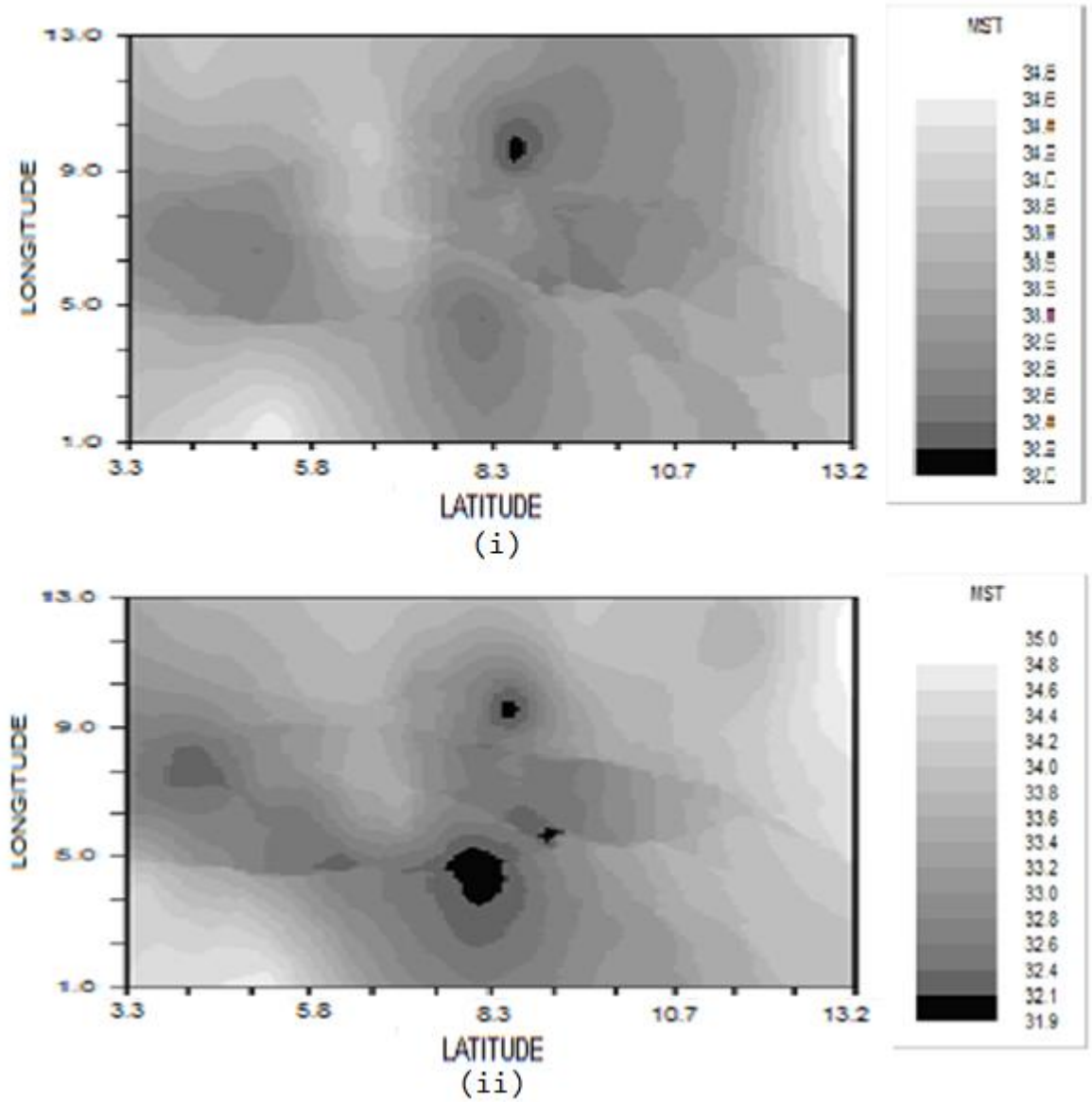

Figure 6: (i) OK and (ii) RK of anisotropic variogram using exponential model: Spatial prediction of MST

For a comparison, the predictions at all locations of OK and RK were compared side-by-side in figures 5 and 6. Visually, there are clear differences in the two maps. It could be observed that low MST predictions occur in the North Central region in OK maps in the model with isotropy and anisotropy as compared to RK models . Since visual comparison may not be enough, the study also used the leave-one-out cross validation method as in (Pebesma, 2004).

4.4 The Semivariogram

To compute the values for the Γ matrix in equation (3), we examined the structure of the data by creating the semivariogram. In a semivariogram, half the difference squared between the pairs of locations of longitude is plotted relative to the distance that separates them:

Table 4: Semivariance of Pairs of Locations

S/N	Pairs of Sampled Locations (MST Value)	Distance	Difference^2	Semivariance
1	L(1, 2) = 57	1055	1	0.5
2	L(1, 3) = 58	537	4	2
3	L(1, 4) = 54	729	4	2
4	L(1, 5) = 54	743	4	2
5	L(1, 6) = 55	1275	1	0.5
6	L(2, 3) = 59	1204	1	0.5
7	L(2, 4) = 55	1331	9	4.5
8	L(2, 5) = 55	820	9	4.5
9	L(2, 6) = 56	891	4	2
10	L(3, 4) = 56	1257	16	8
11	L(3, 5) =56	1050	16	8
12	L(3, 6) = 57	849	9	4.5
13	L(4, 5) = 52	652	0	0
14	L(4, 6) = 53	131	1	0.5
15	L(5, 6) = 53	1110	1	0.5

With larger dataset the number of pairs of locations will increase rapidly and will quickly become unmanageable. Therefore, pairs of locations are grouped, which is referred to as binning. A bin is a specified range of distances. That is, all points that are within 100 to 300 kilometres apart are grouped into the first bin, those that are within 300 to 500 kilometres apart are grouped into the second bin, and so forth.

The average semivariance of all pairs of points is obtained after grouping the observations into bins and result is presented in Table 5.

The semivariance for any distance can be determined by semivariance = 0.907*h.

Table 5: Binning the Semivariance

Lag Distance	Paired Distance	Average Distance	Paired Semivariance	Average Semivar.
100 - 300	131	131	0.5	0.5
300 - 500	0	0	0	0
500 - 700	537, 652	594.5	2, 0	1
700 - 900	727, 743, 820, 849, 891	806	2, 2, 4.5, 4.5, 2,	3
900 -1100	1050, 1055	1052.5	8, 0.5	4.25
1100 - 1300	1110, 1204, 1257, 1275, 1331	1235.4	0.5, 0.5, 8, 0.5, 4.5	2.8

Distance is the distance between pairs of locations and is symbolized as *h*. The semivariance for any distance is determined by:

Γ Matrix (Gamma)

	1	2	3	4	5	6	
1	0						
2	118.817	0					
3	487.059	591.364	0				
4	659.389	673.901	743.740	0			
5	952.350	956.885	956.885	952.350	0		
6	100.677	1092.028	1140.099	1156.425	1207.217	0	
	1	1	1	1	1	1	0

Now the Γ gamma matrix and its inverse are used to obtain weights (λ_i) to assign to the measured values surrounding the prediction location. Thus, the inverse of Γ^{-1} is obtained.

Γ^{-1} Matrix

	1	2	3	4	5	6	
1	0.0025						
2	-0.0016	-0.0002					
3	-0.0001	0.0006	-0.0011				
4	0.0003	0.0002	0.0003	-0.0010			
5	0.0004	-0.0001	0.0002	0.0003	-0.0007		
6	-0.0015	0.0011	0.0002	-0.0002	-0.0001	0.0003	
	0.8128	-0.4088	0.1136	0.2505	0.3957	-0.1638	−532.346

Next, the ℓ vector was created for the unsampled location that we wish to predict. For example, to use location 7 (Abuja), the distance from Abuja to each of the sampled locations could be determined using the formula Semivariance = 0.907* *h*, which was derived earlier. The ℓ vector for Abuja is given in table 6.

Table 6: ℓ vector for un-sample location

Pairs of Un sampled Location with Sampled Locations	**Distance**	**ℓ vector for Abuja**
L(7, 1) = 56	117	106.12
L(7, 2) = 57	918	832.63
L(7, 3) = 58	793	719.25
L(7, 4) = 54	498	451.69
L(7, 5) = 54	467	423.57
L(7, 6) = 55	857	777.30

The kriging equation becomes:

$$\begin{bmatrix} & 1 & 2 & 3 & 4 & 5 & 6 & \\ 1 & 0.0025 & & & & & & \\ 2 & -0.0016 & -0.0002 & & & & & \\ 3 & -0.0001 & 0.0006 & -0.0011 & & & & \\ 4 & 0.0003 & 0.0002 & 0.0003 & -0.0010 & & & \\ 5 & 0.0004 & -0.0001 & 0.0002 & 0.0003 & -0.0007 & & \\ 6 & -0.0015 & 0.0011 & 0.0002 & -0.0002 & -0.0001 & 0.0003 & \\ & 0.8128 & -0.4088 & 0.1136 & 0.2505 & 0.3957 & -0.1638 & -532.346 \end{bmatrix} \begin{bmatrix} \\ 106.119 \\ 832.626 \\ 719.251 \\ 451.686 \\ 423.569 \\ 777.299 \\ 1 \end{bmatrix} = \begin{bmatrix} \\ -1.2068 \\ 0.5937 \\ 0.1461 \\ 0.3112 \\ 0.2281 \\ 0.9277 \\ -551.376 \end{bmatrix}$$

4.5 Making a Prediction

Table 7 is on kriging predictor for the six locations on which measurements were taken.

Table 7: Prediction of kriging predictor

Location	**Weights (λ)**	**MST Values**	**Weights (λ)*MST Values**
1	-1.2068	28	-33.7904
2	0.5937	29	17.2173
3	0.1461	30	4.3830
4	0.3112	26	8.0912
5	0.2281	26	5.9306
6	0.9277	27	25.0479

			kriging predictor =26.8796

Kriging variance

According to Webster and Oliver, (2001) the kriging variance of the prediction error is defined as the weighted average of the covariances from the new location (S_0) to all calibration points $(X_1,\ldots,X_n)$ and the Lagrange multiplier. The square root of the kriging variance is called the kriging standard error.

Table 8: Kriging variance

Location	**Weights (λ)**	**ℓ vector**	**Weights (λ)* ℓ vector**
1	-1.2068	106.119	-128.0644
2	0.5937	832.626	494.3301
3	0.1461	719.251	105.0826
4	0.3112	451.686	140.5646
5	0.2281	423.569	96.6161
6	0.9277	777.299	721.1003
	-551.376	1	-551376
			Kriging Variance = 878.2533

In this case, the Kriging Standard Error (KSE) is 29.6353. If it is assumed that the errors are normally distributed, with 95 percent prediction interval using: Kriging Predictor $\pm$ 1.96*KSE

The value 1.96 comes from the standard normal distribution where 95 percent of the probability within the interval -1.96 to 1.96. This means that if predictions are made again and again from the same model, in the long run 95 percent of the time the prediction interval will contain the value at the prediction location. In this problem the prediction interval ranges from 31.21 to 84.96.

The proposed mean surface temperature (MST) prediction derived by RK is:

$$\hat{T}(S_0) = \sum_{k=0}^{6} b_K q_K(S_0) + \sum_{i=1}^{6} \lambda_i e(S_i)$$

$$\hat{T}(s_0) = 27.852 + 0.114LONG(s_0) + 0.033LAT(s_0) - 0.006MRH(s_0) + 0.204MRAD(s_0)$$

$$-0.003ELEV(s_0) + 0.564EVAP(s_0) + 0.001DIST(s_0) - 1.2068e(s_1) + 0.5937e(s_2) + 0.1461e(s_3)$$

$$+0.3112e(s_4) + 0.2281e(s_5) + 0.9277e(s_6)$$

4.6 Validation and Kriging Error Distribution

Using cross-validation, the study compared six error statistics summaries. To estimate how much of variation has been explained by OK and RK models, it shows that OK is not much worse than RK. Although RK is a better predictor, the difference is only about 12%. This is possibly because variables ELEV, EVAP and DIST are also spatially continuous, and because the samples are equally spread in geographic space. Indeed, Figures 5 and 6 again, shows that the two maps do not differ much. Furthermore, the amount of variation explained by RK is about 78%, which is satisfactory.

Table9 : Comparison of RK to MLR and OK

Method	MPE	RMSPE	AKSE	MSPE	RMSSPE	R^2
OK	-0.014	1.06	2.50	0.221	0.76	0.66
RK	-0.017	1.02	2.06	0.203	0.85	0.78
MLR						0.62

4.7 Relationship between the MST, MRH, MRAD, ELEV, EVAP and DIST

Figure 7 is the individual relationship between MST, MRH, MRAD, ELEV, EVAP and DIST. It shows that MST drops with MRH, ELEV and DIST whereby MRAD and EVAP have linear trend and scatter around the regression lines. Nevertheless, figure 7 also shows that there is a significant scatter around the regression lines, which means that the residuals are significant.

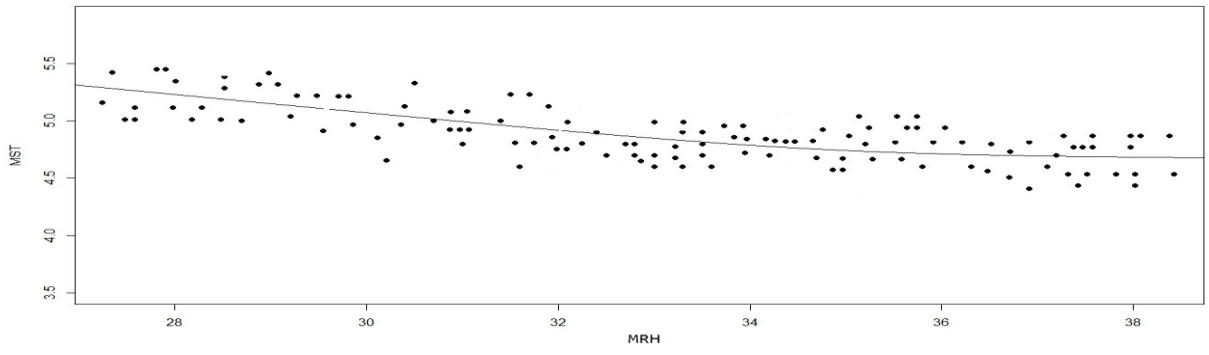

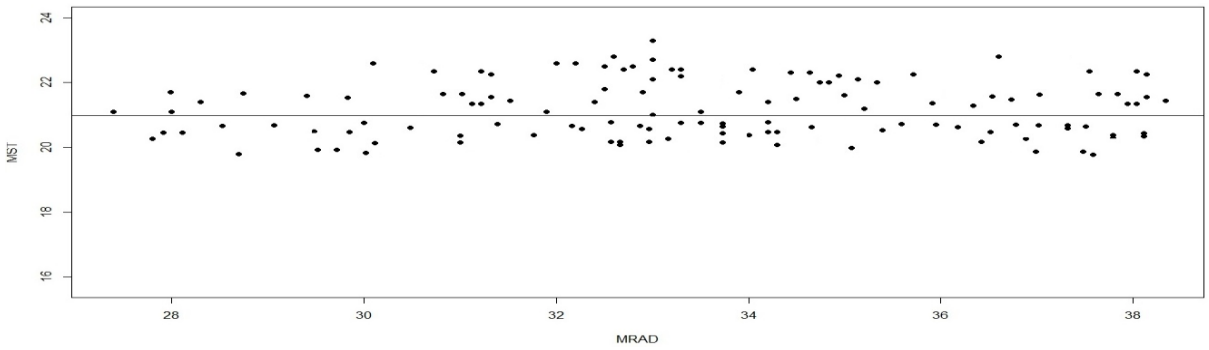
MST
16
18
20
22
24
28
30
32
34
36
38
MRAD

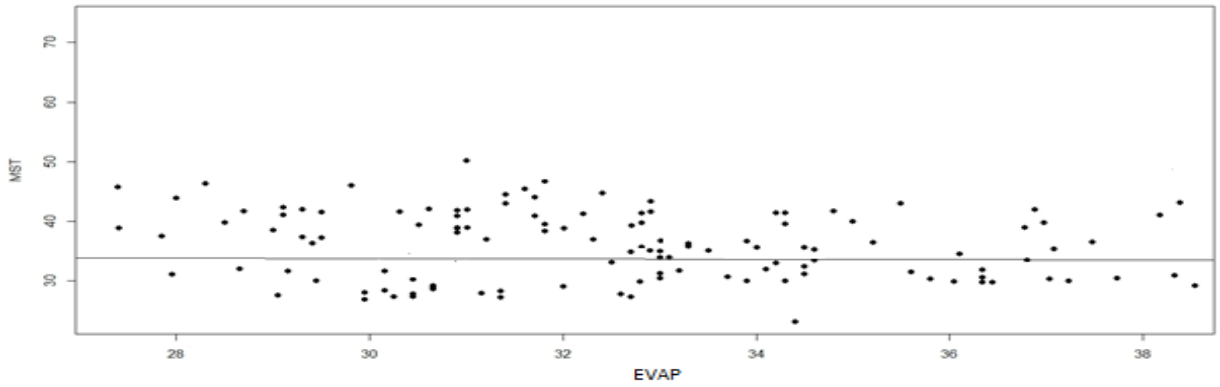
MST
30
40
50
60
70
28
30
32
34
36
38
EVAP

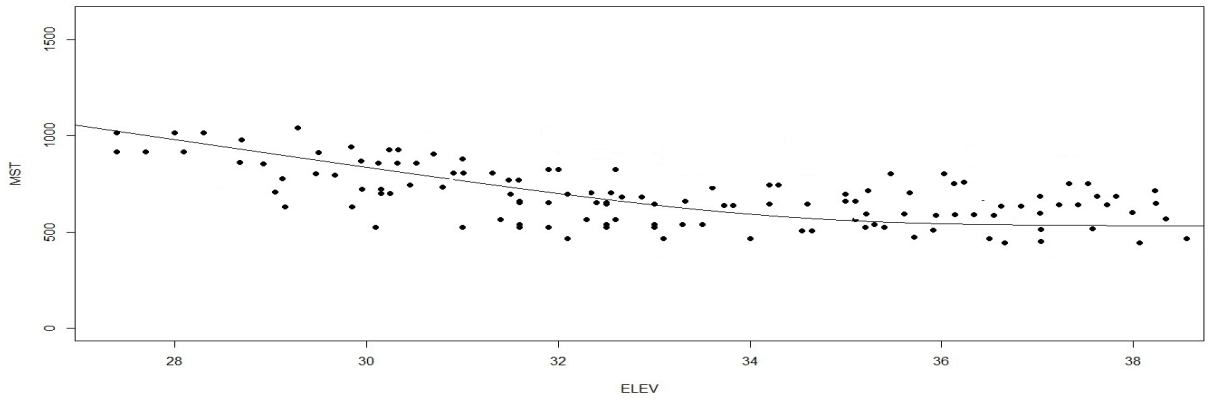
MST
0
500
1000
1500
28
30
32
34
36
38
ELEV

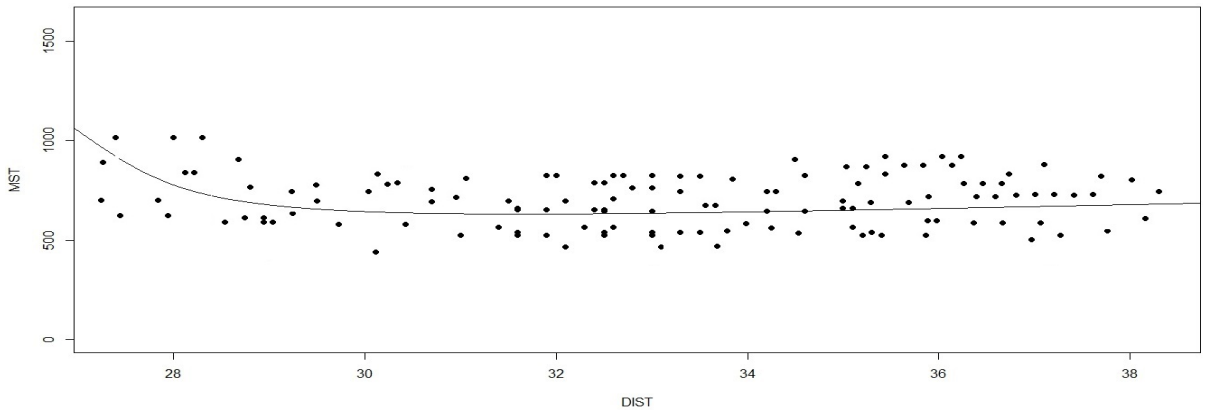
MST
0
500
1000
1500
28
30
32
34
36
38
DIST

Fig. 7: Scatter plots showing the general relationship between mean surface temperature (MST) against mean relative humidity (MRH), mean radiation (MRAD), evaporation (EVAP), elevation (ELEV) and distance (DIST).

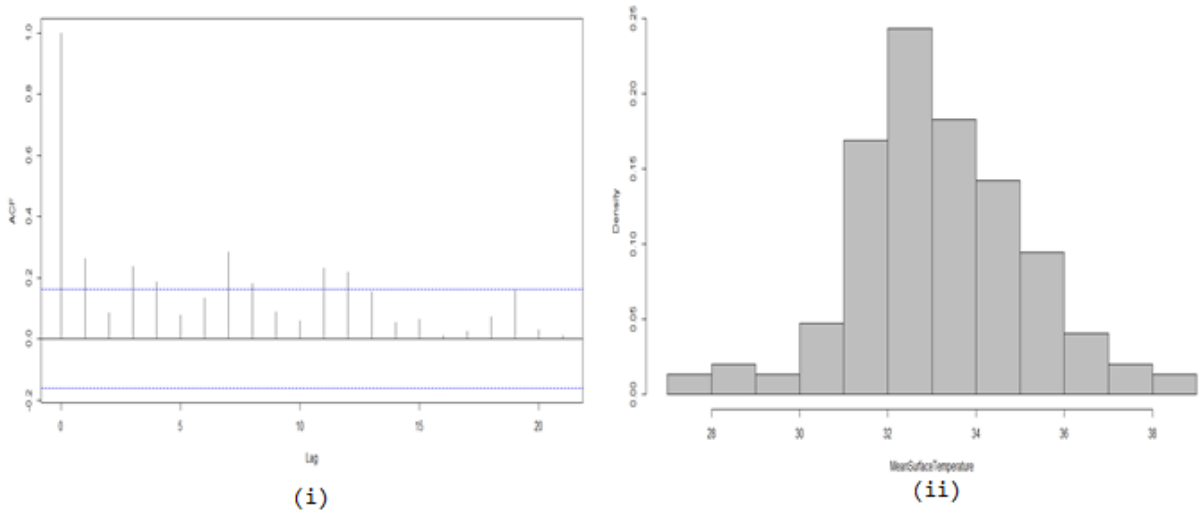

Figure.8: (i) Auto correlation function (acf) of MST (ii) A histogram of MST

5. Conclusion

The study has developed MST model using geostatistical technique with mean relative humidity, mean radiation, elevation, evaporation, distances of monitoring station Lagos (ocean/sea), longitude and latitude (position of each of the state capitals) as explanatory variables. The relationships between MST and the predictors in OLS and MLR models were positive and significant at 0.05 level. The experimental variogram is isotropic with Gaussian model, and the four directional variogram in the XYZ plane is anisotropic with exponential model as the best for the OK model. The OK XYZ with zonal anisotropic in the Z direction shows that the spatial continuity is in the North-East direction. The result also shows that predictions of estimates and kriging variances for OK and RK were similar as shown in the maps. The predictions are reasonable with RK model performing best.

References

Cressie, N. A. C., (1993). Statistics for Spatial Data, revised edition. John Wiley & Sons, New York, p. 416.

Davis, B. M., (1987). Uses and abuses of cross-validation in geostatistics. Math. Geol., 19: 241- 248

Draper, N. R., Smith, H., (1998). Applied Regression Analysis, 3rd Edition. John Wiley, New York, p. 697.

Hengl, T.,(2009). A practical Guide to Geostatistical Mapping, Europa Technology, Luxembourg

Hudson, G., Wackernagel, H., (1994). Mapping temperature using kriging with external drift: theory and example from Scotland. Int. J. Climatol. 14, 77–91.

Isah A. (2011). Multivariate spatial modeling and prediction of meteorological data; *International Journal of Engineering and Management Sciences (IJEMS); Vol.2, No.3 pp101-109.*

Ishida, T., Kawashima, S., (1993). Use of cokriging to estimate surface air temperature from elevation. Theor. Appl. Climatol. 47, 147–157.

Kutner, M. H., Nachtsheim, C. J., Neter, J., Li, W. (Eds.), (2004). Applied Linear Statistical Models, 5th Edition. McGraw-Hill, p. 1396.

Lapen, D.R., Hayhoe, H.N., (2003). Spatial analysis of seasonal and annual temperature and precipitations normals in Southern Ontario, Canada. J. Great Lakes Res. 29 (4), 529–544.

Matheron, G., (1969). Le krigeage universel. Vol. 1. Cahiers du Centre de Morphologie Mathématique, École des Mines de Paris, Fontainebleau, p. NA. De Iaco, S., Myers, D.E.,

Nalder, I.A., Ross, W.W., (1998). Spatial interpolation of climatic normal: test of a new method in Canadian boreal forest. Agric. Forest Meteorol. 92, 211–225.

Robinson, T. P. & G. Metternicht, (2006). Testing the performance of spatial interpolation techniques for mapping soil properties. J. Comput. Elect. Agric., 50: 97-108.

Annual Abstract of Statistics (2009). National Bureau of Statistics

Webster, R., Oliver, M. A., 2001. Geostatistics for Environmental Scientists. Statistics in Practice. Wiley, Chichester.

(http://www.nigeria-weather.com).

https://www.researchgate.net/figure/279459974_fig6_Map-of-Nigeria-showing-the-locations-of-meteorological-stations

PHYSICOCHEMICAL PROPERTIES AND ANTIFUNGAL ACTIVITY OF ESSENTIAL OIL OF *LANTANA CAMARA* SEEDS FROM NIGERIA

Abdullahi Mann*and Aishat Funmilayo Shuaib

[1]Department of Chemistry, Federal University of Technology, Minna, Nigeria

abdumann@gmail.com

* Corresponding author

Abstract

Lantana camara is a very well-known ornamental plant which is regarded as notorious weed used in the treatment of many ailments. *Lantana camara* seeds possess essential oil which can be used in cosmetics, paint, food and pharmaceuticals industries. In the present study, physicochemical properties and antifungal activity of the essential oil obtained from Nigerian *Lantana camara* seeds were investigated. The oil was extracted using cold extraction (maceration) and analyzed for its physicochemical parameters using standard procedures. The mean of fungicidal activity of the essential oil was calculated from different zones of inhibition obtained from five microorganisms used (*Aspergillus flavus, Aspergillus fumigatus, Aspergillus niger, Alternaria alternata* and *Penicillium notatum*) on different extract concentrations (40mg/cm^3, 60 mg/cm^3, 80 mg/cm^3,100 mg/cm^3, 120 mg/cm^3 respectively). Results obtained revealed that Nigerian *Lantana camara* seeds gave oil yield of 4.2% and had the following physicochemical properties. The colour (dark green), moisture content (61.6%), density (0.84 g/cm^3), viscosity (1.43pa.s) refractive index (1.481), acid value (14) free fatty acid (7%), iodine value (38), ester value (56), glycerin (3.1%) and saponification value (105.2). The oil extract shows activity on the five microbes used in which *Penicillium notatum* had the least activity and they are said to possess antifungal activity and it can be used in soap, paint, food, cosmetic and pharmaceutical industries. However, further studies have to be done to identify the bioactive constituents and to determine its mechanism of action.

Keywords: Antifungal activity, *Lantana camara*, physicochemical properties

1. Introduction

Plants produce a vast number of metabolites that are either primary or secondary (Croteau *et al.*, 2000). The secondary metabolites are those compounds that are produced in response to stress, and other physiological conditions. These compounds are able to perform their roles in plants because of their special features which include odor, physiological actions and taste. The essential oils (EOs) or volatile oils are produced to attract pollinators, or deterrent against herbivores. Many of these secondary metabolites have been exploited by humans for beneficial purposes and have diverse human applications (Hamid *et al.*, 2011).

Essential oils are known as volatile oils, and they are natural liquid aromatic oily compounds from natural sources usually plants. EOs can be found in different parts of a plant and therefore, they are extracted from

different plant parts such as: flowers, buds, seeds, leaves, twigs, bark, herbs, wood, fruits and roots) and the oils may differ both in composition and characteristics (Pannizi *et al*., 1993). For instance, geranium yields essential oils from both the flowers and the leaves and the oils from both parts differ in constituents, scents and some other properties. Some volatile oils are found in the leaves (oregano), seed (almond), flower (jasmine), peel (bergamot), berries (juniper), rhizome (ginger), root (angelica archangelic), bark (sassafras), wood (agar wood), resin (frankincense), petals (rose) (Pannizi *et al*., 1993). The quantity of essential oils extracted from the plant is determined by many interrelated factors like: climate, seasonal and geographical conditions, harvest period, and extraction techniques (Pannizi *et al*., 1993). Essential oils have been reported to have therapeutic effects by researchers; these properties were established after the oils have been extracted from the plant materials (Cappello *et al*., 2007). EOs or their components have been shown to exhibit antibacterial, antiviral, antimitotic, antiparasitic, and insecticidal properties. Currently the EOs are used as flavoring agents, or in perfumes as fragrances and aftershaves and in pharmaceuticals (due to their functional properties). The modern use of essential oils will continued to grow rapidly as health scientists and medical practitioners continue to research and validate the numerous health and wellness benefits of therapeutic-grade essential oils. Essential oils can be extracted by various techniques, depending on the stability of the oil to heat, and susceptibility of the oil constituents to chemical reactions. These techniques include: hydro distillation, hydro diffusion, effleurage, cold pressing, steam distillation, solvent extraction, microwave assisted process and carbon monoxide extraction (Husnu and Buchbauer, 2010).

2. Literature Review

Lantana camara (Verbenaceae) is widely known in subtropical and tropical regions of the world. It is an erect or subs cadent aromatic branching shrub with prickles and popularly known as wild or red sedge (Ghizalberti, 2000). *Lantana camara* is also called ewonadele in Yoruba, kimbamahalba in Hausa and anya nnunu in Igbo.

Lantana camara has been used in various parts of the world to treat varieties of disorders (Ross, 1999) and the flowers and leaves of this plant is used as remedies for tumors, cancers, chicken pox, measles, asthma, ulcers, swellings, eczema, high blood pressure, bilious fevers, malaria fevers, catarrhal infections, tetanus, rheumatism, cold, scratching, stomach ache, rheumatism, wound healing, toothache, bronchitis, antiseptic and other affections (Irvine, 1961; Rose, 1999; Deena and Thoppil, 2000; Begum *et al*., 2000).

This plant has been reported to possess numerous biological activities such as antimicrobial, fungicidal, insecticidal, biocidal and nematicidal activity (Sharma and Sharma, 1989; Begum *et al*. 2000; Sharma *et al*., 2007).

Lantana oil is sometimes used for the treatment of skin itches, as an antiseptic for wounds and externally for leprosy and scabies (Ghisalberti, 2000). The essential oil of *Lantana camara* showed a wide spectrum of antibacterial, antimicrobial and antifungal activity (Kumar *et al*., 2006). Phytochemically, a lot of phytocompounds have been isolated from aerial parts of *L. camara* extracts (Begum *et al*., 2002; 2003a;

2006; Hart *et al*., 1976a; Sharma *et al*., 1987; 1988; Pattabhi *et al*., 1991; Mirsa *et al*., 1997; Ma *et al*., 2004; Fatope *et al*., 2002; Yadav & Tripathi, 2003; Lai *et al*., 1998). However, no attempt has been made to investigate the physicochemical properties of the essential oil of Nigerian *Lantana camara* seeds and knowing these properties are important criteria for proper utilization of the essential oil. Therefore, the aim of this study is to determine physicochemical properties of the essential oil extracted from *Lantana camara* seeds grown in Nigeria and to evaluate its antifungal activity.

3. Methodology

3.1 Materials

The *Lantana camara* seed was collected from a farm square at the front of a public toilet in Bitrus Sawa square and Staff Quarter, Bosso Campus, Federal University of Technology Minna, Niger State.

3.2 Methods

3.2.1 Extraction of oil from Samples

The pulverized samples were macerated (using hexane as solvent) for 24 h, before filtering. After maceration and filtration, the hexane was removed by evaporation at reduced pressure and low temperature (room temperature) to yield the high fragrant essential oil (or absolute). After extraction was completed, the oils were stored in airtight vials for further study. Assay was carried out on the oil obtained from the sample to determine the antifungal activities and physicochemical properties of the oil.

3.2.2 Preparation of Agar

Sabouraud Dextrose agar of about 67 g was weighed into a conical flask and distilled water was added to make up to 1000 cm^3 marks. This mixture was then sterilized using autoclave machine. After it has been removed, the agar is then allowed to decreased in temperature before gelling and dispensed into sterilized petri dishes to solidified and form a media.

3.2.3 Agar Diffusion Test

Agar diffusion was carried out with Sabouraud Dextrose agar. Holes were bored in the agar and labeled in their respective extract concentration. The inoculum was prepared using 72 h plate cultures of *Aspergillus flavus, Aspergillus fumigatus, Aspergillus niger, Alternaria alternata* and *Penicillium notatum*. The colonies were suspended in already autoclave or sterilized broth. The suspension was loaded on a sterile cotton swab that was rotated several times and press firmly against the inside wall of the tube to remove excess inoculum from the swab. The dried surface of a Sabouraud Dextrose agar plate was inoculated by streaking the swab over the entire sterile agar surface. This procedure was repeated two more times, rotating the plate many time to ensure a uniform distribution of inoculum. Already prepared different extract concentration were introduced into their respective bored holes. Concentrations used are 40, 60, 80, 100 and 120 mg/ml which is equivalent to 8, 18, 32, 50 and 72 mg of oil per hole. The plates were incubated at 35^oC for 24 h, 48 h and 72 h respectively, for the fungi. The zone diameter was read to the nearest whole millimeter at the point at which there is a sharp reduction in growth occurs (Clinical and Laboratory Standards Institute, 2009). The control was griseofulvin at a concentration of 6.2 mg/ml.

3.3.0 Physical Properties

3.3.1 Color

Color measurement was done by physical appearance.

3.3.2 Determination of percentage (%) yield

The percentage (%) yield was calculated using the equation;

Percentage yield of oil = (Weight of oil/ Weight of sample) x 100

3.3.3 Determination of Moisture Content

The crucible was weighed and 5g of the oil sample was added. The sample was dried to constant weight in an oven at 105°C, cooled in desiccators and weighed. The procedure was repeated twice the sample and the average value was determined (Edcey, 1957).

3.3.4 Determination of Saponification Values (AOAC, 1990)

Approximately 2 g of the oil was put in a 250 cm^3 conical flask and 2.5 cm^3 of ethanol was added.10cm^3 of ethanolic potassium hydroxide solution (0.5 N) was added to the mixture and shaken to mix well. The conical flask was then attached to a reflux condenser and its contents were heated on a boiling water bath for 30mins with occasional shaking. 3 drops of phenolphthalein indicator was added to the solution while it was still warm and then it was titrated with 0.5N hydrochloric acid. The volume of HCl consumed at end point was recorded. Another blank (or control) solution was prepared, without the presence of any oil sample and heated and titrated against HCl, and the volume of HCl consumed at end point was also recorded. The saponification number was then calculated using the following equation

$$SV = \frac{56.1(B-S) \times N \text{ of KOH}}{\text{Gram of sample}}$$

Where;

SV: Saponification Value

B: ml of HCl required by Blank

S: ml of HCl required by Sample

N: normality

3.3.5 Determination of Acid Values, % Free Fatty Acids (AOAC, 1990)

Five grams of oil sample were placed in a conical flask to which 25 cm^3 absolute ethanol was added and 3 drops of phenolphthalein. The mixture was heated in a warm bath (65°C) and occasionally shaken for 10 min after which it was cooled and titrated with 0.1 N KOH until a faint pink color appeared.

Calculation:

Acid Value (AV) = ml of KOH x N x 5/Weight of sample

% Free Fatty Acid (FFA) = AV x 0.503

AV = Acid value

N = Normality of KOH

3.3.6 Determination of Ester Value (AOAC, 1990) Principle

The ester value is defined as the mg of KOH required to react with glycerin (glycerol / or glycerin) after saponifying 1gram of fat. It is calculated from the saponification Value (SV) and the acid Value (AV).

Calculation:

Ester Value (EV) = Saponification Value (SV) – Acid Value (AV)

% glycerin = Ester Value X 0.054664

3.3.7 Determination of specific gravity:

A density bottle was used in determining the density of the oil. A clean and dry bottle of 25 cm^3 capacity was weighed and assigned as *Wo,* and then filled with the oil, a stopper was inserted and reweighed to give a weight recorded as W1. The oil was substituted with the water after washing and drying the bottle and weighed and was recorded as W2. The expression for specific gravity (Sp.gr) is as given (ASTMD4052);

3.3.8 Determination of viscosity

Viscosity is the ease with which a fluid will flow. 20 cm^3 of the oil sample poured into a capillary of a calibrated viscometer at a closely controlled and known temperature and the time for the volume of the oil to flow under gravity through a calibrated glass capillary tube was noted and recorded. The viscosity was obtained by multiplying the time of flow obtained and the factor on the glass calibrated viscometer (ASTMD445).

3.3.9 Refractive index

This was determined using a refractor meter. About 2-3 drops of the oil was drop on the lens of the refractor meter to clean it. After which 3 cm^3 of ethanol sample was placed on the surface of the lens and then closed. The micro-gauge was adjusted until a sharp color is shown in the lens, from which the reading was taking. The value from the micro-gauge was the refractive index of the oil (Ademiluyi and Mepba, 2012).

3.3.10 Iodine value

Approximately 0.5 g of the oil was weighed into 250 cm^3 conical flask and 10 cm^3 of chloroform was also added. 10 cm^3 of iodine solution was added to the solution and shark vigorously. After which 10 cm^3 of 15% potassium iodide and 50 cm^3 of distilled water were also added, the obtain solution is been placed in a dark cupboard for 30 mins and shark after every 5mins. After that, the solution is then titrated against 0.1M of sodium thiosulphate. The procedure was repeated for the blank without oil (AOAC, 1990).

4. Results and Discussion

Table 4.1: Physicochemical characteristics of *Lantana camara* crude seed oil

Property	Value
Acid value (mg KOH/g of oil)	14
Saponification value(mg KOH/g of oil)	105.2
Iodine value gI_2/100g	38
%Free fatty acid	7
Ester value	56
%Glycerin	3.1
Viscosity (pa.s)	1.43
Refractive index	1.481
Color	Dark green
Solubility	Insoluble in water
Density(g/cm^3)	0.84
%Moisture content	61.6
%yield	4.2
Physical state	Liquid
Stability	Stable at room temperature

Table 4.2: The mean of fungicidal activity of *Lantana camara* seed oil

Organism	40 mg/ml	60 mg/ml	80 mg/ml	100 mg/ml	120 mg/ml	negative control
A. flavus	22.0±7.94	12±2.00	17.0±12.14	09.0±2.83	17.3±8.74	—
A.fumigatus	25.0±0.00	17.0±4.24	16.5±0.71	26.0±19.80	19.5±7.78	—
A. niger	32.0±7.55	21.0±4.00	20.0±2.00	18.7±3.22	18.7±5.51	—
A. alternata	29.7±11.24	20.3±6.11	20.7±11.02	20.5±14.85	23.0±11.53	—
P. notatum	21.5±9.19	14.5±0.71	19.3±9.51	13.7±5.51	18.3±3.79	—

Essential oil was obtained by cold maceration with a yield of 4.2% and was dark green in color. This yield is higher than that obtained by Alitonou *et al*. (2004) and Sonibare and Effiong (2008). This difference could be due to the zone of collection, the stage of development, the nature of the ground where the plant was grown (Adjou and Soumanou, 2013) and also the extraction method used (Ogunsina *et al.,* 2010).

The fungal isolates used in this study include *Aspergillus flavus, Aspergillus fumigatus, Aspergillus niger, Alternaria alternata* and *Penicillium notatum.* Essential oil of *Lantana camara* seed exhibited notable antifungal activity against all the fungi strains tested. The antifungal activity was less pronounced on *Aspergillus flavus* when compared with *Penicillium notatum, Aspergillus fumigatus, Aspergillus niger, Alternaria alternata* which may be due to the presence of some highly fungitoxic components in the oil, such as terpenoïds. Similar results were found by Adjou *et al*.(2012) and several studies has revealed the antibacterial and antifungal (Kumar *et al*., 2006), antioxidant (Basu *et al*., 2006), insecticidal (Abdel-Hady *et al*., 2005), nematicidal activities (Oamar *et al*., 2006) and the used of this plant in folk remedies for cancers and tumours (Ghisalberti, 2000).

Essential oil of *Lantana camara* seed exhibited pronounced antifungal activity against the growth of these fungi. If they are isolated from any food such as cowpea, essential oil of *Lantana camara* seed can be use as an antifungal preservatives for such food, it can also be use as antifungal preservative for paint productions, body creams and soaps.

The physicochemical analysis (Table 1), determined for the extracted indigenous *Lantana camara* seed oil includes; Saponification value of 105.2mgKOH/g. The value obtained was lower than that of *Dennettia tripatala* fruit oil (Pepper fruit) 159.33±1-20 suitable for soap making (Nwinuka, and Nwiloh, 2009) but higher than that of beeswax (93 mgKOH/g) which are also commonly used in soap making (Mabrouk, 2005). This indicates that the oil could be used in soap making since its saponification value falls within the range of these oils. Saponification value is used in checking adulteration. Higher saponification justifies the usage of fat or oil for soap production. The high saponification values indicate oxidation and its decrease suggest the unset of oxidation. Rossel (2004) reported similar observation. The high saponification value may be connected to the nature of the oils and the metallic ions present among other factors (Gray, 1978; Magnus, 1992; Nkafamiya *et al.,* 2007).

The ester value is the number of mg of potassium hydroxide (KOH) required for saponifying the esters in 1 g of a sample. Esterification value is the difference between the saponification value and the free fatty acid value of the fats and oils.

The Iodine Value (IV) is a measure of the relative degree of unsaturation in oils. The greater the iodine value, the more the unsaturation and the higher the susceptibility to oxidation. Iodine value of 38 I2/100g (less than 100) was obtained, which shows that the oil belongs to the class of Non-drying oils, which are useful in the manufacture of soaps (Kochhar,1998). High iodine value indicates dehydrogenation. It is a measure of unsaturation in lipid, which again determines the degree of flow. Decrease in iodine value indicates lipid oxidation and this might be due to metallic ions present among other factors, which enhances or promotes oxidation after the formation of hydro peroxide (Joseph, 1977; Tanlor *et al*., 1983; Chan and Cotton, 1987; Ruize et al., 1995; Rossel, 2004).

An Acid value of 14mgKOH/g was obtained which is lower than that of olive oil 17 mgKOH/g (Davine, J and Williams,P.N. 1961) higher than the 10.49 3mgKOH/g reported suitable for soap production (Oyedele, 2002). The acid and Free Fatty Acid (FFA) values are used to indicate the level of rancidity of oils (edibility)

and their suitability for use in the paint industry. The acid value obtained for *Lantana camara* seed oil was 14 mg/KOH and the percent FFA values obtained was 7%. Probably because crude might contain impurities that could cause the hydrolysis of the ester linkage thereby increasing the free fatty acid level. The allowable limit for FFA for edible oils is 1.0- 3.0% (Paul and Mittal, 1997). The lower the FFA level, the better the quality of the oil for human consumption.

Lantana camara seed oil has moisture content of 3.8. The higher the value of the moisture content of the oil, the greater the value used for food texturing (baking and frying) and industrially in the manufacture of soaps, detergents, cosmetics and oil paints.

The viscosity obtains for *Lantana camara* seed oil is 1.43. Viscosity of fats and oils decreases slightly with an increase in unsaturation, therefore viscosity is increased slightly by hydrogenation. Oils and fats containing a greater proportion of fatty acids of relatively low molecular weight are slightly less viscous than ones of an equivalent degree of unsaturation, but containing a higher proportion of high molecular weight acids (Lawson, 1995).
The density of *Lantana camara* seed oil is 0.84. The obtained results are in close agreement to those reported by Erickson (1990) for the density value of edible animal fat (lard) which ranged from 0.896 to 0.904.
The refractive index is related to the ease with which light passes through the fat. Temperature and degree of saturation affect the value. The RI of the oil (1.481) is also within the range of some edible oils like cottonseeds and groundnut (Kamal and Kamal, 1992). Refractive index is the degree of refraction of a beam of light that occurs when it passes from one transparent medium to another.

5. Conclusion

From the findings of this study, it was found that *Lantana camara* seed oil contained higher level of all the physicochemical properties and antifungal activity against tested fungi which is an indication of some important use of this oil in different applications such as soap production, cosmetics, paint, antibacterial, antifungal and antioxidant. The allowable limit for FFA for edible oils is 1.0- 3.0% (Paul and Mittal, 1997). The lower the FFA level, the better the quality of the oil for human consumption which makes *Lantana camara* seed oil with FFA 7% non edible oil. I recommended that further research should be carried out on the essential oil *Lantana camara* seed oil due to its antifungal activity.

References

Ademiluyi, F. T., and Mepba, H.D. (2012), Yield and properties of ethanol biofuel produced from different whole cassava flours, *Biotechnol.*, 1-6.

Alitonou, G. Avlessi, F., Bokossa, I. , Ahoussi, E., Dangou, J. and. Sohounhloué, D. C. K. (2004), Composition Chimique et Activité Biologique de l'Huile Essentielle de *Lantana camara* L, *Compte Rendue de Chimie*, Vol. 73, 1101–1105.

Adjou, E.S., Dahouenon-Ahoussi, E., Degnon, R. G., Soumanou, M. M. and Sohounhloue, D. C. K. (2012), Bioefficacy of Essential Oil of *Lantana camara* from Benin against the Growth of Fungi and Aflatoxin Production. *Journal Recent Advanced Agriculture*, Vol.1(4), 112-121.

AOAC (1990). Official Methods of Analysis (15th Ed.). Washington, VA: Association of Official Analytical Chemists.

Abdel-Hady NM, Abdei-halim AS, Al- Ghabdam AM. **(**2005), Chemical composition and insecticidal activity of the volatile oils of leaves and flowers of Lantana camara L. cultivated in Egypt. *Egyptian Society of Parasitology*, Vol.35(2), 687-698.

Basu, S. and Hazra, B. (2006), Evaluation of nitric oxide scavenging activity; in vitro and ex vivo. of the selected medicinal plants traditionally used in inflammatory diseases. *Phytotherapy Research*, Vol. 20(10), 896-900.

Begum, S., Wahab, A., Siddiqui, B. S. and Qamar, F. (2000), Nematicidal constituents of the aerial parts of Lantana *camara*. *Journal Natural Product*, Vol. 63, 765-767.

Begum, S., Wahab, A. and Siddiqui, B. S. (2000), Pentacyclic triterpenoids from the aerial parts of *Lantana camara*. *Chemical and Pharmaceutical Bulletin*, Vol. 51, 134-137.

Begum, S., Wahab, A. and Siddiqui, B. S. (2002), Ursethoxy acid, a new triterpene from *Lantana camara*. *Natural Product Letter*, Vol. 16, 235-238.

Begum, S., Wahab, A. and Siddiqui, B. S. (2003a), Pentacyclic triterpenoids from the aerial parts of *Lantana camara*. *Chemical and Pharmaceutical Bulletin*, Vol. 51, 134-137.

Begum, S., Syeda, Z. Q., Wahab, A. and Siddiqui, B. S. (2006), Triterpenoidal secondary metabolites from *Lantana camara* Linn. *Helv.Chim. Acta*, Vol. 89, 1932-1941.

Chan, H. W. S. and Cotton, D. T. (1987), The mechanism of autoxidation.Academic Press, Inc., Orland. Fla: p. 49.

Cappello, G., Spezzaferro, M. Grossi, L., Manzoli, L. and Marzio, L. (2007), Peppermint oil (MintolR) in the treatment of irritable bowel syndrome: A prospective double blind placebo controlled randomized trial, *Digestive Liver Diseases*, Vol. 39, 530–536.

Clinical and Laboratory Standards Institute (CLSI). (2009), *Method for antifungal disk diffusion susceptibility testing of yeasts*. 2th ed. CLSI document M44-A2. Pennsykvania, USA.

Davine, J. and Williams, P. N. (1961), The chemistry and technology of edible oils and fats. 1st Edition, Pergamon press, London.

Deena, M. J. and Thoppil, J. E. (2000), Antimicrobial activity of the essential oil of *Lantana camara*. *Fitoterapia*, 71, 453-455.

Edcey, E. W. (1957), Vegetable Fats and Oils. American Chemical Society Monograph Series, Reinhold Publication Company, New York, pp. 582-584.

Erickson, D. R. (1990), Edible Fats and Oils Processing, Basic Principles and Modern Practices, Illionis.

Fatope, M. O., Salihu, L. Asante, S. K. and Takeda, Y. (2002). Larvicidal activity of extracts and triterpenoids from *Lantana camara*. Pharmaceutical Biology, Vol. 40, 564-567.

Ghisalberti, E. L. (2000), *Lantana camara* Linn. (Verbenaceae). (Review). *Fitoterapia*, Vol.71, 467–486.

Gray, J. T. (1978), Measurement of lipid oxidation: A review. *JAOCS*, Vol.55, 535-545.

Hamid, A. A., Aiyelaagbe, O. O. and Usman, L. A. (2011), Essential oils: it medicinal and pharmacological uses, *International Journal of Current Research*, Vol. l3 (2), 86-98.

Hart, N.K., Lamberton, J. A., Sioumis, A. A. and Suares, H. (1976), New triterpenes of Lantana camara. A comparative study of the constituents of several taxa, *Australia Journal Chemistry*, Vol. 29, 655-671.

Husnu, K. C. B. and Buchbauer, G. (2010), Handbook of Essential Oils: Science, Technology and Applications. CRC Press, Boca Raton, London, New York.

Irvine, F.R. (1961). Woody plants of Ghana. London: Oxford University Press.

Joseph, A. F. (1977). Measuring Flavour Deterioration of Fats, Oils and Foods. General Food Cooperation Technical Center, New York.

1-7.Kamal, S. and Kamal, U. (1992). Fats and oils. *Nigeria Journal of Science*, Vol.18, 76-78.
Kochhar, S. L. (1998), Economic Botany in the Tropics. 2nd Edition. 1998; Macmillan India

Kumar, V.P., Chauhan, N.S., Padhand, H. and Rajani, M. (2006), Search for the antibacterial and antifungal agent from selected Indian Medicinal plants. *Journal of Ethnopharmacology*, Vol. 107, 182-188.

Lai, J.S., Chan, Y. F. and Huang, K. F. (1998). Constituents from the stems of *Lantana camara*. *China Pharmaceutical Journal*, Vol.50, 385-392.

Lawson, H. (1995), Food Oils and Fats, Technology, Utilization and Nutrition p 35.
Ma,W., Xiao, D. and Deng. S. (2004), Terpenoid constituents of the leaves of *Lantana camara*. *Guangzhou Huaxue*, Vol. 29, 14-19.

Mabrouk, S.T. (2005), Making Useable, Quality Opaque or Transparent Soap. *Journal of Chemistry Education,* Vol.82(10),1534-1537.

Magnus, P. (1992), Food science and Technology. Bristol. Great Britain, pp. 140-146.

Misra, L. N., Dixit, A. K. and Sharma, R. P. (1997). High concentration of hepatoprotective oleanolic acid and its derivatives in *Lantana camara* roots. *Planta Medica*, Vol.63, 582.

Morton, J. F. (1994), Lantana, or red sedge (*Lantana camara* L. [Verbenaceae]), notorious weed and popular garden flower; some cases of poisoning in Florida. *Economic Botany*, Vol. 48, 259-270

Nkafamiya, I. I., Aliyu, B. A., Manji, A. J. and Modibbo, U. U. (2007), Evaluation of Deterioration of Traditionally Produced Groundnut Oil on Storage. *Journal Chemical Society of Nigeria*, Vol. 32(1), 137-142.

Nwinuka, N. M. and Nwiloh, B. I. (2009). Physico-chemical Properties and Fatty Acid Composition of Dennettia tripetala Fruit Oil (Pepper Fruit). *Nigerian Journal Biochemistry Molecular Biology*, Vol. 24 (1), 42 - 46.

Oamar F, Begum S, Razar SM, Wahab A, Siddiqui BS. 2005. Nematicidal natural products from aerial parts of *Lantana camara*. *Natural Product Research*, Vol.19 (6), 609-613.

Ogunsina O, Oladimeji M, Lajide L. 2010. Insecticidal action of hexane extracts of three plants against bean weevil, *Callosobruchus maculatus* (F.) and maize weevil, *Sitophilus zeamais* motsch. *Journal of Ecology and the Natural Environment*, Vol.3, 64-68.

Panizzi, L., Flamini, G., Cioni, P. L. and Morelli, I. (1993), Composition and antimicrobial properties of essential oils of four Mediterranean Lamiaceae, *Journal of Ethnopharmacology*, Vol.39 (3), 167-170.

Paul, S. and Mittal, G.S. (1997), Regulating the use of degraded oil/fat in deep fat/oil food frying. Critical Rev. *Food Science Nutrition*, Vol. 37, 635-662.

Pattabhi, V., Sukumar, N. and Sharma, O.P. (1991), Structure of lantadene A, the major triterpenoid of *Lantana camara*, red variety. *Acta Cryst. C,* Vol. C47, 810-812.

Ross, I.A. (1999), Medicinal plants of the world. Chemical constituents, traditional and modern medical uses. 487 p. Humana Press, Totowa, New Jersey, USA

Sharma, V.S. and K.N. Kaul. 1959. Indian 59418. *Chem. Abstr*., Vol.53, 652.

Rossel, J.B (1984), Vegetable oils and Fats. *C.M.E. Casterberg*, 263-265.

Ruiz, M. C, Margaret, T. M. and Dobarganea, M. C. (1995), Quantitative and distribution of altered fatty acids in frying fats, JAOCS, Vol.72(10), 1171-1176.

Sharma, P., R.K. Dawra and H.P.S. Makkar. 1987. Isolation and partial purification of lantana (*Lantana camara* L.) toxins. *Toxicology Letters*, 37, 165-172

Sharma, O.P. and Sharma, P. D. (1989), Natural products of the Lantana plant — the present and prospects. *Journal of Scientific & Industrial Research*, Vol. 48, 471–478.

Sharma, O. P., Sharma, S., Pattabhi, V., Mahato, S. B. and Sharma, P. D. (2007), A Review of the Hepatotoxic Plant. *Lantana camara*, *Journal of Scientific & Industrial Research*, Vol.37, 313-352.

Sonibare, O.O. and Effiong, I. (2008). Antibacterial activity and cytotoxicity of essential oil of *Lantana camara* L. leaves from Nigeria, *African Journal of Biotechnology,* Vol. *7*, 2618-2620.

Tanlor, S. L., Beg, C. M., Shoptangh, N. H. and Traisman, E. (1983), Mutagive formation in deep fat fried foods as a function of frying conditions. *JAOCS*, Vol.60, 576-580.

Yadav, S.B. and Tripathi, V. (2003). A new triterpenoid from *Lantana camara*. *Fitoterapia*, Vol.74, 320-321

KINETIC AND ISOTHERM STUDIES OF HOG PLUM SEED COAT POWDER AS AN ADSORBENT

Ndamitso, M.M.[1], Mustapha, S.[1], Etsuyankpa, M.B.[2], Umar, M.T.[3], Sumaila, A.[1], Ovansa, A.A.[1]

[1]Department of Chemistry, Federal University of Technology, Minna, Nigeria

[2]Department of Chemistry, Federal University Lafia, Nassarawa State, Nigeria

[3]Department of Chemistry, IBBU, Lapia, Nigeria

E-mail address: ***muhd.ndamitso@futminna.edu.ng***

ABSTRACT

Hog plum was evaluated as a raw adsorbent for the removal of Fe(II), Cu(II) and Pb(II) ions from aqueous solutions. The physicochemical properties of the adsorbent investigated were: moisture content, ash, bulk density, cellulose, hemicellulose and lignin. Batch adsorption studies were performed by varying parameters such as contact time, pH, dosage and initial concentration. The obtained optimum contact times were 20 min for Pb(II), 40 min for Cu(II) and Fe(II) at optimum pH of 4 for Fe(II) and 6 for Cu(II) and Pb(II) ions respectively. Studies on the adsorption isotherm and kinetics were conducted and the adsorption followed Langmuir model for Pb(II) while Freundlich for Cu(II) and Fe(II) ions. The results showed that the adsorption processes obeyed the pseudo-second-order kinetic models, indicating that the adsorption mechanisms followed both chemical and physical adsorption processes. Thus, the Hog plum seed coat can be used as an alternative, cost effective and environmentally friendly adsorbent for the metal ions employed in this study.

Keywords: Hog plum, adsorbent, aqueous solutions, physicochemical properties, adsorption

1.0 Introduction

The significance of water for human sustenance has been a principal concern for both governmental and non-governmental organizations across the globe. This is because, over the years, there has been increase in the consumption of water of low quality especially in the rural areas of developing countries. As a result of advancement in globalization, toxic chemicals are produced and released into the environment without proper monitoring. Thus, increased industrial activities in the mining, pharmaceutical, smelting, dyeing and tanning, smelting, electroplating and other anthropogenic activities have caused serious problems to human and aquatic lives. Effluents from these industries

contain large amounts of inorganic and organic substances making it challenging to be treated by some conventional technologies.

Furthermore, removal and reclamation of heavy metals via conventional technologies which include osmosis, oxidation, filtration, precipitation, adsorption, filtration, flocculation, sedimentation and ion-exchange have been used for sequestering heavy metals from wastewater (Hegazi, 2013). Among these techniques, biosorption known as physicochemical process, is found to be accessible, reliable, and cheap for the removal of both organic and inorganic substances from wastewater. In the past, several agricultural wastes have been used as low cost sorbents for the removal of heavy metals from wastewater. Among these were peanut hull (Ali *et al.,* 2016), *Colocasia esculenta* (Banerjee *et al.*, 2016), barley (Arshadi *et al.*, 2014) and *Ngella sativa* seeds (Al-Tohami *et al.*, 2013).

Hog plum tree known as *Spondias mombin* or *Spondias purpurea* var. lutea, is a tree, a species of flowering plants that belongs to the family Anacardiaceae. It is a native to the tropical Americas, including the West Indies. The tree is commonly cultivated in some parts of Africa countries, India, Bangladesh, Sri Lanka and Indonesia. In Nigeria, the fruit from the plant is called Iyeye or Yeye in the Yoruba language, Ngulungwu in Igbo and Isada in Hausa (Ayoka *et al.,* 2009). *Spondias mombin* consists of pectin (Adepoju, 2009), cellulose (Afolabi *et al.,* 2008), proteins (Olayiwola *et al.,* 2013) and carotenoids (Tiburski *et al.,* 2011). The presence of the functional groups such as hydroxyl (cellulose) and carboxyl (pectin) can easily form surface-based process (adsorption) between the adsorbate on the surface of the adsorbent. The present study investigated the potential use of Hog plum seed coats as a cost effective adsorbent for the removal of iron (II), copper (II) and lead (II) ions from aqueous solutions through batch mode adsorption studies. The physicochemical properties of the adsorbent and batch mode adsorption studies were conducted by varying the parameters such as contact time, pH, adsorbent dosage and initial metal ion concentration. The equilibrium adsorption data were evaluated by Langmuir and Freundlich isotherms. The adsorption of Fe, Cu and Pb on Hog

plum seed coats using pseudo-first-order and pseudo-second-order kinetics were studied in order to predict the nature of adsorption.

2 Materials and Methods

2.1 Preparation of adsorbent

Hog plum (HP) fruits were obtained from a local market located at Bosso, Niger State, Nigeria and washed with tap water several times and afterwards with distilled water. After thorough washing, they were cut into small pieces and dried under sun light for seven (7) days to remove the seed coats from the fruits. Later, the dried pieces were washed with hot water (80 ^{o}C) to remove any soluble matter present and dried in an oven at 105 ^{o}C for 12 h. The oven dried seed coats were powdered using conventional mixer and sieved through 250 µm mesh. The sieved powder was stored and used for physicochemical analysis and batch adsorption experiments.

2.2 Preparation of synthetic stock solutions

The aqueous stock solutions of Fe(II), Cu(II) and Pb(II) ions were prepared from their respective stock salts of $FeSO_4$, $CuSO_4$ and $Pb(NO_3)_2$ by dissolving 4.90, 2.50 and 1.60 g into 1000 cm^3 volumetric flask for each metal and diluted with deionized water to give the concentrations of 1000ppm and other concentrations were prepared by serial dilutions prepared from the 1000 ppm stock solutions. The pH adjustments were done using 0.1 M HCl and 0.1 M NaOH solutions. All reagents were of Analytical grade (AR grade) and deionised water was used for dilutions.

2.3 Compositional analysis of the raw lignocellulosic materials

The gravimetric method was employed for the compositional analysis of Hog plum coat seeds and the following components were determined.

Extractive

2.50 g of the dried raw sample was loaded into the thimble of the Soxhlet extractor. 200 cm^3 of n-hexane was introduced, allowed to boil at 70 ^oC and heated for 4 h a the heating mantle. After extraction, the sample was air dried at room temperature for some minutes and constant weight of the extracted material was achieved in an oven at 105 ^oC for 12 hr. The % (w/w) of the extractives content of the sample was evaluated as the difference in weight between the raw extractive-loaded biomass and extractive-free biomass (Lin *et al.,* 2010).

Hemicellulose

1.00 g of dried extract was transferred into a 250 cm^3 conical flask and 150 cm^3 of 0.5 mol/dm^3 NaOH was added, boiled for 3.5 h and the mixture was filtered after cooling and washed until neutral pH was achieved. The residue was dried to a constant weight at 105 ^oC in an oven for 12 h. The difference between the sample weight before and after this treatment was measured as the hemicellulose content (%w/w) (Ayeni *et al.,* 2013).

Lignin

The weight of 0.5 g of the dried extract was weighed in glass test tube and 3 cm^3 of 72 % H_2SO_4 was added. The sample was shaken for 30 min and kept for 2 h to allowed complete hydrolysis. After the initial hydrolysis, 84 cm^3 of distilled water was added. The second step of hydrolysis was made to occur in an autoclave for 1 h at 121 °C. The slurry was then cooled at room temperature. The hydrolyzate was filtered and the acid insoluble lignin was determined by drying the residues at 105 ^oC. The hydrolyzed sample was heated at 575 ^oC in a muffle furnace after which the acid soluble lignin fraction was determined by measuring the absorbance of the acid hydrolyzed samples at 320 nm. The lignin content was calculated as the addition of acid insoluble lignin and acid soluble lignin.

Cellulose

The percentage cellulose content (%w/w) was obtained by difference:

$$\% \text{ Cellulose} = 100 - (\text{Ash} + \% \text{ Hemicellulose} + \% \text{ Lignin})$$

Determination of the moisture content

This was done by weighing 2.00 g of hug plum seed coat into a crucible. It was placed in the oven and heated for 3hours at constant temperature of 105°C. The sample was then removed and put rapidly into a desiccator in order to prevent more moisture uptake from the atmosphere. The sample was re-weighed. This procedure was repeated several times until a constant weight was obtained. The difference in the mass constitutes the amount of moisture content of the adsorbent.

$$\% \text{ Moisture content} = \frac{W_2 - W_3}{W_2 - W_1} \times 100$$

W_1 = the weight of the crucible

W_2 = the Initial weight of crucible with the sample

W_3 = the Final weight of crucible with the sample

Bulk Density

A known weight of sample was placed in a 25 cm^3 cylinder to a specified volume and tapping the cylinder for at least 10 min and measuring the volume of sample. The bulk density was measured as:

$$\text{Bulk density } \left(\frac{g}{cm^3}\right) = \frac{\text{Weight of dry sample (g)}}{\text{Volume of packed dry sample } (cm^3)}$$

Ash Content (%)

Ash content was determined by weighing 2.00 g of sample in a crucible and heating the sample to 105 ^{0}C for 4 h. The sample was then heated in a muffle furnace at 600 ^{0}C for 2 h. The crucible was then removed and placed in a desiccator and weighed after cooling. The ash content was calculated as:

$$\text{Ash } (\%) = \frac{\text{Final solid weight (g)}}{\text{Initial carbon weight (g)}} \times 100$$

2.4 Batch mode adsorption studies

Batch experiments were conducted at room temperature on an orbital shaker at 180 rpm using 100 cm^3 conical flasks. Effect of pH was evaluated by varying pH from 2 to 8 using 0.1 M HCl and 0.1 M NaOH for adjustments. The contact times were varied between 10 and 60 min to study the effect

of time on the sorption and adsorbent dosage was varied from 1.0 to 2.5 g for the respective optimum times for the metal ions while the other parameters were kept constant for each parameter studied. The percentage removal of the metal ions were determined by contacting 0.5 g of the prepared adsorbent with 40 cm^3 of known concentrations of the metal ion solutions. The residual metal concentrations in the supernatants were determined using an atomic absorption spectrophotometer (AAS), model, Buck Scientific Model 210. The results obtained in these batch studies were used to calculate the percentage removal of metal ions by using the following relationship:

$$\% \text{ Removal} = \frac{C_o - C_e}{C_o} \times 100$$

Where C_o and C_e are the initial and equilibrium concentrations (mg/dm^3) of the metal ion respectively.

The solutions containing different initial concentrations of Cu(II), Pb(II) and Fe(II) ions were prepared and the batch adsorption studies were done under the specific conditions. The solution pH of 6, contact time of 40 min, adsorbent dosage of 0.5 g and initial concentration range of 10-25 mg/dm^3 were employed. The residual concentrations of metal ions in various solutions were achieved by atomic absorption spectrometer. The data obtained in the batch equilibrium studies were used to calculate the equilibrium metal ions adsorptive capacity by the following equation:

$$q_e = \frac{C_o - C_e}{M} \times V$$

Where q_e is the amount of metal ions adsorbed (mg/g), V is the volume of the solution (dm^3), and M is the mass of the adsorbent (g).

3. Results and Discussion

Chemical analysis

The results of lignocellulosic material are presented in Table 1. The Hog plum seed coat contained 44.61 % cellulose, 7.02 % hemicelluloses and 47.3 % lignin. This was therefore, considered as adsorbent materials that can be used for biosorption of heavy metals which constituted. This material is rich in cellulose, hemicelluloses

and lignin which may adhere to the metal ions on the surface (Li *et al.*, 2016). It has been evidently reported that cellulosic adsorbent for metal ions sequestration exhibit efficient adsorption capacity (Pareek *et al.*, 2013).

Table 1: The physicochemical parameters of the hog plum seed coat

Parameter	Result
Ash content (%)	1.06
Moisture content (%)	1.2
Bulk density (g/cm^3)	0.4
Lignin (%)	47.3
Hemicelluloses (%)	7.02
Cellulose (%)	44.61

Effect of contact time

Equilibrium time is an important parameter used to determine the economical viability of an adsorbent for industrial scale adsorption processes. The effect of contact time on the removal of Fe(II), Cu(II) and Pb(II) by Hug plum seed coat is given in Fig. 1. The adsorption processes of the metal ions were very fast for the first 20 to 40 min where high amounts of the metal ions were adsorbed until they got to their optimum points. The optimum times were established at 20 and 40 min for the metal ions. These results show that the rates of removal of metal ions from the sorbate were initially rapid due to the abundant vacant sites on the surface of the adsorbent and the rapid occurrence is always controlled by diffusion process from the bulk solution to the adsorbent surface. However, further increase in contact time beyond the optimum time led to decrease in the percentage removal of the metal ions which may be as a result of less available active sites for adsorption process. This process is often accompanied by desorption process where the concentrations of the metal ions in the bulk phase are lowered with the release of the metal ions from or through the adsorbent surface which is similar to the findings of (Nasrullah *et al.*, 2015).

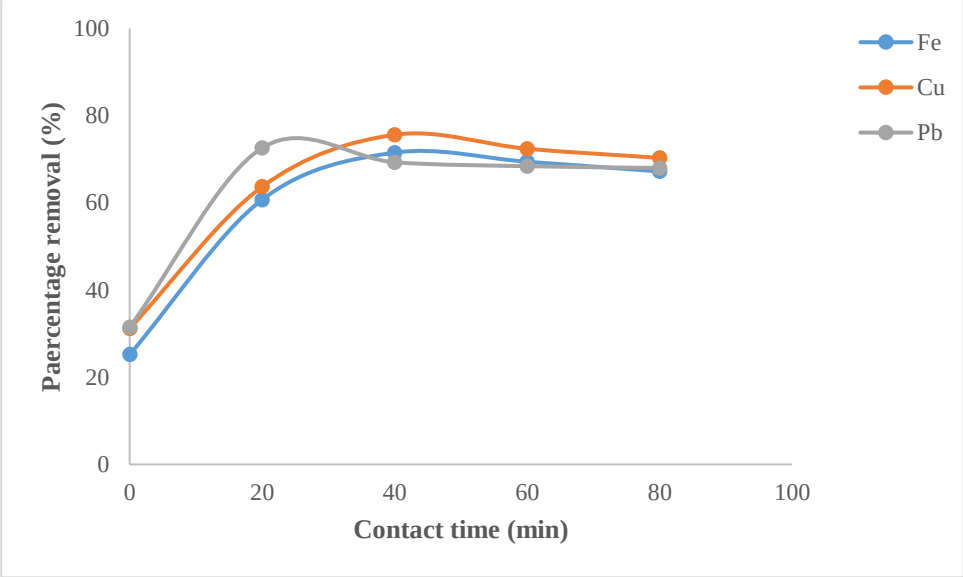

Figure 1: Effect of time on the percentage removal of Pb(II), Fe(II)and Cu(II) ions on HP at 28 ºC using 0.5 g adsorbent dose, particle size of 250 µm and at 180 rpm shaking speed

Effect of pH

Fig 2 shows the effect of pH on the removal of Fe(II), Cu(II) and Pb(II) by raw Hog plum seed coat. The initial pH of solution is a prime factor in the adsorption of metal ions onto adsorbents as it affects the surface charge of the adsorbent and the degree of ionization and specification of the adsorbate. From the results, the metal ions removal increased with increase in pH and it is obvious that the adsorbent for the removal of the metal ions is effective at high pH. That is, at the acidic media for the removal of the metals but decrease in the percentage removal at basic media as a result of hydroxyl ions in the aqueous solution. This is better explained based on deprotonation as a result of increase in the electrostatic interaction between the negatively charged of the adsorbent and the metal ions (Wang *et al.*, 2016). This study conform to the finding of Salem and Awwad (2014).

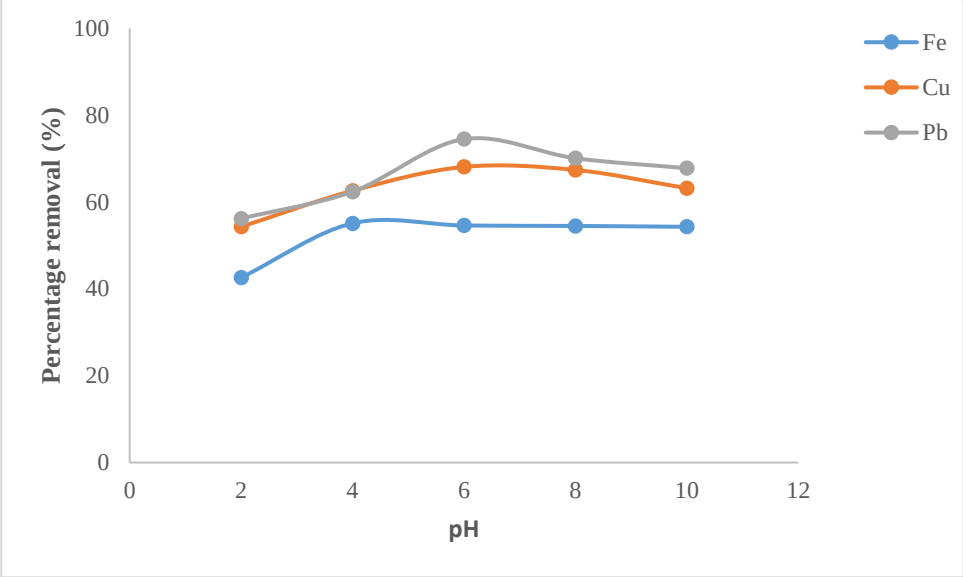

Figure 2: Effect of pH on the percentage removal of Pb(II), Fe(II)and Cu(II) ions on HP (40 cm^3 solution, 28 ºC, 0.5 g adsorbent dose, particle size 250 µm and 180 rpm shaking speed)

Effect of initial concentration

The effects of different initial concentrations of Fe(II), Pb(II) and Cu(II) ions were investigated and is shown in Fig. 3. It was observed that there were decrease in the percentage removal with increase in metal ion concentrations. The higher initial metal ion concentration adhere at the initial could be explained by the availability of higher internal surface area on the adsorbent that gets saturated with time (Ali *et al.*, 2016). At higher concentrations, decrease in adsorption could be due to the fact that the adsorbent has less available surface active sites for the attachment of the metal ions.

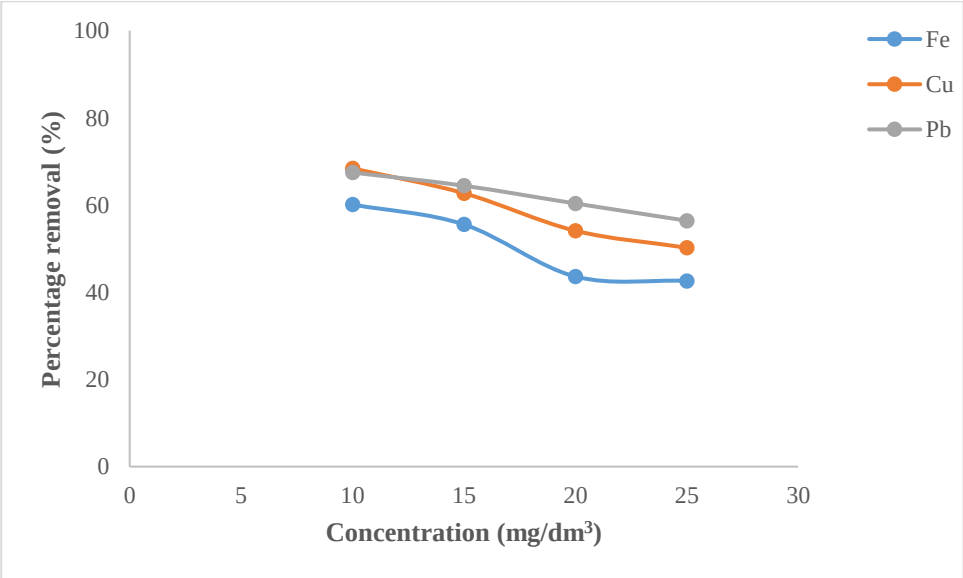

Figure 3: Effect of concentration on the percentage removal of Pb(II), Fe(II)and Cu(II) ions on HP (40 cm^3 solution, 28 ºC, 0.5 g adsorbent dose, particle size 250 µm and 180 rpm shaking speed)

Effect of adsorbent dose

The effect of adsorbent dose on the percentage removal of the metal ions from solutions is shown in Fig. 4. It was observed that as the mass of the adsorbent increased from 1.0 to 2.5 g a corresponding increase in the percentage removal was obtained for the metal ions. This is mainly due to an increase in the sorptive surface area and the availability of more active binding sites on the surface of the adsorbent (Zare *et al.,* 2015). However, the maximum adsorption capacity of metal ion onto the adsorbent could be achieved from the batch experiment by the use of laden amount of this adsorbent.

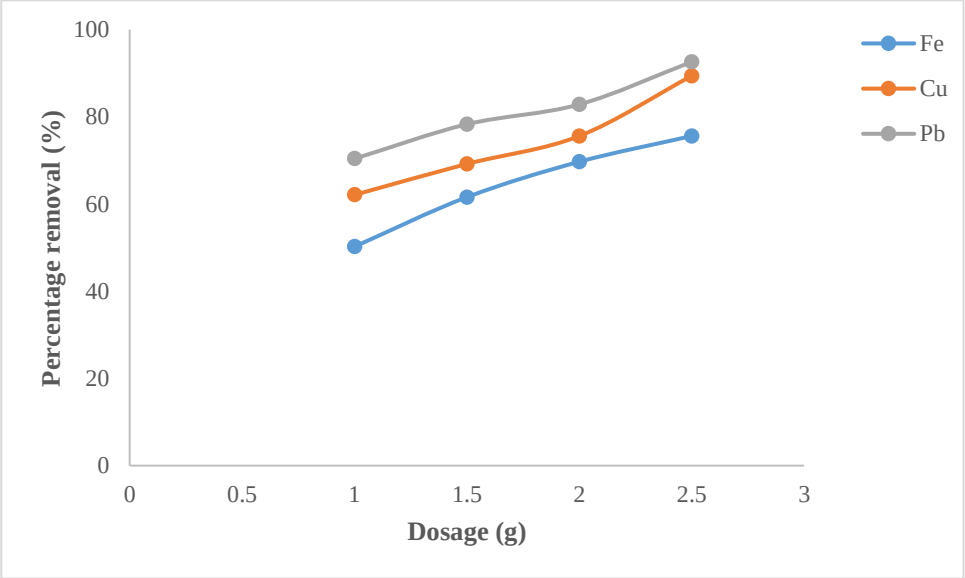

Figure 4: Effect of dosage on the percentage removal of Pb(II), Fe(II)and Cu(II) ions by HP (40 cm^3 solution, 28 ºC, particle size 250 µm and 180 rpm shaking speed)

Equilibrium isotherm

The isotherm data is used to determine the adsorption capacity of the adsorbent when the concentration of the adsorbate in solution reaches the state of equilibrium with the liquid-adsorbent interface. In this study, the Langmuir and Freundlich models were used to describe the experimental data analysis.

Langmuir isotherm

The Langmuir model describes a monolayer adsorption layer of solutes onto the adsorptive sites which comprises of homogeneous adsorption energy. The linearized form of the Langmuir model is depicted as follows:

$$\frac{C_e}{q_e} = \frac{1}{K_L Q_m} + \frac{1}{Q_m} C_e$$

Where Q_m and K_L are the Langmuir constants, describing the maximum adsorption capacity for the solid phase laden and the energy constant related to the heat of biosorption, respectively.

On the other hand, the regression correlation coefficient (R^2) values measure the fitness of the experimental data to the model. The R^2 values greater than 0.99 only for Pb(II) ion was deduced from the mathematical model as illustrated in Table 2. The Langmuir isotherm model was fitted for the adsorption process of the metal ion.

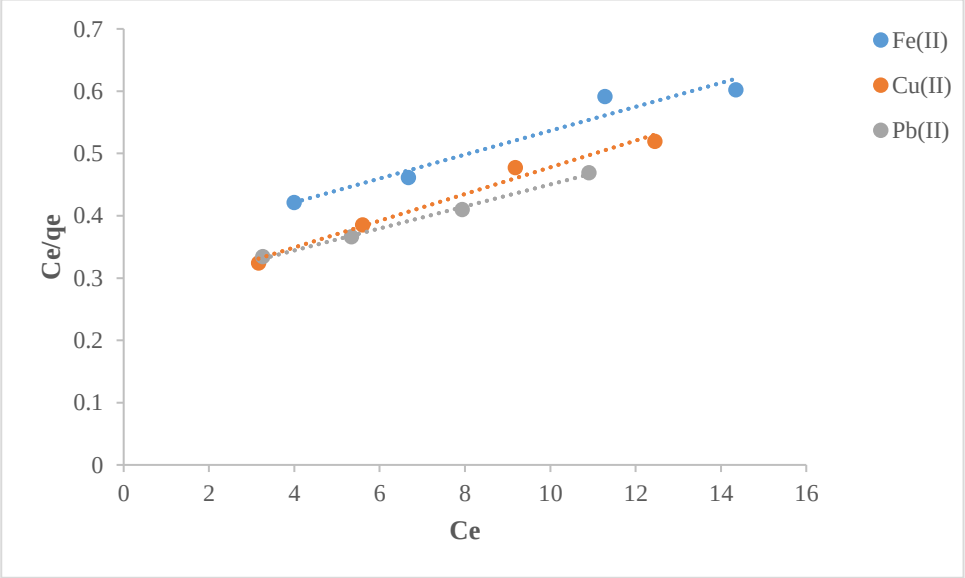

Figure 5: Plot of Langmuir isotherm model for the removal of Pb, Cu and Fe from aqueous solution by HP

Freundlich isotherm

The experimental uptake values for the metal ions were analyzed using Freundlich equation and the fundamental description of this model on adsorption studies is for a multilayer adsorption process indicating a heterogeneous system. This is expressed as:

$$\ln q_e = \ln K_F + \frac{1}{n}\ln C_e$$

Where K_F and $\frac{1}{n}$ are Freundlich constants related to adsorption intensity and adsorption capacity, respectively. From Table 2, the comparison of correlation coefficient values for the two employed models indicates that the adsorption processes of Pb(II) ions followed the Langmuir model while those of Cu(II) and Fe(II) ions were favoured by Freundlich isotherm model. The adsorption intensity (n) indicates the favorability of the adsorption. The n values for the three metal ions correspond to the favorable adsorption process of $0 < n < 10$. This findings follow the observation made by Gonzalez and Pliego-cuerio (2014).

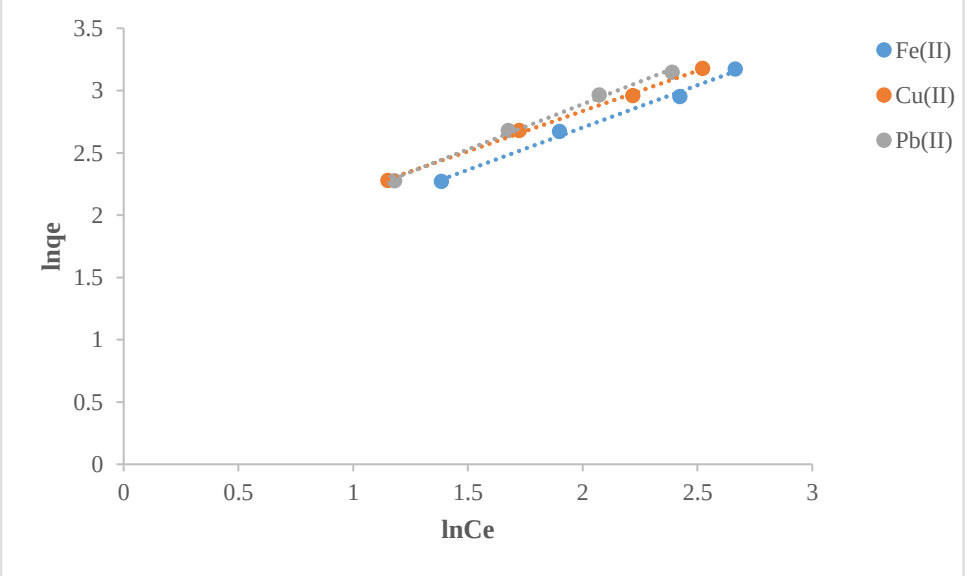

Figure 6: Plot of Freundlich isotherm model for the removal of Pb, Cu and Fe from aqueous solution by HP

Table 3: Estimated equilibrium parameters of Langmuir and Freundlich isotherms for the adsorption of Pb(II), Cu(II) and Fe(II) ions onto hog plum seed coat

Model	Parameter	Pb(II)	Fe(II)	Cu(II)
Langmuir	Q_m(mg/g)	56.497	52.083	46.729
	K_L(L/mg)	0.0647	0.0557	0.0889
	R^2	0.997	0.946	0.980
Freundlich	K_F (mg/g)	0.365	0.297	0.434
	n (g/L)	1.379	1.435	1.547
	R^2	0.995	0.992	0.998

Kinetics of the adsorption

The sorption kinetics defines the rate of the solute uptake at the adsorbent-adsorbate interface which provide an insight on the reaction pathways and mechanisms for the adsorption process. The kinetic of Fe(II), Pb(II) and Cu(II) adsorption on the coat of Hog plum seed coat was analyzed using pseudo-first and pseudo-second-order models.

Pseudo-first-order model

The rate of the adsorptive interaction provides the adsorption process based on the unoccupied sites of the sorbent. The equation designated to this reaction is given as:

$$\ln(q_e - q_t) = \ln q_e + k_1 t$$

Where q_e and q_t are the amounts of metal ions adsorbed (mg/g) at equilibrium and at time t (min), respectively while k_1 is the pseudo-first-order adsorption rate constant (L/min). The values of k_1 and q_e were calculated from the equation and the correlation coefficient (R^2) values of the equation model are presented in Table 4. The R^2 values for the pseudo-first order model are less than 0.9, suggesting that the adsorption processes of Fe(II), Cu(II) and Pb(II) could not be better explained by this adsorption mechanism.

Pseudo-second-order model

The pseudo second-order model predicts that the rate of adsorption rate is equivalent to the square of unoccupied adsorption sites. The model is expressed as:

$$\frac{t}{q_t} = \frac{1}{k_2 q_e^2} + \frac{1}{q_e} t$$

Where k_2 is the equilibrium rate constant for the pseudo-second order (g/mgmin), q_e is the calculated adsorption equilibrium and R^2 is the determined correlation coefficient as presented in Table 3. The values of the correlation coefficient from the linearized form of the pseudo-second-order model as presented in Fig. 8 were extremely high showing the best quality of linearization. It is palpable from the result that the adsorption process showed a better compliance with the pseudo second order model compared to the pseudo-first-order. This indicate that the rate determining steps in the adsorption of these ions in the study could be chemical adsorption processes that involved valency forces between the adsorbent and adsorbate.

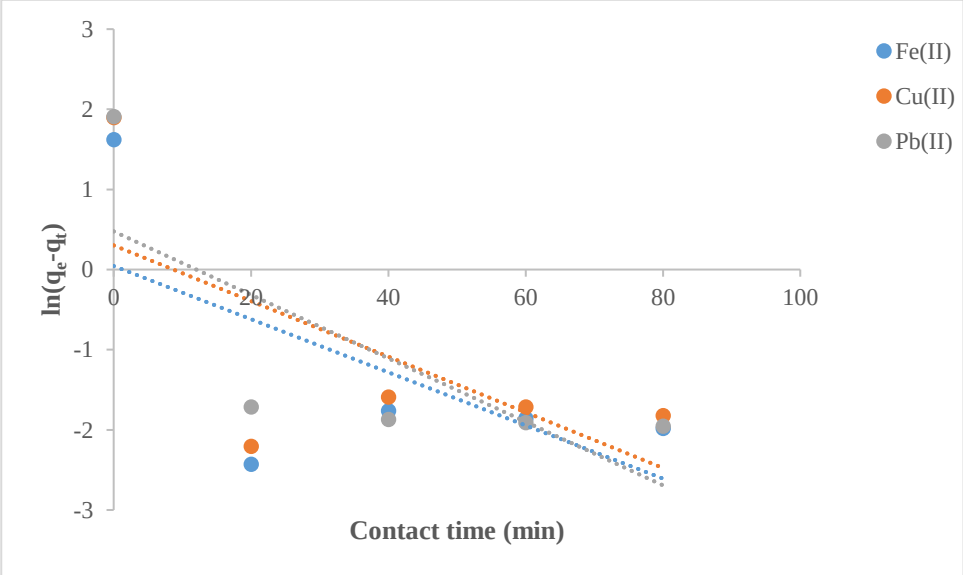

Figure 7: Plot of pseudo-first-order kinetic model for the removal of Pb, Cu anf Fe ions from aqueous solution by HP

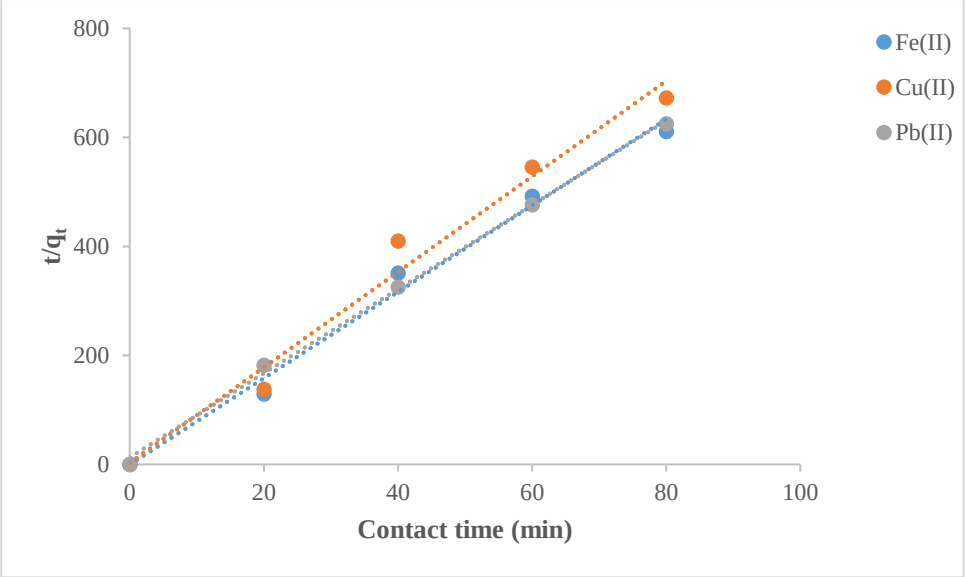

Figure 8: Plot of pseudo-second-order kinetic model for the removal of Pb, Cu anf Fe ions from aqueous solution by HP

Table 4: Constants and correlation coefficients of pseudo-first-order and pseudo-second-order models of Fe(II), Cu(II) and Pb(II) ions onto hog plum seed coat

Model	Parameter	Pb(II)	Fe(II)	Cu(II)
Pseudo-first-order	K_1(min^{-1})	0.0396	0.0332	0.0347
	q_e (mg/g)	2.998	1..107	2.004
	R^2	0.5494	0.407	0.425
Pseudo-second-order	K_2 (g/mg.min)	4.667	179.966	28.647

q_e (mg/g)	0.130	0.126	0.114
R^2	0.998	0.989	0.981

Conclusion

Hog plum seed coat is an effective adsorbent for the removal of Pb(II), Fe(II) and Cu(II) ions from aqueous solutions. The use of this adsorbent could be useful for the economic treatment of wastewater containing these heavy metals. The presence of substantial amounts of lignocellulosic material such as cellulose, hemicelluloses and lignin in this coat could help to adhere toxic pollutants on the adsorbent surface given the fact that when applied for metal sequestration it exhibited high efficient adsorption capacity. However, the adsorption was dependent on contact time, dosage, pH and concentration. Also, the results revealed Langmuir isotherm model best fitted the removal of Pb(II) ions while the Freundlich isotherm best fitted the removal of Cu(II) and Fe(II) ions. The pseudo-second-order kinetic was a better model for their adsorption rather that the pseudo-first-order kinetic. Therefore, it is believed that this biosorbent could serve as a less expensive alternative to the commercially available activated carbon.

REFERENCES

Adepoju, O.T. (2009). Proximate composition and micronutrient potentials of three locally available wild fruits in Nigeria. *African Journal of Agricultural Research*, 4(9), 887-892.

Afolabi, T.A., Onadeji, R.S., Ogunkunle, O.A. and Bamiro, F.O. (2009). Comparative Analysis of the Nutritional Quality of Browse Leaves (*Spondias Mombin* and (*Albizia Saman*) and Tuber Peels (Yam and Cassava) used as Ruminant Feeds. *Ife Journal of Science*, 14(2), 337-344.

Ali, R.M., Hamada, H.A., Husseinb, M.M. and Malash, G.F. (2016). Potential of using green adsorbent of heavy metal removal from aqueous solutions: Adsorption kinetics, isotherm, thermodynamic, mechanism and economic analysis. *Ecological Engineering*, 91, 317–332.

Al-Tohamia, F., Ackachab, M.A., Belaidc, R.A. and Hamaadid, M. (2013). Adsorption of Zn (II) Ions from Aqueous Solutions by Novel Adsorbent: *Ngella sativa* Seeds. *APCBEE Procedia*, 5, 400-404

Arshadi, M., Amiri, M.J. and Mousavi, S. (2014). Kinetic, equilibrium and thermodynamic Investigations of Ni(II),Cd(II),Cu(II)and Co(II) adsorption on barley straw ash. *Water Resources and Industry*, 6, 1-17.

Ayeni, A.O., Hymore, F.K., Mudliar, S.N., Deskmukh, S.C., Satpute, D.B., Omoleye, J.A. and Pandey, R.A. (2013). Hydrogen peroxide and lime based oxidative pretreatment of wood waste to enhance enzymatic hydrolysis for a biorefinery: process parameters optimization using response surface methodology, *Fuel,* 106, 187-194.

Ayoka, A.O., Akomolafe, R.O., Akinsomisoye, O.S. and Ukponmwan, O.E. (2008). "Medicinal and Economic Value of Spondias mombin" (PDF online reproduction). *African Journal of Biomedical Research,* Ibadan, Nigeria: Ibadan Biomedical Communications Group. 11, 129-136.

Banerjee, S., Mukherjee, S., LaminKa-ot, A., Joshi, S.R., Mandal, T. and Halder, G. (2016). Biosorptive uptake of Fe^{2+}, Cu^{2+} and As^{5+} by activated biochar derived from *Colocasia esculenta*: Isotherm, kinetics, thermodynamics, and cost estimation. *Journal of Advanced Research,* 7, 597-610.

Gonzáleza, P.G. and Pliego-Cuerio, Y.B. (2014). Adsorption of Cd(II), Hg(II) and Zn(II) from aqueous solution using mesoporous activated carbon produced from *Bambusa vulgarisstriata. Chemical Engineering Research and Design,* 92, 2715-2724.

Hegazi, H.A. (2013). Removal of heavy metals from wastewater using agricultural and industrial wastes as adsorbents. *Housing and Building National Research Center,* 9, 276-282.

Li, Y., Sun, Z., Ge, X. and Zhang, J. (2016). Effects of lignin and surfactant on adsorption and hydrolysis of cellulases on cellulose. *Biotechnology for Biofuels,* 9, 1-20

Lin, L., Yan, R., Liu, Y. and Jiang, W. (2010). In-depth investigation of enzymatic hydrolysis of biomass wastes based on three major components: cellulose, hemicellulose, and lignin. *Bioresource Technology,* 101(21), 8217-8223.

Nasrullah, A., Khan, H., Khan, A., Man, Z., Muhammad, N., Khan, M. and Abd El-Salam, N. (2015). Potential biosorbent derived from calligonum polygonoides for removal of methylene blue dye from aqueous solution. *Science World Journal,* 1, 1-11.

Olayiwola, I.O., Akinfenwa, V.O., Oguntona, C.O., Sanni, S.A., Onabanjo, O.O. and Afolabi, W.A.O. (2013). Phytonutrient, Antioxidant and Mineral Composition of Some Wild Fruits in South West Nigeria. *Nigerian Food Journal,* 31(2), 33–40.

Pareek, N., Gillgren, T. and Jonson, L.J. (2013). Adsorption of proteins involved in hydrolysis of lignocellulose on lignins and hemicelluloses. *Bioresource Technology,* 148, 170-177.

Salem, N.M. and Awwad, A.M. (2014). Biosorption of Ni(II) from electroplating wastewater by modified (*Eriobotrya japonica*) loquat bark. *Journal of Saudi Chemical Society,* 18, 379-386.

Tiburski, J.H., Rosentha, A., Ronoe, R.D., de Oliveira-Godoy, L. and Pacheco, S. (2011). Nutritional properties of yellow mombin (*Spondias mombin L.*) pulp. *Food Research International,* 44, 2326-2331.

Wang, C., Maneerung, T., Liew, J., Dai, Y.,Kawi, S. and Chong, C. (2016). Activated carbon derived from carbon residue from biomass gasification and its application for dye adsorption: Kinetics, isotherms and thermodynamic studies. *Bioresource Technology,* 200, 350-359.

Zare, H., Heydarzade, H., Rahimnejad, M., Tardast, A., Seyfi, M. and Peyghambarzadeh, S.M. (2015). Dried activated sludge as an appropriate biosorbent for removal of copper (II) ions. *Arabian Journal of Chemistry,* 8, 858-864.

RAIN-INDUCED ATTENUATION AT KU-BAND IN A TROPICAL REGION

Oyedum Onyedi David[1], Olubusade Joseph*[2], Moses Abiodun Stephen[3]
[1,2,3]Department of Physics, Federal University of Technology Minna, P.M.B. 65 Minna, Niger State, Nigeria
[1]oyedumod@yahoo.com
[2]olubusadejoseph@gmail.com*
[3]abiodun.moses@futminna.edu.ng
* Corresponding author

Abstract

The global increase in the use of wireless communication and the need to explore new technologies has resulted in the congestion of the communication system operating at lower frequency bands. Hence, there is need to open up higher frequency bands that could provide wide bandwidth and higher data rate transfer for human consumption. Communication at higher frequency bands has lots of benefits but is susceptible to rain impairments. Rain-induced attenuation becomes more prominent as the carrier frequency and rain rate increase. Hence, precise knowledge of rain rate can help in predicting level of rain-induced attenuation. In this work, point cumulative rainfall rate was determined at 0.1 percentage of time exceedance and converted from five minutes to one minute integration time. The specific and the total rain-induced attenuation were predicted at 0.1 percentage of time exceedance from 12 GHz to 18 GHz, for both horizontal and vertical polarisations. Lavergnat-Gole rain rate conversion model and ITU-R P.838-3 model were employed using a four year rainfall data obtained from Port Harcourt, Nigeria. Results revealed that the peak activities of rainfall rates were recorded at lower integration times and the total rain-induced attenuation increases with increasing operating frequencies, which is greater for horizontally polarised than vertically polarised waves. Therefore, periodic measurement and prediction of rain rate, specific rain-induced attenuation and possible total rain-induced attenuation are essential because of the varying nature of rainfall over time and region.

Keywords: Conversion factor, Integration time, Rain attenuation, Rainfall rate, Operating frequency

1.0 Introduction

All forms of wireless communication make use of electromagnetic wave which is either propagated vertically, horizontally or as a combination of both. Wireless communication provides us with huge opportunity to get possible access to the world at any time in any place. The modern day digital information and wireless communication system is reliant on radio waves for its transmission. Radio wave ranges from the very low frequency (VLF) up to the extremely high frequency (EHF).

Transmissions of wireless information at the lower frequency bands are however associated with long wavelength but very little bandwidth. On the other hand, transmissions of wireless information at the higher frequency bands are characterized by short wavelength and higher bandwidth. Thus, the carrier frequency and bandwidth increases as the wavelength becomes thinner. Owing to the low bandwidth associated with transmission at the lower frequency bands, there is a restriction to the size of transmittable data which often results in congestion at the lower frequency bands. Transmission at higher frequency band is the solution to the problem of this congestion. Moreover, higher frequency bands have numerous merits like wide spectrum availability and higher data transfer rate, more so, smaller antenna size are employed (Owolawi, Afullo and Malinga, 2009). On this note, there is need to open up higher frequency bands for human exploitation. But radio signals at frequencies above 10 GHz are susceptible to rain-induced attenuation.

In order to predict the possible level of system outage, several empirical and physical attenuation models have been designed by various researchers which aimed at providing a margin between system outage and availability. For the purpose of achieving optimal system availability, unavailability of satellite communication link can be limited to 0.01 percentage of time exceedance, while the unavailability of a terrestrial communication link can be limited to 0.1 percentage of time exceedance which both approximately corresponds to 53 minutes and 526 minutes respectively, in a year. Rain is an important element of the weather which has its own season and duration. Prediction of possible rain induced attenuation is carried out so as to help communication engineers design a system with the least system loss, which could ensure good quality of

service during rainfall. Thus, for the fact that the occurrence of rainfall cannot be controlled, accurate prediction of possible signal outage is not enough to minimize rain attenuation. Hence, a better approach in ensuring a low percentage of link outage during rain event is to employ suitable attenuation mitigation technique.

2.0 Theoretical Background

According to Ojo and Ajewole (2008), the activity of rain on a roving wave is more severe in the tropical regions, compared to the temperate regions. Rainfall in the tropical region is characterized by heavy downpour and large rain drop-size. The International Telecommunication Union-Radio bureau (ITU-R) has set a standard for the use and allocation of radio spectrum. The sector also developed several recommendations both for satellite and terrestrial communication links in order to ensure effective transmission and reception of radio signals globally. With regards to the recent recommendation by the sector (ITU-R, 2009), it was affirmed that rain rate measured at one minute interval of time is most efficient to obtain accurate prediction of rain-induced attenuation.

There is lack of sufficient rain rate data of one minute integration time in the non-developed parts of the world. Hence, there is need to convert the available rain rate data from higher integration times to the required one minute integration time. However, Segal (1986) and Burgueno *et al.* (1998) stated that there is no unified regression coefficient for the conversion of rain rates from higher integration times into corresponding one minute integration time. In response to this, several empirical studies were carried out globally in bid to device means for the conversion of rain rates. These include the works of Moupfouma (1995), Lavergnat and Gole (1996), and Chebil and Rahman (1999) to mention but a few.

Olsen *et al.* (1978) demonstrated the existing theoretical relationship between specific rain-induced attenuation and point rain rate which is given as:

$$\gamma = kR^{\alpha} \text{ (dB/km)} \quad (1)$$

where γ = specific rain attenuation

R = rain rate (mm/hr)

k and α are known as regression coefficients which are frequency, polarisation and canting angle dependent.

2.1 Rain Rate and Rain-Induced Attenuation

The term, rain rate is a measure of the intensity of rainfall per unit time. It is synonymous to the thickness of rainfall precipitating over a given period of time. It is a crucial parameter needed in predicting rain-induced attenuation. Rain rate (R) at (T) minute integration time is expressed as:

$$R_T = V_p \div \frac{T}{60} \text{ (mm/hr)} \quad (2)$$

where V_p = volume of precipitated rain (mm) at T integration time (minutes).

Dated back in 1996, Lavergnat and Gole (LG) developed a conversion method for converting point rain rate from higher integration times to one minute integration time. The method was developed as an application of stochastic process which was achieved by modelling the time interval between two consecutive rain drops as a renewal process using a disdrometer. The LG model employed a conversion factor h to scale both the rain rate and the probability (Emiliani and Luini, 2010). It is expressed as;

$$P_1 (R_1) = h^z P_T (R_T) \quad (3)$$

$$R_1 = \frac{R_T}{h^z} \quad (4)$$

$$R_1 = R_T \times \left(\frac{t_T}{t_1}\right)^z \quad (5)$$

where, P_1 and P_T are percentage probabilities of exceedance at one-minute and T-minute integration time respectively, R_1 and R_T are rain rates at one minute and T minute integration time, h is the conversion factor which is the ratio of the integration time at which the rain rate is required (t_1) to that at which it is available (t_T). Z is an empirical parameter which is given to be 0.143 for the tropical regions (Emiliani *et al.*, 2009).

According to ITU-R recommendation P.838-3 (ITU-R, 2012), total rain-induced attenuation is defined as the product of specific attenuation and effective path length. It is expressed as:

$$A_{(p)} = \gamma L_s \quad (6)$$

where A is the total attenuation, γ is the specific attenuation and L_s is the effective path length. However, rain impairs a roving wave either by scattering or absorption. Raindrops scatter radio waves whose wavelength is comparatively larger than the drop size of the rain drops. That is, radio waves are scattered when they hit small rain drops whose drop size are smaller compared to the wavelength of the roving waves. Rain-induced attenuation by scattering is a physical process. It is either caused by refraction or diffraction in which radio wave deviates from its original path. During this process energy is not used up by the molecules of water but scattered in different directions. As a result of forward scattering, rainfall sometimes cause radio signals to be received beyond the ordinary radio communication range.

Absorption of radio waves' energy by raindrops occurs as a result of the periodic change in the magnitude of a propagating radio wave from a positive value to a non-positive value. This periodic

change further causes water molecules (bi-polar molecules) to jostle, there by inducing a displacement current corresponding to a slight increase in heat energy and temperature in water molecules. Owing to shorter wavelength, there will be more interaction between radio waves and the molecules of water. Attenuation of radio waves by absorption involves energy transformation from radiant energy to heat energy, which is the main process through which the energy of a roving wave is lost.

3.0 Materials and Method

The major material involved in this research work is the rain gauge. The gauge employed is that of the tipping bucket type, which measures the amount of rainfall (mm) at every five minutes time intervals. A four year rainfall data is acquired from the rain gauge installed at National Space Research and Development Agency Port Harcourt, by the Nigeria Environmental and Climate Observing Program (NECOP).

Physical and empirical methods are the main known methods for the modeling of rain-induced attenuation. The empirical method is based on the relationship between observed attenuation distribution and the cumulative distribution of rain rate while the physical method is based on the attempt to reproduce the physical behaviour involved in the attenuation process. The empirical method is employed for this research work in conjunction with a physical-stochastic method, which is a combination of the physical principles and stochastic approach. But more emphasis is laid on the empirical method because of its ease to use simple analytical laws in predicting the extent to which rain event will impair a propagating radio wave.

However, due to in-homogeneity in rain drop size and the irregular distribution of rainfall along a specified path, a correction factor is therefore employed based on the assumption that an equivalent rain cell of uniform rain rate over a propagation path can model a non-uniform rain rate over the same propagation path (ITU-R, 2012). The correction factor is expressed as:

$$r_{(p)} = \left(1 + \left(\frac{L}{Lo}\right)\right)^{-1} \quad (7)$$

$$L_o = 35e^{-0.015}R_{(p)} \quad (8)$$

In the above equations, r represents the correction factor at (p) percentage of time exceedance, L is the path length (km), L_o is a rain rate dependent factor and R is the rain rate at (p) percentage of time exceedance. The effective path length (L_s) is defined as:

$$L_s = L \times \left(1 + \left(\frac{L}{Lo}\right)\right)^{-1} \quad (9)$$

Hence, the total rain-induced attenuation (A) at (p) percentage probability of time exceedance is redefined by combining equations (1) and (9) into equation (6), which gives:

$$A_{(p)} = kR^{\alpha} \times L \times \left(1 + \left(\frac{L}{Lo}\right)\right)^{-1} \quad (10)$$

4.0 Results

From the graphical relationship in Figure 1, at 0.001 percentage probability of time exceedance, the accumulated rain rate is 151.05 mm/hr and 120 mm/hr for one minute and five minutes integration times respectively. Also at 0.01 percentage probability of time exceedance, the accumulated rain rate is 100.7 mm/hr for one minute and 80 mm/hr for five minutes integration time. At 0.1 percentage probability of time exceedance, 50.35 mm/hr and 40 mm/hr are recorded for one minute and five minutes integration times respectively. Finally, at 1.0 percentage of time exceedance, 6.29 mm/hr is recorded for one minute integration time and 5 mm/hr is recorded for five minutes integration time.

Figure 2 represents the graphical relationship between specific rain attenuation and frequency for horizontal and vertical polarisations. At frequencies of 12 GHz, 13 GHz, 14 GHz, 15 GHz, 16 GHz, 17 GHz and 18 GHz the predicted specific rain induced attenuation for horizontally polarised wave are, 24.46 dB/km, 28.33 dB/km, 32.36 dB/km, 36.36 dB/km, 40.46 dB/km, 44.66 dB/km and 48.84 dB/km respectively. Also at frequencies of 12 GHz, 13 GHz, 14 GHz, 15 GHz, 16 GHz, 17 GHz and 18 GHz the predicted specific rain induced attenuation for vertically polarised wave are, 19.83 dB/km, 23.30 dB/km, 26.63 dB/km, 29.8 dB/km, 32.87

dB/km, 35.92 dB/km and 38.98 dB/km respectively and each is lower than the corresponding value for horizontal polarisation

Figure 3 shows the graphical relationship between total rain-induced attenuation and frequency for horizontal and vertical polarisations. At operating frequencies of 12 GHz, 13 GHz, 14 GHz, 15 GHz, 16 GHz, 17 GHz and 18 GHz the predicted total rain-induced attenuation for horizontally polarised radio wave are, 24.46 dB, 28.33 dB, 32.36 dB, 36.36 dB, 40.46 dB, 44.66 dB and 48.84 dB respectively, as against 19.83 dB, 23.30 dB, 26.63 dB, 29.8 dB, 32.87 dB, 35.92 dB and 38.98 dB respectively predicted for vertically polarised radio wave. The highest estimated rain-induced attenuation is recorded at the operating frequency of 18 GHz for horizontally polarised radio wave, while the least predicted value of rain-induced attenuation is recorded at an operating frequency of 12 GHz for vertically polarised radio wave.

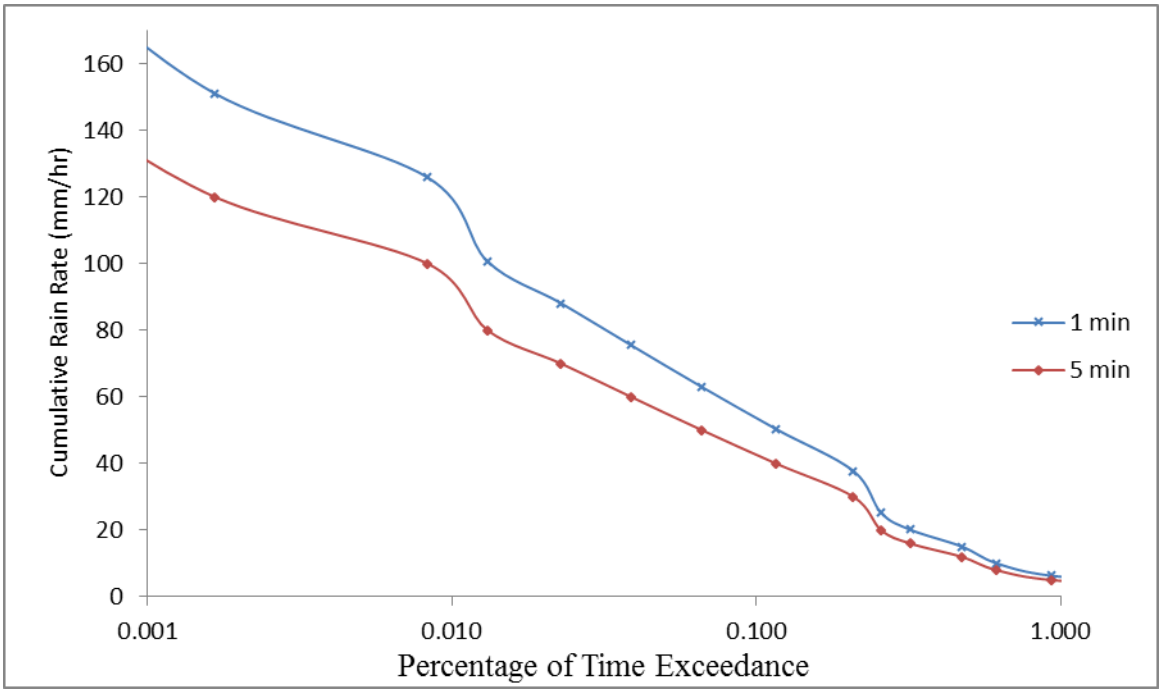

Figure 1: Relationship between Percentage of Time Exceedance and Cumulative Rain Rate

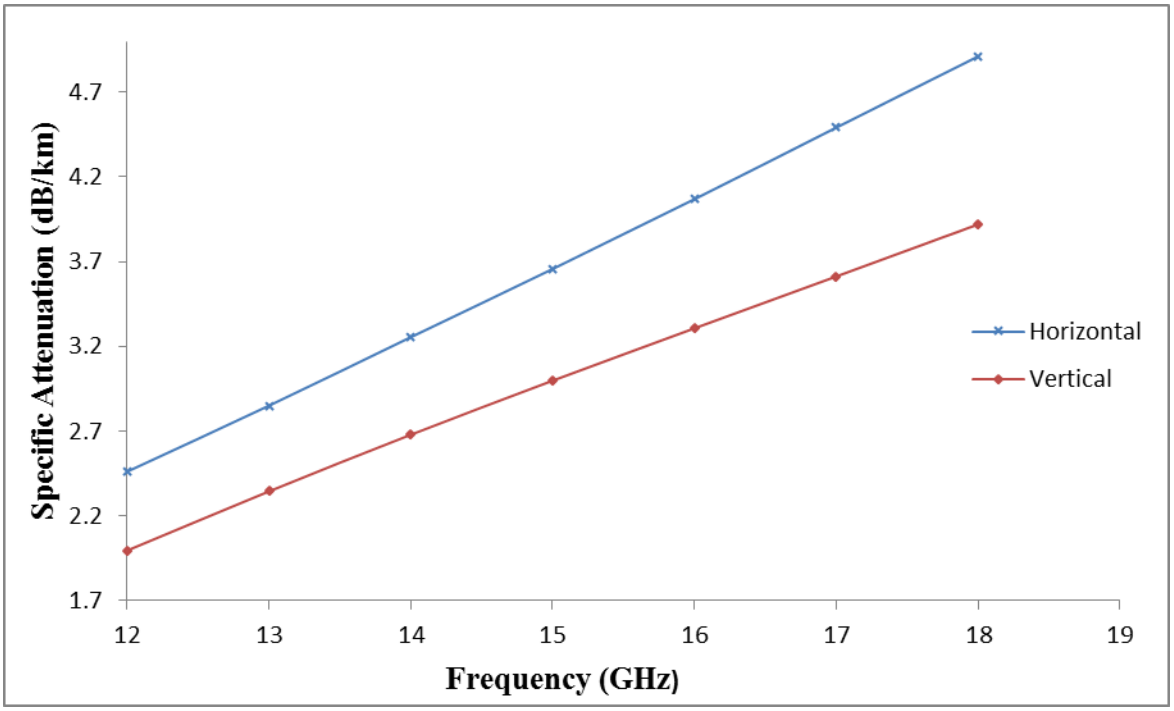

Figure 2: Relationship between Specific Attenuation and Frequency

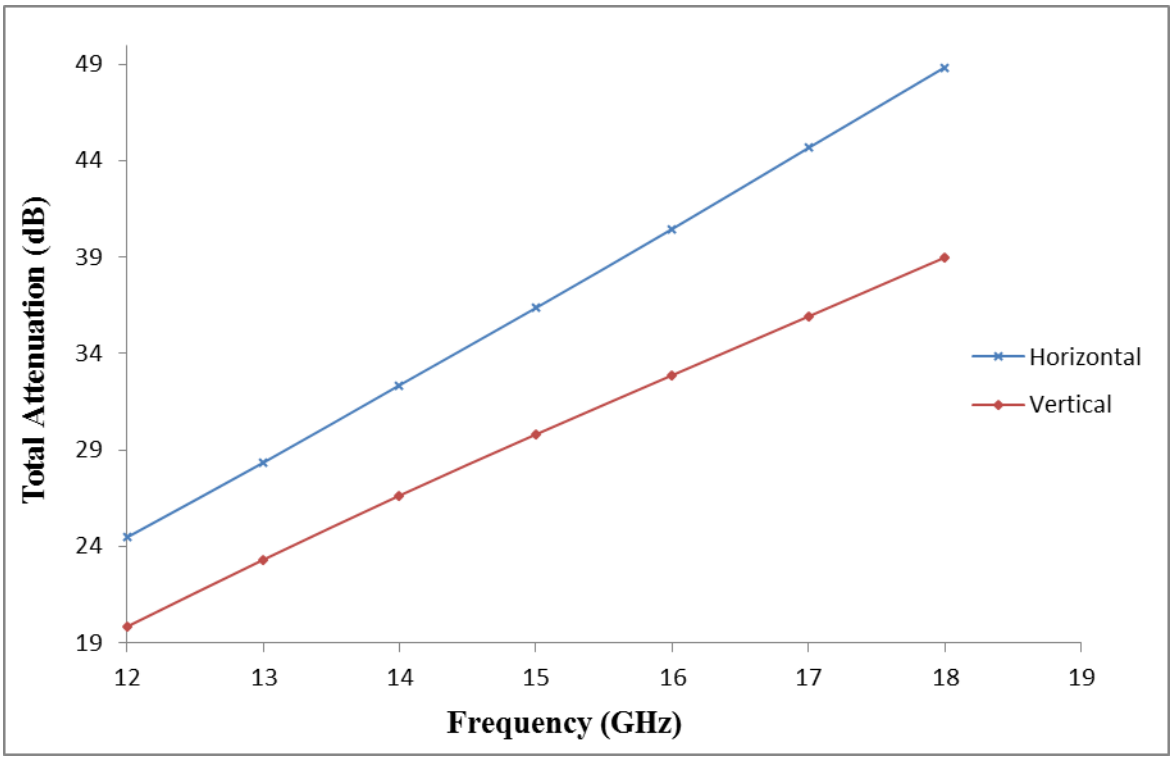

Figure 3: Relationship between Total Attenuation and Frequency

5.0 Conclusion

The cumulative rain rate distribution of rainfall over Port Harcourt for a period of four years (2008 – 2011) has been utilised to predict rain-induced attenuation on terrestrial line-of-sight link for a path length of 10 km,

at operating frequencies of 12 GHz, 13 GHz, 14 GHz, 15 GHz, 16 GHz, 17 GHz and 18 GHz respectively. The rain rate for one minute integration time at 0.1 percentage of time exceedance was determined from the cumulative distribution of rain rate to be 50.35 mm/hr. Considering the graphical relationship between cumulative distribution of rain rate against percentage of time exceedance. The peak rain rate values are attainable at lower percentage probability of time exceedance which implies that the peak activities of rain rates are hidden at higher integration times. Also, the correlation between the graph of one minute and five minutes integration times revealed that a power law relationship exists between them. From the results, it is evident that the total rain-induced attenuation increases with increasing operating frequencies and that horizontally polarised radio waves are more attenuated than vertically polarised radio waves.

References

Burgueno, A. M., Puigcever, M., and Vilar, E. (1998). Influence of rainguage integration time on the rain rate statistics used in microwave communication. *Annals of Telecommunications, 43, 9 – 10. 522 -527.*

Chebil, J. and Rahman, T. A. (1999). Rain rate statistics conversion for the prediction of rain attenuation in Malaysia. *Electronic letters.* 35 (12) 1019-1021.

Emiliani, L. D., Luini, L. and Capsoni, C. (2009). Analysis and parameterisation of methodologies for the conversion of rain-rate cumulative distributions from various integration times to one minute.

Emiliani, L. and Luini, L. (2010). Evaluation of models for the conversion of *T-min* rainfall distributions to an equivalent one-minute distribution to be used in Colombia. *Rev. Fac. Ing. Univ. Antioquia No. 56.*

ITU-R P.618–10 (2009). Transmission data and forecast methods required for the design of Earth–space telecommunication systems. *International Telecommunication Union.*

ITU-R Recommendation P.530-14 (2012). Propagation data and prediction methods required for the design of terrestrial line-of-sight systems. *International Telecommunication Union.*

Ojo, J.S. and Ajewole, M.O. (2008). Rain Rate and Rain Attenuation Prediction for Satellite Communication in Ku and Ka bands over Nigeria. *Progress in Electromagnetic Research B, Vol. 5, 2008, 207–223.*

Olsen, R. L., Rogers, D. V. and Hodge, D. B. (1978). "The *aRb* relation in the calculation of rain attenuation", *IEEE Trans. Antennas and Propag.*, vol. 26, pp. 547 – 556.

Lavergnat, J. and Gole, P. (1996). "A Stochastic Raindrop Time Distribution Model," *AMS Journal of Applied Meteorology,* 37, 8, August 1998, pp. 805-818.

Moupfouma, F. and Martin L. (1995). Modelling of the rainfall rate cumulative distribution for the design of satellite and terrestrial communication systems," *International Journal of Satellite Comm., Vol. 13,No. 2, 105-115, 1995.*

Segal, B. (1986). The influence of rainguage integration time on measured rainfall intensity distribution functions. *Journal of Atmospheric Oceanic Tech, 3, 4. 662 – 671.*

SYSTEMATIC PALYNOLOGY OF MAIGANGA COAL FACIES, NORTHERN BENUE TROUGH, NIGERIA

ONODUKU, U. S.

Department of Geology, Federal University of Technology, Minna, Nigeria.

Abstract

The Palynostratigraphy of the Maiganga coal mine is based on the available and recovered palynomorphs whose systematic Palynology of both existing and new palynoforms is vital in the palyno-characteristics of the Gombe Formation. Sixty-one [61] palynoforms which comprise of spores, pollen grains and algae have been identified and their systematic Palynology was described. The palynoforms are characteristic of typical Maastrichtian period which form part of the larger Cretaceous age that dominate the Gombe Formation in which the Maiganga coal deposit was formed. This study will serve as reference to future palynological studies for the study area as the described palynoforms were recovered from subsurface samples for the first time as against the previous similar studies on surface samples in the study area.

Key words: Palynostratigraphy, Maiganga, systematic Palynology, Gombe formation, Maastrichtian

1.0 INTRODUCTION

Palynology is the branch of Earth Sciences that is concerned with the study of acid-resistant microscopic organic matters recovered from sediments or sedimentary rocks (Onoduku, 2013). These organic matters can be recent or fossilized materials which have been deposited in a variety of environments that range from terrestrial to aquatic (Andrew, 2004). Palynological studies usually attempt to qualify and/or quantify the abundance and diversification of the organic matter species that characterize a given portion (depth) of a penetrated well or borehole. The quality of the palynoforms that characterize a particular range of depth of the well or borehole are used to deduce the biozonation, age, infer the paleoenvironment/paleoecology and correlation of such depth interval. The forgoing parameters of a defined depth interval of a well or borehole are useful for general mineral exploration program, oil and gas exploration, assessment of climate change as well as dating of a formation. The use of various palynoforms (pollen, spores, dinoflagellates, acritarchs, algae and other organic matters) for the above listed geoscientific purposes is usually based on their adequate recognition, identification and description, the last being the scope of this paper which fits adequately into the field of systematic Palynology. Systematic Palynology involves the microscopic study and description of palynoforms based on their various forms such as apertures, shapes, sculptures, structures, scars, number and arrangement of furrows/pores.

1.1 The Gombe Formation

The present study area is located within the Gombe Formation, precisely at Maiganga coal mine, near Kumo in Akko LGA. The Gombe Formation had been mapped as a unit by several workers (e.g. Falconer, 1911; Berber *et al*., 1954; Reyment and Barber, 1956 and Carter *et al.*, 1963). The Formation consists of estuarine and deltaic sandstones, siltstones, shales and limestone. There are thin coal beds reported by the above earlier workers and this has been confirmed by the successful exploration and on-going exploitation of the coal deposit at Maiganga coal mine which serve as the source of samples for this study. The exact age of the formation as at that time is unknown but a tentative assignation of Upper (Campanian) senonain-masstrichtian has been suggested. Its type locality is Gombe according to the earlier workers.

Carter *et al.* (1963) mapped the northeastern part of the Benue Trough and stated that the Maastrichtian Gombe Sandstone rests uncomformably on the older folded rocks of the Upper Benue depression and that the Maastrichtian rocks are themselves folded. However, mapping reveals that the strong fold which affected the Upper Benue Trough is pre-Gombe, i.e. probably pre-Maastrichtian and that, as in the Abakaliki and Lower Benue Trough, the main folds were generated in Santonian times (Murat, 1972; Burke *et al.*, 1972; Whiteman, 1973). The Gombe Formation is restricted to the western

part of the Gongola basin. It weathers to produce ferruginous capping. The weathering is responsible for the rugged hilly topography that characterizes most of the outcrops.

The Gombe Formation is made of 3 major lithofacies which were later proved as separate distinguishable members. At its base, it consists of rapidly alternating thin beds of silty shales, sometimes with plant remains and fine to medium-grained sand stones with some intercalated thin flaggy Ironstones. Passing upwards, the Gombe sandstone beds become more persistent and make up the greater of what was referred to as "bedded facies" by Zaborski (1997). South of Gombe, the Upper part of the Gombe Formation was termed "Red Sandstones Facies" by Zaborski (1997) probably due to its reddish colouration. Dike (1995) had reported coal horizons within the Gombe Formation and this was later proved by other workers. The coal seams are presently being mined by the Ashaka Cement Company.

According to Hamidu (2012), the type locality of the Gombe formation was designated as the "Kware Stream" by Carter *et al*. (1963) which is about 3 km south of Gombe where 300 m of sediments were described as exposed. He however asserted that the 1:250,000 scale geological map (Gombe sheet 36) provided in Carter *et al*. (1963) is inadequate to determine with certainty which of the "Kware" streams in the area actually contains the type section. He concluded, based on his field findings, that the type section for the Gombe Formation proposed by Carter *et al*. (1963) actually belongs to the Arowa member (a member of the Gombe Formation)(Figure 1).

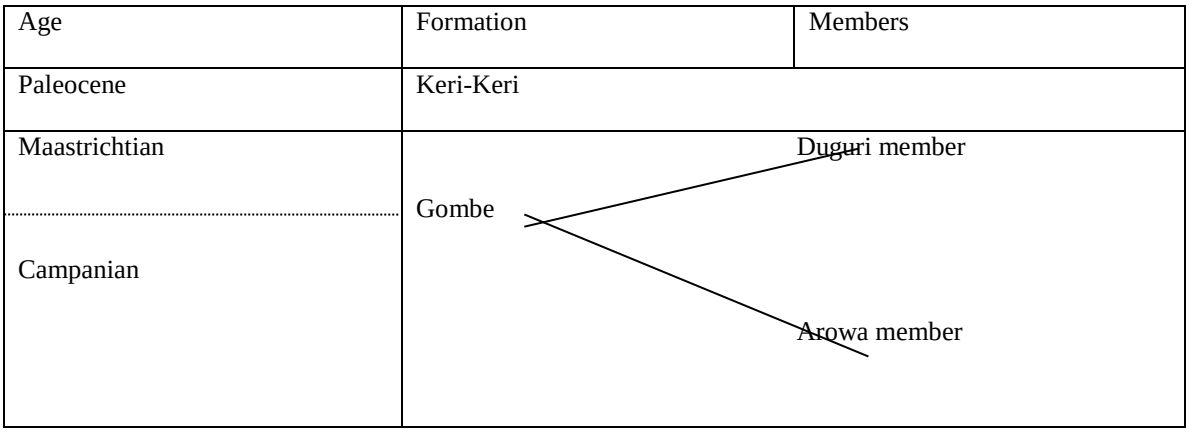

Figure 1: Lithostratigraphic subdivision of Gombe Formation (After Hamidu, 2012).

1.2 Coal seams

There are three distinct seams of coal within the Maiganga coal mine as observed during the field work and these three seams are currently being mined. The coal seams are intercalated in between an overlying sandstone and underlying shale facies. The uppermost seam 3 is about 1.2 m thick; the underlying seam 2 is about 1.5 m thick while the

lowermost seam 1 is about 4.5 m thick. The coals are dark, hard, striated and easily crumble into fragment.

Figure 1: Maiganga Coal Seams

1.3 MORPHOLOGICAL DESCRIPTION AND TERMINOLOGIES USED IN PALYNOMORPH DESCRIPTION

The first main distinction for the morphological description and grouping of palynomorphs is usually made between spores and pollen grains (Jzuora, 1980). In general, it can be stated that with an ordinary light microscope, no differentiation can be observed in the wall or exine of spores. For pollen grains, however, a differentiation between a more or less structured outer layer (extexine) and a Structureless inner layer (endexine) can usually be seen. The main criteria for morphological grouping for spores are based on the preserved nature of a scar and for pollen grains, on the number and arrangement of furrows and spores.For both pollen grains and spores, the sculpture of the exine is a distinct feature used for selection, which can be further subdivided based on the size of the grains. Other additional features used for morphological description of palynomorphs include their view and shape (monolete and trilete), structure of pollen grains, sculpture and apertures.The terminologies used in the description of palynomorphs are as briefly stated below just for the guidance and refresh of the readers' memory in Palynology. These terminologies include

(i) View and shape – This refers to the manner of arrangement of the spores in the sporangium which dictate the array of the tetrad marks. These marks could be trilete scar for radially symmetric spores and monolete for bilaterally symmetric spores. Also, a group of 4 pollen grains resulting from the division of one pollen mother cell is called a tetrad while an individual grain being arranged in a tetrahedron. The point of contact between a spore and other adjacent three within a sporangium is called the proximal pole and the area opposite is called the distal pole.

(ii) Structure of pollen grains – Pollen grains are structurally made of an outer coat called the exine and an inner layer called intine. The exine usually forms the preserved fossil while the intine usually disintegrates and disappears with the plant's exit. Under the light microscope, two layers of the exine are distinguishable into an inner layer called endexine and an outer layer called extexine. The extexine is further subdivided into an outermost tegillum or tectum and inner pillar-like elements called columellae or granulae. The term structure defines all the characteristics arising from the form and arrangement of the exine elements inside the tegillum or tectum.

(iii) Sculpture – This is defined as the ornamentation that is formed on or in the outer wall of a palynomorph. When it protrudes outwards of the grain, it is called positive sculpture like psilate, scabrate, verrucate, areolate, gemmate, baculate, clarate, regulate, striate, perforate, foveolate, fossulate and reticulate.

(iv) Apertures – These refer to scars, furrows, pores, as they characterize palynomorphs. They provide growth point(s) foe the gametes. Aperture can be simple or compound. Palynomorphs without apertures are said to be inaperturate. Elongated apertures are called colpi (sing. Colpus) or furrows or sulcus while circular ones are called Pori (sing. Porus) or pores. They can be either situated in the extexine and/or in the endexine.

2.0 MATERIALS AND METHODS

The major materials employed in this study comprised of ditch cuttings, palynomorph charts and palynomorph albums. Others include a palynological microscope (Zeiss 230, bifocal and transmitted light source) attached with camera,

standard and individual past authors' palynological albums and various literatures on systematic Palynology by various authors. The methodology used in the study involved the systematic microscopic study of the palynoslides prepared. In doing so, each palynoslides was thoroughly viewed under transmitted palynological microscope, searching for, marking any palynomorph seen, describing it and taking the photomicrograph of the specie. Marker or diagnostic species were specially described in detail. The depth of the studied wells at which the palynoforms described were encountered was equally recorded to correlate with the age of the formation from which they are deposited.

3.0 RESULTS AND DISCUSSION

The results of the systematic study and description of the palynoforms found in the palynoslides are as explained in 3.1 and shown on the photomicrograph.

3.1 Systematic Palynology

The systematic Palynology adopted in this work generally follows the patterns of Potonie` (1956, 1958, 1960), Dettmann (1963) and Atta-Peters and Salami (2004). Other relevant previous works by Salami (1983), Van Hoeken-Klinkenberg (1964), Ojo (2009), Obianuju (2008), Aboul Ela (1978) and Onoduku (2013) were also consulted especially for synonyms and general descriptions of forms. Finally, the work of Ames and Spackman, 1985 on the catalog of fossil spores and pollen, was widely consulted for species names, general description, authors and references. All species magnification is X 1000.In this work, the analyzed palynomorphs have generally been grouped into three, namely Pollen, Spores, and Fresh Water Algae. For easy and less cumbersome systematic, the palynomorphs have further been grouped and described under palyno-designated headings such as sporites and pollenites divisions (Aboul Ela, 1978), Pteridopytes spores, Gymnosperm pollen, Angiosperm pollen and Dinoflagellates. Pteridopytes spores are discussed under sporites while gymnosperms and angiosperms pollen are discussed under pollenites.

Division: Sporites Potonie`, 1956

Family: Pteridopytes spores

Subdivision: TRILETES

Genus: Cyathidites (Couper, 1953).

Cyathidites minor Couper, 1953
BA – 7, 32.7 m
Fig. 25

Description: Trilete spore, amb triangular with straight to slightly concave sides and rounded apices. Exine psilate and thick

Age: Maastrichtian

Genus: Rugulatisporites (Pflug and Thomson, 1953).

Rugulatisporites caperatus Van Hoeken-Klinken-berg, 1964
BA – 7, 35 m
Fig. 35

Description: Trilete microspore, amb sub-triangular, triangular or spherical, sides convex, radial corners round triangular or sub-triangular forms, trilete mark thin, arms moderate, slightly raised but without Margo, exine moderate, rugulate and cavaliculate, both proximal and distal surfaces are sculptured.

Age: Maastrichtian

Genus: Foveotriletes (Van der Hammen, 1954, ex Protonie, 1956).

Foveotriletes margaritae (Van der Hammen) Germeraad *et al.*, (1968)
BA – 7, 32 m
Fig. 23

Description: The species has foveolate distal surface, thin wall and short less pronounced trilete mark

Age: Maastrichtian

Genus: Osmunda (Martin and Rouse, 1966).

*Osmundacidites sp.*Martin and Rouse, 1966
BA – 16, 40 m
Fig. 19

Description: Trilete spores, sub-spherical in outline, folded and crumpled. Faint Laesurae, thin Margo subtending the commissure. The ornamentation consists of slender bacula which are slightly clavate. The bacula are straight and relatively uniform in size, shape and spacing.

Age: Maastrichtian

Genus: Gleicheniidites (Potonie, 1956)

Gleicheniidites senonicus Potonie, 1956

BA – 16, 37m

Fig. 30

Description: Trilete microspore, trilete mark, thin, amb triangular to sub-triangular, sides moderately concave, corners round, tricrassate but crassitudes are compressed as to appear cicatricose.

Age: Maastrichtian

Genus: Cingulatisporites (Van Hoeken-Klinken-berg, 1964).

Cingulatisporites ornatus Van Hoeken-Klinken-berg, 1964

BA – 16, 37 m

Fig. 59

Description: Trilete microspore, amb triangular-round, sides convex, central body surrounded by a distinct ornamented cingulum, trilete mark thin, armed long and extended to the margins of the central body, not bordered by Margo, proximal surface convex, smooth but covered by low vernicae, cingulum split into several clavate structures

Age: Maastrichtian

Subdivision: MONOLETE (Potonie, 1956).

Genus: Laevigatosporites (Protonie, 1956)

Laevigatosporites haardtii Protonie and Venitz

BA – 17, 3 m

Fig. 11

Description: Monolete spore, posses limited sculptures and usually appears as tiny particles

Age: Maastrichtian

Subdivision: CINGULATISPORATES

Genus: Zlivisporites (Pacltova, 1959)

Zlivisporites blanensis (Pacltova, 1959)

BA – 17, 27 m

Fig. 15

Description: Specimen has cingulated sculptures which appear to represent residual perisporal membranes.

Age: Maastrichtian

Subdivision: VERRUCATI (Muller, 1968).

Genus: Distaverrusporites (Muller, 1968)

Distaverrusporites simplex (Muller, 1968)

BA – 16, 29 m

Fig. 28

Description: Trilete microspore, amb triangular, sides convex, trilete mark thin, arms long and extend to the equatorial margin, not bordered by any Margo, exine thick.

Age: Maastrichtian

Division: Pollenites Potonie, 1956

Class: Gymnospermae

Genus: Ephedripites (Boltenhagen and Azema, 1974)

Ephedripites ambigus (Boltenhagen and Azema, 1974)

BA – 7, 32 m

Fig. 4

Description: The Ephedripites is regarded as a taxonomic synonym of Equisotosporites (Singh, 1964, 1971), multicostate oval in outline, twice as long as broad, narrow ridges, covering the colpi.

Age: Maastrichtian

Class: Monocolpates (Iversen and Troels-Smith, 1950).

Genus: Auriculiidites (Elsik, 1964, Elsik and Thanikaimoni, 1970)
Auriculiidites sp.
BA – 7, 32 m
Fig. 60
Description: Oval monosulcate pollen grain with auriculate structures at the extremities of the grain. Sulcus long, extending to diameter of the grain, exine thin, and microreticulate. The microreticulate ornamentation and the overall smaller size differentiate this species from A. reticulatus.

Age: Maastrichtian

Genus: Spinizonocolpites (Muller, 1968).

Spinizonocolpites echinatus (Muller, 1968)
BA – 16, 42 m
Fig. 55
Description: *S. echinatus* has smooth to finely reticulate ornamentation, closely spaced processes and expanded or bulbous bases.

Age: Maastrichtian

Genus: Longapertites (Van Hoeken-Klinkenberg, 1964).

Longapertites microfoveolatus (Jan du Chene and Adegoke, 1978)
BA – 16, 47 m
Fig. 52
Description: Palm pollen, fine foveolate sculpture.
Age: Maastrichtian
Genus: Longapertites (Van Hoeken-Klinkenberg, 1964)
Longapertites chlonovae (Boltenhagen, 1978)
BA – 16, 53 m
Fig. 34
Age: Maastrichtian

Genus: Monocolpites (Van der Hammen, Pierce, 1961).

Retimonocolpites sp. (Pierce, 1961)
BA – 7, 22 m
Fig. 8
Description: Intectate reticulate, Monocolpates pollen grain, endocolpi only. The lumina of the reticulum vary in size, appearing smaller on the two extremes of the pollen grain.

Class: Porosa (Potonie, 1970).

Sub-class: Triporines (Potonie, 1956)
Genus: Proteacidites (Cookson, 1950)
Proteacidites sigalii Boltenhagen, 1978
BA – 17, 20 m
Fig. 24
Description: Pollen sub-isopolar, oblate, angular apertures, triporate. Amb angular, sides nearly straight, apertures sub-circular, exine slightly thicker in the equatorial inter-aperture regions, sexine about half as thick as nexine, ornamented with reticulum.

Age: Maastrichtian

Sub-class: Triporines (Potonie, 1960).

Genus: Echitriporites (Van Hoeken-Klinkenberg, 1964)
Echitriporites trianguliformis (Van Hoeken-Klinkenberg, 1964)
BA – 17, 21 m
Fig. 39

Description: It is characterized by fine echinate or spinose form. Triporate, triangular in polar view, pores circular, thick wall, Structureless, surface psilate, rather densely and even covered with spines, conical shaped with fairly sharp points.

Age: Maastrichtian

Class: Tricolpates (Iversen and Troels-Smith, 1950).

Genus: Retitricolpites (Van der Hammen, 1956a)
Retitricolpites irregularis (Van der Hammen, 1956b)
BA – 7, 47 m
Fig. 48
Description: Tricolpate pollen grain, probably iso-polar, radially symmetrical, short colpi, exine thick and coarsely reticulate.

Age: Maastrichtian

Class: Psilatricolpates (Van der Hammen and Wymstra, 1964)

Genus: Psilatricolpites (Van der Hammen and Wymstra, 1964)
Psilatricolporites Crassus (Van der Hammen and Wymstra, 1964)
BA – 17, 38 m
Fig. 20
Description: Psilatectate pollen grain with clearly visible columellae, Tricolpate, indistinct and short Constricticolpate.

Age: Maastrichtian

Class: Proxaperturates (Van der Hammen, 1956).

Genus: Proxapertites (Van der Hammen, 1956b)
Proxapertites cursus (Van Hoeken-Klinkerberg, 1966)
BA – 17, 37 m
Fig. 17
Description: Proxaperturates pollen grains, reticulate, under the muri of the reticulum are columellae, but most of the lumina are without columellae, semi-tectate

Age: Maastrichtian

Class: Stephanocolpates

Genus: Tubistephanocolpites (Salami, 1983).
Tubistephanocolpites cylindricus (Salami, 1983)
BA – 7, 33 m
Fig. 5
Description: Stephanocolpates pollen, it is circular to sub-circular in outline, encircled by meridionally arranged colpi with pores. Exine is smooth.

Age: Maastrichtian

Class: Droseraceae

Genus: Droseridites (Cookson, 1950 ex. potonie, 1956).
Droseridites senonicus (Cookson, 1950)
BA – 7, 23 m
Fig. 22
Description: The species is characterized by inaperturate and spinose pollen grains that are united in loose tetrahedral tetrads. The grains are prolate, striate and Tricolpate. The colpi are slender and long, the striae are very fine, densely packed and situated parallel to the polar axis.
Age: Maastrichtian

Class: Monoporates

Genus: Monoporites (Cookson, 1950)
Monoporites annulatus (Van der Hammen, 1954)
BA – 17, 23 m
Fig. 61
Description: The species consists of a spherical, often thin-walled and rather large grain, with a single pore. They are characteristics of grasses.
Age: Maastrichtian

Genus: Monocolpopollenites (Pflug and Thomson, 1953).

Monocolpopollenites sphaeroidites (Pflug and Thomson, 1953)
BA – 7, 29 m
Fig. 51
Description: Monocolpates copus, spherical in shape.
Age: Maastrichtian

PHOTOMICROGRAPHS OF PALYNOMORPHS

ALL MAGNIFICATION IS X 1000

Monocolpites marginatus

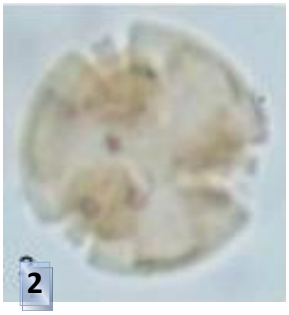

Psilatricolporites Crassus

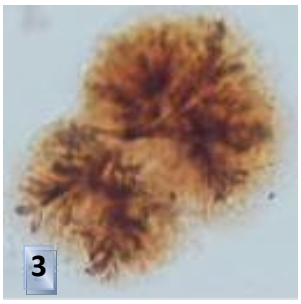

Botryococcus braunii (A)

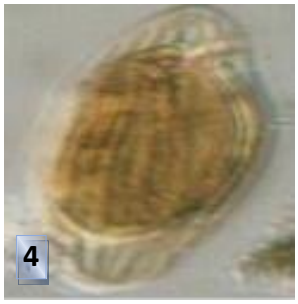

Ephedripites ambiguous

Tubistephanocolpites cylindricus

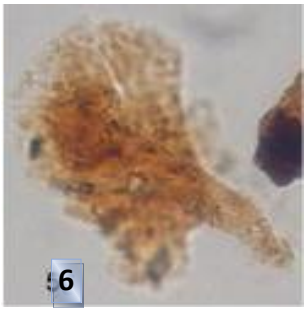

Botryococcus braunii (B)

Monocolpopollenites

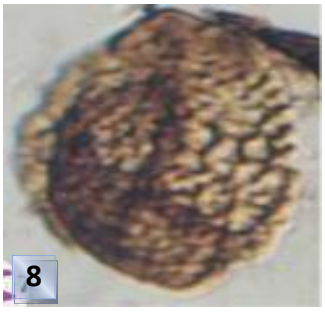

Retimonocolpites sp.

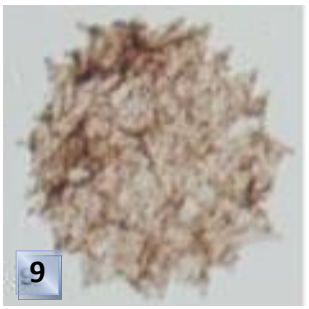

Pediastrum sp

7 8 9

Sapotaceoidaepollenites sp.

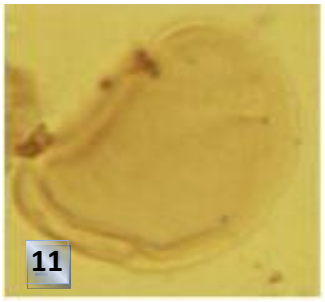

Laevigatosporites haardtii

Ctenolophonidites costatus

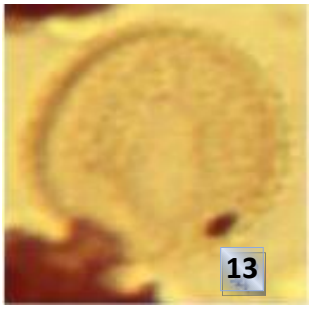

Arecipites crassimuratus

Germmamonoporites

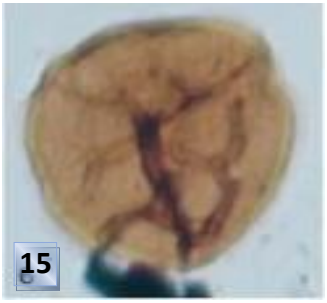

Zlivisporites

Fungal spore (A)

Proxapertites cursus

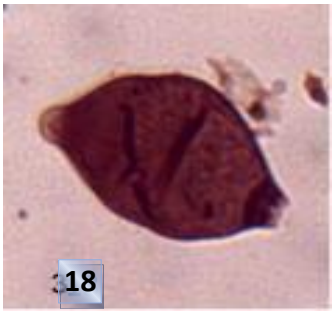

Fungal spore (B)

Osmundacidites sp.

Psilatricolporites crassus

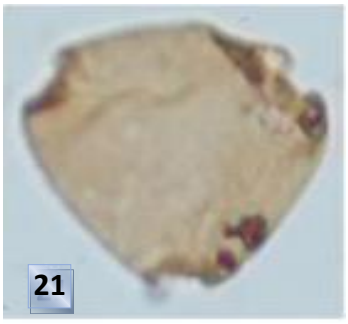

Cupanieidites sp.

Droseridites Senonicus

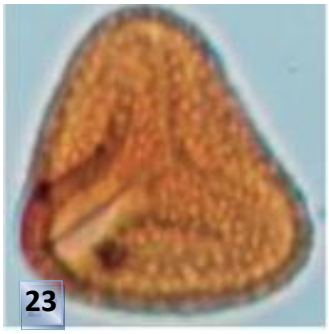

Foveotriletes margaritae

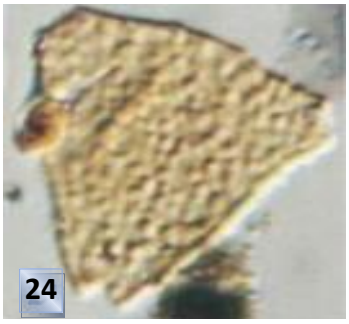

Proteacidites sigalii

Cyathidites sp.

Tricolporopollenites sp.

Leoisphaeridia sp.

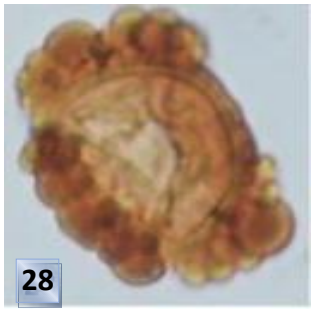

Distaverrusporites simplex

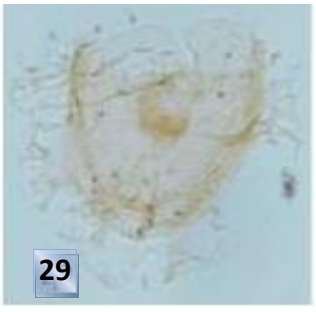

Nematosphaeropsis sp.

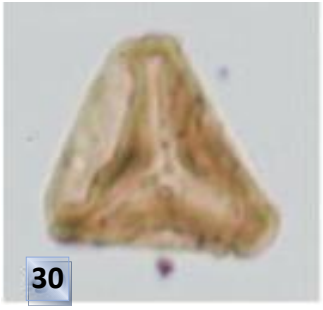

GlecheniditesSenonicus

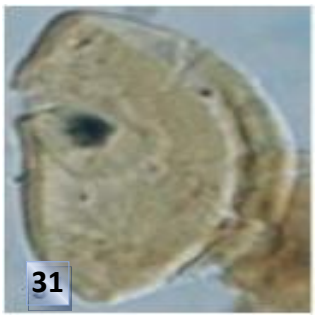

Longapertites

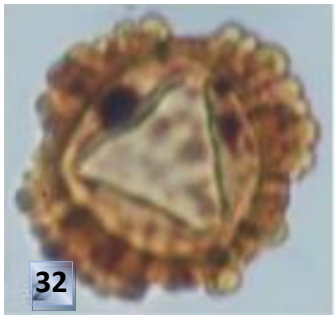

Cingulatisporites Ornatus

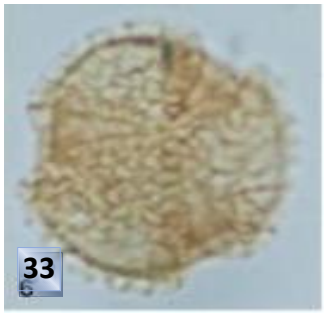

Retitricolporites

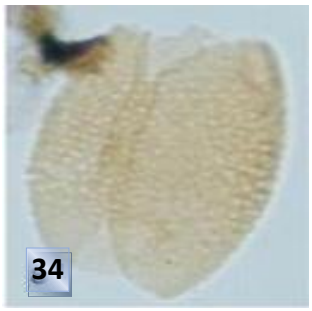

Longapertites chlonovae

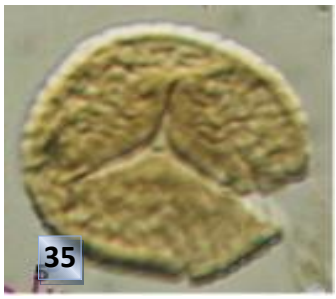

Rugulatisporites caperatus

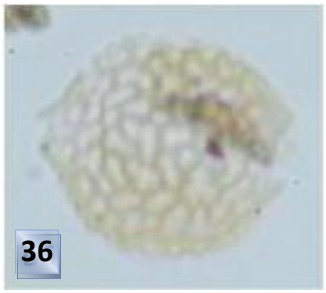

Auriculiidites sp.

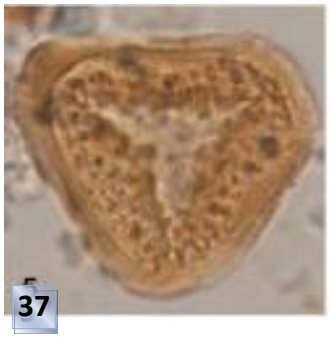

Polypodiaceoisporites sp.

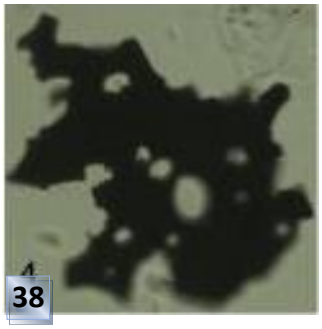

Charred Graminae Cuticle

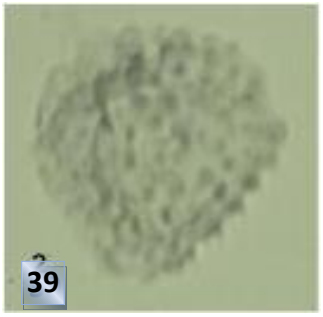

Echitriporites trianguliformis

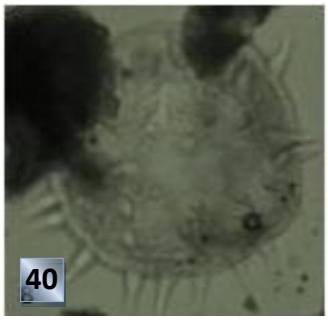

Spinizonocolpites echinatus

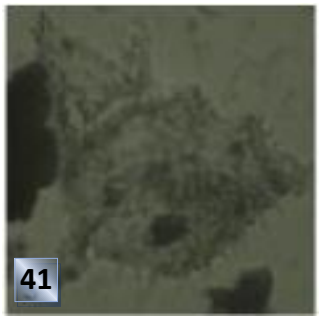

Auriculopollenites

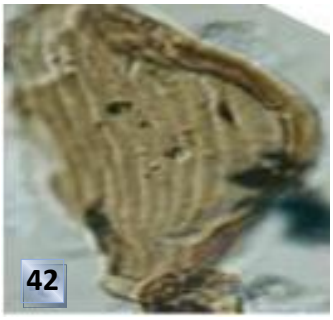

Gnetaceaepollenites sp.

Monoporites annulatus

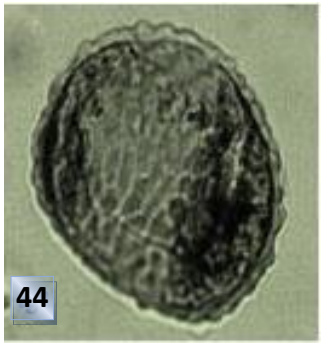

Verrucatosporites sp.

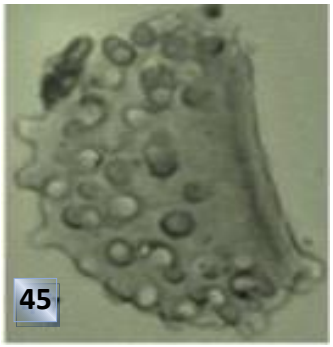

Verrucatosporites usmensis

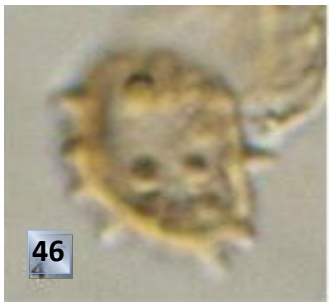

Laevigatosporites haardti sp.

Cingulatisporites ornatus

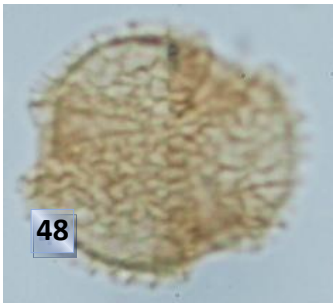

Retitricolporites irregularis

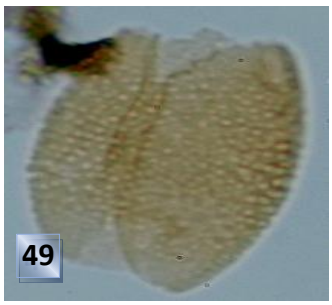

Longapertites chlonovae

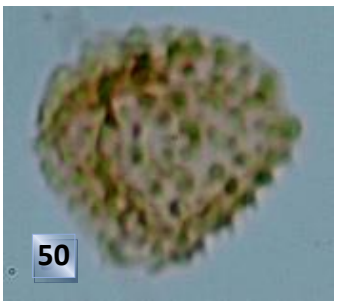

Echitriporites trianguliformis

Monocolpopollenites sphaeroidites sp

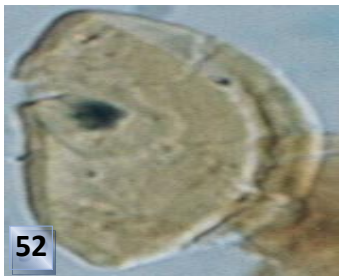

Longapertites microfoveolatus

Rugulatisporites caperatus

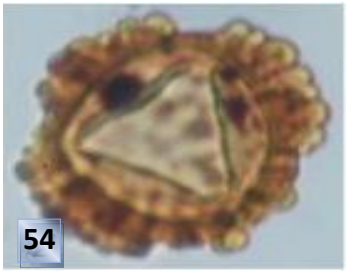

Droseridites senonicus sp.

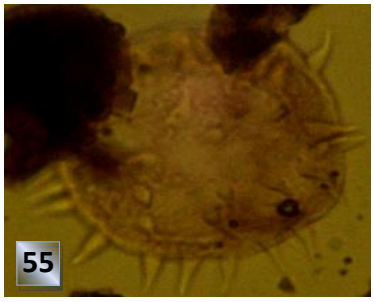

Spinizonocolpites echinatus

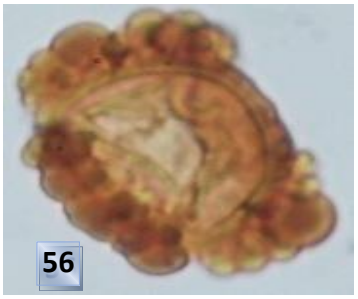

Distaverrusporites simplex

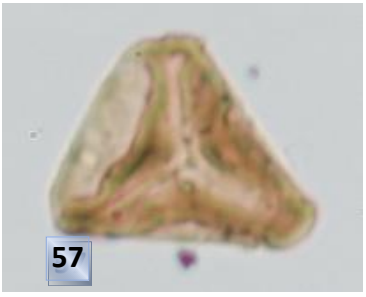

Glecheniidites senonicus

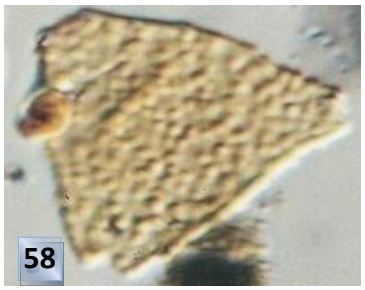

Proteacidites Sigalii

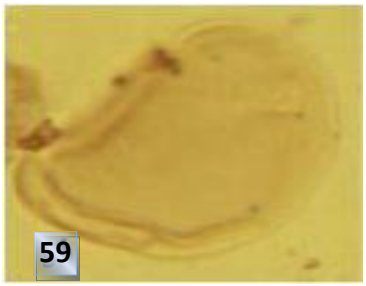

Cingulatisporites ornatus sp.

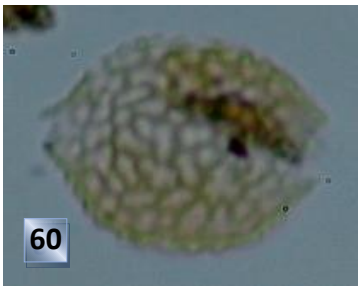

Auriculiidites spp.

Monoporitesannulatus

4.0 CONCLUSION

The paper has aptly dwelt on the descriptive systematic Palynology of the various palynoforms recovered from the Maiganga coal mine situated within the Gombe Formation. The observed and described forms include various Spores and Pollen grains as well as algal spores, totaling 61 species.

5.0 REFERENCES

Aboul Ela, N. M. (1978). The Palynological Characteristics of the Upper Cretaceous Sediments in Abu Tarkur Plateau, Kharga Oasis, Egypt. *Revista Espanola de Micropaleontologia*. X, (3) 421 – 442.

Ames, H. T. & Spackman, W. (1985). Catalog of fossil, spores and pollen. Tertiary and Upper Cretaceous Spores and Pollen from Africa, Europe, Canada, Australia and New Zealand. 44, *University Park, Pennsylvania*. 182.

Andrew, F. W. (2004). The semi – automated classification of sedimentary organic matter and dinoflagellate cysts in palynological preparations. An unpublished PhD thesis 1 – 4.

Atta-Peters, D. & Salami, M. B. (2004). Late Cretaceous to Tertiary Pollen grains from Offshore Tano Basin, Southwestern Ghana. Instituto *Geologico Minero de Espana* 451 – 465.

Barber, W., Tait, E. A. & Thompson, J. A. (1954). The Geology of the Lower Gongola. In: *Annual Report of the Geological Survey of Nigeria*. 1952 – 53, 18 – 20.

Boltenhagen (1978). Introduction a la palynology stratigrapique du basins sedimentaire de Afrique equitoriale, *Memoire du Bureau de Researches de Geologique et Mineres*, 32, 305 – 327.

Boltenhagen, E. & Azema, A. (1994). Spores et pollen du Cretace Supericur du Gabon: *Pollen et Spores*. 9, 191 – 199.

Burke, K. C., Dessauvagie, I. F. J. & Whiteman, A. J. (1972). Geological History of the Benue Valley and adjacent areas In: Dessauvagie, T. F. J. and Whiteman, A. J. (Eds). *African Geology, Ibadan University Press*, Ibadan. 187 – 205

Carter, J. D., Barber, W. and Tait, E. A. (1963). The Geology of parts of Adamawa, Bauchi and Bornu Provinces in North – Eastern Nigeria. *Geological Survey of Nigeria Bulletin.* 56 – 59.

Cookson, I. C. (1950). Fossil pollen grains of the protaceous type from Tertiary deposits in Australia. *Australian Journal of Scientific Research*. B. 3.

Couper (1953). Uppermost Cenonian-basal Turonian ammonites from Salinas, Angola. *Annals of South.Africa Museum*, Cape Town, 75, 51 – 152.

Dettmann, M. E. (1963). Upper Mesozoic Microfloras from Southeastern Australia. *Proceedings of the Royal Society of Victoria,* 77, 1 – 148.

Dike, E. F. C. (1995). Stratigraphy and Structure of the Kerri-Kerri Basin, Northeastern Nigeria. *Journal of Mining and Geology,* 29 (2). 77 – 92.

Elsik, W. C. (1964). New Sporomorph genera from the Upper Cretaceous of Peru. *Pollen et Spores* 6 (2), 553 – 564.
Elsik, W. C. (1964). New Sporomorph genera from the Upper Cretaceous of Peru. *Pollen et Spores* 6 (2), 553 – 564.

Elsik, W. C. & Thanikamoni, L. (1970). Palynology of Paleocene Rockdale Lignite, Milan County, Texas. II Morphology and Taxanomy. *Pollen et Spores*. 10 (3), 599 – 664.

Falconer, J. D. (1911). The Geology and Geography of Northern Nigeria. *Macmillan London*, 295.

Gutjahr, C. C. M, (1960): Palynology and its application in petroleum exploration. *Gulf Coast Association Geological Society Trans*. 10. 175, 187.

Hamidu, I. (2012). The Campanian to Maastrichtian Stratigraphic Succession in the Cretaceous Gongola Basin of North-East Nigeria. Ph.D thesis A.B.U, Zaria. 41.

Iversen, J. & Troels-Smith, J. (1950). Pollen morphologische Definitionen Und typen. *Denmark Geologische Unders*. IV Rackke Bd. 3.8 Copenagen.

Martin, H. A. & Rouse, G. E. (1966). Palynology of Late Tertiary Sediments from Queen Charlotte Islands, British Colombia: *Canadian Journal of Botany*; 44, 171 – 208.

Muller, J. (1968). Palynology of Pedawan and Plateau sandstone formation (Cretaceous – Eocene) in Sarawak, Malaysia. *Micropaleontology*, 14 (1), 1 – 39.

Murat, R. C. (1972). Stratigraphy and Paleogeography of the Cretaceous and Lower Tertiary of Southern Nigeria. In T. F. J. Dessauvagie and Whiteman (Eds), *African Geology, Ibadan University Press,* Nigeria. 251 – 266.

Obianuju, P. U. (2005): Palynological study of the Okaba Coal Mine section in the Anambra Basin, Southeastern Nigeria. *Journal of Mining and Geology,* 41 (2) 193 – 203.

Ojo, O. J. (2009). Occurrence of some Maastrichtian Dinoflagellate Cysts from the Upper Cretaceous Sediments in Southeastern Bida Basin, Nigeria: Implications for Age and Paleoenvironments. *Ozean Journal of Applied Sciences* 2 (3), 291 – 305.

Onoduku, U.S. (2013). The Geochemistry, Palynology and Palynofacies characteristics of Maiganga Coal deposit, Upper Benue Trough, Northeastern Nigeria. An unpublished *PhD Thesis*. Federal University of Technology, Minna, Nigeria. pp 179.

Pacltova, B. (1959) On some plant microfossils from fresh-water sediments of the Upper Cretaceous (Senonian) in the South Bohenian Basin. *Sbornik Ustred Geologie*, 26, 38 – 50.

Pacltova, B. (1970). New types of spores (genera and species) from the Bohemian Miocene: *Palaont; Abh. B-Palaobot*; III; (3 & 4) 599 – 617. Pflug, H. & Thompson, P. W. (1953). Pollen und Sporen. *Mitteleuro Paischen Tertiars. Palaeontographica*. 94.

Pierce, R. C. (1961). Lower Upper Cretaceous plant microfossils from Minnesota. University of Minnesota, *Minnesota Geological Survey Bulletin*. 42.

Potonie, R. (1956). Synopsis der Gattungen der Sporae dispersae I. Teil Sporites, I. *Beiheffe zum Geologischen Jahrb* 23, 3 – 103.

Potonie, R. (1958). Synopsis der Gattungen dispersae II. Teil: Sporites Machuridge saccite Aletes praecolpates, tricolpates, monoclpates. *Beiheffe zum Geologischen Jahrb* 39, 3 – 139.

Potonie, R. (1960). Synopsis der Gattungen der Sporae dispersae III. Teil nachtrage Sporites, Fotsetziang pollenites. Micropaleon. General register zu Teil I – IV. *Beiheffe zum Geologischen Jahrb*, 39: 189

Reyment, R. A. (1965). Aspects of the geology of Nigeria. The Stratigraphy of the Cretaceous and Cenozoic deposits. *Ibadan University Press.* 23 – 73.

Salami, M. B. (1983). Some Late Cretaceous and Early Tertiary Pteridophytic Spores From the Southern Nigeria Sedimentary Basin. *Revista Espanola de Micropaleontologia*. XV (2). 257 – 272.

Salami, M. B. (1990). Palynomorph taxa from the "Lower Coal Measures" deposits(? Campanian – Maastrichtian) of Anambra Trough, Southeastern Nigeria. *Journal of African Earth Sciences* 11: 135 – 150.

Simpson, A. (1954). The Nigerian Coal Field: The Geology of Parts of Onitsha, Owerri and Benue Provinces: *Nigeria Geological Survey Bulletin*. 24, 85.

Thompson, J. H. (1958). The Geology and Hydrogeology of Gombe, Bauchi Province. *Records of the Geological Survey of Nigeria*, 1956. 46 – 65.

Van der Hammen, T. (1954). The development of Colombian flora throughout geological periods, I: Maastrichtian to Lower Tertiary. *Boletin Geologico* (Bogota), 2(1). 49 – 106

Van der Hammen, T. (1956a). A palynological systematic nomenclature. *Boletin Geologico* 4, 2 – 3, Bogota. 63 – 101.

Van der Hammen, T. (1956b). Description of some genera and species of fossils.

Van der Hammen, T. & Pierce, R. L. (1961). Lower Upper Cretaceous plant microfossils. *University of Minnesota – Mines Geological Survey Bulletin*. 42.

Van der Hammen, T. & Wymstra, T. A. (1964). A palynological study on the Tertiary and Upper Crateceous of British Guiana. *Leidse Geologische Mediedelingen*. ded 30.

Van Hoeken-Klinkenberg P. M. J. (1964). A Palynological Investigation of Some Upper-Cretaceous Sediments in Nigeria. Palynological Laboratory, *Geological Institute, Leiden*. Netherlands

Whiteman, A. J. (1973). Nigeria: Its petroleum geology, resources and potentials. (1) 176, (2) 238. *Graham and Trotman*, London, U.K.

Zaborski, P. M., Ugoduluwa, F., Idornigie, A., Nnabo, P. & Ibe, K. (1997). Stratigraphy and Structure of the Cretaceous Gongola Basin, Northeastern Nigeria. *Bulletin des Centres de Recherches Exploration – Production Elf – Aquitaine*, 21. 153 – 185.

MODELLING AND ANALYTICAL SIMULATION OF DRYING BEHAVIOUR OF LEATHER

MUDASIRU O.D; ; OLAYIWOLA, R. O

Department of Mathematics

Federal University of Technology, Minna, Nigeria

E-mail: drlarry2012@yahoo.com

ABSTRACT

A mathematical model capable of predicting the behavior of drying leather has been presented. The criteria for existence and uniqueness of the solution of the model were established.

The equations governing the phenomenon were solved using parameter expanding method and eigenfunction expansion technique. The results obtained revealed that ratio of moisture content, rare constant and scale thermal conductivity play an important role in the drying process.

Keywords:Leather, Drying behaviors, Eigenfunction expansion technique.

INTRODUCTION

Leather is a durable and flexible material created by tanning animals rawhide and often cattle hide. It can be produce at manufacturing scales ranging from cottage industry to heavy industry. It can be made from animals such as cows, pigs, goats, sheep etc. Exotics animals such as Alligators, Ostriches, Kangaroos, Dogs, and Cats who are slaughtered for their meat and skin in some parts of the world which exports their skins around the world. Because of no indication of leather, you never really know where or from whom it comes from.(Encyclopedia of science clarified 2015).

Leather is one of the earliest and most useful discoveries. Our ancestors used leather to protect themselves from the elements. Primitive man hunted wild animals for food then made clothing, footwear and tents from hides. Also for sources of income generation i.e trade by barters. Also as protector of man from elements.

Leather has numerous uses, because it is a versatile material, such as; rugs, foams, protectors,clothing, binding, saddles, foot wears, furniture, gloves, watches, balls, bags, cases, holsters accessories also used as income generations.

In this chapter a literature review of simulation of drying behavior of lather that are relevant to this research work is presented. Emphasis is given drying behaviors of leather.

Among the first studies of this type was carried out by (Vaskoval et al.,2006) where it was it was dealt with an area of leather product like footwear, clothing, wallet, bags etc are among the object of our everyday use. Achieving the final products comprises a lot of waste arising from the raw material processing and creating specific item only in tanneries. Million tons of waste generated annually.Kkolomaznik et al.,(2014) worked on significant amount of waste that is produce in the manufacturing sector of natural polymers especially in the leather industry. The leather tanning industry is historically one of the first industries occupying an important function in term of by- product of the other industries.

Jaroslav et al.,(2013) worked on the theoretically tools of chemical engineering of optimizing of real technological demining procedure on leather. Haghi et al.,(2001) also worked on convective drying to have an essential role, that leather fabrication has become an important industrial development worldwide, also emphasis is made on transient temperature and moisture concentration distribution on the leather in a dryer.

Goldsim (2004) defined simulation as the process of creating a computer model to represent existing a computer model to represent existing or proposed system(in this case drying leather behaviour) in order to identify and understand the factor that control the system. Any system that can be quantitatively described using equations and rules can be be simulated. Arma et al.,(1988) also make his contribution by saying some of the unit operations involved in the leather industry especially the drying processing are still based on empiricism and tradition with little use of science principal

In a dynamic simulation, the system changes and evolves with time and the objective in modeling such a system is to understand the way in which it is likely to evolve, predict the future behavior of the system and determine how to influence the future behavior.

Also Behzat et al., (2004) discuss some technological parameter of ostrich skin and leathers, which are considered to be important in the leather industry were analyzed, it was observed that these parameter vary according to the weather skin comes from the neck, leg and back side. However on basis of area and strength value, leg and backside are more appropriate for upper leather production and neck side maybe use as accessories.

Also Nordon et al.,(1967) has been modified to determine the transient temperature and moisture concentrating distribution of leather in a radiator or dryer. Beard et al.,(1976) also worked on leather where he assumed leather can exist in two layer one been dry and the other wet. However, his analysis did not describe what is going inside the leather. He used two experimental result of fit his data to the experimental results of the measured temperature

variation inside the dryer. Milan et al.,(2007) also worked on leather manufacturing procedure considerable amount of water which means unfavorable impact on elementary component especially soil, water and air. Haghi (2014) also worked on convective drying as usually encountered in many industrial field(food industry, building industry, leather industry etc Therefore ,the study of this of problem becomes very important and for very several decades attracted the attention of many investigator. He also presented a comprehensive mathematical model for the drying process which emphasis on convective drying model to be used to describe the drying behaviors of leather.

MATERIALS AND METHODS

Among the many processes that are performed in the leather industry, convective drying has an essential role. Leather fabrication has become an important industry development worldwide. To simplify the model the following assumptions are made:

1. Both the initial temperature and initial moisture concentrated of air in leather pores depend on space variable x;
2. The rate constant is small, the evaporation rate is also so small that the moisture content decreases very slowly;
3. When the moisture content is high ,the initial temperature rise of the leather also become high ;
4. An analogy was assured between heat and mass transfer and both heat and mass transfer coefficient were determined;
5. That the leather can consist of two layer one dry and another wet;
6. No chemical reaction takes place during drying i.e. chemical properties of material, air and moisture are constant within the range of temperatures considered.

Product is uniformly distributed in the drying chamber.

Following Haghi(2001),the mathematical model describing the drying behaviors of leather is given as;

$$\frac{\partial C_A}{\partial t} + \frac{\partial C_f}{\partial x} = D\frac{\partial^2 C_A}{\partial x^2} \quad (1)$$

$$K\frac{\partial^2 t}{\partial x^2} + \lambda\frac{\partial c_f}{\partial t} = Pc_p\frac{\partial T}{\partial t} \quad (2)$$

For mass transfer of the leather

$\frac{1}{\rho(1-\varepsilon)}\frac{\partial c_f}{\partial t}$=K$(y_{A-y_f})$ (3)

Also, the relative humilities of air and leather are assumed to be

$y_{A=}\frac{c_{ART}}{P_s}$ (4)

And

$y_{A=}\frac{c_F}{\rho(1-\varepsilon)}$ (5)

The initial and boundary conditions are formulated as follow;

$c_{A(X,0)}$=$(c_{e-c_{A0}})\frac{x}{l}\left(1-\frac{x}{l}\right)+\frac{\partial c_A}{\partial x}|_{x=0}=0,\ \frac{\partial c_A}{\partial x}|_{x=L}=lm(c_{e-c_A})$

T(x,o)=$(T_{e-T_0})\frac{x}{l}\left(1-\frac{x}{l}\right)+T_0,\frac{\partial c_A}{\partial x}|_{x=0}=0,\quad \frac{\partial c_A}{\partial x}|_{x=L}=lm\left(T_{e-T_0}\right)$

$c_{f(x,o)=}c_{f0}$

Where C_A is moisture content of air in the leather pores $(\frac{kg}{m^3})$, c_e is moisture content of the externalair$(\frac{kg}{m^3})$, c_f $(\frac{kg}{m^3})$, c_p is specificheat$(\frac{KJ}{\frac{Kg}{K}})$,Disdiffusion coefficient$(\frac{m^2}{s})$, $h_e$is heat transfer coefficient$(\frac{w}{m^2k})$, h_m is heat transfer coefficient (m/s),K isthermalconductivity$(\frac{w}{mk})$,mismasstransferrate$(\frac{kg}{m^2s})$, p_s is saturated pressure(pa),qis convective heat transfer rate$\frac{w}{m^2}$),R is gas constant$(\frac{kj}{k})$,T is temperature(k), T_e is external air temperature(k),t is time(s), y_A is relative humidity of air pole of leather, y_f relative humidity of leather,ε is porosity, $\lambda\ is\ l$atent heat of evaporation(kj/kg),β is scale thermal conductivity,γ evaporation rate parameter is rate constant,α is the ratio of moisture content.

Substituting equations (4) and (5) into (3), we have

$\frac{\partial c_f}{\partial t}=\frac{K(\rho(1-\varepsilon))c_{ART-p_s}}{ps}$ (6)

Non dimensionalization

Here we non dimensionalize equation (1) – (6), using the following dimensionless variable:

$\theta=\frac{T-T_0}{T-T_0},\ \phi=\frac{c_{A-c_{A0}}}{c_{e-c_{A0}}},\ \psi=\frac{c_f}{c_{f0}},\quad x'=\frac{x}{L},\ t'=\frac{DT}{l^2}$ (7)

Then

x=x'L, T=$\theta(T_{e-}T_0)+T_0,\ c_A$= $\phi(c_{e-}CA_0)+c_{A0},\quad c_{f=}\ \psi c_{f0,}$ t=$\frac{l^2t'}{D}$

$\partial x=L\partial x',\ \partial t=\partial t'\frac{L^2}{D},\ \partial c_{f=\partial}\varphi c_{f0},\ \partial c_{A=\partial}\phi(c_{e-}CA_0),\ \partial T=\partial\theta(T_{e-}T_0).$ (3.9)

Substituting 7 into 1, 2,and 5 we obtain

For equation (1),

$\frac{\partial\phi}{\partial t'}+\frac{\partial\varphi c_{f0}}{\partial t'(c_{e-}CA_0)}=\frac{\partial^2\phi}{\partial^2x'^2}$ (8)

Dropping prime we have

$\frac{\partial\phi}{\partial t}=\frac{\partial^2\phi}{\partial x^2}-\alpha\frac{\partial\varphi}{\partial t}$ (9)

Where α =$\frac{c_{f0}}{c_{e-c_{A0}}}$

For equation (2)

$$\frac{\partial\theta}{\partial t} = \frac{k}{D\rho c_p}\left(\frac{\partial^2\theta}{\partial^{2x12}}\right)+\frac{\lambda}{D\rho c_p}\left(\frac{\partial\varphi c_{f0}}{\partial t'(T_{e-T_0})}\right) \quad (10)$$

Dropping prime we have,

$$\frac{\partial\theta}{\partial t} = \beta\frac{\partial^2\theta}{\partial x^2}+\gamma\frac{\partial\psi}{\partial t} \quad (11)$$

Where $\beta=\frac{K}{D\rho c_p}$ and $\gamma = \frac{\lambda}{D\rho c_p}\left(\frac{c_{f0}}{T_{e-T_0}}\right)$

For equation (5)

$$\frac{\partial\psi}{\partial t'} = \frac{KL^2(\rho(1-\varepsilon))(\phi(c_{e-}cA_0)+c_{A0})R(\theta(T_{e-}T_0)+T_0)-p_s\varphi c_{f0}}{p_s D c_{f0}(\rho(1-\varepsilon))} \quad (12)$$

Dropping prime we have,

$$\frac{\partial\psi}{\partial t} = K(\sigma\theta\phi+\delta\phi+\mu\theta-\varphi\upsilon+\eta) \quad (13)$$

Where;

$$\sigma = \frac{\rho(1-\varepsilon)L^2R(c_{e-c_{A0}})(T_{e-T_0})}{Dc_{f0}p_s}$$

$$\delta = \frac{\rho(1-\varepsilon)L^2RT_0(T_{e-T_0})}{Dc_{f0}p_s}$$

$$\mu = \sigma = \frac{\rho(1-\varepsilon)L^2Rc_{A0}(T_{e-T_0})}{Dc_{f0}p_s}$$

$$\upsilon = \frac{pL^2}{D}$$

$$\eta = \frac{\rho(1-\varepsilon)L^2c_{A0}T_0}{Dc_{f0}}$$

For the boundary conditions we have,

$c_A(x,t)$ =$(c_{e-}c_{A0})\phi(x',t')$+$c_{A0}$

Then

$c_A(x,0)$ = $(c_{e-c_{A0}})\phi(x',0)$+$c_{A0=}$=$(c_{e-c_{A0}})\frac{x}{L}(1-\frac{x}{L})$+ c_{A0}

i.e

$\phi(x',0)$= $x'(1-x')$

Dropping prime we have,

$\phi(x,0) = x(1-x)$

$\frac{\partial c_A}{\partial x}|_{x=0} = \left(c_{e-c_{A0}}\right), \frac{\partial\phi}{\partial x'}|_{x=0} = 0$

$\frac{\partial\phi}{\partial x'}|_{X'=0} = 0$

Dropping prime we have

$\frac{\partial\phi}{\partial X}|_{x=0} = 0$

$\frac{\partial c_A}{\partial x}|_{x=L} = \frac{(c_{e-c_{A0)}}}{L} = \frac{\partial\phi}{\partial x'}|_{Lx'=L} = hm\left(c_{e-\left(c_{e-c_{A0}}\right)\phi-c_{A0}}\right)$

i.e

$\frac{\partial\phi}{\partial x'}|_{x'=1} = Llm(1-\phi)$

Dropping prime, we have

$\frac{\partial\phi}{\partial x}|_{x=0} = a(1-\phi)$

Where a =Lhm

T(x,t)=$(T_{e-T_e})\theta(x'-t')+T_0$

i.e

$\theta(x',0) = x'(1-x')$

Dropping prime we have,

$\theta(x,0) = x(1-x)$

$\frac{\partial T}{\partial x}|_{x=0} = 0$ =(T_{e-T_e}), $\frac{\partial\theta}{\partial x'}|_{x'=0} = 0$

i.e

$\frac{\partial\theta}{\partial x'}|_{x'=0} = 0$

Dropping prime we have ,

$\frac{\partial T}{\partial x}|_{x=0} = 0$

$\frac{\partial T}{\partial x}|_{x=L} = \frac{(T_{e-}}{L}T_0)$ $\frac{\partial\theta}{\partial x'}|_{Lx'=L}$ =he $(T_{e-(T_{e-T_e})} - T_0)$

i.e

$\frac{\partial\theta}{\partial x'}|x'_{=1} = \frac{Lhe}{T_e - T_0}((T_e - T_0) - (T_e - T_0)\theta)$

Dropping prime, we have,

$\frac{\partial\theta}{\partial x}|_{x=1} = b(1-\theta)$

Where b=Lhe

$c_{f(x,t)=}\, c_{f0}\, \varphi(x', t') = c_{f0}$

$\varphi(x', 0) = 1$

Dropping prime, we have

$\varphi(x, 0) = 1$

Therefore, the dimensionless equations with boundary conditions are as follows;

$$\frac{\partial\phi}{\partial t} = \frac{\partial^2\phi}{\partial x^2} - \alpha\frac{\partial\varphi}{\partial t} \quad (14)$$

$$\frac{\partial\theta}{\partial t} = \beta\frac{\partial^2\phi}{\partial x^2} - \gamma\frac{\partial\varphi}{\partial t} \quad (15)$$

$$\frac{\partial\varphi}{\partial t} = \sigma\phi\theta + \delta\phi + \mu\theta - \upsilon\varphi + \eta \quad (16)$$

With Initial and Boundary conditions

$$\left.\begin{array}{c} \phi(x,0) = x(1-x), \frac{\partial\phi}{\partial x}|_{x=0} = 0, \quad \frac{\partial\phi}{\partial x}|_{x=1} = a(1-\phi) \\ \theta(x,0) = x(1-x), \frac{\partial\theta}{\partial x}|_{x=0} = 0, \frac{\partial\theta}{\partial x}|_{x=1} = b(1-\theta) \\ \varphi(x,0) = 1 \end{array}\right\}$$

Using eigenfunctions expansion method and direct integration, we obtain the solution of equations (14) - (16) as

$$\phi_0(x,t) = \frac{1}{3} - \sum_{n=1}^{\infty} \quad w exp^{-vt} cosn\pi x$$

Where

w=$-2\left[\frac{1+(-1)^n}{(n\pi)^2}\right]$

v=$(n\pi^2)$

$$\theta_0(x,t) = \frac{1}{3} - \sum_{n=1}^{\infty} \quad w exp^{-mt} cosn\pi x$$

$$\psi_0(x,t) = q\left(\frac{1}{3}t - \frac{w}{v}\sum_{n=1}^{\infty} \quad exp^{-vt}\cos n\pi x\right) + \mu\left(\frac{1}{3} - \frac{w}{m}\sum_{n=1}^{\infty} \quad exp^{-mt}\cos n\pi x\right) + \eta t + 1 - q\left(\frac{w}{v}\sum_{n=1}^{\infty} \cos n\pi x\right) + \mu\left(\frac{w}{m}\sum_{n=1}^{\infty} \quad \cos n\pi x\right)$$

Where;

Where q =$(\delta + \upsilon)$

$\phi_1(x,t)$=$\frac{mv}{3v^2}\sum_{n=1}^{\infty}(1-exp^{-vt})+\frac{2m}{v}\sum_{n=1}^{\infty}(-1)^n(1-exp^{-vt})+\frac{4mt}{3}-\frac{t}{3}(6\eta+2q+2\mu)+$
$\sum_{n=1}^{\infty}(2\sum_{n=1}^{\infty}(-1)^n)\frac{mw}{v}exp^{-vt}+qw\sum_{n=1}^{\infty}exp^{-vt}+\mu\sum_{n=1}^{\infty}\frac{wt}{m})cosn\pi x$

$$\theta_{1(x,t)=}cp\sum_{n=1}^{\infty}\frac{w}{m^2v}(1-exp^{-mt})+2\frac{cpw}{v}\sum_{n=1}^{\infty}(-1)^n(1-exp^{-vt})+\frac{ct}{3}(2p-2q-2\mu-6\eta)$$
$$+\left(\sum_{n=1}^{\infty}\frac{cqw}{f}exp^{-mt}\sum_{n=1}^{\infty}\left(1-exp^{-ft}\right)\right)$$
$$+2exp^{-mt}\sum_{n=1}^{\infty}\frac{cpw}{m}+exp^{-mt}\sum_{n=1}^{\infty}\frac{cqw}{f}(1-exp^{-ft})cosn\pi x$$

$$\psi_1(x,t)=\frac{dt}{9}+\frac{d}{3t}\sum_{n=1}^{\infty}mexp^{-mt}\cos n\pi x+(\frac{d}{t})^2\sum_{n=1}^{\infty}wexp^{-vt}cosn\pi x-2\delta m(-1)^n(t-exp^{-vt})$$
$$+\frac{2\delta wt^2}{3}-\frac{\delta t}{3}-\frac{\delta}{t}(2q+2\mu+6\eta)$$
$$-\frac{2m\delta}{Bv}\sum_{n=1}^{\infty}exp^{-vt}cosn\pi x$$
$$-\frac{\delta qw}{Bv}\sum_{n=1}^{\infty}\sum_{n=1}^{\infty}exp^{-vt}cosn\pi x$$
$$+\frac{\delta\mu wt^2}{m}\sum_{n=1}^{\infty}\sum_{n=1}^{\infty}exp^{-vt}cosn\pi x$$
$$-\frac{\mu g}{m}\sum_{n=1}^{\infty}(t-exp^{-mt})-\frac{2\mu K}{v}(-1)^n(t-exp^{-vt})+\frac{c\mu t^2}{3}(2p-2q-2\mu-6\eta)$$
$$-\frac{L\mu}{d}\sum_{n=1}^{\infty}\sum_{n=1}^{\infty}\left(t-exp^{-dt}\right)cosn\pi x-\frac{2\sigma R}{m}\sum_{n=1}^{\infty}exp^{-mt}\sum_{n=1}^{\infty}cosn\pi x$$
$$-\frac{L}{m}\sum_{n=1}^{\infty}\sum_{n=1}^{\infty}exp^{-mt}\left(t-exp^{-dt}\right)\cos n\pi x$$
$$+\frac{\omega g}{m}\sum_{n=1}^{\infty}(1-exp^{-mt})-\frac{2\omega K}{v}\sum_{n=1}^{\infty}(-1)^n(t-exp^{-vt})+\frac{\mu+ct}{3}(2p-2q-2\mu-6\eta)$$
$$-\frac{L}{d}\sum_{n=1}^{\infty}\sum_{n=1}^{\infty}(t-exp^{-dt})\,cosn\pi x$$
$$+\frac{2K}{m}\sum_{n=1}^{\infty}\sum_{n=1}^{\infty}exp^{-mt}cosn\pi x$$
$$+\frac{L}{md}\sum_{n=1}^{\infty}(t-exp^{-dt})\sum_{n=1}^{\infty}(t-exp^{-dt})\sum_{n=1}^{\infty}exp^{-mt}$$
$$+\sum_{n=1}^{\infty}\sum_{n=1}^{\infty}\frac{L}{md}+\sum_{n=1}^{\infty}\sum_{n=1}^{\infty}\frac{2\mu R}{m}cosn\pi x+2\delta m(-1)^n-\frac{2m\delta}{Bv}cosn\pi x-\frac{\delta qw}{Bv}\sum_{n=1}^{\infty}\sum_{n=1}^{\infty}cosn\pi x$$

Where;

g =$\frac{cpw}{m^2 v}$,
w=-2$\left[\frac{1+(-1)^n}{(n\pi)^2}\right]$,
L=$\frac{cqw}{f}$,
R = $\frac{cpw}{m}$,

q= $(\delta + \upsilon)$
f=v-m,
v=$(n\pi)^2$
m=$\beta(n\pi)^2$
a=mα
b=pα
r =$\frac{\gamma}{\alpha}$
d=$\frac{\delta}{\alpha}$
The computations were done using computer symbolic algebraic package MAPLE.

RESULTS AND DISCUSSION

The system of partial differential equations describing the physical and drying behavior and simulation of leather. The analytical solution is solved using Eigen function expansion.

The numerical result for the temperature, moisture content of the air leather pores and the moisture content in the leather using maple software are displayed in figure 1 – 3

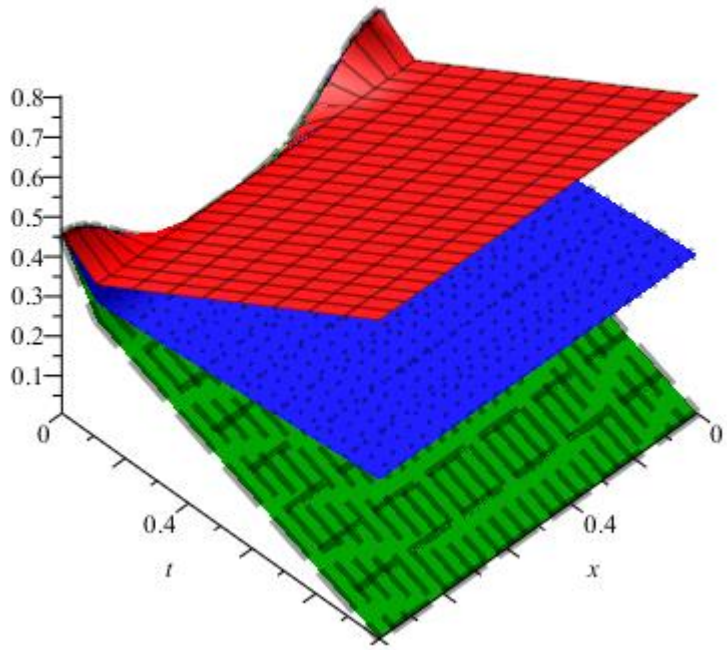

Figure 1: variation of temperature ($\theta(x,t)$) with ratio of moisture content. (α)

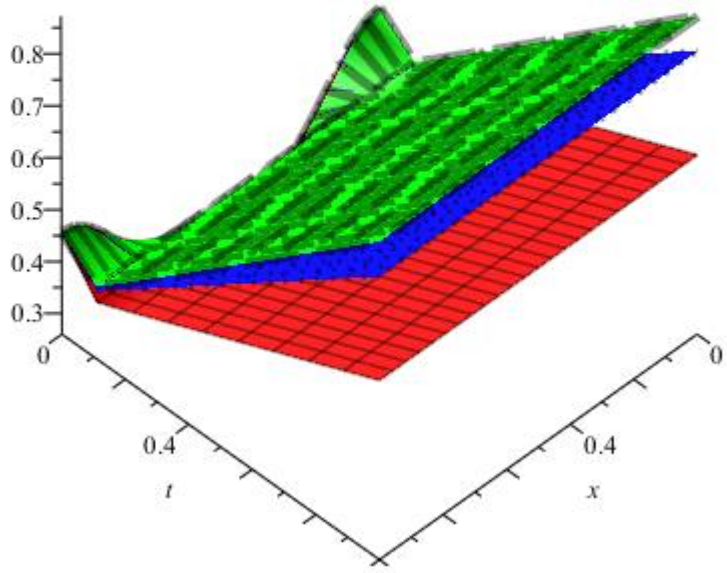

Figure 2: variation of temperature ($\theta(x,t)$) with rare constant (K)

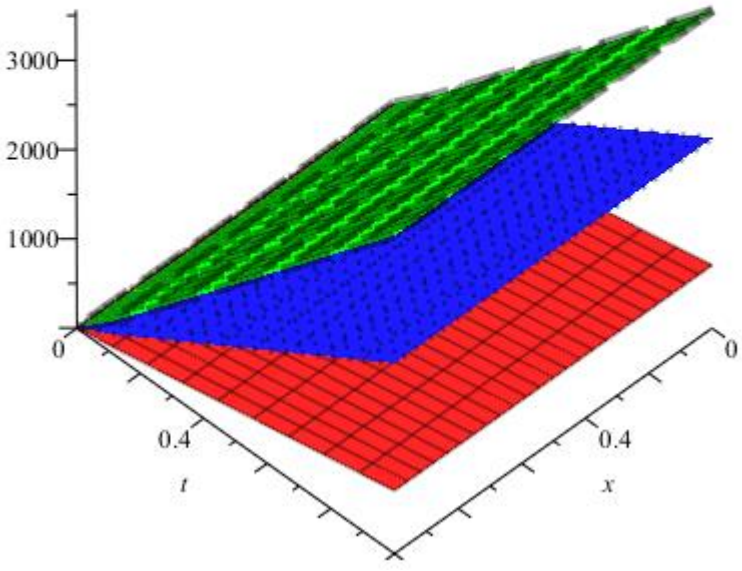

Figure 3: variation of moisture content of the air leather pores ($\phi(x,t)$) with scale thermal conductivity (β)

Figure 1 shows the effect of ratio of moisture content (α) on temperature. Its observe that the temperature decreases with time and distance. Clearly, the ratio of moisture content decreases the temperature

Figure 2 shows the effect of rare constant (K) on the temperature. It is observed that temperature increases with distance and time. Clearly, the rare constant increase with temperature.

Figure 3 shows the scales thermal conductivity (β) on moisture content of air leather pores. It is observed that the moisture content of the air leather pore increases with distance and time. Clearly the scales thermal conductivity increases with moisture content of the air leather pores

CONCLUSION

We have formulated and solved analytically a modeling and analytical simulation of drying behavior of leather in the presences of temperature, rare constant and thermal conductivity. In particular, we have provedby actual solution method that the model formulated has a unique solution for all $t \geq 0$ .We decoupled the equations using parameter expanding method and solved the resulting equations using eigenfunctions expansion technique. Finally, we have provided the graphical summaries of the system responses.

REFERENCES

Aima C.R,Gortary J.C(1988). Experimental data and premilinary desigh of a non- conventional dryer of leather. Sixth international drying symp. 85:59-63

Beard J.N(1976). More effect tenter frame operation through mathematical modeling 3:47- 50

Behzat Oral Bitiliz, Bahri Basaran,Oscan Sari, Ahmed Ajlan & Goklan Zenjin (2004). Some physical and chemical properties of ostrich skins and leather 11:654-659.

Bienkiewiez, K.J: physical chemistry of leather making.Robert E.kriger publication Co., 1983

Carnahan, B., Luther, H.A, Wilkes, J.O:. Applied Numerical method John Wiley and Sons, NY, 1969

Charvatova H.,D Janacova, Kolomaznik,Vasek V., Drja R.,and Mokrejs (2014). Mathematically modeling of leather fatliquoring. 2004 international conference on mechanical fluid mechanics, heat and mass transfer.

Encyclopia of science clarified (2015). We are surrounded , retrieved from http://www.scienceclarified.com/scitech/leather are surrounded on 23rd march,2015.

Farnworth,B.: A numerical Model of combined Diffusion of Heat and water vapor Through Clothing. Tectile Res J.,No. 56/1986,pp.653-655

Goldslim technology group LLC(2007). Dynamic simulation and supply chain magement.5:12-23

Haghi A.K(2001). A mathematical model of the drying process 41:20-25

Haghi K., Rondot D.,and Akbar(2014). Heat and mass transfer in leather drying process.

Henry, P.S.: Diffusion in Absorbing Media Proc.R. soc.,171A, 1986,PP.215-655

Jaroslav solc, Hona Charvatona, Michaela Barinova, Karel Kolomaznik(2013). Mathematically modeling on chemical delliing and simulation of economical parameter in Galatin production.8:820-832

Milan Nevratul,Karel Kolomaznik, and Kreselek Vojtech(2007). Approach to mathematical

model of cross linking reaction of polymer composite. AT&P journal 17-25\

ON THE APPLICATION OF OPTIMAL CONTROL IN A MILITARY ENVIRONMENT

[1]M. D. Shehu, [2] H. O. Ahmed

[1,2]Mathematics/Statistics Department, Federal University of Technology, Niger State, Nigeria

e-mail: m.shehu@futminna.edu.ng

Abstract

In this paper, we formulated a mathematical model using the concept of optimal control, where the state of the system is governed by a differential equation controlled by two combatants (combatant A and combatant B) refer to as the evader and pursuer respectively, with conflicting motives. A control *u(.)* defines a notion where the combatant A tries to escape capture from the combatant B defined by control *v(.)*. The game terminates if capture occurs prior to a pre-assigned time *t* or at a time *t*. In a situation where capture has not occurred prior to *t*, the control u(.) sole-aim would be to escape capture, while combatant B sole-aim is to ensure that combatant A is captured.

Key words: Optimal control, terminal miss, dynamics, perturbation and differential games

1.0 Introduction

The existence of optimal control theory can be traced back to the days of Newton, Lagrange and Cauchy, (Emilo, 2012). One of the first instances of optimization theory concerns the finding of a geometric curve of given length which will together with a straight line, enclose the largest possible area, (Francis, 2014). The fundamental problem of optimal control problems is concerned with the choosing of a function that minimizes certain functional, (Jack,2014).

The theory of optimization involves the maximization or minimization of a function (sometimes unknown), which represent the performance of a system, (Jery, 2012). This is carried out by finding values for those variables (which are both quantifiable and controllable) which cause the function to yield an optimal value.

The Optimal control problem can be stated, (Rao ,1984), (Robert,2015) as:

Find the control vector;

$$U = \begin{bmatrix} u_1 \\ u_2 \\ : \\ u_n \end{bmatrix} \tag{1.1}$$

which minimizes the functional called the *Performance* index;

$$J = \int_0^T f_0(x,u,t) \tag{1.2}$$

where

$$X = \begin{bmatrix} x_1 \\ x_2 \\ : \\ x_n \end{bmatrix} \qquad (1.3)$$

Equation (1.3) is called the state vector,

t = time parameter

T = terminal time

f_0 = is a function of x, u, t

In this paper, we formulate a mathematical model by extending the notion of equation (1.1) to a two control problem defined by control *u(.)* and control *v(.)*.

2.0 Model Formulation

We considered a dynamic system, (Shehu, (2004), given by equation (2.1)

$$\dot{x} = \mathbf{f}(x, u, v, t), \qquad x(t_0) = x_0 \qquad (2.1)$$

Where;
control *u(.)* = combatant A
control *v(.)* = combatant B

Equation (2.1) is a state a system that is governed by a differential equation controlled by two combatants (combatant A and combatant B) refers to as the evader and pursuer respectively, with conflicting motives.

A control *u(.)* defines a notion where the combatant A tries to escape capture from combatant B defined by control *v(.)*.

We define a terminal constraints;

$$\psi(x(t_f), t_f \qquad (2.2)$$

and the performance criterion;

$$P = \phi(x(t_f), t_f) + \int_0^{t_f} f_0(x, u, v, t)dt \qquad (2.3)$$

Where;

t_f = Terminal Time

u = Control for Combatant A

v = Control for Combatant B

A strategy Γ for combatant A is a sequence of instructions given by Γ_n

A strategy ∇ for combatant A is a sequence of instructions given by ∇_n

We define the following saddle point property for both controls;

$$p(u^0, v^0) = \min_u p(u, v^0) \tag{2.4}$$

Where,

$$v^0 = v(t : x_0, t_0) \tag{2.5}$$

Similarly;

$$e\ (u^0, v^0) = \max_v e(u^0, v\ ) \tag{2.6}$$

$$u^0 = u(t : x_0, t_0) \tag{2.7}$$

Where,

u, v are controls for Combatant A and B respectively

and

u^0, v^0 are optimal controls for Combatant A and B respectively.

The equation of motion for the two controls is defined as;

$$\dot{v} = ap - ae \quad v(t_0) = v_0 \tag{2.8}$$

$$\dot{y} = v \quad y(t_0) = 0 \tag{2.9}$$

Where,

$v(t)$ = Relative Velocity to the Initial Line of Site

$y(t)$ = Relative Displacement to the initial Line of Site

Combatant B whishes to minimize the terminal miss ($y(t_f)$,to make capture possible whereas combatant A wishes to maximize the terminal miss to make capture invariably impossible.

We define the performance index as;

$$J = \frac{1}{2}\left(y(t_f)\right)^2 \tag{2/10}$$

We now form the Hamiltonian system for the two combatants as

$$H = \lambda_v (a_p - a_e) + \lambda_y v \tag{2.11}$$

Where;

λ = Control parameter for both the velocity and the displacement

a_p = Acceleration of the Pursuer (combatant B)

a_e = Acceleration of the Evader (combatant A)

The adjoint equations are;

$$\dot{\lambda}_v = -\lambda_y, \qquad \lambda_v(t_f) = 0 \tag{2.12}$$

$$\dot{\lambda}_y = 0, \qquad \lambda_y(t_f) = y(t_f) \tag{2.13}$$

The optimality conditions are;

$$a_p(t) = -a_{pm} \operatorname{sgn} \lambda_v \tag{2.14}$$

$$a_e(t) = -a_{em} \operatorname{sgn} \lambda_v \tag{2.15}$$

Integrating the adjoint equations we have;

$$\lambda_v(t) = (t_f - t)\ y(t_f) \tag{2.16}$$

Where;

$$\lambda_y(t_f) = y(t_f) \tag{2.17}$$

$$\lambda_y(t\ ) = y(t\ ) = constatnt \tag{2.18}$$

We note that

$$\operatorname{sgn} \lambda_v(t) = \operatorname{sgn} y(t_f) = constatnt \tag{2.19}$$

Substituting (2.19) into equations (2.14) and (2.15) we have;

$$a_p(t) = -a_{pm}\ \operatorname{sgn} y(t_f) \tag{2.20}$$

$$a_e(t) = -a_{em}\ \operatorname{sgn} y(t_f) \tag{2.21}$$

Substituting equations (2.20) and (2.21) into equations (2.8) and (2.9) yields;

$$\dot{v} = (-a_{pm} + a_{em}) \operatorname{sgn}\ y(t_f) \tag{2.22}$$

$$\dot{v} = (a_{pm} - a_{em}) \operatorname{sgn} y(t_f) \tag{2.23}$$

$$v(t_f - t_0) = (t_f - t_0)(a_{pm} - a_{em})\operatorname{sgn} y(t_f) \tag{2.24}$$

$$v(t_f) - v(t_0) = (t_f - t_0)(a_{pm} - a_{em})\operatorname{sgn} y(t_f) \tag{2.25}$$

$$v(t_f) = v_0 - (t_f - t_0)(a_{pm} - a_{em})\operatorname{sgn} y(t_f); \quad v(t_0) = v_0 \tag{2.26}$$

$$\dot{y} = v_0 - (t_f - t_0)(a_{pm} - a_{em})\operatorname{sgn} y(t_f); \qquad \dot{y} = v \tag{2.27}$$

Whose solution may be written as;

$$y(t_f) = v_0(t_f - t_0) - 1/2(a_{pm} - a_{em})(t_f - t_0)^2 \operatorname{sgn} y(t_f); \; y(t_0) = 0 \tag{2.28}$$

We then have;

$$y(t_f) = \begin{bmatrix} 1/2(t_f - t_0)^2[2v_0/(t_f - t_0) - (a_{pm} - a_{em})] \\ \\ -1/2(t_f - t_0)^2[-2v_0/(t_f - t_0) - (a_{pm} - a_{em})] \end{bmatrix} \tag{2.29}$$

3.0 Discussion of Results

It is possible for Combatant B to bring the terminal miss to zero, by making $y(t_f) = 0$ in equation (2.29) This can be achieved by choosing;

$$a_p(t) = a_e(t) + 2v(t)/(t_f - t) \tag{2.30}$$

Substituting equation (2.30) into equation (2.29) $y(t_f)$ becomes;

$$y(t_f) = 1/2(t_f - t_0)^2[2v(t)/(t_f - t) - (a_e(t) + 2v(t)/(t_f - t) - a_e(t))] \tag{2.31}$$

The sole aim of the Combatant B (the pursuer) is to make capture possible by minimizing the terminal miss as minimum as possible, and Combatant B (the evader) sole aim is to maximize the terminal miss to make capture invariably impossible.

RFFERENCES

Emilo O. Roxin (2012). Modern Optimal Control; Books/Cole Publishing Company, California. pp. 123-155.

Francis Sheid (2014). Numerical Analysis; Second Edition, Schaum's Outline Series. pp. 7-23.

Jack Mack (2014). Introduction to Optimal Control. MIR Publishing Moscow. pp. 27-53.

Jery B. Marion (2013). Classical Dynamics of Particles and Systems. Academic Press New York. pp. 1-23.

Robert H. Martin (2015). Ordinary Differential Equation. Addison-Wesley Publishing Company, Inc. pp. 17-23.

S. S. Rao (1984). Optimization Theory and Application. Second Edition, Willey Eastern Limited. pp. 8-12.

Shehu D. M (2004). Optimal Control Strategy in Differential Games. M. Tech. Thesis (Unpublished).

DYNAMICS OF VEGETAL COVER AND URBANIZATION TREND IN JOS SOUTH LOCAL GOVERNMENT AREA OF PLATEAU STATE, NIGERIA A GEOSPATIAL APPROACH.

Muhammed M.[1], Joseph M. M[1]. And Hassan, A.B[1]
[*1]ummubahiyya@futminna.edu.ng
matmayebam@gmail.com
aisha.hassan@futminna.edu.ng

[1]Department of Geography Federal University of Technology Minna

Abstract

The high rate of urbanization coupled with population growth has caused changes in land use. Therefore, understanding and quantifying the spatio- temporal dynamics of vegetal cover due to urbanization is essential for monitoring mechanisms and decision making. The study aimed at determining how dynamics of vegetal cover relates to urbanization trend in Jos South Area. Landsat TM for 1991, ETM$^+$ and operational land imager (OLI) for 2003 and 2015 was obtained and preprocessed using Erdas Imagine 2014, Idrisi software and ArcGIS 10.2. Maximum Likelihood Classification was used to generate land use and land cover maps of the area. Confusion matrix was used to derive overall accuracy and results were above the minimum and acceptable threshold level. Land Change Modeler was run to model land use and land cover changes in Jos South Area to predict future urban land use trend and changes. Six land cover transitions were incorporated in the modeling process. Makovian transition estimator was used to model the transition potential matrix. This result of which was used to make prediction using CA_ Markov chain analysis for year 2039. The results revealed there was an increase in built up areas in the last 24 years from 535.68ha (1.18%) in 1991 to 4608.99ha (10.17%) in 2003 and 15600.96ha (34.43%) in 2015 at the expense of vegetal cover. The prediction results showed built up will increase from 15600.96ha (34.43%) to 20972.88ha (46.29 while vegetatal cover will decrease from 4675.86ha (10.32%) to 3125.34ha (6.90. The study concluded that geospatial techniques are a viable tool for assessing urbanization trend and dynamics of vegetal cover. It was recommended that high resolution imageries such as IKONOS be made readily available, because urban areas have complex and heterogonous features, and this will provide better information in mapping these areas.
Key words: Geospatial, Dynamics, Urbanization, land cover, vegetation, Remote sensing

INTRODUCTION

Settlement expansion have now become a central component in current strategies for managing land as a resource and in monitoring environmental changes. Settlements represent the most profound human alteration of the natural environment through a spectrum of urban land use activities (Ifatimehin and Ufuah, 2006) which include, but are not restricted to, transportation, commercial, industrial, residential, institutional, and recreational land uses. The expansion that ensues as a result of increase in the demand for these land uses explains the underlying and fundamental cause of urban expansion which is population increase.

The rapid changes of land use and cover than ever before, particularly in developing nations, are often characterized by rampant urban sprawling, land degradation, or the transformation of agricultural land to shrimp farming ensuing enormous cost to the environment (Sankhala and Singh, 2014). The increase in carbon dioxide temperature of the atmosphere, regulation of Nutrient cycle of carbon dioxide and photosynthesis shifting in population provision of income through the sale of fuel wood/firewood has increased rate of evaporation and alteration of fluvial competence and capacity (Mustafa 2010).

Usually land uses and urban growth in remote sensing involves the analysis of two registered, aerial or satellite multi-spectral bands from the same geographical area obtained at two different times. Such an analysis aims at identifying changes that have occurred in the same geographical area between the two times considered (Radke et al., 2005). Herold *et al* (2005) also noted that one of the advantages of remote sensing is its ability to provide spatially consistent data sets covering large areas with both high detail and high temporal frequency, including historical time series.

The basic premise in using remote sensing data for change detection is that the process can identify change between two or more dates that is uncharacteristic of normal variation. Numerous researchers have addressed the problem of accurately monitoring land-cover and land-use change in a wide variety of environments (Shalaby and Tateishi, 2007).

Jos south is a mid-sized city under the pressure of urban growth. Timely and accurate assessments of urbanization trend scenarios and associated environmental impacts are crucial for urban planning, policy decision, and natural resource management (Adzandeh *et al,* 2015).Many Studies have shown that there remain only few landscapes on the earth surface that is still in their natural state (Fasal, 2000). This is due to natural processes and disasters, as well as intense pressure from anthropogenic activities such as deforestation, urbanization, intensive agriculture and mineral exploitation (CARPE, 2003, Lambin *et al.,* 2003; Ndjomo, 2008; Sarma *et al.,* 2008).

Jos South Local Government Area of Plateau State in Nigeria is witnessing rapid urbanization largely due to high population growth (Vivan *et al* 2013). Understanding the rapid growth dynamics, developments of urban sprawl and quantifying the spatial extent of urbanization requires a geospatial tool (Araya and Cabral, 2010). Living conditions deteriorate continually, particularly in cities of the developing countries. This is due to poorly planned human interference and limited access to adequate information and appropriate technology. Hence, in order to effectively monitor urbanization trend and how it affects the dynamics of vegetal cover, it is not only necessary to have information on existing land use land cover but also the capability to monitor the dynamics of land use resulting out of both changing demands of increasing population and forces of nature acting to shape the landscape.

The aim of the study was to analyze urbanization trend and how it affects vegetal cover in Jos south LGA, Plateau state. With the objectives to create a land use land cover map of the study area, determine the effect of land use land cover change on vegetal cover and project the future pattern of land use land cover in as it affects urbanization trend and dynamics of vegetal cover of the area for 24years (2039).

The Study Area

Jos Plateau is situated between latitudes 10°11′N and 8°55′N and longitude 8°21′E and 9°30′E (Figure 1).The study area **(**Jos south LGA) is located between latitudes 9° 30’ to 10° N and longitude 8° 30’ E. It is situated at the north western part of the state with its headquarters at Bukuru, which is about 15 km from the state capital, Jos. The local government area has total land area of about 1,037 km^2 with a population of 306,716 (NPC, 2006). It has an average elevation of about 1,150 metres above mean sea level and the highest peak some 20 km eastwards from Jos-shere hill, rising to 1777 meters above mean sea level. It has a cool climatic condition due to its altitude. The coldest period is between November and February with an average mean daily temperature of 18°C, while it gets warm between March and April before the onset of rain. The rainy season, which is between the months of May and October, has its peak in August. The mean annual rainfall varies between 1347.5 and 1460 mm per annum (Michael, 2012).

The Jos Plateau is dominated by three rock types. The Older Granites date to the late Cambrian and Ordovician. The Younger Granites are emplacements dating to the Jurassic, and forming part of a series that includes the Air Massif in the central Sahara. There are also many volcanoes and sheets of basalt extruded since the Pliocene.The Younger Granites contain tin which was mined since the beginning of the 20th century, during and after the colonial period The original woodland vegetation of the Jos region has long been cleared

for mining and agricultural activities, turning the region into open savannah grassland with widely spread eucalyptus and acacia trees, and cactus hedges which are used for land/boundary delineation.. (Michael 2012).

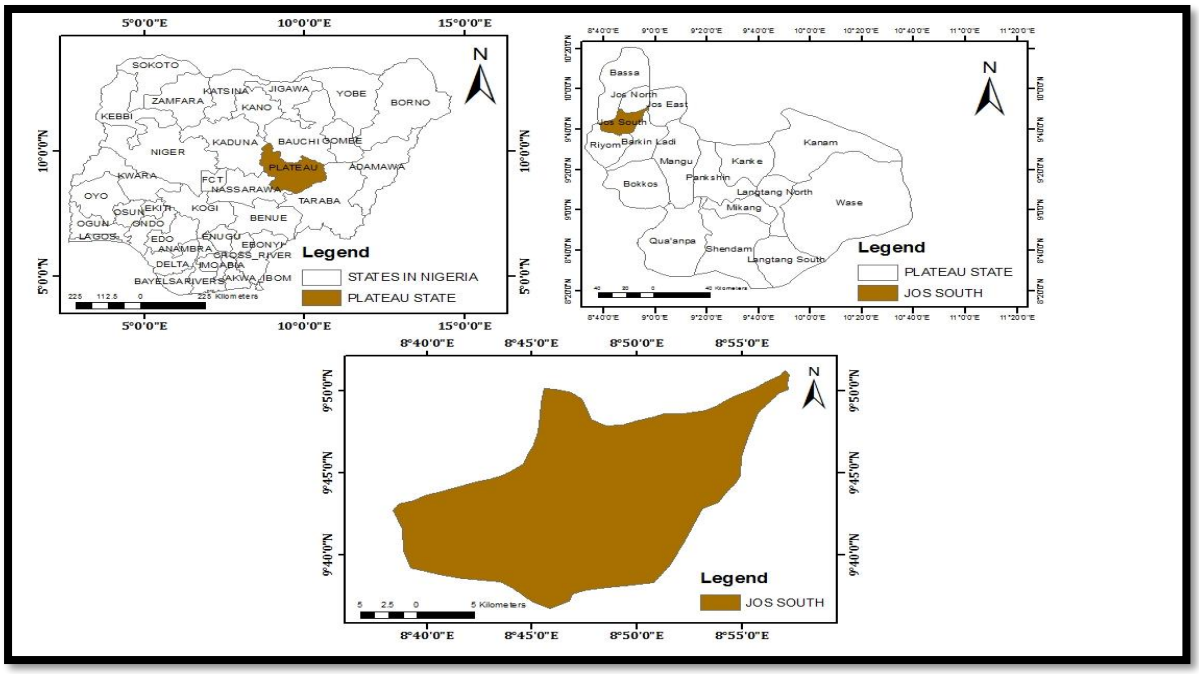

Figure 1: Plateau State showing Jos south Local Government

Materials and Methods

Three, Landsat imageries of TM, ETM^{+}, and OLI of the same season and resolutions were acquired for the periods 1991, 2003 and 2015. The images were downloaded from the United States Geological Survey (USGS). It is also important to state that Jos south L.G.A which was carved out using the local government boundary map and Nigerian Administrative map was obtained from NASRDA. And spatially referenced in the Universal Transverse Mercator (UTM) projection with datum World Geodetic System (WGS) 1984 UTM zone 32N

The Landsat Thematic Mapper (TM) of 1991,the enhanced Thematic Mapper (ETM+) of 2003 and Operational land imager of 2015 were Pre-Processed (Mosaicking, Clipping Study Area, Image Stretching And Layer Stacking). A supervised classification was performed on false colour composites (bands 4, 3 and 2) into the following land use and land cover classes; Built-up area, vegetation, Bare land, Rock out crop, Farmland, and water bodies. Information collected during the field surveys was used to assess the accuracy of the classification.

Because classified land cover maps from remotely sensed images contain various types of errors, the accuracy of a classified map was assessed and compared with a referenced data using an error matrix. The accuracy assessment in this study was made using the original sub-sected image for 1991 for the study periods of 2003 and 2015. It was computed by dividing the total number of correctly classified pixels (i.e., the sum of the elements along the major diagonal) by the total number of reference pixels. It shows an overall result of the tabular error matrix.

The classified land cover maps of 1991, 2003 and 2015 were used as input parameters and LCM was applied to identify the locations and magnitude of the major land use and land cover changes and persistence. Moreover, the spatial trends of major transitions between land use and land cover categories of special interest in the study area were quantified.

Results and Discussions

Land use land cover maps of the study area

The land cover maps generated after running a maximum likelihood supervised classification as well as a post classification algorithm are presented in figures 2a, 2b and 2c. As shown, there has been an increase of built up areas with respective values 1.18% of the study area in 1991 to 10.17% in 2003 and 34.43% in 2015, the statistics is indicated in table 1.

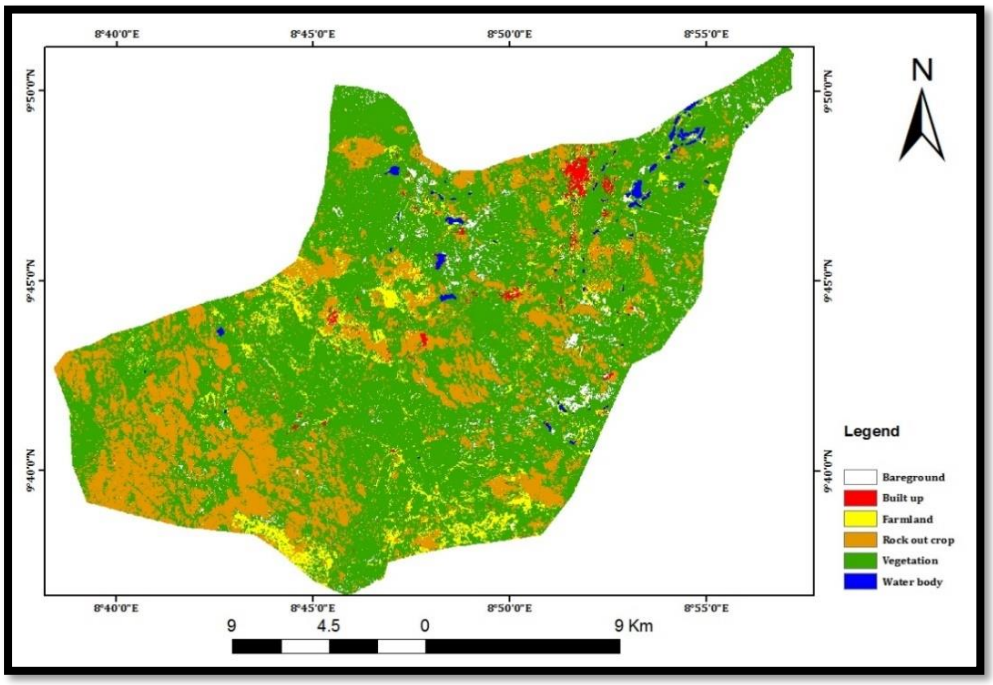

Land Use Land Cover Map of Jos South LGA in 1991

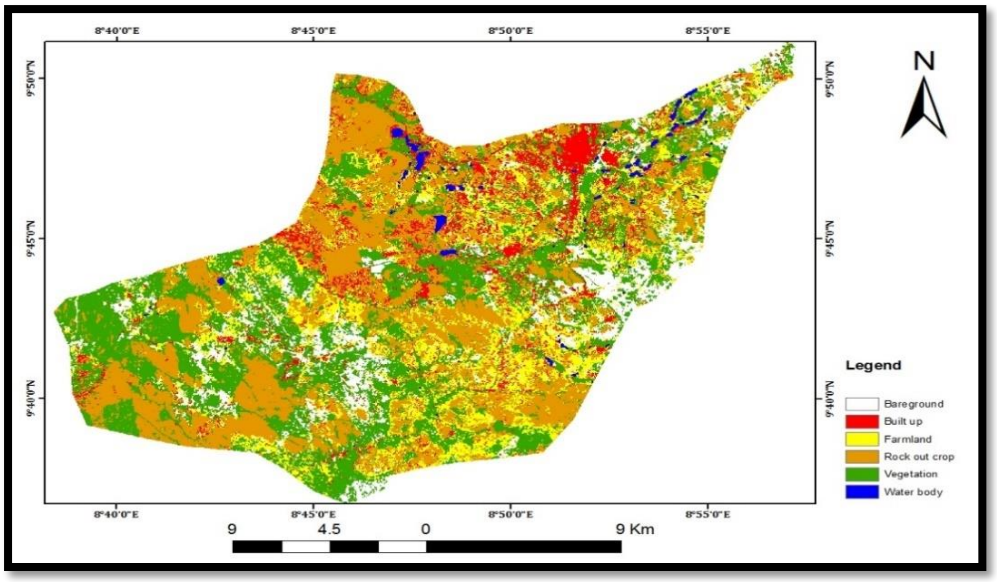

Land Use Land Cover Map of Jos South LGA in 2003

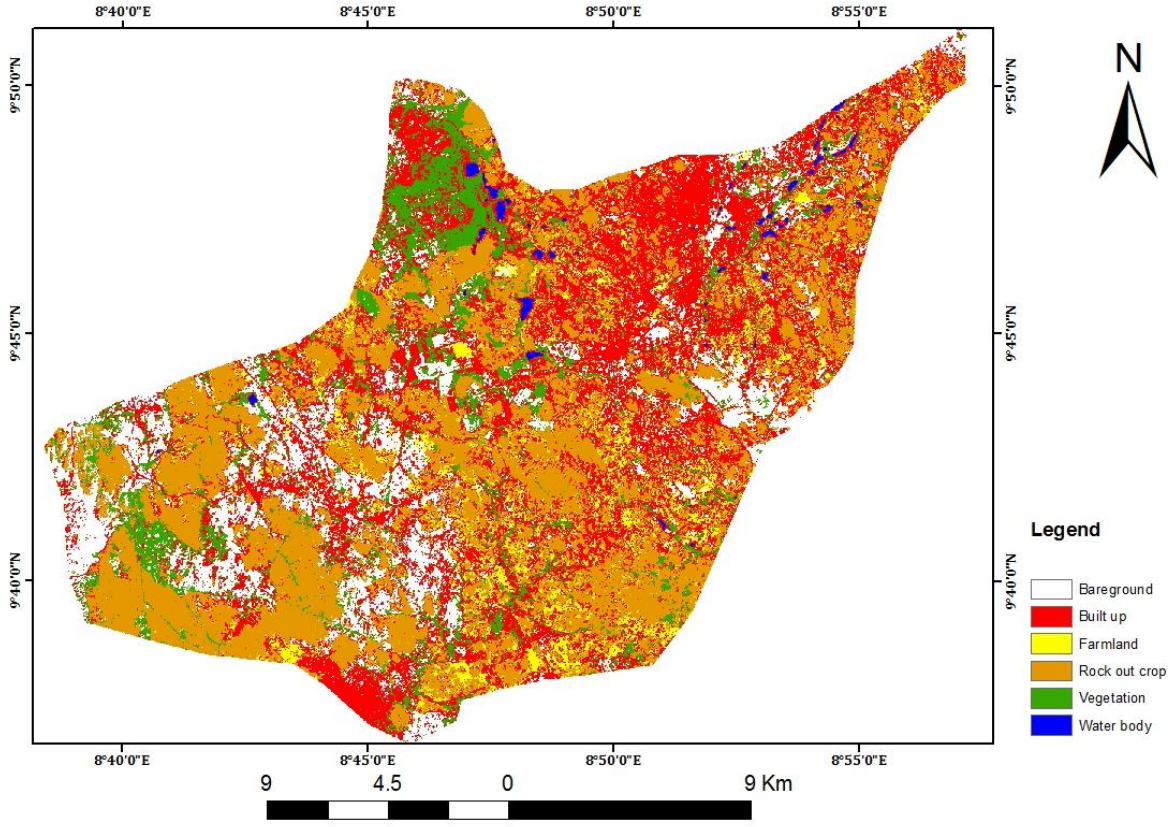

Land Use Land Cover Map of Jos South LGA in 2015

Figure 2; Land Use Land Cover Map of Jos South LGA 1991-2015

Open areas (bare ground) have also shown a consistent increase between the study periods. However, there have been a decrease of vegetated areas as clearly shown in 1991, 2003 and 2015 images (figures 2a, b and c) respectively. In 1991 vegetated areas covered 66.40% of the study area (from figure 2a and table 4.1) vegetation was the most dominant land cover class in the study area but showed a continuous decrease from 66.40% in 1991 to 10.32% in 2015. Because of the successive decrease of vegetation areas, built up areas have dramatically increased in the study periods. This could be due to an increase of population growth associated with high demand for land and urban supplies.

The values presented in table 1 represents the distribution area of each land use land cover category for each study year. Built-up in 1991 occupies the least class with just 1.18% of the total classes. Furthermore, vegetation occupies the highest portion with 66.40% in 1991 and decreased to 31.46% and 10.32% in 2003 and 2015 respectively. Also, farming seems to be practiced moderately, occupying 5.73% of the total classes in 1991, was increased to 19.07% in 2003 and drastically reduced to 8.55% in 2015. This may be due to the fact that the city is just moving away from the rather traditional setting where farming seems to form the basis for living. Apart from this, the time of the year in which the area was imaged which happens to fall within the onset of harmatan could also be a major contributing factor to the observed classification, contributing to the high percentage of bare ground and the low percentage of water bodies.

Table 1 Land Use Land Cover Distribution (1991, 2003, 2015)

Land cover classes	1991		2003		2015	
	Area(Ha)	Area (%)	Area(Ha)	Area (%)	Area(Ha)	Area (%)
Bare ground	1146.6	2.53	4629.51	10.22	6691.23	14.77
Built up	535.68	1.18	4608.99	10.17	15600.96	34.43
Farmland	2597.31	5.73	8638.29	19.07	3874.32	8.55
Rock out crop	10633.68	23.47	12730.5	28.10	14208.3	31.36
Vegetation	30084.21	66.40	14255.01	31.46	4675.86	10.32
Water body	312.12	0.69	447.3	0.99	258.93	0.57
Total	45309.6	100	45309.6	100	45309.6	100

In addition rock out-crop occupies 23.47% in 1991, 28.10% in 2003 and increased to 31.36% due loss of vegetation in 2015. Bare ground on the other hand occupies 2.53% in 1991 and increased to 10.22% and 14.77% in 2003 and 2015 respectively. It is also visible from figure 2a and table 1 that water body had the lowest proportion occupying 0.69% in 1991, increased to 0.99% in 2003 and showed a little decrease to 0.57% of the study area in 2015.

Accuracy Assessment of the Classification

The overall accuracies performed in this study period 1991 was 75.06% (table 2), in 2003 was 98.26% (table 3) and during 2015 it was 93.26 % (table 4). As mentioned by Anderson *et. al,* (1976) for a reliable land cover classification, the minimum overall accuracy value computed from an error matrix should be 85%. However, Foody (2002) showed that this baseline makes no sense to be a universal standard for accuracy under practical applications. This is because a universal standard is not exactly related to any specific study area.

Table 2: Confusion matrix for land cover map of 1991

Table 3: Confusion matrix for land cover map of 2003

	Reference map								
Classified Map	Landcover classes	Bare ground	Built up	Farmland	Rock out crop	Vegetation	Water body	Total	Users accuracy
	Bare ground	211	0	0	0	0	0	211	100
	Built up	0	124	0	0	0	0	124	100
	Farmland	1	67	70	0	0	0.49	138.49	50.55
	Rock-out crop	0	2	163	472	0	0.259	637.26	74.07
	Vegetation	0	2	102	3	281	0.2758	388.28	72.37
	Water body	0	0	0	0	0	0	0	0
	Total	212	195	335	475	281	1.0276	1499.03	
	Producers accuracy	99.4	60.72	13.89	98.99	100	100		
	Over all accuracy	75.06							

		Reference Map							
Classified Map	Landcover classes	Bare Ground	Built Up	Farmland	Rock Out Crop	Vegetation	Water Body	Total	Users Accuracy
	Bare Ground	519	0	0	0	0	0	519	100
	Built Up	2	757	0	0	0	0.0026	759.003	99.74
	Farmland	0	13	82	0	0	0.1368	95.1368	86.19
	Rock-Out Crop	0	25	0	1526	0	0.0161	1551.02	98.39
	Vegetation	0	0	0	0	51	0	51	100
	Water Body	0	0	0	0	0	0	0	
	Total	521	796	82	1526	51	0.1555	2975.16	
	Producers Accuracy	99.54	98.8	100	100	100	100		
	Overall Accuracy	98.26							

Table 4: Confusion matrix for land cover map of 2015

	Reference Map								
	Landcover classes	Bare Ground	Built Up	Farmland	Rock Out	Vegetation	Water	Total	Users Accuracy

					Crop				
Classified Map	Bare Ground	320	0	0	0	0	0	320	100
	Built Up	133	832	0	0	0	0.1196	965.1196	86.20693228
	Farmland	0	2	122	0	0	0.0161	124.0161	98.37432398
	Rock-Out Crop	0	58	10	2067	0	0.0319	2135.0319	96.81354176
	Vegetation	0	0	0	0	205	0	205	100
	Water	0	0	0	0	0	0	0	
	Total	433	892	132	2067	205	0.1676	3749.1676	
	Producers Accuracy	71.64	91.2	92.18	100	100	100		
	Overall Accuracy	93.05							

Overall Accuracy

Foody (2002) also noted that Anderson *et. al.*, (1976) did not explain in detail about the criteria of map evaluation for universal applications. Moreover, Lu *et al* (2004) noted that the accuracies of change detection results highly depend on many factors, such as: availability and quality of ground truth data, the complexity of landscape of the study area, the change detection methods or algorithms used as well as classification and change detection schemes. So, the overall accuracies for 2003 and 2015 maps were above 85% based on Anderson's criteria, but the overall accuracy of 1991 was 75.06% which is not up 85% based on Anderson's criteria, however this may be due to the availability and quality of ground truth data, the complexity of landscape of the study area, the change detection methods or algorithms used as well as classification and change detection schemes, (Lu *et, al.* 2004).

Change Analysis Results of Land Change Modeler (LCM)

The results of the cross-tabulation comparison of both land use and land cover maps in figures 3a, b, and c, revealed that there have been marked changes in all land use and land cover classes between 1991, 2003 and 2015. During the period 1991 - 2003 the total built up areas increased by 4227ha (representing an increase of 9.33% of the total study area) and lost 154 ha (0.34%) of the study area) as indicated in figure 4.3a. While vegetation areas decreased by 19409 ha (42.84%) of the total study area) and gained 3580 ha (7.90%) with a net loss of 15829 ha. Similarly water bodies lost 80 ha (0.18%) and gained 216 ha (0.48%). Furthermore rock out-crop lost 4606ha (10.17%) and gained 6703ha (14.79%).The proportion of areas covered with farmland areas gained 7361 ha (16.25%) and lost 1320 ha (2.91%), while the proportion of bare ground gained 4153 ha (9.17%) and lost 670ha (1.48%). The increase in farmland areas in 2003 study period has been associated to an increasing trend of plantation of Common food crops grown in the area which include Irish potatoes, sweet-potatoes, maize, millet, Acha, tomato and many other varieties of vegetables.

The built up areas have also continued to increase with a gain of 12671 ha (27.97%) in the period 2003-2015 shown in figure 3b. Similarly the consistent decrease of vegetation areas have been also seen in this time with a loss of 11476 ha (25.33%). From figure 4.3c, the overall changes occurred for the last 24years in built up areas have shown an increase of 15177 ha gain (representing an increase of 33.50% of the total study area) with a loss of 112 ha (0.25 % of the study areas). Whereas vegetation areas have lost 26458 ha (58.38% of the study area) and gained only about 1050 ha (2.32%) of the study area.

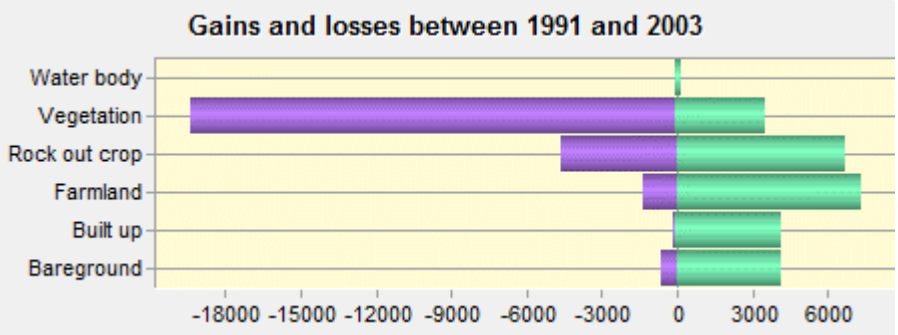

Figure 3a Gains and losses of land cover classes in (ha).1991-2003

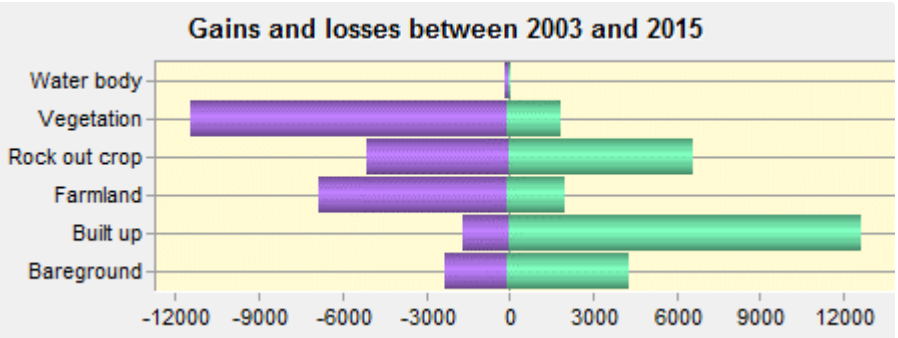

Figure 3b Gains and losses of land cover classes in (ha).2003-2015

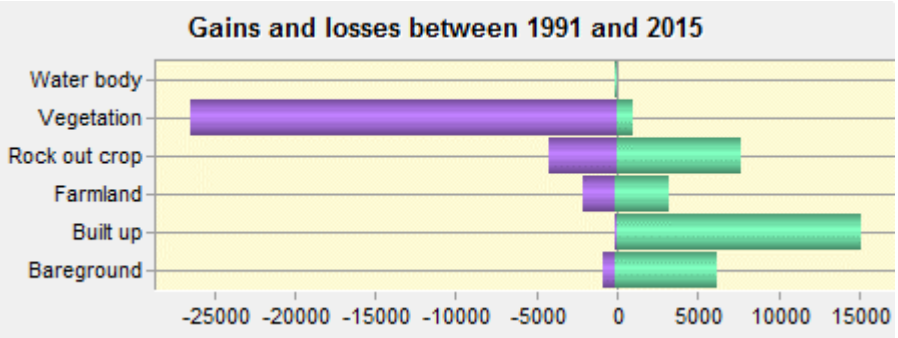

Figure 3c; Gains and losses of land cover classes in (ha) 1991-2015.

The land cover changes between the study periods were quantified by using differences from the late periods to early study periods. Table 5 shows the changes that was seen in the past three distinct study years quantified through LCM. Built-up areas showed a big change of 24.26% between 2003 -2015 rather than 1991-2003with only 8.99% which was a 13 years period. Following this, there has been a great loss of vegetation area from 15829.2ha(34.94%) in 1991-2003 to 9579.15ha (21.14%) in 2003-2015 which contributed to an increase in the changes of built up areas, bare ground as shown in table 4.5.

Table 5; Comparison of changes in land cover classes between 1991-2015 using LCM

Land cover classes	2003-1991		2015-2003		2015-1991	
	Area(Ha)	Area (%)	Area(Ha)	Area (%)	Area(Ha)	Area (%)
Bare ground	3482.91	7.69	2061.72	4.55	5544.63	12.24

Built up	4073.31	8.99	10991.97	24.26	15065.28	33.25
Farmland	6040.98	13.33	-4763.97	-10.51	1277.01	2.82
Rock out crop	2096.82	4.63	1477.8	3.26	3574.62	7.89
Vegetation	-15829.2	-34.94	-9579.15	-21.14	-25408.35	-56.08
Water body	135.18	0.30	-188.37	-0.42	-53.19	-0.12

Transition Probability Matrix

The transition probability matrix records the probability that each land cover category will change to the other category. This matrix is produced by the multiplication of each column in the transition probability matrix , the number of cells of corresponding land use in the later image.

For the 5 by 5 matrix table presented below, the rows represent the older land cover categories and the column represents the newer categories. Although this matrix can be used as a direct input for specification of the prior probabilities in maximum likelihood classification of the remotely sensed imagery, it was however used in predicting land use land cover of 2039.

Table 6; Transitional Probability table derived from the land use land cover map of 1991 and 2015

Land cover classes	Bare ground	Built up	Farmland	Rock out crop	Vegetation	Water body
Bare ground	0.2431	0.4354	0.1256	0.1319	0.0402	0.0239
Built up	0.1087	0.6722	0.0582	0.0998	0.0506	0.0105
Farmland	0.0742	0.5405	0.1786	0.1739	0.0315	0.0012
Rock out crop	0.0878	0.257	0.037	0.5178	0.0996	0.0008
Vegetation	0.1824	0.3756	0.0968	0.2411	0.1024	0.0017
Water body	0.0313	0.2577	0.0061	0.0452	0.1972	0.4625

Row categories represent land use land cover classes in 1991 whilst column categories represent 2039 classes. As seen from the table, bare ground land has a 0.2431 probability of remaining bare ground and a 0.4354 of changing to built-up in 2039. This therefore shows an undesirable change (reduction), with a probability of change which is much higher than stability. Bare ground has a 0.2431 the probability of changing to bare ground, Built up during this period will likely be class with a 0.6722 probability of increasing built up in 2039.farmland also has a 0.5405 probability as high as to decrease to built-up in 2039 which signifies stability. Rock out crop has a 0.5178 probability of remaining Rock out crop.

On the other hand, the 0.3756 probability of change from vegetation land to built-up shows that there might likely be a high level of instability in vegetation land during this period. Water body which is the last class has a 0.4625 probability of remaining as water body.

Land Use Land Cover Projection for 2039

The table 7 shows the statistic of land use land cover projection for 2039. Comparing the percentage representations of this table 7 and that of table 1, there exist similarities in the observed distribution particularly in 2015.

Table 7: Projected Land use land cover table for 2039

Land cover classes	2039

	Area(Ha)	Area (%)
Bare ground	5719.23	12.62
Built up	20972.88	46.29
Farmland	3418.74	7.55
Rock out crop	11608.11	25.62
Vegetation	3125.34	6.90
Water body	465.75	1.03
Total	45310.05	100.00

This may tend to suggest no change in the classes between 2015 and 2039, but a careful look at the area in hectares between these two tables shows a change though meager. Thus in table 7, built up (46.29%) still maintains the highest position in the class whilst water body (1.03%) retains its least position.

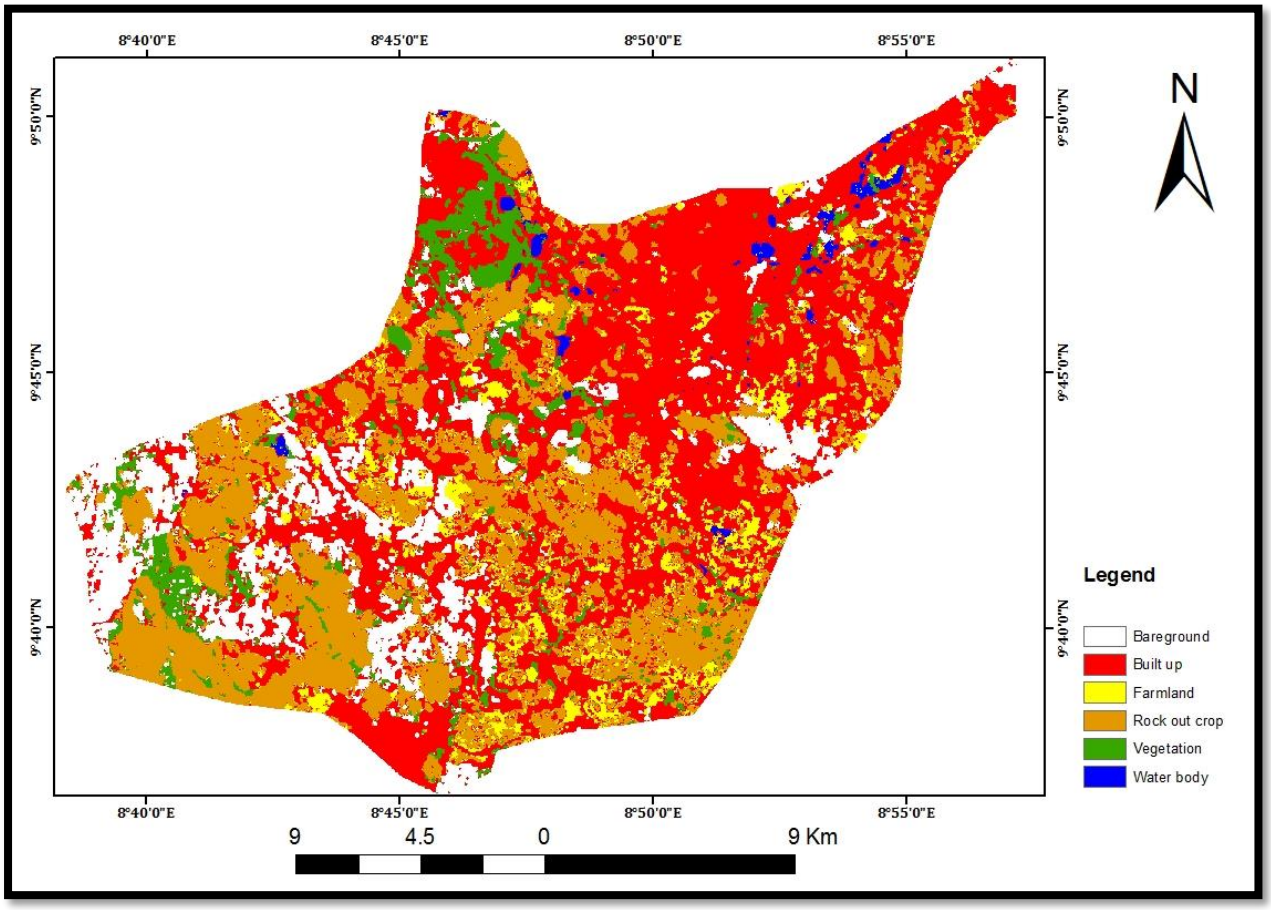

Figure 4; Projected Land Use Land Cover Map of Jos South LGA for 2039, Map Derived From the 1991 And 2015 Land Use Land Cover Map

Rock out crop (25.62%) takes up the next position, followed by bare ground (12.62%), farmland (7.55%) and finally, vegetation (6.90%). As seen in figure 4.5, there is likely to be compactness in Jos south local government area by 2039 which signifies crowdedness.

4.6 Implications of Findings

Jos south local government is experiencing a fast developmental growth where government allocated land for building at the detriment of vegetation and farmland which needs to be looked in to With the changes shown on the map, if precautionary measures were not taken land for agricultural purposes will start to have a set back and may affect the agricultural activities of the area.

Both Adzandeh, *et,al.* (2015) and (Vivan *et, al.* 2013) used remote sensing and GIS techniques in capturing spatial-temporal data to study the land use land cover of Jos metropolis and Jos south respectively. Vivan *et al* (2003) didn't carry out accuracy assessment in their work but Adzandeh, *et,al*, (2015) carried out accuracy assessment, they both came to a conclusion that Jos metropolis and Jos south has continued to experience unprecedented growth both in population size and spatial coverage due to migration, educational development, economic growth residential development and pattern of transportation routes at the detriment of farm land and vegetation which also corroborate with findings of this study.

Conclusions

The study has shown that Jos south will continued to experience unprecedented growth both in population size and spatial coverage due to rural-urban migration, educational development, residential development, economic growth and pattern of transportation routes. Similarly infrastructural facilities, which are regarded as agents of development, should be evenly distributed at various segment of the town so as to achieve a more balanced city growth. The major factors responsible for city growth apart from natural increase (population increase) are through rural-urban migration, economic growth, urbanization, transportation, tourist attraction, good weather and educational development. The study also proved geospatial techniques as a viable tool for assessing urbanization trend.

It was recommended that high resolution imageries such as IKONOS be made readily available, because urban areas have complex and heterogonous features, and this will provide better information in mapping these areas

REFERENCE

Adzandeh,E.A, Akintunde,J.A,andAkintunde,E.A. (2015). AnalysisOfUrbanGrowthAgentsInJosMetropolis,Nigeria, *InternationalJournalOf RemoteSensingAndGIS*,Volume 4, Issue2, 2015,41-50

Anderson, J.R., Hardy, E.E., Roach, J.T., and Witmer, R.E. (1976). A Land Use and Land Cover Classification System for Use with Remote Sensor Data. *Geological Survey Professional Paper* No. 964, U.S. Government Printing Office, Washington, D.C. p. 28.

Araya, Y. H and Cabral, P. (2010). Analysis and Modeling of Urban Land Cover Change in Setúbal and Sesimbra, Portugal. *Remote Sensing*, 2(6), 1549–1563

Central African Regional Program for the Environment CARPE (2003). The USAID CARPE Program, 2003-2010. In: Njomo, D. Mapping Deforestation in the Congo Basin Forest Using Multi-Temporal SPOT-VGT Imagery from 2000-2004. EARSeL Proceedings 7, 1. Available On-line at http://www.eproceedings.org/static/vol07_1/07_1_njomo1.pdf?Sessio nID=49c6647bb6b81ad3fe Accessed July 31, 2015.

Fasal, S. (2000). *"Urban Expansion and Loss of Agricultural Land-A GIS Based Study of Saharanpur City, India"*. Environ. Urban. 12:2.

Foody, G. M. (2002). Status of land cover classification accuracy assessment. *Remote Sensingof Environment*, 80(1), 185–201.

Herold, M., Couclelis, H and Clarke, K. C. (2005). The role of spatial metrics in the analysis and modeling of urban land use change. *Computers, Environment and Urban Systems*, 29(4), 369–399. doi:10.1016/j.compenvurbsys.2003.12.001.

Ifatimehin OO, Ufuah ME (2006). "An Analysis of Urban Expansion and Loss of Vegetation Cover in Lokoja, Using GIS Techniques". *Zaria Geogr*., 17(1): 28-36.

Lambin, E. F., Geist, H. J and Lepers, E. (2003). Dynamics of land-use and land-cover change in tropical regions. *Annual Review of Environment and Resources*, 28(1), 205–241.

Lu, D., Mausel, P., Brondizio, E and Moran, E. (2004). Change detection techniques. *International Journal of Remote Sensing*, 25(12), 2365–2401.

Michael, A. A., (2012) Effect of mining on farming in Jos South Local Government Area of Plateau State. Federal College of Land Resources Technology, Kuru, Plateau State. *Nigeria. Journal of Soil Science and Environmental Management. 3*(4):77-83.

Mustafa, M. (2010). *Seasonal Change in the Greenness of Soybean Leaves: Groundtruthing of NDVI*; research presented to Illinois Junior Science and Humanities Symposium at Southern Ill. Univ. at Carbondale.

Njomo D (2008). *"Mapping Deforestation in the Congo Basin Forest Using Multi-Temporal SPOT-VGT Imagery from 2000-2004". EARSeL Proceedings* 7, 1. Available On-line at http://www.eproceedings.org/static/vol07_1/07_1_njomo1.pdf?Sessio nID=49c6647bb6b81ad3fe Accessed July 31, 2016.

Radke et al., (2005). J. Radke, S. Andra, O. Al-Kofani, B. Roysan, Image change detection algorithms: a systematic survey**,** IEEE Trans. *Image Process.* 14 (3) (2005), pp. 291–307

Sarma P.K, Lahkar B.P, Ghosh, S, Rabha A, Das J.P, Nath N.K, Dey S, Brahma N (2008). "Land Use and Land Cover Change and Future Implication Analysis in Manas National Park, India Using Multi-Temporal Satellite Data". *Curr. Sci.*, 95(2)2: 23-227.

Shalaby, A and Tateishi, R. (2007).Remote sensing and GIS for mapping and monitoring land-cover and land-use changes in the Northwestern coastal zone of Egypt.*Appl. Geogr*., 27 (2007), pp. 28–41

Sankhala, S and Singh, B (2014).Evaluation of urban sprawl and land use land cover change using remote sensing and GIS techniques: a case study of Jaipur City, India.*Int. J. Emerging Technol. Adv. Eng.*, 4 (1) (2014), pp. 66–72

Vivan Ezra Lekwot, Julius Andrew Baji, Okafor Christian I. And Ali Andesikuteb Yakubu, (2013), An Appraisal Of Urban Land Use And Land Cover Changes In Jos South Local Government Area Of Plateau State, Nigeria Using *Remote Sensing And Gis*. Department of Environmental Management, Faculty of Environmental Sciences**,** Kaduna State University, Nigeria. Un-Habitat Juba, South-Sudan, *Ph.D. Candidate***,**Department Of Geography and Planning, University Of Jos, Nigeria.

IMPACT OF URBANIZATION ON AGRICULTURAL LANDS IN LAFIA LOCAL GOVERNMENT AREA, NASARAWA STATE

Dantijani, N[1], Hassan, A.B[1], Muhammed, M[1,] Emigilati, M.A[1] and Kuta, G.I[1]

[1]Department of Geography Federal University of Technology, Minna, Niger State, Nigeria

e-mail :aisha.hassan@futminna.edu.ng

ABSTRACT

Lafia is one of the fastest growing city in Nigeria, yet it lacks reliable, modern, scientific monitoring techniques to effectively monitor and manage land use/cover changes brought about by urbanization. This research looks at the impact of urbanization on agricultural lands in Lafia local government area, Nasarawa state. The capabilities of satellite remote sensing in terms of large spatial coverage, spatial and temporal resolutions adequate for these types of studies, as well as the ability of GIS to handle spatial and non-spatial data, make it the optimal approach for this research. To achieve this, Landsat Thematic Mapper (1986), Landsat ETM+ (1999) and Landsat 8(2016) were used to provide maps for land use/cover change and analysis. A post classification approach was adopted with a maximum likelihood classifier algorithm. The analysis revealed that, Agricultural land has decreased by 8.5% while Built-up has increased by 39%, population increase and executive lowliness are the driving factors of land use change and farmland has 0.6% of converting to built-up in the next 10 years. Agricultural lands and vegetal cover are most threatened, and most land allocated for these uses has been legally or illegally converted to other land uses. The continual increase of the aerial coverage of built up area needs to be checked by promulgating a law of unlawful expansion to achieve sustainable urban and environmental development and planning in the study area.

Keywords: Urbanisation, GIS, Remote sensing

1. **Introduction**:

Agriculture is the main source of livelihood for many developing countries. In Nigeria, the sector contribute about 55% of gainful employment and almost 40% of the share of GDP. Before the discovery of oil, this figure is as high as 75 – 80% of GDP (Yusuf, 2014). The modernization of Agriculture in any economy is dependent on the amount of fertile land allocated to it. Urbanization in recent times tends to deprive agriculture of its needed land.

World population is currently growing at a rate of 1.2% annually, which is a net addition of 77 million people every year, six countries accounts for half of the increase: India 21%, china 12%, Pakistan 5%, Bangladesh, Nigeria and the united states of America 4% each (UN, 2011). Global proportion of urban population has been rising rapidly over the last decade. The average increase in global urban population between 1950 and 2005 was 2.6%, while Africa's average increase urban growth was 3.6% for the same period. At the regional level,

West African average growth was 4.3% and Nigeria 4.4% (Adepoju, 2007) . World population projected to reach 9.7 billion by 2050 with most growth on developing regions especially Africa (UN, 2015).

Africa is urbanizing fast. Its rate of urbanization soared from 15% in 1960 to 40% in 2010, and is projected to reach 60% in 2050 (UN habitat, 2010). Urban population in Africa are expected to triple in the next 50 years, changing the profile of the region and challenging policy makers to harness urbanization for sustainable and inclusive growth. According to UN (2004), Africa is the least urbanized but most rapidly urbanizing and it is expected to experience rapid rate of urbanization during 2000 – 2030. By 2030, 53% of its inhabitants will live in urban areas, Africa and Asia will each have higher numbers of urban dwellers than any other major area of the world (UN, 2004).

Since the end of World War II, West Africa has been distinguished by extremely high urban growth due to a high population growth rate (Africapolis, 2000). Spurred by the oil boom prosperity of the 1970s and the massive improvements in roads and the availability of vehicles, Nigeria since independence has become an increasingly urbanized and urban oriented society (Olorunfemi, 2014). Nigeria is a vast agricultural country "endowed with substantial natural resources" which include: 68 million hectares of arable land; fresh water resources covering about 12 million hectares, 960 kilometers of coastline and an ecological diversity which enables the country to produce a wide variety of crops and livestock, forestry and fisheries products (Arokoyo, 2012). Agriculture is the dominant occupation of the inhabitants of Nasarawa state. Some of the major agricultural products in the state include maize, sorghum, millet, rice, groundnut cowpea, soya beans, melon, yam, cassava, sweet potatoes, Mango, cashew, oil palm, cattle, sheep, goats, poultry, and fisheries. Nasarawa state (the home of solid minerals) is blessed with numerous solid minerals such as Beryl, tourmaline, quartz, columbite, granite, limestone, Barytes, glass sand, marble and salt (Salau, and Attah, 2012) . Lafia being a state capital has experienced rapid expansion since 1996 when it was designated state capital owing to the influx of formal and service workers as well as business entrepreneurs. Growth and developmental activities such as buildings, road construction, deforestation, and many other anthropogenic activities. For the reasons of its size and status as state capital as well as the location near the federal capital territory (FCT), Lafia is now the first order town in the state.

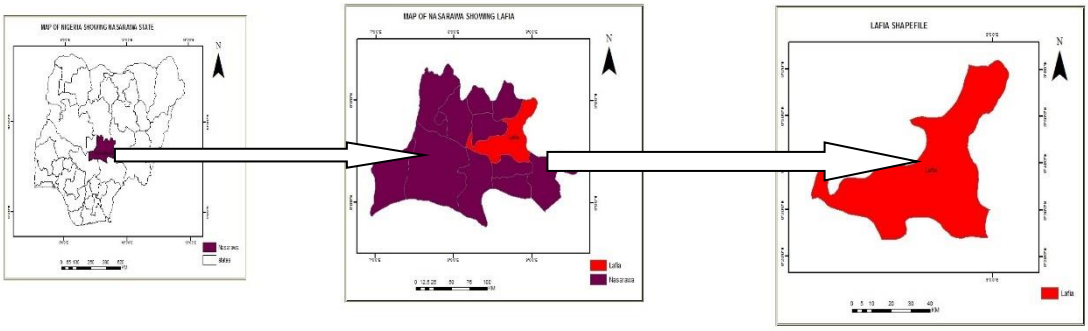

Figure 1, Map of the Study Area

2. **Literature Review:**

Adepoju, 2007 integrated Landsat imageries, Maps and Census data to analyze Land use Land cover change detection in Metropolitan Lagos, Nigeria. The study revealed that rapid population growth in the study area has been, and continues to be, the main driving force for the rapid land cover change. He also used Landsat TM, Landsat ETM and SPOT HRV2 for the study. Ejaro and Abdullahi, (2013) worked on the spatiotemporal analysis of Land use Land cover changes in Suleja Local government area, Niger state, Nigeria. They utilized ILWIS 3.3 Software and Satellite imageries such as NigSat-1, Landsat-TM and Landsat ETM+ to analyze the rate of change and Factors responsible for this changes. Anthropogenic activities have been identified to cause the changes in land use/land cover and these are driven by synergetic factors of rapid growth of population and urbanization.

Nuhu and Ahmed, (2013), merged information obtained from field work and Google earth images digitized with ArcGIS 9.3 version which was used as the base map for the study. The land use types and their characteristics were identified based on their physiographic characteristics which satisfied the research; Agricultural land use in sub-Saharan Lafia of Nassarawa State, Nigeria. The methodology developed by Adepoju, (2007) was adopted for this research.

3. **Methodology**

3.1 *Data and Data Source*

S/N	DATA	YEAR	PATH/ROW	SCALE	SOURCE
1	Landsat 5 (TM)	1986	188/54	30m™	USGS
2	Landsat 7 (ETM+)	1999	188/54	30m™	USGS
3	Landsat 8 (OLIS)	2016	188/54	30m™	USGS
4	Administrative and Local govt. Map of Nigeria	2016		1:500000	NASRDA

Landsat images of Nasarawa state for the years 1986, 1999 and 2016 were imported and pre-processed in ERDAS imagine 2014 for sub-setting of the image on the basis of Area of Interest (AOI) using Lafia shape file.

The data was unzipped and imported into ERDAS Imagine software 2014, which converted the data to imagine (.img) image format. The importation was on band by band basis. Bands 1 - 5 and 7 were then layer stacked for both Landsat TM 1986, ETM+ and OLIS. Bands 6 (TM), band 6 (ETM+) and 8 (ETM) were excluded in both images because in Thermal Infrared (TIR) and 15 meters spatial resolution this was considered not as useful for this research as band 8 (ETM). The resolution merge spatial enhancement technique was used for the improvement of Landsat ETM (28.5 meter) image. The main importance of this technique is that it retains the thematic information of the multiband raster image. Using Erdas imagine 2014 software, spatial enhancement from the image interpreter menu was used, where convolution (filtering on images) and kernel selection was carried out.

Both inverse and reverse options of the image inversion function to enhance images was used. Inverse emphasizes details in the dark portions of an image, while reverse simply reverses the DN vales. All satellite data were studied by assigning per-pixel signatures and differentiating the land use/land cover into six classes on the bases of the specific Digital Number (DN) value of different landscape elements. The objective of image classification in this research is to create cluster classes from multispectral images to make sense of

spectral information contained in the images. The area coverage of different classes of multitemporal images was compared for changes that have taken place between dates of the images.

Supervised classification with maximum likelihood classifier was used because it gives a better result than any other algorithms such as neural network, contextual, minimum distance etc.

Supervised image classification was carried out. The delineated classes are built-up, bare-ground, rock, farmland, vegetation and water body. For each of the predetermined land cover landuse type, training samples were selected by delimiting polygons around representative sites. Spectral signatures for the respective land cover types derived from the satellite imagery were recorded by using the pixels enclosed by these polygons.

The digital format of the imagery was imported into the GIS environment which serves as a valuable platform for data capturing, storage, manipulation, analysis and display of partially referenced data.

Change detection

Change detection is the process of identifying differences in the state of an object or phenomenon by observing it at different times (Lu et al., 2003). This research is focused on the changes between class (conversion between land cover types) and within-class (changes within a land cover type). Post classification change detection approach was employed due to its ability to bypass the problems and difficulties associated with analysis of images acquired at different times of the year and sensors. In this research, land cover change is detected as a change in land cover label between two image dates. It is based on two independent true land cover class classifications, and was achieved by supervised classification. Erdas imagine software 2014 and Idrisi software were used for this analysis.

The survey, part of the qualitative research, served as broad and quantifiable background data in which the case studies were conceptualized. Interviews and questionnaires were considered the best means of unraveling the silent issues behind the factors of land cover land use change in the study area. The reconnaissance survey conducted in August 2016 revealed that there were several other factors that are responsible and encouraging land cover/use change besides population growth.

A number of 130 questionnaires were administered, 3 was missing and 17 returned, giving a total of 150 questionnaires for this research. The data and information gotten was collated and analyzed using SPSS analysis.

The visual analysis of the satellite images used in this research provided insight into the landscape structure of the study area. This helped with understanding the spatial distribution and arrangement of different land use/ landcover types as shown by textural difference throughout the study area. Though visual analysis does not reveal quantitative or statistical data facts, it provided a good knowledge of the general pattern of land use and land cover distribution in Lafia. This played a crucial role in understanding the direction of growth and salient issues that have led to land use/cover conversion and differential rates.

Markovian chain analysis was used to describe land use change from one period to another and this was used as the basis for projecting future changes. This was achieved by developing a transition probability matrix of land use change from time one to time two, which showed the nature of change while still serving as the basis for projecting to a later time period using Idrisi software .The transition probability may be accurate on a per category basis, but there is no knowledge of the spatial distribution of occurrences within each land use category. Hence, Cellular Automata (CA) was used to add spatial character to the model. CA Markov used the output from the Markov Chain Analysis particularly Transition Area file to apply a contiguity filter to "grow out" land use from time two to a later time period. In essence, the CA develop a spatially explicit weighting more heavily areas that proximate to existing land uses. This ensured that land use change occurs proximate to existing like land use classes, and not wholly random.

4. Results and Analysis

- ✓ **Production of Landuse/Landcover maps of the study area**

  The land use land cover maps of Lafia town, Nasarawa state is generated after running a maximum likelihood supervised classification as well as a post classification algorithm for the period of 30 years [1986, 1999 and 2016].

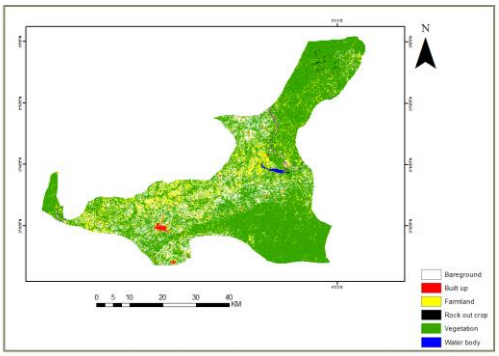

Figure 4.1: 1986 Land Use Land Cover Map of Lafia town

Source: Author's GIS Analysis 2016

Figure 4.2: 1999 Land Use Land Cover Map of Lafia town

Source: Author's GIS Analysis 2016

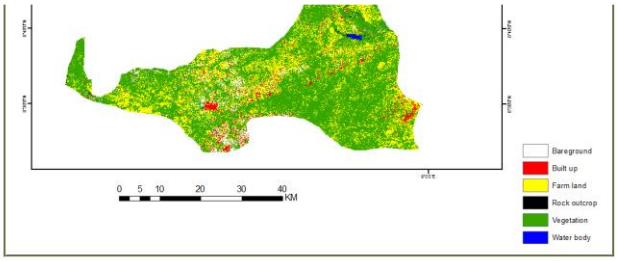

From the 1999 land use map, there is a significant increase on the Farmland and Built-up areas, this is due to migration of people from nearby areas to Lafia as a result of favorable weather condition and available land for Agriculture.

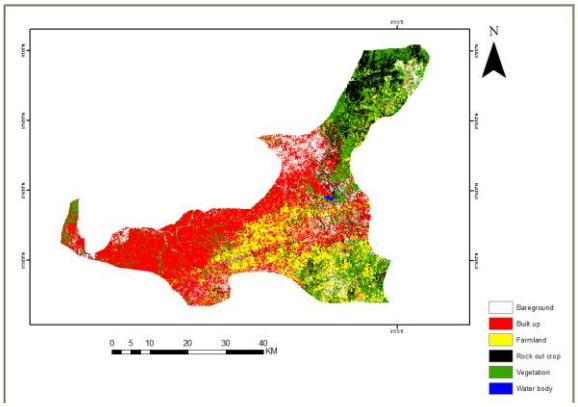

Figure 4.3: 2016 Land Use Land Cover Map of Lafia town

Source: Author's GIS Analysis 2016

Figure 4.3 above shows the landuse map of Lafia in 2016, most of the other land use type are being converted to Built-up, especially Vegetation and Farmlands. As the population of the area increase, urbanization is set to occur in such areas, and this leads to the erection of buildings. The three Landuse/Land cover maps shows distinct differences in the classes classified. The Table below gives the analysis of the above images.

Land cover Type	1986 Area [Ha]	1986 %	1999 Area [Ha]	1999 %	2016 Area [Ha]	2016 %
Bare-ground	31332.06	13.71303	8807.22	3.854635	26994.69	11.8147
Built-up	1295.82	0.567138	7590.78	3.322238	89864.1	39.3306
Farmland	30382.38	13.29738	58163.58	25.45631	38607.03	16.89705
Rock out-crop	876.78	0.383738	2634.39	1.152987	25529.13	11.17327
Vegetation	163577.3	71.5925	150836	66.01601	46861.02	20.50955
Water body	1019.52	0.446211	451.98	0.197817	627.93	0.274825
Total	228483.9	100	228483.9	100	228483.9	100

- ✓ **Rate of change of Landuse from Agriculture to Urbanization**

The post classification comparison of land use/landcover classes gives the change that took place between 1986 and 1999; 1999 and 2016; and 1986 to 2016 in hectares (Table 4.2). The land cover classes show detail of spatio-temporal changes between different land cover types.

Table 4.2: 1986 and 1999 Land Cover Change derived from Post-Classification Comparison.

Land cover Type	1986 Area [Ha]	1986 %	1999 Area [Ha]	1999 %	Change Area	% Change
Bare-ground	31332.06	13.71303	8807.22	3.854635	-22524.8	-9.85839
Built-up	1295.82	0.567138	7590.78	3.322238	+6294.96	2.7551
Farmland	30382.38	13.29738	58163.58	25.45631	+27781.2	12.15893
Rock out-crop	876.78	0.383738	2634.39	1.152987	+1757.61	0.769249
Vegetation	163577.3	71.5925	150836	66.01601	-12741.4	-5.57649
Water body	1019.52	0.446211	451.98	0.197817	-567.54	-0.24839
Total	228483.9	100	228483.9	100		

Table 4.2 above shows detail of temporal change between land cover types. The urban/built-up area has increased by 2.6%, and farmland has increased by 12.16%. Increase in Farmland is due to prevalent Agricultural activities within 1986 and 1999 which caused drastic reduction of Bare-ground. Water body reduced by 0.25%. There is an increase of 0.77% in Rock out-crop which is due to the decrease in Vegetation, as vegetation decrease, Rocks which are covered by vegetation is exposed. Below is the graphical representation of this analysis

Figure 4.4a, chart showing Land cover change between 1986 and 1999

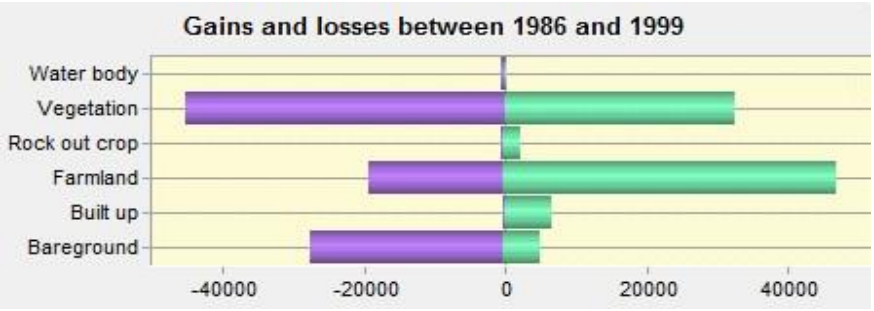

Source: Author's GIS Analysis 2016

Table 4.3: 1999 and 2016 Land Cover Change derived from Post-Classification Comparison.

Land cover Type	1999 Area [Ha]	1999 %	2016 Area [Ha]	2016 %	Change Area	% Change
Bare-ground	8807.22	3.854635	26994.69	11.8147	+18187.47	7.960066
Built-up	7590.78	3.322238	89864.1	39.3306	+82273.32	36.00837
Farmland	58163.58	25.45631	38607.03	16.89705	-19556.6	-8.55927
Rock out-crop	2634.39	1.152987	25529.13	11.17327	+22894.74	10.02029
Vegetation	150836	66.01601	46861.02	20.50955	-103975	-45.5065
Water body	451.98	0.197817	627.93	0.274825	+175.95	0.077008
Total	228483.9	100	228483.9	100		

From table 4.3 above, the urban/built-up area has drastically increased by 36%, and farmland has decreased by 8.56%. As Lafia town becomes urbanized which means increased in Built-up areas, Rock out-crop 10.02% and Bare-ground 7.96%; Farming activities is reduced, Vegetation is also reduced by 45% as it is cleared to make room for space. Water body increased by 0.1% due to sensor difference or canalization projects in the study area. Below is the graphical representation of this analysis.

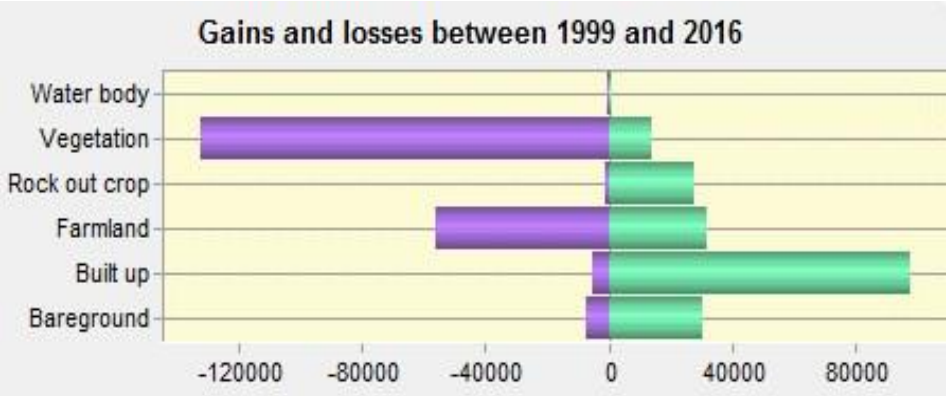

Figure 4.4b, chart showing Land cover change between 1999 and 2016

Source: Author's GIS Analysis 2016

The spatial growth or expansion in other land cover types especially built-up has directly taken place on the agricultural land and vegetation as this is the only land cover type with a decrease in area coverage for the period under study.

Table 4.4: 1986 - 2016 Land Cover Change derived from Post-Classification Comparison.

Land cover Type	[Ha]	1986 %	2016 Area [Ha]	2016 %	Change Area	% Change
Bare-ground	31332.06	13.71303	26994.69	11.8147	-4337.37	-1.89833
Built-up	1295.82	0.567138	89864.1	39.3306	+88568.28	38.76347
Farmland	30382.38	13.29738	38607.03	16.89705	+8224.65	3.599663
Rock out-crop	876.78	0.383738	25529.13	11.17327	+24652.35	10.78953
Vegetation	163577.3	71.5925	46861.02	20.50955	-116716	-51.083
Water body	1019.52	0.446211	627.93	0.274825	-391.59	-0.17139
Total	228483.9	100	228483.9	100		

Through the period of 30years in Lafia town, Nasarawa state, Landuse undergone a severe change where a land cover is either reduced or increased. This change is calculated in percentage and area (hectares) within each land use class as represented in the Table above.

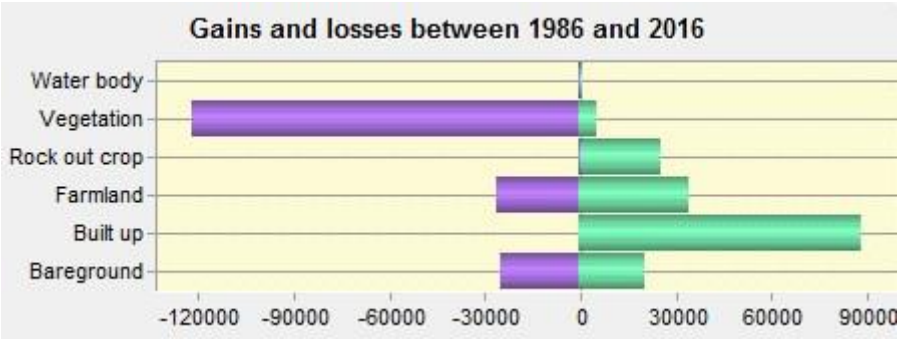

Figure 4.4c, chart showing Land cover change within 1986 - 2016

Source: Author's GIS Analysis 2016

Below are figures showing changes specifically on Built-up and Farmland areas.

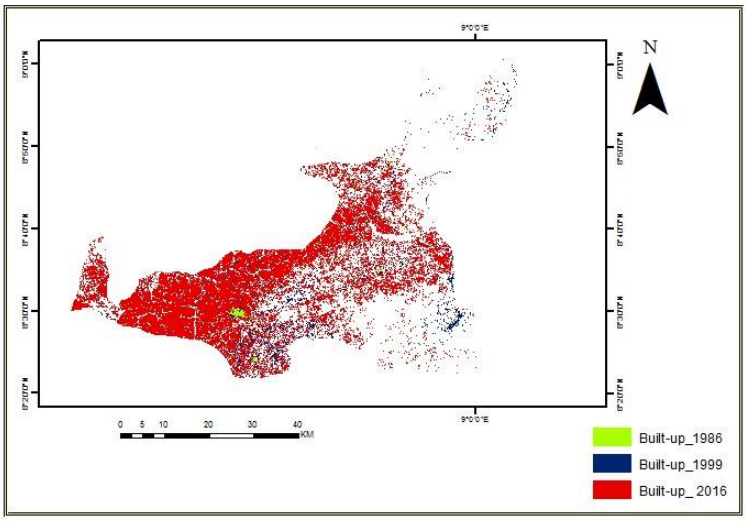

Figure 4.5, changes in Built-up from 1986 - 2016

Source: Author's GIS Analysis 2016

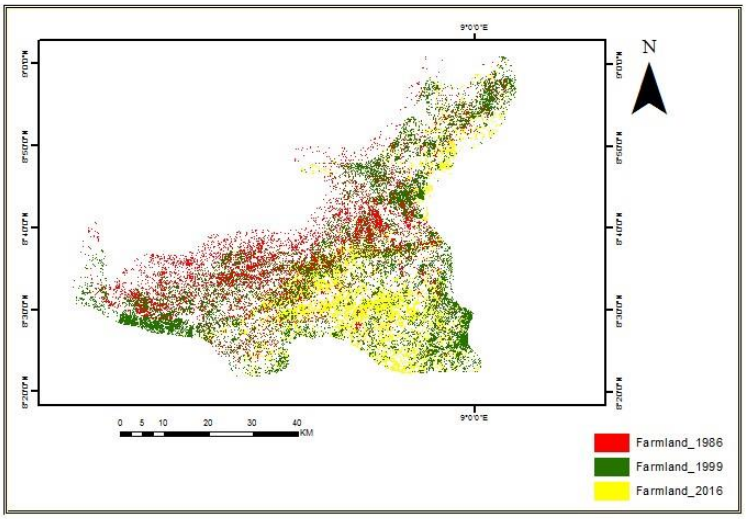

Figure 4.6, changes in Farmland from 1986 - 2016

Source: Author's GIS Analysis 2016

In 1968 Built-up accounted for 1% of the study area, 3% in 1999, while in 2016 Built-up areas accounted for 39%. The rate of Built-up growth, which is faster than any other land use/cover types, does not do justice to the Farmland land use conversion in the study area as this is primarily a result of the dominant growth in Built-up at the outskirts of the Town. The change

in Agricultural land use area is clearly visibly from Figures 4.6. Most of the growth associated with Agricultural land use is due to transformation between land use classes.

- ✓ Future pattern of land use land cover in 10years (2026).

The transition probability matrix is used to record the probability that each land cover category will change to other category. This matrix is produced by the multiplication of each column in the transition probability matrix by the number of cells of corresponding land use in the later image.

For the 6 by 6 matrix table presented below, the rows represent the older land cover categories and the column represents the newer categories. Although this matrix can be used as a direct input for specification of the prior probabilities in maximum likelihood classification of the remotely sensed imagery, it was however used in predicting land use land cover of 2026.

Table 4.5: Transitional Probability table derived from the land use land cover map of 1986 to 2016

Landuse classes	2026					
	Bare ground	Built up	Farm land	Rock out crop	Vegetation	Water body
Bare ground	0.283	0.5256	0.1287	0	0.0628	0
Built up	0.0506	0.7261	0.1607	0.0039	0.0293	0.0295
Farm land	0.1412	0.5547	0.1386	0.0285	0.137	0
Rock out crop	0	0	0.2217	0.5289	0.2462	0.0031
Vegetation	0.1344	0.1066	0.2505	0.1828	0.3258	0
Water body	0.0286	0	0.1574	0	0.2632	0.5509

Source: Author's GIS Analysis 2016

From table 4.5 above, Row categories represent land use land cover classes in 2016 whilst column categories represent 2026 classes. Bare ground has a 0.5256 probability of becoming Built-up and a 0.283 of remaining Bare-ground in 2026. This therefore shows an undesirable change (reduction), with

a probability of change which is much higher than stability. Built up during this period will likely be class with a 0.7261 probability of increasing built up in 2026; Farmland also has a 0.5547 probability of becoming Built-up; Rock out crop has a 0.5289 probability of remaining Rock out crop, this signifies stability so as Vegetation and Water body with a probability of 0.3258 and 0.5509 respectively. From the transitional probability matrix, the Landuse classes for 2026 can be deduced.

Table 4.6: Projected Land use land cover for 2026

Land use classes	2026	
	Area(Ha)	Area (%)
Bare ground	23950.89	10.48227
Built up	105846.3	46.32436
Farmland	40757.13	17.83764
Rock out crop	23525.91	10.29628
Vegetation	31335.12	13.71403
Water body	3074.13	1.345414
Total	228489.5	99.99999

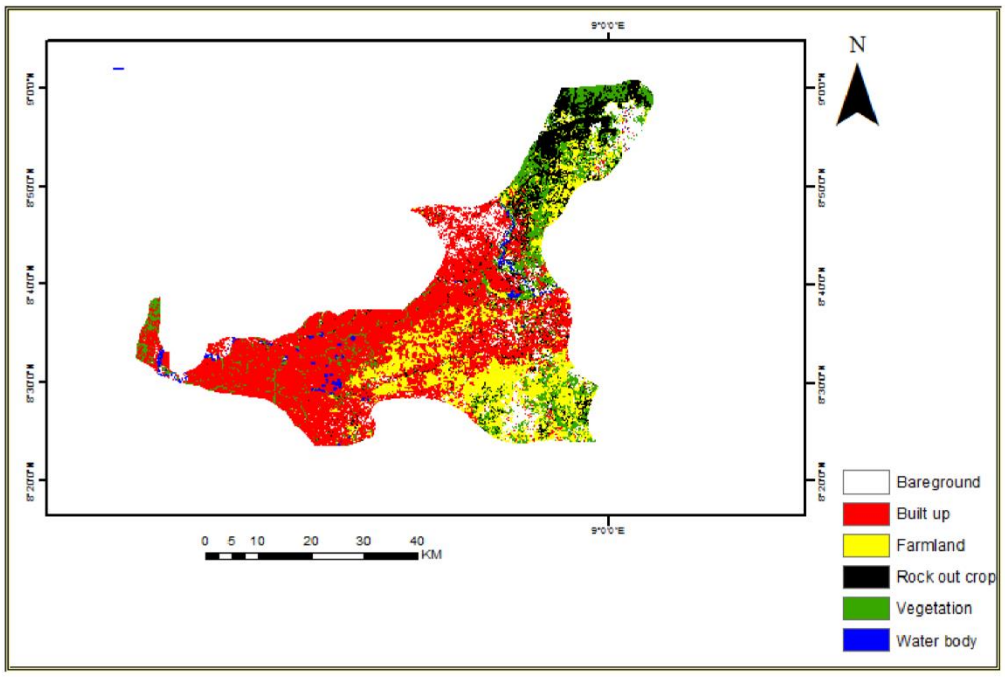

Figure 4.8; Projected Land Use Land Cover Map of Lafia for 2026, Map Derived From the 1986, 1999 And 2016 Use Land Cover Map

Source: Author's GIS Analysis 2016

- ✓ **Factors responsible for change in Landuse**

Several factors are responsible for the fast growth of Lafia town which are summarized in this section as represented in the chart below.

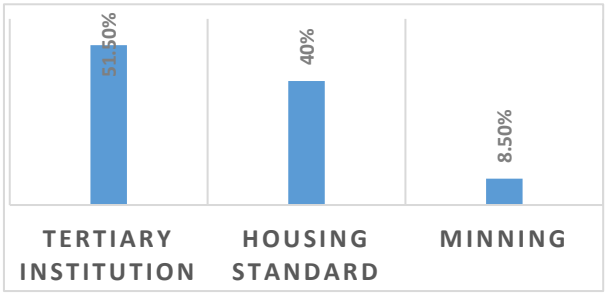

Figure 4.7 Drivers of urbanization in Lafia

In the first instance population dynamics manifested in urban population growth and rural to urban migration are by far the most significant driving forces of urban expansion of Lafia, Nasarawa state, through natural increase due to high fertility rate and decline in mortality.

The state has a federal polytechnic in Nasarawa local government area of the state, college of education in Akwanga, college of Agriculture in Lafia, Nasarawa state polytechnic in Lafia, Nasarawa state university in Keffi, a newly established federal university of Lafia in Lafia town,

and other vocational training schools. This account for high population in the area thereby driving urbanization at a high rate.

since the establishment of the FCT, Abuja in 1976 and the movement of the federal government offices and parastatals in 1991 as well as the demolition of informal settlements in 2006, mass movements of people into the suburbs has been unparalleled. As a result, settlements in Nasarawa have experienced unprecedented urbanization, increase in demand for land and rapid development of infrastructural facilities, social services and housing, changes in land tenure, increase in real property development and value, economic, social and political activities which are each contributing significantly to rapid urbanization of the area.

Additionally, there is demand for larger suburban lands and the desire of individuals for more living space. This explains why developers have preferred Nasarawa where large parcels of land is available at relatively cheaper rates than the Federal Capital city where land acquisition is restricted, costly and development control is more stringent. It also further explains why majority of the low and medium income groups whose houses were demolished from the FCT Abuja relocated to Nasarawa where about 40% of both the federal government and private sector workers reside and only transit to the capital city to work.

Nasarawa state is home to the Farin Ruwa falls in Wamba local government area of the state. Farin Ruwa falls is reputed to be one of the highest falls in Africa. This influence Tourism in the state. There is also the salt village in Keana local government area of the state. It produces naturally iodized salt from the lake located near it. The town is also the cradle of Alago civilization.

5. **Conclusion**

This study has shown clearly the extent to which the use of Remote Sensing technique can be helpful in providing bio- physical information necessary for assessing and monitoring the environmental impact of development projects. Urban growth analysis of Lafia town, Nasarawa state has been mapped out in this

research and it has shown a rapid growth and decrease in the classes that was developed, Since the results obtained showed a rapid growth of built- up area this can cause shortage in food production, pollution, congestion, traffic, urbanization, and high rate of crime in the study area.

References

Aberra E., King R., (2005); Additional Knowledge of livelihoods in the Kumasi Peri-urban interface, Ashanti region, Ghana development planning unit, University College London.

Addison, K. K. (2000). City farms. http;//journey.to.Forever.org. Retrieved 23/6/2010

Agbamu, J. U. (2006). Essentials of Agricultural Communication in Nigeria. Malthouse Press Limited, Lagos.

Adepoju M.O, Halilu S.A, Ozigis S.M, Mohammed S.O. Idris I, Adeluyi S.A, Eta J., Mapping and Monitoring Of Slum Development in Abuja, Nigeria with Satellite Remote Sensing and Geographical Information System, National Space Research and Development Agency, Abuja, Nigeria.

Adepoju, M. O. (2007). Land use and land cover change detection with remote sensing and GIS at metropolitan Lagos , Nigeria (1984 - 2002) by Matthew Olumide Adepoju MSc . (Nottingham).

Africapolis. (2000). AFRICAPOLIS : Urbanization Trends in West Africa 1950-2020, 1–12.

Cohen, B. (2004). Urban growth in developing countries: A review of current trends and a caution regarding existing forecasts. *World Development*, *32*(1), 23–51. http://doi.org/10.1016/j.worlddev.2003.04.008

Ejaro, S. P., & Abdullahi, U. (2013). Spatiotemporal Analyses of Land Use and Land Cover Changes in Suleja Local Government Area, Niger State, Nigeria. *Journal of Environment and Earth Science*, *3*(9), 72–84.

FAO (Food and Agriculture Organisation of the United Nations), 1996. World Food Summit. Plan of Action, Rome. FAO

FAO, (2004), Globalisation of Food Systems in Developing Countries: Impact on Food Security and Nutrition. FAO Food and Nutrition Paper. 83, Rome, FAO

FAO, (2008).Urbanization and food security in sub-saharan Africa. Paper prepared for regional conference for Africa, Nairobi, Kenya; June 16-20-2008

Lipton, N. (1977). Why poor people stay poor: Urbanization in World Development. London, Temple SmithMabogunje, A.L. (2007). Global urban poverty research: The Africa case, Urban update, no 10, Washington DC, Wilson International centre for scholars.

Montgomery, M.R., Stren, R., Cohen, B., & Reed, H. (eds) (2003). Cities transformed: Demographic change and its implications in the Developing World. Washington DC. The National Academy press.

Naab, F. Z., Dinye, R. D., & Kasanga, R. K. (2013). *Urbanisation and its impact on agricultural lands in growing cities in developing countries: a case study of Tamale in Ghana*. *Modern Social Science Journal*, *2*(2), 256–287. Retrieved from http://scik.org/index.php/mssj/article/view/993

Namara, H. (2011). The impacts of urbanization on the agricultural land use : a case study of kawempe division , By Harriet Namara Supervisor.

Nation, U. (2015). World population projections. *Uma ética Para Quantos?*, *XXXIII*(2)

87. http://doi.org/10.1007/s13398-014-0173-7.2

National Bureau of Statistics. (2010). National bureau of statistics annual abstract of statistics , Federal Republic of Nigeria, 698.

Nuhu, Z., & Ahmed, M. (2013). Agricultural landuse in sub-urban lafia of Nasarawa state , Nigeria, *4*(4), 607–617.

Ojo, S. S. (2015). Urbanization and urban growth : challenges and prospects for national development, *1*(4), 1–8.

Olorunfemi, S. (2014). Determinants of urbanization in Nigeria : implication for sustainable development, *4*(4), 50–57.

Salau, E.S. and Attah, A. J. (2012). A Socio-Economic Analysis of Urban Agriculture In Nasarawa State, Nigeria ., *8*(1), 17–29.

United Nations Centre for Human Settlements (UNCHS) (1996). An Urbanizing World. Global Report on Human Settlements. Oxford, Oxford University Press.

UN. (2002). World Urbanization Prospects. The 2003 Revision Data Tables and Highlights. *World Urbanization Prospects: The 2003 Revision*, (March), 1–195. Retrieved from papers2://publication/uuid/F44D048C-4507-42E9-87CE-A360409DE2B7

United Nation Population Fund (UNFPA) (2007). The state of World Population 2007: Unleashing the potential of urban growth. NewYork, United Nations Population Fund.

UN-Habitat (2007). Meeting Development Goals in small urban centres: water and sanitation in World Cities, London, UN-Habitat and Earthscan.

UN. (2011). World population prospects: the 2002 revision. *Un*, *III*, 164. Retrieved from http://books.google.com/books?hl=en&lr=&id=YQNVJ7RkKrYC&oi=fnd&pg=PP5&dq=World+Population+Prospects+The+2010+Revision&ots=AoYMX54Zdi&sig=9YDTWdMjtf6EefrQWqRPy4CyT60

Various. (2001). The Components of Urban Growth in Developing Countries, 1 – 64.

World Bank, (2000). World Development Report 1999/2000. Entering the 21st Century. New York, World Bank.

Yusuf, S. A. (2014). Role of Agriculture in Economic Growth & Development: Nigeria Perspective, (39922), 0–29. Retrieved from http://mpra.ub.uni-muenchen.de/55536/

MODELING AND ANALYTICAL SIMULATION OF OIL SHALE ARRHENIUS COMBUSTION

Oyedeji Saheed[1*].; Olayiwola, R. O[1].

Department of Mathematics,

Federal University of Technology, Minna, Nigeria.

Saflex24@gmail.com

Abstract

A mathematical model of the oil shale Arrhenius Combustion process is described by a pair of nonlinear partial differential equation. The paper presents an analytical solution to describe this phenomenon. The nonlinear coupled governing equation are decoupled using parameter expanding method and solved analytically using Eigenfunction Expansion technique. The results obtained revealed that the Frank-kameneskii number and heat transfer coefficient have significant effect on temperature and concentration of fuel.
Keywords: Oil Shale, Combustion, Arrhenius Equation, Eigenfunction Expansion Technique

Introduction

Oil shale is commonly defined as a fine-grained sedimentary rock containing organic matter that yields substantial amounts of oil and combustible gas upon destructive distillation. Most of the organic matter is insoluble in ordinary organic solvents therefore, it must be decomposed by heating to release such materials.Oil shales are distributed throughout the world, although the richest and most abundant identified deposits are contained in the Green River Formation of Utah, Wyoming and Colorado

Oil shale also contains a material rich in mineral matter: both marine and terrestrial oil shales have been found. The oil shale industry started in Scotland in 1694, oil was produced by heating Shropshire oil shale.The direct combustion of oil shale to produce hot water, steam, and, finally, electricity has developed in accordance with the general trends in solid fuel combustion technology. At the beginning of the 19th century, industrialized countries became more interested in obtaining oil and gas from coal pyrolysis (the decomposition or transformation of the kerogen organic matter into hydrocarbons by heat).

Oil shale pyrolysis was developed in France, where in 1832, a method for producing lighting oil was realized. However, the plants were later closed because of the rapid development of the crude oil industry. Data from 1860 indicate that oil shale from the Volga basin in Russia was industrially mined and used as fuel. During the 19th century oil shale thermal processing factories also operated in Australia, the United States, Brazil, Germany, and Scotland. During the 20th century oil shale processing factories were built in several countries, including China and Israel. However, later most of them were closed. In Estonia and Germany oil shale has been used also in cement production both as a fuel and as a constituent of the clinkers.

Today, considerable quantities of oil shale are mined in Estonia, Russia, China, Brazil, Australia, and Germany. Estonia's oil shale industry is currently the most developed in the world.

Oil shale can be used for several purposes: to obtain heat by direct combustion (for example, in the generation of electricity); to produce shale oil (SO); and as a source of other valuable chemicals. Underlying most definitions of oil shale is its potential for the economic recovery of energy, including shale oil and combustible gas, as well as a number of byproducts. A deposit of oil shale having economic potential is generally one that is at or near enough to the surface to be developed by open-pit or conventional underground mining or by in-situ methods

Retorting of oil shale can be performed in different environments. Pyrolysis is a process of heating oil shale in an inert environment. Primary products of pyrolysis are liquid, gas and coke. The extent of decomposition (yield) and the quality of pyrolysis products depend on the composition of the source material, the temperature-time history, pressure, residence time and presence of other reactants such as water, methane etc. Because of the chemical composition of the oil produced, moderate to significant upgrading (nitrogen removal and/or hydrogen addition) may be required to convert the oil into a refinery feedstock.

Literature Review

In situ combustion (ISC) is an established method for recovery of crude oil from heavy oil reservoirs. The method relies on the heat, generated from combustion of a small fraction of the in-place oil to reduce the viscosity, and improve the fluidity of the crude oil. The foot print of carbon dioxide from the ISC reaction is as such insignificant, and can be reduced to zero by recycling the flue gas back to the reservoir (Liu et al., 2011).

Olayiwola and Ayeni (2007, 2009) presented a mathematical model of in-situ combustion using high activation energy asymptotics. The effect of Frank-Kamenetskii parameter and flame velocity on the temperature and concentration field was discussed. The numerical solution was provided using large activation energy asymptotics and shooting method

R.Davies (1990) who tracked an in-situ combustion front using thin flame technique. Schecter and Marchesin (2003) who constructed a two-phase model for oxidation, involving air or oxygen and oil that include heat loss to the rock formation. Souza et al. (2006) who studied the Riemann problem with forward combustion due to injection of air into a porous medium containing solid fuel.

Methodology

We assume linear heat flow in a homogeneous system that we consider to be represented by a one dimensional, infinitely long, constant pressure system in which the temperatures of the shale, oil, and gas are the same at any given spatial point, x, and temporal point, t. All physical parameters are assumed to be temperature invariant; the parameters are assigned values that are appropriate for the ranges of temperature involved.

Temperature Distribution Equation

Conservation of energy accounting for conduction, convection, head generation and heat loss, gives the following partial differential equation for the distribution of temperature with respect to space and time (Berry and Parrish 1960)

$$\left(\phi_g \rho_g c_{pg} + \phi_s \rho_s c_{ps}\right)\frac{\partial T}{\partial t} + \dot{m}_g\, c_g \frac{\partial T}{\partial x} = k\frac{\partial^2 T}{\partial x^2} + g(T) - L(T) \qquad (3.1)$$

Where,

x = Distance, feet

T = Temperature

t = Time

k = Gross thermal conductivity

m_g = Mass gas flux

c_g = Heat capacity of gas

ρ_g = Density of gas

c_{ps} = Heat capacity of solid

Φ_g= Gas space porosity

g(T) = Heat generation function

L(T) = Heat loss function

Oxygen Concentration Equation

Conservation of mass, accounting for convection and reaction gives the following differential equation for the oxygen concentration with respect to space and time

$$\phi_g \rho_g \frac{\partial c_{ox}}{\partial t} + \dot{m}_g \frac{\partial c_{ox}}{\partial x} = -\frac{\phi_g}{N_o} G(T) \tag{3.2}$$

Fuel Concentration

The fuel concentration equation is thus needed to provide a complexity of the problem. Thomas(1963) simplifies his model by considering only a single element of time Δt, chosen sufficiently small so that it may supposed that

$$\rho_f \frac{\partial c_f}{\partial t} = G(T) \tag{3.3}$$

Where,

$$L(T) = hp(T - T_e) \tag{3.4}$$

$$G(T) = AC_{ox} e^{-E/RT} \tag{3.5}$$

$$g(T) = \phi_g \Delta H G(T) \tag{3.6}$$

A= Reaction rate coefficient

C_f= Concentration of fuel

E=Activation energy
R= Gas constant

T= Temperature

T_e= External temperature

ΔH= Heat generation constant

p= Perimeter shape factor

c_{ox}= Fraction of original oxygen remaining unreacted

t_{out}= Time at which the combustion front leaves the reactor

Substituting equation (3.4) – (3.6) into (3.1) – (3.3), we obtain

$$\phi_g \rho_g c_{pg} + \phi_s \rho_s c_{ps} \frac{\partial T}{\partial t} + \dot{m}_g c_g \frac{\partial T}{\partial x} = K \frac{\partial^2 T}{\partial x^2} - hp(T - T_e) + \phi_g \Delta \mathrm{H} A c_{ox} e^{-E/RT} \tag{3.7}$$

$$\phi_g \rho_g \frac{\partial c_{ox}}{\partial t} + \dot{m}_g \frac{\partial c_{ox}}{\partial x} = -\frac{\phi_g}{N_o} A c_{ox} e^{-E/RT} \tag{3.8}$$

$$\rho_f \frac{\partial c_f}{\partial t} = A c_{ox} e^{-E/RT} \tag{3.9}$$

Together with initial and boundary conditions

$$\left.\begin{aligned} &T(x,0)=T_o, \quad T(0,t)=T_o \quad \frac{\partial T}{\partial x}|_{x=L}=0 \quad 0\le x\le L \\ &c_{ox}(x,0)=c_o\frac{x}{L}(1-\frac{x}{L}), \quad c_{ox}(0,t)=c_o, \quad c_f(x,0)=c_{fo} \end{aligned}\right\} \tag{3.10}$$

Method of Solution

Non-dimensionalization

We non-dimensionalized equation (3.7) - (3.10)

Let $\phi_g\rho_g c_{pg}+\phi_s\rho_s c_{ps}=\phi_g\rho c_p$ in (3.7) and non-dimensionalized using the following dimensionless variable

$$x'=\frac{x}{L}, \quad t'=\frac{t}{t_{out}}, \quad \in=\frac{RT_o}{E}, \quad \theta=\frac{E}{RT_o^2}(T-T_o), \quad \phi=\frac{c_{ox}}{c_o}, \quad \psi=\frac{c_f}{c_{fo}}$$

And we obtain

$$\frac{\partial\theta}{\partial t}+\alpha\frac{\partial\theta}{\partial x}=\lambda\frac{\partial^2\theta}{\partial x^2}-\beta\theta-\sigma+\delta\phi.e^{\frac{\theta}{1+\in\theta}} \tag{3.44}$$

$$\frac{\partial\phi}{\partial t}+\alpha_1\frac{\partial\phi}{\partial x}=-\beta_1\phi.e^{\frac{\theta}{1+\in\theta}} \tag{3.45}$$

$$\frac{\partial\varphi}{\partial t}=\beta_2\phi e^{\frac{\theta}{1+\in\theta}} \tag{3.46}$$

$$\left.\begin{aligned} &\theta(x,0)=0, \quad \theta(0,t)=0 \quad \frac{\partial\theta(1,t)}{\partial x}=0 \\ &\phi(x,0)=x(1-x), \quad \phi(0,t)=1 \\ &\varphi(x,0)=1 \end{aligned}\right\} \tag{3.47}$$

Where

$\alpha=\dot{m}_g c_g\frac{t_{out}}{L\phi_g\rho c_p}$ $\quad MassGas\,flux$

$\lambda=k\frac{t_{out}}{L^2\phi_g\rho c_p}$ Scaled thermal conductivity

$\beta=\frac{hpt_{out}}{\phi_g\rho C_p}$ Heat transfer coefficient

$$\sigma = \frac{hpt_{out}(T_o - T_e)}{\phi_g \rho c_p \in T_o}$$ Heat transfer coefficient

$$\delta = \frac{t_{out}}{\rho c_p \in T_o} \Delta H A c_o . e^{-E/RT_o}$$ Frank-Kameneskii parameter

Here, we solve equations (3.44) – (3.47) using parameter-expanding method (where details can be found in He, 2006) and eigenfunctions expansion method (where details can be found in Myint-U and Debnanth, 1987).

Let $0 < \alpha << 1$ $and\, \alpha_1 = a\alpha,\ \delta = b\alpha,\quad \beta_1 = d\alpha$

Such that

$$\left.\begin{aligned} \theta(x,t) &= \theta_o(x,t) + \alpha\theta_1(x,t) + h.o.t \\ \phi(x,t) &= \phi_o(x,t) + \alpha\phi_1(x,t) + h.o.t \\ \varphi(x,t) &= \varphi_o(x,t) + \alpha\varphi_1(x,t) + h.o.t \end{aligned}\right\} \tag{3.48}$$

Substituting (3.48) into (3.44) – (3.47), we have

$$\frac{\partial}{\partial t}(\theta_o + \alpha\theta_1 + ...) + \alpha\frac{\partial}{\partial x}(\theta_o + \alpha\theta_1 + ...) = \lambda\frac{\partial^2}{\partial x^2}(\theta_o + \alpha\theta_1 + ...) - \beta(\theta_o + \alpha\theta_1 + ...) + b\alpha(\theta_o + \alpha\theta_1 + ...)\left[1 + (e-2)(\theta_o + \alpha\theta_1 + ...)\right] - \sigma \tag{3.49}$$

Collecting the like powers of α,

For

$\alpha^{\,o}$:

$$\frac{\partial\theta_o}{\partial t} = \lambda\frac{\partial^2\theta}{\partial x^2} - \beta\theta_o - \sigma \tag{3.50}$$

$$\theta_o(x,0) = 0, \quad \theta_o(0,t) = 0 \quad \frac{\partial\theta_o}{\partial x}|_{x=1} = 0 \tag{3.51}$$

$\alpha^{\,1}$:

$$\frac{\partial\theta_1}{\partial t} + \frac{\partial\theta_o}{\partial x} = \lambda\frac{\partial^2\theta_1}{\partial x^2} - \beta\theta + b\phi_o\left[1 + (e-2)\theta_o\right] \tag{3.52}$$

$$\theta_1(x,0) = 0, \quad \theta_1(0,t) = 0 \quad \frac{\partial\theta_1}{\partial x}|_{x=1} = 0 \tag{3.53}$$

$$\frac{\partial}{\partial t}(\phi_o + \alpha\phi_1 + ...) + a\alpha\frac{\partial}{\partial x}(\phi_o + \alpha\phi_1 + ...) = -d\alpha(\phi_o + \alpha\phi_1 + ...)\left[1 + (e-2)(\theta_o + \alpha\theta_1 + ...)\right]$$

(3.54)

Collecting the like powers of α,

For

α^{o}:

$$\frac{\partial \phi_o}{\partial t} = 0 \tag{3.55}$$

$$\phi_o(x,0) = x(1-x), \quad \phi_o(0,t) = 1 \quad \frac{\partial \phi_o}{\partial x}|_{x=1} = 0 \tag{3.56}$$

α^{1}:

$$\frac{\partial \phi_1}{\partial t} + a\frac{\partial \phi_o}{\partial x} = -d\phi_o\left[1 + (e-2)\theta_o\right] \tag{3.57}$$

$$\phi_1(x,0) = 0, \quad \phi_1(0,t) = 1 \quad \frac{\partial \phi_1}{\partial x}|_{x=1} = 0 \tag{3.58}$$

$$\frac{\partial}{\partial t}(\varphi_o + \alpha\varphi_1 + ...) = \beta_2(\phi_o + \alpha\phi_1 + ...)\left[1 + (e-2)(\theta_o + \alpha\theta_1 + ...)\right] \tag{3.59}$$

Collecting the like powers of α,

For

α^{o}:

$$\frac{\partial \varphi_o}{\partial t} = \beta_2\phi_o\left[1 + (e-2)\theta_o\right] \tag{3.60}$$

$$\varphi_o(x,0) = 0, \quad \varphi_o(0,t) = 0 \quad \frac{\partial \varphi_o}{\partial x}|_{x=1} = 0 \tag{3.61}$$

α^{1}:

$$\frac{\partial \varphi_1}{\partial t} = \beta_2\phi_1\left[1 + (e-2)\theta_o\right] + \beta_2\phi_o(e-2)\theta_1 \tag{3.62}$$

$$\varphi_1(x,0) = 0, \quad \varphi_1(0,t) = 0 \quad \frac{\partial \varphi_1}{\partial x}|_{x=1} = 0 \tag{3.63}$$

Then , we have the following system of equations

$$\frac{\partial \theta_o}{\partial t} = \lambda \frac{\partial^2 \theta}{\partial x^2} - \beta \theta_o - \sigma \tag{3.64}$$

$$\theta_o(x,0) = 0, \quad \theta_o(0,t) = 0 \quad \frac{\partial \theta_o}{\partial x}|_{x=1} = 0 \tag{3.65}$$

$$\frac{\partial \theta_1}{\partial t} + \frac{\partial \theta_o}{\partial x} = \lambda \frac{\partial^2 \theta_1}{\partial x^2} - \beta \theta_1 + b\phi_o[1 + (e-2)\theta_o] \tag{3.66}$$

$$\theta_1(x,0) = 0, \quad \theta_1(0,t) = 0 \quad \frac{\partial \theta_1}{\partial x}|_{x=1} = 0 \tag{3.67}$$

$$\frac{\partial \phi_o}{\partial t} = 0 \tag{3.68}$$

$$\phi_o(x,0) = x(1-x), \quad \phi_o(0,t) = 0 \quad \frac{\partial \phi_o}{\partial x}|_{x=1} = 0 \tag{3.69}$$

$$\frac{\partial \phi_1}{\partial t} + a\frac{\partial \phi_o}{\partial x} = -d\phi_o[1 + (e-2)\theta_o] \tag{3.70}$$

$$\phi_1(x,0) = 0, \quad \phi_1(0,t) = 0 \quad \frac{\partial \phi_1}{\partial x}|_{x=1} = 0 \tag{3.71}$$

$$\frac{\partial \varphi_o}{\partial t} = \beta_2 \phi_o[1 + (e-2)\theta_o] \tag{3.72}$$

$$\varphi_o(x,0) = 1, \quad \varphi_o(0,t) = 0 \quad \frac{\partial \varphi_o}{\partial x}|_{x=1} = 0 \tag{3.73}$$

$$\frac{\partial \varphi_1}{\partial t} = \beta_2 \phi_1[1 + (e-2)\theta_o] + \beta_2 \phi_o (e-2)\theta_1 \tag{3.74}$$

$$\varphi_1(x,0) = 1, \quad \varphi_1(0,t) = 0 \quad \frac{\partial \varphi_1}{\partial x}|_{x=1} = 0$$

Using eigenfunctions expansion method and direct integration, we obtain the solution of equations (3.64) - (3.74) as

$$\theta_o(x,t) = \sum_{n=1}^{\infty} \frac{A_1}{B}\left(1 - e^{Bt}\right)\sin\left(\frac{2n-1}{2}\right)\pi x \tag{3.75}$$

$$\phi_o(x,t) = x(1-x) \tag{3.76}$$

$$\phi_1(x,t) = d\left(x-x^2\right)\left[t+(e-2)\left(\sum_{n=1}^{\infty}\frac{A_1}{B}\left(t-\frac{e^{Bt}}{B}\right)\sin\left(\frac{2n-1}{2}\right)\pi x\right)\right] - a(1-2x)t - d\left(x-x^2\right)(e-2)\left(\sum_{n=1}^{\infty}\frac{A_1}{B^2}\sin\left(\frac{2n-1}{2}\right)\pi x\right)$$

(3.77)

$$\varphi_o(x,t) = \beta_2\left(x-x^2\right)\left[t+(e-2)\left(\sum_{n=1}^{\infty}\frac{A_1}{B}\left(t-\frac{e^{Bt}}{B}\right)\sin\left(\frac{2n-1}{2}\right)\pi x\right)\right] + 1 + \beta_2\left(x-x^2\right)\left[(e-2)\left(\sum_{n=1}^{\infty}\frac{A_1}{B^2}\sin\left(\frac{2n-1}{2}\right)\pi x\right)\right]$$

(3.78)

$$\Rightarrow \theta_1(x,t) = \sum_{n=1}^{\infty}\left[\frac{A_2}{B}\left(e^{Bt}-1\right) + A_1\sum_{n=1}^{\infty}\frac{A_3}{B}\left(\frac{e^{Bt}-1-e^{Bt}Bt}{B}\right) + \sum_{n=1}^{\infty}\frac{A_1}{B}\left(\frac{e^{Bt}-1-e^{Bt}Bt}{B}\right)\right]\sin\left(\frac{2n-1}{2}\right)\pi x$$

(3.79)

$$\varphi_1(x,t) = \beta_2\left(\begin{array}{c} d\left(x-x^2\right)\left[\frac{t^2}{2}+(e-2)\left(\sum_{n=1}^{\infty}\frac{A_1}{B}\left(\frac{t^2}{2}-\frac{e^{Bt}}{B^2}\right)\sin\left(\frac{2n-1}{2}\right)\pi x\right)\right] - a(1-2x)\frac{t^2}{2} \\ -d\left(x-x^2\right)(e-2)\left(\sum_{n=1}^{\infty}\frac{A_1}{B^2}\sin\left(\frac{2n-1}{2}\right)\pi x t\right)\left(t+(e-2)\sum_{n=1}^{\infty}\frac{A_1}{B}\left(t-\frac{e^{Bt}}{B}\right)\sin\left(\frac{2n-1}{2}\right)\pi x\right)\end{array}\right)$$

$$+\beta_2(x-x^2)(e-2)\left(\sum_{n=1}^{\infty}\left[\frac{A_2}{B}\left(\frac{e^{Bt}}{B}-t\right)+A_1\sum_{n=1}^{\infty}\frac{A_3}{B^2}\left(e^{Bt}\left(\frac{2}{B}-t\right)-t\right)+\sum_{n=1}^{\infty}\frac{A_1}{B^2}\left(e^{Bt}\left(\frac{2}{B}-t\right)-t\right)\right]\sin\left(\frac{2n-1}{2}\right)\pi x\right)$$

$$-\beta_2\left(d\left(x-x^2\right)\left[(e-2)\left(\sum_{n=1}^{\infty}\frac{A_1}{B^3}\sin\left(\frac{2n-1}{2}\right)\pi x\right)\right]\left((e-2)\sum_{n=1}^{\infty}\frac{A_1}{B^2}\sin\left(\frac{2n-1}{2}\right)\pi x\right)\right)$$

$$-\beta_2(x-x^2)(e-2)\left(\sum_{n=1}^{\infty}\left[\frac{A_2}{B}\left(\frac{1}{B}\right)+A_1\sum_{n=1}^{\infty}\frac{A_3}{B^2}\left(\frac{2}{B}\right)+\sum_{n=1}^{\infty}\frac{A_1}{B^2}\left(\frac{2}{B}\right)\right]\sin\left(\frac{2n-1}{2}\right)\pi x\right)$$

(3.80)

where

$$B = -\beta-\lambda\left(\frac{(2n-1)\pi}{2}\right)^2, \quad A_1 = \frac{4\sigma}{(2n-1)\pi}$$

$$A_2 = \frac{8b\left(4-\pi(-1)^n+2\pi n(-1)^n\right)}{\pi^3(2n-1)^3}, \quad A_3 = b(e-2)\frac{8\pi^3n^3-12\pi^3n^2+6\pi^3n-\pi^3}{6\pi^3(2n-1)^3}$$

The computations were done using computer symbolic algebraic package MAPLE

RESULTS AND DISCUSSION

The system of partial differential equations describing the Oil Shale Arrhenius Combustion are solved analytically. We decouple the equations using parameter-expanding method and solve the resulting equations using eigenfunctions expansion technique and direct integration method.

Analytical solutions of equation (3.75) – (3.80) are computed for the following values

$\delta = 0.4, \quad \lambda = 0.3, \quad \alpha = 0.002, \quad \sigma = 0.01,$

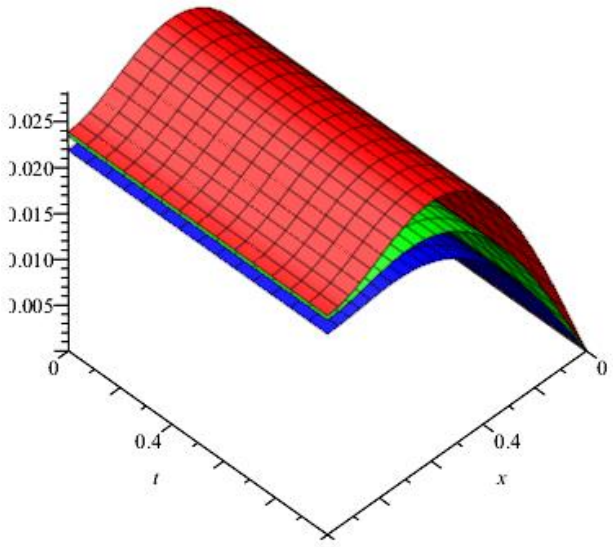

Fig.1: *Variation of with temperature* $\theta(x,t)$ *with Scaled thermal Conductivity*

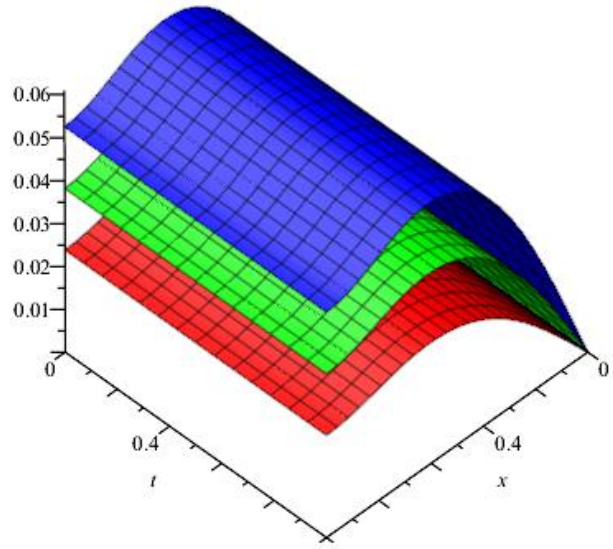

Fig.2: *Variation of temperature* $\theta(x,t)$ *with Frank-Kamenetskii number* δ

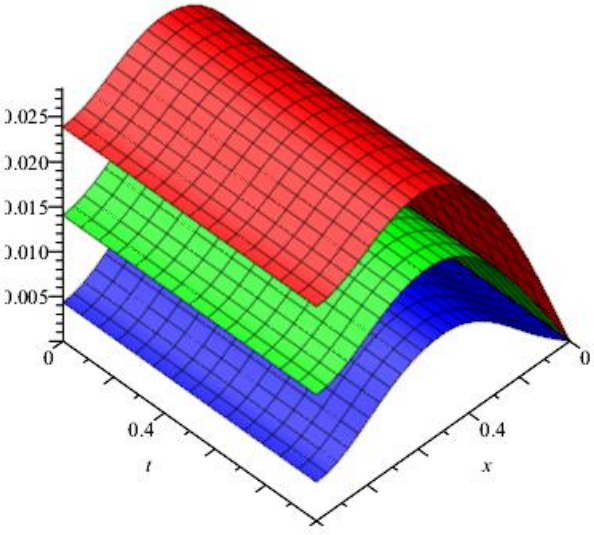

Fig.3: *Variation of temperature* $\theta(x,t)$ *with Heat transfer coefficient* σ,

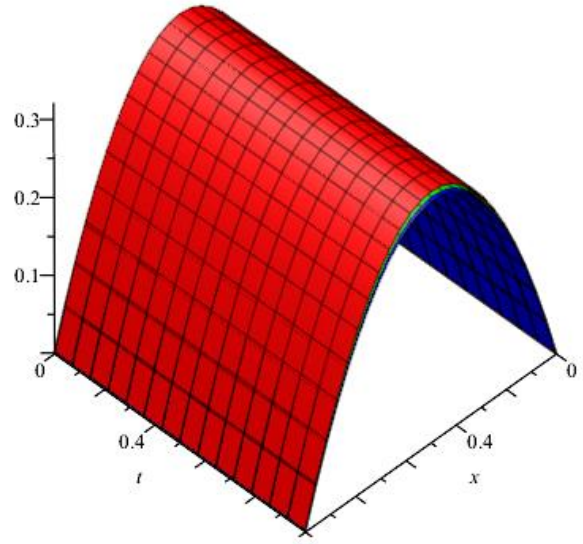

Fig.4: *Variation of Fraction of original oxygen remaining unreacted* $\phi(x,t)$ *with Heat transfer coefficient* σ,

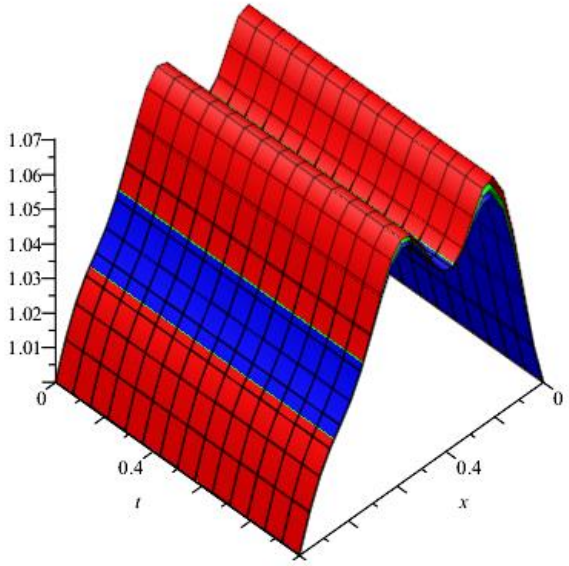

Fig.5: *Variation of concentration of fuel* $\varphi(x,t)$ *with Heat transfer coefficient* σ.

Fig. 1 shows the effect of scaled thermal conductivity (λ) on the reactive layer temperature profile. It is observed that the reactive layer temperature increases significantly with time and decreases with distance.

Fig. 2: Shows the effect of Frank-Kamenetskii number (δ) on the inert layer temperature profile. It is observed that the inert layer temperature increases significantly with time and distance. Clearly, the Frank-Kamenetskii number enhances the inert layer temperature. This is as a result of exchange of heat between the layers.

Fig.3: Displays the effect of Heat Transfer Coefficient on the inert layer temperature profile. It is observed that the reactive layer temperature increases significantly with time and decreases with distance.

Fig.4: shows the effect of Heat Transfer Coefficient on the Fraction of original oxygen remaining unreacted. It is observed that the Fraction of original oxygen remaining unreacted increases with time and decreases with distance.

Fig.5: presents the effect of heat transfer coefficient on concentration of fuel. It is observed that the maximum concentration of fuel decrease with distance and increases with time Clearly, the heat transfer coefficient decreases the concentration of fuel.

Conclusion

We have formulated and solved analytically a mathematical model of Oil shale Arrhenius combustion to determine the concentration of fuel and temperature distributions. In particular, we have proved by actual solution method that the model formulated has a unique solution for all $t \geq 0$ .We decoupled the equations using parameter expanding method and solved the resulting equations using eigenfunctions expansion technique. Finally, we have provided the graphical summaries of the system responses.

Reference

Abbasbandy, S., 2007. Application of He's homotopy perturbation method to functional integral equations. Chaos Solitons Fractals, 31: 1243-1247.

A.J. Souza ; D. Marchesin; I.Y. Akkutlu,Wave Sequences for Solid Fuel Adiabatic In-Situ Combustion in Porous Media., Comp. Appl. Math. 1 (54) 27-54, 2006

Ayeni, R.O., 1982. *On the explosion of chain thermal reaction*. J. Aust. Math. Soc. Series,24: 194-2023.

Burnham and Braun 2005. Comprehensive utilization strategy of Huandian oil shale // Oil Shale. 2005.Vol. 22, No. 3. P. 305–316.

Babolian, E. and J. Biazar, 2002. On the order of convergence of a domian method. Applied Math.Compute., 130: 383-387.

Biazar, J.,2008. He's homotopy perturbation method for solving helmholtz equation.

Int. J Contemp. Math. Si.., 3: 739-7443.

Duncan, D. C. and Swanson, V. E., Organic Rich Shales of the United States and World Land Areas, Geol. Survey Circ. No. 523 (1965).

D'alembert, Jean Le Rond (1749) Essai d'une nouvelle théorie de la résistance des fluides

Derrick,N.R., Grossman,S.L,Differential Equation with applications. Addison Wesley Publishing Company,Inc.Phillipines,1976
Dainton, F.S., 1960. Chain Reaction: An introduction Wiley, New York.
Enring, H., 1990. The Encyclopedia: Am. Grolier Incorporated, 2: 377

Fausett, D. W., 1974, *Mathematical study of an oil shale retort*: Ph.D. thesis, Math.Dept., Univ. Wyoming.

Fazeli, M., S.A. Zahedi and N. Tolou, 2008. Explicit solution of nonlinear fourth order parabolic equations via homotopy perturbation method. J. Applied Sci., 8: 2619-2624.

Ghotbi, A.R., A. Avaei, A. Barari and D.D. Ganji, 2008. Assessment of He's homotopy perturbation method in burgers and coupled burgers' equations.

He, J.H. (2001): Bookkeeping parameter in perturbation methods, International Journal of NonlinearSciences & Numerical Simulation vol.2, no. 3 pp. 257-264.
He, J.H. (1999): Variational iteration method – a kind of non-linear analytical technique: some examples, Int. J. Non-Linear Mech. vol.34 pp. 699–708.
He, J.H. (2000): A coupling method of a homotopy technique and a perturbation Applications of Parameter-Expanding Method 233 technique for non-linear problems, International Journal of Non-linear Mechanics vol.35,no.1,pp. 37–43.
He, J.H. (2006): Some asymptotic methods for strongly nonlinear equations, Int. J. Modern Phys. Vol.20, pp. 1141–1199.

H.M. Liu, Variational approach to nonlinear electrochemical system, Chaos Soliton.Fract (2005) 573-576.

J. C. Da Mota,D. Dantas and D. Marchesin, Traveling waves for Combustion in porous media, Int. Ser.Num. Math. Birkhauser,(129) 177-187, 1999.
J. C. Da Mota,D. Dantas and D. Marchesin,Combustion fronts in porous media.Bowes, P.C., 1984.Self-Heating: Evaluating and Controlling the Hazard. Elsevier.

J.H. He, Variational iteration method: a kind of nonlinear analytical technique:some examples, Int. J. Nonlinear Mech. 34 (4) (1999) 699-708.

J.H. He, X.H. Wu, Construction of solitary solution and compacton-like solution by variational iteration method, Chaos Soliton. Fract. 29 (2006) 108-113.

M. El-Shahed, Application of He's homotopy perturbation method to Volterra's integrodi.erential equation,Int. J. Nonlinear Sci. Numer. Simul. 6 (2) (2005) 163-168.
Mickens, R.E. (2007): Harmonic balance and iteration calculations of periodic solutions . Sound Vib. vol.306, pp. 968–72.
Mohyud-Din, S.T.; Noor,M.A.; Noor, K.I. (2009): Parameter-expansion Techniques for Strongly Nonlinear Oscillators, International Journal of Nonlinear Sciences and Numerical Simulation,vol.10,no.5,pp. 581-583
Nayfeh, A. H. (1973): Perturbation Methods, Wiley-Interscience, New York.

Ozis T.; Yildirim A. (2007): A study of nonlinear oscillators with u1/3 force by He's variational iteration method, J Sound Vib vol.306, pp.372–376
Ozis, T.; Yildirim, A. (2007): A comparative study of He's homotopy perturbation method for determining frequency–amplitude relation of a nonlinear oscillator with discontinuities, International Journal of Nonlinear Sciences and Numerical Simulation vol.8, no.2, pp. 243248.
Ozis T.; Yildirim, A. (2007): A note on He's homotopy perturbation method for van der Pol oscillator with very strong nonlinearity. Chaos Solitons Fractals vol.34, pp.989–991
Okoya, S.S., 2001. Similarity temperature profiles for some nonlinear reaction-diffusion equations.MEch.Res. Comm., 28: 477-484.
Olaytwola R.O. and Ayeni R.O. (2007) "A note on the temperature field of an in-situ combustion," Int. J. Numerical Mathematics (IJNM), 2(2): 399 -40/.
Olayiwola R.O. and Ayeni R.O. (2009) "A note on reactant consumption of an in-sit combustion," Nig. J. Mathematics and Application (NJMA), 19:7- 14

Okoya, S.S., 2004. Reactive-diffusive equation with variable pre-exponential factor.Mech. Res Comm.31: 263-267.

P.O. Olanrewaju (2007) Departmnet of Pure and Applied Mathematics, Ladoke Akintola University of Technology, Ogbomoso, Nigeria Journal of Engineering and Applied

Sciences 2 (7): 1144-1146, 2007 © Medwell Journals, 2007

R. Davies, Tracking an In-Situ Combustion Front Using the Thin Flame Technique A paper presented in a conference on oil recovery. 631- 648